Modern Nuclear Chemistry

Second Edition

Walter D. Loveland
Oregon State University

David J. Morrissey
Michigan State University

Glenn T. Seaborg
University of California, Berkeley

WILEY

Contents

Preface to the Second Edition

In this second edition of *Modern Nuclear Chemistry*, we have added new chapters on nuclear medicine, particle physics, and nuclear forensics. We have edited and updated all the chapters in the first edition reflecting the substantial progress that has been made in the past 12 years. We have dropped the chapter on radiotracer methods. We have tried to remove all the typographical errors in the first edition, without, we hope, introducing new errors. We continue to be grateful to the many colleagues and students who have taught us about a wide range of nuclear chemistry. In addition to our colleagues acknowledged in the first edition of this book, we gratefully acknowledge the helpful comments of J. Cerny and L.G. Sobotka on various portions of the book.

Walter D. Loveland
Corvallis, OR
March, 2016

David J. Morrissey
East Lansing, MI
March, 2016

Preface to the First Edition

There are many fine textbooks of nuclear physics and chemistry in print at this time. So the question can be raised as to why we would write another textbook, especially one focusing on the smaller discipline of nuclear chemistry. When we began this project over five years ago, we felt that we were a unique juncture in nuclear chemistry and technology and that, immodestly, we had a unique perspective to offer to students.

Much of the mainstream of nuclear chemistry is now deeply tied to nuclear physics, in a cooperative endeavor called "nuclear science." At the same time, there is a large, growing, and vital community of people who use the applications of nuclear chemistry to tackle wide-ranging set of problems in the physical, biological, and environmental sciences, medicine, engineering, and so on. We thought it was important to bring together, in a single volume, a rigorous, detailed perspective on both the "pure" and "applied" aspects of nuclear chemistry. As such, one might find more detail about any particular subject than one might like. We hope this encourages instructors to summarize the textbook material and present it in a manner most suitable to a particular audience. The amount of material contained in this book is too much for a one quarter or one semester course and a bit too little for a yearlong course. Instructors can pick and choose which material seems most suitable for their course.

We have attempted to present nuclear chemistry and the associated applications at a level suitable for an advanced undergraduate or beginning graduate student. We have assumed that a student has prior or concurrent instruction in physical chemistry or modern physics and has some skills in handling differential equations. We have attempted to sprinkle solved problems throughout the text, as we believe that one learns by working problems. The end-of-the-chapter homework problems are largely examination questions used at Oregon State University. They should be considered to be integral part of the textbook as they are intended to illustrate or amplify the main points of each chapter. We have taken some pains to use quantum mechanics in a schematic way, that is, to use the conclusions of such considerations without using or demanding a rigorous, complete approach. The use of hand-waving quantum mechanics, we

believe, is appropriate for our general audience. We summarize, in the appendices, some salient features of quantum mechanics that may be useful for those students with limited backgrounds.

Our aim is to convey the essence of the ideas and the blend of theory and experiment that characterizes nuclear and radiochemistry. We have included some more advanced material for those who would like a deeper immersion in the subject. Our hope is that the reader can use this book for an introductory treatment of the subject of interest and can use the end-of-chapter bibliography as a guide to more advanced and detailed presentations. We also hope the practicing scientist might see this volume as a quick refresher course for the rudiments of relatively unfamiliar aspects of nuclear and radiochemistry and as an information booth for directions for more detailed inquiries.

It is with the deep sense of loss and sadness that the junior authors (WDL, DJM) note the passing of our dear friend, colleague, and coauthor, Prof. Glenn T. Seaborg, before the completion of this work. Glenn participated in planning and development of the textbook, wrote some of the text, and reviewed much of the rest. We deeply miss his guidance and his perspective as we have brought this project to conclusion. We regret not paying closer attention to his urging that we work harder and faster as he would remark to us, "You know I'm not going to live forever." We hope that the thoughts and ideas that he taught us are reflected in these pages.

Walter D. Loveland
Corvallis, OR
October, 2004

David J. Morrissey
East Lansing, MI
October, 2004

1

Introductory Concepts

1.1 Introduction

Nuclear chemistry consists of a four-pronged endeavor made up of (a) studies of the chemical and physical properties of the heaviest elements where detection of radioactive decay is an essential part of the work, (b) studies of nuclear properties such as structure, reactions, and radioactive decay by people trained as chemists, (c) studies of macroscopic phenomena (such as geochronology or astrophysics) where nuclear processes are intimately involved, and (d) application of measurement techniques based on nuclear phenomena (such as activation analysis or radiotracers) to study scientific problems in a variety of fields. The principal activity or "mainstream" of nuclear chemistry involves those activities listed under (b).

As a branch of chemistry, the activities of nuclear chemists frequently span several traditional areas of chemistry such as organic, analytical, inorganic, and physical chemistry. Nuclear chemistry has ties to all branches of chemistry. For example, nuclear chemists are frequently involved with the synthesis and preparation of radiolabeled molecules for use in research or medicine. Nuclear analytical techniques are an important part of the arsenal of the modern analytical chemist. The study of the actinide and transactinide elements has involved the joint efforts of nuclear and inorganic chemists in extending knowledge of the periodic table. Certainly the physical concepts and reasoning at the heart of modern nuclear chemistry are familiar to physical chemists. In this book we will touch on many of these interdisciplinary topics and attempt to bring in familiar chemical concepts.

A frequently asked question is "what are the differences between *nuclear physics* and *nuclear chemistry*?" Clearly, the two endeavors overlap to a large extent, and in recognition of this overlap, they are collectively referred to by the catchall phrase "nuclear science." But we believe that there are fundamental, important distinctions between these two fields. Besides the continuing close ties to traditional chemistry cited previously, nuclear chemists tend to study nuclear problems in different ways than nuclear physicists. Much of nuclear

physics is focused on detailed studies of the fundamental interactions operating between subatomic particles and the basic symmetries governing their behavior. Nuclear chemists, by contrast, have tended to focus on studies of more complex phenomena where "statistical behavior" is important. Nuclear chemists are more likely to be involved in applications of nuclear phenomena than nuclear physicists, although there is clearly a considerable overlap in their efforts. Some problems, such as the study of the nuclear fuel cycle in reactors or the migration of nuclides in the environment, are so inherently chemical that they involve chemists almost exclusively.

One term that is frequently associated with nuclear chemistry is *radiochemistry*. The term radiochemistry refers to the chemical manipulation of radioactivity and associated phenomena. All radiochemists are, by definition, nuclear chemists, but not all nuclear chemists are radiochemists. Many nuclear chemists use purely nonchemical and therefore physical techniques to study nuclear phenomena, and thus, their work is not radiochemistry.

1.2 The Excitement and Relevance of Nuclear Chemistry

What do nuclear chemists do? Why do they do it? Who are the nuclear chemists? What is exciting and relevant about nuclear chemistry? The answers to these questions and many more similar questions are what we will discuss in this book.

Nuclear chemists ask questions about the sizes of things like nuclei and their constituents. But because nuclear reactions are what makes the stars shine, the laboratory for many nuclear chemists is the universe with attention focusing on supernova and neutron stars (the largest known "nuclei"). The size scale for the nuclear chemistry laboratory ranges from zeptometers (10^{-21} m) to zettameters (10^{21} m). Nuclear chemists are always trying to make/discover new things about the natural world. From using radioactivity to measure the temperature of the planet Earth to tracing the flow of groundwater or the circulation patterns of the oceans, nuclear chemists explore the natural world. What makes the stars shine or how do they shine? A nuclear chemist, Ray Davis, won the 2002 Nobel Prize in Physics for his pioneering work on the neutrinos emitted by the sun (see Chapter 12).

Speaking of Nobel Prizes, the junior authors (WDL, DJM) would be remiss not to mention that our coauthor (GTS) won the 1951 Nobel Prize in Chemistry for his discoveries in the chemistry of the transuranium elements. In total, nuclear chemists and physicists have discovered 26 new elements, expanding the fundamental building blocks of nature by about 30%. The expansion of the nuclear landscape from the 3000 known nuclei to the 7000 possibly bound

nuclei remains an agenda item for nuclear science. Understanding why only about 228 of these nuclei are stable is also important.

Understanding the sizes and shapes of nuclei remains an important item. Shapes such as spherical, oblate, prolate, and hexadecapole are all observed; sometimes there are coexisting shapes even in the decay products of a single nucleus, such as ^{190}Po, which decays to spherical, oblate and prolate-shaped products. Some nuclei like ^{11}Li appear to have spatially extended structures due to weak binding that make them huge.

The applications of nuclear chemistry to the world around us enrich our lives in countless ways. One of these ways is the application of nuclear chemistry to the diagnosis and treatment of disease (nuclear medicine). Over 400 million nuclear medicine procedures are performed each year for the diagnosis of disease. The most widely used (over 10 million procedures/year) radionuclide is ^{99}Tc^m, which was discovered by one of us (GTS). Positron emission tomography (PET) is used in over 1.5 million procedures/year in the United States. In PET, compounds of short-lived β^+ emitters, like ^{18}F, are injected into a patient, concentrating in particular organs. When the positron emitters decay, the β^+ particles contact ordinary electrons, annihilating to produce two 0.511 MeV photons moving in opposite directions. When enough of these photon pairs are detected, one can form an image of the location of the decay. Studies of these images can be used to understand the location of tumors, brain functions, and so on. Targeted radiopharmaceuticals can be used to deliver a radiation dose to a specific location in the body.

Nuclear chemistry plays a role in our national security. In the United States, 300 portal monitors detect the possible entry of clandestine nuclear material. Several of these monitors employ advanced technologies to combat sophisticated schemes to shield the clandestine material. In the event of a nuclear radioactivity release, such as what occurred at the Fukushima reactor complex in Japan, simple ray spectroscopy of exposed air filters has proven to be useful.

Nuclear power remains an important source of electricity for several countries. Nuclear chemists play key roles in waste remediation from nuclear power plants and providing solutions for nuclear fuel cycle issues. As chemists, they are also able to contribute to studies of material damage in reactor components.

There is a significant demand for people trained as nuclear chemists and radiochemists. In the United States, the demand for trained nuclear chemists at the PhD level exceeds the supply by a factor of 10 and has done so for decades.

1.3 The Atom

Before beginning a discussion of nuclei and their properties, we need to understand the environment in which most nuclei exist, that is, in the center of atoms. In elementary chemistry, we learn that the atom is the smallest unit a chemical
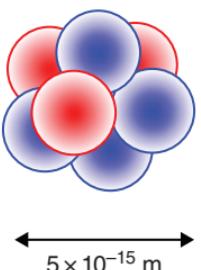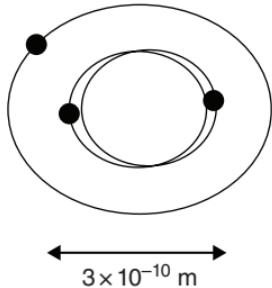
Figure 1.1 Schematic representation of the relative sizes of a lithium atom and its nucleus. The nucleus is too small to be represented in the image of the atom even with the smallest printable dot. (*See insert for color representation of the figure.*)

3×10^{-10} m

5×10^{-15} m

element can be divided into that retains its chemical properties. As we know from our study of chemistry, the radii of atoms are ~ 1 to 5×10^{-10} m, that is, 1–5 Å. At the center of each atom, we find the *nucleus*, a small object ($r \approx 1$ to 10×10^{-15} m) that contains almost all the mass of the atom (Fig. 1.1). The atomic nucleus contains Z protons where Z is the *atomic number* of the element under study. Z is equal to the number of protons and thus the number of positive charges in the nucleus. The *chemistry* of the element is controlled by Z in that all nuclei with the same Z will have similar chemical behavior. The nucleus also contains N neutrons where N is the *neutron number*. Neutrons are uncharged particles with masses approximately equal to the mass of a proton (≈ 1 u). The protons have a positive charge equal to that of an electron. The overall charge of a nucleus is $+Z$ electronic charge units.

Most of the atom is empty space in which the electrons surround the nucleus. (Electrons are small, negatively charged particles with a charge of -1 electronic charge units and a mass of about 1/1840 of the proton mass.) The negatively charged electrons are bound by an electrostatic (Coulombic) attraction to the positively charged nucleus. In a neutral atom, the number of electrons in the atom equals the number of protons in the nucleus.

Quantum mechanics tells us that only certain discrete values of E, the total electron energy, and J, the angular momentum of the electrons, are allowed. These discrete states have been depicted in the familiar semiclassical picture of the atom (Fig. 1.1) as a tiny nucleus with electrons rotating about it in discrete orbits. In this book, we will examine nuclear structure and will develop a similar semiclassical picture of the nucleus that will allow us to understand and predict a large range of nuclear phenomena.

1.4 Atomic Processes

The sizes and energy scales of atomic and nuclear processes are very different. These differences allow us to consider them separately.
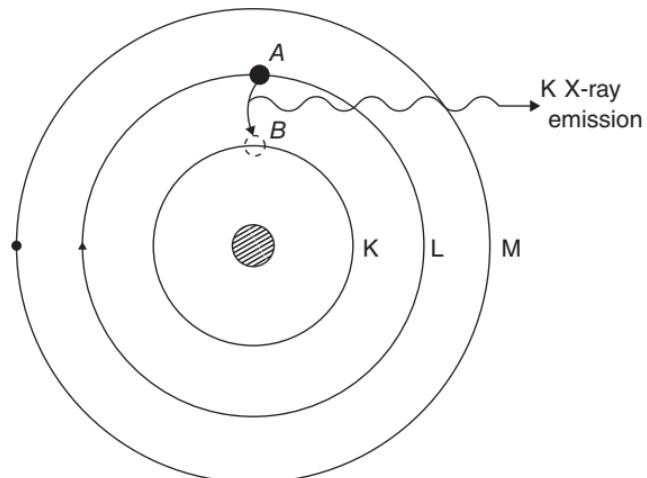
1.4.1 Ionization

Suppose one atom collides with another atom. If the collision is *inelastic*, (the kinetic energies of the colliding nuclei are not conserved), one of two things may happen. They are (a) *excitation* of one or both atoms to an excited state involving a change in electron configuration or (b) *ionization* of atoms, that is, removal of one or more of the atom's electrons to form a positively charged ion. For ionization to occur, an atomic electron must receive an energy that is at least equivalent to its binding energy, which, for the innermost or K electrons, is $(Z_{effective}/137)^2(255.5)$ keV, where $Z_{effective}$ is the effective nuclear charge felt by the electron (and includes the effects of screening of the nuclear charge by other electrons). This effective nuclear charge for K electrons can be approximated by the expression $(Z - 0.3)$. As one can see from these expressions, the energy necessary to cause ionization far exceeds the kinetic energies of gaseous atoms at room temperature. Thus, atoms must be moving with high speeds (as the result of nuclear decay processes or acceleration) to eject tightly bound electrons from other atoms.

1.4.2 X-Ray Emission

The term *X-ray* refers to the electromagnetic radiation produced when an electron in an outer atomic electron shell drops down to fill a vacancy in an inner atomic electron shell (Fig. 1.2), such as going from the M shell to fill a vacancy in the L shell. The electron loses potential energy in this transition (in going to a more tightly bound shell) and radiates this energy in the form of X-rays. (X-rays are not to be confused with generally more energetic γ-rays that result from transitions made by the neutrons and protons in the nucleus of the atom,

Figure 1.2 Schematic representation to show X-ray emission to fill vacancy caused by nuclear decay. An L shell electron (*A*) is shown filling a K shell vacancy (*B*). In doing so, it emits a characteristic K X-ray.

not in the atomic electron shells.) The energy of the X-ray is given by the difference in the binding energies of the electrons in the two shells, which, in turn, depends on the atomic number of the element. Thus X-ray energies can be used to determine the atomic number of the elemental constituents of a material and are also regarded as conclusive proof of the identification of a new chemical element.

In X-ray terminology, X-rays due to transitions from the L to K shell are called K_α X-rays; X-rays due to transitions from the M to K shells are called K_β X-rays. In a further refinement, the terms $K_{\alpha1}$ and $K_{\alpha2}$ refer to X-rays originating in different subshells ($2p_{3/2}$, $2p_{1/2}$) of the L shell. X-rays from M to L transitions are L_α and so on. For each transition, the changes in orbital angular momentum, $\Delta\ell$, and total angular momentum, Δj, are required to be

$$\Delta\ell = \pm 1 \tag{1.1}$$

$$\Delta j = 0, \pm 1 \tag{1.2}$$

The simple Bohr model of the hydrogen-like atom (one electron only) predicts that the X-ray energy or the transition energy, ΔE, is given as

$$\Delta E = E_{\text{initial}} - E_{\text{final}} = R_\infty hcZ^2 \left(\frac{1}{n_{\text{initial}}^2} - \frac{1}{n_{\text{final}}^2} \right) \tag{1.3}$$

where R_∞, h, c, and n denote the Rydberg constant, the Planck constant, the speed of light, and the principal quantum number for the orbital electron, respectively. Since the X-ray energy, E_x, is actually $-\Delta E$, we can write (after substituting values for the physical constants)

$$E_x = 13.6Z^2 \left(\frac{1}{n_{\text{final}}^2} - \frac{1}{n_{\text{initial}}^2} \right) \text{eV} \tag{1.4}$$

where E_x is given in units of electron volts (eV).

For K_α X-rays from ions with only one electron,

$$E_x^K = 13.6 \left(\frac{1}{1^2} - \frac{1}{2^2} \right) Z^2 \text{ eV} \tag{1.5}$$

while for L_α X-rays, we have

$$E_x^L = 13.6 \left(\frac{1}{2^2} - \frac{1}{3^2} \right) Z^2 \text{ eV} \tag{1.6}$$

In reality, many electrons will surround the nucleus, and we must replace Z by $Z_{\text{effective}}$ to reflect the screening of the nuclear charge by these other electrons. This correction was done by Moseley who showed that the frequencies, ν, of the K_α series X-rays could be expressed as

$$\nu^{1/2} = \text{const}(Z - 1) \tag{1.7}$$

while for L_α series X-rays,

$$v^{1/2} = \text{const}(Z - 7.4) \tag{1.8}$$

Moseley thus demonstrated the X-ray energies ($= h\nu$) depend on the square of some altered form (due to screening) of the atomic number. Also, the relative intensities of the $K_{\alpha 1}$, $K_{\alpha 2}$, etc X-rays will be proportional to the number of possible ways to make the transition. Thus, we expect the $K_{\alpha 1}/K_{\alpha 2}$ intensity ratio to be ~2 as the maximum number of electrons in the $2p_{3/2}$ level is 4 while the maximum number of electrons in the $2p_{1/2}$ level is 2. The relative intensities of different X-rays depend on the chemical state of the atom, its oxidation state, bonding with ligands, and other factors that affect the local electron density. These relative intensities are, thus, useful in chemical speciation studies. We should also note, as discussed extensively in Chapters 7–9, that X-ray production can accompany radioactive decay. Radioactive decay modes, such as electron capture (EC) or internal conversion (IC), directly result in vacancies in the atomic electron shells. The resulting X-rays are signatures that can be used to characterize the decay modes and/or the decaying species.

1.5 The Nucleus: Nomenclature

A nucleus is said to be composed of *nucleons*. There are two "kinds" of nucleons, the neutrons and the protons. A nucleus with a given number of protons and neutrons is called a *nuclide*. The *atomic number Z* is the number of protons in the nucleus, while N, the *neutron number*, is used to designate the number of neutrons in the nucleus. The total number of nucleons in the nucleus is A, the *mass number*. Obviously $A = N + Z$. Note that A, the number of nucleons in the nucleus, is an integer, while the actual mass of that nucleus, m, is not an integer.

Nuclides with the same number of protons in the nucleus but with differing numbers of neutrons are called *isotopes*. (This word comes from the Greek *iso + topos*, meaning "same place" and referring to the position in the periodic table.) Isotopes have very similar chemical behavior because they have the same electron configurations. Nuclides with the same number of neutrons in the nucleus, N, but differing numbers of protons, Z, are referred to as *isotones*. Isotones have some nuclear properties that are similar in analogy to the similar chemical properties of isotopes. Nuclides with the same mass number, A, but differing numbers of neutrons and protons are referred to as *isobars*. Isobars are important in radioactive decay processes. Finally, the term *isomer* refers to a nuclide in an excited nuclear state that has a measurable lifetime ($>10^{-9}$ s). These labels are straightforward, but one of them is frequently misused, that is, the term isotope. For example, radioactive nuclei (radionuclides) are often *incorrectly*

referred to as radioisotopes, even though the nuclides being referenced do not have the same atomic numbers.

The convention for designating a given nuclide (with Z protons, N neutrons) is to write $^A_Z\text{Chemical Symbol}_N$ with the relative positions indicating a specific feature of the nuclide. Thus, the nucleus with 6 protons and 8 neutrons is $^{14}_6\text{C}_8$ or completely equivalently, ^{14}C. (The older literature used the form $^N_Z\text{Chemical Symbol}^A$, so ^{14}C was designated as C^{14}. This nomenclature is generally extinct.) Note that sometimes the atomic charge of the entity containing the nuclide is denoted as an upper right-hand superscript. Thus a doubly ionized atom containing a Li nucleus with 3 protons and 4 neutrons and only one electron is designated as $^7\text{Li}^{2+}$.

Sample Problem 1.1: Labels

Consider the following nuclei: ^{60m}Co, ^{14}C, ^{14}N, ^{12}C, ^{13}N. Which are isotopes? isotones? isobars? isomers?

Solution

^{60m}Co is the isomer, ^{14}C and ^{12}C are isotopes of carbon, ^{13}N and ^{14}N are isotopes of nitrogen, ^{14}C and ^{14}N are isobars ($A = 14$), while ^{12}C and ^{13}N are isotones ($N = 6$).

1.6 Properties of the Nucleus

We can now make an estimate of two important quantities, the size and the density of a typical nucleus. We can say

$$\rho \equiv \text{Density} = \frac{\text{Mass}}{\text{Volume}} \approx \frac{A\ (\text{amu})}{\frac{4}{3}\pi R^3} \tag{1.9}$$

if we assume that the mass of each nucleon is about 1 u and the nucleus can be represented as a sphere. It turns out (Chapter 2) that a rule to describe the radii of stable nuclei is that radius R is

$$R = 1.2 \times 10^{-13} A^{1/3}\ \text{cm} \tag{1.10}$$

Thus we have

$$\rho = \frac{(A\ (\text{u}))\left(1.66 \times 10^{-24}\ (\text{g/u})\right)}{\frac{4}{3}\pi \left(1.2 \times 10^{-13} A^{1/3}\ \text{cm}\right)^3} \tag{1.11}$$

where we have used the value of 1.66×10^{-24} g for 1 u (Appendix A). Before evaluating the density ρ numerically, we note that the A factor cancels in the expression, leading us to conclude that all nuclei have approximately the

same density. This is similar to the situation with different sized drops of a pure liquid. All of the molecules in a drop interact with each other with the same short-ranged forces, and the overall drop size grows with the number of molecules. Evaluating this expression and converting to convenient units, we have

$$\rho \approx 200,000 \text{ metric tons/mm}^3$$

A cube of nuclear matter that is 1 mm on a side contains a mass of 200,000 tonnes. WOW! Now we can realize what all the excitement about the nuclear phenomena is about. Think of the tremendous forces that are needed to hold matter together with this density. Relatively small changes in nuclei (via decay or reactions) can release large amounts of energy. (From the point of view of the student doing calculations with nuclear problems, a more useful expression of the nuclear density is 0.17 nucleons/fm^3.)

1.7 Survey of Nuclear Decay Types

Nuclei can emit radiation spontaneously. The general process is called *radioactive decay*. While this subject will be discussed in detail in Chapters 3, 7, 8, and 9, we need to know a few general ideas about these processes right away (which we can summarize in the following).

Radioactive decay usually involves one of three basic types of decay, α-decay, β-decay, or γ-decay in which an unstable nuclide spontaneously changes into a more stable form and emits some radiation. In Table 1.1, we summarize the basic features of these decay types.

The fact that there were three basic decay processes (and their names) was discovered by Rutherford. He showed that all three processes occur in a sample of decaying natural uranium (and its daughters). The emitted radiations were designated α, β, and γ to denote the penetrating power of the different radiation types. Further research has shown that in α-decay, a heavy nucleus spontaneously emits an ^{4}He nucleus (an α- particle). The emitted α-particles are monoenergetic, and as a result of the decay, the parent nucleus loses two protons and two neutrons and is transformed into a new nuclide. All nuclei with $Z > 83$ are unstable with respect to this decay mode.

Nuclear β decay occurs in three ways, β^-, β^+, and EC. In these decays, a nuclear neutron (proton) changes into a nuclear proton (neutron) with the ejection of neutrinos (small neutral particles) and electrons (or positrons). (In EC, an orbital electron is captured by the nucleus, changing a proton into a neutron with the emission of a neutrino.) The total number of nucleons in the nucleus, A, does not change in these decays, only the relative number of neutrons and protons. In a sense, this process can "correct" or "adjust" an imbalance between the number of neutrons, and protons in a nucleus. In β^+ and β^- decays,

ctive Decay.

				Typical Energy of		
	N	ΔA	Emitted Particle	Example		Occ
	2	-4	$4 \le E_\alpha \le 10$ MeV	$^{238}\text{U} \to ^{234}\text{Th} + \alpha$		$Z >$
	1	0	$0 \le E_\beta \le 2$ MeV	$^{14}\text{C} \to ^{14}\text{N} + \beta^- + \overline{\nu}_e$		$N/$
	1	0	$0 \le E_\beta \le 2$ MeV	$^{22}\text{Na} \to ^{22}\text{Ne} + \beta^+ + \nu_e$		$N/$
	1	0	$0 \le E_\nu \le 2$ MeV	$e^- + ^{207}\text{Bi} \to ^{207}\text{Pb} + \nu_e$		$N/$
		0	$0.1 \le E_\gamma \le 2$ MeV	$^{60}\text{Ni}^* \to ^{60}\text{Ni} + \gamma$		An
		0	$0.1 \le E_e \le 2$ MeV	$^{125}\text{Sb}^m \to ^{125}\text{Sb} + e^-$		Cas

the decay energy is shared between the emitted electrons, the neutrinos, and the recoiling daughter nucleus. Thus, the energy spectrum of the emitted electrons and neutrinos is continuous ranging from zero to the decay energy. In EC decay, essentially all the decay energy is carried away by the emitted neutrino. Neutron-rich nuclei decay by β^- decay while proton-rich nuclei decay by β^+ or EC decay. β^+ decay is favored in the light nuclei and requires the decay energy to be > 1.02 MeV (for reasons to be discussed later), while EC decay is found mostly in the heavier nuclei.

Nuclear electromagnetic decay occurs in two ways, γ-decay and IC. In γ-ray decay a nucleus in an excited state decays by the emission of a photon. In IC the same excited nucleus transfers its energy radiationlessly to an orbital electron that is ejected from the atom. In both types of decay, only the excitation energy of the nucleus is reduced with no change in the number of any of the nucleons.

Sample Problem 1.2: Balancing equations

The conservation of the number of nucleons in the nucleus and conservation of charge during radioactive decay (Table 1.1) makes it relatively easy to write and balance nuclear decay equations. For example, consider

- The β^- decay of ^{90}Sr
- The α decay of ^{232}Th
- The β^+ decay of ^{62}Cu
- The EC decay of ^{256}Md

Solution

These decay equations can be written, using Table 1.1, as

- $^{90}_{38}\text{Sr} \rightarrow ^{90}_{39}\text{Y}^+ + \beta^- + \overline{\nu}_e$

- $^{232}_{90}\text{Th} \rightarrow ^{228}_{88}\text{Ra} + ^4_2\text{He}$

- $^{62}_{29}\text{Cu} \rightarrow ^{62}_{28}\text{Ni}^- + \beta^+ + \nu_e$

- $e^- + ^{256}_{101}\text{Md}^+ \rightarrow ^{256}_{100}\text{Fm} + \nu_e$

Besides its qualitative description, radioactive decay has an important quantitative description. Radioactive decay can be described as a first-order reaction, that is, the number of decays is proportional to the number of decaying nuclei present. It is described by the integrated rate law

$$N = N_0 e^{-\lambda t} \tag{1.12}$$

where N is the number of nuclei present at time t while N_0 is the number of nuclei present at time $t = 0$. The decay constant λ, a characteristic of each nucleus, is related to the half-life $t_{1/2}$ by

$$\lambda = \frac{\ln 2}{t_{\frac{1}{2}}} \tag{1.13}$$

The *half-life* is the time required for the number of nuclei present to decrease by a factor of 2. The number of decays that occur in a radioactive sample in a given amount of time is called the *activity A* of the sample. The activity is equal to the number of nuclei present, N, multiplied by the probability of decay per nucleus, λ, that is, $A = \lambda N$. Therefore, the activity will also decrease exponentially with time, that is,

$$A = A_0 e^{-\lambda t} \tag{1.14}$$

where A is the number of disintegrations per unit time at time t and A_0 is the activity at time $t = 0$. The half-lives of nuclei with respect to each decay mode are often used to identify the nuclei.

Sample Problem 1.3

^{14}C decays to ^{14}N by β^- decay with a half-life of 5730 years. If a 1 g sample of carbon contains 15.0 dis/min, what will be its activity after 10,000 years?

Solution

- $A = A_0 e^{-\lambda t}$
- $\lambda = \dfrac{\ln 2}{5730 \text{ years}} = 1.210 \times 10^{-4}/\text{year}$
- $A = (15 \text{ dis/min}) \, e^{-(1.210 \times 10^{-4})(10,000)} = 4.5 \text{ dis/min}$

All living things maintain a constant level of ^{14}C per gram of carbon through exchange with their surroundings. When they die, this exchange stops, and the amount of ^{14}C present decreases exponentially with time. A measurement of the ^{14}C content of a dead object can be used to determine the age of the object. This process and other geologically important decay processes are discussed in Chapter 3.

1.8 Modern Physical Concepts Needed in Nuclear Chemistry

While we shall strive to describe nuclear chemistry without using extensive mathematics and physics, there are several important concepts from modern physics that we need to review because we will use these concepts in our discussions.

1.8.1 Elementary Mechanics

Let us recall a few elementary relationships from classical physics that we shall use. Force can be represented as a vector, **F**, which describes the rate of change of the momentum with time:

$$\mathbf{F} = \frac{d\mathrm{p}}{dt} \tag{1.15}$$

where the momentum $p = mv$ and where m is the mass and v is the velocity of the particle. Neglecting relativistic effects (Section 1.8.2) that are important for particles whose velocity approaches the speed of light, we can say that the kinetic energy of a moving body T is given as

$$T = \frac{1}{2}mv^2 \tag{1.16}$$

For the situation depicted in Figure 1.3 for the motion of a particle past a fixed point, we can say that the orbital angular momentum of the particle, ℓ, with mass m with respect to the point Q is
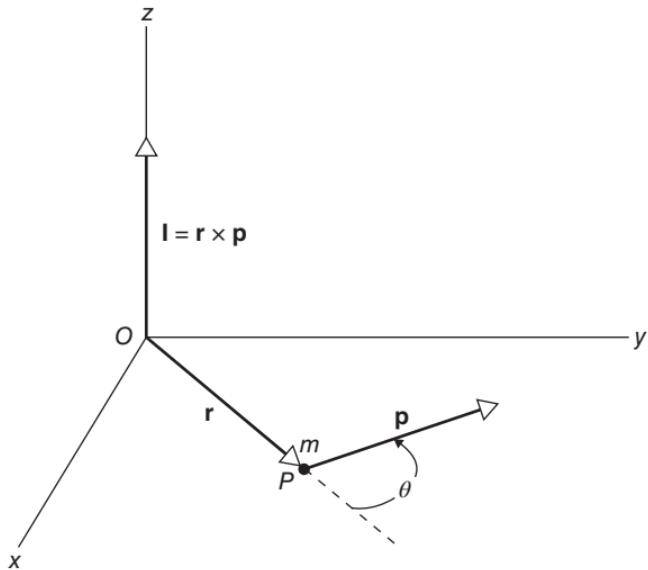
$$\mathbf{l} = \mathbf{r} \times \mathbf{p} \tag{1.17}$$

The quantity ℓ is a vector whose magnitude is mvr for circular motion. For motion past a stationary point, the magnitude is mvb where b is the distance of closest approach called the *impact parameter*.

Let us also recall the relationship between the magnitude of a force $F(r)$ that depends on the distance between two objects, r, and the potential energy, $V(r)$, that is,

$$F = \frac{-\partial V}{dr} \tag{1.18}$$

Figure 1.3 A particle of mass, m, moving with a velocity, v, has a linear momentum $\mathbf{p} = mv$. Relative to point O, the particle has an angular momentum of $\ell = \mathbf{r} \times \mathbf{p}$, where $\mathbf{r}$ is a vector connecting point O and the particle. At the point of closest approach, r is equal to impact parameter b.

Thus, if the Coulomb potential energy between two charged objects is given as

$$V = \frac{+kq_1q_2}{r_{12}} \tag{1.19}$$

where r_{12} is the distance separating charges q_1 and q_2 (and where k is a constant), we can say t the magnitude of the Coulomb force, F_C, is

$$F_C = \frac{-\partial V}{dr} = \frac{kq_1q_2}{r_{12}^2} \tag{1.20}$$

Since forces are usually represented as vectors, it is more convenient when discussing nuclear interactions to refer to the scalar, potential energy. From the previous discussion, we should always remember that a discussion of potential energy $V(r)$ is also a discussion of force $F(r)$.

1.8.2 Relativistic Mechanics

As Einstein demonstrated, when a particle moves with a velocity approaching that of light, the classical relations (Section 1.8.1) describing its motion in a stationary system are no longer valid. Nuclear processes frequently involve particles with such high velocities. Thus we need to understand the basic elements of relativistic mechanics. According to the special theory of relativity, the mass of a moving particle changes with speed according to the equation

$$m^* = \gamma m_0 \tag{1.21}$$

where m^* and m_0 are the mass of a particle in motion and at rest, respectively. The Lorentz factor, γ, is given as

$$\gamma = \left(1 - \beta^2\right)^{-1/2} \tag{1.22}$$

where β is the speed of the particle, v, relative to the speed of light, c, that is, $\beta = v/c$. Thus, as the speed of the particle increases, the mass also increases, making further increases in speed more difficult. Since the mass m^* cannot be imaginary, no particle can go faster than the speed of light. The total energy of a particle, E_{tot}, is given as

$$E_{tot} = m^*c^2 \tag{1.23}$$

Since the total energy equals the kinetic energy plus the rest mass energy, we can write

$$E_{tot} = T + m_0c^2 \tag{1.24}$$

where T is the particle's kinetic energy. Thus

$$T = (\gamma - 1)m_0c^2 \tag{1.25}$$

A series of relationships have been derived between the stationary coordinate system (the scientist in his or her laboratory) and a moving (intrinsic, invariant)

Table 1.2 Comparison of Relativistic and Classical Expressions for a Free Particle.

Classical Expression	Relativistic Expression
$\Delta t = t_2 - t_1$	$\Delta t' = \gamma \Delta t$
Mass m	$m = \gamma m_0$ ($m_0 \equiv$ rest mass)
Momentum $p = mv$	$p = \gamma mv$
$T \equiv$ kinetic energy $= \frac{1}{2}mv^2$	$T = (\gamma - 1)m_0 c^2$
Total energy $E_{\text{tot}} = E_k$ (free particle)	$E_{\text{tot}} = \gamma m_0 c^2$
Energy–momentum relationship $E = p^2/2m$	$E_{\text{tot}}^2 = p^2 c^2 + m_0^2 c^4$

coordinate system that can be compared to classical calculations of dynamic variables (Table 1.2).

Note that for a particle at rest

$$E_{\text{tot}} = m_0 c^2 \tag{1.26}$$

where m_0 is the rest mass and c the speed of light. For a massless particle, such as a photon, we have

$$E_{tot} = pc \tag{1.27}$$

where p is the momentum of the photon. These equations make it clear why the units of MeV/c^2 for mass and MeV/c for momentum are useful. An important question is when do we use classical expressions and when do we use relativistic expressions? A convenient but arbitrary criterion for making this decision is to use the relativistic expression when $\gamma \geq 1.1$. This corresponds roughly to a 13% error in the classical expression. What does this criterion mean, in practice? In Table 1.3, we indicate the values of the kinetic energy at which $\gamma = 1.1$ for different particles. Thus, one should always use the relativistic expressions for photons, neutrinos, and electrons (when $T_e > 50$ keV) or for nucleons when the kinetic energy/nucleon exceeds 100 MeV.

Sample Problem 1.4: Relativistic Mechanics

Consider a ^{20}Ne ion with a kinetic energy of 1 GeV/nucleon. Calculate its velocity, momentum, and total energy.

Solution

The kinetic energy = 20×1 GeV/nucleon = 20 GeV = 20,000 MeV. But we know the kinetic energy is $T = (\gamma - 1)m_0 c^2$, and the rest mass is ~ 20 u or $(20)(931.5)$ MeV/c or 18,630 MeV. So we can write

$$\gamma = \frac{T}{m_0 c^2} + 1 = 1 + \frac{20,000}{18,630} = 2.07$$

$$\gamma = \left(1 - \beta^2\right)^{-1/2} \rightarrow \beta = \left(1 - \frac{1}{\gamma^2}\right)^{1/2} = 0.88$$

Thus the velocity, v, is $0.88c$ or $(0.88)(3.00 \times 10^8$ m/s$) = 2.6 \times 10^8$ m/s. The momentum is given by

$$p = \frac{mv}{\sqrt{1 - \beta^2}} = \gamma m v$$
$$= (2.07)(20)\left(1.67 \times 10^{-27}\ \text{kg}\right)\left(2.6 \times 10^8\right)$$
$$= 1.8 \times 10^{-17}\ \text{kg} \cdot \text{m/s}$$

or in other units

$$pc = \frac{mcv}{\sqrt{1 - \beta^2}} = \frac{mc^2\beta}{\sqrt{1 - \beta^2}} = mc^2 \beta \gamma$$
$$= (20)(931.5)(0.88)(2.07)$$
$$= 33.9\ \text{GeV} \rightarrow p = 33.9\ \text{GeV/c}$$

The total energy is given by

$$E_{\text{tot}} = T + m_0 c^2 = \gamma m_0 c^2$$
$$= (2.07)(20)(931.5) = 38.6\ \text{GeV}$$

1.8.3 de Broglie Wavelength: Wave–Particle Duality

There is no distinction between wave and particle descriptions of matter. It is simply a matter of convenience, which we choose to use in a given situation. For example, it is quite natural to describe matter in terms of particles with values of momenta, kinetic energies, and so on. It is also natural to use a wave

Table 1.3 When Does One Use Relativistic Expressions?.

Particle	T (MeV) when $\gamma = 1.1$
γ, ν	0
e	0.051
μ	11
π	14
p, n	94
d	188
α	373

description for light. However, associated with each material particle, there is a wave description in which the particle is assigned a wavelength (the de Broglie wavelength λ) whose magnitude is given as

$$\lambda = \frac{h}{p} \tag{1.28}$$

where p is the momentum of the particle and h is Planck's constant. (Note that Planck's constant is extremely small, 6.6×10^{-34} J s. Thus the wave length of a particle is only important when the momentum is small, such as with electrons whose mass is 9×10^{-31} kg.) The expression for the de Broglie wavelength may be written in rationalized units

$$\lambdabar = \frac{\hbar}{p} \tag{1.29}$$

where $\hbar$ is $h/2\pi$. The aforementioned expressions are classical and should be replaced by their relativistic equivalents where appropriate, that is,

$$\lambdabar = \frac{\hbar c}{\left[E_{\mathrm{k}} \left(E_{\mathrm{k}} + 2m_0 c^2 \right) \right]^{1/2}} \tag{1.30}$$

We can calculate typical magnitudes of these wavelengths of particles encountered in nuclear chemistry (Table 1.4). Given typical nuclear dimensions of 10^{-13} cm, the data of Table 1.4 indicate the energy at which such particles might have a wavelength similar or smaller than nuclear dimensions. These particles can be used as probes of nuclear sizes and shapes. In a similar manner, it is quite natural to associate a wave description to photons (Table 1.4). Here we recall that

$$\lambda = \frac{c}{\nu} = \frac{hc}{E_\gamma} \tag{1.31}$$

where ν is the frequency associated with the wave of length λ. A convenient form of this equation is

$$\lambda \, (\mathrm{cm}) = \frac{1.2397 \times 10^{-10}}{E_\gamma (\mathrm{MeV})} \tag{1.32}$$

Table 1.4 Typical Magnitudes of de Broglie Wavelengths.

Energy (MeV)	Photon	Electron	Proton
0.1	1.2×10^{-9}	3.7×10^{-10}	9.0×10^{-12}
1	1.2×10^{-10}	8.7×10^{-11}	2.9×10^{-12}
10	1.2×10^{-11}	1.2×10^{-11}	0.9×10^{-12}
100	1.2×10^{-12}	1.2×10^{-12}	2.8×10^{-13}
1000	1.2×10^{-13}	1.2×10^{-13}	0.7×10^{-13}

which was used to calculate the values in Table 1.4. But it is often useful to speak of photons as particles particularly when they are emitted or absorbed by a nucleus, when we write

$$E_\gamma = h\nu = pc \qquad (1.33)$$

Sample Problem 1.5: de Broglie Wavelength

Consider the case of a beam of 1 eV neutrons incident on a crystal. First-order Bragg reflections are observed at 11.8°. What is the spacing between crystal planes?

Solution

Low-energy neutrons are diffracted like X-rays. The Bragg condition is that $n\lambda = 2d \sin \theta$ where the index $n = 1$ for first-order diffraction.

$$\lambda = 2d \sin \theta$$

$$d = \frac{\lambda}{2 \sin \theta} = \frac{h/p}{2 \sin \theta} = \frac{h/\sqrt{2mE_k}}{2 \sin \theta}$$

$$d = \frac{6.63 \times 10^{-34} \text{ Js}/\sqrt{2 \times 1.67 \times 10^{-27} \text{ kg} \times 1.60 \times 10^{-19} \text{ J}}}{2 \sin(11.8°)}$$

$$d = 7.0 \times 10^{-11} \text{ m}$$

1.8.4 Heisenberg Uncertainty Principle

Simply put, the Heisenberg uncertainty principle states that there are limits on knowing both where something is and how fast it is moving. Formally, we can write

$$\Delta p_x \cdot \Delta x \geq \hbar$$
$$\Delta p_y \cdot \Delta y \geq \hbar$$
$$\Delta p_z \cdot \Delta z \geq \hbar$$
$$\Delta E \cdot \Delta t \geq \hbar$$

where Δp_x, Δx are the uncertainties in the x-component of the momentum and the x coordinate, respectively, while Δt is the lifetime of a particle and ΔE is the uncertainty in its total energy. These limits on our knowledge are not due to the limitations of our measuring instruments. They represent fundamental limits even with ideal or perfect instruments. It is instructive to consider a practical example to see the effect of these limits. Consider an electron with a kinetic

energy of 5.0 ± 0.05 eV. Its speed can be calculated (nonrelativistically since KE $\ll m_0 c^2$):

$$v = \left(\frac{2E_k}{m}\right)^{1/2} = \left(\frac{(2)(5.0)(1.602 \times 10^{-19} \text{ J/eV})}{9.11 \times 10^{-31} \text{ kg}}\right)^{1/2} = 1.3 \times 10^6 \text{ m/s} \tag{1.34}$$

The electron's momentum is then

$$p = mv = 1.21 \times 10^{-24} \text{ kg} \cdot \text{m/s} \tag{1.35}$$

The uncertainty in its measured momentum is $0.05/5.0 = 1.0\%$. The uncertainty principle then tells us

$$\Delta x = \frac{\hbar}{\Delta p} = \frac{1.06 \times 10^{-34} \text{ J/s}}{0.01 \times 1.21 \times 10^{-24} \text{ kg} \cdot \text{m/s}} = 8.8 \times 10^{-9} \text{ m} \tag{1.36}$$

which is about 40 atomic diameters. In short, if you know the momentum relatively well, you don't know where the electron is in space.

1.8.5 Units and Conversion Factors

Every field has its own special units of measure, and nuclear chemistry is no different. The unit of length is the femtometer (10^{-15} m), which is called a *fermi*. The unit of mass is the *atomic mass unit* (amu or u) that has a numerical value of 1.66×10^{-24} g or expressed in units of MeV/c^2; it is 931.5 MeV/c^2. The unit of energy is MeV (10^6 eV) that is 1.602×10^{-13} J, the energy gained when a proton is accelerated through a potential of 10^6 V. Appendix A contains a list of the exact numerical values of these and other convenient units. Special attention is called to five very useful quantities:

- $\frac{e^2}{4\pi\epsilon_0} = 1.43998$ MeV fm
- $\hbar = 6.58212 \times 10^{-22}$ MeV $\cdot$ s
- $c = 2.9979 \times 10^{23}$ fm/s $= 29.979$ cm/ns
- $\hbar c = 197.3$ MeV fm
- 1 year (sidereal) $= 3.1558 \times 10^7$ s $\approx \pi \times 10^7$ s

Problems

1.1 Define or describe the following terms or phenomena: radiochemistry, isotone, internal conversion.

1.2 In an experiment one observes the characteristic K_α X-rays of two elements at energies of 6.930 and 7.478 eV. The higher energy line is due to Ni. What element is responsible for the lower energy line?

1.3 Calculate the speed of a particle whose kinetic energy is three times its rest energy, $T/m_0c^2 = 3$.

1.4 Given the following energies of the K_α X-rays for the following elements, make a Moseley plot of the data:
- V 4.952 eV
- Cr 5.415 eV
- Mn 5.899 eV
- Fe 6.404 eV

1.5 Predict the mode of decay of the following nuclei: ^{14}C, ^3H, ^{11}C, ^{233}U, ^{138}La.

1.6 Write complete, balanced equations for the following decays:
- The α decay of ^{230}Th
- The β^- decay of ^{95}Zr
- The β^+ decay of ^{17}F
- The EC decay of ^{192}Au

1.7 Consider the decay of ^{238}U to ^{206}Pb. How many α-particles and β-particles are emitted in this decay?

1.8 If a rock has a ratio of ^{206}Pb to ^{238}U of 0.6, what is the age of the rock?

1.9 How long will it take for a sample of ^{239}Pu ($t_{1/2} = 24,119$ years) to decay to 1/10 its original amount?

1.10 If a radioactive sample of ^{59}Fe ($t_{1/2} = 44.496$ days) has an activity of 1000 dis/min, what weight of ^{59}Fe is present?

1.11 The environmental concentration of ^{239}Pu ($t_{1/2} = 24,119$ years) in a lake is 3.7×10^{-6} dis/s/L. What is the molarity of the solution?

1.12 ^{32}P ($t_{1/2} = 14.262$ days) is a popular tracer in biochemistry. If I need to have 0.1×10^6 dis/s 60 days from now, how many ^{32}P tracer must I purchase today?

1.13 Calculate the speed of a particle whose kinetic energy is three times its rest energy.

1.14 Calculate the speed parameter β and the Lorentz factor γ for the following particles: an electron with $E_K = 1$ MeV; a proton with $E_K = 1$ MeV; and a ^{12}C nucleus with $E_K = 12$ MeV.

1.15 Consider the following free particles: a 1-eV photon, a 1-MeV electron, and a 10-MeV proton. Which is moving the fastest? slowest? has the most momentum? the least momentum?

1.16 How much energy is necessary to increase the speed of a proton from $0.2c$ to $0.3c$ from $0.98c$ to $0.99c$?

1.17 A nonrelativistic particle is moving five times as fast as a proton. The ratio of their de Broglie wavelengths is 10. Calculate the mass of the particle.

1.18 What are the wavelengths of a 500-MeV photon, a 500-MeV electron, and a 500-MeV proton?

1.19 What is the wavelength of a "thermal" neutron? Assume that its kinetic energy is 3/2 kBT and room temperature is 20°C, T=293 K.

1.20 Consider a nuclear excited state with a lifetime of 10 ps that decays by the emission of a 2 MeV γ-ray. What is the uncertainty in the γ-ray energy?

Bibliography

There are many fine textbooks for nuclear and radiochemistry that cover the material covered in this book. A limited selection of some of the authors' favorites appears as follows.

Simple Introductions to Nuclear Chemistry

J.C. Bryan, Introduction to Nuclear Science, 2nd Edition (Taylor & Francis, Boca Raton, 2013) An introduction to nuclear physics and chemistry for students with limited backgrounds in math and the physical sciences.

W.D. Ehmann and D.E. Vance, Radiochemistry and Nuclear Methods of Analysis (John Wiley & Sons, Inc., New York, 1991). A survey of nuclear chemistry that emphasizes its applications in analytical chemistry.

B.G. Harvey, Nuclear Chemistry (Prentice-Hall, Englewood Cliffs, 1965). A dated but elegant summary of the essential features of nuclear science.

C.H. Wang, D.L. Willis, and W.D. Loveland, Radiotracer Methodology in the Biological, Environmental and Physical Sciences (Prentice-Hall, Englewood Cliffs, 1975). An out-of-date survey of radiotracer methods which includes an introduction to nuclear science for life scientists.

History

A. Romer, Radiochemistry and the Discovery of Isotopes (Dover, New York, 1970). An intriguing view of the beginning of nuclear chemistry.

A. Romer, The Discovery of Radioactivity and Transmutation (Dover, New York, 1964). A presentation of the earliest explorations of radioactivity.

G.T. Seaborg and W. Loveland, Nuclear Chemistry (Hutchinson-Ross, Stroudsberg, 1982). Reprints of the most significant papers in nuclear chemistry from the earliest work to present with annotations and English translations.

Intermediate Level Textbooks -Similar to This Book

G.R. Choppin, J.O. Liljenzin, and J. Rydberg, Radiochemistry and Nuclear Chemistry, 4th Edition (Academic, Oxford, 2013). A very good, broad discussion of nuclear chemistry that is oriented toward nuclear power and nuclear power applications.

R. Evans, The Atomic Nucleus (McGraw-Hill, New York, 1955). A dated, but encyclopedic treatment of nuclear science that has set the standard for its successors.

G. Friedlander, J. Kennedy, J.M. Miller, and E.S. Macias, Nuclear and Radiochemistry (John Wiley & Sons, Inc., New York, 1981). The bible of nuclear chemistry.

B.G. Harvey, Introduction to Nuclear Physics and Chemistry, 2nd Edition (Prentice-Hall, Englewood Cliffs, 1969). A wonderful, clear description of the physics of nuclei and their interaction that is somewhat dated.

K.S. Krane, Introductory Nuclear Physics (John Wiley & Sons, Inc., New York, 1987). A clear discussion from the point of view of a practicing experimental nuclear physicist.

J.V. Kratz and K.H. Lieser, Nuclear and Radiochemistry (John Wiley & Sons, Inc., Weinheim, 2013). A comprehensive two volume detailed survey of nuclear chemistry.

J.S. Lilley, Nuclear Physics: Principles and Applications (John Wiley & Sons, Inc., West Sussex, 2001). Nuclear physics and its applications.

W. Meyerhof, Elements of Nuclear Physics (McGraw-Hill, New York, 1967). A very concise summary of the essential ideas of nuclear science.

S.G. Prussin, Nuclear Physics for Applications (John Wiley & Sons, Inc., Weinheim, 2007). Nuclear physics from a nuclear engineering perspective.

More Advanced Textbooks

C.A. Bertulani, Nuclear Physics in a Nutshell (Princeton, Princeton, 2007). A clear concise summary of nuclear physics.

A. de Shalit and H. Feshbach, Theoretical Nuclear Physics, Vol. I: Nuclear Structure, Vol. II: Nuclear Reactions (John Wiley & Sons, Inc., New York, 1974). A comprehensive treatment of the theory of nuclear structure and reactions.

E.M. Henley and A. Garcia, Subatomic Physics, 3rd Edition (World Scientific, Singapore, 2007). An up-to-date and lucid introduction to both particle and nuclear physics.

K. Heyde, Basic Ideas and Concepts in Nuclear Physics, 3rd Edition (IOP, Bristol, 2004). A clear, up-to-date description of the basics of nuclear physics.

P. Marmier and E. Sheldon, Physics of Nuclei and Particles, Volumes I and II (Academic, New York, 1969). A dated, but accessible treatment aimed at experimentalists.

E. Segre, Nuclei and Particles, 2nd Edition (Benjamin, Reading, 1977). Remarkable for its breadth and insight in nuclear physics.

S.S.M. Wong, Introductory Nuclear Physics, 2nd Edition (Prentice-Hall, Englewood Cliffs, 1998). A very up-to-date, readable treatment of nuclear physics.

General Physics Textbooks

D. Halliday, R. Resnick, and K.S. Krane, Physics, 5th Edition (John Wiley & Sons, Inc., New York, 2002). A remarkable encyclopedic treatment of introductory physics.

K.S. Krane, Modern Physics, 3rd Edition (John Wiley & Sons, Inc., New York, 2012). A recent revision of a modern classic.

Nuclear Properties

In this chapter we will turn to a systematic look at the general properties of nuclei, including their masses and matter distributions. A very large number of nuclei have been studied over the years, and the general size, shape, mass, and relative stability of these nuclei follow patterns that can be understood and interpreted with two complementary models of nuclear structure. The average size and stability of a nucleus can be described by the average binding of the nucleons to each other in a macroscopic model, while the detailed energy levels and decay properties can be understood with a quantum mechanical or microscopic model. We will consider the average behavior in this chapter and a detailed description of nuclear structure is given later in Chapter 6.

2.1   Nuclear Masses

One of the most important nuclear properties that can be directly measured is the mass. Nuclear or atomic masses are usually given in atomic mass units (amu or u) or their energy equivalent. The mass unit u is defined so that the mass of one atom of ^{12}C is equal to 12.00000 u. Note we said "atom." For convenience, the masses of atoms rather than nuclei are used in all calculations. When needed, the nuclear mass m^{nucl} can be calculated from the relationship

$$m^{nucl}c^2 = M^{atomic}c^2 - [Zm_0c^2 + B_e(Z)] \tag{2.1}$$

where m_0 is the rest mass of the electron and $B_e(Z)$ is the total binding energy of all the electrons in the atom. $B_e(Z)$ can be estimated using the Thomas–Fermi uniform density model of the atom with the equation

$$B_e(Z) = 15.73Z^{7/3} \ eV \tag{2.2}$$

Since the values of the binding energies, $B_e(Z)$, are generally small compared to the masses of the nuclei and electrons, we shall neglect this factor in most calculations. We can make a few simple calculations to illustrate the use of masses

in describing nuclear phenomena. Consider the β^- decay of ^{14}C:

$$^{14}C \rightarrow^{14} N^+ + \beta^- + \overline{\nu}_e + Energy \tag{2.3}$$

Neglecting the electron binding and the mass of the electron antineutrino, $\overline{\nu}_e$ known to be less than an eV, and rearranging we have

$$\text{Energy} = [(m(^{14}C) + 6m_0) - (m(^{14}N) + 6m_0) + m(\beta^-)]c^2 \tag{2.4}$$

where $m(x)$ is the mass of only the nucleus x. Substituting in atomic masses as appropriate and recognizing that the β^- particle is an electron, we get simply

$$\text{Energy} = [M(^{14}C) - M(^{14}N)]c^2 \tag{2.5}$$

Let us now consider the related case of the β^+-decay of ^{64}Cu:

$$^{64}Cu \rightarrow^{64} Ni^- + \beta^+ + \nu_e + \text{Energy} \tag{2.6}$$

Rewriting the equation for the energy release in the decay using the nuclear masses, $m(x)$, and again ignoring the electron binding energies and the electron neutrino, we have

$$\text{Energy} = [(m(^{64}Cu) + 29m_0) - (m(^{64}Ni) + 28m_0) - (m_0) - m(\beta^+)]c^2 \tag{2.7}$$

Notice the extra electron for the net charge on the nickel leftover after the decay. Substituting in atomic masses and the fact that the positron mass is exactly equal to the electron mass, we have

$$\text{Energy} = [M(^{64}Cu) - (M(^{64}Ni) + 2m_0)]c^2 \tag{2.8}$$

The straightforward bookkeeping for the number of electrons has shown us that for β^+-decay, the difference between the initial and final nuclear masses must be at least $2m_0c^2$ (i.e., 1.022 MeV) for the decay to be energetically possible. This energy represents the cost of creating the positron antiparticle.

To complete our survey of the energy release in β-decay, let us consider the case of electron capture the process that is important in heavy nuclei or in β unstable nuclei that do not have the enough decay energy to create an electron/positron pair. For example, the electron capture decay of ^{207}Bi:

$$e^- +^{207}Bi^+ \rightarrow^{207}Pb + \nu_e + \text{Energy} \tag{2.9}$$

Notice that we have separated the initial bismuth atom into an electron and a positive bismuth ion to indicate that the electron to be captured was in an atomic level of that atom. For the energy release in the decay, with the same assumptions as mentioned earlier, we have

$$\text{Energy} = [(m(^{207}Bi) + 83m_0) - (m(^{207}Pb) + 82m_0)]c^2 \tag{2.10}$$

Notice that the resulting ^{207}Pb atom would be neutral when the bismuth atom captures one of its orbital electrons. Substituting in atomic masses, we get the simple relation:

$$\text{Energy} = [M(^{207}\text{Bi}) - M(^{207}\text{Pb})]c^2 \qquad (2.11)$$

There are two final points on using atomic masses in nuclear energy calculations that we should consider. First, the most precise mass measurements possible at present rely on measuring the masses of singly charged ions in Penning traps. The masses of these ions will reflect the binding energies of all of the electrons, except the last one, of course, and the mass of the singly charged ion plus one electron will be extremely close to that of the neutral atom. Since we are almost always considering *mass differences* in nuclear energy calculations, using the masses of neutral atoms will take into account nearly all of the effects of electron binding.

Second, the energy change in nuclear reactions is called the *Q value* of that reaction, and as we have seen, its value can be obtained by strict bookkeeping for all the components in the reaction, particularly the electrons. If we consider the reaction

$$^{56}\text{Fe} + {}^{4}\text{He} \rightarrow {}^{59}\text{Co} + {}^{1}\text{H} + Q \qquad (2.12)$$

Rearranging for the Q value, we get

$$Q = [M(^{56}\text{Fe}) + M(^{4}\text{He}) - M(^{59}\text{Co}) - M(^{1}\text{H})]c^2 \qquad (2.13)$$

Note that the sign convention used in nuclear chemistry and physics assigns a positive Q value for exoergic reactions, which is (unfortunately) opposite to that used in chemistry where exoergic reactions have negative values of ΔH and ΔE.

Sample Problem 2.1: Energy Release

Calculate the energy release in the β^- and in β^+ decay of ^{64}Cu.

Solution

$$\begin{aligned} E \text{ for } {}^{64}\text{Cu } \beta^- \text{ decay} &= [M(^{64}\text{Cu}) - M(^{64}\text{Zn})]c^2 \\ &= [-65.421 - (-65.999)] \text{ MeV} \\ &= 0.578 \text{ MeV} \end{aligned}$$

$$\begin{aligned} E \text{ for } {}^{64}\text{Cu } \beta^+ \text{ decay} &= [M(^{64}\text{Cu}) - M(^{64}\text{Zn}) - 2m_0]c^2 \\ &= [-65.421 - (-67.096) - 1.022)] \text{ MeV} \\ &= 0.653 \text{ MeV} \end{aligned}$$

2.2 Terminology

The difference between the actual nuclear mass and the mass of all the individual nucleons (free protons and neutrons) that must be assembled to make the nucleus is called the total binding energy, $B_{tot}(A, Z)$. This binding energy represents the energy that would be released if all the nucleons come together to form the nucleus or the work necessary to dissociate the nucleus into separate nucleons We can write

$$B_{tot}(A, Z) = [ZM(^1H) + (A - Z)M(n) - M(A, Z)]c^2 \qquad (2.14)$$

where $M(A, Z)$ is the atomic mass of the nuclide with mass number A, and atomic number Z, $M(n)$, and $M(^1H)$ are the mass of a neutron and a hydrogen atom, respectively. Using the mass of a hydrogen atom here brings along the electron mass. The *average* binding energy per nucleon, $B_{ave}(A, Z)$ is given by

$$B_{ave}(A, Z) = \frac{B_{tot}(A, Z)}{A} \qquad (2.15)$$

In many tabulations of nuclear properties, such as that in *Appendix B*, the tabulated quantity is the *mass excess* rather than the mass. The mass excess, Δ, is defined as $M(A, Z) - A$, usually given in units of the energy equivalent of mass. Since in most, if not all, nuclear reaction calculations, the number of nucleons remains constant and the use of mass excesses in the calculations introduces an arithmetic simplification. Another related term is the *mass defect*. The mass defect is defined as $M(A, Z) - ZM(^1H) - NM(n)$. Note that the mass defect is a negative number for all bound nuclei, while the mass excess could be either a negative or a positive number. Unfortunately sometimes the terms mass defect and mass excess are incorrectly used as synonyms. Another term that is sometimes used is the *mass excess per nucleon* also called the packing fraction, which is Δ/A.

The work necessary to remove a neutron, proton, or α particle and others. from a nucleus is called the (neutron, proton, or α particle) separation energy and given the symbol S with a subscript to identify the particle. The neutron separation from the nucleus ^AZ:

$$S_n = [M(A - 1, Z) + M(n) - M(A, Z)]c^2 \qquad (2.16)$$

Such separation energies can also be expressed in terms of the total binding energy by

$$S_n = B_{tot}(A, Z) - B_{tot}(A - 1, Z) \qquad (2.17)$$

Sample Problem 2.2: Separation Energies

Calculate the neutron separation energy for ^{236}U and for ^{239}U.

Solution

For ^{236}U : $S_n = [M(^{235}\text{U}) + M(\text{n}) - M(^{236}\text{U})]c^2$

$\qquad\qquad = [\Delta(^{235}\text{U}) + \Delta(\text{n}) - \Delta(^{236}\text{U})]$

$\qquad\qquad = 40.914 + 8.071 - 42.441 \text{ MeV}$

$\qquad\qquad = 6.544 \text{ MeV}$

For ^{239}U : $S_n = [M(^{238}\text{U}) + M(\text{n}) - M(^{239}\text{U})]c^2$

$\qquad\qquad = [\Delta(^{238}\text{U}) + \Delta(n) - \Delta(^{239}\text{U})]$

$\qquad\qquad = 47.304 + 8.071 - 50.596 \text{ MeV}$

$\qquad\qquad = 7.779 \text{ MeV}$

Notice that the neutron separation energy of $^A Z$ is the excitation energy of the nucleus $^A Z$ produced when ^{A-1}Z captures a neutron with "zero energy," that is, the reverse reaction. Thus, when the even–odd ^{235}U nucleus absorbs a very low-energy neutron, the ^{236}U is produced at an excitation energy of 6.5 MeV, while the same process with ^{238}U nuclei gives an excitation energy of only 4.8 MeV. If it takes 5–6 MeV to cause these nuclei to fission, then ^{235}U would be "fissionable" with zero-energy neutrons, while ^{238}U would not be.

2.3 Binding Energy Per Nucleon

The *binding energy per nucleon* is a measure of the relative stability of a nucleus. The more tightly bound a nucleus is, the larger the binding energy per nucleon is. The values of the average binding energy per nucleon are shown as function of the mass number in Figure 2.1. Several features visible in this figure are worth noting. The highest stability is associated with medium mass nuclei and the most stable nucleus is ^{62}Ni. This means that the heaviest nuclei could increase their (thermodynamic) stability by fissioning into two pieces, while the lightest nuclei could increase their stability by fusing to make nuclei in the Fe–Ni region.

The most striking feature of Figure 2.1 is probably the nearly constant value of the average binding energy per nucleon for most nuclei (ranging only from 7.4 to 8.8 MeV except for the lightest nuclei). This small variation is a direct consequence of the short range and saturated character of the nuclear force. Suppose that the nuclear force was long range and not saturated and further that the binding energy of one nucleon to every other nucleon was some constant value, K. In a nucleus with A nucleons, there would be $A(A-1)/2$ "bonds" and thus the total binding energy would be $KA(A-1)/2$ with the binding energy per nucleon being $K(A-1)/2$. In other words, one would predict that the average binding energy per nucleon should increase linearly with mass number A. That does not happen, of course, as shown in Figure 2.1. Thus, one has to conclude that the nuclear force is not long range but only extends over a short range.
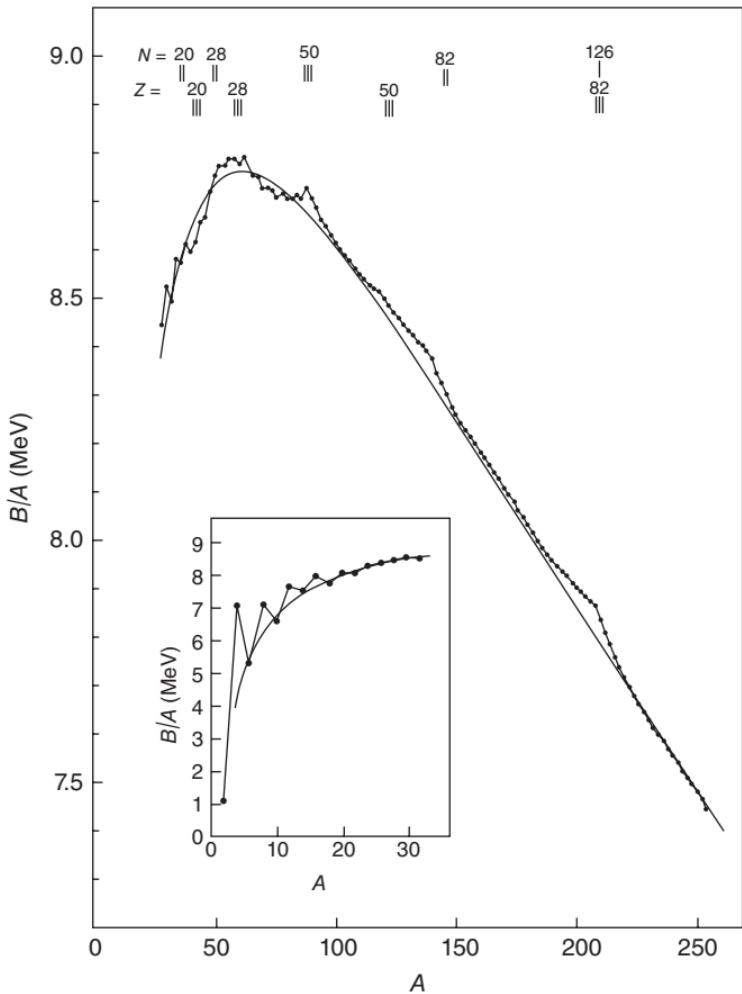
Figure 2.1 Average binding energy per nucleon versus mass number *A* for the stable nuclei (Valentin (1981). Reproduced with the permission of North-Holland Publishing Company).

One can also observe definite peaks in the average binding energy per nucleon in Figure 2.1 at certain values of *A*. This is quite reminiscent of the variation of the electron ionization potential for atoms and suggests that there are certain special stable nucleonic configurations similar to the inert gas structures of atoms. The general decrease of B_{ave} at larger values of *A* is due to the increasing influence of the Coulomb force, a long-range force, with all the protons repelling one another.

Sample Problem 2.3: Binding Energies

Contrast the binding energy per nucleon in an ^{16}O nucleus with the binding energy per molecule in liquid water.

Solution

$$\text{For } {}^{16}\text{O} : \frac{B(16, 8)}{16} = \frac{[8M({}^1\text{H}) + 8M(\text{n}) - M(16, 8)]931.5}{16}$$

$$= 7.97 \text{ MeV}$$

$$\text{For water} : \frac{\Delta \overline{H}_{\text{vap}}}{N_A} = \frac{40700 \text{ J/mol}}{6.02 \times 10^{23} \text{/mol}}$$

$$= \frac{6.76 \times 10^{-20} \text{ J}}{1.602 \times 10^{-19} \text{ J/eV}}$$

$$= 0.42 \text{ eV}$$

Notice that these values are constants, but different by ~ 7 orders of magnitude!

2.4 Separation Energy Systematics

Figure 2.2 shows the variation of the neutron separation energy for several isotopes of lead. Notice that for a given value of Z (i.e., isotopes), S_n is larger for isotopes with an even value of N than that for isotopes with an odd value of N. Similarly for a given value of N (i.e., isotopes), S_p is larger for even values of Z compared with that for odd values of Z. This difference is caused by that part of the nuclear force that favors having neutrons paired with neutrons (with
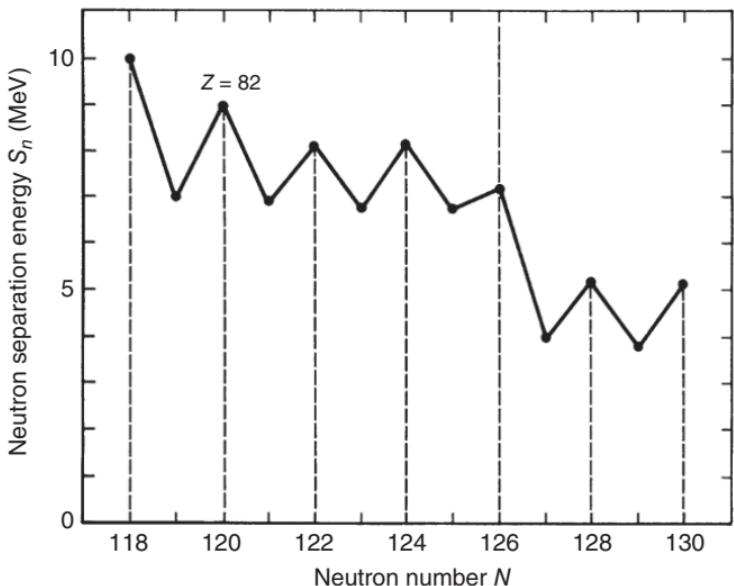
Figure 2.2 Neutron separation energy S_n for a range of lead isotopes.

antiparallel spin) and, at the same time, having protons paired with protons but favors to a much lesser extent n–p pairing. This nucleon pairing causes so-called even–even nuclei (Z even, N even) to be more stable than even-odd or odd-even nuclides, which, in turn, are more stable than odd–odd nuclei.

2.5 Abundance Systematics

In Figure 2.3, we compare the positions of the known stable nuclides of odd A with those of even A in the chart of the nuclides. Note that as Z increases the line of stability moves from $N = Z$ to $N/Z \sim 1.5$ due to the influence of the Coulomb force. For odd A nuclei, only one stable isobar is found, while for even A nuclei, there are, in general, very few stable odd–odd nuclei. This is further demonstrated by the data of Table 2.1 showing the distribution of stable isotopes.
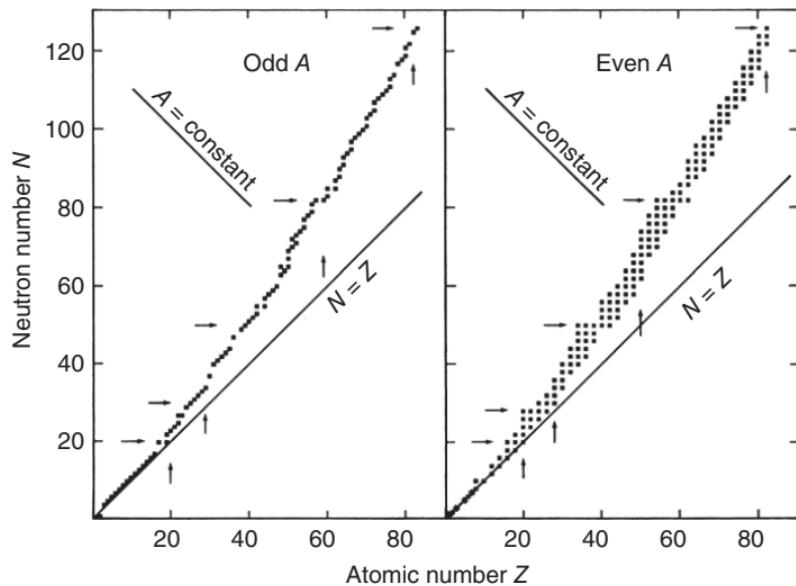
Figure 2.3 Positions of the stable odd A and even A nuclei in a Segre chart (Meyerhof 1967). Reproduced with the permission of McGraw-Hill Book Company).

Table 2.1 Distribution of Stable Nuclei.

N	Even	Odd	Even	Odd
Z	Even	Even	Odd	Odd
	160	53	49	4

2.6 Semiempirical Mass Equation

C.F. von Weizsäcker developed a crude theory of nuclear masses in 1935 that is still widely used. The theory uses the basic idea that nuclei behave as if they are incompressible uniformly charged liquid drops. How can we describe the variation of the total mass of a nuclear drop of incompressible liquid that has a uniform electric charge? We begin by writing an expression for the mass in terms of the total binding energy:

$$M(Z,A)c^2 = [ZM(^1H) + (A - Z)M(n)]c^2 - B_{tot}(Z,A) \qquad (2.18)$$

The total binding energy is clearly the most important part of Weizsäcker's equation, and it has evolved into what is called the *semiempirical mass equation*, which consists of a parameterization of the total binding energy of a nucleus with Z, A with five separate parts:

$$B_{tot}(A,Z) = a_v A - a_s A^{2/3} - a_c \frac{Z^2}{A^{1/3}} - a_a \frac{(A-2Z)^2}{A} \pm \delta \qquad (2.19)$$

The justification for the five parts of this representation of the total binding energy of the nucleus is as follows:

1) Since there are A nucleons in the nucleus and the short-ranged nuclear force saturates, we expect each nucleon to contribute the same amount to the total binding energy. Thus, the first term is known as the volume term. The coefficient a_v is the energy by which a nucleon in the interior of the nucleus is bound to its nearest neighbors and is a parameter to be determined experimentally.

2) Not all nucleons are in the interior, of course. Those nucleons on the surface are less tightly bound because they do not have a full complement of neighbors. A correction term should be applied to the binding energy proportional to the surface area of the nucleus. The surface area of a spherical nucleus can be taken to be $4\pi R^2$. If, as asserted earlier, the nuclear radius is given by $R = A^{1/3}$, then $4\pi R^2 \propto A^{2/3}$. (Notice that the volume is $(4/3)\pi R^3$ that is proportional to A, hence the form of the first term.) The $A^{2/3}$ factor is multiplied by another coefficient, a_s, that also has to be determined experimentally.

3) The third term reflects the decrease in binding due to the Coulomb repulsion among all of the protons. The Coulomb energy of a uniform sphere can be written as

$$E_C = \frac{3}{5} \frac{Z^2 e^2}{R} \qquad (2.20)$$

where we have taken $\frac{1}{4\pi\epsilon_0} = 1$ for simplicity. If we again substitute $R = r_0 A^{1/3}$, then we find that the Coulomb energy for a spherical nucleus is $E_C = 0.72 Z^2/A^{1/3}$ MeV. Note that the coefficient a_c is usually fitted along

with the other parameters, and one usually obtains the slightly smaller value of 0.6 rather than 0.72.

4) The fourth term (along with the fifth term) represents quantum mechanical effects on the binding energy. The fourth term is called the asymmetry correction and describes a decrease in the binding energy of a nucleus when $N \neq Z$ relative to a nucleus with $Z = N = A/2$. To determine the general form of this term, we should recall the quantum mechanical picture with neutrons and protons occupying orbitals in the nucleus at well-defined energies and that the neutrons and protons obey the Pauli principle for fermions. An oversimplified model such as that shown in Figure 2.4 will suffice to identify the mathematical form of this correction. Assume that the neutron and proton levels of a nucleus are equidistant with spacing Δ and that we can have only one nucleon per level. To build up the neutron-rich nucleus $^A Z$ (with $Z > N$) from the neighboring nucleus with $N' = Z' = A/2$, we must take $x = N - N'$ protons and transform them into neutrons. Mathematically we would have $Z = A/2 - x$ and $N = A/2 + x$ and solving for x, $x = (N - Z)/2$. Notice that all of the protons must be raised in energy to reach an unoccupied orbital. The amount of energy increase for the first one is $\delta E = \Delta$, the second one will require $\delta E = 2\Delta$, and so on. The total energy needed to transform the nucleus with $N' = Z'$ into the nucleus with $N > Z$ is thus $\Delta E = \Sigma(x \delta E) \propto x^2 \Delta$. Notice that we could have made exactly the same argument for changing neutrons into protons to form a proton-rich nucleus. Finally, we should note that the energy levels in a bound nucleus are not equally spaced but bunch closer together as the total number of nucleons increases so that $\Delta \propto 1/A$. As a final matter of notation, we can replace $(N - Z)$ by $(A - 2Z)$ to remove the explicit dependence on N in the final expression.

5) The last term represents the special stability associated with completely paired proton and neutron spins in a nucleus called pairing. The pairing
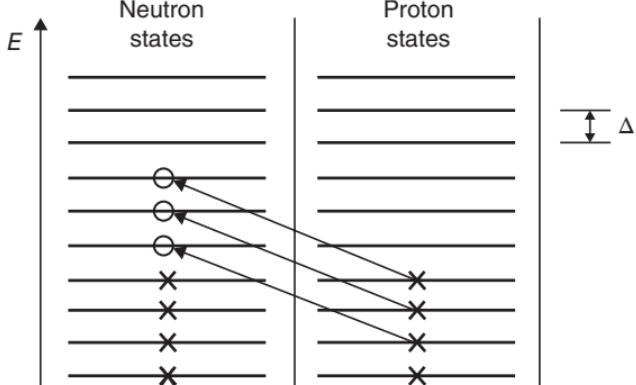
Figure 2.4 Schematic model of the energy changes when the nucleus $^A Z$ is created from an $N = Z$ nucleus (Meyerhof 1967). Reproduced with the permission of McGraw-Hill Book Company).
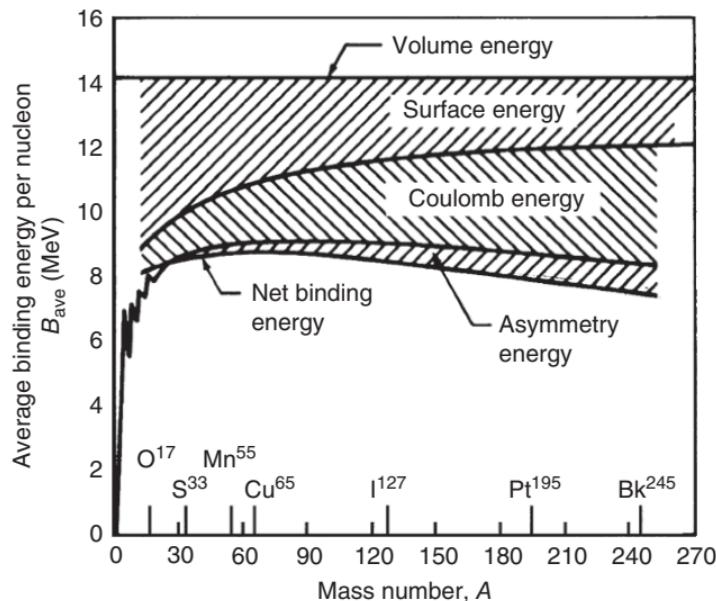
Figure 2.5 Relative contribution of the various terms in the semiempirical mass equation to the average binding energy per nucleon (Meyerhof 1967). Reproduced with the permission of McGraw-Hill Book Company).

energy term is chosen to be zero for odd A nuclides; select the additive form for e–e nuclides, and select the subtractive form for o–o nuclides.

The constants of the semiempirical binding energy equation have been determined by fitting the measured masses of a wide range of nuclei. A recent set of values of the coefficients are $a_v = 15.56$ MeV, $a_s = 17.23$ MeV, $a_c = 0.7$ MeV, $a_a = 23.285$ MeV, and $\delta = 11/A^{1/2}$ MeV. The relative contribution of each term to the binding energy per nucleon is shown in Figure 2.5. As expected, the largest constant contribution to the average binding energy per nucleon comes from the volume energy. The surface energy correction is most important for the lighter nuclei where the fraction of nucleons in the surface is greatest. Similarly the Coulomb energy correction is most important for the heaviest nuclei since it depends on Z^2. The asymmetry energy makes a smaller contribution that is most important in the heaviest nuclei where the N/Z ratio is the largest.

Sample Problem 2.4: Semiempirical Mass Equation

Calculate the average binding energy per nucleon of ^{58}Fe using the semi-empirical mass equation.

Solution

$$B_{\text{tot}}(A, Z) = a_v A - a_s A^{2/3} - a_c \frac{Z^2}{A^{1/3}} - a_a \frac{(A - 2Z)^2}{A} \pm \delta$$

$$= 15.56(58) - 17.23(58^{2/3}) - 0.7 \frac{26^2}{58^{1/3}} - 23.285 \frac{(58 - 52)^2}{58}$$

$$+ \frac{11}{58^{1/2}}$$

$$= 902.48 - 258.17 - 122.25 - 14.45 + 1.44 = 509.05 \text{ MeV}$$

and per nucleon:

$$\frac{B_{\text{tot}}(58, 26)}{A} = \frac{509.05}{58} \text{ MeV}/A$$

$$= 8.78 \text{ MeV}/A$$

Notice the relative contribution of the various terms of the binding energy.

Myers and Swiatecki (1966) have proposed a modification of the semiempirical mass equation that gives a better description of the experimental masses. This modification can be summarized in the following equation:

$$B_{\text{tot}}(A, Z) = c_1 A \left[1 - k \left(\frac{N - Z}{A} \right)^2 \right] - c_2 A^{2/3} \left[1 - k \left(\frac{N - Z}{A} \right)^2 \right]$$

$$- c_3 \frac{Z^2}{A^{1/3}} + c_4 \frac{Z^2}{A} + \delta \tag{2.21}$$

where c_1=15.677 MeV, c_2=18.56 MeV, c_3=0.717 MeV, c_4=1.211 MeV, $k = 1.79$, and $\delta = 11/A^{1/2}$. Myers and Swiatecki have added an asymmetry energy correction term (in the square brackets) to the volume and surface energy and also a correction to the Coulomb energy term (the c_4 term) due to the diffuseness of the nuclear surface.

We will now look at some of the predictions of the semiempirical mass equation. The first question we pose is what happens if we hold the mass number, A, constant and vary the atomic number, Z, (neglecting for a moment the pairing term). Recall from earlier that the mass is given by

$$M(Z, A) = [Z * M(^1\text{H}) + (A - Z)M(\text{n})]c^2 - B_{\text{tot}}(Z, A) \tag{2.22}$$

and without pairing

$$B_{\text{tot}}(Z, A) = a_v A - a_s A^{2/3} - a_c Z^2/A^{1/3} - a_a(A - 2Z)^2/A \tag{2.23}$$

we can expand the symmetry term:

$$\frac{a_a(A - 2Z)^2}{A} = \frac{a_a(A^2 - 4AZ - 4Z^2)}{A} = \frac{a_a(A - 4Z - 4Z^2)}{A} \tag{2.24}$$

Substituting back into the equation for the mass and collecting terms, we have

$$
\begin{aligned}
M = A &\left[\left(M(\text{n})c^2 - a_\text{v} + \left(\frac{a_\text{s}}{A^{1/3}} \right) + a_\text{a} \right) \right] \\
&+ Z[(M(^1\text{H})c^2 - M(\text{n})c^2 - 4a_\text{a})] + Z^2 \left(\frac{a_\text{c}}{A^{1/3}} + \frac{4a_\text{a}}{A} \right)
\end{aligned}
\tag{2.25}
$$

Thus, the mass equation at constant A takes on the form of a parabola ($\alpha + \beta Z + \gamma Z^2$) with respect to atomic number. The second term, β, is negative but the coefficient of Z^2, γ, is positive and so the parabola goes through a minimum for some value of Z, which is termed Z_A. Note that Z_A is not necessarily an integer. We can now ask ourselves how can we find the value of Z_A for a given atomic mass number, that is, what is the most favored value of Z for a given value of A? We can evaluate this by minimizing M with respect to Z at constant A, that is, we need to solve a simple partial differential equation:

$$
\left(\frac{\partial M}{\partial Z} \right)_{Z_A} = 0 = \beta + 2\gamma Z_A
\tag{2.26}
$$

$$
Z_A = \frac{-\beta}{2\gamma} = -\frac{M(^1\text{H}) - M(\text{n}) - 4a_\text{a}}{2\left(\frac{a_\text{c}}{A^{1/3}} + \frac{4a_\text{a}}{A} \right)}
\tag{2.27}
$$

Substituting numerical values for the coefficients from the semiempirical mass equation, we can write

$$
Z_A \sim \left(\frac{1}{2} \right) \frac{81}{80 + 0.6A^{2/3}}
\tag{2.28}
$$

Thus as A goes to 0, Z_A/A becomes equal to 1/2, that is, the most stable light nuclei are predicted to have $Z = N = A/2$. As A gets large, the Z_A/A becomes $< 1/2$, typically taking on a value of about 0.4. The underlying physics behind this trend is that, in the absence of a Coulomb repulsion between the protons, equal numbers of neutrons and protons are favored due to the asymmetry energy term. When Z gets large, the Coulomb energy becomes large. Nuclei with a larger number of neutrons are more stable among a given set of isotopes. Stability results when we have a balance between the Coulomb energy and the asymmetry energy.

Let us now consider the specific case of $A = 111$. From the previously mentioned relations, we can calculate $Z_A = 47.76$. The measured masses of the nuclei with $A = 111$ are shown in Figure 2.6. Note that the expected parabolic dependence of the mass on Z is present. The most stable nucleus has $Z = 48$ (Cd). All of the $A = 111$ nuclei that have more neutrons than ^{111}Cd can release energy when they decay by β^- decay, while the nuclei with fewer neutrons than ^{111}Cd will become more bound by β^+ or EC decay.

Now let us consider the neighboring case of nuclei with $A = 112$ (an even mass number). We calculate that $Z_A = 48.15$. Plotting the measured masses of

Figure 2.6 Mass excesses of the known nuclei with $A = 111$.
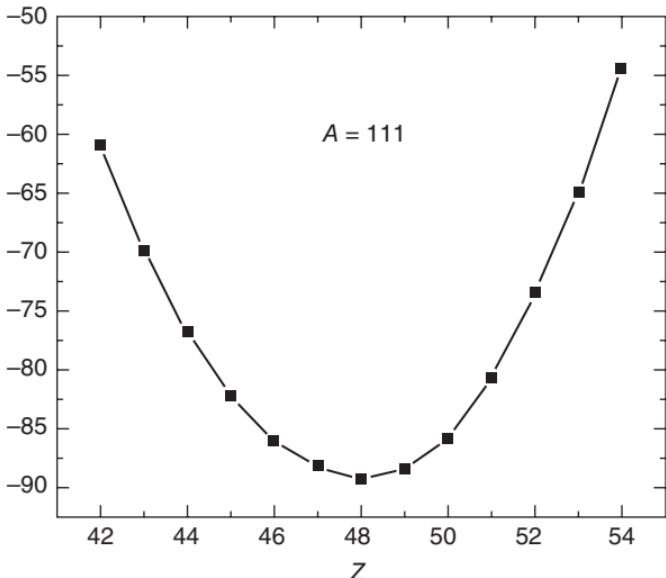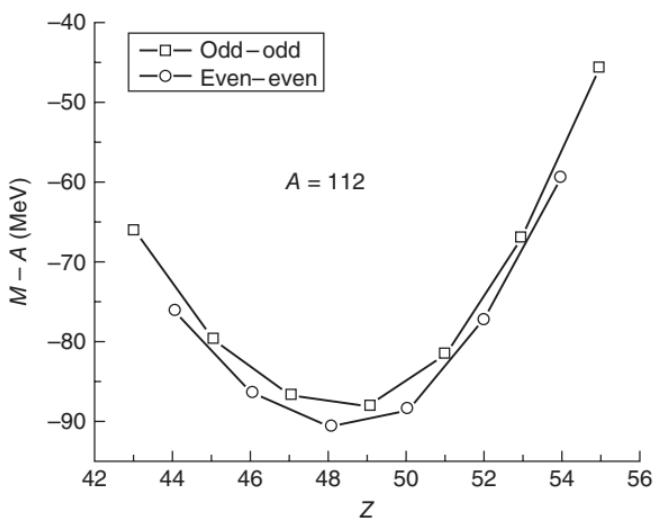
Figure 2.7 Mass excesses of the known nuclei with $A = 112$.

the $A = 112$ nuclei versus Z (Fig. 2.7) indicates that two parabolas are present, one for the even–even nuclei and one for the odd–odd nuclei, displaced from one another by an energy difference of 2δ, the pairing energy. Since all nuclei on the upper parabola (the o–o nuclei) can decay to a nucleus on the lower parabola (the e–e nuclei), we conclude that there should be no stable odd–odd nuclei. The only known exceptions to this prediction occur in the lightest nuclei where nuclear structure effects make ^{2}H, ^{6}Li, ^{10}B, and ^{14}N stable. Note that some odd–odd nuclei near stability can thus decay by both β^- and β^+ emission.
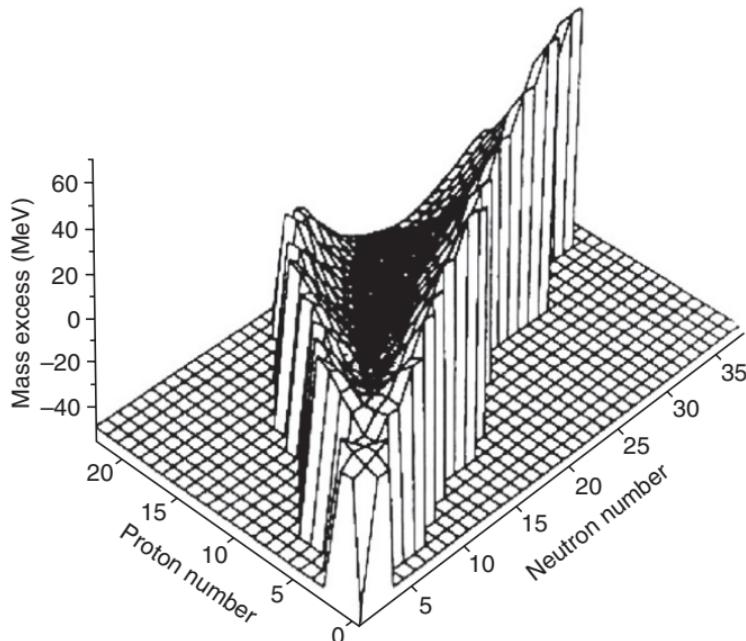
Figure 2.8 Plot of the nuclear mass excesses versus neutron number *N* and proton number *Z* for the light nuclei showing the nuclear mass surface and the valley of β stability (Halliday et al. (1992)). Reproduced with the permission of John Wiley & Sons).
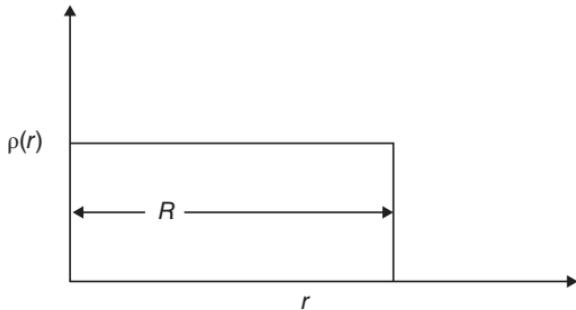
Note also that so-called double β decay is energetically possible ($^{112}\text{Pd} \rightarrow ^{112}\text{Cd} + 2\beta^- + 2\overline{\nu}_e$). This mode of decay has been observed in a few rare cases such as ^{130}Te and ^{82}Se and the half-lives for this mode of decay are very long ($t_{1/2} = 10^{20} - 10^{21}$ years). Active searches are underway for the so-called neutrinoless double β decay, for example, $^{136}\text{Xe} \rightarrow ^{136}\text{Ba} + 2\beta^-$, that would only be possible if the electron neutrino is its own antiparticle. Notice also that we can have more than one stable isotope for a given *A* but all of them will be even–even nuclei.

This parabolic dependence of the nuclear mass upon *Z* for fixed *A* can be used to define an overall nuclear mass surface for all *A* (Fig. 2.8). The position of the minimum mass for each *A* (most bound isobar) defines what is called the valley of β stability. β Decay is then visualized as moving down the walls of the valley toward the valley floor.

2.7 Nuclear Sizes and Shapes

We can ask: how big are nuclei? The basic answer is that the radii of *all* nuclei have been found to lie in the range of 1–10 fm. Our mathematical answer to this question begins by assuming the nucleus is spherical with a uniform density out to some sharp cutoff radius, that is, the nucleus has the shape and density

Figure 2.9 Schematic diagram of a nuclear density model with a constant density and a sharp cutoff (or hard edge).

distribution of a billiard ball. Such a uniform density distribution is shown in Figure 2.9. One can characterize this distribution by writing that the nuclear radius R is a simple function of A:

$$R = r_0 A^{1/3} \tag{2.29}$$

where the nuclear radius constant can be taken to be 1.2 fm for the "charge radius" and 1.4 fm for the "matter radius." What do we mean by this dichotomy? When one measures the nuclear radius by scattering high-energy electrons from the nucleus or when one measures the radius by scattering other nuclei from a given nucleus, one gets slightly different answers for the nuclear size. The electrons probe the charge distribution via the electromagnetic force, that is, the distribution of the protons, while other nuclei are sensitive to the matter distribution (neutrons plus protons) or the region over which the nuclear force can act. Which value of r_0 should one use in calculations? The answer depends upon the nuclear property being calculated and whether it is sensitive to the distribution of the nuclear charge or the nuclear matter.

A somewhat more sophisticated approach to the problem of defining the nuclear size and density is to assume that the nuclear density distribution, $\rho(r)$, has a diffuse surface, such as that given by the form of a Fermi distribution, that is,

$$\rho(r) = \frac{\rho_0}{1 + e^{(r-R)/a}} \tag{2.30}$$

where ρ_0 is the density in the interior of the nucleus (one can show that $\rho_0 = 0.172$ nucleons/fm^3), the parameter a is a measure of the diffuseness of the nuclear surface, and R is the half-density radius of the nucleus (Fig. 2.10). The half-density radius is given by the already familiar expression: $R = r_0 A^{1/3}$ with $r_0 = 1.12$ fm. The thickness of the nuclear skin, t, indicated in Figure 2.10 can be numerically connected to the diffuseness parameter as $t = 4a \ln(3) \sim 4.4a$. Most nuclei show a skin thickness, t, in the range of 2.4–2.5 fm. A physical meaning of this value of t can be gained by calculating the faction of the nucleons that lie in the skin region of the nucleus as a function of the nuclear size (Table 2.2).

Figure 2.10 Nuclear density distribution: (a) in a schematic presentation and (b) in an artist's conception (Mackintosh et al. (2001). Reproduced with the permission of The Johns Hopkins University Press). (*See insert for color representation of the figure.*)
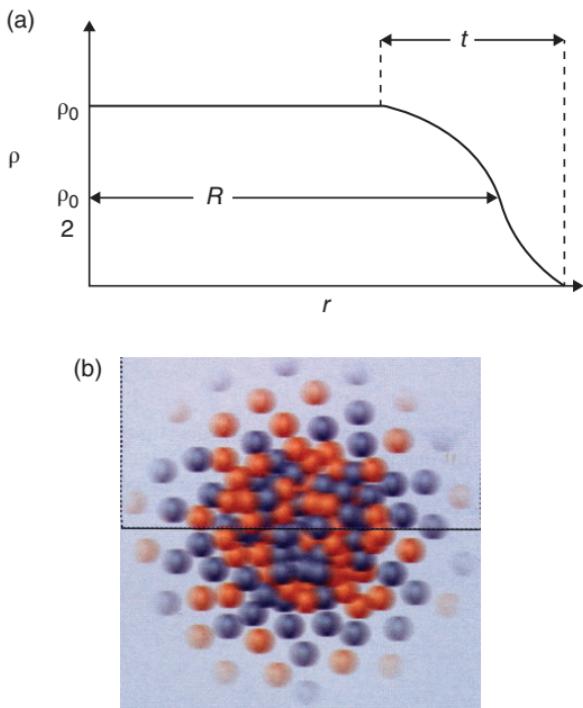
Table 2.2 Fraction of Nucleons in the Nuclear "Skin".

Nuclide	Fraction in "Skin"
^{12}C	0.90
^{24}Mg	0.79
^{56}Fe	0.65
^{107}Ag	0.55
^{139}Ba	0.51
^{208}Pb	0.46
^{238}U	0.44

Thus the lighter nuclei are mostly "skin" and the heaviest nuclei still have substantial "skin" regions. These approximate models for the nuclear size and density distribution can be compared (favorably) to the measured distributions for typical nuclei (Fig. 2.11).

Up to this point, we have assumed that all nuclei are spherical in shape. That is not true. Most nuclei can stretch when they are rapidly rotated, called dynamic deformation, and there are regions of nuclei that have substantial nuclear deformation in their ground states, for example, the rare earths ($150 < A < 180$) and
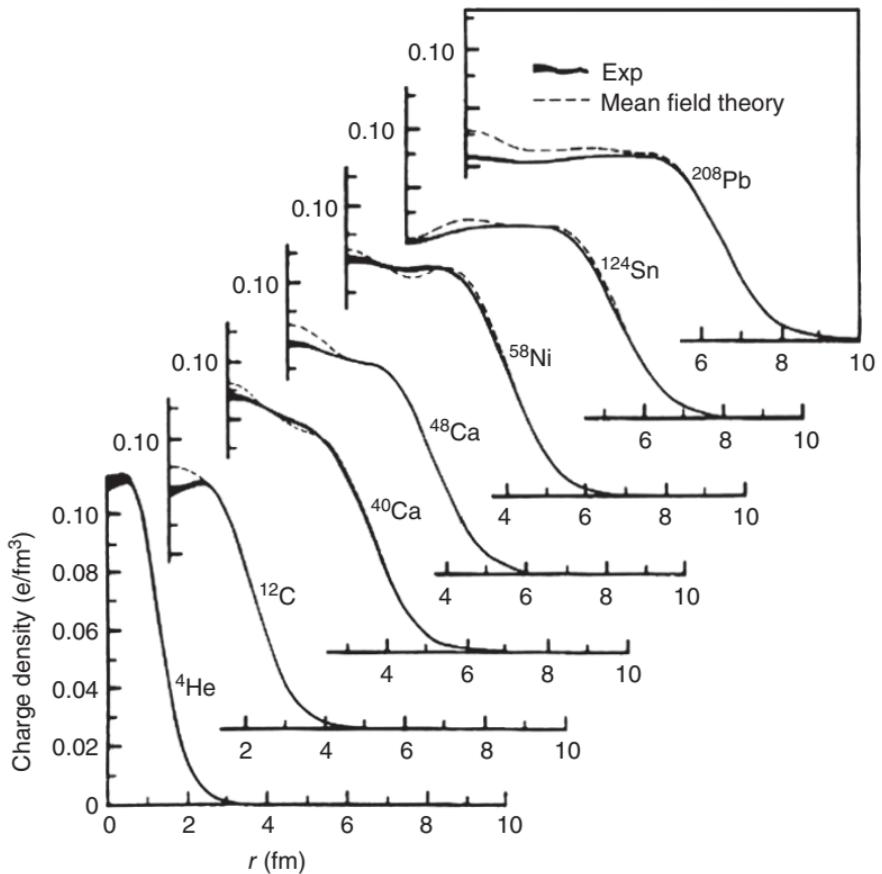
Figure 2.11 Measured nuclear ground state charge distributions for a sample of nuclei from across the periodic table (From Frois (1983)).

the actinides ($220 < A < 260$). We shall discuss these cases in more detail later in this chapter as we discuss the electric moments of nuclei.

Another question we might pose to ourselves is whether the neutron and proton distributions in nuclei are the same. Modern models for the nuclear potential predict the nuclear skin region to be neutron rich. The neutron quantum mechanical well is predicted to extend out to larger radii than the proton potential. Extreme examples of this behavior are the halo nuclei. A halo nucleus is a very neutron-rich (or perhaps proton-rich) nucleus (up to now only observed for small values of A) where the outermost nucleons are very weakly bound. The density distribution of these weakly bound outermost nucleons extends beyond the radius expected from the $R = A^{1/3}$ rule. Proven examples of these nuclei are ^{11}Be, ^{11}Li, and ^{19}C. The most well-studied case of halo nuclei at present is ^{11}Li. In this nucleus the two outermost nucleons are so weakly bound (a few hundred keV each) as to make the apparent size of ^{11}Li equal to the size of a ^{208}Pb nucleus (see Fig. 2.12).
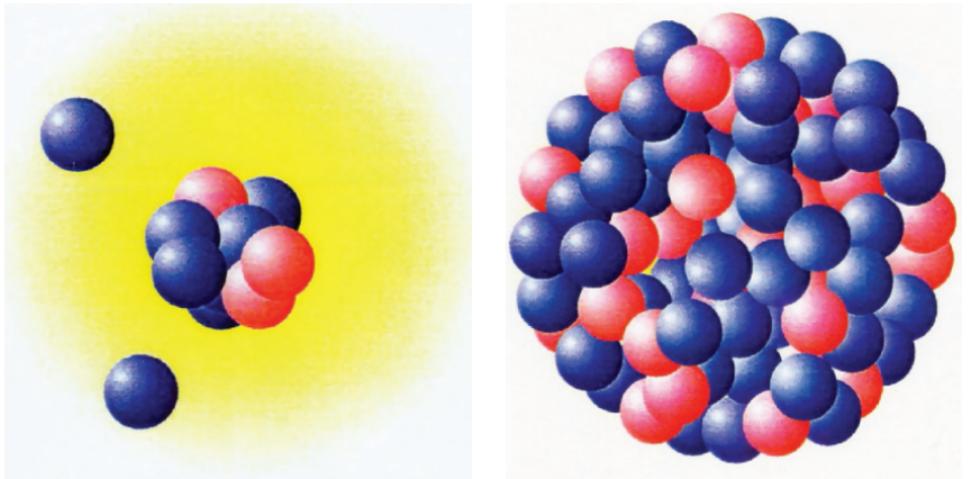
Figure 2.12 Artistic representation of the relative sizes of the halo nucleus ^{11}Li and ^{208}Pb. (*See insert for color representation of the figure.*)

2.8 Quantum Mechanical Properties

2.8.1 Nuclear Angular Momentum

In fact, an essential underlying part of chemical behavior is that the electron has an intrinsic angular momentum, called spin with a value of $1/2\ \hbar$. That is, the electron behaves as if it is rotating or spinning about an internal axis. The electron spin angular momentum provides an important criterion for assigning quantum numbers to atomic electrons through the Pauli principle and thus has far-reaching consequences. The electrons occupy quantum mechanical states or orbitals that carry two labels: the principal quantum number, N, with a numerical value of one plus the number of radial nodes in the atomic wave function and the angular momentum quantum number, ℓ, the number of angular nodes in the wave function. The electrons distribute themselves among those states with degenerate energies so that their spin angular momenta, s, are aligned to the maximal extent (described by Hund's rules). The atom can be characterized by a total angular momentum, J, that is made up from the total orbital motion of all the electrons given the symbol, L, and a total intrinsic spin given the symbol, S. The values of L and S are obtained by separate vector couplings of the two types of angular momenta of the electrons. The electrons in all but the heaviest atoms exhibit such "LS" coupling.

The neutron and the proton also have an intrinsic angular momentum, $s = 1/2\hbar$, and so each appears as if it is spinning about an internal axis. Thus, we can expect that a large nucleus, which contains a number of neutrons and protons, will have a total intrinsic angular momentum, or a nuclear spin from

the combination of the intrinsic spins of the neutrons and protons. Similarly, we can imagine that neutrons and protons will occupy discrete states in the nucleus, and some of these states will have orbital angular momenta in a manner similar to the orbital angular momenta of electronic states ($\ell = 1$, p-states, etc.), and there should be a total angular momentum of the nucleons. While there are such similarities, the fact that the potential well for nucleons has a dramatically different shape from the central Coulomb potential for electrons introduces several important differences in the concepts needed to describe nuclear states and levels. The detailed discussion of the quantum mechanical structure of nuclei is presented in Chapter 6. At this point we only need to address the overall features.

The orbital angular momenta of the nuclear (and atomic) states are all integer multiples of $\hbar$ starting with zero. Individual nucleons exhibit a strong coupling of their orbital and spin angular momenta such that $j = \ell + s$ is the appropriate quantum number to describe the orbit of a nucleon. We can immediately see that the sum of the intrinsic spins of all the nucleons with their orbital motion in a nucleus will always give half-integer values for the total spin given the label, I, of any odd A nucleus and will give integer values for any even A nucleus.

$$\text{odd } A \text{ nuclei} : I = \frac{1}{2}, \frac{3}{2}, \frac{5}{2}, \ldots \tag{2.31}$$

$$\text{even } A \text{ nuclei} : I = 0, 1, 2, \ldots \tag{2.32}$$

The numerical value obtained for a specific nucleus will depend on the filling of the nuclear states with angular momenta j and on the coupling of all of those angular momenta. At first glance we might expect that a large nucleus could have a very large intrinsic angular momentum. However, recall that the nuclear force has a short range and that the nucleons are more strongly bound when they are in close proximity. Two nucleons will be in the closest proximity when they are in the same orbital. If the two nucleons in the same orbital are both neutrons or both are protons, then their spins must be opposed in order to satisfy the Pauli Principle so that each has a unique set of quantum numbers. So we find that the nuclear force tends to put pairs of nucleons into the same orbitals, and their orbital angular momenta and intrinsic spins will cancel, summing to zero. (This behavior is opposite from that of atomic electrons.) Thus, the angular momenta of the ground states of nuclei tend to be small, even for nuclei with hundreds of nucleons in states with very high angular momenta. For example, the ground state nuclear spins of all even–even nuclei are zero!

Parity, as used in nuclear science, refers to the symmetry properties of the wave function for a particle or a system of particles. If the wave function that specifies the state of the system is $\Psi(r, s)$ where r represents the position coordinates of the system, for example, (x, y, z), and s represents the spin orientation, then $\Psi(r, s)$ is said to have positive or even parity when

$$\Psi(r, s) = +\Psi(-r, -s) \tag{2.33}$$

where the minus signs indicate the sign of the spatial coordinates has been reversed as well as the direction of the spin. On the other hand, when

$$\Psi(r, s) = -\Psi(-r, -s) \qquad (2.34)$$

the system is said to have negative or odd parity. For a central potential, one in which the potential energy, $V(r)$, only depends on the distance from the center and not the spatial orientation, the parity, denoted as π, for a state with angular momentum, ℓ, is given by

$$\pi = (-1)^{\ell} \qquad (2.35)$$

Thus, s and d orbitals have positive or even parity, while p and f orbitals have negative parity. The spin and parity of a given nuclear state are usually used as labels for that state so that a state with $j = 7/2$ and negative parity is referred to as a 7/2-state.

2.9 Electric and Magnetic Moments

2.9.1 Magnetic Dipole Moment

The magnetic moment of a nucleus is a measure of the average electric current in that nucleus, while the electric moment is a measure of the distribution of electric charge. These are both fundamental properties of the nucleus and can be used to test models of nuclear structure. Since the magnetic moment may not be a familiar concept, we will begin by discussing a simple example of a "classical" magnetic moment that arises from the motion of an electron. An electron moving with a velocity v in a circular orbit with a radius r as indicated in Figure 2.13. The magnetic dipole moment of this moving charge is defined as the product of the area of the loop made by the electron, A, and the current, i. The area of the circle is πr^2 and the current i is given by the ratio of the electron charge to the time to complete a loop or $i = e/(2\pi r/v)$. Combining these parts, we get for the magnetic moment
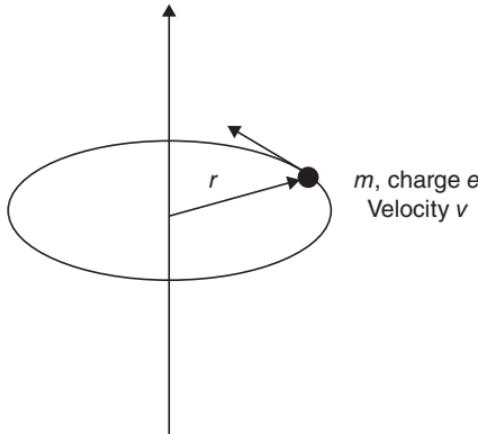
$$|\mu| = iA = \left(\frac{ev}{2\pi r}\right)(\pi r^2) = \frac{evr}{2} \qquad (2.36)$$

The absolute value sign on the magnetic moment is to emphasize that the electron motion has a direction. Recall that the angular momentum of the electron moving in a circle, $\ell \hbar = m_0 v r$. Substituting for vr,

$$|\mu| = \frac{e\ell \hbar}{2m_0} \qquad (2.37)$$

Notice that $e/2m_0$ is a constant, which is called the gyromagnetic ratio, and given the symbol γ, so that $|\mu| = \gamma \ell \hbar$. We can remove the absolute value sign by recalling that the projection of the angular momentum $\ell \hbar$ is $m_\ell \hbar$, which

Figure 2.13 Representation of a moving system that would generate a classical dipole moment.

includes information on the direction of rotation. The usual expression for magnetic dipole moment due to the orbital motion of the electron is thus

$$\mu = \left(\frac{e}{2m_0} \right) m_\ell \hbar = m_\ell \mu_B \tag{2.38}$$

where the constants are collected into a single number, μ_B, called the Bohr magneton with the value of 5.78×10^{-5} eV/Tesla or 9.27×10^{-21} erg/gauss. Recall that the electron also has an intrinsic spin, $s = 1/2\hbar$, and so the electron will have an intrinsic additional component to its magnetic moment due to this spin.

Extending these ideas to nucleons, we can expect that a proton in a nucleus will have an intrinsic magnetic moment due to its spin and an additional part if it has orbital motion. A neutron, on the other hand, will only have the intrinsic magnetic moment. We can define a nuclear magneton, μ_N, similar to that mentioned earlier as $\mu_N = e\hbar/2m_p$ that has the numerical value of 3.15×10^{-8} eV/Tesla or 5.50×10^{-24} erg/gauss. Note that the nuclear magneton is smaller than the Bohr magneton by the ratio of the proton to electron masses of ~ 1840. Thus, the magnetic moment of a proton due to orbital motion is

$$\mu_\ell^{\text{proton}} = m_\ell \mu_N \tag{2.39}$$

It is traditional to expand the definition of the magnetic moment by including a constant of proportionality called the gyromagnetic ratio or simply *g*-factor:

$$\mu = g_\ell m_\ell \mu_N \tag{2.40}$$

By adding a constant of proportionality, we are anticipating that the magnetic moment for a nucleus will be the net result of a complicated cancellation process. For example, we would expect $g_\ell = 1$ for the orbital motion of a proton due to its charge, but $g_\ell = 0$ for a neutron since it is uncharged. Both neutrons and protons have intrinsic spins and so, by extension, we can expect additional contributions to the total magnetic moment with the form

$$\mu_s = g_s m_s \mu_N \tag{2.41}$$

where the projection $m_s = 1/2$ for a proton or neutron. The spin g-factor for electrons, $g_s = 2.0023$, has been calculated exactly with the relativistic Dirac equation for electrons and includes known higher-order correction terms. This value is in excellent agreement with a long series of very precise measurements of the magnetic moment of electrons. However, the measured values of g_s for both the proton and the neutron are different and surprisingly large:

$$\text{Proton}: g_s = 5.5856912(22) \tag{2.42}$$

$$\text{Neutron}: g_s = -3.8260837(18) \tag{2.43}$$

Thus, if the electron is an "elementary" particle with no internal components, both the proton and the neutron do not appear to be elementary particles based on their magnetic moments. Rather they both seem to have internal (moving) constituents. For example, the neutron that has exactly zero net charge has a nonzero magnetic moment that is opposite in direction to that of a proton. It was noted some time ago that the magnetic moment of the proton is larger than the expected value of "2" and that of the neutron is smaller than its expected value of "0" by about the same amount of 3.8 units. Older models of the nuclear force attributed these differences to "clouds" of mesons surrounding the nucleons. In the modern theory of quantum chromodynamics, the nucleons are themselves made up from three quarks, each quark with its own magnetic moment and electronic charge.

Similar to the total angular momentum of a nucleus, the net magnetic moment of a nucleus will be made up from all of the contributions from the individual nucleons. As before, a very large fraction of the nucleons will be paired and the two contributions from the partners will cancel. Thus, the net magnetic moment of a given nucleus will tend to be small and may be dominated by a small number of unpaired nucleons.

The presence of a net magnetic dipole moment in nuclei that have an intrinsic spin has found enormous application in nuclear magnetic resonance (NMR) and magnetic resonance imaging (MRI). NMR is extensively used in chemical laboratories to identify the structural and chemical environments of the nuclei in molecules, whereas MRI uses a tomographic technique to locate specific molecules on a microscopic scale. Both techniques rely on the splitting of the energies of the magnetic substates by a (strong) external magnetic field. NMR measures tiny shifts in the relative energies of the magnetic substates due to induced magnetization of the local electron density by the nuclear spin to provide information on the chemical environment. These states have a fine structure or splitting due to the presence of neighboring magnetic nuclei that provide information on the structure of the molecule. MRI applies a spatially varying magnetic field to detect the resonance of a single type of nucleus, originally the hydrogen nuclei in water and aliphatic compounds, and to measure the concentration in a three-dimensional space. More recent functional-MRI

or f-MRI uses transitions in specific molecules. Both techniques are nondestructive and can be applied to living systems. The concentration of water molecules varies widely in tissues and other biological media and can easily provide detailed microscopic images for medical purposes.

Sample Problem 2.5: Magnetic Moment

Make an estimate of the ground state magnetic moment of ^{15}N if the nuclear spin, $I = 1/2$, is due to an unpaired proton in an $\ell = 0$ orbital.

Solution

Since all the nucleons are paired except one proton,

$$
\begin{aligned}
\mu_{tot} &= \mu_\ell^p + \mu_s^p \\
&= g_\ell^p m_\ell \mu_N + g_s^p m_s \mu_N \\
&= (2*0 + 5.5856912 * 1/2)\mu_N = +2.7928456\mu_N
\end{aligned}
$$

2.9.2 Electric Quadrupole Moment

Up to this point we have considered nuclei to be spherical with a uniform distribution of electric charge. If the nucleus had a static dipolar charge distribution, then the distributions of protons would be asymmetric in space—something that has never been observed. A number of studies have been carried out and others are underway to determine if static dipolar nuclear charge distributions are possible. On the other hand, a nucleus could be symmetrically stretched or squashed, which would give rise to a quadrupolar charge distribution.

Measurements of a nonzero electric quadrupole moment of a nucleus implies a nonspherical charge distribution. We can use a little calculus to obtain an expression for the shape of a nucleus in terms of its quadrupole moment. Imagine the nucleus is an extended charged object as sketched in Figure 2.14. Consider trying to calculate the electric potential energy at some point P, which is at a distance D from the center of this charged object (nucleus). First we can evaluate the potential, $d\Phi$, at point P due to a charge at a distance r from the
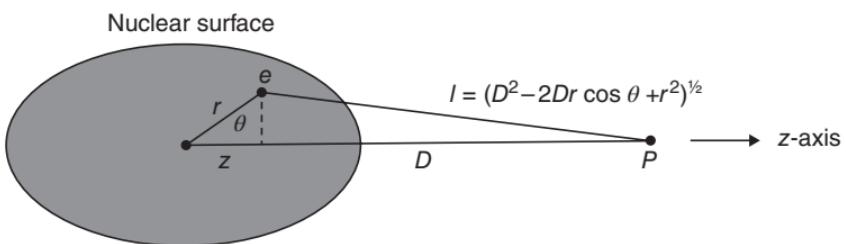
Figure 2.14 Geometry used for the potential at an external point due to an extended charged object (Harvey (1969). Reproduced with the permission of Pearson Education).

center of the charge object where the line from the center of the object to the charge makes an angle θ with the line connecting the center of the object with the point P (cf. Fig. 2.14). If the density of charge in the object as a function of position is given by the function $\rho(\theta, \phi, r)$, then the total charge at point P is $\rho(r, \theta, \phi)d\tau$ or $\rho(r, \theta, \phi)(r^2 dr \sin \theta d\theta d\phi)$. We can write the potential at P using the law of cosines for the distance

$$\frac{d\Phi = \rho(\theta, \phi, r)d\tau}{\ell} = \frac{\rho(\theta, \phi, r)d\tau}{[D^2 + r^2 - 2Dr \cos \theta]} \tag{2.44}$$

Factoring out the distance, D, and substituting the first and second Legendre polynomials

$$P_1(\cos \theta) = \cos \theta, P_2(\cos \theta) = \frac{3}{2}\cos^2 \theta - \frac{1}{2} \tag{2.45}$$

we get a series expansion for the potential

$$d\Phi = \frac{\rho d\tau}{D}\left(1 + \frac{r}{D}P_1(\cos \theta) + \left(\frac{r}{D}\right)^2 P_2(\cos \theta) + \ldots\right) \tag{2.46}$$

This expression can be integrated over the entire volume of the charged object to get an expression for the total charge:

$$V = \frac{1}{D}\left[\int \rho d\tau\right] + \frac{1}{D^2}\left[\int \rho r \cos \theta d\tau\right] + \frac{1}{D^3}\left[\int \rho r^2 \left(\frac{3}{2}\cos^2 \theta - \frac{1}{2}\right)d\tau + \ldots\right] \tag{2.47}$$

The first term in the square bracket in this equation is the electric monopole moment, which is equal to the nuclear charge, Ze. The second term in the square bracket is the electric dipole moment, while the third term in the square bracket is the electric quadrupole moment. For a quantum mechanical system in a well-defined quantum state, the charge density ρ is an even function and because the dipole moment involves the product of an even and an odd function, the corresponding integral is identically zero. Therefore, there should be no electric dipole moment for nuclei or any other odd electric moment. For spherical nuclei, the charge density ρ does not depend on θ, and thus the quadrupole moment Q, given by the expression

$$Q = \int \int \int \rho(r)r^2\left(\frac{3}{2}\cos^2 \theta - \frac{1}{2}\right)r^2 dr \sin \theta d\theta d\phi \tag{2.48}$$

would be exactly zero. However, an axially deformed shape has a dependence on θ (but not ϕ), then the quadrupole moment becomes a measure of the non-sphericity or shape of the nucleus. We can further elaborate on this by making a simple model (Fig. 2.15) for nonspherical nuclei. We shall assume such nuclei are ellipsoids with a shape generated by rotating an ellipse about one of its axes. We can define a semiminor axis of the ellipse, c, and a
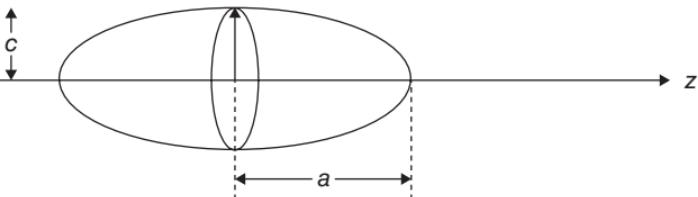
Figure 2.15 A sketch of the semimajor, a, and semiminor axis, c in a prolate ellipsoid.

semi-major axis, a. (a is the axis about which the ellipse was rotated.) If a is the long axis, we have generated a prolate spheroid (the shape of a rugby ball). If a is the short axis, we have generated an oblate spheroid (a flattened sphere). The quadrupole moment of these ellipsoids is given by,

$$Q = \frac{2}{5}Ze(a^2 - c^2) \tag{2.49}$$

and we also know the square of the mean radius R of the spheroid is related to the two semiaxes by

$$R^2 = \frac{1}{2}(a^2 + c^2) = \left(r_0 A^{1/3}\right)^2 \tag{2.50}$$

Given a measurement of Q, we can solve the two axes of the spheroid. Thus, the quadrupole moment gives us a direct measure of the shape of nuclei. Note further that Q has the dimensions of charge times area. It is common to tabulate Q/e, which has the dimensions only of area. The nuclear dimension of area is the barn, which is equal to 10^{-24} cm^2, hence quadrupole moments are frequently tabulated in barns. Some of the experimental values of the electric quadrupole moments are shown in Figure 2.16. Note (Fig. 2.16) that the rare earth and actinide nuclei have prolate shapes (positive values of Q), while there are other nuclei with oblate shapes (negative values of Q). The amount of deformation of nuclei is rather small overall and one often sees exaggerated depictions of deformed nuclei.

Sample Problem 2.6: Quadrupole Moment

Calculate the ratio of the semimajor to semiminor axes of the prolate nucleus ^{177}Hf given $Q = +3.0$ e-barns.

Solution

Two equations are required. First equation:

$$Q = \frac{2}{5}Ze(a^2 - c^2)$$
$$(a^2 - c^2) = \frac{Q/e}{2Z/5} = \frac{+3.0 \times 10^{-24}\ \text{cm}^2}{2 \times 72/5}$$
$$= 1.04 \times 10^{-25}\ \text{cm}^2$$
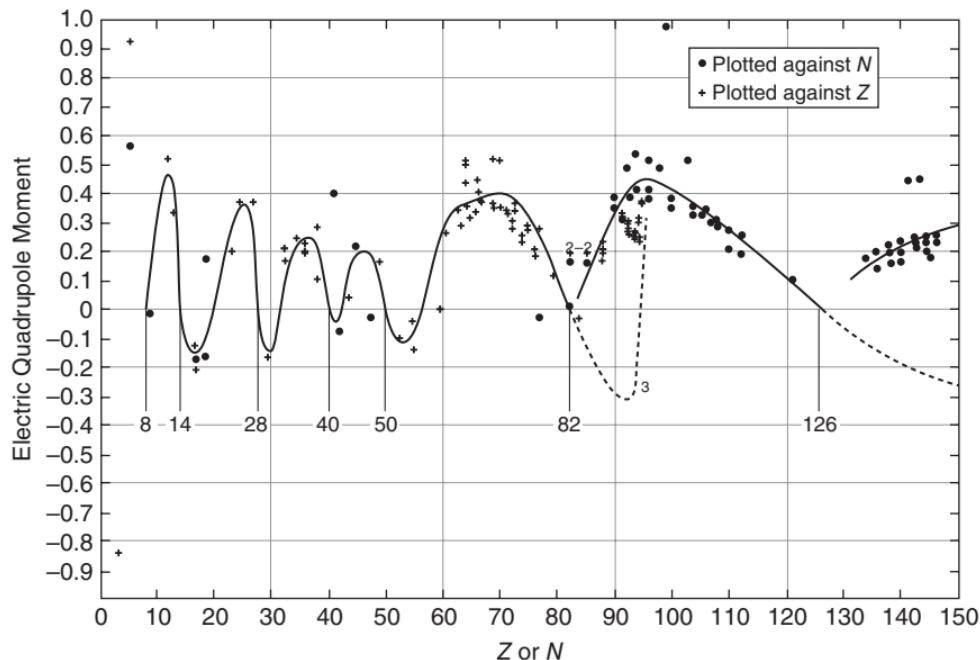
Figure 2.16 Experimental values of the electric quadrupole moment of nuclei. The lines are drawn through the data to emphasize the (Preston (1962). Reproduced with the permission of Pearson Education).

Second equation:

$$R^2 = \frac{1}{2}(a^2 + c^2) = \left(r_0 A^{1/3}\right)^2$$

$$(a^2 + c^2) = 2r_0^2 A^{2/3} = 2(1.2 \times 10^{-13} \text{ cm})^2 (177)^{2/3}$$

$$= 9.08 \times 10^{-25} \text{ cm}^2$$

Add the two results:

$$(a^2 + c^2) + (a^2 - c^2) = 2a^2 = 1.012 \times 10^{-24} \text{ cm}^2$$

$$a = 7.1 \times 10^{-13} \text{ cm}$$

$$c = 6.3 \times 10^{-13} \text{ cm}$$

Notice that the difference between the two axes is only ~12%.

Problems
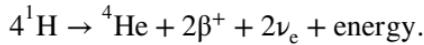
2.1 Define or describe the following terms or phenomena in your own words: nuclear surface energy, parity, asymmetry energy, packing fraction, nuclear magneton, mass defect, and magnetic dipole moment.

2.2 The total nuclear binding energies of ^{27}Mg, ^{27}Al, and ^{27}Si are 244.2667, 246.8741, and 241.6741 MeV, respectively. Determine the values of the Coulomb energy and asymmetry energy coefficients of the semiempirical mass equation using (only) these data.

2.3 Explain why we expect that there should not be any stable odd–odd nuclei. What are the exceptions to this rule?

2.4 Explain why in the sequential decay of ^{238}U to ^{206}Pb by successive α and β^- decays, one sees one or two successive α decays followed by β^- decays and others. That is, why are there no β^+ or EC decays in this chain?

2.5 Use the semiempirical mass equation to derive an expression for the energy released in α decay. For fixed Z, how does the predicted energy release depend on A?

2.6 Assume that a reanalysis of mass data gave the following set of parameters for the semiempirical mass equation: $a_v = 15.835$, $a_s = 18.33$, $a_a = 23.20$ and $a_c = 0.714$. Show that the binding energy per nucleon reaches a maximum for $Z \sim 26$ (iron) with the assumption that $Z = N = A/2$ and neglect pairing.

2.7 Some nuclei can decay by either β^- or β^+ emission. Use the semiempirical mass equation to show that such nuclei must have even A and odd N.

2.8 Use the semiempirical mass equation to compute, for a given A, a relation between Z and N for a nucleus that has $S_n = 0$ (i.e., a nucleus on the neutron "drip-line"). Compute the value of N/Z for the neutron drip line nucleus with $A = 100$.

2.9 Use the semiempirical mass equation to calculate the percentage contribution to the average binding energy per nucleon of each of (a) the volume energy, (b) the surface energy, (c) the Coulomb energy, and (d) the asymmetry energy for ^{56}Fe and ^{235}U.

2.10 The red giant stars, which are cooler than the sun, are thought to produce energy from reactions such as

$$^9\text{Be} + {}^1\text{H} \rightarrow {}^6\text{Li} + {}^4\text{He} + \text{energy}$$

From the masses tabulated in the Appendix B, calculate the energy release for this reaction and the fraction of the initial mass of the reactants converted to energy.

2.11 The sun yields ~ 2 cal/min-cm^2 at the surface of the Earth. Assuming that all the sun's energy is produced by the reaction,

$$4{}^1\text{H} \rightarrow {}^4\text{He} + 2\beta^+ + 2\nu_e + \text{energy}.$$
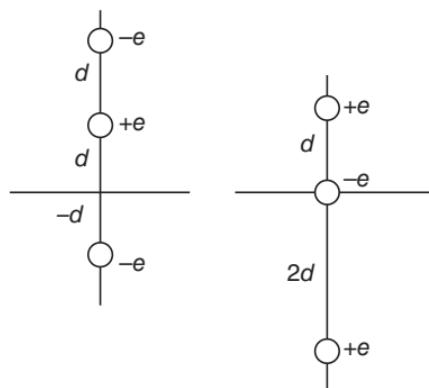
How much helium does the sun produce per year? The distance of the Earth from the sun is 1.49×10^6 km.
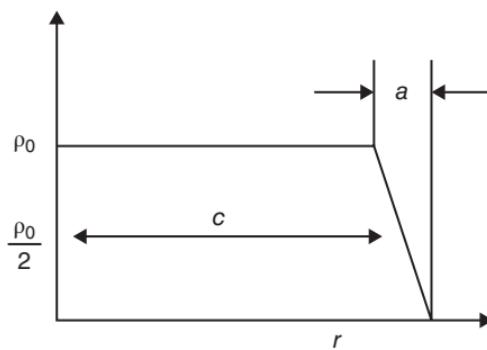
2.12 Consider the three isobaric nuclei ^{15}C, ^{15}N, and ^{15}O. Which of these nuclei is stable? What type(s) of radioactive decay would the other two undergo? Calculate the binding energy difference between ^{15}N and ^{15}O. Assuming this difference comes from the Coulomb term in the semiempirical binding energy equation, estimate the nuclear radius of these nuclei.

2.13 Compute and graph the mass parabola(s) for $A = 180$. Which isobar or isobars are stable against radioactive decay? Predict the type(s) of decay and their energies for the isobars near stability.

2.14 Calculate the electric quadrupole moment along the z-axis of a charge with a magnitude of Ze distributed over a ring of radius R centered on and perpendicular to that axis.

2.15 The ground state quadrupole moment of ^{152}Eu is $+3.16 \times 10^2$ fm^2. Assuming that it is an ellipsoid, deduce the ratio of semimajor to semiminor axes for this nucleus.

2.16 Find the electric dipole moment and electric quadrupole moment of the system with two positive point charges with a value of $+q$, both positioned along the z-axis, one at $z = -a/2$ and the other at $z = -a/2$.

2.17 Show that the quadrupole moment, Q, of a uniformly charged ellipsoid about the axis of symmetry is $(2/5)Z(b^2 - a^2)$ where a and b are the semiaxes, b being along the axis of symmetrical distortion of the sphere. Show that the quadrupole moment about an axis making an angle β with respect to the axis of symmetry is $[(3/2)\cos^2\beta - 1/2]Q$.

2.18 For ^{181}Ta, $Q/e = 4.20$ barns. Calculate the ratio of the semimajor to semiminor axes of this nucleus.

2.19 The quadrupole moments of ^{176}Lu and ^{127}I are 7.0 and -0.6 e-barns, respectively. Assume that ^{176}Lu and ^{127}I are ellipsoids of revolution obtained by deforming (without volume change) a sphere of radius

$R = 1.4A^{1/3}$ fm. Calculate the ratio of the semimajor to semiminor axes, a/b for each of these nuclei.

2.20 Calculate the electric monopole, dipole, and quadrupole moments of the arrangements of charge shown below. Hint: The integrals over the charges can be replaced by a sum in these systems with discrete charges.

2.21 Suppose that the nuclear density ρ varies with radial distance r from the center of the nucleus as shown below. What fraction of the nucleons would lie in the surface region (taken to be the sloping region) for the nuclei: ^{28}Si, ^{132}Sn, and ^{208}Pb if $\rho_0 = 0.17$ nucleons/fm^3, $c = 1.2 \, A^{1/3}$fm, and $a = 2.4$ fm?

2.22 (a) What regions of the periodic table are characterized by large permanent prolate nuclear deformations? (b) What nuclei in the periodic table have the highest binding energy per nucleon?

Bibliography

R.D. Evans, *The Atomic Nucleus* (McGraw-Hill, New York, 1955).

B. Frois, Proceedings of the International Conference on Nuclear Physics, Florence, August 29 to September 3 (1983), P. Blasi and R.A. Ricci, Eds. (Tipografia Compositori, Bologna), Volume **2**, p. 221.

B.G. Harvey, *Introduction to Nuclear Physics and Chemistry*, 2nd Edition (Prentice-Hall, Englewood Cliffs, 1969).

R.W. Hasse and W.D. Myers, *Geometrical Relationships of Macroscopic Nuclear Physics* (Springer, Berlin, 1988).

K.S. Krane, *Introductory Nuclear Physics* (John Wiley & Sons, Inc., New York, 1988).

R. Mackintosh, J. Al-Khalili, B. Jonson, and T. Pena, *Nucleus: A Trip to the Heart of Matter* (Johns Hopkins University Press, Baltimore, 2001).

W.E. Meyerhof, *Elements of Nuclear Physics* (McGraw-Hill, New York, 1967).

W.D. Myers and W.J. Swiatecki, Nucl. Phys. **81**, 1 (1966).

M.A. Preston, *Physics of the Nucleus* (Addison-Wesley, Reading, 1962).

R. Resnick, D. Halliday, and K.S. Krane, *Physics*, 4th Ed., Wiley, New York 1992.

L. Valentin, Subatomic Physics: Nuclei and Particles, Volume **II** (North-Holland, Amsterdam, 1981).

S.S.M. Wong, *Introductory Nuclear Physics, Second Edition* (John Wiley & Sons, Inc., New York, 1998).

3

Radioactive Decay Kinetics

The number of nuclei in a radioactive sample that disintegrate during a given time interval decreases exponentially with time. Because the nucleus is insulated by the surrounding cloud of electrons, this rate is essentially independent of pressure, temperature, the mass action law, or any other rate-limiting factors that commonly effect chemical and physical changes.[1]

As a result, this decay rate serves as a very useful means of identifying a given nuclide. Since radioactive decay represents the transformation of an unstable radioactive nuclide into a more stable nuclide, which may also be radioactive, it is an irreversible event for each nuclide.

The unstable nuclei in a radioactive sample do not all decay simultaneously. Instead the decay of a given nucleus is an entirely random event. Consequently, studies of radioactive decay events require the use of statistical methods. With these methods, one may observe a large number of radioactive nuclei and predict with fair assurance that, after a given length of time, a definite fraction of them will have disintegrated but not which ones or when.

3.1 Basic Decay Equations

Radioactive decay is what chemists refer to as a first-order reaction; that is, the rate of radioactive decay is proportional to the number of each type of radioactive nuclei present in a given sample. So if we double the number of a given type of radioactive nuclei in a sample, we double the number of particles emitted by the sample per unit time.[2]

---

1 In the case of electron capture and internal conversion, the chemical environment of the electrons involved may affect the decay rate. For L-electron capture in ^{7}Be ($t_{1/2} = 53.3$ days), the ratio of $t_{1/2}^{\mathrm{BeF_2}}/t_{1/2}^{\mathrm{Be}}$ is 1.00084. Similarly, a fully stripped radioactive ion cannot undergo either EC or IC decay, a feature of interest in astrophysics.
2 To make this statement completely correct, we should say that as we double the number of nuclei present, we double the rate of particle emission. This rate is equal to the number of particles emitted per unit time, provided that the time interval is small.

This relation may be expressed as follows:

- The rate of particle emission = the rate of disintegration of radioactive nuclei $\propto$ the number of radioactive nuclei present

Note that the foregoing statement is only a proportion. By introducing the decay constant, it is possible to convert this expression into an equation as follows:

- The rate of disintegration of radioactive nuclei = decay constant × number of radioactive nuclei present

The decay constant, λ, represents the average probability per nucleus of decay occurring per unit time. Therefore we are taking the probability of decay per nucleus, λ, and multiplying it by the number of nuclei present so as to get the rate of particle emission. The units of rate are (disintegration of nuclei/time) making the units of the decay constant (1/time), that is, probability/time of decay.

To convert the preceding word equations to mathematical statements using symbols, let N represent the number of radioactive nuclei present at time t. Then, using differential calculus, the preceding word equations may be written as

$$-\frac{dN}{dt} \propto N \tag{3.1}$$

$$-\frac{dN}{dt} = \lambda N \tag{3.2}$$

Note that N is constantly decreasing in magnitude as a function of time. Rearrangement of this equation to separate the variables gives

$$\frac{-dN}{N} = -\lambda dt \tag{3.3}$$

If we say that at time $t = 0$ we have N_0 radioactive nuclei present, then integration of Equation 3.3 gives the radioactive decay law:
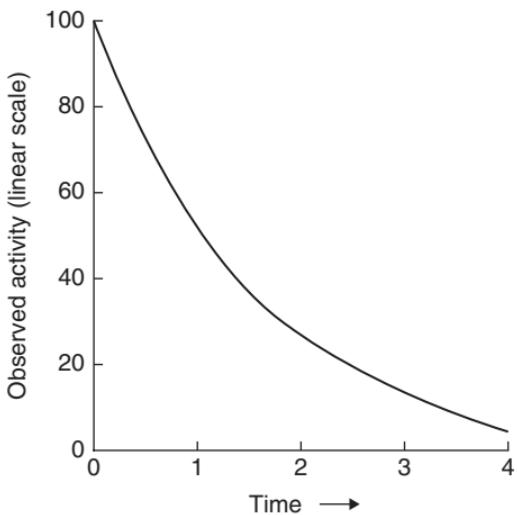
$$N = N_0 e^{-\lambda t} \tag{3.4}$$

This equation gives us the number of radioactive nuclei present at time t. However, in many experiments, we want to know the counting rate that we will get in a detector as a function of time. In other words, we want to know the *activity* of our samples.

Still, it is easy to show that the counting rate in one's radiation detector, C, is equal to the rate of disintegration of the radioactive nuclei present in a sample, A, multiplied by a constant related to the efficiency of the radiation measuring system. Thus,

$$C = \epsilon A = \epsilon \left(-\frac{dN}{dt}\right) = \epsilon \lambda N \tag{3.5}$$

Figure 3.1 Example of a linear plot of an exponential decay curve.
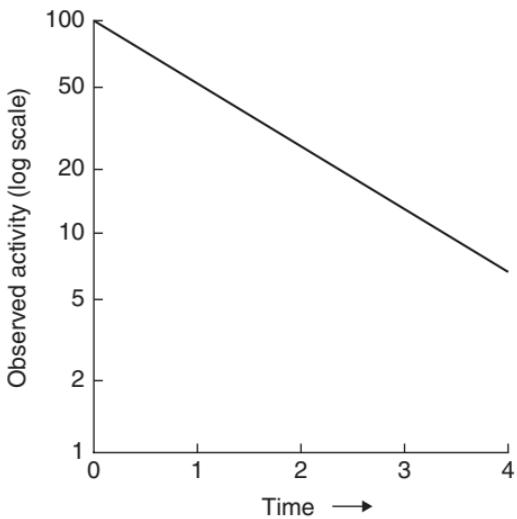
where ϵ is the efficiency. Substituting into Equation 3.4, we get

$$C = C_0 e^{-\lambda t} \tag{3.6}$$

where C is the counting rate at some time t due to a radioactive sample that gave counting rate C_0 at time $t = 0$. Equations 3.4 and 3.6 are the basic equations governing the number of nuclei present in a radioactive sample and the number of counts observed in one's detector as a function of time. Equation 3.6 is shown graphically in Figure 3.1. As seen in the figure, this exponential curve appears to flatten out on a linear scale and asymptotically approaches zero. If the same plot is made on a semilogarithmic scale (Fig. 3.2), the decay curve is a straight line, with a slope equal to the value of $(\lambda/\ln(10) \approx \lambda/2.303)$.

Figure 3.2 Example of a semilogarithmic plot of an exponential decay curve.
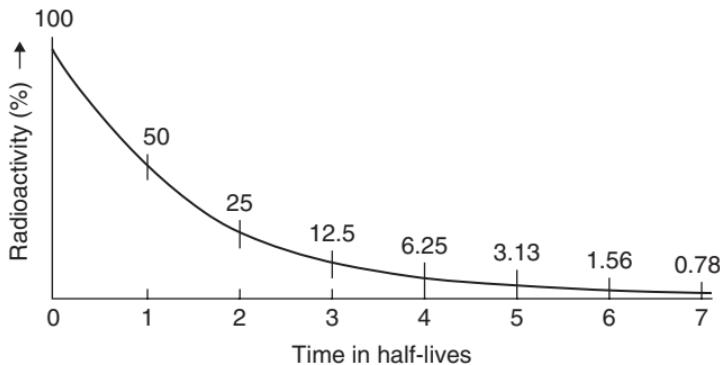
Figure 3.3 Example of the relation between half-life and radioactivity.

The *half-life* ($t_{1/2}$) is another representation of the decay constant. The half-life of a radionuclide is the time required for its activity to decrease by one-half. Thus after one half-life, 50% of the initial activity remains. After two half-lives, only 25% of the initial activity remains. After three half-lives, only 12.5% is yet present and so forth. Figure 3.3 shows this relation graphically.

The half-life for a given nuclide can be derived from Equation 3.6 when the value of the decay constant is known. In accordance with the definition of the term half-life, when $C/C_0 = 1/2$, then $t = t_{1/2}$. Substituting these values into Equation 3.6 gives

$$\frac{C}{C_0} = \frac{1}{2} = e^{-\lambda t_{1/2}} \tag{3.7}$$

Hence,

$$t_{1/2} = \frac{\ln(2)}{\lambda} \approx \frac{0.693}{\lambda} \tag{3.8}$$

Note that the value of the expression for $t_{1/2}$ has the units of $1/\lambda$ or dimensions of (time).

The half-lives for different nuclides range from much $<10^{-6}$ s to 10^{10} years. The half-life has been measured very precisely for all the commonly used radionuclides. When an unknown radioactive nuclide is encountered, a determination of its half-life is normally one of the first steps in its identification. This determination can be done by preparing a semilog plot of a series of activity observations made over a period of time. A short-lived nuclide may be observed as it decays through a complete half-life and the time interval observed directly (Fig. 3.4).

Sample Problem: 3.1: Simple Decay

Given the data plotted in Figure 3.5 for the decay of a single radionuclide, determine the decay constant and the half-life of the nuclide.

Figure 3.4 Example of the direct graphic determination of a half-life.
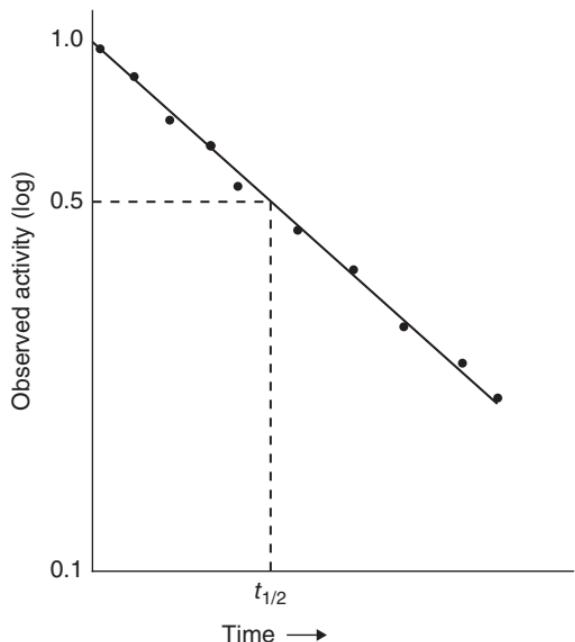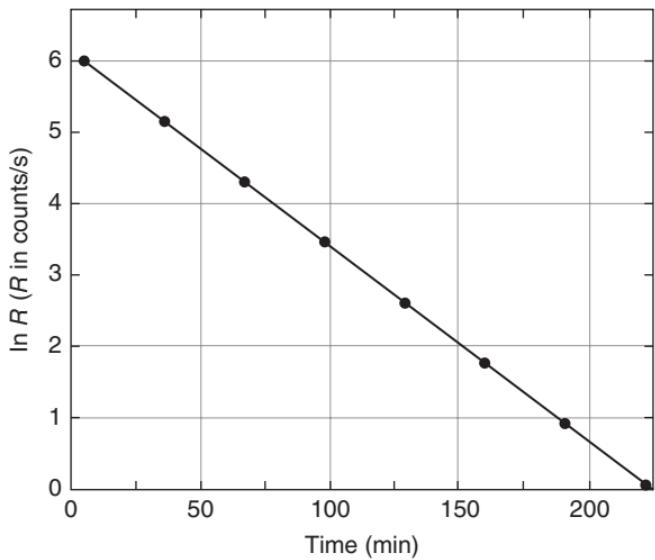
Figure 3.5 Single radionuclide decay data.

Solution

From the data plotted in Figure 3.5, the slope $(-\lambda)$ can be determined as

$$-\lambda = \frac{0 - 6.06}{220 - 0 \text{ min}}$$

$$\lambda = 0.027/5\text{min}^1$$

$$t_{1/2} = \frac{\ln(2)}{\lambda} = \frac{0.693}{0.0275} = 25.2 \text{ min}$$

What nuclide might this be?

It is difficult to measure the half-life of a very long-lived radionuclide. Here variation in disintegration rate may not be noticeable within a reasonable length of time. In this case, the decay constant must be calculated from the absolute decay rate according to Equation 3.2. The absolute number of atoms of the radioisotope present (N) in a given sample can be calculated according to

$$N = \frac{6.02 \times 10^{23} \left(\text{Avogadro's number} \right)}{\text{Atomic weight radionuclide}} \times \text{Mass of radionuclide} \quad (3.9)$$

The total mass of the radioisotope in the given sample can be determined once the isotopic composition of the sample is ascertained by such means as mass spectrometry. When the decay constant is known, the half-life can then be readily calculated. A table for the half-lives of a number of the known nuclei can be found in Appendix B.

Although the half-life of a given radionuclide is a defined value, the actual moment of disintegration for a particular atom can be anywhere from the very beginning of the nuclide's life to infinity. The average or mean life of a population of nuclei can, however, be calculated. The mean life τ is naturally related to the decay constant and is, in fact, simply the reciprocal of the decay constant

$$\tau = \frac{1}{\lambda} \quad (3.10)$$

or the mean life can be expressed in terms of the half-life:

$$\tau = \frac{1}{\ln(2)} \, t_{1/2} \approx 1.443 t_{1/2} \quad (3.11)$$

One can understand the preceding relationship by recalling that the decay constant, λ, was defined as the average probability of decay per unit time, so the $1/\lambda$ is the average time between decays. The concept of average life allows us to calculate the total number of particles emitted during a defined decay period. This number is essential in determining total radiation dose delivered by a radioisotope sample, as in medical research and therapy. During the time equal to one mean life, τ, the activity falls to $1/e$ of its original value. For a sample of N_0 nuclei with lifetimes t_i, we can write for the mean life τ

$$\tau = \frac{\sum_1^{N_0} t_i}{N_0} \quad (3.12)$$
$$= -\frac{1}{N_0} \int_{t=0}^{t=\infty} t \, dN$$

$$= \frac{1}{N_0} \int_0^\infty t\lambda N dt$$

$$= \lambda \int_0^\infty te^{-\lambda t} dt$$

$$= \left[\frac{-\lambda t + 1}{\lambda} \right]_0^t$$

$$= \frac{1}{\lambda}$$

The average or mean life is also of fundamental physical significance because it is the time to be substituted in the mathematical statement of the Heisenberg uncertainty principle, that is,

$$\Delta E \cdot \Delta t \geq \hbar \tag{3.13}$$

In this expression relating the uncertainty in energy of a system, ΔE, to its lifetime Δt, $\tau \equiv \Delta t$:

$$\Delta E = \frac{\hbar}{\tau} = \frac{0.658 \times 10^{-15} \text{ eV}}{\tau(\text{s})} \tag{3.14}$$

The quantity ΔE is called the width Γ.

The natural unit of radioactivity is disintegrations/time, such as disintegration per second (dps) or disintegrations per minute (dpm) The SI unit of radioactivity is the becquerel (Bq) where

$$1\text{Bq} \equiv 1 \text{ dis/s} \equiv 1 \text{ decay/s} \tag{3.15}$$

Counting rates in a detection system are usually given in counts per second (cps), counts per minute (cpm), and so on and differ from the disintegration rates by a factor representing the detector efficiency, ϵ. Thus,

$$(\text{dpm})\epsilon = (\text{cpm}) \tag{3.16}$$

The historical unit of radioactivity that still finds some use is the curie (Ci). It is defined as

$$1 \text{ Ci} = 3.7 \times 10^{10} \text{ Bq} = 3.7 \times 10^{10} \text{ dis/s} \tag{3.17}$$

The curie is a usually large unit of radioactivity for laboratory work and is approximately equal to the activity of 1 g of radium. The inventories of

radioactivity in a nuclear reactor upon shutdown are typically 10^9 Ci, while radiation sources used in tracer experiments have activities of μCi, and the environmental levels of radioactivity are nCi or pCi.

Note also that because radionuclides, in general, have different half-lives, the number of nuclei per curie will differ from one species to another. For example, let us calculate how many nuclei are in 1 MBq ($\sim$27 μCi) of tritium (^3H, $t_{1/2}$ = 12.33 years). We know that

$$N = \frac{-dN/dt}{\lambda} = \frac{10^6/s}{\lambda} \tag{3.18}$$

but

$$\lambda = \frac{\ln(2)}{t_{1/2}} \approx \frac{0.693}{12.33 \text{ years}(\pi \times 10^7 \text{ s/year})} = 1.789 \times 10^{-9}/s^1 \tag{3.19}$$

Thus,

$$N = \frac{A}{\lambda} \approx \frac{10^6 \text{ s}^{-1}}{(1.789)(10^{-9}/s)} = 5.59 \times 10^{14} \text{ nuclei} \tag{3.20}$$

The same calculation carried out for ^{14}C ($t_{1/2}$) = 5730 years) would give 2.60×10^{17} nuclei/MBq. It is also interesting to calculate the mass associated with 1 MBq of tritium. We have

$$M = \frac{N(\text{atomic weight})}{\text{Avogadro's number}} = \frac{5.59 \times 10^{14}(3.00 \text{ g/mol})}{6.02 \times 10^{23}/\text{mol}} = 2.78 \times 10^{-9} \text{ g} \tag{3.21}$$

In other words, 1 MBq of tritium contains about 3 ng of tritium. Thus an important feature of radionuclides becomes apparent—radiochemists routinely work with extremely small quantities of material. Pure samples of radioisotopes are called "carrier-free."

Unless a radionuclide is in a carrier-free state, it is mixed homogeneously with the stable nuclides of the same element. It is therefore desirable to have a simple expression to show the relative abundances of the radioisotope and the stable isotopes. This specification is readily accomplished by using the concept of specific activity, which refers to the amount of radioactivity per given mass or other similar units of the total sample. The SI unit of specific activity is Bq/kg. Specific activity can also be expressed in terms of the disintegration rate (Bq or dpm), counting rate (counts/min, cpm, or counts/s, cps), or curies (or mCi, μCi) of the specific radionuclide per unit mass of the sample.

3.2 Mixture of Two Independently Decaying Radionuclides

Where two or more unrelated (see in the following) radioisotopes with different half-lives are present in a sample and one does not or cannot distinguish the particles emitted by each isotope, a composite decay rate will be observed. The decay curve, in this situation, drawn on a semilogarithmic plot, will not be a straight line. The decay curves of each of the isotopes present usually can be resolved by graphic means if their half-lives are sufficiently different and if not more than three radioactive components are present. In the graphic example shown in Figure 3.6, line C represents the total observed activity. Only the activity of the longer-lived component A is observed after the shorter-lived component B has become exhausted through decay. Extrapolation of this long-time portion of the curve back to zero time gives the decay curve for component A and the activity of component A at $t = 0$. The curve for component B is obtained by subtracting out, point by point, the activity values of component A from the total activity curve. If the half-lives of the two components in such samples are not sufficiently different to allow graphic resolution, a differential detection method may be needed. If the radiation characteristics of the nuclides in the mixture are suitably distinct, that is, emission of different particles or γ-rays, it may be possible to measure the activity of one component without interference from the radiation emitted by the other component. A case in point would be where one nuclide was a pure β-emitter while the other emitted both β- and

Figure 3.6 Graphic resolution of a two-component decay curve.
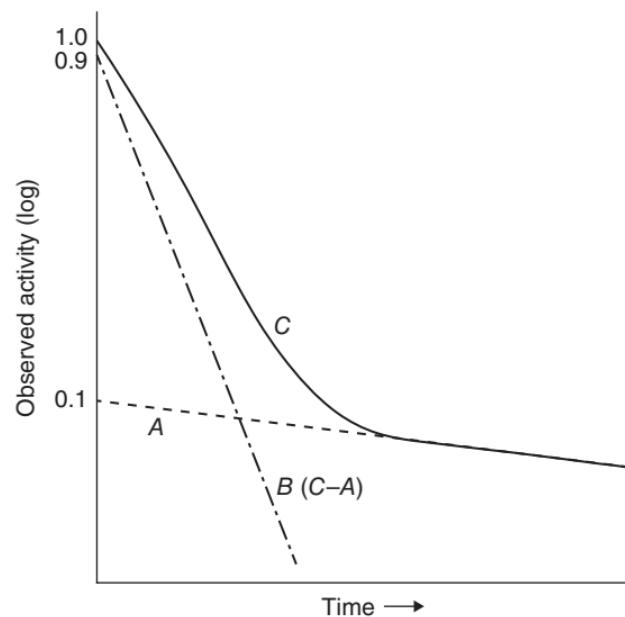
Table 3.1 Typical Decay Data.

t (h)	A (cpm)
0.1	270
0.5	210
1.0	170
1.5	130
2.0	110
2.5	90
3	80
4	65
5	55
7	44
10	34
15	22

γ-rays. In the case where the half-lives of the components are known but are not sufficiently different to allow graphical resolution of the decay curve, computer techniques that utilize least squares fitting to resolve such a case are also available.

Sample Problem 3.2: Resolution of Decay Curves

Given the following decay data (Table 3.1 and Fig. 3.7), determine the half-lives and initial activities of the nuclides (*B* and *C*) present.

Solution

From the data in the table and graph, we can determine
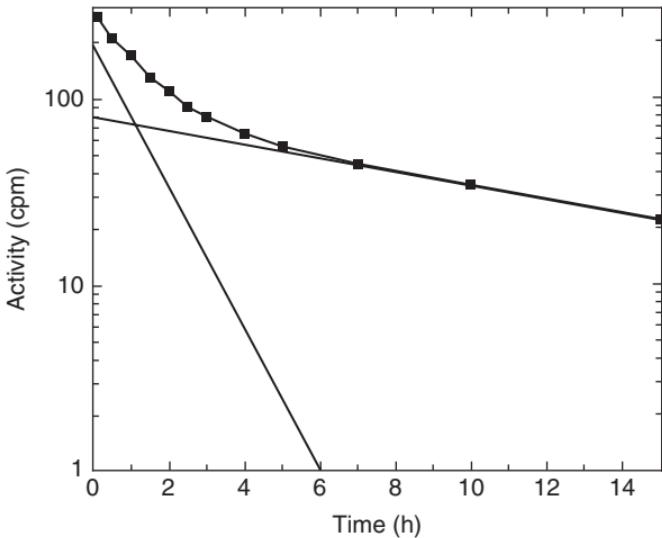
$$t_{1/2}(B) = 8.0 \text{ h}$$
$$A_0(B) = 80 \text{ cpm}$$
$$t_{1/2}(C) = 0.8 \text{ h}$$
$$A_0(C) = 190 \text{ cpm}$$

3.3 Radioactive Decay Equilibrium
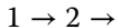
When a radionuclide decays, it does not disappear but is transformed into a new nuclear species of lower total energy and often differing Z, A, J, π, and so on. The equations of radioactive decay discussed so far have focused on the decrease of

Figure 3.7 Radionuclide mixture decay data.

the parent radionuclides but have ignored the formation (and possible decay) of daughter, granddaughter, and so on, species. It is the formation and decay of these "children" that is the focus of this section.

Let us begin by considering the case when a radionuclide (1) decays with decay constant λ_1, forming a daughter nucleus (2), which in turn decays with decay constant λ_2. Schematically we have

$$1 \to 2 \to$$

We can write terms for the production and depletion of 2, that is,

Rate of change of 2 = production rate of 2 − decay rate of 2

$$\frac{dN_2}{dt} = \lambda_1 N_1 - \lambda_2 N_2 \tag{3.22}$$

where N_1 and N_2 are the numbers of (1) and (2) present at time t. Rearranging and collecting similar terms

$$dN_2 + \lambda_2 N_2 dt = \lambda_1 N_1 dt \tag{3.23}$$

Remembering that

$$N_1 = N_1^0 e^{-\lambda_1 t} \tag{3.24}$$

we have

$$dN_2 + \lambda_2 N_2 dt = \lambda_1 N_1^0 e^{-\lambda_1 t} dt \tag{3.25}$$

This is a first-order linear differential equation and can be solved using the method of integrating factors, which we show in the following. Multiplying both sides by $e^{\lambda_2 t}$, we have

$$e^{\lambda_2 t} dN_2 + \lambda_2 N_2 e^{\lambda_2 t} dt = \lambda_1 N_1^0 e^{(\lambda_2 - \lambda_1)t} dt \tag{3.26}$$

The left-hand side is now a perfect differential:

$$d\left(N_2 e^{\lambda_2 t}\right) = \lambda_1 N_1^0 e^{(\lambda_2 - \lambda_1)t} dt \qquad (3.27)$$

Integrating from $t = 0$ to $t = t$, we have

$$N_2 e^{\lambda_2 t}\Big|_0^t = \frac{\lambda_1 N_1^0 e^{(\lambda_2 - \lambda_1)t}}{\lambda_2 - \lambda_1}\Big|_0^t \qquad (3.28)$$

$$N_2 e^{\lambda_2 t} - N_2^0 = \frac{\lambda_1}{\lambda_2 - \lambda_1} N_1^0 (e^{(\lambda_2 - \lambda_1)t} - 1) \qquad (3.29)$$

Multiplying by $e^{-\lambda_2 t}$ and rearranging gives

$$N_2(t) = \frac{\lambda_1}{\lambda_2 - \lambda_1} N_1^0 \left(e^{-\lambda_1 t} - e^{-\lambda_2 t}\right) + N_2^0 e^{-\lambda_2 t} \qquad (3.30)$$

where N_2^0 is the number of species (2) present at $t = 0$. The first term in Equation 3.30 represents the growth of the daughter due to the decay of the parent, while the second term represents the decay of any daughter nuclei that were present initially. Remembering that $A_2 = \lambda_2 N_2$, we can write an expression for the activity of (2) as

$$A_2(t) = \frac{\lambda_1 \lambda_2}{\lambda_2 - \lambda_1} N_1^0 \left(e^{-\lambda_1 t} - e^{-\lambda_2 t}\right) + A_2^0 e^{-\lambda_2 t} \qquad (3.31)$$

These two Equations 3.30 and 3.31 are the general expressions for the number of daughter nuclei and the daughter activity as a function of time, respectively.

The general behavior of the activity of parent and daughter species, as predicted by Equation 3.31, is shown in Figure 3.8. As one expects qualitatively for the case with $N_2^0 = 0$, the initial activity of the daughter is zero, rises to a maximum, and, if one waits long enough, eventually decreases.

Thus there must be a time when the daughter activity is the maximum. We can calculate this by noting the condition for a maximum in the activity of (2) is

$$\frac{dN_2}{dt} = 0 \qquad (3.32)$$

Taking the derivative of Equation 3.31 and simplifying,
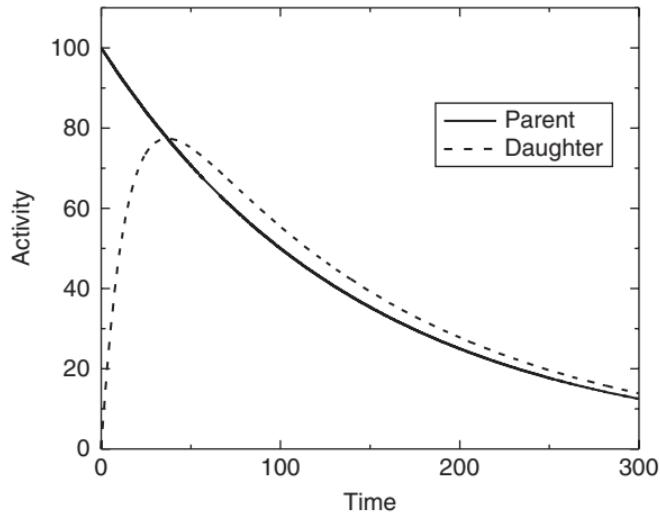
$$\lambda_1 e^{-\lambda_1 t} = \lambda_2 e^{-\lambda_2 t} \qquad (3.33)$$

Solving for t

$$t_{\max} = \frac{\ln(\lambda_2/\lambda_1)}{\lambda_2 - \lambda_1} \qquad (3.34)$$

All of this development may seem like something that would be best handled by a computer program or just represents a chance to practice one's skill with differential equations. But that is not true. It is important to understand the

Figure 3.8 The general case of radioactive decay equilibrium is shown for a shorter-lived parent.

mathematical foundation of these expressions to gain insight into practical situations. Let us consider some cases that illustrate this point.

Consider the special case where $\lambda_1 = \lambda_2$. Plugging into Equations 3.30 or 3.31 or a computer program based upon them leads to a division by zero. Does nature therefore forbid λ_1 from equaling λ_2 in a chain of decays? Nonsense! One simply understands that one must redo the derivation (Equations 3.22 through 3.30) of these equations for this special case (see Sample Problem 3.3).

Let us now consider a number of other special cases of Equations 3.30 or 3.31 that are of practical importance. *Suppose the daughter nucleus is stable*; $\lambda_2 = 0$. Then we have

$$\frac{dN_2}{dt} = \lambda_1 N_1 \tag{3.35}$$

$$dN_2 = \lambda_1 N_1 dt = \lambda_1 N_1^0 e^{-\lambda_1 t} dt \tag{3.36}$$
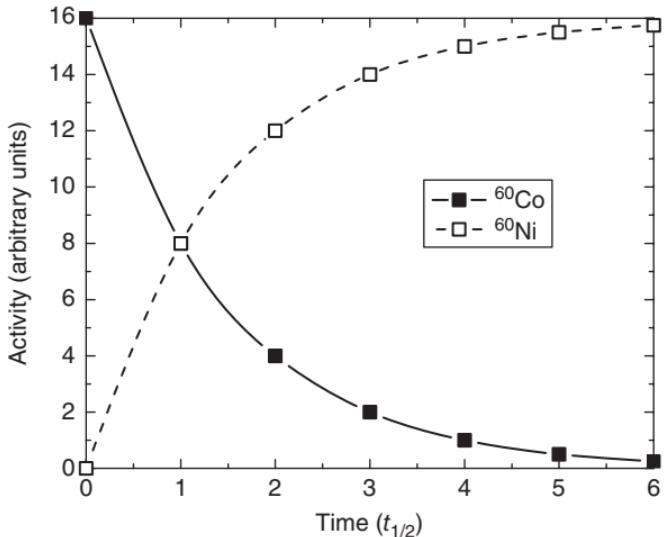
$$N_2 = \frac{\lambda_1 N_1^0}{-\lambda_1} \left(e^{-\lambda_1 t} \right) \Big|_0^t = N_1^0 \left(1 - e^{-\lambda_1 t} \right) \tag{3.37}$$

These relations are shown in Figure 3.9. They represent the typical decay of many radionuclides prepared by neutron capture reactions, the type of reaction that commonly occurs in a nuclear reactor.

In Figure 3.10, we show the activity relationships for parent and daughter (as predicted by Equation 3.31) for four choices of the relative values of the half-lives of the parent and daughter nuclides.

In the first of the cases shown in the figure, we have $t_{1/2}(parent) < t_{1/2}(daughter)$, that is, the parent is shorter lived than the daughter. This is called the *no equilibrium* case because the daughter buildup (due to the decay of the parent) is faster than its loss due to decay. Essentially all of the parent nuclides, are converted to daughter nuclides, and the subsequent activity is

Figure 3.9 Decay of ^{60}Co (half-life 5.27 years) and the growth of ^{60}Ni (stable).

due to the decay of the daughters only. Thus the name "no equilibrium" is used. Practical examples of this decay type are ^{131}Te $\rightarrow$ ^{131}I, ^{210}Bi $\rightarrow$ ^{210}Po, and ^{92}Sr $\rightarrow$ ^{92}Y. This situation typically occurs when one is far from stability and the parent nuclei decay by β-decay toward stability.

A second special case of Equations 3.30 and 3.31 is called *transient equilibrium* (Figs. 3.10c and 3.11a). In this case, the parent is significantly ($\sim$10×) longer lived than the daughter and thus controls the decay chain. Here $\lambda_2 > \lambda_1$, so in Equation 3.30, as $t \rightarrow \infty$

$$e^{-\lambda_2 t} \ll e^{-\lambda_1 t} \text{ and } N_2^0 \, e^{-\lambda_2 t} \rightarrow 0 \tag{3.38}$$

and we have

$$N_2 \approx \frac{\lambda_1}{\lambda_2 - \lambda_1} N_1^0 \, e^{-\lambda_1 t} \tag{3.39}$$
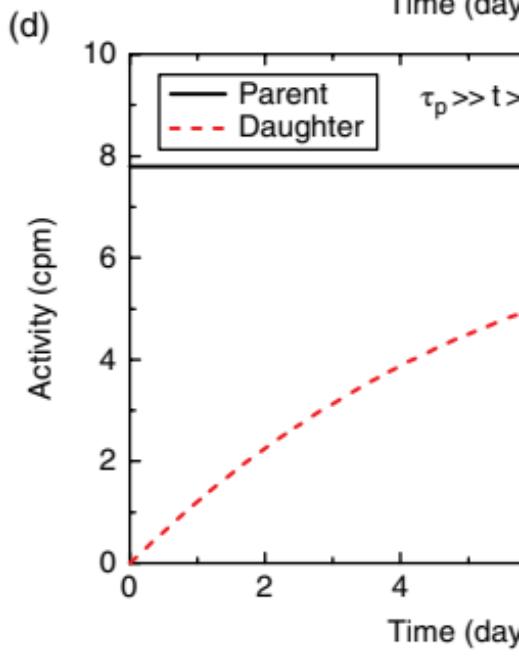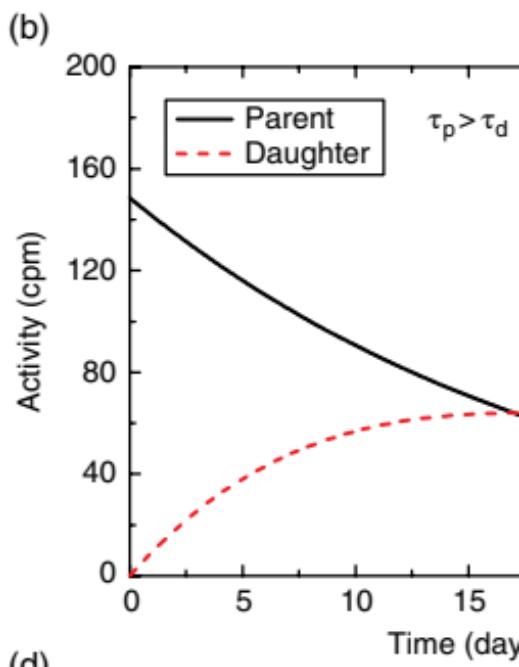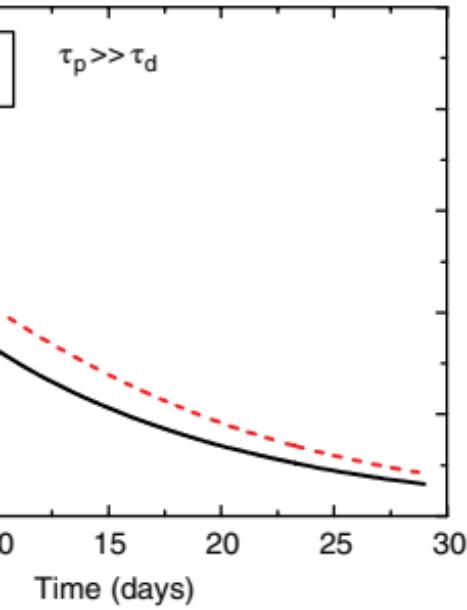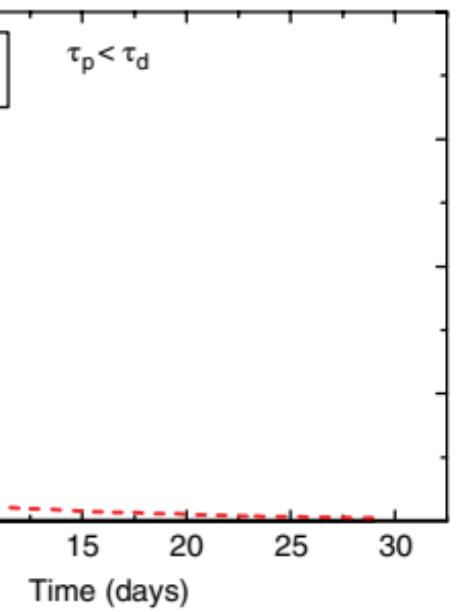
Substituting the expression for N_1,

$$N_1 = N_1^0 \, e^{-\lambda_1 t} \tag{3.40}$$

We get

$$\frac{N_1}{N_2} = \frac{\lambda_2 - \lambda_1}{\lambda_1} \tag{3.41}$$

At long times, the ratio of daughter-to-parent activity becomes constant, and both species disappear with the effective half-life of the parent. The classic examples of this decay equilibrium are the decay of ^{140}Ba ($t_{1/2} = 12.8$ days) to ^{140}La ($t_{1/2} = 40$ h) or the equilibrium between ^{222}Rn ($t_{1/2} = 3.8$ days) and its much short-lived decay products.

(b)

(d)

y curves for various parent–daughter relationships: (a)
ved parent ($\tau_p > \tau_d$); (c) very long-lived parent ($\tau_p >> $
y replenished, parent ($\tau_p >> t >> \tau_d$).

A third special case of Equations 3.30 and 3.31 is called *secular equilibrium* (Figs. 3.10d and 3.11b). In this case, the parent is very much longer lived ($\sim 10^4 \times$) than the daughter, or the parent is constantly being replenished through some other process. During the time of observation, there is no significant change in the number of parent nuclei present, although several half-lives of the daughter may occur. In the previous case of transient equilibrium, we had

$$\frac{N_1}{N_2} = \frac{\lambda_2 - \lambda_1}{\lambda_1} \tag{3.42}$$

Since we now also have $\lambda_1 \ll \lambda_2$, so we can simplify even more to give

$$\frac{N_1}{N_2} = \frac{\lambda_2}{\lambda_1} \tag{3.43}$$

$$\lambda_1 N_1 = \lambda_2 N_2 \tag{3.44}$$

$$A_1 = A_2 \tag{3.45}$$

In short, the activity of the parent and daughter are the same, and the total activity of the sample remains effectively constant during the period of observation. It usually takes about 10 half-lives of the daughter to establish secular equilibrium.

The naturally occurring heavy element decay chains (see in the following) where $^{238}\text{U} \rightarrow {}^{206}\text{Pb}$, $^{235}\text{U} \rightarrow {}^{207}\text{Pb}$ and $^{232}\text{Th} \rightarrow {}^{208}\text{Pb}$ and the extinct heavy element decay series $^{237}\text{Np} \rightarrow {}^{209}\text{Bi}$ are examples of secular equilibrium because of the long half-lives of the parents. Perhaps the most important cases of secular equilibrium are the production of radionuclides by a nuclear reaction in an accelerator, a reactor, a star, or the upper atmosphere. In this cases, we have

$$\text{Nuclear reaction} \rightarrow (2) \rightarrow \tag{3.46}$$

which produces the radionuclide 2 with rate R. If the reaction is simply the decay of a long-lived nuclide, then $R = \lambda_1 N_1^0$ and $N_2^0 = 0$. Substitution into Equation 3.30 gives the expression

$$N_2 = \frac{\lambda_1}{\lambda_2 - \lambda_1} N_1^0 \left(e^{-\lambda_1 t} - e^{-\lambda_2 t} \right) \tag{3.47}$$
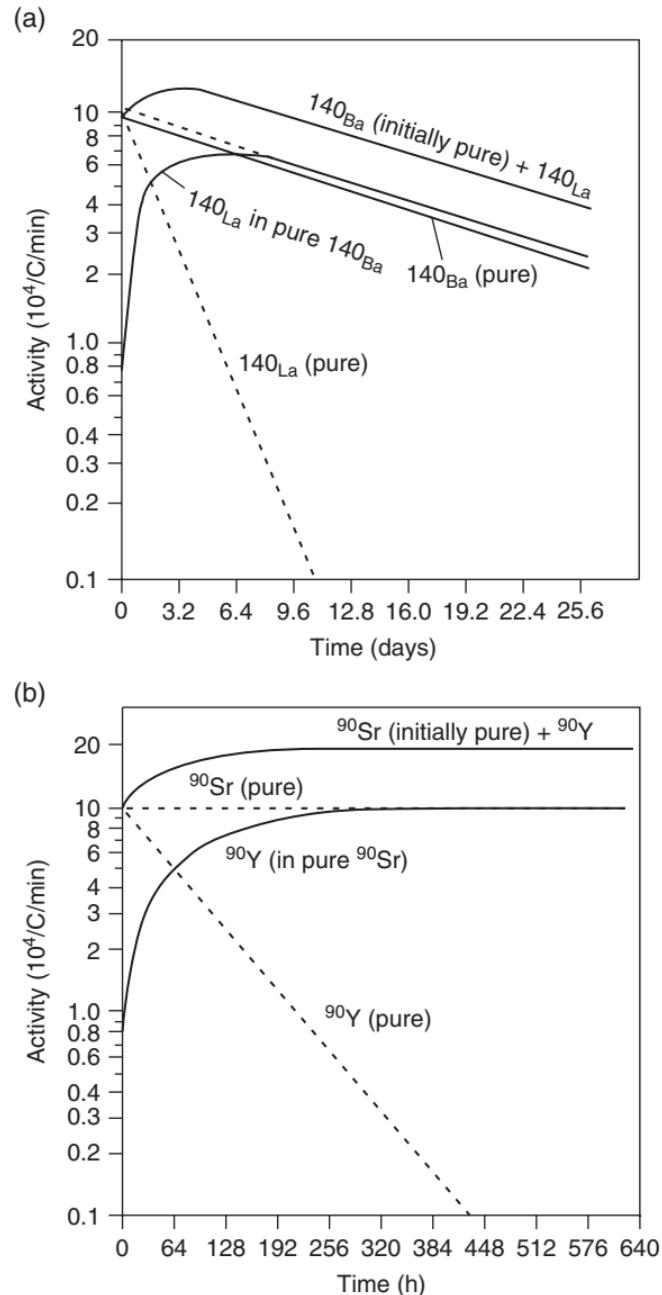
If the reaction is slower than the decay or $\lambda_1 \ll \lambda_2$, it is most appropriate to say (since $\lambda_1 \approx 0$)

$$N_2 \approx \frac{\lambda_1}{\lambda_2} N_1^0 \left(1 - e^{-\lambda_2 t} \right) \tag{3.48}$$

or in terms of the activities

$$A_2 = \lambda_2 N_2 = R \left(1 - e^{-\lambda_2 t} \right) \tag{3.49}$$
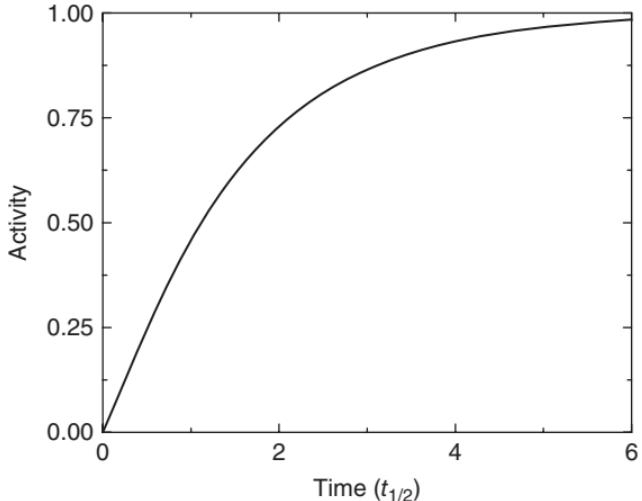
Figure 3.11 Typical examples of (a) transient and (b) secular equilibrium.

Equation 3.49 is known as the activation equation and is shown as a function of time in Figure 3.12.

Initially the growth of the product radionuclide activity is nearly linear (due to the behavior of $\left(1 - e^{-\lambda_2 t}\right)$ for small values of $\lambda_2 \times t$), but eventually

Figure 3.12 Growth of the activity of a primary nuclear reaction product created during a constant bombardment.

the product activity becomes "saturated" or constant, decaying as fast as it is produced. At an irradiation time of one half-life, half the maximum activity is formed; after two half-lives, 3/4 of the maximum activity is formed, after three half-lives, 7/8 of the maximum activity is formed, and so on. This situation gives rise to the rough rule that irradiations that extend for periods that are > 3 three times $t_{1/2}$ of the desired radionuclide are usually not cost effective.

Equation 3.31 may be generalized to a chain of decaying nuclei of arbitrary length in using the Bateman equations (Bateman, 1910). If we assume that at $t = 0$, none of the daughter nuclei are present, $(N_2^0 = N_3^0 = \cdots N_n^0 = 0)$, we get

$$1 \rightarrow 2 \rightarrow 3 \rightarrow \cdots (n) \rightarrow$$
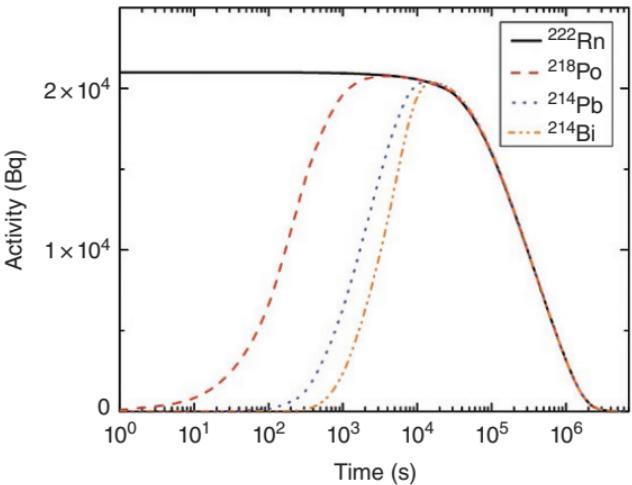
$$N_n = C_1 e^{-\lambda_1 t} + C_2 e^{-\lambda_2 t} + C_3 e^{-\lambda_3 t} + \cdots C_n e^{-\lambda_n t} \tag{3.50}$$

where

$$C_1 = \frac{\lambda_1 \lambda_2 \cdots \lambda_{n-1}}{(\lambda_2 - \lambda_1)(\lambda_3 - \lambda_1) \cdots (\lambda_n - \lambda_1)} N_1^0$$

$$C_2 = \frac{\lambda_1 \lambda_2 \cdots \lambda_{n-1}}{(\lambda_1 - \lambda_2)(\lambda_3 - \lambda_2) \cdots (\lambda_n - \lambda_2)} N_2^0$$

$$C_n = \frac{\lambda_1 \lambda_2 \cdots \lambda_{n-1}}{(\lambda_1 - \lambda_n)(\lambda_2 - \lambda_n) \cdots (\lambda_{n-1} - \lambda_n)} N_n^0 \tag{3.51}$$

These equations describe the activities produced in new fuel as a nuclear reactor begins to operate. No fission or activation products are present when the fuel is loaded, and they grow in as the reactions take place.
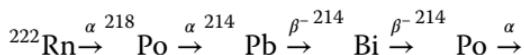
Figure 3.13 Graph of the variation of activities in Sample Problem 3.3.

Sample Problem 3.3: Application of the Bateman Equations

Consider the decay of a 1 μCi sample of pure ^{222}Rn ($t_{1/2} = 3.82$ days). Use the Bateman equations to estimate the activity of its daughters (^{218}Po, ^{214}Pb, ^{214}Bi, and ^{214}Po) after a decay time of 4 h. The decay sequence is

$$^{222}\text{Rn} \xrightarrow{\alpha} {}^{218}\text{Po} \xrightarrow{\alpha} {}^{214}\text{Pb} \xrightarrow{\beta^-} {}^{214}\text{Bi} \xrightarrow{\beta^-} {}^{214}\text{Po} \xrightarrow{\alpha}$$

Solution

$$A = A_0 e^{-\lambda_A t} = 1\ \mu\text{Ci} \left(e^{-(\ln 2)(4)/(24)(3.82)} \right)$$
$$A = 0.97\ \mu\text{Ci}$$

$$B = \lambda_B \left(C_1 e^{-\lambda_1 t} + C_2 e^{-\lambda_2 t} \right)$$

$$C_1 = \frac{\lambda_A N_A^0}{\lambda_B - \lambda_A} = \frac{A_0}{\lambda_B - \lambda_A}$$
$$C_2 = \frac{\lambda_A N_A^0}{\lambda_A - \lambda_B} = \frac{A_0}{\lambda_A - \lambda_B}$$

$$B = \lambda_B \left(\frac{A_0 e^{-\lambda_A t}}{\lambda_B - \lambda_A} + \frac{A_0 e^{-\lambda_B t}}{\lambda_A - \lambda_B} \right)$$
$$B = 37.3 \left(\frac{0.97}{37.3 - 0.021} + \frac{e^{(-\ln 2 \times 4)/(3.1/60)}}{0.021 - 37.3} \right)$$
$$B = 0.97\ \mu\text{Ci}$$

(Actually $B/A = 1.00056$)

The reader should verify that for C, D, and E, the only significant term is the term multiplying $e^{-\lambda_A t}$ as it was for B. Thus for D/A, we have

$$\frac{D}{A} = \frac{\lambda_B}{\lambda_B - \lambda_A} \cdot \frac{\lambda_C}{\lambda_C - \lambda_A} \cdot \frac{\lambda_D}{\lambda_D - \lambda_A} = 1.0091$$

3.4 Branching Decay

Some nuclides decay by more than one mode. Some nuclei may decay by either β^+-decay or electron capture, others by α-decay or spontaneous fission, still others by γ-ray emission or internal conversion, etc. In these cases, we can characterize each competing mode of decay by a separate decay constant λ_i for each type of decay where the total decay constant, λ, is given by the sum

$$\lambda = \lambda_1 + \lambda_2 + \cdots = \sum_{i=1}^{N} \lambda_i \tag{3.52}$$

Corresponding to each partial decay constant λ_i, there is a partial half-life $t_{1/2}^i$ where

$$t_{1/2}^i = \frac{\ln(2)}{\lambda_i} \approx \frac{0.693}{\lambda_i} \tag{3.53}$$

and the total half-life, $t_{1/2}$, is the sum of the reciprocals

$$\frac{1}{t_{1/2}} = \frac{1}{t_{1/2}^1} + \frac{1}{t_{1/2}^2} + \cdots = \sum_{i=1}^{N} \frac{1}{t_{1/2}^i} \tag{3.54}$$

The fraction of decays proceeding by the ith mode is given by the obvious expression

$$f_i = \frac{\lambda_i}{\sum \lambda_i} = \frac{\lambda_i}{\lambda} \tag{3.55}$$

By analogy, the energy uncertainty associated with a given state, ΔE, through the Heisenberg uncertainty principle can be obtained from the lifetime contributed by each decay mode. If we introduce the definition $\Delta E = \Gamma$, the level width, then we can express Γ in terms of the partial widths for each decay mode Γ_i such that

$$\Gamma = \Gamma_1 + \Gamma_2 + \Gamma_3 + \cdots = \sum_{i=1}^{N} \Gamma_i \tag{3.56}$$

where

$$\Gamma_i = \frac{1}{\tau_i} \tag{3.57}$$

in which τ_i is the partial mean life associated with each decay mode. This approach is especially useful in treating the decay of states formed in nuclear reactions in which a variety of competing processes such as α, proton neutron emission, and so on may occur as the nucleus de-excites. In such cases, we can express the total width as

$$\Gamma = \Gamma_\alpha + \Gamma_p + \Gamma_n + \cdots \qquad (3.58)$$

Sample Problem 3.4: Branching Decay

Consider the nucleus ^{64}Cu ($t_{1/2} = 12.700$ h). ^{64}Cu is known to decay by electron capture (61%) and β^--decay (39%). What are the partial half-lives for EC and β^--decay? What is the partial width for EC decay?

Solution

$$\lambda = \frac{\ln(2)}{12.700 \text{ h}} = 5.46 \times 10^{-2}/\text{h}^1$$

$$\lambda = \lambda_{EC} + \lambda_{\beta^-} = \lambda_{EC} + (39/61)\lambda_{EC}$$
$$\lambda_{EC} = 3.329 \times 10^{-2}/h^1$$
$$t_{1/2}^{EC} = \frac{\ln(2)}{\lambda_{EC}} = 20.8 \text{ h}$$
$$\lambda_{\beta^-} = (39/61)\lambda_{EC} = 2.128 \times 10^{-2}/\text{h}^1$$
$$t_{1/2}^{\beta^-} = (\ln 2)/\lambda_{\beta^-} = 32.6 \text{ h}$$
$$\tau^{EC} = t_{1/2}^{EC}/\ln(2) = 30.0 \text{ h} = 108131 \text{ s}$$
$$\Gamma_{EC} = \hbar/\tau^{EC} = 6.582 \times 10^{-22} \text{ MeV s}/108131 \text{ s}$$
$$\Gamma_{EC} = 6.1 \times 10^{-27} \text{ MeV}$$

3.5 Radiation Dosage

Up to now, we have discussed radioactivity (defined as disintegrations/time.) To fully discuss radioactivity we must consider the consequences of the interaction of radiation with matter. (A full discussion of this subject can be found in Chapter 16. Here we summarize some aspects of that discussion related to human health.)

When radiation interacts with matter, the matter is altered by ionization or atom or nuclear displacement. To characterize this effect, we need to know the amount of energy absorbed by the matter in question. The modern unit for absorbed "dose" is the gray (Gy). Formally 1 gray corresponds to the absorption

Table 3.2 Radiation Weighting Factors.

	γ	β	Protons (10 MeV)	α	Neutrons (14 MeV)	(Thermal)
Radiation weighting factor	1	1	2	20	7.7	5

of 1 J/kg = 6.24×10^{12} MeV/kg. (This is a large amount of absorbed energy, and doses are more frequently measured in microGy.)

In living systems, we are concerned with the effect of the absorbed energy, not just its magnitude. Different types of radiation deposit energy at different rates as they interact with matter. Radioactive decay α-particles deposit their energy in $\sim 10^{-4}$ m in condensed matter. Typical β^--particles are stopped in a few millimeter of material, while γ-rays have an infinite range in matter, and it is only their intensities that are attenuated exponentially as they pass through matter. This linear energy transfer (LET), which is approximately dE/dx, can be used to quantify the biological effects of various types of radiation as they interact with matter. For example, α-particles deposit their energy in a small volume compared with γ-radiation, and thus α-particles have a greater biological effect compared with γ-rays when they interact with matter. The differing biological effects of various types of radiation are expressed in the *radiation weighting factors*, w_r. The values of w_r for various types of radiation are shown in Table 3.2.

We express the idea of the biological effect of radiation dose by defining a quantity called the *equivalent dose*. The equivalent dose is measured in *sieverts* (Sv) where 1 sievert is the dose (Grays) $\times w_r$. The sievert (named after the Swedish medical physicist Rolf Maximilian Sievert) is a large amount of radiation dose for most biological systems. An equivalent dose of 1 Sv carries with it a 5.5% chance of eventually developing cancer, and doses of >1 Sv delivered over a short time can lead to serious health consequences. Most radiation exposures are expressed in millisieverts (mSv). The International Commission on Radiological Protection (ICRP) recommends that radiation exposures be limited to equivalent doses of <1 mSv/year, excluding medical and other "natural" exposures.

In the United States, there is an older unit of equivalent dose, the roentgen equivalent man (rem), that is also used. The relation to the SI unit of sieverts is that 1 Sv = 100 rem, or in more useful units, 10 μSv = 1 millirem.

3.6 Natural Radioactivity

3.6.1 General Information

There are ~70 naturally occurring radionuclides on earth. Most of them are heavy element radioactivities present in the natural decay chains, but there are several important light element activities, such as ^{3}H, ^{14}C, ^{40}K, and so on. These radioactive species are ubiquitous, occurring in plants, animals, the air we breathe, the water we drink, the soil, and so on. For example, in the 70 kg "reference man," one finds ~4400 Bq of ^{40}K and ~3600 Bq of ^{14}C, that is, about 8000 dps due to these two radionuclides alone. Imagine that. Every second 8000 nuclei in your body decay. You are "radioactive." In a typical US diet, one ingests ~1 pCi/day of ^{238}U, ^{226}Ra, and ^{210}Po. The air we breathe contains ~0.15 pCi/l of ^{222}Rn, the water we drink contains >10 pCi/L of ^{3}H, while the earth's crust contains ~10 and ~4 ppm of the radioelements Th and U, respectively. One should not forget that the interior heat budget of planet Earth is dominated by the contributions from the radioactive decay of uranium, thorium, and potassium.

The naturally occurring radionuclides can be classified as (a) *primordial*, that is, nuclides that have survived since the time the elements were formed, (b) *cosmogenic*, that is, shorter-lived nuclides formed continuously by the interaction of cosmic rays with matter, and (c) *anthropogenic*, that is, a wide variety of nuclides introduced into the environment by the activities of man, such as nuclear weapons tests, the operation (or mis-operation) of nuclear power plants, and so on. The primordial radionuclides have half-lives > 10^9 years or are the decay products of these nuclei. This class includes ^{40}K ($t_{1/2} = 1.277 \times 10^9$ years), ^{238}U ($t_{1/2} = 4.5 \times 10^9$ years), ^{235}U ($t_{1/2} = 0.74 \times 10^9$ years), ^{232}Th ($t_{1/2} = 14.05 \times 10^9$ years), and ^{87}Rb ($t_{1/2} = 47.5 \times 10^9$ years) as its most important members. (Some additional members of this group include ^{115}In, ^{123}Te, ^{138}La, ^{144}Nd, ^{147}Sm, ^{148}Sm, ^{176}Lu, ^{174}Hf, ^{187}Re, and ^{190}Pt.)

3.6.2 Primordial Nuclei and the Uranium Decay Series

^{40}K is a β-emitting nuclide that is the predominant radioactive component of normal foods and human tissue. Due to the 1460 keV γ-ray that accompanies the β^--decay, it is also an important source of background radiation detected by γ-ray spectrometers. The natural concentration in the body contributes about 0.17 mSv/year to the whole body dose. The specific activity of ^{40}K is ~ 855 pCi/g potassium.

Despite the high specific activity of ^{87}Rb of ~2400 pCi/g, the low abundance of rubidium in nature makes its contribution to the overall radioactivity of the environment small.

There are three naturally occurring decay series. They are the *uranium* ($A = 4n + 2$) series in which ^{238}U decays through 14 intermediate nuclei to form the stable nucleus ^{206}Pb; the *actinium* or ^{235}U ($A = 4n + 3$) series in which ^{235}U
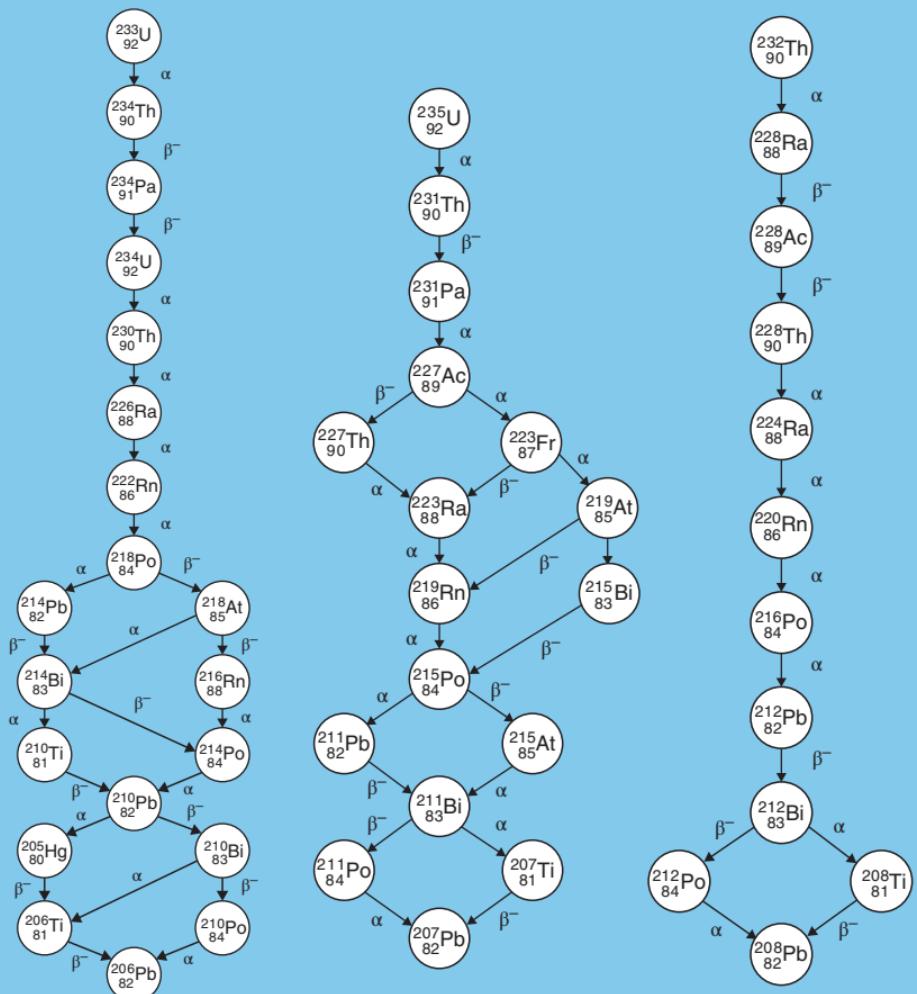
Figure 3.14 Representations of the three naturally occurring decay series.

decays through 11 intermediate nuclei to form stable ^{207}Pb; and the *thorium* ($A = 4n$) series in which ^{232}Th decays through a series of 10 intermediates to stable ^{208}Pb (Fig. 3.14). A little arithmetic will suffice to figure out what the number of decays and their types are in these series. Take the uranium series as an example. ^{238}U decays to ^{206}Pb. $\Delta Z = 10$, $\Delta A = 32$. To change ΔA by 32 requires eight α-particles be emitted or a change in Z of 16. Note that U to Pb is a change of only 10 units of Z. To compensate for the observed Z change requires six β^--decays that would each increase the atomic number by one. So we expect a combination of eight α-decays and six β^- decays in going from ^{238}U to ^{206}Pb.

Because the half-lives of the parent nuclei are so long relative to the other members of each series, all members of each decay series are in secular equilibrium in undisturbed samples, that is, the activities of each member of the chain are equal at equilibrium if the sample has not been chemically fractionated. Thus, the activity associated with ^{238}U in secular equilibrium with its daughters is 14× the activity of the ^{238}U. The notation $4n + 2$, $4n$, $4n + 3$ refers to the fact that the mass number of each member of a given chain is such that it can be represented by the product $4n$, $4n + 2$, $4n + 3$ where n is an integer. (There is an additional decay series, the $4n + 1$ series, that is extinct because its longest-lived member, ^{237}Np, has a half-life of only 2.1×10^6 years, a time that is very short compared with the time of element formation.)

The uranium series contains two radionuclides of special interest, ^{226}Ra ($t_{1/2} = 1600$ years) and its daughter, 38 d ^{222}Rn. ^{226}Ra and its daughters are responsible for a major fraction of the radiation dose received from internal radioactivity. Radium is present in rocks and soils and, as a consequence, in water, food, and human tissue. The high specific activity and gaseous decay products of radium also make it difficult to handle in the laboratory.

^{226}Ra decays by α-emission to ^{222}Rn. This latter nuclide is the principal culprit in the radiation exposures from indoor radon, although radon is an inert gas and is not trapped in the body. However, if the decay happens to decay in the lungs, the short-lived decay products are retained in the body. Indoor radon contributes about 2 mSv/year (200 mrem/year) to the average radiation exposure in the United States, that is, about 2/3 of the dose from natural sources. Under normal circumstances, radon and its daughters attach to dust particles and are present in their equilibrium amounts. These dust particles can also deposit in the lungs. It has been estimated that in the United States, 15,000–22,000 cases annually of lung cancer are due to radon exposure.

3.6.3 Cosmogenic Nuclei

The second class of naturally occurring radionuclides is the *cosmogenic* nuclei produced by the interactions of primary and secondary cosmic radiation with nuclei in the stratosphere. The most important of these nuclei are ^{3}H (tritium), ^{14}C, and ^{7}Be. Less importantly, ^{10}Be, ^{22}Na, ^{32}P, ^{33}P, ^{35}S, and ^{39}Cl are also produced. These nuclei move into the troposphere through normal exchange processes and are brought to the earth's surface by rainwater. Equilibrium is established between the production rate in the primary cosmic ray interactions and the partition of the radionuclides among the various terrestrial compartments (atmosphere, surface waters, biosphere, etc.) leading to an approximately constant specific activity of each nuclide in a particular compartment when the cosmic ray flux is constant. When an organism dies after being in equilibrium with the biosphere, the specific activity of the nuclide in that sample will decrease since it is no longer maintained in equilibrium.

This behavior allows these nuclides to act as tracers for terrestrial processes and for chronological dating.
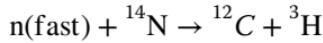
^{14}C ($t_{1/2}$ = 5730 years) is formed continuously in the upper atmosphere by cosmic rays that produce neutrons giving the reaction

$$n(\text{slow}) + {}^{14}\text{N} \rightarrow {}^{14}\text{C} + {}^{1}\text{H}$$

or, in a shorthand notation, $^{14}N(n, p)^{14}C$. ^{14}C is a soft (low-energy) β^--emitter ($E_{max} \sim 158$ keV). This radiocarbon (^{14}C) reacts with oxygen in the atmosphere and eventually exchanges with the stable carbon (mostly ^{12}C) in living things. If the cosmic ray flux is constant, and the terrestrial processes affecting ^{14}C incorporation into living things are constant, and there are no significant changes in the stable carbon content of the atmosphere, then a constant level of ^{14}C in all living things is found (corresponding to ~ 1 atom of ^{14}C for every 10^{12} atoms of ^{12}C or about 227 Bq/kg C). When an organism dies, it ceases to exchange its carbon atoms with the pool of radiocarbon, and its radiocarbon content decreases in accord with Equation 3.31. Measurement of the specific activity of an old object allows one to calculate the age of the object (see in the following).

^{14}C reaches the earth's surface at the rate of ~ 2.3 atoms/cm^2/s after production by cosmic ray interactions in the atmosphere, corresponding to a total production of $\sim 1.4 \times 10^{15}$ Bq/year. ^{14}C is (was) also formed by the $^{14}N(n, p)$ reaction from atmospheric tests of nuclear weapons. About 2.2×10^{17} Bq were made in the atmospheric test "spike" of the 1950s and 1960s that has been primarily transferred to the oceans and the biosphere. This means that ^{14}C is the most significant fallout nuclide from the point of view of population dose. Nuclear power plants also release ^{14}C as part of their normal operation, contributing $\sim 0.1 \times 10^{15}$ Bq/year.

Tritium (^3H) is produced naturally through atmospheric cosmic ray interactions via the reaction

$$n(\text{fast}) + {}^{14}\text{N} \rightarrow {}^{12}C + {}^{3}\text{H}$$

Tritium is also produced in ternary fission and by neutron induced reactions with ^6Li and ^{10}B. Tritium is a very weak β^- emitter with a half-life of 12.33 years. The global inventory of naturally produced tritium is 9.6×10^{17} Bq. Tritium is readily incorporated in water and is removed from the atmosphere by rain or snow. Its residence time in the stratosphere is 2–3 years; after reaching the troposphere it is removed in 1–2 months. The "natural" concentration of ^3H in streams and freshwater is ~ 10 pCi/L.

The nuclear weapons tests of late 1950s and early 1960s also injected a huge spike of tritium into the atmosphere along with the ^{14}C. The tritium levels in the troposphere increased by a factor of 100 at this time. Estimates of 2.4×10^{20} Bq for this spike have been made. Assuming that there will not be more atmospheric testing of nuclear weapons, the tritium from fallout should decrease with a half-life of 12.3 years. At present the fallout tritium in surface waters is

Table 3.3 Events Leading to Large Injections of Radionuclides into the Atmosphere.

Source	Country	Time	Radioactivity(Bq)	Important Nuclides
Hiroshima and Nagasaki	Japan	1945	4×10^{16}	Fission products and actinides
Atmospheric weapons tests	United States and USSR	1963	2×10^{20}	Fission products and actinides
Windscale	United Kingdom	1957	1×10^{15}	^{131}I
Chelyabinsk (Kysthym)	USSR	1957	8×10^{16}	Fission products
Three Mile Island	United States	1979	1×10^{12}	Noble gases, ^{131}I
Chernobyl	Russia	1986	5.2×10^{18}	^{137}Cs
Fukashima	Japan	2011	$3.4 - 8.0 \times 10^{17}$	^{137}Cs

Source: From Choppin et al. (1995).

approximately equal to that generated by nuclear power plant operation (from neutron capture on deuterium in water, as a ternary fission product or from neutron reactions with ^{10}B). (Nuclear plant operation generates $\sim 10^{16}$ Bq/year.) As a result of all of these developments, the current tritium content of surface waters is $\sim 10\times$ the "natural" level.

3.6.4 Anthropogenic Nuclei

The third principal component of environmental radioactivity is due to the activities of man, the *anthropogenic* radionuclides. This group of nuclides includes the previously discussed cases of ^{3}H and ^{14}C along with the fission products and the transuranium elements. The primary sources of these nuclides in the environment are nuclear weapons tests and nuclear power plant accidents. These events and the gross nuclide releases associated with them are listed in Table 3.3. Except for ^{14}C and ^{3}H, the anthropogenic contributions from nuclear weapons testing or use (which is the most significant source of man-made environmental exposure) are negligible compared to other sources of natural radioactivity. (The principal component of these large releases of radioactivity was shorter-lived fission products like ^{131}I, which have decayed, leaving ^{137}Cs, ^{90}Sr, and the Pu isotopes as the nuclides of most concern. For further descriptions of these events and their environmental consequences, the reader is referred to the material in Bibliography.)

3.6.5 Health Effects of Natural Radiation

As indicated previously, humans receive radiation doses from radionuclides in the body, from external exposure to naturally occurring and man-made

Table 3.4 Average Annual Human Exposure to Ionizing Radiation (mSv).

Radiation Source	World	United States
Inhalation of air	1.26	2.28
Medical	0.60	3.00
Terrestrial radiation from ground	0.48	0.21
Cosmic radiation	0.39	0.33
Ingestion of food and water	0.29	0.28
Cigarettes, air travel		0.13
Occupational exposure	0.005	0.005
Miscellaneous	0.002	0.003
Total	3.01	6.24

radionuclides in the environment, and from cosmic radiation. The worldwide average equivalent dose to humans is ~3.0 mSv/year, with significant variations depending on country. Table 3.4 summarizes the various contributions to this dose for the world and the United States (where the average annual dose is ~6.2 mSv.).

Inhalation of airborne radon is the principal contribution to the nonanthropogenic radiation exposure. The dose varies from country to country and depends on geology, house construction, and so on. For the United States, indoor radon is thought to account for 15,000–22,000 lung cancer deaths per year, second only to smoking.

The global annual radiation exposure due to medical procedures is 0.6 mSv, with US exposure being about 3.0 mSv/year due to diagnostic procedures. All other man-made sources of radiation contribute a negligibly small dose.

3.7 Radionuclide Dating

An important application of the basic radioactive decay law is using the decay of an activity to estimate the age of the sample called "radonuclide dating." From Equation 3.4, we know the expression for the number of atoms present as a function of time if there is no additional source:

$$N = N_0 e^{-\lambda t} \tag{3.59}$$

We can solve this equation for t

$$t = \frac{\ln(N_0/N)}{\lambda} \tag{3.60}$$

where N_0 and N are the number of radionuclides present at times $t = 0$ and $t = t$ and λ is the decay constant. The quantity t is the age of the object, and it can be determined from a knowledge of the nuclear decay constant ($\ln 2/t_{1/2}$) and the number of radioactive nuclei present in the object now, N, and initially, N_0. Clearly, N can be determined by counting the sample ($A = \lambda N$), but the trick is to determine N_0. One obvious approach is to recognize that for a decay of parent P to daughter D, the total number of nuclei is constant

$$D(t) + P(t) = P(t_0) \equiv P^0 \tag{3.61}$$

and

$$P(t) = P^0 e^{-\lambda t} \tag{3.62}$$

so that

$$t = \frac{1}{\lambda} \ln\left(1 + \frac{D(t)}{P(t)}\right) \tag{3.63}$$

Thus by measuring the current ratio of daughter to parent atoms $\frac{D(t)}{P(t)}$, one can deduce the age of the sample. (This assumes, of course, that there are no daughter atoms present at $t = 0$, that they are all due to the parent decay, and that none have been lost.)

Sample Problem 3.5: Simple Dating Problem

In a rock, one finds a nuclidic ratio of ^{206}Pb to ^{238}U of 0.60. Estimate the age of the rock.

Solution

$$t = \frac{1}{\lambda} \ln\left(1 + \frac{D(t)}{P(t)}\right)$$
$$t = \frac{1}{\ln 2/(4.5 \times 10^9)} \ln(1 + 0.60)$$
$$t = 3.1 \times 10^9 \text{ years}$$

If we want to relax the condition that no daughter atoms were present at $t = 0$ (i.e., $D(t = 0) \neq 0$), then we need an additional term in the equation

$$D(t) + P(t) = D^0 + P^0 \tag{3.64}$$

and we need another measured quantity or to make an estimate of D^0. Suppose there is another isotope of the daughter element that is stable, D_s, and is not formed in the decay of anything else. We can assume that

$$D_s(t) = D_s^0 \equiv D_s \tag{3.65}$$
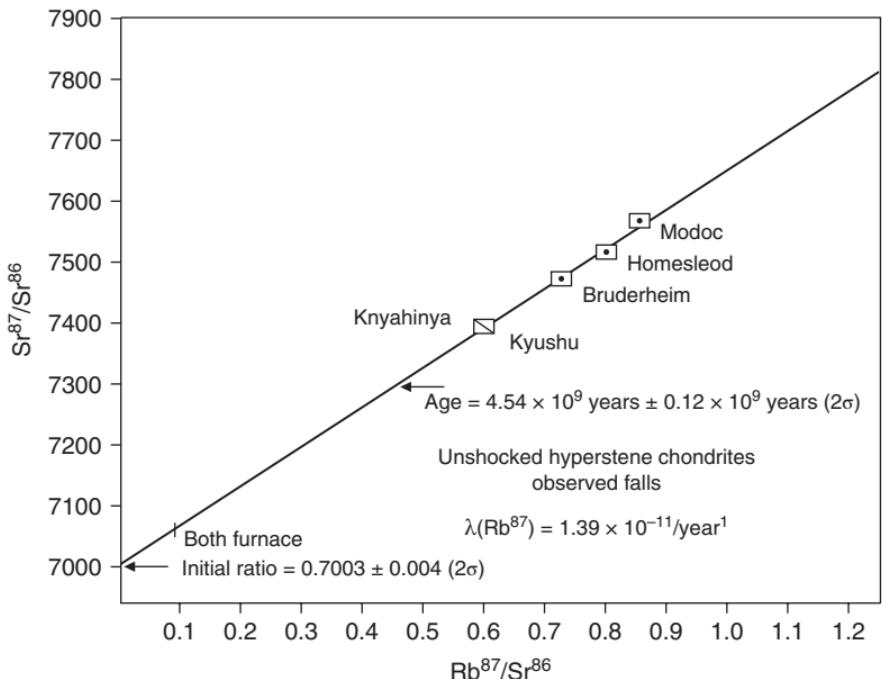
Figure 3.15 $^{87}Rb-^{87}Sr$ evolution diagram for six hypersthene chondrite meteorites. The data can be interpreted as showing that 4.54 billion years ago, all of these rocks had the same $^{87}Sr/^{86}Sr$ ratio of 0.7003 (From Wetherill (1975)).

where D_s is the number of such stable atoms. Then, dividing by D_s

$$\frac{D(t)}{D_s} + \frac{P(t)}{D_s} = \frac{D^0}{D_s} + \frac{P^0}{D_s} \tag{3.66}$$

Substituting $P^0 = Pe^{\lambda t}$ and rearranging

$$\frac{D(t)}{D_s} = \frac{D^0}{D_s} + \frac{P(t)}{D_s}(e^{\lambda t} + 1) \tag{3.67}$$

Thus, if we plot a set of measurements of $\frac{D(t)}{D_s}$ versus $\frac{P(t)}{D_s}$, we will get a straight line with the intercept $\frac{D^0}{D_s}$ and a slope of $(e^{\lambda t} \approx 1)$. Figure 3.15 shows such a plot of a set of meteorite samples using the $^{87}Rb \rightarrow ^{87}Sr$ decay as a chronometer ($t_{1/2} = 4.75 \times 10^{10}$ years).

Other geochronometers that can be used in a similar manner involve the decay of 1.277×10^9 years ^{40}K to ^{40}Ar (K/Ar dating) or the decay of ^{235}U or ^{238}U to their ^{207}Pb and ^{206}Pb daughters. Each chronometer poses special problems with regard to the loss of daughter species over geologic time by diffusion, melting, or chemical processes. The "normalizing" stable nuclide in the case of the uranium decay series is ^{204}Pb, and in the case of K/Ar dating, the normalizing nuclide is ^{36}Ar.

Table 3.5 Properties of Nuclidic Pairs Used in Dating.

Parent	Daughter	Parent Half-life (G year)	Normalizing Nuclide
^{235}U	^{207}Pb	0.70	^{204}Pb
^{40}K	^{40}Ar	1.28	^{36}Ar
^{238}U	^{206}Pb	4.47	^{204}Pb
^{232}Th	^{208}Pb	14.1	^{204}Pb
^{87}Rb	^{87}Sr	47.5	^{86}Sr
^{147}Sm	^{147}Nd	106.0	^{144}Nd

The U–Pb system is one of the most widely used chronometers in geology. There are two geo chronometers, the ^{238}U–^{206}Pb system and the ^{235}U–^{207}Pb system. If one adopts a primordial ratio of $^{238}U/^{235}U$ of 137.818 ± 0.045 for bulk silicate material, one can use the $^{207}Pb/^{206}Pb$ ratio to directly calculate an age. Uranium–lead dating is often done using the mineral zircon ($ZrSiO_4$) because this mineral incorporates uranium into its crystal lattice but rejects Pb, eliminating a possible correction.

In Table 3.5, we summarize the various dating methods, describing the parent nuclide (P), the daughter nuclide (D), and the "normalizing" nuclide (D_s).

The dating methods discussed up to now are been based on the use of long-lived radionuclides that are present in nature. Dating is also possible using "extinct radionuclides," that is, nuclei whose half-lives are so short that if they existed at the time of formation of our solar system, they would have decayed away essentially completely by now. The nuclides ^{129}I ($t_{1/2} = 1.57 \times 10^7$ years) and ^{244}Pu ($t_{1/2} = 8.08 \times 10^7$ years) are noteworthy examples of this type of nuclide.

The decay of extinct radionuclides is measured by measuring anomalies in the isotopic abundance of their stable daughters. For example, ^{129}I decays to ^{129}Xe, and its decay will lead to an anomalously high concentration of ^{129}Xe in the mass spectrum of Xe isotopes found in a rock system. What is dated is the "formation age" of the rock, that is, the time interval between the isolation of the solar system material from galactic nucleosynthesis and the time at which the rock cooled enough to retain its Xe. Formally this formation age, Δ, may be calculated as from the isotopic ratios in a fashion similar to that of Equation 3.67:

$$\Delta = \frac{1}{\lambda} \ln \frac{(^{129}I/^{127}I)_0}{^{129}Xe^*/^{127}I} \tag{3.68}$$

where $^{129}Xe^*$ is the excess Xe attributed to the decay of ^{129}I, ^{127}I is the concentration of stable, nonradiogenic ^{127}I, λ is the decay constant for ^{129}I, and $(^{129}I/^{127}I_0)$ is the ratio of the abundance of the iodine isotopes at the time

of isolation from galactic nucleosynthesis. This latter ratio is derived from theories of nucleosynthesis and is ~10^{-4}.

The decay of extinct ^{244}Pu is deduced from excess abundances of the nuclides ^{136}Xe, ^{134}Xe, and ^{132}Xe produced by the spontaneous fission of ^{244}Pu. Uncertainties arise because there is no stable isotope of Pu that can be used in the way that ^{127}I is used in Equation 3.68, and the use of other heavy nuclides ^{238}U or ^{232}Th as "substitutes" leads to difficulties due to differences in primordial production and chemistry.

By far the most important dating method involves the decay of ^{14}C ($t_{1/2}$ = 5730 years). As indicated previously, ^{14}C is formed continuously by the cosmic ray induced ^{14}N(n, p)^{14}C reaction in the upper atmosphere. This radiocarbon (^{14}C) exchanges with stable carbon (^{12}C) in living things leading to the existence of a constant level of ^{14}C in living systems as indicated schematically in Figure 3.16. When an organism dies, it will cease to exchange its carbon atoms with the pool of radiocarbon, and its radiocarbon will decay. Measurement of the specific activity of an old object allows the determination of the age. When organic matter has decayed for 10 or more half-lives of ^{14}C, it is no longer possible to directly measure the ^{14}C radioactivity of an object. In these cases, one can use *accelerator mass spectrometry* (AMS) to count the atoms of ^{14}C directly. An accelerator, such as a cyclotron or tandem Van de Graaff, is used as a mass spectrometer to separate the ^{14}C atoms from the more prevalent ^{12}C or ^{13}C. Another difficulty is the separation of ^{14}C from the ubiquitous ^{14}N isobar and various molecular ions, so accelerators are used to provide energetic ions that can be identified with standard nuclear techniques to identify the nuclear charge of the ion. The advantage of AMS can be realized by the following example. If one has 1 mg of organic material, a typical ^{14}C concentration might be 6×10^7 ^{14}C nuclei. Using modern AMS techniques, one can collect about 10^5 ^{14}C nuclei /h, while counting the same sample will result in a count rate of 1 count/h. Using this technique, it has been possible to determine ages as long as 100,000 years.

As noted earlier, the fundamental assumption in radiocarbon dating is that the specific activity of ^{14}C in nature (dpm ^{14}C/g^{12}C) is and has remained constant. This assumes the cosmic ray flux that generates the ^{14}C has been constant, and there are no sources of ^{14}C or ^{12}C that would change its equilibrium specific activity. Neither of these assumptions is strictly true, and corrections must be used to obtain correct ages from radiocarbon dating. Tree-ring data are available from present to about 12,500 years ago and serve to calibrate carbon dating in this interval. Recent data from sediments and terrestrial plant microfossils may help to extend this calibration to 52,500 years ago. The primary cosmic ray flux changes due to fluctuations in solar activity or the earth's magnetic field over time. More importantly, since the Industrial Revolution, the global carbon cycle is out of balance due to fossil fuel burning (of "old" or "dead" nonactive fossil carbon). This has caused a 1–3% dilution of the prehistoric ^{14}C/^{12}C ratio. As noted earlier, atmospheric testing of nuclear weapons contributed a spike to the global ^{14}C inventory that perturbed the ^{14}C/^{12}C ratio by
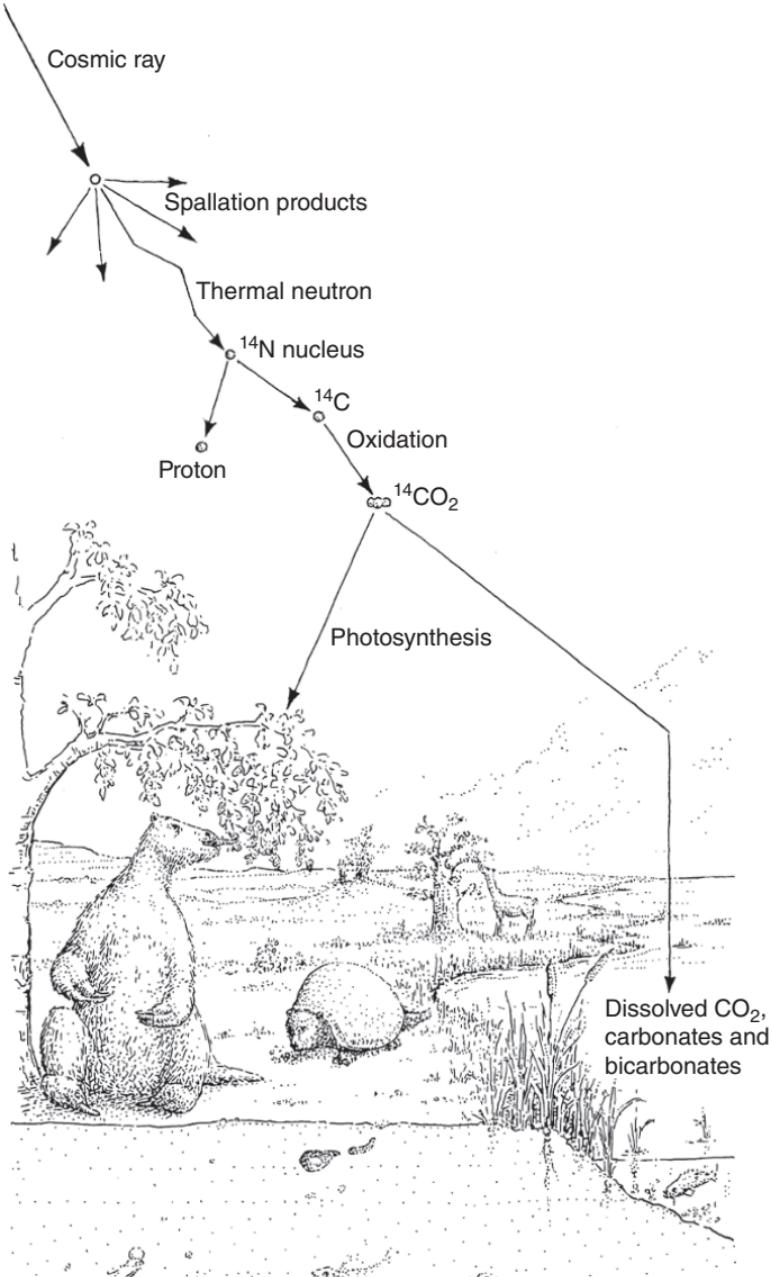
Figure 3.16 Artist's conception of how ^{14}C is generated and incorporated into living things (Reprinted by permission from Taylor (2000)).

a factor of two in the opposite direction. Continued operation of nuclear power plants also contributes an amount that is $\sim 10\%$ of the "natural" ^{14}C production rate. Similarly, a dating scheme for water-containing objects, such as wines, based upon the equilibrium production of tritium (^3H) and its decay has been
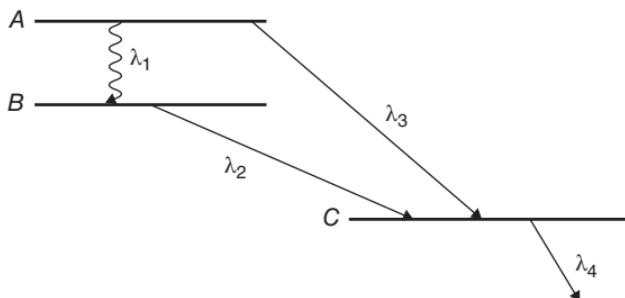
similarly perturbed by an injection of thousands of times the natural levels due to atmospheric testing.

Problems

3.1 Calculate the expected activity in Bq and in Ci for the following radionuclides (see Appendix B for nuclear data): (a) 1.0 g ^{239}Pu, (b) 1.0 g ^{14}C, (c) 1.0 g ^{137}Cs, (d) spontaneous fission activity for 1.0 g ^{252}Cf, and (e) 1 g ^{226}Ra.

3.2 Consider the decay sequence ^{239}U $\rightarrow$ ^{239}Np $\rightarrow$ ^{239}Pu $\rightarrow$
If you start with 1 mCi of initially pure ^{239}U, what is the activity of ^{239}Pu after (a) 1 day, (b) 1 month, and (c) 1 year?

3.3 Calculate the time necessary to reduce the activities of the following nuclei to 1% of their initial values: (a) ^{131}I, (b) ^{3}H, (c) ^{137}Cs, (d) ^{14}C, and (e) ^{239}Pu.

3.4 What is the mass (g) of the following activities: (a) 1 μCi ^{241}Am and (b) 1 pCi ^{239}Pu?

3.5 What is the partial half-life for decay by spontaneous fission for ^{252}Cf?

3.6 If ^{222}Rn is initially purified from its daughters, how long does it take for them to grow back to 50% of their values at secular equilibrium?

3.7 What are the partial half-lives of ^{22}Na for decay by (a) EC and (b) β^+ emission?

3.8 Calculate the relative mass ratios of ^{238}U, ^{226}Ra, and ^{222}Rn in an old uranium ore.

3.9 Consider the decay of ^{140}Ba to ^{140}La. At what time does the ^{140}La activity reach a maximum?

3.10 Consider a reactor in which the production rate of ^{239}U via the ^{238}U (n, γ) ^{239}U reaction is 10^5 atoms/s. Calculate the activity of ^{239}Pu after an irradiation of (a) 1 day, (b) 1 month, and (c) 1 year.

3.11 What is the probability of a ^{222}Rn atom decaying in our lungs? The atmospheric concentration of ^{222}Rn may be assumed to be 1 pCi/L. In an average breath we inhale 0.5 L of air and exhale it 3.5 s later.

3.12 Consider a radionuclide (decay constant λ) with activity A Bq at time t_1. Calculate the number of nuclei that decay between times t_1 and t_2.

3.13 Consider the following decay scheme shown in the following (from Evans, 1955): (a) derive expressions for the activity of B and C as a function of time if at $t = 0$, $A = A$, $B = C = D$. (b) What happens when the cross over transition $\lambda_3 = 0$?

3.14 If one "milks" a sample of ^{99}Mo to remove the daughter nuclide ^{99}Tc, how long does it take before the ^{99}Mo "cow" has an equilibrium amount of ^{99}Tc present?

3.15 Consider the case where $A \rightarrow B \rightarrow C$ and where $\lambda_A = \lambda_B$. Derive an expression for the activity of B as a function of time. Calculate the time t_{max} when the activity of B reaches a maximum. Show that $t_{max} \approx (\tau_A \tau_B)^{1/2}$ where τ_A, τ_B are the mean lives for A and B.

3.16 A uranium mineral was found to contain the Pb isotopes ^{204}Pb, ^{206}Pb, and ^{207}Pb in the ratio of $1 : 1000 : 400$. Estimate the age of this mineral (From Choppin et al. (1995).).

3.17 What was the rate of production of ^{24}Na in a 30 m reactor irradiation of ^{23}Na if the activity of ^{24}Na was found to be 1.0 µCi 3 h after the end of irradiation?

3.18 Calculate the heat generated per kilogram of natural uranium by the ^{238}U and the ^{235}U in secular equilibrium with their decay products. Assume all emitted radiation is absorbed.

3.19 Given the following data, determine the age of the rock and the initial ^{87}Sr/^{86}Sr ratio.

Table 3.6 Rb–Sr Dating Data.

Sample Number	Rb/Sr Weight Ratio	^{87}Sr/^{86}Sr Atom Ratio
1	1.06	0.7597
2	3.51	0.8248
3	6.61	0.9085
4	9.33	0.9796
5	10.67	1.0200

3.20 When counting a radioactive sample, one measures the number of counts C that occur between two times, t_1 and t_2. In plotting a decay curve, one will commonly plot this measurement at the time $t = (t_1 + t_2)/2$ and assign a count rate of $C/\Delta t$ where $\Delta t = t_2 - t_1$ to this point. What is the error associated with this procedure?

Bibliography

H. Bateman, *Proc Cambridge Phil. Soc.* **15**, 423 (1910).

C. Bronk Ramsey, et al., Science, **338**, 370 (2012).

P.J. Collon, W. Kutschera, and Z.-T. Liu, Ann. Rev. Nucl. Part. Sci. **54**, 39 (2004).

M. Eisenbud, *Environmental Radioactivity*, 3rd Edition, (Academic, Orlando, 1987).

J. Heiss, D.J. Condon, N. McLean, and S.R. White, Science **335**, 1610 (2012).

T.R. Ireland, Rev. Sci. Instru. **84**, 011101 (2013).

W. Kutschera, and M. Paul, Ann. Rev. Nucl. Part. Sci. **40**, 411 (1990).

D. Lal and H. Suess, Ann. Rev. Nucl. Sci. **18**, 407 (1968).

NCRP 160, Report No. 160, Ionizing Radiation Exposure of the Population of the United States (2009), ISBN: 9780929600987.

G. Steinhauser, A. Brandl, and T.E. Johnson, *Sci. Tot. Env.* **470**, 800 (2014).

R.E. Taylor, Fifty Years of Radiocarbon Dating, Am. Sci. **88**, 60 (2000).

UNSCEAR, Sources and Effects of Ionizing Radiation, United Nations Scientific Committee on the Effects of Atomic Radiation, (2008).

G.W. Wetherill, Ann. Rev. Nucl. Sci. **25**, 283 (1975). Treatments of radioactive decay in other textbooks that are especially recommended.

C.A. Bertulani, Nuclear Physics in a Nutshell (Princeton, Princeton, 2007).

G. Choppin, J. Rydberg, and J.O. Liljenzin, Radiochemistry and Nuclear Chemistry, 4th Edition (Academic, Oxford, 2013).

R.D. Evans, The Atomic Nucleus (McGraw-Hill, New York, 1955).

G. Friedlander, J.W. Kennedy, E.S. Macias, and J.M. Miller, Nuclear and Radiochemistry (John Wiley & Sons, Inc., New York, 1981).

4

Nuclear Medicine

4.1 Introduction

The most rapidly expanding area of radionuclide use is in **nuclear medicine**. Nuclear medicine deals with the use of radiation and radioactivity to diagnose and treat disease. The two principal areas of endeavor, **diagnosis** and **therapy**, involve different methods and considerations for radioactivity use. (As an aside, we note that radiolabeled drugs that are given to patients are called **radiopharmaceuticals**.) Recent work in this area has focused on developing combinations of two isotopes in one delivery system: one isotope provides a therapy function and another isotope provides a diagnostic function, called **theranostics.**

In **diagnosis (imaging)** emitted radiation from injected radionuclides is detected by special detectors (cameras) to give images of the body. A list of radionuclides commonly used in diagnosis is shown in Tables 4.1 and 4.2. At present, most nuclear medicine procedures (>90%) use either $^{99}Tc^m$ or one of the iodine isotopes. Most diagnostic use of radionuclides is for imaging of specific organs, bones, or tissue. Typical administered quantities of radionuclides are 1–30mCi for adults. Nuclides used for imaging should emit photons with an energy between 100 and 200 keV, which have small decay branches for particle emission (to minimize radiation damage) and have a half-life that is ~1.5 times the duration of the test procedure and be inexpensive and readily available. $^{99}Tc^m$ is used in more than 80% of nuclear medicine imaging because its 143 keV γ-rays produce excellent images with today's gamma cameras, and it has a convenient 6 h half-life. In **therapy**, radionuclides are injected into the body and concentrated in the organ of choice and damage the tissue.

Nuclear medicine combines nuclear and radiochemistry, pharmacy, medicine, and radiation biology in a challenging and satisfying career. Nuclear medicine is a major employer of today's nuclear and radiochemists, with an ever increasing demand for trained people. It can be intellectually and financially rewarding.

Table 4.1 Commonly Used Diagnostic Radionuclides, $Z < 28$.

Nuclide	Application
^{11}C	PET brain scans
^{14}C	Radiolabeling
^{13}N	PET scans
^{15}O	PET scans of cerebral blood flow
^{18}F	PET brain scans
^{32}P	Bone disease diagnosis
^{33}P	Radiolabeling
^{35}S	Heart disease diagnosis, nucleic acid labeling
^{47}Ca	Cell function and bone formation
^{46}Sc	Blood flow studies
^{47}Ca	Cancer diagnosis
^{51}Cr	Red blood cell survival studies, intestinal blood loss
^{51}Mn	Myocardial localizing agent
^{52}Mn	PET scans
^{59}Fe	Bone marrow scanning, iron metabolism studies
^{57}Co	Scanning of various organs
^{58}Co	Tracer for pernicious anemia

4.2 Radiopharmaceuticals

Radiopharmaceuticals are radioactive compounds used for diagnosis and therapy. Most (95%) radiopharmaceuticals are presently used for diagnosis. These compounds must be suitable for administration to humans, that is, they must be sterile. A radiopharmaceutical generally has two parts, the radionuclide and the pharmaceutical. The pharmaceutical component allows the compound to preferentially locate in organs or to participate in some function of the organ. The radiation from the nuclide must be easily detected and lead to a controlled dose to the patient. The effective half-life of the radionuclide in the target organ or the body should be short to minimize unnecessary radiation exposure. Radiopharmaceuticals used for imaging should involve γ-emitting radionuclides, while those intended for therapy will involve α or β emitters. Therapy with α emitters is used for small tumors due to the short range of the α-particles in matter, while the β-emitters are used with larger tumors.

There are a variety of ways that the pharmaceutical can bind to an organ. Among them are (Saha, 2010) (a) passive diffusion (^{99}Tc^m-DTPA in bone imaging), (b) ion exchange (uptake of ^{99}Tc^m phosphonate complexes in the bone),

Table 4.2 Commonly Used Diagnostic Radionuclides, $Z > 28$.

Nuclide	Application
^{64}Cu	PET scans
^{67}Cu	Cancer diagnosis
^{67}Ga	Tumor and inflammatory lesion imaging
^{68}Ga	Thrombosis and atherosclerosis studies
^{72}Se	Brain imaging
^{75}Se	Protein studies, liver and pancreas imaging
^{81}Kr^{m}	Lung imaging
^{82}Rb	Myocardial localizing agent
^{85}Sr	Measurement of bone metabolism
^{99}Tc^{m}	Brain, heart, lung, thyroid, gall bladder, skin, lymph node, bone, liver, spleen, and kidney imaging; blood flow studies
^{109}Cd	Cancer detection, pediatric imaging, heart disease diagnostics
^{111}In	Detection of heart transplant rejections, imaging of abdominal infections, imaging of metastatic melanoma
^{123}I	Thyroid disorders
^{125}I	Osteoporosis detection, tracer for drugs
^{127}Xe	Lung imaging, neuroimaging for brain disorders
^{133}Xe	Lung ventilation studies
^{169}Yb	Gastrointestinal tract diagnosis
^{191}Ir^{m}	Cardiovascular angiography
^{195}Pt^{m}	Pharmacokinetic studies of antitumor agents

(c) active transport (^{131}I intake of the thyroid), (d) metabolic mechanisms (^{18}F-FDG uptake in myocardial and brain tissues), and (e) antigen–antibody complex formation (^{131}I, ^{111}In, and ^{99}Tc^{m} labeled antibodies to attach to tumors).

There are certain obvious aspects of radiopharmaceuticals worth noting. The radiopharmaceutical label must be attached stably and easily to the molecule in question. For metals this frequently means the use of a chelate complex that hides the metal. DTPA complexes are typical compounds of this type. The size of the radionuclide complex must be small enough to pass through various natural filters such as the glomeruli in the kidneys. The pH of blood is 7.4, and the radiopharmaceutical needs to be compatible with this. The protein binding and lipid solubility of the radiopharmaceutical will help to determine the in vivo distribution and localization of the tracer. High lipid solubility will facilitate

diffusion through the cell membrane and concentration in a target organ. Protein binding will reduce this lipid solubility.

Some general labeling techniques include isotopic exchange (used for ^3H, ^{125}I, and ^{14}C), use of bifunctional chelating agents (that attach to the radioactive metal label and a macromolecule involved in localization), biosynthesis, and chemical synthesis (where a "foreign" radioactive label is attached to a biologically active molecule).

4.3 Imaging

Most people are familiar with the medical or dental use of x-rays for providing images of the tissue or bones where an external radiation source is used to do the imaging. To improve contrast, agents like barium sulfate, which attenuate the x-rays, are frequently administered to the patient. In the 1970s, a significant improvement in medical imaging occurred with the advent of **computerized tomography** (CT). In this technique, photographic plates are replaced by one or more radiation detectors, and an apparatus is used to move the source of imaging radiation relative to the patient with a digital computer system with appropriate software to provide online images from observed changes in counting rates as the source–patient geometry changes. (Tomography is from the Greek words "to cut or section" (tomos) and "to write" (graphein)). Tomography shows slices of the body with typical resolution of <1 mm. A simple conceptual diagram of such apparatus is shown in Figure 4.1.

Tomography can involve images generated by the transmission of radiation through the body (Fig. 4.1) or by incorporating radionuclides into the body and detecting the emitted radiation (emission tomography). For emission
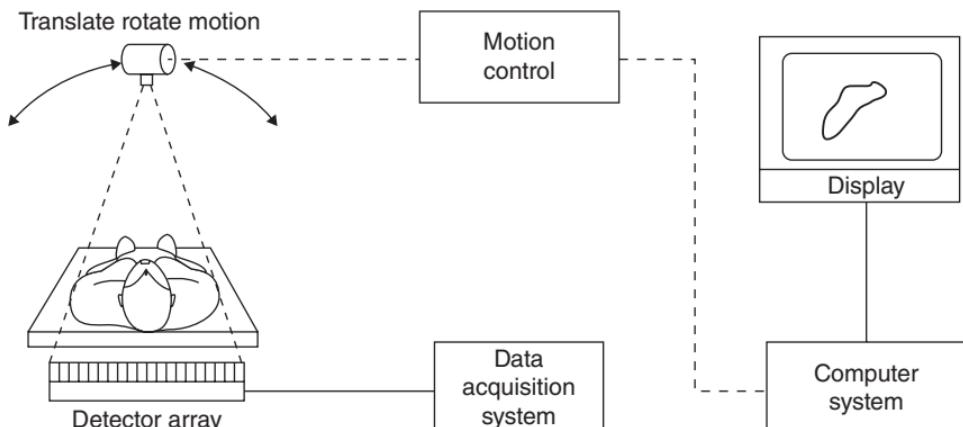
Figure 4.1 A conceptual diagram of a CT system.
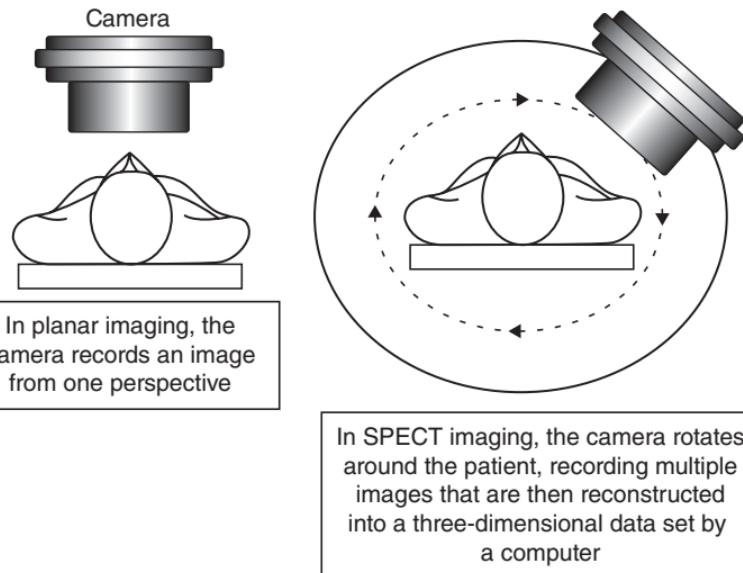
Figure 4.2 Schematic overview of planar (left) and SPECT (right) imaging (Reproduced by permission).
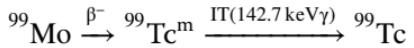
tomography, the imaging techniques can involve (a) planar images where a two-dimensional view of an organ is obtained (Fig. 4.2-left), (b) single-photon emission computerized tomography (SPECT) (Fig. 4.2-right) where a 3D computer reconstructed image is obtained, or (c) a two-photon process called positron emission tomography (PET). In PET, specific positron-emitting nuclides, such as ^{18}F, ^{11}C, ^{15}O, or ^{13}N, are introduced into a region to be studied. The two coincident 0.511 MeV photons produced when a β^+ annihilates emerge in exactly opposite directions and define a line passing through the point where the decay occurred. The two photons are detected in coincidence by an array of scintillation detectors. After the observation of many decays, computer techniques are used to reconstruct a 3D image of the area where the positrons annihilated.

Most imaging is of the planar type in which a stationary γ-ray detector is used. Typically a single picture is taken of the patient's liver, heart, and so on to determine the presence and distribution of the radionuclide. Sometimes, multiple images are taken over a short time to study the dynamic behavior of an organ through its radionuclide uptake. In SPECT imaging, the camera rotates around the patient, and the resulting images are woven together to give a 3D image. SPECT is used mostly for the brain and cardiac imaging with typical resolutions of 3–5 mm. The radionuclides used, ^{99}Tc^{m}, ^{201}Tl, ^{67}Ga, ^{111}In, and ^{123}I, are all single photon emitters.

4.4 $^{99}Tc^m$

$^{99}Tc^m$ is now the most widely used radionuclide for diagnostic purposes. It is used in ∼ 10 million procedures per year in the United States and 20 million per year in the world. It was discovered in 1938 by one of us (GTS) and Emilio Segre. As discussed previously, its single 142.7 keV photon is ideal for imaging, and its 6 h half-life accommodates most procedures without excessive radiation dose to the patients. Very importantly, this isomer is easily obtained as the daughter activity from its longer-lived parent, ^{99}Mo in a Mo–Tc generator (a so-called cow), and thus is available for continuous use at a reasonable cost.

How does a $^{99}Mo/^{99}Tc^m$ generator work? The parent ^{99}Mo (which can be obtained as a fission product or from the $^{98}Mo(n, \gamma)$ reaction) decays to $^{99}Tc^m$ as follows:

$$^{99}Mo \xrightarrow{\beta^-} {}^{99}Tc^m \xrightarrow{IT(142.7\,keV\gamma)} {}^{99}Tc$$

The decay of ^{99}Mo goes ∼ 87.6% of the time to the isomeric state of ^{99}Tc. This state decays by the emission of a single 142.7 keV photon to the ground state. ^{99}Mo, as a reaction product, is purified and dissolved in acid media to form the anionic species molybdate (MoO_4^{2-}) and paramolybdate ($Mo_7O_{24}^{6-}$). The molybdate anions are adsorbed on an aluminum oxide column. This column can be "milked" at will to extract the $[^{99}Tc^mO_4^{2-}]$ ion formed by the decay of ^{99}Mo. The daughter $^{99}Tc^m$ is eluted from the column with 0.9% NaCl. The ^{99}Mo remains bound to the column as it is insoluble in 0.9% NaCl. (See Figs. 4.3 and 4.4.) After elution from the column, the $^{99}Tc^m$ grows in again, and the maximum activity is reached ∼ 1 day later. Useful activities are available 3–6 h after a given elution. Typical commercial columns are used for a week and then discarded. After separation from the molybdenum, the technetium is converted to a suitable complex prior to use in a patient. This is frequently done using "chemistry kits" where the $^{99}Tc^mO_4^-$ is mixed with the contents of the kit to create the radiopharmaceutical. The kit usually contains a reducing agent that reduces the $^{99}Tc^m$ to a lower oxidation state allowing it to bind to a suitable ligand.

The $^{99}Mo/^{99}Tc^m$ system represents a case of **transient equilibrium** as indicated in Figure 4.5—left. If all of the ^{99}Mo decayed to $^{99}Tc^m$, then the activity of $^{99}Tc^m$ would exceed that of the ^{99}Mo after equilibrium. Since only 87.6% of the ^{99}Mo decays to $^{99}Tc^m$, then there is slightly less $^{99}Tc^m$ than ^{99}Mo. We can use Equations 3.6 and 3.31 to trace out the activity of the ^{99}Mo and $^{99}Tc^m$ as a function of time (Fig. 4.5-right) during "milking" of the cow. The $^{99}Tc^m$ activity grows in after each milking of the cow, with a maximum amount being present ∼ 22 h after separation. However Equations 3.6 and 3.31 do not exactly predict the amount of $^{99}Tc^m$ available from the cow because the efficiency of the elution process is typically 80–90% and the elution efficiency changes slightly from one elution to another.

Figure 4.3 Schematic diagram of a Mo–Tc cow (Reprinted from *Ehmann and Vance (1991)*).

Production of parent
↓
Radiochemical separation and chemical treatment
↓
Addition to alumina column
↓
Decay of ^{99}Mo to ^{99}Tc^m
↓
Elution with physiological saline
↓
Eluted ^{99}Tc^{m}O$_4^-$

^{235}U fission → ^{99}Mo ← ^{98}Mo (n,γ)
↓
^{99}MoO$_4^{2-}$
↓
0.9% NaCl

^{99}MoO$_4^{2-}$
$\downarrow$ β^-
^{99}Tc^{m}O$_4^-$

"Cow"

^{99}Tc^{m}O$_4^-$
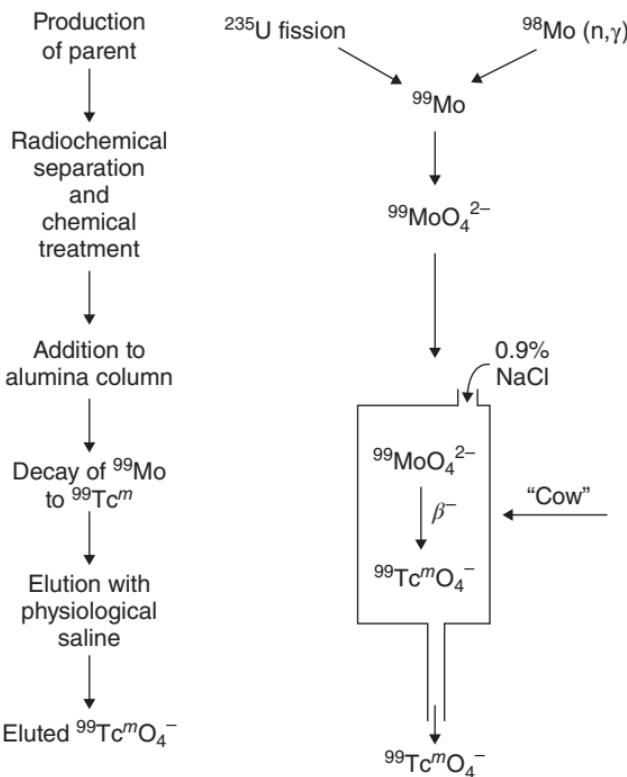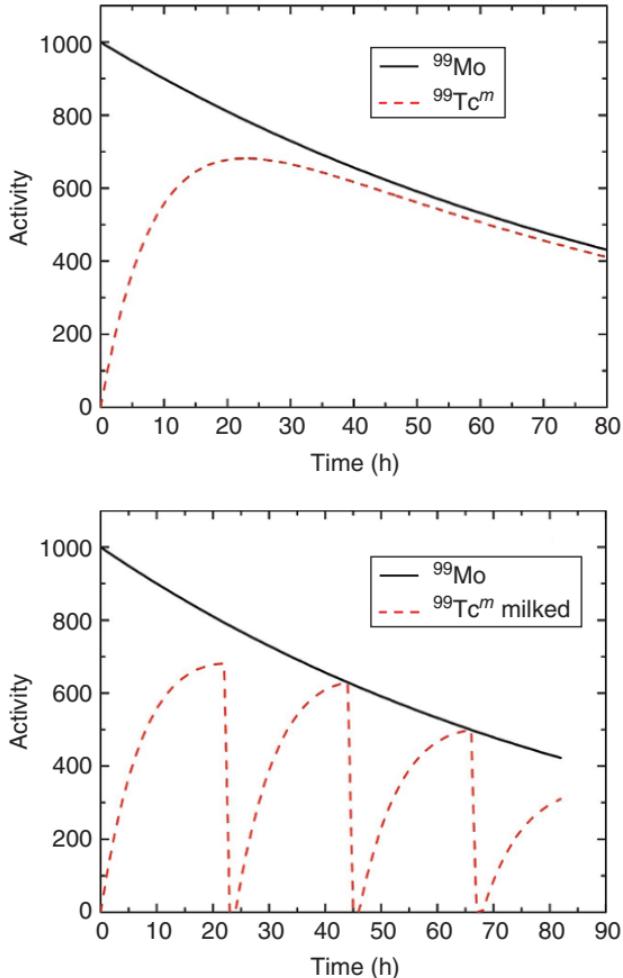
Figure 4.4 Photograph of the first ^{99}Tc^m generator (From Brookhaven National Laboratory).

Figure 4.5 (Left) example of the transient equilibrium between ^{99}Mo and ^{99}Tc^m and (right) how the equilibrium is affected by multiple milkings.

In 2014 ^{99}Tc^m came into short supply (the so-called isotope crisis) due to the combination of safety concerns at the small number of production reactors. The parent nuclide ^{99}Mo can be produced in four different ways: (a) the neutron-induced fission of ^{235}U in reactors, (b) neutron capture reactions on ^{98}Mo (^{98}Mo(n, γ)^{99}Mo) also carried out at reactors, (c) photofission of ^{238}U (^{238}U(γ, f)), and (d) charged-particle-or photon-induced reactions on ^{100}Mo (^{100}Mo(γ, n)^{99}Mo or ^{100}Mo(p, pn)^{99}Mo). The first two reactor-based methods gave the highest production rates for ^{99}Mo and came to dominate the market.

The nuclear reactors used for ^{99}Mo production in Canada, Belgium, the Netherlands, and South Africa were ~50 years old at that time and nearing the end of their lifetimes. Operation of these reactors is not reliable. The United States is a large consumer of ^{99}Mo, requiring 34,000–46,000 Ci/week. The United States had no domestic suppliers of ^{99}Mo at that time. (US production

of ^{99}Mo stopped in 1989 because US suppliers could not compete with subsidized non-US suppliers).

The most efficient reaction for the production of ^{99}Mo is the neutron-induced fission of ^{235}U. The specific activity of the fission generated samples of ^{99}Mo is typically a factor of 10–20 times greater than neutron capture generated samples. The best technique for this reaction involves the use of high enrichment uranium (HEU, 19.7% ^{235}U). Use of this material poses security problems as this level of enrichment is involved in nuclear weapons and the waste from this production method is highly radioactive.

Various solutions to this "isotope crisis" continue to be developed. These solutions involve the use of low enrichment uranium (LEU) in reactors, neutron capture using reactors, and accelerator-based methods. It is not clear which method or methods will be the "winners" in this competition.

As discussed earlier, ^{99}Tc^m is widely used in diagnostic imaging. Common imaging studies include: (a) whole body bone scans, (b) myocardial perfusion imaging, (c) cardiac ventriculography, and (d) functional brain imaging. To use ^{99}Tc^m in these applications, the common pertechnetate ion (^{99}Tc^{m}O$_4^-$) is eluted from ^{99}Mo cows and must be converted to a biologically more useful form. For example, bone imaging frequently involves the use of ^{99}Tc^m-methylene diphosphonate (^{99}Tc^m-MDP). This radiopharmaceutical is taken up by the cells that build the bone and serve as a marker of active bone growth making it sensitive to fractures and bone tumors. Imaging can be done with a simple gamma camera or using the SPECT technique.

4.5 PET

PET is arguably the most powerful imaging technique in nuclear medicine. Positron-emitting radionuclides (such as ^{11}C ($t_{1/2} = 20.3$ m), ^{19}F ($t_{1/2} = 109.7$ m), ^{64}Cu ($t_{1/2} = 12.7$ h) are produced in one of several hundred medical cyclotrons located in hospitals or very close to the delivery site. These relatively short-lived nuclides are incorporated into biologically active molecules, which, in turn, are injected into patients. The active molecule concentrates in the organ of interest, and the patient is placed in a three-dimensional scanner. The positron-emitting radionuclides decay and the resulting positrons annihilate when they strike ordinary electrons. The annihilation occurs within ∼1–10 mm from the site of the radionuclide. Each annihilation event produces two 0.511 MeV photons, moving in exactly opposite directions from one another. These two photons are simultaneously detected by an array of scintillation detectors surrounding the patient. Each pair of 0.511 MeV photons defines a line passing through the point of annihilation of the positron. Detection of multiple events provides a three-dimensional image of the emitting radionuclide distribution. The imaging is shown schematically in Figure 4.6.
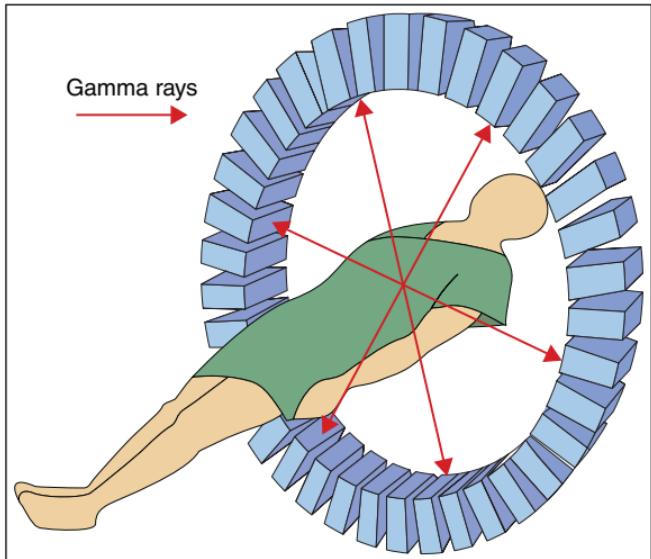
Figure 4.6 Basics of PET imaging, the gamma rays (red arrow) are simultaneously detected in radiation detectors on opposite sides of the patient.
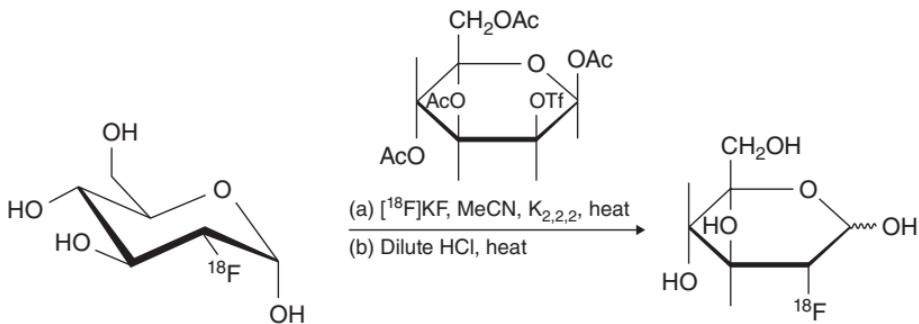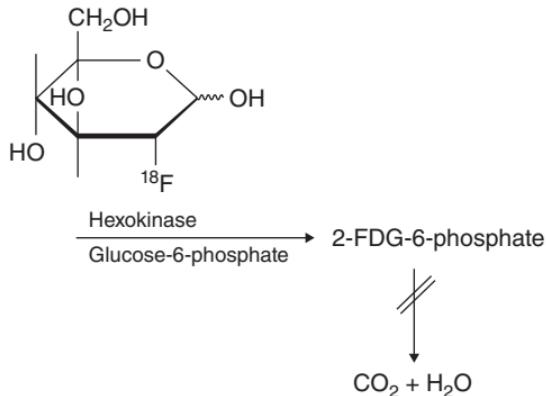
Figure 4.7 (Left) the chemical structure of FDG. (Right) chemical synthesis of FDG.

Approximately 90% of the use of PET at present is in oncology. The approved clinical radiopharmaceutical for these studies is 2-[^{18}F]fluoro-2-D-glucose ([^{18}F]FDG). (See Fig. 4.7-left.) This radiopharmaceutical must be synthesized rapidly since the half-life of ^{18}F is only 109.7 m. The ^{18}F is produced by proton bombardment of ^{18}O-enriched water via the ^{18}O(p,n)^{18}F reaction. This reaction produces ^{18}F$^-$ ions in the water. The ^{18}F$^-$ is separated from the solution by ion exchange and eluted with an acetonitrile solution of 2,2,2-cryptand and K$_2$CO$_3$. Evaporation of the eluate gives [crypt $-$ 222K]$^{+\,18}$F$^-$ salt. The reaction shown schematically in Figure 4.7-right is then carried out to make the ^{18}F-FDG. ^{18}F-FDG is an analog of glucose. When it is absorbed in the body, the fluoroglucose is converted to fluoroglucose-6-phosphate, which cannot be metabolized further (see Fig. 4.8). Note that ordinary glucose also forms glucose-6P in the cells, which in turn is destroyed by glycolysis.

Figure 4.8 Chemical pathway for the uptake of ^{18}F-FDG in the body.

^{18}F–FDG is used to image cancer metabolism by indicating areas of high glucose use, that is, cancer cell activity; thus, FDG-PET can be used for the diagnosis and monitoring of the treatment of cancer. It can also be used to diagnose Alzheimer's disease (Fig. 4.9).
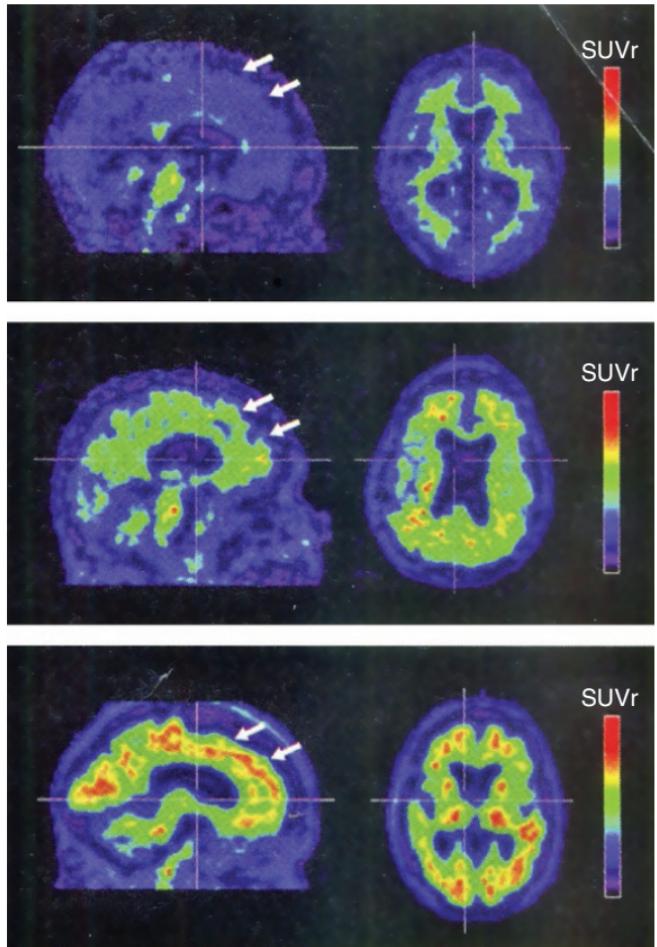
Among the more fascinating uses of PET is real-time imaging of brain functions. By using the PET nuclides ^{11}C, ^{15}O, ^{13}N, and ^{18}F, scientists at the Brookhaven National Laboratory have made a number of pioneering studies of the brain chemistry of substance abuse, the acute effects of cocaine and Ritalin, and the chronic effects of cocaine and tobacco smoke on the human brain (see Fig. 4.10). The "addiction circuitry" of the human brain has been studied. The effects of alcohol and sleep deprivation have also been assessed using PET.

4.6 Other Imaging Techniques

^{201}Tl in the form of thallous chloride is used in perfusion imaging of the heart. Imaging is performed under resting and stress conditions (Fig. 4.11) using SPECT/CT methods. A redistribution image is also measured some 3–4 h after the stress images. In panel (a) of Figure 4.11, one sees the response of a normal heart to stress and redistribution with uptake of the tracer in all sections of the heart. (ii) In subjects with ischemia (b), there are areas of the heart where there is no uptake during stress, but uptake is present during redistribution. (iii) In patients with an infarct (c), there is no uptake of the tracer during stress or redistribution, reflecting permanent heart damage.

Tumors have distinctive characteristics, such as increased metabolic activity and blood flow, high vascular permeability, and the presence of tumor associated antigens. These characteristics can be used with a variety of radiopharmaceuticals to form images of the tumors. ^{18}F-FDG is the most effective, widely used radiopharmaceutical for general tumor imaging in that it can be used to image brain tumors, breast cancer, lung tumors, head and

Figure 4.9 Amyvid-PET images are shown for three subjects where red in the highest standard uptake value ratio (SUVr). Top row, normal subject with no β-amyloid plaques, middle row moderate load of β-amyloid plaques associated with early stage Alzheimer's disease, and bottom row high load of β-amyloid plaques associated with late stage Alzheimer's disease (From Butler Hospital). (*See insert for color representation of the figure.*)
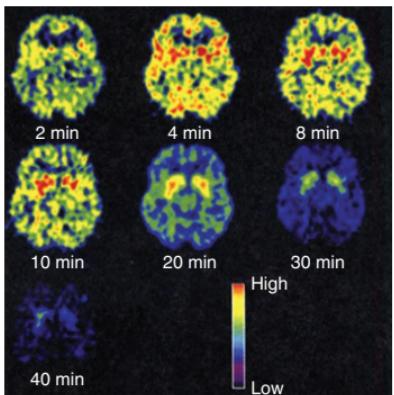
neck cancer, esophageal cancer, melanoma, colorectal cancer, lymphoma, and thyroid follicular cancer.

4.7 Some Random Observations about the Physics of Imaging

It is beyond the scope of our discussion of imaging to discuss in detail the physical principles at work in imaging. However, there are certain short observations that we believe can inform the reader about the nature of some of the problems encountered in nuclear medical imaging. In Figure 4.12, we show a more detailed schematic view of a gamma camera. (These cameras are also referred to as "Anger cameras" after a developer of this device.) One notices two important features of the gamma camera that would not be present if the detector were an ordinary NaI(Tl) scintillation detector. The first is an imagining collimator, typically a lead plate with holes drilled in it, that restricts which photons
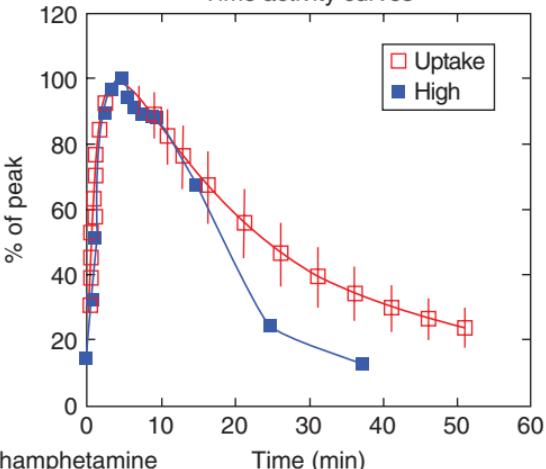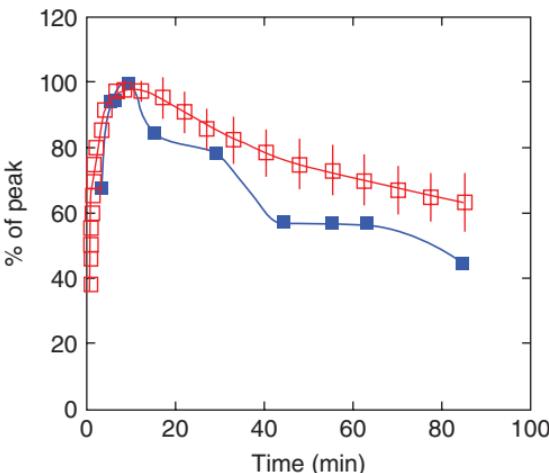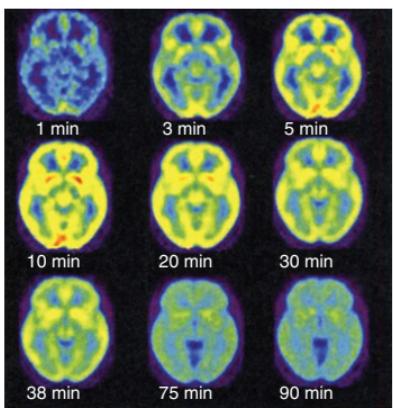
Figure 4.10 Pharmacokinetics of cocaine and methamphetamine in the human brain. (a) Axial brain scans (b) Time activity curves. The fast brain uptake of the drugs corresponds to the user "high". Reproduced with permission from Annu. Rev. Pharmcol. Toxicol. **52**, 321 (2012). (*See insert for color representation of the figure.*)

are detected by the scintillator. This collimator is crucial in forming an image if a large, coarsely segmented scintillator is used. Without it, one would have a jumbled set of photon trajectories at every point on the scintillator. The second feature is the use of an array of phototubes to view the light output of the scintillator. This allows the determination of the X and Y coordinates associated with the detection of a single photon. Such gamma cameras can be used for either static or dynamic imaging depending on the computer routines for signal processing.
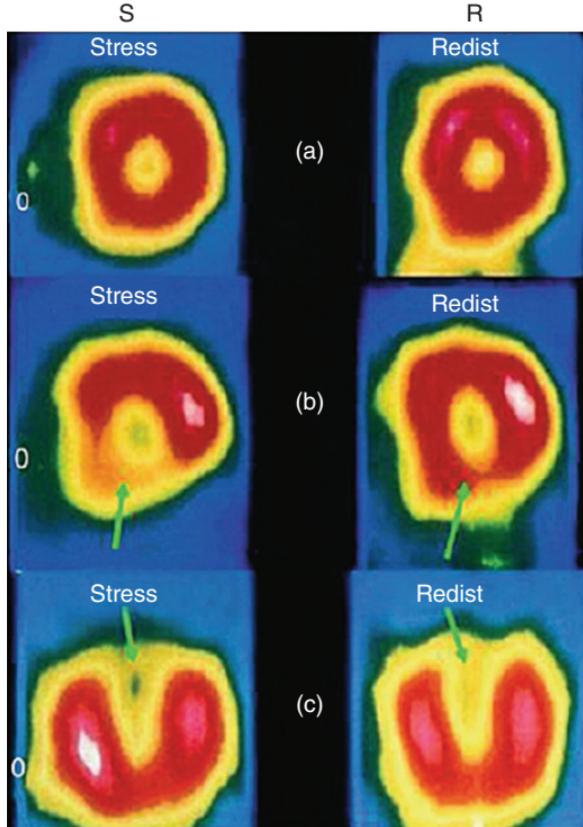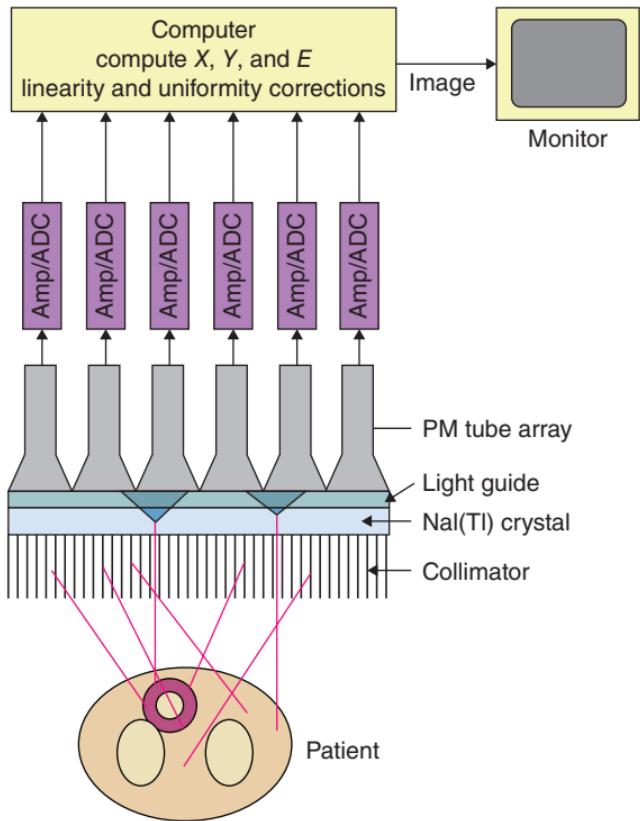
Figure 4.11 Images from ^{201}Tl cardiac imaging (Saha (2010). Reproduced with the permission of Springer). (*See insert for color representation of the figure.*)

A feature that medical uses of radioactivity share with ordinary radiotracer studies is an appropriate treatment of background activity. While one hopes an injected radionuclide will concentrate in a particular organ, it will also be taken up by surrounding tissue, giving rise to a radioactive "background" for an attempts at imaging. The usual rules about proper counting of sample and background and estimation of the total uncertainty in a result must take this into account.

In our simple picture of PET imaging, we indicated that the intersection of several straight-line trajectories of 0.511 MeV photon pairs would clearly define the three-dimensional image of the emitting source. In reality, there are a number of complications or problems with that simple picture. For example, the positrons generally travel a (small) distance before annihilating, creating a dispersion of emitting points. The emitted photons may be scattered by surrounding material, and random coincidences can occur that will further distort the reconstructed image.

Most SPECT and PET scanners are combined in hybrid imaging systems that also involve X-ray or MRI computer tomography. X-ray or MRI tomography has superior resolution (~1 mm) compared with SPECT and PET. Typically these

Figure 4.12 Schematic representation of the important components in a gamma camera (Cherry et al. (2012). Reproduced with the permission of Elsevier).

hybrid systems that involve both types of tomography, PET/CT or SPECT/CT, generally are a single machine to minimize patient time in the machine and facilitate accurate combination of the images.

In assessing the dose given to patients during imaging, one must account for both the physical and biological half-lives of the nuclides involved. For example, imagine we are dealing with a radionuclide that is instantaneously taken up in the body with no excretion. Then we would have the simple radioactive decay

$$A(t) = A_0 e^{-\lambda t} \tag{4.1}$$

where $A(t)$ is the activity of the radionuclide as a function of time and A_0 is the amount taken up. We can then define the "accumulated activity" of the radio-pharmaceutical as

$$A_{\text{accum}} = A_0 \int_0^\infty e^{-\lambda t} dt \tag{4.2}$$

where λ is the familiar decay constant of the radionuclide. Now let's consider the case where there is both physical decay of the radionuclide and elimination of the radionuclide by biological processes. The effective decay constant is the

sum of the two contributions for the disappearance of the nuclide:

$$\lambda_{\text{eff}} = \lambda_{\text{decay}} + \lambda_{\text{biol}} \tag{4.3}$$

If we prefer to use the effective half-life of the radionuclide as $t_{1/2}^{\text{eff}}$, we can write:

$$\frac{1}{t_{1/2}^{\text{eff}}} = \frac{1}{t_{1/2}^{\text{decay}}} + \frac{1}{t_{1/2}^{\text{biol}}} \tag{4.4}$$

$$t_{1/2}^{\text{eff}} = \frac{t_{1/2}^{\text{decay}} t_{1/2}^{\text{biol}}}{t_{1/2}^{\text{decay}} + t_{1/2}^{\text{biol}}} \tag{4.5}$$

$$\lambda_{\text{eff}} = \frac{\ln(2)}{t_{1/2}^{\text{eff}}} \tag{4.6}$$

If we want to calculate the dose associated with this radionuclide, we must also account for the energy deposit associated with the activity. We can define the energy emitted per unit of accumulated dose as Δ_i where $\Delta_i = 1.6 \times 10^{-13} \ N_i E_i$ (Gy-kg/Bq-s) where E_i is the average energy of the emitted particles and N_i is the number of particles emitted per disintegration. Similarly we can define ϕ_i as the fraction of the emitted radiation i that is absorbed in the tissue, we can write for the total absorbed energy, $A_{\text{accum}}\phi_i\Delta_i$, and the dose is then given by the expression

$$\text{Dose} = \frac{A_{\text{accum}}}{\text{Mass}} \sum_{i=1}^{n} \phi_i \Delta_i \tag{4.7}$$

4.8 Therapy

The therapeutic uses of radiation and radioactivity are no less important than the diagnostic uses. Radiotherapy plays an important role in the treatment of cancer. More than half the patients with localized tumors are treated using radiotherapy. The challenge with radiotherapy is similar to that encountered in chemotherapy, how to kill the diseased cells without killing so many (nearby) normal cells that the organism does not survive. A problem that must be overcome is that cancer cells are less oxygenated than normal cells and are thus more radiation resistant.

One approach to this problem is to use an internal source of radiation in the form of a physically or chemically implanted radionuclide. One common example is the treatment of hyperthyroidism. The therapeutic agent is ^{131}I. Iodine in general and thus ^{131}I is accumulated in the thyroid, and when it decays it irradiates the nearby tissue with β- and γ-rays. About 90% of the

damage is done by the β-particles. The thyroid gland resides in the throat and that is somewhat removed from other organs. The treatment has proven to be highly successful.

A promising development in radiotherapy is the development of monoclonal antibodies that seek out particular cancer cells and bind to them. If one can radiolabel these antibodies with nuclides such as the α-emitting ^{211}At or β-emitters like ^{131}I, ^{186,188}Re, ^{125}I, or ^{90}Y, then one can deliver a large dose to the cancer cells with reduced damage to the normal tissue.

The spread of cancer to the bone results in severe pain. Relief of this pain improves the quality of life. ^{32}P-orthophosphate has been used for some time in this manner. The drug localizes mostly in the hydroxyapatite crystals in the bone. The high-energy β-particle from ^{32}P decay ($E_\beta^{max} = 1.7$ MeV) provides the dose.

An alternative approach, using external radiation, is to deposit, by various means, a large amount of energy into the tumor cell with as little loss of energy elsewhere as possible. One straightforward way to do this is to deposit a radiation absorbing compound preferentially in the cancer cell and to irradiate the organism, thus localizing the dose. One such material is boron, which can undergo the ^{10}B(n, α) reaction, splitting into two large fragments (^{4}He and ^{7}Li) with short ranges (5–9 μm) in tissue. Two boron compounds have been utilized, Sodium borocaptate (BSH) and boronophenylalanine (BPA); epithermal neutrons (0.5 eV< E_n < 10 keV) are used for the ^{10}B(n, α) reaction as a compromise between a larger cross section (thermal neutrons) and the
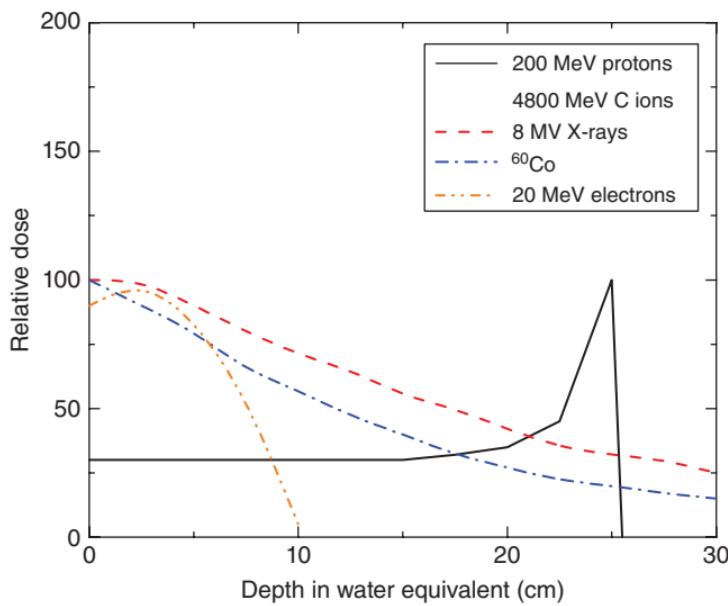
Figure 4.13 Comparison of the Bragg curves of several therapy agents.

ability of higher-energy neutrons to penetrate tissue. This technique is referred to as boron neutron capture therapy (BNCT). While clinical trials of BNCT have been pursued for some time in connection with treatment of brain, neck, and head cancers, it has not been widely adopted at present because the boron delivery agents have not met the criteria of low toxicity, normal tissue uptake, high tumor uptake, and rapid clearance from the body.

The most common form of radiotherapy is irradiation of the cancerous tissue with ionizing radiation, that is, photons or charged particles. Figure 4.13 shows the dose associated with various types of ionizing radiation as a function of depth of penetration in tissue. The X-rays and γ-rays generally deliver a continuously decreasing dose as they penetrate matter. (High-energy photons show an initial increase in dose and then a decrease, due to forward scattered Compton electrons.) This continuous slowly varying dose at all depths means that the radiation damage delivered by the photons is not concentrated in a tumor but occurs in healthy tissue as well. Only the charged particles (protons or heavy ions) show an energy deposition pattern that has a maximum near the end of its range in matter (the Bragg peak). In theory, carefully choosing the incident energy would allow one to localize the radiation damage to the tumor. Furthermore, the higher linear energy transfer associated with heavy ions compared to photons results in more severe DNA damage. This enhanced relative biological effect of the heavy-ion radiation allows greater tumor destruction.

Problems

4.1 Compute the amount of a radionuclide necessary to perform an experiment with a sample count rate of 1000 cpm, a detector efficiency of 33%, and a sample aliquot for counting consisting of 10% of the total isolated sample and where the percent incorporation of the nuclide into the total isolated sample was 0.5%.

4.2 Isotope X, with a half-life of 5 days, is to be used in an experiment that includes the following factors: (a) sample count rate of 100 cpm, (b) detector efficiency of 10%, (c) assume the sample with the lowest count rate will represent a 0.5% incorporation, and (d) assume all samples will represent only 5% of the total isotope administered. What amount of X must be used?

4.3 Three tracers, 90-year ^{151}Sm (0.076 MeV β$^-$, 100% of the disintegrations and 0.022 MeV X-ray, 4%), 244.3 days ^{65}Zn (0.33 MeV β$^-$, 1.7% of disintegrations and 0.511 MeV γ-rays, 3.45), and 14.3 days ^{32}P (1.71 MeV β$^-$, 100% of the disintegrations) will be used simultaneously in a multi-tracer

experiment. Suppose you wish to measure the uptake of these three elements in the blood of a rat and the loss of these elements to the rest of the rat's organs and tissue from the blood. What levels of the tracer will you inject into the rat? Why? (Assume that you will withdraw 0.1 mL blood volumes every hour for 24 h. The total blood volume of an adult rat is about 15 mL.)

4.4 A 10-mL sample of blood is withdrawn from a patient, and the red cells are labeled with ^{51}Cr, a 27-day γ-emitter. One milliliter of the labeled blood diluted to 15 mL with water gave a net counting rate of 33,000 cpm (background corrected). The remaining labeled blood is injected back into the patient, and after several hours 10 mL of blood is withdrawn and counted as before. The net counting rate (background corrected) was 500 cpm. What is the total volume of the patient's blood?

4.5 Compound X, molecular weight of 150 (specific activity 1.0 mCi/mmole), was checked for purity by carefully weighing 1.5 mg of the radiochemical, mixing with 1000 mg of unlabeled compound X, and recrystallizing until a constant specific activity. Radioassay gave a value of 2500 dpm/mg. What was the purity of the radiochemical in percent?

4.6 A sample of $^{99}Tc^{m}$ is labeled "100 kBq/mL at 09:00." What volume should be withdrawn to prepare an injection for a patient of 50 kBq at 16:00?

4.7 Consider two radiopharmaceuticals, A and B. Radiopharmaceutical A generates contrast in imaging by enhanced uptake in the organ of interest by uptake in this organ that is 10 times the uptake in the surrounding tissue. Radiopharmaceutical B generates contrast in imaging the same organ by reducing the uptake in the surrounding tissue by a factor of 10. Assume the organ to be imaged has a volume of 1 cm^3, while the total tissue affected has a volume of 10 cm^3. Assume the background counting rate in the tissue is 10 cpm/cm^3. Which is the better choice for imaging, A or B and why?

4.8 What is the specific activity of $^{99}Tc^{m}$ in Bq/g? Ci/g?

4.9 What is the accumulated activity in the liver if 50 MBq of $^{99}Tc^{m}$ is injected in the body, assuming 50% is trapped by the liver and remains there? The accumulated activity is a measure of the total number of decays occurring in the organ during the time radioactivity is present in the organ.

4.10 What is the activity in the lungs after 8 h if 50 MBq of ^{99}Tc^m is injected into the patient? Assume the biological half-life is 30 min.

4.11 A radionuclide decays by emitting 0.695 MeV β-particles. Its physical half-life is 14.5 days. Assume its biological half-life is 7.1 days. What is the total energy deposited per kilogram in the body in one week from the absorption of 250 MBq?

4.12 A Mo–Tc cow is measured to contain 3.2 Ci of ^{99}Mo (in equilibrium with ^{99}Tc^m) at 08:00 on Monday. What is the total ^{99}Tc^m activity that could be eluted from this cow at 12:00 on Wednesday?

Bibliography

V. Carroll, D.W. Demoin, T.J. Hoffman, and S.S. Jurisson, Radiochim. Acta **100**, 653 (2012).

S.R. Cherry, J.A. Sorenson, and M.E. Phelps, *Physics in Nuclear Medicine*, 4th Edition (Elsevier, Philadelphia, 2012).

Ehmann, W. D. and D.E. Vance, *Radiochemistry and Nuclear Methods of Analysis*, Wiley, New York, 1991.

T.J. McCarthy, S.W. Schwarz, and M.J. Welch, J. Chem. Educ. **71**, 830 (1994).

G.B. Saha, *Fundamentals of Nuclear Pharmacy*, 6th Edition (Springer, New York, 2010).

D. Schardt, T. Elsässer, and D. Schulz-Ertner, Rev. Mod. Phys. **82**, 383 (2010).

R.F. Service, Science **331**, 277 (2011).

Science **335**, 898 (2012).

N.D. Volkow, G.-J. Wang, J.S. Fowler, and D. Toman, Annu. Rev. Pharmacol. Toxicol. **52**, 521 (2002).

N.D. Volkow, et al., Psychiatry Res. Neuroimaging **162**, 205 (2008).

N.D. Volkow, et al., J. Neurosc., **28**, 8454 (2008).

N.D. Volkow, J.S. Fowler, and G.-J. Wang, Neuropharmacology **47**, 3 (2014).

G.-J. Wang, et al., PNAS, **106**, 1249 (2009).

L. Zhu, K. Ploessl, and H.F. King, Science **342**, 429 (2013).

5

Particle Physics and the Nuclear Force

5.1 Particle Physics

Elementary particle physicists (also known as "high-energy physicists") study the fundamental particles of nature and the symmetries found in their interactions. The study of elementary particle physics is an important endeavor in its own right and well beyond the scope of this book. Here we will introduce some of the basic concepts of this area of physics that are needed for our discussion of nuclei.

The particles that make up all matter can be classified as either fermions or bosons. Fermions obey the Pauli exclusion principle, have antisymmetric wave functions, and half-integer spins. For example, neutrons, protons, and electrons are all fermions. Bosons do not obey the Pauli exclusion principle and have symmetric wave functions and integer spins. Photons are the most common example of bosons.

The two groups of particles can also be further divided into the hadrons (such as the neutron and proton) and the leptons (such as the electron). The hadrons can interact via the nuclear or strong interaction, while the leptons do not. Both the hadrons and leptons can, however, interact via other forces, such as the electromagnetic force. Figure 5.1 contains an artist's conception of the standard model, a theory that describes these fundamental particles and their interactions. Among the hadrons, a large fraction of nuclear physics can be described only considering the familiar neutron and proton. On the other hand, the leptons play an important role in the nuclear force and in β decay, and we need to look a little into their properties. Note that each of these particles has a corresponding antiparticle. Similarly, only the antiparticle of the electron, called the positron, plus the antiparticle of the electron neutrino play an important role in nuclear physics.

There are six different kinds of leptons (Table 5.1), and they are arranged in three pairs. The electron (e), the mu lepton (μ or muon), and the tau lepton (τ) each carry a charge of −1 e and each has an associated neutrino: the electron and the electron neutrino (ν_e), the muon and the muon neutrino (ν_μ), and the

The standard model

All the *matter* in the universe, including atoms, stars, rocks, plants, and animals, is made of...

The particles *carrying* the forces between the matter are...

Fermions

Two types ▾

Quarks
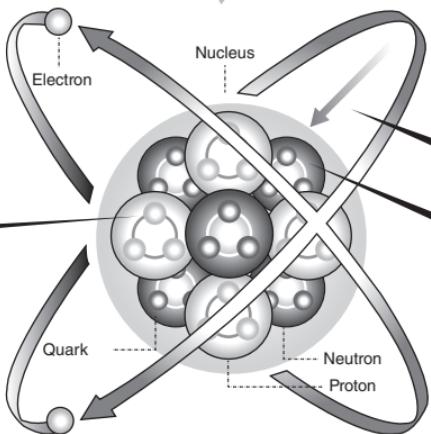
The **protons** and **neutrons** of an atom's nucleus are themselves complex structures, made up of groups of three basic particles called **quarks.** Quarks can also bind with **antiquarks** to make other particles called **mesons.**

Leptons

Leptons are not made of quarks, and include the **electrons** that orbit the atomic nucleus, and their more esoteric relatives, like **muons, taus,** and **neutrinos.**

Structure of the atom ▾

Nucleus

Electron

Quark

Neutron
Proton

Bosons

A family of particles called **gauge bosons** transmit the forces between the fermions. There is a different kind of particle for each force:

- **Photons** (the particles of light) carry the electromagnetic force.
- **Gluons** carry the strong force.
- **W** and **Z** bosons carry the weak force.
- **Gravitons** — not yet observed — are believed to be responsible for gravity, which is not a part of the standard model.

Forces

There appear to be four basic forces at work:

1. **Strong force** is responsible for holding together protons and neutrons.
2. **Weak force** causes certain forms of radioactivity.
3. **Electromagnetic force** holds atoms and molecules together.
4. **Gravity** is responsible for the large-scale structure of the universe, binding stars, and galaxies together.
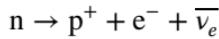
Figure 5.1 An artist's conception of the standard model of particle physics.

Table 5.1 Leptons in Standard Model.
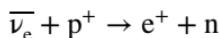
Flavor	Mass GeV/c^2	Electric Charge
ν_e, electron neutrino	$<1 \times 10^{-11}$	0
e, electron	0.000511	−1
ν_μ, muon neutrino	<0.0002	0
μ, muon	0.106	−1
ν_τ, tau neutrino	<0.02	0
τ, tau	1.7771	−1

tau lepton and the tau neutrino (ν_τ). All of these neutrinos are electrically neutral and have very small rest masses that have not been determined at present. Determining the masses of the neutrinos is a subject of current research (see Chapter 12). The first experimental evidence for neutrinos (the electron neutrino) came from nuclear β decay, while the existence of the other neutrinos was demonstrated in higher energy processes.
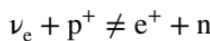
One important aspect of leptons is that their total number is conserved by type in nuclear processes. Consider, for example, the decay of a free neutron:

$$n \rightarrow p^+ + e^- + \overline{\nu}_e$$

where the line over the symbol for a given particle, for example, $\overline{\nu}_e$, indicates the antimatter version of that particle, here the electron antineutrino. In this equation, the number of leptons on the left hand side is zero (only one hadron), so that number of leptons on the right hand side must also be zero. This equivalence can only be true if we assign a lepton number of +1 to electron (by convention) and −1 to the antineutrino (being antimatter). Consider on the other hand, a scattering reaction used to observe the presence of antineutrinos:

$$\overline{\nu}_e + p^+ \rightarrow e^+ + n$$

Here the lepton number is −1 on both sides of the equation again using the convention of lepton numbers of +1 for every lepton and −1 for every antilepton (the positron, e^+, is an anti-lepton, of course). Finally, in contrast, the putative reaction to observe a neutrino

$$\nu_e + p^+ \neq e^+ + n$$

would conserve hadron number and electrical charge but not lepton number. Note that lepton conservation applies separately to the pairs of electrons, muons, and taus, so many other combinations would also be disallowed.

Sample Problem 5.1: Lepton Conservation

Is the reaction $\mu^- \rightarrow e^- + \overline{\nu}_e + \nu_\mu$ allowed?

Solution

Check lepton number conservation: $1 = 1 - 1 + 1$

Thus the reaction would be allowed, and based on the masses of the particles, the reaction should be exothermic as written.

If we return our focus to neutrons and protons (the nucleons), we note that they have similar masses ($\sim$1 u). We also should note that the neutron is slightly more massive than the proton with the mass difference being 1.29 MeV ($\sim$0.14%, Appendix A). This small energy difference causes/allows all free neutrons to decay into protons with a half-life of $\sim$10 min. As remarked earlier,
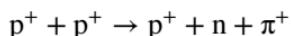
the neutron has no net electric charge, while the proton has a positive charge exactly equal to the negative charge on the electron. The electric charge on the proton appears to be uniformly and symmetrically distributed about the center of the proton with a charge radius of about 0.8 fm (again, this is an active area of research at present). The neutron, although electrically neutral, appears to have an extended charge distribution with a net positive charge near the center being canceled by a net negative charge at larger radii. The values of the magnetic dipole moment of the neutron and proton indicate their complex (inner) structure (see Chapter 2). The neutrons and protons respond equally to the nuclear or strong force, (the "charge independence" of the nuclear force) and are regarded collectively as "nucleons." The nucleons can be treated as a single hadron type with a mass of 938 MeV/c^2. By extension, the nucleon can have excited states such as the particle identified with a mass of 1232 MeV/c^2, which is called the Δ resonance.

The fermionic hadrons are called baryons and according to the standard model are made up of three fundamental fermions called quarks. There are six different kinds (or so-called flavors) of quarks: u (up), d (down), s (strange), c (charm), t (top), and b (bottom). The masses and charges of the quarks are given in Table 5.2. The size of each quark is thought to be $<10^{-18}$ m. The lightest two quarks, the u and d quarks, are thought to combine in groups of three to make up a nucleon. The proton is an "uud" combination with a net charge of $(2/3 + 2/3 - 1/3)e$, while the neutron is an "udd" combination with a net charge of $(2/3 - 1/3 - 1/3)e$. The effective diameter of the proton consistent with scattering reactions is about 1 fm. The up and down quarks are both light ($m \sim 5 - 10$ MeV/c^2) and point-like. The quarks account for $\sim 2\%$ of the mass of the proton. The remainder of the mass comes from "gluons," which bind the quarks together. The most massive of the quarks is the top quark with a mass approximately equivalent to that of a ^{197}Au nucleus and a short lifetime ($\sim 10^{-24}$ s).

Table 5.2 Quarks in Standard Model.

Flavor	Approx. Mass GeV/c^2	Electric Charge
u, up	0.003	+2/3
d, down	0.006	−1/3
c, charm	1.3	+2/3
s, strange	0.1	−1/3
t, top	175	+2/3
b, bottom	4.3	−1/3

Similar to the leptons, the number of baryons is conserved in a nuclear reaction. Each baryon, such as the neutron or proton, is assigned the value +1 and −1 to each antibaryon (such as the antiproton) in exact analogy to the lepton number. The total baryon number must be conserved in any nuclear process. As well as binding three quarks (or antiquarks) together to make baryons (or antibaryons), the nuclear or strong interaction can bind a quark–antiquark pair $(q, \bar{q})$ together to form unstable particles called mesons. The π^+ and π^- mesons $(u\bar{d}, d\bar{u})$ are especially important to describe the nuclear force. Notice that the quark/antiquark pairs will always couple to have zero spin, and thus the mesons are bosons. For example, consider the proton scattering reaction:

$$p^+ + p^+ \rightarrow p^+ + n + \pi^+$$

The number of baryons on the left side of the equation is 2, and the number on the right hand side is also 2 because the mesons (a π^+ in this case) as we just saw are leptons.

5.2   The Nuclear Force

There are four forces of nature: the electromagnetic, the strong (nuclear), the weak, and the gravitational force. In dealing with the structure, reactions, and decay of nuclei, we have to consider the electromagnetic, strong, and weak interactions. The principal force we shall concern ourselves with is the strong or nuclear force. In this chapter, we shall summarize some important features of the nuclear force and some underlying concepts building on some of the high-energy physics concepts we just introduced.

One basic characteristics of all the fundamental forces is their so-called exchange character. The forces are said to operate through the **virtual** exchange of particles that act as force carriers. First of all, the force carriers (or "exchange") particles are all bosons. Second, what do we mean by this term virtual? We mean that the particles that are exchanged or passed back and forth only exist for a very short time and cannot be observed externally. The time limit for their existence comes from the Heisenberg uncertainty principle. How is this possible? Consider the familiar electromagnetic interaction. Two charged particles can be imagined to interact electromagnetically by the emission of virtual photons that are continuously emitted and absorbed by the particles (i.e., exchanged) as long as the photons are absorbed (and disappear) before the clock runs out. The Heisenberg uncertainty principle tells us for a given system that

$$\Delta E \cdot \Delta t \geq \hbar$$

where ΔE represents the uncertainty of the total energy of that system, and Δt is the uncertainty in the time that system exists in that state. Thus, we can "violate"

the law of conservation of energy by exchanging a photon with an amount of energy ΔE for a length of time Δt given by

$$\Delta t \approx \frac{\hbar}{\Delta E}$$

Recall that $\hbar$ is a very, very small number, but also notice that if the energy of the photon is smaller, the length of time is longer. Since photons travel at the speed of light, the virtual photon could travel a distance R:

$$R = c\Delta t \approx \frac{\hbar c}{\Delta E} = \frac{\hbar c}{E_\gamma}$$

where E_γ is the kinetic energy of the photon, which has a rest mass of zero. If the exchanged particle is not a photon but has a rest mass m, the total energy is the rest mass plus the kinetic energy, but the minimum energy is its rest mass mc^2, so

$$\Delta t \approx \frac{\hbar c}{\Delta E} \Rightarrow R \leq \frac{\hbar}{mc}$$

The exchange particles for the four forces are the *graviton* for the gravitational force, the *pi-meson* or pion for the strong interaction between nucleons, the *photon* for the electromagnetic force, and the *$W_\pm$ and Z bosons* for the weak interaction. The mass of the graviton is unknown but must be nearly zero because the gravitational force appears to have an infinite range. The exchange particles for the electromagnetic force, the photons, have a zero rest mass, which allows the range of the force to be infinite. However, In the case of the strong interaction between nucleons, the range of the force is <1.5 fm, so $m_{\text{exchange}} \geq 140$ MeV/c^2. In the case of the weak interaction, the exchange particles called the $W_\pm$ and Z bosons have masses $m \approx 90$GeV/c^2, so $R \approx 10^{-3}$fm.

Sample Problem 5.2: Virtual Particle Range

Show that the maximum range of the virtual exchange of a pi meson is 1.4 fm.

Solution

There are three pi-mesons, one positively charged, π^+, one negatively charged, π^-, and one neutral, π^0. Their masses are 139.57, 139.57, and 134.98 MeV, respectively. Taking the lowest mass to get the longest range

$$R \leq \frac{\hbar}{M(\pi^0)c} = \frac{\hbar c}{M(\pi^0)c^2}$$
$$\leq \frac{197.327 \text{ MeV fm}}{134.98 \text{ MeV}}$$
$$\leq 1.46 \text{ fm}$$

When dealing with atoms and molecules and their interactions, one is almost always dealing primarily with the electromagnetic interaction, which is well described theoretically. In principle, the problems of atomic and molecular structure are exactly soluble, albeit sometimes with a great deal of mathematical complexity. The case for the nuclear or strong interaction is different. While we have gained much information about nucleons and their interactions, there are some features of the nuclear force that are poorly understood even today, and there is no complete theory of nuclear interactions. Since the nucleon is a composite particle, it is not surprising that the interaction between nucleons is complicated. Nonetheless, an exploration of some of the features of the nuclear force will greatly aid us in understanding nuclear phenomena.

5.3   Characteristics of the Strong Force

As discussed earlier, the range of the nuclear force R is thought to be short with $R \leq 1.4$ fm. What evidence do we have for this? The fact that the strong force plays no role in atomic or molecular structure restricts its range to less than the nuclear radius. In our discussion of the semiempirical binding energy equation, we showed that nuclear forces "saturate" and that nucleons only interact with their nearest neighbor. Thus, the range of the nucleon–nucleon interaction must be of the order of the size of a nucleon, that is, a few femtometers (10^{-15} m).

We also know that the nuclear force is strongly attractive, binding nucleons together to form a densely packed nucleus. We also know that the nucleons take up some volume because the nucleus does not collapse down to a point. Experiments based on the scattering of high-energy particles (protons or neutrons) from nuclei have shown the nuclear force also has a repulsive core below a femtometer or so. That is, below some value of the separation between nucleons (~0.5 fm), the nuclear force becomes repulsive instead of attractive. This feature, due to the quark substructure of the nucleon, is required to keep the nucleus from collapsing on itself.

The simplest bound nuclear system, the deuteron, consists of a neutron and a proton. The deuteron is known to have a quadrupole moment, 0.00286 barns, which tells us that the deuteron is not perfectly spherical and that the force between two nucleons is not spherically symmetric. Formally, we say the force between two nucleons has two components, a spherically symmetric central force and an asymmetric tensor force that depends on the angle between the spin axis of each nucleon and the line connecting each pair.

The deuteron has only one bound state, a triplet angular momentum state, in which the intrinsic spins of the neutron and proton are parallel, adding to make a $I = 1$ state. The singlet $I = 0$ state in which the nucleon spins are antiparallel is unbound, and if the deuteron is excited into this state, it simply comes apart.
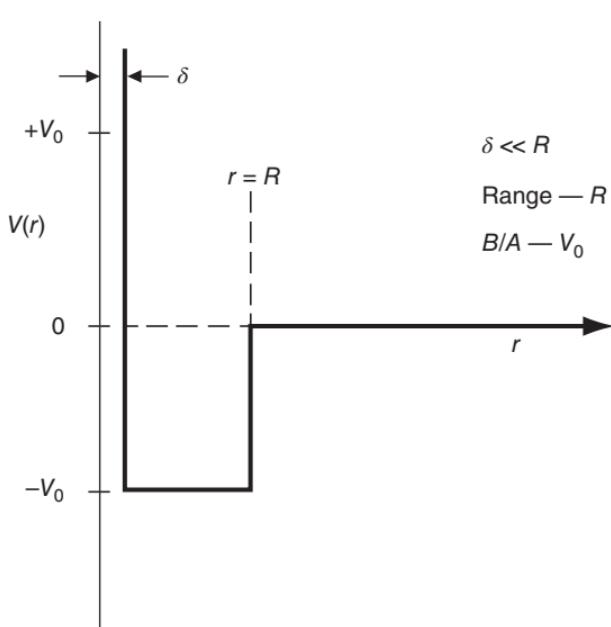
Figure 5.2 Schematic representation of the radial dependence of the simplest version of the nuclear potential energy with a sharp edge at R and a central repulse core at δ.

$\delta \ll R$

Range — R

B/A — V_0

Thus, the nuclear force is spin dependent. Also we shall see that the nuclear force depends on the coupling of the nucleon spin and nucleon orbital angular momentum. The ground state of the deuteron has the neutron and proton primarily in an $L = 0$ state (an S state). The deuteron magnetic dipole moment, 0.857 nuclear magnetons, is close to the sum of the neutron (-1.913) and proton magnetic moments (2.793). Detailed studies show a small portion ($\sim$4%) of the time the neutron and proton are in a ^{3}D-state ($L = 2$, $S = 1$, $I = 1$) rather than ground-state ^3S configuration ($L = 0$, $S = 1$, $I = 1$).

Using the relationship between force and potential energy discussed earlier, we can represent the nuclear force in terms of a simple graph of the nuclear potential energy as a function of distance to the center (Fig. 5.2). Since low-energy particles cannot probe the interior of nucleons or the nucleus, we can usually ignore the repulsive core in most problems involving low-energy nuclear structure and just use a square well potential with a sharp edge ($V(r) = -V_0$ for $r < R$, $V(r) = 0$ for $r > R$). Occasionally the so-called Yukawa form of the potential is used where $V(r) = -V_0 \exp(-r/R)/(r/R)$ or the Woods–Saxon form where $V = -V_0/(1 + \exp((r - R)/a))$. The typical values of the constant R for these potentials are 1.5–2 fm with $V_0 = $30–60 MeV. Other important components of the nuclear force are discussed as they become important in our subsequent discussions of nuclear structure.

5.4 Charge Independence of Nuclear Forces

The nuclear force between two nucleons has been found to be charge independent. By this we mean that the strong interaction between (a) two

Table 5.3 Distribution of Stable Nuclei.

A	Nuclide	Total Binding Energy (MeV)	Coulomb Energy (MeV)	Net Nuclear Binding Energy (MeV)
3	^{3}H	-8.49	0	-8.49
	^{3}He	-7.72	0.83	-8.55
13	^{13}C	-97.10	7.66	-104.76
	^{13}N	-94.10	10.72	-104.82
23	^{23}Na	-186.54	23.21	-209.75
	^{23}Mg	-181.67	27.85	-209.52
41	^{41}Ca	-350.53	66.12	-416.65
	^{41}Sc	-343.79	73.08	-416.87

protons or (b) two neutrons, or (c) a neutron and a proton is the same. Of course, the electromagnetic force will be acting at the same time in these pairs of nucleons, and the total resulting force will be slightly different in these three cases. The nuclear force is much stronger than the electromagnetic force, and the different resulting forces will only be slightly different. Evidence for the charge independence of nuclear forces can be found in nucleon–nucleon scattering and in the binding energies of light mirror nuclei shown. (Mirror nuclei are isobars where the number of protons in one nucleus is equal to the number of neutrons in the other nucleus and vice versa.) Table 5.3 lists the total nuclear binding energy of some light mirror nuclei, the difference in Coulomb energy between the nuclei, and the resulting net "nuclear" binding energy. Notice that the net nuclear binding energy is remarkably similar for these mirror nuclei, supporting the idea of charge independence of nuclear forces.

The simple relation of the masses of mirror nuclei suggests that the nuclear force between two neutrons, two protons, or a proton and a neutron is the same. This equivalence leads naturally to imagining that the neutron and the proton are two states of the same particle, *the nucleon*. (A similar situation holds for the π meson that we just encountered, where the π^0, π^+, and π^- mesons are three states of a single particle, the pion, that all show the same strong force behavior.) To solidify this idea, we say there is a new quantum number T for the nucleon (or the π meson) called its isotopic spin or isospin. In analogy to the nucleon angular momentum called spin, we say that for the nucleon $T = 1/2$ and in this hypothetical isospin space, there are two valid projections of T, $T_Z = +1/2$ (the proton) and $T_Z = -1/2$ (the neutron). (An alternate notation system refers to the isospin projection as T_3.) For a system with isospin T, there are $2T + 1$ members of the isospin multiplet, thus the pion has $T = 1$ with three members. In a nucleus of N neutrons and Z protons: $T_Z = (Z - N)/2$, a number

that can be quite large in heavy nuclei. For even nuclei, $0 \leq T \leq A/2$, while for odd nuclei, $1/2 \leq T \leq A/2$.

Sample Problem 5.3: Charge Independence

Consider the mirror nuclei ^{25}Mg and ^{25}Al. What is the energy difference between their ground states?

Solution

Note the "conversion" of neutral ^{25}Mg into ^{25}Al will require the change of one neutron into one proton plus an electron. The neutron and proton have slightly different masses, of course. The extra proton will interact electromagnetically with the other 12 protons giving a second part to the energy difference:

$$\begin{aligned}
\Delta E &= \Delta E_C - (m_n - m_H)c^2 \\
&= \frac{6Ze^2}{5R} - (8.071 - 7.289 \text{ MeV}) \\
&= \frac{6 \times 12 \times 1.44 \text{ MeV fm}}{5 \times 1.2 \times (25)^{1/3} \text{ fm}} - 0.782 \text{ MeV} \\
&= 5.128 \text{ MeV}
\end{aligned}$$

We can check this with the total mass change (count electrons) or simply the difference in mass defects from the appendix:

$$\begin{aligned}
\Delta E &= \text{BE}(A, Z + 1) - \text{BE}(A, Z) = \Delta(A, Z + 1) - \Delta(Z, A) \\
&= -8.916 - (-13.934 \text{ MeV}) = +5.018 \text{ MeV}
\end{aligned}$$

These results are quite close so we have the ground state of ^{25}Al to be ~ 5 MeV above the ground state of ^{25}Mg.

Isospin is a useful concept in that it is conserved in processes involving the strong interaction between hadrons. The use of isospin can help us to understand the structure of nuclei and forms the basis for some selection rules for nuclear reactions and nuclear decay processes. While a detailed discussion of the effects of isospin upon nuclear structure, decay, and reactions is reserved for later chapters, a few simple examples will suffice to demonstrate the utility of this concept.

Consider the $A = 14$ isobars, ^{14}C, ^{14}N, and ^{14}O. ^{14}C and ^{14}O are mirror nuclei, and their ground states should have very similar nuclear properties and can be labeled with $T_Z = +1$ and -1, respectively. As such they must be part of an isospin triplet with $T = 1(T_Z = 0, -1)$. Thus, in the $T_Z = 0$ nucleus, ^{14}N, there must be a state with $T = 1$, $T_Z = 0$, that is, the *isobaric analog* of the $T_Z = 0$ ground states of ^{14}C and ^{14}O and also have very similar nuclear properties. (See problems for further details.) We also expect the three members of this multiplet to have approximately the same energy levels after correction for the Coulomb effect.
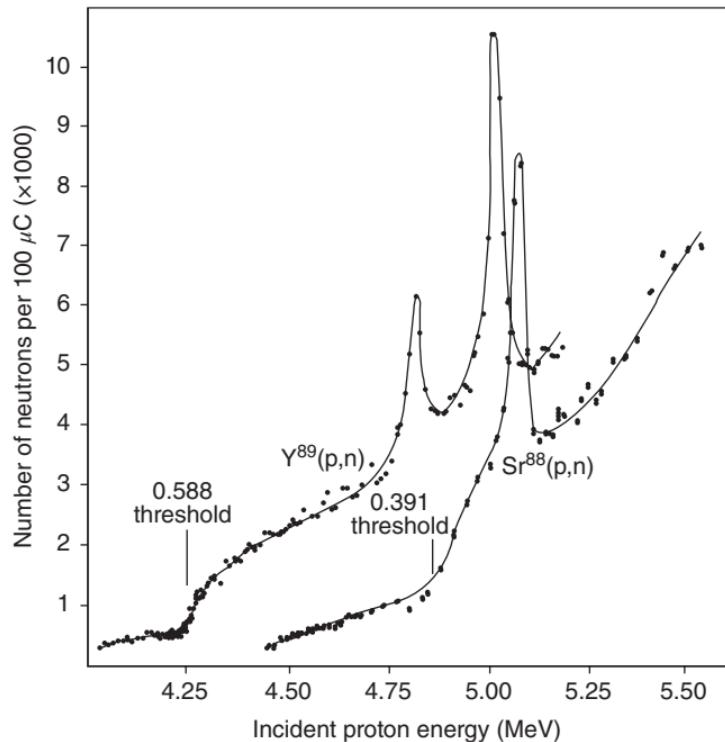
Figure 5.3 Neutron yields versus proton energy for the (p,n) charge-exchange reactions on ^{89}Y and ^{88}Sr (Fox et al. (1964). Reproduced with the permission of American Physical Society).

In heavy nuclei, the Coulomb energy shift between members of an isospin multiplet can be large due to the large number of protons in the nucleus. Thus, the isobaric analog of the ground state of one member of an isospin multiplet can have an excitation energy of several MeV. Some years ago when Fox et al. (1964, 198) were doing routine excitation function measurements of the ^{89}Y(p,n)^{89}Zr reaction, a net charge-exchange reaction that essentially converts the incident proton into a neutron and vice versa in the target nucleus, and they observed two sharp peaks in the neutron yields near $E_p = 5$ MeV, as shown in Figure 5.3. This observation was unexpected at the time, since the reaction was populating levels in the ^{90}Zr compound nucleus at an excitation energy of ~10 MeV where the spacing between levels was small, and no states were known that would produce a large resonances (see later discussion of nuclear reactions). Angular distributions quickly showed that the spin and parity of these states were 2^- and 3^-. It was pointed out that the ground and first excited state of ^{90}Y had spins and parities of 2^- and 3^- and were separated by only ~200 keV. Calculations of the Coulomb energies showed these resonances in the compound nucleus ^{90}Zr corresponded to the isobaric analogs of the ground state and first excited state of ^{90}Y. The yield of the reaction was enhanced because

the intermediate state represents a particularly simple nuclear configuration in contrast to the nearby states found at excitation energies of 10 MeV.

Problems

5.1 Calculate the Q value for the reaction $\mu^- \to e^- + \overline{\nu}_e + \nu_\mu$ in the sample problem.

5.2 Define or describe the following terms or phenomena: quark, lepton, hadron conservation, and pi meson.

5.3 What is the quark composition of the antiproton and the antineutron?

5.4 Which of the following decays are NOT allowed by conservation laws and why: (a) $p^+ \to e^+ + \gamma$, (b) $p^+ \to \pi^+ + \gamma$, (c) $n \to p^+ + \gamma$, (d) $p^+ + n \to p^+ + p^+ + \pi^-$ and (e) $p^+ + p^+ \to p^+ + p^+ + p^+ + \overline{p}$ +

5.5 Make a table similar to Table 5.3 showing the total binding energy, the Coulomb energy, and the net nuclear binding energy for the ground states of ^{14}C and ^{14}O and the 2.31 MeV excited state of ^{14}N.

5.6 If the difference in energy of the ground state of ^{14}C and the $T = 1$ analog of the ^{14}C ground state in ^{14}N of 2.31 MeV is due to the Coulomb energy difference between the nuclei, calculate an average nuclear radius R for these two $A = 14$ nuclei.

5.7 For a Yukawa nuclear potential with $V_0 = 40$ MeV and $R = 1.5$ fm, calculate the ratio between the nuclear and Coulomb potential for at the values of $r = 1, 2, 4, 8$, and 16 fm for the reaction of a proton with ^{89}Y nucleus.

5.8 Fox et al. (1964, 198, Fig. 5.3) also observed a large resonance in the $^{88}Sr(p,n)$ reaction at ~5.05 MeV. What is the nuclear product of thisreaction? (For practice, what is the Q value of this reaction?) Whatis the isospin, T, and isospin projection, T_Z, of the target nucleus? What is the isospin, T, of the strong resonance in the reaction and in what nucleus does it occur?

Bibliography

J.D. Fox, C.F. Moore, and D. Robson, Phys. Rev. Lett. **12**, 198 (1964).

6

Nuclear Structure

6.1   Introduction

Nuclei have been shown to have a very regular structure with many general and simple properties that are predicted by quantum mechanical treatment of particles (nucleons) moving in a potential well. The nuclear structure is very similar to the structure of electrons in the atomic potential energy well created by the Coulomb force; however the shape of the potential well is substantially different from the atomic case to the nuclear force. The previous chapter contained an introduction to the basic properties of the nuclear force and how we have been able to determine its important features. In summary, the exact form of the nuclear force is unknown at present, but the force is known to be short ranged (~1 fm) with a repulsive core, and it saturates. That is, the force acts primarily between nearest neighbors to hold them together without letting them penetrate into one another. We use these features to form the basis of our description of nuclear structure.

We can also learn a great deal about the basic features of nuclear structure and the nature of the force that holds the nucleus together if we simply carefully analyze the properties of the lightest stable and unstable nuclei. The building blocks of nuclei are the nucleons, protons, and neutrons, of course. The proton is stable and is usually found as a hydrogen atom bound to a single electron. The mass of the electron is small compared with that of the proton (511 keV/ 938,232 keV ~ 1/1800), and the binding energy of the electron in a hydrogen atom is even smaller (13 eV/ 938,232,000 eV ~ 10^{-8}). The electrons are almost always carried along by the nuclei, so it is most convenient to imagine building nuclides up from hydrogen atoms, ^{1}H, rather than bare protons. On the other hand, the free neutron is unstable and decays with a half-life of ~10 min into a proton, an electron, and an antineutrino. Thus, imagining that we will construct nuclei from these constituents, we should not expect to be able to make arbitrary heavy isotopes of any given chemical element because eventually if there are too many neutrons, they will be able to decay as if they were independent.

If we now bring together two nucleons, we find a rather important and interesting fact: only one combination produces a stable (bound) nucleus. One proton and one neutron will combine to form a deuteron, or one hydrogen atom plus one neutron will form a deuterium atom with its atomic electron. Both of the other combinations, two protons that can be labeled ^{2}He and two neutrons, are unbound and come apart almost as rapidly as the constituents come together. It is easy to see that the diproton or ^{2}He is more unstable than the dineutron due to the Coulomb repulsion between the two positively charged protons. Thus, we find a preference for equal numbers of neutrons and protons even in the smallest nucleus.

If we look more carefully at the deuteron, we expect that there should be two possible combinations of the spins of the two nucleons. Both the proton and neutron have $S = 1/2$, and we can have the parallel combination $S_p + S_n = 1$ and the antiparallel combination $S_p + S_n = 0$. Both of these states exist in a deuterium nucleus, the $S = 1$ state is the ground state (lowest energy), and the $S = 0$ state is an excited state and is, in fact, unbound. Therefore, the alignment of the spins of the two unlike nucleons has an important effect on the total binding energy. This provides part of the explanation as to why the dineutron is unbound. Notice that the intrinsic spins of two neutrons in a $\ell = 0$ or s-state must be paired (antiparallel, according to the Pauli principle). However, the nuclear force prefers the parallel alignment. In order to align the spins in the same direction in a dineutron, the neutrons have to be in an $\ell = 1$ or p-state, which requires more relative energy. In addition, the fact that the deuteron has an intrinsic electric quadrupole moment and is thus not spherical tells us that there is a noncentral component of the nuclear force.

We can continue our survey of the lightest nuclei with $A = 3$. Only the combinations of two protons and one neutron, ^{3}He, and one proton with two neutrons, ^{3}H, are bound, while the combinations of three protons, ^{3}Li, and three neutrons are unbound. Again we see a balance between the numbers of neutrons and protons with the extreme cases being unbound. The nuclear spins of both bound $A = 3$ nuclei are 1/2 indicative of two paired nucleons plus one unpaired nucleon; three unpaired nucleons would have had a total spin of 3/2. In the $A = 3$ system the more neutron-rich nucleus, tritium, ^{3}H, is very slightly less stable than ^{3}He, and it decays by β^- emission with a 12.3 year half-life.

Only one combination of four nucleons is bound, ^{4}He, with two protons and two neutrons. All other combinations of four nucleons are unbound. Moreover, ^{4}He, or the α particle, is especially stable (very strongly bound), and the nucleons are paired to give a total spin $S = 0$. Interestingly, if we add a nucleon to the α particle of either type, we produce an unbound nucleus! Thus, there are no stable nuclei with $A = 5$ as both ^{5}He and ^{5}Li break apart very rapidly after formation. This creates a gap in the stable masses and poses a problem for the building up of the elements in stars that is discussed in Chapter 12. Going on, there are two bound nuclei with $A = 6$, ^{6}He and ^{6}Li, with the helium

isotope decaying into the lithium isotope by β^- decay with a half-life of only 0.801 s. The other combinations are unbound. Continuing further, there are no stable isotopes with $A = 8$ since ^{8}Be very rapidly decays into ^{4}He nuclei, which also complicates the production of heavier nuclei in stellar environments. Then between mass 9 and 209, all mass numbers have at least one stable nucleus. There is generally one stable nucleus for each odd mass number, and in heavy nuclei there are often two stable nuclei for each even mass number. There are at most three stable isobars for a given A.

We can summarize our observations about light nuclei and the nuclear force as follows; the nuclear force acts between nucleons in a uniform way; protons have an additional Coulomb repulsion that can destabilize proton-rich nuclei, but very neutron-rich nuclei are also unstable. The symmetric nuclei with equal numbers of neutrons and protons are favored (at least in light nuclei), and finally the nuclear force depends on the spin alignment of the nucleons. Because the underlying nature of the nuclear force is unknown at present, several parameterizations of an effective force have been developed. A detailed discussion of these effective forces or equivalently the nucleon potentials is beyond the scope of this book. Now imagine the complexity of describing a nucleus in which each nucleon is interacting with its nearest neighbors through the nuclear force and at the same time all the protons are pushing on each other with the Coulomb force! This problem and the closely related problem of molecular motion in a liquid drop have not been solved in detail yet, and so we will present models of the average behavior of the nucleons in effective energy potentials.

6.2 Nuclear Potentials

The combined interactions of the neutrons and protons can be described in terms of a "nuclear potential well." Since the protons are charged particles, we generally treat the neutrons and protons as if they move inside separate potential wells (superimposed on one another). It is useful to imagine in a very schematic and simple way the forces that would act on a neutron as it is brought up to a nucleus. At large distances (>few fm), there will be no force (no change in the potential energy); when the neutron reaches the surface of the nucleus (or more precisely comes within the range of the nuclear force ~1 fm from the "edge"), there will be an attraction from the nearest neighbor nucleons, and the neutron will be pulled into the nucleus. This attraction will increase rapidly in the surface region as the nucleon comes in contact with other nucleons until it is surrounded by nucleons and is in the interior of the nucleus. The potential energy will stay approximately constant if the neutron moves inside the nucleus and is not near the edge. This behavior is summarized in the potential energy function shown as a function of distance from the center of the nucleus shown on the left side of Figure 6.1.
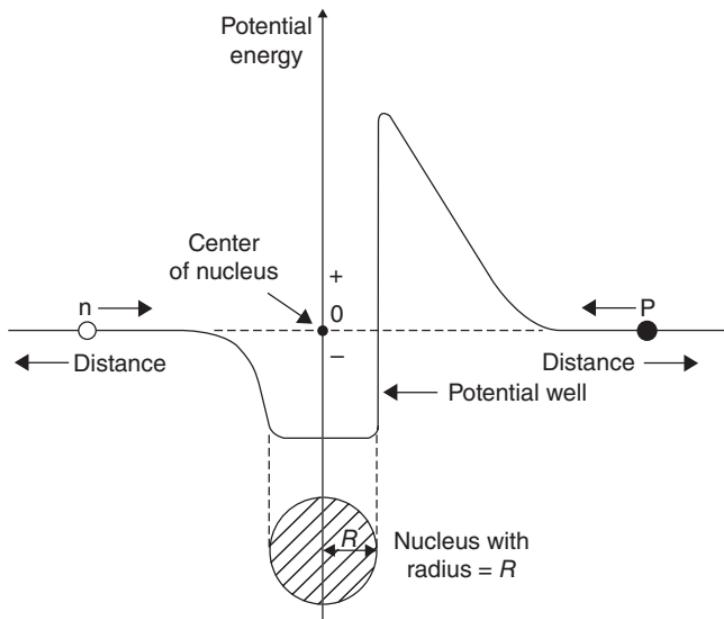
Figure 6.1 Schematic representations of a general neutron–nucleus potential (left side) and a proton–nucleus potential (right side) as a function of radius.

On the other hand, if we bring a proton up to the same nucleus, we will have a slightly different behavior. At first, the nucleus will repel the proton due to the long-range Coulomb force, and then as we bring the proton very near to the surface, the same nuclear attraction that the neutron felt will begin to overcome the Coulomb repulsion. The nuclear attraction will again increase until the proton is surrounded by nucleons as in the neutron case, but there will always be a net repulsion from the other protons. The Coulomb repulsion decreases the overall attraction, and the proton potential energy well will not be as deep as the neutron potential well. The models that we will describe later in this chapter will rely on the ideas behind these simple schematic potentials.

Before going on to describe the models of nuclear structure in detail, it is useful to make a short comparison of the characteristics of the atomic and the nuclear potential energies. The atomic potential is, in some sense, easier to describe because it is created by an extremely small central nucleus that can be ignored in many atomic calculations. The nucleus supplies the overall attraction that gets stronger as the electron approaches it, but the nucleus does not interact with the electrons. In the nuclear case the potential is created by the nucleons themselves, and if we disturb the nucleons (add or subtract one), then the overall potential will have to be readjusted. Fortunately, the changes in the potential energy for a large nucleus are often relatively small, and the general behavior of the whole nucleus remains the same. There can be, of course, major changes that cannot be described with a simple potential energy.

6.3 Schematic Shell Model

With a general understanding of the form of nuclear potentials, we can begin to solve the problem of the calculation of the properties of the quantum mechanical states that will "fill" the energy well. One might imagine that the nucleons will have certain finite energy levels and exist in stationary states or orbitals in the nuclear well, similar to the electrons in the atomic potential well. This interpretation is quite valid and forms the basis of the "shell model" of the nucleus. The potential well for nucleons has a very different shape from that for atomic electrons, and so we should expect that the energy levels and their filling patterns will be different.

As a very first approximation, we could model the nucleus as a rigid spherical container (also called a square-well potential). The potential energy is assumed to be exactly zero when the particle is inside the walls of the container, and the walls are so strong and high that the particle can never get out. An analogy would be a gaseous atom inside a very small spherical balloon. We could compare these energy levels to the known nuclei, but this potential is so unrealistic that we cannot expect to have much success. For example, notice that this potential goes to infinity at the edge of the nucleus, but the nuclear potential felt by a neutron goes to zero at the edge.

A much more useful potential is the harmonic oscillator potential, which has a parabolic shape. As indicated in Figure 6.2, this potential also has steep sides that continue upward and will be useful only for the low-lying energy levels in nuclei. The harmonic oscillator potential has the feature of equally spaced energy levels. This potential does not "saturate," rather it has a rounded bottom and so will not be very good for large nuclei with large central volumes. Nevertheless, the harmonic oscillator potential is used extensively for light nuclei, and harmonic oscillator wave functions are often used in reaction calculations. The harmonic oscillator states are labeled by their total angular momentum starting at 0. Each principal quantum number level is said to form a shell of orbitals. The energy gap between each shell will be exactly the same in the harmonic oscillator potential, and all the sublevels with a given principal quantum number will be degenerate. The number of orbitals is given by the expression $2N + 1$ where $N = 0, 1, 2, \ldots$. The Pauli principle states that the number of nucleons (fermions) needed to fill each orbital is 2, as for electrons in atomic orbitals, so the number of nucleons needed to fill the shells are $2[2N + 1] = 2, 6, 12, \ldots$. This filling agrees with the enhanced stability of the lightest nuclei (^{4}He, ^{16}O), taking the neutrons and protons in separate orbits, but does not agree with that of heavier nuclei.

A dramatic improvement was made to the simple harmonic oscillator potential by the addition of a spin–orbit correlation. It is known that relativistic particles have a tendency to align their orbital and intrinsic angular momenta (spins). This alignment is the basis of the familiar change in the chemistry of
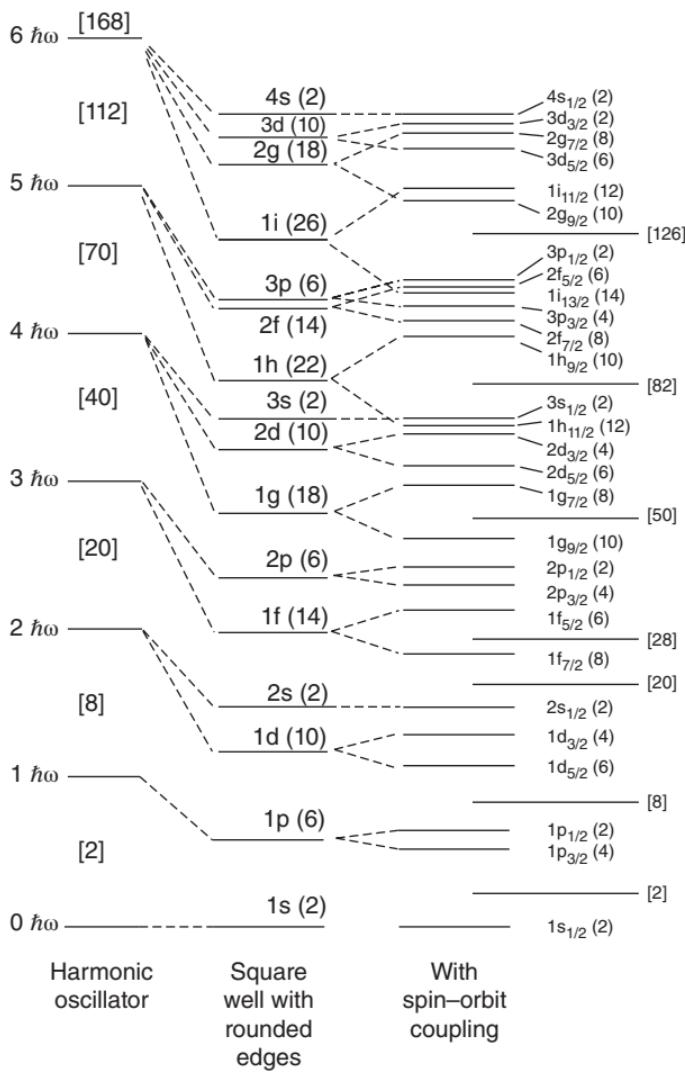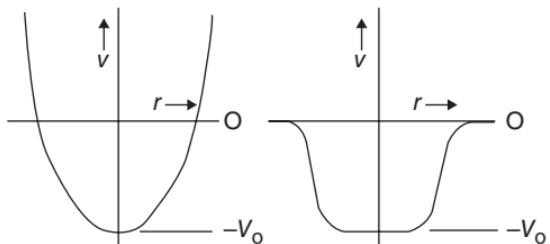
Figure 6.2 Energies of single particle orbitals in harmonic oscillator and "rounded square-well" potentials, the latter with and without spin–orbit coupling. Numbers in parenthesis indicate orbital capacities, and those in brackets give cumulative capacity up to the given point (Gordon and Coryell (1967). Reproduced with the permission of American Chemical Society).

the bottom-row elements in the periodic table. For example, thallium favors the 1^+ oxidation state even though thallium is the heaviest member of group 13 (IIIA). This preference for a low oxidation state comes about because the three atomic p-states separate (or split apart) into two groups in energy according to the alignment of the orbital ($\ell = 1$) and intrinsic spin ($s = 1/2$) angular momentum. The $p_{1/2}$ state with the spin and angular momentum coupled in opposite directions comes lower in energy and holds two electrons, while the third electron lies in the higher-lying $p_{3/2}$ state and is easily ionized.

The addition of the spin–orbit term to the nuclear harmonic oscillator potential causes a separation or removal of the degeneracy of the energy levels according to their total angular momentum ($j = \ell + s$). In the nuclear case, the states with the parallel coupling and larger total angular momentum values are favored and move lower in energy than those with smaller total spin values for a given combination. The ordering of the energy levels from a spin–orbit/harmonic oscillator shell model is shown in Figure 6.3 with their spectroscopic notation. Each total angular momentum state has $2j + 1$ suborbitals or projections of the angular momentum ($m_j = -j \ldots 0 \cdots +j$) just like the ℓ values of atomic electrons. Recall that we always have separate neutron states and proton states and the Pauli principle will put a maximum of two neutrons or protons into each orbital.

Let us consider placing nucleons into these shell model states. The lowest level is called the $1s_{1/2}$, s for $\ell = 0$, and $j = \ell + s = 1/2$. This level has only $2\ell + 1 = 1$ m-value and can hold only two protons in the proton well and two neutrons in the neutron well. Going up the scale, the next levels are the $1p_{3/2}$ and $1p_{1/2}$ pair in the next highest shell ($N = 1\hbar\omega$). Thus, ^{4}He represents the smallest nucleus with exact filling of both $N = 0$ harmonic oscillator levels for neutrons and protons and thus might be expected to have an enhanced stability. The next shell filling occurs when the $N = 0\hbar\omega$ and $N = 1\hbar\omega$ shells are filled. This requires eight protons and eight neutrons, so ^{16}O should be the next especially stable nucleus. The other shell closures occur at 20, 28, 50, 82, and 126 nucleons. These values correspond to places in the chart of nuclides with unusually large numbers of isotopes and isotones due to their enhanced stability. A few stable nuclei have both closed neutron and proton shells and are very strongly bound (relative to their neighbors), such as ^{4}He, ^{16}O, ^{40}Ca, ^{48}Ca, and ^{208}Pb. A few doubly closed shell nuclei have been produced outside the range of stable nuclei like ^{56}Ni, ^{100}Sn, and ^{132}Sn, and others that are more exotic have been sought like ^{10}He and ^{28}O but have been shown to be unbound.

Sample Problem 6.1: Shell Model Filling

Describe the configurations of the nucleons in ^{7}Li expected in the Shell Model.
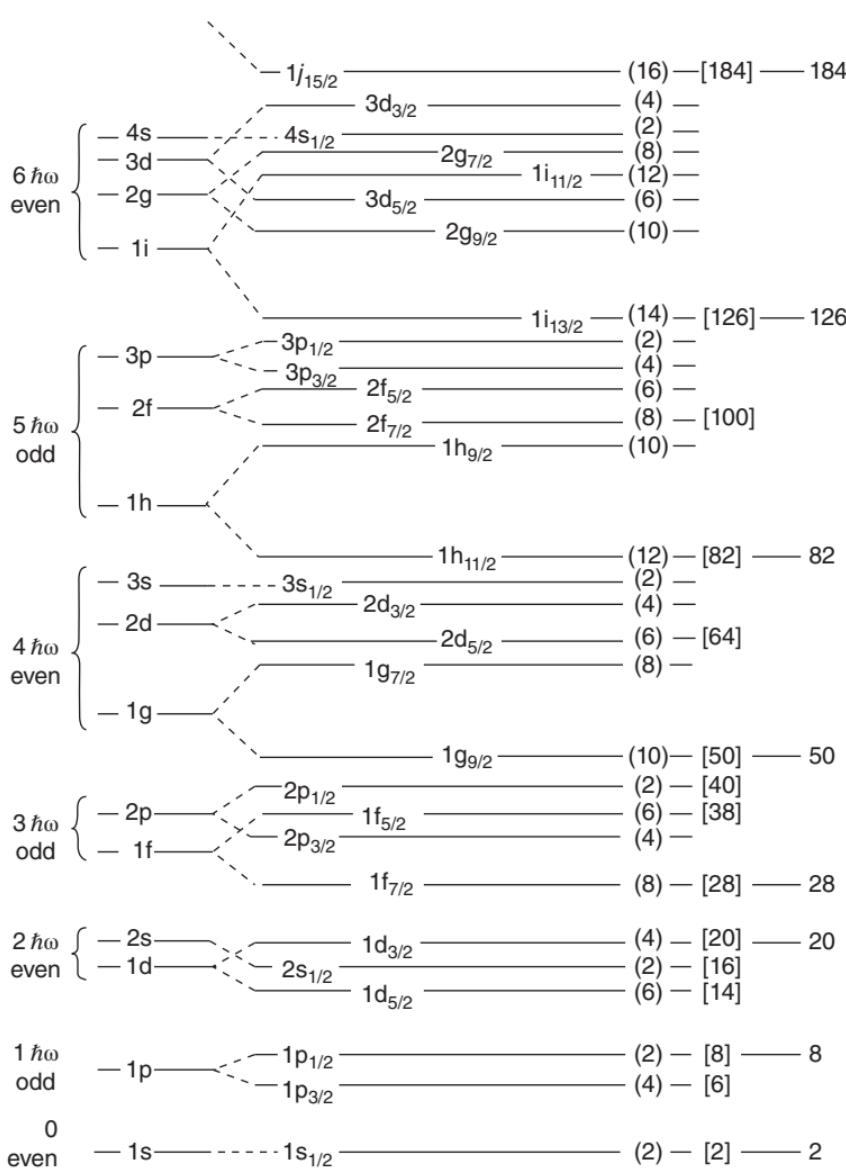
Figure 6.3 The energy level pattern and spectroscopic labeling of states from the schematic shell model. The angular momentum coupling is indicated at the left side, and the numbers of nucleons needed to fill each orbital and each shell are shown on the right side.

Solution

1) Place the three protons into the lowest available orbitals. The protons in the $1s_{1/2}$ state must be paired according to the Pauli principle, so we have a configuration of $(1s_{1/2})^2(1p_{3/2})$.[1]

2) Place the four neutrons into their lowest available orbitals. The neutrons should be paired in the partially filled orbital (this is in contrast to the case for atomic electrons), giving a configuration of $(1s_{1/2})^2(1p_{3/2})^2$

Prediction: All nucleons are paired except for the $1p_{3/2}$ proton. Therefore, the spins and angular momenta of the nucleons will cancel except for this proton. The nuclear spin should be 3/2, and the nuclear parity should be negative, corresponding to the parity of a p-state (odd π value).

Further question: What would this model predict for an excited state of ^{7}Li? Two possibilities should be apparent. We could promote the $p_{3/2}$ proton to the $p_{1/2}$ state or we could uncouple the $p_{3/2}$ neutrons, giving three unpaired neutrons in the $p_{3/2}$ level. Experimentally it has been found that ^{7}Li has only one bound excited state and it corresponds to promotion $p_{3/2} \rightarrow p_{1/2}$ of the proton. The breaking of pairs has a significant energy cost and causes the nucleus to become unbound.

Notice that the light nuclei are extremely fragile due to the large level spacing and relatively small number of levels. The small numbers of nucleons are very sensitive to small changes in the configurations and have relatively few excited states. Heavy nuclei are much more "resilient" due to the large number of nearby energy levels with slightly different configurations, and these nuclei almost always have very large numbers of bound excited states.

The reality of this scheme of assigning nucleons to various simple shell model states can be checked very directly by nuclear reactions that give or take a nucleon from the nucleus. The (p, 2p) reaction is such a reaction that removes a single proton from the nucleus. The energy required to remove a given proton is thus a measure of the energy of the corresponding nuclear state. In Figure 6.4,
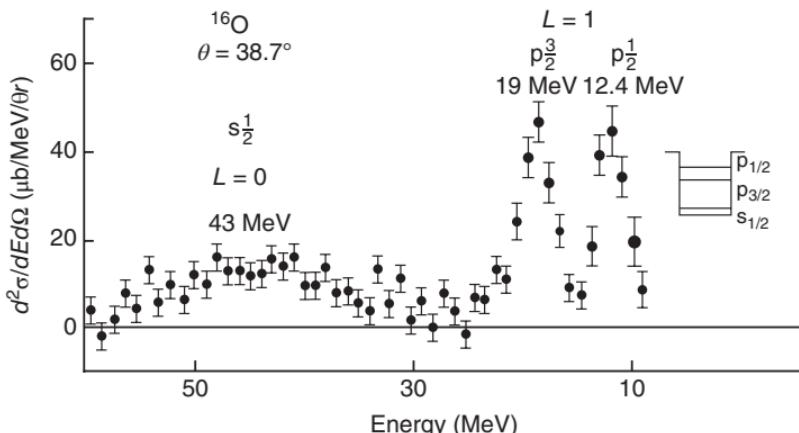
Figure 6.4 Energy spectrum of emitted protons from the ^{16}O(p, 2p) reaction, showing the single particle states (Tyrén et al. (1958). Reproduced with the permission of Elsevier.).

we show the results of such a study of the $^{16}O(p, 2p)$ reaction. Three peaks are seen corresponding to the removal of protons from the $1p_{1/2}$, $1p_{3/2}$, and $1s_{1/2}$ orbitals.

The energy level diagram for the schematic shell model, shown in Figure 6.3, allows us to make a large number of predictions about the ground states of broad ranges of nuclei. *First, the strong pairing of nucleons in the individual orbitals tells us immediately that the (net) spin of all nuclei with both even numbers of protons and even numbers of neutrons will be zero. Also the parities of the wave functions of all these nuclei will be positive. Thus, the ground state spin and parity of all even–even nuclei is* 0^+. These predictions are exactly correct, and the fact that all even–even nuclei have no net nuclear spin is the reason why relatively few nuclei can be used in NMR studies. *Second, we expect that the ground states of odd A nuclei, those with an even number of one kind of nucleon and an odd number of the other kind, will be described by the spin and parity of that single odd nucleon.* These predictions are often correct, particularly if we recognize that single vacancies or holes in subshells will give the same angular momentum and parity as a single particle in the same subshell. This equivalence of "particles" and "holes" can be shown by detailed angular momentum coupling calculations that we will not go into here. However, recall that a completely filled subshell will couple to a spin of 0, so by symmetry if we add one particle to get a given j-value, we should expect to get the same spin value when we take one particle from the completely full subshell.

The shell model can also be used to predict the ground state spins and parities of odd-proton/odd-neutron nuclei by combining the individual $j\pi$ values of the two unpaired particles. Notice that two combinations will always be possible and we will need a way to decide which of the two alignments of the total nucleon angular momenta will be lower in energy (i.e., be the ground state). The ground state of the deuteron with its single proton and single neutron provides the key to this selection. The spin angular momenta of the neutron and proton are aligned in the deuteron ground state; thus for the ground state of an odd–odd nucleus, we should couple the total j-values so that the intrinsic spins of the odd particles are aligned. We can do this by inspection of the angular momenta or by applying a set of rules based on the systematics of the shell model orbitals. Brennan and Bernstein have summarized these data in the form of three rules. When the odd nucleons are both particles or both holes in their respective subshells, Rule 1 states that when $j_1 = \ell_1 \pm 1/2$ and $j_2 = \ell_2 \mp 1/2$, then $J = |j_1 - j_2|$. Rule 2 states that when $j_1 = \ell_1 \pm 1/2$ and $j_2 = \ell_2 \pm 1/2$, then $J = |j_1 \pm j_2|$. Rule 3 states that for configurations in which the odd nucleons are a combination of particles and holes, such as ^{36}Cl, $J = j_1 + j_2 - 1$.

Sample Problem 6.2: Shell Model Coupling

Consider the odd–odd nuclei, ^{38}Cl, ^{26}Al, and ^{56}Co. Predict the ground state spin and parity for these nuclei.

Solution

a) ^{38}Cl has 17 protons and 21 neutrons. The last proton is in a $d_{3/2}$ level, while the last neutron is in a $f_{7/2}$ level (see Fig. 6.3).

$$j_p(d_{3/2}) = 2 - 1/2, \quad j_n(f_{7/2}) = 3 + 1/2$$
$$J = |7/2 - 3/2| = 2$$
$$\pi = (+1)(-1) = -$$

b) ^{26}Al has 13 protons and 13 neutrons. The last proton and the last neutron are in $d_{5/2}$ hole states, that is, $j_p = j_n = 2 + 1/2$:

$$J = |5/2 + 5/2| = 5$$
$$\pi = (+1)(+1) = +$$

c) ^{56}Co has 27 protons and 29 neutrons. The last proton is in a $f_{7/2}$ hole state, and the last neutron is in a $p_{3/2}$ state $(1 + 1/2)$:

$$J = 7/2 + 3/2 - 1 = 4$$
$$\pi = (-1)(-1) = +$$

The simple shell model is very robust and is even successful in describing nuclei at the limits of stability. For example, ^{11}Li is the heaviest bound lithium isotope. The shell model diagram for this nucleus is indicated in Figure 6.5. Notice the prediction of two filled neutron shells. The binding energy is only 300 keV for the whole nucleus, so it is very fragile, and we expect it to rapidly decay toward the stable isobar ^{11}B. It is also known that ^{10}Li that does not have a filled p-shell is unbound. This again emphasizes the importance of pairing in nuclei. The two neutrons in the highest energy level in ^{11}Li, a level that is very close to zero, are alone in a $p_{1/2}$ state, and the empty $d_{s/2}$ state is very close in energy. This nucleus has an unusually large interaction radius (or size) and a high probability to dissociate into ^{9}Li + 2n that have been attributed to a large
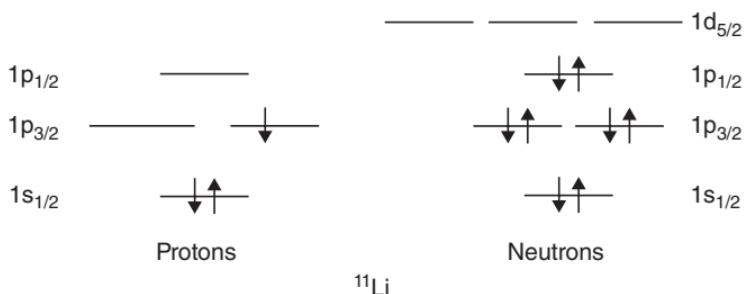
Figure 6.5 The energy level pattern and filling for the exotic nucleus ^{11}Li in the schematic shell model.

physical extent of the very weakly bound neutrons in the highest energy level. In fact, there is some debate in the current literature as to the relative ordering of the s- and p-states.

In addition to the spin and parity, another fundamental nuclear parameter that can be determined experimentally that depends on nuclear structure is the **magnetic dipole moment**. The magnetic moment of a nucleus is a measure of the response of that nucleus to an external magnetic field and is made up from the net effect of the motion of the protons plus the intrinsic spins of both the protons and neutrons. The magnetic moment μ_i of one particle can be written as

$$\mu_i = g_\ell L_i + g_s S_i \tag{6.1}$$

where L_i is the angular momentum and S_i is the intrinsic spin of particle i. The gyromagnetic ratios g_ℓ and g_s are

$$g_\ell = \mu_0, g_s = 5.5845\mu_0 \text{ for protons} \tag{6.2}$$

and

$$g_\ell = 0, g_s = -3.8263\mu_0 \text{ for neutrons} \tag{6.3}$$

where μ_0 is the nuclear magneton $\mu_0 = e\hbar/2m_p c$. Due to the large cancellation of the spins and angular momenta due to the strong coupling of nucleons in matching orbitals and the pairing of spins, we should expect that the magnetic moments will be small and strongly dependent on the number and orbits of any unpaired particles. A relatively simple formula for the magnetic moments of nuclei with single unpaired nucleons, called the Schmidt limits, depends on the relative orientation of the angular momentum and the spin:

$$\text{For } j = \ell + s : \mu = g_\ell \left(j - \frac{1}{2}\right) + \frac{1}{2g_s} \tag{6.4}$$

$$\text{For } j = \ell - s : \mu = \left(\frac{j(j + 3/2)}{(j + 1)}\right) g_\ell - \left(\frac{j}{(2(j + 1))}\right) g_s \tag{6.5}$$

The measured magnetic moments of the odd-mass nuclei are similar in magnitude to the Schmidt limits as shown in Figure 6.6. Notice that the measured values fall into two groups at ∼60% of the predicted values. The fact that the magnetic moments are less than those expected for single particles indicates that the nuclear wave function is not completely dominated by one particle. (If we were to show only the magnetic moments of nuclei that have one particle more than a closed shell configuration, we would see better agreement with the Schmidt limits). Also there is a large amount of variation in the magnetic moments that indicates the complexity of the underlying structure and that the cancellation effect of paired particles is not as complete as we might hope.

Up to this point we have concentrated on the properties of the ground states of nuclei predicted by the schematic shell model. However, we can use these
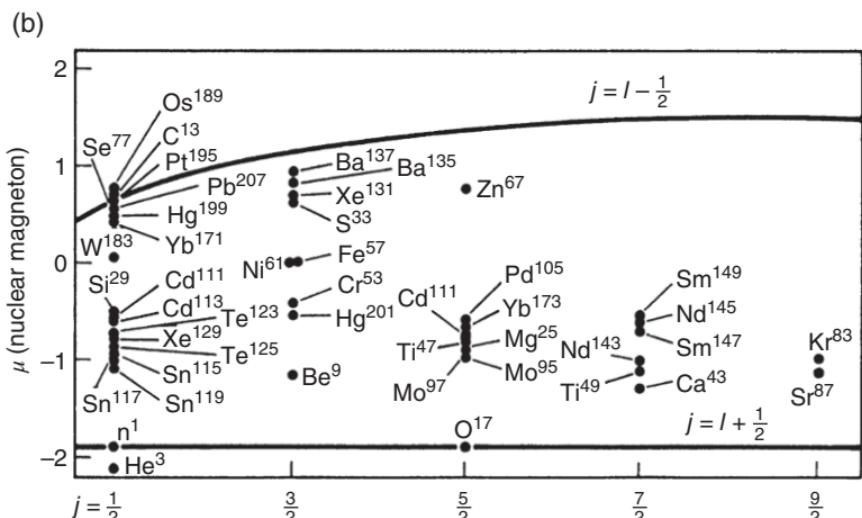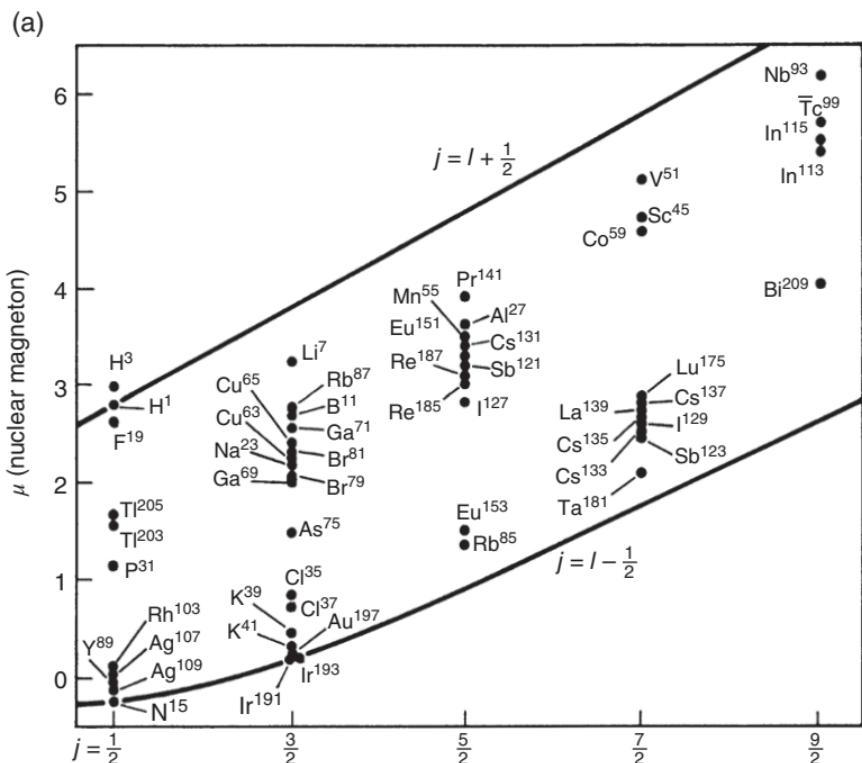
Figure 6.6 The magnetic moments of the odd-proton (*A*) and of the odd-neutron nuclei plotted as a function of the nuclear spin *j*. The Schmidt limits are shown by the solid lines. The data generally fall inside the limits and are better reproduced as 60% of the limits.

energy levels to construct excited states by the promotion of particles and the appropriate coupling of odd (unpaired) particles. First of all, the shell model has already shown that odd–odd nuclei always have two possible couplings of the angular momenta of the odd particles. One coupling leads to a high spin $J = j_1 + j_2$ and other a low total spin $J = j_1 - j_2$. We have already described how to decide which state will lie lower in energy, but notice that the state will always be present. This state will be an isomeric state that will decay to the ground state by γ-ray emission (usually with a relatively long half-life due to the large change in angular momentum between the states). The relative energy splitting of the two levels decreases as the mass increases due to the dilution effect of more and more nucleon–nucleon interactions. Examples of isomeric pairs of levels and excited states in the simple shell model are given in the accompanying examples.

Sample Problem 6.3: Shell Model Isomers

Identify the shell model isomeric spin states in ^{26}Al and ^{198}Au.

Solution

a) ^{26}Al is a nucleus with 13 protons and 13 neutrons, and filling the shell model energy level diagram from the bottom, we find the following configurations:

$$\text{Protons } (1s_{1/2})^2 (1p_{3/2})^4 \ (1p_{1/2})^2 (1d_{5/2})^5 \tag{6.6}$$

$$\text{Neutrons } (1s_{1/2})^2 (1p_{3/2})^4 \ (1p_{1/2})^2 (1d_{5/2})^5 \tag{6.7}$$

Recall that a $1d_{5/2}$ level is filled by six particles. Therefore, the net configuration contains a proton hole coupled to a neutron hole in $1d_{5/2}$ states. This is written as $\pi(1d_{5/2})^{-1} \otimes \nu(1d_{5/2})^{-1}$. Coupling the proton and neutron angular momenta, we expect $j_p \pm j_n = 0$ and 5 for the nuclear spins. The Brennan–Bernstein rules predict that the high spin isomer has the lower energy for identical orbitals, in agreement with observation. The parities of both orbitals are positive, so the parities of both coupled states are positive.

b) ^{198}Au is a nucleus with 79 protons and 119 neutrons, and filling in the shell model energy level diagram, we find that the highest partially filled or valence orbitals are

$$\text{Valence} : \pi(1h_{11/2})^9 \text{ and } \nu(1i_{13/2})^7 \tag{6.8}$$

both of which are partially filled subshells near major shell closures. If we make the simplest assumption that all the neutrons and protons are paired except the last odd particles, then we would expect a configuration of $\pi(1h_{11/2}) \otimes \nu(1i_{13/2})$ with $j_p \pm j_n = 1$ and 12 for the nuclear spins. The parities of these orbitals are negative and positive,

respectively, making the product negative. Notice that we could add or remove a pair of neutrons from this configuration, making ^{200}Au and ^{196}Au, and we would leave an odd neutron in the same orbital. Therefore, we would make the same predictions for the ground and isomeric states of these nearby nuclei.

An interesting subset of nuclei is those nuclear pairs in which the numbers of protons and neutrons are interchanged, for example, ^{3}He and ^{3}H. These sets of nuclei are called mirror pairs, and the schematic shell model predicts that they will have identical ground and excited states, after correcting for the (small) upward shift of the proton levels by the Coulomb force and the difference in mass of a neutron and a proton. This shift caused by increasing the nuclear charge by one unit while keeping the mass constant can be readily calculated from the Coulomb energy inside a uniformly charged sphere:

$$E_C = \frac{3}{5}\frac{Ze^2}{R} \tag{6.9}$$

where Z is the atomic number and R is the radius. The Coulomb energy difference between a mirror pair, where Z refers to the higher atomic number, is then

$$\begin{aligned}
\Delta E_C &= \frac{3}{5}\frac{e^2}{R}\left(Z^2 - (Z-1)^2\right) \\
&= \frac{3}{5}\frac{e^2}{R}(2Z-1) \\
&\approx \frac{Ze^2}{R}
\end{aligned}$$

This estimate of the Coulomb shift is an overestimate as it assumes that the nuclei are rigid spheres, but, nonetheless, it is straightforward to calculate. A large number of mirror pairs have been studied, and the agreement between the energy levels after compensating for the Coulomb shift in the mirrors is dramatic. An example of the energy level matching in the mirror pair ^{17}F, ^{17}O is shown in Figure 6.7. The agreement of the levels is quite remarkable and can be taken as strong evidence for the charge independence of the nuclear force, that is, the protons and neutrons move in essentially identical but separate orbitals in the nucleus.

After all these successes of the very simple shell model, we should be careful to note that there are a number of other well-established and simple properties of nuclei that it cannot describe. For example, the energy levels of essentially all nuclei, and particularly the even–even nuclei with all paired particles, have series of states that are arranged in groups (or bands) with energy spacings and state-to-state transitions that are characteristic of a collective vibration and/or rotation of the entire nucleus. Specifically, even–even nuclei have low-lying

Figure 6.7 The energy levels of the ground state and first few excited states of the mirror pair ^{17}F, ^{17}O are shown. The states are labeled by their intrinsic spin and parity. The matching of these mirror states is remarkable and strongly supports the idea of the neutrons and protons moving in identical orbitals.

2^+ and 4^+ excited states that are very strongly related to the 0^+ ground state that, once excited, cascades rapidly back to the ground state by γ-ray emission. Examples of such collective states are shown in Figure 6.8. These states correspond to macroscopic vibration of the entire nucleus around the spherical ground state shape.

Another example of collective motion that is outside the shell model is found in the rare earth and actinide elements. These nuclei lie between the major shell closures in the shell model and the filling of the mid-shell high spin orbitals that cause the nuclei to be deformed (stretched like a rugby ball) in the ground state. The orbitals that are being filled in these regions have relatively large ℓ-values, for example, g and h states. The angular part of these orbitals is relatively concentrated in space (due to the large number of angular nodes in the wave function), and each suborbital is relatively planar. Recall that s orbitals are spherically symmetric and orbitals with larger ℓ-values are divided by more and more planar nodes. Thus, the mid-shell nucleons in this region fill relatively nonspherical suborbitals. As we have already discussed, the simple shell model was developed with a spherically symmetric potential. We should expect that the energy levels would shift if the shape of the potential was changed. We will consider the effects of just such a change later in this chapter.

Recent studies of nuclei far from stability, such as ^{11}Li, ^{31}Na, ^{36}Mg, ^{38}Si, and ^{48}Ca, have shown orderings of single particle levels that are different from that predicted by the shell model. The positions of the single particle levels that define the relevant shell gap are inverted relative to their normal position. The regions where this occurs are referred to as "islands of inversion."
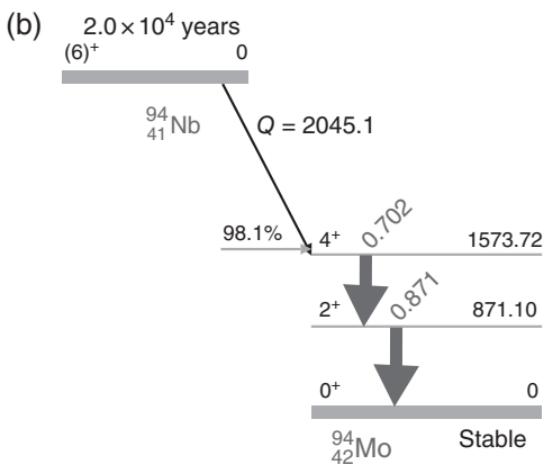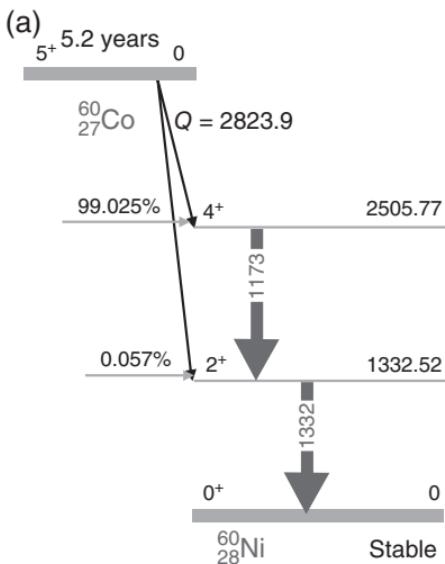
Figure 6.8 (a) The energy level diagram showing the first (lowest energy) 2^+ and 4^+ states in ^{60}Ni. The high spin ground state, 5^+, of ^{60}Co β decays primarily to the 4^+ state and initiates a well-known γ-ray cascade to the 2^+ state and then the 0^+ ground state. (b) For comparison, the energy level diagram showing the first (lowest energy) 2^+ and 4^+ states in ^{94}Mo. The high spin ground state, 6^+, of ^{94}Nb also primarily feeds the 4^+ state initiating a γ-ray cascade.

6.4 Independent Particle Model

A more detailed model can be constructed for the nucleons in terms of a central potential that holds all the nucleons together plus a "residual potential" or "residual interaction" that lumps together all of the other nucleon–nucleon interactions. Other such important one-on-one interactions align the spins of unlike nucleons (p–n) and cause the pairing of like nucleons (p–p, n–n). The

nucleons are then allowed to move independently in these potentials, that is, the Schrödinger equation is solved for the combined interaction to provide the energy levels and wave functions for the individual particles. Once again there will be a large amount of cancellation of the effects of the independent nucleons, and the overall properties of the nucleus are again determined by the last (few) unpaired nucleons or holes.

The central potential can be a simple harmonic oscillator potential $f(r) \sim kr^2$ or more complicated such as the Yukawa function $f(r) \sim (e^{-ar}/r)^{-1}$ or the Woods–Saxon function that has a flat bottom and goes smoothly to zero at the nuclear surface. The complete Woods–Saxon potential has two parts:

$$U(r) = \frac{U_0}{1 + \exp[(r - R_0)/a]} + \frac{U_{ls}}{r_2} \frac{1}{r} \frac{d}{dr}\left(\frac{1}{1 + \exp[(r - R_0)/a]}\right) \vec{\ell} \cdot \vec{s}$$

(6.10)

where the first term is the overall potential and the second term is the spin–orbit contribution with $R_0 = r_0 A^{1/3}$, with $r_0 = 1.27$ fm and $a = 0.67$ fm, and strength of the contributions are given by

$$U_0 = (-51 + 33(N - Z)/A) \text{ MeV and } U_{ls} = -0.44 U_0$$

(6.11)

The spin–orbit strength (second term) is peaked on the nuclear surface as shown in Figure 6.9.

A residual interaction that is also quite simple has been developed and applied with good results. Recall that the nucleon–nucleon force is attractive and very short ranged, so one might imagine that the nucleons must be in contact to interact. Thus, the simplest residual interaction is an attractive force that only acts when the nucleons touch or a delta interaction (in the sense of a Kronecker delta from quantum mechanics). This can be written as $V(r_1, r_2) = a\delta_{1,2}$ where a is the strength of the interaction and the delta function only allows the force to be positive when the nucleons are at exactly the same point in space. In practice the strength of the potential must be
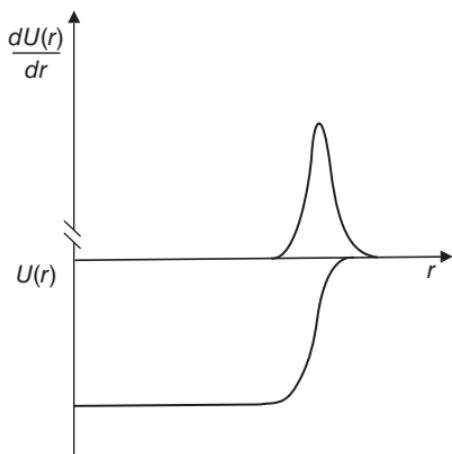
Figure 6.9 Radial dependence of the strength of the spin–orbit potential compared with a Woods–Saxon potential well.

determined by comparison to experimental data. Notice, however, that such models have a very small number of parameters to be adjusted to give an overall or average agreement with the data. The "best-fit" values are then used to calculate the properties of other nuclei and their excited states.

6.5 Collective Model

As we have seen the nucleons reside in well-defined orbitals in the nucleus that can be understood in a relatively simple quantum mechanical model, the shell model. In this model, the properties of the nucleus are dominated by the wave functions of one or two unpaired nucleons. Notice that the bulk of the nucleons, which may even number in the hundreds, only contribute to the overall central potential. These core nucleons cannot be ignored in reality, and they give rise to large-scale macroscopic behavior of the nucleus that may be very different from the behavior of single particles. There are two important collective motions of the nucleus that we have already mentioned that we should address: collective or overall rotation of deformed nuclei and vibrations of the nuclear shape about a spherical ground-state shape.

Rotational motion is characteristic of nonspherical nuclei, and the deformation can be permanent (i.e., the ground state remains deformed), or it can be induced by centrifugal stretching of a nucleus under rapid rotation. The nuclei with masses in the region $150 < A < 190$ and $220 < A$ lie between the major shells and generally have permanent deformations in their ground states. An example of the regular spacing of the energy levels of deformed nucleus are shown in Figure 6.10. On the other hand, the rapid rotation of a nucleus can be dynamically induced by nuclear reactions. It is common to create rapidly rotating nuclei in compound nuclear reactions that decay by γ-ray emission, eventually slowing down to form spherical ground states.

The deformation can be very complicated to describe in a single particle framework, but a good understanding of the basic behavior can be obtained with an overall parameterization of the shape of the whole nucleus in terms of quadrupole distortions with ellipsoidal symmetries. If we start from a (solid) spherical nucleus, then there are two axially symmetric quadrupole deformations to consider. The deformations are indicated schematically in Figure 6.11 and give the nuclei ellipsoidal shapes (an ellipsoid is a three-dimensional object formed by the rotation of an ellipse around one of its two major axes). The prolate deformation in which one axis is longer relative to the other two produces a shape that is similar to that of a rugby ball but more round on the ends. The oblate shape with one axis shorter than the other two becomes a pancake shape in the limit of extremely large deformations.

The surface of the ellipsoid can be written in terms of the expansion

$$R(\theta, \phi) = R_{\text{average}} \left[1 + \beta Y_{20}(\theta, \phi) \right] \tag{6.12}$$

16⁺ ———— 4.143	

16^+ ———— 4.143

14^+ ———— 3.499

12^+ ———— 2.884

10^+ ———— 2.300

8^+ ———— 1.747

6^+ ———— 1.227

4^+ ———— 0.755

2^+ ———— 0.344

0^+ ———— 0

Figure 6.10 The low-lying energy levels of ^{152}Gd that clearly fit the pattern of a rotational band. The rotational constant $\hbar^2/2\mathcal{J} = 57.3$ keV can be extracted from the separation of the 2^+ to 0^+ states. The energy units are MeV.

Oblate nucleus
Quadrupole moment < 0

Spherical nucleus
Quadrupole moment = 0

Prolate nucleus
Quadrupole moment > 0
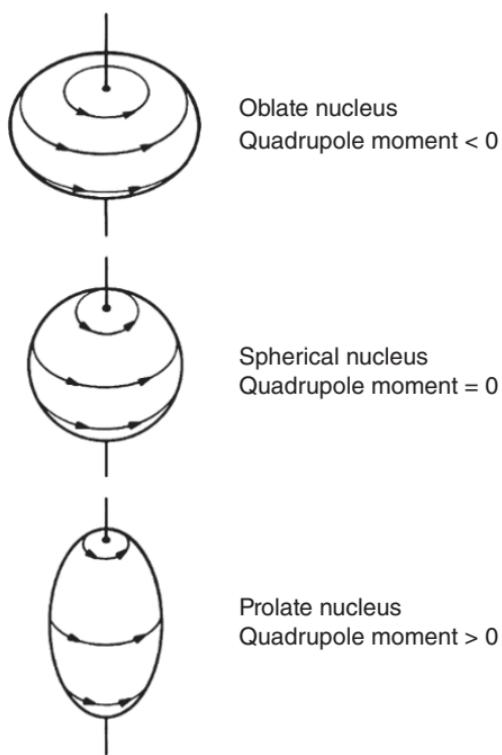
Figure 6.11 Schematic representations of prolate and oblate deformations of a uniform sphere. A prolate deformation corresponds to the stretching of the distribution along only one axis, while the distribution shrinks equally along the other two axes. An oblate deformation corresponds to the compression of the distribution along one axis with increases along the other two axes. Note that nuclear deformations are much smaller than those displayed here.

where R_{average} is the average radius of the two major axes, β is the dimensionless measure of the deformation, and Y_{20} is the spherical harmonic function. Formally,

$$\beta = \frac{4}{3}\sqrt{\frac{\pi}{5}}\frac{b-a}{R_{\text{avg}}} \tag{6.13}$$

where b and a are the semi-major and semi-minor axes of the ellipsoid and R_{avg} is the average radius, $R_{\text{avg}}^2 = (a^2 + b^2)/2$. The deformation parameter can be positive (prolate shapes) or negative (oblate shapes) and is generally a small number. For example, the superdeformed prolate shape with an axis ratio of 2 : 1 has $\beta \sim 0.6$.

The energy levels from the quantum mechanical solution of the rotation of a rigid body have the characteristic feature of increasing separation with angular momentum. The energy levels are given by the expression

$$E_{\text{rot}} = \frac{J(J+1)\hbar^2}{2\mathcal{J}} \tag{6.14}$$

where J is the rotational quantum number describing the amount of rotation and $\mathcal{J}$ is the moment of inertia of the rigid body. For reference, the moment of inertia of a solid sphere with mass, m, is $\mathcal{J}_{\text{rigid}} = 2mR^2/5$. Substituting in constants and using $R = 1.2A^{1/3}$ fm, we find that the rotational energy levels of a sphere at $E_{\text{rot}} = 36.29J(J+1)/A^{5/3}$ MeV for J in $\hbar$ units. Note the large power of A in the denominator, which causes the expression for the rotational constant, $\hbar^2/2\mathcal{J}$, to be on the order of keV-s. This expression is called the rigid-body limit, and spherical rigid-body values for rotational energies are generally smaller than those observed, meaning that the real nuclear moment of inertia is smaller. The spherical moment of inertia expression can be readily extended to nuclei with static or rigid deformations by substituting the appropriate moment of inertia; thus, $\mathcal{J} = 2mR_{\text{avg}}^2/5(1+0.31\beta)$. The result is similar in that the deformed rigid-body estimate of the moment of inertia is too large and the rotational energy is too small.

We have already seen that nuclei have some properties that are similar to those of a liquid drop; in fact, the overall binding energy is well represented in these terms. The moment of inertia for the rotation of the liquid in a rigid deformed container, for example, a large water balloon with a negligible mass wall, is $\mathcal{J}_{\text{irro}} = (9/8\pi)mR^2\beta^2$. This moment of inertia is smaller than that of a rigid body because the liquid can "flow" inside the container to follow the motion of the walls, and the moment of inertia goes to zero at $\beta = 0$ as expected by symmetry. This rotational behavior is called irrotational flow. The irrotational flow moment of inertia gives a value that is usually smaller than the experimental value, leading to rotational energies that are larger than the experimental data. Thus, we have the general situation that

$$\mathcal{J}_{\text{irro}} < \mathcal{J}_{\text{exp}} < \mathcal{J}_{\text{rigid}} \tag{6.15}$$

which allows us to bracket the experimental value with predicted numerical estimates.

Sample Problem 6.4: Rotational Constant

The ground-state rotational band of ^{152}Gd is shown in Figure 6.10. Use the energy separation between the 2^+ and 0^+ levels to estimate the rotational constant in keV and the moment of inertia in amu-fm^2, and then compare your result to that obtained to the rigid body result with a deformation parameter of $\beta = 0.2$. Finally, evaluate the irrotational flow moment of inertia for this nucleus.

Solution

$$E_{\text{rot}} = \frac{J(J+1)\hbar^2}{2\mathcal{J}}$$

$$\Delta E_{\text{rot}}(2 \to 0) = \frac{(6-0)\hbar^2}{2\mathcal{J}} = 344.3 \text{ keV}$$

$$\frac{\hbar^2}{2\mathcal{J}} = 57.3 \text{ keV}; \mathcal{J} = 364.7 \text{ amu-fm}^2$$

$$\mathcal{J}_{\text{rigid}} = \frac{2}{5}mR_{\text{avg}}^2(1 + 0.31\beta)$$

$$\mathcal{J}_{\text{rigid}} = 2494 \text{ amu-fm}^2(1 + 0.31(0.2)) = 2648 \text{ amu-fm}^2$$

$$\mathcal{J}_{\text{irro}} = \frac{9}{8\pi}mR^2\beta^2$$

$$\mathcal{J}_{\text{irro}} = 2232 \text{ amu-fm}^2(0.2)^2 = 89.3 \text{ amu-fm}^2$$

Different rotational bands in a given nucleus can have differing effective moments of inertia. This could reflect a larger deformation or a change in the number of paired nucleons or a different alignment of a pair of nucleons of high spin. The result is that each band can have a different pattern of energy versus spin (Fig. 6.12, left). If one plots $2\mathcal{J}/\hbar^2$ versus the rotational frequency $\hbar^2\omega^2$ for a given nucleus, then one observes a kink or "backbend" in the plot corresponding to the region where the two bands cross (Fig. 6.12, right). A special class of quantum rotors are the superdeformed nuclei. The moments of inertia, after scaling by $A^{5/3}$, are all similar due to the fact that the shape of these nuclei is largely independent of mass. All these nuclei have similar shapes with an axis ratio of 2 : 1 due to shell stabilization effects discussed in the succeeding text.

Another interesting case of nuclear rotation occurs in the spherical nuclei. Ordinarily equally spaced γ-ray transitions imploy collective rotation, but such bands have been observed in the nearly spherical ^{199}Pb. It has been suggested
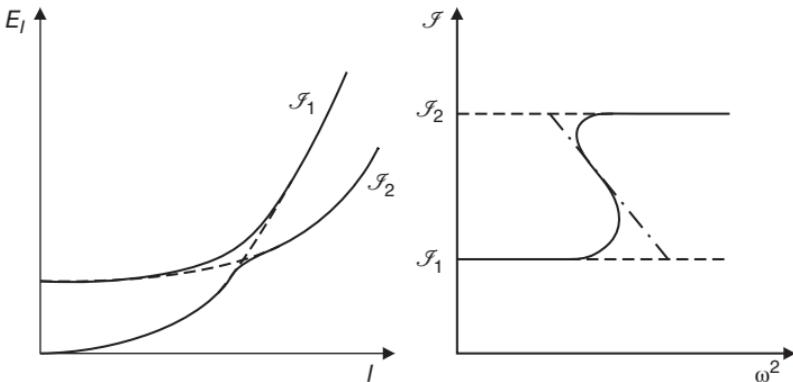
Figure 6.12 (Left) Schematic picture of two intersecting bands with different moments of inertia, $\mathcal{J}_1$ and $\mathcal{J}_1$. (Right) The backbending plot corresponding to the intersecting bands (From Heyde (1999)).

that these bands arise by another type of nuclear rotation called the "shears mechanism." A few valence neutron and proton holes couple to form to large or "long" angular momenta, j_n and j_p, which couple to give the total spin j. By varying the angle between these two "blades of the shears," states of differing spin are created. This gives rise to a magnetic moment, and the radiation associated with the γ-ray transition is $M1$.

The other important macroscopic motions of nuclei are the vibrations of the nuclear volume around the spherical ground state. Recall that the great majority of nuclei have spherical ground states, but they also can behave like liquid drops, so we might imagine that the surface of the nucleus could be caused to vibrate harmonically, back and forth, around the spherical ground state. In this picture we could parameterize the shape vibrations, also called surface oscillations, in terms of the spherical harmonic functions with their characteristic multipolarities. We should also be careful to differentiate between the characteristic motion labeled by the multipolarity or "shape symmetry" of the mode and the number of quanta or phonons in each vibrational mode. We will label the multipolarity of the mode by λ and use integers for the number of quanta. One might imagine multiple excitation of a single mode, single excitation of several modes simultaneously, or any other combination of modes and excitations.

The lowest-order vibration is a swelling/compression of the whole nucleus with $\lambda = 0$. This is sometimes called the "breathing" mode. The next macroscopic vibration, labeled $\lambda = 1$, is a dipole motion. However, the motion of the entire surface, first in one direction and then back in the other, imply corresponds to translation of the nucleus and not internal vibration. This motion would have to be caused by a "restoring force" that was outside the nucleus (e.g., an alternating electric field), and so there cannot be an intrinsic dipole motion of a (whole) nucleus. The next-order vibration, labeled $\lambda = 2$, is the

quadrupole motion in which the nucleus symmetrically stretches out and then in without moving its center or mass. This is clearly a vibrational motion with a "restoring force" generated by the nuclear potential. The third-order vibration, labeled $\lambda = 3$, is the octupole motion in which the nucleus asymmetrically expands on one end while pinching in on the other. This vibration creates pair shaped figures and requires significantly more energy to excite compared with the more symmetric quadrupole shapes.

Recall that the energy levels of the quantum mechanical harmonic oscillator are all equally spaced having energies $E_N = (N + 1/2)\hbar\omega_0$, $N = 0, 1, 2$, (see Fig. 6.13). The fundamental frequency of the oscillation ω_0 is equal to the square root of the force constant divided by the effective mass. Considering even–even nuclei with 0^+ ground states, single excitation of quadrupole motion with $\lambda = 2$ will require an $N = 2$ state as $N = 1$ is not allowed because it would break the symmetry of the nuclear wave function. This $N = 2$ excitation gives rise to a 2^+ state with two $\hbar\omega_0$ units of energy. We would expect that the subsequent multiple excitation of this mode would create a 4^+ state with twice the excitation energy and so on. Because there are three ways to couple two quadrupole phonons together ($J\pi = 4^+$, 2^+, and 0^+), the two-phonon state is triply degenerate. The three phonon state at an energy of three $\hbar\omega_0$ will include 6^+, 4^+, 3^+, 2^+, and 0^+ states. From a global perspective, the observed ratios of the energy of the 4^+ to 2^+ states in even–even nuclei are $\sim 2 : 1$ in good agreement with this model, but there are two strong deviations. First, the deformed rotational nuclei
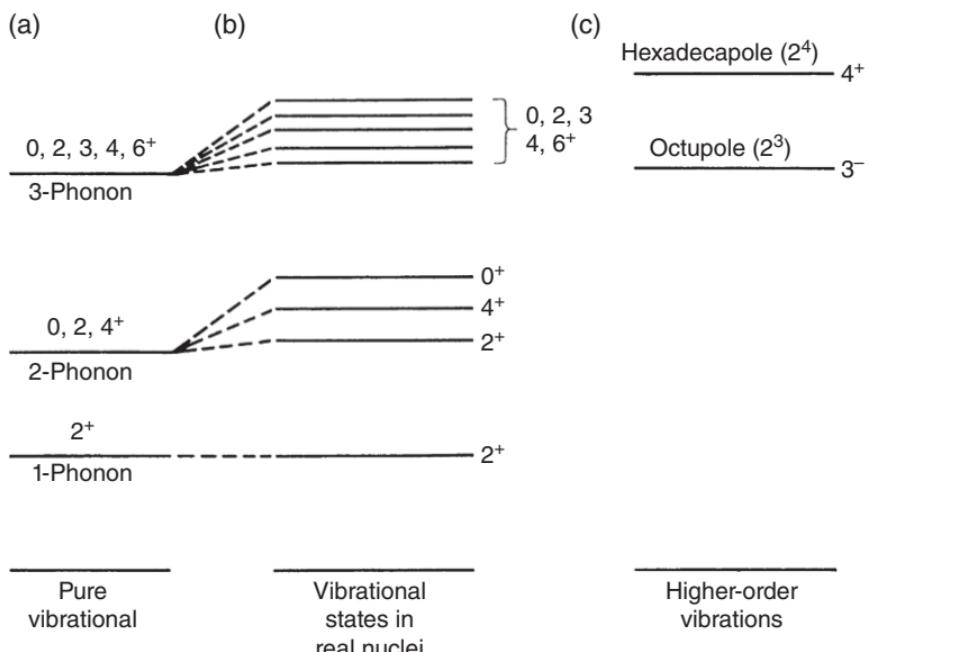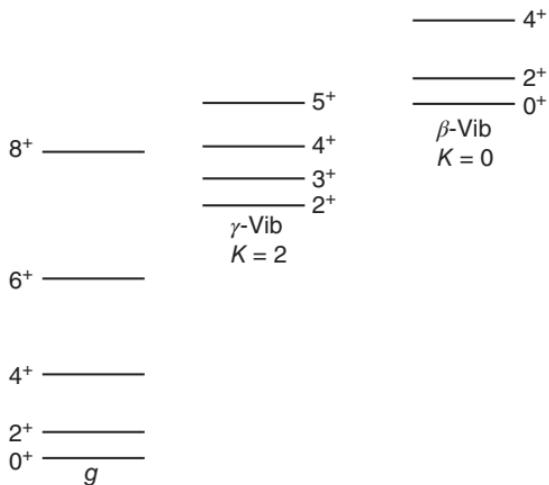
Figure 6.13 Schematic vibrational energy level diagrams of medium-mass even–even nuclei (Eichler (1964). Reproduced with the permission of American Physical Society).

Figure 6.14 Example of the energy variation of the positive parity levels with K in a typical deformed nucleus.

have $4^+/2^+$ ratios of $10:3$ as discussed previously. And, second, when the number of neutrons or protons are close to the magic numbers for closed spherical shells, the nucleus becomes more resistant to oscillation, and the energies of the 2^+ and 4^+ states increase dramatically as well as their ratio.

It is interesting to note that the vibrational model of the nucleus predicts that each nucleus will be continuously undergoing zero-point motion in all of its modes. This zero-point motion of a quantum mechanical harmonic oscillator is a formal consequence of the Heisenberg uncertainty principle and can be seen in the fact that the lowest-energy state $N = 0$ has the finite energy of $\hbar\omega/2$. From another standpoint, the superposition of all of these shape oscillations can be viewed as a natural basis for the diffuseness of the nuclear surface.

The energy of rotational states built on vibrations is given by

$$E = \frac{\hbar^2}{2\mathcal{J}} \left[j(j + 1) - K^2 \right] \tag{6.16}$$

where K is the projection of J on the nuclear symmetry axis. For so-called β vibrations ($\lambda = 2$, $K = 0$), $J\pi = 0^+$, 2^+, 4^+; for so-called γ vibrations ($\lambda = 2$, $K = 2$), $J\pi = 2^+$, 3^+, 4^+. A typical sequence of states is shown in Figure 6.14.

6.6 Nilsson Model

Up to now, we have discussed two extremes of nuclear structure, those aspects that can be explained by the properties of single or individual particles moving in a spherically symmetric central potential and those aspects corresponding to large-scale collective motions of groups of nucleons away from spherical symmetry. Additional insight into the structure of nuclei can be obtained by considering the states of single particles moving in a deformed nuclear
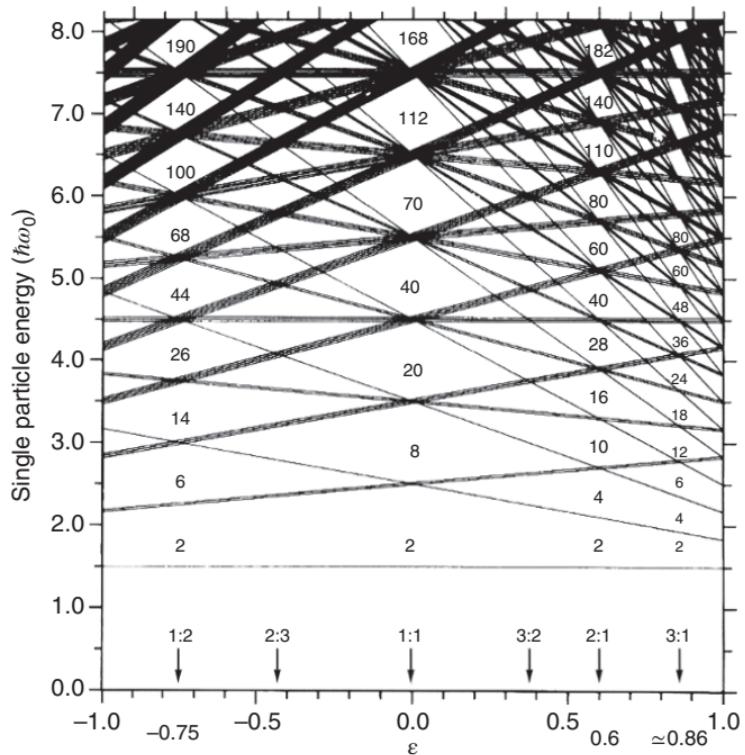
Figure 6.15 Variation of the single particle levels of a deformed harmonic oscillator as a function of the deformation of the potential. The ratios of the semi-major to semi-minor axes of the oscillator are also shown for reference.

potential. S.G. Nilsson extensively studied this problem, and the resulting model of nuclear structure is referred to as the Nilsson model.

Using a deformed harmonic oscillator potential, one can make several useful observations about the nuclear structure of deformed nuclei. In Figure 6.15, we show the variation of the energies of single particle states of such a potential as a function of the deformation of the potential. At spherical symmetry, one observes the gaps in the level spacings corresponding to the major harmonic oscillator shells that we have already discussed. But as the deformation changes, the levels move in energy, and new magic numbers (shell gaps) occur when the ratio of the semi-major and semi-minor axes of the nucleus equals a simple whole number. Thus, nuclei with axes ratios of 2 : 1 have special stability (the superdeformed nuclei). In addition, each spherical shell model state, for example, a $f_{7/2}$ state, is split into $(2j + 1)/2$ levels labeled with a new quantum number Ω defined as the projection of the single particle angular momentum on the nuclear symmetry axis (Fig. 6.16). For prolate deformation, states of highest Ω lie the highest in energy.
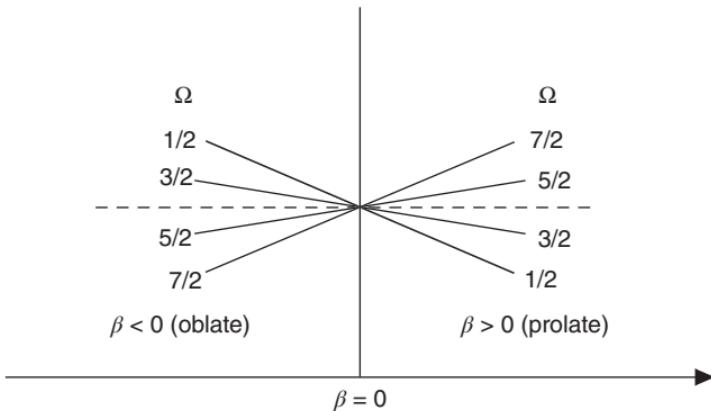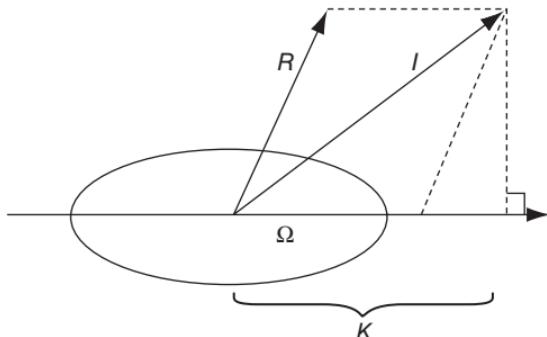
Figure 6.16 Schematic variation of the energies of the $f_{7/2}$ spherical shell model substates as the potential deforms. Positive deformations correspond to prolate shapes, while negative deformations correspond to oblate shapes.

The angular momentum of an odd A deformed nucleus, J, is the vector sum of the angular momentum of the last unpaired nucleon and the rotational angular momentum, R, of the core of remaining nucleons as shown schematically in Figure 6.17. The projection of the total nuclear angular momentum J upon the nuclear symmetry axis is again given the symbol K. For axially symmetric nuclei, the direction of R is perpendicular to the symmetry axis and $J = \Omega = K$. Each Nilsson single particle level may be the ground state of a rotational band. For the ground state of such bands, $J = \Omega = K$. When $J = 3/2$ or greater, the allowed nuclear spins of the members of the band are $J_0, J_0 + 1, J_0 + 2$, etc. The energies of the members of the band are given as

$$E(J) = \frac{\hbar^2}{2\mathcal{J}} \left[J(J+1) - J_0(J_0+1) \right] \tag{6.17}$$

The Nilsson model is also able to predict the ground state and low-lying states of deformed odd A nuclei. Figure 6.18 presents a more detailed picture of how the energies of the Nilsson levels vary as a function of the deformation parameter β_2 for the first 20 nucleons in the nucleus. Let us consider the nuclei ^{19}F,

Figure 6.17 Schematic display of the addition of angular momenta in a deformed odd A nucleus. Ω is the projection of the total angular momentum of the odd nucleon. It is added vectorially to the rotational angular momentum of the core R to give the total angular momentum I whose projection on the symmetry axis is K.
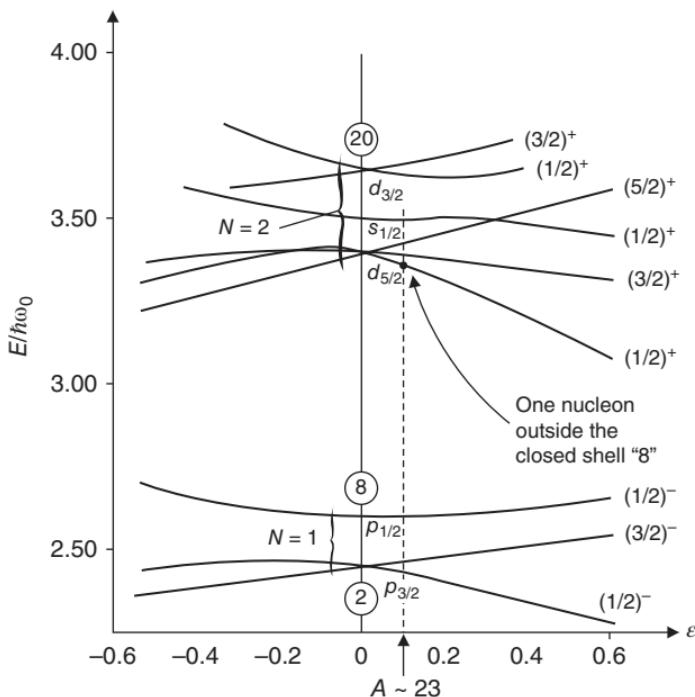
Figure 6.18 Variation of the energy of a single nucleon in a deformed potential as a function of deformation parameter ϵ. This diagram pertains to either $Z < 20$ or $N < 20$. Each state can accept two (spin-paired) nucleons, as usual.

^{19}Ne, ^{21}Ne, and ^{23}Na. According to the simple shell model (Fig. 6.3), the last odd nucleon in these nuclei should be in a $d_{5/2}$ state, giving rise to a ground state spin and parity $J\pi$ of $5/2^+$. One observes $J\pi$ for these four nuclei to be $1/2^+$, $1/2^+$, $3/2^+$, and $3/2^+$, respectively. None of them are $5/2^+$. The Nilsson model allows us to understand these observations. The quadrupole moments of these nuclei are all ∼0.1 barns, from which we can deduce that β = 0.1. Thus, from the variation of the $d_{5/2}$ levels with deformation shown in Figure 6.18, we expect the 9th particle to be in the substate with $J\pi = 1/2^+$, while the 11th particle will have $J\pi = 3/2^+$ in agreement with the observations. The low-lying excited states of many nuclei can also be explained by considering the filling of sublevels with small deformations in the Nilsson diagrams.

6.7 Fermi Gas Model

The preceding discussion of nuclear structure and models was mostly aimed at explaining the detailed properties of the ground states and small excitations of nuclei. These nuclei are produced and take part in nuclear reactions that are usually very complicated dynamical situations compared with the (simple)

situation of nucleons confined in a static central potential. Detailed calculations with wave functions in dynamical potentials associated with scattering and absorption have only been carried out in a very few specific cases. On the other hand, a very wide variety of nuclear reactions have been studied experimentally and often exhibit amazing simplicity. Models have been developed that treat the average behavior of the large number of nucleons in a nucleus on a statistical basis. An important statistical model developed to describe the average behavior of medium and large nuclei, particularly useful in reactions, treats the nucleus as a gas of fermions. This approximation, called the Fermi gas model, uses the now familiar concept of confining the nucleons to a fixed spherical shape with a central potential, but in this case the nucleons are assumed to be all equivalent and independent. This situation loosely corresponds to an ideal gas confined to a fixed volume with the addition of Fermi–Dirac statistics and Pauli blocking to prevent spatial overlap of the particles.

An important feature of the Fermi gas model is that it allows us to describe the average behavior of a nucleus with thermodynamical functions. The fact that the energy levels in a (large) nucleus with a finite excitation energy are so closely spaced allows us to use entropy to predict the evolution of the system. (This idea is somewhat opposite to the ground-state situation that is dominated by the wave functions of individual particles.) The concept of thermodynamic entropy is closely linked to a thermodynamic nuclear temperature. Nuclear reactions are often described in terms of the imagined temperature of the internal particles, and excited nuclei emit light particles and γ-rays as they lose their excitation energy and "cool" as they approach the ground state.

The first step in developing the Fermi gas model is to determine the highest level that is occupied by nucleons. Next the average energies and momenta can be calculated because we will assume that all the lower levels are exactly filled. In this model the nucleons are confined to a fixed total volume and are assumed to have a uniform density. When quantum mechanical particles are confined in a rigid container, then they occupy fixed states that can be labeled with appropriate quantum numbers, that is, n_x, n_y, n_z for a rectangular box with three dimensions, L_x, L_y, L_z. The particle will have a specific momentum in each state, so, alternatively, we could label the states by their momenta, p_x, p_y, p_z, or by their wave numbers, k_x, k_y, k_z, where $k_i = (n_i \pi / L_i = p_i / \hbar)$, which explicitly incorporates the dimensions of the box. We would like to know what is the highest quantum number n or the largest momentum p_f or the wave number k_f of the highest filled level, called the Fermi level. The number of states for a particle to move with momentum in the range of p to $p + dp$ in a volume Ω is given by the expression

$$dN_{\text{states}} = \frac{\Omega}{(2\pi\hbar)^3} 4\pi p^2 dp \tag{6.18}$$

which can be integrated from zero up to the maximum momentum value to give the number of states up to that momentum:

$$N_{\text{states}} = \int_0^{p_f} dN_{\text{states}} = \frac{\Omega}{(2\pi\hbar)^3} \int_0^{p_f} 4\pi p^2 dp = \frac{4\pi\Omega}{3(2\pi\hbar)^3} p_f^3 \tag{6.19}$$

Remember that the Pauli principle allows us to put particles with two spins (up/down) into each state, and if the nucleons are all in their lowest possible states, the number of filled states can be assumed to be equal to the number of each type of nucleon:

$$n_{\text{particles}} = 2N_{\text{states}} = \frac{\Omega}{3\pi^2\hbar^3} p_f^3 \rightarrow p_f = \left(\frac{3\pi^2\, n_{\text{particles}}}{\Omega} \right)^{1/3} \hbar \tag{6.20}$$

Thus, the Fermi wave number for protons is

$$p_f(\text{protons}) = \left(\frac{3\pi^2 Z}{\Omega} \right)^{1/3} \hbar = \left(\frac{3\pi^2 Z}{(4/3)\pi r_0^3 A} \right)^{1/3} \hbar = \left(\frac{9\pi Z}{4A} \right)^{1/3} \frac{\hbar}{r_0} \tag{6.21}$$

and similarly for neutrons where we have taken the volume to be that of a sphere $\Omega = (4/3)\pi R^3$ and the nuclear radius, $R = r_0 A^{1/3}$. Notice that we have obtained an expression that depends only on Z/A (or N/A) and the radius constant r_0 so the value of the Fermi energy will be similar for most nuclei because the variation of Z/A is small for stable nuclei and only varies with the cube root. The Fermi energy for nucleons in those nuclei with $Z/A = 1/2$ taking $r_0 = 1.2$ fm is

$$E_f = \frac{p_f^2}{2m} \approx 32 \text{ MeV} \tag{6.22}$$

If the number of neutrons is greater than the number of protons, as in heavy nuclei, then the Fermi energies will be slightly different for the two kinds of particles. An approximate representation of the Fermi energy for protons and neutrons is

$$E_f^{\text{protons}} = 53 \left(\frac{Z}{A} \right)^{2/3} \text{ MeV} \tag{6.23}$$

$$E_f^{\text{neutrons}} = 53 \left(\frac{A-Z}{A} \right)^{2/3} \text{ MeV} \tag{6.24}$$

The average kinetic energy of the nucleons in the well can be shown to be $3/5\, E_f$ or $\sim$20 MeV. Notice that the nucleons are moving rapidly inside the potential well but not extremely fast.

Sample Problem 6.5: Fermi Energy

What is the de Broglie wavelength of a neutron moving with the average kinetic energy in a ^{208}Pb nucleus according to the Fermi gas model? You can assume that the neutron is nonrelativistic and use $r_0 = 1.2$ fm.

Solution

$$p_f(\text{neutrons}) = \left(\frac{9\pi N}{4A}\right)^{1/3} \frac{\hbar}{r_0}$$

$$k_f = \frac{p_f}{\hbar} = \left(\frac{9\pi N}{4A}\right)^{1/3} \frac{1}{r_0} = 1.353 \text{ fm}^{-1}$$

$$E_f = \frac{p_f^2}{2m} = \frac{(k_f\hbar)^2}{2m} = \frac{(1.353 \times 197.3)^2}{2 \times 939} = 38 \text{ MeV}$$

$$E_{\text{avg}} = \frac{3}{5} E_f = 23 \text{ MeV}$$

$$\lambda_{\text{deB}} = \frac{2\pi\hbar}{p} = \frac{2\pi}{k_f} = 4.64 \text{ fm}$$

Notice that this wavelength is slightly smaller than the lead radius $R = 1.2A^{1/3} = 7.1$ fm.

A schematic version of the Fermi gas potential energy well for a large nucleus is shown in Figure 6.19. Recall that nucleons are bound by $\sim$8 MeV, on average, so the uppermost filled energy level (Fermi level) should be approximately at -8 MeV. The lowest level is then $\sim$32 MeV below this, which makes the Fermi
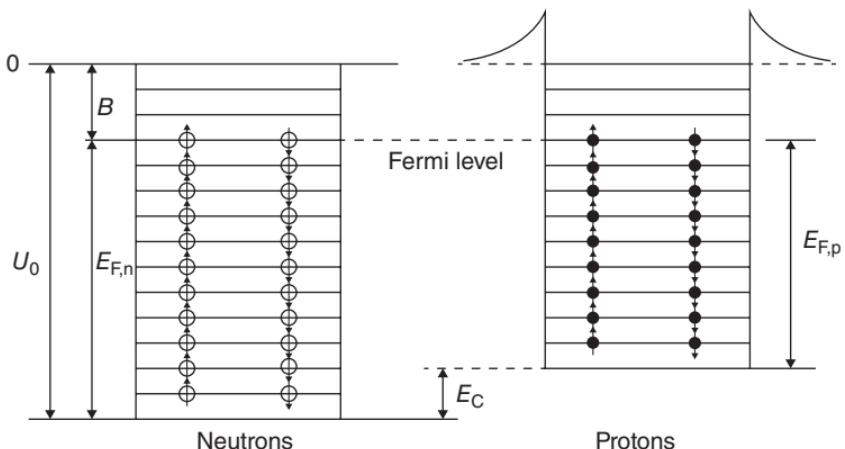
Figure 6.19 A schematic version of the potential energy well derived from the Fermi gas model. The highest filled energy levels reach up to the Fermi level of $\sim$32 MeV. The nucleons are bound by $\sim$8 MeV, so the potential energy minimum is relatively shallow.

gas potential energy well relatively shallow. The levels between the Fermi level and zero potential energy are assumed to be completely empty in the ground state and become occupied when the nucleus absorbs excitation energy.

As a nucleus absorbs energy, nucleons are promoted from the filled levels into the unfilled region between the Fermi level and zero potential energy. Each promotion leads to a specific excitation energy, and combinations of multiple excitations can lead to the same or similar energies. At high excitations the number of combinations of different possible promotions for a specific excitation energy grows dramatically. The tremendous growth of the number of energy states with excitation energy is one of the interesting features of nuclei. The number of levels is so large that we can describe the system by an average level density, $\rho(E^*, N)$, which is simply the number of levels per unit excitation energy, E^*, for a fixed number of nucleons, N. The fact that excited nuclei, even with a finite number of particles, have very dense and nearly continuous distributions of levels is the feature that allows us to describe their de-excitation with statistical techniques.

The connection between the microscopic description of any system in terms of individual states and its macroscopic thermodynamical behavior was provided by Boltzmann through statistical mechanics. The key connection for nuclei is that the entropy of a system is proportional to the natural logarithm of the number of levels available to the system, thus

$$S(E, N) = k_B \ln \Gamma(E, N) = k_B \ln[\rho(E, N)\Delta E] \qquad (6.25)$$

where Γ is this total number of levels. The entropy of an excited nucleus is thus proportional to the level density in some energy interval, ΔE, and goes to zero as the excitation energy goes to zero. (Recall that there is only one nuclear ground state.) The thermodynamic temperature can be calculated from the entropy with the expression

$$\frac{1}{T} = \frac{\partial S(E^*, N)}{\partial E} = k_B \frac{\partial \ln \rho(E^*, N)}{\partial E} \qquad (6.26)$$

In statistical mechanics the Boltzmann constant k_B with dimensions of energy per degree is included in expressions so that the temperatures can be given in degrees Kelvin. The numerical values of nuclear temperatures in Kelvin are very large, for example, 10^9 K, so the product of k_B and T is usually quoted in energy units (MeV), and the Boltzmann factor is often not written explicitly.

At this point we have not distinguished between nuclear systems and macroscopic systems. There is, however, at least one important difference between the two types of systems. The difference is the way the entropy $S(E^*, N)$ can be evaluated. In statistical mechanics one has different physical situations (ensembles) for evaluating thermodynamic quantities: (a) fixed energy and particle number (called the micro-canonical ensemble), (b) fixed temperature and particle number (the canonical ensemble), and (c) fixed temperature and chemical potential

(the grand canonical ensemble). In the evaluation of thermodynamic quantities for macroscopic systems, each of these approaches provides essentially the same result so that the entropy may be evaluated by calculating any of the following: $S_{\text{micro−canonical}}$, $S_{\text{canonical}}$, or $S_{\text{grand canonical}}$. This is not the case for nuclear systems because only the micro-canonical ensemble with a fixed energy and particle number can be evaluated for an isolated nucleus. Thus, the fundamental definition of nuclear temperature should be written as

$$\frac{1}{T} = \frac{\partial S_{\text{micro−canonical}}(E^*, N)}{\partial E} \tag{6.27}$$

and it is not correct to substitute an entropy obtained with a different ensemble into this expression.

Standard procedures are available to evaluate the entropy of a Fermi gas under the conditions of a grand canonical ensemble, which we will have to adjust to obtain the useful micro-canonical entropy. For low excitation energies, E^*, the entropy is

$$S_{\text{grand canonical}}(E^*, N) = 2\sqrt{aE^*} \tag{6.28}$$

where a is a constant proportional both to the number of particles and to the density of the single particle levels of the Fermi gas at the Fermi energy E_f. If $S_{\text{grand canonical}}$ is used to replace $S_{\text{micro−canonical}}$, one obtains $T = (E/a)^{1/2}$ as the link between temperature and excitation energy. This result is appropriate for macroscopic systems, but as we said it must be modified for isolated nuclear systems. For small systems with a fixed small number of particles

$$S_{\text{micro−canonical}} = S_{\text{grand canonical}} + \Delta S \tag{6.29}$$

where ΔS becomes vanishingly small compared with $S_{\text{grand canonical}}$, as the number of particles or the excitation energy becomes large. An approximate expression for ΔS for a Fermi gas at relatively low energy is

$$\Delta S = -\gamma \ln(E^*) \tag{6.30}$$

with γ being a number of the order of unity, ranging from 1 to 2 depending on whether isospin and angular momentum are explicitly considered in the labeling of the states. When the appropriate $S_{\text{micro−canonical}}$ is used to evaluate the nuclear temperature, one finds

$$\frac{1}{T} = \frac{\partial S_{\text{grand canonical}}(E^*, N)}{\partial E} + \frac{\partial \Delta S}{\partial E} \tag{6.31}$$

For the moderately low energies, this provides

$$\frac{1}{T} \approx \sqrt{\frac{a}{E^*}} - \left(\frac{\gamma}{E^*}\right) \tag{6.32}$$

as the link between excitation energy and nuclear temperature. For large excitation energies, E^*, and large particle number, the correction term proportional to γ becomes small, and one can write $E^* \approx aT^2$.

The density of nuclear states can be written

$$\rho(E^*) \propto \frac{a}{(aE^*)^\gamma} \exp\left(2\sqrt{aE^*}\right) \tag{6.33}$$

The factor a that appears here and in the previous text is called the level density parameter and is adjusted to correspond to level densities measured at low excitation energies. The analyses of data over a broad mass range suggest that a is proportional to the mass of the nuclear system A with a value of $\sim A/8.5 \text{ MeV}^{-1}$. The level densities can be corrected for the effect of angular momentum on the thermal excitation energy by including pre-exponential statistical factors and subtracting the collective energy that is involved in rotation. The rotational energy is often included with an effective moment of inertia, a parameter adjusted to match experimental spectra and yields.
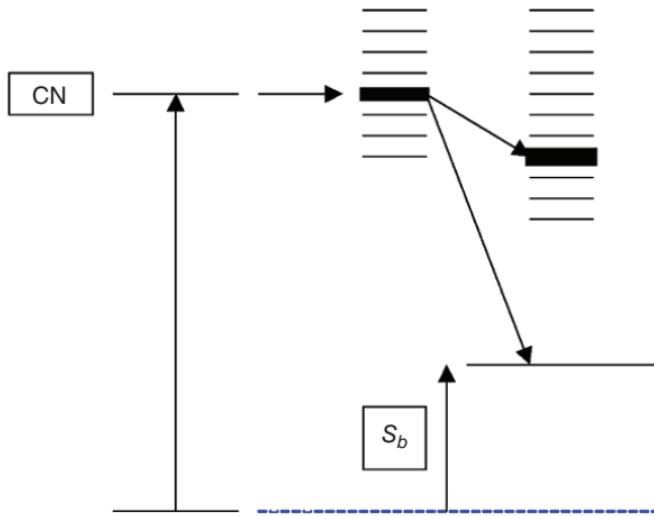
We can extend the Fermi gas level density analysis to predict the relative probability of various decay modes of excited nuclei if we make the assumption that the nuclei are in full thermal equilibrium. That is, we assume that all of the energy levels corresponding to a given excitation energy are fully populated. It is not possible for a single nucleus to be in many states simultaneously, that is, it can only be in one. So the thermal equilibrium that we require can only be used to describe a set of nuclei created in many (identical) reactions. This is, of course, how chemical reactions take place when Avogadro's number of atoms or molecules with various kinetic energies but one temperature follows a path from reactant to products based on a specific reaction mechanism. Nuclear reactions are usually detected by producing large numbers of nuclei, $\gg 10^3$, and then observing various reaction products and determining the probabilities of each process.

Excited nuclei that have attained statistical equilibrium will decay into different products in proportion to the number of states available to the whole system after the decay. The different decays are often called reaction channels or exit channels, and we speak of the probability to decay into a given channel. A very schematic representation of the energy levels and the energies involved in the decay of an excited nucleus into various channels is shown in Figure 6.20. The total sum of the probabilities for decay into all channels is, of course, one. We can simply count the number of states available for a decay channel and obtain a general expression for the relative probability, $P(\epsilon, n)$, for an excited nucleus to emit a portion with size n, requiring an energy ϵ. The expression is

$$P(\epsilon, n) \propto \Gamma(\epsilon, n) \times \Gamma(E - \epsilon, N - n) \tag{6.34}$$

where $\Gamma(E, N)$ is the number of states in the vicinity of energy E for a system of mass number N. The first factor on the right hand side is contributed by the

Figure 6.20 A representation of the branching decays from a highly excited compound nucleus. In the statistical model, the relative probability for the excited nucleus to decay into a specific channel is proportional to the number of possibilities or statistical weight of that channel divided by the sum of all of the statistical weights of all of the channels.

states in the emitted object, and the second is contributed by the states in the (large) residual nucleus. The number of internal states can be taken to be the log of the level densities used to define the entropy, shown previously, and we will need to include a term for the kinetic energy of the emitted object. However, we need to integrate the emission rates over the whole course of the nuclear reaction to obtain the total yields that can be measured in the laboratory.

Focusing on comparisons to measurable quantities, the relative probability of a reaction (exit) channel can be written as the ratio of the cross section for that channel, σ_i, to the total reaction cross section, σ_T. The ratios are labeled as the relative decay widths, Γ_i, in a notation, that is, unfortunately, easy to confuse with the number of states discussed previously. The sum of the decay widths is the total width of the state and can be used to calculate the lifetime of the excited state. Thus,

$$\frac{\sigma_i}{\sigma_T} = \frac{\Gamma_i}{\Gamma_T} \tag{6.35}$$

and notice that the ratio of the relative probability of two decay channels i and j does not depend on the total reaction cross section:

$$\frac{\sigma_i}{\sigma_j} = \frac{\Gamma_i}{\Gamma_j} \tag{6.36}$$

The width for the emission of a particle with a binding energy of B_n that has no internal states (i.e., proton, neutron, deuteron, alpha) has been shown to have the form

$$\Gamma_i \propto \Gamma(E, N) \int_0^{E-B_i} \epsilon \rho(E - B_i - \epsilon) d\epsilon \tag{6.37}$$

with E as the excitation of the excited parent nucleus. Therefore, the relative intensities of the channels change because the binding energies of the emitted

particles change the density of states through the exponential dependence of the level density. This approach can be extended to the case of fission decay leading, in the simplest approximation, to a slightly different integral:

$$\Gamma_f \propto \Gamma(E, N) \int_0^{E-E_f} \rho(E - E_f - \epsilon)d\epsilon \tag{6.38}$$

in terms of the fission barrier E_f. The ratio Γ_n/Γ_f is very important in determining the survival of the heaviest elements when they are synthesized in nuclear reactions. Notice that if the nucleus emits a neutron to remove excitation, it retains its large atomic number; however, if it fissions then it is converted into two nuclei with much smaller atomic numbers. The integrals in the previous expressions can be evaluated in the Fermi gas approximation with the following approximate result (Vandenbosch and Huizenga, 1973):

$$\frac{\Gamma_n}{\Gamma_f} \approx \frac{2TA^{2/3}}{K_0} \exp\left[\frac{(E_f - B_n)}{T}\right] \tag{6.39}$$

where $K_0 = \hbar^2/2mr_0^2 \sim 15$ MeV and T is the nuclear temperature created by the initial reaction. The exponential function contains the difference between the fission barrier and the neutron separation energy. Therefore, this ratio is only near unity when these two values are nearly equal. If there is a large difference between the fission barrier and the separation energy, then the overall ratio will be very large or very small.

Sample Problem 6.6: Nuclear Temperature

In a certain nuclear reaction, a beam of ^{18}O was combined with ^{238}U nuclei to form a compound nucleus of ^{256}Fm. The nuclei were produced with an excitation energy of 95 MeV. Calculate the nuclear temperature assuming that $\gamma = 1$, and then calculate the relative probability of neutron to fission decay of the excited system.

Solution

$$\frac{1}{T} \approx \left(\frac{a}{E^*}\right)^{1/2} - \frac{1}{E^*}$$

with $a = A/8.5 = 256/8.5 = 30.1$ MeV^{-1}

$$\frac{1}{T} \approx \left(\frac{20.1}{95}\right)^{1/2} - \frac{1}{95} \rightarrow T \approx 1.8 \text{ MeV}$$

We need to find the neutron separation energy and the fission barrier for this nucleus in order to evaluate the ratio. The neutron separation energy is 6.38 MeV, and the fission barrier is 5.90 MeV.

$$\frac{\Gamma_n}{\Gamma_f} \approx \frac{2TA^{2/3}}{K_0} \exp\left[\frac{(E_f - B_n)}{T}\right]$$

$$\frac{\Gamma_n}{\Gamma_f} \approx \frac{2 \times 8 \times 256^{2/3}}{15} \exp\left[\frac{(5.90 - 6.38)}{1.8}\right]$$

$$\frac{\Gamma_n}{\Gamma_f} \approx 9.68 \exp[-0.266] = 7.4$$

Problems

6.1 Predict the ground state spins and parities for ^{41}K, ^{44}Ca, and ^{60}Co.

6.2 An odd A nucleus has a $J\pi = 7/2^+$ ground state. (a) What are J, K for the first two excited states? (b) If the energy of the first excited state is 100 keV, what is the energy of the second excited state?

6.3 Define or describe the following terms or phenomena: nuclear isomerism, spin–orbit coupling, β-vibration, Schmidt limits, and Nilsson diagram.

6.4 The α decay of ^{241}Am ($t_{1/2} = 420$ years, $J\pi = 5/2^+$) populates members of at least two rotational bands (A and B) in ^{237}Np shown in Table 6.1. (a) Using the collective model, predict the energies of the $9/2^+$, $9/2^-$, and $11/2^-$ levels. (b) Calculate the effective moment of inertia of ^{237}Np.

Table 6.1 Energy Levels in ^{237}Np.

Band	J, π	E (keV)
B	$11/2^-$	?
B	$9/2^-$	?
B	$7/2^-$	103
A	$9/2^+$	?
B	$5/2^-$	59.6
A	$7/2^+$	33.2
A	$5/2^+$	0

6.5 What is the energy of the $2^+ \rightarrow 0^+$ γ-ray transition in ^{172}Hf assuming that ^{172}Hf is a perfect rigid rotor with a moment of inertia, $\mathcal{J} = (2/5)mR^2$?

6.6 Calculate the energy of the 4^+, 6^+, 8^+, and 10^+ members of the ground-state rotational band of an even–even nucleus if the energy of the 2^+ member of the band is 0.044 MeV above the ground state.

6.7 An odd A nucleus has levels at 0, 33, 60, 75.5, 127 and 189 keV. Which of these levels are likely to be part of a ground state rotational band built on the $5/2^-$ ground state?

6.8 Identify the single particle makeup of the following levels in the odd–odd ^{131}Tm nucleus using the collective and Nilsson models if $\beta = 0.25$ (Table 6.2).

Table 6.2 Energy Levels in ^{131}Tm.

J, π	E (keV)
$7/2^-$	425
$7/2^+$	129
$5/2^+$	117
$3/2^+$	5
$1/2^+$	0

6.9 Identify the single particle makeup of the following levels in the even–even ^{24}Mg nucleus using the collective and Nilsson models if $\beta = 0$ (Table 6.3).

Table 6.3 Energy Levels in ^{24}Mg.

J, π	E (MeV)
4^+	6.000
3^+	5.220
2^+	4.230
4^+	4.113
2^+	1.369
0^+	0

6.10 A deformed even–even nuclide has energy levels characterized by the following values of spin, parity, and K value. You will note that not all of the information is given for each level. Fill in the blanks with

Table 6.4 Energy Levels in Even–Even Nuclide.

E (keV)	J, π	K
400	1⁻	0
376	3⁺	?
?	4⁺	0
349	6⁺	0
310	2⁺	2
?	2⁺	0
200	0⁺	0
166	4⁺	?
0	0⁺	0

the required values. In the appropriate space, assign each of the levels to a particular mode of excitation, for example, vibrational or rotational. Assume all bands are characterized by the same value of the moment of inertia (Table 6.4).

6.11 Using the shell model calculate the ground state spins, parities, and magnetic moments for ^{32}S, ^{33}S, and ^{41}K.

6.12 Predict the following characteristics of the ground states of ^{25}Mg and ^{63}Cu: the state of the odd nucleon, the total nuclear angular momentum, the nuclear magnetic dipole moment, the sign of the nuclear quadrupole moment, and the parity. Explain the probable cause of any important discrepancies between your predictions and the following measured values: ^{25}Mg, I = 5.2, μ = −0.96, Q = (−) and ^{63}Cu, I = 3/2, μ = +2.22, Q = −0.1.

6.13 The energies (in MeV) of the lowest excited states of ^{182}W for $J = 2, 4, 6$ are $E = 0.100, 0.329$, and 0.680, respectively. Do these values agree with a rotational model?

6.14 For the nucleus ^{236}U at an excitation energy of 30 MeV, (a) what is the nuclear temperature at this energy and (b) what is the ratio of Γ_n to Γ_f at this excitation energy if the fission barrier $B_f = 6$ MeV?

6.15 ^{249}Bk is known to have the following level scheme. Fill in the missing energies and J, π value (Table 6.5).

Table 6.5 Energy Levels in ^{249}Bk.

E (keV)	J, π
1540	4^+
1415	?
1318	2^+
656	2^+
0	0^+

6.16 Given the shell model state $k_{17/2}$, show qualitatively how it might split as a function of increasing prolate deformation. (a) How many fermions are needed to fill this orbital. Label each state as to its Ω value and indicate the maximum number of particles in each Ω state.

6.17 Show that the Brennan–Bernstein rules forbid the existence of odd-mass nuclei with ground states spin/parity of 0^+ or 1^-. Can you find exceptions?

6.18 ^{121}Sb has a spin of 5/2 and a magnetic moment of 3.36 nm. What is the shell model state of the 51st proton? What would the shell model predict for the spin?

Bibliography

E. Eichler, Rev. Med. Phys. **36**, 809 (1964).

R. Vandenbosch, and J. R. Huizenga, *Nuclear Fission* (Academic, New York, 1973).

General

Most, if not all, textbooks in nuclear science have a chapter discussing nuclear structure. Among the favorites of the authors are:

A. Das and T. Ferbel, *Introduction to Nuclear and Particle Physics* (John Wiley & Sons, Inc., New York, 1994).

H.A. Enge, *Introduction to Nuclear Physics* (Addison-Wesley, Reading, 1966).

G. Friedlander, J.W. Kennedy, E.S. Macias, and J.M. Miller, *Nuclear and Radiochemistry* (John Wiley and Sons, Inc., New York, 1981).

K. Heyde, *Basic Ideas and Concepts in Nuclear Physics*, 2nd Edition (IOP, Bristol, 1999).

P.E. Hodgson, E. Gadioli, and E. Gadioli-Erba, *Introductory Nuclear Physics*. (Clarendon, Oxford, 1997).

K.S. Krane, *Introductory Nuclear Physics* (John Wiley & Sons, Inc., New York, 1987).

More Specialized, Advanced Treatments

A. Bohr and B.R. Mottelson, *Nuclear Structure, Volumes I and II* (Benjamin, New York, 1969).

R.F. Casten, *Nuclear Structure from a Simple Perspective* (Oxford, New York, 1990).

G.E. Gordon and C.D. Coryell, J. Chem. Ed. **44**, 636 (1967).

A. de Shalit and H. Feshbach, *Theoretical Nuclear Physics, Vol I Nuclear Structure* (John Wiley and Sons, Inc., New York, 1974).

S.G. Nilsson and I. Ragnarsson, *Shapes and Shells in Nuclear Structure* (Cambridge, Cambridge, 1995).

H. Tyren, P. Hillman, and T. Maris, Nucl. Phys. **7**, 10 (1958).

7

α-Decay

7.1 Introduction

In a series of seminal experiments, Ernest Rutherford and his collaborators established the important features of α decay. The behavior of the radiations from natural sources of uranium and thorium and their daughters was studied in magnetic and electric fields. The least penetrating particles, labeled "α-rays" because they were the first to be absorbed, were found to be positively charged and quite massive in comparison with the more penetrating negatively charged "β-rays" and the most penetrating neutral "γ-rays." In a subsequent experiment the α-rays from a needle-like source were collected in a very small concentric discharge tube, and the emission spectrum of helium was observed in the trapped volume. Thus, α rays were proven to be energetic helium nuclei. The α-particles are the most ionizing radiation emitted by natural sources (with the extremely rare exception of the spontaneous fission of uranium) and are stopped by as little as a sheet of paper or a few centimeters of air. The particles are quite energetic (E_α = 4–12 MeV) but interact very strongly with electrons as they penetrate into material and stop within 100 μm in most materials.

Understanding these features of α-decay allowed early researchers to use the emitted α-particles to probe the structure of nuclei in scattering experiments and later, by reaction with beryllium, to produce neutrons. In an interesting dichotomy, the α-particles from the decay of natural isotopes of uranium, radium, and their daughters have sufficient kinetic energies to overcome the Coulomb barriers of light elements and induce nuclear reactions but are not energetic enough to induce reactions in the heaviest elements.

α particles played an important role in nuclear physics before the invention of charged particle accelerators and were extensively used in research. Therefore, the basic features of α decay have been known for some time. The process of α decay is a nuclear reaction that can be written as

$$_Z^A (Z)_N \rightarrow {_{Z-2}^{A-4}} (Z)_{N-2}^{2-} + {_2^4}\mathrm{He}_2^{2+} + Q_\alpha \tag{7.1}$$

where we have chosen to write out all of the superscripts and subscripts. Thus the α-decay of ^{238}U can be written as

$$^{238}\text{U} \rightarrow {}^{234}\text{Th}^{2^-} + {}^4\text{He}^{2^+} + Q \qquad (7.2)$$

The Q_α value is positive (exothermic) for spontaneous α decay. The helium nucleus emerges with a substantial velocity and is fully ionized, and the atomic electrons on the daughter are disrupted by the sudden change, but the whole process conserves electrical charge. We can rewrite the equation in terms of the masses of the neutral atoms:

$$^{A}_{Z}(Z)_N \rightarrow {}^{A-4}_{Z-2}(Z)_{N-2} + {}^4_2\text{He}_2 + Q_\alpha \qquad (7.3)$$

and then calculate the Q_α value because the net change in the atomic binding energies ($\sim 65.3Z^{7/5} - 80Z^{2/5}$ eV) is very small compared with the nuclear decay energy.

What causes α-decay? (Or what causes Q_α to be positive?) In the language of the semiempirical mass equation, the emission of an α-particle lowers the Coulomb energy of the nucleus, which increases the stability of heavy nuclei while not affecting the overall binding energy per nucleon very much because the tightly bound α-particle has approximately the same binding energy/nucleon as the original nucleus.

Two important features of α decay are that the energies of the α particles are known to generally increase with the atomic number of the parent but the kinetic energy of the emitted particle is less than that of the Coulomb barrier in the reverse reaction between the α-particle and the daughter nucleus. In addition, all nuclei with mass numbers greater than $A \approx 150$ are thermodynamically unstable against α emission (Q_α is positive), but α emission is the dominant decay process only for the heaviest nuclei, $A > 210$. The energies of the emitted α-particles can range from 1.8 MeV (^{144}Nd) to 11.6 MeV (^{212}Po^m) with the half-life of ^{144}Nd being 5×10^{29} times as long as that of ^{212}Po^m. Typical heavy element α decay energies are typically in the range from 4 to 9 MeV, as noted earlier.

In general, α decay leads to the ground state of the daughter nucleus so that the emitted particle carries away as much energy as possible and as little angular momentum as possible. The ground state spins of even–even parents and daughters (including the α particle, of course) are zero, which makes $\ell = 0$ α particle emission the most likely process for these nuclei. Small branches are seen to higher excited states, but such processes are strongly suppressed. Some decays of odd A heavy nuclei populate low-lying excited states that match the spin of the parent so that the orbital angular momentum of the α-particle can be zero. For example, the strongest branch (83%) of the α decay of ^{249}Cf goes to the ninth excited state of ^{245}Cm because this is the lowest-lying state with the same spin and parity as that of the parent. α Decay to several different excited states of a daughter nucleus is called *fine structure*; α-decay from an excited

state of a parent nucleus to the ground state of the daughter nucleus is said to be *long-range* α *emission* because these α-particles are more energetic and thus have longer ranges in matter than ground state to ground state-emission. A famous case of long-range α-emission is that of ^{212}Po^m where a 45 s isomeric level at 2.922 MeV decays to the ground state of ^{208}Pb by emitting a 11.65 MeV α-particle.

We will consider the general features of α emission, and then we will describe them in terms of a simple quantum mechanical model. It turns out that α emission is a beautiful example of the quantum mechanical process of tunneling through a barrier that is forbidden in classical mechanics.

7.2 Energetics of α Decay

As we have seen in the overview of the nuclear mass surface in Chapter 2, the α particle, or ^{4}He nucleus, is an especially strongly bound particle. This, combined with the fact that the binding energy per nucleon has a maximum value near $A \approx 56$ and systematically decreases for heavier nuclei, creates the situation that nuclei with $A > 150$ have positive Q_α values for the emission of α particles. This behavior can be seen in Figure 7.1. For example, one of the
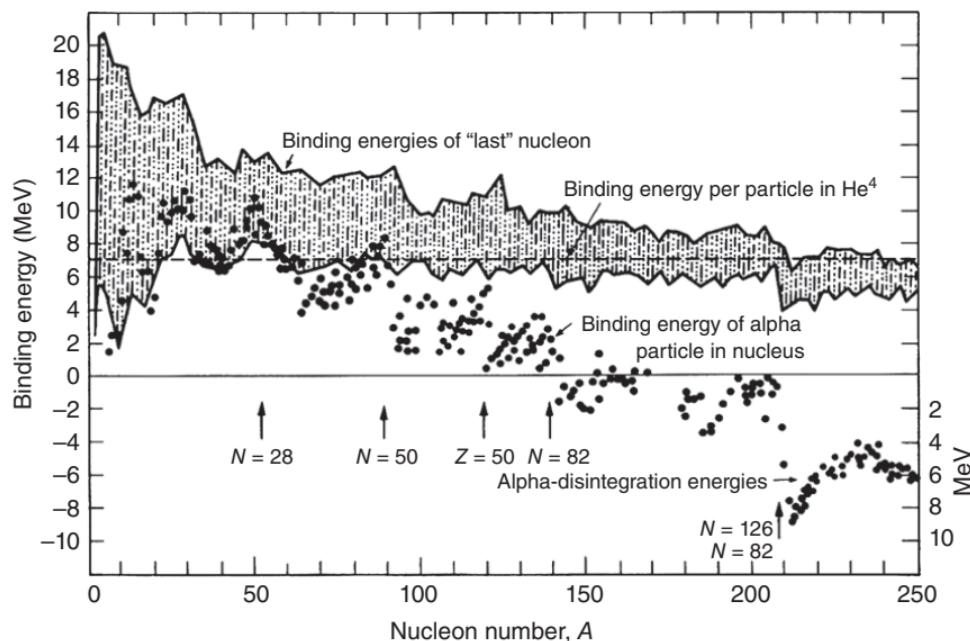
Figure 7.1 The variation of the α particle separation energy as a function of mass number is shown in comparison to the average nuclear binding energy (Valentin (1981). Reproduced with the permission of North-Holland Publishing Company).

heaviest naturally occurring isotopes, ^{238}U (with a mass excess, Δ, of $+47.3070$ MeV), decays by α emission to ^{234}Th ($\Delta = +40.612$ MeV), giving a Q_α value of

$$Q_\alpha = 47.3070 - (40.612 + 2.4249) = 4.270 \text{ MeV} \tag{7.4}$$

Note that the decay energy will be divided between the α-particle and the heavy recoiling daughter so that the kinetic energy of the α-particle will be slightly less than the Q value. (The kinetic energy of the recoiling ^{234}Th nucleus produced in the decay of ^{238}U is ~0.070 MeV.) Conservation of momentum and energy in this reaction requires that the kinetic energy of the α-particle, T_α, is

$$T_\alpha = \frac{234}{238} Q_\alpha = 4.198 \text{ MeV} \tag{7.5}$$

The kinetic energies of the emitted α particles can be measured very precisely, so we should be careful to distinguish between the Q_α value and the kinetic energy T_α. The very small recoil energy of the heavy daughter is very difficult to measure, but it is still large compared to chemical bond energies and can lead to interesting chemistry. For example, the daughter nuclei may recoil out of the original α-source. This can cause serious contamination problems if the daughters are themselves radioactive.

The Q_α values generally increase with increasing atomic number, but the variation in the mass surface due to shell effects can overwhelm the systematic increase (Fig. 7.2). The sharp peaks near $A = 214$ are due to the effects of the $N = 126$ shell. When ^{212}Po decays by α-emission, the daughter nucleus is doubly magic ^{208}Pb (very stable) with a large energy release. The α-decay of neighboring ^{211}Pb and ^{213}Po will not lead to such a large Q_α because the products are not doubly magic. Similarly, the presence of the 82 neutron closed shell in the rare earth region causes an increase in Q_α, allowing observable α-decay half-lives for several of these nuclei (with $N = 84$). Also one has observed short-lived α-emitters near doubly magic ^{100}Sn, including ^{107}Te, ^{108}Te, and ^{111}Xe. And, in addition, α emitters have been identified along the proton dripline above $A = 100$. For a set of isotopes (nuclei with a constant atomic number), the decay energy generally decreases with increasing mass. These effects can be seen in Figure 7.2. For example, the kinetic energy of α particles from the decay of uranium isotopes is typically 4–5 MeV, those for californium isotopes are >6 MeV, and those for rutherfordium isotopes are >8 MeV. However, recall that the kinetic energy from the decay of ^{212}Po to the doubly magic ^{208}Pb daughter is 8.78 MeV, showing the dramatic effect of the underlying nuclear structure.

The generally smooth variation of Q_α with Z, A of the emitting nucleus and the two body nature of α decay can be used to deduce masses of unknown nuclei. One tool in this effort is the concept of closed decay cycles (Fig. 7.3).
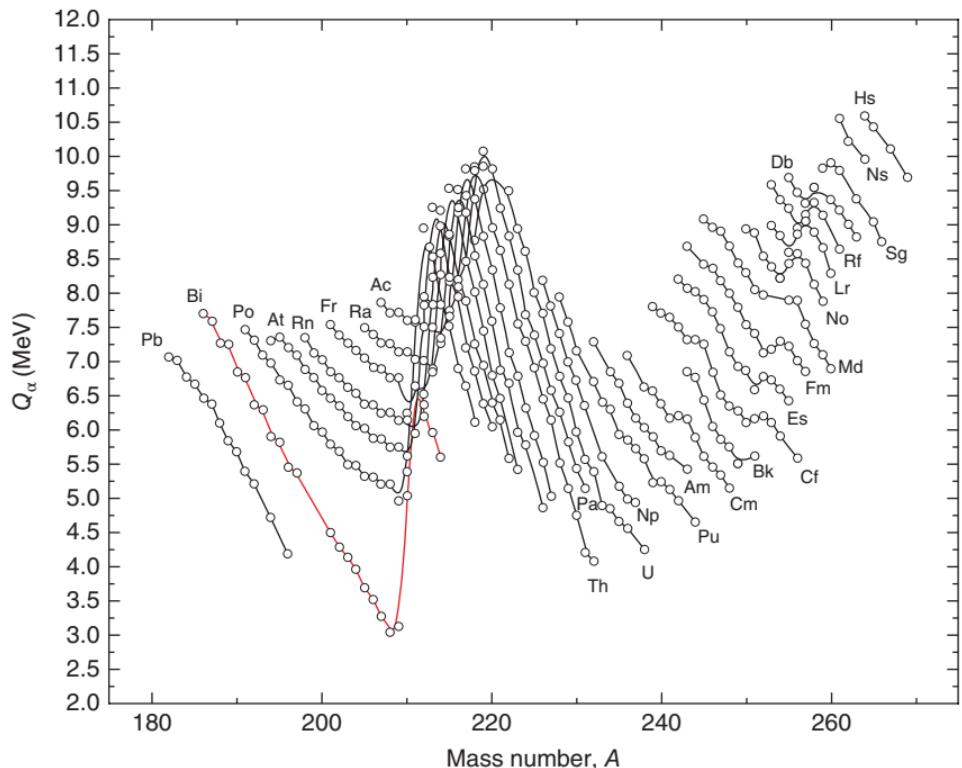
Figure 7.2 The variation of α decay energies indicating the effect of the $N = 126$ and $Z = 82$ shell closures along with the $N = 152$ subshell.
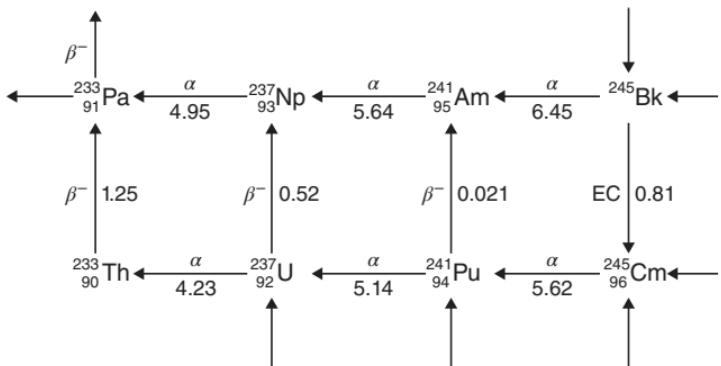
Figure 7.3 Decay cycles for part of the $4n + 1$ family. Modes of decay are indicated over the arrows; the numbers indicate total decay energies in MeV.

Consider the α- and β-decays connecting $^{237}_{93}\text{Np}$, $^{241}_{95}\text{Np}$, $^{241}_{94}\text{Pu}$, and $^{237}_{92}\text{U}$. By conservation of energy, one can state that the sum of the decay energies around the cycle connecting these nuclei must be zero (within experimental uncertainty). In those cases where experimental data or reliable estimates are available for three branches of the cycle, the fourth can be calculated by difference.

Even though the energies released by the decay of a heavy nucleus into an α particle and a lighter daughter nucleus are quite substantial, the energies are paradoxically small compared to the energy necessary to bring the α particle back into nuclear contact with the daughter. The electrostatic potential energy between the two positively charged nuclei, called the Coulomb potential, can be written as

$$V_C = \frac{2Z}{R} \frac{e^2}{4\pi\epsilon_0} \tag{7.6}$$

where Z is the atomic number of the daughter and R is the separation between the centers of the two nuclei. (As pointed out in Chapter 1, $\frac{e^2}{4\pi\epsilon_0}$ is 1.440 MeV-fm.) To obtain a rough estimate of the Coulomb energy, we can take R to be $1.2(A^{1/3} + 4^{1/3})$ fm, where A is the mass number of the daughter. For the decay of ^{238}U, we get

$$V_C = \frac{(2)(90)(1.440 \text{ MeV fm})}{1.2(234^{1/3} + 4^{1/3}) \text{ fm}} \approx \frac{259 \text{ MeV fm}}{9.3 \text{ fm}} = 28 \text{ MeV} \tag{7.7}$$

which is 6–7 times the decay energy. This factor is typical of the ratio of the Coulomb barrier to the Q value for α decay. If we accept for the moment the large difference between the Coulomb barrier and the observed decay energy, then we can attribute the two general features of increasing decay energy with increasing atomic number, Z, and decreasing kinetic energy with increasing mass among a set of isotopes to the Coulomb potential. The higher nuclear charge accelerates the products apart, and the larger mass allows the daughter and α particle to start further apart.

Sample Problem 7.1: α Decay Energies

Calculate the Q_α value; kinetic energy, T_α; and Coulomb barrier, V_C, for the primary branch of the α decay of ^{212}Po to the ground state of ^{208}Pb.

Solution

Using tabulated mass excesses we have
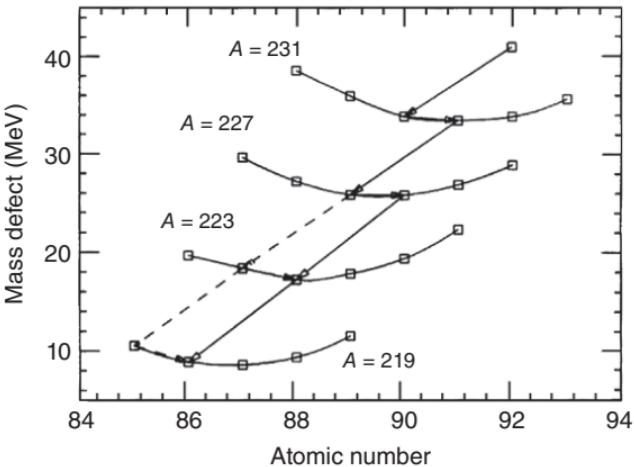
$$Q_\alpha = -10.381 - (-21.759 + 2.4249) = 8.953 \text{ MeV}$$
$$T_\alpha = \frac{208}{212} Q_\alpha = 8.784 \text{ MeV}$$
$$V_C = \frac{(2)(82)(1.440 \text{ MeV fm})}{1.2(208^{1/3} + 4^{1/3}) \text{ fm}} \approx 26 \text{ MeV}$$

The ^{212}Po parent also decays with a 1% branch to the first excited state of ^{208}Pb at an excitation energy of 2.6146 MeV. What is the kinetic energy of this α particle?

Figure 7.4 Mass parabolas for some members of the $4n + 3$ natural decay series. The main decay path is shown by a solid line, while a weak branch is indicated by a dashed line.

$$Q'_\alpha = 8.953 - 2.6146 \text{ MeV} = 6.338 \text{ MeV}$$
$$T'_\alpha = \frac{208}{212}Q'_\alpha = 6.22 \text{ MeV}$$

As discussed previously, many heavy nuclei ($A \geq 150$) are unstable with respect to α-decay. Some of them also undergo β^- decay. In Chapter 3, we discussed the natural decay series in which heavy nuclei undergo a sequence of β^- and α-decays until they form one of the stable isotopes of lead or bismuth, ^{206,207,208}Pb or ^{209}Bi. We are now in a position to understand why a particular sequence occurs. Figure 7.4 shows a series of mass parabolas (calculated using the semiempirical mass equation) for some members of the $4n + 3$ series, beginning with ^{235}U. Each of the mass parabolas can be thought of as a cut through the nuclear mass surface at constant A. ^{235}U decays to ^{231}Th. ^{231}Th then decays to ^{231}Pa by β^-decay. This nucleus, being near the bottom of the mass parabola, cannot undergo further β^- decay but decays by α-emission to ^{227}Ac. This nucleus decays by β^- emission to ^{227}Th, which must α-decay to ^{223}Ra, drop etc.

7.3 Theory of α Decay

The allowed emission of α particles could not be understood in classical pictures of the nucleus. This fact can be appreciated by considering the schematic potential energy diagram for ^{238}U shown in Figure 7.5. Using simple estimates we have drawn a one dimensional potential energy curve for this system as a function of radius. At the smallest distances, inside the parent nucleus, we
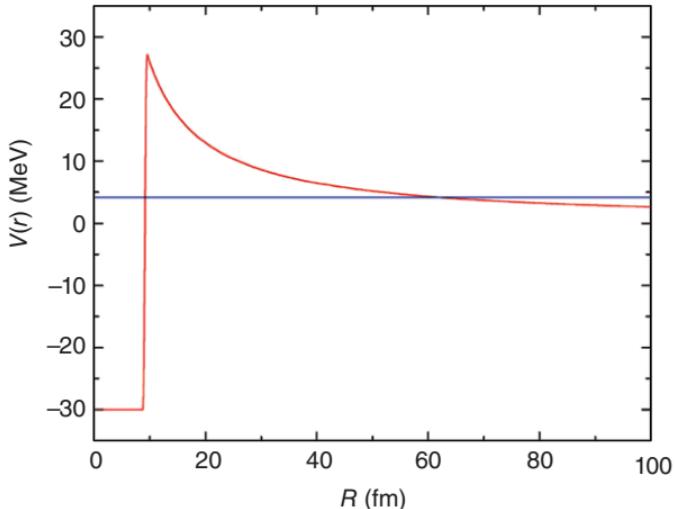
Figure 7.5 A (reasonably accurate) one-dimensional potential energy diagram for ^{238}U indicating the energy and calculated distances for α decay into ^{234}Th. Fermi energy ≈30 MeV, Coulomb barrier ≈28 MeV at 9.3 fm, $Q_\alpha = 4.2$ MeV, distance of closest approach 62 fm.

have drawn a flat-bottomed potential with a depth of ∼30 MeV (as discussed in Chapter 6). The potential rapidly rises at the nuclear radius and comes to the Coulomb barrier height of $V_C \sim +28$ MeV at 9.3 fm. At larger distances the potential falls as $\frac{1}{r}$ according to Coulomb's law.

Starting from a separated α particle and the daughter nucleus, we can determine that the distance of closest approach during the scattering of a 4.2 MeV α particle will be ∼62 fm. This is the distance at which the α particle stops moving toward the daughter and turns around because its kinetic energy has been converted into potential energy of repulsion. Now the paradox should be clear: the α particle should not get even remotely close to the nucleus, or from the decay standpoint, the α particle should be trapped behind a potential energy barrier that it cannot get over. The solution to this paradox was found in quantum mechanics. A general property of quantum mechanical wave functions is that they are only completely confined by potential energy barriers that are infinitely high. Whenever the barrier has a finite size, the wave function solution will have its main component inside the potential well plus a small but finite part *inside* the barrier (generally exponentially decreasing with distance) and another finite piece *outside* the barrier. This phenomenon is called tunneling because the classically trapped particle has a component of its wave function outside the potential barrier and has some probability to go through the barrier to the outside. The details of these calculations are discussed in Appendix E and in many quantum mechanics textbooks. Some features of tunneling should be
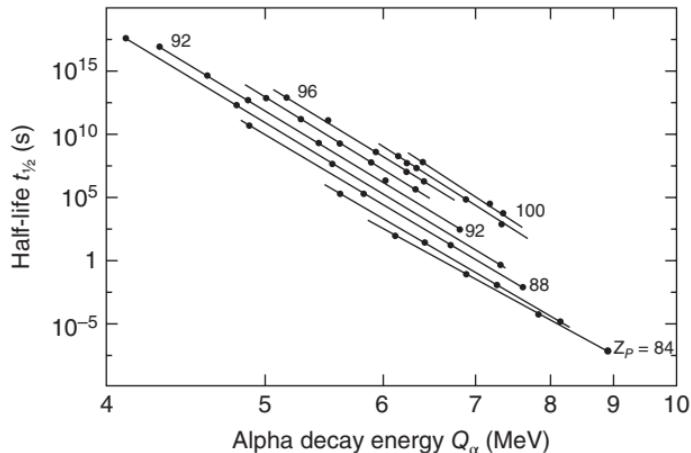
Figure 7.6 A Geiger–Nuttall plot of the logarithm of the half-life (s) versus the square root of the Q_α value (MeV).

obvious: the closer the energy of the particle to the top of the barrier, the more likely that the particle will get out. Also, the more energetic the particle is relative to a given barrier height, the more frequently the particle will "assault" the barrier, and the more likely that the particle will escape.

It has been known for some time that half-life for α-decay, $t_{1/2}$, can be written in terms of the square root of the α particle decay energy, Q_α, as follows:

$$\log_{10}(t_{1/2}) = A + \frac{B}{\sqrt{Q_\alpha}} \tag{7.8}$$

where the constants A and B have a Z dependence. This relationship, shown in Figure 7.6, is known as the Geiger–Nuttall law of α-decay (Geiger and Nuttall, 1911, 1912) due to the fact that they found a linear relationship between the logarithm of the decay constant and the logarithm of the range of α particles from a given natural radioactive decay series. This simple relationship describes the data on α-decay, which span over 20 orders of magnitude in decay constant or half-life. Note that a 1 MeV change in α-decay energy results in a change of 10^5 in the half-life. A modern representation of this relationship due to Parkhomenko and Sobiczewski has the form

$$\log_{10}\left(t_{1/2}(\text{s})\right) = aZ\left(Q_\alpha(\text{MeV}) - E_{\text{d}}\right)^{-1/2} + bZ + c \tag{7.9}$$

where $a = 1.5372$, $b = -0.1607$, $c = -36.573$, and $E_{\text{d}} = 0$ for e–e nuclei; 0.0113 MeV for o–e nuclei; 0.171 MeV for e–o nuclei; and 0.284 MeV for o–o nuclei. Z refers to the parent nuclide. The effect of the E_{d} term is to account for the excitation energy of the daughter.

This modern relationship is useful for predicting the expected α-decay half-lives for unknown nuclei.

The theoretical description of α emission relies on calculating the rate in terms of two factors. The overall rate of emission consists of the product of the rate at which an α particle appears at the inside wall of the nucleus times the (independent) probability that the α particle tunnels through the barrier. Thus, the rate of emission, or the partial decay constant λ_α, is written as the product of a frequency factor, f, and a transmission coefficient, T, through the barrier:

$$\lambda_\alpha = fT \tag{7.10}$$

Some investigators have suggested that this expression should be multiplied by an additional factor to describe the probability of preformation of an α particle inside the parent nucleus. Unfortunately, there is no clear way to calculate such a factor, but empirical estimates have been made. As we will see in the following text, the theoretical estimates of the emission rates are higher than the observed rates, and the preformation factor can be estimated for each measured case. However, there are other uncertainties in the theoretical estimates that contribute to the differences.

The frequency with which an α particle reaches the edge of a nucleus can be estimated as the velocity divided by the distance across the nucleus. We can take the distance to be twice the radius (something of a maximum value), but the velocity requires a more subtle estimate. A lower limit for the velocity could be obtained from the kinetic energy of emitted α particle, but the particle is moving inside a potential energy well, and its velocity should be larger and correspond to the well depth plus the external energy. Therefore, the frequency can be written as:

$$f = \frac{v}{2R} = \frac{\sqrt{2(V_0 + Q_\alpha)/\mu}}{2R} \tag{7.11}$$

where we have assumed that the α particle is nonrelativistic, V_0 is the well depth indicated in Figure 7.5 of $\sim$30 MeV, μ is the reduced mass, and R is the radius of the daughter nucleus (because the α-particle needs only to reach this distance before it is emitted). We use the reduced mass because the α particle is moving inside the nucleus, and the total momentum of the nucleus must be zero. The frequency of assaults on the barrier is quite large, usually on the order of 10^{21} /s.

The quantum mechanical transmission coefficient for an α-particle to pass through a barrier is derived in Appendix E. Generalizing the results summarized in the Appendix to a three-dimensional barrier shown in Figure 7.5, we have

$$T = e^{-2G} \tag{7.12}$$

where the Gamow factor ($2G$) can be written as

$$2G = \frac{2}{\hbar} \int_R^b \left[2\mu \left(\frac{Z_\alpha Z_d e^2}{r} - Q_\alpha \right) \right]^{1/2} dr \tag{7.13}$$

where the classical distance of closest approach, b, is given as a function of Q_α by

$$b = \frac{Z_\alpha Z_d e^2}{Q_\alpha} \tag{7.14}$$

In these equations, $e^2 = 1.440$ MeV-fm, Q_α is given in MeV, and Z_α, Z_d are the atomic numbers of the α-particle and daughter nucleus, respectively. Rearranging we get

$$2G = \frac{2}{\hbar}\sqrt{2\mu Q_\alpha} \int_R^b \left(\frac{b}{r} - 1\right)^{1/2} dr \tag{7.15}$$

That can be integrated to give

$$2G = \frac{2b}{\hbar}\sqrt{2\mu Q_\alpha} \left(\arccos(\sqrt{y}) - \sqrt{y(1-y)}\right) \tag{7.16}$$

with $y = R/b$. Substituting back and collecting terms,

$$2G = 2\sqrt{\frac{2\mu}{\hbar^2 Q_\alpha}}(Z_\alpha Z_d e^2)\left(\arccos(\sqrt{y}) - \sqrt{y(1-y)}\right) \tag{7.17}$$

For thick barriers where $R/b \ll 1$ or ($Q_\alpha/V_C \ll 1$, we can approximate the arccos as

$$\arccos\left(\sqrt{\frac{R}{b}}\right) \approx \frac{\pi}{2} - \sqrt{\frac{R}{b}} \tag{7.18}$$

so that we get

$$2G = 2\sqrt{\frac{2\mu}{\hbar^2 Q_\alpha}}(Z_\alpha Z_d e^2)\left(\frac{\pi}{2}\right) \tag{7.19}$$

with an "effective" Coulomb barrier of

$$B = \frac{Z_\alpha Z_d e^2}{r_\alpha + R_d} \tag{7.20}$$

Typically, the Gamow factor is large ($2G \sim 60\text{-}120$), which makes the transmission coefficient T extremely small ($\sim 10^{-55}$ to 10^{-27}). Combining the various equations, we get a prediction for the half-life of

$$t_{1/2} = \frac{\ln 2}{\lambda} = \frac{\ln 2}{fT} = \frac{\ln 2}{\frac{(2(V_0 + Q_\alpha)/\mu)^{1/2}}{2R}e^{-2G}} \tag{7.21}$$

which has the form

$$\log t_{1/2} = a + \frac{b}{\sqrt{Q_\alpha}} \tag{7.22}$$
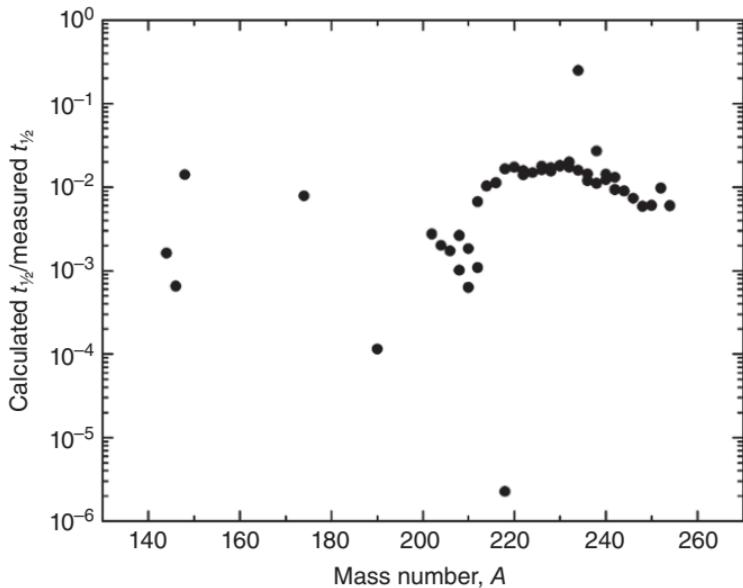
Figure 7.7 Plot of the ratio of the calculated partial α-decay half-life for ground-state $\ell = 0$ transitions of even–even nuclei to the measured half-lives. The calculations were made using the simple theory of α-decay.

that is, we get the Geiger–Nuttall law of α-decay, where $a + b$ are constants, which depend on Z and A.

This simple estimate tracks the general behavior of the observed emission rates over the very large range in nature. The calculated emission rate is typically one order of magnitude larger than that observed, meaning that *the observed half-lives are longer than predicted.* This has led some researchers to suggest that the probability to find a "preformed" α particle inside a heavy nucleus is on the order of 10^{-1} or less. One estimate of the "preformation factor" can be obtained from a plot of the ratio of the calculated half-life to the measured half-life for even–even nuclei undergoing $\ell = 0$ decay. Such a plot can be seen in Figure 7.7. The average preformation factor is $\sim 10^{-2}$ from this analysis.

Sample Problem 7.2: α Particle Emission Rate

Calculate the emission rate and half-life for ^{238}U decay from the simple theory of α decay. Compare this to the observed half-life.

Solution

$$\lambda = fT$$

$$f = \frac{\sqrt{2(V_0 + Q)/\mu}}{2R}$$

$$R = r_0 \left(A_d^{1/3} + A_\alpha^{1/3}\right) = 1.2(234^{1/3} + 4^{1/3}) = 9.3 \text{ fm}$$

Note: We previously estimated $b \gg 62$ fm for this decay; $R/b = 8.63/62 \ll 1$.

$$\mu = 4 \times 234/238 = 3.933 \text{ amu}$$

$$f = \frac{c \times \sqrt{2\,(30 + 4.2)/(3.933 \times 931.5)}}{2 \times 9.3} = 2.20 \times 10^{21}/\text{s}$$

We know that $T = e^{-2G}$, where

$$2G \approx 2 \left(\frac{2\mu}{\hbar^2 Q_\alpha}\right)^{1/2} Z_\alpha Z_d e^2 \left(\frac{\pi}{2} - 2\sqrt{\frac{Q}{B}}\right)$$

$$2 \left(\frac{2\mu}{\hbar^2 Q_\alpha}\right) = 2 \left(\frac{(2)(3.933)(931.5)}{(197.3)^2(4.27)}\right) = 0.420 \text{ (MeV fm)}^{-1}$$

$$Z_\alpha Z_d e^2 = (2)(90)(1.440) \text{ MeV fm}$$

$$\left(\frac{\pi}{2} - 2\sqrt{\frac{Q}{B}}\right) = \frac{\pi}{2} - 2\left(\frac{4.27}{27.9}\right)^{1/2} = 0.788$$

$$T = e^{85.5} = 5.68 \times 10^{-38}$$

$$\lambda = fT = (2.26 \times 10^{21})(5.43 \times 10^{-38}) = 1.23 \times 10^{-16}/\text{s}$$

$$t_{1/2} = \frac{\ln 2}{\lambda} = 5.53 \times 10^{15} \text{ s} = 1.8 \times 10^8 \text{ years}$$

Note that the observed half-life of ^{238}U is 4.47×10^9 years, which is a factor of ~25 times longer than this calculated value. Be aware of the
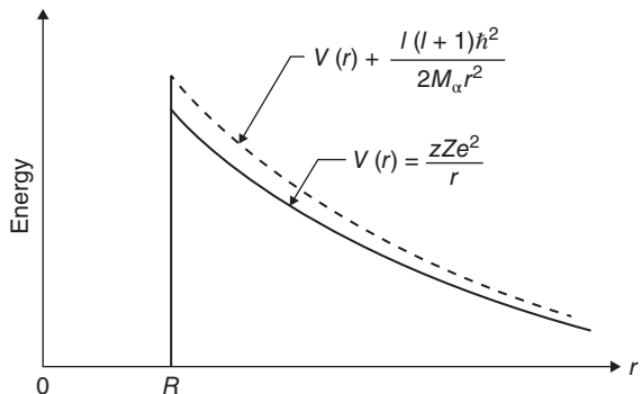
Figure 7.8 Modification of the potential energy in α-decay due to the centrifugal potential. Note that the centrifugal potential is defined slightly differently than given in the text with M_α replacing the reduced mass μ since $\mu \approx? M_\alpha$ (Meyerhof (1967). Reproduced with the permission of McGraw-Hill Book Company).

qualitative aspects of this calculation; the α-particle must hit the border of the parent nucleus $\sim 10^{38}$ times before it can escape and the extreme sensitivity of this calculation to details of the nuclear radius. A 2% change in R changes λ by a factor of 2. In our example, we approximated R as $R_{\text{Th}} + R_\alpha$. In reality, the α-particle has not fully separated from the daughter nucleus when it enters the barrier. One could attempt to correct for this by approximating $R \approx 1.4 A^{1/3}$.

The theory presented previously neglects the effects of angular momentum in that it assumes the α-particle carries off no orbital angular momentum ($\ell = 0$). If α-decay takes place to or from an excited state, some angular momentum may be carried off by the α-particle with a resulting change in the decay constant. In a quantum mechanical sense, we say that the α-particle has to tunnel through a barrier that is larger by an amount called the centrifugal potential:

$$V_\ell = \frac{\ell(\ell + 1)\hbar^2}{2\mu R^2} \tag{7.23}$$

where ℓ is the orbital angular momentum of the α-particle, μ is the reduced mass, and R is the appropriate radius. This centrifugal potential must be added to the potential energy $V(r)$, resulting in a thicker and higher barrier and increasing the half-life (Fig. 7.8).

One can evaluate the effect of this centrifugal potential upon α-decay half-lives by simply adding this energy to the Coulomb barrier height. If we define the ratio of barrier heights, σ,

$$\sigma = \frac{\text{Centrifugal barrier height}}{\text{Coulomb barrier height}} \tag{7.24}$$

Then substituting in the expressions from the preceding text:

$$\sigma = \frac{\ell(\ell + 1)\hbar^2}{2\mu R^2} \frac{R}{Z_\alpha Z_d} = \frac{\ell(\ell + 1)\hbar^2}{2\mu R Z_\alpha Z_d} \tag{7.25}$$

Then all we need to do is to replace all occurrences of B by $B(1 + \sigma)$ in the expression for the half-life. A simple pocket formula that results from such a substation is

$$\lambda_{\ell \neq 0} \approx \lambda_{\ell = 0} \exp[-2.027\ell(\ell + 1)Z^{-1/2}A^{-1/6}] \qquad (7.26)$$

This centrifugal barrier correction is a very small effect compared to the effect of Q_α or R upon the decay rate.

We should also note that conservation of angular momentum and parity during the α-decay process places some constraints on the daughter states that can be populated. Since the α-particle has no intrinsic spin, the total angular momentum of the emitted α-particle must equal its orbital angular momentum ℓ, and the α-particle parity must be $(-1)^\ell$. Since parity is conserved in α-decay, the final states are restricted. If the parent nucleus has $J\pi = 0^+$, then the allowed values of $J\pi$ of the daughter nucleus are $0^+(\ell = 0)$, $1^-(\ell = 1)$, $2^+(\ell = 2)$, etc. These rules only specify the required spin and parity of the state in the daughter, while the energy of the state is a separate quantity. Recall from Chapter 6 that the heaviest elements are strongly deformed and are good rotors. The low-lying excited states of even–even nuclei form a low-lying rotational band with spins of 2, 4, 6, etc., while odd angular momenta states tend to lie higher in energy. Because of the decrease in the energy of the emitted α-particle when populating these states, decay to these higher-lying states will be inhibited. Thus the lower available energy suppresses these decays more strongly than the centrifugal barrier.

Sample Problem 7.3: Angular Momentum in α Decay

^{241}Am is a long-lived α emitter that is used extensively as an ionization source in smoke detectors. The parent state has a spin and parity of $5/2^-$ and cannot decay to the $5/2^+$ ground state of ^{237}Np because that would violate parity conservation. Rather it decays primarily to a $5/2^-$ excited state (85.2%, $E^* = 59.5$ keV) and to a $7/2^-$ higher-lying excited state (12.8%, $E^* = 102.9$ keV). Estimate these branching ratios using the theoretical equations, and compare them to the observed values.

Solution

$$Q_\alpha(5/2^-) = 5.578 \text{ MeV} ; \qquad Q_\alpha(7/2^-) = 5.535 \text{ MeV}$$
$$f(5/2^-) = 2.24 \times 10^{21}/\text{s} ; \qquad f(7/2^-) = 2.24 \times 10^{21}/\text{s}$$
$$G(5/2^-) = 33.91 ; \qquad G(7/2^-) = 34.21$$
$$\lambda(5/2^-) = 7.9 \times 10^{-9}/\text{s} ; \qquad \lambda(7/2^-) = 4.3 \times 10^{-9}/\text{s}$$

Assuming that the branches to other states are small and do not contribute to the sum of the partial half-lives, we can write

$$\text{Branching ratio}(5/2^-) = \frac{\lambda(5/2^-)}{\lambda(5/2^-) + \lambda(7/2^-)} = 0.65$$

Note that the observed half-life of 433 years is again significantly longer than the predicted half-life of $\sim$3 years. This difference is attributed to the combined effects of the preformation factor and the hindrance effect of the odd proton in the americium parent ($Z = 95$), discussed in the following text.

7.4 Hindrance Factors

The one-body theory of α-decay applies strictly to e–e α emitters only. The odd nucleon α-emitters, especially in ground-state transitions, decay at a slower rate than that suggested by the simple one-body formulation as applied to e–e nuclei. Consider the data shown in Figure 7.9 showing the α-decay half-lives of the e–e and odd A uranium isotopes. The odd A nuclei have substantially longer half-lives than their e–e neighbors.

The decays of the odd A nuclei are referred to as "hindered decays," and the "hindrance factor" is defined as the ratio of the measured partial half-life for a given α-transition to the half-life that would be calculated from the simple one-body theory applied to e–e nuclides. In general, these hindrances for odd A nuclei may be divided into five classes:

1) If the hindrance factor is between 1 and 4, the transition is called a "favored" transition. In such decays, the emitted α particle is assembled from two low-lying pairs of nucleons in the parent nucleus, leaving the odd nucleon
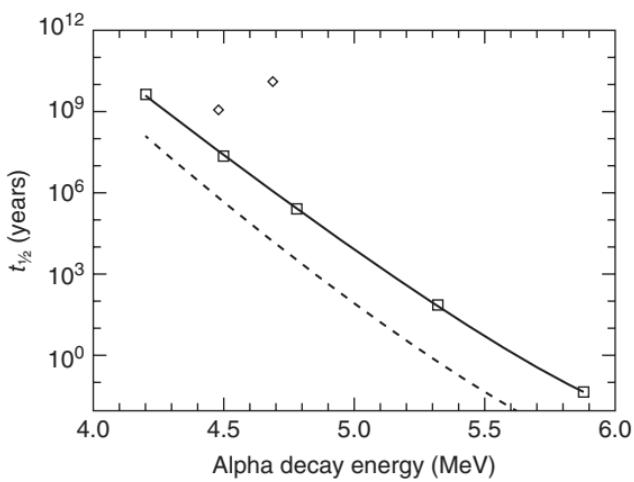
Figure 7.9 The α-decay half-lives of the e–e (squares) and odd A (circles) isotopes of uranium. The measured values are connected by the solid line; the estimates from the one-body theory of α decay is shown by the dashed line.

in its initial orbital. To form an α-particle within a nucleus, two protons and two neutrons must come together with their spins coupled to zero and with zero orbital angular momentum relative to the center of mass of the α-particle. These four nucleons are likely to come from the highest occupied levels of the nucleus. In odd A nuclei, because of the odd particle and the difficulty of getting a "partner" for it, one pair of nucleons is drawn from a lower-lying level, causing the daughter nucleus to be formed in an excited state.

2) A hindrance factor of 4–10 indicates a mixing or favorable overlap between the initial and final nuclear states involved in the transition.

3) Factors of 10–100 indicate that spin projections of the initial and final states are parallel, but the wave function overlap is not favorable.

4) Factors of 100–1000 indicate transitions with a change in parity but with projections of initial and final states being parallel.

5) Hindrance factors >1000 indicate that the transition involves a parity change and a spin flip, that is, the spin projections of the initial and final states are antiparallel, which requires substantial reorganization of the nucleon in the parent when the α-particle is emitted.

7.5 Heavy Particle Radioactivity

As an academic exercise one can calculate the Q values for the emission of heavier nuclei than α particles and show that it is energetically possible for a large range of heavy nuclei to emit other light nuclei. For example, contours of the Q values for carbon ion emission by a large range of nuclei are shown in Figure 7.10 calculated with the smooth liquid drop mass equation without shell corrections. Recall that the binding energy steadily decreases with increasing mass (above $A \sim 60$), and several light nuclei have large binding energies relative to their neighbors similar to the α particle. As can be seen in Figure 7.10, there are several nuclei with positive Q values for carbon ion emission. Such emission processes or heavy particle radioactivity have been called "heavy cluster emission."

We should also note that the double shell closures at $Z = 82$ and $N = 126$ lead to especially large positive Q values, as already shown in Figure 7.2. Thus, the emission of other heavy nuclei, particularly ^{12}C, has been predicted or at least anticipated for a long time. Notice also that ^{12}C is an even–even nucleus, and s-wave emission without a centrifugal barrier is possible. However, the Coulomb barrier will be significantly larger for higher Z nuclei than that for α particles.

We can use the simple theory of α decay to make an estimate of the relative branching ratios for α emission and ^{12}C emission from ^{220}Ra, a very favorable parent that leads to the doubly magic ^{208}Pb daughter. In this case we find
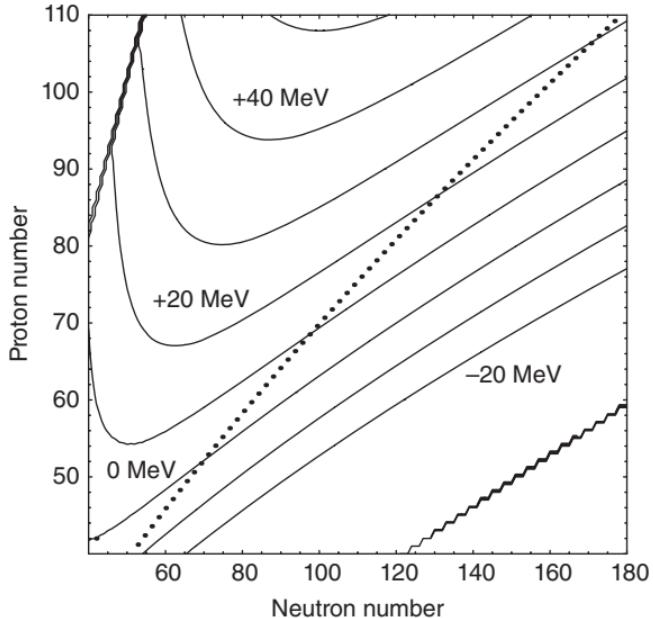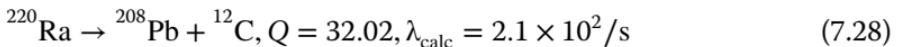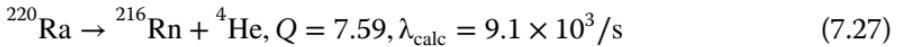
Figure 7.10 Contours of the *Q* value for the emission of a ^{12}C nucleus as a function of neutron and proton numbers calculated with the liquid drop model mass formula. The contour lines are separated by 10 MeV. The dotted curve indicates the line of β stability.

$Q_\alpha = 7.59$ MeV and $Q_C = 32.02$ MeV. Using the simple theory and ignoring differences in the preformation factor, the predicted half-life for ^{12}C emission is only longer than that for α emission by a factor of 40!

$$^{220}\text{Ra} \rightarrow {}^{216}\text{Rn} + {}^{4}\text{He}, Q = 7.59, \lambda_{\text{calc}} = 9.1 \times 10^3/\text{s} \tag{7.27}$$

$$^{220}\text{Ra} \rightarrow {}^{208}\text{Pb} + {}^{12}\text{C}, Q = 32.02, \lambda_{\text{calc}} = 2.1 \times 10^2/\text{s} \tag{7.28}$$

The encouraging results from simple calculations like this have spurred many searches for this form of radioactivity.

It was relatively recently that heavy cluster emission was observed at a level enormously lower than these estimates. Even so, an additional twist in the process was discovered when the radiation from a ^{223}Ra source was measured directly in a silicon surface barrier telescope. The emission of ^{14}C was observed at the rate of $\sim 10^{-9}$ times the α emission rate, and ^{12}C was not observed. Thus, the very large neutron excess of the heavy elements favors the emission of neutron-rich light products. The fact that the emission probability is so much smaller than the simple barrier penetration estimate can be attributed to the very small probability to "preform" a ^{14}C residue inside the heavy nucleus. This first observation has been confirmed in subsequent measurements with magnetic spectrographs. The more rare emission of other larger neutron-rich light nuclei have been reported in very sensitive studies with nuclear track detectors.

7.6 Proton Radioactivity

For very neutron-deficient (i.e., proton-rich) nuclei, the Q value for proton emission, Q_p, becomes positive. One estimate, based on the semiempirical mass equation, of the line that describes the locus of the nuclei where Q_p becomes positive for ground state decay is shown in Figure 7.11. This line is known as the proton drip line. Our ability to know the position of this line is a measure of our ability to describe the forces holding nuclei together. Nuclei to the right of the proton dripline in Figure 7.11 can decay by proton emission.

Proton decay should be a simple extension of α-decay with the same ideas of barrier penetration being involved. A simplification with proton decay relative to α-decay is that there should be no preformation factor for the proton. The situation is shown in Figure 7.12 for the case of the known proton emitter ^{151}Lu. One can see certain important features/complications from this case. The proton energies, even for the heavier nuclei, are low ($E_p \sim 1$–2 MeV). As a consequence, the barriers to be penetrated are quite thick ($R_{out} = 80$ fm), and one is particularly sensitive to the proton energy, angular momentum changes, etc.

The measurements of proton decay are challenging due to the low energies and short half-lives involved. Frequently there are interfering α-decays (Fig. 7.13). To produce nuclei near the proton dripline from nuclei near the valley of β-stability requires forming nuclei with high excitation energies that emit neutrons relative to protons and α-particles to move toward this proton dripline. This, along with difficulties in studying low-energy proton emitters, means that the known proton emitters are mostly in the medium to high mass

Figure 7.11 Locus of neutron and proton driplines as predicted by the liquid drop model.

Limits of nuclear stability
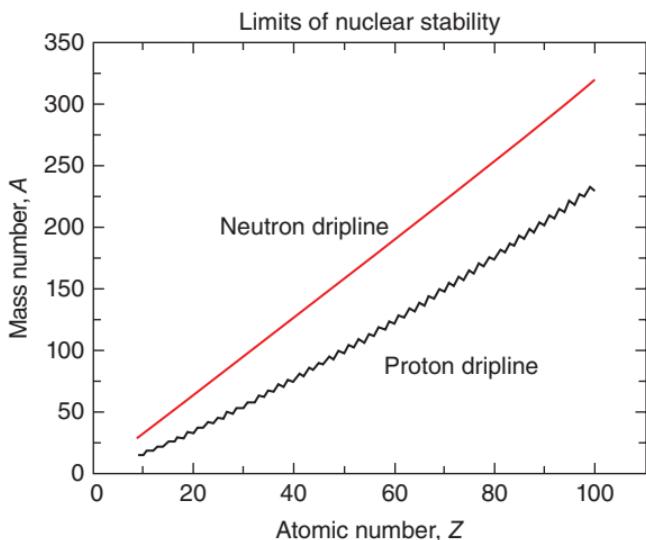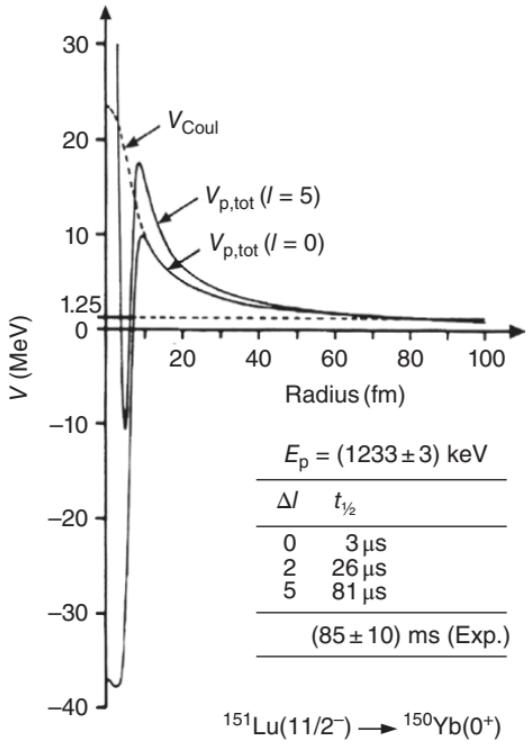
Figure 7.12 Proton–nucleus potential for the semiclassical calculation of the [151]Lu partial proton half-life (From Hofmann (1996), Copyright 1996 by IOP Publishing, reprinted by permission of IOP Publishing).

Within the figure:

V_{Coul}

$V_{p,tot}$ ($l = 5$)

$V_{p,tot}$ ($l = 0$)

V (MeV)

Radius (fm)

$E_p = (1233 \pm 3)$ keV

Δl	$t_{1/2}$
0	3 µs
2	26 µs
5	81 µs

(85 ± 10) ms (Exp.)

[151]Lu($11/2^-$) $\longrightarrow$ [150]Yb(0^+)

nuclei. Single proton decay occurs in odd Z nuclei beyond the proton dripline. About 40 cases of this decay mode, ranging from [109]I to [185]Bi, have been identified. Two proton decay has also been observed. Recent review articles by Hofmann (1996) and Pfutzner and Karny (2012) summarize the details of proton decay.

Problems

7.1 Using the conservation of momentum and energy, derive a relationship between Q_α and T_α.

7.2 All nuclei with $A > 210$ are α-emitters yet very few emit protons spontaneously. Yet both decays lower the Coulomb energy of the nucleus. Why isn't proton decay more common?

7.3 Use the Geiger–Nuttall rule to estimate the expected α-decay half-lives of the following nuclei: [148]Gd, [226]Ra, [238]U, [252]Cf, and [262]Sg.
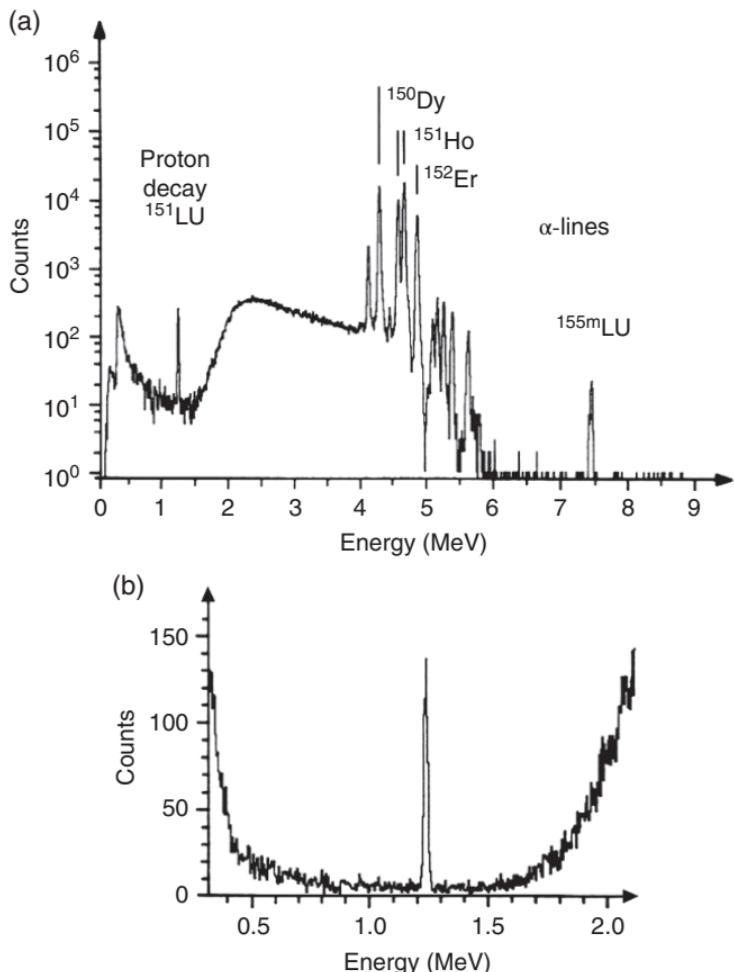
Figure 7.13 (a) Energy spectrum obtained during the irradiation of a ^{96}Ru target with 261 MeV ^{58}Ni projectiles. (b) Expanded part of the spectrum showing the proton line from ^{151}Lu decay (From Hofmann (1996), Copyright 1996 by IOP Publishing, reprinted by permission of IOP Publishing).

7.4 Use the one-body theory of α-decay to estimate the half-life of ^{224}Ra for decay by emission of a ^{14}C ion or a ^{4}He ion. The measured half-life for the ^{14}C decay mode is 10^{-9} relative to the ^{4}He decay mode. Estimate the relative preformation factors for the α-particle and ^{14}C nucleus in the parent nuclide.

7.5 ^{212}Po^{m} and ^{269}Ds both decay by the emission of high-energy α-particles ($E_{\alpha} = 11.6$ and 11.1 MeV, respectively). Calculate the expected lifetime of these nuclei using the one-body theory of α-decay. The observed

half-lives are 45.1 s and 170 μs, respectively. Comment on any difference between the observed and calculated half-lives.

7.6 What is the wavelength of an α-particle confined inside a ^{238}U nucleus?

7.7 ^{8}Be decays into two α-particles with $Q_\alpha = 0.094$ MeV. Calculate the expected half-life of ^{8}Be using one-body theory, and compare this estimate to the measured half-life of 2.6×10^{-7} s.

7.8 Calculate the kinetic energy and velocity of the recoiling daughter atom in the α-decay of ^{252}Cf.

7.9 Calculate the hindrance factor for the α-decay of ^{243}Bk to the ground state of ^{239}Am. The half-life of ^{243}Bk is 4.35 h, the decay is 99.994% EC and 0.006% α-decay. Further, only 0.0231% of the α-decays lead to the ground state of ^{239}Am. Q_α for the ground state decay is 6.874 MeV.

7.10 Calculate Q_α for gold. Why don't we see α-decay from gold nuclei?

7.11 The natural decay series starting with ^{232}Th has the sequence αββα. Show why this is the case by plotting the mass parabolas (or portions thereof for A = 232, 228, and 224).

7.12 Using the semiempirical mass equation, verify that Q_α becomes positive for $A \geq 150$.

7.13 Calculate the heights of the centrifugal barrier for the emission of α-particles carrying away two units of angular momentum in the decay of ^{244}Cm. Assume $R_0 = 1 \times 10^{-13}$ cm. What fraction of the Coulomb barrier height does this represent?

7.14 Use one-body theory to calculate the expected half-life for the proton decay of ^{185}Bi.

Bibliography

L. Valentin, *Subatomic Physics: Nuclei and Particles, Volume II* (North-Holland, Amsterdam, 1981).

Textbook discussions of α decay that are especially good:

R. Evans, *The Atomic Nucleus* (McGraw-Hill, New York, 1953), pp. 511–535.

K. Heyde, *Basic Ideas and Concepts in Nuclear Physics*, 3rd Edition (Taylor & Francis, London, 2004), pp. 82–103.

K.S. Krane, *Introductory Nuclear Physics* (John Wiley & Sons, Inc., New York, 1988), pp. 246–271.

W.E. Meyerhof, *Elements of Nuclear Physics* (McGraw-Hill, New York, 1967), pp. 135–145.

S.S.M. Wong, *Introductory Nuclear Physics*, 2nd Edition (John Wiley & Sons, Inc., New York, 1998).

More advanced discussion can be found in:

J.O. Rasmussen, "Alpha Decay," in *Alpha-, Beta-, and Gamma-Ray Spectroscopy*, K. Siegbahn, Ed. (North-Holland, Amsterdam, 1965) Chapter XI.

Proton decay is discussed in:

S. Hofmann, "Proton Radioactivity," in *Nuclear Decay Modes*, D.N. Poenaru, Ed. (IOP, Bristol, 1996).

M. Pfutzner, M. Karny, L.V. Grigorenko, and K. Riisager, Rev. Mod. Phys. **84**, 567 (2012).

8

β-Decay

8.1 Introduction

We have seen that many thousands of nuclei can be produced and studied in the lab. However, only <300 of these nuclei are stable; the rest are radioactive. We have also seen that the degree of instability grows with the "distance" a given nuclide is from the stable nuclide with the same mass number. In the previous chapter we considered the process of a decay in which heavy nuclei emit α particles to reduce their mass and move toward stability. The Coulomb barrier limits this process to those regions where the *Q* value provides sufficient energy to tunnel through the barrier. The vast majority of unstable nuclei lie in regions in which α− decay is not important and the nuclei undergo one or another form of β decay in order to become more stable. In a certain sense, the stable nuclei have a balance between the numbers of neutrons and protons. Nuclei are said to be unstable with respect to β decay when these numbers are "out of balance." In a very qualitative way, β decay "converts" a neutron into a proton (or vice versa) inside a nucleus, which becomes more stable while maintaining a constant mass number. The β decay process is more complicated than α emission, and we will provide an overview and a discussion of its basic features in this chapter.

β decay is named for the second most ionizing rays that were found to emanate from uranium samples. The naturally occurring β rays were identified as fast-moving (negative) electrons relatively easily, but it took many years to obtain a full understanding of the emission process. The difficulty lies in the fact that two particles are "created" during the decay as compared to the "disruption" of a heavy nucleus in α decay. In contrast to α decay, angular momentum plays a crucial role in understanding the β decay process. Let us consider the simplest form of β decay to illustrate the difficulties. The proton and the neutron are the two possible isobars for *A* = 1. We know that the neutron has a larger mass than the proton and is thus unstable with respect to the combination of a proton and an electron. A free neutron will undergo

β decay with a half-life of approximately 10.2 min. We might expect to write the decay equation as

$$\,^1_0\text{n} \rightarrow \,^1_1\text{p}^+ + \,^{\ 0}_{-1}\text{e}^- + Q_\beta \text{ (Incomplete Equation)} \tag{8.1}$$

However, all three particles in this equation are fermions with intrinsic spins $S = 1/2\hbar$. Therefore, we cannot balance the angular momentum in the reaction as written. The spins of the proton and the electron can be coupled to 0 or $1\hbar$ and can also have relative angular momenta with any integral value from the emission process. This simple spin algebra will never yield the half-integral value on the left-hand side of the equation. Another fermion must be present among the products.

Another feature of β decay that was puzzling at first but really pointed to the incompleteness of the previous equation is that the β rays have a continuous energy distribution. That is, electrons are emitted from a source with a distribution of energies that extends from a maximum at the Q value all the way down to zero. Recall that if there are only two products from a reaction, then they will precisely share the decay energy according to conservation of momentum. We have clearly seen such sharp energy spectra in α decay. (Note: the continuous energy distribution is not an instrumental artifact nor does it come from electron scattering.) Quite dramatic pictures of the tracks of charged particles from β decay show events in which the two ionizing particles do not move in exactly opposite directions also in clear violation of conservation of linear momentum. The way out of this mounting paradox with violations of very strongly held conservation laws is to recognize that another unseen particle must be created and emitted and introduce an additional conservation law. The conservation law is conservation of the number of "particles" in a reaction, and the unseen particle must be an antiparticle to cancel the creation of the electron particle. This new beast is called the neutrino, literally the little neutral one in Italian, because it had a small mass and is electrically neutral.

8.2 Neutrino Hypothesis

Enrico Fermi on his voyage to the new world postulated that a third particle was needed to balance the emission of the electron in β decay. However, the existing conservation laws also had to be satisfied, so there were a number of constraints on the properties of this new particle. Focusing on the decay of a neutron as the simplest example, the reaction is already balanced with respect to electric charge, so any additional particle must be neutral. The electrons were observed with energies up to the maximum allowed by the decay Q value, so the mass of the particle must be smaller than the instrumental uncertainties in these measurements. Initially this limit was <1 keV, but this value has been reduced to <10 eV in more recent work. Recent experiments have shown that

the neutrinos have mass (see Chapter 12). The third constraint on the neutrino from the decay is that it must be an "antiparticle" in order to cancel or compensate for the creation of the electron, a "particle." The fourth constraint is that the neutrino must have half-integral spin and be a fermion in order to couple the total final angular momentum to the initial spin of $1/2\hbar$.

Combining all of these constraints, we can now rewrite the previous equation properly as

$$\begin{matrix} 1 \\ 0 \end{matrix}\text{n} \rightarrow \begin{matrix} 1 \\ 1 \end{matrix}\text{p}^+ + \begin{matrix} 0 \\ 1 \end{matrix}\text{e}^- + \begin{matrix} 0 \\ 0 \end{matrix}\overline{\nu}_e + Q_\beta \tag{8.2}$$

where we have used the notation of placing a bar over the Greek character nu to indicate that the neutrino is an antiparticle and a subscript indicating the neutrino is an electron–neutrino (see Chapter 5). As indicated in Chapter 5, the existence of antiparticles and antimatter extends quite generally, and we can produce and observe the decays of antielectrons (usually called positrons), antiprotons, antineutrons, and so on and even combine positrons and antiprotons to make antihydrogen!

The spins of all of the final products in the neutron decay equation can be combined in two ways and still couple to the initial spin of the neutron. Focusing on the spins of the created particles, they can vector couple to $S_\beta = 1$ in a parallel alignment or to $S_\beta = 0$ in an antiparallel alignment. Both of these can combine with $S = 1/2$ of the proton for a resultant vector of $1/2$. The two possible relative alignments of the "created" spins are labeled as Fermi (F) ($S_\beta = 0$) and Gamow–Teller (GT) ($S_\beta = 1$) decay modes after the people that initially described the spin alignment in the decay mode. Both modes are often possible, and a radioactive source can produce a mixture of relative spins. However, in some cases, particularly the decay of even–even nuclei with $N = Z$ (the so-called mirror nuclei), the neutron and protons are in the same orbitals so that 0^+ to 0^+ decay can only take place by a Fermi transition. In heavy nuclei with protons and neutrons in very different orbitals (shells), the GT mode dominates. In complex nuclei, the rate of decay will depend on the overlap of the wave functions of the ground state of the parent and the state of the daughter. The final state in the daughter depends on the decay mode. Notice that in the example of neutron decay, the difference between the two modes is solely the orientation of the spin of the bare proton relative to the spins of the other products. The decay constant can be calculated if these wave functions are known. Alternatively, the observed rate gives some indication of the quantum mechanical overlap of the initial and final state wave functions.

The general form of β^- decay of a heavy parent nucleus, $^A Z$, can be written as

$$^A Z_N \rightarrow {}^A (Z+1)^+_{N-1} + \text{e}^- + \overline{\nu}_e + Q_{\beta^-} \tag{8.3}$$

where we have written out the charges on the products explicitly. Notice that the electron can be combined with the positive ion to create a neutral atom

(with the release of a relatively small atomic binding energy). This allows us to use the masses of the neutral atoms to calculate the Q value, again assuming that the mass of the antineutrino is very small. Thus,

$$Q_{\beta^-} = M[^A Z] - M[^A(Z+1)] \tag{8.4}$$

Up to this point we have concentrated on the β decay process in which a neutron is converted into a proton. There are a large number of unstable nuclei that have more protons in the nucleus than the stable isobar and so will decay in the opposite direction by converting a proton into a neutron. We can write an equation for β^+ decay that is exactly analogous to the previous equation:

$$^A Z_N \rightarrow \,^A(Z-1)^-_{N+1} + e^+ + \nu_e + Q_{\beta^+} \tag{8.5}$$

where we have replaced both the electron and the electron antineutrino with their respective antiparticles, the positron and the electron–neutrino. Note in this case, in contrast to β^- decay, the charge on the daughter ion is negative. This means that there is an extra electron present in the reaction compared with writing the reaction with a neutral daughter atom. Thus, the Q value must reflect this difference:
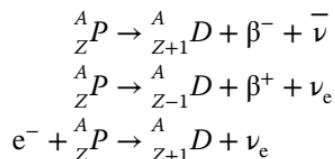
$$Q_{\beta^+} = M[^A Z] - \left(M[^A(Z-1)] + 2m_e c^2 \right) \tag{8.6}$$

where m_e is the electron mass. Recall that particles and antiparticles have identical masses. This equation shows that spontaneous β^+ decay requires that the mass difference between the parent and daughter atoms be $>2m_e c^2 = 1.022$ MeV. Nature takes this to be an undue restriction and has found an alternative process for the conversion of a proton into a neutron (in an atomic nucleus). The process is the capture of an orbital electron by a proton in the nucleus. This process, called electron capture is particularly important for heavy nuclei. The reaction is written as

$$^A Z_N \rightarrow \,^A(Z-1)_{N+1} + \nu_e + Q_{EC} \tag{8.7}$$

where all of the electrons are implicitly understood to be present on the atoms. This process also has the property that the final state has only two products, so conservation of momentum will cause the neutrino to be emitted with a precise energy depending on the binding energy of the captured electron and the final state of the daughter nucleus.

To summarize, there are three types of decay, all known as β decay. They are

$$^A_Z P \rightarrow \,^A_{Z+1} D + \beta^- + \bar{\nu}$$
$$^A_Z P \rightarrow \,^A_{Z-1} D + \beta^+ + \nu_e$$
$$e^- + \,^A_Z P \rightarrow \,^A_{Z+1} D + \nu_e$$

indicating β^- decay of neutron-rich nuclei, β^+ decay of proton-rich nuclei, and the electron capture decay of proton-rich nuclei, respectively. Neglecting the electron binding energies in computing the decay energetics, we have

$$Q_{\beta^-} = (M_P - M_D)c^2$$
$$Q_{\beta^+} = (M_P - M_D)c^2 - 2m_e c^2$$
$$Q_{EC} = (M_P - M_D)c^2$$

where M is the atomic mass of the nuclide involved and m_e is the electron mass. Typical values of Q_{β^-} are ~0.5–2 MeV, Q_{β^+} ~2–4 MeV, and Q_{EC} ~0.2–2 MeV.

As a final point in the general discussion of β decay, it is interesting to note that the analogous process of positron capture by neutron-excessive nuclei should be possible in principle. However, such captures are hindered by two important facts: first, the number of positrons available for capture is vanishingly small in nature, and second, both the nucleus and the positron are positively charged and will repel one another. Compare this to the situation for electron capture in which the nucleus is surrounded by (negative) electrons that are attracted to the nucleus, of course, and the most probable position to find the electrons in an "s" atomic orbital is at the nucleus ($r = 0$).

Sample Problem 8.1: Equation Balancing

Write the balanced equation for positron capture on the β unstable nucleus, ^{24}Na. Calculate the Q value for this process.

Solution

On the left-hand side of the equation, we assume that we have a ^{24}Na nuclide (with 11 electrons) and a single positron, which is an antilepton. The conservation rules imply that the mass number of the product will be 24, the atomic number will be $Z = 11 + 1$, the 11 electrons will carry over, and an antilepton has to be created to conserve lepton number. Thus,

$$^{24}\text{Na} + \text{e}^+ \rightarrow {}^{24}\text{Mg}^+ + \overline{\nu} + Q_{PC}$$

We must be careful about the numbers of electrons on both sides of the equation when we calculate the Q value. If we use mass excesses rather than the masses and assume a zero mass neutrino, then

$$Q_{PC} = \left(\Delta(^{24}\text{Na}) + m_e c^2 \right) - \left(\Delta(^{24}\text{Mg}) - m_e c^2 \right)$$

or, rearranging,

$$Q_{PC} = \left(\Delta(^{24}\text{Na}) + 2m_e c^2 \right) - \Delta(^{24}\text{Mg})$$
$$Q_{PC} = (-8.417 + 1.022) - (-13.933) = +4.494 \, \text{MeV}$$

8.3 Derivation of the Spectral Shape

β decay is clearly a process that follows first-order kinetics, and the rate of decay should be described by a single decay constant. Experimentally, β decay has been observed with a huge range of half-lives, from a few milliseconds (and no shorter) to $\sim 10^{16}$ years. This large range is reminiscent of the range of half-lives for α decay, and we should expect that the nuclear structure of the parent, the ground state, and the available daughter states will play important roles in determining the half-life. We should also recognize that the calculation of the rate will require a full quantum mechanical approach because the decay process involves the creation of two particles and the kinetic energy spectrum is continuous for the relativistic electron because $Q_\beta \sim m_e c^2$.

Enrico Fermi developed a quantum mechanical theory of β decay building on the foundation of the theory for the spontaneous emission of photons by atomic and molecular systems in excited states. At first blush these may seem unrelated, but in both cases a system in a very well-defined single quantum mechanical state that has excess energy releases the energy spontaneously by the creation of a particle (or particles). The decay constant for the emission of a photon was shown in the appendix to be given by the general expression:

$$\lambda = \frac{2\pi}{\hbar} |\int \Psi_{\text{final}}^* V_p \Psi_{\text{initial}} \, d\tau|^2 \rho(E_f) \tag{8.8}$$

which is also called Fermi's golden rule. The wave functions, Ψ, represent the complete initial and final states of the entire system, and V_p is a (very) small perturbative interaction that stimulates the transition. The form and the strength of the perturbation will have to be determined. Fermi assumed that the interaction responsible for β decay is different from the gravitational, Coulomb, and nuclear forces. This interaction between the nucleons, electron, and neutrino is called the weak interaction, and a new constant expressing its strength, like $e^2/4\pi\epsilon_0$ and G, had to be defined. This constant, g, has the numerical value of 0.88×10^{-4} MeV/fm^3, which is $\sim 10^{-3}$ of the electromagnetic force constant. The last factor, $\rho(E_f)$, is the density of quantum mechanical states that are available to the system after the transition and is often written as dn/dE where n is the number of states per unit energy interval. In this case the final energy is the decay Q value. The initial wave function contains only the parent nucleus, whereas the final wave function will have contributions for all of the resultant particles. Specifically for β decay $\Psi_{\text{initial}} = \phi_{\text{gs}}(^A Z)$, the complete wave function for the parent in its ground state. The final wave function will have three parts, $\Psi_{\text{final}}^* = \phi_j^*(^A Z)\phi^*(e)\phi^*(\nu)$, with a part for the daughter nucleus in the appropriate final state j, a part for the traveling wave of the electron, and a part for the corresponding traveling wave of the neutrino, all of which must be coupled so that energy and angular momentum is conserved.

The quantum mechanical problem can be separated into two parts, the determination of $\rho(E_f)$ and the matrix element $|\int \phi_{\text{final}}^* V_p \phi_{\text{initial}} d\tau|^2$, to make the calculation tractable. The determination of the density of final states, dn/dE, is done using quantum statistical mechanics. It is basically the problem of counting the number of ways the decay energy can be divided between the electron and the neutrino, neglecting, for the moment, the recoiling daughter nucleus. Classically, the number of states of a free electron with momentum between p_e and $p_e + dp_e$ in a volume V is $\frac{V4\pi p_e^2 dp_e}{h^3}$. (This is the volume of a spherical shell in phase space where the volume of a unit cell is h^3.) Similarly for the neutrino, the number of states of the free neutrino with momentum between $p\nu$ and $p_\nu + dp_\nu$ in a volume V is $\frac{V4\pi p_\nu^2 dp_\nu}{h^3}$. The total number of states is the product of these two factors:

$$dn = \frac{16\pi^2 V^2 p_e^2 p_\nu^2 dp_e dp_\nu}{h^6} \tag{8.9}$$

If we assume the neutrino has zero rest mass, then

$$p_\nu = \frac{T_\nu}{c} = \frac{Q - T_e}{c} \tag{8.10}$$

$$dp_\nu = \frac{dQ}{c} \tag{8.11}$$

substituting back, we get

$$dn = \frac{16\pi^2 V^2}{h^6 c^3} \left(Q - T_e\right) p_e^2 dp_e dQ \tag{8.12}$$

$$\frac{dn}{dQ} = \frac{16\pi^2 V^2}{h^6 c^3} \left(Q - T_e\right) p_e^2 dp_e \tag{8.13}$$

(One must understand this equation expresses the variation of the number of final states with changes in the Q value of the decay and does not represent differentiation with respect to a constant Q.) The electron and neutrino wave functions can be written as radial plane waves

$$\phi_e(r) = Ae^{ik_e r} = \frac{1}{\sqrt{V}} e^{ik_e r} \tag{8.14}$$

$$\phi_\nu(r) = Be^{ik_\nu r} = \frac{1}{\sqrt{V}} e^{ik_\nu r} \tag{8.15}$$

where we have to apply a normalization condition to determine the constants A and B. We can expand the exponentials around $r \sim 0$ (the nuclear volume) as

$$e^{ikr} = 1 + ikr + \cdots \approx 1 \tag{8.16}$$

$$\phi(r \sim 0) \approx \frac{1}{V} \tag{8.17}$$

The probability of emitting an electron with a momentum p_e between p_e and dp_e becomes

$$\lambda(p_e)dp_e = \frac{1}{2\pi^3 \hbar^7 c^3} |M_{fi}|^2 g^2 (Q - T_e)^2 p_e^2 dp_e \tag{8.18}$$

where $|M_{fi}|$ is a nuclear matrix element representing the overlap between the initial and final nuclear states. This matrix element must be evaluated with the detailed nuclear wave functions, for example, those available from the shell model.

Collecting all constants for a given decay, the probability of a decay as a function of the electron momentum is

$$\lambda(p_e)dp_e = (\text{constants})(Q - T_e)^2 p_e^2 dp_e \tag{8.19}$$

This form (even though it is mixed with a momentum part and an energy part for the electron) clearly goes to zero at $p_e = 0$ and also at $T_e = Q$ and has a maximum in between. The shape of this function is shown in Figure 8.1. This function is often called the statistical or phase space factor for the decay.
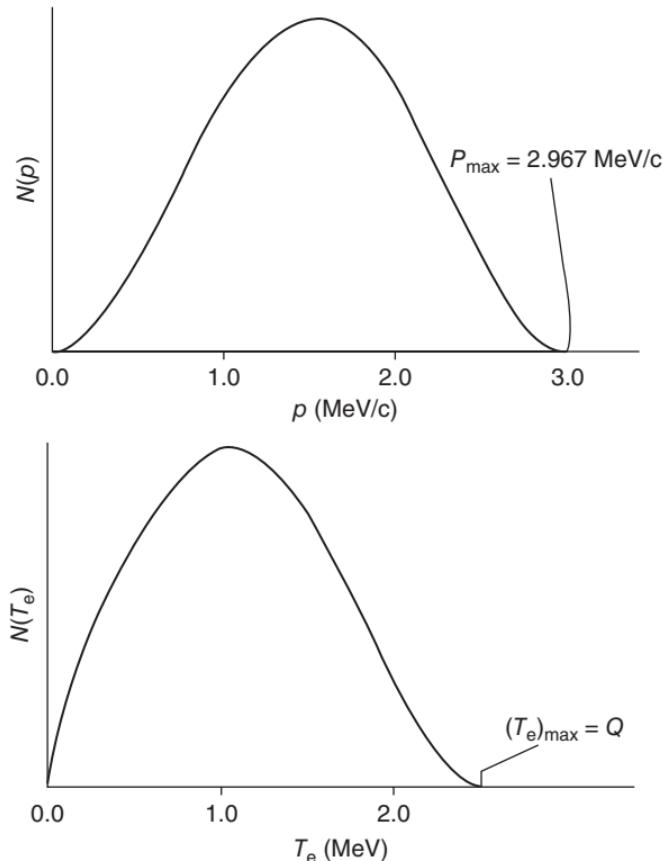
We should be sure to note that we have made a big approximation in ignoring the charge on the emitted electron. Positively charged β particles (positrons) will be repelled by the nucleus and shifted to higher energies, while negatively charged β particles (electrons) will be attracted and slowed down. These effects were incorporated by Fermi by using Coulomb-distorted wave functions and are contained in a spectrum distortion expression called the Fermi function, $F(Z_d, p_e)$, where Z_d is the atomic number of the daughter nucleus. The more accurate β spectrum thus has the form

$$\lambda(p_e)dp_e = (\text{constants})F(Z_d, p_e)(Q - T_e)^2 p_e^2 dp_e \tag{8.20}$$

The effects of the Coulomb distortion can be seen in the measured spectra from the decay of ^{64}Cu shown in Figure 8.2. This odd–odd nucleus undergoes both β$^-$ and β$^+$ decay to its even–even neighbors with very similar Q values, thus providing a relatively clear indication of the distortion. The restriction that the neutrino rest mass is zero can be removed and provides the slightly more complicated expression (Heyde, 2005):

$$\lambda(p_e)dp_e = \frac{|M_{fi}|^2}{2\pi^3 \hbar^7 c^3} F(Z_d, p_e)(Q - T_e)^2 \left(1 - \frac{m_\nu^2 c^4}{(Q - T_e)^2}\right)^{1/2} p_e^2 dp_e \tag{8.21}$$

Figure 8.1 The shape of the statistical factor for β decay, which represents the expected shape of the electron momentum distribution (top) and the kinetic energy distribution (bottom) before distortion by the Coulomb potential.

$P_{max} = 2.967$ MeV/c

$(T_e)_{max} = Q$

8.4 Kurie Plots

We have seen that the β spectrum has an endpoint at the Q value, but the form of equation for the spectrum does not allow us to easily identify the endpoint because it slowly drops toward zero. Notice that with a little rearrangement, this spectrum can be represented as

$$\left(\frac{\lambda(p_e)}{p_e^2 F(Z_d, p_e)} \right)^{1/2} \propto (Q - T_e)|M_{fi}|^2 \tag{8.22}$$

If the nuclear matrix element does not depend on the electron kinetic energy, as we have assumed so far, then a plot of the reduced spectral intensity, the left-hand side, versus the electron kinetic energy will be a straight line that intercepts the abscissa at the Q value. Such a graph is called a Kurie plot and an example is shown in Figure 8.3. This procedure applies to allowed transitions (see following text). There are correction terms that need to be taken into account for forbidden transitions.
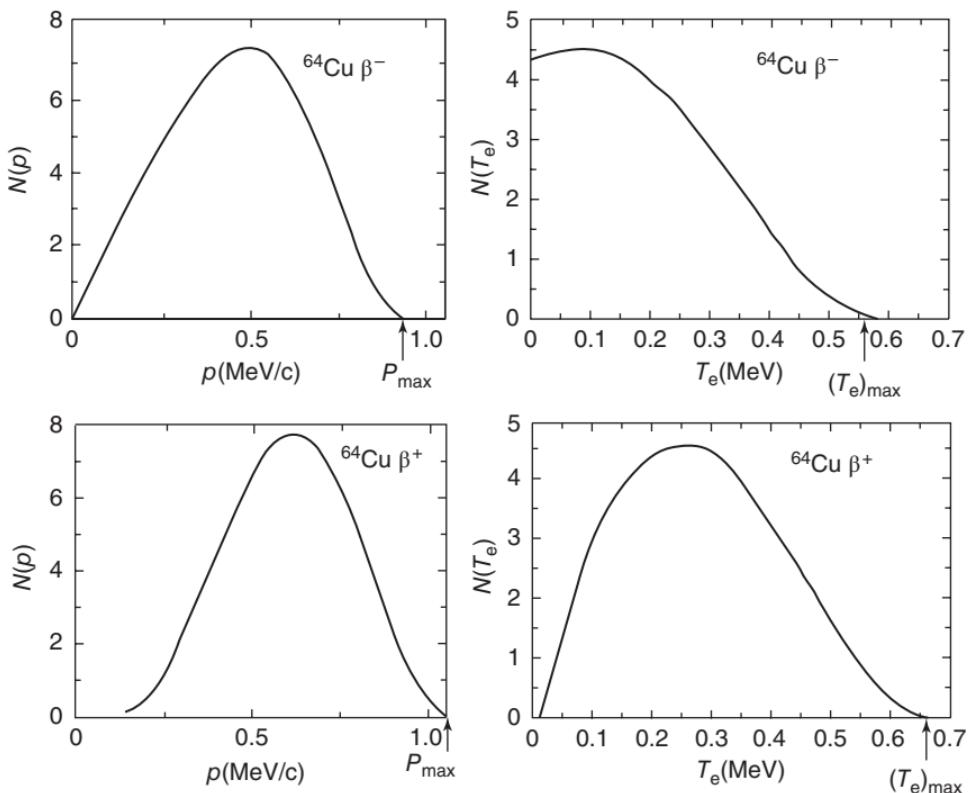
Figure 8.2 The momentum and kinetic energy (left and right) spectra from the decay of ^{64}Cu for β^- and β^+ decay (top and bottom, respectively). The Q values for these decays are 0.5782 and 0.6529 MeV, respectively.
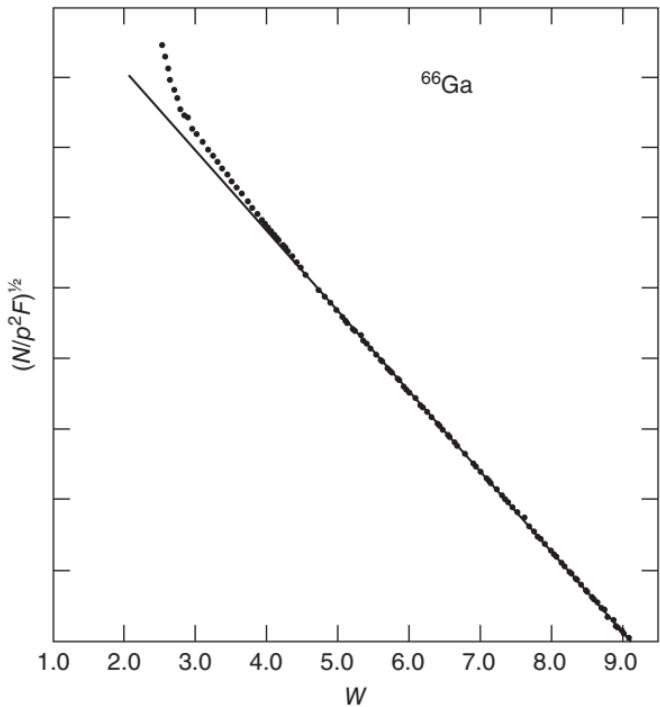
8.5 β Decay Rate Constant

The differential form of the β decay spectrum can be integrated over all electron momenta to obtain the total decay constant. The expression, for a constant nuclear matrix element, to be integrated is

$$\lambda = \frac{g^2 |M_{fi}|^2}{2\pi^3 \hbar^7 c^3} \int_0^{p_{max}} F(Z_d, p_e) p_e^2 (Q - T_e)^2 dp_e \tag{8.23}$$

Note that an appropriate relativistic substitution for T_e in terms of the momentum is still needed. This integral has been shown to only depend on the atomic number of the daughter and the maximum electron momentum. The integral, called the Fermi integral, $f(Z_d, Q)$, as distinct from the Fermi function, F, is complicated, but numerical expressions or tables of the solutions are available. Note that the differential Fermi function, $F(Z_d, p_e)$, contains the momentum,

Figure 8.3 An example of a Kurie plot (Camp and Langer (1963). Reproduced with the permission of American Physical Society).

whereas the Fermi integral, $f(Z_d, Q)$, contains the Q value. The Fermi integral is a constant for a given β decay and has been presented in many forms. For example, curves of the Fermi function are shown in the nomograph in Figure 8.4.

The decay constant is now reduced to an expression with the nuclear matrix element, here written simply as $M \ (\equiv |M_{fi}|)$, and the strength parameter, g, written as

$$\lambda = \frac{g^2 M^2}{2\pi^3 \hbar^7 c^3} f(Z_d, Q) \tag{8.24}$$
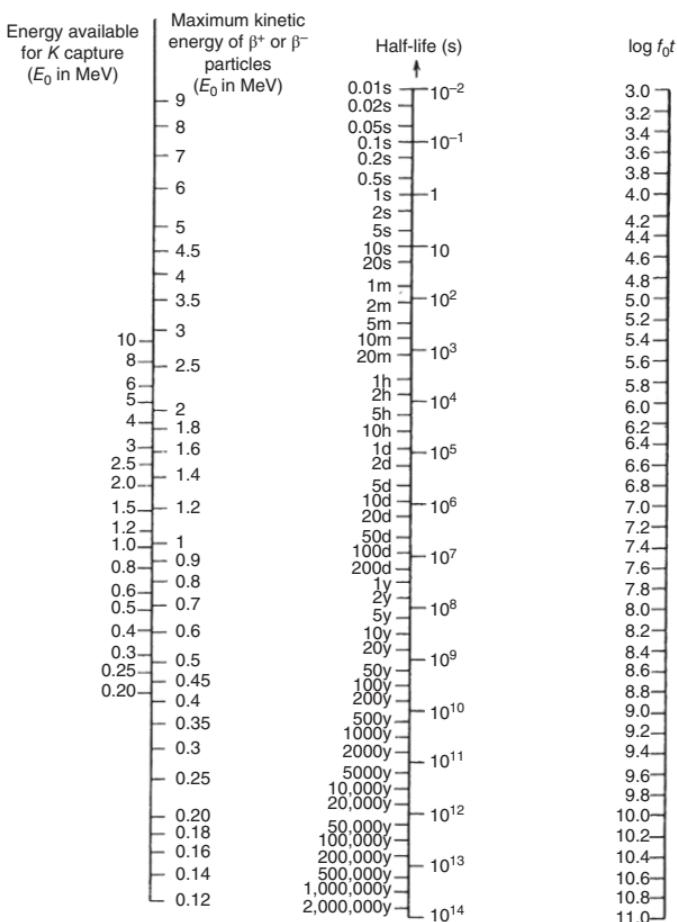
or in terms of the half-life of the parent, $t_{1/2}$:

$$ft_{1/2} = \ln 2 \frac{2\pi^3 \hbar^7 c^3}{g^2 |M|^2 m_e^5 c^4} \propto \frac{1}{g^2 |M|^2} \tag{8.25}$$
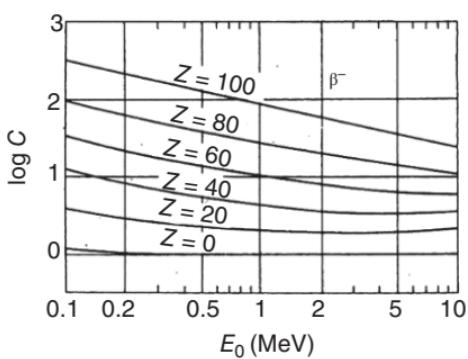
The left-hand side of this equation is called the comparative half-life, or "ft value," because this value can be readily measured in experiments and should only depend on the nuclear matrix element and the β decay strength constant. Recall that β decay half-lives span many orders of magnitude so the ft values will span a similarly large range. It is therefore convenient to use the common logarithm of the ft value (with $t_{1/2}$ in seconds) to characterize observed β decays.

Values of $\log(ft)$ may be calculated from the nomograph and curves in Figure 8.4, which are due to Moszkowski (1951). Log(ft) values can be calculated for β−, β+, and EC decay. These ft values roughly fall into groups, which
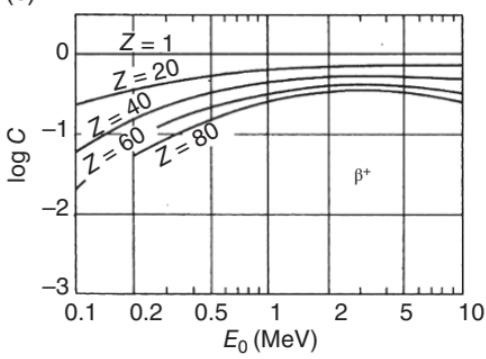
Figure 8.4 Nomograph for the rapid determination of $\log_{10}(ft)$ values. This figure provides information for the rapid calculation of $\log_{10}(ft)$ for a given type of decay, given energy, branching ratio, and so on. Notation: E_0 for $\beta\pm$ emission is the maximum kinetic energy of the particles in MeV; E_0 for K electron capture is the Q value in MeV. When a β^+ emission and
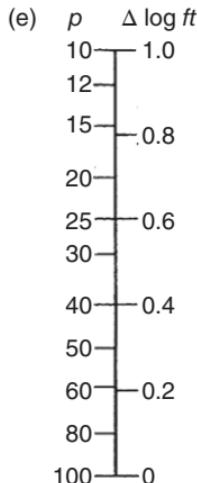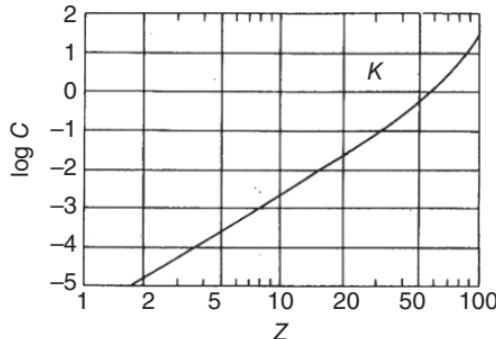
Figure 8.4 *(Continued)* K electron capture go from and to the same level, E_0 for the K capture = E_0 for β^+ emission plus 1.022 MeV. Z is the atomic number of the parent, t is the total half-life, and p is the percentage of decay occurring in the mode under consideration. When no branching occurs, p = 100. To obtain $\log_{10}(ft)$, find $\log(f_0 t)$ using part (a). Read off $\log(C)$ from parts (b), (c), and (d) for β^-, β^+, and K_{EC}, respectively. Get $\Delta \log(ft)$ from part (e) if p < 100. For p = 100, $\Delta \log(ft) = 0$. Finally, $\log(ft) = \log(f_0 t) + \log(C) + \Delta \log(ft)$. Moszkowski (1951). Reproduced with the permission of American Physical Society.

can be correlated with the spin and parity change in the decay (see following text) and can, then, be used to assign spins and parities in nuclei whose structure is not known. However, there is significant overlap between the *ft* groups, and caution must be exercised in using the ft values to characterize transitions.

Sample Problem 8.2: Log ft Values

Using the graph of the Fermi integral in Figure 8.4, estimate the $\log(ft)$ value for the decay of ^{32}P ($t_{1/2} = 14.28$ days).

Solution

This is a neutron-rich nucleus and undergoes β^- decay, thus
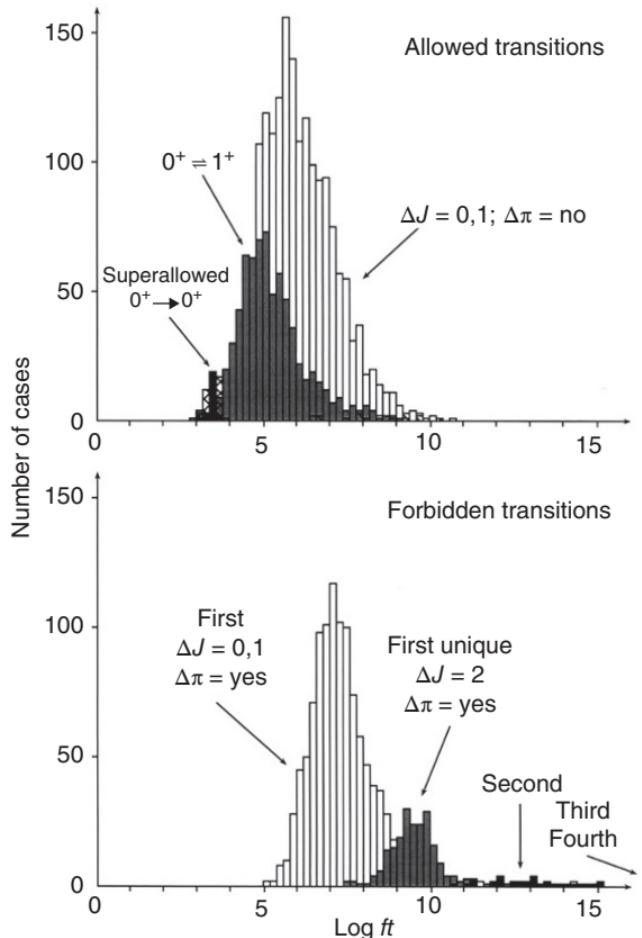
$$Q_{\beta^-} = M(^{32}P) - M(^{32}S) = \Delta(^{32}P) - \Delta(^{32}S)$$
$$Q_{\beta^-} = (-24.305) - (26.015)\ \text{MeV} = +1.710\ \text{MeV}$$

From the figure with $Z = 15$, $Q = 1.710$ MeV, $\log(ft) = \log(f_0 t) + \log(C) = 7.8 + 0.2 = 8.0$.

The creation of relative angular momentum in β decay is even more difficult than that in α decay due to the lighter masses of ejecta and causes more severe

Figure 8.5 Summary of the experimental values of log(*ft*). The shading indicates the transition type (Singh et al. (1998). Reproduced with the permission of Elsevier.)

"hindrance" for each unit of relative angular momentum. The difficulty is easy to see with a simple calculation. We can write the relative angular momentum for two bodies as the cross product $L = r \times p$ where r is the radius of emission and p is the momentum. Taking a typical nuclear radius of 5 fm and a typical β decay energy of 1 MeV, we find the maximum of the cross product to be $L = 5$ fm $\times$ $(1.4 \text{ MeV/c}) = 7.90$ MeV-fm/c or $L = 0.035\hbar$ units. Log(*ft*) values increase by an average of 3.5 units for each unit of orbital angular momentum, also called the "degree of forbiddenness." Each unit of angular momentum, that is, each degree of forbiddenness, leads to an increase in the lifetime (or a hindrance) of $\sim 3 \times 10^{-4}$. There is a large spread in the values, however, due to the strong effect of the nuclear overlap on each decay. The overall variation of log(*ft*) in β decay is shown in Figure 8.5.

The quantum mechanical selection rules for β decay with no relative angular momentum in the exit channel ($\ell = 0$) are $\Delta I = 0, 1$ and $\Delta \pi = 0$. The two

Table 8.1 Representative Allowed β Decays.

Parent	Daughter	Half-Life (s)	Q_β (MeV)	Log(ft)	Character
^{1}n ($1/2^+$)	^{1}p ($1/2^+$, gs)	612	0.7824	−0.27	Mixed
^{6}He (0^+)	^{6}Li (1^+, gs)	0.808	3.5097	2.42	Gamow–Teller
^{14}O (0^+)	^{14}N (0^+, 2.313)	71.1	1.180	2.81	Fermi
^{14}O (0^+)	^{14}N (1^+, gs)	1.16×10^4	4.123	7.36	Gamow–Teller

values for the spin change come directly from the two possible couplings of the spins of the electron and neutrino as discussed previously. Some representative "allowed" β decays are described in Table 8.1 along with their log(ft) values and the character of the decay.

The decay of ^{14}O to the 0^+ excited state of ^{14}N can only take place by a Fermi decay where the created spins couple to zero. This parent nucleus also has a weak branch to the 1^+ ground state that takes place by a Gamow–Teller transition. In contrast, the decay of ^{6}He to the ground state of ^{6}Li must take place by a Gamow–Teller transition in order to couple the total resultant angular momentum to zero.

As mentioned earlier, the decay of the neutron into a proton can take place with no change in angular momentum between the spin 1/2 particles. (The angular momentum coupling rules allow both decay modes.) The decay of the neutron into the proton is an important example of decay between mirror nuclei. In the β decay of mirror nuclei, the transformed nucleons (neutron → proton or proton → neutron) must be in the same shell and have very similar wave functions. This gives rise to a large matrix element $|M_{fi}|^2$ and a very small log(ft) value. For the β decay of mirror nuclei to their partners, log(ft) values are about 3, which is unusually small. Such transitions are called "super-allowed" transitions.

When the initial and final states in β decay have opposite parities, decay by an "allowed" transition cannot occur. However such decays can occur, albeit with reduced probability compared with the "allowed" transition. Such transitions are called "forbidden" transitions even though they do occur. The forbidden transitions can be classified by the spin and parity changes (and the corresponding observed values of log(ft)) as in Table 8.2. Remember that in β decay

$$\vec{J}_P = \vec{J}_D + \vec{L}_\beta + \vec{S}_{\beta\nu} \tag{8.26}$$

$$\pi_P = \pi_D(-1)^{L_\beta} \tag{8.27}$$

where the subscripts P and D refer to the parent and daughter, L_β is the orbital angular momentum carried away by the emitted electron, and $S_{\beta\nu}$ is the coupled

Table 8.2 Classification of β Decay Transitions.

Transition Type	Log(ft)	L_β	$\Delta\pi$	Fermi ΔJ	Gamow–Teller ΔJ
Super-allowed	2.9–3.7	0	No	0	0
Allowed	4.4–6.0	0	No	0	0,1
First forbidden	6–10	1	Yes	0,1	0, 1, 2
Second forbidden	10–13	2	No	1,2	1, 2, 3
Third forbidden	>15	3	Yes	2, 3	2, 3, 4

spin of the electron–neutrino pair ($S_{\beta\nu} = 0$ for a Fermi transition and $S_{\beta\nu} = 1$ for a Gamow–Teller transition).

8.6 Electron Capture Decay

When the decay energy is <1.022 MeV ($2m_e c^2$) but larger than 0, the β decay of a proton-rich nucleus to its daughter must take place by electron capture (EC). For decay energies >1.022 MeV, EC, and β^+ decay compete. In EC decay, only one particle, the neutrino, is emitted from the nucleus with a kinetic energy $(M_P - M_d)c^2 - B_e$ where B_e is the atomic binding energy of the captured electron. The decay constant for electron capture can be written, again assuming a zero neutrino rest mass, as

$$\lambda_{EC} = \frac{g^2 |M_{fi}|^2 T_\nu^2}{2\pi^2 \hbar^3 c^3} |\phi_K(0)|^2 \tag{8.28}$$

where we have assumed that the capture of an atomic 1s (or K) electron will occur because the electron density at the nucleus is the greatest for the K electrons. The K electron wave function in this expression can be written as

$$\phi_K(0) = \frac{1}{\sqrt{\pi}} \left(\frac{Z m_e e^2}{4\pi\epsilon_0 \hbar^2} \right)^{3/2} \tag{8.29}$$

Thus, on substitution

$$\lambda_{K-EC} = \frac{g^2 Z^3 |M_{fi}|^2 T_\nu^2}{\text{constants}} \tag{8.30}$$

Comparison of the decay constants for EC and β^+ decay leads to the ratio

$$\frac{\lambda_{K-EC}}{\lambda_{\beta^+}} = \text{constants} \frac{Z^3 T_\nu^2}{f(Z_d, Q)} \tag{8.31}$$

Thus EC decay is favored for high-Z nuclei. Of course, the decay energy must be >1.022 MeV for β^+ decay to even occur, a situation found mostly in low-Z

nuclei where the slope of the wall of the valley of β stability is large (see Fig. 2.8) and decay energies >1.022 MeV are common. Note that electron capture decay produces a vacancy in the atomic electron configuration and secondary processes that lead to filling that vacancy by the emission of X-rays and Auger electrons occur. These X-rays permit the detection of EC decay to the ground state of the daughter that would otherwise be difficult to detect.

8.7 Parity Nonconservation

In Chapter 1, we introduced the concept of parity as a measure of the response of the wave function to an operation in which the signs of the spatial coordinates were reversed. As we indicated in our discussion of α decay, parity conservation provides an important selection rule for α decay. Emission of an α particle of orbital angular momentum ℓ carries a parity change $(-1)^\ell$ so that $1^+ \rightarrow 0^+$ or $2^- \rightarrow 0^+$ α decays are forbidden. In general, we find that parity is conserved in strong and electromagnetic interactions.

In the late 1950s, it was found (Wu et al., 1957) that parity was not conserved in weak interaction processes such as nuclear β decay. Wu et al. (1957) measured the spatial distribution of the β^- particles emitted in the decay of a set of polarized ^{60}Co nuclei (see Fig. 8.6). When the nuclei decay, the intensities of electrons emitted in two directions, I_1 and I_2, were measured. As shown in Figure 8.6, application of the parity operator will not change the direction of
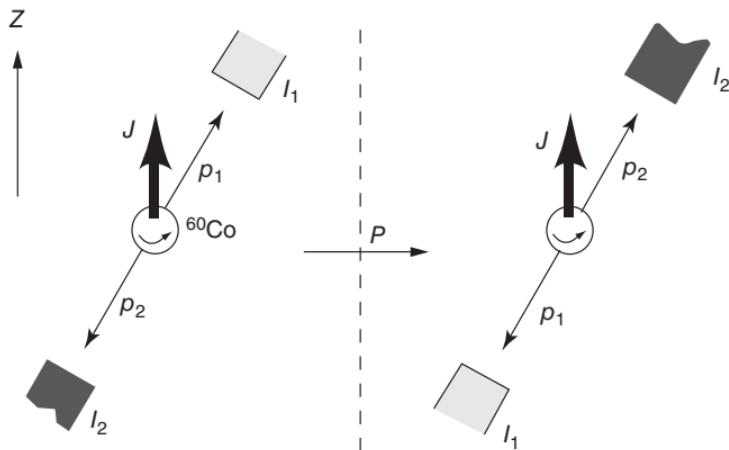
Figure 8.6 Schematic diagram of the Wu et al. (1957) apparatus. A polarized nucleus emits electrons with momenta p_1 and p_2 that are detected with intensities I_1 and I_2. The left figure shows the "normal" situation, while the right figure shows what would be expected after applying the parity operator. Parity conservation implies the two situations cannot be distinguished experimentally (which was not the case) (Frauenfelder and Henley (1991). Reproduced with the permission of Pearson Prentice-Hall).

the nuclear spins but will reverse the electron momenta and intensities, I_1 and I_2. If parity is conserved, we should not be able to tell the difference between the "normal" and "parity reversed" situations, that is, $I_1 = I_2$. However, Wu et al. (1957) found that $I_1 \neq I_2$, that is, the β-particles were preferentially emitted along the direction opposite to the spin of the ^{60}Co nucleus. (God is "left handed.")

8.8 Neutrinos Again

A number of studies have been undertaken of the interaction of neutrinos with nuclei, to determine the neutrino mass and to show that neutrinos and antineutrinos are produced in β⁺ and β⁻ decay, respectively. Neutrinos also provide important information about stellar nuclear reactions because they have a very low probability for interacting with matter and come directly out from the stellar interior. Starting with the simple equation for the β⁻ decay of the neutron and the β⁺ decay of the proton, we can write two closely related reactions that are induced by neutrinos:

$$\overline{\nu}_e + p^+ \rightarrow n + e^+ \tag{8.32}$$

$$\nu_e + n \rightarrow p^+ + e^- \tag{8.33}$$

These reactions, called inverse β decay, were obtained by adding the antiparticle of the electron in the normal β decay equation to both sides of the reaction. When we did this we also canceled (or annihilated) the antiparticle/particle pair. Notice that other neutrino-induced reactions such as $\overline{\nu}_e + n \rightarrow p^+ + e^-$ would not conserve lepton number because an antilepton, $\overline{\nu}_e$, is converted into a lepton, e^-. Proving that this reaction does not take place, for example, provides evidence that there is a difference between neutrinos and antineutrinos. One difficulty with studying these reactions is that the cross sections are extremely small, on the order of 10^{-19} barns, compared with typical nuclear reaction cross sections, on the order of 1 barn (recall 1 barn = 10^{-24}cm²).

The combination of two studies of inverse β decay clearly showed that the neutrinos emitted in β⁻ and β⁺ decay were different. Both used nuclear reactors to provide strong sources of antineutrinos. Recall that nuclear fission produces very neutron-rich products that undergo a series of rapid β decays emitting antineutrinos. In the first experiment, performed by Reines and Cowan (1953), a large volume of liquid scintillator was irradiated, and protons in the organic solution were reacted into a neutron and a positron. The positron rapidly annihilated with an electron in the liquid providing the first signal of an interaction. The neutron was captured within a few microseconds by Cd nuclei that were added to the

scintillator and provided a second correlated signal. The flux of neutrinos from the reactor was sufficient to produce a few events per hour in a 1 m^3 volume of scintillator.

In the second study, Ray Davis and coworkers irradiated a large volume of liquid carbon tetrachloride (CCl_4) with antineutrinos from a reactor. The putative reaction, $\overline{\nu}_e + {}^{37}Cl \rightarrow {}^{37}Ar + e^-$, could be detected by periodic purging of the liquid, collection of the noble gas, and then detection of the induced activity (^{37}Ar is unstable, of course). The reaction was not observed to occur. Thus, they concluded that the reactor emits antineutrinos and that lepton number is conserved in the reactions.

Sample Problem 8.3: Antineutrino Flux

Estimate the flux of antineutrinos from an operating nuclear power reactor. For this estimate assume the power plant produces 1 GW of thermal power, given that fission produces 200 MeV per event and that there are ~6 rapid β^- decays per fission.

Solution
There is one antineutrino per β^- decay, of course, so this is simply a problem in dimensional analysis.

$$\text{Rate} = 1\ GW(10^6 J/s)/GW(1\ \text{fission}/200\ MeV)$$
$$\times (1\ MeV/1.602 \times 10^{-13} J/MeV)(6\overline{\nu}_e/\text{fission})$$
$$\text{Rate} = 2 \times 10^{17}\overline{\nu}_e/s$$

8.9   β-Delayed Radioactivities

The central feature of β decay is that, for example, in the β^- direction, the decay converts a neutron into a proton at a constant mass number. This conversion will clearly change the number of pairs of like nucleons in the nucleus, and we have already seen that unpaired nucleons influence the overall stability. β decay in even mass chains will convert odd–odd nuclei into the even–even isobar with potentially large Q values due to a gain of twice the pairing energy. The large Q values lead to high-energy β particles and rapid decays, but the relative stability of the daughter may be less than that of the parent. The large Q values also allow the population of higher lying states in the daughter. If the nuclei are far from the (most) stable isobar, the decay may have sufficient energy to populate states in the daughter that are above the neutron binding energy.

^{90}Sr provides an important example of a change in relative stability following β decay. This even–even parent is an important fission product that has a 29-year half-life. It decays to the odd–odd ^{90}Y, which subsequently decays to the stable isobar ^{90}Zr with a half-life of only 64 h. Thus, a pure preparation of ^{90}Sr will come into equilibrium with its daughter after about a week, and the observed activity will be the sum of the two decays. A chemical separation can be used to strip out the daughter activity and repurify the preparation. The daughter will decay away in the separated sample and will grow back into the parent sample. There are several examples of these parent/daughter pairs that provide convenient sources of short-lived activities. For example, the 66-h ^{99}Mo decays predominantly to a 6-h excited state in ^{99}Tc because the decay to ground state would require a very large spin change. The daughter ^{99}Tc^m is used extensively in nuclear medicine. Current estimates are that 40 million medical procedures are carried out with ^{99}Tc^m each year.

The natural decay chains have several examples of short-lived α activities that are "delayed" by a longer-lived parent. In fact, the existence of these activities on earth is possible by the fact that the "head" of the chain has a half-life on the order of the age of the earth. Another more practical example near the end of the 4n chain is ^{212}Pb with a half-life of 10.6 h that decays to ^{212}Bi. The daughter rapidly decays by α or β emission. The lead nucleus is also preceded by a short-lived and gaseous Rn parent, which can produce very thin sources of α particles by emanation of the gas and collection of the nongaseous daughters.
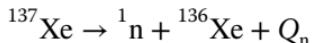
The β decay of nuclei far from the bottom of the valley of β stability can feed unbound states and lead to direct nucleon emission. This process was first recognized during the discovery of fission by the fact that virtually all the neutrons are emitted promptly but on the order of 1% are delayed with respect to the fission event. These delayed neutrons play a very important role in the control of nuclear reactors. The fission products are very neutron rich and have large β decay energies. For example, ^{87}Br is produced in nuclear fission and decays with a half-life of 55 s to ^{87}Kr with a Q value of 6.5 MeV. The decay populates some high-lying states in the krypton daughter; notice that ^{87}Kr has 51 neutrons, one more than the magic number 50, and the neutron separation energy of 5.1 MeV is less than the Q value. Thus, β decays that lead to excited states that lie above the neutron separation energy will be able to rapidly emit a neutron and form ^{86}Kr.

Sample Problem 8.4: β Delayed Neutron Emission

An important delayed neutron emitter in nuclear fission is ^{137}I. This nuclide decays with a half-life of 25 s and emits neutrons with an average energy of 0.56 MeV and a total probability of ~6%. Estimate the energy of an excited state in ^{137}Xe that would emit a 0.56 MeV neutron.

Solution

First obtain the Q value for the neutron emission reaction. This is the minimum amount of energy necessary to "unbind" the 83rd neutron and should be negative, of course:
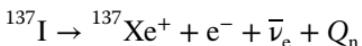
$$^{137}\text{Xe} \rightarrow {}^{1}\text{n} + {}^{136}\text{Xe} + Q_\text{n}$$
$$Q_\text{n} = \Delta(^{137}\text{Xe}) - [\Delta(^1 n) + \Delta(^{136}\text{Xe}]$$
$$Q_\text{n} = -82.218 - [8.0174 + -86.425] = -3.864 \text{ MeV}$$

The average energy of the excited state will be Q_n plus the kinetic energies of the particles, that is, the neutron plus the energy of the recoil. In this case the recoil energy is very small and could have been ignored. The recoil energy is obtained by conservation of momentum in the two-body decay:

$$E^* = -Q_\text{n} + T_\text{n} + T_\text{n}\left(\frac{1}{137}\right) = 3.864 + 0.56 + 0.01 = 4.43 \text{ MeV}$$

Now as a check, obtain the Q value for the β decay, and verify that it is more than the excitation energy:

$$^{137}\text{I} \rightarrow {}^{137}\text{Xe}^+ + \text{e}^- + \overline{\nu}_\text{e} + Q_\text{n}$$
$$Q_\beta = \Delta(^{137}\text{I}) - \Delta(^{137}\text{Xe}) = -76.72 - -82.21 = 5.49 \text{ MeV}$$

The population of high-lying unbound states by β decay is an important feature of nuclei near the drip lines. β-delayed proton emission and β-delayed neutron emission have been studied extensively and provide important insight into the structure of exotic nuclei.

8.10 Double β Decay

The periodic variation of the mass surface caused by the pairing energy also causes a large number of even–even nuclei near the bottom of the valley of stability to be unstable with respect to two successive β decays. This process is called double β decay, and extensive searches have been carried out for it. The difficulty is that the probability of a double transition is extremely low. A gross estimate can be made by squaring the rate constant obtained previously for a single decay; one finds that the number of decays from even large samples is at best one per day and at worst a few per year.

Two reactions have been studied as possible candidates for double β decay. The first reaction is simply two times the normal β decay process where the four particles are emitted simultaneously:

$$^{A}Z \rightarrow {}^{A}(Z-2) + 2\text{e}^- + 2\overline{\nu}_\text{e} \tag{8.34}$$

and thus follows the usual conservation laws. A second, more exotic reaction has been proposed as a test of weak interaction theory and proceeds without creation of neutrinos:

$$^A Z \rightarrow {}^A(Z-2) + 2e^- \tag{8.35}$$

which does not appear to follow the lepton conservation law. The speculation is that if the neutrino is its own antiparticle then the second, neutrinoless double β decay would be possible. Instrumental searches for this latter neutrinoless process have been made, but there is no strong evidence for its existence at present. The former two neutrino decay has been observed with a variety of techniques that were carefully tuned to detect the rare products.

As an example of the energetics of the double decay process, the ^{86}Kr nucleus just mentioned previously in delayed neutron emission is stable with respect to single β⁻ decay to ^{86}Rb having a Q value of −0.526 MeV. However, ^{86}Kr is unstable with respect to the double β decay to ^{86}Sr as it has a Q value of +1.249 MeV. In this case decay to the intermediate state is energetically forbidden, and only the simultaneous emission of two β particles can take place to reach strontium. To obtain the gross estimate, we can rewrite the aforementioned expression for the decay constant as

$$\lambda = \left(\frac{m_e c^2}{\hbar} \right) \left(\frac{|M|^2 m_e^4 c^2}{2\pi^3 \hbar^6} g^2 f(Z_d, Q) \right) \tag{8.36}$$
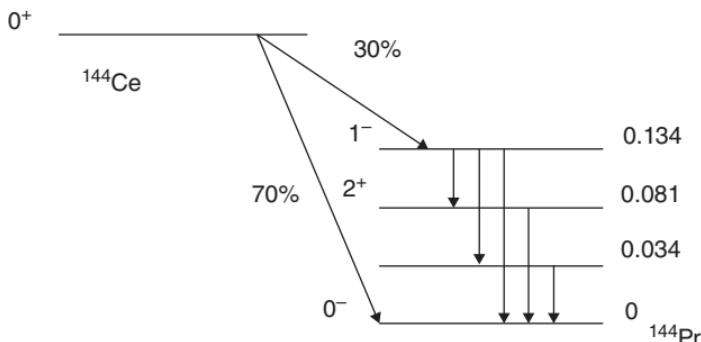
The first term is the constant 8×10^{20}/s, while the second term reflects the nuclear structure details of the decay. Using the value of $|M| = \sqrt{2}$ for the Fermi decay from the 0^+ ground state to the 0^+ ground state of the daughter, the second term becomes $1.5 \times 10^{-25} f$. For this Fermi decay case, $\log(f) \sim 1.5$ then taking the first term times the square of the second term with the nuclear structure factors for double β decay, we get $\lambda \sim 10^{-26}$ /s or $\sim 10^{-19}$/year! If we had a mole of this gas with $\sim 10^{24}$ atoms, we expect about one double decay every few minutes in the entire sample.

The techniques used to observe double β decay fall into three general categories: geochemical, radiochemical, and instrumental. The geochemical studies rely on assumptions that are similar to those used in geochemical dating (see Chapter 3). A sample of an ore containing the parent nuclide is processed; the daughter atoms are chemically extracted and then assayed, for example, with a mass spectrometer. The number of daughter atoms is then compared to the number of parent atoms, and with an estimate of the lifetime of the ore, the double β decay half-life can be calculated. Difficulties with this technique are discussed in Chapter 3. The radiochemical searches for double β decay relied
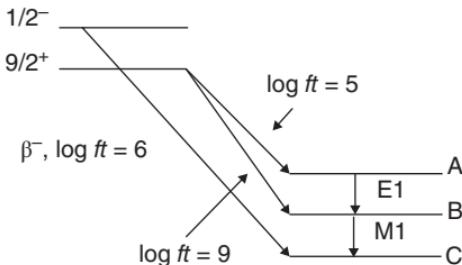
on chemically separating and identifying a radioactive daughter of the process in a previously purified sample. Such cases are relatively rare, but the decay $^{238}U \rightarrow ^{238}Pu$ was observed by chemically separating a uranium ore and observing the characteristic α decay of the plutonium isotope. The successful instrumental searches for double β decay up to this point have used time projection chambers in which sample of the parent was introduced into the active volume of the detector. The tracks of the two coincident β particles can be observed providing a clear signal for the exotic process.

Problems
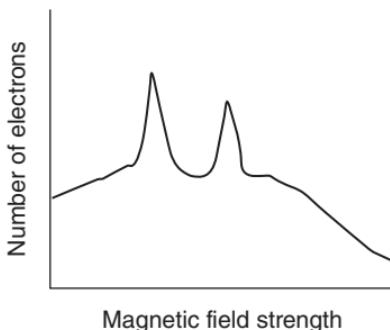
8.1 The β^- decay of ^{144}Ce is shown schematically in the following:

- What $\log(ft)$ value should we expect for the β^- decay to the 1^- level of ^{141}Pr?
- Why is there no β decay observed to the 2^+ level?

8.2 Sketch quantitatively the shape of the neutrino energy spectrum for the following types of decay. Label all axes carefully and indicate the types of neutrinos involved:
- The electron capture decay of ^{207}Bi, $Q_{EC} = 2.40$ MeV.
- The β^+ decay of ^{22}Na, $Q_\beta = 2.842$ MeV.
- The β^- decay of ^{14}Na, $Q_\beta = 0.156$ MeV.

8.3 Consider the β decay scheme shown in the accompanying figure for the decay of a pair of isomers into three excited states A, B, and C of the daughter nucleus. List the spins and parities of the three levels A, B, and C:

8.4 Suppose a state in a bismuth isotope decays by EC to the 2^+ state of an even–even Pb nucleus in which the three lowest states have spins/parities of 0^+, 2^+, and 4^+, with $E_{EC} = 1.0$ MeV. Assume that $Q_{EC} = 4.0$ MeV, $t_{1/2} = 4.0$ s, and calculate $J\pi$ for the initial state of the bismuth nucleus.

8.5 The results of some measurements with a β ray spectrometer of the radiation coming from a newly discovered radionuclide are shown in the figure later. The two sharp peaks were labeled "K" and "L" by the experimenter. Explain what the labels K and L mean. Which peak is the K peak and why?

8.6 A 1^- excited state of a lutetium isotope decays to a 0^+ state of a ytterbium isotope with a maximum β^+ energy of 4.6 MeV. Estimate the half-life for the transition. Do not neglect electron capture.

Bibliography

D.C. Camp and L.M. Langer, Phys. Rev. **129**, 1782 (1963).

H. Frauenfelder and E.M. Henley, *Subatomic Physics*, 2nd Edition (Prentice-Hall, Englewood Cliffs, 1991).

K. Heyde, *Basic Ideas and Concepts in Nuclear Physics*, 3rd Edition (Taylor & Francis, New York, 2005).

S.A. Moszkowski, Phys. Rev. **82**, 35 (1951).

T. Reines and C.L. Cowan, Jr. Phys. Rev. **92**, 830 (1953).

B. Singh et al., Nucl. Data Sheets **84**, 487 (1998).

C.S. Wu et al., Phys. Rev. **105**, 1413 (1957).

Textbook discussions of β decay that are especially good:

R. Evans, *The Atomic Nucleus* (McGraw-Hill, New York, 1953).

K. Heyde, *Basic Ideas and Concepts in Nuclear Physics*, 3rd Edition (Taylor & Francis, New York, 2005).

K.S. Krane, *Introductory Nuclear Physics* (John Wiley & Sons, Inc., New York, 1988).

J.R. Lamarsh, *Introduction to Nuclear Reactor Theory* (Addison-Wesley, Reading, 1967).

W.E. Meyerhof, *Elements of Nuclear Physics* (McGraw-Hill, New York, 1967).

M. Moe and P. Vogel, Ann. Rev. Nucl. Sci. **44**, 247 (1994).

T. Reines and C.L. Cowan, Jr. Phys. Rev. **92**, 830 (1953).

More advanced discussion can be found in:

K. Siegbahn, *Alpha, Beta and Gamma Ray Spectroscopy* (North-Holland, Amsterdam, 1966).

C.S. Wu and S.A. Moszkowski, *Beta Decay* (John Wiley & Sons, Inc., New York, 1966).

C.S. Wu et al., Phys. Rev. **105**, 1413 (1957).

9

γ-Ray Decay

9.1   Introduction

γ-Ray decay occurs when a nucleus in an excited state releases its excess energy by emission of electromagnetic radiation, that is, a photon. Thus we have

$$^{A}Z^* \rightarrow {}^{A}Z + \gamma \qquad (9.1)$$

where the symbol ∗ indicates an excited state of the nucleus. Note that there is no change in Z or A during this type of decay, only the release of energy. One can also get γ-ray emission from a high lying excited state to a lower-lying excited state of the same nucleus. Thus, γ-ray transitions do not have to go to the ground state of the nucleus. Figure 9.1 depicts a hypothetical situation in which a series of γ rays de-excite the evenly spaced levels of a nucleus with so-called "crossover transitions" also occurring (e.g., from top to bottom). Also note that the γ-ray energy spectrum shows discrete, sharp lines corresponding to each transition. The energies of the γ rays can vary from a few keV to many MeV. Any nucleus from deuterium to the heaviest one can emit γ rays if suitably excited.

In some unusual cases a nucleus can have two configurations of nucleons that have very similar low-lying energy states that have very different total angular momenta. One of these states will lie lower in energy, but the transition between the two states will be strongly hindered due to the fact that the photon will have to balance the large change in angular momentum. This hindered decay is similar to the hindrance of the decay of triplet states in atomic and molecular systems to lower-lying singlet states. The long-lived nuclear states are called *isomeric states* or *isomers*, since the only difference between the states is structural, and their γ-ray decay is called an *isomeric transition* or simply IT decay. An example of an isomeric state is shown in Figure 9.2 for ^{69}Zn. The ground state of the zinc nucleus is unstable with respect to β decay with a half-life of 56 min. The lowest excited state of this nucleus has an energy of only 439 keV, but it has a much larger spin and opposite parity compared with the ground state. The transition from the excited state to the ground state is hindered by the large
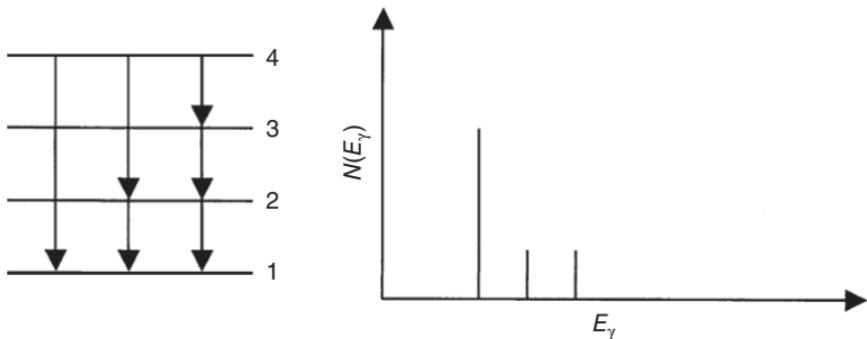
Figure 9.1 Schematic diagram of the γ-ray transitions among the evenly spaced levels of a hypothetical nucleus (left) and the resulting γ-ray energy spectrum (right).
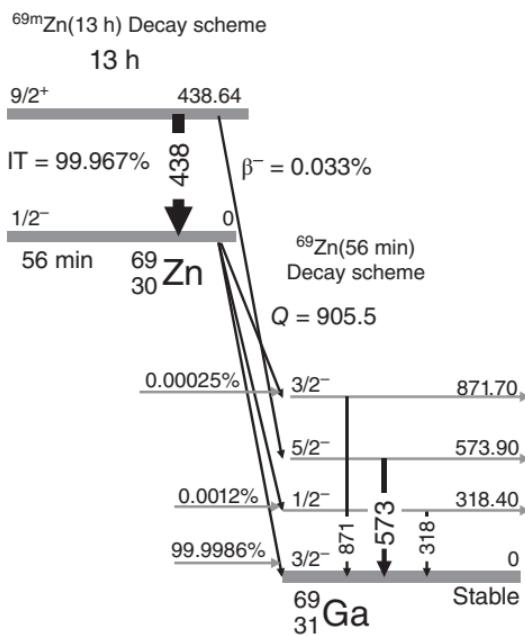
Figure 9.2 Decay scheme for the isomeric state of ^{69}Zn^m and the ground state of ^{69}Zn.

change in angular momentum, $4\hbar$, combined with a change in parity (discussed in the following text), which leads to an IT half-life of 14 h. The β decay of the isomeric state is slower than the IT decay in this case.

9.2 Energetics of γ-Ray Decay

Imagine a γ transition between two nuclear states. Applying the law of conservation of energy, we have

$$M_0^* c^2 = M_0 c^2 + E_\gamma + T_r \tag{9.2}$$

where E_γ is the photon energy, T_r is the kinetic energy of the recoiling nucleus after γ-ray emission, and M_0^* and M_0 are the masses of the higher and lower nuclear states, respectively. Applying the law of conservation of momentum, we have only two bodies in the final state so that

$$p_\gamma + p_r = 0 \tag{9.3}$$

where p_γ and p_r are the momenta of the photon and recoiling nucleus, respectively. The kinetic energy of the recoil is so small that nonrelativistic mechanics can be used for it but not for the photon. Hence we have

$$T_r = \frac{p_r^2}{2M} \tag{9.4}$$

where M is the mass of the recoiling nucleus. Since $p_r^2 = (-p_\gamma)^2 = p_\gamma^2$:

$$T_r = \frac{p_\gamma^2}{2M} \tag{9.5}$$

further $E_\gamma = p^2c^2$ so that

$$T_r = \frac{E_\gamma^2}{2M_0c^2} \tag{9.6}$$

For example, if $E_\gamma = 2$ MeV (a relatively large value for nuclei) and $A = 50$, then the recoil energy is about 40 eV, which is larger than typical molecular bond energies but negligible for nuclei except for Mössbauer studies (discussed later in this chapter).

Sample Problem 9.1: γ-Ray Recoil Energies

Calculate the recoil energy for the IT decay of ^{69}Zn^m to the ground state of ^{69}Zn and the recoil energy from the emission of a 15.1 MeV photon by an excited ^{12}C nucleus. Recall that the mass excess of ^{12}C is exactly zero so that the mass of ^{12}C is 12 amu.

Solution
Using the energy of the excited state from Figure 9.2, we have

$$\left(M_0^* - M_0\right) c^2 = E_\gamma = 0.439 \text{ MeV}$$

Recall that $M_0c^2 = \text{amu} * 931.5$ MeV/amu. Using the mass excess of 68.418 MeV found in the wallet cards for ^{69}Zn, the mass is 68.927 amu. (This is obtained by 69 amu + (−68.418 MeV/931.5 MeV/amu) = 69 amu + 0.073 amu = 68.927 amu.)

$$T_r = \frac{E_\gamma^2}{2M_0c^2} = \frac{(0.439 \text{ MeV})^2}{2(68.927 \times 931.5 \text{ MeVc}^2)} = 1.5 \times 10^{-6} \text{ MeV}$$

The recoil energy from the emission of the 15.1 MeV photon from an excited ^{12}C nucleus is

$$T_r = \frac{E_\gamma^2}{2M_0 c^2} = \frac{(15.1 \text{ MeV})^2}{2(12 \times 931.5) \text{ MeVc}^2}$$
$$T_r = 1.02 \times 10^{-2} \text{ MeV} = 10.2 \text{ keV}$$

9.3 Classification of Decay Types

The conservation of angular momentum plays a controlling role in the γ-ray decay process and has provided an enormous amount of information on the structure of nuclei. From a schematic viewpoint, a stationary nucleus in a definite quantum mechanical state makes a transition to a lower-energy state during γ decay and emits a single photon. Both the initial and final states of the nucleus will have definite angular momentum and parity, and so the photon must connect the two states and conserve both parity and angular momentum. Photons each carry an exact integer number of angular momentum units ($\hbar$), and each has a definite parity. The conservation of angular momentum and parity are different, of course, and conservation of each has a different effect on the possible properties of the emitted photon.

The angular momenta of the initial and final states of final nucleus can be labeled as $I_i \hbar$ and $I_f \hbar$, and the change in the intrinsic nuclear angular momentum, ΔI is, of course, $\ell = \Delta I = (I_f - I_i)\hbar$. A photon must carry at least one unit of angular momentum so that $\Delta I = 0$ is forbidden for single photon emission. The emitted photon should have a minimum intrinsic spin of $\ell \hbar$ units to connect the two nuclear states. However, the standard coupling rules for angular momenta allow the photon to carry away up to a maximum of $(I_f + I_i)\hbar$ units. Therefore, given known values of the spins of initial and final states of the nucleus, the angular momentum carried by the photon can take any value in the range:

$$|(I_f - I_i)| \leq \ell \leq (I_f + I_i) \tag{9.7}$$

The *multipolarity* of the photon is a label for the amount of angular momentum carried by the photon. The nomenclature is that a photon with ℓ units of angular momentum is called a 2^ℓ-pole photon. (The nomenclature comes from the classical radiation patterns of electromagnetic radiation and the design of the antennas used to create those patterns.) For example, a photon with $\ell = 1$ is called a dipole photon, $\ell = 2$ a quadrupole photon, and so on as indicated in Table 9.1. The transition rate, discussed in the following text, depends strongly on the angular momentum change so that the smallest value of $\ell = |(I_f - I_i)|\hbar$ is usually observed although conservation of parity plays an important role.

Table 9.1 γ-Ray Selection Rules and Multipolarities.

Radiation Type	Name	$\ell = \Delta I$	$\Delta\pi$
E1	Electric dipole	1	(Yes)
M1	Magnetic dipole	1	(No)
E2	Electric quadrupole	2	(No)
M2	Magnetic quadrupole	2	(Yes)
E3	Electric octupole	3	(Yes)
M3	Magnetic octupole	3	(No)
E4	Electric hexadecapole	4	(No)
M4	Magnetic hexadecapole	4	(Yes)

Transitions with the maximum change in the angular momentum of the nuclear states are called *stretched transitions*.

To understand the parity of electromagnetic transitions, we need to recall that each of the initial and final states of the nucleus undergoing the transition can be viewed as having a definite distribution of matter and charge. When the excited nucleus makes a transition from the excited state to a lower-energy state, the distribution of matter and charge will change in some way. For example, a nucleus that is spinning with a certain value of angular momentum will slow down as it de-excites and reaches the ground state. Thus, the emission of the photon can be associated with the change in the overall distribution of neutrons and protons, but we can identify two different changes that are analogous to classical antennas. A shift in the distribution of charge (e.g., the transition of a proton from one orbital to another) will give rise to an electric field, but a shift in the distribution of current in the nucleus (e.g., the shift of the direction of a proton orbital) will give rise to a magnetic field. The parity of the photon depends on both the angular momentum and the type (electric or magnetic) of transition indicated in Table 9.1. Notice that electric and magnetic radiation with a given multipole character has opposite parities.

With the list of properties of photons, we can generalize the procedure to identify the probable type of photon for a given transition between nuclear states. First the parity of the photon will be given by the difference in parities of the two nuclear states. Then the angular momentum of the photon will be limited to be in the range of $|I_f - I_i|$ to $I_f + I_i$. The combination of allowed angular momenta and parity will determine the character of the electromagnetic radiation. For example, the first excited state in ^{7}Li has spin and parity $1/2^-$ and the ground state is $3/2^-$. Possible electromagnetic transitions between the two states must have $\Delta\pi = $ no and $1 \leq \ell \leq 2$. Consulting Table 9.1, we find that the only candidates are M1($\ell = 1$, $\Delta\pi = $ no) and E2 ($\ell = 2$, $\Delta\pi = $ no) while the

other potential angular momentum combinations of E1 and M2 are ruled out by the lack of a parity change. As we will see in the next section, all of the allowed radiation types will be emitted but at substantially different rates so that the overall radiation usually has one predominant character.

Sample Problem 9.2: Application of Selection Rules

Use the electromagnetic selection rules to identity the character of all of the transitions that could link the second excited state at 2.080 MeV $(7/2^+)$ in ^{23}Na with the ground state $(3/2^+)$.

Solution

First, we should note that $\Delta\pi = $ no. Then

$$|I_f - I_i| \leq \ell \leq I_f + I_i$$
$$|2| \leq \ell \leq 5$$

so the allowed transitions are

ℓ	$\Delta\pi$	Type
2	No	E2
3	No	M3
4	No	E4
5	No	M5

As a final point on the topic of selection rules, we noted that $\Delta\ell = 0$ is forbidden for the emission of a single photon. The electric monopole distribution (E0) corresponds to the static distribution of charge in the nucleus and is constant. Similarly the M0 distribution corresponds to the nonexistent magnetic monopole moment. Nonetheless there are a few examples of even–even nuclei that have first excited and ground states that are both 0^+. Once populated, these excited states decay by internal conversion processes in which the atomic electrons, particularly s electrons with significant penetration into the nucleus, are directly emitted from the atom or by direct pair production if the energy difference is >1.022 MeV.

Sample Problem 9.3: Wavelength Calculation

Calculate the ratio of the wavelength of the 439 keV IT photon emitted when the isomeric state of ^{69}Zn^m to the ground state of this nucleus.

Solution

Recall for a photon

$$E_\gamma = h\nu$$
$$\lambda\nu = c$$

$$\lambda = \frac{hc}{E_\gamma} = \frac{(6.626 \times 10^{-34} \text{ Js}) \left(2.998 \times 10^8 \text{ m/s}\right)}{(439 \times 10^3 \text{ eV}) (1.602 \times 10^{-19} \text{ J/eV})}$$
$$\lambda = 2.82 \times 10^{-12} \text{ m}$$

thus

$$\frac{\lambda}{2R} = \frac{2.82 \times 10^{-12} \text{ m}}{2 \times 1.2 \times (69)^{1/3} \times 10^{-15} \text{ m}} = 287$$

A nucleus is not an effective antenna due to its small size compared to the wavelength of the radiation. γ-Rays are in the long-wavelength limit and are not very sensitive to the detailed internal structure of the emitting nucleus.

9.4 Electromagnetic Transition Rates

Determining the rate at which an excited state will decay by the emission of a photon is a very general quantum mechanical problem that is not limited to the world of nuclei. The detailed derivation of the transition rate is beyond the scope of this text, and we will only sketch out the results. The decay constant for the emission of a photon by a very well-defined single state that has excess energy is shown in the Appendix E to be given by the general expression

$$\lambda = \frac{2\pi}{\hbar} | \int \phi_{\text{final}}^* V_P \phi_{\text{initial}} dv |^2 \rho(E_f) \tag{9.8}$$

which is also called Fermi's golden rule. The wave functions, ϕ, represent the complete initial and final states of the entire system, and V_P is a (very) small perturbative interaction between the nuclear and electric fields that stimulates the transition. The form and the strength of the perturbation will depend on the multipolarity of the transition. The last factor, $\rho(E_f)$, is the product of the density of nuclear and electromagnetic states that are available to the system after the transition. The initial wave function contains only the nuclear excited state, whereas the final wave function will have parts for the electromagnetic wave and the daughter nuclear state.

After some extensive calculus and input from the theory of electromagnetism, we come to an expression for the electromagnetic decay rate, one can write

$$\lambda(\ell, I_i, \pi \to I_f, \pi) = \frac{8\pi(\ell+1)}{\ell[(2\ell+1)!!]^2} \frac{k^{2\ell+1}}{\hbar} B(\ell, I_i, \pi \to I_f, \pi) \tag{9.9}$$

where k is the photon wave number ($k = \frac{E_\gamma}{\hbar c}$). The symbol !! calls for the double factorial of its argument, which for the case of $\ell = 2$ and $(2\ell + 1) = 5$ would be the product of the odd integers: $5!! = 5 * 3 * 1 = 15$. The reduced transition probability, $B(\ell, I_i, \pi \to I_f, \pi)$, is the matrix element for the reduced nuclear wave functions (i.e., summed over magnetic orientations) using the multipole operator (either electric or magnetic in character)

$$B(\ell, I_i, \pi \to I_f, \pi) = \frac{1}{2I_i + 1} |\langle I_f \xi | O_\ell | I_i \xi \rangle|^2 \tag{9.10}$$

in which the symbols ξ in the nuclear wave functions are meant to represent all the other relevant quantum numbers. (As an aside we should note that the two "types" of electric and magnetic radiation are only different in terms of their parity and in the orientation of their plane of polarization.) This expression is still somewhat complicated and is difficult to evaluate. Victor Weisskopf derived a general expression for the reduced transition probability with the assumption that the transition results from the change of a single particle/proton inside a nucleus with a uniform density with the familiar radius function, $R = r_0 A^{1/3}$. His expression for *electric* multipole radiation, called the *Weisskopf single particle limit*, is
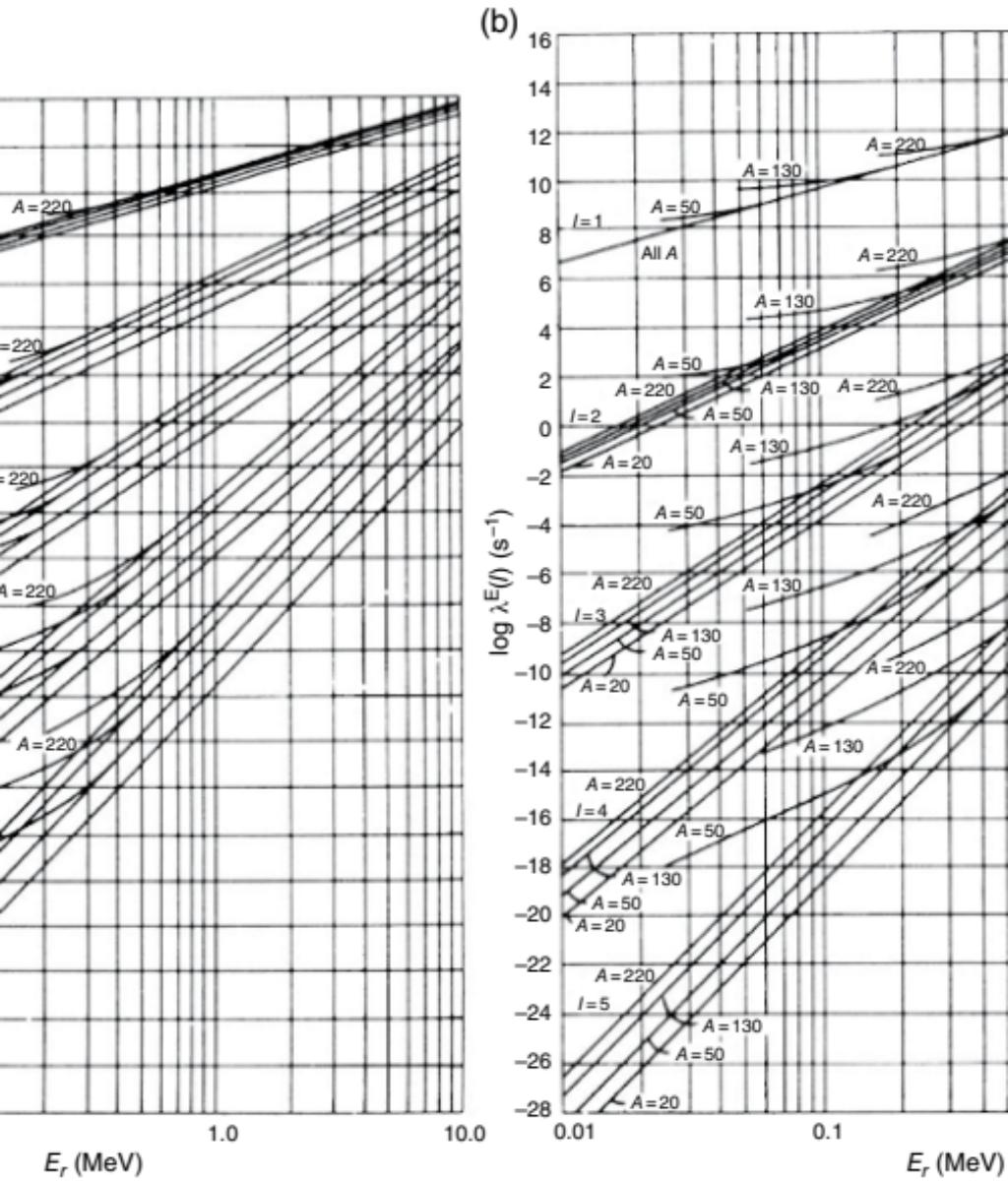
$$B_{sp}(E, \ell) = \frac{1}{4\pi} \left[\frac{3}{(\ell+3)} \right]^2 (r_0)^{2\ell} A^{2\ell/3} e^2 \, \text{fm}^{2\ell} \tag{9.11}$$

Similarly, the single particle limit for *magnetic* multipole radiation obtained by assuming that the change in current is due to a single nucleon is

$$B_{sp}(M, \ell) = \frac{10}{\pi} \left[\frac{3}{(\ell+3)} \right]^2 (r_0)^{2\ell-2} A^{(2\ell-2)/3} \mu_n^2 \, \text{fm}^{2\ell-2} \tag{9.12}$$

One of the nagging features of these expressions is that the radial integral from the multipole expansion introduces a factor of $r^{2\ell}$, and thus the dimensions of $B(E, \ell)$ and $B_{sp}(E, \ell)$ depend on ℓ.

Either of the single particle limits for the reduced electric or magnetic transition, probability can be substituted into the expression for the transition rate to obtain numerical estimates of the de-excitation rates under the assumption that one particle was responsible for the change in electric charge or electric current associated with the change in nuclear states. The transition rates vary over an enormous range as shown in Figure 9.3 depending most strongly on the value of ℓ. Electric transitions are faster than magnetic transitions by about

(b)

pf single particle estimates of the transition rates for electric multipoles (b) (Condon and Odishaw (1967). Reproduced ... aw-Hill Book Company, Inc.).

two orders of magnitude. Looking back to the discussion of the fact that several different types of photons can be associated with a given nuclear transition, we now see that we expect the rates of emission to favor the lowest multipolarity. This fact can be simply demonstrated by evaluating the expressions for the transition rate for electric dipole, $\ell = 1$, and electric quadrupole, $\ell = 2$, radiation with a typical nuclear radius parameter of $r_0 = 1.2$ fm. Combining the expressions for the transition rate and the reduced transition probability for an E1 transition, we get

$$\lambda_{sp}(E, \ell) = \frac{8\pi(\ell + 1)}{\ell[(2\ell + 1)!!]^2} \frac{k^{2\ell+1}}{\hbar} \frac{1}{4\pi} \left[\frac{3}{(\ell + 3)}\right]^2 (r_0)^{2\ell} A^{2\ell/3} e^2 \text{ fm}^{2\ell} \quad (9.13)$$

Substituting in $\ell = 1$,

$$\lambda_{sp}(E1) = \frac{8\pi(2)}{[(3)!!]^2} \frac{k^3}{\hbar} \frac{1}{4\pi} \left[\frac{3}{4}\right]^2 (r_0)^2 A^{2/3} e^2 \text{fm}^2 \quad (9.14)$$

Recall that $\hbar c = 197$ MeV-fm and $e^2/4\pi\epsilon = 1.44$ MeV-fm, so that

$$\lambda_{sp}(E1) = \frac{16\pi}{9} \left(\frac{E_\gamma(\text{MeV})}{197.3 \text{ MeV fm}}\right)^3 \frac{1.44 \text{ fm}}{4\pi\hbar} \left[\frac{3}{4}\right]^2 (1.2 \text{ fm})^2 A^{2/3}/\text{s}^1 \quad (9.15)$$

$$\lambda_{sp}(E1) = 1.03 \times 10^{14} E_\gamma^3 A^{2/3}/\text{s}^1 \quad (9.16)$$

Similar substitution into the expression for $\lambda_{sp}(E\ell)$ with $\ell = 2$ for electric quadrupole radiation will eventually yield

$$\lambda_{sp}(E2) = 7.28 \times 10^7 E_\gamma^5 A^{4/3}/\text{s}^1 \quad (9.17)$$

So we see that the rates depend very strongly on the energy of the photon and on the size (mass number) of the emitting nucleus. If we consider the specific hypothetical case of a 1 MeV transition in a medium mass nucleus, $A = 100$, the ratio of transition rates is

$$\frac{\lambda_{sp}(E1)}{\lambda_{sp}(E2)} = \frac{1.03 \times 10^{14} E_\gamma^3 A^{2/3}}{1.03 \times 10^{14} E_\gamma^3 A^{2/3}} = 1.41 \times 10^6 E_\gamma^{-2} A^{-2/3} \quad (9.18)$$

$$\frac{\lambda_{sp}(E1)}{\lambda_{sp}(E2)} = 6.54 \times 10^4 \quad (9.19)$$

The formulas for the Weisskopf transition rates are summarized in Table 9.2 for the lowest five multipoles of each character. The transition rates always increase with a high power of the γ-ray energy so that low-energy transitions, say below 100 keV, are much slower than high-energy transitions, say above 1 MeV. The table also shows that in some cases, particularly in heavy nuclei, an $\ell + 1$ electric transition can compete favorably with an ℓ magnetic transition. The Weisskopf estimates are usually good to within a factor of 10, which

Table 9.2 Weisskopf Single Particle Transition Rates (E_γ in MeV).

Multipolarity ℓ	$E\ell$ $\lambda(s^{-1})$	$M\ell$ $\lambda(s^{-1})$
1	$1.0 \times 10^{14} A^{2/3}E_\gamma^3$	$3.1 \times 10^{13}E_\gamma^3$
2	$7.4 \times 10^7 A^{4/3}E_\gamma^5$	$2.2 \times 10^7 A^{2/3}E_\gamma^3$
3	$3.5 \times 10^1 A^2 E_\gamma^7$	$1.1 \times 10^1 A^{4/3}E_\gamma^3$
4	$1.1 \times 10^{-5} A^{8/3}E_\gamma^9$	$3.3 \times 10^{-6} A^2 E_\gamma^3$
5	$2.4 \times 10^{-12} A^{10/3}E_\gamma^{11}$	$7.4 \times 10^{-13} A^{8/3}E_\gamma^3$

is remarkable given the large number of orders of magnitude that they span, and provide important references for comparison to the observed transition rates. Notice that if a transition occurs more rapidly than the single particle rate, then the transition is more collective, that is, more particles participate in the change. If the transition is significantly slower than the Weisskopf estimate, then the nuclear matrix element must be smaller than the single particle limit, that is, the overlap of the initial and final states must be smaller. The ratio of the observed decay rate to the Weisskopf estimated rate is often quoted in the literature as the transition rate in Weisskopf units (W.u.).

Sample Problem 9.4: Weisskopf Transition Rate

Use the electromagnetic selection rules to identity the character of the isomeric transition from the first excited state at 0.439 MeV ($9/2^+$) in ^{69}Zn^m with the ground state ($1/2^-$). Then calculate the Weisskopf single particle rates for the allowed transitions.

Solution

First, we should note that $\Delta\pi = $ yes. Then, recall from the previous discussion:

$$|I_f - I_i| \leq \ell \leq I_f + I_i$$
$$|4| \leq \ell \leq 5$$

Thus, only M4 and E5 transitions are allowed. Using the expressions in Table 9.2,

$$\lambda_{sp}(M4) = 3.3 \times 10^{-6} E_\gamma^9 A^2/s^1$$
$$\lambda_{sp}(M4) = 9.5 \times 10^{-6}/s^1$$

and

$$\lambda_{sp}(E5) = 2.4 \times 10^{-12}E_\gamma^{11} A^{10/3}/s^1$$
$$\lambda_{sp}(E5) = 3.8 \times 10^{-10}/s^1$$

so we expect that the transition will be predominantly M4 in character due to its higher decay rate. The observed transition occurs almost twice as fast as the single particle estimate since

$$\lambda_{\text{expt}} = \ln(2)/(14\,\text{h} \times 3600\,\text{s/h}) = 1.4 \times 10^{-5}/\text{s}^1$$

indicating that a change in the "current" from more than one particle contributes to the magnetic transition.

It should be noted that E2 transitions are often enhanced by an order of magnitude compared to the single particle estimates. This enhancement of these specific transitions stems from collective nuclear motion, and the enhancement is particularly strong for nuclei that lie in between major shell closures. An example of a set of E2 transitions to the ground state of ^{160}Dy and the first three excited (collective) states are shown in Figure 9.4. The excited nucleus cascades down from the 6^+ level in a series of three E2 transitions with no crossover transitions. The lifetimes of the states, indicated in the figure, were used to calculate the transition rates in Weisskopf units, also indicated in the figure. Notice that the rate of emission in this case ranges from 200 to 1100 times the single particle rate. If we take a closer look at the transition rate for electric quadrupole transitions, then we would find that the reduced transition probability could be written in terms of the quadrupole moment, Q_0:

$$B(\text{E2}, J_i \rightarrow J_f) = \frac{5}{16\pi} e^2 Q_0^2 \langle J_i, K, 2, 0|J_j, K\rangle^2 \tag{9.20}$$

in which the last term is a Clebsch–Gordan coefficient, which is a very general normalization coefficient for the values of the spins and the spin projections. In the present case of transitions between the states of a rotational band, $K = 0, J_i = J$, and $J_f = J - 2$, the normalization coefficient only contains values of J:

$$\langle J_i, K, 2, 0|J_j, K\rangle^2 \rightarrow \langle J_i, 0, 2, 0|(J-2), 0\rangle^2 = \frac{3J(J-1)}{2(2J+1)(J-1)} \tag{9.21}$$
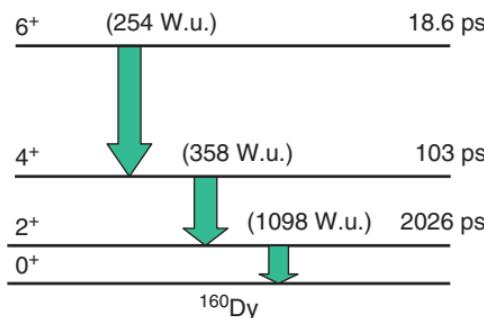

Figure 9.4 Schematic diagram of the ground-state rotational band transitions for ^{160}Dy.

so that the reduced transition probability is

$$B(\text{E2}, J_i \rightarrow J - 2) = \frac{15}{32\pi} e^2 Q_0^2 \frac{J(J-1)}{(2J+1)(J-1)} \tag{9.22}$$

Thus, the experimental transition rate provides a measurement of the quadrupole moment of the nucleus, and we should not be surprised that a strongly deformed nucleus with a large quadrupole moment will have a larger E2 transition rate because the whole nucleus can participate in the transition compared to a single particle.

The single particle estimates of γ-ray decay presume a single nucleon interacts with a photon. This means there is an isospin selection rule ($\Delta T = 0$ or 1) for γ-ray decay between two pure isospin states. Further, E1 γ-ray transitions cannot occur when $\Delta T = 0$ in a self-conjugate or mirror nucleus ($N = Z$).

9.5 Internal Conversion

Internal conversion is a competing process to γ-ray decay that can occur when an excited nucleus interacts electromagnetically with an orbital electron and ejects it. This transfer of the nuclear excitation energy to the electron occurs radiationlessly without the emission of a photon. The energy of the internal conversion electron, E_{IC}, is given by the expression

$$E_{\text{IC}} = E_{\text{transition}} - E_{\text{electron binding energy}} \tag{9.23}$$

For example, if a nuclear transition with $E_{\text{transition}} = 0.412$ MeV, one would expect to see a spectrum of emitted internal conversion electrons indicated in Figure 9.5. Note that the conversion electrons are superimposed on the continuous spectrum of β particles (also electrons!) and the different lines corresponding to the ejection of electrons from the K, L, and M shells. The nucleus will interact more readily with the K electrons than with the L electrons, than with the M electrons, and so on because the K electrons spend more time in the nucleus than the L electrons, than the M electrons, and so on.

To characterize this decay process and its competition with γ-ray emission, we define the internal conversion coefficient, α_{total}, by the relationship

$$\alpha_{\text{total}} = \frac{\text{Number of internal conversion decays}}{\text{Number of γ-ray decays}} = \frac{\lambda_{\text{IC}}}{\lambda_\gamma} \tag{9.24}$$

where the coefficient, α, can take on values from zero to infinity. Note further that

$$\lambda = \lambda_\gamma + \lambda_{\text{IC}} = \lambda_\gamma (1 + \alpha) \tag{9.25}$$

One can define an internal conversion coefficient for electrons only from the K shell or for electrons only from the M shell, and so on, giving rise to α_K, α_L,
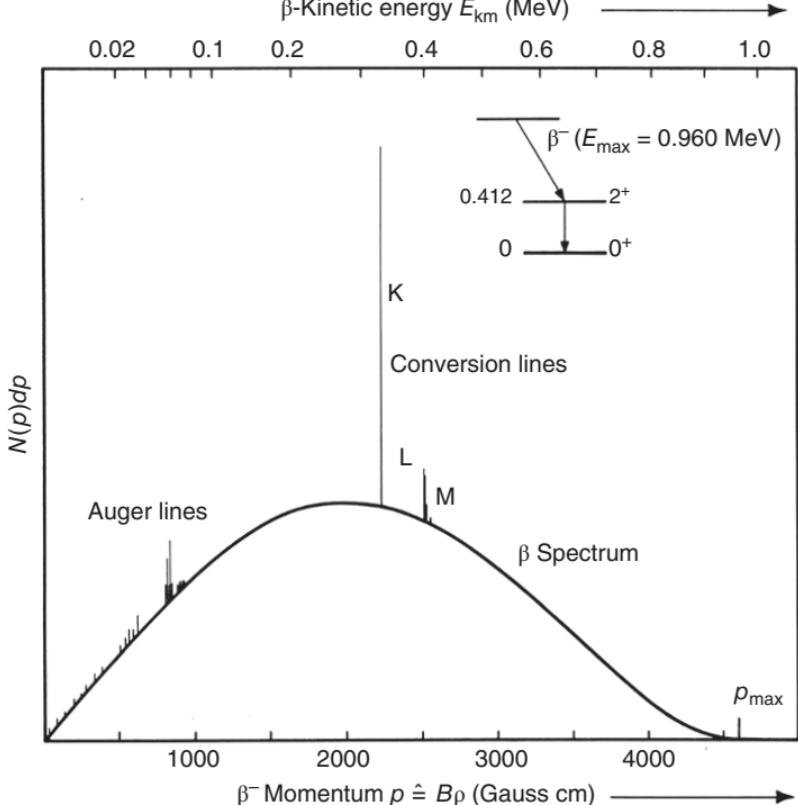
Figure 9.5 The kinetic energy spectrum of internal conversion electrons for a 412-keV nuclear transition in ^{198}Hg. Superimposed on this spectrum is the accompanying spectrum of β^- particles from the β decay that feeds the excited state. The peaks labeled K, L, and M represent conversion of electrons with principal quantum numbers of 1, 2, or 3, respectively (Marmier and Sheldon (1969). Reproduced with the permission of Elsevier).

α_M, and so on. Since the total probability of decay must equal the sum of the probabilities of decay via various paths, we have

$$\alpha_{\text{total}} = \alpha_K + \alpha_L + \alpha_M + \cdots \tag{9.26}$$
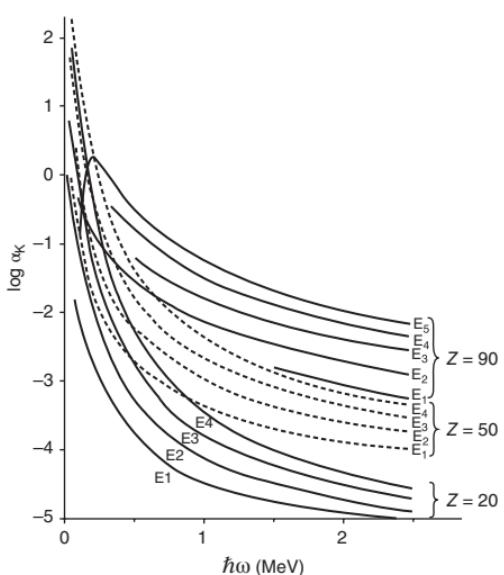
The internal conversion coefficient depends primarily on the density of the atomic electrons at the center of the nucleus, and thus it can be calculated using principles from atomic physics. Large tables and nomographs of internal conversion coefficients exist, such as those shown in Figure 9.6.

Rough approximate formulas for the internal conversion coefficients are

$$\alpha(E, L) = \frac{Z^3}{n^3} \left(\frac{L}{L+1} \right) \left(\frac{e^2}{4\pi\epsilon_0 \, \hbar c} \right)^4 \left(\frac{2m_e c^2}{E} \right)^{L+5/2}$$

$$\alpha(M, L) = \frac{Z^3}{n^3} \left(\frac{e^2}{4\pi\epsilon_0 \, \hbar c} \right)^4 \left(\frac{2m_e c^2}{E} \right)^{L+3/2}$$
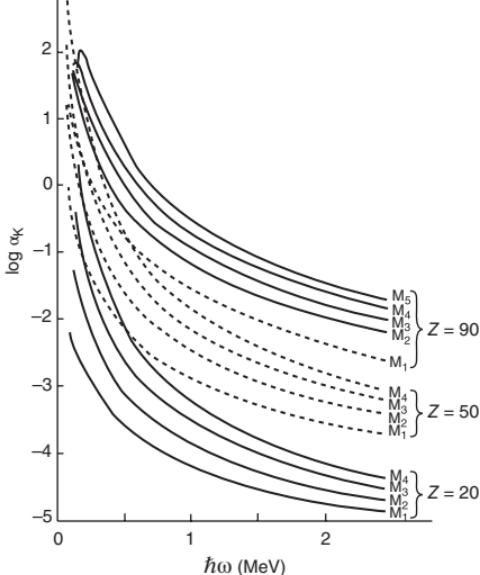
Figure 9.6 Calculated internal conversion coefficients for (a) electric transitions and (b) magnetic transitions (Preston (1962). Reproduced with the permission of Pearson Education).

where Z is the atomic number of the atom in which the conversion is taking place, n is the principal quantum number of the bound electron being ejected, and $e^2/4\pi\epsilon_0\hbar c$ is the fine structure constant and is $\sim 1/137$. Note that the internal conversion coefficient, α, increases approximately as Z^3, making internal conversion most important for heavy nuclei. The last factor in the equations gives the energy and multipolarity dependence with internal conversion increasing for low energies and higher transition multipolarities. Notice that the ratio of α_K to α_L is ~ 8 due to the n^3 factor.

Sample Problem 9.5: Internal Conversion Coefficients

Use a standard reference such as the *Table of Isotopes, 8th Ed.*, to determine the internal conversion coefficients for each shell for the transition from the first excited state at $0.08679\,\text{keV}$ (2^+) in ^{160}Dy to the ground state (0^+). Then calculate the decay rates for internal conversion and for γ-ray emission.

Solution

First, this transition can be identified as an E2 photon using Appendix F in the *Table of Isotopes, 8th Ed.* Interpolation in a graph gives

$\alpha_K(\text{E2}, Z \approx 65,\ 0.090\,\text{MeV}) = 1.5$

$\alpha_{L1}(\text{E2}, Z \approx 65,\ 0.090\,\text{MeV}) = 0.1$

$$\alpha_{L2}(E2, Z \approx 65, \ 0.090 \text{ MeV}) = 5.$$
$$\alpha_{L3}(E2, Z \approx 65, \ 0.090 \text{ MeV}) = 2.5$$
$$\alpha_{\text{total}} = \alpha_K + \alpha_{L2} + \alpha_{L3} + \alpha_{L1} = 9.1$$

$$\lambda = \ln(2)/2.02 \times 10^{-9} \text{ s} = 3.34 \times 10^8 \text{ s} = \lambda(1 + \alpha_{\text{total}})$$

$$\lambda_\gamma = \frac{\lambda}{(1 + \alpha_{\text{total}})} = 3.4 \times 10^7 \text{ s}^{-1}$$

$$\lambda_{\text{IC}} = \lambda - \lambda_\gamma = 3 \times 10^8 \text{ s}^{-1}$$

Note that internal conversion occurs ~10 times FASTER than γ-ray emission for this transition in this (heavy) nucleus.

9.6 Angular Correlations

One part of the derivation of the emission rate for γ rays that we glossed over is that the angular distribution of the emitted radiation from a single state must be isotropic. The isotropy comes from the fact that the nuclei are oriented at random, and the process sums over all the internal magnetic substates and thus includes all possible angular distributions. We used this fact in the derivation by using the "reduced (or double-barred) matrix elements." Anisotropic angular distributions can only be observed when a preferred direction or nuclear orientation is established prior to the emission of the photon. There are several techniques to establish such preferred orientations that rely on observing an angular correlation with either an external magnetic field or another particle or photon emitted in "cascade" from the same nucleus. All of these techniques rely on unequal populations of the magnetic substates of the observed emitting nuclear state. Two of these techniques are shown schematically in Figure 9.7. Another important application of angular correlations is to determine the multipolarity of the electromagnetic transition. We have seen that the selection rules often provide a range of possibilities for the spin change and the lifetimes of the states depend on the nuclear matrix elements as well as the multipolarity. To reliably identify the multipolarity, we have to measure the angular distribution of the radiation; however, as just noted, we need a reference axis.

The conceptually simplest technique to observe an angular correlation is to measure the angular distribution of radiation from an excited nucleus relative to an external, applied magnetic field. The magnetic substates of nuclear excited states that have angular momenta, I, greater than 0 will split in proportion to the strength of the external magnetic field, B_{ext}, and the magnetic field provides the reference axis. This substate splitting provides the basis for NMR and MRI techniques, of course. The difficulty with this correlation technique is that the (Zeeman) splitting of the nuclear spin substates, ΔE_m, given by the simple expression

$$\Delta E_m = gIB_{\text{ext}}\mu_n \tag{9.27}$$
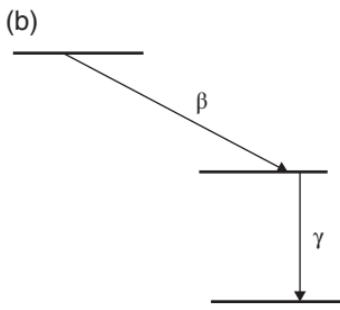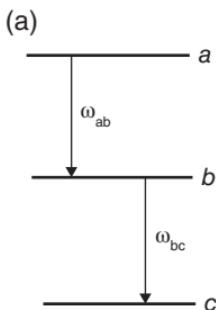
Figure 9.7 Schematic examples of two techniques to prepare a nuclear state with unequal populations of the internal magnetic substates: (a) correlating the sequential emission of two γ rays and (b) correlating the emission of a β-particle with a subsequent γ-ray (de Shalit and Feshbach (1974). Reproduced with the permission of John Wiley & Sons, Inc.).

is a very small energy. In this expression "g" is the gyromagnetic ratio or g factor for the state, and $\mu_n = e\hbar/2m_p c^2$ is the nuclear magneton. We should note that this energy splitting is much too small compared with the energy of a nuclear transition so we could not expect to directly observe different energy transitions with different angular distributions. Rather we can obtain unequal populations of the substates through the Boltzmann distribution of thermal energy when the sample is cooled to a temperature where $k_B T$ is small compared to the energy splitting. The typical temperature to maintain nuclear orientation in an external magnetic field is on the order of 10 mK. Cooling small samples to such low temperatures is possible, but it requires special techniques such as ^{3}He dilution refrigeration.

Sample Problem 9.6: Boltzmann Distribution and Nuclear Orientation

Determine the temperature at which $k_B T$ is equal to the energy level splitting for the metastable state of ^{123}Te at 247.6 keV in an external magnetic field of 4.0 Tesla. This state $I = 11/2$ decays by (M4) IT to the ground state 1/2 with a half-life of 119.7 days. The gyromagnetic ratio or g-factor for this state is 0.1685.

Solution

$$\Delta E_m = g I B_{ext} \mu_n = k_B T$$
$$T = \frac{g I B_{ext} \mu_n}{k_B}$$
$$T = (0.1685)(11/2)(4.0T)(5.05080 \times 10^{-27} J/T)/$$
$$1.380066 \times 10^{-23} J/K$$
$$T = 1.4 \times 10^{-3} \text{ K}$$

A much more common technique for observing angular correlations relies on detecting the direction of radiation from a process that feeds the excited state and then observing the angular distribution relative to that direction. As indicated in Figure 9.7, this process could be a γ-ray transition from a higher lying excited state, or it could be a β- or α-particle emitted by a parent nucleus prior to the γ-ray transition. The first particle provides the reference axis, but it must also introduce an unequal population of the magnetic substates of the intermediate state in order for the second transition to have an anisotropic angular distribution.

The angular distribution of the intensity of electromagnetic radiation is given by specific analytic functions written in terms of an angle, $W(\theta, m_I)$, relative to the quantization axis, Z, and the magnetic quantum number, m_I. The patterns depend on the order of the multipole (dipole, quadrupole, etc.), but they are the same for electric and magnetic transitions with the same order. For example, the angular distributions for dipole radiation are

$$W_{\text{dipole}}(\theta, m_I = 0) = \frac{3}{8\pi} \sin^2 \theta$$

$$W_{\text{dipole}}(\theta, m_I = +1) = \frac{3}{16\pi}(1 + \cos^2 \theta)$$

$$W_{\text{dipole}}(\theta, m_I = -1) = \frac{3}{16\pi}(1 + \cos^2 \theta)$$

A schematic representation of the dipole angular distributions is shown in Figure 9.8. First we should notice that these functions depend on only one angle, and thus they are cylindrically symmetric. Therefore, we will not find any asymmetry in radiation from systems with only two states, that is, $I = 1/2$, $m_I = \pm 1/2$. Notice also that the intensity of $m = 0$ for dipole radiation is exactly zero along the Z axis because the sine function becomes zero, whereas the $m = \pm 1$ distributions have nonzero minima perpendicular to the Z axis.

(a) z, $L = 1$, $\Delta m = 0$

(b) z, $L = 1$, $\Delta m = \pm 1$
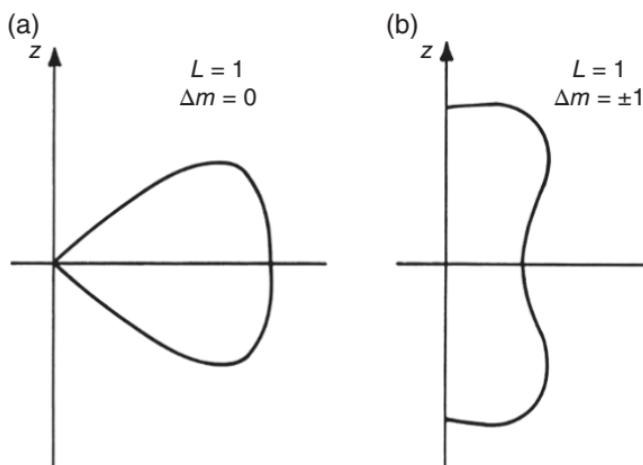
Figure 9.8 The angular distribution of dipole radiation for $\Delta m = 0$ (left) and $\Delta m = \pm 1$ (right) (Marmier and Sheldon (1969). Reproduced with the permission of Elsevier).
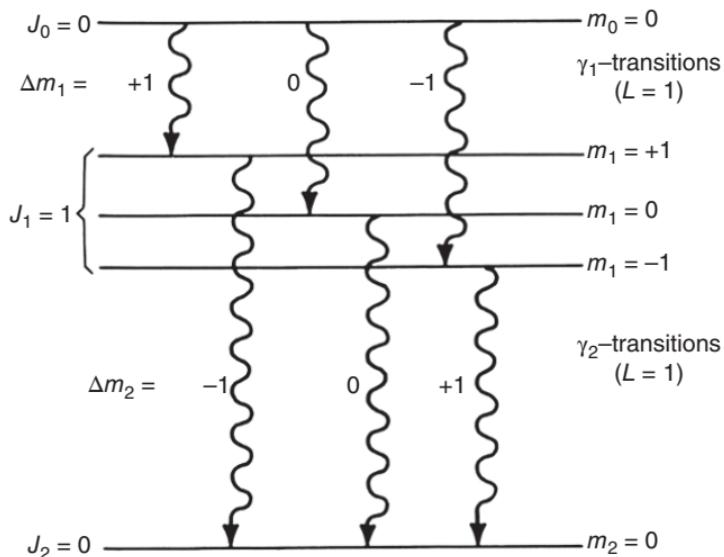
Figure 9.9 Schematic diagram of how angular correlations occur. The magnetic substates populated in a $\gamma_1\gamma_2$ cascade from a state with $J_0 = 0$ to $J_1 = 1$ to $J_2 = 0$. When γ_1 defines the Z axis, then the $m_1 = 0$ state cannot be fed, and one has only $\Delta m_1 = \pm 1$ and $\Delta m_2 = \mp 1$, causing γ_2 to have an anisotropic distribution relative to γ_1 (Marmier and Sheldon (1969). Reproduced with the permission of Elsevier).

Let us consider the specific case of the cascade of two electromagnetic dipoles from nuclear states with $J_0 = 0$ to $J_1 = 1$ to $J_2 = I_{gs} = 0$ as a specific example of the creation of an aligned system by a γ-ray cascade, shown in Figures 9.9 and 9.10. The energy level diagram is shown in Figure 9.9. The radiation pattern of the second photon will have the $(1 + \cos^2\theta)$ form relative to the direction of the first photon in this case. The fact that the radiation will not be isotropic can be seen from a classical as well as from a quantum mechanical standpoint. The simple definition that the Z axis is the direction of this first photon forces the observed photon to have $m_I = \pm 1$ because $W_{\text{dipole}}(\theta, m_I = 0) = 0$ at $\theta = 0$ and such a photon will not be observed along the Z axis. The first dipole transition from $J_0 = 0$ to $J_1 = 1$ will carry away one unit of angular momentum, and the angular momentum of the residual nucleus must be oriented in such a way as to be equal and opposite to that of the photon. Then to conserve angular momentum in the second transition, the next photon must also have $m_I = \mp 1$ and will follow the $(1 + \cos^2\theta)$ distribution relative to the first photon emitted along the Z axis. From a quantum mechanical standpoint, the argument depends simply on spin algebra. The only allowed magnetic substates for the initial and final states are $m_1 = m_2 = 0$ (because $J_0 = J_2 = 0$). The only allowed value for the multipolarity of both photons, $\ell_1 = \ell_2$, is one by the relation $|0 - 1| \leq \ell \leq (0 + 1)$. The coupling of the angular momentum of the photon with that of the initial state to create the intermediate state requires that
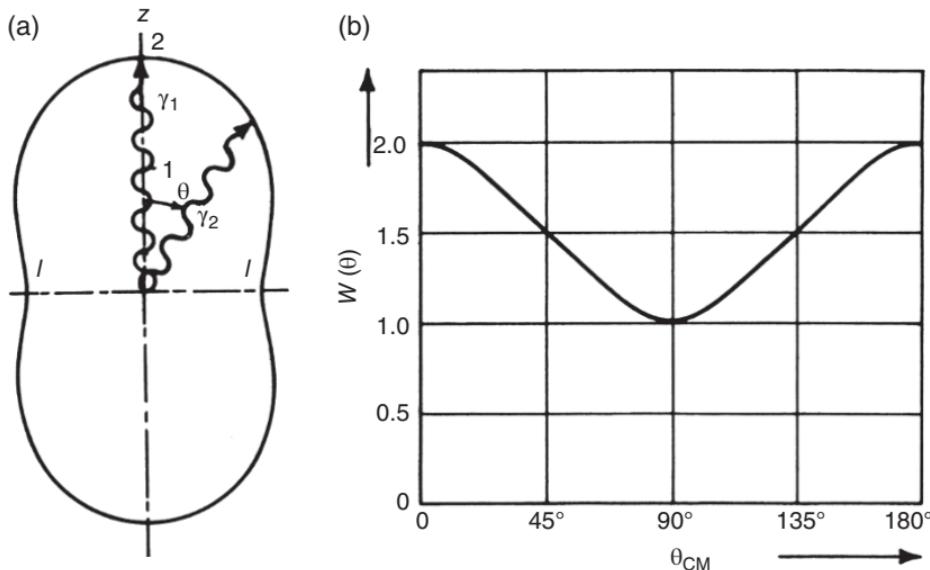
Figure 9.10 Schematic diagram of how angular correlations occur. The anisotropic distribution of γ_2 relative to γ_1 in the cascade shown in Figure 9.9 (Marmier and Sheldon (1969). Reproduced with the permission of Elsevier).

only allowed magnetic substate of $J_1 = 1$ be $m_1 = \pm 1$. Thus, both photons must have $m = \pm 1$ and follow the $(1 + \cos^2 \theta)$ distribution.

The angular distributions for γ-ray cascades have been worked out, but each case requires substantial and sophisticated algebra that will not be presented here. The general result is that the angular distributions can be written in terms of a sum of Legendre polynomials that depends on the multipolarities of the photons, ℓ_1, ℓ_2, and the spin of the intervening state. It is common to analyze the observed angular correlations in terms of a power series of $\cos \theta$ that is normalized with $W(\theta = 90°) = 1$ so that

$$W(\theta) = (1 + a_2 \cos^2 \theta + a_4 \cos^4 \theta + a_6 \cos^6 \theta + \cdots + a_{2L} \cos^{2L} \theta)$$

(9.28)

where the coefficients, a_2, a_4, and so on are fitted to the data and can be compared to predicted values for assumed values of J_0, J_1, J_2, and ℓ_1 and ℓ_2. The number of radiation patterns or angular distributions may seem extensive with these five variables, but there are certain rules that simplify the situation. The highest even power of the cosine function, $2L$, is determined by the smallest value of $2J_1$, $2\ell_1$, and $2\ell_2$ and is one unit less than the smallest value if the smallest of these three numbers is an odd number. For example, when $J_1 = 0$ or $1/2$ then $2L = 0$ and $W(\theta) = 1$ (a_2, etc. $= 0$); when $J_1 = 1$ then $2L = 2$ and $(1 + a_2 \cos^2 \theta)$. The theoretical coefficients for a few types of pure dipole and pure quadrupole transitions are given in Table 9.3.

Table 9.3 Angular Correlation Coefficients for Some $\gamma-\gamma$ Cascades with Pure Multipolarities.

$J_0(\ell_1); J_1(\ell_2); J_2$	a_2	a_4
0(1); 1(1); 0	1	0
1(1); 1(1); 0	−1/3	0
1(2); 1(1); 0	−1/3	0
2(1); 1(1); 0	1/13	0
3(2); 1(1); 0	−3/29	0
0(2); 2(2); 0	−3	4
1(2); 2(2); 0	−1/3	0
2(2); 2(2); 0	3/7	0
3(2); 2(2); 0	−15/13	16/13
4(2); 2(2); 0	1/8	1/24

Source: From (Evans (1955).

The third technique for establishing a reference axis for angular correlations can be applied to nuclear reactions when the direction of a particle involved in the reaction is detected. This direction provides a reference axis that can be related to the angular momentum axis, but each nuclear reaction has its own peculiarities and constraints on the angular momentum vector. For example, the direction of an α particle from a decay process that feeds an excited state can be detected as indicated in Figure 9.7, but, as is discussed in Chapter 7, the energetics of α decay are such that decay to excited states or decays with large orbital angular momenta are hindered and not very common. On the other hand, nuclear reactions can produce nuclei with large amounts of angular momenta with characteristic distributions. The motion of the center of mass provides a good reference that coincides with the direction of the initial beam for the usual case of a target at rest in the lab system. The angular momentum vector must lie in the plane perpendicular to the beam direction in compound nuclear reactions. The angular momentum vector is further confined in two-body scattering reactions to be normal to the plane containing the beam (or center or mass vector) and the two particles. The effects of angular momentum on nuclear reactions are discussed further in Chapter 10.

At this point we have established techniques to identify the multipolarity of a transition through its angular distribution. We still have the ambiguity of the parity of the electromagnetic wave, that is, whether it was produced by an electric or a magnetic transition in the nucleus. The parity of the radiation corresponds to the plane of polarization of the electromagnetic radiation. The polarization of the wave can be determined from knowledge of the direction

of the plane of the electric vector of the photons relative to the plane containing two coincident photons. The direction of the electron emitted in the Compton scattering process is sensitive to the direction of the electric vector of the incoming photon and has been used to determine the parity of electromagnetic transitions. Alternatively the number and type of conversion electrons emitted in the decay is also sensitive to the electric or magnetic nature of the radiation. Measurements of the conversion coefficients are also used to establish the character of the radiation.

9.7 Mössbauer Effect

We could imagine that the inverse of γ-ray emission from an excited nuclear state to the ground state might be possible if a nucleus in its ground state was bathed in sufficient photons that exactly correspond to the transition. A large difficulty with causing this absorption to take place is the relatively large amount of energy associated with individual nuclear transitions (MeV) compared with the amount of available (terrestrial) thermal energies (10^{-6} MeV). This inverse process can occur in two situations: (a) in nuclear reactions called Coulomb excitation that take place when heavy ions pass very near to large target nuclei (cf. Chapter 10) and (b) when there is a resonant absorption of a γ-ray emitted by nuclear de-excitation in another identical nucleus. The latter process is called the **Mössbauer Effect**, and the process requires some special conditions in order to take place. The energies of the nuclear states are very precise so that the resonant absorption or energy matching is very sensitive to the chemical environment of the nucleus. As we will see there are relatively few nuclei that are suitable for Mössbauer studies due to the requirements of a half-life that allows a high specific activity with a reasonable useful period and a single γ-ray transition, and the absorbing nucleus must be a stable isotope of an important/practical chemical element. The important examples are ^{57}Fe, ^{191}Ir, and ^{198}Hg.

The first nucleus in which the resonant absorption of photons was observed was ^{191}Ir. The excited states of this nucleus are fed by the electron capture decay of ^{191}Pt, one of which decays by a 129.43 keV M1 transition to the ground state. Now we can ask what will happen if we shine γ rays from a radioactive source of ^{191}Pt onto a set of stable ^{191}Ir nuclei? We could use an iridium foil because iridium only has two stable isotopes 191 (37.3%) and 193 (72.7%). Without careful preparation, the answer is that very few photons will be absorbed by the ^{191}Ir nuclei! The difficulty comes from the fact that in order to be absorbed, the γ ray will have to exactly match the energy of the transition. Remember that quantum mechanics dictates that the absorption of the γ ray will move the nucleus from its ground state to a single and specific excited state that has an exact energy. A single nucleus cannot absorb a random amount of energy. Several important effects shift the energy of the emitted photon, but first we could ask how

accurately do we have to match the energy of the state in order to be absorbed? This corresponds to the natural width of the state.

The measured half-life of the state is 89.4 ps, which corresponds to an energy width, Γ, or ΔE, due to the Heisenberg uncertainty principle of

$$\Gamma = \frac{\hbar}{\tau} = \hbar\lambda = \hbar \times \frac{\ln(2)}{t_{1/2}} = \frac{4.6 \times 10^{-16} \text{ (eV s)}}{t_{1/2} \text{ (s)}} \tag{9.29}$$

where τ is the mean life or the reciprocal of the decay constant $\lambda = \ln(2)/t_{1/2}$. In this case the energy width of the excited state is only the tiny amount of 5.1×10^{-6} eV, a factor of 2×10^{-10} less than the energy of the state. Such narrow widths are a general property of nuclear excited states that decay by γ-ray emission. Thus, the energy matching of the nuclear state and photon energy has to be incredibly exact for significant absorption to take place.

The linewidth of an observed transition is broadened by the random thermal motion of the nuclei that emit the photon. That is, the energies of photons emitted along the direction of thermal motion of the atom will be slightly higher than the average and vice versa for those emitted opposite. The value of the energy of a photon emitted by a moving source is shifted according to the expression:

$$E'_\gamma = E_{\gamma 0}(1 \pm \beta_x) \tag{9.30}$$

where $E_{\gamma 0}$ is the energy of the transition and $\beta_x = v_x/c$ is the familiar ratio of the velocity along the photon direction to the speed of light. As an upper limit, we could use the kinetic theory of gases and the Maxwell–Boltzmann velocity distribution to estimate the width of the velocity distribution for gaseous iron nuclei. (The motion of atoms in liquids and the vibrations of atoms in solids are smaller but not zero.) The Boltzmann (thermal) probability distribution for the kinetic energy of an atom, $P(KE)$, is always a decreasing exponential function, $P(KE) \propto e^{-mv^2/2k_B T}$, and it applies to the total kinetic energy and to the kinetic energy along one coordinate of a normal gas in a closed container. Solving the Doppler expression for v_x in terms of E'_γ

$$v_x = c\left[1 \mp \left(\frac{E'_\gamma}{E_{\gamma 0}}\right)\right] \tag{9.31}$$

and substituting that expression into the Boltzmann probability, we get

$$P(E'_\gamma) \propto e^{-mc^2[1\mp(E'_\gamma/E_{\gamma 0})]^2/2k_B T} \tag{9.32}$$

Selecting one sign for the direction, multiplying through, and collecting constants, we find

$$P(E'_\gamma) \propto e^{-mc^2\, E'^2_\gamma/(2E^2_{\gamma 0}k_B T)} \tag{9.33}$$

This expression shows that the distribution of emitted γ-ray energies follows a Gaussian distribution with a variance something like

$$\sigma^2 \approx \frac{E_{\gamma 0}^2 k_B T}{mc^2} \tag{9.34}$$

In the present example of ^{191}Ir excitation at room temperature, $k_B T = 0.025$ eV, $E_{\gamma 0} = 0.1294$ MeV, and $mc^2 = 191 * 931.5$ MeV which, when combined, give $\sigma \sim 7 \times 10^{-2}$ eV, which, although small and an upper limit for gaseous atoms, is still six orders of magnitude larger than the natural linewidth of the state. Therefore, it is not very easy to be able to actually observe the natural linewidth of a γ-ray emitting state. However, this broadening works in favor of the absorption of a photon because it allows the thermal motion to help match the energy of the whole system, nucleus in the atom, to the photon energy.

In addition, as we have already discussed, the emission of a photon induces a recoil by the nucleus in order to conserve momentum. The energy of the photon is less than the energy of the nuclear transition by the amount $T_r = E\gamma^2/(2mc^2)$. Notice that to conserve energy and momentum in the reverse process of γ-ray absorption, a nucleus initially at rest will recoil with the same value of the recoil energy after absorbing a photon. In the present example of ^{191}Ir, the recoil energy is $T_r = 4.7 \times 10^{-2}$ eV and is a similar magnitude to the thermal Doppler shift for a gas. We probably can expect the radioactive platinum atoms to be in a metal lattice so their motion would correspond to lattice vibrational motion and be somewhat less than that in a gas. The relative energy distributions expected for the emitted and absorbed photons are shown schematically in Figure 9.11 using the estimate of the thermal widths. Notice that the recoil energy moves the peaks apart and the thermal width provides only a partial overlap. It is these photons in the overlap region that have the proper energy to be absorbed; they must encounter a nucleus, of course, in order to actually be absorbed.

We might imagine that we could prepare a system that physically moves the source of the radiation toward the absorbing nuclei with sufficient speed that the Doppler shift compensates for the energy difference. Restricting the motion to the approaching direction, we can rearrange the previous expression to obtain the velocity in terms of the Doppler shift:

$$\Delta E = (E_\gamma' - E_{\gamma 0}) = E_{\gamma 0} \left(\frac{v_x}{c} \right) \tag{9.35}$$

The necessary velocity that would create a Doppler shift corresponding to twice the recoil energy is

$$\Delta E = 2\, T_r = \frac{2E_{\gamma 0}}{2mc^2} = E_{\gamma 0} \left(\frac{v_x}{c} \right)$$
$$\frac{v_x}{c} = \frac{E_{\gamma 0}}{mc^2} \tag{9.36}$$
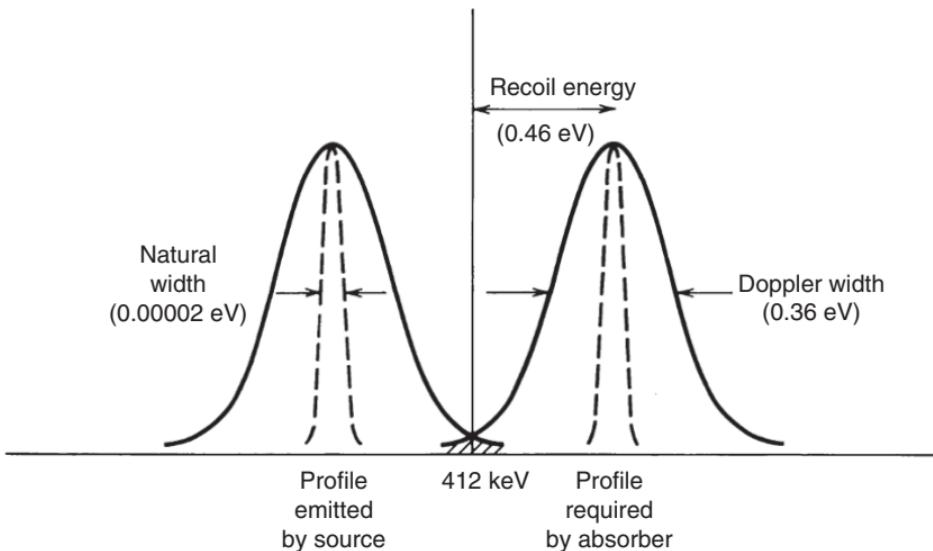
Figure 9.11 A schematic indication of the position and widths of the emitted and absorbed radiation corresponding to the 412 keV transition in ^{198}Hg (Krane (1988). Reproduced with the permission of John Wiley & Sons).

For the example of ^{198}Hg, in Figure 9.11, $\beta_x = 2.2 \times 10^{-6}$ or $v_x = 670$ m/s and corresponds to a kinetic energy of 0.92 eV. The magnitude of this difference is visible in Figure 9.11 as the separation between the two peaks and is about twice the thermal width. Such a high velocity is difficult to attain with any macroscopic, that is, physical radioactive source.
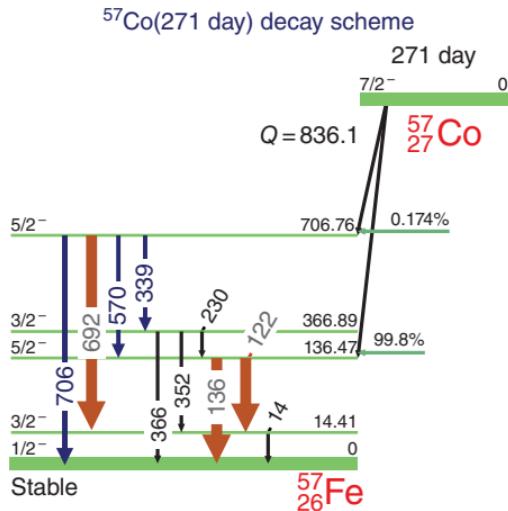
The Mössbauer effect relies on a very different technique for overcoming the energy mismatch of twice the recoil energy between nuclear emission and nuclear absorption. Notice that the recoil energies that we have calculated are small fractions of an electron volt per atom. You might recall that chemical bonds have energies on the order of a few electron volts per bond and may be stronger in some sense than the recoil effect from γ-ray emission in some cases. Mössbauer showed that the resonant emission/absorption of photons could be strongly enhanced by binding both the emitting atoms and the absorbing atoms into crystal lattices. In practice the emitter is produced by a β decay of a parent nuclide, that is, a different chemical element from the absorber; thus, two separate crystals are used. Due to the chemical bonds or the lattice energy of the crystal, the atom that absorbs the photon is held in place and the entire macroscopic, lattice "recoils" to conserve momentum. The mass of the entire lattice should be used to calculate the recoil velocity, but this mass is on the order of Avogadro's number larger than that of an atom so that there is effectively no recoil. One analogy is to compare the difference that you would feel if you hit a single stone with a bat compared with that you would feel if you hit the same stone if it were part of a cement wall in a concrete building.

The actual difference in the atomic case is orders of magnitude larger. Thus, with the atoms bound into the crystal lattice, the Doppler motion is limited to the vibrational motion of the atoms, and the linewidth shrinks essentially to the natural width of the state. In this case the energy of the emitted photon and the energy absorbed in the nuclear excitation overlap. The Mössbauer experiment is then to remove the overlap between the photon energies by moving one crystal lattice with respect to the other. The relative velocity is on the order of cm/s, which is, of course, much smaller than that necessary to compensate for the nuclear recoil. The resonance is then seen as a preferential absorption as a function of relative velocity between the emitter and absorber.

Notice that the Mössbauer effect is very sensitive to the energy of the nuclear state; changes on the order of 10^{-6} eV are readily detected. This is the level at which atomic orbitals can shift nuclear states through the penetration of electron density into the nucleus. As a first approximation we could imagine that the interaction of the electron wave function with the nucleus will depend on the size, that is, radius, of the nuclear wave function. The nuclear wave function for the excited state will be (slightly) different, and thus the penetration of the electrons into the excited nucleus will be slightly different. Thus, the transition energy will be different, albeit by a very small amount, from the pure nuclear transition that would occur in a bare nucleus (no electrons). When the chemical state or environment of both the absorber and the emitter are the same, the transition will occur at a definite but different energy, but one could not perform the measurement of the pure nuclear transition (without electrons). Finally, when the chemical environment of the emitter and absorber is different, then the transition will occur at a new energy. The shift of the energy of the resonance between the identical environments and different environments is called the chemical shift in analogy to NMR work. In practice, the chemical shift in the Mössbauer resonance lines provides a probe for the overall chemical environment of the absorbing nuclei.

The most extensively used nuclide for Mössbauer studies at present is ^{57}Fe due to the very low energy of the nuclear transition. Let us consider the low-lying excited states of ^{57}Fe shown in Figure 9.12. The first excited state in ^{57}Fe lies at only 14.4125 keV, and it decays to the ground state with a half-life of 98 ns. As shown in Figure 9.12, the β decay of the parent nucleus, ^{57}Co, feeds this excited state of the daughter nucleus so that we can imagine producing a strong source of the low-energy γ rays. As shown in the example calculation in the following text, the energy of this transition is so low that the recoil energy is also quite low and comparable with the thermal energy. Thus, studies can be performed with the source bound in a crystal lattice, but the absorber can be in solution.

Figure 9.12 Energy level diagram of two members of the $A = 57$ mass chain. ^{57}Co decays to excited states of ^{57}Fe, which result in the M1 transition from the 3/2$^-$ state at 14.41 keV to the 1/2$^-$ ground state. (*See insert for color representation of the figure.*)

^{57}Co(271 day) decay scheme

Sample Problem 9.7: Mössbauer Linewidth and Velocity

Calculate the natural linewidth of the state at 14.4 keV in ^{57}Fe given that $t_{1/2} = 98$ ns. Then calculate the velocity of the source lattice that would correspond to twice the natural width and would lie outside the Mössbauer resonance effect.

Solution

$$\Delta E = \Gamma = \hbar/\tau = \hbar \left(\frac{\ln(2)}{t_{1/2}} \right)$$

$$\Delta E = \Gamma = \frac{4.135 \times 10^{-15} \text{ eV s}}{2\pi} \left(\frac{\ln(2)}{98 \times 10^{-9} \text{ s}} \right)$$

$$\Delta E = \Gamma = 4.65 \times 10^{-9} \text{ eV}$$

The velocity that would correspond to twice this energy can be found from the nonrelativistic expression for the kinetic energy:
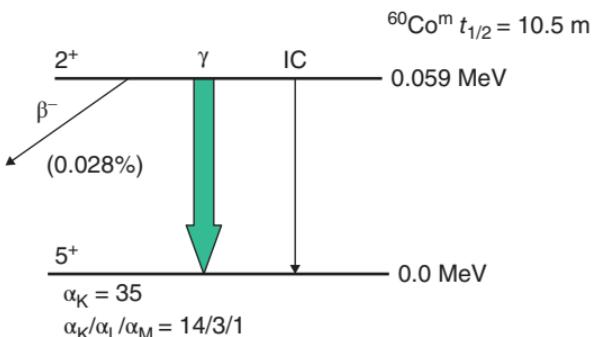
$$\text{KE} = \frac{1}{2} m v_x^2 = 2\Gamma$$

$$\frac{v_x}{c} = \sqrt{\frac{4\Gamma}{mc^2}} = \sqrt{\frac{4 \times 4.65 \times 10^{-9} \text{ eV}}{57 \times 931.5 \times 10^6 \text{ eV}}}$$

$$\frac{v_x}{c} = 5.92 \times 10^{-10} \Rightarrow v_x = 0.178 \text{ m/s}$$

Problems

9.1 ^{195}Pt has a ground-state spin and parity of $1/2^-$, with excited states at 0.029 MeV ($3/2^-$) and 0.130 MeV ($5/2^-$). Would you expect the 5/2 level decay primarily to the $3/2^-$ level or to the $1/2^-$ level? Why? What is the transition multipolarity?

9.2 The $1/2^-$ isomeric state of ^{95}Nb decays to the $9/2^+$ ground state by means of an M4 transition. The half-life of the isomeric state is 90 h, while the half-life of the ground state is 35 days ($\alpha_{total} = 4.5$). Calculate the partial half-life for the γ-ray decay of the isomeric state.

9.3 Consider the following decay scheme for ^{60}Co^m shown schematically in the following:

- Classify the most likely multipolarity for the γ-ray decay of ^{60}Co^m.
- Calculate the partial decay constants for β^-, internal conversion, and γ-ray decay.
- What is the width of ^{60}Co^m in eV?

9.4 ^{52}Mn has an excited state at 0.377 MeV above the ground state. This excited state decays to the ground state with $t_{1/2} = 21.1$ min. The $J\pi$ values of initial excited state and the ground state are 2^+ and 6^+, respectively. (a) What is the lowest multipole order that can contribute to the transition? Calculate the decay constant and compare it to the experimental value. (b) Suppose we wanted to check whether, in the initial state, there was any mixture of other angular momenta than 2. Set a rough upper limit to the amplitude of a $J = 1$ component of the initial

state, using as data only the measured half-life and transition energy. Assume parity conservation.

9.5 Consider ^{10}B. The ground state has $J\pi = 3^+$, and the excited states, in order of increasing excitation energy, are $1^+, 0^+, 1^+, 2^+, 3^+, 2^-, 2^+ \ldots$ (a) Explain why ^{10}B is stable even though it is an odd–odd nucleus. (b) The first excited state is at 0.72 MeV, and the second excited state is at 1.74 MeV. What are the energies, multipolarities, and relative intensities of the γ rays that are emitted in the de-excitation of the second excited state?

9.6 A 64 d isomer of an even Z, odd A nucleus with $A \sim 90$ occurs at 105 keV above the ground state. The isomeric state decays 10% by EC and 90% by IT. If the internal conversion coefficient $\alpha_{total} = 50$, what is the γ-ray lifetime and the most likely multipolarity of the isomeric transition? If this is a magnetic transition and the isomeric state has $J\pi = 1/2^-$, what is the $J\pi$ of the ground state?

9.7 ^{51}V has a ground-state spin and parity of $7/2^-$ with excited states at 0.3198 MeV ($5/2^-$) and at 0.930 MeV ($3/2^-$). What is the energy and multipolarity of the principal γ-ray that de-excites each excited state?

9.8 The ground state of ^{61}Ni has $J\pi = 3/2^-$. ^{61}Co ($t_{1/2} = 1.65$ h) decays by β^- emission with $E_{max} = 1.24$ MeV to a 0.067 MeV excited state of ^{61}Ni. The 0.067 MeV transition has $\alpha_K = 0.10$, $\alpha_K/\alpha_L = 8$. The branching ratio for the transition from ^{61}Co to the ^{61}Ni ground state is 10^{-6}. What is $J\pi$ for the ground state of ^{61}Co and the first excited state (0.067 MeV) of ^{61}Ni?

Bibliography

E.U. Condon and H. Odishaw, *Handbook of Physics*, 2nd Edition (McGraw-Hill, New York, 1967).

A. de Shalit and H. Feshbach, *Theoretical Nuclear Physics*, Vol. 1 (John Wiley and Sons, Inc., New York, 1974).

R.D. Evans, *The Atomic Nucleus* (McGraw-Hill, New York, 1955).

P. Marmier and E. Sheldon, *Physics of Nuclei and Particles*, Vol. 1 (Academic, New York, 1969).

M.A. Preston, *Physics of the Nucleus* (Addison-Wesley, Reading, MA, 1962).

Some useful general references on γ-ray decay include the following textbooks and monographs:

A. Bohr and B. Mottelson, *Nuclear Structure*, Volume 1 (Benjamin, New York, 1969).

R. Evans, *The Atomic Nucleus* (McGraw-Hill, New York, 1953).

K.S. Krane, *Introductory Nuclear Physics* (John Wiley and Sons, Inc., New York, 1988).

S.S.M. Wong, *Introductory Nuclear Physics*, 2nd Edition (John Wiley and Sons, Inc., New York, 1998).

10

Nuclear Reactions

10.1   Introduction
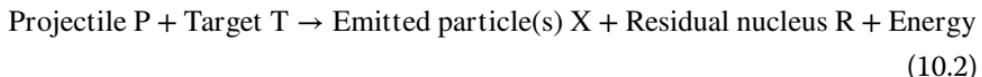
The study of nuclear reactions is important for a number of reasons. Progress in the understanding of nuclear reactions has occurred at a faster pace, and generally a higher level of sophistication has been achieved, compared with similar studies of chemical reactions. Individual nuclear reactions can be observed in the laboratory and the energy balance, and the effects of conservation laws can be clearly visible. The approaches used to understand nuclear reactions are of value to any chemist who wishes a deeper insight into chemical reactions. There are certain nuclear reactions that play a preeminent role in the affairs of man and our understanding of the natural world in which we live. For example, life on earth would not be possible without the energy provided to us by the sun. The sun's energy is released in the nuclear reactions that build up helium from hydrogen. Other astrophysical systems and explosions build up the heavier elements. For better or worse, the nuclear reactions, fission and fusion, are the basis for nuclear weapons, which have shaped much of the geopolitical dialog for the last 75 years. Apart from the intrinsically interesting nature of these dynamic processes, their practical importance would be enough to justify their study. In this chapter we will focus on nuclear reactions that occur between a projectile and a target; in the following chapter, we will focus on the fission process.

For an efficient and effective discussion of nuclear reactions, we must understand the notation or jargon that is widely used to describe them. Let us begin by considering one of the first nuclear reactions to be studied:

$$^{4}\text{He} + {}^{14}\text{N} \rightarrow {}^{17}\text{O} + {}^{1}\text{H} + Q \tag{10.1}$$

Here, an α particle reacts with a nitrogen nucleus-producing oxygen, a proton, and some energy, Q. Most nuclear reactions are studied by inducing a collision between two nuclei where the heavier reacting nucleus is at rest (the target nucleus) while the other nucleus (the projectile nucleus) is in motion, and this is called "normal kinematics." Exceptions to this normal situation occur both

in nature and in the laboratory where both the colliding nuclei are in motion relative to one another before the collision, but let us stick to the scenario of a moving projectile and a stationary target nucleus for the present. Such nuclear reactions might be described generically as

Projectile P + Target T → Emitted particle(s) X + Residual nucleus R + Energy

$$(10.2)$$

For example, the reaction introduced earlier might occur by bombarding ^{14}N gas with α particles to generate an emitted particle, a proton, and a residual nucleus ^{14}O. A shorthand way to denote such reactions is, for the general case

$$T(P, x)R \tag{10.3}$$
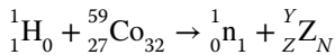
or for the specific example discussed earlier:

$$^{14}N(^{4}He, ^{1}H)^{17}O \tag{10.4}$$

In a nuclear reaction moderated by the strong force in contrast to the weak force, there is conservation of the number of protons and neutrons (and thus the number of nucleons). Thus the total number of neutrons (protons) on the left and right sides of the equations must be equal. There is also conservation of energy, momentum, angular momentum, and parity, which will be discussed later.

Sample Problem 10.1: Balancing Nuclear Reactions

Consider the reaction ^{59}Co(p, n). What is the product of this reaction?

$$^{1}_{1}H_{0} + ^{59}_{27}Co_{32} \rightarrow ^{1}_{0}n_{1} + ^{Y}_{Z}Z_{N}$$

Solution

On the left side of the equation, we have $27 + 1$ protons. On the right side we have $0 + Z$ protons where Z is atomic number of the product. Obviously $Z = 28$ or the element Ni. On the left hand side, we have $59 + 1$ nucleons, and on the right side, we must have $1 + Y$ nucleons so that $Y = 59$. Thus, the product of this nuclear reaction is ^{59}Ni.

10.2 Energetics of Nuclear Reactions

Consider the T(P, x)R reaction with only two products. Neglecting electron binding energies, we have, for the energy balance in the reaction,

$$m_{P}c^{2} + T_{P} + m_{T}c^{2} = m_{R}c^{2} + T_{R} + m_{x}c^{2} + T_{x} \tag{10.5}$$

where T_i is the kinetic energy of the i-th particle and m_i represents the mass energy of the i-th species. Note that since R and x may be complex nuclei, they could be formed in excited states so that the values of m may be different than the ground state masses. The Q value of the reaction is defined as the difference in mass energies of the product and reactants, that is,

$$Q = \left[m_P + m_T - m_x - m_R \right] c^2 = T_x + T_R - T_P \tag{10.6}$$

Note that if Q is positive, the reaction is *exoergic*, while if Q is negative, the reaction is *endoergic*. Thus the sign convention for Q is exactly the opposite of the familiar ΔH used in chemical reactions. Note that a necessary but not sufficient condition for the occurrence of a nuclear reaction is that

$$Q + T_P > 0 \tag{10.7}$$

Q is an important quantity for nuclear reactions. If the masses of both the products and reactants are known (see, e.g., the Appendices), the Q value can be calculated using the mass excess as
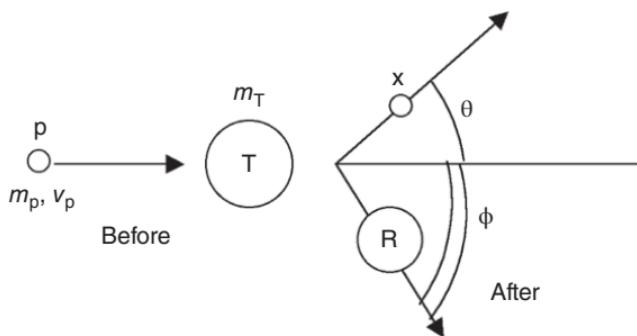
$$Q = \Delta(\text{Projectile}) + \Delta(\text{Target}) - \Sigma\, \Delta(\text{Products}) \tag{10.8}$$

The Q value can be measured by measuring the masses or kinetic energies of the reactants and products in a nuclear reaction. However, we can show, using conservation of momentum, that only T_x and the angle θ of x with respect to the direction of motion of P suffice to determine Q if there are only two products in a so-called two-body reaction.

In the laboratory system, a typical two-body nuclear collision can be depicted as shown in Figure 10.1. Note that all of the reactants and products from this type of reaction lie in one plane. Conserving momentum in the horizontal direction parallel to v_P, we can write

$$m_P v_P = m_x v_x \cos\theta + m_R v_R \cos\phi \tag{10.9}$$

Figure 10.1 Schematic diagram of the kinematics in a two-body nuclear reaction.

Applying conservation of momentum in the vertical direction (perpendicular to v_P), we have

$$0 = -m_x v_x \sin\theta + m_R v_R \sin\phi \tag{10.10}$$

where m_i and v_i are the mass and velocity of the i-th species. If we remember that the momentum $p = mv = (2m_T E_T)^{1/2}$, we can substitute in the earlier equation and get

$$(m_P T_P)^{1/2} - (m_x T_x)^{1/2} \cos\theta = (m_R T_R)^{1/2} \cos\phi$$
$$(m_x T_x)^{1/2} \sin\theta = (m_R T_R)^{1/2} \sin\phi \tag{10.11}$$

Squaring and adding the equations, we have

$$m_P T_P - 2(m_P T_P m_x T_x)^{1/2} \cos\theta + m_x T_x = m_R T_R \tag{10.12}$$

Previously we had said that $Q = T_x - T_P - T_R$. Plugging in this definition of Q and the value of T_R we have just calculated, we get what is called the *Q-value equation*
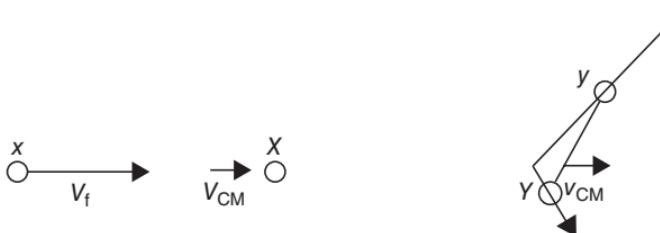
$$Q = T_x \left(1 - \frac{m_x}{m_R}\right) - T_P \left(1 - \frac{m_P}{m_R}\right) - \frac{2}{m_R} \left(m_P T_P m_x T_x\right)^{1/2} \cos\theta \tag{10.13}$$

What does the Q-value equation say? It says that if we measure the kinetic energy of the emitted particle x and the angle at which it is emitted in a two-body reaction and we know the identities of the reactants and products of the reactions, then we can determine the Q value of the reaction. In short, we can measure the energy release for any two-body reaction by measuring the properties of one of the products. If we calculate the Q value of a reaction using a mass table, then we can turn this equation around to calculate the energy of the emitted particle using the equation

$$T_x^{1/2} =$$
$$\frac{(m_P m_x T_P)^{1/2} \cos\theta \pm \left\{m_P m_x T_P \cos^2\theta + (m_R + m_x)[m_R Q + (m_R - m_P)T_P]\right\}^{1/2}}{m_R + m_x} \tag{10.14}$$

For additional insight, let us now consider the same reaction as described in the center of mass (CM) coordinate system. In the CM system the total momentum of the particles is zero, before and after the collision. The reaction as viewed in both the laboratory and CM system is shown in Figure 10.2.
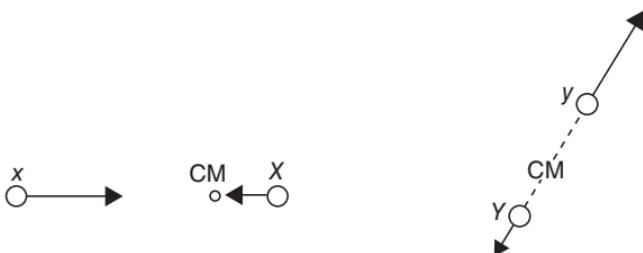
The kinetic energy of the cm is $T_{CM} = (m_P + m_T)v_{CM}^2/2$ where $v_{CM} = v_P m_P/(m_P + m_T)$ is the speed of the cm. Then substituting in the earlier equation, we find that

(a) Before collision   (b) After collision

As seen in the laboratory

(c) Before collision   (d) After collision

As seen from the center of mass

Figure 10.2 Schematic diagram of the kinematics in a two-body nuclear reaction as seen in the laboratory and center of mass systems.

$$T_{CM} = \frac{1}{2}(m_P + M_T)\left[\frac{v_P m_P}{m_P + m_T}\right]^2 = \frac{1}{2}m_P v_P^2\left[\frac{m_P}{m_P + m_T}\right] \qquad (10.15)$$
$$= T_{lab}\left[\frac{m_P}{m_P + m_T}\right]$$

where T_{lab} is the kinetic energy in the lab system before the reaction, that is,

$$T_{lab} = \frac{1}{2}m_P v_P^2 \qquad (10.16)$$
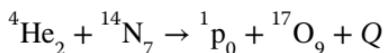
The kinetic energy carried in by the projectile, T_{lab}, is not fully available to be dissipated in the reaction. Instead, an amount, T_{CM}, must be carried away by the motion of the CM. Thus, the available energy to be used (dissipated) in the collision is only $T_{lab} - T_{CM} \equiv T_0 = [m_T/(m_T + m_P)]T_{lab}$. The energy available for the nuclear reaction is $Q + T_0$. To make an endothermic reaction go, the sum $Q + T_0$ must be ≥ 0. Rearranging a few terms in the equation, the condition for having the reaction occur is that

$$T_P \geq -Q\frac{m_P + m_T}{m_T} \qquad (10.17)$$

This minimum kinetic energy that the projectile must have to make the reaction go forward is called the *threshold energy* for the reaction.

Sample Problem 10.2: Threshold Energy

What is the threshold energy for the $^{14}N(\alpha, p)$ reaction?

$$^{4}He_2 + {}^{14}N_7 \rightarrow {}^{1}p_0 + {}^{17}O_9 + Q$$

Solution

$$Q = (m_\alpha + m_{14-N} - (m_p + m_{17-O}))c^2$$
$$Q = \Delta_\alpha + \Delta_{14-N} - (\Delta_p + \Delta_{17-O})$$
$$Q = 2.425 + 2.863 - 7.289 - (-0.809) \text{ MeV} = -1.19 \text{ MeV}$$
$$T_\alpha = -(-1.19 \text{ MeV}) \times \frac{4.0026 + 14.0031}{14.0031} = +1.53 \text{ MeV}$$

10.3 Reaction Types and Mechanisms

Nuclear reactions, like chemical reactions, can occur via different reaction mechanisms. Weisskopf has presented a simple conceptual model (Fig. 10.3) for illustrating the relationships between the various nuclear reaction mechanisms.

Consider a general nuclear reaction of the type *A (a, b) B* where the projectile is limited to a nucleon (p or n), and also bear in mind that for some cases, the product nuclei b and B could be identical to a and A. As the projectile nucleon a moves near the target nucleus A, it will have a certain probability of interacting via the nuclear force field of A, causing it to change direction but not to lose any energy: $Q = 0$. This reaction mechanism is labeled *shape elastic scattering* in Figure 10.3. If shape elastic scattering does not occur, then the projectile nucleon may interact further with A via a two-body collision between the projectile and some nucleon inside A, raising the nucleon in A to an unfilled level: $Q \leq 0$. If the struck nucleon leaves the nucleus and the projectile is captured, a *direct reaction* is said to have occurred. If the struck nucleon does not leave the nucleus but the projectile does, then *compound elastic and inelastic scattering* occurred, the name depending on the Q value. Further two-body collisions may occur, and eventually the entire kinetic energy of the projectile nucleus may be distributed among the a + A nucleons, leading to the formation of a compound nucleus (CN) with an excitation energy given by the combination of the Q value and kinetic energy of the projectile above the threshold energy (discussed earlier). The complicated set of interactions leading to the formation of the CN that occur inside the CN cannot be followed in detail, and, loosely speaking, the CN "forgets" its mode of formation, and its subsequent breakup or decay only depends on the
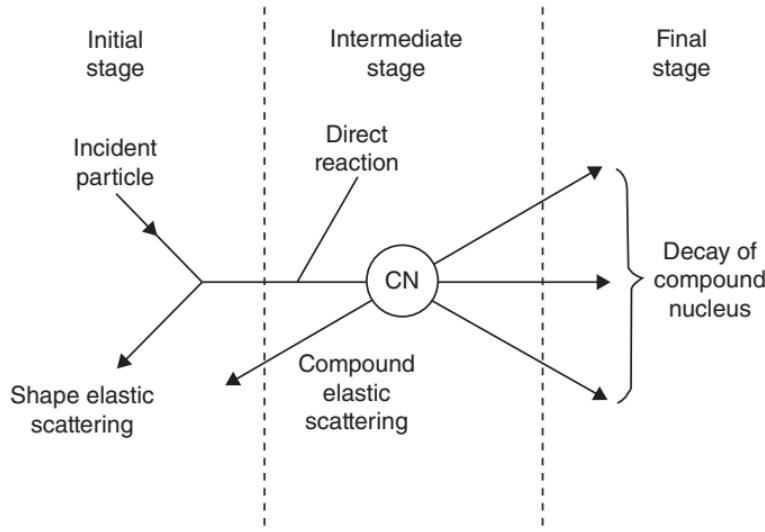
Figure 10.3 Conceptual view of the stages of a nuclear reaction (Weisskopf (1959). Reproduced with the permission of American Physical Society).

excitation energy, angular momentum, and so on, of CN and not on the nature of the projectile and target nuclei. The CN may decay into various reaction products that are unlike the projectile and target nuclei. We shall spend much of this chapter discussing these reaction mechanisms and some others not yet mentioned. But before doing so, let us see what general properties of nuclear reactions we can deduce from relatively simple arguments about the sizes of nuclei.

10.4 Nuclear Reaction Cross Sections

Consider the situation illustrated in Figure 10.4 where a beam of projectile nuclei of intensity Φ_0 particles per second is incident upon a thin foil of target nuclei with the result that the beam is attenuated by reactions in the foil such that the transmitted intensity is Φ particles per second.

We can ask what fraction of the incident particles disappear from the beam, that is, in some way react, in passing through the foil. Let us assume the beam intersects an area A (cm^2) on the foil. We can then assert that the fraction of beam particles that is blocked (reacts) by the nuclei is the **fraction** of the area A that is covered by the target nuclei.

If the foil contains ρ_n atoms/cm^3, where the foil thickness is dx(cm), then the **area** that is covered by nuclei is ρ_n atoms/cm$^3 \times dx$(cm) $\times A$(cm^2)$\times$ (the effective area subtended by one atom) (cm^2/atom).
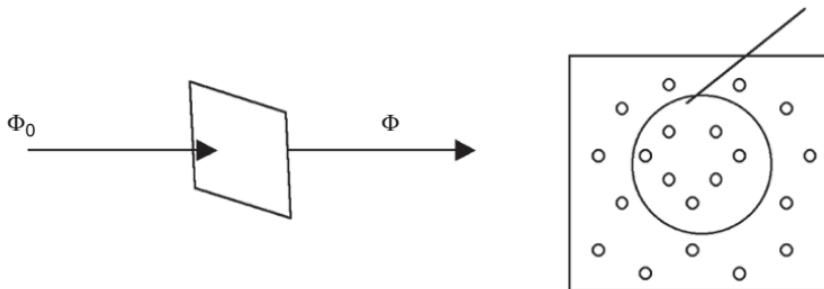
Figure 10.4 Schematic diagram showing the attenuation of an incident projectile beam in a thin foil by scattering centers.

This latter term, the effective area subtended by one atom, is called the **cross section**, σ, for the reaction under study. Then the fraction of the area A that is blocked is $\rho_n dx\sigma$. If we say the number of projectile nuclei incident on the foil is the flux Φ and the number absorbed per unit time is $\Delta\Phi$, then we have

$$\Delta\Phi = -\Phi\rho_n dx\sigma \tag{10.18}$$

where the minus sign indicates that the beam intensity is decreasing as the beam propagates through the foil. Expressing the earlier equation as a differential, we get

$$-d\Phi = \Phi\rho_n dx\sigma \tag{10.19}$$

$$\frac{d\Phi}{\Phi} = -\rho_n\sigma dx \tag{10.20}$$

This simple differential equation can be solved by integration:
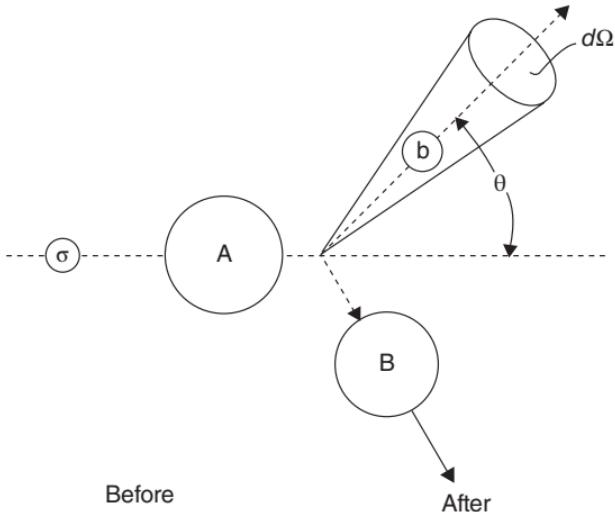
$$\int_{\Phi_0}^{\Phi_{\text{trans}}} \frac{-d\Phi}{\Phi} = -\rho_n\sigma \int_0^x \mathrm{d}x$$

$$\ln\left(\frac{\Phi_{\text{trans}}}{\Phi_0}\right) = -\rho_n\sigma x$$

$$\Phi_{\text{trans}} = \Phi_0 e^{-\rho_n\sigma x}$$

which is the familiar exponential attenuation of the incident projectile beam (and have thus derived a form of the Lambert–Beer law). The number of reactions that are occurring is the difference between the initial and transmitted flux, that is,

$$\left(\Phi_{\text{initial}} - \Phi_0\right) = \Phi_0\left(1 - \exp^{-\rho_n\sigma x}\right) \tag{10.21}$$

The foregoing discussion relied only on the *attenuation* of the incident beam and thus refers to all reactions and is called the *total reaction cross section*. In many cases, we are interested in only one of several reactions that may be taking

Figure 10.5 Schematic diagram of a typical experimental setup in the laboratory frame.

place. We can measure and refer to the cross section for that particular reaction, which will be some fraction of the total reaction cross section. In addition, we may be interested in not only a specific product but also a particular product moving in a particular direction relative to the direction of the projectile beam (see Fig. 10.5 for a sketch of a typical experimental measurement). In this case, we can speak of a differential cross section or the cross section per unit solid angle $d\sigma/d\Omega$. For a thin target, we have

$$\frac{dN}{d\Omega} = \Phi\rho_n \left(\frac{d\sigma}{d\Omega} \right) dx \tag{10.22}$$

where $dN/d\Omega$ is the number of particles detected moving in a particular direction per unit solid angle, $d\Omega$. The total cross section, σ, is given by integration over all space, which, written in terms of spherical coordinates, is

$$\sigma = \int_0^{2\pi} \int_0^{\pi} \frac{d\sigma}{d\Omega} \sin\theta \, d\theta \, d\phi \tag{10.23}$$

Be aware of the distinction between the flux Φ earlier and the azimuthal angle ϕ in this expression.

The description given earlier is appropriate for work at accelerators, where one has a beam of particles that is generally smaller in diameter than the target. In this case, the beam intensity Φ is given in particles per second, and the areal target density ρ_n is given in atoms per square centimeter. In a nuclear reactor, we immerse a small target in a sea of neutrons. In this case, the neutron flux Φ represents the number of neutrons passing through the target per square centimeter per second, and N is the total number of atoms in the target. Otherwise the arithmetic is the same. For charged particles from an accelerator, the beam

intensity is usually measured as a current. Thus, for a beam of protons with a current of 1 μA, we have

$$\Phi = 1 \,\mu\text{A} \left(\frac{10^{-6} \,\text{C/s}}{\mu\text{A}} \right) \left(\frac{1 \,\text{proton}}{1.602 \times 10^{-19} \,\text{C}} \right) \tag{10.24}$$
$$= 6.24 \times 10^{12} \,\text{protons/s}$$

For a beam of some other ion with charge q, one simply divides by the charge on the ion to get the projectile beam intensity. Thus, for a beam of 4 μA of Ar^{17+} ions, we have

$$\Phi = 4 \,\mu\text{A} \left(\frac{10^{-6} \,\text{C/s}}{\mu\text{A}} \right) \left(\frac{1 \,\text{ion}}{17 \times 1.602 \times 10^{-19} \,\text{C}} \right) = 1.47 \times 10^{12} \,\text{ions/s} \tag{10.25}$$

To put the intensities of beams of differing charge states on the common footing of particles/s, it is common to quote charged-particle beam intensities in units of *particle microamperes* or *particle nanoamperes* where, for example, 1 particle microampere $= 6.24 \times 10^{12}$ ions/s.

It is easy to calculate the number of product nuclei produced during an irradiation, N. If we assume the product nuclei are stable, then the number of nuclei produced is simply the rate of production, R, times the length of the irradiation, t. For a thick target irradiation, we have

$$N = \Phi(1 - \exp^{-\rho_n \sigma \Delta x}) \, t \tag{10.26}$$

For a thin target and Δx is small, we can expand the exponential function to get

$$N = \phi \left(-\rho_n \sigma dx \right) t \tag{10.27}$$

But, what if the products are radioactive? Then some of the product nuclei will decay during the irradiation. In this case, we can set up the familiar differential equations

$$\frac{dN}{dt} = (\text{Rate of production}) - (\text{Rate of decay})$$
$$\frac{dN}{dt} = (\Phi \rho_n \sigma \Delta x) - \lambda N$$
$$\frac{dN}{(\Phi \rho_n \sigma \Delta x) - \lambda N} = dt$$

Multiplying by λ to get a decay rate and rearranging

$$\frac{d(\lambda N)}{\lambda N - (\Phi \rho_n \sigma \Delta x)} = -\lambda dt \tag{10.28}$$

On integration one gets

$$\ln(\lambda N - (\Phi\rho_n\sigma\Delta x)|_0^N = -\lambda t|_0^t$$

$$\frac{\lambda N - (\Phi\rho_n\sigma\Delta x)}{-(\Phi\rho_n\sigma\Delta x)} = \exp^{-\lambda t}$$

$$A = \Delta N = (\Phi\rho_n\sigma\Delta x)(1 - \exp^{-\lambda t})$$

where A is the disintegration rate of product nuclei (i.e., the activity) at the end of the irradiation. The number of product nuclei, N, present at the end of the irradiation is A/λ or

$$N = \frac{\Phi\rho_n\sigma\Delta x}{\lambda}\left(1 - \exp^{-\lambda t}\right) \tag{10.29}$$

The variation of this function with time is shown in Figure 10.6. Note that in the limit of an infinitely long irradiation, $e^{-\lambda t} \to 0$, and thus the activity present becomes $\Phi\rho_n\sigma\Delta x$, which is called the *saturation activity*. Note also that for very short times (compared with the half-life of the product nuclei), $e^{-\lambda t} \to 1 - \lambda t + \cdots$. Thus, the activity increases approximately linearly with time at the beginning. In general, we note that we achieve one-half of the saturation activity after an irradiation of one half-life, three-quarters of the saturation activity after irradiating two half-lives, seven-eighths of the saturation activity after irradiating three half-lives, and so on. Thus, it does not generally pay to make the irradiation longer than 2–3 half-lives. (This effect can be used to find the optimal length of an irradiation to maximize the yield of the product of interest relative to the other reaction products that might be present.)
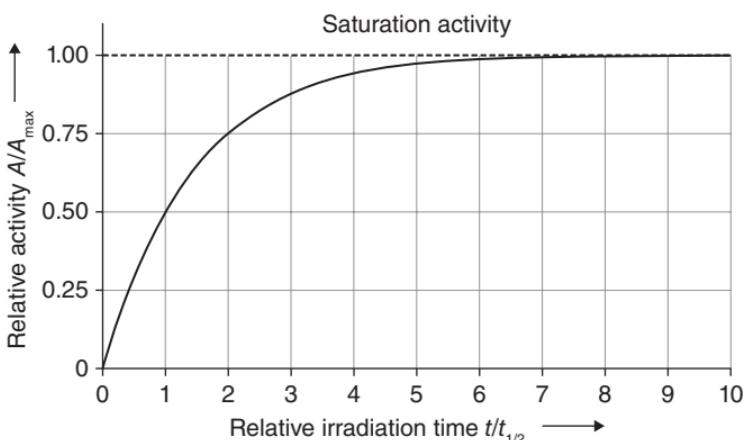
Figure 10.6 Temporal variation of the product activity during a constant irradiation.

Sample Problem 10.3: Radioactive Product of Reaction

Calculate the activity of ^{254}No ($t_{1/2}$ = 55 s) produced in a 1-min irradiation of ^{208}Pb by ^{48}Ca. Assume the ^{208}Pb target thickness is 0.5 mg/cm²; the ^{48}Ca beam current is 0.5 particle microamperes, and the ^{208}Pb(^{48}Ca, 2n) reaction cross section is 3.0 µb.

Solution

$$A = \Phi N \sigma (1 - e^{-\lambda t})$$

$$\Phi = \frac{0.5 \times 10^{-6} \text{ C/s}}{1.602 \times 10^{-19} \text{ C/ion}} = 3.12 \times 10^{12} \text{ ions/s}$$

$$N = (0.5 \times 10^{-3} \text{ g/cm}^2) \frac{6.02 \times 10^{23} \text{ /mol}}{208 \text{ g/mol}} = 1.44 \times 10^{18} \text{ /cm}^2$$

$$\sigma = 3 \times 10^{-6} \, b \times 10^{-24} \text{ cm}^2/b = 3 \times 10^{-30} \text{ cm}^2$$

$$t = 60 \text{ s}, \quad \lambda = \frac{\ln(2)}{55 \text{ s}} = 1.26 \times 10^{-2} \text{ /s}$$

$$A = 7.2 \text{ /s}$$

Let us consider what else we can learn about cross sections from other general considerations. Consider the reaction of a neutron (an uncharged particle) with a nucleus as shown in Figure 10.7. When the neutron makes a grazing collision with the nucleus, the impact parameter b can be taken as the sum of the radii of the neutron and the target nucleus. Thus, the geometrical cross section can be written as

$$\sigma \approx \pi(R + r')^2 = \pi r_0^2 (1 + A_T)^{2/3} \tag{10.30}$$

where r' is the radius of the neutron. Using classical mechanics to describe this problem, we can write the orbital angular momentum ℓ as

$$\ell_{\text{classical}} = \vec{r} \times \vec{p} = (R + r')p = b \, p \tag{10.31}$$
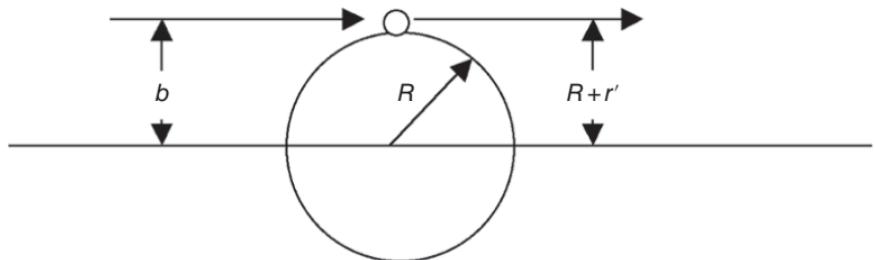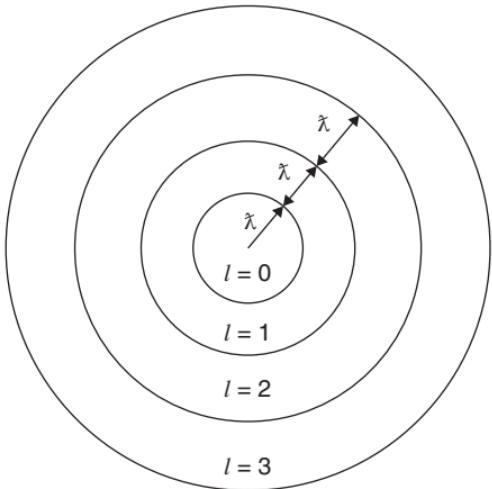
Figure 10.7 Schematic diagram of a grazing collision of a neutron with a nucleus.

Figure 10.8 Schematic bull's-eye view of the target nucleus in terms of the reduced de Broglie wavelength of a neutron projectile.

Whereas if quantum mechanics is used to describe the same problem, we know that $\ell_{classical} \to \ell \hbar$ and from de Broglie that the momentum is connected to the wavelength λ (unfortunately the same symbol as the mean lifetime) through the expression

$$p = \frac{h}{\lambda} = \frac{\hbar}{\lambdabar} \tag{10.32}$$

And then write the quantized angular momentum ℓ as

$$\ell \hbar = \frac{\hbar b}{\lambdabar} \Rightarrow b = \ell \lambdabar \tag{10.33}$$

This expression is not quite right because ℓ is quantized whereas b is not. We can get around this by associating each b with a certain ring or zone on the target. Figure 10.8 shows this concept with a head-on collision ($\ell = 0$), associated with the range of b is from 0 to $\lambdabar$, while $\ell = 1$ collisions range from $\lambdabar$ to $2\lambdabar$. Thus, the cross section grows with impact parameter, and larger impact parameters are associated with larger angular momenta. We can write the cross section for a specific value of ℓ as the difference between two circular areas:

$$\sigma_\ell = \pi (\ell + 1)^2 \lambdabar^2 - \pi (\ell)^2 \lambdabar^2 \tag{10.34}$$

$$\sigma_\ell = \pi \lambdabar^2 \left(\ell^2 + 2\ell + 1 - \ell^2 \right) \tag{10.35}$$

$$\sigma_\ell = \pi \lambdabar^2 (2\ell + 1) \tag{10.36}$$

The total reaction cross section is obtained by summing over all ℓ values up to the grazing trajectory as

$$\sigma_{total} = \sum_\ell \sigma_\ell = \sum_{\ell=0}^{\ell_{max}} \pi \lambdabar^2 (2\ell + 1) = \pi \lambdabar^2 (\ell_{max} + 1)^2 \tag{10.37}$$

where the maximum angular momentum ℓ_{max} is determined by the grazing distance

$$\ell_{max} = \frac{b_{max}}{\hbar} = \frac{R + r'}{\hbar} \tag{10.38}$$

$$\ell_{max} + 1 = \frac{b_{max}}{\hbar} + \frac{\hbar}{\hbar} = \frac{R + r' + \hbar}{\hbar} \tag{10.39}$$

Thus for the total cross section in terms of radii

$$\sigma_{total} = \pi \left(R + r' + \hbar \right)^2 = \pi \left(R_{total} + \hbar \right)^2 \tag{10.40}$$

The total cross section is proportional to the size of the target nucleus and the "size" of the projectile nucleus ($r' + \hbar$). Since the reduced wavelength of the projectile, $\hbar$, goes to infinity as the projectile momentum or kinetic energy goes to zero, the cross sections should increase dramatically at the lowest energies. This is true for neutrons, and their reaction cross sections at low energies can be very large; however, reactions at low energies between two charged particles are suppressed by the Coulomb barrier (discussed later). Note that the discussion earlier relies on classical mechanics. We should indicate how the problem would look if we used quantum mechanics to treat it. In quantum mechanics, we can write a similar expression for the total reaction cross section:

$$\sigma_{total} = \pi \hbar^2 \sum_{\ell=0}^{\infty} (2\ell + 1) T_\ell \tag{10.41}$$

where the transmission coefficient T_ℓ varies between 0 and 1. The transmission coefficient expresses the probability that a given angular momentum value ℓ will contribute to the reaction. At high neutron energies, $T_\ell = 1$ for $\ell \leq \ell_{max}$ and $T_\ell = 0$ for $\ell \geq \ell_{max}$. At the lowest neutron energies, $T_\ell = \epsilon^{1/2}$ for $\ell = 0$ and $T_\ell = 0$ for $\ell > 0$, where ϵ is the neutron kinetic energy. Thus, at very low energies, the total neutron interaction cross section is

$$\sigma_{total} \propto \pi \hbar^2 \sqrt{\epsilon} \propto \pi \left(\frac{\hbar^2}{2m\epsilon} \right) \sqrt{\epsilon} \propto \frac{1}{\sqrt{\epsilon}} \tag{10.42}$$

Such behavior of the cross sections for low-energy neutron-induced reactions is referred to as "$1/v$" behavior.

Now let us consider the interaction of a charged particle with a nucleus as shown in Figure 10.9. As the projectile approaches the target nucleus, it feels the long-range Coulomb force and begins to be deflected. As a consequence, the range of possible collisions where the nuclei will come into contact corresponds to a smaller range of impact parameters than in neutron-induced reactions. If the incident projectile has an energy ϵ at an infinite separation from the target nucleus, it will have a kinetic energy of $\epsilon - V_B$ where V_B is the Coulomb barrier
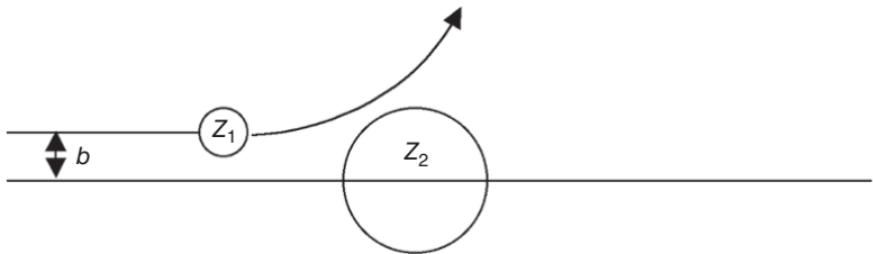
Figure 10.9 Schematic side view of a charged-particle-induced reaction.

at the distance of closest approach R. Numerically, the Coulomb barrier is given by the expression

$$V_B = \frac{Z_1 Z_2 e^2}{R} \tag{10.43}$$

At the distance of closest approach, the momentum p of the projectile will be $(2mT)^{1/2}$. Thus, we can write

$$p = (2mT)^{1/2} = (2\mu)^{1/2}(\epsilon - V_B)^{1/2} = (2\mu\epsilon)^{1/2}(1 - V_B/\epsilon)^{1/2} \tag{10.44}$$

where μ is the reduced mass of the system and $\mu = A_1 A_2/(A_1 + A_2)$. Classically we can write the orbital angular momentum

$$\ell_{classical} = \vec{r} \times \vec{p} \tag{10.45}$$

$$\ell_{max} = R\sqrt{2m\epsilon\left(1 - V_B/\epsilon\right)} \tag{10.46}$$

Quantum mechanically, again we have $\ell_{classical} \to \ell\,\hbar$, so

$$\sigma_{total} = \pi\lambdabar^2 \left(2\ell_{max} + 1\right)^2 \approx \pi\lambdabar^2 \ell_{max}^2 \tag{10.47}$$

$$\sigma_{total} \approx \pi\lambdabar^2 \frac{2\mu\epsilon}{\hbar^2}(1 - V_B/\epsilon) = \pi\lambdabar^2 R^2 \frac{1}{\lambdabar^2}(1 - V_B/\epsilon) \tag{10.48}$$

$$\sigma_{total} \approx \pi R^2(1 - V_B/\epsilon) \tag{10.49}$$

Note this last classical expression is valid only when $\epsilon > V_B$. The combined general properties of cross sections for charged and uncharged particles (neutrons) are shown in Figure 10.10.

Sample Problem 10.4: Charged-particle-induced reaction cross sections

Calculate the energy dependence of the total reaction cross section for the ^{48}Ca + ^{208}Pb reaction above the Coulomb barrier.
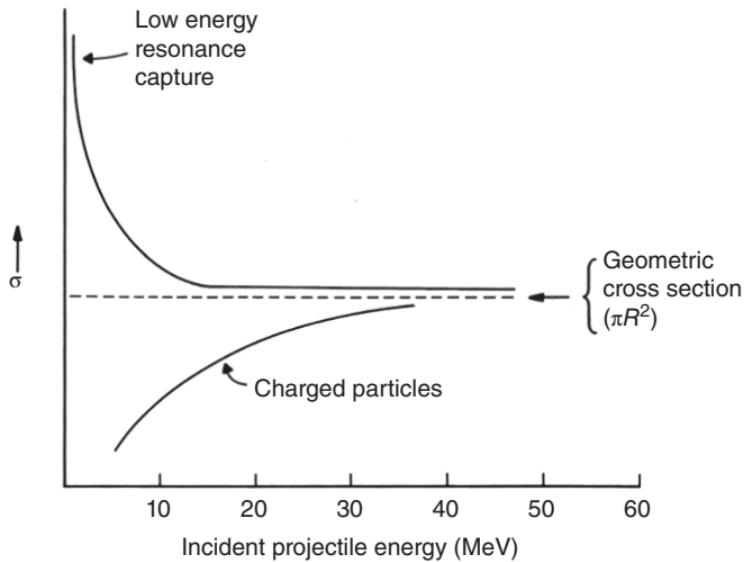
Figure 10.10 Schematic variation of the near threshold cross sections for neutron and charged-particle-induced reactions (Ehmann and Vance (1993). Reproduced with the permission of John Wiley & Sons, Inc.).

Solution

$$\sigma_{\text{total}} \approx \pi R^2 (1 - V_B/\epsilon)$$
$$R = R_{\text{Pb}} + R_{\text{Ca}} = 1.2(208^{1/3} + 48^{1/3}) = 11.47 \, \text{fm}$$
$$V_B = Z_1 Z_2 e^2/R = (82)(20)(1.44 \, \text{MeV} - \text{fm})/11.47 \, \text{fm} = 205.9 \, \text{MeV}$$
$$\epsilon = \text{energy of the projectile in the CM system}$$

ϵ (MeV)	σ_{total} (mb)
208	41.7
210	80.7
220	264.9
230	433.1
240	587.2
250	729.1

Aside on Barriers

In our semiclassical treatment of the properties of charged-particle-induced reaction cross sections, we have equated the reaction barrier V_B to the Coulomb barrier. That is, in reality, a simplification that is applicable to many but not all charged-particle-induced reactions.
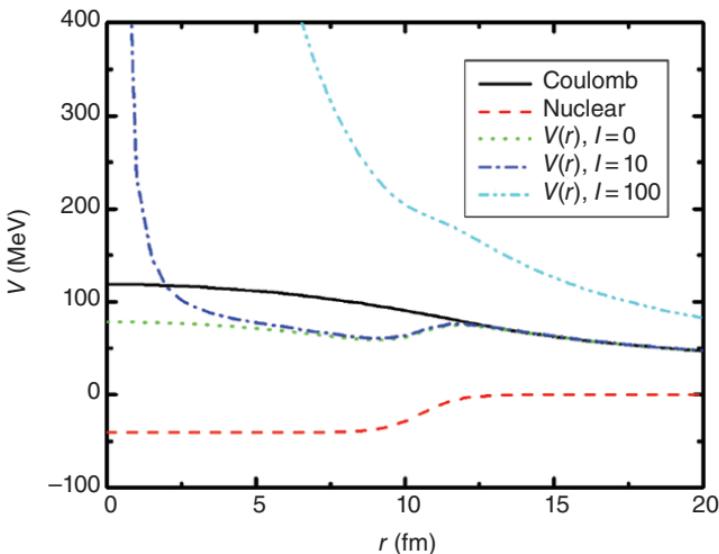
Figure 10.11 The nuclear Coulomb and total potentials for the interaction of ^{16}O with ^{208}Pb for several values of the orbital angular momentum. (*See insert for color representation of the figure.*)

The force (negative derivative of the potential energy) felt by an incoming projectile results from the sum of the nuclear, Coulomb and centrifugal forces (Fig. 10.11). The Coulomb potential $V_C(r)$ is approximated as the potential between a point charge Z_1e and a homogeneous charged sphere with charge Z_2e at a radius R_C as

$$V_C(r) = \frac{Z_1 Z_2}{r} \text{ for } r > R_C \tag{10.50}$$

$$V_C(r) = \left(\frac{Z_1 Z_2}{R_C}\right)\left(\frac{3}{2} - \frac{(r^2/R_C^2)}{2}\right) \text{ for } r < R_C \tag{10.51}$$

The nuclear potential is frequently represented by a Woods–Saxon potential (see Chapter 5) that is written as

$$V_{nucl}(r) = \frac{V_0}{1 + \exp^{(r-R)/a}} \tag{10.52}$$

where the strength of the potential is on the order of 40 MeV but must be adjusted for each reaction. The centrifugal potential has the standard form of

$$V_{cent}(r) = \frac{\hbar^2}{2\mu} \frac{\ell(\ell+1)}{r^2} \tag{10.53}$$

where $\ell\,\hbar$ is the orbital angular momentum of the incident projectile. The total potential $V_{total}(r)$ is the sum of the three contributions: $V_C(r) + V_{nucl}(r) + V_{cent}(r)$. An example of the different strengths and radial variation of these potentials is shown in Figure 10.11 using the ^{16}O + ^{208}Pb reaction as an

example with entrance channel angular momenta of $\ell = 0$, 10, and $100\hbar$. Note that for the highest angular momentum, $\ell = 100\hbar$, the total potential is repulsive at all distances, that is, the ions are not predicted to fuse with such a large angular momenta.

The actual *interaction barrier* is the value of $V_{\text{total}}(r)$ at the point when the colliding nuclei touch. Note that is a slightly different value from that of $V_C(r)$ at $r = R_C$, the *Coulomb barrier* due to the nuclear contribution.

10.5 Reaction Observables

What do we typically measure when we study a nuclear reaction? We might measure σ_R, the total reaction cross section. This might be measured by a beam attenuation method ($\Phi_{\text{transmitted}}$ vs. Φ_{incident}) or by summing up the cross sections for all possible exit channels for a reaction, which could be written as

$$\sigma_R = \sum_i^{b+B} \sigma_i(b, B) \tag{10.54}$$

but this is problematic because we would need to know beforehand what are all the possible combinations of products. Instead, we might measure the cross section for producing particular isotopic products at the end of the reaction, $\sigma(Z, A)$, by measuring the radioactivity of the reaction products. We might, as discussed previously, measure the products emerging in a particular angular range, $d\sigma(\theta, \phi)/d\Omega$. This measurement is especially important for experiments with charged-particle-induced reactions where the incident beam provides a reference axis for θ and ϕ. The energy spectra of the emitted particles can be measured as the differential cross section $d\sigma/dE$, or more likely we might observe the products emerging at a particular angle and with a particular energy and obtain a double differential cross section, $d^2\sigma/dEd\Omega$. As a bit of jargon, if the cross section for only one product is measured at a time, then it is called an "inclusive" cross section because it *includes* all possible pathways to the single product. If the cross section for the production of two or more simultaneously generated products is measured, then this is called an "exclusive" cross section.

10.6 Rutherford Scattering

One of the probable outcomes of the collision of a charged particle with a nucleus at large impact parameters is Rutherford or Coulomb scattering. The incident charged particle feels the long-range Coulomb force of the positively charged nucleus and is deflected from its path along a so-called Coulomb trajectory. A particle on a trajectory where the nuclei do not interact, as in

Figure 10.12 Schematic diagram of the kinematics in Rutherford scattering (Satchler (1990). Reproduced with the permission of Springer).
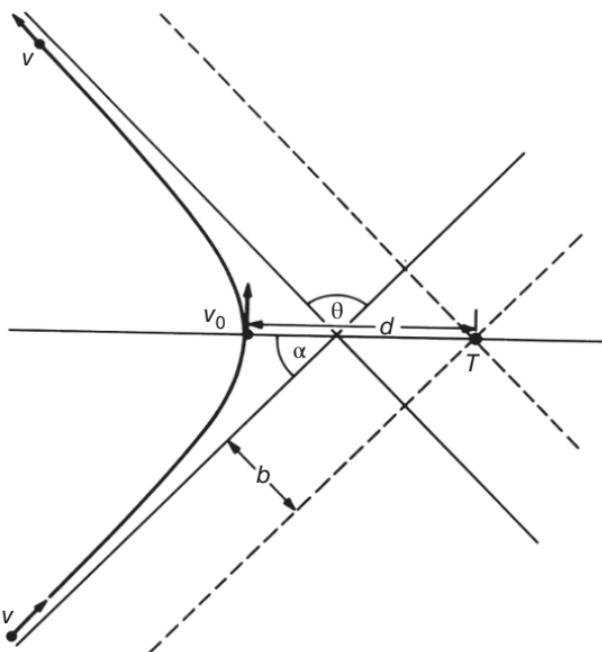
Figure 10.12, is "elastic scattering" in that the kinetic energy of motion is conserved. The Coulomb potential energy between a projectile of charge Z_1e and a target nucleus with charge Z_2e was given earlier as

$$V_C = \frac{Z_1Z_2e^2}{r} \tag{10.55}$$

where r is the distance between the projectile and target nuclei. The Coulomb force is the negative derivative of the potential energy and thus

$$F_C = -\frac{d}{dr}V_C = -\frac{Z_1Z_2e^2}{r^2} \tag{10.56}$$

The force is repulsive between two nuclei that have the same (positive) charge, that is, it acts in the opposite direction to r. In the case that the target nucleus is much heavier than the projectile nucleus, we can neglect the recoil of the target nucleus in the interaction. The projectile will follow a hyperbolic orbit, as shown in Figure 10.12 where b is the impact parameter, T_p is the kinetic energy of the projectile, and d is the distance of closest approach. We can connect the hyperbola with the initial collision variables by beginning at infinitely far apart where the projectile velocity is v. At the distance of closest approach $r = d$, the projectile velocity will become v_0. Conservation of energy for a projectile with mass, m, gives

$$\frac{1}{2}mv^2 = \frac{1}{2}mv_0^2 + \frac{Z_1Z_2e^2}{d} \tag{10.57}$$

Rearranging, we find that

$$\left(\frac{v_0}{v}\right)^2 = 1 - \frac{d_0}{d} \tag{10.58}$$

where the reduced distance of closest approach, d_0, is

$$d_0 = \frac{2Z_1 Z_2 e^2}{mv^2} = \frac{Z_1 Z_2 e^2}{T_P} \tag{10.59}$$

If we now invoke the conservation of angular momentum in the process, the product of linear momentum and distance must be conserved:

$$mv\,b = mv_0\,d \tag{10.60}$$

$$b^2 = \left(\frac{v_0}{v}\right)^2 d^2 = d(d - d_0) \tag{10.61}$$

Recall that one of the properties of the hyperbola shown in Figure 10.12 is that

$$d = b \cot\left(\frac{\alpha}{2}\right) \tag{10.62}$$

Again rearranging and substituting for d from earlier,

$$\tan \alpha = \frac{2b}{d_0} \tag{10.63}$$

The angles in Figure 10.12 are such that $\theta = \pi - 2\alpha$, and thus the scattering angle for Rutherford scattering is directly connected to the initial impact parameter b and the reduced distance of approach that contains the information on the Coulomb potential:

$$\cot\left(\frac{\theta}{2}\right) = \frac{2b}{d_0} \tag{10.64}$$

Figure 10.13 shows the expected orbits of the projectile nuclei after undergoing Rutherford scattering for a typical case. Note that the most probable trajectories (large values of b) result in the projectile being scattered to forward angles but that nearly head-on collisions (b almost zero) result in large-angle scattering. It was these latter large-angle scattering events that led Ernest Rutherford to conclude that there was a massive object at the center of the atom.

We can make the observations about elastic scattering more quantitative by considering the situation where a flux of I_0 particles/unit area is incident on a plane normal to the beam direction. The flux of particles passing through a ring with a differential width db and with impact parameters between b and $b + db$ is given as

$$dI = \left(\frac{\text{Flux}}{\text{Unit area}}\right)(\text{Area of ring}) = I_0(2\pi\,b\,db) \tag{10.65}$$
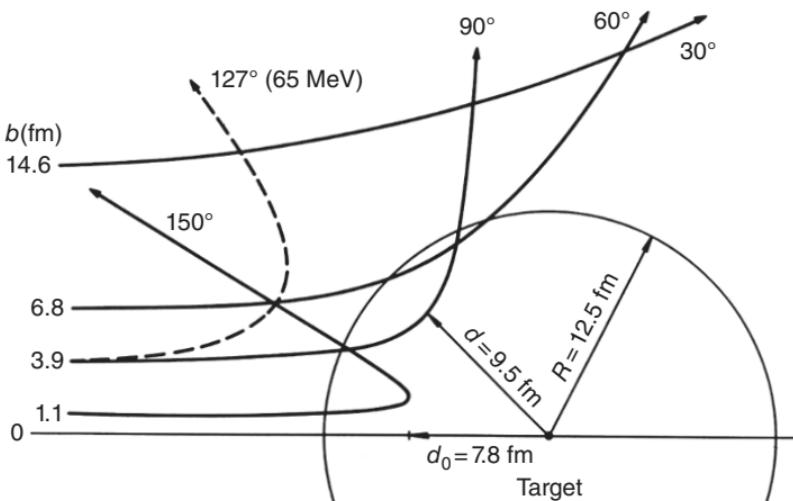
Figure 10.13 Diagram showing some representative projectile orbits for the interaction of 130 MeV ^{16}O with ^{208}Pb (Satchler (1990). Reproduced with the permission of Springer).

Substituting for the impact parameter from earlier, we get the differential equation for the angular distribution of intensity:

$$dI = \frac{\pi}{4} I_0 d_0^2 \frac{\cos(\theta/2)}{\sin^3(\theta/2)} d\theta \tag{10.66}$$

If we want to calculate the number of projectile nuclei that undergo Rutherford scattering into a solid angle $d\Omega$ at a plane angle of θ, we can write

$$\frac{d\sigma}{d\Omega} = \frac{dI}{I_0} \frac{1}{d\Omega} = \left(\frac{d_0}{4}\right)^2 \frac{1}{\sin^4(\theta/2)} \tag{10.67}$$

$$\frac{d\sigma}{d\Omega} = \left(\frac{Z_1 Z_2 e^2}{4 \, T_P^{CM}}\right)^2 \frac{1}{\sin^4(\theta/2)} \tag{10.68}$$

in which we have also used the definition of the solid angle in spherical coordinates after integration over the azimuth $d\Omega = 2\pi \sin\theta \, d\theta$ to convert from $d\theta$ to $d\Omega$.

Note the strong dependence of the Rutherford scattering cross section upon scattering angle. Remember that Rutherford scattering is not a nuclear reaction, as it does not involve the nuclear force, only the Coulomb force between the charged nuclei. Remember also that Rutherford scattering will occur to some extent in all studies of charged-particle-induced reactions and will furnish a "background" of scattered particles at forward angles due to so-called distant collisions.

Sample Problem 10.5: Rutherford Scattering

Calculate the differential Rutherford scattering cross section for the reaction of 215 MeV (lab energy) ^{48}Ca with ^{208}Pb at an angle of 20°. Note that this is close to the Coulomb barrier and a relatively small angle.

Solution

$$\frac{d\sigma}{d\Omega} = \left(\frac{Z_1 Z_2 e^2}{4\,T_P^{CM}}\right)^2 \frac{1}{\sin^4(\theta/2)}$$

$$T_P^{CM} = 215\ \text{MeV} \times \left(\frac{208}{208+48}\right) = 174.7\ \text{MeV}$$

$$\frac{d\sigma}{d\Omega} = \left(\frac{20 \times 82 \times 1.44\ \text{MeV fm}}{4 \times 174.7\ \text{MeV}}\right)^2 \frac{1}{\sin^4(20/2)}$$

$$\frac{d\sigma}{d\Omega} = 12{,}562\ \text{fm}^2 = 125.6\ b$$

10.7 Elastic (Diffractive) Scattering

Suppose we picture the interaction of the incident projectile nucleus with the target nucleus as it undergoes shape elastic scattering. It is convenient to think of this interaction as that of a plane wave with the nucleus as depicted in Figure 10.14. Imagine further that all interactions take place on the nuclear surface. If only points A and B in Figure 10.14 on the nuclear surface scatter particles and all other points absorb them, then an interference will occur between (particle) waves going around the two sides of the nucleus. To get
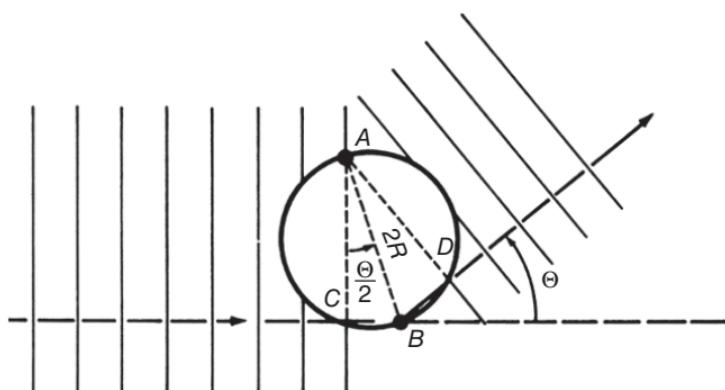
Figure 10.14 Schematic diagram of the interaction of a plane wave with a nucleus (Meyerhof (1967). Reproduced with the permission of McGraw-Hill Book Company).

constructive interference between the incoming and outgoing wave, we must fulfill the condition that the distances from C to B plus from B to D must be an integral number of wavelengths, or

$$CB + BD = n\lambda \tag{10.69}$$

where λ is the wavelength of the incident particle and n is an integer. From simple geometry, peaks should occur in the scattering cross section when

$$n\lambda = 2 \times 2R \times \sin(\theta/2) \tag{10.70}$$

In Figure 10.15, we show the angular distribution for the elastic scattering of 800 MeV protons from ^{208}Pb. The de Broglie wavelength of the projectile is 0.85 fm, while the nuclear radius R is about 7.6 fm ($1.28(208)^{1/3}$). We expect peaks in the cross section at ($n = 2, 3, 4, ...$) with a spacing between them, $\Delta\theta$, of approximately 3.2° while one observes a spacing of 3.5°. (This example was taken from Bertsch and Kashy, 1993.)
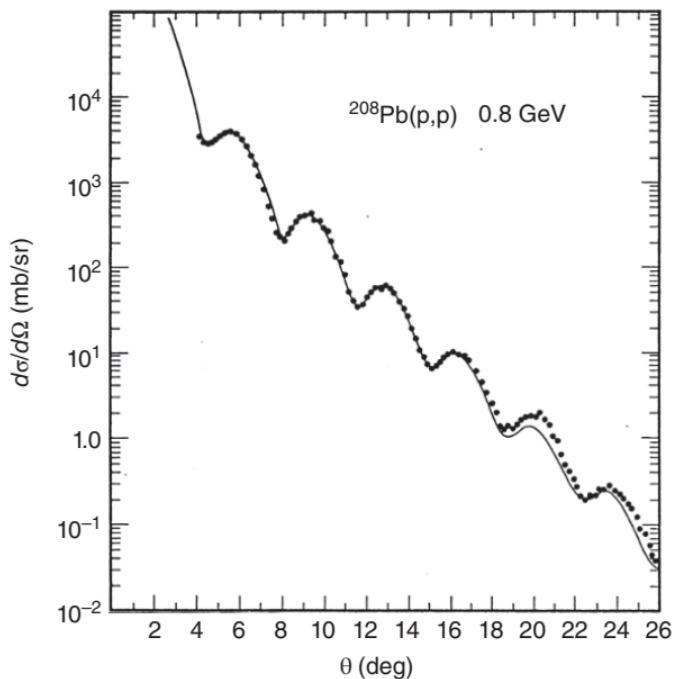
Figure 10.15 Angular distribution of 800 MeV protons that have been elastically scattered from ^{208}Pb Blanpied et al. (1978). Reproduced with the permission of American Physical Society).

10.8 Aside on the Optical Model

The optical model is an important tool to understand and parameterize studies of nuclear scattering. It likens the interaction of projectile and target nucleus with that of a beam of light interacting with a glass ball. To simulate the occurrence of both elastic scattering and absorption (reactions) in the interaction, the glass ball is imagined to be somewhat cloudy.

In formal terms, the nucleus is represented by a nuclear potential that has a real and an imaginary part:

$$U_{\text{nucl}}(r) = V(r) + iW(r) \tag{10.71}$$

where the imaginary potential $W(r)$ describes absorption (reactions) as the depletion of the total flux by that going into nonelastic channels and the real potential $V(r)$ describes the elastic scattering. Frequently the nuclear potential is taken to have the Woods–Saxon form:

$$U_{\text{nucl}}(r) = -V_0(r)f(r, R_R, a_R) - W_0 f(r, R_I, a_I) \tag{10.72}$$
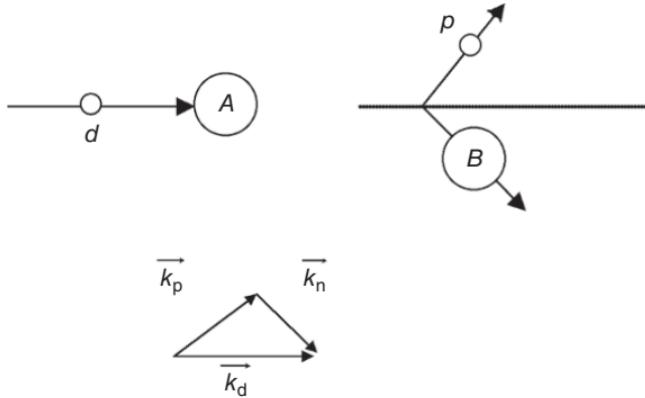
$$f(r, R, a) = \left[1 + \exp\left(\frac{r-R}{a}\right)\right] \tag{10.73}$$

The complete nuclear potential thus has six parameters, the potential depths V_0, W_0; the radii R_R, R_I; and the surface diffusenesses a_R, $a_I$. By solving the Schrödinger equation with this nuclear potential (along with the Coulomb and centrifugal potentials), one can predict the cross section for elastic scattering, the angular distribution for elastic scattering, and the total reaction cross section given the values of these six parameters. Alternatively, one can measure the elastic scattering cross sections and use the data to determine the parameters. It has been shown that the six parameters are not linearly independent, so extracting the parameters from the data can be ambiguous. The meaning of the imaginary potential depth W can be understood by noting that the mean free path of a nucleon in the nucleus, Λ, can be written as

$$\Lambda = \frac{v\,\hbar}{2\,W_0} \tag{10.74}$$

where v is the relative velocity. By fitting measured elastic scattering cross sections and angular distributions over a wide range of projectiles, targets, and beam energies, one might hope to find a universal set of parameters to describe elastic scattering (and the nuclear potential). That hope is only partially realized because only the tail of the nuclear potential affects elastic scattering, and there are families of parameters that fit the data equally well, as long as they agree in the exterior regions of the nucleus.

Figure 10.16 Sketch of a (d, p) reaction and the associated linear momentum triangle in terms of the wave numbers, k.

10.9 Direct Reactions

As we recall from our general description of nuclear reactions, a direct reaction is said to occur if one of the participants in the initial two-body interaction involving the incident projectile leaves the nucleus. This definition is too restrictive. Generally speaking, these direct reactions are said to occur when the interaction between the projective and the target occurs in one step and only a single particle or one pair of particles is involved in the reaction. As such, direct reactions can be divided into two classes, *stripping reactions* in which part of the incident projectile is "stripped away" and is captured by the target nucleus and *pickup reactions* in which the outgoing emitted particle is a combination of the incident projectile plus a nucleon (or perhaps two) target nucleon(s) picked up as it went by.

Let us consider stripping reactions first and in particular, the most commonly encountered stripping reaction, the (d, p) reaction. Formally the result of a (d, p) reaction is to introduce a neutron into the target nucleus, and thus this reaction should bear some resemblance to the simple neutron capture reaction. But because of the generally higher angular momenta associated with the larger kinetic energy necessary to get over the Coulomb barrier in the (d, p) reaction, there can be differences between the two reactions. Consider the A (d, p) B^* reaction where the recoiling nucleus $B = A + n$ is produced in an excited state B^*. We sketch out a simple picture of this reaction and the momentum relations in Figure 10.16.

The momentum diagram for the reaction shown in Figure 10.16 writes the momentum of the incident deuteron as k_d, the momentum of the emitted proton as k_p, while k_n as the momentum of the stripped neutron. From conservation of momentum, we have

$$k_n^2 = k_d^2 + k_p^2 - 2k_d k_p \cos \theta \tag{10.75}$$

If the neutron is captured at impact parameter R, the orbital angular momentum transferred to the nucleus, $\ell_n \hbar$, is given by

$$\ell_n \hbar = \tilde{r} \times \tilde{p} = R k_n \hbar \tag{10.76}$$

$$\ell_n = R k_n \tag{10.77}$$

Since we have previously shown that k_n is a function of the angle θ, we can now associate each orbital angular momentum transfer in the reaction with a given angle θ corresponding to the direction of motion of the outgoing proton. Thus the (d, p) reaction becomes a very powerful spectroscopic tool to measure angular momentum transfer. By measuring the energy of the outgoing proton, we can deduce the Q value of the reaction and thus the energy of any excited state of the residual nucleus that is formed. From the direction of motion of the proton, we can deduce the orbital angular momentum transfer in the reaction ℓ_n. If we know the ground state spin and parity of the residual nucleus, we can deduce information about the spin and parity of the excited states of the residual nucleus using the rules

$$||(I_A - \ell_n)| - \frac{1}{2}| \leq I_{B^*} \leq I_A + \ell_n + \frac{1}{2} \tag{10.78}$$

$$\pi_A \pi_{B^*} = (-i)^{\ell_n} \tag{10.79}$$

Other stripping reactions have been used with greater or lesser success such as (α, t), (α, d), and so on, but the more complex the projectile and ejectile nuclei, the more complicated the transfer process. Typical pickup reactions that have been studied include (p, d), (p, t), $(\alpha, {}^6Li)$, and so on.

Sample Problem 10.6: Direct Reactions

Calculate the angle at which the (d, p) cross section has a maximum for $\ell = 0, 1, 2, 3$ and $4\hbar$. Assume a deuteron kinetic energy of 7 MeV and a proton energy of 13 MeV with $R = 6$ fm.

Solution

$$k_d = 0.82/\text{fm}$$
$$k_p = 0.79/\text{fm}$$
$$k_n = \frac{\ell}{R}$$

Thus for $\ell = 0, 1, 2, 3, 4$, $k_n = 0, 0.17, 0.33, 0.50, 0.67/\text{fm}^1$. Then from the momentum triangle in each case

$$\cos \theta = \frac{-k_n^2 + k_d^2 + k_p}{2 k_d k_p} \tag{10.80}$$

$$\theta = 0°, 12°, 24°, 36°, 49° \text{ for } \ell = 0, 1, 2, 3, 4, \text{ respectively} \qquad (10.81)$$

Note that a somewhat more correct expression would be $k_n R = \sqrt{\ell(\ell + 1)}$.

10.10 Compound Nuclear Reactions

A compound nucleus (CN) is a relatively long-lived reaction intermediate that is the result of a complicated set of two-body interactions in which the energy of the projectile is distributed (thermalized) among all of the nucleons of the composite system. How long does the CN live? From our definition earlier, we can say the CN must live for at least several times the time it would take a nucleon to traverse the nucleus ($\sim 10^{-22}$ s). Thus, the time scale of compound nuclear reactions should be on the order of 10^{-18} to 10^{-16} s. Lifetimes as long as 10^{-14} s have been observed, all of which are clearly long times compared with the typical time scale of a direct reaction of 10^{-22} s.

Another important feature of CN reactions is the mode of decay of the CN is independent of its mode of formation (the *Bohr independence hypothesis* or the *amnesia assumption*). While this lack of memory of the entrance channel is not true in general, it remains a useful tool for understanding certain features of compound nuclear reactions. For example, consider the classical work of Ghoshal (1950) who formed the CN ^{64}Zn in two ways, that is, by bombarding ^{63}Cu with protons and by bombarding ^{60}Ni with α particles. He examined the relative amounts of ^{62}Cu, ^{62}Zn, and ^{63}Zn found in the two bombardments, and within his experimental uncertainty of 10%, he found the amounts of the products were the same in both bombardments. (Later experiments have shown smaller scale deviations from the independence hypothesis.)

Because of the long time scale of the reaction and the "amnesia" of the CN as to its mode of formation, one can show that the angular distribution of the products must be symmetric about 90° (in the frame of the moving CN).

The cross section for a compound nuclear reaction can be written as the product of two factors, the probability of forming the CN and the probability that the CN decays in a given way. As described earlier, the probability of forming the CN can be written as

$$\sigma_{CN} = \pi \lambdabar^2 \sum_{\ell=0}^{\infty} (2\ell + 1) \ T_\ell \qquad (10.82)$$

The probability of decay of the CN, P, into a given set of products, β, can be written as

$$P(\beta) = \left[\frac{T_\ell^\beta(E_\beta)}{\sum_{\ell_i, E_i} T_\ell^i(E_i)} \right] \qquad (10.83)$$

Figure 10.17 Schematic view of the exponential increase in the number of levels in a nucleus with excitation energy.

$\Gamma/D \gg 1$

$\Gamma/D \ll 1$

where T_ℓ^i is the transmission coefficient for CN decay into products i with some energy E_i. We have encountered the fact that nuclei can exist in various excited states, but it turns out the arrangements of nucleons become increasingly numerous as the amount of internal energy increases. Figure 10.17 shows a schematic view of the energy levels of a typical nucleus, which would include a CN formed in a reaction. The number of levels in the CN excitation energy actually increases exponentially. Quantitatively, the Fermi gas model of the nucleus predicts that the number of levels per mega-electron volt of excitation energy, E^*, increases approximately exponentially with $\sqrt{E^*}$. It should not be surprising that the complexity of the deexcitation of a CN grows with its excitation energy due to the increasing number of excited states at that energy.

Compound nuclear reactions can be grouped by the ratio of the width of the CN level, Γ, which is formed to the average spacing between compound nuclear levels, D. Recall from the Heisenberg uncertainty principle that $\Gamma \tau \geq \hbar$, where τ is the mean life of that quantum mechanical level. The categories are (a) the lowest energies where $\Gamma/D \ll 1$, that is, the CN has isolated nonoverlapping levels and (b) $\Gamma/D \gg 1$, that is, the CN is formed in a region with many overlapping levels. Intuitively the excited CN in category (a) will only be able to decay in relatively few ways, whereas those in CN category (b) will be able to follow many decay paths.

Let us first consider the case of $\Gamma/D \ll 1$. In this case, generally only low excitation energies and individual levels of the CN can be produced in the reaction (i.e., when the excitation energy exactly matches the energy of a given CN level). During a scan of the bombarding energy, there will be a sharp rise or *resonance* in the reaction cross section at that specific energy akin to the absorption of infrared radiation by a molecule when the radiation frequency equals one of the natural oscillation frequencies. The formula for the cross section of a resonance (called the *Breit–Wigner single level formula*) for the reaction $a + A \rightarrow (CN) \rightarrow b + B$ is

$$\sigma = \pi \lambdabar^2 \left(\frac{(2J_{CN} + 1)}{(2J_A + 1)(2J_a + 1)} \right) \frac{\Gamma_{aA} \Gamma_{bB}}{(\epsilon - \epsilon_0)^2 + (\Gamma/2)^2} \tag{10.84}$$

where J_i is the spin of i-th nucleus and Γ_{aA}, Γ_{bB}, and Γ are the partial widths for the formation of the CN, the decay of the CN into $b + B$, and total width for the all the decays of the CN, respectively. The symbols ϵ and ϵ_0 refer to the CM energy of the projectile nucleus and the exact CM projectile energy that corresponds to the excitation of a single isolated level. Applying this formula to the case of (n, γ) reactions gives

$$\sigma = \pi \lambdabar^2 \left(\frac{(2J_C + 1)}{(2J_A + 1)(2)} \right) \frac{\Gamma_n \Gamma_\gamma}{(\epsilon - \epsilon_0)^2 + (\Gamma/2)^2} \tag{10.85}$$

An example of the energy variation of an isolated resonance in a neutron-capture reaction is shown in Figure 10.18. Resonances are seen in the energy spectra of low-energy neutron-induced reactions where levels in the CN are populated at excitation energies on the order of the neutron binding energy (roughly 8 MeV) with a spacing between levels on the order of an electronvolt. Notice that for neutron energies much smaller than ϵ_0, the $(\epsilon - \epsilon_0)^2$ term becomes a constant at approximately ϵ_0^2, and the cross section for the (n, γ) reaction will be governed by the energy variation of the wavelength and the width for formation of the CN. Recall that $\lambdabar = \hbar/mv$ and the width for neutron capture $\Gamma_n \propto v$ at low energies, while the width for γ-ray decay does not depend on the bombarding energy since it is a property of the CN state so that $\sigma \propto 1/v$, as indicated earlier.

Let us now consider the case where $\Gamma/D \gg 1$, that is, many overlapping levels of the CN are populated in a reaction. We do not need a large range of compound nuclear excitation energies, rather we need a high energy with many levels, some number of which have short lifetimes and large widths.
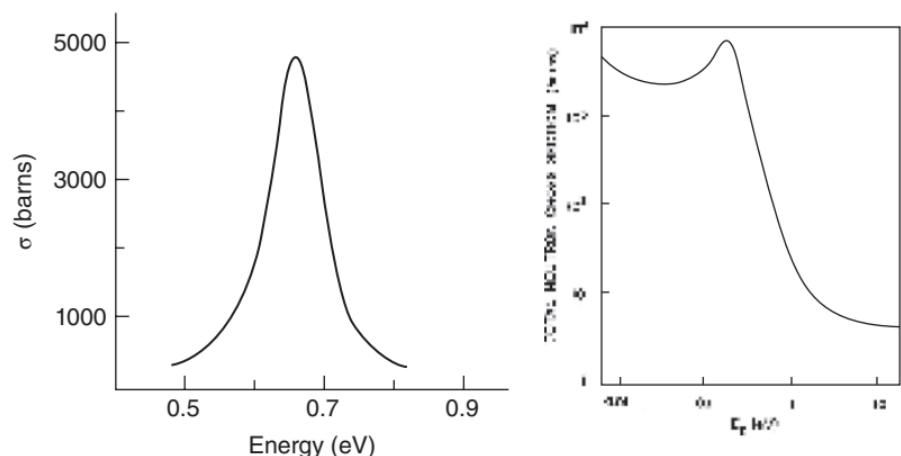

Figure 10.18 (left) The cross section for an isolated resonance in the energy spectrum of a (n, γ) reaction. (right) The variation of the neutron capture cross section at low energies for ^{113}Cd showing resonant behavior with a $1/v$ dependence at low energies.

In this case the cross section for the same reaction $a + A \rightarrow (\text{CN}) \rightarrow b + B$ can be written as

$$\sigma_{ab} = \sigma_{\text{CN}}(aA) \sum P_{\text{CN}}(bB) \tag{10.86}$$

where $\sigma_{\text{CN}}(aA)$ is the cross section for the formation of the CN and $P_{\text{CN}}(bB)$ describes the probabilities that the CN will decay to form $b + B$ in various ways. Here we will not evaluate all of the contributions of their individual resonances (there could be a very large number) but rather consider the average behavior. Now let us consider in a little more detail the probability that emitted particle b has an energy ϵ_b in the exit channel. First, we can write down that the maximum energy that b can have is the difference between the excitation energy of the CN and the separation energy of b from the CN, $E^*_{\text{CN}} - S_b$. Notice that b can be emitted with a range of kinetic energies less than the maximum with the result that the nucleus B will be left in a corresponding range of excited states. The number of excited states in B grows exponentially, and so the CN will strike a balance between kinetic energy of b and internal excitation of B. By using the arguments of detailed balance from statistical mechanics (see Lefort (1968), FKMM), we can write for the probability of the CN emitting a particle b with an energy $\epsilon_b < \epsilon_{\text{max}}$ and leaving the nucleus B at an excitation energy E^*_B as

$$W_b(\epsilon_b)d\epsilon_b = \frac{(2J_b + 1)\mu}{\pi^2 \, h^3}\epsilon_b\sigma_{\text{inv}}\frac{\rho(E^*_B)}{\rho(E^*_{\text{CN}})}d\epsilon_b \tag{10.87}$$

In this equation, μ is the familiar reduced mass of the system, and σ_{inv} is the cross section for the inverse process in which the particle b is captured by the nucleus B and b has a (CM) kinetic energy, ϵ_b. The symbols $\rho(E^*_B)$ and $\rho(E^*_{\text{CN}})$ refer to the level density in the nucleus B with an excitation energy E^*_B and the level density in the CN with an excitation energy, E^*_C. The inverse cross section can be calculated using the same formulas used to calculate the compound nucleus formation cross sections. Using the Fermi gas model of a nucleus, we find that the level densities of the excited nucleus are given by the expression

$$\rho(E^*) = C \exp(2\sqrt{aE^*}) \tag{10.88}$$

where C is a constant scaling factor and the *level density parameter*, a, depends on the mass number of the nucleus and generally falls in the range of $A/12$ to $A/8$. One can also define a *nuclear temperature*, T, in the Fermi gas model based on the statistical mechanical definition that the temperature is related to the derivative of the level density of a system:

$$E^* = aT^2 - T \tag{10.89}$$

Often an excited CN will be able to emit different particles, and the relative amounts will be determined by the separation energies and the level density in the (excited) daughter nucleus, B, after the particle is emitted. If we consider

the ratio of emission widths for two kinds of emitted particles, x and y, then some terms cancel in the ratio, leaving

$$\frac{\Gamma_x}{\Gamma_y} = \frac{g_x \mu_x}{g_y \mu_y} \frac{R_x}{R_y} \frac{a_x}{a_y} \exp\left[2(a_x R_x)^{1/2} - 2(a_y R_y)^{1/2}\right] \tag{10.90}$$

where g_i is the spin factor $2J_i + 1$, or statistical weight of each channel; μ_i the reduced mass of each channel with a_i; and E_i^* the level density parameter and maximum excitation energy for the residual nucleus that results from the emission of the i-th particle. E^* is formally equal to $E^* - S_i - \epsilon_t$ where ϵ_t is the threshold for the emission of a charged particle ($\epsilon_t = 0$ for neutrons).

When the emitted particles are neutrons, the emitted neutron energy spectrum has the form

$$N(\epsilon)d\epsilon = \frac{\epsilon}{T^2} \exp^{-\epsilon/T} d\epsilon \tag{10.91}$$

As shown in Figure 10.19.

The neutrons are emitted with a Maxwellian energy distribution, and the most probable energy is T while the average energy is twice the nuclear temperature. Thus, the CN can be thought of as "evaporating" particles similar to molecules leaving the surface of a hot liquid. We can measure the energy spectrum of the particles emitted in a compound nuclear reaction and use it as a "nuclear thermometer" in that

$$\frac{d}{d\epsilon} \ln(N(\epsilon)d\epsilon) = \frac{-1}{T} \tag{10.92}$$

Charged particles can be evaporated from excited nuclei except that the minimum kinetic energy is not zero as it is for neutrons. Rather there is a threshold for each type of charged particle, ϵ_t, (which is approximately the Coulomb barrier) that determines its minimum energy (see Fig. 10.10). The energy spectrum of evaporated charged particles is then
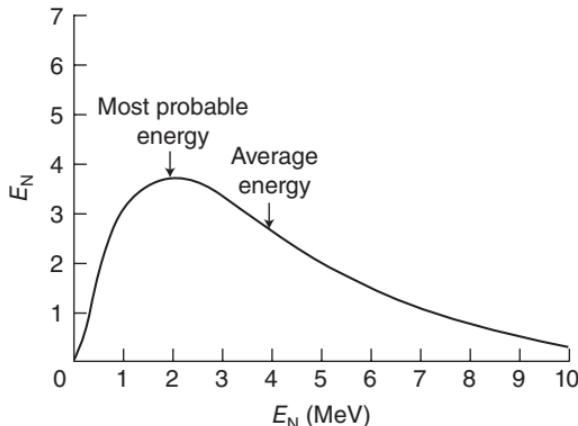
$$N(\epsilon)d\epsilon = \frac{\epsilon - \epsilon_t}{T^2} \exp^{-(\epsilon-\epsilon_t)/T} d\epsilon \tag{10.93}$$

What can be said about the distribution in space of the reaction products? We might think that because the CN has "forgotten" its mode of formation, there would be no preferential direction for the emission of the decay products. Thus, we might expect that all angles of emission of the particles, θ, to be equally probable and that $P(\theta)$, the probability of emitting a particle at an angle θ, would be a constant. Then we would expect that $d\sigma/d\Omega(\theta)$ would be simply

$$\frac{d\sigma}{d\Omega} = \int P(\theta) \frac{d\theta}{d\Omega} \tag{10.94}$$

This expression assumes that we are making the measurement of the angular distribution in the frame of the moving CN. In the laboratory frame, there will appear to be more particles emitted in the forward direction (with higher energies) than are emitted in the backward direction due to the motion of the cm.

Figure 10.19 An example of the kinetic energy spectrum of neutrons emitted (so-called evaporated neutrons) from a compound nucleus.

We should realize that this picture of uniform emission of evaporated particles is too simplistic. The CN will form a range of angular momenta due to the orbital motion in the entrance channel. This angular momenta will have to be conserved during the decay of excited states, and it will tend to focus the particles into the plane perpendicular to the emission axis. However, the affect of angular momentum will depend strongly on the particle emitted.

The energy variation of the cross section (the so-called *excitation function*) for processes involving evaporation is fairly distinctive as can be seen in Figure 10.20, where the excitation function for the ^{209}Bi(α, xn) reaction is shown. Starting from the overall threshold for the α-induced reaction, the cross section rises with increasing energy because the formation cross section for the CN is increasing for the reasons discussed earlier. Initially the ^{213}At nucleus only has enough energy to emit one neutron as the thresholds for emitting charged particles like protons, or α particles are relatively high. Eventually the excitation energy of the CN becomes large enough that emission of two neutrons is energetically possible. At this stage, the "2n out" process will dominate the "1n out" process because the sequential emission of two neutrons has a higher probability than the emission of a single high-energy neutron due to the effect of the level density of the daughter nucleus. We expect subsequent peaks for the individual "xn out" processes to occur at approximately $(S_{n1} + 2T)$, $(S_{n1} + S_{n2} + 4T)$, $(S_{n1} + S_{n2} + S_{n3} + 6T)$, and so on, where we have neglected the decrease in T during the emission process.

Let us review what we have said about compound nuclear reactions. CN reactions are nuclear reactions with a long-lived reaction intermediate that is formed by a complex and variable set of two-body interactions. We developed a set of equations that describe the overall compound nuclear cross section. We have shown how this general formula simplifies for specific cases, the case of exciting a single level of the CN with spikes or resonances in the cross section as a function of energy and the case of higher excitation energies where the CN behaves like a hot liquid, evaporating particles to remove excitation energy.
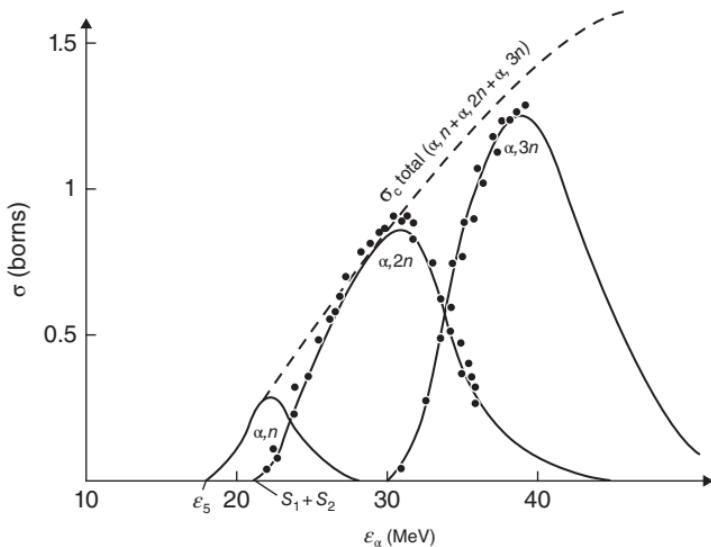
Figure 10.20 Excitation function for the ^{209}Bi(α, xn) reaction showing the contributions of the first three individual neutron evaporation channels to the total cross section for compound nucleus formation.

At all excitation energies, the angular distribution of the reaction products is symmetric with respect to a plane perpendicular to the incident particle direction.

10.11 Photonuclear Reactions

Photonuclear reactions are nuclear reactions in which the incident projectile is a photon and the emitted particles are either charged particles or neutrons. Examples of such reactions include (γ, p), (γ, n), (γ, α), and so on. The energetic photons needed to induce these reactions can be furnished from the annihilation of positrons in flight (producing monoenergetic photons), more commonly by the energetic bremsstrahlung from slowing down high-energy electrons (producing a continuous distribution of photon energies), and the related technique of coincident detection of the scattered electron (producing a narrow energy beam). Most recently the technique of Compton backscattering laser light from monoenergetic electrons stored in a ring (producing a tunable energy photon beam) has been used. These sources produce electric dipole ($E1$) photons. Thus, the reactions that have been studied involve the absorption of an $E1$ photon and have been carried out on stable nuclei. The absorption of an $E1$ photon would create a spin change of $+1$ and a parity change. Thus, a photonuclear reaction

with an even–even nucleus would produce excited states with a spin/parity of 1^- that had a large nuclear overlap with the ground state.

The incident photon can interact with individual protons in the nucleus or simultaneously with all of the protons. An interesting and unusual feature of the excitation function for photonuclear reactions is the appearance of a large enhancement of the cross section at ~25 MeV for reactions with low mass targets, for example, ^{16}O, which is present in the cross sections for all nuclei, but the energy slowly decreases with mass number until it reaches ~15 MeV for ^{208}Pb. An example of the total photonuclear cross section for a heavy nucleus is shown in Figure 10.21.

The large bump in the total photonuclear cross section, common to all nuclei, is called the *giant dipole resonance* or GDR. Goldhaber and Teller provided the first description of this reaction in which they ascribed the GDR to the collective vibration of all the neutrons against all the protons. Their model was based on the oscillation of the density of a proton fluid against a neutron fluid inside the nucleus. Their model suggested the energy of the GDR should vary as $A^{-1/6}$, in fair agreement with the observed variation. As a confirmation of the giant oscillation, it was found that the GDR in deformed nuclei splits into two components with different energies, corresponding to oscillation along the major and minor nuclear axes of the deformed ellipsoidal nuclei. One further
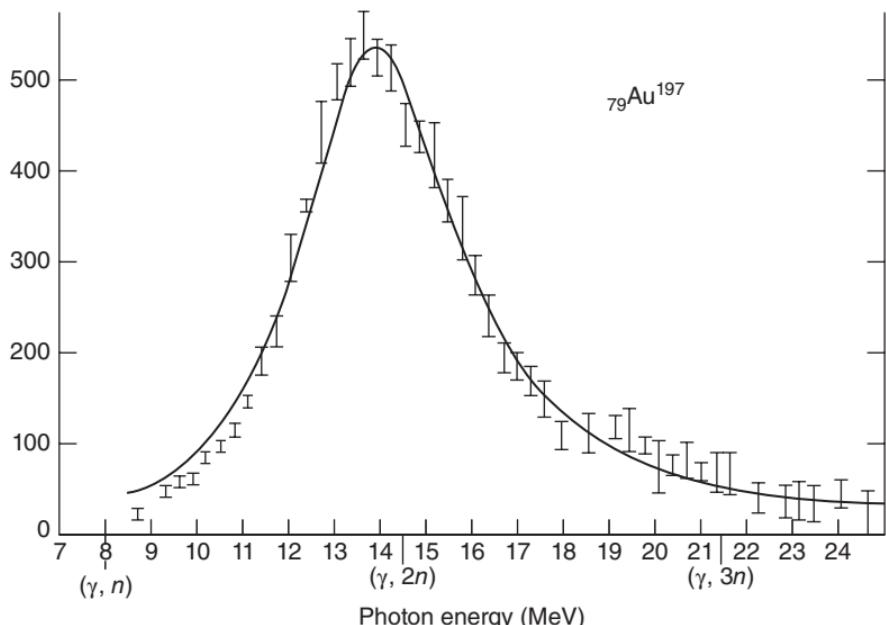

Figure 10.21 The photonuclear total reaction cross section of ^{197}Au (Fultz et al. (1962). Reproduced with the permission of American Physical Society).

fact about photonuclear reactions and the GDR should be noted. The sum of the absorption cross section for dipole photons (summed over all energies) is approximately constant, that is,

$$\int_0^\infty \sigma_{abs}(E_\gamma)\,dE_\gamma \propto \frac{NZ}{A} \approx 0.058\frac{NZ}{A} \text{ MeV barns} \qquad (10.95)$$

This expression is called the dipole sum rule.

Sample Problem 10.7: Giant Dipole Resonance

Calculate the ratio of the wavelength of the GDR E1 photon to the nuclear diameter for ^{16}O that occurs with 25 MeV photons and for ^{208}Pb with 15 MeV photons.

Solution

$$^{16}O$$

$$\lambda = \frac{hc}{E_\gamma} = \frac{197.3 \text{ MeV fm}}{25 \text{ MeV}} = 7.9 \text{ fm}$$

$$\text{Diameter} = 2 \times 1.2(16)^{1/3} \text{ fm} = 6.0 \text{ fm}$$

$$\text{Ratio} = \frac{\lambda}{\text{Diameter}} = \frac{7.9 \text{ fm}}{6.0 \text{ fm}} = 1.3$$

$$^{208}\text{Pb}$$

$$\lambda = 13.1 \text{ fm}; \text{diameter} = 14.1 \text{ fm}; \text{ratio} = 1.1$$

10.12 Heavy-Ion Reactions

Heavy-ion-induced reactions are usually taken as reactions induced by projectiles heavier than an α particle. The span of projectiles studied is large, spanning essentially all of the stable elements in the periodic table from the light ions, C, O, and Ne to the medium mass ions, such as S, Ar, Ca, and Kr to the heavy projectiles, Au, Bi, and even U. Reactions induced by heavy ions have certain unique characteristics that distinguish them from other nuclear reactions. First of all, the Coulomb barrier between the beam and target nucleus always puts a significant threshold on their reaction. Second, the de Broglie wavelength of a heavy ion at an energy of 5 MeV/nucleon (above the barrier) or higher is small compared to the dimensions of the ion. As a result, the interactions of these ions can be described semiclassically. In addition, the small wavelengths allow relatively large angular momentum in these collisions. For example, we can write

$$\ell_{max} = \frac{R}{\lambdabar}\left(1 - \frac{V_B}{E_{CM}}\right) \qquad (10.96)$$

As an example, for the near-barrier reaction of 226 MeV (lab) ^{40}Ar + ^{165}Ho, we calculate $\ell_{max} = 163\hbar$. This value is relatively large compared to the angular momenta involved in nucleon-induced reactions. Lastly, quite often the product of the atomic numbers of the projectile and target is quite large (>1000), indicating the presence of large Coulomb forces acting in these collisions.

The study of heavy-ion-induced reactions is a forefront area of nuclear research at present. By using heavy-ion-induced reactions to make unusual nuclear species, one can explore various aspects of nuclear structure and dynamics "at its limits" and thus gain insight into nuclear structure and reactions not possible with stable nuclei. Another major thrust is to study the dynamics and thermodynamics of the colliding nuclei. The bombarding energy plays a very important role in determining the course of heavy-ion reactions. The vast majority of work has been carried out with bombarding energies near the interaction barrier and much of the discussion later relates to so-called low-energy reactions.

In Figure 10.22, we show a cartoon of the various impact parameters and trajectories one might see in a heavy-ion reaction. The most distant collisions lead to elastic scattering and Coulomb excitation. Coulomb excitation is the transfer of energy to the target nucleus via the long-range Coulomb interaction that excites levels above the ground state in the target or the projectile nucleus (or both). Grazing collisions lead to inelastic scattering and the onset of nucleon exchange through the short-ranged nuclear force. Head-on or near head-on collisions at low kinetic energy can lead to fusion of the reacting nuclei and to
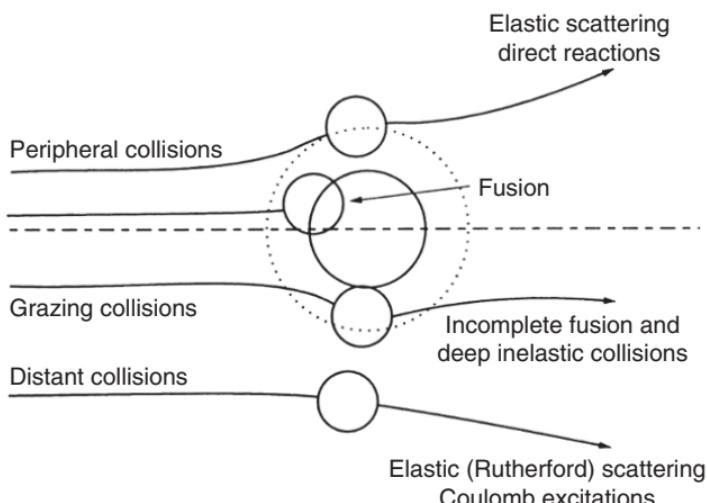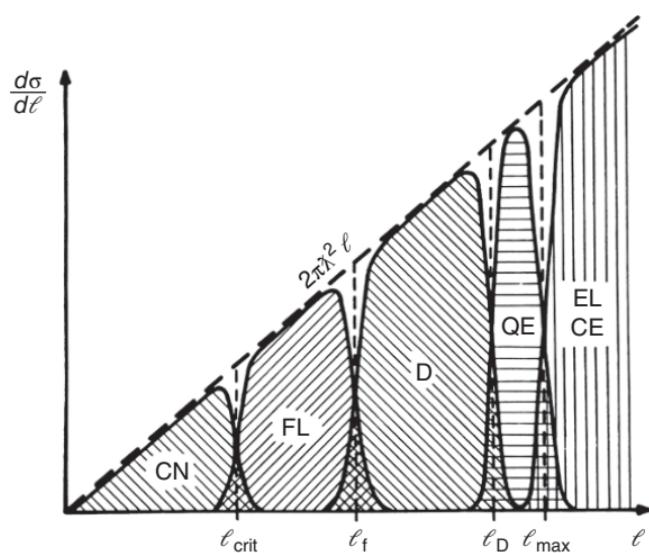

Figure 10.22 Classification scheme of near-barrier heavy-ion induced collisions based upon impact parameter (Hodgson et al. (1997). Reproduced with the permission of American Physical Society).

the formation of a CN, particularly if the reaction partners have very different masses. On the other hand, a "quasi-fusion" reaction in which there is substantial mass and energy exchange between large projectile and target nuclei without the "true amnesia" characteristic of CN formation can take place. At high incident kinetic energies, the complete disruption of both the target and projectile nuclei can occur in central collisions. For impact parameters between the grazing and head-on collisions, one observes an unusual type of nuclear reaction mechanism called deep inelastic scattering. In deep inelastic scattering, the colliding nuclei touch, partially amalgamate, exchange substantial amounts of energy and mass, continue to rotate due to the large angular momenta as a binuclear complex, and then reseparate primarily due to their mutual Coulomb repulsion.

The same range of reaction mechanisms can be depicted in terms of the angular momentum of the reaction in the entrance channel since we have already seen that $\ell \propto b$. An example of the schematic assignment of ranges of ℓ to reaction mechanisms is shown in Figure 10.23. The most peripheral collisions lead to elastic scattering and thus the highest values of the angular momentum transfer, ℓ. The grazing collisions lead to inelastic scattering and nucleon exchange reactions, which are lumped together as "quasi-elastic" reactions in this picture. Solid-contact collisions lead to deep inelastic collisions, corresponding to intermediate values of ℓ. The most head-on collisions correspond to CN formation and thus the lowest values of the angular momenta. Slightly more peripheral collisions lead to the fusion-like or quasi-fusion reactions.

Figure 10.23 Schematic illustration of the dependence of the partial cross sections for compound nucleus (CN), fusion-like (FL), deep inelastic (D), quasi-elastic (QE), Coulomb excitation (CE), and elastic (EL) processes on the entrance channel angular momenta (Schröder and Huizenga (1984, 242. Reproduced with the permission of Springer).

10.12.1 Coulomb Excitation

The potential energy due to the Coulomb interaction between a heavy-ion projectile and a target nucleus can be written as

$$E_{CM}^C = \frac{Z_1 Z_2 e^2}{R} \sim \frac{1.2 \, Z_1 Z_2}{A^{1/3}} \text{ MeV} \tag{10.97}$$

Because of the strong, long-range electric field between projectile and target nuclei, it is possible for the incident heavy ion to excite the target nucleus electromagnetically. This is called Coulomb excitation or Coulex for short. Rotational bands in deformed target nuclei may be excited by the absorption of so-called virtual photons created by the strongly varying electric field as the nuclei move past one another. This excitation technique is useful for studying the energy levels of nuclei. Since the cross sections for these reactions can be very large (involving long-range interactions with the nucleus at large impact parameters), the reactions are especially suitable for studying the structure of exotic nuclei with radioactive beams where the intensities are low. At relativistic energies, the strongly and rapidly varying electric fields can lead to large excitations of the nuclei that lead to particle emission or fission of the heaviest nuclei (electromagnetic dissociation).

10.12.2 Elastic Scattering

In Figure 10.24, the results for the angular distributions from the elastic scattering of two light nuclei can be contrasted with that observed in the collision involving a light ion with a much heavier target nucleus. Collisions between the light nuclei show the characteristic Fraunhofer diffraction pattern discussed earlier for nucleon scattering. The large Coulomb force associated with the heavier nucleus acts as diverging lens, causing the diffraction pattern to be that of Fresnel diffraction. For the case of Fresnel diffraction, special emphasis is given to the point in the angular distribution of the scattered particle where the cross section is 1/4 that of the Rutherford scattering cross section. This "quarter-point angle" corresponds to the classical grazing angle. Note that the elastic scattering cross section equals the Rutherford scattering cross section at scattering angles significantly less than the quarter point angle. Since the Rutherford scattering cross section is calculable, this fact allows experimentalists to measure the number of elastically scattered particles at angles less than the quarter point angle to deduce/monitor the beam intensity in heavy-ion-induced reaction studies.

10.12.3 Fusion Reactions

In Figure 10.25, we show another representation of the difference between the various near-barrier reaction mechanisms in terms of the energy needed to induce the reactions. From a very abstract view, in the entrance channel there
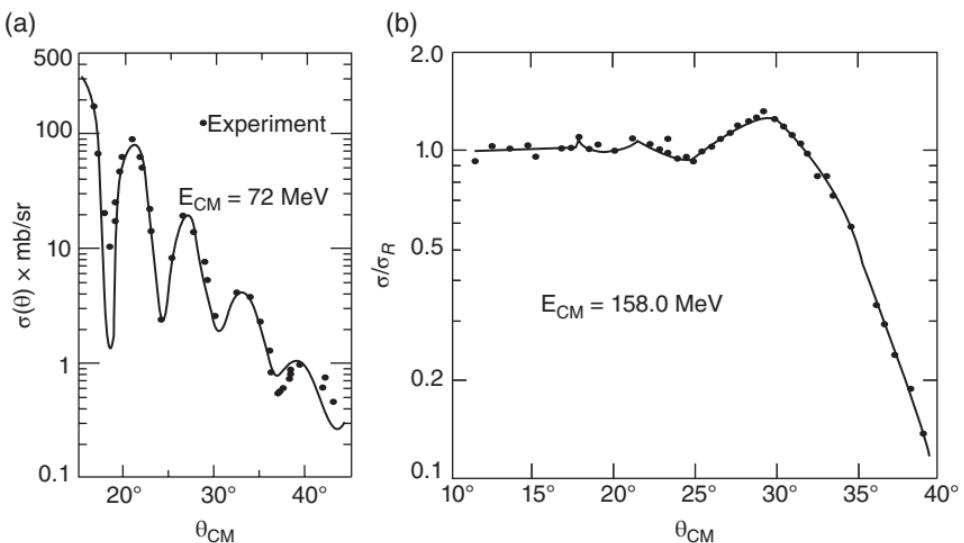
Figure 10.24 Angular distribution for $^{12}C + ^{16}O$ elastic scattering reaction showing a Fraunhofer diffraction pattern and the elastic scattering of ^{16}O with ^{208}Pb showing a Fresnel diffraction pattern (Valentin et al. (1981). Reproduced with the permission of Elsevier).
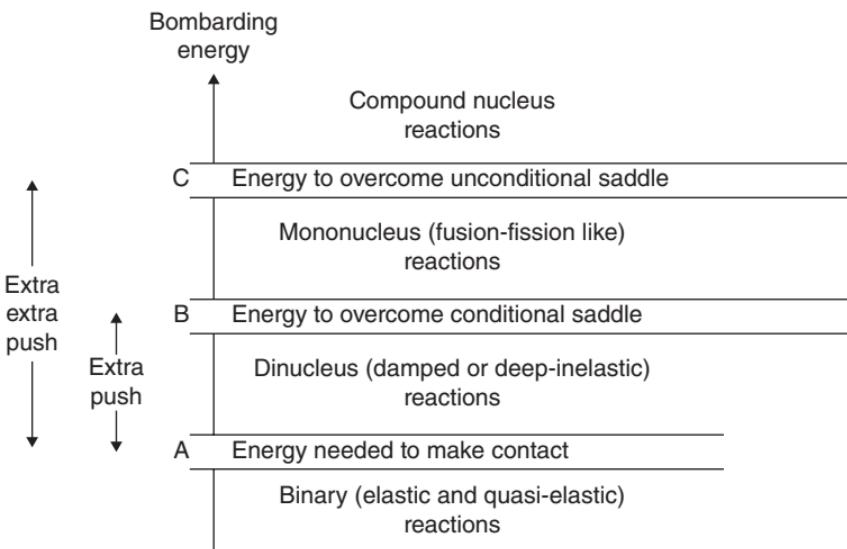
Figure 10.25 Schematic illustration of the three critical energies and the four types of near-barrier heavy-ion-induced nuclear reactions (Schroeder and Huizenga (1984). Reproduced with the permission of Springer).

are two distinct nuclei in their ground states with some relative kinetic energy. If the system fuses then the product is a CN then two separate nuclei have to undergo a large transition in shape and character to form one (approximately) spherical nucleus. From the kinetic energy standpoint, there is the minimum energy needed to bring the ions in contact and thus interact, the interaction barrier $V(R_{int})$. Bass has formally shown that the reaction cross section can be expressed in terms of this interaction barrier as

$$\sigma_R = \pi R_{int}^2 \left[1 - \frac{V(R_{int})}{E_{CMS}} \right] \tag{10.98}$$

where the interaction radius is given by Bass as

$$R_{int} = R_1 + R_2 + 3.2 \, \text{fm} \tag{10.99}$$

and the radius of each nucleus is

$$R_i = 1.12 A_i^{1/3} - 0.94 A_i^{-1/3} \, \text{fm} \tag{10.100}$$
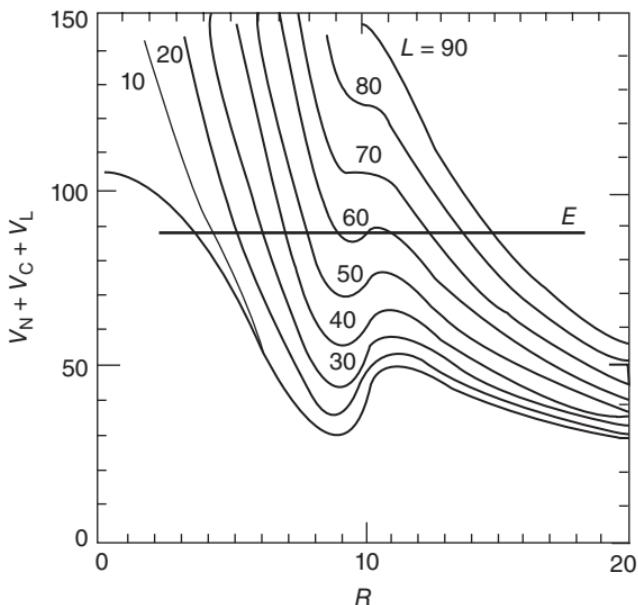
and the Bass interaction barrier is given by the expression

$$V_{Bass}(R_{int}) = 1.44 \, \text{MeV} \left(\frac{Z_1 Z_2}{R_{int}} \right) - b \left(\frac{R_1 R_2}{R_1 + R_2} \right) \tag{10.101}$$

where $b \sim 1 \, \text{MeV/fm}$. The energy necessary to cause the ions to interpenetrate where the ions have not fully merged and leading to quasi-fusion is called the extra-push energy in this framework. The higher energy necessary to cause the ions to truly fuse and forget their mode of formation is referred to as the extra–extra push energy.

The probability of fusion is also a sensitive function of the product of the atomic numbers of the colliding ions due to the large influence of Coulomb repulsion between two heavy ions. The abrupt decline of the fusion cross section observed in the formation of the heaviest nuclei as the Coulomb force between the ions increases leads to the emergence of the deep inelastic reaction mechanism. This decline and other features of the fusion cross section can be explained in terms of the potential energy surface on which the colliding ions move. As before with nucleon projectiles, this potential has of three contributions, the Coulomb potential, the nuclear potential, and the centrifugal potential. The variation of this potential as a function of the angular momentum ℓ is shown in Figure 10.26 for the reaction of ^{16}O with ^{120}Sn. One can image that the projectile approaches from the right side of the figure and slows down as it rides up the potential energy curve. Note that at small values of the angular momentum, there is a pocket in the potential. Fusion occurs when the ions get trapped in this pocket. If they do not get trapped they do not fuse. With high values of the Coulomb potential, there are few or no pockets in the potential for any value of ℓ, thus no fusion occurs. For a given projectile energy and Coulomb potential, there is a value of the angular momentum

Figure 10.26 Sum of the nuclear, Coulomb, and centrifugal potentials for the reaction of ^{18}O with ^{120}Sn as a function of radial distance for various values of the orbital angular momentum ℓ in the Bass model. The entrance channel kinetic energy (CMS) in this example is shown by the horizontal solid line.
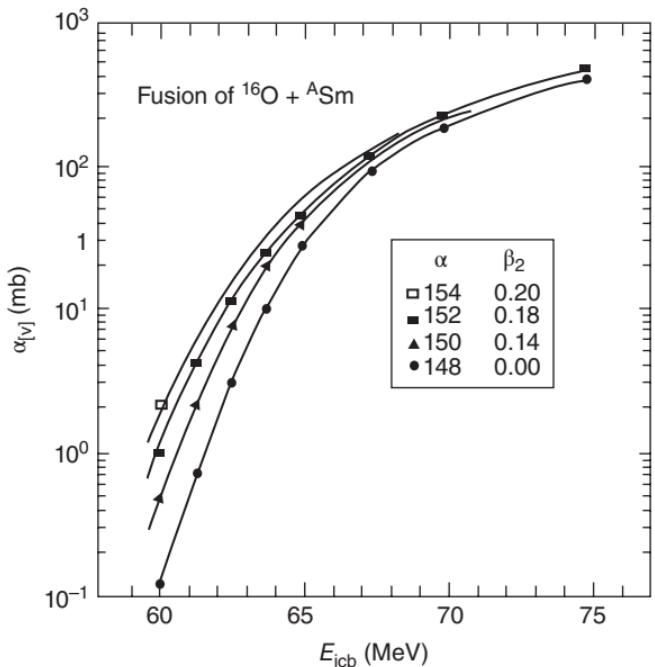
above which there are no pockets in the potential (the critical value of the angular momentum), and thus no fusion occurs for trajectories with these angular momenta.

Most of the stable nuclei are spherical, and one can construct an ℓ-dependent barrier to fusion that is the sum of the nuclear, Coulomb, and centrifugal potentials for these nuclei. However, this barrier is a sensitive function of the relative distance between the nuclei and thus would depend on the orientation of deformed nuclei. The cross section is a very steeply rising function of energy near the interaction barrier, and a small change in the Coulomb energy due to the orientation of a deformed nucleus would change the cross section. In Figure 10.27, the excitation function for fusion of ^{16}O with various isotopes of Sm is shown. Samarium is an even-Z element with many stable isotopes having neutron numbers that range from the closed shell at $N = 82$ into the region of nuclei with deformed ground states. One would have a significantly lower threshold and enhanced cross section for fusion where the ^{16}O ion interacts with a deformed ^{154}Sm nucleus compared with the reaction with a near-spherical ^{148}Sm nucleus. This enhancement is the result of the lowering of the fusion barrier for the collision with the deformed nucleus due to the fact that the ions can come into contact at a larger value of, R resulting in a lower Coulomb component of the potential.

Let us now consider what happens after the formation of a CN in a heavy-ion fusion reaction. In Figure 10.28, we show the predictions for the decay of the compound nuclei formed in the reaction of 147 MeV ^{40}Ar with ^{124}Sn to form ^{164}Er at an excitation energy of 53.8 MeV. The probability distribution is shown

Figure 10.27 Fusion cross sections observed for the reaction of ^{16}O with several samarium isotopes as indicated in the figure.
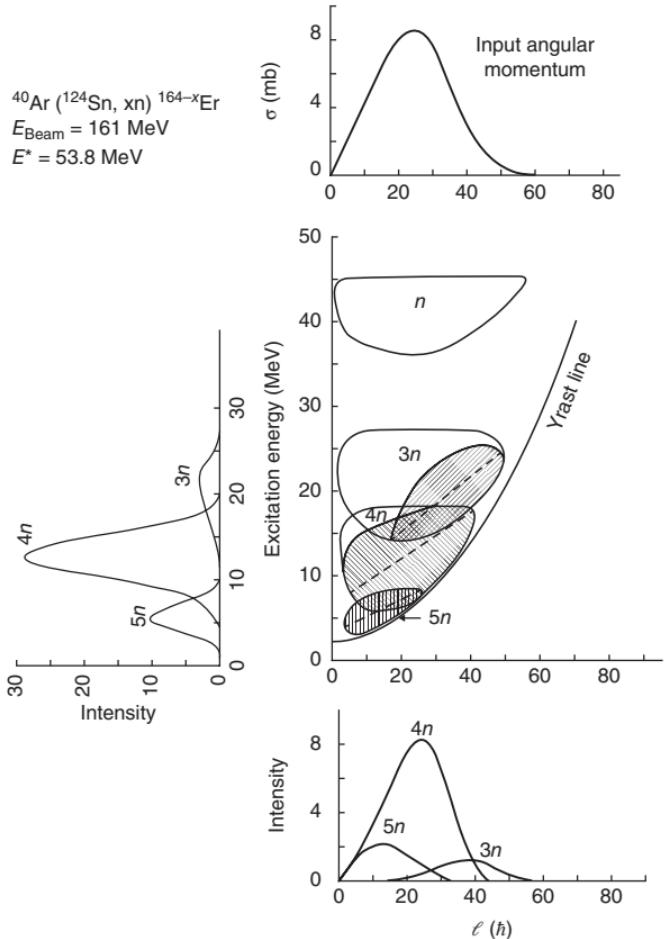
as a function of the angular momentum and the excitation energy of the CN. The angular momentum distribution in the CN populates states with $\ell = 0$ to $60\hbar$. The excitation energy is such that the preferred reaction channel is the evaporation of four neutrons from the CN with lesser amounts of three and five neutron emission. As the CN evaporates neutrons, the angular momentum does not change much since each neutron removes a relatively small amount of angular momentum. Eventually the yrast line restricts the population of states in the E^*-I plane. The yrast line is the locus of the excitation energy of the lowest lying state of a given angular momentum in a nucleus (and thus depends on the moment of inertia). Below the yrast line for a given spin, there cannot be any excited states in that nucleus. (The word yrast is from the Old Norse for the "dizziest.") When the system reaches the yrast line, it must decay by γ-ray emission to remove both excitation energy and angular momentum. Heavy-ion fusion reactions are thus a tool to excite the highest spins in nuclei allowing the study of nuclear structure at high angular momentum.

10.12.4 Incomplete Fusion

In the course of the fusion of the projectile and target nuclei, it is possible that one of the reaction partners will emit a single nucleon or a nucleonic cluster prior to the formation of a completely fused system. Such processes are referred to as pre-equilibrium emission (in the case of nucleon emission) or incomplete fusion (in the case of cluster emission). This process is particularly important for reactions induced by the α-cluster nuclei such as ^{12}C, ^{16}O, and ^{20}Ne. As the

Figure 10.28 The predicted population and decay of the ^{164}Er compound nuclei formed in the reaction of ^{40}Ar with ^{124}Sn at a bombarding energy of 161 MeV (lab). The probability distribution is shown in the plane of excitation energy and spin in the compound nucleus and projected onto the two axes (Stokstad (1985). Reproduced with the permission of Annual Reviews).

projectile energy increases above the interaction barrier, these processes can become more important and can dominate complete fusion at projectile energies above 20 MeV/nucleon. As a consequence of these processes where some part of the projectile is emitted with a high kinetic energy, the resulting product nucleus (close in mass to the CN) will have a momentum that is reduced relative to that for complete fusion. Measurement of the cross section as a function of momentum transfer in the collision provides a measure of the mass loss and the probability of these phenomena. A high energy component added to the expected evaporation distribution in the spectra of emitted particles is another signature or pre-equilibrium emission.

10.12.5 Deep-Inelastic Scattering

Now let us turn our attention to the case of deep inelastic scattering that primarily occurs between heavy-ion projectiles and heavy targets. In the early

1970s, as part of a quest to form superheavy elements by the fusion of Ar, Ca, and even Kr ions with the heaviest target nuclei, a new nuclear reaction mechanism was discovered called *deep-inelastic scattering*. For example, studies of the reaction of ^{84}Kr with ^{209}Bi (some results are shown in Fig. 10.29) did not observe the fission products of the completely fused nuclei ($Z_{CN} = 119$, $A_{CN} = 293$), rather projectile-like and target-like nuclei were produced with velocities close to those of the projectile and target along with a new and unexpected group of fragments with masses similar to those of the target and projectile at relatively low kinetic energies. These nuclei appeared to have undergone a very inelastic process that had resulted in the conversion of a large amount of the incident projectile kinetic energy into internal excitation energy of the two fragments. Further measurements revealed this to be a general phenomenon in heavy-ion reactions where the product of the atomic numbers of the colliding ions was very large (e.g., >2000). As indicated earlier, the colliding heavy ions come together, interpenetrate slightly, exchange neutrons and protons, dissipate kinetic energy in a diffusion process, and then reseparate under the influence of their mutual Coulomb repulsion. In this case the Coulomb and centrifugal energies are so large that the system never proceeds to a single CN but retains a di-nuclear character. The initial projectile energy is said to be
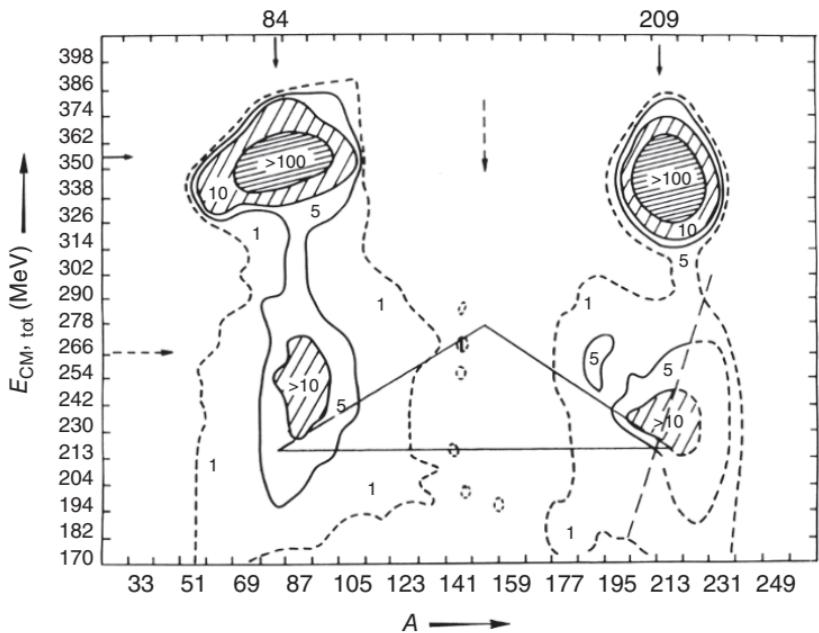
**Figure 10.29** Distributions of the cross sections as a function of kinetic energy (CMS) and mass number from the reaction of ^{84}Kr with ^{209}Bi. The contours are in mb and the solid arrows indicate the projectile and target masses; the dashed arrow and the solid triangle indicate the expected position of mass-symmetric fission products (Lefort et al. (1973). Reproduced with the permission of Elsevier).

"damped" into the excitation energy of the projectile-like and target-like fragments. These excited fragments undergo deexcitation cascades, evaporating particles, and eventually γ rays. As a consequence, the larger the kinetic energy loss in the collision process, the broader the distribution of the final products.

10.13 High-Energy Nuclear Reactions

A nuclear reaction is said to be a low energy reaction if the projectile energy is close to the interaction barrier, for example, $E/A \leq 10$ MeV/nucleon. A nuclear reaction is termed a high-energy reaction if the projectile energy is much higher and beginning to approach the rest mass, for example, ≥ 250 MeV/nucleon. (Not surprisingly the reactions induced by 20–250 MeV/nucleon heavy-ion projectiles are called intermediate energy reactions.)

What distinguishes low and high-energy reactions? In low energy nuclear collisions, the nucleons of the projectile interact with the average or mean nuclear force field associated with the entire target nucleus. In a high-energy reaction, the nucleons of the projectile generally interact with the nucleons of the target nucleus individually, as nucleon–nucleon collisions. To see why this might occur, we should compare the de Broglie wavelength of a 10 MeV proton with that of a 1000 MeV proton. We get $\lambda(10$ MeV $)= 9.0$ fm and $\lambda(1000$ MeV$)=$ 0.73 fm. The average spacing between nucleons in a nucleus is ~ 1.2 fm. Thus, we conclude that at low energies, a projectile nucleon will interact with the nucleus as a whole, while at high energies, collisions can occur between the incident nucleon and individual nucleons in the nucleus.

10.13.1 Spallation/Fragmentation Reactions

At high incident energies we must deal with nucleon–nucleon collisions and we should not expect any significant amount of CN formation. Instead most reactions should be reactions taking place on a short time scale that leave the target and projectile in very excited states. If we limit the incident particle to protons (as was true from a historical standpoint) after the collision, we would be left with one of a set of target nuclei in a variety of excited states depending on the number of struck target nucleons. In Figure 10.30, we show a typical distribution of the masses of the residual nuclei from the interaction of protons at energies near 1 GeV with the heavy nucleus, ^{209}Bi. One observes a continuous distribution of product masses ranging from the target mass to very low masses at the highest incident energies. Three regions can be readily identified in the yield distributions. One region is centered around one-half of the target mass ($A = 50$–140) and consists of the products of the fission of a target-like nucleus. There is a region with larger masses ($A_{obs} \geq (2/3)A_{target}$) that are the products from a fast knockout reaction process called **spallation**. The incident
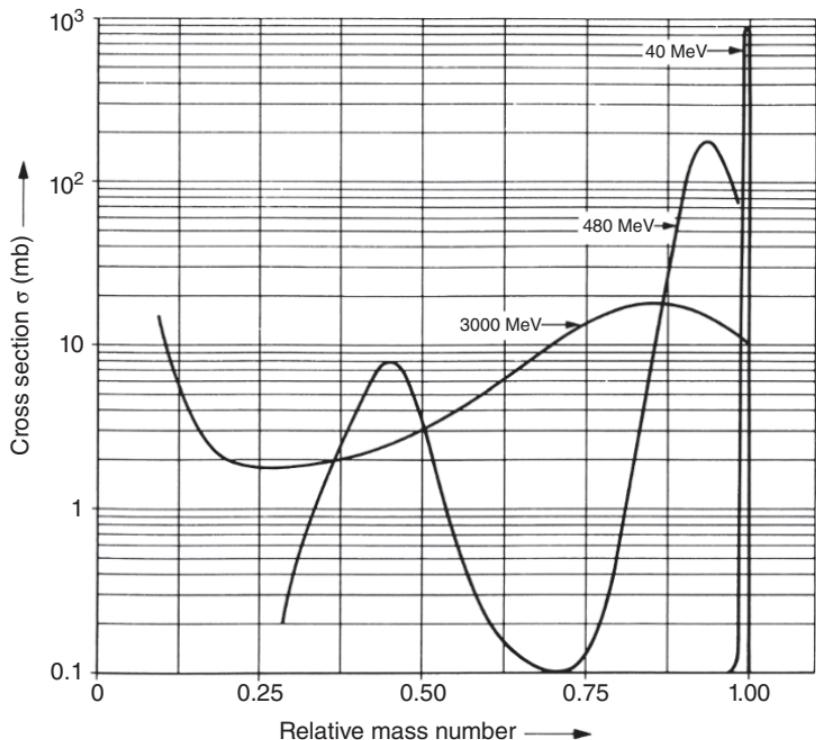
Figure 10.30 Distributions of the cross sections as a function of mass number from the reaction of high energy protons with ^{209}Bi (Miller and Hudis (1959). Reproduced with the permission of Annual Reviews).

proton knocks out several nucleons in a series of two-body collisions, leaving behind a highly excited heavy nucleus (see following text). This highly excited nucleus goes on to decay by the evaporation of charged particles and neutrons, forming a continuous distribution of products ranging downward in mass from that of the target. The spread of the distribution in mass is correlated with the incident energy. The term "spallation" was given to this phenomenon by one of us (GTS) after consultation with a professor of English who assured him that the verb "to spall" was a very appropriate term for this phenomenon. In the region of the lowest mass fragments ($A_{obs} \leq (1/3)A_{target}$), one observes another group of fragments that are called "intermediate mass fragments (IMF)." These lightest fragments are thought to arise from the extremely excited remnants of the most head-on collisions that decay by either long chains of sequential particle emission or nuclear shattering with simultaneous explosive disintegration of the remnant.

Looking at spallation in a little more detail, the course of these reactions at high energies is significantly different than that occurring at lower energies. As mentioned earlier, high-energy collisions occur between pairs of nucleons

rather than having the incident nucleon (or nucleus) interact with the nucleus as a whole. The cross section for nucleon–nucleon scattering varies inversely with projectile energy. At the highest energies, this cross section may become so small that some nucleons will pass through the nucleus without undergoing any collisions, that is, the nucleus appears to be transparent. In this regard, a useful quantitative measure of the number of collisions a nucleon undergoes in traversing the nucleus is the mean free path Λ. Formally we have

$$\Lambda = \frac{1}{\rho\sigma} \tag{10.102}$$

where σ is the average nucleon–nucleon scattering cross section ($\sim$30 mb at high energies) and ρ is the nuclear density ($\sim 1.5 \times 10^{38}$ nucleons/cm^3 or $\sim$0.15 nucleons/fm^3). Thus, the mean free path of a high-energy nucleon in a nucleus is $\sim 3 \times 10^{-13}$ cm or $\sim$3 fm, which is about 1/4 the diameter of a large nucleus. In each collision, the kinetic energy imparted to the struck nucleon is $\sim$25 MeV and thus the struck nucleon may collide with other nucleons depending on its initial position in the nucleus, generating a cascade of struck particles (see Fig. 10.31). If the energy of the incident nucleon exceeds $\sim$300 MeV, then it is possible to generate π-mesons in the nucleon–nucleon collisions, which, in turn, can interact with other nucleons. A typical time scale for the fast cascade is the time for the particles to propagate across the target nucleus or $\sim 10^{-22}$ s. The result of this intranuclear cascade is an extremely excited (if not disrupted)
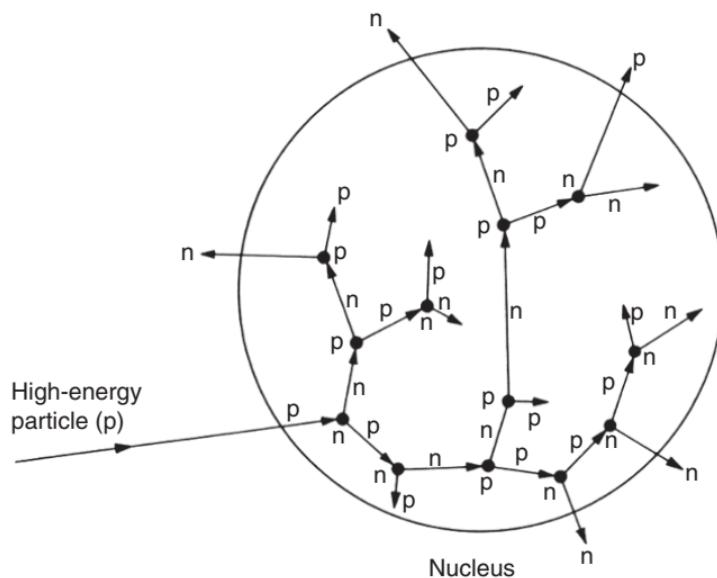
Figure 10.31 Schematic view of an intranuclear cascade in a large nucleus induced by a high energy proton. Note that the size and localization of the nucleons are exaggerated and small relative to the nucleus (Lieser (1997). Reproduced with the permission of VCH).

nucleus, which may decay by pre-equilibrium emission of particles, evaporation of nucleons or heavier nuclei (alphas, etc.) or even disintegration into multiple fragments. The spallation products are produced nearly at rest in the target frame and most remain in the target. Most of these products are radioactive, and this mechanism provides an important technique for making radioactive nuclei for study and is the basis of the isotope separator online (ISOL) facilities. The difficulty is extracting the activity of interest from the target material in a timely manner.

The Bevalac accelerator complex was constructed in the mid-1970s at Berkeley to provide heavy-ion beams at relativistic energies for the first time. This initiated the study of heavy-ion reactions at very high energies (0.250–2.1 GeV/nucleon), which were qualitatively different from low-energy heavy-ion reactions and even high-energy proton-induced reactions. At these high projectile energies, the distributions of observed products (extremely high-energy protons and neutrons along with significant residues of the target and projectile) that were interpreted in terms of a simple geometric model referred to as the abrasion–ablation or fireball model. The geometrical or so-called macroscopic view of these collisions is outlined in Figure 10.32. In the abrasion–ablation model, part of the incoming projectile is rapidly sheared off and itself shears off a sector of the target (corresponding to the geometrical
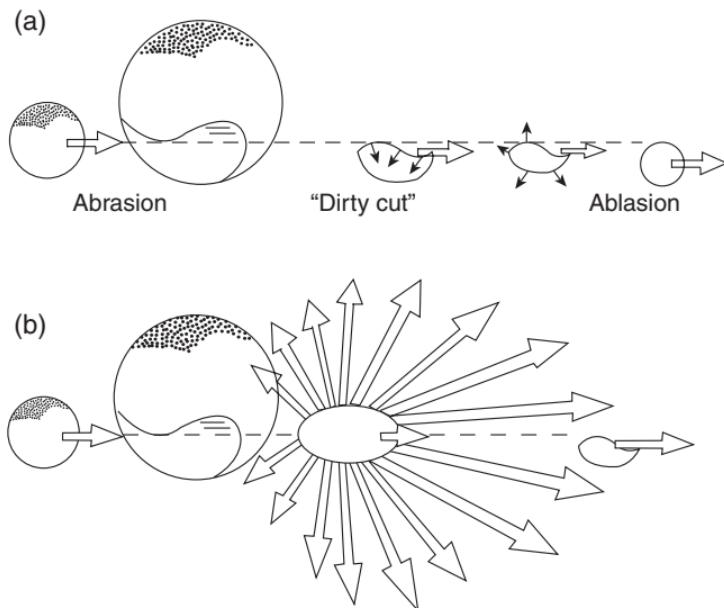
Figure 10.32 Schematic views of the abrasion–ablation model of high energy nucleus–nucleus collisions: (a) emphasis on the formation of the target and projectile fragments by the geometrical overlap of the densities; (b) emphasis on the formation of a hot fireball of nuclear matter in the region of geometrical overlap of the two nuclei.

overlap region of the projectile and target nuclei—the "abrasion" step). The nonoverlapping regions of the target and projectile nuclei were assumed to be left essentially undisturbed and unheated because the projectile and target move past one another before the unstruck nucleons can react, the so-called spectators to the collision. The overlap region consists of high-excited nuclear matter (the "participants" in the collision) that form a "fireball" that decays explosively into nucleons and the lightest fragments. The distorted target and projectile nuclei were expected to have a region of extra surface area exposed by the cuts through them. Associated with this extra surface area is a relatively small excitation energy; the surface area term of the semiempirical mass equation indicates about 1 MeV per excess fm^2 of surface area. As the nucleus relaxes, this excess surface energy becomes available as excitation energy and results in the normal emission of nucleons and fragments (the "ablation" step). This surface energy was found to be too small to explain the distribution of products, and various other mechanisms were developed to deliver more energy into the spectators.

The use of this simple model for high-energy nucleus–nucleus collisions has resulted in a general categorization of energetic nucleus–nucleus collisions as either "peripheral" or "central." The peripheral reactions take place at large impact parameters with large residues of the target and projectile that have small momentum transfer and relatively low excitation energies. Such reactions that produce significantly large, surviving spectators are referred to as fragmentation reactions. Notice that the projectile fragment from these reactions will be moving close to the (vector) velocity of the beam. Most of these fragments are radioactive nuclei, and some of the them have never been studied because they are very exotic. The projectile fragments leave the target very rapidly (less than a nanosecond) without undergoing any chemical reactions. Various devices have been developed to collect and use the projectile fragments. Modern radioactive beam facilities can accelerate heavy nuclei and collide them with light targets such as beryllium to produce beams of the most exotic nuclei for study and to induce secondary reactions (see following text).

10.13.2 Reactions Induced by Radioactive Projectiles

There are <300 stable nuclei but several thousand nuclei that are radioactive and have experimentally accessible lifetimes. In the recent past, one of the fastest growing areas of research in nuclear science has been the study of nuclear reactions induced by radioactive projectiles. Both the ISOL and projectile-fragmentation (PF) techniques discussed in Chapter 14 have been used to produce several hundred new radioactive nuclear beams for study of the ions themselves or to induce secondary reactions. One of the principal attractions in these studies is the ability to form reaction products or reaction

intermediates with very unusual N/Z ratios that are not possible by combining the stable isotopes. The high-energy reaction of stable nuclei that are either very proton-rich or very neutron-rich can produce radioactive nuclei through fragmentation in regions of nuclei cannot be reached in direct or fusion reactions. At higher energies, the isospin of the intermediate species may be unusual, allowing one to determine the effect of isospin on the properties of highly excited nuclear matter. Occasionally the radioactive beams themselves have unusual structure, that is, ^{11}Li, and their properties and reactions are of interest.

10.13.3 Multifragmentation

In central collisions of high energy, heavy ions take place at the smallest impact parameters and transfer the largest amount of energy and momentum from the projectile motion into the participants. In central nucleus–nucleus collisions at intermediate energies (∼20–200 MeV/nucleon), large values of the nuclear excitation energy (>1000 MeV) and temperature (>10 MeV) may be achieved for short periods of time (10^{-22} s). Nuclei at these high excitation energies can decay by the emission of small nuclei also called IMF. Colloquially, an IMF is defined as a reaction product whose mass is >4 and less than that of a fission fragment. Multifragmentation occurs when several IMFs are produced in a reaction. This could be the result of sequential binary processes, "statistical" decay into many fragments (described by passage through a transition state or the establishment of statistical equilibrium among fragments in a critical volume), or dynamical process in which the system evolves into regions of volume and surface instabilities leading to simultaneous fragment production.

To investigate these phenomena, it is necessary to simultaneously measure as many of the emitted fragments and particles from a reaction as possible. As a result, various multidetector arrays have been constructed specifically to study these reactions. Quite often these arrays consist of several hundred individual detectors to detect the emitted IMFs, light charged particles, sometimes neutrons, and even products from the target. As a consequence of the high granularity of these detectors, the analysis of the experimental data is time consuming and difficult. Nonetheless, several interesting developments have occurred in recent years. One theory to describe multifragmentation postulates the formation of a hot nuclear vapor during the reaction, which subsequently condenses into droplets of liquid nuclear matter (IMFs) somewhere near the critical temperature. First postulated to occur in the interaction of giga-electron volt protons with xenon nuclei, recent experiments with heavy ions have resulted in the deduction of the variation of the temperatures and excitation energies (Fig. 10.33) that resemble that expected for a liquid- to gas-phase transition. This "caloric curve" shows an initial rise in temperature with excitation energy typical of heating a liquid, followed by a flat region (the
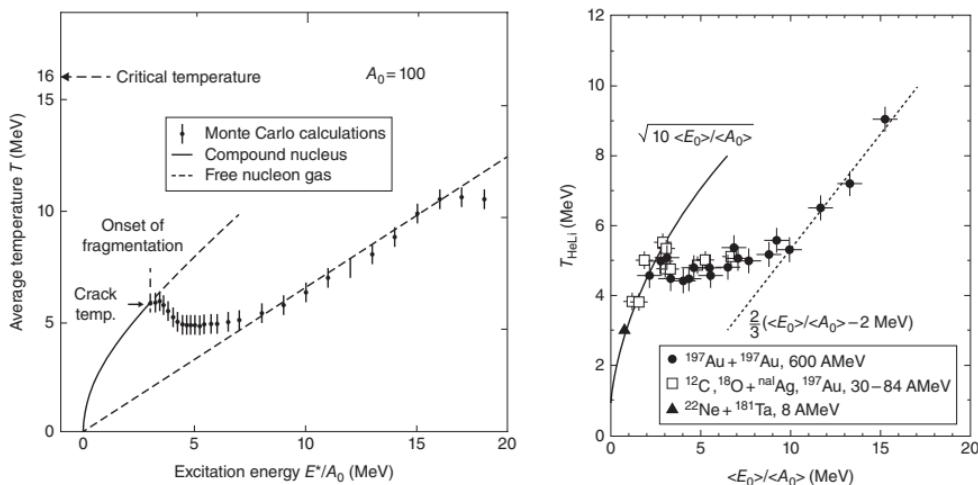
Figure 10.33 Example of the comparison of the calculated caloric curve indicating a nuclear phase transition in a multifragmentation model (left) and the results of the measurement of the light products from several nuclear reactions (right).

phase transition), and followed by a region corresponding to heating a vapor. There has been an extended debate and much discussion of the relative role of statistical and dynamical factors in multifragmentation. The debate has focussed on the observation that the data from several reactions indicate that the probability of emitting multiple fragments, P, could be expressed in a form, $P \propto \exp(-B/T)$, where B is constant and T is a nuclear temperature extracted from the data. This variation suggests that the fragment emission probabilities depend on a single fragment emission barrier, B, a feature that is consistent with a statistical decay. Others have criticized this observation by focussing on the details of the correlation and evidence for dynamic effects in the reactions.

10.13.4   Quark–Gluon Plasma
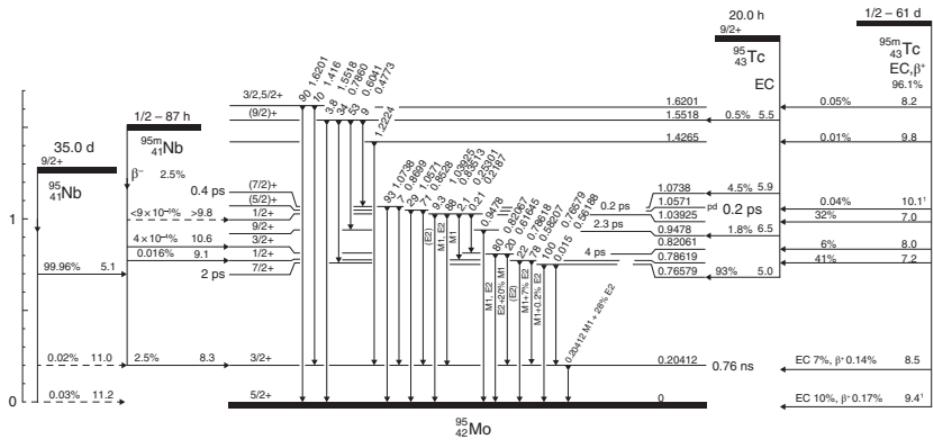
An important thrust in studies of central collisions at ultra-relativistic energies (>5 GeV/nucleon) is to create and observe a new form of matter called the *quark–gluon plasma* (QGP). The modern theory of the strong interaction, quantum chromodynamics, predicts that while quarks and gluons will be confined within a nucleon or colloquially a "nucleonic bag" under normal conditions, they can become deconfined at sufficiently high thermal energies and densities. A phase transition from normal nuclear matter to the QGP is predicted to occur at energy densities of 1–3 GeV/fm^3, which is thought to be achievable in central collisions of large nuclei at CMS energies of 17 GeV/nucleon.

The experimental signatures of a phase transition include (a) suppression of production of the heavy vector mesons such as the J/Ψ and Ψ' resonance and the upsilon states, (b) the creation of a large number of $s\bar{s}$ strange quark-strange antiquark pairs, and (c) the momentum spectra, abundance, and direction of emission of pairs of leptons (so-called di-lepton pairs). The first phase experiments in this field have been carried out, and it is believed that energy densities of ~2 GeV/fm^3 were created. Strong J/Ψ suppression has been observed relative to that observed in proton–nucleus collisions along with an increase in strangeness production.

Problems

10.1   Consider the reaction of ^{16}O with ^{64}Ni at a CMS energy of 48 MeV. What is the lab kinetic energy of the ^{16}O ? What is the Coulomb barrier for the reaction? What is the total reaction cross section at this energy? What is the maximum angular momentum brought in by the ^{16}O projectile at this energy?

10.2 One reaction proposed for the synthesis of Darmstadtium ($Z = 110$) is the reaction of ^{59}Co with ^{209}Bi at a laboratory energy of 300 MeV. Calculate the expected total reaction cross section for this reaction.

10.3 Define or describe the following terms or phenomena: direct reaction, compound nucleus, and stripping reaction.

10.4 A piece of gold metal that is 1.0 mm thick is bombarded for 15 h by a slow neutron beam of intensity 10^6/s. How many disintegrations per second of ^{198}Au are present in this sample 24 h after the end of the bombardment? $\sigma(n, \gamma) = 98.8$ b at this neutron energy, $t_{1/2}(^{198}\text{Au}) = 2.7$ days.

10.5 What was the rate of production, in atoms per second, of ^{128}I during a constant 1 h cyclotron (induced neutron) irradiation of a pure iodine sample if the sample was found to contain 2.00 mCi of ^{128}I activity at 15 min after end of the irradiation?

10.6 What is the excitation energy of the ^{116}Sb compound nuclei formed by the bombardment of ^{103}Rh with 50 MeV ^{13}C ions?

10.7 Recall that neutrons evaporated from a compound nucleus are known to have an average kinetic energy of $2T$, where T is the nuclear temperature of the residual nucleus. What is the optimum bombarding energy for the production of ^{66}Ga via the ^{65}Cu($\alpha, 3n$) reaction if the average nuclear temperature is 1.6 MeV?

10.8 What is the number of ^{60}Co atoms produced in a 10 mg sample of cobalt metal exposed for 2.0 min to a thermal neutron flux of 2×10^{13} n/cm^2/s in a reactor? The cross section for producing 10.5 min ^{60}Co^m is 16 barns, while the cross section for producing 5.3 y ^{60}Co ground state is 20 barns. What is the disintegration rate of the cobalt sample 4 h after the end of the irradiation?

10.9 Consider the ^{48}Ca + ^{248}Cm reaction where the lab energy of the ^{48}Ca is 300 MeV. What is the excitation energy of the putative compound nucleus ^{296}116? What is the expected total reaction cross section at this energy?

10.10 A 100 mg/cm^2 thick natural zirconium target was bombarded with a beam of 11 MeV protons for 1 h (beam current = 25μA). The ^{95}Nb^m

Nuclear decay scheme for mass number 95: $^{95}_{41}$Nb, $^{95m}_{41}$Nb, $^{95}_{42}$Mo, $^{95}_{43}$Tc, and $^{95m}_{43}$Tc.
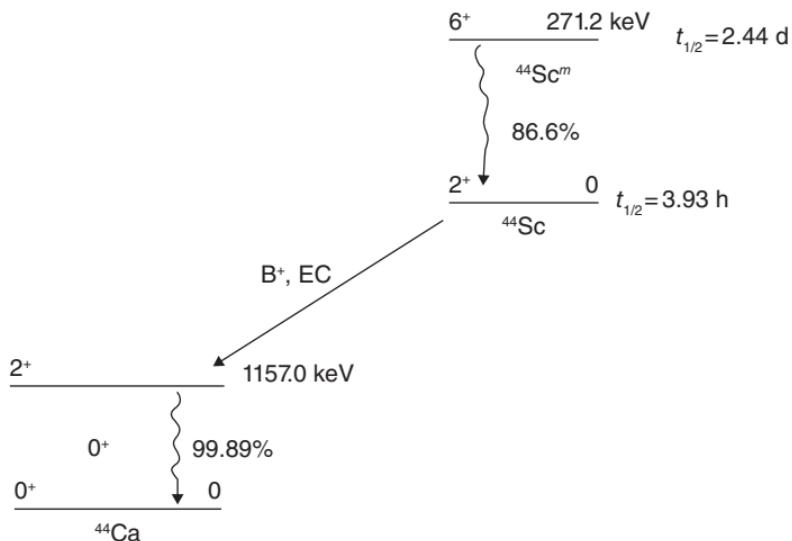
from the reaction $^{96}Zr(p, 2n)$ was isolated chemically (with a 100% yield), and the *k*-X-rays resulting from the internal conversion decay of $^{95}Nb^m$ were counted. In a 2-h long count beginning 20 h after the end of bombardment, 1000 counts were observed in the Nb Kα-X-ray peak. Given the ^{95}Nb decay scheme shown below and the data given below, calculate the cross section for the $^{96}Zr(p, 2n)^{95}Nb^m$ reaction. Fluorescence yield = 0.7 and efficiency of detection of the K-X-ray is 10^{-3}, $\alpha_k = 2.21$.

10.11 Consider the reaction of 10 MeV/nucleon ^{129}Xe with ^{238}U. What is the kinetic energy of the elastically scattered ^{129}Xe detected at 10° in the lab system?

10.12 Consider the $^{40}Ca(d, p)$ reaction. What would be the most probable angle to detect the protons leading to the first excited state $(3/2^-)$ of ^{41}Ca? What would be the proton kinetic energy at this angle if the energy of the incident deuteron beam was 21.0 MeV?

10.13 Consider you want to make ^{18}F for use in PET studies. What would be the maximum specific activity (dpm/g F) of the ^{18}F made by irradiating 1.0 g of KF in a flux of 10^{10} fast neutrons/cm^2/s. You may assume the $^{19}F(n, 2n)$ cross section is 300 mb. Imagine you want to produce the ^{18}F carrier-free (i.e., with no stable fluorine present). Devise a synthetic scheme for producing the carrier-free ^{18}F. Defend your choice of nuclear reaction.

10.14 Consider the nuclide $^{99}Tc^m$ that is the daughter of ^{99}Mo. Most diagnostic procedures involving radioactivity in the United States involve $^{99}Tc^m$. Explain how you would produce ^{99}Mo (the 66.0 h parent of 6.0 h $^{99}Tc^m$). Compare and contrast two possible choices, production of ^{99}Mo as a fission product or via the $^{98}Mo(n,\gamma)$ reaction.

10.15 Calculate the activity of ^{254}No $(t_{1/2} = 55$ s) present 5.0 min after a 10 min irradiation of a 0.0010 in thick ^{208}Pb foil by ^{48}Ca projectiles $(\Phi = 6.28 \times 10^{12}$ particles/s). Assume $\sigma(^{48}Ca, 2n)$ is 3×10^{-30} cm^2.

10.16 Consider the reaction $^{12}C(\alpha, n)$ where the laboratory energy of the incident α particle is 14.6 MeV. What is the excitation energy of the compound nucleus? The reaction cross section is 25 mb. Assuming a carbon

target thickness of 0.10 mg/cm² and a beam current of 25 pnA, compute the ^{15}O activity after a 4.0 min irradiation.

10.17 The cross section for the ^{60}Ni(α, pn) reaction is 0.9 barn for 32 MeV α-particles. Calculate the number of disintegrations per minute of ^{62}Cu at 15 min after a 15 min bombardment of a 50 mg/cm² foil of ^{60}Ni with 10 pμA of 32 MeV α-particles.

10.18 Consider the reaction ^{29}Si(^{18}O,p2n) that populates the metastable and ground states of ^{44}Sc. Using the decay scheme shown later, and the fact that at EOB one observed 1000 photons/s at an energy of 271.2 keV and 1000 photons/s at an energy of 1157.0 keV, calculate the ratio of the cross section for the production of ^{44}Sc^m, σ_m, to the cross section for the production of ^{44}Sc, σ_{gs}. Neglect any decay of ^{44}Sc^m to ^{44}Sc during the irradiation and assume the length of the irradiation was 6 h.

Bibliography

G.F. Bertsch and E. Kashy, Am. J. Phys. **61**, 858 (1993).
C. Fultz, et al., Phys. Rev. **127**, 1273 (1962).
S.N. Ghoshal, Phys. Rev. **80**, 939 (1950).
J.M. Miller and J. Hudis, Ann. Rev. Nucl. Sci. **9**, 159 (1959).
V.F. Weisskopf, Rev. Mod. Phys. **29**, 174 (1959).

Most textbooks on nuclear physics and chemistry have chapters on nuclear reactions. Among the favorites of the authors are the following:

W.D. Ehmann and D.E. Vance, *Radiochemistry and Nuclear Methods of Analysis* (John Wiley & Sons, Inc., New York, 1991).

P.E. Hodgson, E. Gladioli, and E. Gladioli-Erba, *Introductory Nuclear Physics* (Clarendon, Oxford, 1997).

N.A. Jelley, *Fundamentals of Nuclear Physics* (Cambridge University Press, Cambridge, 1990).

K.S. Krane, *Introductory Nuclear Physics* (John Wiley & Sons, Inc., New York, 1988).

M. Lefort, *Nuclear Chemistry* (Van Nostrand, Princeton, 1968).

K.H. Lieser, *Nuclear and Radiochemistry* (VCH, Wertheim, 1997).

J.S. Lilley, *Nuclear Physics* (John Wiley & Sons, Ltd, Chichester, 2001).

W.E. Meyerhof, *Elements of Nuclear Physics* (McGraw-Hill, New York, 1967).

L. Valentin, *Subatomic Physics: Nuclei and Particles*, Volume II (North-Holland, Amsterdam, 1981).

S.S.M. Wong, *Introductory Nuclear Physics*, 2nd Edition (John Wiley & Sons, Inc., New York, 1998).

Some specialized references to nuclear reactions that are specially recommended include:

R. Bass, *Nuclear Reactions with Heavy Ions* (Springer-Verlag, Berlin, 1980).

J.R. Parrington; *General Electric Company, Nuclides and Isotopes*, 15th Edition (General Electric, San Jose, 1996).

G.R. Satchler, *Introduction of Nuclear Reactions*, 2nd Edition (Oxford, New York, 1990).

W.U. Schröder and J.R. Huizenga, in *Treatise on Heavy-Ion Science*, Volume 2, D.A. Bromley, Ed. (Plenum Press, New York, 1984).

R. Stokstad, in *Treatise on Heavy Ion Science*, Volume 3, D.A. Bromley, Ed. (Plenum, New York, 1985).

11

Fission

11.1 Introduction

Fission has a unique importance among nuclear reactions. Apart from the nuclear reactions that drive the sun, no other nuclear reaction has had such a profound impact on the affairs of man. The discovery of fission and the developments that proceeded from it have altered the world forever and have impinged on the consciousness of every literate human being. The exploitation of nuclear energy that followed the discovery of fission, particularly in weapons of mass destruction, has been of profound importance to humankind.

Chemists have played an important role in the study of fission. Fission was discovered by the chemists Otto Hahn and Fritz Strassmann in 1938 (cf. translation by Graetzer (1964)). By painstakingly difficult chemical separations, they were able to show the neutron irradiation of uranium led not to many new elements as had been thought but to products like barium, lanthanum, and so on. The uranium nucleus had not increased in size by adding a neutron but had been split! That conclusion caused Hahn and Strassmann much concern as they wrote "As 'nuclear chemists' working very close to the field of physics, we cannot bring ourselves yet to take such a drastic step (to conclude that uranium had fissioned), which goes against all previous experience in nuclear physics" (Am. J. Phys. 32, (1964), 15). Nuclear chemists have continued their role in studying fission, first using chemical techniques and, more recently, using physical techniques.

Knowledge of fission and its consequences is important for the nuclear power industry and the related fields of nuclear waste management and environmental cleanup. From the point of view of basic research, fission continues to be interesting in its own right as an example of large-scale collective motion of the nucleus, as an important exit channel for many nuclear reactions, and as a source of neutron-rich nuclei for nuclear structure studies and use as radioactive beams.

The reader should be cautioned that understanding the fission process represents a very difficult problem. Some of the best minds in chemistry and

physics have worked on the problem since the discovery of fission. Yet while we understand many aspects of the fission process, there is no overall theoretical framework that gives a satisfactory account of the basic observations. Figure 11.1 presents a schematic view of the fission process. A nucleus with some small equilibrium (ground-state) deformation absorbs energy through some process, becomes excited, and deforms into a configuration known as the "transition-state" or "saddle point" configuration. As the nucleus deforms, the nuclear Coulomb energy decreases (as the average distance between the protons in the excited nucleus increases), while the nuclear surface energy increases (as the nuclear surface area increases). At the saddle point, the rate of change of the Coulomb energy is equal to the rate of change of the nuclear surface energy. The formation and decay of this transition state of the nucleus is the rate-determining step in the fission process and corresponds to the passage over an activation energy barrier to the reaction. If the nucleus deforms beyond this point, it is irretrievably committed to fission. When the nucleus crosses the transition state, then in a very short time, the neck between the nascent fragments disappears (ruptures) and the nucleus divides into two fragments at the "scission point." At the scission point, one has two highly charged, deformed nuclear fragments in contact with each other. The large Coulomb repulsion between the two fragments accelerates them to ~90% of their final kinetic energy within ~10^{-20} s. As these accelerated primary fragments move away from one another, they contract to more spherical shapes, converting the potential energy of deformation into internal excitation energy, that is, they become "hotter." This excitation energy is removed by the emission of so-called prompt neutrons emitted from the fully accelerated fragments, and then, in increasing competition with the last neutrons to be emitted, the nucleus emits γ-rays. Finally, on a longer time scale, the neutron-rich fragments emit β⁻ particles. Occasionally one of these β-decays populates a high-lying excited state of a daughter that is unstable with respect to neutron emission, and the daughter nucleus can emit a neutron long after the fission event. These few neutrons are called "delayed" neutrons and provide the basis for controlled fission reactors. Note that this schematic view conflicts with some presentations of fission in elementary textbooks. For example, since the neutrons are mostly emitted primarily from the fully accelerated fragments, their spatial distribution is concentrated along the direction of motion of the fragments. The neutrons do not emerge randomly from the fissioning nucleus as many artists' conceptions of fission depict. Also note that the energy release in fission is primarily in the form of the kinetic energies of the fragments, not in the neutrons, photons, or other emitted particles. This energy is the "mass–energy" released in fission due to the increased stability of the fission fragments.

Because of the large amount of experimental information available about fission, it is beyond the scope of this chapter to present a complete treatment of fission research. We shall attempt to emphasize the fundamental aspects of the
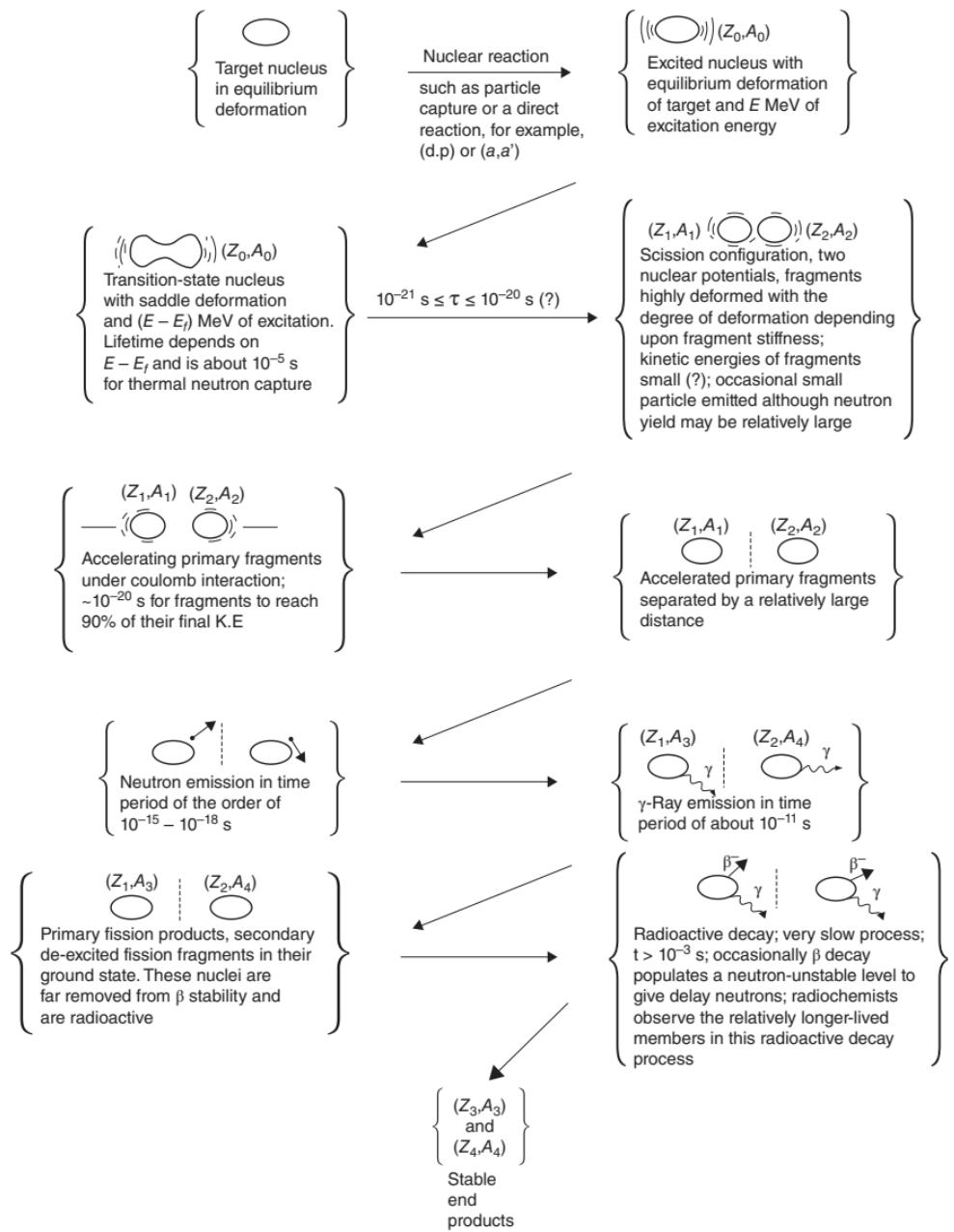
Figure 11.1 Schematic overview of the nuclear fission process (Gindler and Huizenga (1964). Reproduced with the permission of Elsevier).

subject. The reader is referred to one of the excellent monographs or reviews of fission Hoffman et al., 1996; Oganessian and Lazarev, 1985; Vandenbosch and Huizenga, 1973; Wagemans, 1991 for further information.

11.2 Probability of Fission

11.2.1 Liquid Drop Model

Figure 11.1 suggests that fission proceeds in three steps, the ascent to the saddle point, the critical passage over the saddle point, and the descent through the scission point. We shall present our discussion of fission from this point of view where we concentrate on the first two steps. We shall assert that like chemical reactions, the reaction probability is determined by the passage through the transition state. We shall also assert, perhaps more controversially, that the distribution of fission product energies, masses, and so on is determined at or near the scission point.

Let us begin with a discussion of the probability of fission. For the first approximation to the estimation of the fission barrier, we shall use the liquid drop model (Chapter 2). We can parameterize the small nonequilibrium deformations, that is, elongations, of the nuclear surface as

$$R(\theta) = R_0[1 + \alpha_2 \, P_2(\cos \theta)] \tag{11.1}$$

where α_2 is the quadrupole distortion parameter ($=\sqrt{5/4\pi}\beta_2$) and P_2 is the second-order Legendre polynomial. For small distortions of a sphere, the surface, E_S, and Coulomb, E_C, energies are given by

$$E_S = E_S^0 \left(1 + \frac{2}{5}\alpha_2^2\right) \tag{11.2}$$

$$E_C = E_C^0 \left(1 - \frac{1}{5}\alpha_2^2\right) \tag{11.3}$$

where E_S^0 and E_C^0 are the surface and Coulomb energies of the undistorted spherical drops, respectively. When the changes in the Coulomb and surface energies ($\Delta E_C = E_C^0 - E_C, \Delta E_S = E_S - E_S^0$) are equal, the nucleus becomes spontaneously unstable with respect to fission. At that point we find that

$$\frac{E_C^0}{2E_S^0} = 1 \tag{11.4}$$

Thus it is natural to express the fissionability of nuclei in terms of a parameter x, that is, this energy ratio and is called the *fissionability parameter.* Thus

$$x = \frac{E_C^0}{2E_S^0} = \frac{1}{2}\frac{\text{Coulomb energy of a charged sphere}}{\text{Surface energy of that sphere}} \tag{11.5}$$

and will be a constant for a given nucleus. We can approximate the Coulomb and surface energies of a uniformly charged sphere by the following expressions:

$$E_C^0 = \frac{3}{5} \frac{Z^2 e^2}{r_0 A^{1/3}} = \left(a_C \frac{Z^2}{A^{1/3}} \right) \tag{11.6}$$

$$E_S^0 - 4\pi r_0^2 S A^{2/3} = a_S A^{2/3} \tag{11.7}$$

where $a_C = 3e^2/5r_0$, S is the surface tension per unit area ($\approx 1\ MeV/fm^2$), and $a_S = 4\pi r_0^2 S$. Then the equation for x becomes

$$x = \left(\frac{a_C}{2a_S} \right) \left(\frac{Z^2}{A} \right) = \frac{Z^2/A}{(Z^2/A)_{\text{critical}}} \tag{11.8}$$

where the ratio of the constants $(a_C/2a_S)^{-1}$ is referred to as $(Z^2/A)_{\text{critical}}$. The fissility of a given nucleus thus is viewed relative to the value of $(Z^2/A)_{\text{critical}}$. More sophisticated treatments of the fissionability of nuclei show that $(Z^2/A)_{\text{critical}}$ varies slightly from nucleus to nucleus (due to the isospin asymmetry) and should be given by the expression

$$\left(\frac{Z^2}{A} \right)_{\text{critical}} = 50.883 \left[1 - 1.7826 \left(\frac{(N-Z)}{A} \right)^2 \right] \tag{11.9}$$

The parameters Z^2/A and x provide measures of the relative fissionability of nuclei. The greater the value of these parameters, the more "fissionable" the nuclei are, although the scale is rather compressed. Very fissionable nuclei like ^{239}Pu have Z^2/A values of 36.97, while less fissionable nuclei like ^{209}Bi have Z^2/A values of 32.96. Recall that the Z^2/A factor is simply proportional to the ratio of the disruptive Coulomb energy ($\propto Z^2/A^{1/3}$) to the cohesive surface (nuclear) energy ($\propto A^{2/3}$).

Note that the parameter $(Z^2/A)_{\text{critical}}$ is the ratio of two empirical constants related to the strength of the Coulomb and surface (nuclear) forces. If we take the view that the limit to the size of the periodic table is given by the point at which the heaviest nuclei spontaneously undergo fission

$$\frac{E_C^0}{2E_S^0} = 1 \tag{11.10}$$

We can rearrange these equations to find the value of the atomic number Z at which this occurs. Thus, Z_{limit} is given by the expression

$$Z_{\text{limit}}^2 = 2 \left(\frac{a_S}{a_C} \right) A_{\text{limit}} \tag{11.11}$$

If we remember that the neutron/proton ratio in heavy nuclei is about 1.5, then Z_{limit} will be about $5(a_S/a_C)$. Thus, we can set the upper bound to the periodic table from the ratio of two constants relating to the strength of the

fundamental nuclear and Coulomb forces. The ratio a_S/a_C is about 20–25, and so we can expect a fundamental limit of about 100–125 chemical elements!

For all stable nuclei, x must be < 1, and the total deformation energy of nuclei undergoing fission will increase by an amount $(1/5)\alpha_2^2(2E_S^0 - E_C^0)$, as the nucleus deforms toward fission. This increase in potential energy can be thought of as an activation energy barrier for the reaction. Eventually if the deformation proceeds far enough, the decrease in Coulomb energy will overwhelm the increase in surface energy, and the deformation energy will decrease. (In this case, the simple deformation energy formulas used so far in our discussion become inaccurate, and more complicated formulas must be used.) One can appreciate the difficulty of these calculations by a simple example. The liquid drop fission barrier for ^{238}U is 4.8 MeV. Equating this to $(1/5)\alpha_2^2(2E_S^0 - E_C^0)$ and using the values of 983 MeV for E_C^0 and 695 MeV for E_S^0 for ^{238}U, one can estimate that the value of the deformation parameter α_2 is 0.243, which requires changes in the surface and Coulomb energies (ΔE_S^0 and ΔE_C^0) of 16.4 and 11.6 MeV, respectively. Thus, one sees that the resulting fission barrier heights are small differences between two larger numbers that may be difficult to determine. Modern calculations of the potential energy of deformation for the liquid drop model involve many deformation coordinates (as many as five or six at present, not just the α_2 used previously) and represent major computational tasks.
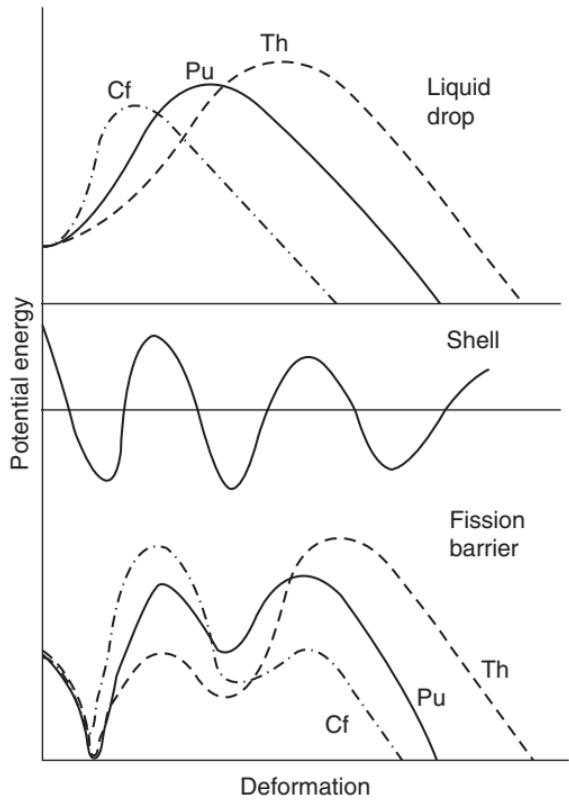
11.2.2 Shell Corrections

Figure 11.2 illustrates how some of the basic features of nuclei combine to give an overall fission barrier. The fission barriers are estimated with the liquid drop model for a range of actinide nuclei along with a qualitative estimate of the variation of the nuclear shells with deformation. Focusing on the upper part of the figure, the fission barrier height decreases, and the maximum (saddle point) moves to smaller deformations as Z^2/A increases. In the lighter nuclei the saddle point and scission point configurations are more similar, that is, have a similar deformation, than in the heavier nuclei.

As we learned in Chapter 2, it is necessary to include shell effects in the liquid drop model if we want to get reasonable agreement of the predictions with nuclear masses. Similarly we must devise a way to include shell effects with the liquid drop model description of the effect of deforming nuclei. Strutinsky (1967) proposed such a method to calculate these "shell corrections" (and also corrections for nuclear pairing) with the framework of the liquid drop model. In this method, the total energy of the nucleus is taken as the sum of a liquid drop model energy, E_{LDM}, and the shell (δS) and pairing (δP) corrections to this energy:

$$E = E_{LDM} + \sum_{p,n}(\delta S + \delta P) \tag{11.12}$$

Figure 11.2 Qualitative features of the fission barriers for some actinide nuclei as a function of deformation (Britt (1982). Reproduced with the permission of Pergammon Press, Ltd.).

The shell corrections, just like the liquid drop energy, are functions of the nuclear deformation. The shell corrections tend to lower the ground-state masses of spherical nuclei with magic or near-magic numbers of neutrons and protons. They also tend to lower the ground-state mass of mid-shell nuclei at various finite deformations (e.g., $\beta_2 \approx 0.3$), thus accounting for deformed nature of the actinides. Large shell correction energies are found when the ratios of the major/minor nuclear axes are in the ratio of small whole numbers, as $3 : 2$ or $2 : 1$ (corresponding to bunching up of the single particle levels). The result of combining these deformation-dependent shell corrections with the liquid drop barriers is shown schematically in Figure 11.2. The stable ground-state shapes of the actinide nuclei in the figure are predicted to have some finite deformation ($\beta_2 \sim 0.2$) rather than zero deformation (a sphere), and a secondary minimum in the barrier appears at $\beta_2 \sim 0.6$ (axes ratio of $2 : 1$). In the heaviest nuclei ($Z \geq 106$), where the liquid drop fission barriers are very small or nonexistent, the observed fission barrier heights are due primarily to a lowering of the ground-state mass by shell corrections. Without these shell effects, the heaviest nuclei could not be observed as they would decay by spontaneous fission on a time scale much shorter than we can observe ($t_{1/2} < \mu s$).

Notice that this combination of macroscopic (LD) and microscopic (shell) effects predicts a double-humped fission barrier with equal barrier heights, and a deep secondary minimum will occur for nuclei in the uranium-plutonium region. For heavier nuclei, like californium, the first barrier is predicted to be much larger than the second barrier, and passage over this first barrier is rate determining. In effect, these heavy nuclei ($Z \geq 100$) behave as though they have a high, thin single barrier to fission. The predicted barrier shape is triple-humped in many cases for lighter nuclei (radium, thorium). The reader should be aware that the situation is even more complicated than this; cursory description would indicate as the variability of nuclear shapes should make it clear that the real fission barriers are multidimensional in character with a complicated dependence on asymmetric and symmetric deformations. In general, there is ample experimental and theoretical evidence that the lowest-energy path in the fission process corresponds to having the nucleus, initially in an axially symmetric and mass (reflection) symmetric shape, pass over the first maximum in the fission barrier with an axially asymmetric but mass symmetric shape and then pass over the second maximum in the barrier with an axially symmetric but mass (reflection) asymmetric shape. Because of the complicated multidimensional character of the fission process, there are no simple formulas for the fission barrier heights. However, the reader can find (Vandenbosch and Huizenga, 1973; Wagemans, 1991) extensive tabulations of experimental characterizations of the fission barrier heights for various nuclei.

Nuclei can be trapped in the secondary minimum of the fission barrier. Such trapped nuclei will experience a significant hindrance of their γ-ray decay back to the ground state (because of the large shape change involved) and an enhancement of their decay by spontaneous fission (due to the "thinner" barrier, they would have to penetrate). Such nuclei are called *spontaneously fissioning isomers*, and they were first observed in 1962 and are discussed in the succeeding text. They are members of a general class of nuclei, called *super-deformed nuclei* that have shapes with axes ratios of 2 : 1. These nuclei are all trapped in a pocket in the potential energy surface due to a shell effect at this deformation.

11.2.3 Spontaneous Fission

In 1940 Petrzhak and Flerov discovered that ^{238}U could decay by spontaneously fissioning into two large fragments (with a probability that was 5×10^{-7} of that of undergoing α-decay). Over 100 examples of this decay mode have been found since then. Spontaneous fission is a rare decay mode in the light actinides and increases in importance with increasing atomic number until it is a stability-limiting mode for nuclei with $Z \geq 98$. The spontaneous fission half-lives change by a factor of 10^{29} in going from the longest-lived uranium nuclei to the short-lived isotopes of fermium.

It is clear from these basic facts and our picture of fission that spontaneous fission is a barrier penetration phenomenon similar to α or proton decay. The nucleus "tunnels" from its ground state through the fission barrier to the scission point. Therefore we would expect the spontaneous fission half-life to have the form

$$t_{1/2}^{SF} = \frac{\ln(2)}{fP} \tag{11.13}$$

where f is the frequency of assaults on the fission barrier in the first minimum ($\sim 10^{20}$/s) and P is the barrier penetrability. As in α or proton decay, the penetrability factor is the most important term. The calculation of the barrier penetrability is complicated by the double-or triple-humped shape of the multi-dimensional barrier. A simple model for the barrier (near its top) is that of an inverted harmonic oscillator potential (a parabola) as indicated in Figure 11.3. The Hill–Wheeler formula describes the transmission coefficient for penetration of such a barrier as
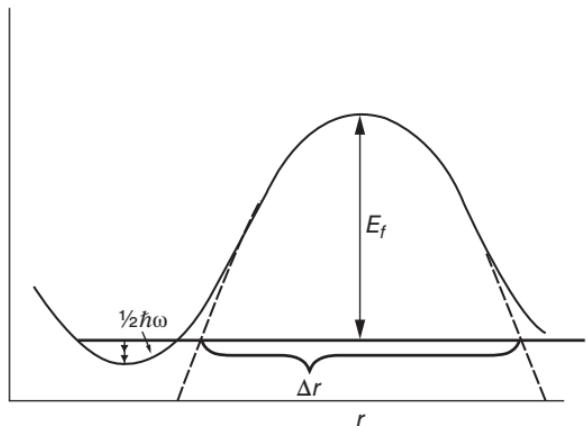
$$P = \left(1 + \exp \left[\frac{2\pi(B_f)}{\hbar \omega} \right] \right)^{-1} \tag{11.14}$$

where B_f is the fission barrier height and $\hbar \omega$ is the barrier curvature (spacing between the levels in the corresponding "normal" harmonic oscillator potential). Large values of $\hbar \omega$ imply tall, thin barriers with high penetrabilities; low values of $\hbar \omega$ imply short, thick barriers with low penetrabilities. Combining equations gives

$$t_{1/2}^{SF} \approx 2.77 \times 10^{-21} \exp \left(\frac{2\pi B_f}{\hbar \omega} \right) \text{ s} \tag{11.15}$$

As an exercise, we can compare the spontaneous fission half-lives of two nuclei with barrier heights of 5 and 6 MeV, respectively, and barrier curvatures of

Figure 11.3 A simple parabolic fission barrier (Vandenbosch and Huizenga (1973). Reproduced with the permission of Elsevier).
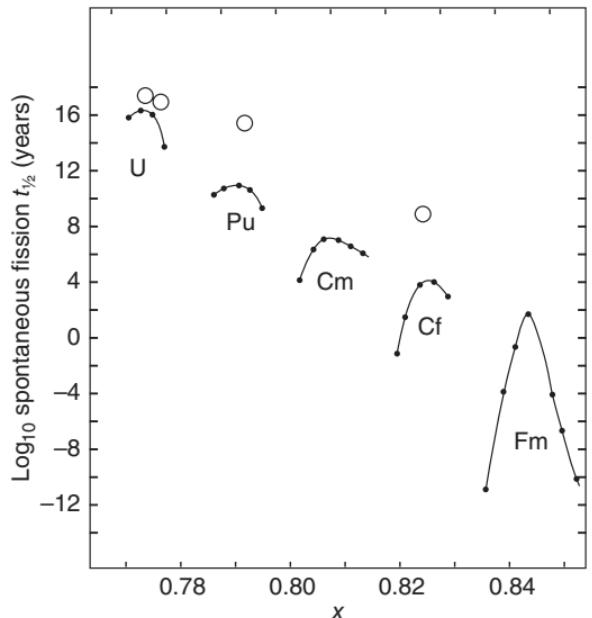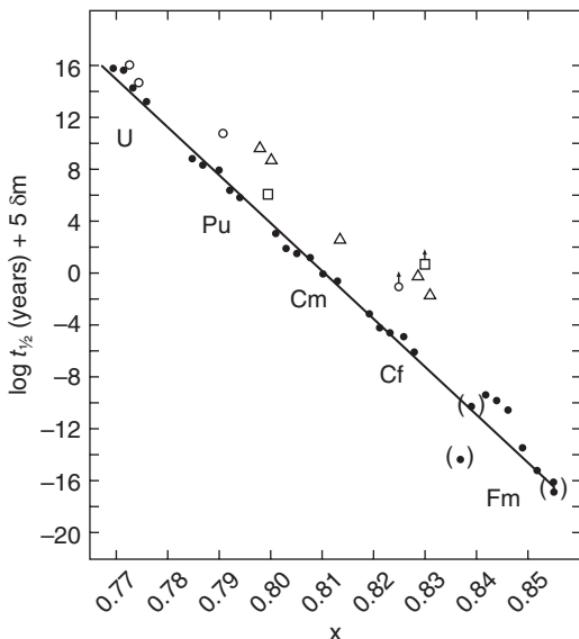
Figure 11.4 Spontaneous fission half-lives of even–even (solid points) and even–odd nuclides (open circles) as a function of fissionability parameter, *x* (Vandenbosch and Huizenga (1973). Reproduced with the permission of Elsevier).

0.5 MeV. One quickly finds that the spontaneous fission half-lives of these two nuclei differ by a factor of 3×10^5. The barrier heights and curvatures in this example are similar to those in the actinides and illustrate the exponential nature of barrier penetration in that a 1 MeV uncertainty in the fission barrier height corresponds to a factor of 10^5 in the spontaneous fission half-life.

In our previous discussion, we showed that the fission barrier heights depend on Z^2/A and thus so should the spontaneous fission half-lives. The dependence of the known spontaneous fission half-lives on x, the fissionability parameter, is shown in Figure 11.4. There is an overall decrease in spontaneous fission half-life with increasing x, but clearly the spontaneous fission half-life does not depend solely on Z^2/A. One also observes that the odd A nuclei have abnormally long half-lives relative to the even–even nuclei. In addition, the spontaneous fission half-lives of the heaviest nuclei ($Z \geq 104$) are roughly similar with values of milliseconds.

Similar observations were made in the discussion of α decay. Swiatecki has shown that there is a correlation between the deviations of the spontaneous fission half-lives from the smooth trend with Z^2/A and the deviations of the ground-state masses from those expected from the liquid drop model. (These deviations are exactly the shell and pairing corrections discussed previously.) Following the prescription developed by Swiatecki, we can plot the function $\log(t_{1/2}) + 5\delta m$ versus x, where δm represents the deviation of the ground-state mass from the liquid drop model. The correlation, shown in Figure 11.5, becomes much better, indicating we have perhaps identified the

Figure 11.5 Spontaneous fission half-lives, corrected according to the method of Swiatecki, versus fissionability parameter *x* (Vandenbosch and Huizenga (1973). Reproduced with the permission of Elsevier).

essence of the phenomenon. However, we should note that the half-lives of the odd *A* nuclei are still significantly longer than those of the neighboring even–even nuclei even though we have corrected the effect of the ground-state masses. We can parameterize this difference with a hindrance factor similar to that used in α decay systematics. In the present case, the hindrance factor is defined as the log of the ratio of the observed half-life for an odd *A* nucleus to that of the neighboring even–even nuclei. For the odd *A* nuclei, typical hindrance factors of 5 are observed, that is, the odd *A* half-lives are $\sim 10^5$ times longer than those of their even–even neighbors (Hoffman et al., 1996).

11.2.4 Spontaneously Fissioning Isomers

Since the discovery of the first spontaneously fissioning isomer, a number of other examples have been found. The positions of these nuclei in the chart of nuclides are shown in Figure 11.6. These isomers range from thorium to berkelium, forming an island with a point of maximum stability near ^{242}Am. γ-ray decay back to the ground-state limits the number of isomers with lower *Z* and *N* than those in this island, while spontaneous fission decay limits the number of cases with high *Z* and *N*. The half-lives range from 10^{-9} to 10^{-3} s, whereas the ground-state half-lives of the same nuclei are $\sim 10^{25}$ to 10^{30} times longer. The typical excitation energy of these isomers is 2–3 MeV. Spectroscopic studies of the transitions between the states in the second minimum has established that the moments of inertia associated with the rotational bands of these excited

		140	141	142	143	144	145	146	147	148	149	150	151
Fm	100												
Es	99												
Cf	98												
Bk	97												
Cm	96												
Am	95												
Pu	94												
Np	93												
U	92												
Pa	91												
Th	90												

Figure 11.6 The positions of the known spontaneously fissioning isomers in the high mass end of the chart of nuclides. The dark-colored boxes indicate one isomeric state, while the light-colored boxes indicate two isomeric states (Vandenbosch and Huizenga (1973). Reproduced with the permission of Elsevier). (*See insert for color representation of the figure.*)

nuclei are those expected for an object with an axes ratio of $2 : 1$, a result confirmed in other quadrupole moment studies.

11.2.5 The Transition Nucleus

In analogy to chemical reactions, we might expect the probability of fission as expressed in terms of the fission width, $\Gamma_f (= \hbar/\tau)$ to be given by the expression

$$\Gamma_f = A \exp\left(\frac{-B_f}{T}\right) \tag{11.16}$$

where B_f is the fission barrier height. It turns out that this approach is an oversimplification, but it has certain pedagogical uses. For example, in an early paper describing fission, Bohr and Wheeler were able to use this idea to show that a rare odd A isotope of uranium, ^{235}U, was responsible for the fission of natural uranium by thermal neutrons, not the more abundant even–even isotope ^{238}U. The ability to cause odd A actinide nuclei to undergo fission when bombarded with thermal neutrons is of great practical importance. Because of the large cross sections associated with thermal neutrons due to their long wavelengths, the fission cross sections for these odd A nuclei are very large. For the "big three" nuclei, ^{233}U, ^{235}U, and ^{239}Pu, of which significant quantities can be produced, the thermal neutron-induced fission cross sections are 530, 586, and 752 barns, respectively. These three actinides are the basis for the fuel in nuclear reactors and nuclear weapons utilizing fission by thermal neutrons.

Sample Problem 11.1: Fission Barriers and Excitation Energy

Why do thermal neutrons whose kinetic energy is 0.025 eV cause ^{235}U to fission, but not ^{238}U?

Solution

Let us calculate the energy released when a neutron is captured by ^{235}U and ^{238}U. (This will be equivalent to the binding energy of the last neutron in ^{236}U and ^{239}U.)

For ^{235}U
$$E_{\text{release}}^{235} = [M(235) + M(\text{n}) - M(236)]c^2$$
$$= 40.913 + 8.071 - 42.440 = 6.544 \text{ MeV}$$

For ^{238}U
$$E_{\text{release}}^{238} = [M(238) + M(n) - M(239)]c^2$$
$$= 47.305 + 8.071 - 50.570 = 4.806 \text{ MeV}$$

The fission barrier in ^{235,238}U is ~5.7 MeV. Thus, for ^{235}U + n, we exceed the fission barrier even with "zero kinetic energy" neutrons, while for ^{238}U + n, we will need ~1 MeV neutrons to get over the fission barrier. In fact, this example suggests ^{235}U would fission even if we bombarded it with "negative kinetic energy" neutrons. Where would we find such neutrons? Consider the reaction ^{235}U(d,p). The Q value for this reaction is negative, and it is equivalent to adding a neutron to the nucleus and can even correspond, at low bombarding energies, to the addition of "negative kinetic energy" neutrons to the nucleus, allowing studies of near-barrier phenomena in this and other odd A actinides.

We should note that once again, the probability of fission is more complicated than what the simple relation given previously would indicate. In a paper written shortly after the discovery of fission, Bohr and Wheeler showed that fission has to compete with other modes of nuclear de-excitation. They showed that Γ_f should be written as

$$\Gamma_f = \frac{N_f}{N_f + N_n + N_\gamma + N_{\text{cp}}} \tag{11.17}$$

where N_i is a measure of the number of ways (open channels) to accomplish each possible de-excitation process ($N_i = 2\pi\Gamma_i/D$). When evaluating N_f, one must evaluate ρ_f, the density of levels in the transition-state nucleus that lead to fission. N_n is the principal term in this equation for heavy nuclei (i.e., it is the most likely decay channel) and is taken as the number of final states
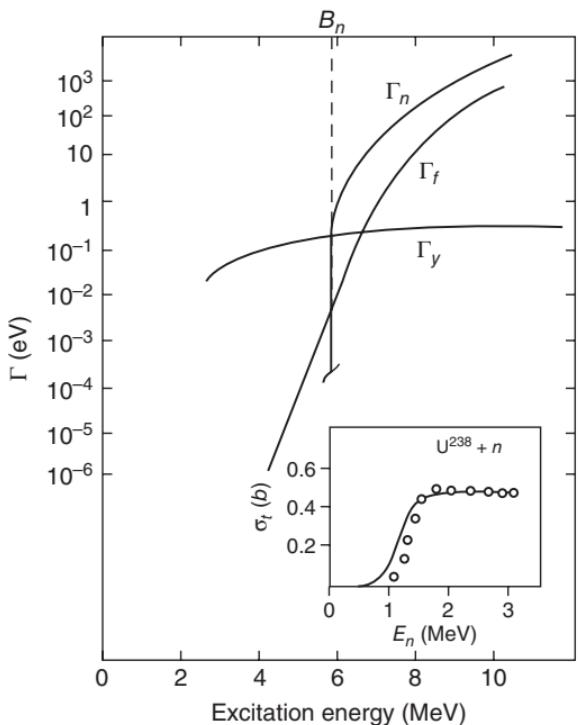
Figure 11.7 Schematic diagram of neutron, fission, and γ-ray widths of a typical excited heavy nucleus with a neutron binding energy slightly < 6 MeV. The inset shows the predicted fission excitation function for a nucleus with $B_f - B_n = 0.75$ MeV together with some recent data (Vandenbosch and Huizenga (1973). Reproduced with the permission of Elsevier).

of the daughter nucleus (after emitting a neutron) times the neutron kinetic energy. N_γ is the number of states decaying by γ-ray emission to a lower-lying level (small but important below the neutron separation energy), and N_{cp} is the number of states decaying by charged-particle emission (negligibly small). Bohr and Wheeler's predictions of the probability of fission in ^{238}U as a function of excitation energy are shown in Figure 11.7.

In nuclear reactors one has neutrons with energies ranging from thermal energies (0.025 eV) to several MeV. There are a series of sharp peaks in the cross section for neutron-induced reactions with energies between 0.2 and 3000 eV that are called "resonances." (See discussion in Chapter 10.) These resonances correspond to exciting specific isolated level in the compound nucleus (CN) that can decay by fission. The situation is particularly interesting for the neutron irradiation of even–even nuclei, like ^{240}Pu at subthreshold energies as shown in Figure 11.8. The resonances associated with fission appear to cluster in bunches, but not all resonances in the CN lead to fission. We can understand this situation with the help of Figure 11.9. The normal resonances correspond to excitation of levels in the CN, which are levels in the first minimum shown schematically in Figure 11.9. When one of these metastable levels exactly corresponds to a level in the second minimum, then there will be enhanced tunneling through the fission barrier and an enhanced
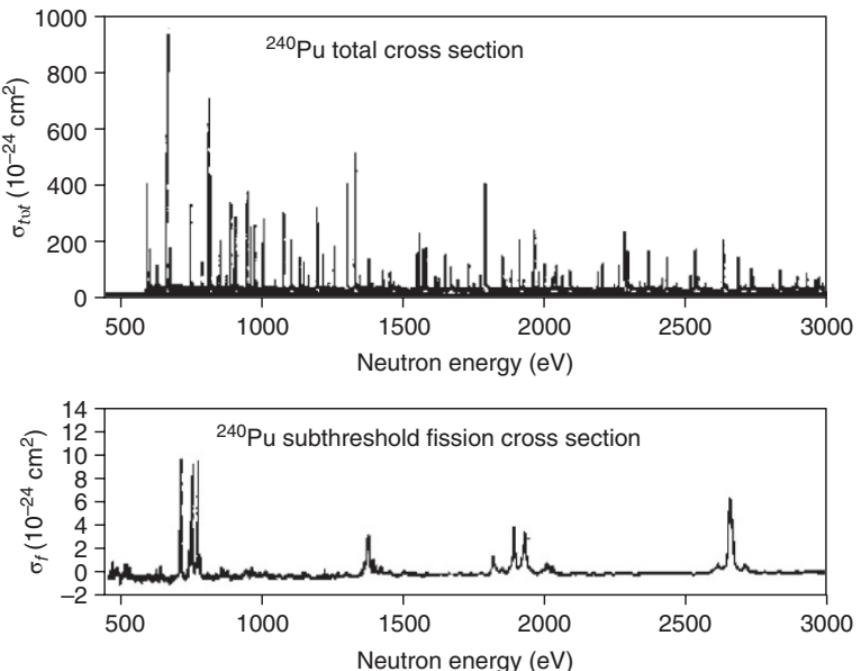
Figure 11.8 The neutron total reaction cross sections (above) and sub-barrier fission cross sections (below) of ^{240}Pu as a function of neutron energy between 0.5 and 3 keV (Wagemans (1991). Reproduced with the permission of CRC Press).

fission cross section. The state in the second minimum can have a significant width due to a short lifetime and could overlap with several states in the ground state well, giving rise to the clusters of states.

When higher-energy ($E > 1$ MeV) neutrons interact with nuclei like ^{238}U where the fission barrier height is greater than the neutron separation energy, a stairstep pattern is observed in the excitation function. The excitation function is the variation of the cross section with energy as seen in Figure 11.10. The first rise and plateau is due to the occurrence of the (n,f) reaction. The second rise and plateau is due to the (n, nf) reaction called "second-chance fission" where one neutron is emitted and the daughter is still highly excited and undergoes fission. The third rise and plateau is due to the $(n, 2nf)$ reaction and called "third-chance fission". For nuclei with $B_f < B_n$, a similar pattern occurs but riding on top of a rapidly decreasing cross section at low energies due to $1/v$ absorption of neutrons.

How do we estimate the factors determining the fission probability when the excitation energy of the fissioning system is 10 MeV or more? (How do we calculate the various widths?) At these excitation energies, we have reached the point where the statistical model of nuclear reactions can be used. The most important terms in the branching ratio are only Γ_n and Γ_f. Some experimental data on the **ratio** of Γ_n to Γ_f at excitation energies of 5–25 MeV is shown
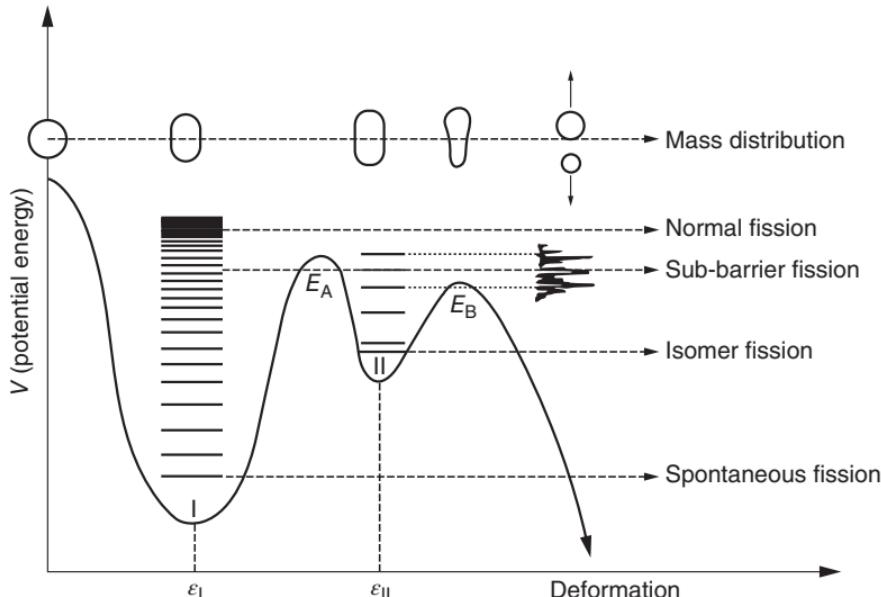
Figure 11.9 Schematic representation of the energy levels in a fissionable nucleus and the double-humped fission barrier. Intrinsic excitations in the first and second minimum are indicated along with the path of spontaneous fission from the ground state, isomeric-state fission, sub-barrier fission, and direct fission from a high excited state.
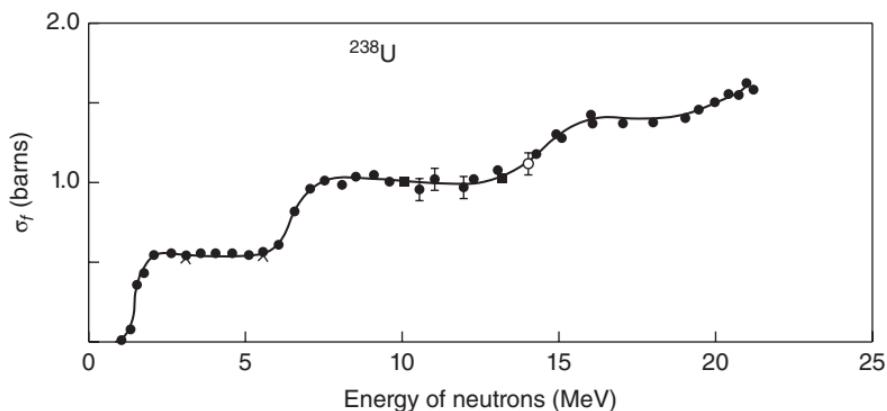
Figure 11.10 Fission excitation function for $n + {}^{238}U$ for incident neutron kinetic energies between 1 and 22 MeV.

in Figure 11.11. One notes the general trend in Γ_n/Γ_f with increasing Z and A (consistent with the qualitative dependence on Z^2/A for fission). For this limited range of energies, the ratio Γ_n/Γ_f can be parameterized as

$$\frac{\Gamma_n}{\Gamma_f} = \frac{2TA^{2/3}}{10\ \text{MeV}} \exp\left[\frac{(B_f - B_n)}{T}\right] \tag{11.18}$$
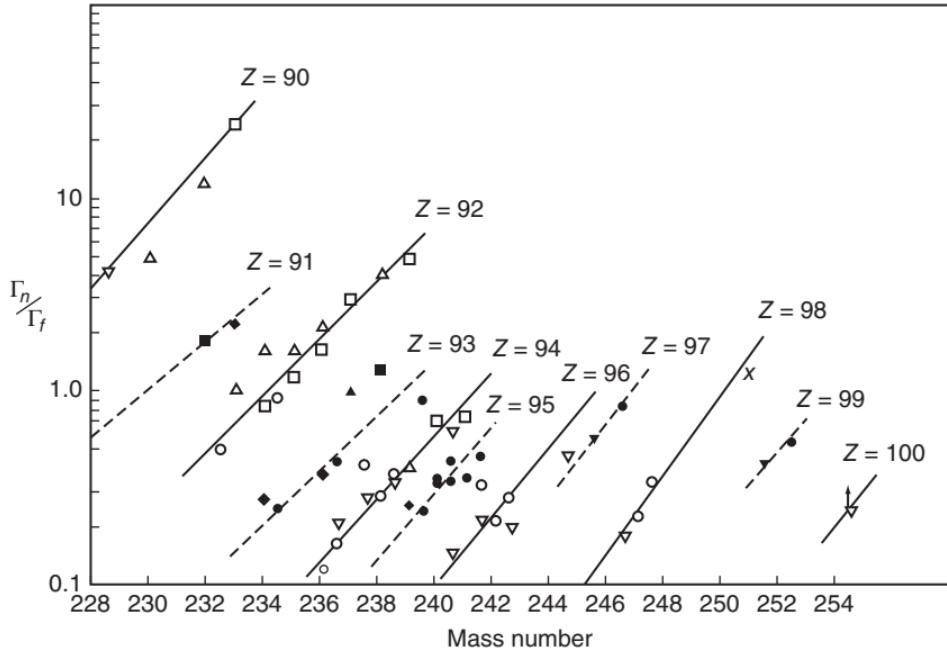
Figure 11.11 Values of the ratio Γ_n/Γ_f as a function of the mass number of the fissioning system (Vandenbosch and Huizenga (1973). Reproduced with the permission of Elsevier).

where B_f, B_n, and the nuclear temperature $T = \sqrt{8E^*/A}$ refer to the fissioning system. A more rigorous expression that can be used over a wider range of excitation energies is

$$
\frac{\Gamma_n}{\Gamma_f} = \frac{g\mu r_0^2}{\hbar^2} \frac{4A^{2/3}a_f(E^* - B_n)}{a_n\left[2\sqrt{a_f(E^* - B_f)} - 1\right]} \\
\times \exp\left[2\sqrt{a_n(E^* - B_n)} - 2\sqrt{a_f(E^* - B_f)}\right]
\tag{11.19}
$$

where a_n is the level density parameter of the residual nucleus after emission of a neutron and a_f is that of the deformed transition-state nucleus. Note that Γ_n/Γ_f is related to the difference $(B_f - B_n)$ as shown in Figure 11.12.

Sample Problem 11.2: Fission Probability

Consider the bombardment of ^{238}U with 42 MeV α-particles. What fraction of the initial nuclei undergoes first-chance fission?

Solution

First evaluate the excitation energy of the compound nucleus ^{242}Pu, E^* and the neutron binding energy B_n and use the figure to estimate Γ_n/Γ_f.

Then recall that the branching ratio is the ratio of one channel to the sum of all channels:

$$E^* = 42 \left(\frac{238}{242} \right) + Q_{CN}$$

$$Q_{CN} = [M(^{238}U) + M_\alpha - M(^{242}Pu)]c^2$$

$$Q_{CN} = 47.305 + 2.425 - 54.712 = -4.982 \text{ MeV}$$

$$E^* = 36.3 \text{ MeV}$$

The neutron binding energy in ^{242}Pu is 6.3 MeV and $B_f = 5.3$ MeV. From Figure 11.12, $\Gamma_n/\Gamma_f = 3$. Assuming that only neutron emission and fission are the important decay channels, $\Gamma_f/\Gamma_n + \Gamma_f = 1/(3 + 1) = 0.25$. Thus, ~25% of the nuclei are expected to undergo nuclear fission before emitting a neutron.
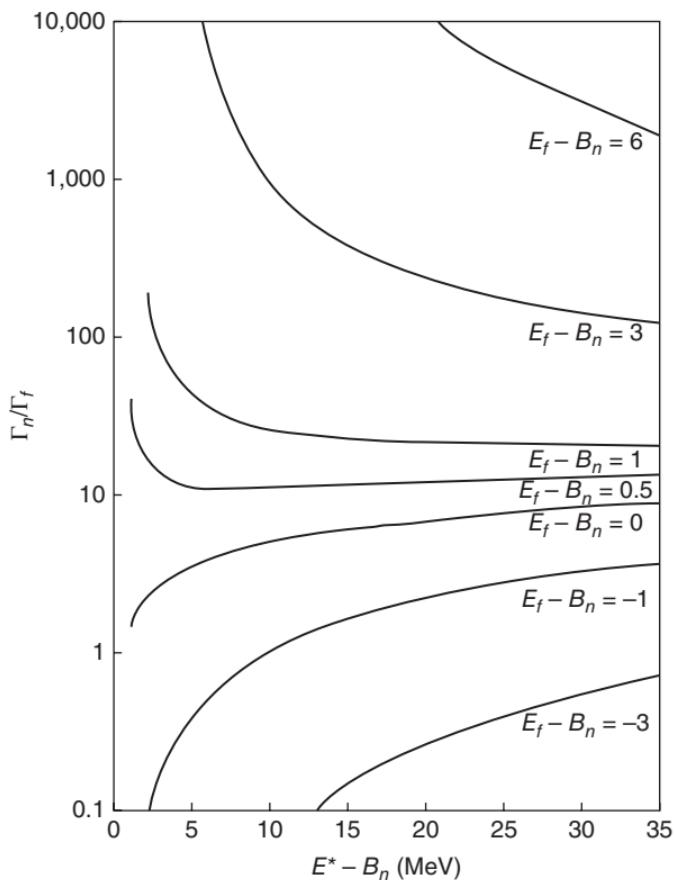
Figure 11.12 Excitation energy dependence of the ratio Γ_n/Γ_f for different values of $(B_f - B_n)$. Note that the figure uses the symbol E_f for the fission barrier (Vandenbosch and Huizenga (1973). Reproduced with the permission of Elsevier).

For reactions induced by heavy ions or high-energy charged particles, these expressions should be corrected for the effect of angular momentum. For example, there will be excitation energy tied up in rotation, which is unavailable for fission (Vandenbosch and Huizenga, 1973), and the fission barriers are lower for rotating nuclei. For reactions involving less fissionable nuclei ($x < 0.7$), especially at higher energies, one frequently sees that the primary reaction products first decay by sequential emission of neutrons or charged particles and then as Z^2/A increases, fission occurs at the last stages of the evaporation chains.

11.3 Dynamical Properties of Fission Fragments

One of the properties of fission fragments that can be exploited is the angular distribution. Fission is generally considered to be a "slow" process, in which the fissioning nucleus stays in statistical equilibrium. The angular distribution of the fission fragments will, therefore, be symmetric with respect to a plane perpendicular to the direction of motion of the fissioning system, that is, the fragment angular distributions will be symmetric about 90° in the frame of the fissioning system.

A typical fission fragment angular distribution for a heavy-in-induced fission reaction is shown in Figure 11.13. As one can see, the fragments are emitted preferentially forward and backward with respect to the direction of motion of the fissioning system. In this case involving a reaction that produces a fissioning system has a significant amount of angular momentum ($\sim 36\hbar$); the distribution closely resembles the function $1/\sin(\theta)$. To understand these distributions, one needs to consider the fissioning transition-state nucleus. Figure 11.14 presents a coordinate system for describing this nucleus in terms of the quantum numbers, J, the total angular momentum; M, the projection of J on a space-fixed axis, usually taken to be the direction of motion of the fissioning system; and K, the projection of J on the nuclear symmetry axis.

In low-energy nuclear fusion reactions, the angular momentum vectors, J, will be concentrated in a plane perpendicular to the beam direction ($M = 0$). In this case, we can easily see a relation among the orientation of J, K and the fission fragment angular distribution. For example, the case with $J = K$, the nuclear symmetry axis is perpendicular to the beam, and the fragments emerge sideways to the beam. Similarly, for $K = 0$, the symmetry axis of the nucleus is oriented perpendicular to J, that is, along the beam direction, and the fragments are emitted preferentially forward and backward. It is this extreme that leads to the $1/\sin(\theta)$ form of the angular distribution. (If J is perpendicular to the beam, and the vectors describing the possible directions of the nuclear symmetry axis are uniformly distributed over the surface of a sphere, then the probability of having a symmetry axis at an angle θ with respect to the beam will go as $1/\sin(\theta)$.)
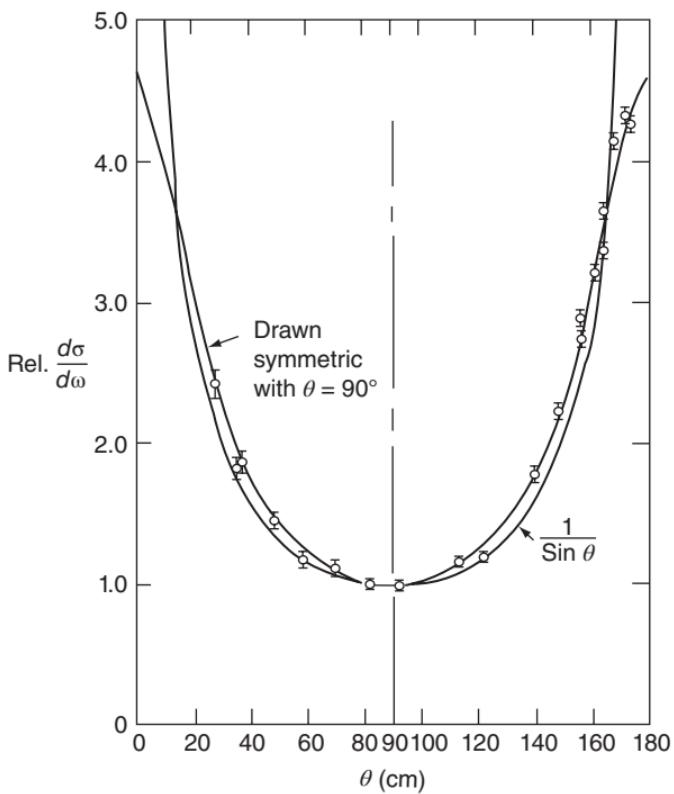
Figure 11.13 An example of the fission fragment angular distribution from the low-energy reaction of carbon with gold, $^{197}\text{Au}(^{12}\text{C,f})$.
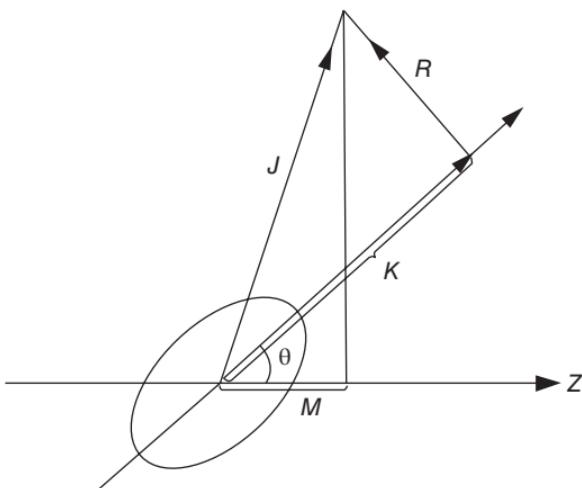

Figure 11.14 Angular momentum coordinate system for a deformed nucleus.

For the general case, Wheeler (1963) showed that the probability of emitting a fragment at an angle θ from a transition nucleus characterized by J, K, and M is

$$P^J_{M,K}(\theta) = (2J + 1) \left(\frac{2\pi R^2 \sin\theta \, d\theta}{4\pi R^2} \right) \left| d^J_{M,K}(\theta) \right|^2 \tag{11.20}$$

where the first term represents a statistical weighting factor, the second term a solid angle factor for the probability of getting the angle θ, and the third term a symmetric top wave function.

In low-energy fission and in photofission, one can populate individual states of the fissioning transition-state nucleus, and one can observe fragment angular distributions that change from forward to sidewise peaked and back again as a function of the J, K, and M of the transition nucleus (Vandenbosch and Huizenga, 1973). At higher energies ($E^* > 10$ MeV), one can describe the states of the transitioning nucleus using a statistical model. Assuming that there is a Gaussian distribution of K values for the transition nucleus,

$$\rho(K) \propto \exp\left(\frac{-K^2}{K_0^2} \right) \text{ for } K \leq J \tag{11.21}$$

$$\rho(K) = 0 \text{ for } K > J \tag{11.22}$$

where the modified Gaussian width parameter, K_0^2, is the root mean square projection of J on the nuclear symmetry axis. In statistical thermal equilibrium the so-called spin cutoff parameter is given by

$$K_0^2 = \frac{\mathcal{J}_{\text{eff}} T}{\hbar^2} \tag{11.23}$$

where $\mathcal{J}_{\text{eff}}$ is the effective moment of inertia of the transitioning nucleus with a temperature T. The fission fragment angular distributions, $W(\theta)$, can be then written as

$$W(\theta) \propto \sum_{J=0}^{\infty} (2J + 1) \, T_J \sum_{K=-J}^{J} \frac{(2J = 1) \left| d^J_{M=0,K}(\theta) \right|^2 \exp(-K/2K_0^2)}{\sum_{K=-J}^{J} \exp(-K/2K_0^2)} \tag{11.24}$$

where T_J is the transmission coefficient for forming the fissioning nucleus with total angular momentum J. Under the assumption that $M = 0$, we get the handy "pocket formula"

$$W(\theta) \propto \sum_{J=0}^{\infty}$$
$$\times \frac{(2J + 1)^2 \, T_J \, \exp[-(J + 0.5)^2 \sin^2\theta \, /4K_0^2] J_0[i(J + 0.5)^2 \sin^2\theta/4K_0^2]}{\text{erf}[(J + 0.5)/(2K_0^2)^{1/2}]} \tag{11.25}$$

where J_0 is the zero order Bessel function with imaginary argument and $erf[(J + 0.5)/(2K_0^2)^{1/2}$ is the error function defined as

$$\text{erf}(x) = (2/\pi^{1/2}) \int_0^x \exp(-t^2)dt \tag{11.26}$$

If one can estimate K_0^2 from the moment of inertia and temperature, then the fission angular distributions can be used to measure the spin J, or vice versa.

One other aspect of the spatial distribution of the fission fragments that has proven to be a useful tool in studying nuclear reactions is the angular correlation between the two fission fragments. When a fission event occurs, the two fragments emerge with an angle of 180° between them (to conserve angular momentum). If the fissioning nucleus is in motion, then the initial linear momentum of the fissioning system must be shared between the two fragments to give the final (laboratory system) fragment momenta. Complete fusion events can thus be differentiated from incomplete fusion events by observing the mean angle between coincident fission fragments. This angle is colloquially called the fission fragment folding-angle, since the CMS angle of 180° is decreased or folded by the motion of the CMS.

Sample Problem 11.3: Fission Folding Angle

Consider the case of 240 MeV ^{32}S interacting with ^{181}Ta, producing a CN that fissions. What would be the laboratory correlation angle between the fragments if the full linear momentum of the projectile was transferred to the fissioning system?

$$^{32}\text{S} + {}^{181}\text{Ta} \rightarrow {}^{213}\text{Ac}$$

Solution

The momentum of the CN is given by

$$p_{\text{CN}} = \sqrt{2mT_p} = \sqrt{2 \times 32 \times 240} = 123.9 \sqrt{\text{MeV} - \text{amu}}$$

leaving the momentum in unusual units. For the total kinetic energy (TKE) of the symmetric fission of ^{213}Ac, we expect

$$\text{TKE} = \frac{(89/2)^2 \, 1.44 \text{ MeV fm}}{1.8(213/2)^{1/3} \times 2 \text{ fm}} = 167 \text{ MeV}$$

The momentum of each fragment in the moving frame is then

$$p_f = \sqrt{2mT_f} = \sqrt{2 \times (213/2) \times (167/2)} = 133.4 \sqrt{\text{MeV} - \text{amu}}$$

Constructing a right triangle from the three momenta with p_{CN} perpendicular to p_f,

$$\theta = \arctan\left[\frac{133.4}{(123.9/2)}\right] = 65°$$

And finally, the correlation angle would be $2\theta = 130°$.

11.4 Fission Product Distributions

Up to this point, we have focused on describing the factors that control the probability of fission to occur. Now we will focus our attention on the distributions of the products in mass, energy, charge, and so on. In doing so, we will mostly be discussing "scission point" or "post-fission" phenomena. Our treatment of these phenomena is, of necessity, somewhat superficial, and the reader is referred to the excellent monograph of Vandenbosch and Huizenga for a more authoritative account.

11.4.1 Total Kinetic Energy (TKE) Release

To a first approximation, one can assume that the kinetic energies of the fission fragments are the result of the Coulomb repulsion of the fragments after scission. A handy pocket formula that gives the TKE is
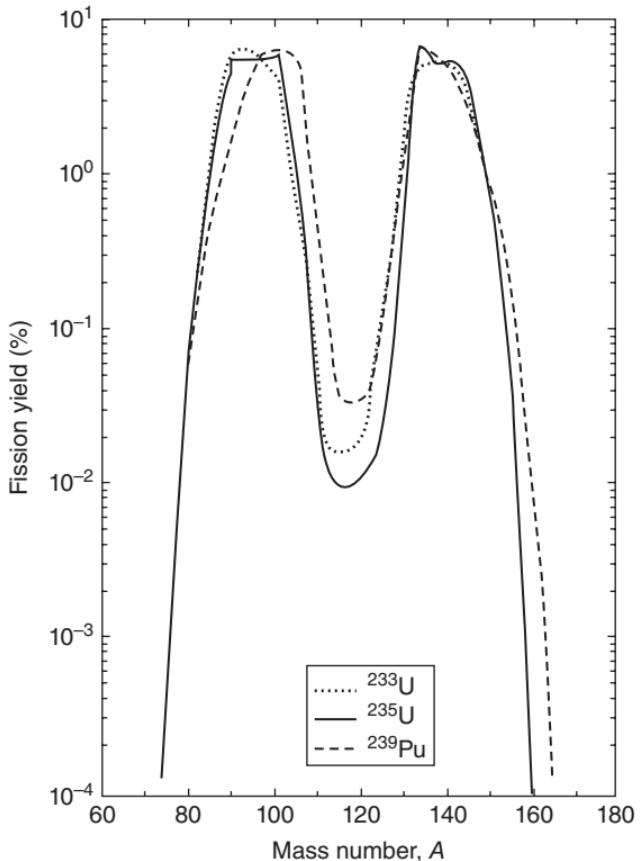
$$\text{TKE} = \frac{Z_1 Z_2 e^2}{1.8(A_1^{1/3} + A_2^{1/3})} \text{ MeV} \tag{11.27}$$

where Z_1, A_1, Z_2, and A_2 refer to the atomic and mass numbers of the two fragments. The factor of 1.8 (instead of the usual value for r_0 of 1.2) results from the fact that the fragments at scission have unusually large deformations. More detailed empirical prescriptions for the TKE are available (Viola et al., 1985), but the previous formula seems to work quite well over a range of excitation energies and fissioning nuclei. The most significant deviations from these formulas appear in the very heavy actinides, ^{258,259}Fm and ^{260}Md, where the observed kinetic energies are evidence (Hoffman et al., 1996) for an unusually compact scission configuration.

11.4.2 Fission Product Mass Distribution

One of the first big surprises in early studies of fission was the fission product mass distribution. Investigations of the thermal neutron-induced fission of uranium and plutonium nuclides (and later the spontaneous fission of ^{252}Cf) showed that the most probable division of mass was asymmetric ($M_{\text{Heavy}}/M_{\text{Light}}$ =1.3–1.5). The liquid drop model would predict that the greatest energy release

Figure 11.15 Smoothed fragment mass distributions for the thermal neutron-induced fission of ^{233}U, ^{235}U, and ^{239}Pu (Seaborg and Loveland (1990). Reproduced with the permission of John Wiley & Sons, Inc.).

and, therefore, the most probable mass split would be a symmetric one, that is, $M_{\text{Heavy}}/M_{\text{Light}} = 1.0$. This situation is shown in Figure 11.15 where the mass distributions for the thermal neutron-induced fission of the "big three nuclides" ^{233}U, ^{235}U, and ^{239}Pu are shown. Symmetric fission is suppressed by at least two orders of magnitude relative to asymmetric fission. Note also that the peak-to-valley ratio of the distributions decrease with increasing mass of the fissioning nucleus.

An important key to understanding the preference for asymmetric mass distributions in the fission of the light actinides is contained in Figures 11.15 and 11.16. In these figures, one can see that the position of the heavy peak in the fission mass distribution remains constant, while the position of the light peak increases with increasing fissioning system mass. This observation, along with the realization that the lower edge of the heavy fragment peak is anchored at $A = 132$, has suggested that the preference for asymmetric fission is due to the special stability of having one fragment being close to $Z = 50$, $N = 82$, a doubly magic spherical nucleus. The lighter fragment makes up the difference in mass and charge.
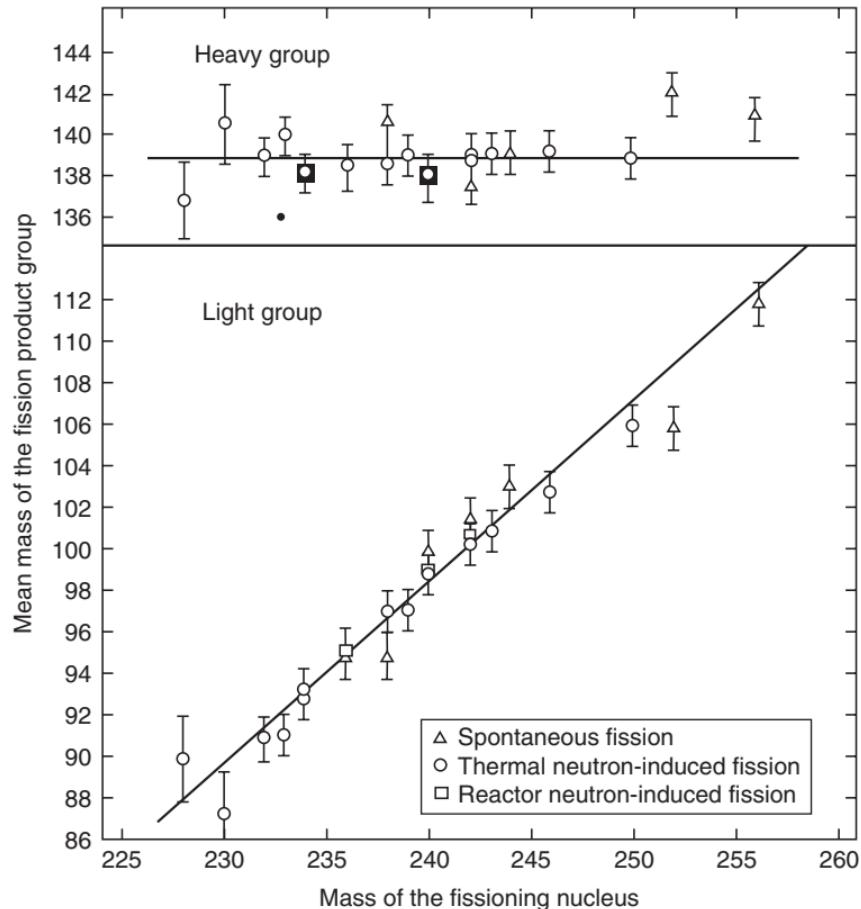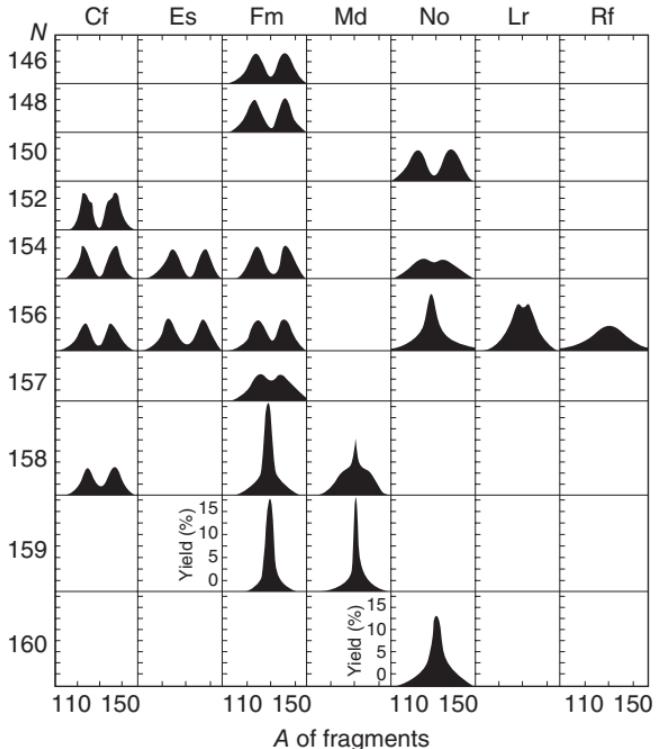
Figure 11.16 Summary of the average masses of the light and heavy fragments as a function of the mass of the fissioning system (Flynn et al. (1972). Reproduced with the permission of American Physical Society).

Further evidence for this influence of "magic" (shell model) configurations on the fission mass distributions is found in the fragment mass distributions for spontaneous fission (Fig. 11.17) and low-energy-induced fission of the "preactinides" (Fig. 11.18). One observes, in the case of spontaneous fission, a sharp transition between asymmetric fission and symmetric fission as one goes from ^{257}Fm to ^{258}Fm. The addition of a single neutron to the nucleus causes a large change in the fission product mass distribution. Similarly, a shift of two protons in going from ^{225}Ac to ^{227}Pa causes the mass distribution to shift from purely symmetric to dominantly asymmetric. These changes occur at neutron and proton numbers that are not the so-called magic numbers for spherical nuclei. The key to remember is that the fissioning system and its fragments

Figure 11.17 Schematic representation of the mass yield distributions for the spontaneous fission of the trans-berkelium nuclides (Hoffman et al. (1996). Reproduced with the permission of IOP Press).

are quite deformed near the scission point. Thus, the relevant "magic numbers," that is, configurations of special stability, are those expected for deformed nuclei and as shown in Chapter 6, the actual configurations change with deformation. A detailed theory of fission scission point properties based on these ideas developed by Wilkins et al. (1976) has been quite successful in describing the observed trends.

Qualitatively, if these explanations of the fission mass distributions for low-energy induced fission are correct, one might expect, as the excitation energy of the fissioning system were raised, the influence of the ground-state shell structure of the nascent fragments would decrease, and the fission mass distributions would show a greater amount of symmetric fission. That is exactly what happens, and at high energy all nuclei fission symmetrically (Fig. 11.19).

11.4.3 Fission Product Charge Distributions

If one were to plot the yield of fission fragments as a function of their atomic numbers (as in Fig. 11.20), the result would look very much like the distribution as a function of mass number. Nuclear matter is not very polarizable, and, to first order, the protons will divide like the neutrons. The primary fission fragments thus have neutron/proton ratios very close to that of the fissioning
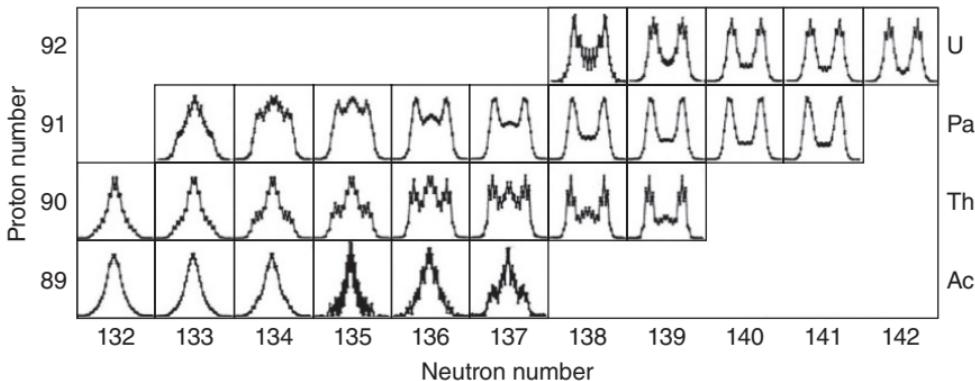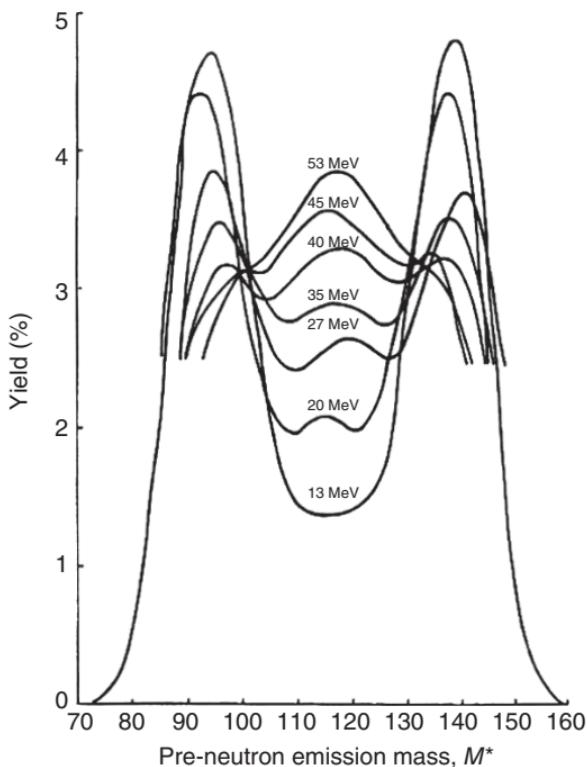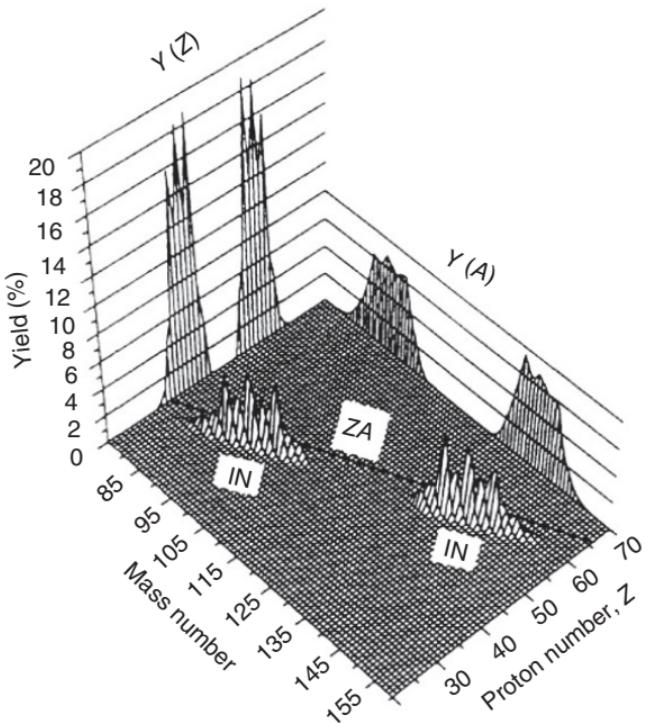
Figure 11.18 Schematic variation of the atomic number (Z) distributions for the low-energy fission of several actinide nuclei that are shown in each panel (Schmidt et al. (1998). Reproduced with the permission of World Scientific).

Figure 11.19 Fission mass distributions for ^{232}Th(p, f). The curves are labeled by the incident proton energy.

system and thus lie on the neutron-rich side of β stability. Enhanced yields for even Z nuclides relative to odd Z nuclides are observed (e.g., Fig. 11.20) due to the stabilization from proton pairing.

Figure 11.20 Yields of products from the thermal neutron-induced fission of ^{235}U (Metropolis et al. (1987). Reproduced with the permission of Elsevier).
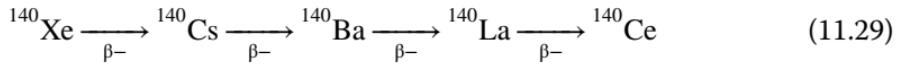
The yield of any given nuclide in fission is called *independent yield*. It can be shown that the independent yield or probability, $P(Z, A)$, of an isobar from fission has a Gaussian form:

$$P(Z, A) = \sigma(A) \frac{1}{\sqrt{c\pi}} \exp\left[\frac{-(Z - Z_p)^2}{c}\right] \tag{11.28}$$

where the width parameter c has an average value of 0.80 ± 0.14 for low-energy fission and Z_p is the most probable primary fragment atomic number (non-integer) for that isobar. The width parameter is related to the more common Gaussian width, σ, by Sheppard's relation: $c = 2(\sigma^2 + 1/12)$. (Also be aware of the distinction in this context of the difference between the Gaussian width parameter σ and the isobaric yield $\sigma(A)$.) Large tables of Z_p exist for common fissioning systems (Wahl, 1988). One consequence of this small value of c is that, for a given A, only a few isobars will have significant yields. Two effects tend to favor the observed narrow charge distributions: (a) the high-energetic cost of unfavorable charge splits and (b) the existence of ground-state correlations between neutrons and protons in the fragments.

In discussions of fission, one frequently hears the terms *cumulative yield* as opposed to the *independent yield* just introduced. The independent yield of a nuclide is just what it appears, the yield of that nucleus as a primary fission product. Because the fission products are essentially all β^- emitters, they will

decay toward the bottom of the valley of β-stability, generally passing through several sequential members of an isobaric series, as, for example, with $A = 140$ fragments:

$$^{140}\text{Xe} \xrightarrow[\beta-]{} {}^{140}\text{Cs} \xrightarrow[\beta-]{} {}^{140}\text{Ba} \xrightarrow[\beta-]{} {}^{140}\text{La} \xrightarrow[\beta-]{} {}^{140}\text{Ce} \qquad (11.29)$$

The yield of each member of the isobaric series integrates, by virtue of the intervening β-decay, the yields of its precursors depending on the time allowed for decay since the fission event. Such integrated (and time-dependent) yields are referred to as cumulative yields. For example, the cumulative yield of the mass 140 chain in the thermal neutron-induced fission of ^{235}U is 6.25% of the total fission yield.

Sample Problem 11.4: Fission Yield

What is the independent yield of ^{140}Ba from the thermal neutron-induced fission of ^{235}U, and what is its cumulative yield?

Solution

The fractional independent yield is given by the expression

$$P(Z, A) = \frac{\sigma(A)}{\sqrt{c\pi}} \exp\left[\frac{-(Z - Z_p)^2}{c}\right]$$

For the mass 140 chain, $Z_p = 54.55$ from Wahl's summary mentioned in the text. Notice that this value of $Z_p/A(= 54.55/140)$ is very close to that of the fissioning system, 92/236, that is, the N/Z ratio of the fragments is approximately that of the fissioning system. This idea is called the unchanged charge distribution (UCD) prescription. Substituting,

$$P(56, 140) = \frac{\sigma(140)}{\sqrt{0.8\pi}} \exp\left[-\frac{(56 - 54.55)^2}{0.8}\right] = 4.56 \times 10^{-2}$$

The text indicates that the fractional yield of $A = 140$ is 6.25% in this system, so in terms of fractional yield

$$P(56, 140) = 0.0625 \times 0.0456 = 2.85 \times 10^{-3}$$

The cumulative yield of an isotope in terms of fractions, called the *fractional cumulative yield* or FCY, is

$$\text{FCY}(Z, A) = \frac{\sigma(A)}{\sqrt{c\pi}} \int_{-\infty}^{Z+1/2} \exp\left[-\frac{(n - Z_p)^2}{c}\right] dn$$

Evaluating the integral in this case gives $FCY = 0.9978$, which is the fraction of the isobaric yield that would pass through ^{140}Ba during the entire production and subsequent decay process.

11.5 Excitation Energy of Fission Fragments

The excitation energy of the fission fragments is equal to the difference between the total energy release, Q, and the TKE of the fragments. The excitation energy should be calculated for each mass split because the Q value depends on the exact nuclides in the split. Here we will do an average accounting to see where the energy goes. For the thermal neutron-induced fission of ^{235}U, the amount of excitation energy corresponds to ~200–172 MeV or about ~28 MeV for the two fragments (~14% of the total energy release), averaged overall mass splits. The average number of emitted prompt neutrons is ~2.4, and each neutron has a kinetic energy of ≈ 2 MeV, while the emitting fragments have average neutron binding energies of ≈ 5.5 MeV. Thus, roughly 18 MeV (= $2.4 \times (2 + 5.5)$) of the fragment excitation energy is carried away by the prompt neutrons. Prompt photon emission carries away ≈ 7.5 MeV, which leaves about 2.5 MeV, in this crude accounting, to be emitted in the form of β particles, neutrinos, delayed neutrons, and so on.

As noted earlier, the prompt neutrons are emitted from the fully accelerated fragments after scission. The variation of the average number of these neutrons, v_{total} (= 2.4 in the previous example), as a function of the mass of the fissioning system is shown in Figure 11.21. The general increase in v_{total} with mass of the fissioning system is due to the increase in fragment excitation energy. For very
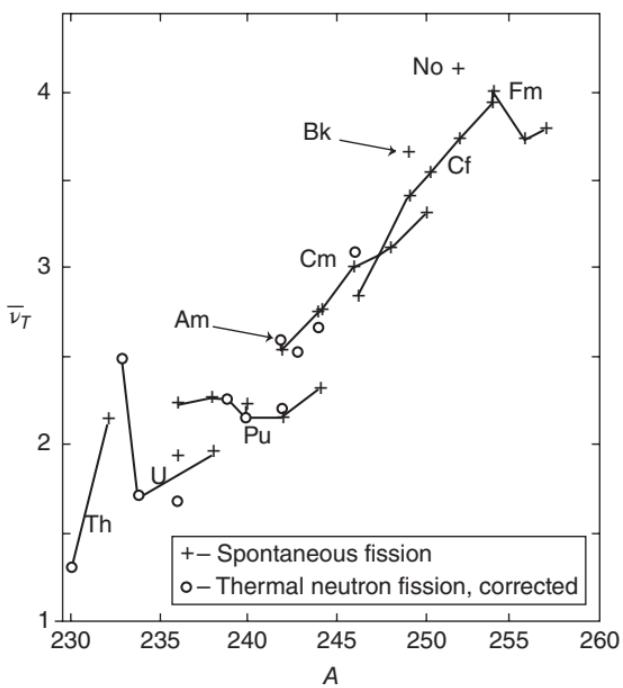
**Figure 11.21** The average total number of neutrons, $\overline{v_T}$, as a function of the mass number of the fissioning system for spontaneous and thermal neutron-induced fission. The values for thermal neutron-induced fission have been corrected to zero excitation energy (spontaneous fission) assuming $d\overline{v}/dE^* = 0.12$ MeV^{-1} (Vandenbosch and Huizenga (1973). Reproduced with the permission of Elsevier).
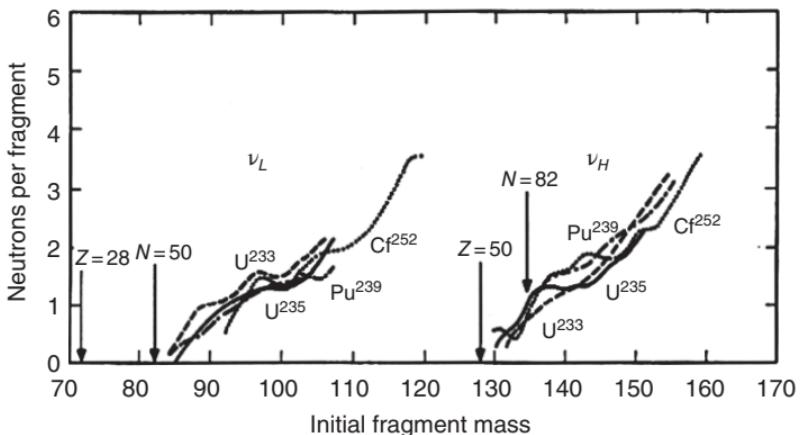
Figure 11.22 The dependence of $\nu(A)$ on fission fragment mass number A for some actinide nuclei.

heavy systems ($Z \sim 114$), ν_{total} is predicted to be almost 7, allowing the critical mass for a self-sustaining fission reaction to be quite small.

The average neutron kinetic energy is ~ 2 MeV. In the frame of the moving fragment, the distribution of fragment energies is Maxwellian, $P(E_n) = E_n \exp(-E_n/T)$. Transforming this spectrum into the laboratory frame gives a spectrum of the Watt form, that is,

$$P(E_n) = \exp\left(\frac{-E_n}{T}\right) \sinh\left(\frac{4E_n E_f}{T^2}\right)^{1/2} \tag{11.30}$$

where E_n and E_f are the laboratory system energies of the neutron and fission fragment (in MeV/nucleon) and T is the nuclear temperature. The mean kinetic energy of each neutron is $\sim 2T$, and a typical temperature in low-energy fission is ~ 1 MeV.

Another important aspect of neutron emission is the variation of the number of emitted neutrons as a function of the fragment mass $\nu(A)$ as indicated in Figure 11.22. The striking features of these data are the nearly universal dependence of $\nu(A)$ on A, independent of fissioning system for these actinide nuclei (which again suggests that the role of fragment shell structure is important in determining this property). Notice also the sawtooth dependence of $\nu(A)$ with a correlation of low values of $\nu(A)$ with those fragments whose structure is that of a "magic" nucleus, that is, a nucleus of special stability. These fragments are expected to have low excitation energies due to shell effects and will have higher kinetic energies (Wilkins et al., 1976).

Prompt γ-ray emission only competes with or follows the last stages of prompt neutron emission. These photons are emitted in times from 10^{-15} to 10^{-7} s. Typical γ-ray multiplicities of 7–10 photons per fission are observed. These photons, as indicated earlier, carry away a total of ~ 7.5 MeV. This γ-ray

yield is considerably larger than one would predict if γ-ray emission followed neutron emission instead of competing with it. Because of the significant angular momentum of the fission fragments ($\sim$7–10$\hbar$) even in spontaneous fission, photon emission can compete with neutron emission because the neutrons cannot efficiently remove angular momentum from a nucleus. The emitted γ-rays are mostly dipole radiation with some significant admixture of quadrupole radiation, due to the so-called stretched $E2$ transitions ($J_f = J_i - 2$). Because of the large number of possible neutron-rich fragments produced in fission, the study of the γ-rays emitted by the fragments can lead to useful information about the nuclear structure of these exotic, short-lived nuclei far from stability.

Sample Problem 11.5: Fission Neutrons

Justify the estimate for v_{total} for the fission of ^{298}114 in the text earlier assuming that this nucleus fissions symmetrically.

Solution

First, the total energy released can be found using a modern mass formula to be 311 MeV for (exactly) symmetric fission. Second, the TKE of the fragments can be calculated as

$$\text{TKE} = \frac{(57)(57)1.44 \text{ MeV fm}}{1.8(149)^{1/3} \times 2} = 245 \text{ MeV}$$

This leaves a total fragment excitation energy of $311 - 245 = 66$ MeV. Since the γ-rays and decay are only emitted after the neutrons, we will assume that the amount of this energy is the same as in ^{235}U(n_{th}, f), which is $\sim$10 MeV. The excitation energy carried away by the neutrons becomes $66 - 10 = 56$ MeV. The mean kinetic energy of each neutron is $\sim 2T$ or 2 MeV, and the neutron binding energy in a typical fission fragment is about 6 MeV (a little lower than that in a stable nucleus). Thus, finally we get that $v_{total} = 56/(6 + 2) = 7$.

As just indicated in our discussion of prompt γ-ray emission, the fission fragments have a significant amount of angular momentum. There are two origins for this angular momentum: (a) the existence of random off-axis torques given to the fragments during the scission process and (b) the excitation of bending and wriggling modes of the nascent fragments against one another at the saddle point, which persist to scission and are amplified by the off-axis torques.

After neutron and γ emission "cools" the fission fragments, the final excitation energy of the fragments is emitted in β decay of the fragments, resulting in the emission of β-particles, antineutrinos, and delayed neutrons. The time scale of this emission is of the order of seconds to minutes to hours to days to years. In nuclear reactors, this emission continues after the reactor is shut down. This

energy release is referred to as "decay heat" and amounts to about 6–7% of the full power of the reactor immediately after shutdown.

A final dynamical scission point phenomenon to be considered here is the violent snapping of the neck between the nascent fragments, which can result in the creation of particles into the region between the fragments. The phenomenon is rare, occurring in about 1 in 300 to 1 in 1000 of the fission events creating α-particles and with a lesser frequency for heavier charged particles. (Neutrons can be emitted by this same mechanism in a few percent of all fission events.) The charged particles, being born in the region between the fragments, are strongly focused by the Coulomb field of the fragments and emerge at 90° with respect to the direction of motion of the separating fragments, with energies (~15 MeV for α-particles) characteristic of the Coulomb fields of the separating fragments.

Problems

11.1 Why is ^{240}Pu not fissionable by thermal neutrons, but ^{239}Pu is?

11.2 What is the expected total kinetic energy release in the fission of ^{272}110 assuming fission occurs symmetrically?

11.3 What is the meaning of the terms "prompt" and "delayed" with respect to the fission neutrons?

11.4 Sketch the fission excitation function for the reaction of ^{232}Th with neutrons. The fission barrier is ~6.5 MeV, and the binding energy of the last neutron in ^{232}Th and ^{233}Th are 6.90 and 4.93 MeV, respectively.

11.5 What are the values of the fissionability parameter x for ^{209}Bi, ^{226}Ra, ^{232}Th, ^{242}Pu, and ^{252}Cf?

11.6 What is the fraction of fission neutrons with energies > 2 MeV from the thermal neutron fission of ^{235}U (in the laboratory frame)?

11.7 What is the independent yield of ^{99}Mo in the thermal neutron-induced fission of ^{239}Pu? Z_p is 39.921 and the yield of the $A = 99$ chain is 6.15% for this fission process.

11.8 What is the value of Γ_n/Γ_f for a ^{210}Po nucleus produced in the bombardment of ^{209}Bi with 10.5 MeV protons? $B_f = 20.4$ MeV.

Bibliography

H.C. Britt, *"Fission properties of the Actinides"*, in *Actinides in Perspective*, N.M. Edelstein, Ed. (Pergamon, Oxford, 1982), p. 245.

K.F. Flynn, E.P. Horwitz, C.A.A. Bloomquist, R.F. Barnes, R.K. Sjoblom, P.R. Fields, and L.E. Glendenin, Phys. Rev. **C5**, 1725 (1972).

J. Gindler and J.R. Huizenga, "Nuclear Fission," in Nuclear Chemistry, Volume **II**, L. Yaffe, Ed. (Academic Press, New York, 1964), p. 1.

O. Hahn and F. Strassmann, Naturwiss 26, 756 (1938); see translation by H. Graetzer, Am. J. Phys. **32**, 15 (1964).

D.C. Hoffman, T.M. Hamilton, and M.R. Lane, *"Spontaneous Fission,"* in Nuclear Decay Modes, D.N. Poenaru, Ed. (IOP, Bristol, 1996), pp. 393–432.

S. Liran and N. Zeldes, At. Data Nucl. Data Tables **17**, 431 (1976).

Y.T. Oganessian and Y.A. Lazarev, "Heavy Ions and Nuclear Fission," in Treatise on Heavy-Ion Nuclear Science, Volume **4**, D.A. Bromley, Ed. (Plenum, New York, 1985), pp. 1–254. A review article with significant insight.

K.-H. Schmidt, et al., *"Electromagnetic-induced fission of short-lived nuclei"*, in Heavy Ion Physics, Y.T. Oganessian and R. Kalpakchieva, Eds. (World, Singapore, 1998), p. 667.

G.T. Seaborg and W. Loveland, *The Elements Beyond Uranium* (John Wiley & Sons, Inc., New York, 1990).

V.M. Strutinsky, Nucl. Phys. **A95**, 420 (1967).

R. Vandenbosch and J.R. Huizenga, *Nuclear Fission* (Academic, New York, 1973). The bible of basic information and insight into the fission process.

V.E. Viola, Jr., K. Kwiatkowski, and M. Walker, Phys. Rev. **C31**, 1550 (1985).

C. Wagemans, *The Nuclear Fission Process* (CRC Press, Boca Raton, 1991). Summary of developments since Vandenbosch and Huizenga (1973) was written.

A.C. Wahl, At. Data Nucl. Data Tables **39**, 1 (1988).

J.A. Wheeler, *"Channel analysis of fission"*, in Fast Neutron Physics, J.B. Marion and J.L. Fowler, Eds. (John Wiley & Sons, Inc., New York, 1963).

B.D. Wilkins, E.P. Steinberg, and R.R. Chasman, Phys. Rev. **C14**, 1832 (1976).

Nuclear Astrophysics

12.1 Introduction

An important mystery that is still unfolding today is *how did the chemical elements that we have here on earth come into existence?* We know that the readily available, **stable** chemical elements are restricted in number to 81 and that they are essentially immutable by chemical reactions. The large-scale nuclear reactions that are taking place on earth are those induced by (external) cosmic rays and radioactive decay; nuclear reactions induced by people, such as fission, take place on a tiny scale by comparison. Thus, the vast bulk of chemical elements that we have today on earth are those that were present when the solar system was formed. The elements have undergone an enormous range of geochemical, geological, and biochemical processes, but all such processes retain the integrity of each nucleus. Thus, the origin of the elements is certainly extraterrestrial, but questions remain as to where and how they were formed.

The answers to these questions lie in the field of *Nuclear Astrophysics*, an area concerned with the connection of fundamental information on the properties of nuclei and their reactions to the perceived and postulated properties of astrological objects and processes that occur in space. The universe is composed of a large variety of massive objects distributed in an enormous volume. Most of the volume is very empty ($<1 \times 10^{-18}$ kg/m³) and very cold ($\sim$3 K). On the other hand, the massive objects, stars and such, are very dense (sun's core density $\sim$1.5 $\times 10^5$ kg/m³) and very hot (sun's core temperature $\sim$1.6 $\times 10^7$ K). These temperatures and densities are such that the light elements are ionized and thermal velocities sufficient to occasionally induce a nuclear reaction. Thus, in contrast to the earth, the elemental makeup of stars is not static. The general understanding of the synthesis of the heavier elements is that they were created by a variety of nuclear processes in massive stellar systems. These massive objects exert large gravitational forces, and so one might expect the new materials to remain in the stars. The stellar processing systems often explode at some point and disperse the heavier elements, which later form new stars and solar systems again due to gravity. When we look at the details of the distribution of

isotopes here on earth, we will find that some number of explosive cycles must have taken place before the earth was formed!

In this chapter we will first consider the underlying information on the elemental and isotopic abundances and some of the implications of these abundances. Then we will consider the nuclear processes that must have taken place to produce the primordial elements and those that processed the primordial light elements into the ones that we have here on earth.

12.2 Elemental and Isotopic Abundances

Many students of chemistry have given little thought to the relative abundances of the chemical elements. Everyone realizes that some elements and their compounds are more common than others. The oxygen in water, for example, must be plentiful compared to mercury or gold. But what if we compare elements that are closer in the periodic table, for example, what is the amount of lead ($Z = 82$) compared with mercury ($Z = 80$) or what is the amount of iron ($Z = 26$) compared with copper ($Z = 27$)? Oddly enough, the answer one gets depends on what material is sampled. The relative abundances of the first forty elements are shown in Figure 12.1 as a percentage by mass in the earth's crust and also as a percentage by mass in our solar system. Notice that the scale is logarithmic and the data spans almost 11 orders of magnitude. The earth is predominantly
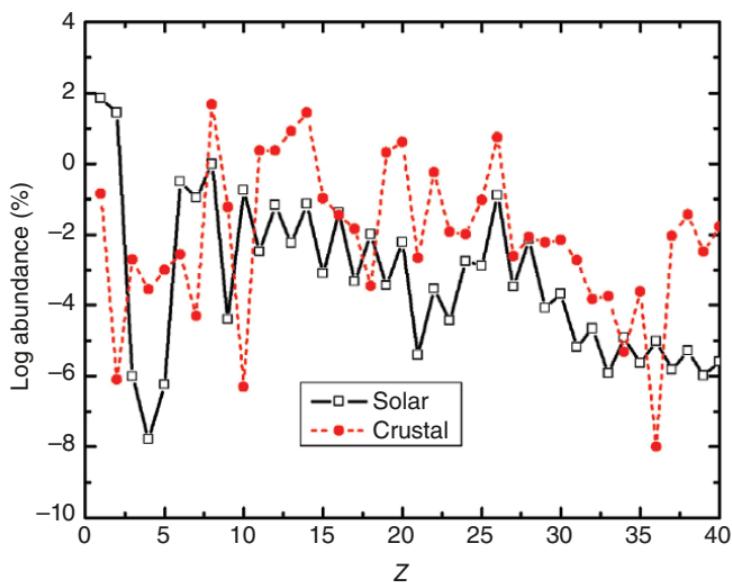

Figure 12.1 The abundances of the first 40 elements as a percentage by mass of the earth's crust (filled circles) and in the solar system (open squares) (Reproduced with the permission of Haynes et al. (1994)). (*See insert for color representation of the figure.*)

oxygen, silicon, aluminum, iron, and calcium, which comprise more than 90% of the earth's crust. On the other hand, the mass of the solar system is dominated by mass of the sun so that the solar system is mostly hydrogen, with some helium, and everything else is present at the trace level. The differences between the solar system abundances and those on the earth are due to astrophysical, geophysical, and geochemical processing of the solar material. In this Chapter we will concentrate on understanding the solar system abundances that reflect nuclear processes. The abundances of the isotopes and the elements are the basic factual information that we have to test theories of nucleosynthesis. We have data from the earth, moon, and meteorites, from spectroscopic measurements of the sun, and recently from spectroscopic measurements of distant stars. Many studies have characterized and then attempted to explain the similarities and differences from what we observe in the solar system.

The solar abundances of all of the chemical elements are shown in Figure 12.2. These abundances are derived primarily from knowledge of the elemental abundances in carbonaceous chondritic meteorites (CI) and stellar spectra. The scale is logarithmic so that ~99% of the mass resides in hydrogen and helium. Notice that there is a general logarithmic decline in the elemental abundance with atomic number with the exceptions of a large dip at beryllium ($Z = 4$) and of peaks at carbon and oxygen ($Z = 6, 8$), iron ($Z \sim 26$), and the platinum ($Z = 78$) to lead ($Z = 82$) region. Also notice that there is a strong odd–even staggering and that all the even Z elements with $Z > 6$ are more abundant than their odd atomic number neighbors. We have already encountered an explanation for this effect, that is, recall from earlier discussions of nuclear stability that there are many more stable nuclei for elements with an
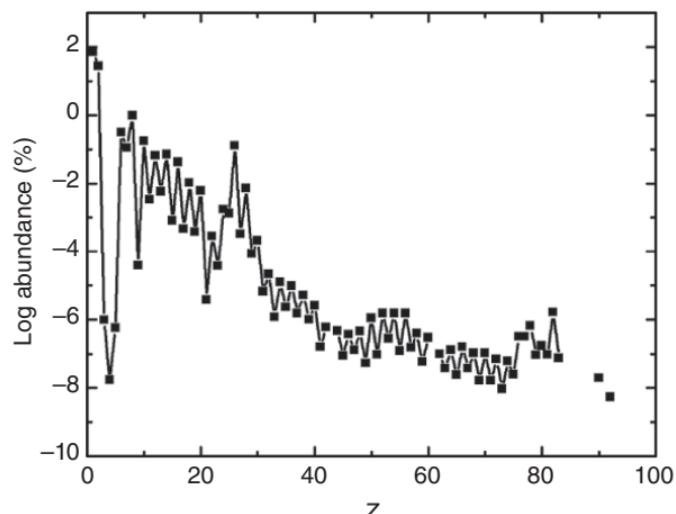
Figure 12.2 The abundances of all of the elements as a percentage by mass of the solar system (Reproduced with the permission of Haynes et al. (1994)).
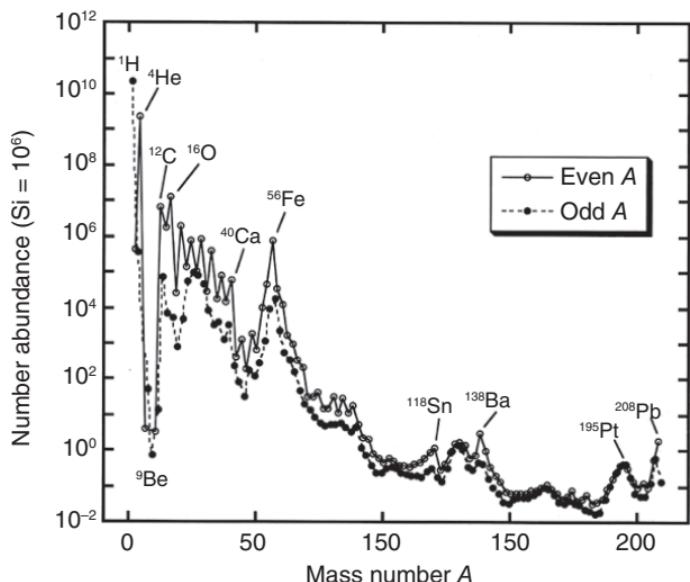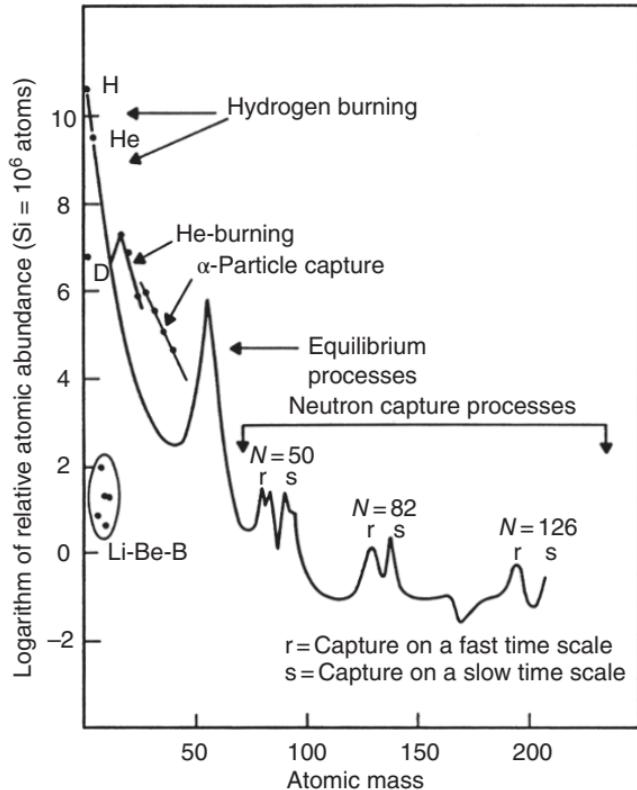
Figure 12.3 The abundances of the nuclides in the solar system (Iliadis (2007). Reproduced with the permission of Wiley).

even number of protons than there are for elements with an odd number of protons simply because there are very few stable odd–odd nuclei. Thus, the simple number of stable product nuclei, whatever the production mechanism, will have an effect on the observed populations because nearly all radioactive decay will have taken place since the astrophysical production, leaving (only) the stable products. There are exceptions, of course, and contemporary research searches out recently produced radioactive nuclei in the cosmos.

Given what we know about nuclear structure, it is reasonable to consider the isotopic distribution rather than the (integrated) elemental distribution. An example of the isotopic abundances of the-top-row elements is shown in Figure 12.3. Once again a very strong staggering is seen, and the depression of masses between 5 and 10 is more apparent. This mass region has gaps (no stable nuclei with $A = 5$ or 8), and the remaining nuclei are all relatively fragile and have small binding energies. For the lightest nuclei, the nuclei whose mass numbers are a multiple of 4 have the highest abundances. Again, simple nuclear stability considerations affect the amount of beryllium we find relative to the amount of carbon or oxygen, but the many orders of magnitude difference in the abundance of elements like beryllium and carbon must be due to the production mechanisms.

The sun is a typical star (discussed later), and in the past the solar abundances were used to represent the elemental abundances in the universe (the "cosmic" abundances). More recently spectroscopic analysis of individual stars has shown that the sun is relatively metal rich compared to most stars. It will turn

Figure 12.4 The atomic abundances of the elements in the solar system and the major nucleosynthetic processes responsible for the observed abundances (Burbridge et al. (1957). Reproduced with the permission of American Physical Society).

out that several nucleosynthetic processes are necessary to explain the details of the observed solar system abundances. In Figure 12.4, we jump ahead of our discussion to show a rough association between the elemental abundances and the nucleosynthetic processes that created them. Figure 12.4 is based upon a pioneering paper by Burbridge, Burbridge, Fowler, and Hoyle (colloquially called B²FH) (1957) and an independent analysis by Cameron (1957). These works have served as a framework for the discussion of nucleosynthesis since their publication in the 1950s, and we will follow a similar route in our discussion.

12.3 Primordial Nucleosynthesis

The universe is between 10 and 20 billion years old, with the best estimate of its age being $14 \pm 1 \times 10^9$ years old. The universe is thought to have begun with a cataclysmic explosion called the big bang. Since the big bang, the universe has been expanding with a decrease of temperature and density.

One important piece of evidence to support the idea of the big bang is the 2.7 K microwave radiation background in the universe. This blackbody radiation was discovered by Penzias and Wilson in 1965 and represents the thermal remnants of the electromagnetic radiation that existed shortly after the big

bang. Weinberg (1977) tells how Penzias and Wilson found a microwave noise at 7.35 cm that was independent of direction using a radio antenna at the Bell Telephone Laboratories in New Jersey. After ruling out a number of sources for this noise, they noted a pair of pigeons had been roosting in the antenna. The pigeons were caught, shipped to a new site, reappeared, were caught again, and were then "discouraged by more decisive means." The pigeons, it was noted, had coated the antenna with a "white dielectric material." After removal of this material, the microwave background was still there. It was soon realized that this 7.35 cm radiation corresponded to an equivalent temperature of the noise of about 3.5 K, which was eventually recognized as the remnants of the big bang. (Subsequent measurements have characterized this radiation as having a temperature of 2.7 K with a photon density of ~ 400 photons/cm^3 in the universe.)

A pictorial representation of some of the important events in the "thermal cooling" history of the universe is shown in Figure 12.5. The description of the evolution of the universe begins at 10^{-43} s after the big bang, the so-called *Planck time*. The universe at that time had a temperature of 10^{32} K ($k_{\rm B}T \sim 10^{19}$ GeV) and a volume that was $\sim 10^{-31}$ of its current volume. (To convert temperature in K to energy $k_{\rm B}T$ in electron volts, note that $k_{\rm B}T$ (eV) $= 8.6 \times 10^{-5} \, T$ (K).) Matter existed in a state more or less unknown to us, a plasma of quarks and gluons. All particles were present and in statistical equilibrium, where each particle had a production rate equal to the rate at which it was destroyed. As the universe expanded, it cooled and some species fell out of statistical equilibrium. At a time of 10^{-6} s ($T \sim 10^{13}$ K), the photons from the blackbody radiation could not sustain the production of the massive particles
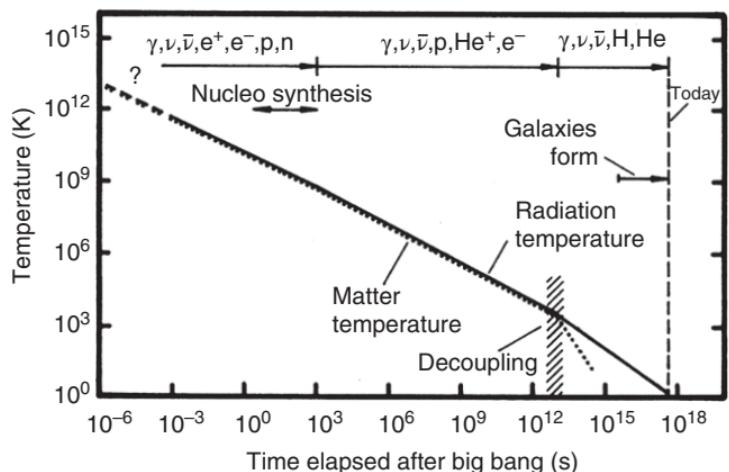

Figure 12.5 An outline of the events in the universe due to thermal cooling since the big bang (Rolfs and Rodney (1988). Reproduced with the permission of Chicago University Press).

and the hadronic matter condensed into a gas of nucleons and mesons. At this point, the universe consisted of nucleons, mesons, neutrinos (and antineutrinos), photons, and electrons (and positrons). The ratio of baryons to photons was ~10^{-9} so that most of the universe was pure energy.

At a time of 10^{-2}s ($T \sim 10^{11}$ K), the density of the universe dropped to ~4×10^6 kg/m^3. In this photon-dominated era, the temperature T (K) was given by the relation

$$T(\text{K}) = \frac{1.5 \times 10^{10}}{\sqrt{t(\text{s})}} \tag{12.1}$$

where t is the age in seconds. During this period, the neutrons and protons interconvert by the weak interactions

$$\overline{\nu}_e + p \leftrightarrow e^+ + n \tag{12.2}$$

$$\nu_e + n \leftrightarrow p + e^- \tag{12.3}$$

(Note that we are following the convention in astrophysics of not indicating the atomic charges in equations resulting in an apparent, but not real, lack of conservation of charge.) One can neglect the free decay of the neutron to the proton because the half-life for that decay (10.3 m) is too long to be relevant. The neutron–proton ratio, n:p, was determined by a Boltzmann factor containing the mass difference between the two particles, that is,

$$n : p = \exp(-\Delta mc^2/k_B T) \tag{12.4}$$

where Δmc^2 in the n–p mass difference of 1.29 MeV. At $T = 10^{12}$ K, n:p~1; at $T = 10^{11}$ K n:p drops to ~0.86, and so on. At T = 10^{11}K, no complex nuclei were formed because the temperature was too high to allow deuterons to form. When the temperature fell to $T = 10^{10}$ K ($t \sim 1$ s), the creation of e^+/e^- pairs (by pair production) ceased because $k_B T$ dropped below 1.022 MeV where the n:p ratio was ~17 : 83. At a time of 225 s, this ratio was 13 : 87, the temperature was $T \sim 10^9$ K, and the density was ~2×10^4 kg/m^3, and the first nucleosynthetic reactions could begin.

The primordial nucleosynthesis reactions began with the production of deuterium by the simple radiative capture process

$$n + p \rightarrow d + \gamma \tag{12.5}$$
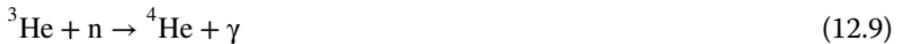
Notice that the deuteron can be destroyed by the absorption of a high-energy photon in the reverse process. At this time, the deuteron could survive long enough to allow the subsequent reactions

$$p + d \rightarrow {}^3\text{He} + \gamma \tag{12.6}$$

and

$$n + d \rightarrow {}^3\text{H} + \gamma \tag{12.7}$$

^{3}H and ^{3}He are more strongly bound than deuterium allowing further reactions that produce the very strongly bound α particles

$$^3\text{H} + \text{p} \rightarrow {}^4\text{He} + \gamma \tag{12.8}$$

$$^3\text{He} + \text{n} \rightarrow {}^4\text{He} + \gamma \tag{12.9}$$

$$^3\text{H} + \text{d} \rightarrow {}^4\text{He} + \text{n} \tag{12.10}$$

$$\text{d} + \text{d} \rightarrow {}^4\text{He} + \gamma \tag{12.11}$$

Further reactions to produce the $A = 5$ nuclei could not occur because there are no stable nuclei with $A = 5$ (or subsequently $A = 8$). A small amount of ^{7}Li is produced in the reactions

$$^4\text{He} + {}^3\text{H} \rightarrow {}^7\text{Li} + \gamma$$

$$^4\text{He} + {}^3\text{He} \rightarrow {}^7\text{Be} + \gamma$$

$$^7\text{Be} + \text{e}^- \rightarrow {}^7\text{Li} + \nu_\text{e} \tag{12.12}$$
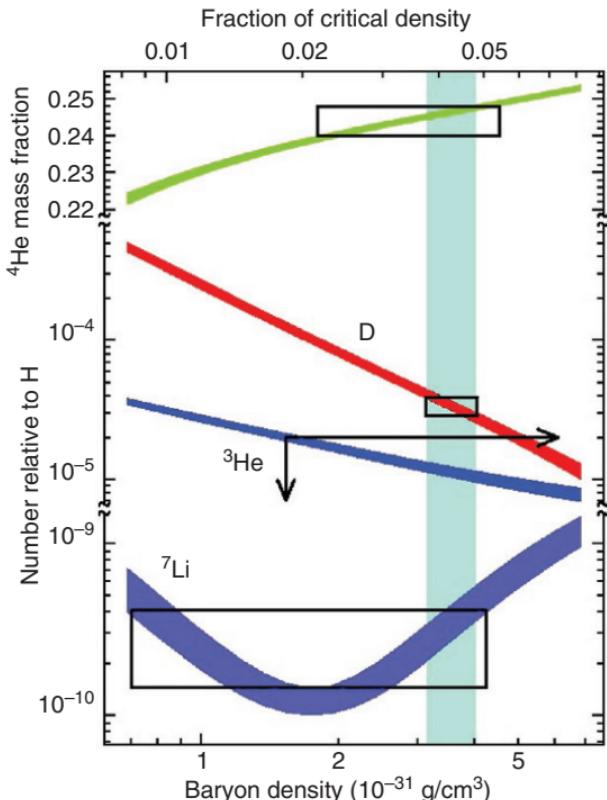
where the last step is an electron capture decay, but the ^{7}Li is also very weakly bound and is rapidly destroyed by (p, α) or (γ, α) reactions. Thus, the synthesis of larger nuclei was blocked. After about 30 m of expansion, nucleosynthesis ceased. The temperature was ~3×10^8 K and the density was ~30 kg/m^3. (For reference, recall that water vapor at 1 atm has a density of ~1 kg/m^3 and liquid water has a density of ~10^3 kg/m^3.) Nuclear matter at this point was 76% by mass protons, 24% α particles with traces of deuterium, ^{3}He, and ^{7}Li. The γ:p:n ratios were 10^9:87:13. The relative ratios of p:^{4}He:d:^{3}He:^{7}Li are a sensitive function of the baryon density of the universe as shown in Figure 12.6, a fact that can be used to constrain models of the big bang. The cross sections for the reactions that convert one product to another are generally known, and complex network calculations of the reaction rates can be performed as a function of temperature and density. The resulting abundances can be compared to estimates from observations of stellar matter. Chemistry began about 10^6 years later, when the temperature has fallen to 2000 K and the electrons and protons (and the helium and lithium) could combine to form hydrogen (and the other) atoms. Further nucleosynthesis that can produce heavier elements continues to occur in the interiors of stars.

Sample Problem 12.1: Temperatures and Velocities

Stellar temperatures are often given in units labeled T_9, which is the temperature in billion degrees kelvin, that is, T in kelvin divided by 1×10^9. What is the average velocity of protons in a stellar environment with $T_9 = 1.5$?

Figure 12.6 The variation of the relative abundances of the big bang nuclei (bottom) and the ^{4}He mass fraction (top) versus the baryon density. The boxes indicate the measured values and estimates of their uncertainty. The curves indicate the dependence of the yield on the baryon density in the big bang models and the vertical bar indicates the region of overlap. (*See insert for color representation of the figure.*)

Solution

First let us recall that the mean kinetic energy of a free particle in thermal equilibrium is $3/2\ k_B T$, and then use the fact that the (nonrelativistic) velocity of a thermal particle is $1/2 m v^2$:

$$E_{\text{thermal}} = \frac{3}{2} k_B T = \frac{3}{2}(1.38 \times 10^{-23})(1.5 \times 10^9)$$
$$= (3.10 \times 10^{-14} J) = 194 \text{ keV}$$

$$E_{\text{thermal}} = \frac{1}{2} m v^2 \rightarrow v = \sqrt{\frac{2 E_{\text{thermal}}}{m}}$$
$$v = \sqrt{\frac{2 \times 0.194 \text{ MeV}}{938 \text{ MeV/c}^2}} = 0.0203\ c$$
$$v = 6.10 \times 10^7 \text{m/s}$$

12.3.1 Stellar Evolution

As discussed previously, nucleosynthesis occurred in two steps, the primordial nucleosynthesis that occurred in the big bang forming only the lightest nuclei

and later processes, beginning $\sim 10^6$ years after the big bang, and then nucleosynthesis shifted to the stars. Big bang nucleosynthesis produced hydrogen, helium, and traces of ^{7}Li, while the rest of the elements are the result of stellar nucleosynthesis. For example, recent observations of stellar spectral lines showing the presence of 2×10^5 y. ^{99}Tc that indicates ongoing stellar nucleosynthesis. To understand the nuclear reactions that make the stars shine and generate the bulk of the elements, one needs to understand how stars work. That is the focus of this section.

After the big bang explosion, the material of the universe was dispersed. Inhomogeneities that developed evolved under the influence of gravity to form the galaxies. Within these galaxies, clouds of hydrogen and helium gas can further collapse under the influence of gravity. At first, the internal heat of this collapse can be radiated away. As the gas becomes denser, however, the opacity increases, and the gravitational energy associated with the collapse is stored in thermal motion in the interior rather than being radiated into space. Eventually a radiative equilibrium is established with the development of a *protostar*. The protostar continues to shrink under the influence of gravity with continued heating of the stellar interior. When the interior temperature reaches $\sim 10^7$ K, thermonuclear reactions between the hydrogen nuclei (protons) can begin because some of the particles have sufficient kinetic energies to overcome the Coulomb repulsion between them.

The first generation of stars that formed in this way is called *Population III stars*. They consisted of hydrogen and helium, were massive, had relatively short lifetimes, and are now extinct. The debris from these stars has been dispersed by explosions and was incorporated into later generation stars.

The second generation of stars is called *Population II stars*, or called as "metal-poor" stars, which consist of hydrogen, helium, and about 1% of the heavier elements like carbon and oxygen. Finally, there is a third generation of stars, like our sun, called *Population I stars*. These stars consist of hydrogen, helium, and 2–5% of the heavier elements.

Our sun, typical for Population I star, has a mass of 2.0×10^{30} kg, a radius of 7.0×10^6 m, an average density of 1.41×10^3 kg/m^3, a surface temperature of ~ 6000 K, and a luminosity of 3.83×10^{26} W. Our sun is 4.5×10^9 years old.

The Danish astronomer Ejnar Hertzsprung and the American astronomer Henry Norris Russell independently observed a very well-defined correlation between the luminosity and surface temperature (color) of stars. That correlation is shown in Figure 12.7 and is called a Hertzsprung–Russell or H–R diagram. Most stars, like our sun, fall in a narrow band on this diagram called the *main sequence*. Stars in the main sequence have luminosities, L, that are approximately proportional to $T_{\text{surface}}^{5.5}$, or in terms of their mass, M, $L \propto M^{3.5}$. Stars radiate energy, of course, and decrease in temperature. The length of time that a star stays on the main sequence depends on its mass, which, in turn, is related to the reaction rates in its interior.
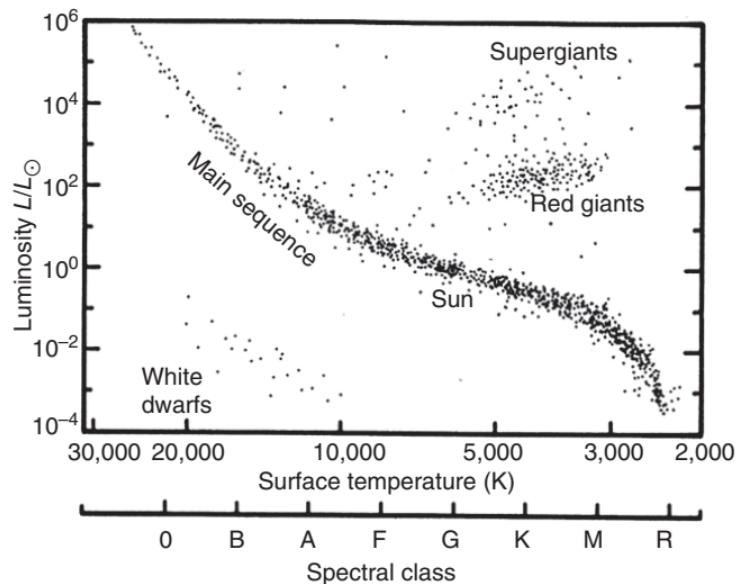
Figure 12.7 A schematic representation of a Hertzsprung–Russell diagram. The spectral class related to the historical grouping by color (Rolfs and Rodney (1988). Reproduced with the permission of Chicago University Press).

In the upper right area of the H–R diagram, one sees a group of stars, the *red giants* or super giants, with large radii that are relatively cool (3000–4000 K). Stars on the main sequence move to this region when the nuclear energy liberated in the nuclear reactions occurring in the star is not enough to sustain main sequence luminosity values.

Our sun is expected to spend $\sim 7 \times 10^9$ more years on the main sequence before becoming a red giant. In the slightly shorter time of $1.1–1.5 \times 10^9$ years, the sun will increase slowly in luminosity by $\sim 10\%$, probably leading to a cessation of life on earth. (In short, terrestrial life has used up $\sim 3/4$ of its allotted time, since its formation $\sim 3.5 \times 10^9$ years ago.)

In the lower left area of the H–R diagram, one sees a group of small dense, bright stars ($T > 10^4$ K) called *white dwarfs*. The white dwarfs represent the evolutionary outcome for the red giants with masses between 0.1 and 1.4 solar masses. A red giant is a helium-burning star (discussed previously), and after the helium is gone, the star becomes unstable, and if there is not sufficient mass to burn higher mass elements, it ejects the envelope, creates a planetary nebula, and moves across the main sequence on the H–R diagram to become a white dwarf. (See Fig. 12.8 for a schematic view of this evolution.)

For massive red giants ($M > 8$ solar masses), one finds they undergo a more spectacular death spiral, with contractions, increases in temperature leading to carbon burning, carbon–oxygen burning, silicon burning, and so on, with the
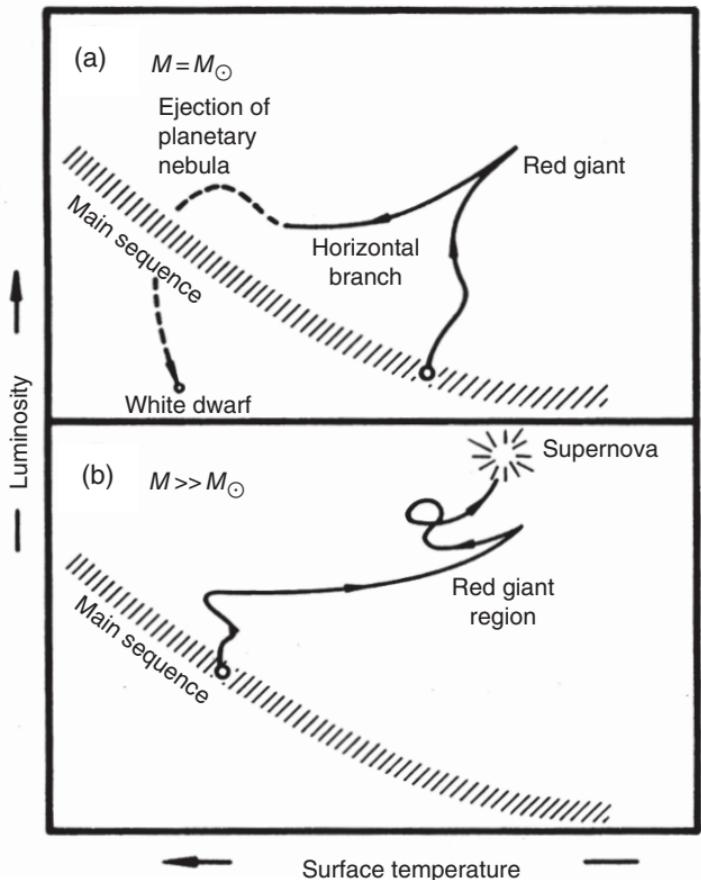
Figure 12.8 Schematic diagram of the evolution of: (a) a star with a mass near that of the sun and (b) a much more massive star (Rolfs and Rodney (1988). Reproduced with the permission of Chicago University Press).

production of the elements extending up to iron, followed by an explosive end (see Fig. 12.8).

The explosive end for main sequence stars can lead to the formation of novae and supernovae. The name "nova" means "new" and connotes a star that undergoes a sudden increase in brightness, followed by fading–a characteristic of an explosion. In this process, the outer part of the star, containing perhaps only $\sim 10^{-3}$ of the stellar mass, is ejected with the release of $\sim 10^{45}$ ergs. (For historical reasons the energy output of novae is usually given in ergs and not joules.) Supernovae are spectacular stellar explosions in which the stellar brightness increases by a factor of 10^{6}–10^{9}, releasing $\sim 10^{51}$ ergs on a time scale of seconds. We have observed about 10 nova/year but only 2–3 supernova per century. Supernovae are classified as type I (low hydrogen, high "heavy" elements, such as oxygen through iron) and type II (primarily hydrogen, with lesser amounts

of the "heavy" elements). Some supernovae lead to the formation of neutron stars, which are giant nuclei of essentially pure neutronic matter.

12.4 Thermonuclear Reaction Rates

Before discussing the nuclear reactions involved in stellar nucleosynthesis, we need to discuss the rates of reactions, which take place in a "thermal soup" as opposed to reactions studied one at a time in the laboratory. The rates of the first kind will tell us what reactions are most important in nucleosynthesis. When we speak of *thermonuclear reactions*, we mean nuclear reactions where the energy of the colliding nuclei is the thermal energy of the particles in a hot gas. Both reacting nuclei are moving, and thus it is their relative velocity (in the center of mass) that is important. In ordinary nuclear reactions in the laboratory, we write for the rate of the reaction, R,

$$R = N\sigma\phi \tag{12.13}$$

where the reaction rate, R, is in reactions/seconds, σ is the reaction cross section (cm^2), ϕ is the incident particle flux in particles/seconds, and N is the number of target atoms/square centimeter. For astrophysical reactions, we write

$$R = N_x N_y \int_0^\infty \sigma(v)v\,dv = N_x N_y \langle \sigma v \rangle \tag{12.14}$$

where v is the relative velocity between nuclei x and y, each present in a concentration of N_i particles/cm^3, and the quantity $\langle \sigma v \rangle$ is the temperature-averaged reaction rate per particle pair. To ensure that double counting of collisions between identical particles does not occur, it is conventional to express the previous equation as

$$R = \frac{N_x N_y \langle \sigma v \rangle}{1 + \delta_{xy}} \tag{12.15}$$

where δ_{xy} is the Kronecker delta (which is 0 when $x \neq y$ and 1 when $x = y$). Note the mean lifetime of component x is then $1/(N_x \langle \sigma v \rangle)$.

In a hot gas the velocity distribution of each component will be given by a Maxwell–Boltzmann function:

$$P(v) = \left(\frac{m}{2\pi k_B T} \right)^{3/2} \exp\left(-\frac{mv^2}{2k_B T} \right) 4\pi v^2 dv \tag{12.16}$$

where m is the particle mass, k_B is Boltzmann's constant, and T is the gas temperature. Integrating over all velocities for the reacting particles, x and y, gives

$$\langle \sigma v \rangle = \left(\frac{8}{\pi\mu} \right)^{1/2} \frac{1}{(k_B T)^{3/2}} \int_0^\infty \sigma(E)E \, \exp\left(-\frac{E}{k_B T} \right) dE \tag{12.17}$$

where μ is the reduced mass $(m_x \times m_y)/(m_x + m_y)$. Since the rates, R, of stellar nuclear reactions are directly proportional to $\langle \sigma v \rangle$, they directly depend on the gas temperature T.

For slow neutron-induced reactions that do not involve resonances, we know (from Chapter 10) that $\sigma(E) \propto 1/v_n$ so that $\langle \sigma v \rangle$ should be a constant at the lowest energies. For charged particle reactions, however, one must overcome the repulsive Coulomb force between the positively charged nuclei. For the simplest reaction, p + p, the Coulomb barrier is 550 keV. But, in a typical star like the sun, $k_B T$ is only 1.3 keV, that is, the nuclear reactions that occur are very much sub-barrier, and any observed reactions are the result of barrier penetration. (At a proton–proton center of mass energy of 1 keV, the barrier penetration probability is $\sim 2 \times 10^{-10}$). At these extreme sub-barrier energies, the barrier penetration factor, P, can be approximated as

$$P = \exp\left(-\frac{2\pi Z_1 Z_2 e^2}{\hbar v}\right) = \exp\left(-31.29 Z_1 Z_2 \left(\frac{\mu}{E}\right)^{1/2}\right) \quad (12.18)$$

where E is in keV and μ in amu. This tunneling probability is referred to as the *Gamow factor*. The cross section (see also Chapter 10) is proportional to $\pi \lambdabar^2 \propto \frac{1}{E}$. Thus, the cross section for nonresonant charged particle-induced reactions can be written as

$$\sigma(E) = \frac{1}{E} \exp\left(-31.29 Z_1 Z_2 \left(\frac{\mu}{E}\right)^{1/2}\right) S(E) \quad (12.19)$$

where the function $S(E)$, the so-called *astrophysical S factor*, contains all the constants and terms related to the nuclei involved in the reaction. Substituting this expression into the equation for $\langle \sigma v \rangle$, we have

$$\langle \sigma v \rangle = \left(\frac{8}{\pi \mu}\right)^{1/2} \frac{1}{(k_B T)^{3/2}} \int_0^\infty S(E) \exp\left[-\frac{E}{k_B T} - \frac{b}{E^{1/2}}\right] dE \quad (12.20)$$
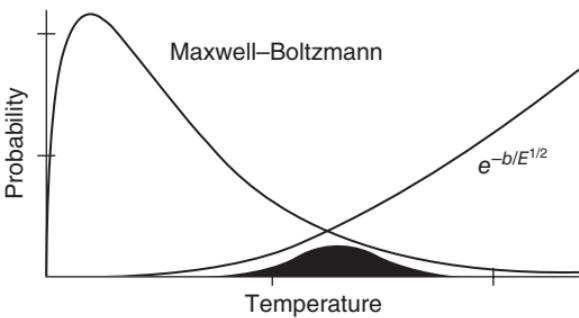
where b is $0.989 Z_1 Z_2 \mu^{1/2} (\text{MeV})^{1/2}$. This equation represents the overlap between the Maxwell–Boltzmann distribution, which is peaked at low energies and the Gamow barrier penetration factor that increases with increasing energy. The product of these two terms produces a peak in the overlap region of these two functions called the *Gamow peak* (see Fig. 12.9). This peak occurs at an energy $E_G = (b k_B T/2)^{2/3}$.

For reactions involving isolated single resonances or broad resonances, it is possible to derive a different formula for $\sigma(E)$ using the Breit–Wigner form, that is,

$$\sigma(E) = \pi \lambdabar^2 \left[\frac{2J_r + 1}{(2J_x + 1)(2J_y + 1)}\right] \frac{\Gamma_{\text{in}} \Gamma_{\text{out}}}{(E - E_r)^2 + \frac{\Gamma_{\text{total}}^2}{4}} \quad (12.21)$$

where J_x, J_y, and J_r are the spins of the interacting particles and the resonance while Γ_{in}, Γ_{out}, and Γ_{total} are the partial widths of the entrance and exit channels and the total width, respectively.

Figure 12.9 Schematic representation of the relative probability of a non-resonant stellar nuclear reaction as a function of temperature. The Gamow peak is shown by the solid black area (Wong (1998). Reproduced with the permission of John Wiley & Sons).

12.5 Stellar Nucleosynthesis

12.5.1 Introduction

After big bang nucleosynthesis is over, we have a compact universe that is ~75% hydrogen and ~25% helium with a trace of ^{7}Li. The synthesis of the chemical elements that we have in the present universe took place by processing this material in stars. Beginning ~10^6 years after the big bang, as described in Section 12.4, the sequence of gravitational collapse of material into a star causes an increasing temperature that allows the onset of nuclear fusion reactions, releasing energy (primarily in the form of kinetic energy of motion of the products) that works against the collapse. Starting from hydrogen and helium, a new set of fusion reactions that operate at lower temperatures and over longer times scales than the big bang produce the nuclei up to the maximum in the nuclear binding energy curve at $A \sim 60$. The temperature of these reactions starts at about 5×10^7 K or $k_B T \sim 2$ keV and builds up due to continued gravitational collapse. A rough outline of the nuclear reactions involved is given in Table 12.1.

The products from these reactions are distributed into the galaxies by slow emission from the red giants and by the catastrophic explosions of novae and supernovae. This dispersed material condenses in the Population II and later the Population I stars where additional nuclear reactions (see in the following text) create the odd A nuclei and sources of free neutrons. These neutrons allow us to get slow neutron capture reactions (s-process) synthesizing many of the nuclei with $A > 60$. High-temperature photonuclear reactions and rapid neutron capture reactions in supernovae complete the bulk of the nucleosynthesis reactions.

12.5.2 Hydrogen Burning

The first stage of stellar nucleosynthesis, which is still occurring in stars like our sun, is *hydrogen burning*. In hydrogen burning, protons are converted to ^{4}He

Table 12.1 Nuclear Reactions Involved in Stellar Nucleosynthesis.

Primary Fuel	T (K)	kT (MeV)	Primary Products
^{1}H	5×10^7	0.002	^{4}He
^{4}He	2×10^8	0.02	^{12}C, ^{16}O, ^{20}Ne
^{12}C	8×10^8	0.07	^{16}O, ^{20}Ne, ^{24}Mg
^{16}O	2×10^9	0.2	^{20}Ne, ^{28}Si, ^{32}S
^{20}Ne	1.5×10^9	0.13	^{16}O, ^{24}Mg
^{28}Si	3.5×10^9	0.3	$A < 60$

nuclei. Since there are no free neutrons present, the reactions differ from those of big bang nucleosynthesis. The first reaction that occurs is

$$p + p \rightarrow d + e^+ + \nu_e \tag{12.22}$$

$$Q = 0.42 \text{ MeV} \tag{12.23}$$

which is a *weak interaction* and involves the production of a positron and a neutrino. Most of the released energy is shared between the two leptons and not the deuteron due to its relatively high mass. In our sun, $T \sim 15 \times 10^6$ K (or $k_B T \sim 1$ keV). Since the *proton–proton (pp) burning* is a weak interaction process, it has a very small cross section, $\sim 10^{-47}$ cm^2, compared with strong interactions at these energies. The resulting reaction rate is 5×10^{-18} reactions/proton/second is only observed due to the extremely large number of protons in the sun.

There is an improbable (0.4%) three-body competitor to this reaction, called the *PEP process*, that also leads to deuteron production. The reaction can be written as

$$p + e^- + p \rightarrow d + \nu_e \tag{12.24}$$

$$Q = 1.42 \text{ MeV} \tag{12.25}$$

This relatively rare reaction is important because it is a source of energetic neutrinos that are emitted by the sun.

Once a significant number of deuterons are created, nuclear reactions take over, and the next reaction in the sequence is

$$d + p \rightarrow {}^3\text{He} + \gamma \tag{12.26}$$

$$Q = 5.49 \text{ MeV} \tag{12.27}$$

leading to the synthesis of ^{3}He. The rate of this strong interaction is $\sim 10^{16}$ times greater than the weak interaction-moderated $p + p$ reaction. At this point the
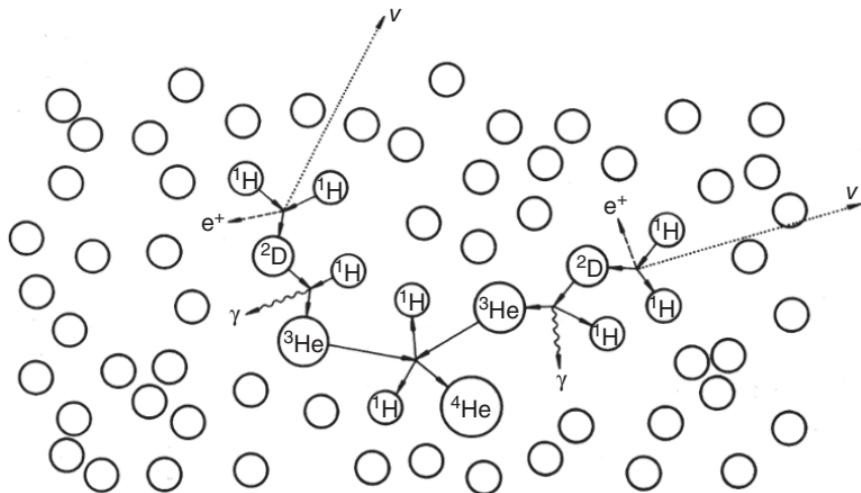
Figure 12.10 A highly schematic view of the ppI chain. The open, unlabeled circles are meant to represent protons, but their relative number would be much greater in the sun (Rolfs and Rodney (1988). Reproduced with the permission of Chicago University Press).

product ^{3}He can undergo two possible reactions. In $\sim$86% of the cases in our sun (Bahcall), the reaction is

$$^3\text{He} + {}^3\text{He} \rightarrow {}^4\text{He} + 2\text{p} \tag{12.28}$$

$$Q = 12.86 \text{ MeV} \tag{12.29}$$
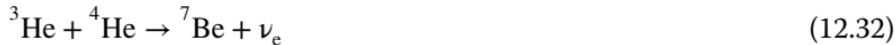
Notice that the net reaction for the combination of this with the two previous reactions (p + p and d + p) corresponds to an overall reaction of

$$4\text{p} \rightarrow {}^4\text{He} + 2\text{e}^+ + 2\nu_e \tag{12.30}$$

$$Q = 24.7 \text{ MeV} \tag{12.31}$$

This sequence of reactions is called the *ppI chain*, with the first step being the rate-limiting step and is responsible for 91% of the sun's energy. A schematic view of this reaction is shown in Figure 12.10.

Approximately 14% of the time(Bahcall), the ^{3}He product undergoes a reaction with an α particle:

$$^3\text{He} + {}^4\text{He} \rightarrow {}^7\text{Be} + \nu_e \tag{12.32}$$

and the ^{7}Be subsequently undergoes an electron capture decay:

$$\text{e}^- + {}^7\text{Be} \rightarrow {}^7\text{Li} + \nu_e \tag{12.33}$$

$$Q_{EC} = 0.86 \text{ MeV} \tag{12.34}$$

Note that this EC decay process does *not* involve capture of the orbital electron of the ^{7}Be since it is fully ionized in a star but rather involves capture of a free

continuum electron. As a consequence, the mean life of this decay is ~120 days rather than the terrestrial mean life of only 77 days. The resulting ^{7}Li undergoes proton capture to form two helium nuclei

$$p + {}^7\text{Li} \rightarrow 2\,{}^4\text{He} \tag{12.35}$$
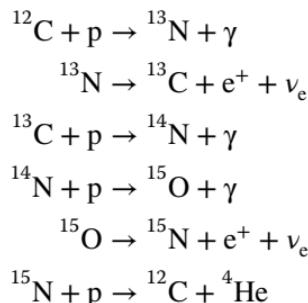
and terminates the process. This sequence of reactions (p + p, d + p, ^{3}He + ^{4}He, ^{7}Be EC, ^{7}Li(p, α)) constitutes the *ppII process*, which accounts for ~7% of the sun's energy and again involves weak interactions.

A small fraction of the ^{7}Be produced by the ^{3}He + ^{4}He reaction can undergo proton capture and follow a different pathway to two helium nuclei:

$$\begin{aligned}
{}^7\text{Be} + \text{p} &\rightarrow {}^8\text{B} + \gamma \\
{}^8\text{B} &\rightarrow {}^8\text{Be} + e^+ + \nu_e \\
{}^8\text{Be} &\rightarrow 2\,{}^4\text{He}
\end{aligned} \tag{12.36}$$

The chain is terminated since the ^{8}Be nucleus is unbound and decays in ~10^{-16} s into the two helium nuclei. This sequence (p+p, p+d, ^{3}He + ^{4}He, ^{7}Be(p, γ), ^{8}B $\rightarrow^8$ Be $\rightarrow 2\,^4$He) constitutes the *ppIII chain* (which provides only about 0.015% of the sun's energy). In each of the pp-processes, some fraction of the energy is carried away by the emitted neutrinos. Quantitatively, in the ppI process, the neutrino fraction is 2%, in the ppII process 4%, and 28.3% in the ppIII process. The large neutrino fraction in the ppIII process is due to the production of the neutrino in the energetic β decay of ^{9}B. The overall path and branchings of the pp chains are shown schematically in Figure 12.11.

In Population II and Population I stars, "heavy" elements like carbon, nitrogen, and oxygen are present at trace levels, leading to the occurrence of another set of nuclear reactions whose net effect is the conversion $4p \rightarrow {}^4\text{He}^{2+} + 2e^+ + 2\nu_e$. The "heavy" nuclei act as catalytic intermediates for this reaction. The basic catalytic cycle consists of the following reaction sequence:

$$\begin{aligned}
{}^{12}\text{C} + \text{p} &\rightarrow {}^{13}\text{N} + \gamma \\
{}^{13}\text{N} &\rightarrow {}^{13}\text{C} + e^+ + \nu_e \\
{}^{13}\text{C} + \text{p} &\rightarrow {}^{14}\text{N} + \gamma \\
{}^{14}\text{N} + \text{p} &\rightarrow {}^{15}\text{O} + \gamma \\
{}^{15}\text{O} &\rightarrow {}^{15}\text{N} + e^+ + \nu_e \\
{}^{15}\text{N} + \text{p} &\rightarrow {}^{12}\text{C} + {}^4\text{He}
\end{aligned}$$

This group of reactions is referred to as *the CNO cycle* and is favored at higher temperatures where the Coulomb barrier for these reactions can be more easily overcome. In our sun, 98% of the energy comes from the pp chain and only 2%
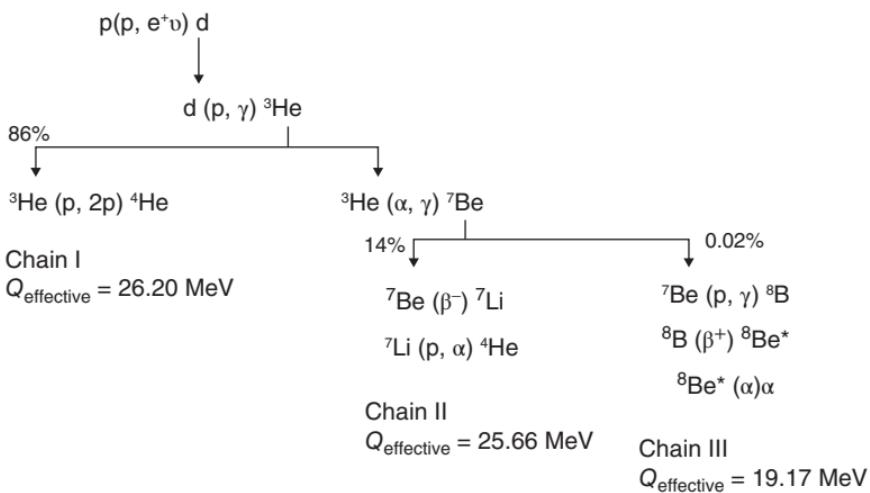
Figure 12.11 The three branching chains of nuclear reactions that constitute hydrogen burning in the sun(Bahcall). The net reaction converts four protons into an ^{4}He nucleus. The rate-limiting step in all reactions is the first reaction that relies on the weak interaction to create the deuterium nucleus.
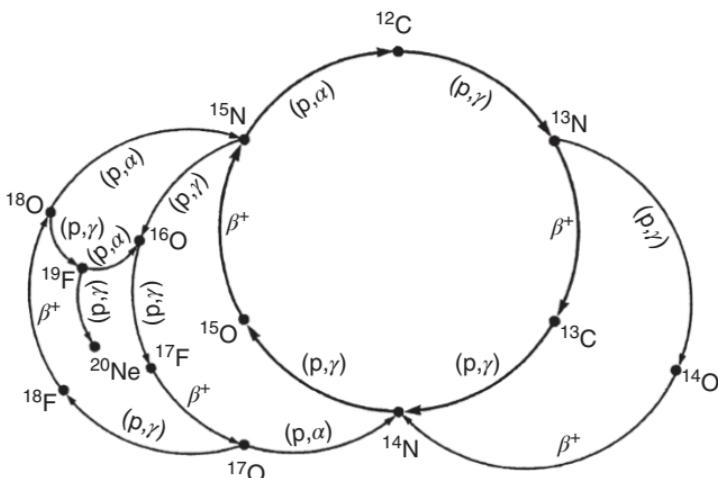
Figure 12.12 A graphical representation of the catalytic CNO cycle including the side chain reactions (Wong (1998). Reproduced with the permission of John Wiley & Sons).

from the CNO cycle. Several side chains of this reaction cycle are possible, as illustrated in Figure 12.12.

12.5.3 Helium Burning

Eventually the hydrogen fuel in the star will be exhausted, and further gravitational collapse will occur. This will give rise to a temperature increase up to

$\sim 1 - 2 \times 10^8$ K (with a density of $\sim 10^8$ kg/m³). When the star reaches this stage, it becomes a red giant and *helium burning* can commence.

One might think the first reaction in this situation is

$$^4\text{He} + {}^4\text{He} \rightarrow {}^8\text{Be} + \gamma \tag{12.37}$$

$$Q = -0.0191 \text{ MeV} \tag{12.38}$$

but ^{8}Be is essentially unstable ($t_{1/2} = 6.7 \times 10^{-17}$ s), and thus that process is hindered by the short lifetime and low transient population of the beryllium nuclei. Instead one gets the so-called 3α process

$$3^4\text{He} \rightarrow {}^{12}\text{C} + \gamma \tag{12.39}$$

$$Q = 7.37 \text{ MeV} \tag{12.40}$$

Three body reactions are usually rare, but the reaction proceeds through a resonance in ^{12}C at 7.65 MeV corresponding to the second excited state of ^{12}C ($J\pi = 0^+$). This excited state has a more favorable configuration than the ^{12}C ground state for allowing the reaction to occur. The difference in the relative reaction rates can be seen in Figure 12.13 by comparing the curve for the resonant reaction with the curve for the nonresonant one. (In a triumph for nuclear astrophysics, the existence of this state, now called the Hoyle State, was postulated by astrophysicists to explain nucleosynthetic rates before it was found in the laboratory.)

After a significant amount of ^{12}C is formed, one gets the follow-on α capture reactions

$$^4\text{He} + {}^{12}\text{C} \rightarrow {}^{16}\text{O} + \gamma \tag{12.41}$$

$$Q = 7.16 \text{ MeV} \tag{12.42}$$

and

$$^4\text{He} + {}^{16}\text{O} \rightarrow {}^{20}\text{Ne} + \gamma \tag{12.43}$$

$$Q = 4.73 \text{ MeV} \tag{12.44}$$
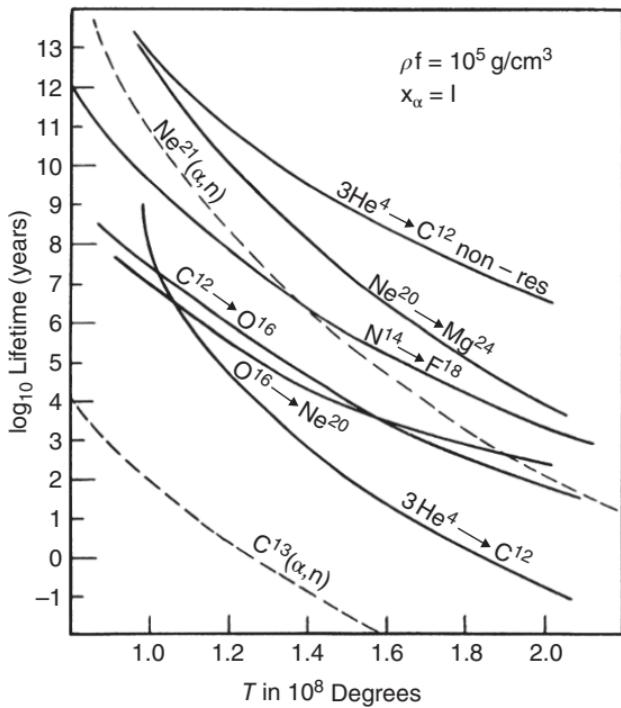
Notice that these reactions will require higher and higher average kinetic energies to overcome the Coulomb barriers for the successively heavier nuclei. Such higher energies will occur deeper and deeper inside the star due to the increasing pressure from the gravitational force. Thus, the star will develop a series of layers where different nuclear reactions are occurring.

If the temperature is high enough, then reverse reactions are possible and the neon will become part of an equilibrium:

$$^{20}\text{Ne} + \gamma \rightarrow {}^{16}\text{O} + {}^4\text{He} \tag{12.45}$$

$$Q = -4.73 \text{ MeV} \tag{12.46}$$

Figure 12.13 Mean lifetimes for various nucleosynthesis reactions involved in the helium-burning stage of a star shown as a function of the stellar temperature. The resonant reaction through the Hoyle state is shown by the solid line labeled 3He⁴ →C¹². Note that the mean lifetime is inversely related to the reaction rate (Burbridge et al. (1957). Reproduced with the permission of American Physical Society).

with a breakout reaction to form magnesium:

$$^{4}\text{He} + {}^{20}\text{Ne} \rightarrow {}^{24}\text{Mg} + \gamma \tag{12.47}$$
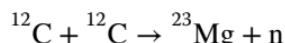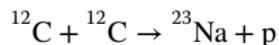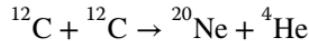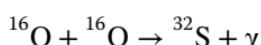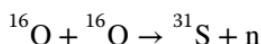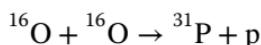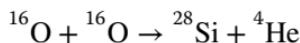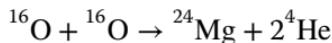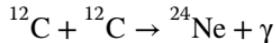
$$Q = +9.32 \text{ MeV} \tag{12.48}$$

with the latter reaction requiring an even higher average kinetic energy in the entrance channel. The relative rates of these and related processes are shown in Figure 12.13.

12.5.4 Synthesis of Nuclei with $A < 60$

Eventually the helium of the star will be exhausted, leading to further gravitational collapse with a temperature increase to $\sim 6 \times 10^8 - 2 \times 10^9 \text{K}$ ($kT \sim 100 - 200$ keV). At this point the fusion reactions of the "α cluster" nuclei formed in the α burning reactions are possible. For example, carbon and oxygen burning occurs in charged particle reactions such as

$$^{12}\text{C} + {}^{12}\text{C} \rightarrow {}^{20}\text{Ne} + {}^{4}\text{He}$$
$$^{12}\text{C} + {}^{12}\text{C} \rightarrow {}^{23}\text{Na} + \text{p}$$
$$^{12}\text{C} + {}^{12}\text{C} \rightarrow {}^{23}\text{Mg} + \text{n}$$

$$^{12}\text{C} + {}^{12}\text{C} \rightarrow {}^{24}\text{Ne} + \gamma$$

$$^{16}\text{O} + {}^{16}\text{O} \rightarrow {}^{24}\text{Mg} + 2\,{}^{4}\text{He}$$

$$^{16}\text{O} + {}^{16}\text{O} \rightarrow {}^{28}\text{Si} + {}^{4}\text{He}$$

$$^{16}\text{O} + {}^{16}\text{O} \rightarrow {}^{31}\text{P} + \text{p}$$

$$^{16}\text{O} + {}^{16}\text{O} \rightarrow {}^{31}\text{S} + \text{n}$$

$$^{16}\text{O} + {}^{16}\text{O} \rightarrow {}^{32}\text{S} + \gamma$$

with the production of ^{28}Si and ^{32}S being the most important branches of the oxygen-burning reactions so that the proportion of protons and neutrons will be low. Again, all of these reactions have substantial Coulomb barriers but are exothermic. The energy release will create thermal motion that acts against the gravitational pressure until the fuel runs out. Further rises in temperature up to $\sim 5 \times 10^9$ K result in a series of silicon burning reactions involving an equilibrium between photodisintegration at the high temperature and radiative capture processes such as

$$^{28}\text{Si} + \gamma \rightarrow {}^{24}\text{Mg} + {}^{4}\text{He} \tag{12.49}$$

$$^{4}\text{He} + {}^{28}\text{Si} \rightarrow {}^{32}\text{S} + \gamma \tag{12.50}$$

Various nuclei up to $A \sim 60$ are produced in sets of equilibrium reactions. In such equilibrium processes, the final yields of various nuclei are directly related to their nuclear stability (binding energies) with the more stable nuclei having higher yields. One observes greater yields of even–even nuclei than odd A nuclei (due to the pairing term in the mass formula), and even N isotopes are more abundant than odd N isotopes of an element.

The relative time scales of the various reactions leading to nuclei with $A < 60$ are shown in Table 12.2. Note these time scales are inversely proportional to the reaction rates. Note also that these processes have to end with nuclei in the region of $A < 60$ because such nuclei have the highest binding energies per nucleon.
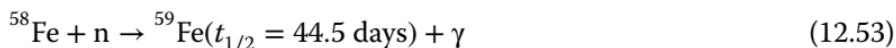
12.5.5 Synthesis of Nuclei with $A > 60$

The binding energy per nucleon curve peaks near $A \sim 60$ and decreases slowly as A increases beyond 60. This indicates that fusion reactions using charged particles are not generally energetically favorable to make heavier nuclei. However, another possible nuclear reaction is neutron capture, that is, (n, γ), if there are free neutrons available. These reactions have no Coulomb barriers, and the rates are then governed by the Maxwell–Boltzmann distribution of velocities in a hot gas and the availability of free neutrons. We have already seen that the cross section for (n, γ) reactions is proportional to 1/velocity at low energies, so that the reaction rate $N_n \langle \sigma v \rangle$ is largely governed by N_n, the neutron density.

Table 12.2 Time Scales of Nucleosynthetic Process in a One Solar-mass Star.

Process	Time Scale
Hydrogen burning	6×10^9 years
Helium burning	0.5×10^6 years
Carbon burning	200 years
Neon burning	1 year
Oxygen burning	Few months
Silicon burning	Day
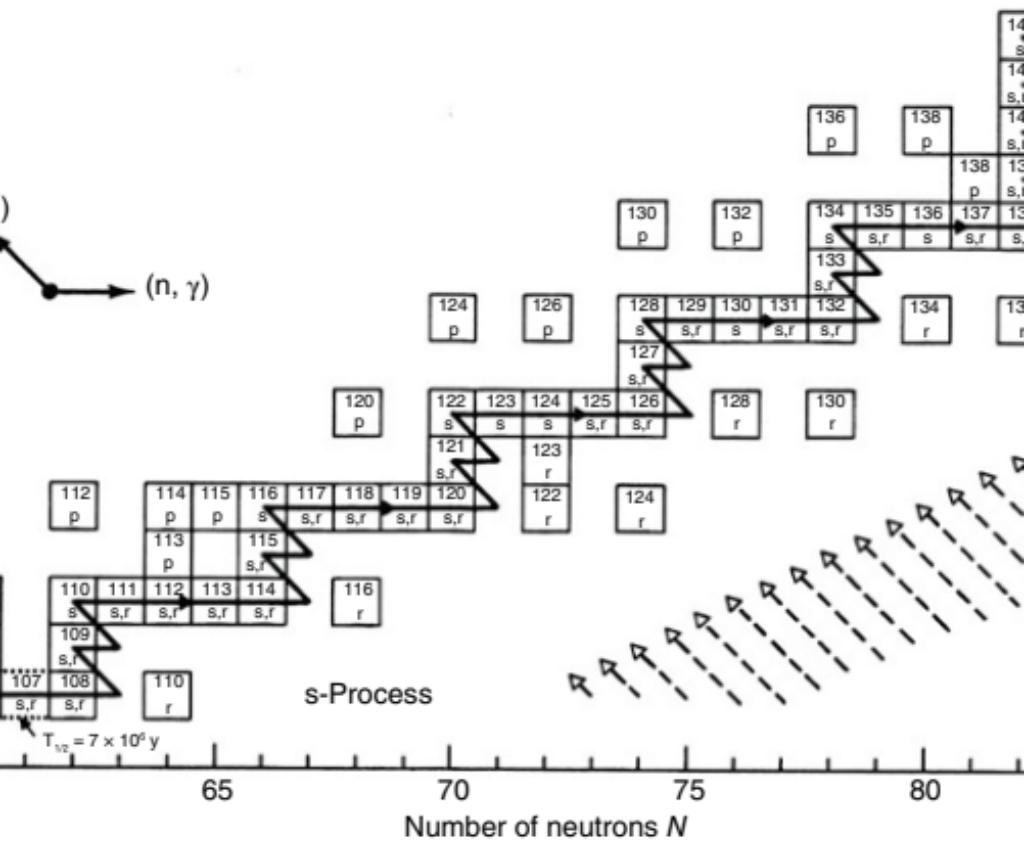
Two main types of neutron capture processes have been identified for nucleosynthesis that depend on the relative numbers of free neutrons and thus on the reaction rate. The first of these is slow neutron capture, the *so-called s-process*, where the time scale of the neutron capture process is much slower than the β decay lifetimes of the nuclei involved ($\tau_{\text{reaction}} \gg \tau_\beta$). In the s-process, each neutron capture proceeds in competition with β⁻ decay. Note that the reaction rates are so low that the process winds its way close to and including the stable nuclei. For example, consider the stable nucleus ^{56}Fe that might be present at the end of the charged particle burning processes (such nuclei are called seed nuclei). If this nuclide is in a neutron flux, the following reactions can occur:

$$^{56}\text{Fe} + \text{n} \rightarrow {}^{57}\text{Fe(stable)} + \gamma \tag{12.51}$$

$$^{57}\text{Fe} + \text{n} \rightarrow {}^{58}\text{Fe(stable)} + \gamma \tag{12.52}$$

$$^{58}\text{Fe} + \text{n} \rightarrow {}^{59}\text{Fe}(t_{1/2} = 44.5 \text{ days}) + \gamma \tag{12.53}$$

The 44.5 days lifetime of ^{59}Fe is short enough that it will undergo β⁻ decay before another neutron is captured, that is,

$$^{59}\text{Fe} \rightarrow {}^{59}\text{Co(stable)} + \text{e}^- + \overline{\nu}_e \tag{12.54}$$
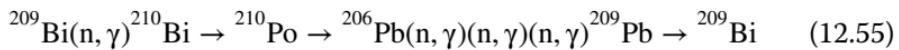
and further captures will continue with ^{59}Co. The mean times of neutron capture reactions $\tau_{\text{reaction}} = \ln 2/\text{rate} = \ln 2/N_n \langle \sigma v \rangle$. If $N_n \sim 10^{11}/\text{m}^3$, $\sigma_\gamma = 0.1 \ b$, and $E_n \sim 50$ keV, then $\tau \sim 10^5$ years under typical stellar conditions. Then neutron capture will be possible by all stable nuclei and many of the long-lived nuclei. A typical s-process path of nucleosynthesis for the nuclei in the region of $Z = 45$–60 is shown in Figure 12.14. The production of nuclei follows a zigzag path through the chart of nuclides, with increases in mass when a neutron is captured and increases in atomic number when β-decay precedes the next neutron capture.

(n, γ)

s-Process

$T_{1/2} = 7 \times 10^6$ y

Number of neutrons N

65   70   75   80

...tion of the chart of nuclides showing the s-process pa... ...rocess proceeds through nuclei far to the right of the v... ...(1988). Reproduced with the permission of Chicago Un...

The s-process terminates at ^{209}Bi because the cyclic α-production sequence

$$^{209}\text{Bi}(n, \gamma)^{210}\text{Bi} \rightarrow {}^{210}\text{Po} \rightarrow {}^{206}\text{Pb}(n, \gamma)(n, \gamma)(n, \gamma)^{209}\text{Pb} \rightarrow {}^{209}\text{Bi} \quad (12.55)$$

cannot proceed to higher mass nuclei. The s-process also has branching points as it proceeds toward higher masses when it encounters an unstable nuclide with a half-life on the order or the reaction lifetime. These branching points are very important for identifying the rate of neutron capture.

The source of the neutrons for the s-process is (α, n) reactions on neutron-rich nuclei such as ^{13}C or ^{21}Ne, with the latter being the most important. In Population II and Population I stars, one can get side reactions in the hydrogen burning process like

$$^{20}\text{Ne}(p, \gamma)^{21}\text{Na} \quad (12.56)$$

$$^{21}\text{Na} \rightarrow {}^{21}\text{Ne} + e^+ + \nu_e \quad (12.57)$$

that produce small amounts of the target nuclei for the (α, n) reactions.

For the slow neutron capture process, there is an equilibrium between the production and loss of adjacent nuclei. Stable nuclei are only destroyed by neutron capture. For such equilibria, we can write for the rate of change of a nucleus with mass number A:

$$\frac{dN_A}{dt} = \sigma_{A-1}N_{A-1} - \sigma_A N_A \quad (12.58)$$

where σ_i and N_i are the capture cross sections and number of nuclei (abundance) for nucleus i, respectively. At equilibrium the derivative is zero, of course, and

$$\sigma_{A-1}N_{A-1} = \sigma_A N_A \quad (12.59)$$

This relationship between the abundances of neighboring stable nuclei in proportion to their neutron capture cross sections is a signature for the s-process production of these nuclei.

If the time scale of neutron capture reactions is very much less than β$^-$ decay lifetimes, then rapid neutron capture or the *r-process* will occur. For r-process nucleosynthesis, one needs large neutron densities, $\sim 10^{28}/\text{m}^3$, which lead to capture times of the order of fractions of a second. (Note that the neutron flux in a small research nuclear reactor is $\sim 10^{17}/\text{m}^2/\text{s}$.) The astrophysical environment where such processes can occur is now thought to be in supernovae but is still uncertain. In the r-process, a large number of sequential captures will occur until the process is terminated by neutron emission or, in the case of the heavy elements, fission or β-delayed fission. The lighter "seed" nuclei capture neutrons until they reach the point where β$^-$ decay lifetimes have decreased and β$^-$ decay will compete with neutron capture. The r-process is responsible for the synthesis of all nuclei with $A > 209$ and many lower mass nuclei. In a
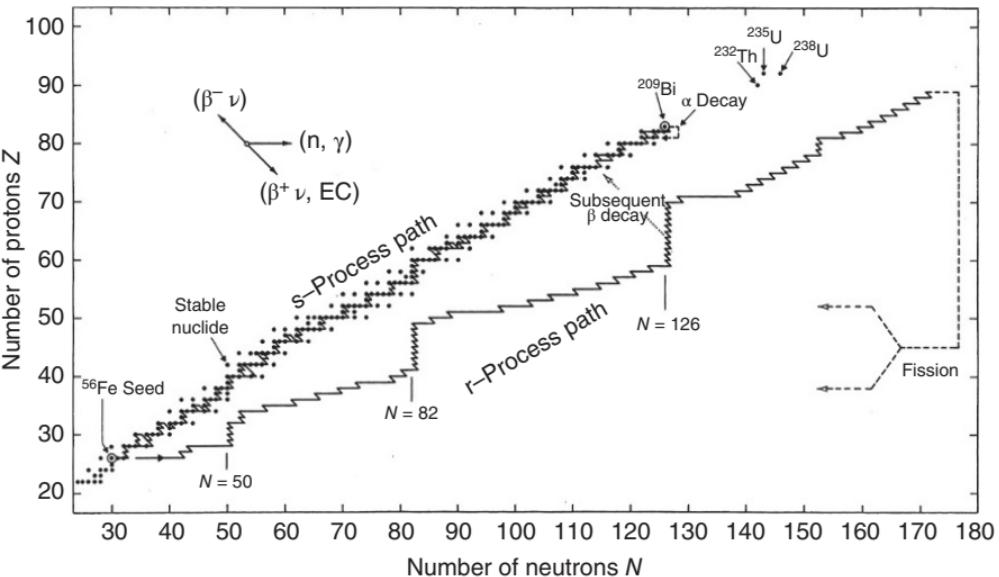
Figure 12.15 Neutron capture paths are shown for the s-process and a typical r-process. The s-process path runs through well-known nuclei, but the nuclei in the r-process path are mostly unknown at present (Rolfs and Rodney (1988). Reproduced with the permission of Chicago University Press).

plot of abundances versus mass number A (Fig. 12.4), one sees two peaks in the abundance distributions near each magic (high) neutron number ($N = 50$, 82, 126). The lower mass peak at each value is due to the r-process, which reaches the magic number of neutrons at a lower Z value than the s-process. The products then decay back to stability. The peaks occur because of the relative stability of $N = 50, 82$ and 126 nuclei against neutron capture compared to their neighbors with just one or two more neutrons. A typical r-process path is shown in Figure 12.15. Notice that the path climbs up in atomic number along the neutron magic numbers. The nuclei in each climbing region are the places of maxima in the isotopic yields after decay. Notice that the r-process creates nuclei that are very far from the valley of stability. The nuclear properties of these nuclei such as half-life and β-delayed neutron emission are needed for an accurate prediction of the r-process. However, only a few nuclei along the predicted r-process path are known at present, and the astrophysical models must rely on theoretical nuclear models. In addition, it seems unlikely that there is only one r-process with a fixed value of the neutron flux in nature, which contributes to the uncertainty of the predictions. Study of the nuclei involved in the r-process is an active field of research at present.

Another important process leading to the synthesis of some specific proton-rich nuclei with $70 < A < 200$ is the so-called *p-process*. The p-process consists of a series of photonuclear reactions (γ, p), (γ, α), (γ, n) on "seed"
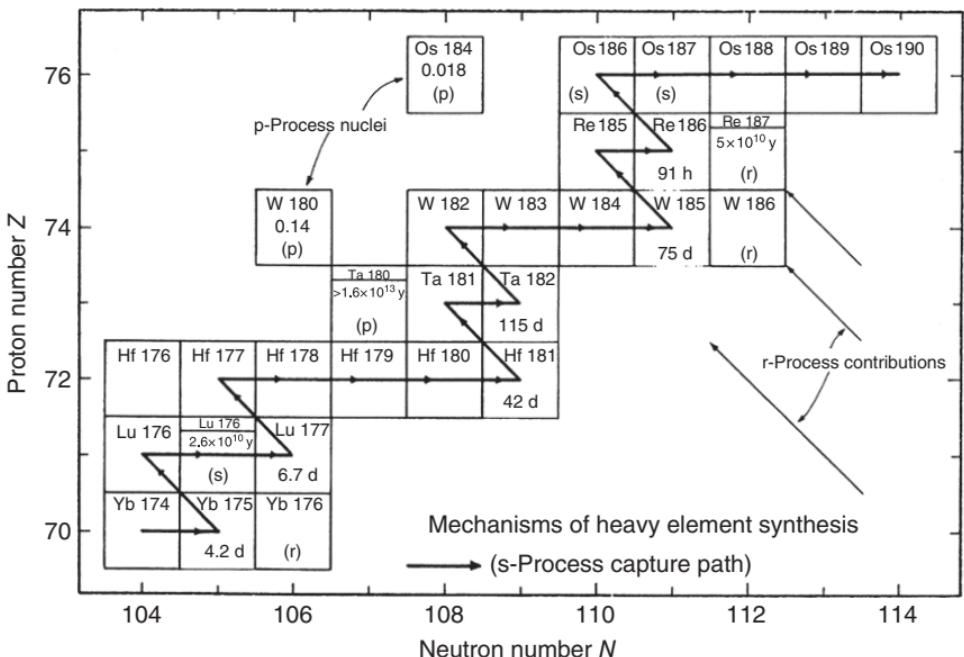
Figure 12.16 A section of the heavy element chart of the nuclides showing the relative paths of the s-, r- and p-processes in nucleosynthesis. Note that certain nuclei are not accessible by the s-process and must be formed in other ways (Truan (1984). Reproduced with the permission of Annual Reviews, Inc.).

nuclei from the s-process that produce these nuclei. (Originally it was believed that proton capture processes during supernovae were responsible for these nuclei, but it was found that the calculated proton densities are too small to explain the observed abundances.) The temperature during a supernovae explosion is $\sim 3 \times 10^9$ K, producing blackbody radiation that can cause these photonuclear reactions. The p-process contribution to the abundances of most elements is very small, but there are some nuclei (^{190}Pt, ^{168}Yb) that seem to have been exclusively made by this process. Putting all three reactions together, the relative importance of s-, r-, and p-processes in nucleosynthesis in a given region is shown in Figure 12.16. Thus, it is clear that the distribution of isotopes in our solar is relatively complex with contribution from several, if not many, stellar processes. The material is highly processed and mixed.

A process that is related to the p-process is that it can produce proton-rich nuclei that are not accessible to the s- or r-processes is the *rp-process*, the rapid proton capture process. This process makes proton-rich nuclei with $Z < 50$ because it encounters a process terminating cycle near tin. The rp-process involves a set of (p, γ) and β$^+$ decays that run near the proton dripline and populate the most proton-rich nuclei. The process is thought to be explosive
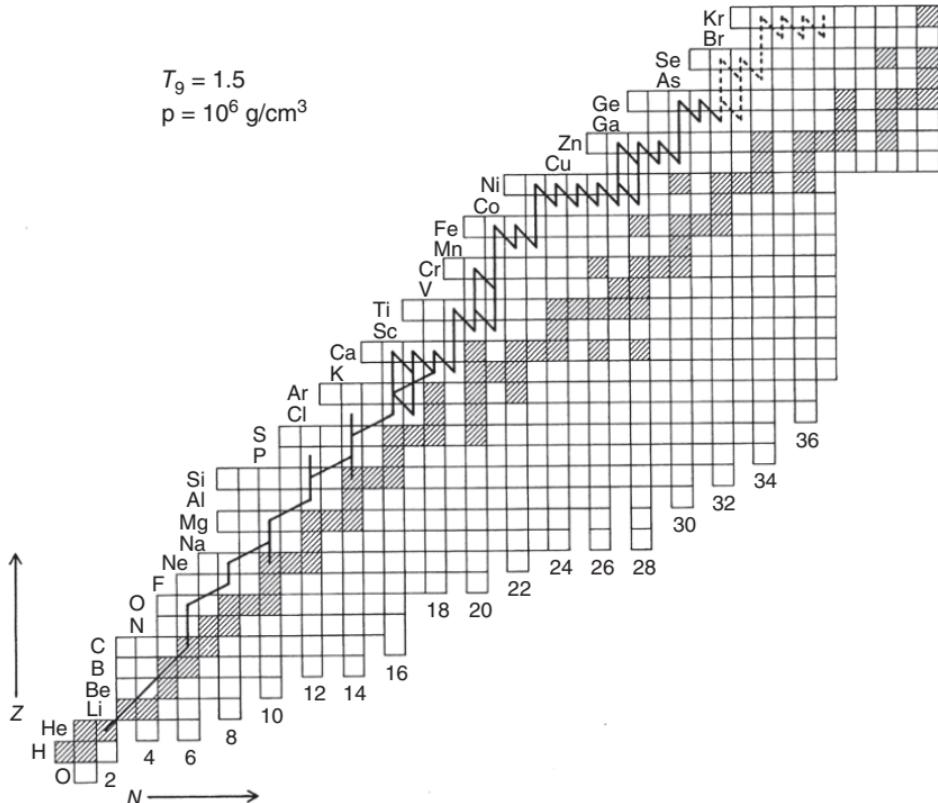
Figure 12.17 The path of the rp-process is shown relative to the line of β stability for the temperature and density conditions as indicated.

with a high flux of energetic protons and starts through a "breakout" from the CNO cycle through a side chain of the CNO cycle that produces the p-rich nuclei ^{21}Na and ^{19}Ne. These "seed" nuclei form the basis for further proton captures that do not cycle back to ^{12}C but rather lead to the nucleosynthetic path shown in Figure 12.17. Note this process, while starting close to the line of β stability, approaches the proton dripline as the nuclei become heavier. The rp-process creates a small number of characteristic nuclei with $A < 100$ that are outside the s-process path. At present, the source of the protons for this process are thought to be certain binary stars where a more dense neutron star is able to accrete hydrogen from a "normal" hydrogen-burning star.

12.6 Solar Neutrino Problem

12.6.1 Introduction

Many of the nuclear reactions that provide the energy of the stars also result in the emission of neutrinos. Because of the small absorption cross

Table 12.3 Solar Neutrino Fluxes on Earth from the Standard Solar Model.

Reaction Source	Flux (particles/s/cm^2)
pp	5.94×10^{10}
pep	1.40×10^8
hep	7.88×10^3
^{7}Be	4.86×10^7
^{8}B	5.82×10^6
^{13}N	5.71×10^8
^{15}O	5.03×10^8
^{17}F	5.91×10^6

Source: From Bacall and Pena-Garay (2004).

sections for neutrinos interacting with matter ($\sigma_{abs} \sim 10^{-44}$cm^2), these neutrinos are not absorbed in the sun or other stars. (This loss of neutrinos corresponds to the emission of ~2% of the energy of our sun.) Because of penetrating power, the neutrinos provide a window into the stellar interior. At the same time the small absorption cross sections also make neutrinos difficult to detect with almost all neutrinos passing through the earth without interacting.

Recently, a good deal of attention has been given to the "solar neutrino problem" and its important solution. The 2002 Nobel Prize in physics was awarded to Ray Davis and Masatoshi Koshiba for their pioneering work on this problem. Of special interest here is the important role of nuclear and radiochemistry in this work as Davis was a nuclear chemist. The definition and solution of this problem is thought to be one of the major scientific advances of recent years.

12.6.2 Expected Solar Neutrino Sources, Energies, and Fluxes

The sun is a major source of neutrinos reaching the surface of the earth due to its close proximity and number of neutrinos from hydrogen burning. The sun emits ~1.8×10^{38} neutrinos/s, which, after the ~8 m transit time, reach the surface of the earth at the rate of 6.4×10^{10} neutrinos/s/cm^2. The predictions of the standard solar model, based on all of the reactions discussed previously, for the neutrino fluxes at the surface of the earth due to various nuclear reactions are shown in Table 12.3. The contributions from the various processes are thought to be relatively reliable because the results must be consistent with many independent measurements of the sun's properties and the number of possible nuclear reactions is limited.
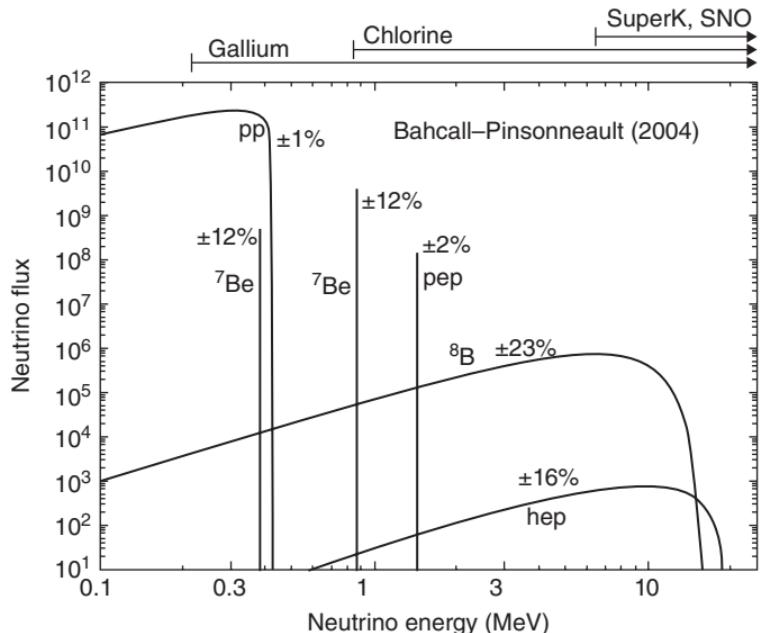
Figure 12.18 Log-log plot of predicted neutrino fluxes from most important solar nuclear reactions. At the top the energy regions to which several neutrino detectors are sensitive are shown (Bahcall, Reproduced with the permission of Bahcall website).

The predicted energy distributions of the neutrinos can be compared in Figure 12.18. Recall that each nuclear reaction will have a characteristic neutrino energy distribution due to the energetics and kinematics of the reaction.
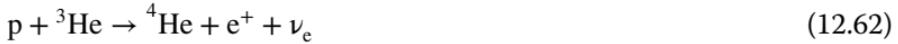
The source labeled "pp" in Table 12.3 and Figure 12.18 refers to the reaction

$$p + p \rightarrow d + e^+ + \nu_e \tag{12.60}$$

and is the most important reaction, producing one neutrino for each ^{4}He nucleus; note that this is a three-body final state and gives a continuous neutrino energy distribution. The "pep" source is the reaction

$$p + p + e^- \rightarrow d + \nu_e \tag{12.61}$$

which produces monoenergetic neutrinos due to the two-body final state, while the "hep" source is another three body reaction

$$p + {}^3He \rightarrow {}^4He + e^+ + \nu_e \tag{12.62}$$
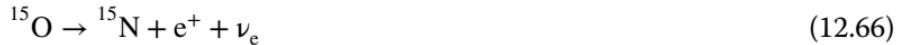
This latter reaction produces the highest energy neutrinos with a maximum energy of 18.77 MeV due to the high reaction Q value. The intensity of the hep source is about 10^7 times less than the pp source. The "^{7}Be" source refers to the electron capture decay reaction that is part of the pp chain

$$e^- + {}^7Be \rightarrow {}^7Li + \nu_e \tag{12.63}$$

that produces two groups of neutrinos, one in which the ground state of ^{7}Li is populated (90% branching ratio) and one that populates the 0.477 MeV excited state (10% branch). The source "^{8}B" refers to the positron decay

$$^{8}\text{B} \rightarrow {}^{8}\text{Be}^{*} + \text{e}^{+} + \nu_{\text{e}} \tag{12.64}$$

in which the first excited state of ^{8}Be (at 3.040 MeV) is populated. The other weak sources "^{13}N," "^{15}O," and "^{17}F" refer to β^{+} decays that occur in the CNO cycle, that is,

$$^{13}\text{N} \rightarrow {}^{13}\text{C} + \text{e}^{+} + \nu_{\text{e}} \tag{12.65}$$

$$^{15}\text{O} \rightarrow {}^{15}\text{N} + \text{e}^{+} + \nu_{\text{e}} \tag{12.66}$$

and

$$^{17}\text{F} \rightarrow {}^{17}\text{O} + \text{e}^{+} + \nu_{\text{e}} \tag{12.67}$$

Looking back at all of these reactions, it is important to note that only electron neutrinos (ν_{e}) are emitted in ALL of these reactions. The nuclear reactions have to convert protons into neutrons in order to form helium nuclei. The reactions that do this conversion are essentially the inverse of neutron β decay that creates a positron and an electron neutrino.

12.6.3 Detection of Solar Neutrinos

As indicated previously, the detection of the weakly interacting solar neutrinos is difficult because of the extremely low absorption cross sections. Two main classes of detectors were used to overcome this obstacle, radiochemical detectors, and Cherenkov detectors. Radiochemical detectors rely on detecting the products of neutrino-induced nuclear reactions, whereas the Cherenkov detectors observe light from the scattering of neutrinos. The most famous radiochemical detector was that constructed by Davis and coworkers in the Homestake Gold Mine in South Dakota. They mounted a massive detector, consisting of 100,000 gallons of a cleaning fluid, C_2Cl_4, in a cavern about 1500 m below the surface of the earth. The cleaning fluid weighed 610 tons and corresponded to the volume of 10 railway tanker cars. The nuclear reaction occurring in the detector was

$$\nu_{\text{e}} + {}^{37}\text{Cl} \rightarrow {}^{37}\text{Ar} + \text{e}^{-} \tag{12.68}$$

The ^{37}Ar product nucleus decays by electron capture back to chlorine with a 35-day half-life. First the cleaning fluid was purged of all gases. After the fluid was irradiated by solar neutrinos for a period of time, the *individual* ^{37}Ar product nuclides were flushed from the detector with a stream of helium gas and put into a proportional counter where the 2.8 keV Auger electrons from the EC

decay were detected with a high efficiency. The detection reaction has a threshold of 0.813 MeV making it sensitive to the ^{8}B, hep, pep, and ^{7}Be (ground-state decay) neutrinos with the ^{8}B being the most important. Typically $\sim$3 atoms of ^{37}Ar are produced per week and must be isolated from the $\sim 10^{30}$ atoms of cleaning fluid in the tank, a radiochemical *tour de force*. The detector was placed deep underground to shield against background reactions induced by cosmic rays.

The Davis- or chlorine-based detector first identified that there was a "solar neutrino problem" in that only a fraction of the expected neutrons were observed. This observation led researchers to build other radiochemical detectors to confirm the problem. These detectors, GALLEX constructed in Italy and SAGE in Russia, were based on the similar reaction

$$\nu_e + {}^{71}\text{Ga} \rightarrow {}^{71}\text{Ge} + e^- \tag{12.69}$$

These detectors have a much lower threshold at 0.232 MeV and can be used to directly detect the dominant pp neutrinos from the sun. The gallium is present as a solution of $GaCl_3$. The ^{71}Ge is collected by sweeping the detector solution with N_2 and converting the Ge to GeH_4 before counting. These detectors utilized 30–100 tons of gallium and contained a significant fraction of the world's yearly gallium production at the time.

The Cherenkov detectors involve the scattering of neutrinos by charged particles where the scattered charged particles then emit Cherenkov radiation when they travel in a condensed medium (water) that can be detected by scintillation detectors. The first of these detectors was placed in a mine at Kamioka, Japan. The largest version of the detectors at Kamioka is called Super-Kamiokande and consists of 50,000 tons of high purity water. The detection reaction in this case is a scattering reaction

$$\nu + e^- \rightarrow \nu + e^- \tag{12.70}$$

and the detection threshold is about 8 MeV, allowing one to observe the ^{8}B neutrinos. The detector is instrumented with literally thousands of very large photomultiplier tubes that are used to create an image of the scattering track.

A related detector, called the Sudbury Neutrino Observatory (SNO), was located at Sudbury, Ontario, Canada, and consisted of 1000 tons of heavy water (D_2O) mounted $\sim$2 km below the surface in the Sudbury nickel mine. In addition to neutrino–electron scattering, this detector can also observe two nuclear reactions involving deuterium:

$$\nu_e + d \rightarrow 2\,p + e^- \tag{12.71}$$

and

$$\nu + d \rightarrow n + p + \nu \tag{12.72}$$

where the reaction can occur with all three types of neutrinos, ν_e, ν_μ, and ν_τ. The former reaction of the previous pair is sensitive to electron neutrinos only. These different types of reactions can be exploited to look for neutrino oscillations (see in the following text). In the latter reaction, the emitted neutron is detected by a subsequent (n, γ) reaction in which the γ-ray is detected by scintillation detectors. (The heavy water of the detector is surrounded by 7000 tons of ordinary water to shield against neutrons from radioactivity in the rock walls of the mine.) This detector also poses radiochemical challenges as the water purity must be such that there are <10 uranium or thorium atoms per 10^{15} water molecules.

12.6.4   The Solar Neutrino Problem

The solar neutrino "problem" was defined by the first results of Davis et al. using the chlorine detector at the Homestake Mine. Davis et al. observed only ~1/3 of the expected solar neutrino flux as predicted by standard models of the sun, which assume 98.5% of the energy is produced by the pp chain and 1.5% of the energy by the CNO cycle. (The final result of the chlorine detector experiment is that the observed solar neutrino flux is 2.1±0.3 SNU compared with the predicted 7.9±2.4 SNU, where the solar neutrino unit (SNU) is defined as 10^{-36} neutrino captures/target atom/second.) The GALLEX and SAGE detectors subsequently reported solar neutrino fluxes of 77±10 SNU and 69±13 SNU, which are to be compared with the standard solar model prediction of 127 SNU for the neutrinos detected by these reactions. Such large discrepancies clearly indicated that either the models of the sun were wrong or something fundamental was wrong in our ideas of the nuclear physics involved.

12.6.5   Solution to the Problem: Neutrino Oscillations

The solution to the solar neutrino problem was found in the previous ideas of the fundamental structure of matter, the so-called Standard Model of particle physics. This difficulty comes from the fact that neutrinos do not retain their individual identities but rather oscillate between forms! The standard model predicts that the three types of neutrinos are massless and that once created, they retain their identity for all time. The basic idea is that as neutrinos come from the sun, they "oscillate," that is, they change from being electron neutrinos to being muon neutrinos and back etc. This oscillation is possible if the neutrinos have a mass and if there is a mass difference between the electron and muon neutrinos. These neutrino oscillations are enhanced by neutrino–electron interactions in the sun.

The direct observational evidence for the occurrence of neutrino oscillations came from observations with the Cherenkov detectors. The SNO detector found 1/3 the expected number of electron neutrinos coming from the sun in agreement with previous work with the radiochemical detectors. The
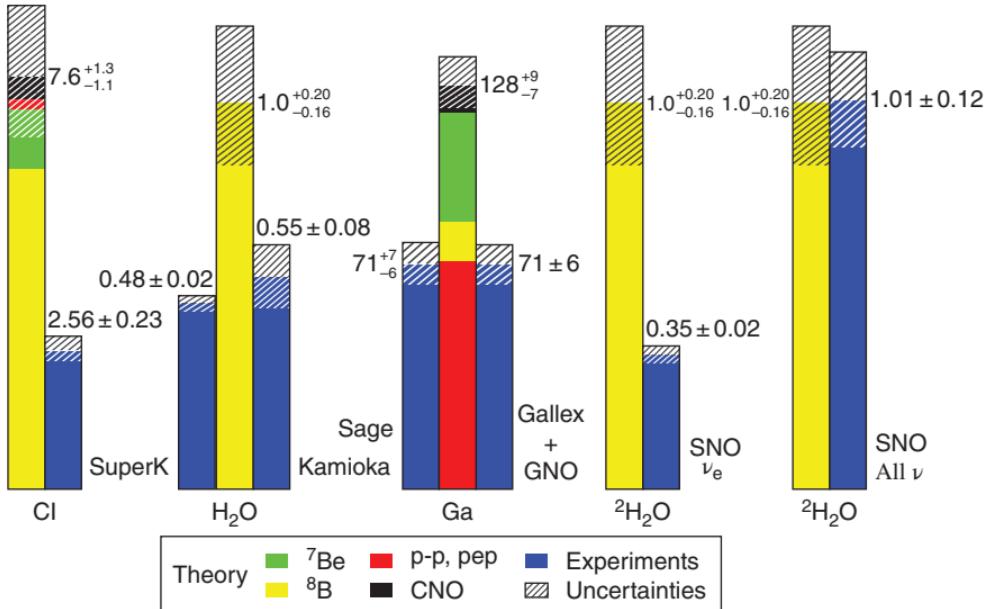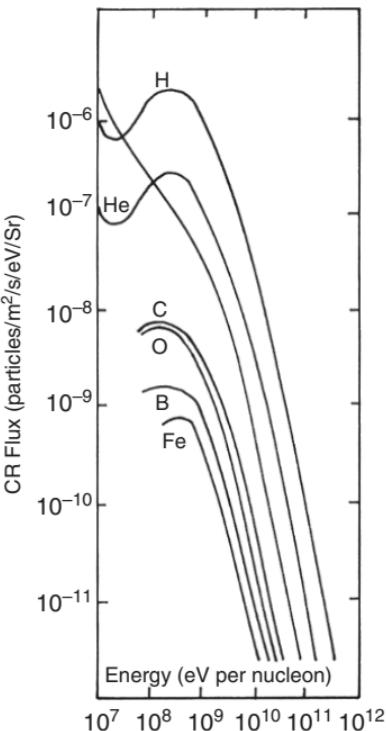
Figure 12.19 A summary of the comparison between standard solar model predictions and experimental measurements emphasizing the effects of neutrino oscillations in detector systems that are sensitive to only one form of neutrino (Bahcall, Reproduced with the permission of Bahcall website). (*See insert for color representation of the figure.*)

Super-Kamiokande detector that is primarily sensitive to electron neutrinos but has some sensitivity to other neutrino types found ∼1/2 the neutrino flux predicted by the standard solar models. If all neutrino types behaved similarly, the SNO and Super-Kamiokande detectors should have detected the same fraction of neutrinos. Further experiments with the SNO detector operating in a mode to simultaneously detect all types of neutrinos found neutrino fluxes in agreement with the solar models. The results for various experiments as they stood in 2000 are summarized in Figure 12.19.

Subsequent experiments have been performed to observed neutrino oscillations from other strong sources of neutrinos. For example, nuclear reactors such as the Chinese complex at Daya Bay provide a strong source of electron neutrinos, and large detectors have been placed at different distances from the complex to monitor the flux. The Super-Kamiokande detector was used to observe the day/night variation of tau and electron neutrinos produced in the atmosphere.

Current work has provided information on the mass differences among the neutrinos but not the absolute scale. There are two orderings of the relative masses, the so-called normal hierarchy with two lower masses separated by

Figure 12.20 Example of the energy spectrum of GCR (Audouze and Vauclair (1980). Reproduced with the permission of An Introduction to Nuclear Astrophysics).

$\sim 7 \times 10^{-5}$ eV^2 that lie below the third mass by $\sim 2 \times 10^{-3}$ eV^2 or the inverted hierarchy where the single mass lies below the pair of nearby masses.

12.7 Synthesis of Li, Be, and B

Big bang nucleosynthesis is responsible for the synthesis of hydrogen and helium and some of the ^{7}Li. (Stellar nucleosynthesis in main sequence stars transforms about 7% of the hydrogen into ^{4}He.) However, neither stellar nucleosynthesis nor big bang nucleosynthesis can produce significant amounts of Li, Be, and B nuclei. For example, the abundances of Li, Be, and B are suppressed by a factor of 10^6 relative to the abundances of the neighboring elements. (cf., Fig. 12.2)

The extremely low abundance is the result of two factors, the relative fragility of the isotopes of Li, Be, and B and the high binding energy of ^{4}He, which makes the isotopes of Li, Be, and B generally unstable with respect to various decay/reactions that lead to ^{4}He. For example, the nuclei ^{6}Li, ^{7}Li, ^{9}Be, ^{11}B, and ^{10}B are destroyed by stellar proton irradiation at the temperatures of 2.0, 2.5, 3.5, 5.0, and 5.3×10^6 K, respectively. Thus, these nuclei can't survive the stellar environment since the temperature in the center of the sun is $\sim 1.5 \times 10^7$ K.
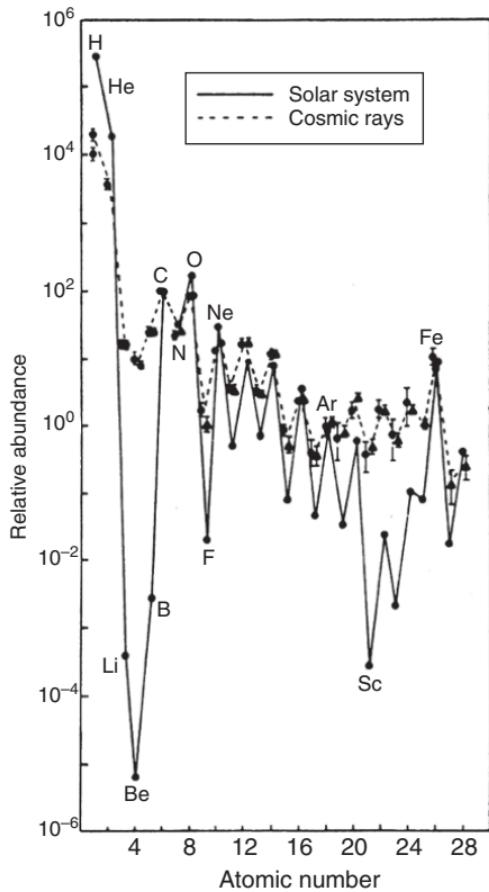
Figure 12.21 The relative elemental abundances in the solar system and cosmic rays (Rolfs and Rodney (1988). Reproduced with the permission of Chicago University Press).

(Only the rapid cooling following the big bang allows the survival of the few lithium products of primordial nucleosynthesis.)

Li, Be, and B are believed to be produced in spallation reactions in which the interstellar ^{12}C and ^{16}O are fragmented by energetic protons in the galactic cosmic rays (GCR). The most likely processes are medium energy reactions with thresholds of 10–20 MeV. The measured energy spectrum of GCR is shown in Figure 12.20. Typical cross sections for these spallation reactions are $\sim$1–100 mb for high-energy protons $E_p > 100$ MeV. The time scale of the irradiation is $\sim 10^{10}$ years. The product nuclei are not subject to high temperatures after synthesis due to the low densities and temperatures in interstellar space, so they can survive. Further support for this mechanism is the relative abundances of the elements in the GCR relative to the solar abundances (Fig. 12.21), which shows enhanced amounts of Li, Be, and B in the GCR. This pattern is similar to the yield distributions of the fragments from the reactions of high-energy projectiles. However it is clear that at most 30% of the solar system, Li is produced by the big bang and cosmic spallation. Core collapse supernovae can account

for at most another 20% that means that 50% must come from other sources. This is known as the "lithium problem."

Problems

12.1 Assume an absorption cross section of 10^{-44} cm^2 for solar neutrinos interacting with matter. Calculate the probability of a neutrino interacting as it passes through the earth.

12.2 What is the most probable kinetic energy of a proton in the interior of the sun ($T = 1.5 \times 10^7$ K)? What fraction of these protons has an energy > 0.5 MeV?

12.3 If we want to study the reaction of ^{4}He with ^{16}O under stellar conditions, what laboratory energy would we use for the ^{4}He?

12.4 If the earth was a neutron star, estimate its radius and density from its mass.

12.5 If the interior temperature of the sun is 1.5×10^7 K, what is the peak energy of the p + ^{14}N → ^{15}O + γ reaction?

12.6 Which nucleosynthetic processes are responsible for the following nuclei: ^{7}Li, ^{12}C, ^{20}Ne, ^{56}Fe, ^{84}Sr, ^{96}Zr, ^{114}Sn, ^{124}Sn, ^{209}Bi, ^{238}U?

12.7 Outline how you would construct a radiochemical neutrino detector based upon ^{115}In.

12.8 Estimate the Coulomb barrier height for the following pairs of nuclei: (a) p + p (b) ^{16}O + ^{16}O (c) ^{28}Si + ^{28}Si.

12.9 Calculate the rate of fusion reactions in the sun. Be sure to correct for the energy loss due to neutrino emission.

12.10 Assuming the sun will continue to shine at its present rate, calculate how long the sun will shine.

12.11 From the data given on the Davis detector and the assumption that the ^{37}Ar production rate is 0.5 atoms/day, calculate the neutrino capture rate in SNU. Assume the effective cross section for the ^{8}B, neutrinos is 10^{-42} cm^2.

12.12 Calculate the evolution of the n/p ratio in the primordial universe from the information given as the temporal dependence of the temperature.

12.13 Make an estimate of the neutron to proton ratio in the center of the sun if the only source of neutrons is thermal equilibrium of the weak interactions.

12.14 Using the information on the r-process and the s-process paths in Figures 12.14 and 12.15, make estimates of the average atomic numbers of the nuclei in the peaks for $N = Z$ in the mass abundance curves. Do the masses of these nuclei correspond to the peaks in Figure 12.4?

Bibliography

E.M. Burbridge, et al., *Rev. Mod. Phys.* **29**, 547 (1957).

W.M. Haynes, T.J. Bruno, and D.R. Lide, *CRC Handbook of Chemistry and Physics*, 75th Edition (CRC Press, Boca Raton, 1994).

C. Iliadis, *Nuclear Physics of Stars* (Wiley-VCH, Weinheim, 2007).

J.W. Truran, *Ann. Rev. Nucl. Part. Sci.* **34**, 53 (1984).

Many elementary textbooks have discussions of nuclear astrophysics. We recommend the following textbooks as being especially good in their coverage.

G.R. Choppin, J.O. Liljenzin, and J. Rydberg, *Radiochemistry and Nuclear Chemistry*, 4th Edition (Academic Press, Oxford, 2013).

W.N. Cottingham and D.A. Greenwood, *An Introduction to Nuclear Physics* (Cambridge University Press, Cambridge, 1986).

R. Dunlap, *An Introduction to the Physics of Nuclei and Particles* (Thomson, Toronto, 2004).

W.D. Ehmann and D.E. Vance, *Radiochemistry and Nuclear Methods of Analysis* (John Wiley & Sons, Inc., New York, 1991).

G. Friedlander, J.W. Kennedy, E.S. Macias, and J.M. Miller, *Nuclear and Radiochemistry*, 3rd Edition (John Wiley & Sons, Inc., New York, 1981).

K. Heyde, *Basic Ideas and Concepts in Nuclear Physics* (IOP, Bristol, 1999).

P.E. Hodgson, E. Gadioli, and E. Gadioli-Erba, *Introductory Nuclear Physics* (Clarendon, Oxford, 1997).

K.S. Krane, *Introductory Nuclear Physics* (John Wiley & Sons, Inc., New York, 1988).

W.S.C. Williams, *Nuclear and Particle Physics* (Clarendon, Oxford, 1991).

S.S.M. Wong, *Introductory Nuclear Physics*, 2nd Edition, (John Wiley & Sons, Inc., New York, 1998).

There are a number of excellent introductory or expository treatments of nuclear astrophysics. Among those we recommend are:

J. Audouze and S. Vauclair, *An Introduction to Nuclear Astrophysics* (D. Reidel Publishing Co., Dordrecht, 1980).

C.A. Barnes, D.D. Clayton, and D.N. Schramm, Editors, *Essays in Nuclear Astrophysics* (Cambridge University Press, Cambridge, 1982).

D.D. Clayton, *Principles of Stellar Evolution and Nucleosynthesis* (University of Chicago Press, Chicago, 1983).

B.W. Filippone, Ann. Rev. Nucl. Part. Sci. 36, 717 (1986).

F. Kappeler. F.-K. Thielemann, and M. Wiescher, Ann. Rev. Nucl. Part. Sci. 48, 175 (1998).

National Research Council (U.S.). Committee on Nuclear Physics, *Nuclear Physics: The Core of Matter, The Fuel of Stars* (NAS, Washington, 1999).

C.E. Rolfs and W.S. Rodney, *Cauldrons in the Cosmos* (University of Chicago Press, Chicago, 1988).

Specific references cited in this chapter are:

A comprehensive account of the solar neutrino problem and its solution is found at the website of J.N. Bahcall (https://www.sns.ias.edu/~jnb).

E. Anders and N. Grevasse, Goechim Cosmochem. Acta 53, 197 (1989).

J.N. Bahcall and C. Pena-Garay, New J. Phys. 6, 63 (2004).

A.G.W. Cameron, Atomic Energy of Canada, CRL-41 (1957).

H. Reeves, Rev. Mod Phys. 66, 193 (1994).

V.E. Viola, in *Origin of Elements in the Solar System: Implications of Post-1957 Observations*, O. Manuel, Ed. (Kluwer, New York, 2000)

S. Weinberg, *The First Three Minutes* (Basic Books, New York, 1977).

Reactors and Accelerators
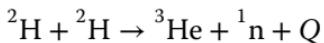
13.1 Introduction

Radioactive decay of primordial nuclides is the most important nuclear transformation that commonly takes place on Earth along with reactions induced by cosmic rays. The reasons that other nuclear reactions do not normally occur on Earth are simple: nuclear reactions that are induced by protons or heavier charged particles have large activation barriers and require energetic charged particles that are only present in space and the highest regions of the atmosphere. On the other hand, nuclear reactions induced by neutrons do not have an activation barrier, but neutrons are unstable, decaying by β-decay into protons with a half-life of ∼10 min. Thus, neutrons cannot be stored very long and have to be produced in other nuclear reactions to use them in subsequent nuclear reactions.

Protons and all nuclei are positively charged and strongly repel one another through the Coulomb force. Colliding nuclei must have kinetic energies that are far in excess of the thermal energies available on Earth to reach distances that are short enough for the nuclear force to be effective (∼1 fm). We must accelerate one of the particles until it has sufficient kinetic energy to get over the Coulomb barrier for the nuclei to react.

Sample Problem 13.1: Temperatures and Velocities

A very simple and potentially useful fusion reaction combines two deuterium nuclei, forming ^{3}He and a neutron:

$$^2\text{H} + {}^2\text{H} \rightarrow {}^3\text{He} + {}^1\text{n} + Q$$

Estimate the Coulomb barrier for this reaction and the temperature of deuterium gas that would give such an average energy.

Solution
The Coulomb barrier, discussed in Chapter 10, is given by

$$V_{\text{C}} = \frac{Z_1 Z_2 e^2}{r} = \frac{[1(1)\ 1.439\ \text{MeV} - \text{fm}]}{(1.93 + 1.93)\text{fm}} = 0.373\ \text{MeV}$$

Setting the kinetic energy equal to the Coulomb barrier as would be appropriate when all the particles are moving (in a gas) and using the thermal energy of an ideal gas,

$$V_C = \text{K.E.} = \frac{1}{2}mv^2 = \frac{3}{2}k_B T$$
$$T = \frac{2V_C}{3k_B} = \frac{2(0.373 \text{ MeV})1.602 \times 10^{-13} \text{ J/MeV}}{3(1.38 \times 10^{-23} \text{ J/K})}$$
$$T = 3 \times 10^9 \text{ K}$$

This extraordinary temperature is characteristic of the interiors of stars, as discussed in Chapter 12, and not of terrestrial objects.

The fact that neutrons can be absorbed by nuclei without overcoming a threshold ($\ell = 0$ or s-wave reactions) makes neutrons extremely effective nuclear "reactants." Neutron-induced reactions are the energy source for present-day commercial nuclear power (fission reactors), while charged-particle-induced reactions remain under study as power sources (fusion reactors). In this chapter we will consider the general features of nuclear fission reactors, followed by the general features of charged-particle accelerators, magnetic spectrometers, and the production of beams of radioactive nuclei.

13.2 Nuclear Reactors

13.2.1 Neutron-Induced Reaction

Nuclear fission reactors ("nuclear power reactors") are devices that use controlled neutron-induced fission to generate energy. The primary form of the generated energy is heat that is converted into electrical energy. While a complete description of the design of these devices is beyond the scope of this book, there are certain basic principles related to nuclear reactors that are worth studying and that can be described and understood with a moderate effort.

Let us begin by reminding ourselves about the energy dependence of the cross section for neutron-induced reactions. In Figure 13.1, we show the (n,f) cross section for ^{235}U and ^{238}U as a function of neutron energy. By examining Figure 13.1, one can see that the highest cross section for fission of ^{235}U occurs at very low energies, so-called thermal energies where $E_n < 1$ eV. Thermal neutrons are neutrons that have come into thermal equilibrium with the environment. As discussed in Chapter 10, the cross section varies approximately as $1/v$ for the lowest neutron energies.

Two other important features of Figure 13.1 deserve further comment. The first of these features is the large difference between the excitation functions for
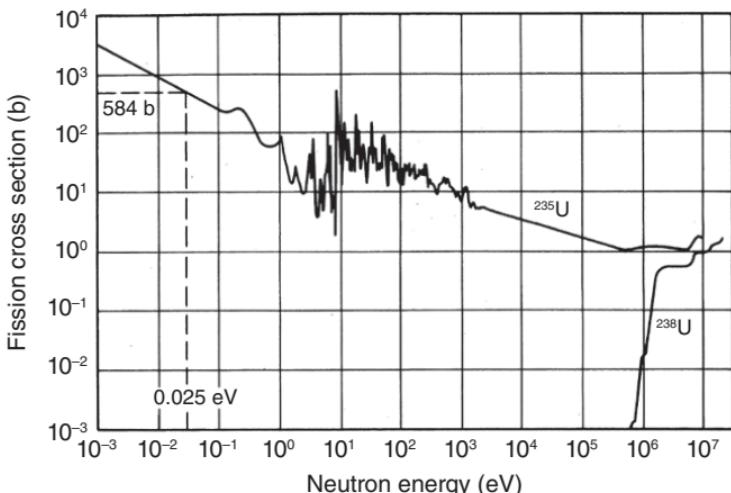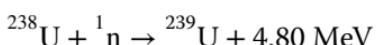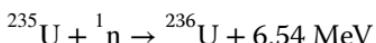
Figure 13.1 Neutron-induced fission cross section for ^{235}U and ^{238}U as function of the neutron energy, E_n (Hughes and Schwartz (1958). Reproduced with the permission of Brookhaven National Laboratory Report).

(n, f) reactions with ^{235}U and ^{238}U. We can understand this difference by noting the Q values for neutron capture by these nuclides:

$$^{235}U + {}^1n \rightarrow {}^{236}U + 6.54 \text{ MeV}$$
$$^{238}U + {}^1n \rightarrow {}^{239}U + 4.80 \text{ MeV}$$

Note the Q value for the $n + {}^{235}$U reaction is 1.7 MeV larger than that for the other reaction. The reaction with the lighter isotope converts an even–odd nucleus into an even–even nucleus, while the other reaction converts an even–even nucleus into an even–odd product. Thus, we would then expect the Q values for these reactions to roughly differ by twice the neutron pairing energy. Since the fission barriers for ^{235}U and ^{238}U are about the same ($B_f \sim 6.2$ MeV), capture of neutrons with any kinetic energy can cause ^{235}U to fission, while it takes ~1.4 MeV neutrons to cause ^{238}U to fission. The "thermally fissionable" nuclei are thus all even–odd nuclei where the energy release in neutron capture is greater than the fission barrier. The most important of these nuclei from a practical point of view are the "big three," ^{233}U, ^{235}U, and ^{239}Pu, one that is available and the other two readily produced.

The other feature of Figure 13.1 worthy of comment is the variation of the cross sections in the different regions of neutron energy. Neutrons with energies <1 eV exhibit the $1/v$ behavior, and this region is referred to as the "thermal" region. Epithermal neutrons have energies from 1 to 100 eV, and their reactions are characterized by large resonances in the cross section caused by neutron capture into specific states in the compound nucleus. In the neutron

energy region from ~ 100 eV to 1 MeV, the energy levels of the excited states in the compound nucleus overlap, and there are no discrete (or separate) resonances. Neutrons with energies > 1 MeV are generally referred to as "fast" neutrons, and they can even cause ^{238}U to fission.

As discussed in Chapter 10, there are other reaction mechanisms besides fission when neutrons interact with heavy nuclei that include:

(a) elastic scattering where $Q = 0$ and kinetic energy is conserved. However, the target nucleus recoils in these events, and the elastically scattered neutron loses some kinetic energy. (For a collision of a neutron of energy E with a nucleus containing A nucleons, the neutron kinetic energy after the collision will be $\frac{A^2+1}{(A+1)^2}E$. Note that the maximum neutron energy loss occurs when $A = 1$ and the neutron energy is halved in each collision.)

(b) inelastic scattering where the neutron gives up some of its kinetic energy in addition to the recoil energy, leaving the struck nucleus in an excited state. The threshold energy for this process in the center-of-mass system will be the energy of the first excited state of the struck nucleus. For ^{235}U and ^{238}U, these energies are 14 and 44 keV, respectively.

(c) radiative capture, that is, the (n, γ) reaction in which part of the energy released by the capture of the neutron is carried away by the emitted photon.

The total cross section, σ_{total}, is the sum of the cross sections for these processes, that is,

$$\sigma_{total} = \sigma_{elas} + \sigma_{inel} + \sigma_{n,\gamma} + \sigma_{f} \tag{13.1}$$

The distance neutrons travel between interactions in a medium, called the mean free path λ, is given as

$$\lambda = \frac{1}{\sigma_{total}\rho} \tag{13.2}$$

where ρ is the number density of nuclei. For uranium, $\rho = 4.8 \times 10^{28}/\text{m}^3$, and if we assume $\sigma_{total} = 7$ barns, then $\lambda = 0.03$ m. If the average neutron energy is 2 MeV, then the time between interactions will be $\sim 10^{-8}$ s. The mean free path places a constraint on the size of a self-sustaining assembly of fissionable material.

Sample Problem 13.2: Neutron Wavelengths

What is the velocity and de Broglie wavelength of a thermal neutron?

Solution

The Maxwell–Boltzmann velocity distribution for the random motion of a thermally equilibrated neutron gas is

$$n(v) = 4\pi v^2 \left[\frac{m}{2\pi k_B T}\right]^{3/2} e^{-mv^2/2k_B T}$$

where we have normalized the function so that $\int_0^\infty n(v)dv = 1$. The most probable velocity can be found from the derivative as

$$v_{\text{MP}} = \left(\frac{2k_B T}{m}\right)^{1/2}$$

If $T = 20°C$, then

$$v_{\text{MP}} = \left(\frac{2(1.38 \times 10^{-23} \text{ J/K})293\text{K}}{1.675 \times 10^{-27} \text{ kg}}\right)^{1/2}$$

$$v_{\text{MP}} = 2200 \text{ m/s}$$

This velocity, 2200 m/s, is taken as the characteristic velocity of thermal neutrons, and the cross section for neutrons at a velocity of 2200 m/s ($E_n = 1/2mv^2 = 0.0253$ eV) is referred to as the "thermal" cross section. The wavelength at this velocity is

$$\lambda_{\text{deBroglie}} = \frac{h}{p} = \frac{6.626 \times 10^{-34} \text{ J/s}}{(1.675 \times 10^{-27} \text{ kg})(2200 \text{ m/s})}$$

$$\lambda_{\text{deBroglie}} = 1.80 \times 10^{-10} \text{ m}$$

Notice that the de Broglie wavelength of thermal neutrons is much larger than the size of a typical nucleus ($r \sim 1$ to 10×10^{-15} m) and similar to the size of a typical atom. Reaction cross sections for thermal neutrons generally exceed the geometrical area of the nucleus.

13.2.2 Neutron-Induced Fission

Let us review some aspects of fission discussed in Chapter 11. Consider the case of the thermal neutron-induced fission of ^{235}U, that is,

$$\,^{1}_{0}\text{n} + \,^{235}_{92}\text{U} \rightarrow (\,^{236}_{92}\text{U})^* \rightarrow \,^{A}_{Z}X + \,^{236-A}_{92-Z}Y \tag{13.3}$$

The two fission fragments X and Y will have a total kinetic energy of ~168 MeV due to their mutual Coulomb repulsion at scission with the lighter fragment carrying away the larger energy. The most probable mass split is asymmetric with $A_{\text{heavy}}/A_{\text{light}} \sim 1.3$–1.4. Following scission, the deformed fragments will contract to a more spherical shape, heating up in the process. The fragments will get rid of this excess energy by the emission of neutrons, emitting ~2.5 neutrons per fission event. These neutrons have a "Watt" spectrum with a broad peak centered below 1 MeV with an energy distribution of the form

$$N(E) = 0.453e^{-1.036E} \sinh(\sqrt{2.29E}) \tag{13.4}$$

The total energy carried away by these neutrons is ~5 MeV. In competition with the last stages of neutron emission and when the excitation energies of the fission fragments are less than the neutron binding energy, the fragments will de-excite by γ-ray emission (so-called "prompt" γ-rays) with the energy carried

away by these γ-rays being ~8 MeV. Following prompt γ-ray emission, one will be left with neutron-rich fragments that will decay by β- and γ-ray emission toward stability. Approximately 8 and 7 MeV will be emitted in the form of β- particles and γ-rays, respectively. Approximately 12 MeV will appear in the form of electron antineutrinos emitted during the β- decay, but these neutrinos will escape any practical reactor assembly. During this β- and γ-decay, the residual nucleus following a small number of β- decays will be excited to an energy greater than the neutron binding energy. Such nuclei can decay by emission of neutrons (so-called beta-delayed neutrons) on a time scale of seconds to minutes rather than the time scale of prompt neutron emission ($\sim 10^{-15}$ s). While the energy carried away by these delayed neutrons is insignificant in the fission energy balance, these neutrons are very important for controlling the chain reaction in reactors.

For the thermal neutron-induced fission of ^{235}U, the total recoverable energy release is ~195 MeV/fission, and it is ~202 MeV/fission for ^{239}Pu. These energy releases can be transformed into nonnuclear units by noting that 200 MeV = 3.2×10^{-11} J. One gram of ^{235}U contains about 3×10^{21} atoms, corresponding to an energy release of $\sim(3.2 \times 10^{-11})(3 \times 10^{21}) = 1$ MW/day. (For reference the burning of 1 ton (10^6 g) of coal releases about 0.36 MW-day, so that 1 g of pure ^{235}U has an energy content of about 3×10^6 more energy than 1 g of coal.)

13.2.3 Neutron Inventory

A reactor designer must pay special attention to the inventory of neutrons in the reactor. Each fission event in the thermal neutron-induced fission of ^{235}U produces ~2.5 fast neutrons. From the data shown in Figure 13.1, we can imagine that the energy of these neutrons could be reduced to thermal energies to induce further fissions. Thus, we could imagine placing lumps of the uranium fuel in a moderator to slow down the fission neutrons to thermal energies. Previously we have demonstrated that neutrons are most effectively slowed by elastic collisions with the lightest nuclei. In addition, the ideal moderator will contain light nuclei whose neutron capture cross sections are low. Graphite is an appropriate solid material as is beryllium or liquid deuterated water (^{2}H$_2$O). The hydrogen in ordinary water (^{1}H$_2$O) has an (n, γ) cross section of 0.33 b for thermal neutrons, making it unsuitable as a moderator unless the fuel is enriched in ^{235}U. The number of collisions necessary to thermalize the fast neutrons from fission is 14.5 for ^{1}H, 92 for ^{12}C, and 1730 for ^{235}U.

Some of the fast neutrons produced in fission will be "moderated" to thermal energies and will induce other fission reactions, while others will be "lost." The ratio of the number of neutrons in the next generation to that in the previous generation is called the multiplication factor, *k*. If the value of *k* < 1 than one then the reactor is *subcritical* and the fission process is not self-sustaining.

If the value of $k > 1$ than one then the number of fissions will accelerate with time and the reactor is *supercritical*. The goal of reactor operation is to maintain the system in the critical state with $k = 1$. The extreme upper limit for the multiplication factor would correspond to the mean number of neutrons per fission in the case where each neutron produces a secondary fission. This scenario is impossible to attain, and, in fact, the neutron inventory must be carefully monitored in order to maintain a critical reactor.

Given that the number of neutrons emitted per fission event $\nu = 2.5$ for the fission of ^{235}U, one would think that designing a system with $k = 1$ would be easy; however there are many ways in which neutrons can be lost. First of all, the core of the reactor that contains the fuel must be finite. Therefore, there will be a limit or surface of the core from which some neutrons can escape. The escaped neutrons can be "reflected" back into the core by a layer of material such as graphite (low absorption cross section and higher mass) surrounding the core, but the reflection is not complete.

A second unavoidable source of neutron loss occurs in the fuel itself. Consider for the moment a hypothetical reactor core made of uranium metal. There are two unavoidable absorption reactions with uranium nuclei, ^{235}U(n,γ)^{236}U, $\sigma_{th} = 98.3$ b and ^{238}U(n,γ)^{239}U, $\sigma_{th} = 2.7$ b, that compete with the ^{235}U(n, f), $\sigma_{th} = 583$ b reaction. As an aside, one should remember that these cross sections for radiative capture and fission, like all nuclear reactions, are energy dependent. For the present discussion we will concentrate on thermal energy ($E_n = 0.0253$ eV) cross sections. Let us define a parameter η as the average number of fission neutrons per thermal neutron absorbed in the fuel. For a pure ^{235}U sample,

$$\frac{\eta}{\nu} = \frac{\sigma_f}{\sigma_a} = \frac{1}{1 + \alpha} \tag{13.5}$$

where $\alpha = \sigma_\gamma/\sigma_f$ and $\sigma_a = \sigma_\gamma + \sigma_f$. For a material like uranium metal that contains both ^{235}U and ^{238}U,

$$\frac{\eta}{\nu} = \frac{x\sigma_f(235)}{x\sigma_a(235) + (1 - x)\sigma_a(238)} \tag{13.6}$$

where x is the atomic fraction (mole fraction) of ^{235}U. For ^{235}U in natural uranium, $\eta = 1.3$. If the ^{235}U content of the fuel is greater than the natural abundance, η will be larger.

The multiplication factor for an infinite-sized reactor core is given by the so-called *four-factor formula*:

$$K = \eta f p \epsilon \tag{13.7}$$

where p is the fraction of fission neutrons that are thermalized (without being captured), f is the fraction of thermal neutrons that are captured in the fuel,

and ϵ is the so-called fast fission enhancement factor that expresses the fact that some fission events are due to fast neutrons. (For a typical thermal reactor, $\eta = 1.65$, $p = 0.87$, $f = 0.71$, and $\epsilon = 1.02$. Because of a leakage of ~4% of neutrons in a finite reactor, $k = 1.00$.)

For safe operation of the reactor, k must be exactly unity. That is difficult to achieve in practice. In fact, if the mean time between generations of neutrons is τ, the multiplication factor is k, and N is the number of neutrons at time t, then there will be kN neutrons at $t + \tau$, $k^2 N$ neutrons at $t + 2\tau$, etc. This relation can be expressed as

$$dN = (kN - N)\frac{d\tau}{\tau} \tag{13.8}$$

or

$$N(t) = N_0\, e^{(k-1)\tau/t} \tag{13.9}$$

Suppose in one case $k = 1.01$ and $\tau = 10^{-3}$s; then $N(1\text{ s}) = 22,000 \times N_0$, a dangerous rate of change. The neutron inventory in a reactor is regulated by inserting **control rods** that contain a neutron-absorbing material such as cadmium or boron in the fissioning assembly. But mechanical regulation of a large system cannot take place on the millisecond time scale. Fortunately, about 0.65% of the fission neutrons are "delayed neutrons" emitted on a time scale of seconds to minutes, mentioned earlier. The resulting average time constant for the "prompt + delayed" neutrons τ is ~0.1 s, instead of 10^{-3} s, which allows control of the reactor.

As mentioned earlier, reactor control is achieved using control rods containing ^{113}Cd ($\sigma_{n,\gamma} = 20,000$ barns) or ^{10}B ($\sigma_{n,\gamma} = 3800$ barns). Another important aspect of reactor control is the fact that certain **fission products** have very high neutron capture cross sections and thus depress the neutron inventory. Foremost among these nuclei, known as *poisons*, are ^{135}Xe ($\sigma_{n,\gamma} = 2.65 \times 10^6$ barns) and ^{149}Sm ($\sigma_{n,\gamma} = 4.1 \times 10^4$ barns). These nuclei lower both the values of f and k. In an ordinary reactor, the amount of these fission product nuclei is regulated by their decay and their destruction by neutron capture although their presence does affect the neutron inventory.

13.2.4 Light Water Reactors

A large number of light water-cooled nuclear reactors have been constructed around the world. All of the reactors rely on the thermal fission of enriched uranium and on normal or "light" water for neutron moderation and heat transfer. These machines fall into two major categories of research reactors and power reactors. We have described the principles that underlie the construction and operation of these machines, but the implementation is different. All nuclear reactors can be categorized by the thermal generating power of the core, usually given in megawatts. Power reactors are also categorized by the electrical

generating power of the plant in giga- or megawatts. Note that ratio of the electrical power to the thermal power of a power plant is the efficiency of the conversion process (a number always < 1; see following text).

Generally speaking, the research reactors are small, on the order of 1 MW of thermal power, and are optimized to provide intense neutron fluxes for the irradiation of samples. These reactors are usually fueled with a few kilograms of enriched uranium (20–90% ^{235}U) in fuel rods that are clad with a zirconium alloy or with aluminum. The entire core assembly of a 1 MW research reactor is on the order of 1 m^3 and can produce an internal neutron flux on the order of 10^{13}/cm^2/s. The two largest research reactors reach internal fluxes of 1×10^{15}/cm^2/s (ILL, Grenoble, France) and 3×10^{15}/cm^2/s (HFIR, Oak Ridge, TN). The small reactors are usually submerged in a pool of water and are cooled by convection. The water layer is designed to be deep enough to provide sufficient radiation shielding so that a person can look through the water and observe the operating reactor. The heat generated by the core of a research reactor is dissipated in the large pool of water.

Nuclear power reactors are generally much larger, on the order of 2 GW of thermal power, and are designed to produce electricity by the adiabatic expansion of steam in a turbine. There are two competing designs in Western countries for nuclear power reactors that differ in the primary coolant loop. In one case the water is allowed to boil (boiling water reactor (BWR)), and in the other design superheated water is held in the liquid phase under pressure (pressurized water reactor (PWR)) (cf. Fig. 13.2). We will briefly consider the two types of power reactors.

BWRs are characterized by having only two coolant loops. The water in the primary coolant loop circulates through the reactor core and boils at ∼ 1 atm pressure and is heated to ∼300°C. The steam is passed to a turbine system to generate electricity, is condensed, and is cycled back to the core. A second coolant loop is used to maintain a constant output temperature at the exit of the turbines; this loop removes the so-called waste heat at the end of the thermodynamic cycle. Such coolant loops are commonly included in machines that use adiabatic expansion to do work, for example, the radiators are connected to gasoline engines in cars. The waste heat loop in a nuclear power plant is usually an external open loop. The waste heat is released into in the atmosphere in large evaporative cooling towers, or released into rivers, lakes, or the ocean. The primary coolant is also the neutron moderator and is subject to intense irradiation in the core. It will contain radioactivities from impurities extracted from the walls, etc., and as a result the turbines will become contaminated. Thus, the important feature of the BWR design with the primary coolant circulating through the turbines necessitates placing them inside the containment shielding.

In the other design, PWRs have two closed loops of water circulating in the plant plus a third external loop to remove the waste heat. Water is pumped
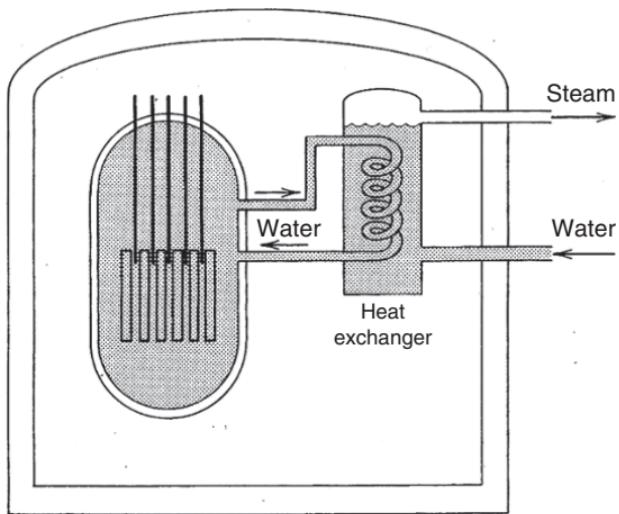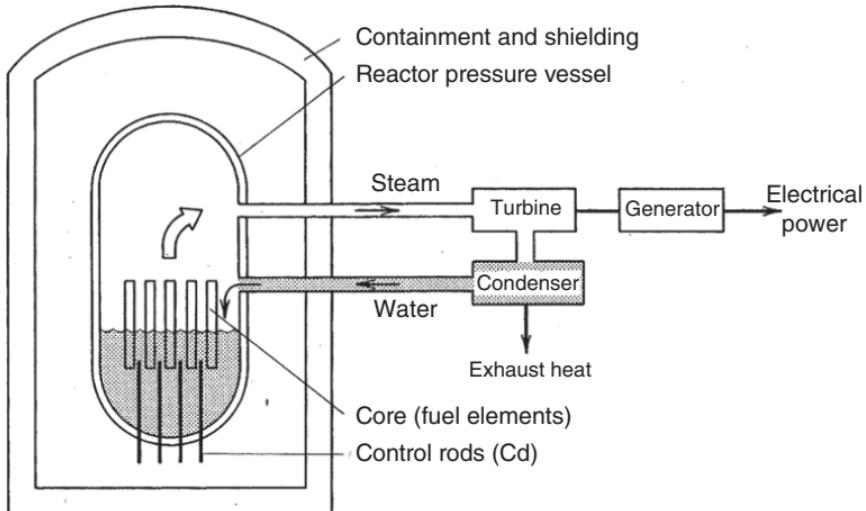
Figure 13.2 Schematic diagram of boiling water (top) and pressurized water reactors (bottom) (Krane (1988). Reproduced with the permission of Wiley).

through the reactor core in the primary coolant loop to moderate the neutrons and to remove the heat from the core as in the BWR. However, the reactor vessel is pressurized so that the water does not boil. Steam is necessary to run the turbines, so the primary loop transfers the heat to a secondary loop. The water in the secondary loop is allowed to boil, producing steam that is isolated from both the core and the outside. The water in the primary loop usually contains boron (as boric acid H_3BO_3 ~0.025 M) to control the reactivity of the reactor. The steam in the secondary loop is allowed to expand and cool through a set of turbines as in the BWR; the cold steam condenses and is returned to the

primary heat exchanger. A third loop of water is used to maintain the low temperature end of the expansion near room temperature and remove the "waste" heat.

The PWR is more expensive to build because the reactor vessel must be stronger to withstand the higher water pressure, and there is a secondary coolant loop with pumps. The BWR, while less expensive to build, is more complicated to service since the turbines are part of the primary coolant loop. The details of the core design are different as well. Approximately twice as many PWRs have been constructed as BWRs.

A limit on the efficiency of the electrical energy conduction can be obtained by applying the second law of thermodynamics to the secondary loop. The maximum thermal efficiency, ϵ_{th}, is given in terms of the input and output heats:

$$\epsilon_{th} = \frac{(q_{in} - q_{out})}{q_{in}} \tag{13.10}$$
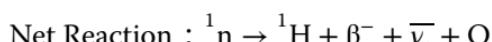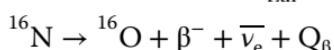
Note that the output heat is the waste heat. In the limit that the machine operates in a Carnot cycle that can be characterized by constant temperatures at the input and output, then the maximum efficiency is given by the expression

$$\epsilon_{Carnot} = \frac{(T_{in} - T_{out})}{T_{in}} \tag{13.11}$$

The output temperature is given by the ambient temperature of the waste heat loop and can be taken to be 30°C for purposes of estimation. The input temperature of the steam is limited by physical constraints on the reactor primary cooland loop to be about 300°C. Therefore, the maximum Carnot efficiency is approximately $\epsilon_{Carnot} = (573\,K - 303\,K)/573\,K = 0.47$, whereas the actual efficiency is typically $\epsilon_{elec} = 0.35$ when measured as electrical power outside the plant to total thermal power in the core. For comparison, a coal-powered plant might have values of $\epsilon_{Carnot} = 0.65$, $\epsilon_{elec} = 0.5$ due to higher steam temperatures.

Sample Problem 13.3: Neutron Reactions in Water

One of the interesting side reactions that occurs in water-moderated nuclear reactors is the (n, p) reaction on ^{16}O, which occurs with a cross section of 0.017 mb. The ^{16}N product rapidly decays back to ^{16}O with a half-life of 7.13 s; thus, the net reaction can be called a catalysis of the neutron beta decay:

$$^{16}O + {}^{1}n \rightarrow {}^{16}N + {}^{1}H + Q_{rxn}$$
$$^{16}N \rightarrow {}^{16}O + \beta^- + \overline{\nu}_e + Q_\beta$$
Net Reaction : $^{1}n \rightarrow {}^{1}H + \beta^- + \overline{\nu}_e + Q$

Make an estimate of the equilibrium activity per liter of cooling water due to ^{16}N in a reactor that has an internal flux of 10^{13} neutrons/cm^2/s.

Solution

Recall that the equilibrium activity, also called the saturation activity, occurs when the rate of production is equal to the rate of decay and requires that the sample be irradiated for more than three half-lives, or $\sim$22 s for ^{16}N. Also, 1 mb is 1×10^{-27} cm^2; thus,

$$\text{Activity} = A = \text{rate of production} = N_0 \sigma \phi$$
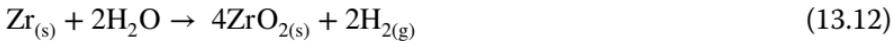
$$A = N_0 \left(10^{13} \frac{1}{\text{cm}^2\text{s}}\right) \left(0.017 \times 10^{-27} \text{cm}^2\right)$$

$$A = \left(\frac{1 \text{ kg}}{\text{L}} \frac{N_A \ 0.9976 \ ^{16}\text{O/mol water}}{0.010 \text{ kg / mol water}}\right) 0.017 \times 10^{-14}/\text{s}$$

$$A = (3.34 \times 10^{25}/\text{L}) \cdot 0.017 \times 10^{-14}/\text{s} = 5.68 \times 10^9 \text{ Bq/L}$$

At this point it is appropriate to mention the three most significant accidents that have occurred at nuclear power plants. In these cases the seriousness of the accidents was dramatically increased by human error. In these cases the difficulties were caused by chemical reactions and not by nuclear fission.

An accident occurred at the Three Mile Island PWR in Pennsylvania in 1979 in which the water stopped flowing due to a mechanical failure in the primary coolant loop. Subsequent actions by the operators caused the water level in the core to drop, uncovering the upper part of the fuel rods. The nuclear fission process rapidly ceased due to the loss of the water moderator, but the fuel continued to generate heat due to the decay of fission products from prior operation. This residual decay heat is a general feature of all nuclear reactors. Parts of fuel rods melted, which indicates that the local temperature reached 3000°C. As part of the accident, contaminated water from the primary coolant loop was released inside the containment building and soaked into the concrete. The noble gas fission products and a fraction of the iodine fission products were released into the environment. The difficulty of melted fuel notwithstanding, the extreme heating of the zirconium alloy that is used to clad the fuel opened the door to an exothermic chemical reaction with steam that produces hydrogen:

$$\text{Zr}_{(s)} + 2\text{H}_2\text{O} \rightarrow 4\text{ZrO}_{2(s)} + 2\text{H}_{2(g)} \tag{13.12}$$

An important concern during the accident was the potential chemical explosion of this hydrogen gas with the oxygen in the air inside the containment building. The cleanup process necessary inside the building continued for many years, and the perception that nuclear power is somehow very dangerous has not subsided after more than 40 years.

A much more serious accident occurred at the Chernobyl power station near Kiev in 1986 that was entirely the result of human error. This reactor relied on a large amount of graphite to moderate the neutrons with water-filled tubes to remove the heat and generate steam. This general reactor design that

also incorporates large amounts of uranium was used in the United States to produce plutonium during the cold war era but were not used for power generation. The accident in Chernobyl occurred when the operators manually removed the control rods from the reactor during a "test." The chain reaction accelerated due to the core design, and the system became very hot. The cooling water was suddenly vaporized and the core exploded. The nuclear fission stopped due to the loss of the moderator by explosion, but the graphite was ignited (since it was open to air) and continued to burn for some time, spewing radioactivity into the air. Approximately 10% of the graphite and large fractions of the radioactive fission products were volatilized, the fraction depending on their chemical nature, all of which was spread across western Europe by the wind. The burning facility was too dangerous to approach, and the fire was extinguished by dropping sand, clay, lead, and boron onto the fire from helicopters. What was left of the reactor was buried in concrete, and a massive cleanup was necessary. The inherent difficulties in the design of this reactor continue to exist in numerous other reactor facilities in the former Soviet Union.

In March 2011, there was a nuclear accident at the Fukushima nuclear power plant in Japan (near the Pacific sea coast). This facility consisted of six BWR reactors, three of which were operating (1-3) and three of which (4-6) were shutdown. The accident was triggered by a magnitude 7.4 earthquake followed by a 13 m tsunami that struck the plant 50 minutes after the earthquake. Immediately after the earthquake, reactors 1-3 shutdown, but had to use emergency diesel generators to run the reactor coolant systems. When the tsunami struck the plant, the emergency pumps failed and the reactor cores suffered a meltdown. Hydrogen-water chemical explosions occurred in reactors 1-4 a few days later. (Reactors 4-6 were shutdown at the time of the accident, but spent fuel was stored in reactor cooling ponds that required cooling water to be furnished continuously). 18,500 people died due to the earthquake/tsunami. No short-term deaths linked to radiation occurred at the power plant. There was extensive release of radioactive material due to the explosions and core meltdowns that are expected to result in 130–640 people dying prematurely in the future. The Fukushima radioactivity release was ~10-40% of the release in the Chernobyl accident. The power plant operator, TEPCO, estimated that 540 PBq of ^{131}I, ^{134}Cs, and ^{137}Cs were released into the atmosphere and the ocean with most of the release being 131I. Subsequent investigations of the accident fault the power company and the civil authorities for poor planning and preparedness and a poor response to the accident.

13.2.5 The Oklo Phenomenon

We should not leave our discussion of nuclear reactors without mentioning "the Oklo phenomenon." In 1972, French scientists analyzing uranium ore from the Oklo uranium mine in Gabon found ore that was depleted in ^{235}U. Further

investigation showed the presence of high abundances of certain Nd isotopes, which are formed as fission products. The relative isotopic abundances of these isotopes were very different from natural abundance patterns. The conclusion was that a natural uranium chain reaction had occurred ~1.8 billion years ago.

At that time, the isotopic abundance of ^{235}U would have been different than today, due to the differing half-lives of ^{235}U and ^{238}U. At $t = 1.9 \times 10^9$ years ago, the isotopic abundance of ^{235}U was ~3%, a number characteristic of the fuels of nuclear reactors. Water apparently entered the ore deposit, acted as a moderator, and initiated chain reactions. These chain reactions appear to have lasted for ~10^6 years, ebbing and flowing as the water boiled away and returned. The power level was ≤10 kW. Some attention has been paid to the fact that these fission product deposits remained stable for more than 10^9 years, possibly supporting the notion of geologic storage of nuclear waste.

13.3   Neutron Sources

Occasionally one may need to use a radionuclide neutron source. For example, in geological applications, one may need to have a portable neutron source. Radionuclide neutron sources are generally based on either the (α, n) reaction or spontaneous fission. Older (α, n) sources utilized the 5.3 MeV α-particles from 138 d ^{210}Po to react with beryllium, but modern sources utilize ^{238}Pu, ^{241}Am, or ^{242}Cm alloyed with beryllium. The α-particles emitted from these nuclei interact with ^{9}Be nuclei to produce neutrons via the (α, n) reaction. The resulting neutron spectrum is broad, usually ranging from a few MeV to >10 MeV. The yield of these sources and the accompanying γ-radiation is shown in Table 13.1. ^{252}Cf is probably the most important pure radionuclide neutron source because it can be produced in high-flux nuclear reactors and 3.2% of its decays are by spontaneous fission, each yielding 3.76 neutrons per fission. The neutron emission rate/Ci of material is quite high, and ^{252}Cf sources have found widespread use.

13.4   Neutron Generators

Commercial neutron generators are compact charged-particle accelerators designed to produce a beam of neutrons by an appropriate nuclear reaction. The most commonly used nuclear reactions are

^{2}H(d, n) $Q = 3.25$ MeV

^{3}H(d, n) $Q = 17.6$ MeV

^{7}Li(p, n) $Q = -1.646$ MeV

^{9}Be(d, n) $Q = 3.79$ MeV
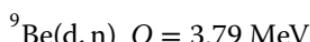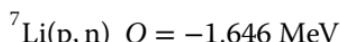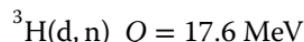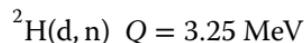
Table 13.1 Properties of Radionuclide Neutron Sources.

Radionuclide	Half-Life	Neutron Yield (n/Ci)	γ Radiation (mR/h at 1 m/Ci)
^{210}Po/Be	138 days	2.5×10^6	–
^{238}Pu/Be	87.8 years	2.2×10^6	<1
^{241}Am/Be	433 years	2.2×10^6	<2.5
^{242}Cm/Be	163 days	2.5×10^6	2.5
^{252}Cf	2.65 years	4.3×10^9	300

The most common sources are based on the ^{3}H(d, n) reaction. Deuterons are accelerated to ~150 keV with currents ~2.5 mA and strike a tritium target. The small accelerators produce $\sim 2 \times 10^{11}$ 14 MeV neutrons/s under these conditions. The neutrons produced are widely used in fast neutron activation analysis for the determination of light elements. The tritium targets are typically metals like Ti, which have been loaded with titanium tritide. The accelerators are usually small Cockcroft–Walton machines or small sealed-tube devices where the ion source and accelerator structure are combined to produce a less expensive device with neutron yields $\sim 10^8$/s.

The ^{7}Li(p,n) reaction is used commonly to produce approximately monoenergetic fast neutrons. The protons are accelerated to an energy of a few MeV by a small Van de Graaff accelerator and strike a cooled rotating lithium target. Thick-target neutron yields are $>10^9$ n/s/μA. The energy of the neutrons can be obtained from the *Q*-value equation (see Chapter 10), which can be expressed (for 0° neutrons) as

$$8T_n - 6T_p - 2(T_n T_p)^{1/2} = -11.522 \tag{13.13}$$

where T_n and T_p are the kinetic energies of the neutron and proton in MeV.

The ultimate in accelerator-based neutron sources is the spallation neutron sources. Neutrons are generated by the spallation reaction that occurs when high-energy (~1 GeV) protons interact with heavy nuclei, like mercury, releasing 20–30 neutrons/reacting proton. The proton beams (and the resulting neutrons) are pulsed, allowing the use of time-of-flight techniques to measure the energies of the neutrons. Expressed as a thermal neutron flux, yields of 10^{17} n/cm^2/s are possible, exceeding the neutron yields of reactors by orders of magnitude. These high intensity neutron fluxes can be used for neutron scattering experiments in materials science and biology.

13.5 Accelerators

As we have already indicated, positively charged particles must be accelerated to kinetic energies on the order of millions of electron volts (MeV) in order to

overcome the Coulomb repulsion of another nucleus and induce a nuclear reaction. The Coulomb potential grows with the inverse of the radial separation, r, between the two nuclei:

$$V_C = Z_1 Z_2 e^2 / r \qquad (13.14)$$

The Coulomb barrier is defined as the value of this potential energy for the two bare nuclei at a separation that corresponds to the sum of their radii. Recall that the nuclei are extremely small compared to atomic dimensions and the electrons do not screen the nuclear charges except in extremely low-energy collisions. The kinetic energy necessary for a moving projectile with mass number A_1 to react with a stationary target with mass number A_2 is

$$\text{KE}_{\text{threshold}} = V_C (A_1 + A_2) / A_2 \qquad (13.15)$$

Note that the actual threshold is larger than the Coulomb barrier to accommodate the recoil due to conservation of momentum.

High kinetic energies can be obtained by producing an ion with charge q on a high-voltage platform held at a static potential E and simply allowing the ion to move (fall) toward ground potential. The kinetic energy gain will be equal to the loss of potential energy; thus, $\text{KE} = qE$. The earliest accelerators were exactly of this type, but physical breakdown of the insulating materials surrounding the platform limits the maximum electrostatic potential. Modern accelerators use electrode structures with alternating electric fields to accelerate charged ions. We will consider the general features of accelerators for heavy charged particles. (The acceleration of electrons is a special case due to the relative ease of production, the very large charge-to-mass (m/q) ratio, and that fact that energetic electrons are relativistic and travel with essentially the same velocity, $v \approx c$.) We will start with consideration of ion sources and then consider the various machines for accelerating charged particles roughly in order of increasing final energy.

13.5.1 Ion Sources

All accelerators operate by the manipulation of charged ions in vacuum. Such particles do not exist naturally and must be produced in ion sources. Positive ions of all chemical elements can be produced, in principle, by electron-impact ionization of atoms already in the vapor phase. The difficulty of producing an ion depends dramatically on the chemical species. A few elements have an exothermic electron affinity and can be produced as singly charged negative ions. As a result only a few accelerators utilize negative heavy ions. Here we will consider three classes of ion sources that are used to produce positively charged ions.

The simplest ion sources create positive ions by bombardment of the residual gas inside a vacuum chamber by electrons emitted from a hot filament (cf. Fig. 13.3). The electrons can be accelerated to a few hundred volts, and the
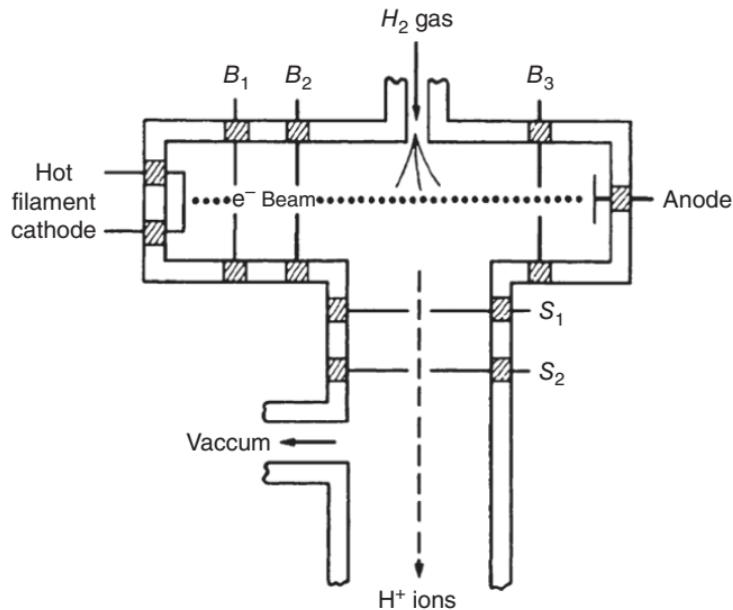
Figure 13.3 Schematic diagram of a hot filament ion source (Choppin et al. (2002). Reproduced with the permission of Elsevier).

electron impact on atoms and small molecules can easily create singly charged positive ions. Filament ion sources work well for producing hydrogen and helium ion beams and low charge states of other gaseous elements that can be bled into the ionization region. These sources can have long lifetimes as the electrodes are not directly damaged by the ionization process and the ions are produced from the feed material.

The energy of the electron beam can be increased in ion sources that are based on the features of a Penning ion gauge (PIG), a vacuum gauge that was developed to measure low pressures. A high-voltage electron arc is created between two electrodes and is confined by an external magnetic field. The arc vaporizes the electrode material and ionizes any residual gas in its path. A PIG source can produce electrons on the order of a few thousand volts and can remove substantial fractions of the electrons from the top-row elements. These sources have erratic and relatively short lifetimes (10 h or less). The electrodes are worn out as they are vaporized by the arc, which also tends to produce metal coating on insulators, leading to short circuits.

Very highly charged ions are produced by modern ion sources that rely on magnetically confined plasmas such as the electron cyclotron resonance ion source (ECRIS or ECR) and the electron beam ion source (EBIS). An ECRIS uses the superposition of axially symmetric magnetic fields with an electric field from end cap electrodes to trap electrons in a magnetic bottle. The electrons are forced to oscillate with radiofrequency radiation that corresponds

to the oscillation frequency in the magnetic field (see the following discussion about cyclotrons). The electrons remain in the plasma for a long time and collide with the residual gas, creating positive ions and more electrons. The positive ions drift toward the extraction electrode and do not absorb the rf power that is tuned to the m/q ratio of the electron. Under optimal conditions, the plasma in an ECRIS can remove even the inner most electrons from second-row elements.

An EBIS ion source relies on passing an extremely intense electron beam (hundreds of amps) at high potential (tens of kilovolts) through a vacuum chamber to ionize the residual gas. The vacuum chamber is surrounded by a coaxial solenoidal magnetic field that compresses the electron beam to a radius of a few microns that produces an extremely intense current density. EBIS ion sources can produce bare nuclei, depending on electron beam kinetic energy, for further acceleration.

All of these ion sources emit beams of positive ions at very low velocities; the ions drift or are pulled out from the ionization region with relatively small electrostatic potentials ($U \sim 20$ kV). These beams of charged particles can be focused and transported in vacuum to the main accelerating machines.

13.5.2 Electrostatic Machines

An ion source that is held at a large and stable positive electrostatic potential, V, will accelerate positive ions to a kinetic energy of $KE = qV$. The maximum potential is limited by the ability to sustain the high voltage without breaking down the intervening dielectric material (sparking). The formula for the electric field E at the surface of a sphere with a radius, r, carrying a total charge, Q, surrounded by a medium with a dielectric constant, ϵ, is $E = Q/\epsilon r^2$, which leads to several common features of electrostatic accelerators. The high-voltage terminal should be as large a sphere as possible without any sharp points (the ends of sharp points have very small radii), and the terminal should be surrounded by a material with a large dielectric constant. A large carefully prepared terminal can be held at a maximum voltage of $\approx + 750$ kV in dry air. The kinetic energies of ions from such systems are (only) sufficient to induce nuclear reactions among the lightest elements and are often used to generate neutrons via the $d + t \rightarrow \alpha + n$ reaction.

The breakdown voltages of various gases were studied as a function of pressure in the 19th century by Paschen, and he showed, not surprisingly, that pure gases have higher breakdown potentials than air and that the breakdown potential increases with gas pressure. Thus, higher electrostatic potentials can be maintained by insulating the platform with an inert gas such as N_2 or SF_6 at high pressure. An important distinguishing feature of electrostatic accelerators is that the beam is emitted "continuously" from the ion source and is literally a "DC" beam of particles. This feature can be good or bad depending on the
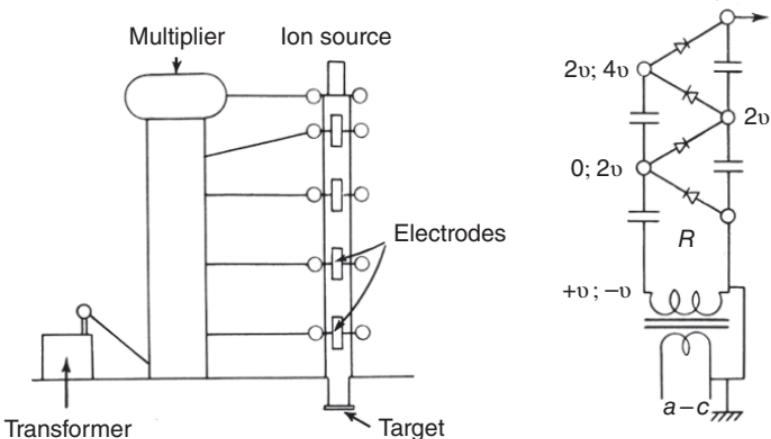
Figure 13.4 A schematic diagram of a Cockcroft–Walton accelerator system on the left and the electronic circuit used to provide the high voltage (Segre (1977). Reproduced with the permission of International Atomic Energy Agency).

application, but a DC beam can be chopped, switched, or bunched to produce an alternating current (AC) beam.

An important principle for production of high voltages is that the leakage current should be as small as possible, microamps or less, so that the dissipated power remains low: $1\ \mathrm{MV} \times 1\ \mu\mathrm{A} = 1\ \mathrm{W}$. The techniques developed for the production of the very high voltages necessary for electrostatic accelerators fall into two categories: direct and mechanical production. Direct production relies on electronic circuits, whereas mechanical production relies on the mechanical transportation of charge to the platform. A schematic drawing of the voltage multiplication circuit for the direct production of very high voltages developed by Cockcroft and Walton is shown in Figure 13.4.

An AC is applied to the transformer at the bottom of the Cockcroft–Walton circuit, which is rectified and multiplied by the stack to produce the high voltage. The resulting voltage depends on the number of elements in the stack and on the input voltage. The high voltage is not precisely constant in that it has a small variation or ripple in proportion to the input frequency. The Cockcroft–Walton design continues to be used in small machines to generate neutrons via the d + t reaction and to provide the bias voltages for ion sources used at large accelerator complexes.

An important feature of all electrostatic machines is that the beam is accelerated down to ground potential by a series of electrodes at intermediate potentials. The electrodes can be shaped to provide a weak focusing effect that causes the beam particles to move toward the center of the tube. The focusing is due to the cylindrically symmetric shape of the electric field combined with the fact that the particle spends more time in the focusing region (first half of the gap
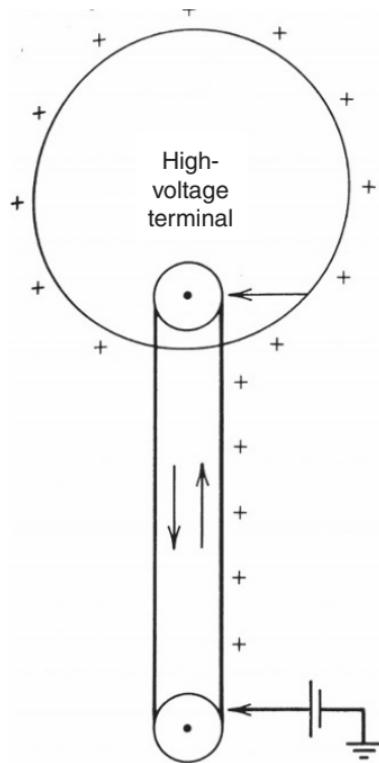
where the field lines move toward the center) than in the defocusing region (second half of the gap) due to acceleration. Note that the Cockcroft–Walton circuit automatically provides these potentials at the intermediate stages in the stacked circuit as shown in Figure 13.4.

Mechanical production of high voltages for ion acceleration is the basis of the class of larger machines called Van de Graaff accelerators. These machines rely on the principle from electrostatics that if a charge is placed *inside* a hollow conducting sphere, then the charge will migrate to the outer surface regardless of the amount of charge already on the sphere. Thus, a Van de Graaff uses the mechanical transportation of positive charges on an insulting belt from ground potential up to a contact on the inside of a large hollow electrode as indicated in Figure 13.5.

The mechanical generation of a few thousand volts is relatively easy, and many, many variations have been developed. You may be familiar with classroom demonstrations that use a small Van de Graaff machine to charge up a metal sphere (radius $\sim$ 10 cm) that can make a person's hair stand on end. Large-scale generators that can produce moderately high potentials, a few MV, have been constructed on a large scale and have been used in spectacular displays of artificial lighting. The electrostatic potential can be written in terms of the capacitance with respect to ground of the terminal, $V = Q/C$, and is limited by the designed breakdown at intermediate points along the insulating support column that provide fixed potentials for focusing or by leakage in the surrounding gas. In practice, the system reaches an equilibrium in which the added charge just compensates for the charge leaking down the column from the terminal. Rapid discharges or sparks need to be avoided because they can damage the components by vaporization of the metal. An important feature of Van de Graaff high-voltage generators is that the terminal voltage can be extremely stable and ripple-free.

To be used as an accelerator, an ion source for positive ions must be mounted inside the high-voltage terminal, and an insulating vacuum tube is needed to allow the ions to be accelerated to ground potential. The positive ions will be accelerated toward ground potential as in the Cockcroft–Walton machines. The terminal, accelerating column, and charging system are usually placed inside a pressurized chamber that is filled with an insulating gas such as pure N_2 or SF_6 at several atmospheres. Constraints on the size and operating power of the ion source inside the terminal generally limit the charge on the ions to be 1+ or 2+ and thus directly limit the energy of the accelerated beam. Even though technically challenging, many so-called single-ended Van de Graaff accelerators were produced in the 1960s and early 1970s and used for detailed studies of low-energy nuclear reactions. Note that the beam itself provides a drain on the terminal voltage and its intensity is therefore limited to be on the order of micro-amperes or less. A number of advances in the technology of the construction of the belt system, the vacuum tube, and electrode structure

Figure 13.5 A highly schematic view of the important components in a Van de Graaff accelerator. Positive ions created by a corona discharge near ground potential are swept upward by a moving belt to a similar corona contact attached to the inside of the high-voltage terminal. The positive ions then evenly distribute themselves on the surface of the terminal (Krane (1988). Reproduced with the permission of John Wiley & Sons).

have been made so that a modern accelerator terminal can routinely sustain 25 MV. For example, the high-voltage generator for the tandem accelerator at Oak Ridge National Laboratory is located inside a 100 ft high, 33 ft diameter pressure vessel that is filled with SF_6 at a pressure of ~75 psig ($P_{total} \sim 6$ atm).

An important improvement of the single-ended Van de Graaff accelerators came through the replacement of the positive ion source inside the high-voltage terminal with an external negative ion source (Fig. 13.6). Negative ions are accelerated toward the high potential in one vacuum column and then strike a very thin foil or a thin layer of gas placed at the center of the terminal. Electrons are readily stripped from the energetic negative ions, and the positive ions are then accelerated away from the high-voltage terminal in a second accelerating column. The final kinetic energy of the ions is the combination of the initial acceleration of the negative ion plus the final acceleration of the (multiply charged) positive ion. The charge state of the positive ion is usually much larger than unity and mostly defines the final beam energy. These devices are called tandem Van de Graaff accelerators, or simply *tandems*. Even though there are serious limits to the number of chemical elements that can be used to produce negative ions, the significantly higher-energy beams from tandems and the relocation of the ion source away from the terminal have generally outweighed the limitations. Tandem accelerators have been used extensively to
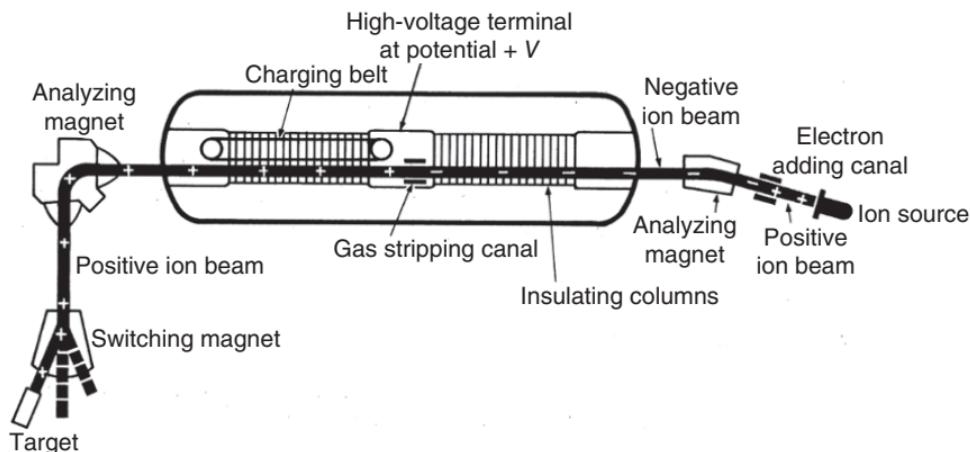
Figure 13.6 A schematic diagram of a two-stage tandem Van de Graaff accelerator (Van de Graaff (1960). Reproduced with the permission of Elsevier).

study low-energy nuclear reactions, particularly direct reactions induced by the lightest ions and fusion reactions induced by elements in the top row of the periodic table. The kinetic energy of the beam can be very precisely controlled and is very stable; however, the total energy is still limited by the terminal voltage. Attaining significantly higher kinetic energies requires a booster accelerator that uses alternating electric fields.
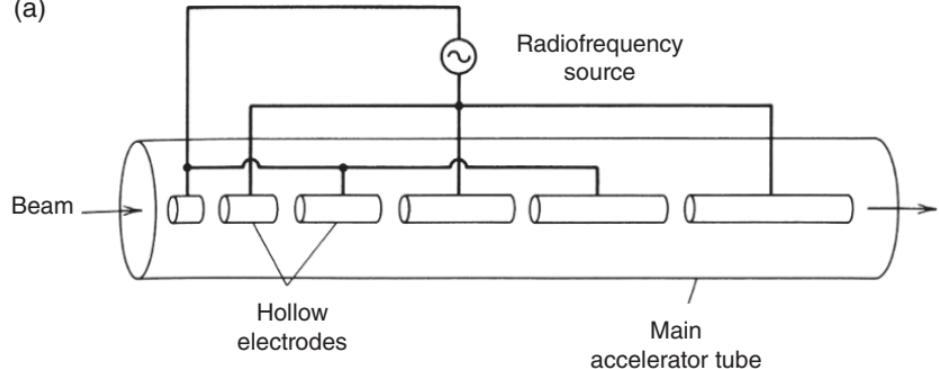
13.5.3 Linear Accelerators

The production of very-high-energy beams that are necessary for the production and study of new and exotic sub-nucleonic particles would require electrostatic acceleration from a high-voltage platform at potentials that are unattainable in a steady state. However, one can imagine that a group of particles can be accelerated in small steps along a series of electrodes if the potential on each electrode is synchronized with the motion of the particles (cf. Fig. 13.7).
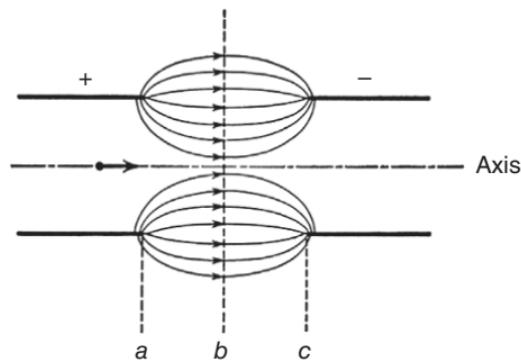
For example, positively charged particles are repelled by positive electrodes and attracted to negatively charged electrodes, gaining kinetic energy as they cross the gap between the two. From a simple standpoint each pair of electrodes acts like an instantaneous electrostatic terminal and ground. The particles will slowly gain energy as they synchronously cross each successive gap.

The synchronization of the arrival of the particles at the electrode gaps with an accelerating electric field can be accomplished with an alternating electric field on a hollow electrode having the polarity that will first attract a set of particles toward it and then later repel the same particles after they have passed through the electrode. The potential difference would follow a sine function:
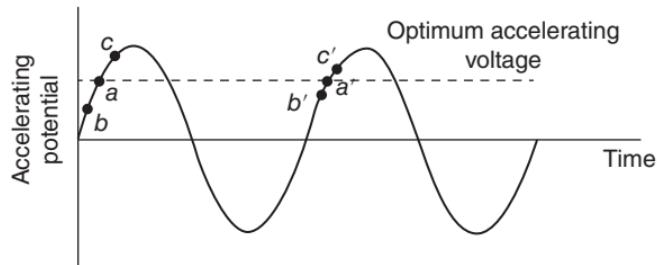
Figure 13.7 (a) Basic design of a linear accelerator. (b) Electric field in the gap between two drift tubes. (c) Phase stability in a linear accelerator. (Krane (1988). Reproduced with the permission of John Wiley & Sons).

$V = V_0 \sin(\omega t)$, where V_0 is the peak voltage and ω is the frequency. An important ingredient in such a simple linear accelerator is that the beam particles pass through the center of each collinear electrode tube. The beam will be accelerated across the gap between the electrodes by the electric field, but the beam will drift while in the field-free region inside the tubular electrodes (hence the electrodes are called drift tubes). The alternating power supply can change the polarity while the beam pulse is inside a drift tube. Notice that the amount of time that the pulse of beam particles spends inside the drift tubes must be held constant to provide a uniform acceleration. The particles should reach the next gap at a time $T = 2\pi/\omega$. Thus, the length of each drift tube must increase along

the path of the beam in proportion to the velocity, $L = v_i T/2$ where v_i is the velocity inside the ith drift tube. The physical dimensions of the drift tubes will have a finite acceptance range in velocity, and so linear accelerators, so-called *linacs*, have to be designed for specific velocity ranges. In practice, linacs are used as energy boosters that accept beams, usually from an electrostatic injector, started with significant initial velocities.

The phasing of the arrival of the particles with respect to the RF has two effects, one good and one bad. At first glance, one might think that the arrival of the particles should coincide with the maximum accelerating voltage. However, this point in time coincides with the top of the sine wave, and particles that arrive slightly earlier (faster particles) or slightly later (slower particles) will receive lower accelerations, and the bunch will spread out in velocity, arriving at the next electrode at different times. If the center of the pulse arrives at the electrode gap while the voltage is increasing somewhat linearly, then the faster particles will receive a lower acceleration than that applied to the average particles and the slower particles will receive a larger acceleration. These small differences in accelerations will tend to compress the velocity distribution of the beam pulse. This feature is called *phase stability* and is a good feature of linacs that works with nonrelativistic particles. Tuning the arrival of the beam pulse to coincide with the increasing portion of the accelerating field has the bad feature that the electric field across the gap sensed by a moving beam particle is asymmetric. A symmetric potential provides the weak focusing in the accelerating columns of electrostatic machines, mentioned earlier. When the potential is asymmetric, then the particle will not be focused toward the center of the drift tube. Phase stability is more important than the weak focusing effect, and linacs include additional components inside the drift tubes to focus the beam.

A classical linac (the Wideröe design) with fixed-length drift tubes connected to an external oscillator has a rather limited velocity acceptance and therefore would be used in specific applications. A much more flexible linac design (the Alvarez linac) relies on creating either a standing electromagnetic wave in a resonant cavity or a traveling wave in a waveguide. Most booster accelerators used to accelerate heavy ions (nuclides more massive than helium) utilize resonant cavities to provide the accelerating voltages. Various shapes have been used to create the accelerating gaps and the drift tube regions. Early designs used copper surfaces to define the distribution, but significant power was still dissipated in the walls. Recent designs have used superconducting niobium or lead surfaces that have a much lower dissipation. Recall that the velocity of all relativistic particles is essentially constant. Thus, accelerating structures for the highest-energy particles generally rely on standing wave cavities with constant drift tube lengths, $L = cT/2$. Electrons become relativistic at comparatively low energies (recall that $m_e = 0.511$ MeV), and so electron accelerators have simpler designs than heavy-ion accelerators.

The number of drift tubes in a linac has to be relatively large because the acceleration per gap is usually modest. A typical value of the effective accelerating electric field in a superconducting cavity is 1–2 MV/q/m of cavity. Booster accelerators for heavy-ion beams can be 50 m long, and the electron linac at Stanford (SLAC) is two miles long. Linacs have the obvious difficulty that the drift tubes have to increase in length as the velocity of the particle grows. For example, the drift tube length for a relativistic particle is inversely proportional to the AC frequency: $L = c(2\pi/2\omega) = c\pi/\omega$. A typical value for the frequency in such an electron accelerator is 300 MHz, so that $L \sim 3$ m. The accelerator has to lie in a straight line, and thus space, alignment, and construction costs are important concerns. Notice that a given pulse of particles will only pass through the accelerating structures one time. The beam from a linac will arrive in pulses that follow the time structure of the oscillations applied to the accelerating gaps. The frequency for heavy ions is usually in the tens of megahertz (radio wave region of the spectrum) so that the pulses are usually separated by tens of nanoseconds. The time structure on this scale is usually called the beam *microstructure*. From a practical standpoint, a beam with such a small time separation appears to be continuous. The beam from a linac with standing wave cavities is usually pulsed on the millisecond time scale to allow time to dissipate heat in the walls and reduce energy consumption. Such pulsing puts a *macrostructure* on the beam and has a large effect on experimental measurements because the particles do not arrive continuously at the target. The fraction of time that the macrostructure of a linac is "on" is called the duty factor. The operating principles of linear accelerators were established in 1930, but the compact design of cyclotrons that use a magnetic field to "reuse" the accelerating electrodes then overtook linac development for low-energy nuclear reactions.

13.5.4 Cyclotrons, Synchrotrons, and Rings

It is well known that when a charged particle moves through a magnetic field, it will experience the Lorentz force that acts perpendicular to the direction of motion. Thus, a moving charged particle can be made to move in a circular orbit by placing it in a suitably large and uniform magnetic field. Essentially all of the accelerators that have been developed to produce very-high-energy beams use a magnetic field to cause the particles to circle through accelerating structures. The first device to rely on a magnetic field was the *cyclotron*, invented in 1929 by E.O. Lawrence.

The original cyclotron had a pancake-shaped vacuum chamber that was placed between the north and south poles of an electromagnet. Figure 13.8 shows a schematic cyclotron with two large electrodes placed inside the vacuum chamber to provide one acceleration gap and two drift regions. Each electrode was a hollow cavity in the shape of the letter "D" and was fitted, back
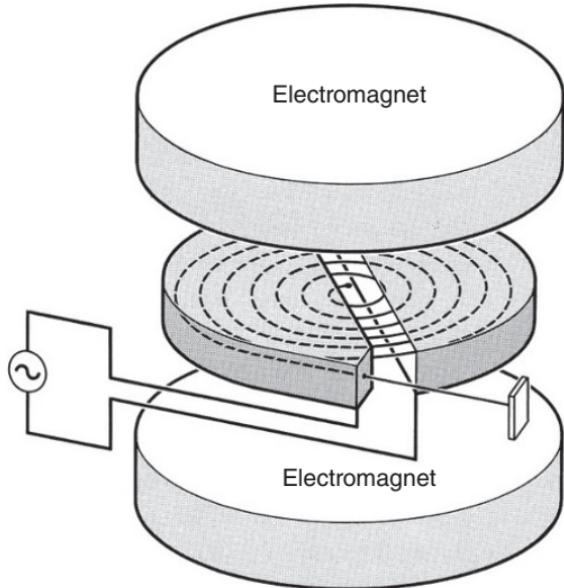
Figure 13.8 A schematic view of the components of a cyclotron. A pulse of beam particles starts in the center of the machine and is accelerated across the gap, circles through the drift space inside the D electrode, and is accelerated again when it returns to the gap. Eventually the beam reaches the edge of the machine and can be extracted along a tangent. (Krane (1988). Reproduced with the permission of Elsevier).

to back, inside the vacuum chamber with the acceleration gap between the straight sides of the two D's. The ions to be accelerated, in the first case H^{2+}, were created at the center of the circle and were accelerated across the gap and enter the drift space. Thus, the moving particles experience the Lorentz force, move on a circular path, and return to the accelerating gap! As the particles drift around, the phase of the accelerating voltage is switched to the opposite polarity as in a linac. When the particles arrive at the gap, they are accelerated again, gain energy, and move into the drift region.

For many years, filament and PIG ion sources were placed in the center of the cyclotrons to provide the ions. However, the development of more complicated and powerful ion sources such as the ECR sources required more space than was available at the center of the machines. Present-day cyclotrons generally have external ion sources, and a low-energy beam from an electrostatic injector is threaded into the center via an axial channel and inflector or via a radial channel in separated-sector machines (described in the following text).

The developers of the cyclotron recognized that the frequency of the circular motion of the particle is constant. Consider the Lorentz force acting on a moving charged particle, $F_{\text{Lorentz}} = B \times qv$, where B is the (vector) magnetic field, q is the charge, and v is the (vector) velocity. The cross product follows the "right-hand rule" so that the force is perpendicular to the motion. The radius of the motion, r, can be found by setting the Lorentz force equal to the mass times the centripetal acceleration:

$$F_{\text{Lorentz}} = Bqv = \frac{mv^2}{r} \tag{13.16}$$

solving for the radius:

$$r = \frac{mv}{Bq} \tag{13.17}$$

The time, t_{cyc}, that it will take a particle to complete one orbit is the circumference divided by the velocity:

$$t_{cyc} = \frac{2\pi r}{v} = \frac{2\pi mv}{Bqv} = \frac{2\pi m}{Bq} \tag{13.18}$$

and is independent of the velocity of the ion for a given value of the magnetic field. The constant time for a charged particle to orbit in a magnetic field is usually stated as a frequency called the *cyclotron resonance* frequency of that particle. As an aside, the circular or cyclotron motion forms the basis of present-day mass measurements in ion cyclotron resonance (ICR) mass spectrometers. As long as the particles are nonrelativistic, all the beam particles in a cyclotron will drift through the D's in the same amount of time and arrive at the accelerating gaps in phase, that is, the orbits are *isochronous*. Notice also that we can use the concept of phase stability from linear accelerators to maintain the bunch structure of the initial beam pulse. The orbital radii will increase as the velocity of the particle increases as they cross each gap so that the particles will appear to spiral out from the center of the cyclotron. The maximum velocity will occur when the particles reach the maximum physical radius, ρ_{max}, of the vacuum chamber and D's. Solving for the maximum kinetic energy, T_{max}, assuming a nonrelativistic beam,

$$T_{max} = \frac{1}{2}mv_{max}^2 = \frac{(Bq\rho_{max})^2}{2m} = \frac{(B\rho_{max})^2}{2}\left(\frac{q^2}{m}\right) \tag{13.19}$$

Notice that the maximum kinetic energy depends on the two machine parameters, B and ρ_{max}, times a ratio of the square of the charge to the mass ratio of the beam particles. The first term in the expression for the maximum beam energy, $(B\rho_{max})^2/2$, is often called the "K" value of the cyclotron (because it is constant that depends on the machine design) and is given in units of MeV. The oscillation frequency of the D's can be tuned over a limited range (e.g., 15–30 MHz) in present-day cyclotrons to provide beams with different values of (q/m) at various energies. Small cyclotrons used to produce specific isotopes for radiopharmaceuticals have $K \sim 30$ MeV and can provide 30 MeV protons ($q^2/m = 1$). The highest-energy cyclotron is presently in Japan with $K = 2600$ MeV that boosts the heaviest ions up to $E/A = 350$ MeV ($q^2/m \sim m/4$) due to limitations in the vertical focusing and the relativistic mass increase of the beam.

The beam has to make many revolutions in a cyclotron in order to be accelerated up to the full energy. For example, a typical accelerating gap might have a potential difference of 100 kV so that a proton beam with total energy of 30 MeV that crosses the gap twice per revolution still requires on the order of

$n_{\text{turns}} \sim E_{\text{total}}/(2qV) = 30/(2 \times 1 \times 0.100) = 150$ turns. It is important that vertical focusing be applied to the beam so that it remains, at least on average, on the central plane of the cyclotron. There are two main techniques for vertical focusing in cyclotrons. A weak focusing effect occurs in the simple case in which the magnetic field of the cyclotron runs between flat, uniform, and *finite-sized* pole faces of an electromagnet. The magnetic field between flat pole faces will only be exactly perpendicular in the center and will increasingly bow out as one moves toward the edge. The curved shape of the magnetic field will provide a weak restoring force for particles that leave the median plane. A stronger focusing effect can be produced by dividing the flat pole face into sections that are higher (hills) and lower (valleys). As indicated in Figure 13.9, the average magnetic field should remain the same as that obtained with a flat pole face, but the local magnetic field is higher between the hills and lower between the valleys. The magnetic field will bow out from the hill region into the valley region along the path of the beam particles and provide a restoring force toward the median plane each time a particle crosses the transition. The vertical focusing can be increased by using a spiraled pole sector rather than a straight-edged sector. Such cyclotrons are usually called *sector-focused cyclotrons* and are extensively used to provide moderate and high-energy beams of charged particles. Another technique to produce strong focusing is to make the hill regions from separate wedge-shaped electromagnets and to leave the valley regions open. There has to be common vacuum chamber for the particles to circulate and to house the D's. The complexity of running four large individual magnets is compensated by the very large variation in the magnetic field between the hills and valleys (called the flutter), leading to a large vertical focusing effect. In addition, it is easier to install and service all the auxiliary equipment needed to inject, accelerate, and extract the beam. Such machines are called *separated-sector cyclotrons*.

An important limitation on the maximum beam energy available from cyclotrons comes from the relativistic increase of the mass of a particle with velocity. We have seen elsewhere that $m = m_0/(1 - (v/c)^2)^{1/2}$; thus, $m = 1.02m_0$ for $v = 0.2c$. Notice that the ratio of the magnetic field to mass, B/m, occurs in all of the cyclotron equations given earlier. There are two classes of isochronous cyclotrons that deal with this variation in mass: low-energy machines where the mass increase is small enough to be ignored, for example, $v_{\text{max}}/c < 0.2$, and medium-energy machines in which the increasing mass is compensated by increasing the strength of the magnetic field with radius. The magnetic field is usually increased by adding extra concentric coils to the magnet pole pieces that are called trim coils. The field could also be increased by decreasing the gap between the pole faces. The field lines in a cyclotron with a magnetic field that increases with radius will bow in toward the middle (opposite to that described earlier), a feature that will produce a weak vertical
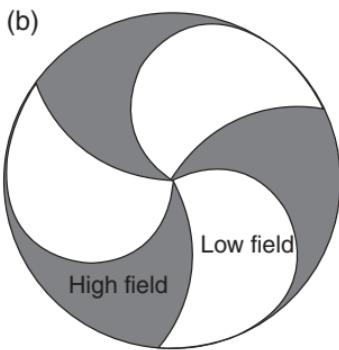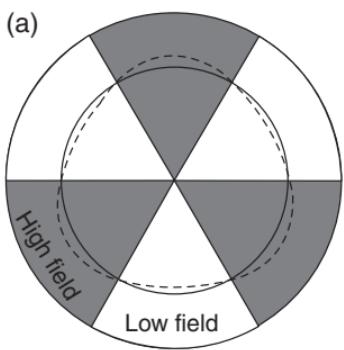
Figure 13.9 A top view of the sectors, or the hills and valleys, in a sector-focused cyclotron. In (a), the concept of strong vertical focusing at the transition regions, edges, of the sectors is shown for straight sectors. A larger focusing effect is obtained by spiraling the sectors as shown in (b). Note that the particles travel counterclockwise in this figure.

defocusing effect! Thus, fixed-frequency cyclotrons cannot be used to produce extremely high-energy beams.

A large number of cyclotrons have been constructed over the years and special-purpose machines continue to be built. For the most part, they have been spiral sector-focused machines with trim coils. The "K" values range from 30 to 150 MeV for electromagnets with normal conducting (or resistive) coils. A number sector-focused cyclotrons have been constructed with superconducting coils based on designs developed at Michigan State University that have "K" values of 500, and the largest machine has $K = 1200$. Several large separated-sector, normally conducting cyclotrons were constructed at the end of the 20th century at GANIL in France ($K = 440$) and at RIKEN in Japan ($K = 540$). A recently completed project at RIKEN includes a separated-sector machine using superconducting coils that is the largest cyclotron in the world. The beams from cyclotrons will have a microstructure on the tens of nanosecond time scale, similar to that from a linac, and will appear to be continuous in most applications. A cyclotron beam will not have a macrostructure unless one is applied to the beam from the ion source for specific experimental reasons. The acceleration of the beam from a cyclotron can be rapidly stopped by simply shifting the relative phases of the D's.

A number of attempts were made to develop cyclotrons that could accelerate protons up to energies on the order of a GeV (the proton rest mass). For example, the resonant frequency of the cyclotron could be decreased in proportion to the mass increase. Such a frequency-modulated (FM) cyclotron, or *synchrocyclotron*, could accelerate a single pulse of particles up to high energy but would have to be reset to start the next pulse and thus would have a low duty factor. In addition, the size of the magnet becomes extremely large and costly. The largest cyclotron magnet ever constructed was a 184 in. diameter

machine at LBL in Berkeley, originally designed to provide 100 MeV protons, but was redeveloped in 1946 as a synchrocyclotron.

The successful acceleration of protons and heavier nuclei to relativistic energies was realized through the compensation of the increasing mass of the particle by increasing the magnetic field. The early machines were fixed-frequency cyclotrons in which the acceleration process was synchronized by changing the magnetic field produced by a very large electromagnet. The mechanical design was changed later to be just a ring of individual magnets where the particles follow the same circular path. Simple geometry indicates that the set of individual magnets necessary to construct a ring requires much, much less iron than that of a single large cyclotron magnet. This *synchrotron* design has proven to be extremely robust and is used in all of the machines built to produce the highest-energy charged-particle beams.

Synchrotrons use the concept that the particles are confined to move in a circular orbit with a constant average radius, that is, a ring, regardless of the energy of the particles. Thus, synchrotrons must be pulsed machines that operate on a cycle in which a modest energy beam is injected into ring, the beam is accelerated, the high-energy beam is extracted, and the magnetic field and ring is returned to the injection state. A low magnetic field is necessary to confine the low-energy particles at injection. After a sufficiently large number of particles have been fed into the ring, one or more accelerating structures (originally drift tubes, now resonant cavities) are turned on, and the beam begins to gain energy as they circulate around the ring. The energy gain per turn is usually low (~100 kV), and during the acceleration process the magnetic field is ramped up toward the maximum value that the magnets can provide. If the synchrotron starts with nonrelativistic particles, then the revolution frequency of the particles will increase as the velocity increases (as the radius of the orbit is constant) so that the frequency of the accelerating structure has to increase as well. Thus, both the magnetic field and the acceleration have to be synchronized with the energy of the particles. The full-energy particles are extracted from the ring, providing a single macrocycle beam pulse. The magnetic field is then returned to the initial low value. The highest-energy synchrotrons accept particles that are already relativistic (from prior acceleration in booster synchrotrons), and the revolution frequency remains essentially constant. The time necessary for a single macrocycle is usually on the order of seconds and is dictated by the maximum rate of change of the magnetic field. Modern rapid cycling synchrotrons run at 1 or 2 Hz, while the original machines from the 1960s typically ran at 1/5 Hz.

The principle of phase stability is also used in synchrotrons to maintain a narrow energy distribution of the beam bunches during acceleration. The problem of vertical focusing in cyclotrons is also present in synchrotrons. The original machines relied on weak focusing in the ring magnets with flat pole faces. A variation of the strong focusing obtained with hills and valleys in

sector-focused cyclotrons can be obtained in synchrotrons. Rather than hills and valleys, though, the ring is divided into sectors in which the gaps between the pole pieces of the magnets are wedge shaped. The thinner side of the wedge is alternately on the inside or the outside of the ring. As in the cyclotron, the average field is set for an isochronous orbit. When the beam circles around the ring, it encounters a vertical focusing region (thin edge inside), and a vertical defocusing region (thin edge outside) which produces a net vertical restoring force. Dipole magnets that have pole pieces that are shaped (tilted) to provide focusing are called *combined function magnets* as they are meant to perform two tasks, and synchrotrons that use this version of strong focusing are called alternating gradient machines. Modern synchrotrons do not use combined function magnets but rather use dipole magnets to bend the beam and quadrupole doublet magnets (discussed in the following text) to focus the beam in straight sections between the dipoles. Such independent function magnets are easier to construct and allow more flexible tuning.

Synchrotrons are used to accelerate protons and heavy nuclei to the highest energies, presently 14 TeV protons in the Large Hadron Collider (LHC) at CERN and 100 GeV/nucleon heavy ions (including ^{197}Au nuclei at almost 20 TeV) in RHIC at Brookhaven National Lab (BNL). The maximum energy of the beam is proportional to $B\rho_{max}$ as in a cyclotron, and the value for the ring is usually given in Tesla-meters or T-m. Even after extensive development, the maximum field strengths in large electromagnets are on the order of a few Tesla; however, the radius of the ring of magnets is constrained by cost. For example, the booster or intermediate-energy synchrotron for the RHIC system is ~20 m radius and provides 1 GeV protons. The main ring of the alternating gradient synchrotron (AGS) at BNL is a 100 T-m system consisting of 240 combined function magnets in a radius of ~85 m. The main rings of the RHIC system are 839.5 T-m and contain 1740 separated function superconducting magnets in a 3.834 km circumference.

A similar but bigger and very versatile combination of big accelerators has been established at CERN in Europe. The complex includes several high-energy injectors for protons, electrons, and heavy ions; a booster synchrotron, the PS, that can accelerate pulses of these ions (e.g., 26 GeV protons); a high-energy synchrotron, the SPS, that can also accelerate the ions (e.g., 400 GeV protons, 170 GeV/nucleon heavy ions in a 1.1 km radius ring); and another ring system, LEP, for electrons and positrons (90 GeV electrons in 4.3 km radius) that was retired. The LEP tunnel was used to house the LHCs, with two rings that is able to accelerate and collide all of these particles (e.g., 7 TeV protons and 1.1 PeV ^{208}Pb nuclei, counter-circulating in the LEP tunnel).

There are two important features of nuclear collisions that we have not yet considered in our discussion of particle accelerators. First, conservation of momentum in the collision dictates that a large fraction of the energy that goes into a collision in the laboratory between a moving particle and a resting target

nucleus will go into kinematic motion of the products and will not be available for excitation of the products or for new particle production. Perhaps more surprisingly, the second feature is that after all the effort to produce a beam of high-energy particles, the huge majority of the beam particles will pass through the target material, interacting with the electrons and slowing down, and not collide with another nucleus! Both of these problems can be resolved if we create counterrotating beams of particles that are circulating at constant orbits in synchrotron rings held at their maximum magnetic fields. The beams can be directed to cross one another at specific points or interaction regions. Circular systems of magnets have also been developed without accelerating structures called storage rings where the beams coast from interaction point to interaction point. Notice that the net momentum of particles that collide head on in the laboratory is zero so that all of the energy is available for excitation of the products. It is much more cost effective to build two storage rings for a synchrotron accelerator and gain a factor of two in energy than to double the radius of the synchrotron. If the counterrotating particles miss during one crossing, as is the most likely event, then they simply continue on their orbit and literally come back around for another try. These features, particularly the higher available energy, lie at the heart of all of the modern high-energy accelerator complexes. All of the modern high-energy synchrotrons mentioned earlier include storage rings and rely on colliding counterrotating beams, for example, the Tevatron collides protons and antiprotons, LEP collides electrons and positrons, and RHIC and the LHC collide heavy-ion beams from separate rings.

13.6 Charged-Particle Beam Transport and Analysis

The goal of accelerating particles is to induce nuclear reactions with target nuclei. Most nuclear targets are pure elemental foils, and the earliest experiments were performed by placing a metal foil in the path of the beam at the end of the acceleration process. For example, a metal foil could be placed at the largest radius of a cyclotron or at the end of a linear accelerator. As we have just discussed, these reactions can also be made to occur between counterrotating beams in storage rings. It is very difficult to perform experiments directly in the accelerator for a number of reasons including the high radiation environment caused by beam loss during acceleration and physical constraints on the available space. Thus, beam transport techniques were developed to bring fully accelerated beams to remote and shielded vaults. These beam handling techniques are directly analogous to optical techniques based on glass prisms and lenses used to transport beams of photons.

In optical systems the light rays are diffracted when they make a transition between two media with different indices of refraction. Prisms use converging flat surfaces to chromatically disperse the light, and lenses use curved surfaces

(spherical lenses are most common) to focus or defocus the light rays. Charged-particle beams are similarly affected by magnetic and electric fields. A beam of charged particles will be deflected as it travels through a uniform magnetic field created between two surfaces and can be focused or defocused as it travels through the radially increasing field created by two, four, six, or more concentric surfaces. The fields are usually labeled as dipole, quadrupole, hexadecapole, and so on. The multipole fields can be created by electrostatic plates or electromagnet poles. The forces acting on the moving particles are different in electrostatic and magnetic systems, of course. Magnetic systems have the most widespread applications primarily for technical reasons since superconducting wire technology provides a means to create extremely large magnetic fields in compact devices, whereas the maximum attainable electric fields are small by comparison.

We have already seen that a moving charged particle will experience a force perpendicular to its direction of motion when it is moving in a magnetic field. The Lorentz force causes the particle to curve with a radius, $\rho = Bq/mv$, that depends on the charge-to-mass ratio (q/m) of the ion. Thus, a simple magnetic dipole can be used to change the direction of a beam of particles. For example, consider the path of a beam that enters the magnetic field in the region between the poles of wedge-shaped magnet as indicated in Figure 13.10. Such magnets are commonly called magnetic sectors or sector magnets and are characterized by their magnetic field, B, their bend radius, ρ, and their bend angle, θ. The beam will follow the path from O to E along an arc with a radius ρ and turn through an angle θ, as indicated in the figure. The path of the beam need not be perpendicular to the straight edges of the sector. These angles are labeled α_1 and α_2 in Figure 13.10. If all the particles are on exactly parallel trajectories when they enter the magnetic field, they will all turn through the angle θ and emerge in a parallel bunch. If, on the other hand, the particles enter the magnetic field in a diverging bunch, then the sector will focus the beam in the horizontal and vertical directions with focal lengths given by

$$f_{\text{horiz}} = \frac{\rho}{\left[\sin(\theta)(1 - \tan(\alpha_1)\tan(\alpha_2)) - \cos(\theta)(\tan(\alpha_1) + \tan(\alpha_2))\right]} \quad (13.20)$$

and

$$f_{\text{vert}} = \frac{\rho}{\left[(\tan(\alpha_1) + \tan(\alpha_2)) - \theta(\tan(\alpha_1)\tan(\alpha_2))\right]} \quad (13.21)$$

Notice that the focal lengths are different in the two dimensions. If the beam enters and exits along a normal to each face, $\alpha_1 = \alpha_2 = 0$, the horizontal focal length becomes $f_{\text{horiz}} = \rho/\sin(\theta)$ and all of the vertical focusing is removed, $f_{\text{vert}} = \infty$. Thus, if a perfectly round beam is deflected by a dipole magnet, it will often lose its symmetry due to the different focal lengths of the dipole magnet. Subsequent ion optical focusing elements have to be
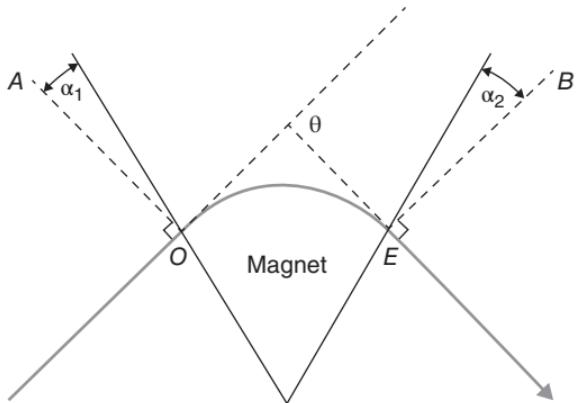
Figure 13.10 A schematic view of the bending of a charged-particle beam in a wedge-shaped dipole magnet with straight edges. The beam will be bent through an angle θ; the angles α_1 and α_2 are used to describe the angles of incidence relative to the straight edges and are important in determining the weak focusing of the magnet due to the fringing field. (Harvey (1964). Reproduced with the permission of Elsevier).
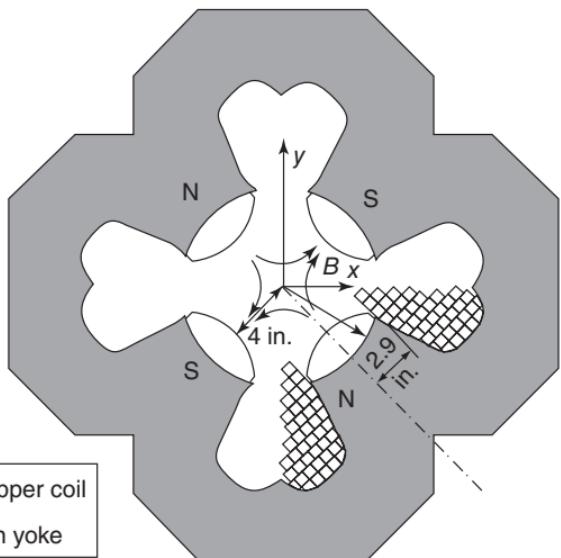

Figure 13.11 A schematic design of a quadrupole magnet. The arrangement of the four poles will provide *x* focusing in the usual right-handed coordinate system with the *z*-axis emerging from the page (Segre (1977). From O. Chamberlin, Ann. Rev. Nucl. Sci. **10**, 161 (1960)).

set to compensate for this difference to produce a round beam at the target position. It is important to remember that the bending radius, ρ, is proportional to the charge-to-momentum ratio of the beam (q/mv) so that the field strengths of all of the magnets will have to be set for each beam particle and energy.

Magnetic focusing of a charged-particle beam can be produced by a collinear solenoidal field or by a pair of magnetic quadrupoles. In both cases the magnets create a fringing field or fields that cause diverging particles to be returned to the optical axis. If we define the *z* axis along the path of the beam, a single solenoid will focus in both *x* and *y* directions. A magnetic quadrupole can be constructed by arranging four equal-strength poles on a circle at 90° from one another with polarities that alternate between north and south. An example of a quadrupole magnet is shown in Figure 13.11. If we examine the magnetic field from such a quadrupole device, we will find that the field along the central

axis is exactly zero and increases linearly to a maximum value at each pole face. (The pole tips should be hyperbolic surfaces to conform to the shape of the magnetic field although cylindrical pole tips are often used for ease of manufacture.) Quadrupole magnets are thus characterized by the gradient of the magnetic field, dB/dr, where r is a radial coordinate and by their length, ℓ, along the beam direction. A particle that moves along the central axis stays in a region of zero magnetic field and goes straight through, while particles that are off-axis will encounter an increasing magnetic field that acts like the fringing field at the edge of a dipole magnet. Notice, however, that the fringing fields will only focus off-axis particles in one direction (e.g., x in Fig. 13.11) and defocus them in the orthogonal direction (e.g., y in Fig. 13.11). If we define the constant $k^2 = (q/mv) * dB/dr$, then the focal length of one quadrupole with a length ℓ (called a singlet) is

$$f_{horiz} = \frac{1}{k \sin(k\ell)} \tag{13.22}$$

At first glance the fact that a singlet is both focusing and defocusing at the same time might imply that uniform focusing of a beam is not possible. However, it is known from light optics that the combination of a converging lens with a diverging lens has a net focusing effect as is indicated in Figure 13.12. Therefore, focusing magnet packages are most often made by combining an x focusing quadrupole with a y focusing quadrupole of equal lengths into a "doublet." Three quadrupoles (y, x, y) with lengths $(\ell, 2\ell, \ell)$ are sometimes combined into "triplets," which provide more flexibility in manipulating the beam shape.

Modern accelerator complexes rely on a large combination of magnetic dipoles and quadrupoles to transport fully accelerated beams for large distances without loss. Solenoidal magnets are only used occasionally when point-to-point foci are needed as quadrupoles are more efficient and allow the two coordinates to be tuned independently. Higher order magnetic multipoles, sextupoles, and octupoles, are used to correct aberrations in high resolution applications such as spectrometers and fragment separators.

Sample Problem 13.4: Magnetic Focal Lengths

A dipole magnet deflects charged-particle beams through an angle of 22.5° with a radius of 2.0 m. For ease of construction the magnet has rectangular pole pieces (0.5×1.5 m long). The beam enters normally at the center of one of the 0.5 m faces and exits at an angle from the opposite 0.5 m edge. What are the focal lengths of this magnet?

Solution

We need to evaluate the angles α_1 and α_2 in order to solve this problem. From the problem definition and consulting Figure 13.10, we know that

$\alpha_1 = 0$. A little geometry will show that in this case the exit angle is equal to the bend angle:

$$f_{horiz} = \frac{\rho}{\left[\sin(\theta)(1 - \tan(\alpha_1)\tan(\alpha_2)) - \cos(\theta)(\tan(\alpha_1) + \tan(\alpha_2))\right]}$$

$$f_{horiz} = \frac{2.0\ \text{m}}{\left[\sin(22.5°)(1 - \tan(0)\tan(22.5°)) - \cos(22.5°)(\tan(0) + \tan(22.5°))\right]}$$

$$f_{horiz} = \frac{2.0\ \text{m}}{\left[\sin(22.5°)(1 - 0) - \cos(22.5°)(0 + \tan(22.5°))\right]}$$

$$f_{horiz} = \frac{2.0\ \text{m}}{\left[0.38268 - 0.92388(0.41421)\right]} = \frac{2.0}{0}$$

$$f_{horiz} = \infty\ \text{m}$$

For the vertical focal length we have

$$f_{vert} = \frac{\rho}{\left[(\tan(\alpha_1) + \tan(\alpha_2)) - \theta(\tan(\alpha_1)\tan(\alpha_2))\right]}$$

$$f_{vert} = \frac{2.0\ \text{m}}{\left[(\tan(0) + \tan(22.5°)) - 22.5°(2\pi/180°)(\tan(0)\tan(22.5°))\right]}$$

$$f_{vert} = \frac{2.0\ \text{m}}{\left[\tan(22.5°) - 0\right]}$$

$$f_{vert} = \frac{2.0\ \text{m}}{0.41421} = 4.83\ \text{m}$$

Such different focal lengths seen in this situation, a weak focus in vertical compared with no focus in the horizontal, are a common occurrence in beam transport systems.

The transport and control of charged-particle beams with electrostatic elements has the nice feature that the equations of motion do not depend
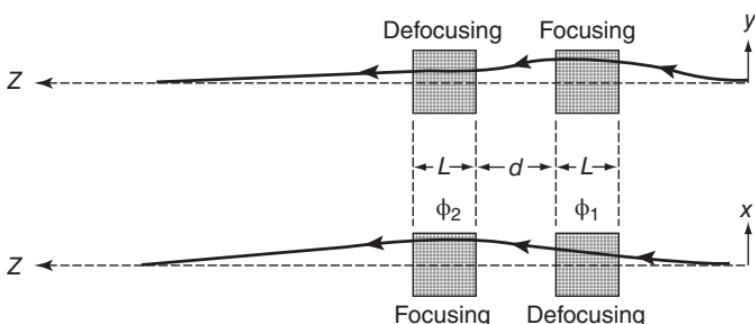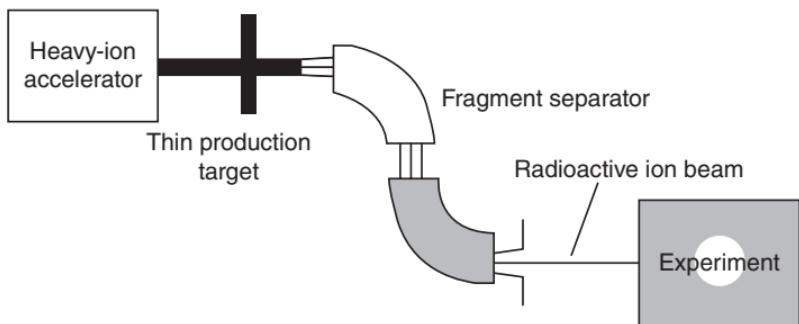

Figure 13.12 The net focusing effect on a diverging charged-particle beam from the combination of a converging and a diverging magnetic quadrupole lens. The key feature of the doublet is that the particles move along paths that are closer to the optical axis in the defocusing element of the pair (Harvey (1964). Reproduced with the permission of Elsevier).

on the mass of the particle. The force felt by a charged particle in an electric field is simply $F_e = qE$ where q is the electric charge and E is the electric field strength. When a positively charged particle enters the region between two parallel plates with a separation d at a voltage V, the particle will feel the electric force pulling it toward the electrode at the lower potential, $F_e = qV/d$, and will move on a circular orbit with a radius, $\rho = mv^2(d/qV)$. Such a device can thus change the direction of the incident beam. (The beam will undergo a weak focusing from the fringing field at the entrance and exit of the device as discussed earlier.) Strong focusing of a beam of charged particles can be produced by an einzel lens (cylindrical focusing from a set of three sequential ring electrodes) and by a quadrupolar arrangement of electrodes. An electrostatic mirror can be produced by an electrode at a potential energy that is greater than the kinetic energy divided by the charge of the particle. The bending and focusing power of electrostatic systems is limited by the maximum electric fields that can be applied across the electrodes. Extensive electrostatic systems have been constructed for the transport of low-energy beams, KE $\leq$ 50 keV, for example, beams extracted from ion sources are usually transported with electrostatic elements.

13.7   Radioactive Ion Beams

Unstable nuclei with modestly short half-lives have been produced and separated into very-low-energy beams for some time. Recently, techniques have been developed to provide much more energetic beams of nuclei with half-lives as short as a few milliseconds with sufficient energy to induce secondary nuclear reactions. The production techniques usually rely on the creation of exotic nuclei in high-energy reactions followed by the collection and separation of a specific exotic nucleus. The physical techniques differ in that the products are either the residues of target (nearly at rest in the laboratory) or of projectile nuclei (moving with nearly the beam velocity), but in both reactions a large nucleus is fragmented into various components. The difference in the initial velocity of the product has large consequences for the physical separation techniques and re-acceleration but no consequences for the reaction mechanism. Thus, the same residues can and have been produced for study in each rest frame. Very energetic proton beams ($E_{\text{lab}} \sim m_0 c^2$) from synchrotrons were used extensively in the 1960s to irradiate various targets, and the process of *target fragmentation* was rapidly exploited for the production of exotic nuclei. The residual nuclei left in the target after a beam pulse were thermalized and then ionized for separation. This technique is usually called the *ISOL* technique (Fig. 13.13). This is an acronym for isotope separator online. Today it may be more precise to associate ISOL with ion source online to more clearly distinguish these devices from in-flight devices used to separate projectile fragments. The proton beam interacts with a target,
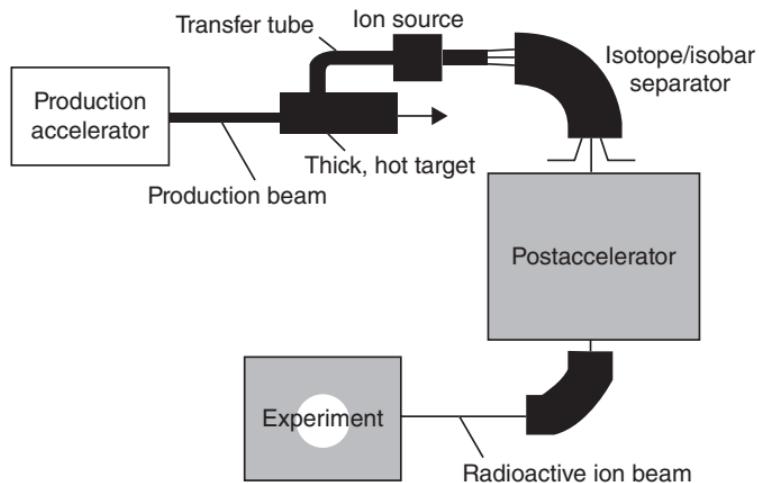
Figure 13.13 Schematic view of the projectile fragmentation (PF) and isotope-separator online (ISOL) techniques for generating radioactive beams.

usually a refractory metal, that is heated to several thousand degrees. The target itself can be quite thick, even thick enough to stop the beam, but it should be thin to allow rapid release of the reaction products. This apparent paradox can be solved by using stacks of thin metal foils. The reaction products come to thermal equilibrium in the target matrix and, depending on their chemical nature, can diffuse out of the matrix. Many techniques have been used to ionize the emergent hot atoms including surface ionization, electron beam or plasma ionization, and resonant laser ionization. Notice that the reaction mechanism creates a broad range of products, many of which diffuse out of the target at some rate but some do not. The ionization process is a second chemical process that creates singly charged ions. After ionization the reaction products can be readily extracted from the target system and accelerated. The chemical selectivity provides a means to select the most exotic nuclei that are only weakly produced in the primary reaction. The

Table 13.2 Examples of ISOL Fragmentation Facilities.

Device	Accelerator System	Reaction[a]	Country
ARENAS	Cyclotron/ECR/Cyclotron	(p, n), (p, 2p), etc.	Belgium
ISAC	Cyclotron/ECR/LINAC	TF	Canada
REX-ISOLDE	Synchrotron/1+/EBIS/LINAC	TF	CERN (Europe)
SPIRAL	HI-Cyclotron/ECR/Cyclotron	PF	France

[a]Class of reactions: low-energy fusion and direct reactions, target fragmentation (TF), projectile fragmentation (PF).

target ion source combination is placed on an electrostatic platform to provide very-low-energy ions (≤ 50 keV, total) for beta decay or other studies. A large number of facilities were operated over the years, the most successful being the ISOLDE facility at CERN that uses pulses of 1 GeV protons from the CERN PS synchrotron to irradiate targets such as Nb, Ta, and U. The ISOLDE facility has a large electrostatic beam handling system with many experimental stations.

A number of facilities around the world are able to accelerate exotic beams from ISOL production to energies sufficient to induce secondary nuclear reactions. These first-generation facilities all rely on using existing accelerators and in some cases existing experimental equipment. A facility at Louvain-la-Neuve produced radioactive beams of light nuclei created in direct reactions induced by a 30 MeV proton beam from a small cyclotron developed to produce radioisotopes for medicine. Neutral gaseous products, atoms and small molecules, were pumped from the target into an ECR ion source, ionized, and then transferred into a K110 cyclotron. Another facility recently completed uses an EBIT charge-breeding source to increase the charge state of positive ions from the ISOLDE separator before injection into a modern linear accelerator. The hallmark of all of these facilities is that they have an accelerator that provides an intense beam to produce the activities (the driver) and another accelerator for the secondary beam. Table 13.2 presents a list of ISOL facilities that is meant to indicate the variety of approaches that have been used to produce radioactive beams from target fragments.

The advent in the 1970s of synchrotrons that were capable of delivering beams of all elements with very high energies allowed the production of the same exotic nuclei observed as target residues with sufficient kinetic energies to allow rapid physical separation and identification. This technique is usually called the *projectile fragmentation* technique but more correctly might be referred to as in-flight separation since other reaction mechanisms besides projectile fragmentation can be used to produce the fast nuclei (cf. Fig. 13.13). The beams of exotic nuclei are not stopped in this technique, and even very short-lived nuclei can be studied and used to induce secondary reactions. In the mid-1970s it was shown that up to 1% of a primary ^{12}C beam could

be converted into ^{11}C ions and separated for implantation into biomedical samples. Nuclear physics experiments to produce exotic nuclei and calibrate space flight instruments using similar techniques based on magnetic rigidity were also pioneered with beam-line elements at LBL (Berkeley, California) and then dramatically extended by using degraders (the LISE spectrometer at GANIL (Caen, France)). This technique has been further extended in four second-generation devices distributed around the world and third-generation devices at the NSCL (Michigan State) and at RIKEN (Japan).

Fast beams of exotic nuclei are separated from the primary beam and from the other reaction products by a combination of magnetic bending dipoles and focusing quadrupole doublets acting on the distribution of ions emerging from the target at high velocities ($\beta \sim 0.5c$). Achromatic magnetic systems are used, where achromatic means that the position and angle of ions at the end of the device (called the focal plane) do not depend on the ion's momentum. Such achromatic magnetic systems are generally most useful for efficient separation at the highest energies because they can collect a large fraction of the produced fragments and focus them to a relatively small spot (~ 5 mm). Achromatic systems have the additional advantage that the final spot size remains small even when the momentum acceptance is large. The key elements in these devices are: (a) an initial bend for momentum-to-charge ratio selection, (b) an energy loss degrader for atomic number separation also called a "wedge," and (c) a second bend for momentum-to-charge ratio selection of a specific ion. This technique is sometimes referred to as the $B\rho - \Delta E - B\rho$ separation technique.

We can consider the in-flight production in more detail. An aperture or a slit is used at an intermediate position (with a momentum dispersion) to limit the momentum acceptance of the device. Since the fragmentation mechanism produces all the nuclei with nearly the same velocity (depending on the target thickness) and initial magnetic rigidity ($B\rho = mv/q$), a momentum-to-charge selection is approximately equal to a separation by mass-to-charge ratio of the products. Under these conditions projectile fragmentation reactions can produce many different ions that have the same mass-to-charge ratio, for example, the fragmentation of an ^{18}O beam can formally produce five ions with $m/q = 3$: ^{3}H, ^{6}He, ^{9}Li, ^{12}Be, and ^{15}B. An energy degrader is inserted into the beam at the intermediate dispersive image in order to introduce a velocity shift that depends on the energy loss in the material and thus on the atomic number of the ion. Recall that all ions will lose some kinetic energy in the degrader and the relative amount will depend on $mZ^2/KE \propto (Z/v)^2$. The ions, therefore, will exit the foil with different magnetic rigidities since v is approximately constant. The contaminants can then be spatially dispersed at the focal plane by an additional bend. This Z-dependent separation is proportional to the degrader thickness and to the ratio of the magnetic rigidity of the second half of the system to that of the first half. A schematic diagram of the A1900 separator operating at the NSCL is shown in Figure 13.14. There are
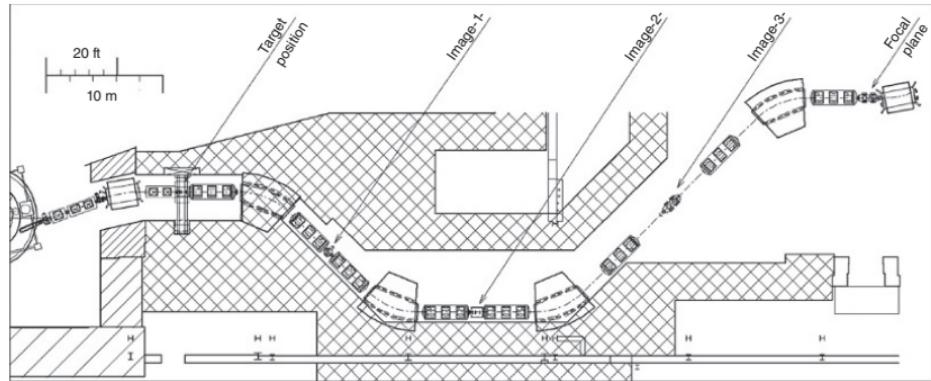
Figure 13.14 A schematic diagram of the A1900, a third-generation projectile fragmentation separator operating at Michigan State University.

Table 13.3 Comparison of Projectile Fragmentation Facilities.

Device	Ω (msr)	$\Delta p/p$ (%)	$B\rho$ (T-m)	Resolving Power	Length (m)	Facility
A1200	0.8–4.3	3.0	5.4	700–1500	22	NSCL (US)
A1900	8.0	4.5	6.0	~2900	35	NSCL (US)
COMBAS	6.4	20	4.5	4360	14.5	JINR (Russia)
LISE3	1.0	5.0	3.2	800	18	GANIL (France)
FRS	0.7–2.5	2.0	9–18	240–1500	73	GSI (Germany)
RIPS	5.0	6.0	5.76	1500	21	RIKEN (Japan)
RCNP	1.1	8.0	3.2	2000	14	RCNP (Japan)

projectile fragmentation separators presently operating in France, Germany, Japan, and the United States. Other similar devices are in the planning stages or are under construction in several laboratories. A comparison of the various parameters that describe these fragment separators is given in Table 13.2. The LISE separator has been operated for more than 15 years at GANIL and has provided beams for a wide variety of experiments. The BigRIPS device at RIKEN in Japan has the largest solid angle and momentum acceptance of third-generation devices. The more recently constructed COMBAS device at the JINR at Dubna has a significantly larger acceptance and is based on using combined function magnets. The A1200 (now retired) and the A1900 (MSU) (shown schematically in Fig. 13.14), RCNP (Osaka), and FRS (GSl) separators are positioned at the beginning of the beam distribution system to allow delivery of radioactive beams to any experimental area. Next-generation devices are being built for the FAIR project in Germany and for the FRIB project in the United States (Table 13.3).

Besides the obvious dependence of the RNB intensity on the intensity of the primary beam, the secondary beam rate is also directly related to the relative separator acceptance. The FRS at GSI and BigRIPS at RIKEN have been designed for very high kinetic energies, where the fragmentation cone and relative energy spread are relatively small. This allows the physical acceptance of the device to be smaller but gives essentially "full acceptance" for individual products. Large solid angle and large momentum acceptance are especially important if the device is to be used to separate light ions at 50–200 MeV/nucleon, the energy region in which most separators are operating. Note that the larger the physical acceptance of the separator, the lower the primary beam energy will be that reaches 100% collection efficiency.

13.8 Nuclear Weapons

While a full discussion of nuclear weapons is beyond the scope of this book, some comments about the operating principles of such devices and their connection to reactors and accelerators are desirable. The techniques used to produce a "nuclear explosion" (i.e., an essentially instantaneous, self-perpetuating nuclear chain reaction) are very complex. A nuclear explosion must utilize a high-energy neutron spectrum (fast neutrons, i.e., neutrons with energies >1 MeV). This requirement results from the fact that, for an explosion to take place, the nuclear chain reaction must be very rapid, on the order of microseconds. Each generation in the chain reaction must occur within about 0.01 μs (a "shake" in the parlance of weaponeers) or less. The energy release takes place over many generations although 99.9% of the energy release occurs within the last seven generations, that is, in a time of the order of 0.1 μs. The rapid time scale of this reaction requires propagation by fast neutrons. The process by which a neutron is moderated in energy is time consuming and largely eliminates the possibility of an explosion. This also explains why power reactors that operate with a slow or thermal neutron spectrum cannot undergo a nuclear explosion, even if the worst accident is imagined. In the case of reactors that operate with higher-energy neutrons, a nuclear explosion is also precluded based on the geometrical arrangement of the fissionable material and the rearrangement of this material if an accident occurs.

The explosive ingredients of fission weapons are limited, in practice, to ^{239}Pu and ^{235}U, because these are the only nuclides that are reasonably long lived, capable of being produced in significant quantities, and also capable of undergoing fission with neutrons of all energies, from essentially zero or thermal to the higher energies of the secondary neutrons emitted in fission. Other nuclides, for example, ^{238}U or ^{232}Th, can undergo fission with some of these higher-energy neutrons, but not with those of lower energy. It is not possible to produce a self-sustaining chain reaction with these latter nuclides, since an insufficient fraction of the neutrons produced in the fission reaction has an appropriate energy to induce, and hence perpetuate, the fission reaction. Fission weapons currently use ^{239}Pu or highly enriched ^{235}U (usually >90%) although, in principle, enrichments as low as 10% are usable. Fission weapons utilizing ^{239}Pu have higher yield-to-weight ratios and can be made with smaller sizes and weights. One problem in plutonium-based weapons is the presence of ^{240}Pu whose high spontaneous fission rate can present problems with pre-initiation of the weapon. Pre-initiation of the weapon is defined as the initiation of the nuclear chain reaction before the desired degree of supercriticality (see following text) is achieved. The neutrons emitted during

the spontaneous fission of ^{240}Pu can cause such a pre-initiation, which will decrease the yield of the weapon and increase the uncertainty in that yield. To prevent this pre-initiation, weapons-grade plutonium contains <7% ^{240}Pu, while ordinary reactor-grade plutonium may contain more than 19% ^{240}Pu. The ^{240}Pu content of plutonium can be regulated by controlling the time ^{238}U is left in the reactor for generating ^{239}Pu. Many US fission weapons contain both ^{239}Pu and ^{235}U as a trade-off between the higher efficiency of using ^{239}Pu and the greater availability of ^{235}U. (About 43 metric tons of Pu is contained in US nuclear weapons.)

If the conditions are such that the neutrons are lost at a faster rate than they are formed by fission, the chain reaction is not self-sustaining. The escape of neutrons occurs at the exterior of the ^{239}Pu (or ^{235}U) object undergoing fission, and thus the rate of loss by escape will be determined by the surface area. On the other hand, the fission process, which results in the formation of more neutrons, takes place throughout the bulk of the material; the rate of growth of neutron population is therefore dependent upon the mass. If the quantity of ^{239}Pu (or ^{235}U) is small, that is, if the ratio of the surface area to the volume is large, the proportion of neutrons lost by escape to those producing fissions will be so great that the propagation of a nuclear fission chain, and hence the production of an explosion, will not be possible. But as the size of the piece of ^{239}Pu (or ^{235}U) is increased and the relative loss of neutrons is thereby decreased, a point is reached at which the chain reaction can become self-sustaining. This is referred to as the "critical mass" of the fissionable material.

The critical mass of a bare sphere of normal density ^{235}U metal has been reported to be 52 kg, while the same number reported for certain phases of plutonium metal is about 10 kg . However, the critical mass may be lowered in a number of ways. Use of a reflector can lower the critical mass by a factor of 2–3. Compression of the material to increase its density will also lower the value of the critical mass, with the critical mass being approximately proportional to the inverse square of the density. Most nuclear weapons employ only a fraction of the critical mass (at normal density). Because of the presence of stray neutrons in the atmosphere or the possibility of their being generated in various ways, a quantity of ^{239}Pu (or ^{235}U) exceeding the critical mass would be likely to melt or possibly explode. It is necessary, therefore, that before detonation a nuclear weapon should contain no single piece of fissionable material that is as large as the critical mass for the given conditions. In order to produce an explosion, the material must then be made supercritical, that is, made to exceed the critical mass, in a time so short as to completely preclude a sub-explosive change in the configuration, such as by melting.

Two general methods have been described for bringing about a nuclear explosion, that is to say, for quickly converting a subcritical system into a

supercritical one. In the first procedure, two or more pieces of fissionable material, each less than a critical mass, are brought together very rapidly in the presence of neutrons to form one piece that exceeds the critical mass. This may be achieved in some kind of gun barrel device, in which a high explosive is used to blow one subcritical piece of fissionable material from the breech end of the gun into another subcritical piece firmly held in the muzzle end. Early nuclear weapons had a mass of ^{235}U in the form of a sphere with a plug removed from its center. The plug was then fired into the center of the sphere creating a supercritical assembly. This technique is largely of historical interest.

The second method makes use of the fact that when a subcritical quantity of an appropriate isotope, that is, ^{239}Pu (or ^{235}U) is strongly compressed, it can become critical or supercritical. The reason for this is that compressing the fissionable material (increasing its density) increases the rate of production of neutrons by fission relative to the rate of loss by escape. The surface area (or neutron escape area) is decreased, while the mass (upon which the rate of propagation of fission depends) remains constant. A self-sustaining chain reaction may then become possible with the same mass that was subcritical in the uncompressed state.

In a fission weapon, the compression may be achieved by encompassing the subcritical material with a shell of chemical high explosives, which is imploded by means of a number of external detonators, so that a uniform inwardly directed "implosion" wave is produced. The implosion wave creates overpressures of millions of pounds per square inch in the core of the weapon, increasing the density by a factor of two. A simple estimate may be made to show that the resulting assembly should have a size of 10 cm, the mean free path of a fast neutron in ^{239}Pu or ^{235}U. The implosion technique is used in modern nuclear weapons. In both methods, high-density heavy metals are used to surround the fissionable material, thereby reducing or preventing the escape of neutrons from the reacting assembly. To contain the fissionable material and ensure that a large enough fraction of the nuclei undergo fission before the expansion of the exploding material causes subcriticality, the fissile material is surrounded by a heavy metal case, which acts as a tamper (and a neutron reflector.)

In a thermonuclear or hydrogen bomb, a significant fraction of the energy release occurs by nuclear fusion rather than nuclear fission. The hydrogen isotopes, ^{2}H (deuterium, D) and ^{3}H (tritium, T), can be made to fuse, as in

$$^{2}\text{H} + {}^{3}\text{H} \rightarrow {}^{4}\text{He} + n + 17 \text{ MeV} \tag{13.23}$$

To initiate such a D–T fusion reaction requires temperatures of 10–100 million degrees. Relatively large amounts of deuterium/tritium and/or lithium deuteride can be heated to such temperatures by a fission explosion where the temperature may be $\sim 10^8$ K. (Tritium is generated in situ by the
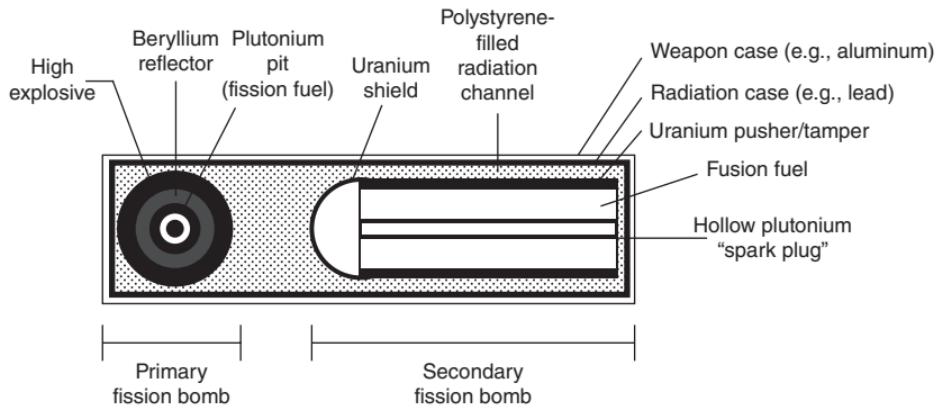
Figure 13.15 A schematic diagram of a hydrogen bomb (From nuclearweaponarchive.org).

neutron bombardment of ^{6}Li during the fusion reaction by the reaction ^{6}Li $+ n \rightarrow$ ^{3}H $+$ ^{4}He $+ n + 17$ MeV thus making the overall fusion reaction ^{6}Li $+$ ^{2}H $\rightarrow 2\,^4$He $+ 21.78$ MeV.)

The energy release can be enhanced further by using the high-energy neutrons released in the fusion reactions to induce fission in the abundant isotope ^{238}U. Thus, we have fission–fusion and fission–fusion–fission weapons, which can give rise to explosions of much greater energy than those from simple fission weapons. In a typical modern multistage thermonuclear weapon, the radiation from a fission explosion is used to transfer energy and compress a physically separate component containing the fusion material. The fissile material is referred to as the primary stage, while the fusion material is called the secondary stage. A third stage can be added in which the fast neutrons from the fusion reaction are used to initiate the fission of ^{238}U. In modern multistage thermonuclear weapons, comparable energy release is said to come from fission and fusion reactions.

A published schematic diagram of the operation of a modern multistage thermonuclear weapon is shown in Figure 13.15. The fission stage is similar to the implosion weapon used over Nagasaki but is only 12 in. in diameter. The chemical explosives are arranged in a soccer ball configuration with 20 hexagons and 12 pentagons forming a sphere. Detonator wires are attached to each face. In this example, the fusion reaction must take place before the expanding fireball of the exploding fission trigger blows apart the fusion materials (i.e., in a time scale of <100 shakes). This is accomplished through the use of x and γ-radiation to transmit the energy of the fission reaction. The x and γ-radiation travels about a 100 times faster than the exploding debris from the fission reaction toward the fusion assembly. As shown in Figure 13.15, the thermonuclear weapon in this example is a 3–4 ft long cylinder with an 18 in. diameter with the fission stage located near one end and the fusion stage near the other.

The x and γ-radiation is directed to a tamper of polystyrene foam, which surrounds the fusion assembly. The radiation energy is absorbed by the polystyrene foam, which is transformed into a highly energized plasma, which compresses the fusion fuel assembly.

The "neutron bomb" or "enhanced radiation" weapon is a thermonuclear weapon in which the energy release in the form of heat and blast is minimized and the lethal effects of the high-energy neutrons generated in fusion are maximized. This is reported to be done by the elimination of the ^{238}U components of the weapon. The suggested net effect of this is that the instantaneously incapacitating radius (dose of 8000 rad) of a neutron bomb is about the same as a fission weapon with 10 times the yield. The instantaneously incapacitating radius for a one kiloton neutron bomb is thus about 690 m.

Nuclear weapon yields are measured in units of kilotons of TNT (1 kiloton of TNT = 10^{12} calories = the explosive energy release from 60 g of fissile material). The energy release is mostly in the form of pressure and heat with a smaller amount (~15%) released in the form of radiation. The first nuclear explosive device, which was detonated at Alamogordo, New Mexico, had a yield of about 20 kT as did the Fat Man bomb dropped over Nagasaki, Japan (both fueled by ^{239}Pu). The Little Boy bomb dropped over Hiroshima, Japan, had a yield of 12–15 kT (fueled by ^{235}U). The efficiency of the plutonium-based devices was about 17%, while the uranium-based device had an efficiency of about 1.3%. For a 20 kT weapon, the radiation dose at 500 m from the center was estimated to be ~70 Gy and dropped to ~4 Gy at 1.1 km. The smallest nuclear weapons have been reported to have weight that is about 0.5% of the Fat Man bomb (10,800 lb) and a total size of 25–30 in. in length and 10–12 inches in diameter, with explosive yields about 0.25 kT. Modern thermonuclear weapons with yields above 100 kT have yield/weight ratios of 1–3 kT/kg, which is far from the theoretical maximum of 80 kT/kg.

Problems

13.1 A Cockcroft–Walton accelerator produces 400 keV protons. What is the maximum energy of the neutrons that can be produced with this accelerator using the $d + T$ reaction?

13.2 Given a reactor that contains 11 kg of ^{235}U and operates at a power level of 1 MWe, what is the antineutrino flux 15 m from the core?

13.3 Verify the statement that the reactor poison ^{135}Xe reaches a maximum ~10 h after shutdown of a high-flux ($>10^{14}$ n/cm^2/s) reactor.

13.4 Given the reactor of Problem 2, how long can it run before it uses up 10% of its fuel?

13.5 Estimate the quantity of ^{140}Ba in a reactor operating at 3000 MWt for a year. Assume the fission yield of ^{140}Ba is 0.06345.

13.6 Given a reactor where the average time between production and absorption of neutrons is 1 ms. and the power level is 1 MWe, calculate the number of free neutrons in the reactor during operation.

13.7 Calculate the number of collisions needed to reduce a neutron's energy from 1 MeV to 0.025 eV in H_2O, D_2O, and C. Calculate the neutron mean free path in each case.

13.8 Given a 1 g source of ^{252}Cf, calculate the neutron flux 1 m from the source and the heat produced in the source.

13.9 For a 1000 MWe nuclear reactor fueled with a fuel containing 5% ^{235}U, calculate the uranium use in a year of full-time operation.

13.10 Describe and compare electron cooling and stochastic cooling of a charged-particle beam.

13.11 Using the web as an information source, compare and contrast either of the current Michigan State University superconducting cyclotrons (K500, K1200) and also the Uppsala University GWI synchrocyclotron with a "classical" simple cyclotron.

13.12 Describe the duty cycles of a typical Van de Graaff accelerator, a linac, and a synchrotron.

13.13 For an accelerator with a radius equal to that of the Earth and a magnetic field of 40 kG, calculate the maximum energy of the protons that could be accelerated in this device.

13.14 A cyclotron accelerates α-particles to a maximum energy of 42 MeV. What is the *K* of this cyclotron? What is the maximum energy deuteron beam that it can produce?

13.15 A cyclotron has a diameter of 60 inches with an RF frequency of 10.75 MHz. Calculate the maximum energy of the proton beam and maximum field strength needed.

13.16 Explain the meaning of the term "phase stability" in regard to a linac and as used with a synchrocyclotron.

13.17 To study the internal structure of the proton, what minimum energy electrons would be needed? Explain your reasoning.

13.18 Consider the following situations: (a) a 20 GeV proton collides with a target electron, (b) a 20 GeV electron collides with a target proton, and (c) a 10 GeV proton collides with a 10 GeV electron. In each case, what is the CM energy available to create new particles?

Bibliography

D. Bodansky, *Nuclear Energy: Principles, Practices and Prospects* (AIP, Woodbury, 1996).

D. Brune, B. Forkman, and B. Persson, *Nuclear Analytical Chemistry* (Chartwell-Bratt, Sweden, 1984).

W.E. Burcham and M. Jobes, *Nuclear and Particle Physics* (Longman, Burnt Mill, 1995).

G. Choppin, J.O. Liljenzin, and J. Rydberg, *Radiochemistry and Nuclear Chemistry*, 3rd Edition (Butterworth-Heinemann, Woburn, 2002).

T.B. Cochran, W.M. Arkin, and M.M. Hoenig, *Nuclear Weapons Databook*, Volume I (Ballinger, Cambridge, 1984).

A. Das and T. Ferbel, *Introduction to Nuclear and Particle Physics* (John Wiley & Sons Inc., New York, 1994).

I.G. Draganic, Z.D. Draganic, and J.P. Adloff, *Radiation and Radioactivity on Earth and Beyond* (CRC Press, Boca Raton, 1993).

H.A. Enge, *Introduction to Nuclear Physics* (Addison-Wesley, Reading, 1966).

H. Frauenfelder and E.M. Henley, *Subatomic Physics*, 2nd Edition (Prentice-Hall, Englewood Cliffs, 1991).

G. Friedlander, J.W. Kennedy, E.S. Macias, and J.M. Miller, *Nuclear and Radiochemistry*, 3rd Edition (John Wiley & Sons, Inc., New York, 1981).

B.G. Harvey, *Introduction to Nuclear Physics and Chemistry*, 2nd Edition (Prentice-Hall, Englewood Cliffs, 1964).

D.T. Hughes and R.B. Schwartz, *Neutron Cross Sections*, 2nd Edition (Brookhaven National Laboratory, Upton, 1958).

K.S. Krane, *Introductory Nuclear Physics* (John Wiley & Sons, Inc., New York, 1988).

P. Kruger, *Principles of Activation Analysis* (John Wiley & Sons, Inc., New York, 1971).

M. LeFort, *Nuclear Chemistry* (van Nostrand, Princeton, 1968).

H. Morland, *The Progressive*, November, 1979; The Secret That Exploded (Random House, New York, 1981).

D.H. Perkins, *Introduction to High Energy Physics*, 4th Edition (Cambridge, Cambridge, 2000).

G.T. Seaborg and W. Loveland, *The Elements Beyond Uranium* (John Wiley & Sons, Inc., New York, 1990).

E. Segre, *Nuclei and Particles*, 2nd Edition (Benjamin, Reading, 1977).

R.J. Van de Graaff, *Nucl. Instr. Meth.* 8, 195 (1960).

The Transuranium Elements

14.1 Introduction

The chemical elements are the building blocks of nature. All substances are combinations of these elements. There are (as of 2016) 118 known chemical elements with the heaviest naturally occurring element being uranium ($Z = 92$). The 26 heaviest chemical elements, the transuranium elements, are man-made. The story of their synthesis, their properties, their impact on chemistry and physics, and their importance to society is fascinating. This story is of particular importance to nuclear chemistry because most of our knowledge of these elements and their properties comes from the work of nuclear chemists, and such work continues to be a major area of nuclear chemical research. One of us (GTS) has been intimately involved in the discovery and characterization of these transuranium elements.

In this chapter, we will discuss how to make these elements, their chemical properties, and their presence in the environment. The current list of transuranium elements is shown in Table 14.1 with a modern view of their place in the periodic table being shown in Figure 14.1.

14.2 Limits of Stability

There are about 290 known transuranium nuclei as of 2015. All these nuclei are unstable, with half-lives ranging from $\sim 10^{-9}$ to 10^{17} s (see Fig. 14.2). The longest-lived nuclei are those with lower atomic numbers. As the atomic number increases, the lifetimes become shorter with the lifetimes of the heaviest elements being tiny fractions of a second.

All transuranium nuclei are unstable with respect to α-decay, meaning that Q_α is positive for all these nuclei. In addition, nuclei with neutron–proton ratios differing from that of nuclei along the valley of β-stability can also decay either by β^- decay (rare in this region at present) or by β^+/EC decay. For most heavy nuclei, EC decay dominates over β^+ decay and consequently

Table 14.1 The Transuranic Elements.

Atomic Number	Element	Symbol
93	Neptunium	Np
94	Plutonium	Pu
95	Americium	Am
96	Curium	Cm
97	Berkelium	Bk
98	Californium	Cf
99	Einsteinium	Es
100	Fermium	Fm
101	Mendelevium	Md
102	Nobelium	No
103	Lawrencium	Lr
104	Rutherfordium	Rf
105	Dubnium	Db
106	Seaborgium	Sg
107	Bohrium	Bh
108	Hassium	Hs
109	Meitnerium	Mt
110	Darmstadtium	Ds
111	Roentgenium	Rg
112	Copernicium	Cn
113	Nihonium	Nh
114	Flerovium	Fl
115	Moscovium	Mc
116	Livermorium	Lv
117	Tennessine	Ts
118	Oganesson	Og

Names for elements 113, 115, 117, and 118 have not been accepted by the IUPAC (as of 2015).
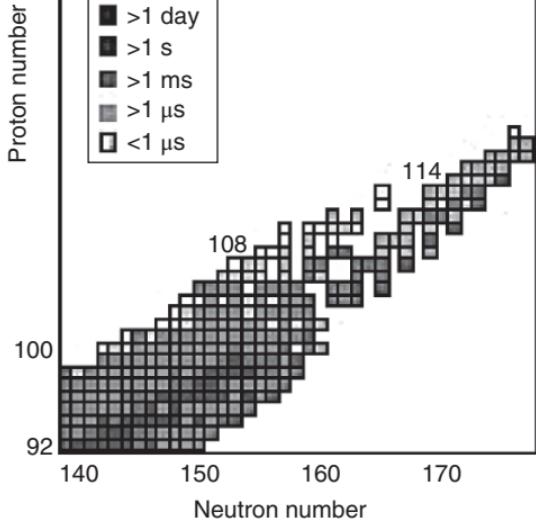
the neutron-deficient heavy nuclei decay by EC decay. As the atomic number of these nuclei increases, the importance of decay by spontaneous fission (SF) increases. Figure 14.3 shows the dominant decay mode for each of the transuranium nuclei. (A subtle bias occurs in preparing Fig. 14.3 in that SF is, in general, not an acceptable way to characterize a nucleus, due to the lack of a

Figure 14.1 The modern periodic table showing the transuranium elements (Reproduced with the IUPAC).

Figure 14.2 The half-lives of the known transuranium nuclei plotted as a function of Z and N (Karpov et al. (2012). Reproduced with the permission of World Scientific Publishing Co Pvt Ltd). (*See insert for color representation of the figure.*)

definitive way of establishing the Z, A of the fissioning system. Consequently, the heaviest *known* nuclei are α-emitters.) As was discussed in Chapter 11, the upper bound of the periodic table is given by SF for fundamental reasons. At some value of (Z,A), the SF half-life becomes so short that it prevents observation ($t_{1/2} < 10^{-9}$ s). Many transuranium nuclei decay by a combination
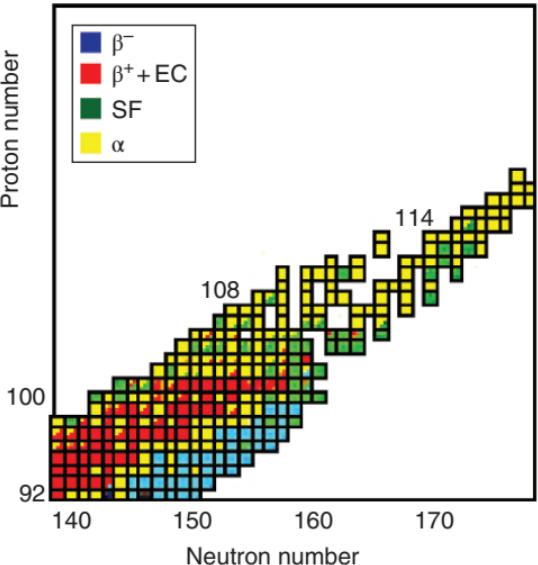
Figure 14.3 The dominant decay modes of the nuclei shown in Firgure 14.2 (Karpov et al. (2012). Reproduced with the permission of World Scientific Publishing Co Pvt Ltd). (*See insert for color representation of the figure.*)

Theoretical half-lives of transuranium nuclei
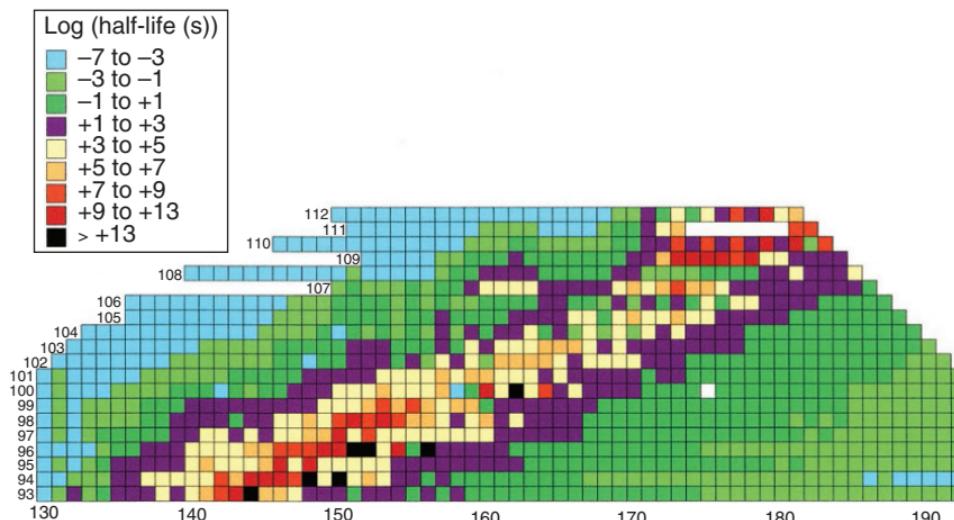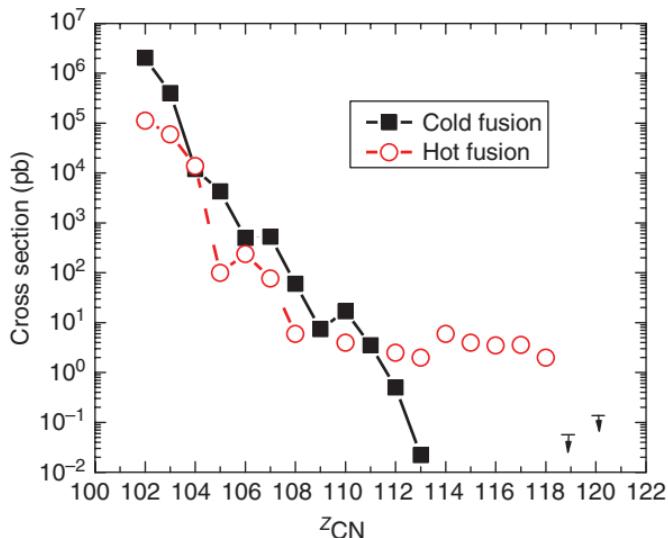
Figure 14.4 The predicted half-lives of the transuranium nuclei with $Z \leq 112$ (Möller (1997). Reproduced with the permission of John Wiley & Sons). (*See insert for color representation of the figure.*)

of EC, α-decay, and SF with the branching ratios for each mode depending on the (Z, A) of the nucleus.

What about the breadth of the distribution of heavy nuclei? What are the limits on $N–Z$? As in the lighter nuclei, the limits are set by the proton dripline ($S_p = 0$) and the neutron dripline ($S_n = 0$). For a typical heavy nucleus, nobelium, the proton dripline is predicted to be $N \sim 132$, while the neutron

Figure 14.5 The observed cross sections for the production of heavy elements by the "cold" and "hot" fusion reactions. (*See insert for color representation of the figure.*)

dripline is predicted to be $N \sim 236$ (Möller et al., 1997). The range of presently known nobelium isotopes goes from $N = 148$ to $N = 160$. Thus, it is unlikely that one will be limited by the neutron dripline for heavy nuclei, while the proton dripline may be reachable with some effort, rather the range of isotopes is limited by the production mechanisms. Figure 14.4 shows the calculated changes in the half-lives of the heavy nuclei, as they become more neutron rich. Comparison of Figures 14.2 and 14.4 show that the predicted half-lives increase by orders of magnitude as the neutron number increases modestly from those currently observed. This effect motivated recent work to make more neutron-rich heavy nuclei to study their chemistry and atomic physics. The underlying science behind these trends is that increasing $N-Z$ decreases Z^2/A (reducing SF decay) and decreases Q_α (reducing the α-decay probability), and this consequently leads to nuclei that decay by β^- decay, a slower process.

The heaviest transuranium nuclei ($Z > 100$) all lie on the n-deficient side of β^- stability. This is due to the fact that they are made in fusion–evaporation reactions where two nuclei on the line of β-stability combine, producing a nucleus that is neutron deficient that de-excites by emitting neutrons. For example, the most neutron-rich isotope of Sg (as of 2016) is ^{271}Sg. The β-stable isotope of Sg is ^{276}Sg. Since the half-lives of the transactinide nuclei generally get larger as their neutron numbers approach the $N = 184$ shell, this neutron-deficient character of the heaviest actinides represents a challenge for people who need or want to make longer-lived nuclei for studies of atomic physics and chemistry.

14.3 Element Synthesis

The synthesis of a new element involves more than just colliding two nuclei whose atomic numbers are such that they sum to an unknown value. Heavy nuclei are, in general, quite fissionable. If they are made with significant excitation, they will decay by fission, leaving no identifiable heavy residue of their formation. So one must balance carefully the factors governing the "production" of a new nucleus with those factors governing its "survival." The "production factors" determine the yield of the primary reaction products, while the "survival factors" determine which primary product nuclei de-excite by particle emission, which allows them to survive, or which nuclei de-excite by fission, which destroys them. Among the "production factors" are items such as the "starting material," the target nuclei, which must be available in sufficient quantity and suitable form. We must have enough transmuting projectile nuclei also. The transmutation reaction must occur with adequate probability to insure a good yield of the product nucleus in a form suitable for further study. Equally important is that the product nuclei be produced with excitation energy and angular momentum distributions such that the product nuclei will de-excite by particle or photon emission rather than the disastrous fission process. The competition between particle emission and fission as de-excitation paths depends on excitation energy, angular momentum, and the intrinsic stability of the product nucleus, which is related to the atomic and mass numbers of the product.

Nuclear synthesis is similar in some ways to inorganic or organic chemical syntheses with the synthetic chemist or physicist having to understand the reactions involved and the structure and stability of the intermediate species. While in principle, the outcome of any synthesis reaction is calculable, in practice such calculations are, for the most part, very difficult. Instead, the cleverness of the scientists involved, their manipulative skills, and the instrumentation available for their use determine the success of many synthetic efforts. The synthesis reactions used to "discover" the transuranium elements are given in Tables 14.2 and 14.3. All these reactions are complete fusion reactions in which the reacting nuclei fuse, equilibrate, and de-excite in a manner independent of their mode of formation. Other production reactions involving a partial capture of the projectile nucleus are also possible.

The cross section for production of a heavy evaporation residue, σ_{EVR}, by a complete fusion reaction can be written as

$$\sigma_{EVR} = (\text{fusion probability})(\text{survival probability}) \tag{14.1}$$

where the "fusion probability" refers to the probability of forming a completely fused system in the reaction and the survival probability refers to the probability that the excited complete fusion product will de-excite by particle emission rather than fission, which destroys the nucleus. Synthesis reactions for heavy nuclei are divided into "cold" or "hot" fusion. Cold fusion reactions involve

Table 14.2 Summary of the Initial Synthesis of the Transuranic Elements, $Z \leq 104$.

Atomic Number	Name (Symbol)	Synthesis Reaction	Half-life
93	Neptunium (Np)	$^{238}\text{U} + n \rightarrow {}^{239}\text{U} + \gamma$	
		$^{239}\text{U} \rightarrow {}^{239}\text{Np} + e^- + \overline{\nu}_e$	2.35 days
94	Plutonium (Pu)	$^{238}\text{U} + {}^{2}\text{H} \rightarrow {}^{238}\text{Np} + 2n$	
		$^{238}\text{Np} \rightarrow {}^{238}\text{Pu} + e^- + \overline{\nu}_e$	86.4 years
95	Americium (Am)	$^{239}\text{Pu} + n \rightarrow {}^{240}\text{Pu} + \gamma$	
		$^{240}\text{Pu} + n \rightarrow {}^{241}\text{Pu} + \gamma$	
		$^{241}\text{Pu} \rightarrow {}^{241}\text{Am} + e^- + \overline{\nu}_e$	433 years
96	Curium (Cm)	$^{239}\text{Pu} + {}^{4}\text{He} \rightarrow {}^{242}\text{Cm} + n$	162.5 days
97	Berkelium (Bk)	$^{241}\text{Am} + {}^{4}\text{He} \rightarrow {}^{243}\text{Bk} + 2n$	4.5 h
98	Californium (Cf)	$^{242}\text{Cm} + {}^{4}\text{He} \rightarrow {}^{245}\text{Cf} + n$	44 min
99	Einsteinium (Es)	"Mike" thermonuclear explosion producing ^{253}Es	20 days
100	Fermium (Fm)	"Mike" thermonuclear explosion producing ^{255}Fm	20 h
101	Mendelevium (Md)	$^{253}\text{Es} + {}^{4}\text{He} \rightarrow {}^{256}\text{Md} + n$	76 min
102	Nobelium (No)	$^{244}\text{Cm} + {}^{12}\text{He} \rightarrow {}^{252}\text{No} + 4n$	2.3 s
103	Lawrencium (Lr)	$^{250,1,2}\text{Cf} + {}^{11}\text{B} \rightarrow {}^{258}\text{Lr} + 3 - 5n$	
		$^{250,1,2}\text{Cf} + {}^{10}\text{B} \rightarrow {}^{258}\text{Lr} + 2 - 4n$	4.3 s
104	Rutherfordium (Rf)	$^{249}\text{Cf} + {}^{12}\text{C} \rightarrow {}^{257}\text{Rf} + 4n$	3.4 s
		$^{249}\text{Cf} + {}^{13}\text{C} \rightarrow {}^{259}\text{Rf} + 3n$	3.8 s

a heavier projectile (Ar to Kr) interacting with a Pb or Bi nucleus, where the excitation energy of the completely fused system is low ($\sim$13 MeV), giving high survival probabilities. Unfortunately the fusion probability in such systems is low. Hot fusion reactions involve the use of lighter projectiles (^{11}B to ^{48}Ca) interacting with actinide nuclei, giving a high fusion probability but a high excitation energy ($E * \sim$30–50 MeV) with a resulting low survival probability.

The reactions shown in Tables 14.2 and 14.3 can be divided into four classes: the neutron-induced reactions ($Z = 93, 95, 99, 100$), the light-charged particle-induced reactions ($Z = 94, 96$–$98, 101$), the "hot fusion" reactions ($Z = 102 - 106, 113$–118), and the "cold fusion" reactions ($Z = 107 - 113$). In the neutron-induced reactions used to make the transuranium nuclei, the capture of a neutron does not create a new element, but the subsequent β^- decays do. Light-charged particle reactions with exotic actinide target nuclei allow one to increase the atomic number of the product one or two units from the target nucleus. To make the heaviest elements, one needs

...ol)	Synthesis Reaction	H...
...b)	$^{249}\text{Cf} + {}^{15}\text{N} \rightarrow {}^{260}\text{Db} + 4n$	1
...m (Rf)	$^{249}\text{Cf} + {}^{18}\text{O} \rightarrow {}^{263}\text{Sg} + 4n$	0
...)	$^{209}\text{Bi} + {}^{54}\text{Cr} \rightarrow {}^{262}\text{Bh} + n$	1
...)	$^{208}\text{Pb} + {}^{58}\text{Fe} \rightarrow {}^{265}\text{Hs} + n$	1
...(Mt)	$^{209}\text{Bi} + {}^{58}\text{Fe} \rightarrow {}^{266}\text{Mt} + n$	3
...m (Ds)	$^{209}\text{Bi} + {}^{59}\text{Co} \rightarrow {}^{267}\text{Ds} + n$	2
	$^{208}\text{Pb} + {}^{62}\text{Ni} \rightarrow {}^{269}\text{Ds} + n$	1
	$^{208}\text{Pb} + {}^{64}\text{Ni} \rightarrow {}^{271}\text{Ds} + n$	5
	$^{244}\text{Pu} + {}^{34}\text{S} \rightarrow {}^{273}\text{Ds} + 5n$	1
...n (Rg)	$^{209}\text{Bi} + {}^{64}\text{Ni} \rightarrow {}^{272}\text{Rg} + n$	3
...(Cn)	$^{208}\text{Pb} + {}^{70}\text{Zn} \rightarrow {}^{277}\text{Cn} + n$	0
...h)	$^{209}\text{Bi} + {}^{70}\text{Zn} \rightarrow {}^{278}113 + n$	0
	$^{243}\text{Am} + {}^{48}\text{Ca} \rightarrow {}^{288}115 + 3n \rightarrow {}^{284}113$	0
...l)	$^{242}\text{Pu} + {}^{48}\text{Ca} \rightarrow {}^{286-288}\text{Fl} + (4-2)n$	0
...Mc)	$^{243}\text{Am} + {}^{48}\text{Ca} \rightarrow {}^{288}115 + 3n$	8
...(Lv)	$^{248}\text{Cm} + {}^{48}\text{Ca} \rightarrow {}^{292,293}\text{Lv} + 4, 3n$	1
...Ts)	$^{249}\text{Bk} + {}^{48}\text{Ca} \rightarrow {}^{283}117 + 4n$	1
...Og)	$^{249}\text{Cf} + {}^{48}\text{Ca} \rightarrow {}^{294}118 + 3n$	0

...l Synthesis of the Transuranic Elements, $Z > 104$.

to add several protons to the target nucleus by a reaction with a heavy ion. Such "hot fusion" reactions with actinide target nuclei lead to highly excited intermediate species that decay mostly by fission but occasionally by emitting neutrons, thus producing new nuclei. However, as the atomic number of the product nuclei increases, so does the probability of fission leading to very poor survival probabilities for the putative new species. The Russian nuclear physicist Yuri Oganessian pointed out that a way around this problem was to fuse heavier projectile nuclei with target nuclei in the lead–bismuth region. Because of the special stability of the lead–bismuth nuclei due to two closed shells, the resulting fused species would be formed "cold" and could, with some reasonable probability, decay by only emitting a single neutron.

Figure 14.5 shows the results of measurements (filled squares) of the cross sections for cold fusion reactions as a function of the atomic number Z of the completely fused system. Also shown (as circles) are the cross sections for hot fusion reactions. The points for elements 119 and 120 represent upper limits for the cross sections. Clearly future efforts will focus on experiments at the femtobarn cross section level or lower. Current technology for cold fusion reaction studies would require ∼12 days to observe one event at a cross section level of 1 pb. Similarly, a cross section of 1 pb in a hot fusion reaction would require ∼6–19 days to observe one event. Using current technology, production of nuclei with femtobarn cross sections is a few atoms per year. From examining the data in Figure 14.5, it would also appear that hot fusion reactions might be the reactions of choice in pursuing future research in this area.

## 14.4 History of Transuranium Element Discovery
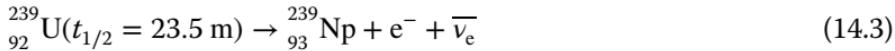
The first scientific attempts to prepare the elements beyond uranium were by Enrico Fermi, Emilio Segrè and coworkers in Rome in 1934, shortly after the existence of the neutron was discovered. This group of investigators irradiated uranium with slow neutrons and found several radioactive products, which were thought to be due to new elements. However, chemical studies by Otto Hahn and Fritz Strassmann in Berlin showed that these species were isotopes of the known elements created by the fission of uranium into two approximately equal parts. This discovery of nuclear fission in December of 1938 was thus a by-product of man's quest for the transuranium elements.

With poetic justice, the actual discovery of the first transuranium element came as part of an experiment to study the nuclear fission process. Edwin McMillan, working at the University of California at Berkeley in the spring of 1939, was trying to measure the energies of the two recoiling fragments from the neutron-induced fission of uranium. He placed a thin layer of uranium oxide on one piece of paper. Next to this he stacked very thin sheets of cigarette paper to stop and collect the uranium fission fragments. During his studies

he found there was another radioactive product of the reaction, one that did not recoil enough to escape the uranium layer, as did the fission products. He suspected that this product was formed by the capture of a neutron by the more abundant isotope of uranium, $^{238}_{92}$U. McMillan and Philip Abelson, who joined him in this research, showed in 1940 by chemical means that this product is an isotope of element 93, $^{239}_{93}$Np, formed in the following sequence:

$$^{238}_{92}\text{U} + ^{1}_{0}\text{n} \rightarrow ^{239}_{92}\text{U} + \gamma \tag{14.2}$$

and

$$^{239}_{92}\text{U}(t_{1/2} = 23.5 \text{ m}) \rightarrow ^{239}_{93}\text{Np} + \text{e}^- + \overline{\nu}_e \tag{14.3}$$
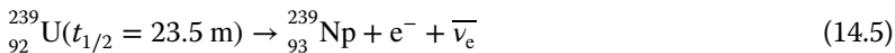
Neptunium, the element beyond uranium, was named after the planet Neptune because this planet is beyond the planet Uranus for which uranium was named.
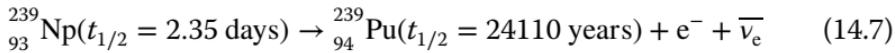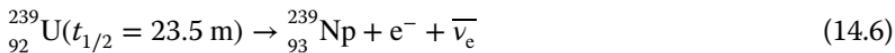
Plutonium was the second transuranium element to be discovered. By bombarding uranium with charged particles, in particular, deuterons (^{2}H), using the 60-in. cyclotron at the University of California at Berkeley, Glenn T. Seaborg, McMillan, Joseph W. Kennedy, and Arthur C. Wahl succeeded in preparing a new isotope of neptunium, ^{239}Np, which decayed by β^- emission to ^{238}Pu, that is,

$$^{238}_{92}\text{U} + ^{2}_{1}\text{H} \rightarrow ^{238}_{93}\text{Np} + 2\,^{1}_{0}\text{n} \tag{14.4}$$

and

$$^{239}_{92}\text{U}(t_{1/2} = 23.5 \text{ m}) \rightarrow ^{239}_{93}\text{Np} + \text{e}^- + \overline{\nu}_e \tag{14.5}$$

Early in 1941, ^{239}Pu, the most important isotope of plutonium, was discovered by Kennedy, Segrè, Wahl, and Seaborg. ^{239}Pu was produced by the decay of ^{239}Np, which in turn was produced by the irradiation of ^{238}U by neutrons, using the sequence of β decays following neutron capture on ^{238}U:

$$^{239}_{92}\text{U}(t_{1/2} = 23.5 \text{ m}) \rightarrow ^{239}_{93}\text{Np} + \text{e}^- + \overline{\nu}_e \tag{14.6}$$

$$^{239}_{93}\text{Np}(t_{1/2} = 2.35 \text{ days}) \rightarrow ^{239}_{94}\text{Pu}(t_{1/2} = 24110 \text{ years}) + \text{e}^- + \overline{\nu}_e \tag{14.7}$$

This isotope, ^{239}Pu, was subsequently shown to have a cross section for thermal neutron-induced fission that exceeded that of ^{235}U, a property that made it important for nuclear weapons, considering that it could be prepared by chemical separation as compared with isotopic separation that was necessary for ^{235}U. Plutonium was named after the planet Pluto, following the pattern used in naming neptunium.

The next transuranium elements to be discovered, americium and curium (Am and Cm; $Z = 95$ and 96, respectively) represent an important milestone in chemistry, the recognition of a new group of elements in the periodic table, the

actinides. According to the periodic table of the early 20th century, one expected americium and curium to be eka-iridium and eka-platinum, that is, to have chemical properties similar to iridium and platinum. In 1944, Seaborg conceived the idea that all the known elements heavier than actinium ($Z = 89$) had been misplaced in the periodic table. He postulated that the elements heavier than actinium might form a second series similar to the lanthanide elements (Fig. 14.1), called the actinide series. This series would end in element 103 (Lr) and, analogous to the lanthanides, would show a common oxidation state of +3.

Once this redox property and the actinide concept was understood, the use of appropriate chemical procedures led quickly to the identification of an isotope of a new element with a new α-emitting nuclide, now known to be $^{242}_{96}$Cm (half-life 162.9 days), which was identified by Seaborg, Albert Ghiorso, and Ralph James in the summer of 1944 by the bombardment of ^{239}Pu with 32-MeV helium ions:

$$^{239}_{94}\text{Pu} + ^{4}_{2}\text{He} \rightarrow ^{242}_{96}\text{Cm} + ^{1}_{0}\text{n} \tag{14.8}$$

The bombardment took place in the Berkeley 60-in. cyclotron after which the target material was shipped to the Metallurgical Laboratory at Chicago for chemical separation and identification. A crucial step in the identification of the α-emitting nuclide as an isotope of element 96, $^{242}_{96}$Cm, was the identification of a previously known isotope, $^{238}_{94}$Pu, as the α-decay daughter of the new nuclide.

Aside 14.1: Element Synthesis Calculations

The reactions used to synthesize heavy nuclei are, quite often, very improbable reactions, representing minor branches to the main reaction. Their probability of occurrence with respect to the main synthesis reaction is frequently $< 10^{-6}$. As such, it is intrinsically difficult to accurately describe these reactions from a theoretical point of view. Instead, workers in this field have frequently resorted to semiempirical prescriptions to guide their efforts.

To give one a feel for the magnitude of the quantities involved, we outline in the following text a very simple schematic method for estimating heavy element production cross sections. It is intended to show the relevant factors and should not be taken too seriously, except to indicate the order of magnitude of a particular formation cross section.

The German physicist Peter Armbruster has made an empirical systematic description of the probability of fusion of two heavy nuclei at energies near the reaction barrier. These systematics are shown in Figure 14.6. To use this graph, one picks values of the atomic number of projectile and target nuclei and reads off the expected value for the cross section for producing a completely fused species. The excitation energy of the completely fused species can then be read from Figure 14.7, which is based upon the nuclear masses of Peter Möller, J. Rayford Nix, and Karl-Ludwig
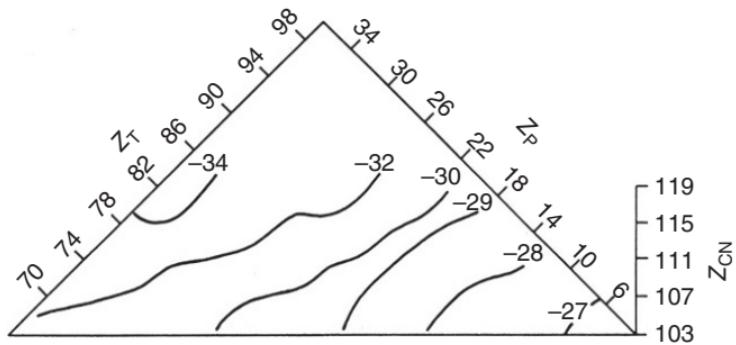
Figure 14.6 Contours of $log_{10}\ \sigma_{fus}$ as functions of the projectile atomic number, Z_p, and target atomic number, Z_T, where σ_{fus} is the s-wave fusion cross section at the interaction barrier.
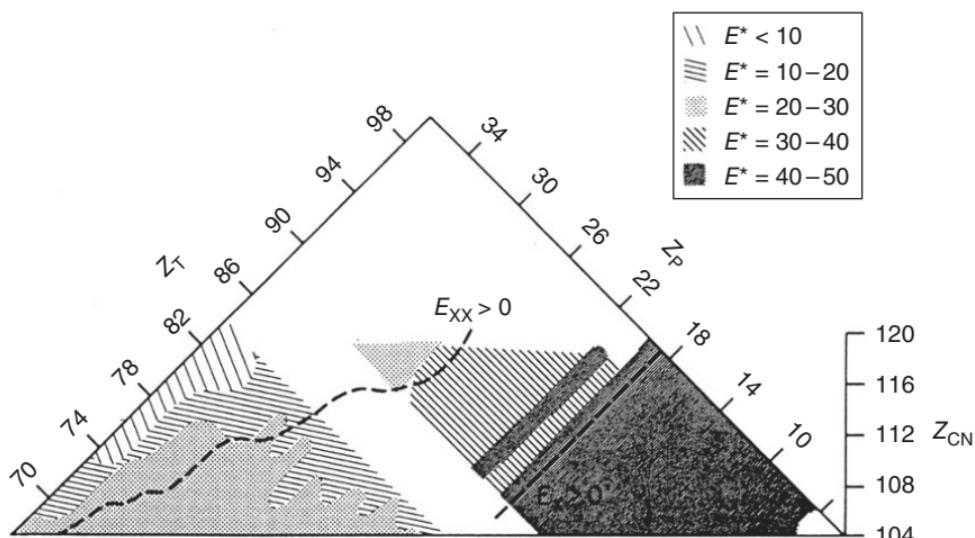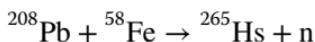

Figure 14.7 Excitation energy of the completely fused system formed from a given target, Z_T, and projectile, Z_p, combination. Reactions are assumed to take place at the interaction barrier.

Kratz. Taking as a rough rule of thumb, for each 10 MeV of excitation energy, the survival probability of the fused system drops by a factor of 10^2, one can then compute the cross section for producing a given species.

For example, the successful synthesis of ^{265}Hs (^{265}108) involved the reaction

$$^{208}\text{Pb} + {}^{58}\text{Fe} \rightarrow {}^{265}\text{Hs} + \text{n}$$
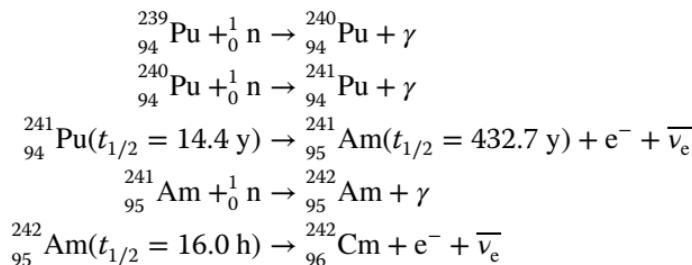
From Figure 14.6, one predicts the fusion cross section to be 10^{-32} cm^2, while Figure 14.7 suggests an excitation energy of $\sim$20 MeV. Thus, one would roughly estimate the overall cross section for producing ^{265}Hs to be

$$(10^{-32}\ \text{cm}^2)(10^{-2})(10^{-2}) = 10^{-36}\ \text{cm}^2$$

Note that the measured cross section was found to be $2 \times 10^{-35}\ \text{cm}^2$.

The identification of an isotope of element 95, by Seaborg, Ghiorso, James, and Leon Morgan in late 1944 and early 1945, followed the identification of this isotope of element 96 (^{242}Cm) as a result of the bombardment of ^{239}Pu with neutrons in a nuclear reactor. The production reactions, starting with multiple neutron capture by plutonium, are

$$^{239}_{94}\text{Pu} + {}^1_0\text{n} \rightarrow {}^{240}_{94}\text{Pu} + \gamma$$
$$^{240}_{94}\text{Pu} + {}^1_0\text{n} \rightarrow {}^{241}_{94}\text{Pu} + \gamma$$
$$^{241}_{94}\text{Pu}(t_{1/2} = 14.4\ \text{y}) \rightarrow {}^{241}_{95}\text{Am}(t_{1/2} = 432.7\ \text{y}) + \text{e}^- + \overline{\nu}_{\text{e}}$$
$$^{241}_{95}\text{Am} + {}^1_0\text{n} \rightarrow {}^{242}_{95}\text{Am} + \gamma$$
$$^{242}_{95}\text{Am}(t_{1/2} = 16.0\ \text{h}) \rightarrow {}^{242}_{96}\text{Cm} + \text{e}^- + \overline{\nu}_{\text{e}}$$

The years after World War II led to the discovery of elements 97–103 and the completion of the actinide series. While the story of the discovery of each of these elements is fascinating, we shall, in the interests of brevity, refer the reader elsewhere (see Bibliography list) for detailed accounts of most of these discoveries. As an example of the techniques involved, we shall discuss the discovery of element 101 (mendelevium).

The discovery of mendelevium was one of the most dramatic in the sequence of transuranium element syntheses. It marked the first time in which a new element was produced and identified one atom at a time. By 1955, scientists at Berkeley had prepared an equilibrium amount of about 10^9 atoms of $^{253}_{99}$Es by neutron irradiation of plutonium in the Materials Testing Reactor in Idaho. As the result of a "back of the envelope" calculation done by Ghiorso during an airplane flight, they thought it might be possible to prepare element 101 using the reaction

$$^{253}_{99}\text{Es} + {}^4_2\text{He} \rightarrow {}^{256}_{101}\text{Md} + {}^1_0\text{n} \tag{14.9}$$

The amount of element 101 expected to be produced in an experiment can be calculated using the formula

$$N_{101} = \frac{N_{\text{Es}}\sigma\phi\left(1 - e^{-\lambda t}\right)}{\lambda} \tag{14.10}$$

where N_{101} and N_{Es} are the number of element 101 atoms produced and the number of $^{253}_{99}$Es target atoms, respectively, σ is the reaction cross section (estimated to be $\approx 10^{-27}\ \text{cm}^2$), ϕ is the helium ion flux ($\approx 10^{14}$ particles/s), λ is the

decay constant of the product, $_{101}^{256}\text{Md}$ (estimated to be $\approx 10^{-4}$/s), and t is the length of the bombardment ($\approx 10^4$s, just under 3 h). Substituting these values,

$$N_{101} = \frac{\left(10^9\right)\left(10^{-27}\right)\left(10^{14}\right)\left(1 - e^{(-10^{-4}10^4)}\right)}{10^{-4}} \approx 1 \qquad (14.11)$$

Thus the production of only one atom of element 101 per experiment could be expected with the available number of target atoms.

Adding immensely to the complexity of the experiment was the absolute necessity for the chemical separation of the one atom of element 101 from the 10^9 atoms of einsteinium in the target and its ultimate, complete chemical identification by separation with the ion exchange method. This separation and identification would presumably have to take place in a period of hours or perhaps even 1 h or less. Furthermore, the target material had a 20-day half-life, and one needed a nondestructive technique allowing the target material to be recycled into another target for a subsequent bombardment.

The definitive experiments were performed in a memorable, all-night session, on February 18, 1955. To increase the number of events that might be observed at one time, three successive 3-h bombardments were made, and, in turn, their transmutation products were quickly and completely separated by the ion exchange method. Some of the target nuclide ^{253}Es was present in each case along with ^{246}Cf produced from ^{246}Cm also present in the target (via the ^{244}Cm ($^4\text{He}, 2n$) reaction). The important chemical step was to define the positions (volumes of extractant) at which the elements were eluted from the column containing the ion exchange resin. Five SF counters then were used to count simultaneously the corresponding drops of solution from the three runs. A total of 5 SF counts was observed in the element 101 position, while a total of 8 SF counts were also observed in the element 100 position. No such counts were observed in any other position. The original data are presented in Figure 14.8.

Aside 14.2: Detection of Heavy Element Atoms

The detection of atoms of a new element has always focused on measuring the atomic number of the new species and showing that it is different from all known atomic numbers, Z. Unambiguous methods for establishing the atomic number include chemical separations, measurement of the X-ray spectrum accompanying a nuclear decay process, or establishment of a genetic relationship between the unknown new nucleus and some known nuclide. As the quest for new elements focuses on still heavier species, the probability of producing the new elements has generally decreased, and one has had to devote increasing attention to the problem of detecting a few atoms of a new species amidst a background of many orders of magnitude more of other atoms. Thus, modern attempts to make new heavy element atoms usually involve some kind of physical separation.
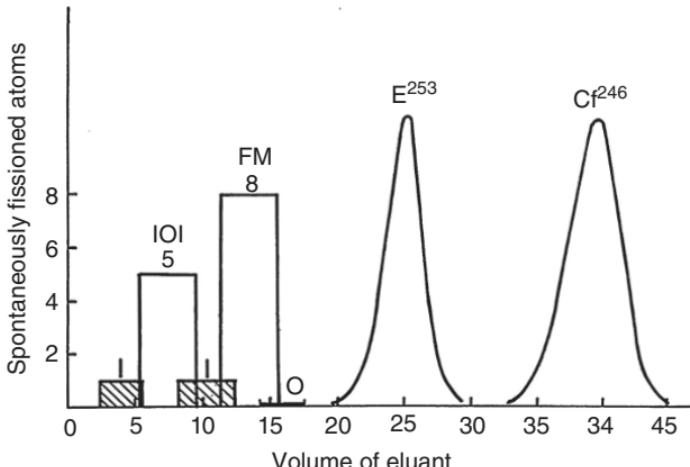
Figure 14.8 Original elution data corresponding to the discovery of mendelevium, February 18, 1955. The curves for ^{253}Es (given the old symbol E253) and ^{246}Cf were determined by α particle emission. (Dowex 50 ion exchange resin was used, and the eluting agent was ammonium α-hydroxyisobutyrate.)
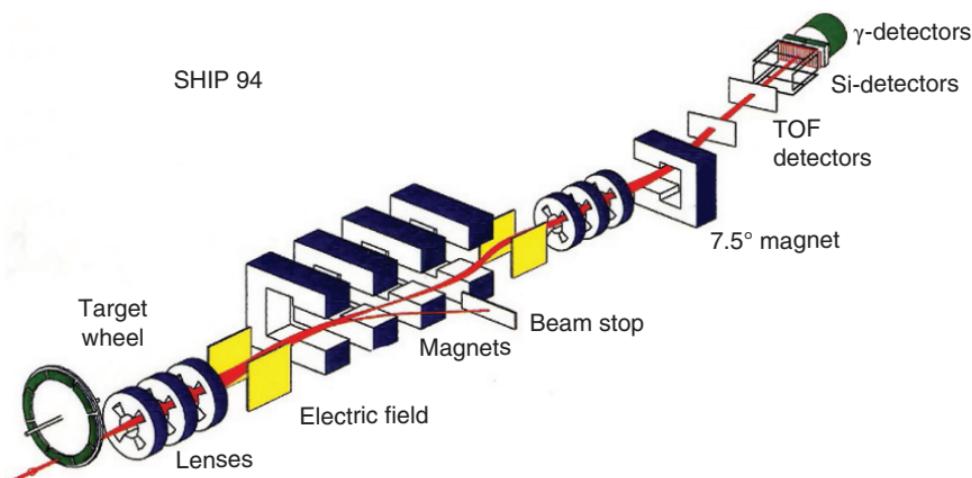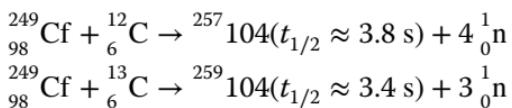

Figure 14.9 A schematic diagram of the SHIP velocity filter separator at the GSI in Germany. (*See insert for color representation of the figure.*)

An example of a modern separator is the SHIP velocity filter (Fig. 14.9) at the GSI in Darmstadt, Germany. In this separator, nuclear reaction products (from the target wheel) undergo different deflections (in crossed electric and magnetic fields) depending on whether they are fission fragments, scattered beam particles, or the desired heavy element residues. The efficiency of the separator is ~50% for heavy element residues, while transfer products and scattered beam nuclei are rejected by factors of 10^{14} and 10^{11}, respectively. The heavy recoil atoms are implanted in the

silicon detectors. Their implantation energy and position are correlated with any subsequent decays of the nuclei to establish genetic relationships to known nuclei.

The synthesis of the **transactinides** is noteworthy from a chemical and a nuclear viewpoint. From the chemical point of view, rutherfordium ($Z = 104$) is important as an example of the first transactinide element. From Figure 14.1, we would expect rutherfordium to behave as a Group 4 (IV-B) element, such as hafnium or zirconium, but not like the heavy actinides. Its solution chemistry, as deduced from chromatography experiments, is different from that of the actinides and resembles that of zirconium and hafnium. More recently, detailed gas chromatography has shown important deviations from expected periodic table trends and relativistic quantum chemical calculations.
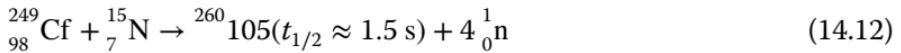
The work on the discovery and identification of elements 104–106 was controversial and contentious due, in part, to the difficulty of the experiments. Looking back now, the following series of experiments clearly identified these elements. Ghiorso et al. (1969) produced isotopes of element 104 in experiments at Berkeley in 1969. The nuclear reactions involved were

$$\,^{249}_{98}\text{Cf} + \,^{12}_{6}\text{C} \rightarrow \,^{257}104(t_{1/2} \approx 3.8 \text{ s}) + 4\,^{1}_{0}\text{n}$$
$$\,^{249}_{98}\text{Cf} + \,^{13}_{6}\text{C} \rightarrow \,^{259}104(t_{1/2} \approx 3.4 \text{ s}) + 3\,^{1}_{0}\text{n}$$

The atomic numbers of these isotopes were identified by detecting the known nobelium daughters of these two nuclei. The group suggested the name of rutherfordium (chemical symbol Rf) for element 104 in honor of Lord Ernest Rutherford.

Contemporaneously with these experiments, Zvara et al. (1970), working at Dubna, produced $^{259}104(3.2 \pm 0.8 \text{ s})$ by the $^{242}_{94}\text{Pu}(^{22}_{10}\text{Ne}, 5\text{n})$ reaction. The chloride of this spontaneously fissioning activity was shown to be slightly less volatile than Hf but more volatile than the actinides using gas chromatography. An international group of reviewers (Barber et al., 1992) has determined that the Berkeley and Dubna groups should share the credit for the discovery of element 104 and has suggested the name of rutherfordium for element 104.

In 1970, Ghiorso et al. (1970) reported the observation of an isotope of element 105 produced in the reaction

$$\,^{249}_{98}\text{Cf} + \,^{15}_{7}\text{N} \rightarrow \,^{260}105(t_{1/2} \approx 1.5 \text{ s}) + 4\,^{1}_{0}\text{n} \tag{14.12}$$

The Z and A of this isotope were established by correlations between the parent $^{260}105$ and its daughter ^{256}Lr. They suggested the name of hahnium (chemical symbol Ha) for this element in honor of the German radiochemist Otto Hahn, codiscoverer of fission. In a series of experiments occurring at a similar time, Druin et al. (1971) identified a mother–daughter pair from the decay of $^{260,261}105$ formed in the reactions $^{243}_{95}\text{Am}(^{22}_{10}\text{Ne}, 4, 5n)$. A name of nielsbohrium
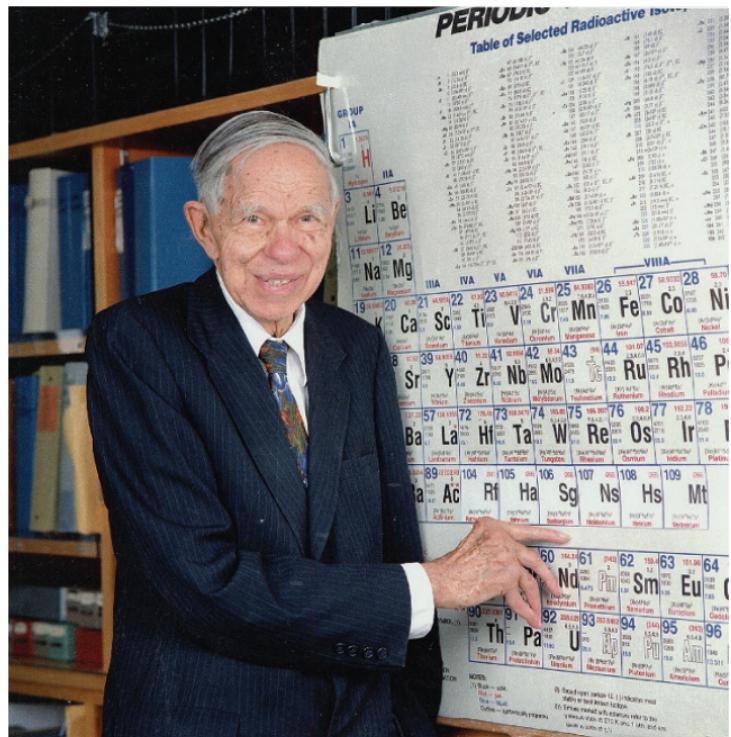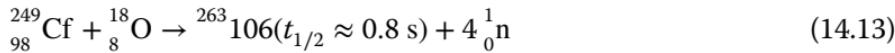
Figure 14.10 Glenn Seaborg points out the position of seaborgium (Sg) in the periodic table. (*See insert for color representation of the figure.*)
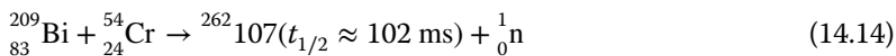
(chemical symbol Ns) was suggested for this element in honor of the Danish physicist Niels Bohr by the Russian group. Later the international group (Barber et al., 1992) also suggested that credit for this discovery be shared and subsequently the name of dubnium (chemical symbol Db) was assigned to this element.

Element 106 was first synthesized by Ghiorso et al. (1974) at Berkeley in 1974 using the reaction

$$^{249}_{98}\text{Cf} + ^{18}_{8}\text{O} \rightarrow ^{263}106(t_{1/2} \approx 0.8 \text{ s}) + 4\,^{1}_{0}\text{n} \tag{14.13}$$

The nuclide was identified by genetic links to its daughters ^{259}Rf and ^{255}No. This synthesis was reconfirmed almost twenty years later in 1993 by Gregorich et al. (1994). Element 106 has been named seaborgium (symbol Sg) after one of the authors of this book. Glenn, the codiscoverer of plutonium and nine other transuranium elements, said upon this occasion (cf. Fig. 14.10), "It is the greatest honor ever bestowed upon me—even better, I think, than winning the Nobel Prize."

In 1981, G. Münzenberg et al. (1981), working in Darmstadt (West Germany at the time) using the velocity filter SHIP, identified the isotope ^{262}Bh produced in the "cold fusion" reaction

$$\,^{209}_{83}\text{Bi} + \,^{54}_{24}\text{Cr} \rightarrow \,^{262}107(t_{1/2} \approx 102 \text{ ms}) + \,^{1}_{0}\text{n} \qquad (14.14)$$

This nuclide was identified by genetic links to the sequence of its α-decay daughters: ^{258}Db, ^{254}Lr, ^{250}Md, ^{250}Fm, and ending with ^{246}Cf. The cross section reported for this reaction was ≈200 pb (~1/5,000,000 of the production cross section assumed for the reaction used in the discovery of Md). This element was named bohrium (chemical symbol Bh) in honor of Niels Bohr.

In 1984, Münzenberg et al., (1981) continuing to work at Darmstadt (Münzenberg et al., 1984b, 1987), produced three atoms of ^{265}Hs using the "cold fusion" reaction ^{208}Pb(^{58}Fe, 1n). ^{265}Hs was identified by genetic links to its α-particle emission daughter and granddaughter: ^{261}Sg and ^{257}Rf. The half-life of this nucleus was ≈1.8 ms. The production cross section was ≈20 pb. At a similar time, Oganessian et al. (1984) reported the production of $^{263-265}$Hs in the reactions ^{209}Bi(^{55}Mn, n), ^{206}Pb(^{58}Fe, n), ^{207}Pb(^{58}Fe, n), and ^{208}Pb(^{58}Fe, n). The Russian group reported observation of SF and α-decays of the granddaughter and great-great-great-granddaughters. Because of this weaker identification, credit for this discovery (Barber et al., 1992) was assigned to the Darmstadt group, who suggested the name of hassium (chemical symbol Hs) in honor of the region of Germany, Hesse, in which the work was done.

In 1982, Münzenberg et al. (1982, 1984a) reported the observation of one atom of element 109 formed in the reaction ^{209}Bi(^{58}Fe, n). The production cross section was 10 pb. This discovery was confirmed by the later observation of more atoms at Darmstadt (Hofmann et al., 1997). The discoverers suggested the name of meitnerium (chemical symbol Mt) in honor of Lise Meitner.

In 1991, Ghiorso et al. (1995a,b) studied the reaction of ^{209}Bi with ^{59}Co. They found one event that they associated with the production of ^{267}110 (^{267}Ds). The evaporation residue formed decayed by the emission of an 11.6 MeV α-particle 4 μs after implantation. Their evidence for the formation of ^{267}110 was weakened by the inability (due to malfunctioning electronics) to detect the decay of the daughter ^{263}Hs although the decay of other members of the decay chain was observed. Further work was not pursued by this group due to the closure of the accelerator used to produce the beam. This observation was probably correct although the evidence presented is not strong enough to justify the claim of element discovery.

On the other hand, there is no doubt that Hofmann et al. (1995b), working in Darmstadt in 1994, observed the production of four atoms of ^{269}Ds in the reaction ^{208}Pb(^{62}Ni, n). This nuclide was identified by genetic links to its daughters ^{265}Hs, ^{261}Sg, ^{257}Rf, and ^{253}No. The neutron-rich isotope of element 110, ^{271}Ds, was produced later (Hofmann, 1998) using the reaction ^{208}Pb(^{64}Ni, n). Nine atoms were observed and identified. This latter reaction was also used by

workers in Berkeley (Ginter et al., 2003) and RIKEN (Morita et al., 2004a) to confirm the discovery of element 110. The very n-rich isotope of element 110, ^{273}Ds, was observed by Lazarev et al. (1996) using the reaction ^{244}Pu(^{34}S, 5n). The name darmstadtium (chemical symbol Ds) has been given to this element in honor of the city in which it was discovered.

An unfortunate footnote to this chapter in the history of the discovery of the heaviest elements is the revelation (Hofmann et al., 2002) that one of the decay chains reported by Hofmann et al. (1995b) for ^{269}Ds was "spuriously created," the result of scientific misconduct, see following text. As disturbing as this finding is, it should not detract from the other correctly identified decay chains.
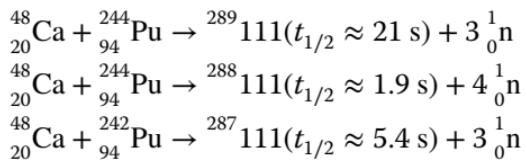
The first production of an isotope of element 111, ^{272}111 ($t_{1/2} \approx 1.5$ ms) was by Hofmann et al. (1995a) in 1994 using the reaction ^{209}Bi(^{64}Ni, n). Three decay chains were observed in 1994. Subsequently three more decay chains corresponding to the decay of ^{272}111 were reported (Hofmann et al., 2002) in 2002. The decay of ^{272}111 is convincingly linked to its daughters ^{268}Mt, ^{264}Bh, ^{260}Db, and ^{256}Lr. This discovery was confirmed in experiments at RIKEN in 2003 (Morita et al., 2004b).

In 1996, Hofmann et al. (1996) reported the formation of ^{277}112 in the reaction ^{208}Pb(^{70}Zn, n). Two decay chains were reported connecting ^{277}112 to its daughters ^{273}Ds, ^{209}Hs, ^{265}Sg, ^{261}Rf, and ^{257}No. Unfortunately one of these decay chains, the first one "observed," is now known (Hofmann et al., 2002) to also have been "spuriously created" by human error or scientific misconduct. A subsequent experiment (Hofmann et al., 2002) in 2000 resulted in the observation of an additional decay chain for ^{277}112. These results were confirmed by experiments at RIKEN in 2004 (Morita et al., 2007). It is now widely believed (S. Hofmann, private communication) that the same individual was responsible for both false reports, that is, one of the ^{269}Ds decay chains and one of the ^{277}112 decay chains along with false reports (see in the following text) of the synthesis of ^{293}118 and its decay products.

Three atoms of element 113 were produced in a cold fusion reaction (^{209}Bi + ^{70}Zn $\rightarrow$ ^{278}113 + n) at RIKEN in a series of experiments spanning the time from 2003 to 2012. 553 days of beam time was used in this effort with a reported production cross section of 22^{+20}_{-13} fb!! (Morita et al., 2012). This remarkable result also points out the special personal characteristics of those "heavy element" hunters. Imagine coming to work each 24-h day for almost 2 years and seeing no events on all but 3 days. It requires an unusual degree of fortitude and courage. Because of this, it will be difficult for another laboratory to confirm these results. This low cross section is usually taken to mean that cold fusion reactions are not useful to synthesizing even heavier elements.

Element 113 has also been produced in hot fusion reactions. Elements 115 and 113 were produced in 2003 using the ^{243}Am + ^{48}Ca → ^{288}115 + $3n$ → ^{284}113 reaction in experiments at Dubna (Oganessian et al., 2005). Element 113 was subsequently produced directly using the reaction ^{237}Np (^{48}Ca, 3n) ^{282}113 in work at Dubna (Oganessian, 2007). Element 113 was named nihonium (Nh) is recognition of the work of the Japanese group.

In 1999, Oganessian et al. (1999a,b, 2000a) reported the successful synthesis of five atoms of element 114 using the ^{48}Ca + ^{242,244}Pu reaction. The long half-lives associated with these atoms (approximately seconds to minutes) represent the possible approach to the long sought "island of stability" of superheavy nuclei near $Z = 114$ and $N = 184$. (All previous heavy nuclei with $Z \geq 110$ have decayed with millisecond half-lives.) The experimental group consisting of scientists from Dubna and the US Lawrence Livermore National Laboratory reported the following observations:

$$^{48}_{20}\text{Ca} + {}^{244}_{94}\text{Pu} \rightarrow {}^{289}111(t_{1/2} \approx 21 \text{ s}) + 3\,{}^{1}_{0}\text{n}$$
$$^{48}_{20}\text{Ca} + {}^{244}_{94}\text{Pu} \rightarrow {}^{288}111(t_{1/2} \approx 1.9 \text{ s}) + 4\,{}^{1}_{0}\text{n}$$
$$^{48}_{20}\text{Ca} + {}^{242}_{94}\text{Pu} \rightarrow {}^{287}111(t_{1/2} \approx 5.4 \text{ s}) + 3\,{}^{1}_{0}\text{n}$$

All these nuclei were observed to decay by a sequence of emitted α-particles with the decay chains ending in SF. Because these nuclei are very n-rich, their descendants have not been characterized before. These observations were confirmed in experiments at GSI (Düllmann et al., 2010) and Berkeley (Ellison et al., 2010). Element 114 was subsequently named flerovium (symbol Fl) after the Russian nuclear physicist G.N. Flerov.

As mentioned earlier, element 115 was synthesized in 2003 using the reaction ^{243}Am (^{48}Ca, 3n) ^{288}115 (Oganessian et al., 2005). Element 115 was named moscovium (Mc) in recognition of the work of the Russian discovery team. The cross section was $2.7^{+4.8}_{-1.6}$ pb. In a subsequent experiment ^{287}115 was observed in the reaction ^{243}Am (^{48}Ca, 4n).

Oganessian et al. (2000b, 2004) reported in 2000 the successful synthesis of three atoms of element 116 using the reaction $^{48}_{20}\text{Ca} + {}^{248}_{96}\text{Cm} \rightarrow {}^{292}\text{Lv} + 4\,{}^{1}_{0}\text{n}$. Each observed decay sequence involved the observation of three energetic α-particle decays followed by an SF. Subsequently the isotope ^{293}Lv was observed. Identification of these nuclei was aided by the previous characterization of their daughters populated in the synthesis of Fl. The synthesis of element 116 was confirmed at GSI (Hofmann et al., 2012). The name of livermorium (symbol Lv) was suggested (and adopted) for this element to reflect the role of the scientists from the Lawrence Livermore National Laboratory in the discovery experiments.

Element 117 was discovered by a collaboration of scientists from Dubna, Livermore, Oak Ridge, and Vanderbilt University. The key part of this effort was the production of a ^{249}Bk target ($t_{1/2} = 320$ days) at the Oak Ridge High Flux

Isotope Reactor. $^{293}117$ and ^{294} were observed in the ^{249}Bk (^{48}Ca, 3–4 n) reaction (Oganessian et al., 2010, 2011). Element 117 was named tennessine (Ts) is recognition of the contributions of the scientists from the Oak Ridge National Laboratory and Vanderbilt University in this experiment.

The isotope $^{294}118$ was synthesized, at Dubna, using the reaction ^{249}Cf (^{48}Ca, 3n) (Oganessian, 2006). A confirming observation was made in the study of the ^{249}Bk + ^{48}Ca reaction due to the decay of ^{249}Bk to form ^{249}Cf, which reacted with ^{48}Ca to form $^{294}118$ (Oganessian, 2012). Element 118 was named oganession (Og) in 2016 in recognition of the seminal contributions of Y.T. Oganessian to this field. As such, it is only the second element to be named after a living person.

In the midst of all the exciting advances in heavy element science in the period from 1994 to 2002, there was a dark chapter, the element 118 fiasco that occurred in Berkeley. In 1999, Ninov et al. (1999) reported the successful synthesis of three atoms of element 118 using the reaction ^{208}Pb(^{86}Kr, n)$^{293}118$. The evidence was stunning, consisting of three decay chains involving highly correlated high-energy α-particle decays after the implantation of a putative $^{293}118$. The reported production cross section was 2 pb, a number later revised to 7 pb. The result was quite unexpected because the empirical systematics of cold fusion cross sections (cf. Fig. 14.5) would have predicted femtobarn cross sections for this reaction.

Other laboratories were not able to reproduce this work (Hofmann and Münzenberg, 2000; Morimoto, 2001; Stodel et al., 2001), and eventually the Berkeley group reported their inability to reproduce the original observation as well (Ninov et al., 2002). A subsequent investigation (Gilchriese et al., 2003) revealed the original data had been fabricated by one individual, who was later connected to similar instances of fraud at Darmstadt in the work with elements 110 and 112 mentioned earlier. From these episodes, one sees that "science works," fraud will be found even in cases with extremely rare events, and the traditional method of independent confirmation of important findings is reaffirmed.

14.5 Superheavy Elements

Up until about 1970, it was thought that the practical limit of the periodic table would be reached at about element 108. By extrapolating the experimental data on heavy element half-lives, people concluded that the half-lives of the longest-lived isotopes of the heavy elements beyond about element 108 would be so short ($<10^{-6}$ s) due to SF decay that we could not produce and study them (cf. Fig. 14.11). However, in the late 1960s and early 1970s, nuclear theorists, using techniques developed by Vilen Strutinsky and Wladyslaw Swiatecki,
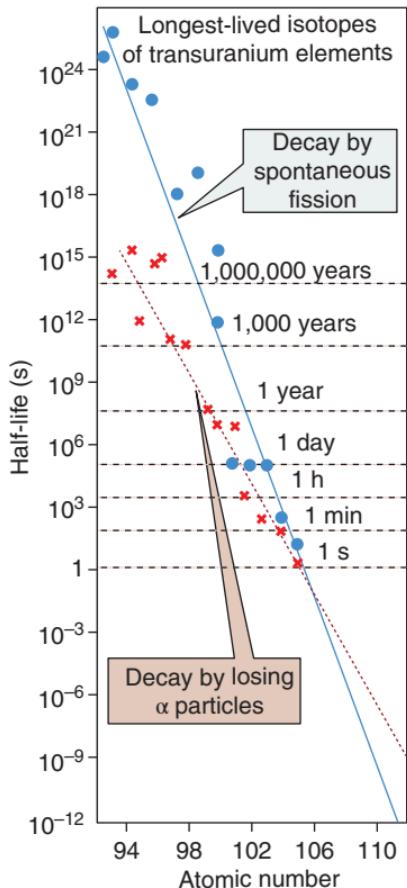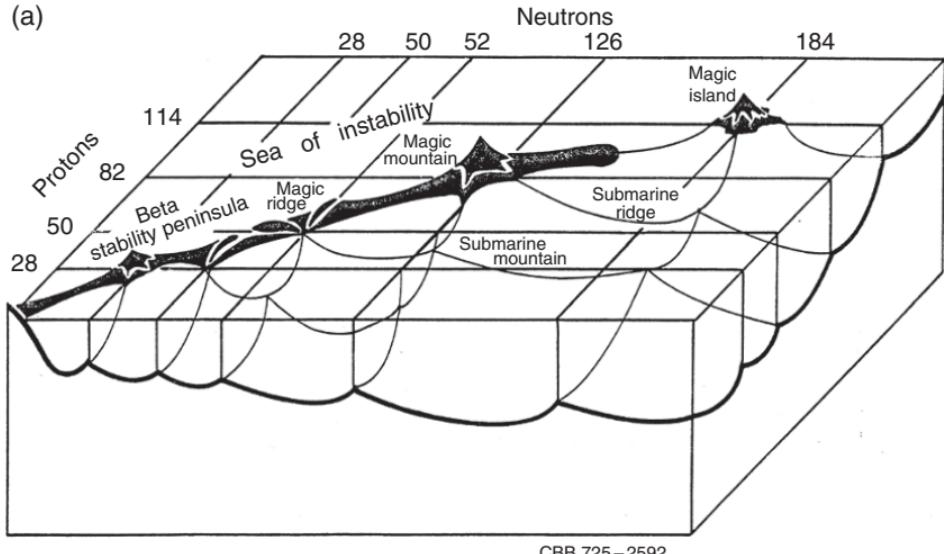
Figure 14.11 Half-lives of the longest-lived isotope of the heaviest elements versus atomic number, Z, circa 1970. (*See insert for color representation of the figure.*)

predicted that special stability against fission would be associated with proton number $Z = 114$ and neutron number $N = 184$. These "superheavy elements" were predicted to have half-lives reaching up to the order of the age of the universe. They were predicted to form an "island" of stability separated from the "peninsula" of known nuclei (see Fig. 14.12a). We now know these predictions were wrong, in part. While we believe there are a group of "superheavy" nuclei whose half-lives are relatively long compared to lower Z elements, we do not believe they form an "island" of stability. Rather, we picture them as a continuation of the peninsula of known nuclei (Fig. 14.12b). We also believe that their half-lives are short compared to geologic time scales. Therefore, they do not exist here on earth or in our solar system. The most stable of the superheavy nuclei, those with $Z = 112$, $N \approx 184$, are predicted to decay by α-particle emission with half-lives ≈ 20 days.

The principal problem associated with observing superheavy nuclei is not their possible existence (which is considered relatively certain) but rather how to make
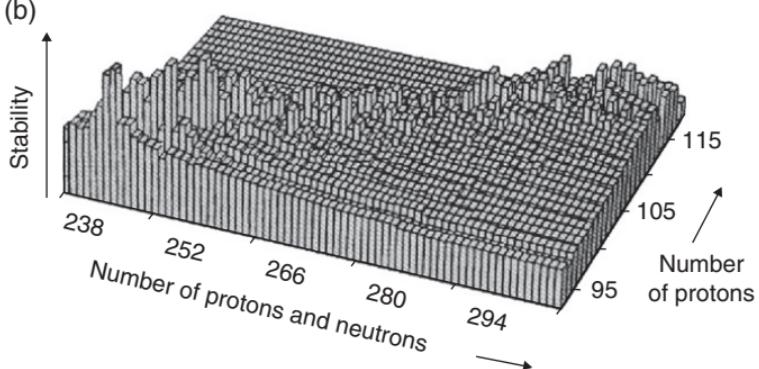
Figure 14.12 (a) An allegorical representation of heavy nuclide stability, circa 1975, showing the "superheavy island." (b) A modern plot of the predicted half-lives of the heaviest nuclei. Note there is a peninsula connecting the known and superheavy nuclei.

them. Literally hundreds of synthesis reactions have been proposed, and a number have been tried. Up to recently, all have failed because either the formation of the fused system is too improbable or its excitation energy is too large, resulting in too small a probability for formation of the product nuclei. For example, the most widely studied synthesis reaction is the ^{48}Ca + ^{248}Cm reaction. Using the information in Figures 14.6 and 14.7 as a guide, we roughly estimate the fusion cross section to be 3×10^{-32} cm^2, the excitation energy $\approx$30 MeV (survival probability $\sim 10^{-6}$), and a predicted formation cross section of 10^{-38} cm^2. With modern technology, this would correspond to one atom per month. This production rate is more or less at the limit of modern technology.
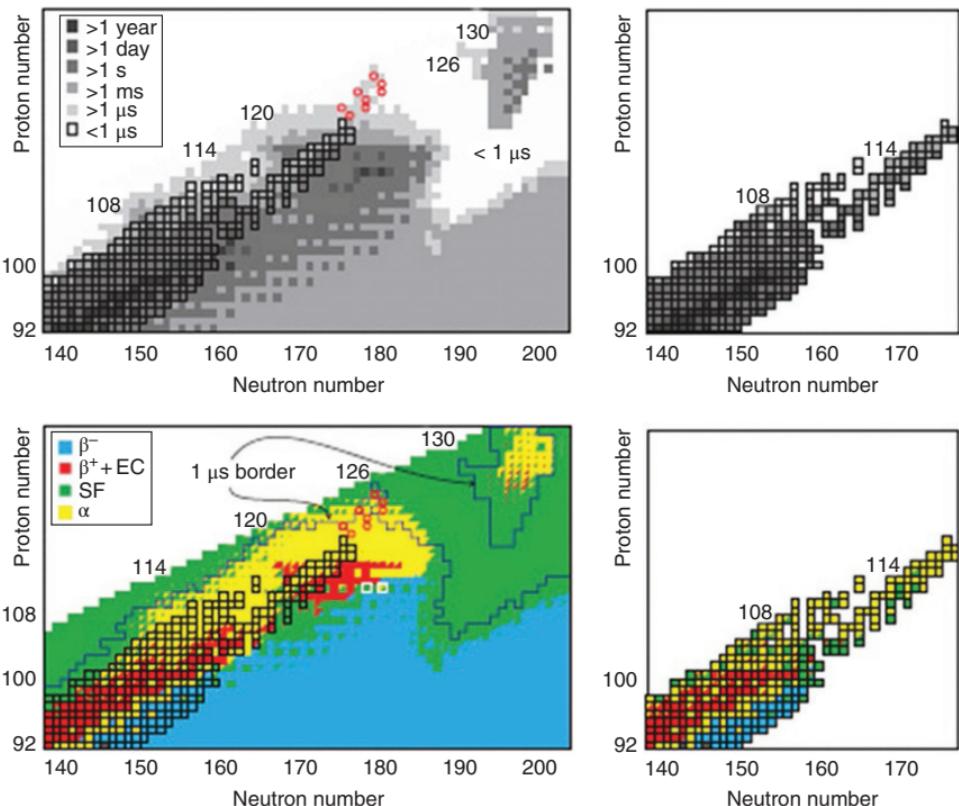
Figure 14.13 Total half-lives (top) and decay modes (bottom) of the transuranium nuclei. The left panels are predictions and the right panels are observations (Karpov et al. (2012). Reproduced with the permission of World Scientific Publishing Co Pvt Ltd). (*See insert for color representation of the figure.*)

As indicated in Section 14.4, observations of the synthesis of elements 113–118 have been reported with low (~pb) cross sections. In addition, instead of following the trends shown in Figure 14.11, the half-lives of the longest-lived known isotopes of elements 106–112 are reported to be approximately milliseconds to seconds, an enhancement of orders of magnitude in their lifetimes. Some have taken the viewpoint that, without the special stability associated with nuclear shell structure, elements as light as $Z = 106$–108 would have negligibly short half-lives. The mere existence of these nuclei with millisecond half-lives is a demonstration that we have already made "superheavy nucleim," according to this view. The shell stabilization of these nuclei, which are deformed, is due to the special stability of the $N = 162$ configuration in deformed nuclei. (The "traditional" superheavy nuclei with $Z \sim 114$, $N = 184$ were calculated to have spherical shapes.)

Our best theoretical predictions (Karpov et al., 2012) (along with what we have discovered to date) of the expected half-lives of the transuranium nuclei are shown in Figure 14.13. Clearly one expects new regions of very heavy nuclei

with half-lives that are substantially longer than those observed to date, but how to make them remains to be seen.

14.6 Chemistry of the Transuranium Elements

The chemical behavior of the transuranium elements is interesting because of its complexity and the insights offered into the chemistry of the lighter elements. The placing of these man-made elements into the periodic table (Fig. 14.1) represents one of the few significant alterations of the periodic table of Mendeleev. Since so little is known about the chemistry of the transactinide elements, one has the unique opportunity to test periodic table predictions of chemical behavior before the relevant experiments are done.

The actinide and known transactinide elements are transition elements, that is, they have partially filled f or d electronic orbitals. As such, they are metals. Similar to the other transition metals, most of them are sufficiently electropositive to dissolve in mineral acids. However, there is an important distinction that separates the actinide elements from the other transition elements, including the transactinide elements. The partially filled d orbitals of most transition elements extend out to the boundary of the atoms and are influenced greatly by (or can influence) the chemical environment of the atom or ion. Thus, the chemical properties of elements with partially filled d orbitals are highly complex and seem to vary somewhat irregularly as one passes from element to element. But the 5f orbitals of the actinides are better screened from the chemical environment of the atom or ion by the higher-lying s and p shell electrons, and thus there is a greater similarity in chemical properties among the actinides compared with the other transition elements. (Correspondingly, the 4f orbitals of the lanthanides are even better screened than the 5f actinide orbitals, and the chemical behavior of the lanthanides is even more homologous.) The greater extension of the 5f orbitals (relative to the 7s and 7p orbitals) compared with the lanthanide 4f orbitals allows some covalency in actinide bonding not seen with the lanthanides.

As the atomic number Z of the nucleus increases, the electrons generally become more tightly bound. As their binding energy increases, so does their velocity. For electrons in the 1 s shell, the average velocity is roughly Z au. (The speed of light, c, is 137.035 au.) Thus, for $Z = 90$, the velocity is $90c/137$ or $0.66c$. The Schrödinger equation is no longer appropriate, and one must use the fully relativistic treatment of Dirac.

The solution of the Dirac equation for the hydrogen-like atoms leads to wave functions that are products of radial and angular factors similar to the solutions of the Schrödinger equation that give the familiar orbitals. The angular factors are shown in Figure 14.14. Each state is specified by four quantum numbers whose meaning is slightly different than for the Schrödinger equation. The
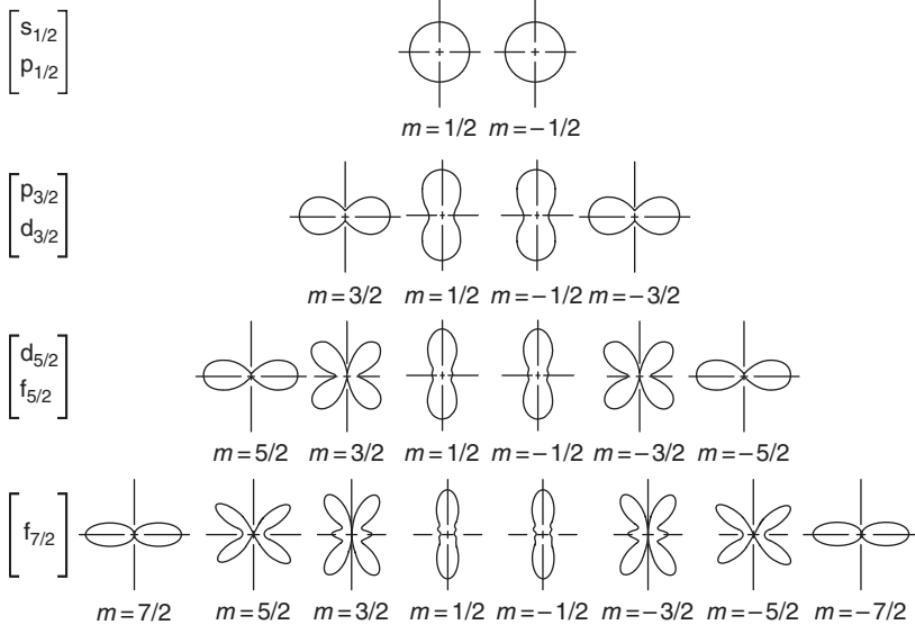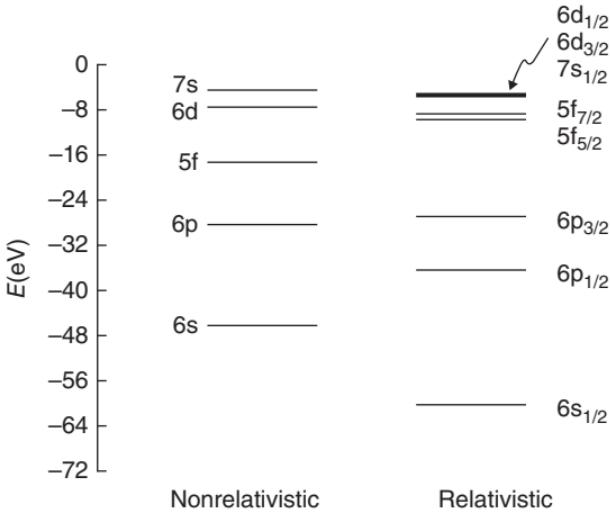
Figure 14.14 Pictorial representation of the relativistic orbital shapes (Adopted from White (1931)).

quantum numbers are n, the principal quantum number with values of 1, 2, 3, ...; ℓ, the azimuthal quantum number with values 0, 1, 2, ..., $n-1$, denoted by s, p, d, f, g; j, the total angular momentum quantum number with values of $\ell \pm 1/2$ (usually denoted as a subscript to ℓ), and m_j, the magnetic quantum number, taking on half-integer values of $\ell - 1/2$ and $\ell + 1/2$. Thus, the three degenerate p orbitals, the five d, and the seven f orbitals in the Schrödinger system split into pairs by total angular momentum: one $p_{1/2}$ plus two $p_{3/2}$ orbitals; two $d_{3/2}$ plus three $d_{5/2}$ orbitals; and three $f_{5/2}$ plus four $f_{7/2}$ orbitals. The maximum occupancy of each orbital is $(2j + 1)$. This arrangement is called "spin orbit" splitting because it represents the effect of coupling the spin and orbital angular momentum of each individual particle. The orbital shapes are governed by j and m_j. What is surprising to the traditional chemist about the shapes shown in Figure 14.14 is that the orbitals have either a spherical shape ($p_{1/2}$), a toroidal or doughnut shape ($p_{3/2}$, $m_j = 3/2$), or a dog-bone shape ($p_{3/2}$, $m_j = 1/2$). One should note that the state with the highest m_j value for a given j value always has a doughnut-shaped distribution, while the lowest value of m_j corresponds to a distribution stretched along the z-axis with no nodes. States of intermediate m are multilobed toroids.

Figure 14.15 A comparison of the predicted (nonrelativistic and relativistic) energies of the valence electronic levels for the uranium atom.
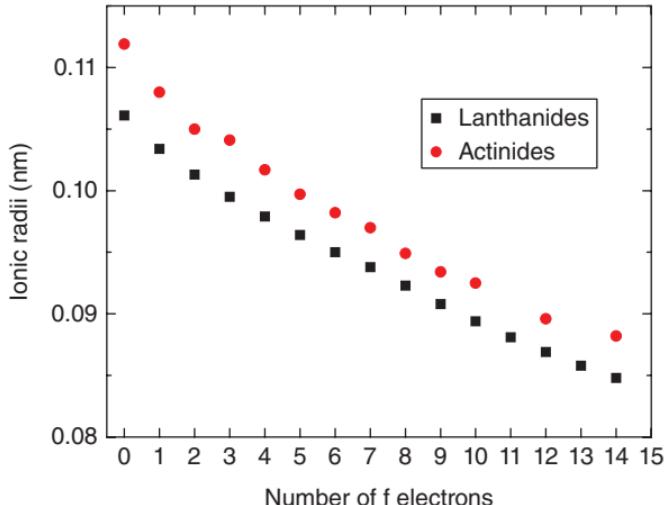
The effect of using relativistic rather than nonrelativistic quantum mechanics to predict the atomic orbitals is threefold: there is (a) a contraction and stabilization of the $s_{1/2}$ and $p_{1/2}$ orbitals, (b) a general splitting of the energy levels due to the spin orbit coupling, and (c) an expansion (and destabilization) of the outer d and all f shells. These effects are of approximately equal magnitude and increase as Z^2. In Figure 14.15, the magnitude of these effects is illustrated for uranium. The chemical consequences of these effects have been well documented for elements such as gold where the yellow color is due to relativistic effects as well as the prominence of the 2^+ oxidation state of lead. (Nonrelativistic quantum mechanics would predict gold and silver to have similar colors and for the 4^+ state to be prominent in lead similar to its lighter homolog tin.)

The ionic radii of the M^{3+} and M^{4+} ions of the actinides decrease with increasing positive charge of the nucleus (the so-called actinide contraction, Fig. 14.16). This contraction is due to the successive addition of electrons in an inner f shell where the incomplete screening of the nuclear charge by each added f electron leads to a contraction of the outer valence orbital due to the net increased nuclear charge. The ionic radii of ions of the same oxidation state are generally similar (see Fig. 14.16), so that the ionic compounds of the actinides are isostructural.

The comparable energies of the 5f, 6d, 7s, and 7p orbitals and their spatial overlap will lead to bonding involving any or all of these orbitals. Thus, complex formation is an important part of actinide chemistry. The most stable oxidation states of the actinides and their solution chemistry depend on the ligands present also because of the small differences among the energies of the electronic levels relative to chemical bond energies.

Figure 14.16 Variation of the ionic radii of trivalent lanthanide and actinide ions with increasing number of f electrons.

The known oxidation states of the actinide elements are shown in Table 14.4 and the transactinide elements in Table 14.5. The lower oxidation states are stabilized by acid, while the higher oxidation states are more stable in basic solutions. In solution, the 2^+, 3^+, and 4^+ species are present as metal cations, while the higher oxidation states are present as oxo-cations, MO_2^+, and MO_2^{2+}. The most common oxidation state is 3^+ for the transplutonium elements like the lanthanide elements. Relativistic quantum mechanics predicts the ground state of lawrencium (Lr) to be $5f^{14}7s^27p_{1/2}^1$ and not $5f^{14}7s^26d^1$. This configuration might lead to a stable 1^+ oxidation state for lawrencium, but experiments designed to look for this state have not observed it. An upper limit for the reduction potential of $E_o < 0.44$ V for the Lr^{3+}/Lr^{1+} half reaction has been determined.

The redox chemistry of the actinide elements, especially plutonium, is complex (Morss et al., 2010). Disproportionation reactions are especially important for the 4^+ and 5^+ oxidation states. Some of the equilibria are kinetically slow and irreversible. All transuranium elements undergo extensive hydrolysis with the 4^+ cations reacting most readily due to their large charge–radius ratio. Pu(IV) hydrolyzes extensively in acid solution and forms polymers. The polymers are of colloidal dimensions and are a serious problem in nuclear fuel reprocessing.

Hydrolysis is actually a special type of complex ion formation. The large positive charge associated with transuranium cations that leads to hydrolysis is also the driving force for the interaction of nucleophiles with the transuranium cations. Water is only one example of a nucleophilic ligand. Other nucleophilic ligands present in solution may replace water molecules directly bound to the metal cation to form inner sphere complexes, or alternatively, they may displace water molecules only from the outer hydrate shell to form outer sphere complexes.

Table 14.4 Oxidation States of the Actinide Elements.

89 Ac	90 Th	91 Pa	92 U	93 Np	94 Pu	95 Am	96 Cm	97 Bk	98 Cf	99 Es	100 Fm	101 Md	102 No	103 Lr
												1?		
	(2)					(2)			(2)	(2)	2	2	2	
3	(3)	(3)	3	3	3	3	3	3	3	3	3	3	3	3
	4	4	4	4	4	4	4	4	4	(4)	4?			
		5	5	5	5	5	5?		5?					
			6	6	6	6	6?							
				7	7	7?								

The most common oxidation states are underlined, and unstable oxidation states are shown in parentheses. Question marks indicate species that have been claimed but not substantiated.
Source: Morss et al. (2010). Reproduced with the permission of Springer.

Table 14.5 Oxidation States of the Transactinide Elements.

104 Rf	105 Db	106 Sg	107 Bh	108 Hs	109 Mt	110 Ds	111 Rg	112 Cn
							−1?	
						0?		0?
					1?			
						2?		2?
3	(3)	(3)	3	3	3?		3?	
4	4	4	4	4		4?		4?
	5	5	5				5?	
		6		6	6?	6?		
			7					
				8				
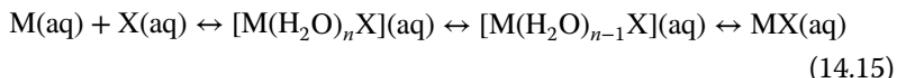
The most common oxidation states are underlined, and unstable oxidation states are shown in parentheses. Question marks indicate species that have been claimed but not substantiated.
Source: Morss et al. (2010). Reproduced with the permission of Springer.

With the competition between water and other ligands for positions in the inner coordination sphere of the central transuranium atom, it should not be surprising that the stability of the complexes formed with a given ligand decreases, in the order: $M^{4+} > MO_2^{2+} > M^{3+} > MO_2^{1+}$. (Note that the strength of complexation does not depend simply on the net cation charge but rather on the charge density seen by the anion or ligand as it approaches

the metal. In the case of MO_2^{2+}, the effective charge is about 3.3 rather than 2.) Although there is some variation within the given cation types, the general order of complexing power of different anions is $F^- > NO_3^- > Cl^- > ClO_4^-$ for singly charged anions and $CO_2^{2-} > C_2O_4^{2-} > SO_4^{2-}$ for doubly charged anions.

The actinide cations form "hard acids," that is, their binding to ligands can be described in terms of electrostatic interactions, and they prefer to interact with hard bases such as oxygen or fluorine rather than softer bases such as nitrogen or sulfur. The actinide cations do form complexes with the soft bases but only in nonaqueous solvents. As typical hard acids, the stabilities of the actinide complexes are due to favorable entropy effects. The enthalpy terms are either endothermic or very weakly exothermic and are of little importance in determining the overall position of the equilibrium in complex formation.

The formation of complexes could be thought to be a three-step process

$$M(aq) + X(aq) \leftrightarrow [M(H_2O)_nX](aq) \leftrightarrow [M(H_2O)_{n-1}X](aq) \leftrightarrow MX(aq)$$
(14.15)
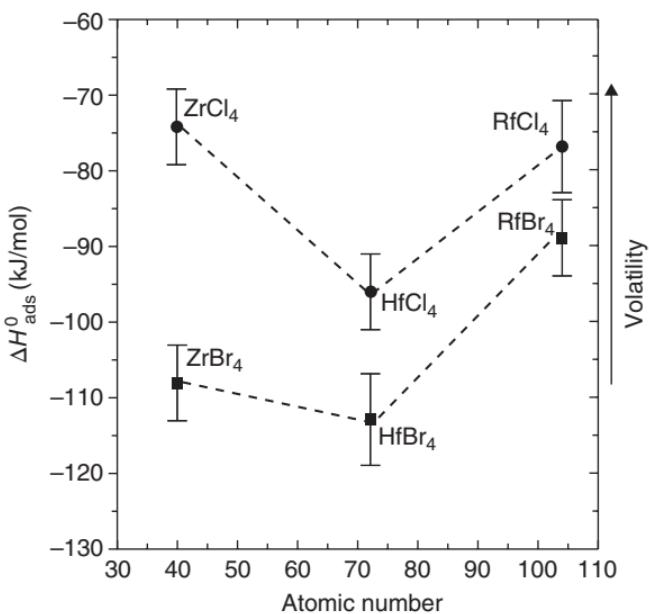
The first step is a diffusion controlled reaction, while in the second step an "outer sphere" complex is formed with at least one water molecule intervening between the ligand and the metal atom. In the third and rate-determining step, a direct connection between the metal and ligand is established with the formation of an "inner sphere" complex. The process could terminate after the second step if the ligand cannot displace water. Actinides form inner and outer sphere complexes; although in most cases, the stronger inner sphere complexes are formed. The halide, nitrate, sulfonate, and trichloroacetate ligands form outer sphere complexes of the trivalent actinides, while fluoride, iodate, sulfate, and acetate form inner sphere complexes.

It should be noted that the study of the chemistry of the elements with $Z > 100$ is very difficult. These elements have short half-lives, and the typical production rates are about one atom/experiment. The experiments must be carried out hundreds of times, and the results summed to produce statistically meaningful results.

The elements Lr–Cn are expected (nonrelativistically) to be d-block elements because they would be filling of the 6d orbital. However relativistic calculations have shown that rutherfordium prefers a $6d^17p^1$ electron configuration rather than the $6d^2$ configuration expected nonrelativistically and expected by a simple extrapolation of periodic table trends. This prediction also implies that $RfCl_4$ should be more covalently bonded than its homologs $HfCl_4$ and $ZrCl_4$. In particular, the calculations predict $RfCl_4$ to be more volatile than $HfCl_4$, which is more volatile than $ZrCl_4$ with bond dissociation energies in the order $RfCl_4 > ZrCl_4 > HfCl_4$. (The periodic table extrapolations would predict the volatility sequence: $ZrCl_4 > HfCl_4 > RfCl_4$.)

Figure 14.17 Adsorption enthalpies, ΔH_ads, on SiO_2 for Group 4 tetrachlorides and tetrabromides (Gregorich (1997). Reproduced with the permission of 41st Conference on Chemical Research - The Transactinide Elements).

The first aqueous chemistry of rutherfordium showed that it eluted from liquid chromatography columns as a 4^+ ion, consistent with its position in the periodic table as a d-block element rather than a trivalent actinide. Gas chromatography of the rutherfordium halides has shown the volatility sequence $ZrCl_4 > RfCl_4 > HfCl_4$ with a similar sequence for the tetrabromides (see Fig. 14.17). Thus rutherfordium does not follow the expected periodic table trend nor is its behavior in accord with relativistic calculations.

The study of the chemistry of seaborgium is remarkable for its technical difficulty as well as the insight offered. In an experiment carried out over a 2-year period, 15 atoms of seaborgium were identified. From this experiment, the group concluded that the volatility of seaborgium was in the sequence: $MoO_2Cl_2 > WO_2Cl_2 \approx SgO_2Cl_2$. This observation agreed with both the extrapolations of periodic table trends and relativistic calculations. In an aqueous chemistry experiment, three atoms of seaborgium were detected, showing seaborgium to have a hexavalent character expected of a Group 6 element. The most stable oxidation state of seaborgium is 6^+ and like its homologs molybdenum and tungsten, seaborgium forms neutral or anionic oxo or oxohalide compounds.

$Sg(CO)_6$ is predicted to be stable because of relativistic effects that lead to stronger molecular bonding. Actinide carbonyls are difficult to synthesize and characterize. ($U(CO)_6$ has only been produced as a transient species using laser ablation.) Recently Even et al. (2014) used a novel separation of recoiling reaction products to produce a carbonyl complex of Sg, probably $Sg(CO)_6$, and
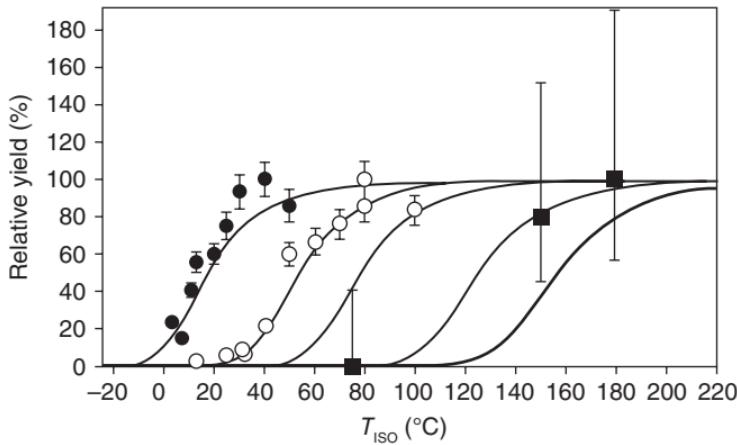
Figure 14.18 Relative yields of the compounds $^{108}TcO_3Cl$ (filled circles), $^{169}ReO_3Cl$ (open circles), and $^{267}BhO_3Cl$ (black squares) as a function of temperature (Eichler et al. (2000). Reproduced with the permission of Nature).

characterized it. This is the first synthesis of a new class of superheavy compounds that could enable studies of the strengths of metal–carbon bonds in the superheavy elements.

To study the chemistry of elements 107 (Bh) and 108 (Hs), one must be able to produce isotopes of these elements with half-lives that are long enough for chemical studies. ^{269}Hs has $t_{1/2} = 9.7$ s, ^{270}Hs has $t_{1/2} = 22$ s, and ^{267}Bh is reported to have a half-life of ≈ 17 s. Because of the small probability of producing these nuclei, methods for chemical study must be very sensitive. Among the projected methods of study, gas-phase thermochemistry is thought to be the most viable.

Thermochromatographic measurements have indicated that Bh is less volatile than Re, which is less volatile than Tc, in agreement with periodic table trends (Fig. 14.18). The chemistry of hassium has been studied using the formation of chemically stable, volatile HsO_4, a property of Group 8 elements. Thermochromatography has shown HsO_4 to be less volatile than OsO_4, a result in agreement with some relativistic predictions (see Fig. 14.19);

One of the most compelling and sophisticated examples of the power of modern chemical techniques is the study of the thermochromatography of Cn and Fl (Eichler et al., 2008). The reaction $^{242}Pu(^{48}Ca, 3n)$ was used to produce 0.48 s ^{287}Fl. ^{287}Fl was then transported in a capillary to a thermochromatography apparatus. During the 2.2 s transport time, the ^{287}Fl decayed to ^{283}Cn. The thermochromatography column was calibrated with Hg (which deposited on the warm end of the column) and Rn (which deposited on the cold end of the column). Five atoms of ^{283}Cn were observed to deposit in the warm (Hg) end of the column (Fig. 14.20), indicating that Cn and Hg have similar behavior—as befitting their place in the periodic table.
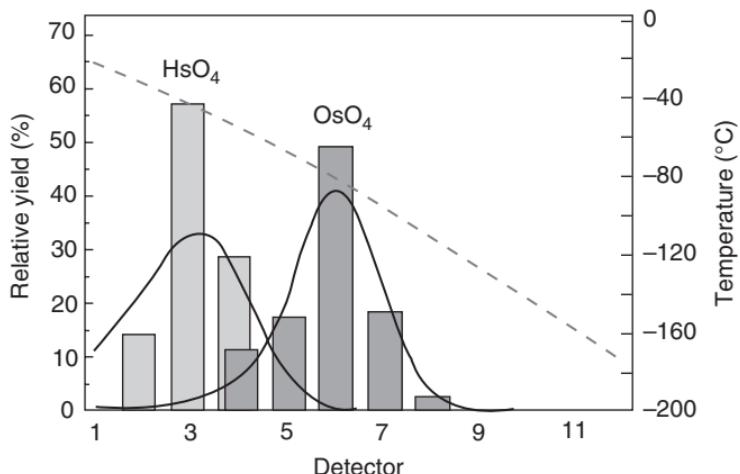
Figure 14.19 Thermochromatogram of HsO$_4$ and OsO$_4$. (Düllmann et al., 2002). The solid bars represent HsO$_4$, the white bars OsO$_4$. The dashed line indicates the temperature profile. The solid lines represent a simulation of the adsorption process with standard adsorption enthalpies of −46.0 kJ/mol for HsO$_4$ and −39.0 kJ/mol for O$_s$O$_4$.

Similar thermochromatography experiments have been carried out with Fl. Fl appears to be more inert than its Pb homolog but can be thought of as a volatile metal.

14.7 Environmental Chemistry of the Transuranium Elements

With the large annual production of neptunium, plutonium, and the higher actinides in the nuclear power industry, there has been increasing concern about the possible release of these elements into the environment. This concern has been heightened by the nuclear reactor accidents at Three Mile Island, Chernobyl, and Fukushima. Coupled with the prospect of cleaning up the detritus of the nuclear weapons programs of the major nations and the general lack of a publicly acceptable method of long-term disposal of nuclear waste, there is considerable interest in the environmental chemistry of the transuranium elements.

Plutonium is clearly the most significant transuranium element in the environment. The plutonium in the environment is due primarily to atmospheric testing of nuclear weapons, secondarily to the disintegration upon reentry of satellites equipped with ^{238}Pu thermoelectric power sources, and lastly, to the processing of irradiated fuel and fuel fabrication in the nuclear power industry and the plutonium production program. Some major radionuclide releases are summarized in Table 14.6. During the period from 1950 to 1963, about
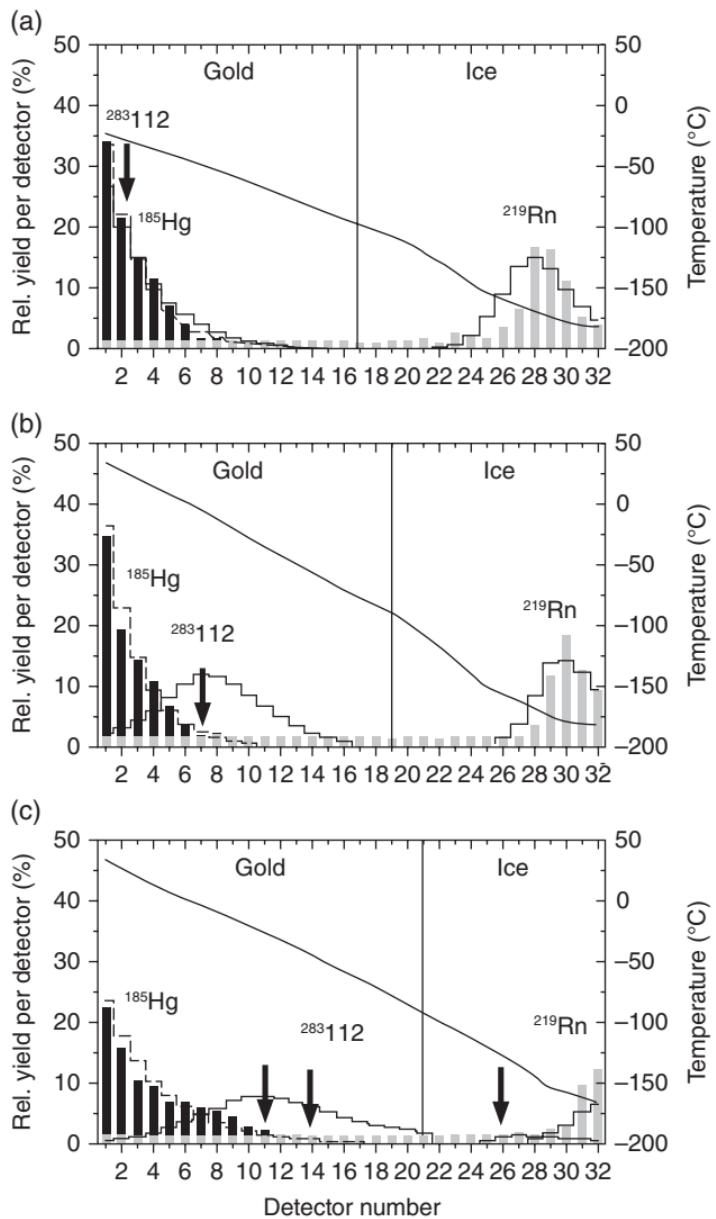
Figure 14.20 Thermochromatographic deposition of Hg (dark bars), Rn (grey bars), and ^{283}Cn (arrows). The labels (a), (b) and (c) refer to different experimental conditions for gas flow and temperature of the column. The dotted line indicates the temperature distribution (right axis) (Eichler et al. (2008). Reproduced with the permission of John Wiley & Sons).

4.2 tons of plutonium (mostly a mixture of ^{239}Pu and ^{240}Pu) was injected into the atmosphere as a result of nuclear weapons testing. Because of the high temperatures at the instant of injection, most of this plutonium was thought to be in the form of a refractory oxide. Most of this plutonium has been

Table 14.6 Events Leading to Large Injections of Radionuclides Into the Atmosphere.

Source	Country Site	Year	Radioactivity (Bq)	Important Nuclides
Hiroshima and Nagasaki	Japan	1945	4×10^{16}	Fission prod. actinides
Atmospheric weapons tests	United States and USSR	Up to 1963	2×10^{20}	Fission prod. actinides
Windscale	United Kingdom	1957	1×10^{15}	^{131}I
Chelyabinsk (Kysthym)	USSR	1957	8×10^{16}	Fission prod. ^{90}Sr, ^{137}Cs
Three Mile Island	United States	1979	1×10^{12}	Noble gases ^{131}I
Chernobyl	USSR	1986	2×10^{18}	^{137}Cs
Fukushima	Japan	2010	2×10^{17}	^{131}I, ^{137}Cs

Source: From Choppin et al. (2013), except Fukushima data from Yamamoto (2015).

redeposited on the earth with the highest concentrations at the mid-latitudes. Of the $\approx 350,000$ Ci of ^{239}Pu and ^{240}Pu originally injected into the atmosphere, about 1000 Ci remained in 1989. Approximately 9.7×10^6 Ci of ^{241}Pu were also injected into the atmosphere during weapons testing. When this isotope completely decays (the $t_{1/2}$ of ^{241}Pu is 14.4 years), a total of $\sim 3.4 \times 10^5$ Ci of ^{241}Am will be formed. There is an additional ~ 1.4 tons of plutonium deposited in the ground (as of 1989) due to surface and subsurface nuclear weapons testing. In addition, $\sim 16,000$ Ci of ^{238}Pu were injected into the atmosphere when a satellite containing an isotopic power source disintegrated over the Indian Ocean in 1964. The Chernobyl nuclear reactor accident caused the release of ~ 800 Ci of ^{238}Pu, ~ 700 Ci of ^{239}Pu, and ~ 1000 Ci of ^{240}Pu, representing $\sim 3\%$ of the reactor core inventory. This activity was dispersed over large areas of the former Soviet Union and Europe. The amount of plutonium in the environment due to fuel reprocessing is small by comparison.

Over 99% of the plutonium released to the environment ends up in the soil and in sediments. The global average concentration of plutonium in soils is 5×10^{-4} to 2×10^{-2} pCi/g dry weight with most of the plutonium being near the soil surface. The concentrations of plutonium in natural waters are quite low with an average concentration being $\sim 10^{-4}$ pCi/l, that is, $\sim 10^{-18}$ M. (Greater than 96% of any plutonium released to an aquatic ecosystem ends up in the sediments. In these sediments, there is some translocation of the plutonium to the sediment surface due to the activities of benthic biota.) Less than 1% (and perhaps closer to 0.1%) of all the plutonium in the environment ends up in the

biota. The concentrations of plutonium in vegetation range from 10^{-5} up to 2% of the Pu, with concentrations in litter and animals ranging from 10^{-4} up to 3% and 10^{-8} up to 1% of the Pu, respectively. None of these concentrations have been observed to cause any discernible effect.

Despite the extremely low concentrations of the transuranium elements in water, most of the environmental chemistry of these elements has been focused on their behavior in the aquatic environment. Note that the neutrality of natural water (pH = 5–9) results in extensive hydrolysis of the highly charged ions, except for Pu(V), and a very low solubility. In addition, natural waters contain organics as well as micro- and macroscopic concentrations of various inorganic species such as metal cations and anions, which can compete with, complex with, or react with the transuranium species. The final concentrations of the actinide elements in the environment are thus the result of a complex set of competing chemical reactions such as hydrolysis, complexation, redox reactions, and colloid formation. As a consequence, the aqueous environmental chemistry of the transuranium elements is significantly different from their ordinary solution chemistry in laboratory.

In natural waters, hydrolysis is the primary factor affecting concentration. The tendency to hydrolyze follows the relative effective charge of the ions. This is known to be

$$An^{4+} > AnO_2^{2+} > An^{3+} > AnO_2^{1+} \tag{14.16}$$
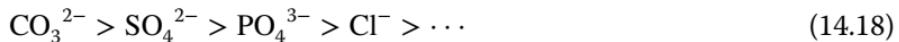
where An represents an actinide element. The hydrolysis reaction can be written as

$$xAn^{m+} + yOH^- \rightarrow An_x(OH)_y \tag{14.17}$$

with $m \times x = y$. The hydrolysis products can be monomeric, polynuclear, or colloidal.

A number of strongly complexing inorganic anions are present in natural waters, such as HCO_3^-/CO_3^{2-}, Cl^-, SO_4^{2-}/HSO_4^{1-}, $PO_4^{3-}/HPO_4^{2-}/H_2PO_4^{1-}$, and so on. The complexation order of these anions is

$$CO_3^{2-} > SO_4^{2-} > PO_4^{3-} > Cl^- > \cdots \tag{14.18}$$

Also present in many natural waters are weak organic acids such as humic–fulvic acid, citric acid, and so on. These organics also can complex actinides. Figure 14.22, 14.23 shows the relative stability constants for the first complexation reaction of various ligands with actinides of different oxidation states. Clearly the carbonate and humate anions along with hydrolysis dominate the chemistry. The tetravalent actinide ions will tend toward hydrolysis reactions or carbonate complexation rather than humate–fulvate formation.

The aquatic solution chemistry of the actinides is also influenced by pH and by the redox potential of the natural water (E_h). The approximate ranges of pH and E_h for natural waters are shown in Figure 14.22. The pH varies from 4 to 9.5 and E_h from −300 to +500 mV. In these pH and E_h ranges, neptunium and

Figure 14.21 Comparison of complexation stability constants for the interaction of various ligands with different actinide oxidation states (Kim (1986). Reproduced with the permission of North-Holland, Amsterdam).
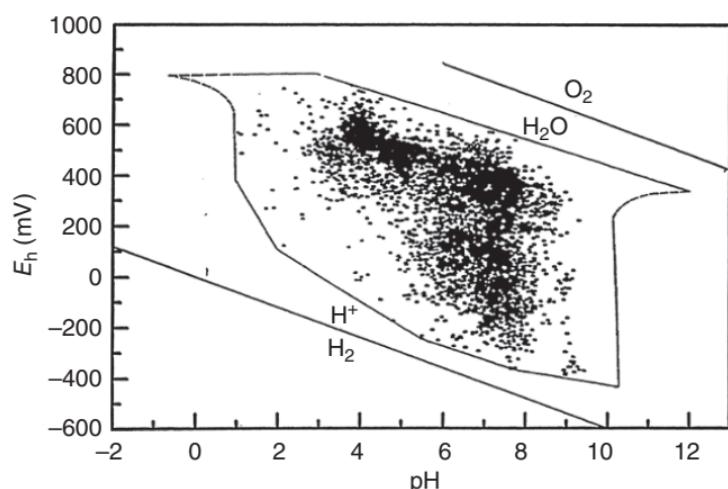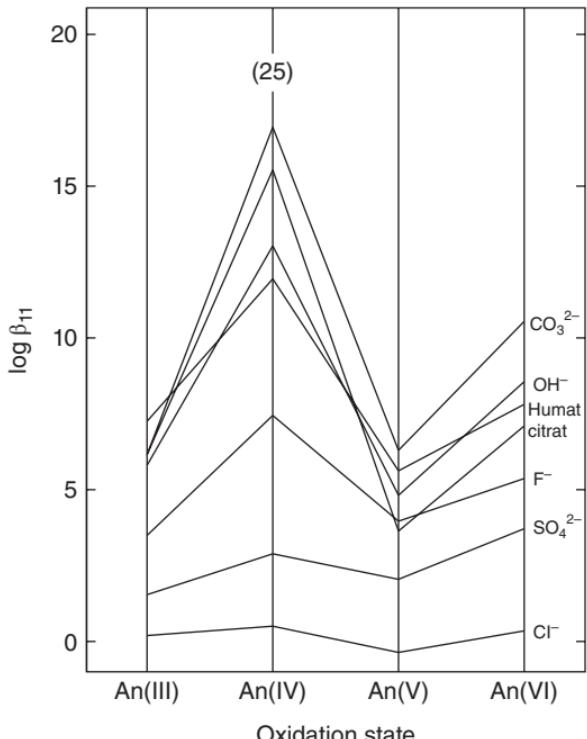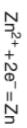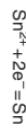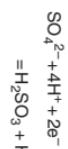

Figure 14.22 A Pourbaix diagram showing the ranges of pH and E_h values in natural waters.

plutonium can be present in several different oxidation states, while americium and curium will be trivalent. In the oxidizing environment of surface waters, $Np(V)$, $Pu(IV)$, $Pu(V)$, and $Am(III)$ will be the dominant species, while other species may be present in the reducing environment of deep groundwater (Figs. 14.21 and 14.23).
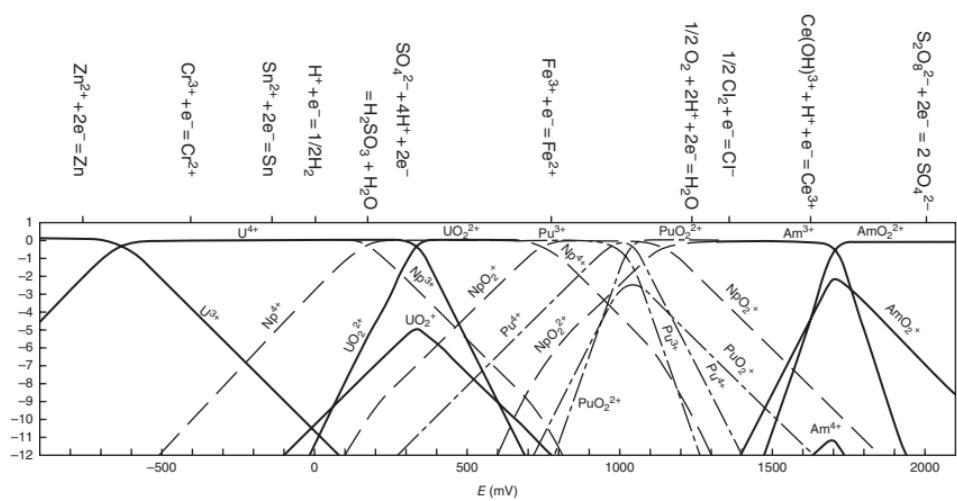
Figure 14.23 Redox diagram for U, Np, Pu, and Am in 1 M $HClO_4$ at 25°C (Choppin et al. (2013). Reproduced with the permission of Academic, London.

Colloids are always present in natural waters containing the transuranium elements. Recall that colloids are defined as aggregated particles with sizes ranging from 1 to 450 nm. These particles form stable suspensions in natural waters. Colloids of the transuranium elements can be formed by hydrolysis of transuranium ions or by the sorption of transuranium elements on the "naturally occurring colloids" already in the water, called pseudo-colloids (since the actinide is not the dominant species). The naturally occurring colloids include such species as metal hydroxides, silicate polymers, organics (such as humates), and so on. The mobility of the transuranium elements in an aquifer is determined largely by the mobility of its pseudo-colloids. The speciation of the transuranium elements in waters is thus a complex function of hydrolysis, colloid formation, redox reactions, and complexation with available ligands. The solubility (mobility) is, thus, highly dependent on the particular aquatic environment and its characteristics.

However, bearing in mind the caveats given earlier, we can make certain generalizations about the behavior of the actinide elements in natural waters. Americium and curium remain in the 3^+ oxidation state over the natural range of environmental conditions. For plutonium, Pu(III) is unstable to oxidation at environmental acidities, and so the other three states are observed with the dominant oxidation state in natural waters being Pu(V). Note that humic materials cause a slow reduction of Pu(V) to Pu(IV) so that Pu(IV) is found to be important in waters containing significant amounts of organic material. Under reducing conditions, neptunium will be present as Np(IV) and behave like Pu(IV); under oxidizing conditions, NpO_2^+ will be the stable species. In marine waters, Pu(IV) and the transplutonium elements will tend to undergo hydrolysis to form insoluble hydroxides and oxides. However, these elements can also form strong complexes with inorganic anions (OH^-, CO_3^{2-}, HPO_4^{2-}, F^-, and SO_4^{2-}) and organic complexing agents that may be present. The speciation and solubility of these elements are largely determined by hydrolysis and formation of carbonate, fluoride, and phosphate complexes. Stable soluble species in marine waters include Pu(V, VI) and Np(V), although under most conditions the actinides will form insoluble species that concentrate in the sediments.

Pu(IV), which forms highly charged polymers, strongly sorbs to soils and sediments. Other actinide III and IV oxidation states also bind by ion exchange to clays. The uptake of these species by solids follows the same sequence as the order of hydrolysis: Pu > Am(III) > U(VI) > Np(V). The uptake of these actinides by plants appears to be in the reverse order of hydrolysis: Np(V) > U(VI) > Am(III) > Pu(IV), with plants showing little ability to assimilate the immobile hydrolyzed species. The further concentration of these species in the food chain with subsequent deposit in man appears to be minor. Of the ~4 tons of plutonium released to the environment in atmospheric testing of nuclear weapons, the total amount fixed in the world population is less than 1 g (of

this amount, most (99.9%) was inhaled and retained as particulates rather than ingested and retained).

Problems

14.1 Predict the aqueous solution chemistry of element 114. What is the expected oxidation state? By extrapolating periodic table trends, estimate the first ionization potential of element 114 (see Nash and Bursten, 1999).

14.2 Suppose you want to synthesize the nucleus ^{271}Mt using the ^{37}Cl + ^{238}U reaction. Estimate the production cross section for this reaction. What is the expected half-life of this nucleus? What is the expected decay mode?

14.3 What is the expected relative population of the 4^+, 5^+, and $6+$ oxidation states of Pu in seawater ($E_h = 1000$ mv)?

14.4 The reported discoveries of elements 114 and 116 do not connect the observed decays to the region of known nuclei. Devise an experimental program to make this connection or to establish the Z of the 114 and 116 nuclei.

14.5 It has been proposed to do a Stern–Gerlach experiment with Lr atoms to better understand the electron configuration of Lr. (a) Describe the original Stern–Gerlach experiment and what it demonstrated about the quantization of electron spin. Why was an inhomogeneous magnetic field used instead of a uniform field? (b) Using nonrelativistic quantum mechanics, one predicts the electron configuration of Lr to be [Rn]5f^{14}6d^{1}s^2. Using relativistic quantum mechanics, the predicted ground-state electron configuration is [Rn]5f^{14}7p$_{1/2}^1$7s^2. Predict the expected pattern of spots one would observe when one passes a beam of neutral Lr atoms through an inhomogeneous magnetic field assuming (a) the nonrelativistic prediction is correct and (b) the relativistic prediction is correct. (c) More sophisticated relativistic calculations predict a spacing of ~1 eV between the ground-state [Rn]5f^{14}7p$_{1/2}^1$7s^2 electron configuration and the electronic excited state with the configuration [Rn]5f^{14}6d^{1}7s^2. If the temperature of an assembly of Lr atoms is 300 K, predict the relative population of the two configurations.

14.6 In the discussion of Figures 14.6 and 14.7, a rough rule of estimating the survival probability as $(E^*/10) \times 10^{-2}$ was given. Using the equations presented in Chapter 11, calculate Γ_n/Γ_f (the survival probability) for

^{254}No with $B_f = 7.1$ MeV and an excitation energy of 50 MeV. Compare this estimate with the rough rule.

14.7 Consider the reaction $^{48}Ca + ^{206}Pb \rightarrow ^{252}No + 2n$. Assume the energy of the ^{48}Ca projectile in the lab system was 217 MeV. Using equations found in Chapters 10 and 11, calculate the formation cross section for this reaction. Compare your calculation with the rough estimate made using Figures 14.6 and 14.7. Assume $B_f = 6.0$ MeV.

14.8 Estimate the total decay power (W) produced in a sample of 10 g of ^{238}Pu.

Bibliography

H.E. White, *Phys. Rev.* 37, 1416 (1931).

M. Yamamoto, J. Radioanal. *Nucl. Chem.* 303, 1227 (2015).

General

J.H. Hamilton, S. Hofmann, and Y.T. Oganessian, *Annu. Rev. Nucl. part. Sci.* 63, 383 (2013). A current summary.

S. Hofmann, Lect. *Notes Phys.* 764, 203 (2009). A definitive review of hot fusion studies.

J.I. Kim, "Chemical Behaviour of Transuranic Elements in Natural Aquatic Systems", in Handbook on the Physics and Chemistry of the Actinides, Volume **4**, A.J. Freeman and C. Keller, Eds. (North-Holland, Amsterdam, 1986) pp. 413–456. A good, critical review of actinide environmental chemistry.

L.R. Morss, N. Edelstein, J. Fuger, and J.J. Katz, Editors, The Chemistry of the Actinide and Transactinide Elements, Volumes **1–6** (Springer, the Netherlands, 2006). An encyclopedic treatment.

Y. Oganessian, *J. Phys. G: Nucl. Part. Phys.* 34, R165 (2007). A definitive review of cold fusion studies.

M. Schadel and D. Shaughnessy, *Editors, The Chemistry of the Superheavy Elements*, 2nd Edition (Springer, Berlin, 2014). A current summary.

G.T. Seaborg and W. Loveland, The Elements Beyond Uranium (John Wiley & Sons, Inc., New York, 1990) and the many references contained therein. The material in this chapter represents a condensation of this book.

Specific to Chapter

R.C. Barber, N.N. Greenwood, A.Z. Hrynkiewics, Y.P. Jeanin, M. Lefort, M. Sakai, I.I. Uleuhla, A.H. Wapstra, and D.H. Wilkinson, Prog. Part. Nucl. Phys. 29, 453 (1992).

G. Choppin, J.O. Liljenzin, J. Rydberg, and C. Ekberg, Radiochemistry and Nuclear Chemistry, 4th Edition (Academic, London, 2013).

V.A. Druin, A.G. Demin, Yu.P. Kharitonov, G.N. Akapev, V.I. Rud, G.Y. Sung-Chin-Yang, L.P. Chelnokov, and K.A. Gavrilov, Yad. Fiz. 13, 251 (1971).

Ch.E. Düllmann et al., Nature 418, 859 (2002).

Ch.E. Düllmann et al., Phys. Rev. Lett. 104, 252701 (2010).

R. Eichler et al., Nature 407, 63 (2000).

R. Eichler et al., Angew. Chem. Int. Ed. 47, 3262 (2008).

P.A. Ellison et al., Phys. Rev. Lett. 105, 182701 (2010).

J. Even et al., Science 345, 1491 (2014).

A. Ghiorso, J.M. Nitschke, J.R. Alonso, C.T. Alonso, M. Nurmia, G.T. Seaborg, E.K. Hulet, and R.W. Lougheed, Phys. Rev. Lett. 33, 1490 (1974).

A. Ghiorso, M. Nurmia, J. Harris, K. Eskola, and P. Eskola, Phys. Rev. Lett. 22, 1317 (1969).

A. Ghiorso, M. Nurmia, K. Eskola, J. Harris, and P. Eskola, Phys. Rev. Lett. 24, 1498 (1970).

A. Ghiorso et al., Nucl. Phys. A583, 861 (1995a) A Ghiorso et al., Phys. Rev. C51, R2293 (1995b).

M. Gilchriese, A. Sessler, G. Trilling, and R. Vogt, Lawrence Berkeley National Laboratory Report, LBNL-51773 (2003).

T.N. Ginter et al., Phys. Rev. C 67, 064609 (2003). K.E. Gregorich, "Radiochemistry of Rutherfordium and Hahnium", *Proceedings of the The RobertWelch Foundation, 41st Conference on Chemical Research—The Transactinide Elements*, Houston, TX, October 27–28 (1997), p. 95.

K.E. Gregorich, M.R. Lane, M.F. Mohar, D.M. Lee, C.D. Kacher, E.R. Sylwester, and D.C. Hoffman, Phys. Rev. Lett. 72, 1423 (1994).

S. Hofmann, Rep. Prog. Phys. 61, 639 (1998). S. Hofmann and G. Münzenberg, Rev. Mod. Phys. 72, 733 (2000) S. Hofmann et al., Z. Phys. A350, 277 (1995a).

S. Hofmann et al., Z. Phys. A350, 281 (1995b).

S. Hofmann et al., Z. Phys. A354, 229 (1996).

S. Hofmann et al., Z. Phys. A. 358, 377 (1997).

S. Hofmann et al., Eur. Phys. J. A 14, 147 (2002).

S. Hofmann et al., Eur. Phys. J. A 48, 62 (2012).

A.V. Karpov et al., Int. J. Mod. Phys. E 21, 1250013 (2012).

J.I. Kim, "Chemical Behaviour of Transuranic Elements in Natural Aqueous Systems", in Handbook on the Physics and Chemistry of the Actinides, Volume 4, A.J. Freeman and C. Keller, Eds. (North-Holland, Amsterdam, 1986), pp. 413–456.

Y.A. Lazarev et al., Phys. Rev. C 54, 620 (1996).

P. Möller, J.R. Nix, and K.L. Kratz, At. Data Nucl. Data Tables 66, 131 (1997).

K. Morimoto, AIP Conf. Series 561, 351 (2001).

K. Morita et al., Eur. Phys. J. A. 21, 257 (2004a).

K. Morita et al., J. Phys. Soc, Jpn 73, 1738 (2004b).

K. Morita et al., J. Phys. Soc. Jpn 76, 043201 (2007).

K. Morita et al., J. Phys. Soc. Jpn 81, 103201 (2012).

L.R. Morss, N.M. Edelstein, and J. Fuger, Editors, The Chemistry of the Actinide and Transactinide Elements, 4th Edition (Springer, Dordrecht, 2010).

G. Münzenberg et al., Z. Phys. A300, 107 (1981).

G. Münzenberg et al., Z. Phys. A309, 89 (1982).

G. Münzenberg et al., Z. Phys. A315, 145 (1984a).

G. Münzenberg et al., Z. Phys. A317, 235 (1984b).

G. Münzenberg et al., Z. Phys. A328, 49 (1987).

V. Ninov et al., Phys. Rev. Lett. 83, 1101 (1999).

V. Ninov et al., Phys. Rev. Lett. 89, 039901 (2002).

Y.T. Oganessian, Phys. Scr., T 125, 57 (2006).

Y. Oganessian, J. Phys. G: Nucl. Part. Phys. 34, R165 (2007).

Y.T. Oganessian, Phys. Rev. Lett. 109, 162501 (2012).

Y.T. Oganessian et al., Z. Phys. A319, 215 (1984).

Y.T. Oganessian et al., Nature 400, 242–245 (1999a).

Y.T. Oganessian et al., Phys. Rev. Lett. 83, 3154 (1999b).

Y.T. Oganessian et al., Phys. Rev. C 62, 041604 (2000a).

Y.T. Oganessian et al., Phys. Rev. C 63, 011301 (2000b).

15

Nuclear Reactor Chemistry

15.1 Introduction
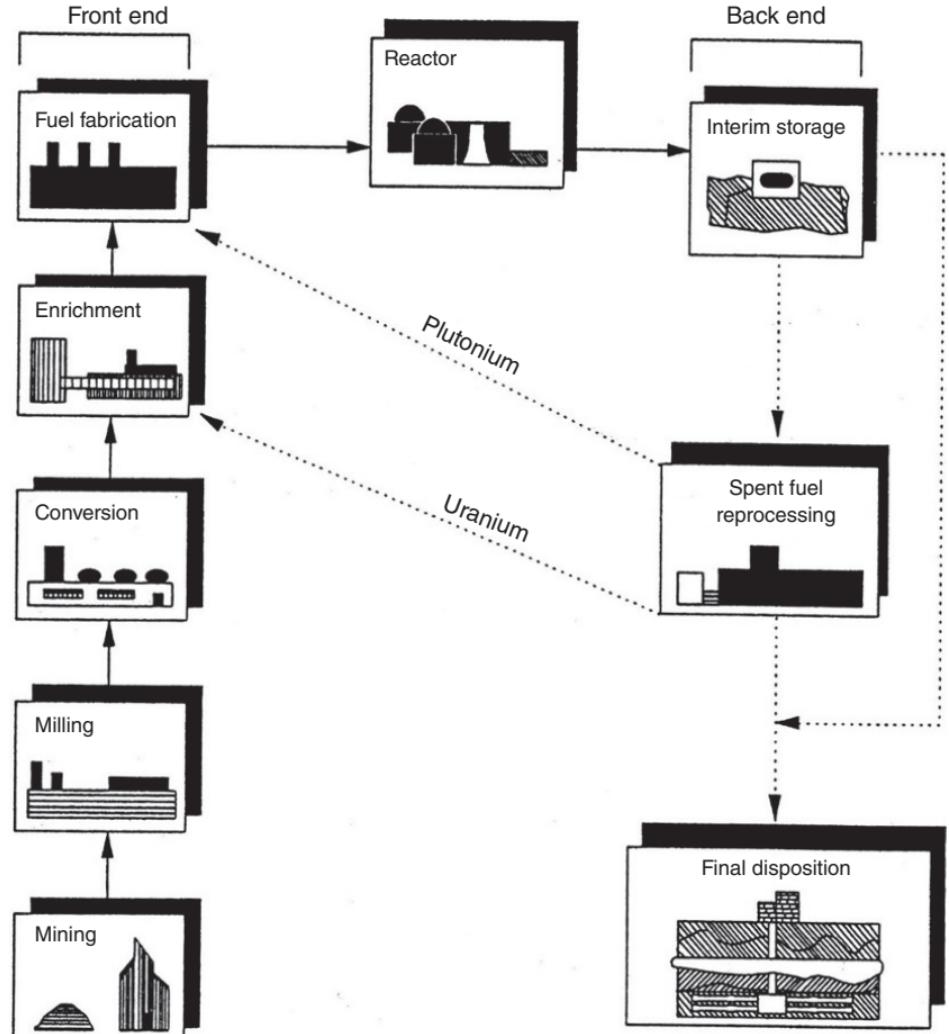
One of the most important applications of nuclear and radiochemistry is the creation of electrical energy from nuclear fission in large nuclear reactors. Chemistry and chemical processes are intimately involved in the preparation and processing of reactor fuel, in reactor operation, and in the storage and ultimate disposal of radioactive waste. In this chapter, we shall examine some of the most important chemistry associated with nuclear power.

The basic principles behind nuclear reactors and the current design of light water reactors are discussed in Chapter 13. The two types of light water reactors, the pressurized water reactor (PWR) and the boiling water reactor (BWR), were shown schematically in Figure 13.2. In these light water reactors, the reactor fuel is enriched to ~3% in ^{235}U, and ordinary water is used as the coolant and moderator. In a PWR, the reactor core is encased in a steel pressure vessel filled with water under a pressure of ~150 bar or greater. The water does not boil due to the high pressure even though the temperature of the water is as high as 350°C. The hot water passes through a heat exchanger where its heat is used to boil water in the secondary coolant loop. The steam is dried and used to drive a turbine and then condensed and returned to the boiler. The water in the primary loop usually contains boron (as 0.025 M boric acid, H_3BO_3) to control the reactivity of the reactor. In contrast, the water passing through the reactor core in a BWR is allowed to boil because it is maintained at a lower pressure, ~75 bar. The steam produced is passed through a turbine, condensed and returned to the reactor.

In PWRs, the fuel is UO_2, enriched typically to 3.3% ^{235}U, while for BWRs, the fuel is also UO_2 but enriched to 2.6%. (Recall that natural uranium is only 0.72% ^{235}U.) The fuel elements are clad in zircaloy, a zirconium alloy that includes tin, iron, chromium, and nickel that is sealed to prevent fission product migration into the water and protects the fuel against corrosion by the coolant.

The control material in BWRs is B_4C, while PWRs generally use Ag-In-Cd or Hf as control materials.

The nuclear fuel cycle is a set of steps in the processing of the reactor's fissile materials that begins with the mining of uranium and extends through the final disposition of the waste from the reactor. These steps are referred to as a cycle because it is possible that the material taken from the reactor after use can be recycled. A schematic diagram of the nuclear fuel cycle is shown in Figure 15.1.

Figure 15.1 A schematic diagram of the nuclear fuel cycle.

This diagram shows two possible paths for this cycle, that is, with and without fuel reprocessing. The majority of reactors in the world and all US reactors operate with a once-through cycle without reprocessing. Some countries, particularly France, perform fuel reprocessing with reuse of the plutonium from spent fuel. The portions of the cycle that precede the introduction of the fissile material into the reactor are referred to as the *front end* of the cycle, while the *back end* includes those steps that occur after the removal of the fuel from the reactor. The details of this cycle and the chemistry involved are discussed in the following.

15.2 Fission Product Chemistry

In the chemistry of the fuel cycle and reactor operations, one must deal with the chemical properties of the actinide elements, particularly uranium and plutonium, and those of the fission products. In this section, we focus on the fission products and their chemistry. In Figures 15.2 and 15.3, we show the chemical
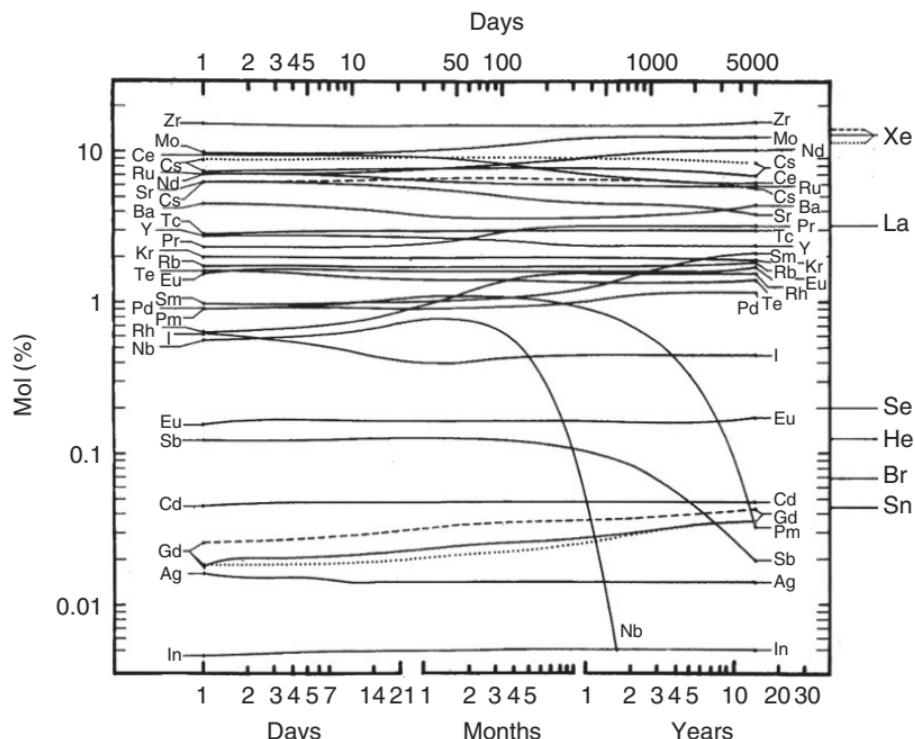
Figure 15.2 The chemical composition of the fission products in irradiated fuel as a function of decay time after a 2-month irradiation (From Prawitz and Rydberg (1958)).
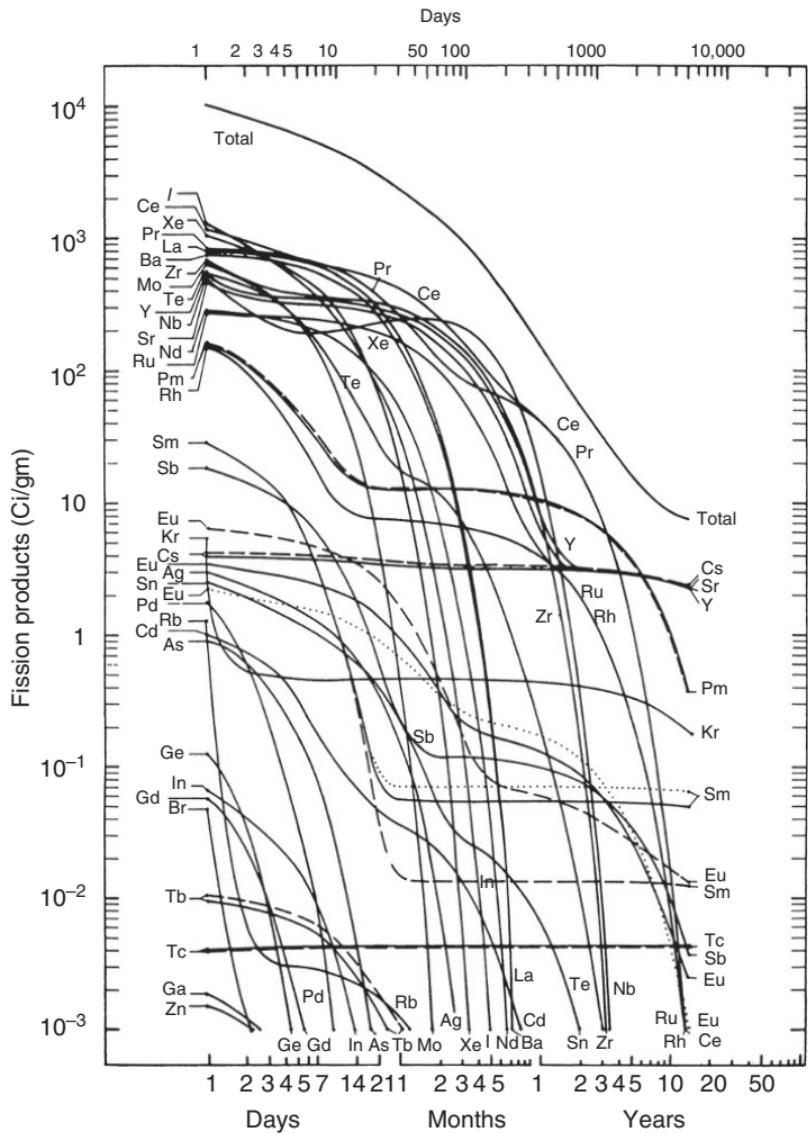
Figure 15.3 The principal fission product activities in irradiated fuel as a function of decay time after a 2-month irradiation. (From Prawitz and Rydberg, (1958)).

composition and associated fission product activities in irradiated fuel. The fission products include the elements from zinc to dysprosium, with all periodic table groups being represented!

The inert gases (Group 18) are represented by isotopes of Kr and Xe. These isotopes are generally short-lived and will decay before fuel reprocessing. As inert gases, they are unreactive and consequently they are isolated using

cryogenic techniques. Note that dissolved argon in the cooling water should be removed to avoid formation of ^{41}Ar by neutron capture on stable ^{40}Ar.

The alkali metals (Group 1) are represented by Rb and Cs where long-lived ^{137}Cs ($t_{1/2} = 30$ years) is the most important (troublesome) nuclide. The solution chemistry of these isotopes is that of the generally soluble 1^+ cations. The alkaline earths (Group 2) are represented by the high-yield nuclides ^{140}Ba, ^{90}Sr, and ^{91}Sr. These nuclides can be separated from the bulk using ion exchange or solvent extraction or gravimetric techniques. The 28-year ^{90}Sr is an important radiation hazard in aged spent fuel, while the 12.8-day ^{140}Ba frequently determines the shielding requirements for fuel during the initial 10–100 day cooling period.

Group 3 contains yttrium and lanthanides. These elements are chemically similar, of course, and can be separated from one another by ion exchange, while their separation from U and Pu can be accomplished using solvent extraction with tributyl phosphate (TBP). These elements have soluble nitrates, chlorides, and sulfates, while their fluorides and hydroxides are insoluble. LaF_3 is frequently used as a carrier for this group. They form stable complexes with strong chelating agents such as DPTA, EDTA, and so on. The most important Group 4 element in fission product mixtures is zirconium whose chemistry is that of the +4 oxidation state. The principal nuclide of interest is the 63-day ^{95}Zr and its 35-day daughter, ^{95}Nb. The chemistry of Zr can be tricky as it readily forms complexes and does form colloids, which can lead to poor separation factors. The fuel is clad with a zirconium alloy, and there could be significant amounts of cold zirconium in the chemical stream.

The most important Group 5 element niobium occurs as the decay product, ^{95}Nb, of ^{95}Zr. Similar to its zirconium parent, ^{95}Nb forms colloids and is readily hydrolyzed. The principal Group 6 fission product is ^{99}Mo ($t_{1/2} = 67$ h), which is important at short cooling times because of its high yield but is insignificant in aged fuel. ^{99}Mo has found extensive use in nuclear medicine since its shorter-lived daughter, ^{99}Tc^{m}, is a very powerful imaging agent. The most important Group 7 fission product is the very long-lived ^{99}Tc ($t_{1/2} = 2.1 \times 10^5$ years). The technetium chemistry is that of the pertechnetate ion TcO_4^{-}. The Group 8, 9, and 10 elements are important because of their activity, and, in the case of ruthenium with multiple oxidation states and slow interconversion kinetics, the chemistry can be troublesome. RuO_4 can be volatilized leading to the loss of Ru in radiochemical procedures. The chemistry of the Group 11 element, Ag, is straightforward (1^+ cation, forming insoluble compounds), and the Group 12 and 13 elements, Zn, Ga, Cd, and In, have low yields and small activities. The Group 14 and 15 elements, Ge, As, Sn, and Sb, also have low activities in aged fuel. The Group 16 element, Te, is present in the form of 30–100 day activities, but most interest has focused on the 78-h ^{132}Te, which

decays to short-lived ^{132}I, which is volatile and can be released when the fuel is processed rapidly. The halogens, Br and I, are not important in fuel reprocessing due to their short half-lives but can be important in reactor operation and accidents due to their volatility.

15.3 Radiochemistry of Uranium

15.3.1 Uranium Isotopes

Natural uranium is 99.274 atom % ^{238}U, 0.7205 atom % ^{235}U, and 0.0056 atom % ^{234}U. The 234/238 ratio is exactly the ratio of their half-lives as expected for nuclei in secular equilibrium in the unprocessed ore. The lightest available isotope ^{233}U is produced by neutron capture on ^{232}Th, followed by β^- decay. ^{232}U is a short-lived nuclide ($t_{1/2} = 72$ years) that is a contaminant in ^{233}U samples irradiated in fast neutron reactions. The daughters of ^{232}U are high-energy γ-ray emitters that complicate working with ^{232}U containing samples. ^{236,237,239}U can be produced by neutron capture reactions on ^{235}U and ^{238}U. ^{236}U is long-lived, but ^{237,239}U are short-lived and decay to produce ^{237}Np and ^{239}Pu, respectively.

15.3.2 Metallic Uranium

Metallic uranium can exist in three different solid phases with differing densities, depending on temperature. At room temperature, the α phase is observed with a density of 19.07 g/cm^3 and a melting point of 1132°C. Metallic uranium is a very reactive metal that is silvery in color. (Frequently a surface oxide layer makes metallic uranium look black.) Uranium powder is pyrophoric. When uranium metal is cut or scratched in the laboratory, a shower of sparks is sometimes observed due to the creation of small particles that ignite. Uranium metal with an oxide coating will burn at 700°C to form U_3O_8. Uranium reacts with hot water to produce UO_2 and UH_3. In reactors, uranium is present as an oxide or is alloyed with zirconium to resist corrosion and radiation damage. Metallic uranium can be produced by the reduction of UF_4, for example,

$$UF_4 + 2Mg \rightarrow 2MgF_2 + U \tag{15.1}$$

15.3.3 Uranium Compounds
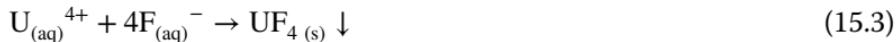
Uranium exists in the $3^+, 4^+, 5^+$, and 6^+ oxidation states. The 5^+ state disproportionates to the 4^+ and 6^+ states and is of little importance. Trivalent uranium reduces water, and therefore there is no stable aqueous chemistry of U^{3+} although compounds do exist.

The most important uranium compounds are the oxides. UO_2 is the compound used in reactor fuel. It is a stable refractory material that is brown–black in color and is nonreactive with H_2O. It has density of 10.97 g/cm^3 and can be prepared by the reduction of UO_3 with hydrogen. U_3O_8 ($UO_2 \cdot 2UO_3$) is a green–black solid that occurs in the mineral pitchblende. It has a density of 8.38 g/cm^3, is soluble in HNO_3, and can be prepared by oxidizing UO_2 or reducing UO_3. UO_3 is a yellow–orange solid (so-called orange oxide) and is important as an intermediate in the production of UO_2 or UF_6. Uranium hydride, UH_3, is a reactive black powder. It is a powerful reducing agent and is pyrophoric. A mixture of uranium and zirconium hydrides is used as the fuel for the small-scale (1 MW thermal) TRIGA research reactors.

Uranium halides exist in the 3^+ oxidation state (UF_3, UCl_3, UBr_3, UI_3), in the 4^+ oxidation state (UF_4, UCl_4, UBr_4, and UI_4), in the 5^+ oxidation state (UF_5, UCl_5), and in the 6^+ oxidation state (UF_6, UCl_6). UF_4 (uranium "green salt") is an intermediate in the production of uranium metal and UF_6 that can be made by reacting UO_2 with excess HF as

$$UO_2 + 4HF = UF_4 + 2H_2O \tag{15.2}$$

or, for laboratory use in small quantities, by the reaction

$$U_{(aq)}^{4+} + 4F_{(aq)}^{-} \rightarrow UF_{4\,(s)} \downarrow \tag{15.3}$$
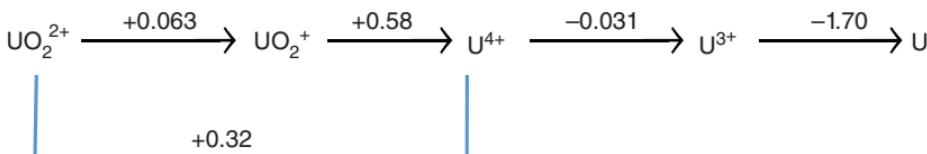
Uranium tetrafluoride when precipitated from aqueous solutions exists as $UF_4 \cdot 5H_2O$, and it is difficult to remove the waters of hydration so that the previous dry reaction is preferred. UF_4 is frequently used to make accelerator targets of uranium by vacuum volatilization.
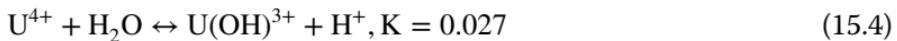
UF_6 (uranium "hex") is the only readily available uranium compound that is volatile at room temperature. It is a colorless solid that is used in the uranium enrichment process that sublimes at room temperature without melting. UF_6 is rapidly hydrolyzed by water and is a fluorinating agent. This latter property means that one must carefully choose the materials used to contain UF_6.

15.3.4 Uranium Solution Chemistry

The solution chemistry of uranium is that of the 4^+ and 6^+ oxidation states, that is, U^{4+} and UO_2^{2+}. The formal reduction potential of uranium in aqueous solution (that is, 1 M $HClO_4$) was shown previously.
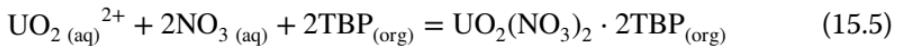
U(IV) chemistry is similar to that of Th^{4+} except for the charge/radius ratio of the ions. U^{4+} solutions are green in color, stable, and slowly oxidized on contact with air to UO_2^{2+}. Solutions of U^{4+} are generally prepared by reduction of solutions of the uranyl (UO_2^{2+}) ion. U(IV) forms complexes with many anions ($C_2O_4^{2-}$, $C_2H_3O_2^{-}$, CO_3^{2-}, Cl^-, and NO_3^-). The chlorides and bromides of U(IV) are water soluble, while the fluorides and hydroxides are insoluble. In aqueous solution, U(IV) hydrolyzes via the reaction

$$U^{4+} + H_2O \leftrightarrow U(OH)^{3+} + H^+, K = 0.027 \tag{15.4}$$

U(VI) can be prepared by dissolving UO_3 in acid or uranium metal in HNO_3. Solutions of the uranyl ion show a characteristic yellow–green color and are very stable. U(VI) shows complex solution equilibria due to the occurrence of hydrolysis, which leads to $[(UO_2)_2OH]^{3+}$, $[(UO_2)_2(OH)_2]^{2+}$, and $[(UO_2)_3(OH)_4]^{2+}$ mixtures. Because of hydrolysis reactions, aqueous solutions of uranyl salts are slightly acidic. Addition of base to uranyl solutions results in precipitation beginning at a pH between 4 and 7.

Uranyl ions form complexes in solutions with most anions. Uranyl sulfate and carbonate complexes are especially strong and are used to extract uranium from its ores. Of great practical importance are the complexes of the uranyl ions with nitrate that are soluble in organic liquids such as alcohols, ethers, ketones, and esters. One of the most important of these reactions is that involving the extraction of uranyl nitrate into tributyl phosphate (TBP) in the so-called PUREX process:

$$UO_{2\ (aq)}^{2+} + 2NO_{3\ (aq)} + 2TBP_{(org)} = UO_2(NO_3)_2 \cdot 2TBP_{(org)} \tag{15.5}$$

Neglecting activity coefficients, the distribution coefficient for the distribution of uranium between the organic and aqueous phases is written as

$$D = \frac{[UO_2(NO_3)_2 \cdot 2TBP]_{(org)}}{[UO_2^{2+}]_{aq}} = K[NO_3]_{aq}^2[TBP]_{org}^2 \tag{15.6}$$

where K is the equilibrium constant ($K \sim 15$–60). One can use the concentration of a salting agent such as NO_3^- to control the extraction process. (In the PUREX process, these salting agents ultimately leave the cycle with the fission products, contributing to the problem of the bulk of these wastes.)

15.4   The Nuclear Fuel Cycle: The Front End
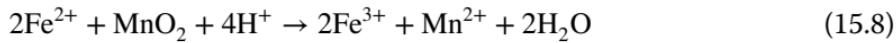
The nuclear fuel cycle (see Fig. 15.1) begins with the mining of uranium ore, of course. Uranium is by no means rare. Its overall abundance in the earth's crust is ~4 ppm, a value that is more abundant than Ag, Hg, Bi, or Cd. There are estimated to be ~10^4 tonnes of uranium in the earth's crust. The problem is one of concentration in that most uranium deposits contain <0.001% uranium.

15.4.1 Mining and Milling

Uranium ore can be classified as high grade (1–4% U), medium grade (0.1–0.5% U), and low grade (<0.1% U). In the high-grade deposits, found in Zaire and Canada, uranium is contained in pitchblende or uraninite, materials with the general composition $x\mathrm{UO_2} \cdot y\mathrm{UO_3}$ where $0 < y/x < 2$. The medium-grade ores are found in places such as the Colorado plateau of the United States, where uranium is incorporated in carnotite ($\mathrm{K_2O \cdot 2UO_3 \cdot V_2O_5 \cdot xH_2O}$) or autunite ($\mathrm{CaO \cdot 2UO_3 \cdot P_2O_5 \cdot xH_2O}$). Low-grade sources include the gold ore residues of South African seawater where the nominal uranium concentration of 3 ppb corresponds to a reservoir of $\sim 10^{10}$ tonnes of uranium or the fertilizer by-products of the phosphate fields of Florida and Idaho, Tennessee shale, or the lignites of Wyoming and the Dakotas. The average uranium content of the ores used in the nuclear fuel cycle in the United States in recent years is $\sim 0.24\%$.

After mining, the uranium must be concentrated before further operations are carried out. This is done in the mills, generally located near the mines. The uranium ore content is increased in the mills from a few tenths of a percent (in the ore) up to 85–95% (into a semi-refined concentrate known as "yellowcake") while eliminating other elements that are present (creating the "tailings"). While very high-grade pitchblende deposits can be concentrated by physical techniques involving their specific gravity, most concentration of uranium involves chemical leaching from the ore. These processes do not affect the isotopic distribution of the material, of course. The ore is prepared for leaching by crushing and roasting (to destroy organic material). It is then subjected to chemical leaching followed by a separation of the liquids and solids and then followed by concentration/purification and final product recovery.

The normal choice ($\sim 80\%$ of all US ores) for chemical leaching is acid leaching with sulfuric acid due to its low cost and great availability. For the ores that have high carbonate content, an alkaline leach with $\mathrm{Na_2CO_3}$ is used to prevent high acid concentrations. The problem in acid leaching is that only U(VI) dissolves in $\mathrm{H_2SO_4}$. Any U(IV) present must be oxidized to U(VI) prior to leaching. The chemical steps can be summarized by the following set of reactions:

$$\mathrm{FeS \ or \ Fe + H_2SO_4 \rightarrow Fe^{2+} + H_2 + SO_4{}^{2-}} \tag{15.7}$$

$$\mathrm{2Fe^{2+} + MnO_2 + 4H^+ \rightarrow 2Fe^{3+} + Mn^{2+} + 2H_2O} \tag{15.8}$$
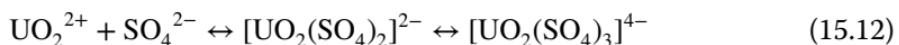
or for the alkaline system

$$\mathrm{6Fe^{2+} + NaClO_3 + 6H^+ \rightarrow 6\ Fe^{3+} + NaCl + 3H_2O} \tag{15.9}$$

allowing the oxidation of the uranium by the ferric ion and complexation with sulfate:

$$\mathrm{UO_2 + 2Fe^{3+} \rightarrow UO_2{}^{2+} + 2Fe^{2+}} \tag{15.10}$$

$$UO_3 + H_2SO_4 \rightarrow UO_2^{2+} + SO_4^{2-} + H_2O \tag{15.11}$$

$$UO_2^{2+} + SO_4^{2-} \leftrightarrow [UO_2(SO_4)_2]^{2-} \leftrightarrow [UO_2(SO_4)_3]^{4-} \tag{15.12}$$

Notice that the final product of this process, UO_2, appears in three chemical forms: UO_2^{2+}, $UO_2(SO_4)_2]^{2-}$, and $[UO_2(SO_4)_3]^{4-}$.

In alkaline leaching of high carbonate materials, one takes advantage of the unique solubility of $[UO_2(CO_3)_3]^{4-}$. One begins with finely divided material and must also deal with the oxidation of any U(IV) that is present. The basic reaction (pun intended) is

$$UO_2 + (\text{oxidant, Ox}) + 3CO_3^{2-} \rightarrow [UO_2(CO_3)_3]^{4-} + Ox^{2-} \tag{15.13}$$

After this leaching, a concentration/purification is done to get rid of other materials leached from the ore. The purification can be done by ion exchange or solvent extraction. In the ion exchange method, three steps are employed: (a) the absorption of uranium from the leach liquor onto the resin, (b) the selective elution of uranium from the resin, and (c) the regeneration of the resin. Anion exchange is the preferred method of ion exchange with the relevant chemical equations for acid leach being

$$[UO_2(SO_4)_3]^{4-} + 4RX = R_4[UO_2(CO_3)_3] + 4X^- \tag{15.14}$$

and for alkaline leach

$$[UO_2(CO_3)_3]^{4-} + 4RX = R_4[UO_2(CO_3)_3] + 4X^- \tag{15.15}$$

The eluant is usually $1\,M\,NO_3^-$ in the form of NH_4NO_3. The physical method for carrying out the extraction can involve (a) a fixed resin bed, (b) a "resin-in-pulp" technique where resin in baskets is passed through a stream of pulp or slurry from the leach process, or (c) a moving bed of resin.

Concentration/purification by solvent extraction usually involves four steps: (a) extraction of uranium from the leach liquor in a solvent, (b) scrubbing to remove impurities from the solvent, (c) *stripping* to remove uranium from the solvent, and (d) *regeneration* of the solvent. The solvent in solvent extraction will contain the extractant, which complexes uranium to make it soluble in the organic phase, a diluent, an inexpensive material to dilute the extractant, and a modifier to improve the solubility of the extractant in the diluent. Typical extractants are amines with isodecanol acting as a modifier to improve the amine solubility in a diluent such as kerosene. The typical chemistry of the extraction would involve the reactions

$$2R_3N_{(org)} + H_2SO_4 \rightarrow (R_3NH)_2SO_{4\,(org)} \tag{15.16}$$

$$2(R_3NH)_2SO_{4\,(org)} + [UO_2(SO_4)_3]_{(aq)}^{4-} \rightarrow \tag{15.17}$$

$$(R_3NH)_4[UO_2(SO_4)_3]_{(org)} + 2\,SO_{4\,(aq)}^{2-} \tag{15.18}$$
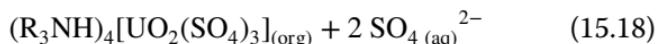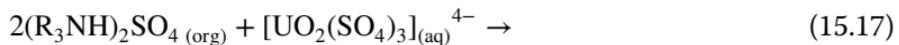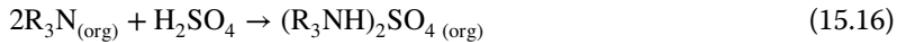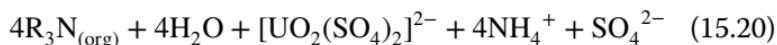
Figure 15.4 Ammonium diuranate (yellowcake) after solvent extraction (Photo from UIC). (*See insert for color representation of the figure.*)

with the stripping reactions being

$$(R_3NH)_4[UO_2(SO_4)_3]_{(org)} + 4NH_4OH \rightarrow \qquad (15.19)$$

$$4R_3N_{(org)} + 4H_2O + [UO_2(SO_4)_2]^{2-} + 4NH_4^+ + SO_4^{2-} \quad (15.20)$$

Following solvent extraction, uranium is precipitated from the solution by the addition of gaseous ammonia with the yellowcake product (see Fig. 15.4) being collected, packaged in 55 gal drums, and shipped to a refinery for further purification and conversion to UF_6 for isotopic enrichment. Alkaline leach mills will use NaOH for final product recovery (in the form of sodium uranate, $Na_2U_2O_7$). Often these uranium ore concentrates (yellowcake) are transformed into U_3O_8 by drying at 200°C to remove water and calcining, that is, heating until decomposition.

15.4.2 Refining and Chemical Conversion

Following milling, the yellowcake is ready for refining and conversion. In most refineries, the uranium ore concentrates are purified by solvent extraction and then converted to UF_6 for enrichment. A schematic diagram of this process is shown in Figure 15.5. The yellowcake is first dissolved in nitric acid. Uranyl nitrate is separated from metallic impurities in the dissolver by solvent extraction with TBP in some organic hydrocarbon solvent such as hexane. The organic extract is scrubbed with 1 M nitric acid, and uranium is stripped from the organic phase by back extraction with 0.01 M HNO_3. The uranyl nitrate hexahydrate, $UO_2(NO_3)_2 \cdot 6H_2O$ (called UNH), is converted to UO_3 (the "orange oxide") in two steps, a concentration by evaporation and a
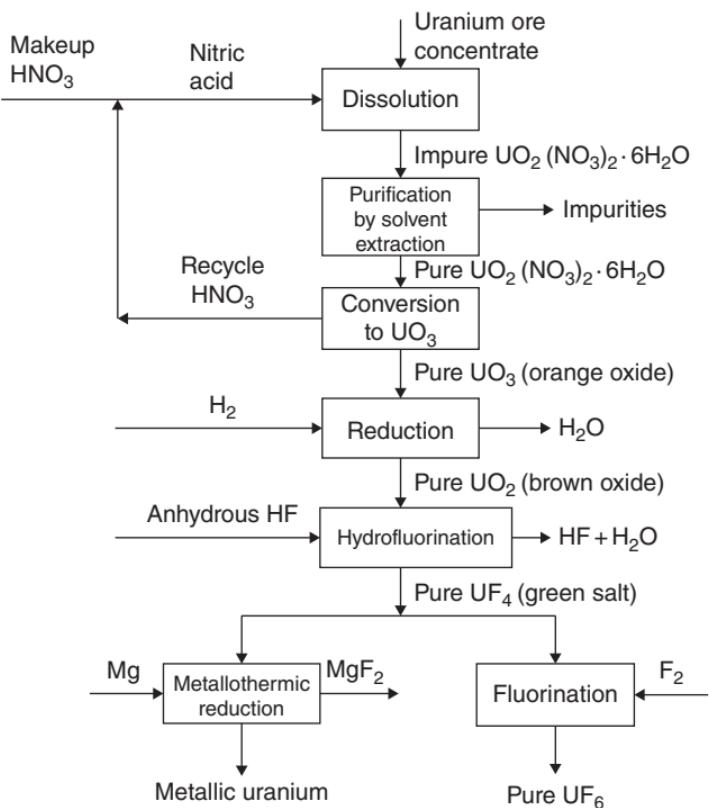
Figure 15.5 A schematic diagram of the refining and conversion of uranium ore concentrates (From Benedict et al. (1981)).

denitrification by heating. UO_3 is reduced to UO_2 (the "brown oxide") using hydrogen via the overall reaction

$$UO_3 + H_2 \rightarrow UO_2 + H_2O \qquad (15.21)$$

UO_2 is then hydrofluorinated via the reaction

$$UO_2 + 4HF \rightarrow UF_4 + 2H_2O \qquad (15.22)$$

using anhydrous HF gas to produce the green salt, UF_4. This green salt can be burned in F_2 gas to produce UF_6. UF_4 can also be reduced to metallic uranium.

15.4.3 Isotopic Enhancement

As discussed earlier, natural uranium is 0.72 atom % ^{235}U, and the fuel used in light water reactors is typically 3% ^{235}U. This means that the refined uranium must be enriched in the lighter 235 isotope prior to fuel fabrication. The enrichment can be accomplished by a variety of physical approaches that take

advantage of the small mass difference between ^{235}U and ^{238}U. We shall discuss four of these methods: electromagnetic separation, gaseous diffusion, gas centrifuges, and laser enrichment.

In *electromagnetic separation*, one uses the fact that when ions of differing mass in the same charge states are accelerated through a potential difference, their kinetic energy is the same, and the radius of curvature in a magnetic field is proportional to the square root of the mass. Thus, the material to be separated is ionized, accelerated, and passed through an analyzing magnet that separates the isotopes into separate beams and a collector for the relevant beams. The technology is straightforward, but there is a high-energy cost to ionize every individual atom and also high for processing macroscopic amounts of material. This technique has largely been abandoned although it was recently attempted in Iraq in an attempt to obtain enriched uranium for nuclear weapons.

In the *gaseous diffusion* process, one takes advantage of the fact that the lighter molecules have higher velocities in a gas. If we assume for simplicity that all of the gas molecules at a given temperature have the average speed, v, given by the temperature, then we can write

$$\frac{3}{2}k_{B}T = KE_{\text{avg}} = \frac{1}{2}mv^2 \tag{15.23}$$

Specifically for the gaseous ^{235}UF$_6$ and ^{238}UF$_6$ molecules, we have

$$\frac{1}{2}mv^2 = \frac{1}{2}m_{235}v_{235}^2 = \frac{1}{2}m_{238}v_{238}^2 \tag{15.24}$$

$$\frac{v_{235}}{v_{238}} = \left(\frac{m_{238}}{m_{235}}\right)^{1/2} = \left(\frac{352}{349}\right)^{1/2} = 1.0043 \tag{15.25}$$

Notice, of course, one has to use the mass of each gaseous molecule, which reduces the separation in this case.

If we introduce a stream of UF$_6$ gas into a vessel with porous walls (see, e.g., Fig. 15.6), then the lighter molecules (with 235) will pass through the pores
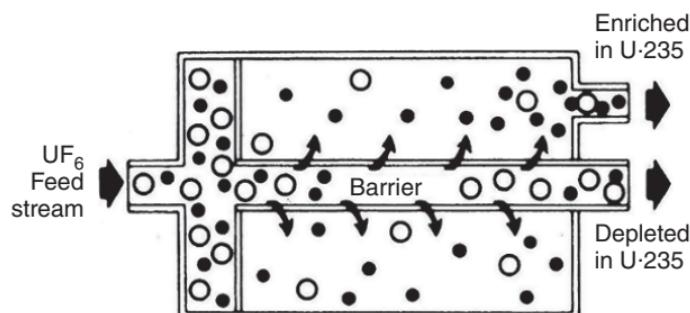
Figure 15.6 A schematic diagram of the operation of a gaseous diffusion cell (From Leuze (1981)).

more frequently (due to their greater number of impacts on the wall per time). The maximum separation factor is 1.0043, but, in practice, this value is not achieved so that more enriched output is passed to another separation chamber and the less enriched remainder of the gas stream is recycled. Typically if one starts with natural uranium (0.72% ^{235}U) and with tails depleted to 0.3%, about 1200 enrichment stages would be needed to achieve an output enriched to 4%. In practice, several million 10–100 nm pores/cm^2 in a membrane are used for the separation, and the process must be carried out at elevated temperatures to increase the average molecular velocity with UF$_6$, a strong fluorinating agent that decomposes upon contact with water. Nonetheless, most isotopic enrichment is done using this technique.

Sample Problem 15.1: Temperatures and Velocities

What is the average velocity of a ^{238}UF$_6$ molecule at $T = 500°C$?

Solution

The molar mass of UF$_6$ is $238 + (6 * 19) = 352$ g/mol. The mean kinetic energy of a gaseous molecule is $1/2mv^2$ and in terms of temperature is $3/2k_B T$.
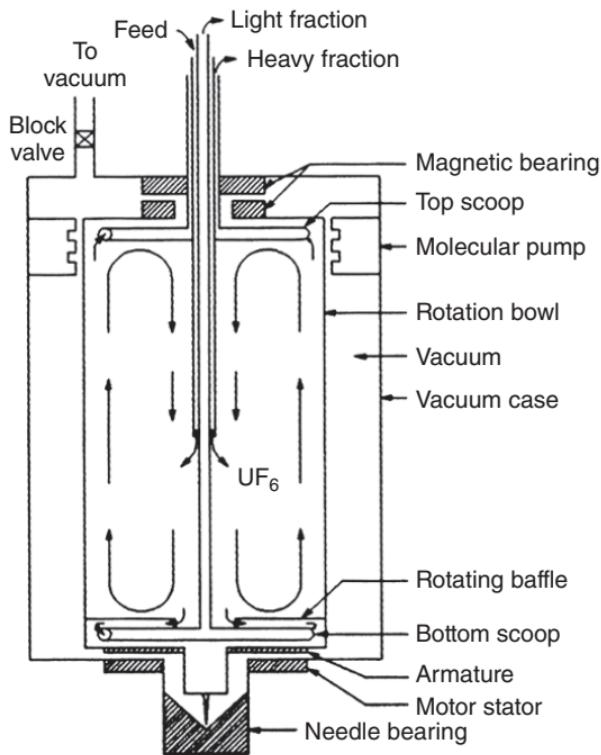
$$E_{molecule} = \frac{3}{2}k_B T = \frac{3}{2}1.38 \times 10^{-23} \text{ J/K } (273.15 + 500 \text{ K})$$
$$= 1.60 \times 10^{-20} \text{ J}$$

$$E_{molecule} = \frac{1}{2}mv^2 \rightarrow v = \sqrt{\frac{2E_{molecule}}{m}}$$

$$v = \sqrt{\frac{2 \times (1.60 \times 10^{-20} \text{ J}) \times 6.02 \times 10^{23}/\text{mol}}{0.352 \text{ kg/mol}}}$$

$$v = 234 \text{ m/s}$$

In *gas centrifuges* such as in Figure 15.7, one takes advantage of the fact that the centrifugal force will preferentially push the heavier ^{238}UF$_6$ molecules to the wall of the centrifuge while the gas near the center will be enriched in ^{235}UF$_6$. A properly designed gas flow pattern will allow the heavier gas to be collected near the top of the device. This separation is more efficient than the simple gaseous diffusion method, requiring only about ten stages to enrich ^{235}U from 0.72 to 3% with a 0.2% tail. The centrifuges have to run at very high speeds if the rotor can change the average velocity of the gaseous atoms, and thus building a working gas centrifuge remains a technical challenge.

In the *laser enrichment* process, one takes advantage of the fact that the atomic energy levels of different isotopes differ slightly. There are two

Figure 15.7 A schematic diagram of a gas centrifuge for isotope enrichment (From Leuze (1981)).
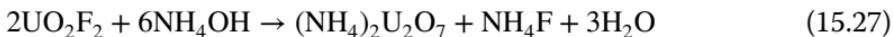
contributions to differences in the energy levels: the so-called mass shift is due the variation of the reduced electron mass in different isotopes, the field shift due to variation of the overlap between the wave functions of the inner electrons and the nucleus due to differences in the nuclear radii. The mass shift is important for the lowest mass elements, and the field shift is more important for heavy elements. Lasers can be tuned precisely enough to excite ^{235}U atoms but not ^{238}U atoms to higher-energy levels. The excited atoms are then ionized with another laser beam. The resulting ionized ^{235}U atoms can be separated electrostatically (or electromagnetically). To date, the feasibility of this technique has been demonstrated, but there are no commercial applications due to the high-energy cost to volatilize the uranium atoms and the cost of the high-power lasers.

15.4.4 Fuel Fabrication

The enriched UF_6 is converted into UO_2 at the fuel fabrication plants. The UF_6 is reacted with water to produce a solution of UO_2F_2 and HF:

$$UF_{6\,(g)} + 2H_2O \rightarrow UO_2F_2 + 4HF \tag{15.26}$$

Ammonium hydroxide is added to the uranyl fluoride solution to quantitatively precipitate ammonium diuranate:

$$2UO_2F_2 + 6NH_4OH \rightarrow (NH_4)_2U_2O_7 + NH_4F + 3H_2O \qquad (15.27)$$

This product is collected, calcined in air to produce U_3O_8, and then heated with hydrogen to make UO_2 powder. The UO_2 powder is pressed into pellets, which are sintered, ground to size and loaded into zircaloy tubing, and finally filled with helium. The tubes are sealed and assembled into fuel bundles for loading into reactors.

15.5 The Nuclear Fuel Cycle: The Back End

At one point in the history of nuclear power, the concept of reprocessing spent reactor fuel to recover its plutonium content to fuel other reactors was considered central to reactor development. The idea of an energy source that could generate its own fuel was very appealing. But, as outlined earlier, most fuel is not reprocessed/recycled but used in a "once-through" manner. The reasons for this are complex, that is, no shortage in near-term uranium supply, low uranium prices, some technical problems in reprocessing, and a concern that reprocessing would make plutonium too readily available for use in weaponry. Nonetheless there are operating plants for reprocessing reactor fuel, particularly in France and Japan, and the overall fate of spent fuel is of great concern and interest.

15.5.1 Properties of Spent Fuel

Periodically a portion of the fuel in a nuclear reactor is removed and replaced with fresh fuel. In the past, the average lifetime of fuel in the reactor was 3 years with approximately one-third of the fuel being removed each year. More recently, attempts have been made to extend fuel lifetimes to increase burnup of the uranium and lower costs associated with spent fuel storage.

Initially the radioactivity levels of the irradiated fuel are quite high (cf. Fig. 15.8). Chemically, the ^{235}U content is reduced from its initial 3 to 1%, while the ^{238}U content is reduced from 97 to 94% (cf. Fig. 15.9). The ^{239}Pu and other Pu isotopes are mixed with the uranium and fission products, of course.

The original plan for the spent fuel from power reactors in the United States was to store it for about 150 days and then transfer it to other facilities for disposal as waste or reprocessing. This proposed transfer has not occurred in the United States, and most of the fuel has remained first in water-filled cooling ponds at the reactor sites and then in dry storage casks, for times that have exceeded 20 years. In fact, dry storage casks have remained in place after power reactors have been decommissioned and the site otherwise remediated. Given this odd situation, a closer look at the properties of irradiated fuel is justified.
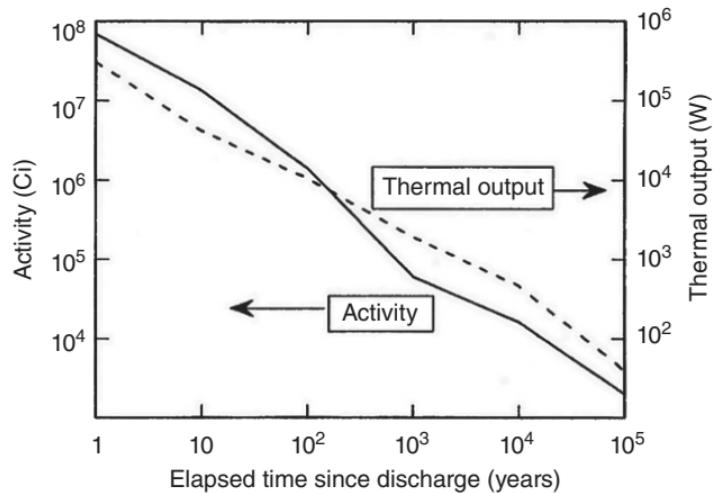
Figure 15.8 General variation of the radioactivity and heat output of spent reactor fuel as a function of time (From Bodansky (1996)).

Figure 15.9 Schematic representation of the general changes in the chemical composition of irradiated fuel (From Murray (1994)).
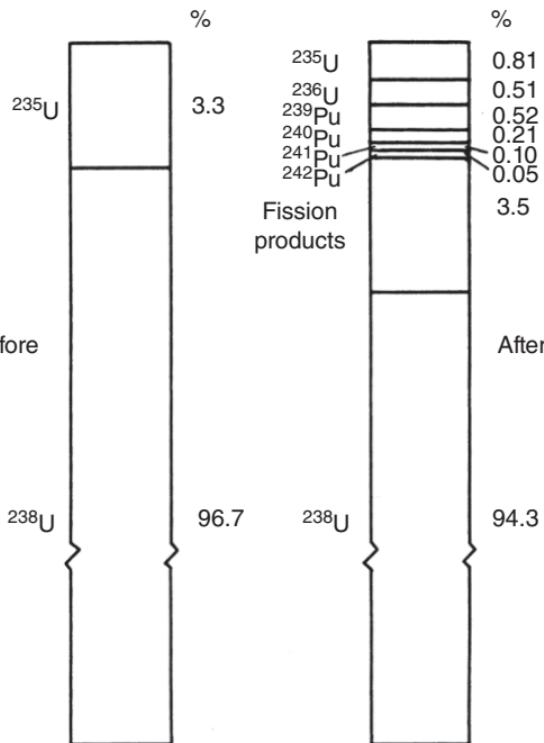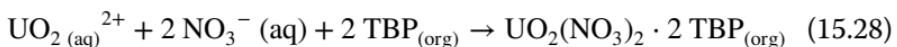
Figure 15.8 shows the activity and heat output for spent fuel beginning 1 year after the end of fission burning in the reactor. During the first year, the activity drops to ≈1% of its initial value and then drops another factor of five in the next 10-year period. The so-called waste disposal problem begins at the 10-year point when the activity level in the fuel has dropped significantly. In this framework, the dominant activities over the long term in unseparated fission waste are ^{90}Sr, ^{137}Cs, ^{241}Pu, ^{241}Am (from the decay of ^{241}Pu), ^{239,240}Pu, ^{99}Tc, and ^{237}Np. The activity level of the waste decreases faster than the heat output due to the shorter half-lives of the β emitters in this group, which do not contribute as much to the heat output as the longer-lived α emitters. The heat output of the waste is sufficiently large to require careful control of the heat during waste storage.
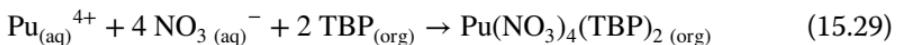
15.5.2 Fuel Reprocessing

Fuel reprocessing has four objectives: (a) to recover U or Pu from the spent fuel for reuse as a nuclear reactor fuel or to render the waste less hazardous, (b) to remove fission products from the actinides to lessen short-term radioactivity problems, and in the case of recycle of the actinides, to remove reactor poisons, (c) to convert the radioactive waste into a safe form for storage, and (d) to reduce the waste volume. Fuel reprocessing was/is important to produce plutonium for weapons use.

The *PUREX process* is used for almost all fuel reprocessing today. As an overview, the irradiated UO_2 fuel is dissolved in HNO_3 with the uranium being oxidized to $UO_2(NO_3)_2$ and the plutonium being oxidized to $Pu(NO_3)_4$. A solution of TBP in a high-boiling hydrocarbon, such as *n*-dodecane, is used to selectively extract the hexavalent $UO_2(NO_3)_2$ and the tetravalent $Pu(NO_3)_4$ from the other actinides and fission products in the aqueous phase. The overall reactions are

$$UO_{2\ (aq)}^{2+} + 2\ NO_3^-\ (aq) + 2\ TBP_{(org)} \rightarrow UO_2(NO_3)_2 \cdot 2\ TBP_{(org)} \quad (15.28)$$

whereas the plutonium reacts

$$Pu_{(aq)}^{4+} + 4\ NO_{3\ (aq)}^- + 2\ TBP_{(org)} \rightarrow Pu(NO_3)_4(TBP)_{2\ (org)} \quad (15.29)$$

These equilibria can be shifted to the right (i.e., improved extraction) by increasing the TBP concentration in the organic phase or by increasing the $[NO_3^-]_{(aq)}$. In the next step, the TBP solution is treated with a dilute nitric acid solution of a reducing agent, such as ferrous sulfamate or U(IV), which reduces the plutonium to a trivalent state but leaves the uranium in a hexavalent state. Plutonium will then transfer to the aqueous phase, leaving uranium in the organic phase. The only fission fragments that extract into the aqueous phase during the initial stripping are Zr, Ru, Nb, and Tc, with the most troublesome being Zr and Ru. Zr forms a number of complex species with the
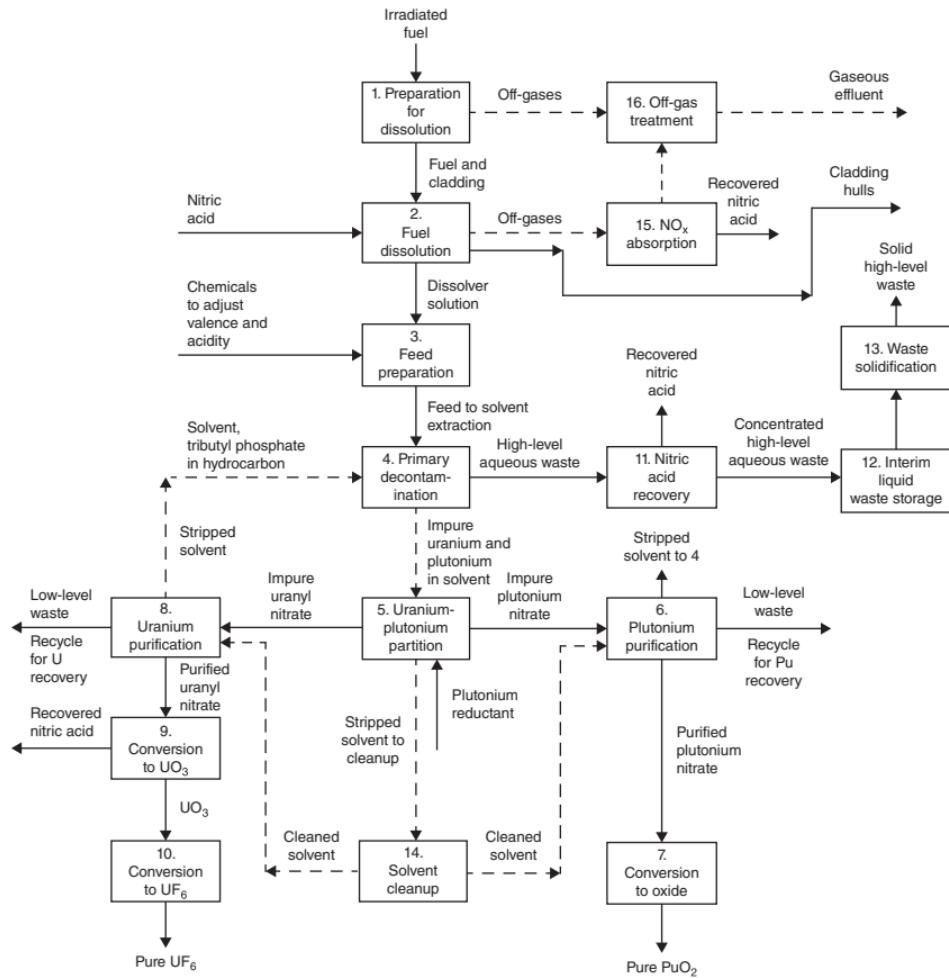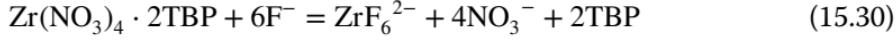
Figure 15.10 Schematic flow diagram of the PUREX process (From Benedict et al. (1981)).

most important being $[Zr(NO_3)_4 \cdot 2TBP]$. The formation of this complex is inhibited by the addition of F^- whereby

$$Zr(NO_3)_4 \cdot 2TBP + 6F^- = ZrF_6^{2-} + 4NO_3^- + 2TBP \tag{15.30}$$

Subsequently the uranium is stripped from the organic phase. An overall schematic view of the PUREX process is shown in Figure 15.10.

Detailed descriptions of the process can be found in the works by Benedict et al. (1981) and Wymer and Vondra (1981). We shall briefly summarize the important parts of the process. The first step is to prepare the irradiated fuel for dissolution by mechanically chopping it into small pieces (1–5 cm long). This opening of the cladding causes the release of ~10% of the Kr and Xe fission products as well as some tritium and volatile fission products. These off-gases are combined with those from the next dissolution step.

In the dissolution step, the fuel pieces are dissolved in near boiling 10 M HNO_3. This step, which takes a few hours, dissolves the uranium, plutonium, and fission products, leaving the cladding to be recovered "intact." NO_x, Kr, and Xe fission products are recovered from the off-gas from this process. The chemical reactions for the dissolution of uranium involve processes like

$$3UO_2 + 8HNO_3 \rightarrow 3UO_2(NO_3)_2 + 2NO + 4H_2O \tag{15.31}$$

and

$$UO_2 + 4HNO_3 \rightarrow UO_2(NO_3)_2 + 2NO_2 + 4H_2O \tag{15.32}$$

The plutonium is oxidized to Pu(IV) and Pu(VI), while the neptunium ends up in the pentavalent or hexavalent states. Small amounts of plutonium and fission products may not dissolve, and they can be leached with acid solutions containing the oxidant Ce^{4+}.

The off-gas treatment involves primarily collecting iodine, krypton, and xenon. There are a variety of chemical processes for capturing the iodine and disposing of it. Kr and Xe are physically captured by either cryogenic techniques or selective absorption, such as absorption in chlorofluoromethane. Most of the off-gas volume is due to Xe ($\sim$800 L/Mg of fuel), whereas the activity is mostly the 10.7-year ^{85}Kr ($\sim$11 kCi/Mg of fuel).

The solution from the dissolution is treated with chemicals to adjust the acidity, valence, and concentrations of the species involved. The HNO_3 concentrations are 2–3 M, the $UO_2(NO_3)_2$ concentrations are 1–2 M, and the Pu is stabilized as Pu(IV) using N_2O_4 or hydroxylamine. In these and subsequent manipulations of these solutions, the concentration of Pu must be carefully monitored with regard to criticality. Criticality is controlled by regulating the solution geometry, the concentrations of fissile materials, and the addition of neutron absorbers such as Gd.

The primary separation of plutonium and uranium from the fission products involves a solvent extraction with 30 vol% TBP at room temperature. The activity levels during this separation are quite high ($\sim$1.7 kCi/L for the fission products), and the aqueous waste, which contains 99$^+$% of the fission products, is a high-level waste. Am and Cm are not extracted and Np is partially extracted. Because of the high radiation levels, the TPB is radiolyzed, leading to general degradation of the solvent. Primary products of the radiolysis of TBP are the dibutyl- and monobutylphosphoric acids along with phosphoric acid. These degradation products must be removed in the solvent purification steps.

Following decontamination of the uranium/plutonium from the fission products, the plutonium is separated from the uranium. This is accomplished by reducing the Pu(IV) to non-extractable Pu(III), leaving uranium in the hexavalent state. In the older PUREX plants, this used Fe^{2+} while the newer plants add U^{4+}. The plutonium thus ends up in an aqueous phase, while the uranium

remains in the organic phase. Uranium is back extracted (and thus removed from the organic phase) with 0.01 M HNO_3 and is purified by a series of solvent extraction cycles until the Pu/U ratio is $<10^{-8}$ and the total βγ activity is less than twice that of aged natural uranium.

15.6   Radioactive Waste Disposal

Radioactive waste management began with the advent of nuclear energy and has been studied continuously since then, with the expenditure of billions of dollars. Despite this Herculean effort, great uncertainty remains about when and how the various aspects of waste disposal (especially high-level waste) will be understood and dealt with effectively.

15.6.1   Classifications of Radioactive Waste

The simplest way to classify radioactive waste is by its physical state, that is, whether it is a gas, liquid, or solid. Gaseous waste arises from gas evolution, during nuclear fuel reprocessing mentioned previously and by activation of air during reactor operation. The principal gaseous activation product is 1.8 h ^{41}Ar, which is usually dispersed into the atmosphere from a stack whose height insures safe ground-level concentrations of the released gas. The off-gases from fuel reprocessing are the largest contributors to the gaseous waste. The fission products krypton and xenon escape when the fuel elements dissolve. Molecular iodine and ruthenium tetraoxide can also be released. Iodine and ruthenium are removed from the waste stream by trapping. Radioxenon has mostly decayed after a cooling time of about 1 year, while ^{85}Kr must be trapped cryogenically. While small quantities of ^{14}C are formed in reactors, the release of this ^{14}C as CO_2 is an important component ($\sim 1/2$) of the public dose due to the fuel cycle.

The most important liquid wastes are the high-level effluents that contain fission products from fuel reprocessing. The liquid waste contains >99% of the fission products in the fuel with small quantities of U and Pu. Medium-level liquid waste has an activity of ~ 4 GBq/L and results from various steps in fuel reprocessing. Low level (<0.1 GBq/m^3) is treated or concentrated. Nonradioactive liquid organic waste is usually incinerated or chemically destroyed. Solid waste comes from the mining and milling of uranium ore and sludge from spent fuel storage. It also includes contaminated equipment and structures. High-level solid waste includes the hulls from the dissolving of spent fuel, ion exchange resin, and so on.

Radioactive waste may also be classified as to origin (defense or commercial waste), the material present (transuranium waste, spent fuel), or the level of radioactivity present (high, medium, low). The principal categories of waste using this classification scheme are *high-level waste* (HLW), which results from

spent fuel reprocessing and consists mainly of fission products and a small portion (<0.5%) of the original U and Pu; *spent nuclear fuel* (SNF), which is irradiated fuel that has not been reprocessed; *transuranic waste* (TRU), which is α-emitting waste with >100 nCi/g of the transuranium nuclei; *low-level waste* (LLW), which is waste with small amounts of radioactivity (but non-TRU) arising from a variety of sources; and *mill tailings*, which are a special type of LLW that contains natural α-emitting radionuclides separated from the ore in uranium mills. Mill tailings are a finely ground sandy material that contains naturally occurring decay products from uranium. Waste may contain also "hazardous" waste (i.e., carcinogens, flammable materials, etc.) as well as "radioactive" waste. Such waste is referred to as "mixed" waste and generally has severe restrictions on disposal.

15.6.2 Waste Amounts and Associated Hazards

The volume and activity of radioactive waste, as of 1996, is summarized in Table 15.1. The largest *volume*, but lowest activity, is the mill tailings, which have a specific activity of $\sim$1.8 nCi/g, mostly due to the ^{238}U decay series daughters (^{230}Th, ^{226}Ra, ^{222}Rn, ^{210}Pb, ^{210}Bi, ^{210}Po, etc). Of special concern is gaseous
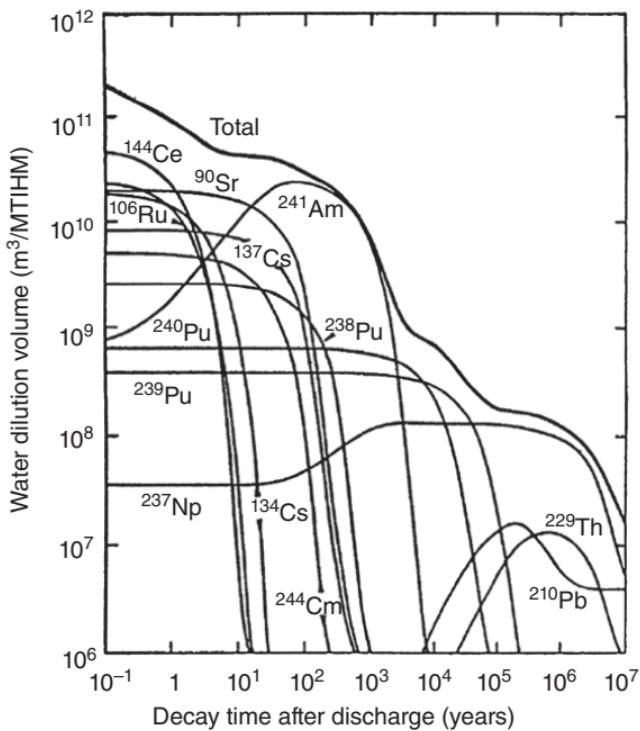
Table 15.1 1996 US Radioactive Waste Inventory.

Type Origin	Volume (10^3 m^3)	Activity (MCi)
Military		
HLW	347	878
LLW	3,389	16
SNF (MTHM)[a]	2,483	9,980
TRU	238	2.6
Mill tailings	28,000	0.08
Commercial		
HLW	2	24
LLW	1,751	8
SNF (MTIHM)[a]	34,253	12,537
Mill tailings	118,700	0.3

Source: Integrated Data Base Report-1996, DOE/RW-0006, Rev 13, U.S. Department of Energy, Washington, DC 1997.

[a]By convention, the quantity of spent fuel is reported in mass units (MTHM or MTIHM, metric tons of heavy metal or metric tons of initial heavy metal).

Figure 15.11 An example of the water dilution volume for radionuclides in PWR spent fuel (From National Research Council (1983)).

^{222}Rn ($t_{1/2} = 38$ s) because it can diffuse and effuse out of the solid material then decay leaving the subsequent decay products at a new, random position. Most of the *activity* associated with radioactive waste is in the unprocessed spent fuel. The military HLW tends to have larger volumes than the commercial HLW because the latter has been compacted. Most of the commercial spent fuel is stored at the reactor sites, while most of the military/USDOE waste is stored at a few major production facilities.

One measure of the hazard associated with this waste is the water dilution volume (m^3) (WDV). The WDV is the volume of water needed to dilute a radionuclide to its maximum permissible concentration in water. For example, the WDV for spent fuel from a PWR is shown in Figure 15.11 as a function of decay time. The quantity of spent fuel is reported in mass units (MTHM or MTIHM, metric tons of heavy metal or metric tons of initial heavy metal). Though the activity of the spent fuel falls by more than a factor of 1000 in the first 1000 years (e.g., Fig. 15.3), the WDV falls more slowly. This is due to the hazards posed by the long-lived α-emitters in the spent fuel. For times > 500 years, the actinide radiotoxicity prevails. On a time scale of 10^4–10^6 years, the WDV values approach those of the original ore used to make the reactor fuel. Note that there are limitations to this measure of hazard due to the ways that radionuclides enter the biosphere and are concentrated in biological systems.

15.6.3 Storage and Disposal of Nuclear Waste

What does one do with the radioactive waste described in the previous section? Clearly the most important component of the waste is the SNF. Currently most spent fuel assemblies from civilian power reactors are first held in cooling ponds at the reactor sites, although one cannot do this indefinitely. After the fuel has cooled for a number of years, the fuel is transferred to dry storage also at the reactor site. The fuel rods are transferred to special casks when the heat output and activity are such that air-cooling will suffice.

Because a permanent disposal strategy has proven illusive due to technical and political considerations, the present "solution" is for interim storage facilities where the fuel is stored in a retrievable manner until a permanent storage facility is developed. The scientifically favored method for permanent storage of radioactive waste is deep geologic repositories. This is the only option for unprocessed spent fuel assemblies and for most HLW. (An alternative, supplemental strategy discussed in the following text is to remove some of the actinides in the HLW by chemical separations prior to geologic storage.)

In general terms, the goal of long-term waste storage is to isolate the radioactive waste from humans and the environment. The prevailing design strategy for waste repositories is to encase the waste inside multiple barriers as indicated schematically in Figure 15.12. The first barrier is the form of waste, which will immobilize the radioactive materials. The waste form should not be damaged by heat or radiation nor be attacked by groundwater. The waste is placed in a steel canister that is resistant to chemical leaching. This canister is surrounded by packing materials that prevent radioactivity from escaping, and the entire
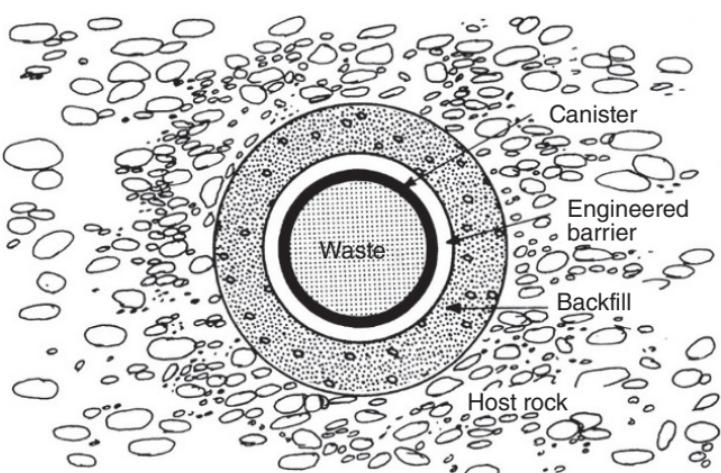
Figure 15.12 Schematic representation of the multiple barrier waste disposal strategy (From Murray (1994)).

repository is backfilled with a material that absorbs or resists chemical intrusion. The final barrier is the bulk host medium that separates the repository from the surrounding area and is generally a thick geological formation.

The host medium can be bedded salt, salt domes, granite, basalt, or volcanic tuff. Each medium has advantages and disadvantages with respect to resistance to water intrusion, site availability, and political considerations. Each medium can be made to work from a scientific standpoint with the most important factor being how the local site is designed. An additional factor is the position of the repository relative to the groundwater table, with most repositories being below the water table. The United States has/had chosen the Yucca Mountain region in Nevada, near the Nevada nuclear weapons test site, as its location for permanent geologic storage. The Yucca Mountain area features welded volcanic tuff as the host medium. Welded volcanic tuff is a material of low permeability, and the Yucca Mountain site is above the water table. Political considerations have blocked placing waste at this site up to the present.

The biggest concern with respect to radionuclides in a waste repository is their movement in groundwater. Attention is focused on the horizontal motion of the groundwater not the upward motion, as the repositories are typically several hundred meters below the surface. The repositories and their boundaries and locations are such that the inhabited biosphere is 10–100 km away from the center of the repository. The velocity of the groundwater in typical geologic media proposed for repositories ranges from 0.01 to 10 m/years. The velocity of radionuclides in groundwater is smaller than the velocity of the groundwater due to sorption phenomena. This sorption can be expressed by a retardation factor R where R is the ratio of the groundwater velocity to the average radionuclide velocity. R has been approximated as

$$R \approx 1 + 10K_{\mathrm{d}} \tag{15.33}$$

where K_{d} is the ratio of the radionuclide concentration in the rock of the repository to that in the groundwater. Retardation factors for radionuclides in geologic media of interest as repository sites range from 1 to 3000 and depend strongly on the ion being sorbed (Saling and Fentimann, 2001). As an example, $R = 200$ for ^{239}Pu in volcanic tuff. The Yucca Mountain groundwater velocities are ~0.025 m/year, meaning that ^{239}Pu will decay before it migrates 6 km. A similar conclusion can be reached for the transplutonium nuclei and for ^{90}Sr. From this standpoint, special concern is (only) necessary for ^{99}Tc and ^{237}Np, whose long half-lives allow significant geologic transport.

15.6.4 Spent Nuclear Fuel

The largest single radioactive waste disposal problem is the spent fuel from military and commercial reactors. As discussed earlier, the spent fuel from commercial reactors is stored in water ponds and then in dry casks at the reactor

sites. The spent fuel storage facility consists of a cooling and cleanup system for the water along with equipment to safely transfer the fuel rods from the reactor to the storage area. A typical pool will have a volume of ~400,000 gal. The water will contain ~2000 ppm boron that acts as a neutron absorber and will be maintained at a temperature of <70°C.

The long-term fate of the spent fuel is (most likely) geologic storage, but this awaits political decisions in the United States. The spent fuel assemblies can be packaged in canisters with a stabilizing material (powder or sand) around the rods in the canister. The fuel canisters are placed in the geologic storage site and covered by a backfill to impede water movement.

15.6.5 HLW

The HLW consists primarily of liquid waste from fuel reprocessing. It contains essentially all of the fission products from the spent fuel along with all the neptunium and transplutonium nuclei but <1% of the uranium and plutonium that has been removed from the fuel. HLW is intensely radioactive with a high heat output (cf. Fig. 15.8). The hazard potential of this waste extends for much greater than the time scale of nuclear energy use. In addition to its radiological hazard, it is very corrosive, being up to 7 M in HNO_3 and containing ~250 g/L salt. This waste is ultimately to be stored in geologic repositories after solidification of the liquid waste. The volume of the solidified waste is modest in that a commercial nuclear power reactor plant running for 1 GW-year produces about 2 m^3 of solidified waste after reprocessing (if such reprocessing were to occur).

The liquid HLW is stored for at least 6 years prior to solidification to reduce the decay heat (again cf. Fig. 15.8) by a factor of 10 or more. The first US military fuel reprocessing wastes were stored as neutralized waste in mild steel tanks at the Hanford Nuclear Reservation in eastern Washington. These steel-lined, reinforced concrete tanks had a capacity of 500,000–1,000,000 gal with provisions for removal of the decay heat and radiolysis products. Corrosion of several tanks occurred with the release of waste below ground level. Fortunately, the soil around these tanks retarded nuclide transport. The mitigation of leakage from the Hanford tanks is an ongoing, large problem at present. A better (and more expensive) design for storage tanks was implemented at the Savannah River Site in South Carolina consisting of a steel tank inside of a Hanford–style tank. The storage of acid waste in these tanks has not encountered the corrosion problems seen with the Hanford tanks.

The solidification of HLW takes place in two steps: a calcining step followed by an incorporation of the calcined material into borosilicate glass. Calcining can be done in various ways but primarily involves the removal of volatile products like water, NO_3^-, and conversion of all species in the HLW to solid stable oxides. The oxides are then mixed with SiO_2, B_2O_3, and so on. to make a borosilicate glass, which is then prepared for geologic storage (see Fig. 15.13).

Vitrified waste

Radioactive material is immobilized in a glass matrix and is only released as the glass is dissolved.

Overpack (steel container)

The vitrified HLW is encapsulated in an overpack (steel container) to prevent contact with groundwater during the time when its radioactivity and beat generation are high.

Buffer (compacted day)

The buffer is mainly bentonite clay compacted to high density so as to have low permeability, which slows the movement of dissolved radioactive waste. The buffer is also designed to protect the overpack.

Figure 15.13 Schematic diagram of the final steps in putting vitrified waste into a geologic repository. (*See insert for color representation of the figure.*)

15.6.6 Transuranic Waste

TRU is generated by fuel reprocessing and fuel fabrication facilities, the production of nuclear weapons, and the decommissioning of nuclear reactors or other fuel cycle facilities. TRU includes protective clothing, equipment, and so on. from reprocessing facilities along with plutonium and other transplutonium elements removed in fuel reprocessing. Because of the relatively low activity levels of this waste, the primary processing steps prior to storage generally involve volume reduction. In the United States, this waste is stored in an interim storage facility called the Waste Isolation Pilot Plant (WIPP), an underground salt-bed facility near Carlsbad, New Mexico.

15.6.7 Low-Level Waste

LLW primarily consists of contaminated dry trash, paper, plastics, protective clothing, organic liquids such as liquid scintillation samples, and so on. LLW is produced by any facility that handles radioactive materials such as nuclear power plants, medical facilities, university laboratories, and so on.

In the United States, commercial LLW is sent to one of three disposal sites (Barnwell, South Carolina, Richland, Washington; and Clive, Utah). Due to the limited size of these sites (and similar disposal sites through the world) and steeply escalating costs for waste disposal, the primary goal of LLW preparation prior to disposal is volume reduction, either by incineration or compaction, followed by immobilization. An important treatment process for LLW from laboratory work is "hold for decay" in which the material is stored in an isolated and secure facility to allow radioactive decay until the level of activity falls to negligible levels. For noncombustible solids, volume reduction can be achieved by mechanical disassembly, crushing, melting, or dissolution. For noncombustible liquids, evaporation, calcination, filtration, or concentration of activities on ion exchange resins are used for volume reduction. Combustible material is oxidized to ashes. Mechanical techniques of volume reduction reduce volume by 5–10 times, while combustion reduces volume by 50–100 times. The products of volume reduction are immobilized using absorbents (vermiculite, clay, etc.), cement, or salt matrices.

15.6.8 Mill Tailings

The tailings from uranium mining and milling contain all the daughters of uranium that were present in the original ore. The mill tailings thus have ~70% of the original activity of the ore. This activity decays with the half-life of the longest-lived isotope remaining in the chain, ^{230}Th ($t_{1/2} = 8 \times 10^4$ years). The radiological hazard is mostly due to ^{226}Ra and its gaseous daughter ^{222}Rn. The inert ^{222}Rn gas can escape from the tailings and can create a radiological inhalation risk. Other radionuclides, such as ^{230}Th or ^{226}Ra, and so on, can be leached from the tailings by exposure to water and transferred to the biosphere. The tailings themselves are finely divided sandy material that can also be dispersed by wind. Remediation of sites containing mill tailings involves covering the tailings by a clay or earth overburden that is 3–8 m thick. This overburden reduces Rn release, minimizes leaching, and prevents wind dispersal.

15.6.9 Partitioning of Waste

As discussed earlier, for a variety of reasons mainly geopolitical, the nuclear fuel cycle is operated in a "once-through" mode in the United States and in the majority of reactors worldwide. The long-lived transuranium nuclides are thus left mixed with the shorter-lived fission products in the HLW and SNF. As concern about the lack of long-term, widely accepted programs to deal with this waste mounts, attention has begun to be focused on partitioning (chemically separating) the transuranium nuclei from the waste and transmuting it to nuclides of shorter half-life by irradiation in high neutron fluxes generated

by high-energy accelerators. These waste destruction steps also can be incorporated into advanced design reactor systems or advanced fuel cycle designs. Other targets for partitioning are the most troublesome fission products such as ^{99}Tc, ^{129}I, ^{90}Sr, and ^{134,137}Cs.

At the outset, it should be noted that there is a division (Benedict et al., 1981; Bodansky, 1996) among scientists as to whether the gains in reduced radiotoxicity of the waste offset the additional cost and risk of further treatment and handling of the waste. Removal of the actinides from a waste repository gives a small reduction in risk because the actinides migrate so slowly through the repository. Several additional problems would be created by partitioning and transmutation such as a greater volume of wastes, the need for large, expensive processing facilities, an increase in the neutron flux coming from the waste that would necessitate increased shielding, and the possibility of additional releases of radioactivity to the environment. A US study has suggested 99.9% removal of the actinides and 95% removal of technetium, and iodine is a minimum requirement to justify the effort.

Nonetheless, the United States and other nations have been developing additional chemical separation processes to partition nuclear waste. Strontium and cesium can be removed from HLW by extraction with crown ethers, such as ditertiarybutyl dicyclohexanone-18-crown-6, which can also extract ^{99}Tc. In the United States, a variation of the PUREX process is being developed to reprocess spent fuel. This modification of the PUREX process is such that only U and Tc are extracted from the fission products and from the TRU nuclei (Np, Pu, Am, Cm). It is called the URanium EXtraction (UREX) process R. It is intended to recover >99.9% of the U, >95% of the Tc, and leave >99.9% of the TRU nuclei in the acid waste. All of the chemicals used in the process are converted to gases in subsequent processing to minimize waste. A PUREX separation is carried out using 30% TBP in kerosene working on a 1 M HNO_3 solution of spent fuel, and then acetohydroxamic acid (AHA), an analog of hydroxylamine, is used to reduce Np(VI) to non-extractible Np(V) and to complex Pu(IV) and Np(IV) to prevent their extraction. Figures 15.14 and 15.15 show the flowsheet for the UREX process and its place in the total, new proposed treatment of spent fuel. Other work on pyrochemical processes involving electrochemical reduction steps in molten salt baths is also underway.

15.6.10 Transmutation of Waste

Transmutation is the term used in connection with waste management to describe nuclear processes in which long-lived nuclides are changed into shorter-lived nuclides by nuclear reactions. Possible sources of bombarding particles are (fast) neutrons from reactors or more realistically accelerators that have been configured to produce large neutron fluxes, by high-energy reactions, such as spallation. Fast neutrons are preferred as the bombarding
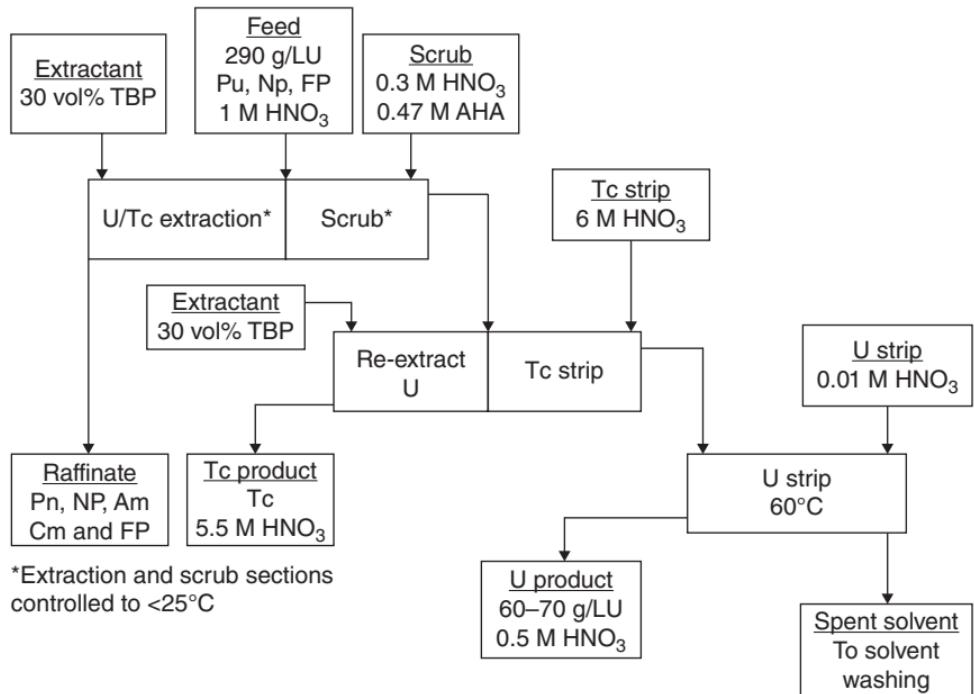
Figure 15.14 Flowsheet for the UREX process.

particle because some of the relevant isotopes of the actinides Np, Am, and Cm are not thermally fissionable. ^{129}I and ^{99}Tc, on the other hand, are readily destroyed in thermal fluxes. Transmutation can also be used to destroy plutonium from dismantled nuclear weapons. Of course, the resulting fission or reaction products from transmutation are usually radioactive and do constitute radioactive waste, albeit with shorter half-lives.

Current attention is centered on methods using charged particle accelerators for transmutation. In a typical scheme, an accelerator is used to produce a 10–200 mA beam of ∼1 GeV protons. The proton beam strikes a liquid lead or lead-bismuth eutectic target giving rise to 30–40 fast neutrons/proton, via spallation. These fast (1–10 MeV) neutrons are slowed down in a graphite moderator surrounding the Pb target. Some designs produce fast (75–225 keV) neutrons in the moderator, while other designs thermalize the neutrons. The actinides and fission products to be transmuted are dissolved in molten salts or other media allowing high heat transfer in channels passing through the moderator. The neutron flux in the channels is as high as 10^{15}–10^{16} n/cm^2/s. Typical heat production in the moderator–fuel blanket is ∼750–1500 MW. The excess heat is used to generate electricity that helps run the operation of the facility. The transmuted material is designed to have ∼20% of the original plutonium and minor actinides of the input material and will contain
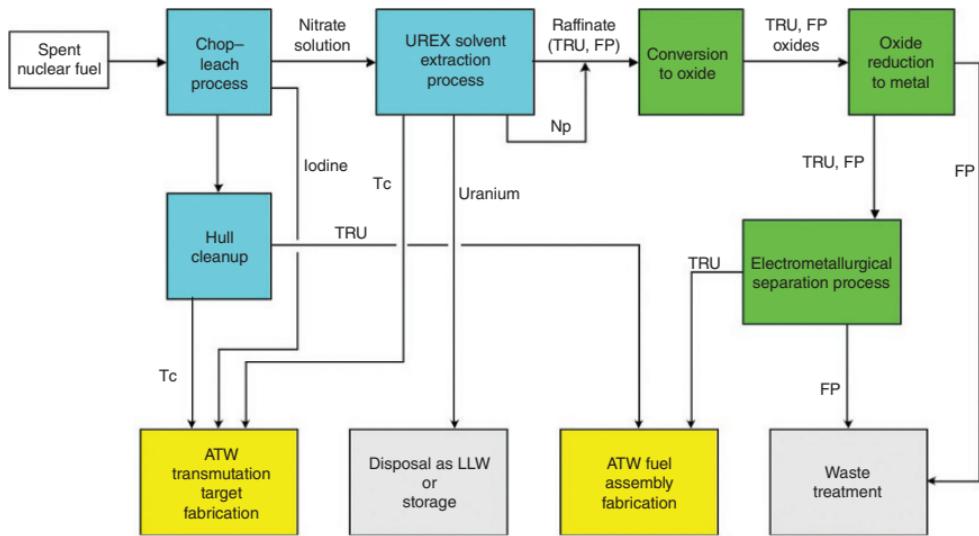
Figure 15.15 Schematic representation of the new schemes for the processing of SNF. (*See insert for color representation of the figure.*)

significant fission product activities. This transmuted material can be put into geologic storage, reducing the long-term hazard of the repository material.

15.7 Chemistry of Operating Reactors
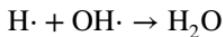
A complex set of chemical processes occurs during the operation of a nuclear reactor. Up to this point, we have concentrated on the chemical, physical, and nuclear processes occurring in the fuel and the consequences of these processes. Now we turn our attention to the coolant, the moderator, and the reactor materials and their changes due to the hostile chemical environment. The reactor environment has coolant temperatures up to 350°C, pressures of ~75–150 atm, and intense neutron and γ radiation. Further complications are introduced by the two phases of water present in BWRs and the use of chemical shims like B to control the reactivity of PWRs. Both reactor types exhibit potentially serious possibilities of corrosion.

15.7.1 Radiation Chemistry of Coolants
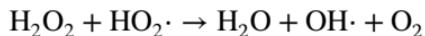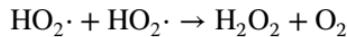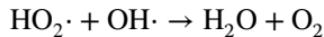
About 2% of the total neutron and γ-ray energy released in a nuclear reactor is deposited in the cooling water. The effects from this energy deposition are of special concern in BWRs where the neutron and γ-ray fluxes near the core are ~10^9 R/h of neutrons and 10^8 R/h of photons. (There is a hydrogen gas overpressure in PWRs that suppresses to some extent water decomposition or oxygen gas production.) The intense radiation fields cause radiolysis of the coolant water, that is, the deposited energy produces a strongly oxidizing environment with 100–300 ppb oxygen and hydrogen peroxide, with lesser concentrations in the vapor phase. The primary process in this radiolysis is

$$H_2O + \text{Energy} \rightarrow H \cdot + OH \cdot \tag{15.34}$$

These radicals go on to react to form H_2 or H_2O_2 by various chain reactions, including chain termination:

$$H \cdot + H \cdot \rightarrow H_2$$
$$H \cdot + OH \cdot \rightarrow H_2O$$
$$OH \cdot + OH \cdot \rightarrow H_2O_2$$

Molecular O_2 is generated by the series

$$H_2O_2 + OH \cdot \rightarrow HO_2 \cdot$$
$$HO_2 \cdot + OH \cdot \rightarrow H_2O + O_2$$
$$HO_2 \cdot + HO_2 \cdot \rightarrow H_2O_2 + O_2$$
$$H_2O_2 + HO_2 \cdot \rightarrow H_2O + OH \cdot + O_2$$

and also destroyed by the reaction

$$O_2 + H\cdot \rightarrow HO_2\cdot \tag{15.35}$$

15.7.2 Corrosion

The oxygen and radiolysis products attack the outer layers of the stainless steel or nickel-based alloys used in the reactor structure, forming a thin oxide layer on these components. Corrosion products are released from this thin oxide layers by the cooling water and become activated as they pass near the reactor core. The activated products can deposit on fuel surfaces, in coolant channels, and on reactor materials. These deposits are referred to as Chalk River Unidentified Deposits (CRUD). In PWRs the chemical composition of the CRUD is primarily $Ni_xFe_yO_4$ where $x/y = 0.25$ and $x + y = 3$. In PWRs, CRUD that also contains boron compounds is thought to cause a phenomenon known as "axial offset anomaly" (AOA), which is an unexpected deviation from predictions of the core axial power distribution during operation of aged reactors. Because it is not well understood, AOA limits the operating power of several PWRs, at great cost to the utilities. Attempts are often made to minimize corrosion by controlling the chemistry of the coolant water. Adding [7]LiOH raises the pH to 8, and one can use oxygen scavengers such as hydrazine to reduce the oxygen concentration.

Sample Problem: 15.2 CRUD
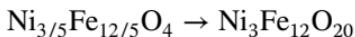
Construct a plausible molecular formula for CRUD based on the description in the text.

Solution
CRUD is described as: $Ni_xFe_yO_4$ where $x/y = 0.25$ and $x + y = 3$. Thus

$$x/y = 0.25 \rightarrow y = 4x$$
$$x + y = 3 \rightarrow 5x = 3; x = 3/5 \text{ and } y = 12/5$$

$$Ni_{3/5}Fe_{12/5}O_4 \rightarrow Ni_3Fe_{12}O_{20}$$

Balancing oxidation states $:$ $Ni(II)_3Fe(II)_2Fe(III)_{10}O_{20}$

15.7.3 Coolant Activities

When corrosion products are deposited on the fuel surfaces, they can become activated by neutron capture. Some of the most prominent corrosion activities are [55]Fe, [63]Ni, ^{60}Co, [54]Mn, [58]Co, and [59]Fe. These radionuclides will then be also found circulating in the reactor coolant.

Fission products can be released from defects in the fuel rods or from tramp uranium on the fuel cladding. Of special importance are the volatile fission

products $^{131-135}$I (^{89}Kr, ^{137,138}Xe in BWR steam). Cations include the Sr and Cs isotopes, which are present along with ^{129}I and ^{99}Tc. One can use the ratio of short-long-lived isotopes such as the ratio of ^{133}I/^{131}I to measure the source of the fission product release, by assuming the short-lived species can only result from tramp fuel or large cracks in the fuel assembly.

Impurities in the water and water activation products also contribute to the radioactivity of the coolant water. Tritium is produced as a low yield (~0.01%) fission product that can diffuse out of the fuel by activation of boron or ^{6}Li impurities in PWRs. ^{24}Na and ^{38}Cl are produced by neutron activation of water impurities. In BWRs, the primary source of radiation fields in the coolant and steam systems during normal operations is 7.1 s ^{16}N. This nuclide is produced by ^{16}O(n, p)^{16}N reactions from fast neutrons interacting with the coolant water. This ^{16}N activity can exist as NO_2^-, NO_3^- in the coolant and as NH_4^+ in the steam.

Problems

15.1 Define or describe the following terms or concepts: (a) CRUD, (b) radiolosis, (c) accelerator transmutation of waste, (d) UREX process, (e) LLW, (f) TRU, (g) HLW, (h) SNF, (i) PUREX process, (j) back end of the fuel cycle, and (k) pyroprocessing.

15.2 Define or describe the following terms or concepts related to the uranium fuel cycle: (a) yellowcake, (b) orange oxide, and (c) green salt.

15.3 Since UO_2 can be converted directly to UF_6, why is it first converted to UF_4 and then to UF_6 in the uranium fuel cycle?

15.4 Write balanced chemical equations for three different methods to produce metallic uranium.

15.5 Nitric acid readily dissolves UO_2. Why doesn't hydrochloric acid dissolve UO_2?

15.6 Given a *G* value of 1.59 for the production of hydrogen gas by the irradiation of TBP with 1 MeV electrons, calculate the rate of hydrogen gas evolution in a liter of TBP irradiated for 1 h at a dose rate of 200 W/L. Assume STP conditions.

15.7 Draw a flowsheet for the PUREX process similar to the one shown in Figure 15.10. Estimate the relative volumes of all streams in the process using data from the references cited in the text.

15.8 Discuss the disposal of the following examples of radioactive waste:
1) Water solutions containing 1 mCi of ^3H from a research lab
2) Gas escaping from the dissolution of 1 kg of irradiated reactor fuel
3) The ion exchange resin used to purify the cooling water of a 1 MW research reactor

15.9 500 grams of natural uranium is irradiated in a neutron flux of 10^{13} n/cm^2/s for 1 year. What is the heat output of this material after cooling for 1 week? One month? One year?

15.10 What is the theoretical maximum separation factor for separation by gaseous diffusion of ^{3}He and ^{4}He?

15.11 If a gaseous diffusion plant produces uranium with a 235/238 ratio of 5 times normal, what is the expected 234/235 ratio in the resulting material?

15.12 Discuss quantitatively the relative merits of using LiOH, NaOH, or KOH for pH control in reactor coolant water.

15.13 In reactors based on a Th fuel cycle, a significant amount of ^{233}Pa is produced. Discuss the radiochemistry of this radionuclide.

Bibliography

M. Benedict, T.H. Pigford, and H.W. Levy, *Nuclear Chemical Engineering*, 2nd Edition (McGraw-Hill, New York, 1981).

D. Bodansky, *Nuclear Energy: Principles, Practices and Prospects* (AIP, Woodbury, 1996).

C.D. Bowman, *Ann. Rev. Nucl. Part. Sci.* 48, 505 (1998).

G. Choppin, J.O. Liljenzin, and J. Rydberg, *Radiochemistry and Nuclear Chemistry*, 3rd Edition (Butterworth-Heinemann, Woburn, 2002).

M. Eisenbud, *Environmental Radioactivity*, 3rd Edition (Academic, Orlando, 1987).

S. Glasstone, *Sourcebook on Atomic Energy*, 3rd Edition (Van Nostrand, New York, 1967).

R.E. Leuze, An overview of the light water reactor fuel cycle in the US, *Light Water React. Nucl.*, Fuel Cycle, R.G. Wymer and B.L. Vondra, eds. (CRC, Boca Raton, 1981), 5–59.

C.C. Lin, *Radiochemistry in Nuclear Power Reactors*, NAS-NS-3119 (National Academy Press, Washington, 1996).

R.L. Murray, *Understanding Radioactive Waste*, 4th Edition (BMI, Columbus, 1994).

National Research Council, A Study of the Isolation System for Geologic Disposal of Radioactive Wastes, (National Academy Press, Washington, 1983).

S. Peterson and R.G. Wymer, *Chemistry in Nuclear Technology* (Addison-Wesley, Reading, 1963).

J. Prawitz and J. Rydberg, *Acta. Chem. Scand.* 12, 393 (1958).

L.E.J. Roberts, *Ann. Rev. Nucl. Part. Sci.* 40, 79 (1990).

J.H. Saling and A.W. Fentimann, *Editors, Radioactive Waste Management*, 2nd Edition (Taylor & Francis, New York, 2001).

R.G. Wymer and B.L. Vondra, *Light Water Reactor Nuclear Fuel Cycle* (CRC, Boca Raton, 1981)

Interaction of Radiation with Matter

16.1   Introduction

At this point we have described nuclear transitions and reactions that produce various forms of nuclear radiation. The radiation propagates out from the originating nucleus and interacts with other matter along its path. These interactions with external matter allow us to observe the radiation, and its effects, and to determine the nature of the transition inside the nucleus. The interaction of radiation with matter is also the cause of chemical, physical, and biological changes that concern the public at large. We will specifically address the operating principles of radiation detectors in the next chapter, but first we will consider the fundamental interactions of nuclear radiation with matter.

It should be clear that radiation (with the exception of neutrons) primarily interacts with bound electrons. For example, a silicon atom contains fourteen electrons in a sphere with a radius of 0.12 nm that presents a geometrical cross section of 4.5×10^{-20} m^2. The silicon nucleus at the center of the sphere has a radius of 3.6 fm with a geometrical cross section of 4.1×10^{-29} m^2. The geometrical probability to strike the electrons in an atom is something like nine orders of magnitude higher than that to strike the nucleus. A scattered electron leaves the original atom and creates an ion pair. The interaction of a single particle of nuclear radiation can lead to tens or hundreds of thousands of ion pairs, and so nuclear radiation is generally called ionizing radiation.

From the starting point that we should consider the interaction of the radiation with electrons, we can divide nuclear radiation into four classes as indicated in Table 16.1. The overall scattering of the particle from an electron will be dominated by the mass and the charge on the particle. Thus, massive charged particles will tend to scatter the much smaller mass electrons widely without losing much energy, while the collision of an electron with another electron will lead to energy sharing, and a photon can be scattered or even absorbed by a single electron. Neutrons only interact very weakly with electrons through their small magnetic moment and predominately interact with nuclei. (As will be discussed later, neutrons are very penetrating and difficult to detect due to the

Table 16.1 Particle Classes for Interaction with Matter.

Relative Mass	Charged Particles	Uncharged Particles
"Heavy"	Protons, heavy ions	Neutrons
"Light"	Electrons	γ-Rays

Table 16.2 Densities of Some Pure Metals.

Element	Atomic Number Z	Atomic Mass (g/mol)	Mass Density ρ (g/cm^3)	Number Density ρ_N (N_A/cm^3)	Electron Density ρ_e (N_A/cm^3)
Beryllium	4	9.0122	1.85	0.205	0.821
Aluminum	13	26.98	2.70	0.10	1.3
Silver	47	107.88	10.5	0.0973	4.6
Gold	79	197.0	19.3	0.0980	7.7
Lead	82	207.2	11.85	0.0572	4.7

small probability of striking a nucleus.) As a general rule, all of the interactions end up in creating energetic electrons. The heavy charged particles and recoiling atoms also scatter electrons. The electrons interact with matter to create moving charged particles, while neutrons create recoiling nuclei and photons create moving electrons.

We will discuss the interaction of each class of radiation starting with the simplest, those charged particles that are more massive than electrons. We will consider what happens as they pass through various types of matter. The radiation generally penetrates through many, many atomic layers, so we can generally assume that the atoms are randomly distributed in space. This assumption is certainly true for liquids and gases, but we usually think of solids as having a regular crystal or lattice structure. The solid material that we encounter in everyday life certainly has a lattice structure on the microscopic scale, but nearly all materials are polycrystalline on a larger scale. Thus, the types of radiation that we will generally consider will cross many crystal (or grain) boundaries in normal materials. The exceptions are single crystals of silicon, germanium, or other special materials that are used in semiconductor-based radiation detectors that rely on their special electronic properties. We have to be aware of the orientation of the crystal axes in these devices relative to the propagation direction of the radiation. One can compare the various densities used in energy-loss calculations with pure metals in Table 16.2.

Also before starting the discussion, it is useful to define a quantity called the *areal density.* We have said that ionizing radiation will pass through a significant amount of material and sometimes will even pass completely through an object. We can imagine that the solid piece of material can be compressed into a thin, two-dimensional sheet as far as the radiation is concerned. The origins of this concept lie in early experiments with α rays in which very thin sheets of metals were necessary to observe scattering reactions. We can easily measure the length, x, and breadth, y, of such thin foils, but it is very difficult to measure the thickness, z, without destroying the foil. On the other hand, we can determine the mass, m, of the foil rather easily and then calculate the thickness using the density of the material. For example, if the foil is made from a pure chemical element, so that the density is known, then

$$\text{Linear thickness} = z = \frac{m/xy}{\rho} = \frac{\text{Areal density}}{\text{Mass density}} \tag{16.1}$$

where ρ is the mass density (and has dimensions of mass per unit volume, of course). The measured quantity of mass per unit area is often used to characterize thin foils of pure materials, and this is the quantity called the *areal density*. The symbol ρ_A is sometimes used for the areal density. Typical dimensions for materials that we might use in nuclear experiments are milligram per square centimeter. Thus, if the density of a typical metal were in the range of 5–10 g/cm^3, the thickness of this typical foil would be on the order of small fractions of a millimeter. Please note that the areal density can be measured easily in that one can take a foil of known area and weigh it.

Sample Problem 16.1: Areal Density

A ream of a certain type of standard letter-sized paper (in the United States) was found to have a mass of 2.26 kg. What is the areal density of one sheet of this paper?

Solution
Recall that a ream of paper contains 500 sheets so that the areal density of one sheet is simply

$$\rho_A = \frac{\text{Mass}}{\text{Area}} = \frac{2260 \text{ g/500 sheets}}{\text{Area of one sheet}}$$
$$= \frac{2260 \text{ g/500 sheets}}{8.5 \times 11 \text{ in.}^2 \times (2.54 \text{ cm/in.})^2}$$
$$= 7.5 \text{ mg/cm}^2$$

16.2 Heavy Charged Particles

We can imagine the progress of any ionizing radiation through material as a series of straight-line segments between scattering events. The scattering events primarily involve electrons as outlined previously. The total path is thus made up of these line segments, and the overall trajectory of the particle in the material will depend on the average kinematics of these scattering events. Elastic scattering is, of course, governed by the conservation of momentum and energy, so we should expect that the mass of the particle will play a large role in determining the overall features of the trajectory of the particle.

The tracks of a few heavy charged particles that have stopped in a photographic film are shown in Figure 16.1. The photographic film, called a nuclear emulsion, is sensitive to the ionization that is caused by the charged particles as they move through it. In normal use, visible photons "expose" photographic film by creating photoelectrons that don't recombine because the emulsion is an insulator, and the trapped ionization is converted into an image through the film development process. All of the heavy charged ions that we have to consider have positive charges. As can be seen in Figure 16.1, energetic charged ions move through material on essentially straight trajectories, giving up or losing kinetic energy through collisions with the atomic electrons of the material. Only rarely by comparison is an ion scattered by the Coulomb potential of a nucleus, and even more rarely does a nuclear reaction take place. Nuclear reactions are excluded when the initial kinetic energy of the heavy charged particle is lower than the Coulomb barrier (as discussed in Chapter 10). Thus the ions will interact with an extremely large number of electrons, and we can examine the average behavior of the ions as they pass through material.

16.2.1 Stopping Power

The *rate* at which charged particles lose energy as they travel through a given material is called the *stopping power* of that material. The stopping power is made up from two parts, the electronic stopping power due to the interaction with the atomic electrons of the material and the nuclear stopping power. Thus,

$$-\frac{dE}{dx} = S_{\text{electronic}} + S_{\text{nuclear reaction}} \approx S_{\text{electronic}} \tag{16.2}$$

because the electronic stopping power is always much larger than the nuclear reaction stopping power. Notice that the minus sign on the rate indicates that the ions are losing kinetic energy. The nuclear reaction stopping power is not zero, of course, because we know that nuclear reactions do take place even if they are rare. The stopping powers are functions of the mass, charge, and velocity of the ion, the atomic number, and the density of the medium.

Niels Bohr suggested that the energy loss rate could be estimated in a very simple picture as the series of impulses delivered to individual electrons by
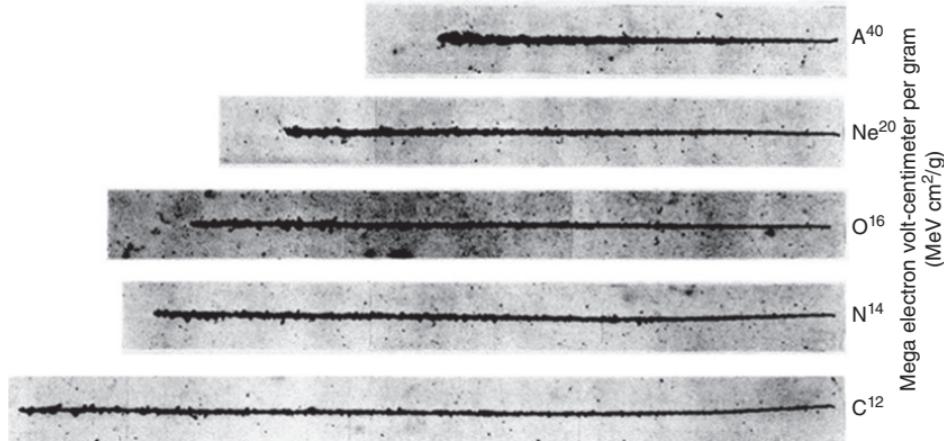
Figure 16.1 The trails of ionization left by heavy charged particles (initial energy of 10 MeV/nucleon) as they penetrate through a photographic plate (nuclear emulsion). The ions interact with the atomic electrons in the emulsion creating ion pairs to "expose" the emulsion, and the tracks become visible after the film is developed. Notice the straight-line tracks (Knoll (2010). Reproduced with the permission of John Wiley & Sons, Inc.).

the ion. Imagine an ion moving on a straight-line trajectory past an electron as indicated in Figure 16.2. A net impulse to the electron will occur in the direction perpendicular to the trajectory of the ion because any impulse due to the approaching ion will be canceled by that of the receding ion. It can be shown that the energy gained by a single electron and thus lost by an ion in one encounter depends on the impact parameter, b, as

$$\Delta E(b) - \frac{2q^2 e^4}{m_e v^2 b^2} \tag{16.3}$$

where q is the charge of the ion (often equal to the atomic number), v is the velocity of the ion, and m_e is the mass of the electron. This expression can be converted to a differential expression by multiplying the electron number density, N_e, times the volume element:

$$- dE(b) = \Delta E(b) N_e dV = \Delta E(b) N_e 2\pi b dx \tag{16.4}$$

by using the cylindrical coordinates of impact parameter and taking x along the ion's path. This expression should not be integrated from $b = 0$ to $b = \infty$ but only over the range b_{min} to b_{max} that are appropriate to the initial assumptions with about the average distance between ion and the electron so that

$$- \frac{dE}{dx} = \frac{4\pi q^2 e^4}{m_e v^2} N_e \ln \frac{b_{max}}{b_{min}} \tag{16.5}$$
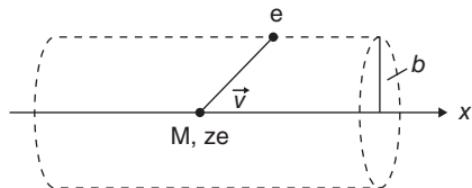
Figure 16.2 Trajectory of a moving ion past an electron (Leo (1987). Reproduced with the permission of Springer).

The minimum impact parameter will correspond to those collisions in which the maximum amount of kinetic energy is transferred to the electron. Due to conservation of momentum, the maximum electron energy is $W_{max} = (1/2)m_e(2\gamma v)^2$ where we have included the relativistic factor, γ, due to the low mass of the electron. Recall that $\gamma = \sqrt{1/(1 - \beta^2)}$ and $\beta = v/c$. Then substituting into the expression for the energy loss at a given impact parameter,

$$\Delta E(b) = \frac{2q^2 e^4}{m_e v^2 b_{min}^2} = 2\gamma^2 m_e v^2 \tag{16.6}$$

and we find that

$$b_{min} = \frac{qe^2}{\gamma m_e v^2} \tag{16.7}$$

The maximum impact parameter has to be estimated from different considerations. The basis of the energy-loss process is that the ion rapidly moves past the electron and delivers a sharp impulse to it. The electrons are bound in atoms and thus are orbiting with their own characteristic frequencies or time scales. The time for the ion to cross the atom should be less than the average time for an electron orbit; otherwise the collision will not be adiabatic or "rapid." The time for the ion to move past can be estimated as the ratio of the impact parameter to the ion's velocity; the average orbital time for an electron will clearly depend on the chemical element, allowing consideration of an average radius, R_e, and velocity, v_e, for each element, thus

$$\frac{b_{max}}{\gamma v} \leq \frac{R_e}{v_e} = f(Z) \tag{16.8}$$

where $f(Z)$ is a function of the atomic number of the stopping material Z. So that we can combine these two limits into the expression for the stopping power or energy loss rate to get Bohr's classical formula, we get

$$\left(-\frac{dE}{dx}\right)_{Bohr} = \frac{4\pi q^2 e^4}{m_e v^2} N_e \ln \frac{\gamma^2 m_e v^3 f(Z)}{qe^2} \tag{16.9}$$

This expression has been superseded by the expression derived by Hans Bethe and Claude Bloch based on momentum transfer in a quantum mechanically correct formalism. Their expression with the expanded form of the electron number density is

$$\left(-\frac{dE}{dx}\right)_{\text{Bethe–Bloch}} = 4\pi N_A r_e^2 m_e c^2 \rho \frac{Zq^2}{A\beta^2} \left[\ln\left(\frac{W_{\max}}{I}\right) - \ln(1-\beta^2) - \beta^2\right]$$

(16.10)

where N_A is Avogadro's number, r_e is the classical radius of the electron, and ρ is the mass–density of the stopping medium with atomic number, Z; mass number, A; and ionization potential, I. Finally, $W_{\max}$ is the maximum energy transfer encountered previously. The structure is very similar to the classical formula as should be expected, but it includes an extra term in the logarithm. Various formulas are available to give the average variation of the ionization potential for the chemical elements. For example, the expressions

$$I/Z = (12 + 7/Z)\,\text{eV}, Z < 13 \tag{16.11}$$

$$I/Z = (9.76 + 58.8\,Z^{-1.19})\,\text{eV}, Z \geq 13 \tag{16.12}$$

result from one empirical fitting of the data, but one should realize that the variation could be quite complicated due to the filling of the atomic shells.

The modern form of the stopping power formula includes two corrections. The first correction applies at high energies at which polarization of electrons by the electric field of the moving ion tends to shield distant electrons; this correction depends on the electron density; it is subtractive and given the symbol δ. The second correction applies at low energies when the collisions are no longer adiabatic, similar to the limit applied by Bohr. This correction is termed the shell correction as it depends on the orbital velocities of the electrons. It is also a subtractive term and given the symbol C. If we evaluate all the constants, then the modern form is

$$\left(-\frac{dE}{dx}\right)_{\text{Bethe–Bloch}} = 0.3071\frac{\text{MeV cm}^2}{\text{g}} \rho \frac{Zq^2}{A\beta^2} \left[\ln\left(\frac{W_{\max}}{I(1-\beta^2)}\right) - \beta^2 - \frac{\delta}{2} - \frac{C}{Z}\right]$$

(16.13)

which has the dimensions of megaelectron volt per centimeter when the usual form of the density in gram per cubic centimeter is used. The actual evaluation of this function is complicated due to the detailed variation of the ionization potential and the two correction terms. The reader is referred to more detailed discussions (see the book by Leo) for actual formulas for the correction factors. In practice, several computer codes and detailed tables of the stopping powers are available. In addition, some authors divide through by the density, ρ, and report the mass stopping power:

$$\frac{-1}{\rho}\frac{dE}{dx} \tag{16.14}$$

with dimensions of MeV cm^2/g which is convenient for ions passing through a combination of materials.

Sample Problem 16.2: Using the Bethe–Bloch Formula

Evaluate the stopping power of beryllium metal for $^{18}O^{8+}$ ions with a kinetic energy of 540 MeV ($E/A = 30$ MeV) using the Bethe–Bloch formula.

Solution

Finding some necessary constants, the density of beryllium metal is 1.85 g/cm^3 and $Z = 4$ so that the ionization potential can be estimated as

$$I/Z = (12 + 7/4)\,\text{eV} = 13.75\,\text{eV} \rightarrow I = 55\,\text{eV}$$

The values of β and γ for the ion can be obtained from the relativistic expressions (derived elsewhere)

$$\beta = \left[1 - \left(\frac{m_0 c^2}{(m_0 c^2 + (E/A))}\right)\right]^{1/2}$$

$$\beta = \left[1 - \left(\frac{931.5}{(931.5 + 30)}\right)\right]^{1/2} = 0.1766$$

$$\gamma = \left[\frac{1}{(1 - \beta^2)^{1/2}}\right] = 1.01598$$

The value of $W_{\max}$ can be evaluated as

$$W_{\max} = 2m_e c^2 (\beta\gamma)^2$$
$$W_{\max} = 2 \times 0.511\,\text{MeV}\,(0.1766 \times 1.01598)^2 = 0.03291\,\text{MeV}$$

Finally, the expression with the leading constants evaluated is

$$\left(-\frac{dE}{dx}\right)_{\text{Bethe–Bloch}} = 0.3071\frac{\text{MeV cm}^2}{\text{g}}\rho\frac{Zq^2}{A\beta^2}\left[\ln\left(\frac{W_{\max}}{I}\right) - \ln(1 - \beta^2) - \beta^2\right]$$

$$\left(-\frac{dE}{dx}\right)_{\text{Bethe–Bloch}} = 0.3071\frac{\text{MeV cm}^2}{\text{g}}(1.85\,\text{g/cm}^3)\frac{(4)(8^2)}{9(0.1766)^2}$$
$$\times \left[\ln\left(\frac{0.03291\,\text{MeV}}{55\times10^{-6}\text{MeV}}\right) + 0.03168 - 0.1766^2\right]$$

$$\left(-\frac{dE}{dx}\right)_{\text{Bethe–Bloch}} = 518.0\,\text{MeV/cm} \times [\ln(598.4) - 0.000492] = 3.3\,\text{GeV/cm}$$

Notice that the answer indicates that an ion with only 540 MeV of kinetic energy will lose all its energy and stop before it travels a fraction of a centimeter. As discussed later, we need to integrate this expression to determine the predicted range.

If we look at the overall form of these equations for the stopping power, we would see that they all have a part that depends on the moving ion and another part that depends on the stopping medium. If we concentrate on the part that only depends on the ion, we find that

$$-\frac{dE}{dx} \propto \frac{q^2}{v^2} \ln(\gamma^2 v^2) g(Z) \tag{16.15}$$

in which we can convert both factors of v^2 into kinetic energy, E, by suitably applying factors of $1/2 m_{\text{ion}}$. The function $g(Z)$ collects all the variation on the absorbing medium. The revised expression shows that the energy loss rate will be proportional to the mass of the ion:

$$-\frac{dE}{dx} \propto \frac{m_{\text{ion}} q^2}{E} \ln\left(\frac{\gamma^2 2E}{m_{\text{ion}}}\right) g(Z) \tag{16.16}$$

and inversely proportional to the kinetic energy. At low ion velocities ($E/A <$ 10 MeV/A), the $\ln(\gamma^2 2E/m_{\text{ion}})$ term is approximately constant so that

$$-\frac{dE}{dx} \propto \frac{m_{\text{ion}} q^2}{E} \tag{16.17}$$

Thus, a more energetic ion will tend to lose energy at a lower rate than a less energetic ion. Be careful to note that we have ignored the relativistic terms γ^2 and β^2 in the parentheses that produce a minimum in the complete function near $\beta \sim 0.96$ and a small rise at higher velocities. (Particles with $\beta \sim 0.96$ are called *minimum ionizing particles*.) The proportionality of the stopping power on the mass and square of the charge of the ion for a given kinetic energy provides the basis for a very effective particle identification using thin silicon semiconductor detectors, as discussed in Chapter 17.

We are now in a position to examine the slowing down of a charged particle as it penetrates into material. Kinetic energy is lost through scattering electrons away from the essentially straight-line path of the ion. If the initial kinetic energy of the ion is a few MeV/A or higher, the rate at which kinetic energy is dissipated slowly increases as the ion penetrates into the material. For example, the stopping power of beryllium metal for a very energetic ^{40}Ar ion is shown in Figure 16.3 along with the residual energy of the ion. (The thickness scale can be converted into a linear distance by dividing the density of beryllium in appropriate units.) Notice that the stopping power is relatively constant over most of the ion's path. The kinetic energy of the ion uniformly decreases as it moves through the material. However, two changes occur as the velocity of the ion approaches the Bohr velocity of the atomic electrons; $v_{Bohr} = \frac{Z\hbar}{m_e n a_0} = 5.51 \times 10^{-3} Zc/n$, where c is the speed of light, n is the Principal Quantum Number of the electron, and a_0 is the fine structure constant. The mean energy loss rate begins to increase dramatically as $\beta \to 0$, but more importantly, the charge state on the ion starts to decrease as the ion captures orbital
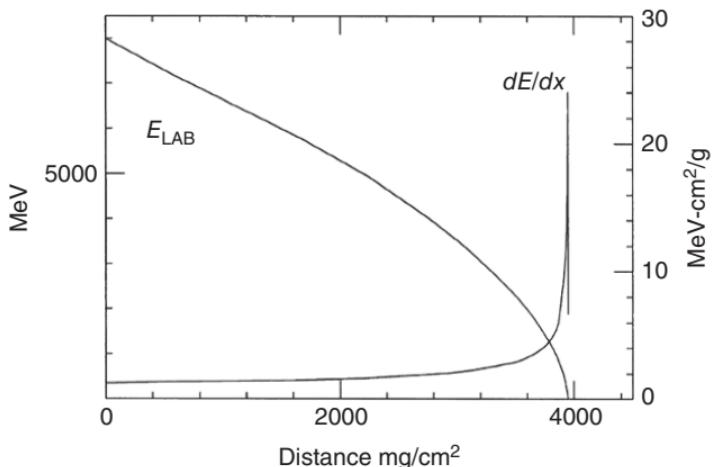
Figure 16.3 The energy loss rate as a function of distance penetrated for an ^{40}Ar projectile stopping in beryllium metal is shown on the scale to the right for an ion that enters the foil at the relatively high energy of 8 GeV. The remaining kinetic energy of the ion is shown on the left scale. Note that the ion penetrates $\sim$21 mm into the metal.
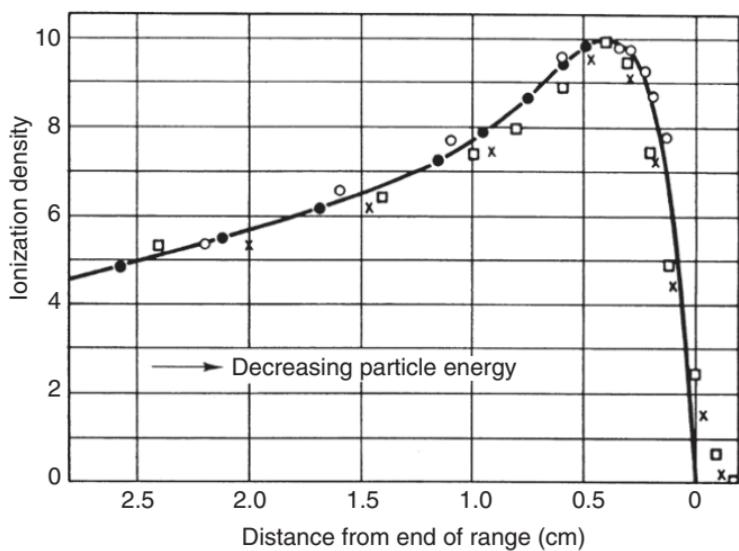
Figure 16.4 Results from an early measurement of the density of ionization along the path of an α particle stopping in air is shown. The Bragg peak in the ionization density is evident (Holloway and Livingston (1938). Reproduced with the permission of American Physical Society).

electrons causing the rate to drop. As indicated in Figure 16.3, the ion rapidly loses energy at the end of its range and stops rather suddenly. The energy loss for an α particle near the end of its range is shown in Figure 16.4. The resulting peak in the energy loss function just before the end of the charged particle's

range is called the *Bragg peak*. The fact that charged particles deliver a significant fraction of their kinetic energy at the end of their range makes charged particles useful for radiation therapy.

All of these expressions for the stopping power only apply to pure chemical elements. The stopping power of a compound or any complicated mixture will depend on the overall density and the relative numbers of electrons from each chemical element. Recognizing that radiation will usually move through macroscopic distances, we can use an averaging procedure called Bragg's rule. The average mass stopping power is

$$\left(\frac{1}{\rho}\frac{dE}{dx}\right)_{\text{total}} = \frac{w_1}{\rho_1}\left(\frac{dE}{dx}\right)_1 + \frac{w_2}{\rho_2}\left(\frac{dE}{dx}\right)_2 + \frac{w_3}{\rho_3}\left(\frac{dE}{dx}\right)_3 + \cdots \quad (16.18)$$

where w_1, ρ_1, and etc refer to the fraction by mass of element 1 in the entire mixture and its elemental density, respectively. The sum ranges over all the elements in the mixture. Thus, if the mixture was a pure compound, then we would combine the numbers of each element in the molecular formula. If the mixture had several components, then we would combine the masses of each element from all the components and so on to get an overall mass stopping power.
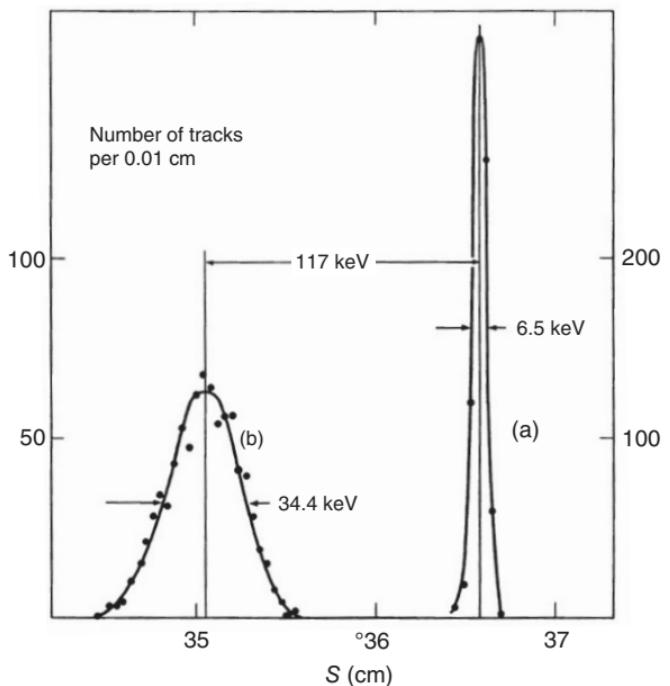
One of the implications of the stopping power formulas for heavy charged particles is that all particles of a given type will follow the same energy loss pattern in a given material. More specifically, the example shown in Figure 16.3 started with 8 GeV ^{40}Ar ions in Be. However, these curves display the expected result for all ^{40}Ar ions with kinetic energies <8 GeV. The energy loss rate for an ion with 4 GeV or even 4 MeV can be read off the graph by finding the point at which the residual energy of the ion is equal to the required energy. This may seem a trivial point, but it has the more subtle meaning that all the ions will follow exactly the same energy loss pattern, within the limits of the statistical stopping process, if we ignore nuclear Coulomb scattering. Formally we can write that the amount of kinetic energy lost, ΔE, in a finite thickness, Δx, of material is

$$\Delta E = \left(\frac{dE}{dx}\right)\Delta x \quad (16.19)$$

and the statistical variation in the energy lost, $\delta(\Delta E)$, would be evidenced as a width in the measured value that is called the amount of *energy straggling*. In a colloquial expression, the ions are said to straggle through the material, and the width of the energy distribution is due to this straggling. Thus, as ions pass through matter, the spread in their energies increases (Fig. 16.5), represented mathematically as a Gaussian distribution:

$$\frac{N(E)}{N}\,dE = \frac{1}{\alpha\sqrt{\pi}}\exp\left[-\frac{(E-\overline{E})^2}{\alpha^2}\right] \quad (16.20)$$

Figure 16.5 Energy spectrum of 3 MeV protons (a) before and (b) after passing through a 3.3 mg/cm^2 gold foil From Nielson (1961).

where the straggling parameter α, that is the half-width at $(1/e)$th height, is given by the expression

$$\alpha = 4\pi q^2 e^4 N_e x_0 \left[1 + \frac{kI}{m_e v^2} \ln\left(\frac{2m_e v^2}{I}\right)\right] \tag{16.21}$$

where x_0 is the mean range of the ion in the absorber and k is a constant (about 4/3).

Sample Problem 16.3: Combining Energy Losses

What is the rate of energy loss of an 8 MeV α-particle in air? Assume air is 21% oxygen and 79% nitrogen.

Solution

$$\left(\frac{1}{\rho}\frac{dE}{dx}\right)_{\text{total}} = \sum_i \frac{w_i}{\rho_i}\left(\frac{dE}{dx}\right)_i$$

where ρ is the total density and ρ_i the density of the i-th element. Neglecting correction terms,

$$\left(\frac{-1}{\rho}\frac{dE}{dx}\right) = 0.3071\frac{\text{MeV cm}^2}{\text{g}}\frac{Zq^2}{A\beta^2}\left[\ln\left(\frac{W_{\max}}{I(1-\beta^2)}\right) - \beta^2\right]$$

For the argon ion

$$\beta = \left[1 - \frac{m_0 c^2}{m_0 c^2 + E/A}\right]^{1/2} = 0.04629$$

$$\gamma = \left[\frac{1}{1 - \beta^2}\right]^{1/2} = 1.0011$$

$$W_{max} = 2 \times 0.511 (\gamma\beta)^2 = 0.002194 \text{ MeV}$$

For oxygen, $I = (12Z + 7) \text{ eV} = 103 \text{ eV}$

$$\left(\frac{-1}{\rho}\frac{dE}{dx}\right)_O = 0.3070 \frac{2^2}{16(0.04629)^2}\left[\ln\left(\frac{0.002194}{103 \times 10^{-6} \times 0.9979}\right) - (0.04629)^2\right]$$

$$\left(\frac{-1}{\rho}\frac{dE}{dx}\right)_O = 109.4 \frac{\text{MeV cm}^2}{\text{g}}$$

For nitrogen, $I = (12Z + 7) \text{ eV} = 91 \text{ eV}$

$$\left(\frac{-1}{\rho}\frac{dE}{dx}\right)_N = 0.3070 \frac{2^2}{14(0.04629)^2}\left[\ln\left(\frac{0.002194}{91 \times 10^{-6} \times 0.9979}\right) - (0.04629)^2\right]$$

$$\left(\frac{-1}{\rho}\frac{dE}{dx}\right)_N = 130.2 \frac{\text{MeV cm}^2}{\text{g}}$$

Finally, for air:

$$\left(\frac{1}{\rho}\frac{dE}{dx}\right)_{total} = 0.21 \times (109.4) + 0.79 \times (130.2) = 125.8 \frac{\text{MeV cm}^2}{\text{g}}$$

16.2.2 Range

The range or distance that a heavy charged particle will travel in a material can be obtained by integrating the energy loss rate *along the path* of the ion. In the approximation that the ion follows a straight-line trajectory, the range for a given kinetic energy, $R(T)$, would be given by the integral

$$R(T) = \int_0^E -\left(\frac{dE}{dx}\right)^{-1} dE \tag{16.22}$$

where the function dE/dx is the appropriate function for the ion in the material. There are two difficulties in applying this simple integral: (a) the ions will suffer a different number of collisions with atomic electrons and (b) more importantly, the ions will undergo some scattering from the Coulomb fields of the atomic nuclei. The *multiple Coulomb scattering* leads to an effect that the ion's trajectory is not straight but rather is made up from a series of straight-line segments. Thus, the apparent range or the projection of the range onto the initial velocity vector of the ion will not be a single value but rather will consist of a statistical
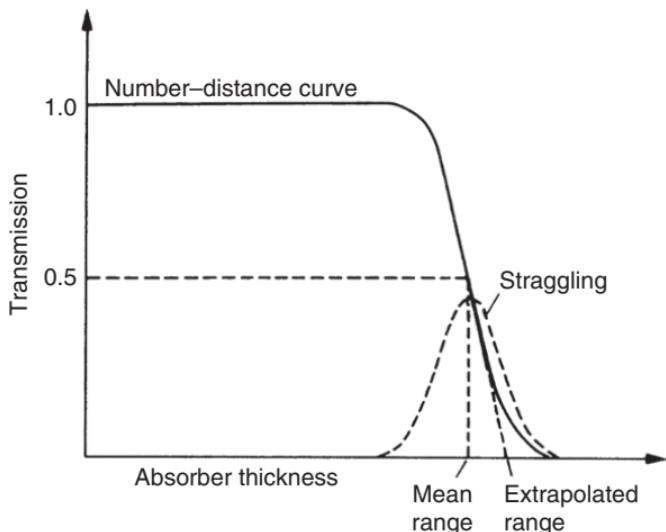
Figure 16.6 The intensity distribution or attenuation curve is shown as a function of absorber thickness for a typical energetic heavy ion penetrating into a metal. The effect of range straggling is indicated by the Gaussian distribution of ranges (Leo (1987). Reproduced with the permission of Springer).

distribution of values. Thus, the distribution of ranges is due to *range straggling*. It is important to note that the size of range straggling will grow as an ion penetrates into material because it will literally add up, in contrast to the energy straggling mentioned previously. The range of an ion and its fluctuations are integral quantities, whereas the energy loss rate and its fluctuations are differential quantities. It is still true that Coulomb and nuclear scattering are relatively rare so that the range straggling for typical ion energies in metals is on the order of a percent of the range. The qualitative features of the range distribution and the attenuation curve for a typical heavy charged particle are shown in Figure 16.6. Heavy charged particles penetrate uniformly into matter with essentially no attenuation in intensity until they are nearly at rest; at this point the intensity of moving ions rapidly drops to zero.

The calculated range energy curves for some low-mass charged particles in silicon are shown in Figure 16.7. We can see from the integral form of the range as a function of initial kinetic energy, given previously, that $R \propto aE^b$. The exponent should be of order two at low energies where the energy loss rate is dominated by the $1/\beta^2$ or $1/E$ term. The range–energy relationships are very useful in determining the kinetic energies of particles by measuring the attenuation curves. More recently, range–energy relationships are used to identify charged particles that are detected in silicon semiconductor telescopes as they emerge from nuclear reactions. The scaling rules that apply to the stopping power for different ions in a given medium can be extended to the range–energy relationship. For example, given the range of ion "1" at an initial kinetic energy E_1, the
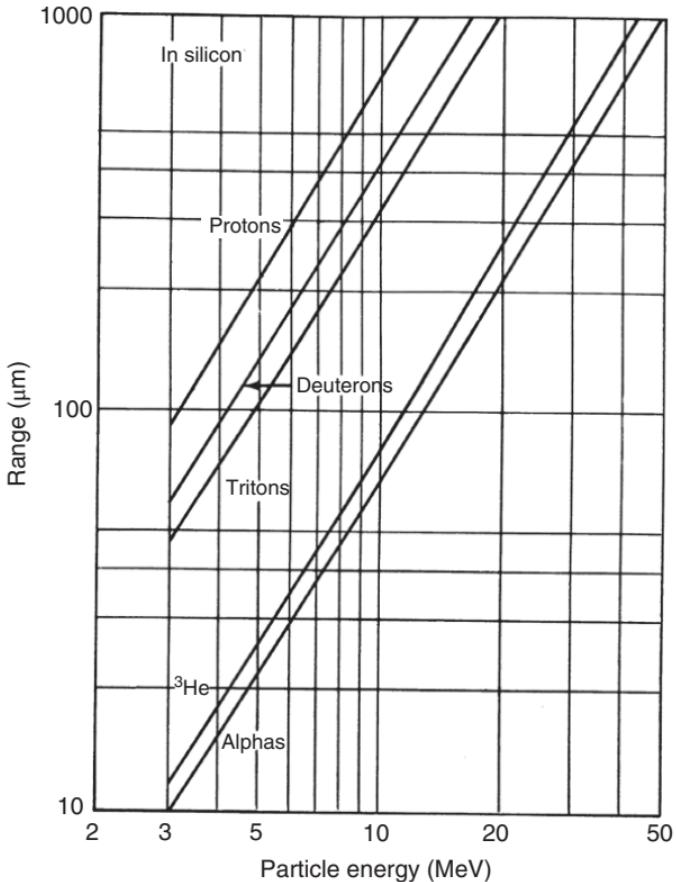
Figure 16.7 The range–energy curves for some charged particles in silicon. Note the data has the form $R = aE^b$ with a similar exponent for all ions (Knoll (2010). Reproduced with the permission of John Wiley & Sons, Inc.).

range of ion "2" with a different mass, charge, and kinetic energy can be found from the range of ion "1" at a scaled energy:

$$R_2(E_2) = \frac{M_2}{M_1}\frac{q_1^2}{q_2^2} R_1\left(E_2 \frac{M_1}{M_2}\right) \tag{16.23}$$

Notice that we have to scale the range of the known first particle obtained at the appropriate energy of the desired second particle.

As a final, more practical point about the stopping power and ranges of charged particles, we should consider the best method to calculate the amount of energy deposited in a thin foil. Clearly the ion will slow down as it passes through the material so that the energy loss rate will change as the particle passes through the foil. Thus, we should use the average energy loss rate but notice that the function is not linear so that we will need a technique to determine the average. Two cases can be identified: *thin foils* in which the

initial, average, and final energy loss rates are nearly the same and *thick foils* in which the particle undergoes a substantial energy loss. In the former example of a thin foil, we can simply use the expression written previously that

$$\Delta E = \left(\frac{dE}{dx} \right) \Delta x \qquad (16.24)$$

and we should verify that the final rate is approximately equal to the initial rate:

$$\left(\frac{dE}{dx} \right)_{\text{initial}} = \left(\frac{dE}{dx} \right)_{\text{final}} \qquad (16.25)$$

If the energy loss rates are not substantially different, then we can use the initial rate to obtain the average in a successive approximation procedure. For the latter case of substantial slowing, we can recall that the range relations come from the integration of dE/dx and thus provide the average energy loss rate that we should use. The technique relies on determining the ranges of ions in graphs or tables of ranges as follows: imagine that an incident particle with an energy, E_0, passes through some material with thickness, t. These are the "known quantities." The particle will emerge from the foil with an energy, E_1, which we would like to determine. We can find the total range of the initial ion in the material from tables, R_0. The particles that emerge from the foil will have a residual range equal to $R_0 - t$. We can then use the range table or graph in the opposite sense to determine the value of E_1 that corresponds to the range $R_1 = R_0 - t$. The slowing down and averaging of the energy loss rate will be contained in the range function and do not have to be explicitly evaluated to find the residual energy E_1.

Sample Problem 16.4: Heavy Ion Ranges

Imagine that a beam of ^{40}Ar ions at 400 MeV (10 MeV/A) is an incident on a 18.5 mg/cm^2 beryllium foil (0.1 mm thick). Do the ions pass through the foil, and if they do, what is their residual kinetic energy?

Solution

Using a standard reference for stopping power, the tables of Northcliffe and Schilling (1970), we find for these ions that $dE/dx = 9.597$ MeV-cm^2/mg in beryllium. Thus, for our first estimate of the energy lost,

$$\Delta E \sim (dE/dx)\,\Delta x = 9.657 \times 18.5 = 177.5 \text{ MeV}$$

giving an estimate of the residual energy of $400{-}177.5 = 222$ MeV, that is, almost half of the initial kinetic energy. The ions will pass through the foil, but this estimate of energy loss is probably too low. Recall that the ions lose more energy per distance traveled as they slow down. Checking, we

see that the energy loss rate for 178 MeV ^{40}Ar ions is substantially larger, that is, $dE/dx = 15.3$ MeV cm^2/mg. Thus, this is not a "thin" foil for these ions.

We can use the range technique with information in the same table for ^{40}Ar ions with $E_0 = 400$ MeV:

$$R(400 \text{ MeV}) = 28.278 \text{ mg/cm}^2$$

$$R(E_2) = 28.278 - 18.5 = 9.8 \text{ mg/cm}^2$$

This range lies between the tabulated values in this table, and by linear interpolation between the range values for $E = 160$ and 200 MeV, one finds that $E_1 \sim 185$ MeV. Thus, just using the initial energy loss rate clearly gave a substantial error.

For the practicing nuclear chemist, range–energy tables or relationships are among the most commonly used tools. The largest collection of data on stopping powers and ranges of ions in matter is that of Ziegler and Biersack in the form of the computer programs SRIM/TRIM. Subsets of these tables exist for low-energy heavy ions interacting with matter (Northcliffe and Schilling, 1970), α particles interacting with matter (Williamson et al., 1966), and energetic heavy ions (Hubert et al., 1990). The ATIMA code (Geissel et al.) provides the most up-to-date calculation of the stopping power and straggling.

For the most commonly encountered heavy charged particles, the α particles from radioactive decay, some semiempirical range–energy rules are often used. For the range of α-particles in air, R_{air}, we have

$$R_{air} \text{ (cm)} = (0.005E_\alpha - 0.285)E_\alpha^{3/2} \tag{16.26}$$

or

$$R_{air} \text{ (mg/cm}^2) = 0.40E_\alpha^{3/2} \tag{16.27}$$

with E_α in MeV in both expressions so that the range of a 7 MeV α particle in air is about 5.9 cm. For a pure element with $10 < Z < 15$, we have the ratio

$$\frac{R_Z}{R_{air}} = (0.90 + 0.0275 \text{ Z}) + (0.06 - 0.0086 \text{ Z}) \log_{10}\left(\frac{E_\alpha}{4}\right) \tag{16.28}$$

where R_Z is the range in a pure element of atomic number Z expressed in milligram per square centimeter, R_{air} is the range in air in milligram per square centimeter, and E_α is the α particle energy in MeV. (For $Z < 10$, substitute 1.00 for the term $(0.09 + 0.0275Z)$.) For $Z > 15$, replace the term R_Z by $(R_Z \times 0.005Z)$.) For compounds or mixtures, the range in the compound or mixture, R_C in milligram per square centimeter, is given as

$$\frac{1}{R_C} = \sum_i \frac{p_i}{R_i} \tag{16.29}$$

where p_i is the weight fraction of the i-th element in the mixture or compound and R_i is the range of an α particle of this energy in the i-th element.

Application of these formulas shows the ranges of decay α particles in solids are very short. A sheet of paper will stop the α-particles from most radioactive sources. α-Emitting nuclei are not external radiation hazards, but because of their high linear energy transfer (LET), they do represent significant hazards when inhaled or ingested.

Sample Problem 16.5: α Particle Ranges

What is the range of an 8 MeV α-particle in cm of air? What is the range of the same particle in aluminum?

Solution

$$R_{air} \text{ (cm)} = [0.005 E_\alpha - 0.285] E_\alpha^{3/2}$$
$$R_{air} \text{ (cm)} = [0.005 \times 8 - 0.285](8)^{3/2} = 7.4 \text{ cm}$$

Scale for aluminum but need range in milligram per square centimeter:

$$\frac{R_Z}{R_{air}} = (0.90 + 0.0275 Z) + (0.06 - 0.0086 Z) \log_{10}\left(\frac{E_\alpha}{4}\right)$$
$$R_{air} \text{ (mg/cm}^2) = 0.40 E_\alpha^{3/2} = 0.0510 \text{ mg/cm}^2$$
$$\frac{R_{Al}}{0.0510} = (0.90 + 0.0275 \times 13) + (0.06 - 0.0086 \times 13) \log_{10}\left(\frac{8}{4}\right)$$
$$R_{Al} = 0.065 \text{ mg/cm}^2$$

Use mass–density for range in cm:

$$R_{Al} = \frac{0.065 \text{ mg/cm}^2}{2700 \text{ mg/cm}^3} = 2.4 \times 10^{-5} \text{ cm or } 0.24 \text{ μm}$$

The long range in air compared to solid Al is due to the very low density of air (at STP).

16.3 Electrons

The passage of energetic electrons through matter is similar to that of heavy charged particles in that the Coulomb interaction dominates the process. However, three clear differences can be easily seen: the incident electrons are generally relativistic particles (notice that 1 MeV of kinetic energy corresponds to nearly twice the rest mass of an electron, 0.511 MeV); the scattering is

predominantly between identical particles and repulsive; and the interactions with nuclei are attractive, and the direction of the electron can be dramatically changed, even reversed, in a collision with a heavy nucleus. A fourth difference that is not so obvious is that a fraction of the kinetic energy is lost through the radiative process of bremsstrahlung. Bremsstrahlung (the German word can be translated literally as "braking radiation") is a general process in which electromagnetic radiation is emitted whenever a charged particle undergoes a substantial acceleration. The scattering of electrons, particularly to large angles, corresponds to a classical acceleration that creates/requires the emission of bremsstrahlung. By comparison, very few heavy charged particles undergo large accelerations as they slow down in material.

Summarizing this overview of the possible interaction mechanisms for fast electrons in material, we find that the rate of energy loss in a material is

$$-\left(\frac{dE}{dx}\right)_{\text{electron}} = S_{\text{electronic}} + S_{\text{radiative}} \tag{16.30}$$

where the electronic stopping power, $S_{\text{electronic}}$, is similar to the electronic interaction between charged particles and electrons discussed earlier, whereas the radiative stopping power, $S_{\text{radiative}}$, is specific to electrons. The electronic stopping power for electrons is written as

$$-\left(\frac{dE}{dx}\right)_{\text{electronic}} = \frac{2\pi Z e^4 \rho_N}{m_e v^2} \left[\ln\left(\frac{m_e v^2 E}{2I^2(1-\beta^2)}\right) - \ln 2\left(2\sqrt{1-\beta^2} - 1 + \beta^2\right) + \left(1-\beta^2\right) + \frac{1}{8}\left(1 - \sqrt{1-\beta^2}\right)^2\right] \tag{16.31}$$

using the same definitions as for the stopping power of heavy charged particles. On the other hand, the expression for the radiative stopping power is

$$\left(\frac{dE}{dx}\right)_{\text{radiative}} = \frac{(Z+1)Z e^4 \rho_N E}{137 m_e^2 c^4} \left[4\ln\left(\frac{2E}{m_e c^2}\right) - \frac{4}{3}\right] \tag{16.32}$$

Note that this expression contains an extra factor of $Z \times E$ in the term in front of the parenthesis. With some algebra and for a typical electron energy, one can show that the ratio of the two contributions to the stopping power depends on the atomic number of the material Z and the electron kinetic energy E:

$$\frac{S_{\text{radiative}}}{S_{\text{electronic}}} \approx \frac{ZE}{800 \text{ MeV}} \tag{16.33}$$

which indicates that the radiative contribution is only significant for large atomic numbers ($Z \sim 80$–90) and high electron energies ($E \sim 10$–100 MeV). Typical β particles from radioactive sources are emitted with only 1–10 MeV
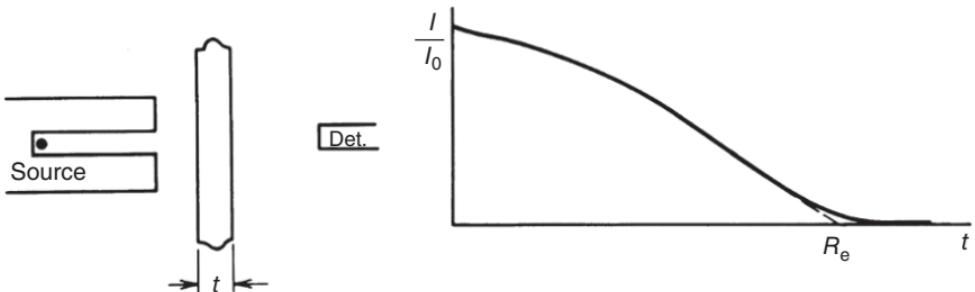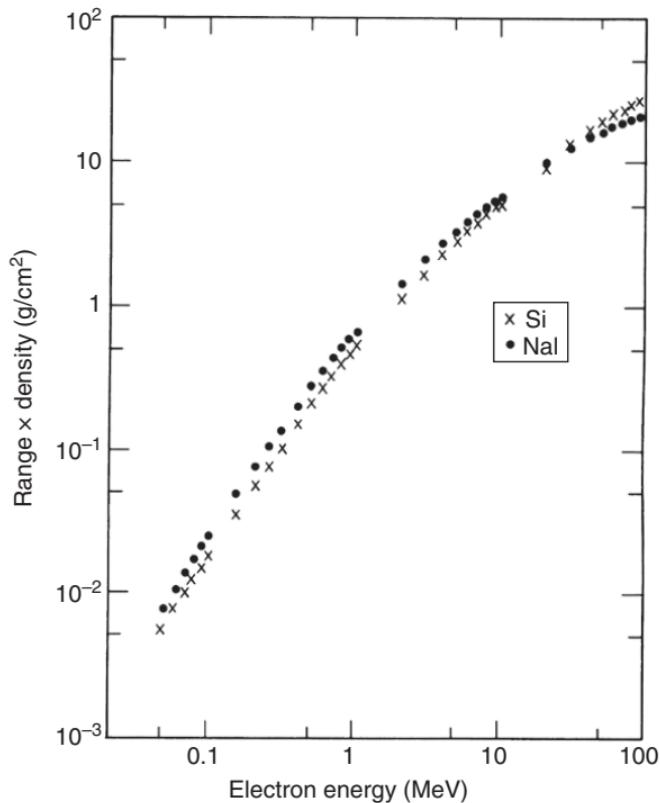
Figure 16.8 A schematic attenuation curve for an energetic electron in a solid material (Knoll (2010). Reproduced with the permission of John Wiley & Sons, Inc.).

of kinetic energy, often much less, and the radiative contribution to the stopping power is very small. The bremsstrahlung spectrum is smooth and continuous ranging from zero energy up to the electron energy due to the random distribution of electron scattering angles.

The important feature that the electrons are occasionally scattered to large angles during the penetration of material causes each electron to follow a tortuous path compared to the straight-line trajectories of heavy ions. Also, a beam of electrons will not have a fixed range in the sense of that a beam of heavy charged particles. In fact, given the identical nature of the particles involved in the scattering process, obtaining the range distribution is problematic. The primary or a secondary electron can be scattered backwards and emitted from the material. A schematic plot of the range distribution is shown in Figure 16.8 for a monoenergetic source of electrons. The falloff of the intensity with penetration depth starts immediately as the electron enters the material and then gradually approaches zero. This figure emphasizes the fact that the concept of range cannot be applied in a simple way to energetic electrons. As an approximation, the electron range is taken as the extrapolation of the linear portion of the attenuation curve to zero. As shown in Figure 16.9, the product of this definition of the range times the density of a material is a smooth function of incident electron energy for a wide range of materials. Such behavior comes from the fact that the range has a strong dependence on the electron density through the electronic stopping and a weak dependence on the atomic number of the material through the ionization potential and radiative stopping.

Many related measurements have been made of the range distribution of electrons emitted in β^- decay. These studies were particularly important before solid-state detectors were available. The measurements have shown that the combination of the Fermi energy distribution of electrons from the decay with

Figure 16.9 The product of the range of an energetic electron in a solid material with the density as a function of the incident kinetic energy is shown (Knoll (2010). Reproduced with the permission of John Wiley & Sons, Inc.).

the sloping range distribution leads to an approximately exponential attenuation of the β decay electrons. This can be expressed as

$$N_t = N_0 e^{-\mu t} \tag{16.34}$$

where N_t is the number of β particles transmitted through a thickness t. The absorption coefficient μ can be related to the endpoint energy E_{max} of the β spectrum as

$$\mu \ (\mathrm{m^2/kg}) = 1.7 E_{max}^{-1.14} \tag{16.35}$$

with E_{max} given in MeV.

Sample Problem 16.6: Electron Ranges

What fraction of the β particles emitted by ^{32}P ($E_{max}(\beta) = 1.71$ MeV) will be stopped by a 1.0 mm sheet of aluminum?

Solution

The mass absorption coefficient μ is

$$\mu = 1.7 \times (1.71)^{-1.14} = 0.922 \ \mathrm{m^2/kg}$$

The fraction of the β particles that are *transmitted* is:

$$N_t/N_0 = e^{-\mu t}$$
$$N_t/N_0 = \exp[-0.922 \text{ m}^2/\text{kg} \times (1 \times 10^{-3} \text{ m}) \times (2.7 \times 10^3 \text{ kg/m}^3)]$$
$$N_t/N_0 = \exp[-2.489] = 0.083$$
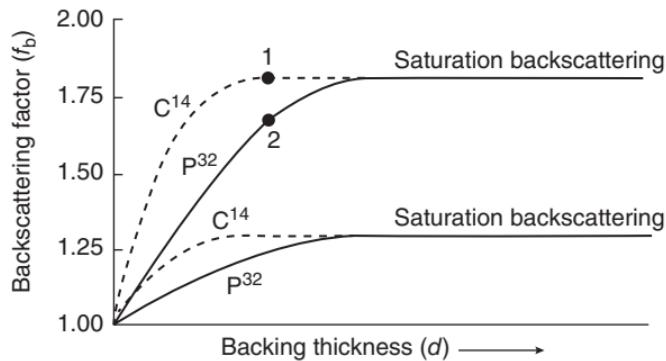
The fraction *absorbed* is then $1 - 0.083 = 0.917$.

In the distant past, measurements of the attenuation of the β spectrum from a newly discovered isotope were used to identify the energy of the β decay. Recently, the attenuation of the radiation from strong sources has been used to monitor the thickness of materials during manufacturing processes. Notice that the monitoring can be continuous, nearly instantaneous, nondestructive, and a physical probe does not need to "touch" the material being measured.

The backscattering of energetic electrons from materials is a feature not seen with heavy charged particles. Backscattering is primarily due to multiple interactions with (heavy) nuclei that significantly alter the direction of the incident electron, a feature that is enhanced by the fact that two energetic electrons are often created when one incident electron scatters from an atomic electron. The coefficient of backscattering is used to quantify the probability that an electron will emerge "backwards" from a surface that is irradiated with electrons. The coefficient is a function of the energy of the incident electron and the atomic number of the absorber. Formally, the coefficient is the fraction of time that an electron is emitted from the surface of a material following the entry of an energetic electron. The coefficient is ~0.5 for $E < 1$ MeV electrons in gold and ~0.3, 0.04, and 0.1 for copper, aluminum, and carbon, respectively. The coefficient falls below 0.1 for $E = 10$ MeV electrons in gold, below 0.05 for copper, and to near zero in aluminum and carbon.

Backscattering is an important phenomenon in the counting of samples containing β-emitting nuclides. Because of backscattering, the recorded number of β^- particles that strike the detector is greater than that expected from the source-detector geometry. For a very thin sample, this effect is small, but the magnitude of this effect is not negligible for most samples (that are not very thin). The observed counting rate will increase with sample thickness until a "saturation" value is reached (15.10). This saturation backscattering thickness is typically 20% of the "range" of the β^- in the sample backing material. What is done in practice is to put a "saturation" thickness of a typical material like Al behind every sample that is being counted so as to have a constant backscattering correction. This is done in practice by using a standard Al planchet that will produce a saturation backscattering for the energy of the β-particle being counted.

Figure 16.10 The effect of β⁻ particle energy and backing thickness on backscattering (Wang et al. (1975). Reproduced with the permission of Prentice-Hall, Englewood Cliffs).

The bremsstrahlung radiation from electron beams has important practical applications even though it is a small contribution to the stopping power. Bremsstrahlung forms the basis for the operation of X-ray tubes and other "controllable" high-fluence sources of radiation. Such devices collide an electron beam with an energy of the order of 10–50 keV with a large electrode, usually made out of a heavy element like tungsten or tantalum. The electrons penetrate the electrode, and the bulk of their kinetic energy is lost through electron scattering and eventually creates heat. However, a small fraction of the incident energy is converted into electromagnetic energy in the X-ray region by bremsstrahlung (and the filling of inner shell electron vacancies). This is called "thick target" bremsstrahlung because the incident electrons are completely stopped inside the material. If we assume that the bremsstrahlung is independent of electron energy, then the fraction of the electron energy would be $f_{rad} = 0.0014Z \times E$ from the previous expression. The observed fraction is about a factor of two lower, which would be consistent with simply taking the average energy of the electron in the material to be 1/2 the initial energy. Some of the energetic electrons can create inner shell atomic vacancies in the atoms that make up the lattice. These vacancies will be filled by outer shell electrons and emit discrete K and L X-ray transitions. These sharp lines will add to the continuous bremsstrahlung spectrum and will depend, of course, on the atomic number of the stopping material.

Another mechanism for electron energy loss in matter is the emission of Cherenkov radiation. When a beam of fast-moving charged particles with a velocity, v, near the speed of light enters another medium with index of refraction, n, that is different from the first medium, the particle velocity will be exceeding the speed of light in the new medium (which is given by c/n). The charged particle radiates the "excess" energy in the form of a blue-white light called Cherenkov radiation. This light is localized in a cone of half-angle, θ, around the direction of motion of the electron such that $\cos \theta = c/nv$. Cherenkov radiation is the blue glow seen in the water around operating

nuclear reactors and is also used to identify extremely high-energy particles. See Figure 17.1.

16.4 Electromagnetic Radiation

As photons move through material, they only interact or "scatter" in localized or discrete interactions, and they do not interact at long distances, that is, they are not subject to the Coulomb or nuclear forces. This behavior is in clear contrast to the long-range interactions felt by charged particles. Thus, as a beam of photons propagates through any material, the intensity of the beam will decrease as the photons that interact are removed, but the energy of all the non-interacting photons will remain constant. The photons will interact in ways that predominantly release fast-moving electrons. Low-energy photons will interact only once and give rise to a single primary electron; energetic photons can interact several times and give rise to a small number of primary electrons. The most energetic photons can create a matter-antimatter pair of primary electrons that induce a cascade of secondary electrons.

The energy of the non-interacting photons remains constant so that the probability that a photon will interact in a fixed thickness of material will also remain constant regardless of the photon energy. This leads immediately to an exponential attenuation of electromagnetic radiation that is called the Beer–Lambert law. The law was applied to the absorption of visible light but applies to all electromagnetic radiation. The derivation of the exponential attenuation law is similar to the derivation of the exponential decay law of radioactive nuclei and will not be repeated here. (The analogy is that the probability of radioactive decay is constant in a given time interval.)

The general expression for the attenuation of photons is

$$I = I_0 e^{-\mu x} \tag{16.36}$$

where I and I_0 are transmitted and incident intensities, respectively, x is the thickness, and μ is an energy-dependent *total linear absorption coefficient* that depends on the nature of the material. The mean free path of the photons in the material is simply $\lambda = 1/\mu$, and we can define a half thickness as $x_{1/2} = \ln(2)/\mu$ in analogy to the radioactive half-life. The exponential nature of the attenuation means that the intensity of the transmitted radiation does not go to zero, although it can be made arbitrarily small. The mass attenuation coefficient is obtained by dividing the linear attenuation coefficient by the density of the material, μ/ρ_m. The mass attenuation coefficient is independent of the physical state of the absorber and comes from the fact that the fundamental interactions can be expressed in terms of cross sections per atom. Extensive tabulations and figures, such as Figure 16.11, are available for the mass attenuation coefficients of photons with energies in the range of 0.01–10 MeV.
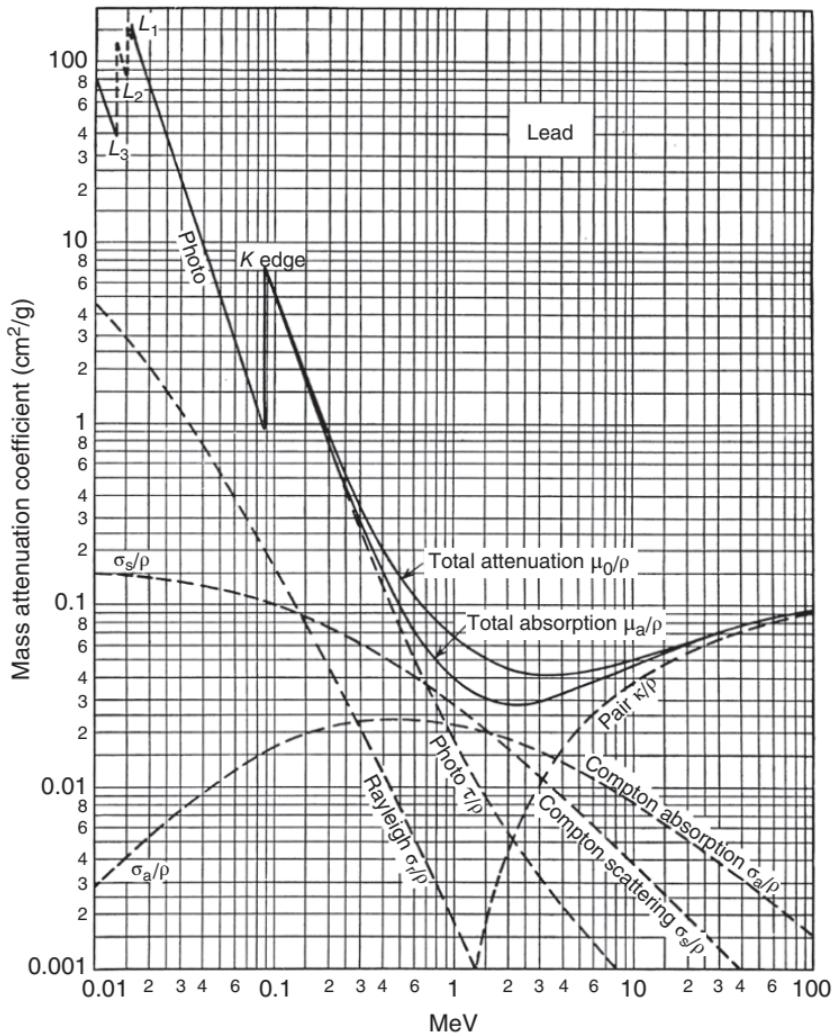
Figure 16.11 The mass attenuation coefficient for energetic photons in lead (Evans (1955). Reproduced with the permission of McGraw-Hill).

Sample Problem 16.7: Photon Attenuation

Estimate the fraction of 1.0 MeV photons that will be transmitted through a lead absorber that is 5 cm thick (the thickness of "lead bricks" commonly used in radiation shields).

Solution

The transmitted fraction is simply

$$\frac{I}{I_0} = e^{-\mu x}$$
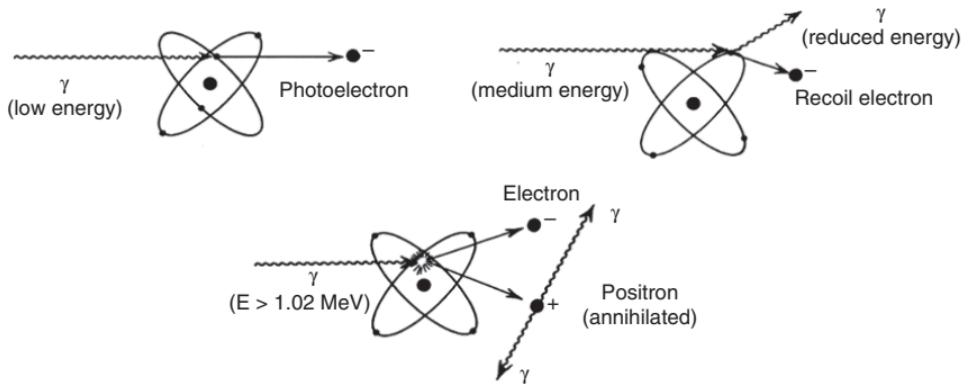
Figure 16.12 Schematic diagrams of (left to right) photoelectric effect, Compton effect, and pair production.

where x is 5 cm and μ can be obtained from the mass attenuation coefficient in Figure 16.11. Reading the value from this figure, $\mu_0/\rho = 0.07$ cm^2/g for the total attenuation and $\mu_0 = (\mu_0/\rho) \times \rho$, of course. Thus,

$$\frac{I}{I_0} = e^{-(0.07 \text{ cm}^2/\text{g} \times 11.35 \text{ g/cm}^3 \times 5\text{cm})} = e^{-0.795 \times 5} = 0.019$$

Approximately 2% will be transmitted. Notice that the half thickness for these photons in lead, $x_{1/2} = \ln 2/\mu$, is 0.87 cm.

Concentrating on photon energies that are associated with nuclear energy levels, those in the region from 10 keV to 10 MeV, we find that only three types of interactions play a role in attenuating a photon beam. These mechanisms are shown schematically in Figure 16.12. Each photon that interacts with an atom via any one of the mechanisms will be lost from the initial beam. The type of interaction is random, but their relative probabilities depend on the photon energy and absorber material. *Photoelectric absorption* dominates at low energies, $E_\gamma < 0.1$ MeV in the heaviest elements, *Compton scattering* is most important at intermediate energies, whereas *pair production* has an absolute threshold at 1.022 MeV and is most important for the highest energy photons. We will consider each of these processes in turn.

16.4.1 Photoelectric Effect

The photoelectric effect was originally described by Einstein and helped to establish the quantized nature of light. The photoelectric effect has many extremely important applications, for example, the detection of visible light by photocells and the photovoltaic conversion of sunlight. The photoelectric effect converts a single photon into a single free electron. When the photon interacts with a bound electron, the photon can be completely absorbed, and

the electron emerges with a kinetic energy that corresponds to the photon energy, $h\nu$, minus the electron binding energy, $KE_{e-} = h\nu - BE$ (see Fig. 16.12). Photocells use a semiconductor like silicon for the absorbing material, and the electrons released by visible light have relatively small kinetic energies and are collected as a photocurrent. In the present application of the absorption of a nuclear photon, a fast electron is usually created in the bulk of a solid medium because the binding energy is often small compared to the photon energy. The fast electron goes on to lose its kinetic energy by scattering through the material (as discussed previously). Conservation of momentum requires that the electron be bound in an atom (that could be in a lattice) that recoils.

The cross section or probability of the photoelectric effect is on the order of the square of the atomic size for photons in the keV region and decreases rapidly with increasing photon energy. The cross section also has a strong dependence on the atomic number of the absorbing material, as there is a sharp increase in the cross section at each threshold for the emission of bound electrons. As an example, the heavy element lead ($Z = 82$) has K, L, and M (principal quantum numbers $n = 1$, 2, and 3) binding energies of ~88, 15, and 3 keV, respectively, which provide strong photoelectric absorption for photons at these exact energies. The sharp increase in the photoelectric cross section can be seen as the sharp peaks on the left side of Figure 16.11. The overall probability for photoelectric absorption follows the very rough expression

$$\sigma_{photoelectric} \propto \frac{Z^n}{E_\gamma^{7/2}} \qquad (16.37)$$

where the exponent n is between 4 and 5. This expression only includes the dramatic effects of the electron binding energies in an overall way and is not meant to replace the measured values. We should note that the photoelectric effect often leaves an inner shell vacancy in the atom that previously contained the "ejected" photoelectron. This vacancy will be filled by an atomic transition, called fluorescence, and generally produce an X-ray photon. In an interesting twist of fate, the X-ray photon will have an energy that is just below the sharp rise in the attenuation coefficient due to conservation of momentum and can often escape from the absorber. Recall that the direction of the fluorescence photon will be uncorrelated with the direction of the incident photon and a fraction will be emitted "backwards" from the absorber. The absorber will thus emit its own characteristic X-rays when it is irradiated with high-energy photons.

Thick lead shields are commonly used in γ-ray spectroscopy. The shields will produce Pb X-rays that can interfere with the measurement of low-energy photons. A "graded shield" can be constructed by lining the Pb shields with a layer of Cu and then a layer of Al to absorb the Pb X-rays and then any Cu X-rays and other subsequent radiation to ameliorate these problems.

Table 16.3 Compton Scattering at Fixed Angles.

θ_γ (°)	Emitted Photon Energy	Electron Kinetic Energy
0	$h\nu$	~ 0
90	$h\nu \left(m_e c^2 / m_e c^2 + h\nu \right)$	$\sim h\nu - m_e c^2$
180	$h\nu \left(m_e c^2 / m_e c^2 + 2\,h\nu \right)$	$\sim h\nu - (m_e c^2 / 2)$

16.4.2 Compton Scattering

If the energy of the incident photon exceeds the typical binding energies of the innermost atomic electrons, the probability of photoelectric absorption drops below the probability that the photon will simply scatter from an electron leading to a moving electron and a lower-energy photon. This process is called Compton scattering. A schematic diagram of this process is shown in Figure 16.12. From the conservation of momentum in the direction of travel of the initial photon, x, we have

$$p = p' \cos\theta + p_e \cos\phi \tag{16.38}$$

where p and p' are the momenta of the initial and scattered photons, p_e is the momentum of the scattered electron, and θ is the scattering angle. From conservation of momentum in the perpendicular direction, y, we have

$$0 = -p' \sin\theta + p_e \sin\phi \tag{16.39}$$

Assuming the collision is elastic, conservation of energy gives us $E = E' + T_e$. Combining these equations (see problems) and utilizing the relativistically correct expressions for the energy and momentum of the electron:

$$p_e^2 = \frac{1}{c^2} \left[T_e \left(T_e + 2m_e c^2 \right) \right] \tag{16.40}$$

We get the relatively simple expression for the wavelength shift of the photon:
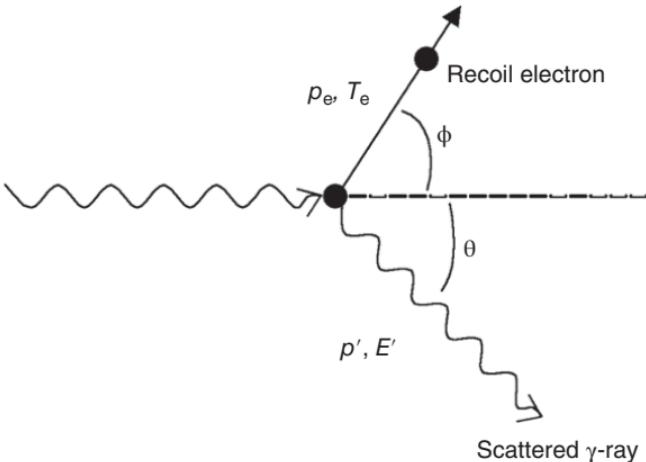
$$\lambda' - \lambda = \frac{h}{m_e c} \left(1 - \cos\theta \right) \tag{16.41}$$

where λ' and λ are the wavelengths of the scattered and incident γ-rays, respectively. The quantity $(h/m_e c)$ is called the Compton wavelength of the electron and is equal to 2426 fm. Note that the shift in γ-ray energy is independent of the incident energy. The expressions for the energies of the scattered photon and electron are given in Table 16.3.

It should be clear that the minimum energy of the scattered γ-ray occurs when $\theta = 180°$ where $\cos\theta = -1$. Thus, we have

$$E_{\gamma'}(\text{min}) = \frac{m_e c^2}{2} \left(1 + \frac{m_e c^2}{2E_\gamma} \right)^{-1} \approx 255 \text{ keV} \tag{16.42}$$

Figure 16.13 Schematic kinematic diagram of Compton scattering.

With the minimum γ-ray energy, the electron energy T_e will be maximum and $T_e = E_\gamma - 0.255$ MeV. If we consider all scattering angles, then the distribution of scattered electron kinetic energies will be as shown in Figure 16.14. The sharp peak at $E_\gamma - 0.255$ MeV is called the *Compton edge*. The minimum energy photon found earlier, $E \approx 225$ keV, will be a noticeable component in γ-ray spectra resulting from the interaction of photons from a radioactive source with the lead shield surrounding the detector, creating a backscattered photon ($E \sim 225$ keV) that can strike the radiation detector.

The Compton scattering cross section per electron of the stopping material is independent of Z, and thus the cross section per atom goes as the number of electrons or as Z. For energies near 0.5 MeV, the cross section varies roughly as $1/E_\gamma$ (Figure 16.15).

16.4.3 Pair Production

Whenever the energy of the initial photon exceeds the rest mass of two electrons, 1.022 MeV, the process of pair production is possible. During the process of pair production, the initial photon interacts with the Coulomb field of a nucleus and is converted into an electron and a positron, a matter–antimatter pair, that shares the initial energy of the photon (see Fig. 16.12). Conservation of energy and momentum in the Coulomb field cause the pair of electrons to move forward along the initial direction of the photon with a small opening angle. The pair of particles will then go on to interact with the electrons and nuclei in the remaining material as described previously.

The process of bremsstrahlung observed in electron stopping is closely related to the process of pair production. From a schematic standpoint, in the first case, a moving electron interacts with the Coulomb field of an atom, making a transition between two energy states, and a (bremsstrahlung) photon
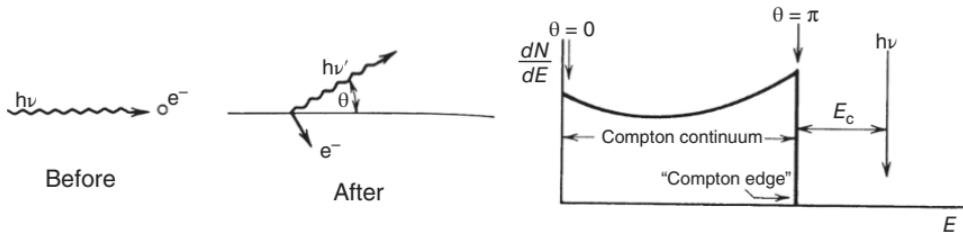
Figure 16.14 Left: Schematic version of Compton scattering. Right: Schematic variation of the distribution of electron kinetic energies produced in Compton scattering (Knoll (2010). Reproduced with the permission of John Wiley & Sons, Inc.).
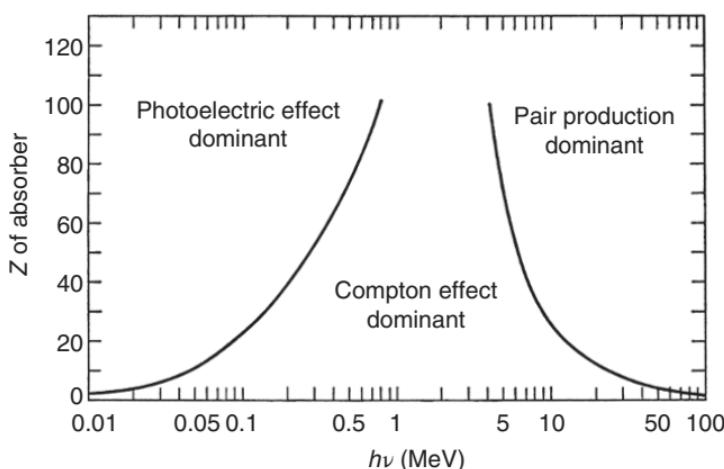
Figure 16.15 A summary of the relative importance of the three mechanisms by which photons interact with matter. The curves indicate the locations in the atomic number-photon energy plane at which the cross section for Compton scattering is equal to that for photoelectric absorption, left side, or is equal to that for pair production, right side. (Evans (1955). Reproduced with the permission of McGraw-Hill).

is emitted. In the second case, a photon is destroyed by interaction with an atomic Coulomb field, and a pair of electrons is created. The probability of pair production has an absolute threshold of 1.022 MeV, that is, this process cannot take place if the photon has a lower energy. The cross section increases relatively rapidly and saturates above ∼10 MeV, as indicated in Figure 16.11. The variation of the pair production cross section with photon energy is complicated, but the cross section depends on the square of the atomic number of the absorber. For large photon energies, $\sigma_{\mathrm{pair}} \propto Z^2 \ln(E_\gamma/mc^2)$. Pair production is the predominant attenuation process for high-energy photons.

Pair production has a threshold energy of 1.022 MeV because two particles are created, one electron and one positron. Thus, some energy is "stored in" or "used to create" the mass of the pair. Notice the total electric charge is conserved because the electron charge is −1 e and the positron charge is +1 e. One of the unique features of this process is that the energy that went into the creation of the two particles will be "released" when the positron comes to rest and annihilates with an electron. The annihilation process is

$$e^+ + e^- \rightarrow \gamma + \gamma \tag{16.43}$$

in which the two γ rays have exactly the same energy, $mc^2 = 0.511$ MeV, and are emitted at 180°, or back to back. The axis along which the two γ rays are emitted will be random with respect to the initial direction of the incident photon because the positron will undergo a slowing down process involving multiple scattering with atoms and atomic electrons before coming to rest and annihilating. Therefore, the characteristic annihilation radiation (photons with an energy of 0.511 MeV) can escape from the absorber whenever pair production occurs.

In summary, photons pass through material until they interact individually with the atoms or nuclei in the material. Depending on the energy of the photons, the interaction will be predominately pair production (high energy), Compton scattering, or photoelectric absorption (low energy). The relative importance of these processes is summarized in Figure 16.15 as a function of atomic number and photon energy. In each interaction, the photon ionizes the material creating one or two fast-moving electrons and leaving a positive ion. Pair production gives two fast-moving electrons, one positive, one negative; Compton scattering gives one fast-moving electron and a lower-energy photon, and the photoelectric effect gives one fast-moving electron. The fast electrons have a much higher rate of ionization than the photons, and the general features of the interactions of these electrons with the material have been described previously. The "path" of the scattered photon will be erratic when Compton scattering is the predominant process. Gamma rays from nuclear decay processes tend to have energies on the order of 1 MeV. From Figure 16.15 we expect these photons to predominantly interact via Compton scattering in all materials. The first interaction will give an electron and a lower-energy photon. The interaction probability of the secondary photon will usually be higher than that of the primary photon and will often result in a photoelectric absorption. Recall also that, depending on the energy of the primary photon, the absorber will weakly emit lower-energy photons such as annihilation radiation, backscatter radiation, or fluorescence X-rays.

16.5 Neutrons

We will now briefly consider the propagation of neutrons through material. Neutrons are the most penetrating radiation for the simple reason that their only significant interaction is with nuclei via the strong force. (Neutrons only have a very small interaction with electrons through their magnetic dipole moment that can be ignored.) As we discussed at the beginning of this chapter, nuclei are very much smaller than atoms, and so the probability that a fast neutron will interact with (strike) a nucleus is very small. On the other hand, neutrons cause significant radiation damage because all of their interactions cause nuclear recoil and many lead to nuclear transmutations.

A neutron will move through material along a straight line with a constant energy until it encounters a nucleus and induces a nuclear reaction. Thus, neutron attenuation follows an exponential law similar to that for photons. Written in terms of an energy-dependent attenuation length, μ_E, we have

$$I = I_0 e^{-\mu_E x} \tag{16.44}$$

where x is a linear dimension and I_0 is the incident intensity. The attenuation length is the inverse of the mean free path, λ, and is proportional to the total nuclear reaction cross section:

$$\mu_E = \frac{1}{\lambda_e} = \rho_N \sigma_{Total}(E) \tag{16.45}$$

ρ_N is a constant that gives the total number of nuclei per unit volume in the material. The total nuclear reaction cross section is a characteristic of each isotope in the absorbing material and has the dimensions of an area. If we have a monoisotopic element such as gold or bismuth, then we will only have to account for the energy dependence of the neutron. If the material contains several isotopes such as silver (^{107}Ag and ^{109}Ag) and nickel (five isotopes) or is a compound NaF (one isotope of each element), etc., then the effective cross section will be the number-weighted cross section:

$$\sigma_{average} = (f_1 \, \sigma_{Total}(E)_1 + f_2 \, \sigma_{Total}(E)_2 + f_3 \, \sigma_{Total}(E)_3 + \cdots) \tag{16.46}$$

where the constants f_i are the fraction by number of each isotope in the sample.

Sample Problem 16.8: Average Cross Sections

Calculate the average thermal neutron capture cross section and the neutron mean free path for LiF, a solid crystalline material at room temperature with a density of 2.635 g/cm^3 and a molar mass of 25.94 g/mole. Lithium has two stable isotopes ^6Li (7.5%) and ^7Li (92.5%) with thermal neutron capture cross sections, $\sigma_{thermal} = 39$ and 45 mb, respectively. Fluorine is monoisotopic, ^{19}F, with $\sigma_{thermal} = 9.6$ mb.

Solution

$$\sigma_{average} = (f_1\,\sigma_{Total}(E)_1 + f_2\,\sigma_{Total}(E)_2 + f_3\,\sigma_{Total}(E)_3)$$

Notice that half the atoms are fluorine and half the atoms are lithium but the lithium atoms are split unevenly between $A = 6$ and $A = 7$. The fractions of each isotope must reflect this distribution:

$$\sigma_{average} = (0.075 \times 0.5 \times 39) + (0.925 \times 0.5 \times 45) + (1 \times 0.5 \times 9.6)\ \text{mb}$$

$$\sigma_{average} = 27.1\ \text{mb}$$

Rearranging the previous equation relating the mean free path to the total reaction cross, one has

$$\lambda_{thermal} = \frac{1}{(\rho_N \sigma_{thermal})}$$

$$\rho_N = \frac{N_A \rho}{molar\,mass} = \frac{6.022 \times 10^{23}\ /\text{mol} \times 2.634\ \text{g/cm}^3}{25.94\ \text{g/mol}}$$

$$\rho_N = 6.11 \times 10^{22}\ /\text{cm}^3$$

And finally for the mean free path of thermal neutrons in LiF,

$$\lambda = \frac{1}{6.11 \times 10^{22}\ /\text{cm}^3 \times 27.1\ \text{mb} \times 10^{-27}\ \text{cm}^2/\text{mb}}$$

$$\lambda = 604\ \text{cm}$$

Thus, the average thermal neutron would travel more than 6 m in solid LiF before undergoing a nuclear capture reaction! Note the total reaction cross section will be larger and the neutrons will most likely scatter before being captured.

Neutrons can interact with matter via a number of different reactions, depending on their energy. Among the most important of these reactions are
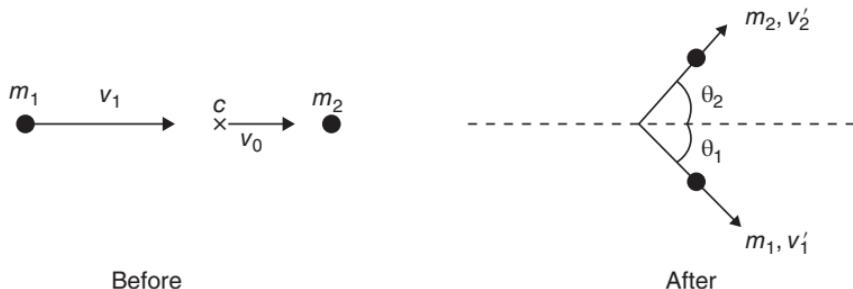
- Elastic scattering, $A(n, n)A$, which is the principal interaction mechanism for neutrons.
- Inelastic scattering, $A(n, n,)A^*$, where the product nucleus A^* is left in an excited state. To undergo inelastic scattering, the incident neutron must have sufficient energy to excite the product nucleus, generally on the order of 0.5 MeV or sometimes more.
- Radiative capture, $A(n, \gamma)A + 1$. As discussed earlier, this cross section shows a $1/v$ energy dependence, and this process is important for low-energy neutrons.
- Fission, $A(n, f)$, which is most likely at thermal energies for certain nuclei but occurs at all energies where the neutron binding energy exceeds the fission barrier height for fissile nuclei.

- Knockout reactions such as (n, p), (n, α), (n, t), etc., *which* are maximum for neutrons of eV–keV energy but also occur at higher energies.
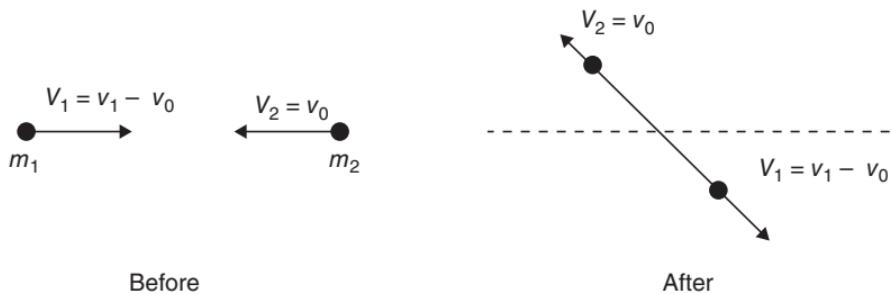
The total neutron interaction cross section, $\sigma_{total}(E)$, is the sum of the various reaction cross sections:

$$\sigma_{total}(E) = \sigma_{elastic} + \sigma_{inelastic} + \sigma_{capture} + \cdots \tag{16.47}$$
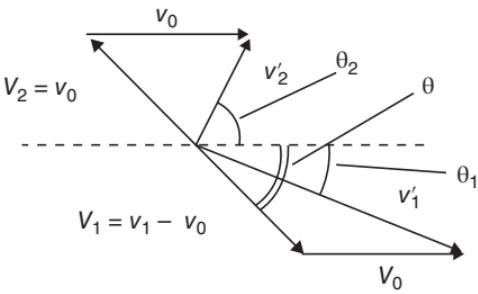
One of the technologically most important interactions of neutrons with matter is their loss of energy ("slowing down") by a series of elastic collisions. We can get an overall understanding of the process if we analyze the scattering using nonrelativistic kinematics. Let's consider the case where particle (#1) with mass m_1 and speed v_1 collides with particle (#2) with mass m_2, at rest in the lab system. After the collision, the particles will have speeds V_1 and V_2 in the lab system. We can represent this in a kinematic diagram in the lab system as

or in the center-of-mass (CM) system as

After the collision, the relationship between the CM and the lab system angles and vectors is

with $v_0 = M_1 v_1/(M_1 + M_2)$ is the velocity of the CM. If we designate the kinetic energy of particle (1) after the collision as $T_1' = 1/2 m_1 (v_1')^2$, we can write using the vectors defined in the figure:

$$T_1' = \frac{1}{2}m_1(V_1 + v_0)^2 = \frac{1}{2}m_1\left(V_1^2 + v_0^2 + 2V_1 v_0 \cos\theta\right) \tag{16.48}$$

Thus T_1' will have a maximum value at $\theta = 0°$ and a minimum value at $\theta = 180°$ due to the cosine function. Specifically we find that

$$T_1'\,(\text{max}) = \frac{1}{2}m_1\left(V_1^2 + v_0^2 + 2V_1 v_0\right) = \frac{1}{2}v_1^2 = T_1 \tag{16.49}$$

$$T_1'\,(\text{min}) = \frac{1}{2}m_1\left(V_1^2 + v_0^2 + -2V_1 v_0\right) = \frac{1}{2}(V_1 - v_0)^2 \tag{16.50}$$

$$T_1'\,(\text{min}) = \frac{1}{2}m_1(v_1 - 2v_0)^2 \tag{16.51}$$

$$T_1'\,(\text{min}) = T_1\left(\frac{m_1 - m_2}{m_1 + m_2}\right)^2 \tag{16.52}$$

For the special case that we are interested in where particle (#1) is a neutron and particle (#2) is a proton, $m_1 \approx m_2$:

$$T_1'\,(\text{min}) = 0; \, T_1'\,(\text{max}) = T_1 \tag{16.53}$$

More algebra will show that

$$T_1' = T_1\frac{1 + \cos\theta}{2} \tag{16.54}$$

$$\theta_1 + \theta_2 = 90° \text{ and } v_1 = v_2 = v_0 \tag{16.55}$$

If we assume that the angular distribution of the scattered neutrons is isotropic in the CM system, then the probability of a neutron scattering into solid angle, $d\Omega$, written as $P(d\Omega)$, is a constant given simply by

$$P(d\Omega) = \frac{d\Omega}{4\pi} \tag{16.56}$$

where the solid angle $d\Omega$ is given in steradians. Substituting for $d\Omega$ using the spherical volume element, we have

$$P(d\Omega) = \frac{2\pi \sin\theta d\theta}{4\pi} = \frac{1}{2}\sin\theta d\theta \tag{16.57}$$

When a neutron is scattered into the angular interval between θ and $\theta + d\theta$, its energy will be changed from T_1 to the interval between T_1' and $T_1' + dT_1'$, where the differential of energy is

$$dT_1' = m_1 V_1 v_0 \sin\theta \, d\theta \tag{16.58}$$

Thus, we get for the probability of scattering into an energy interval dT_1'

$$P(dT_1') = P(d\Omega) = \frac{1}{2}\sin\theta \, d\theta \tag{16.59}$$

$$P(dT_1') = \frac{dT_1'}{2m_1 V_1 v_0} \tag{16.60}$$

With spherical symmetry, there is an equal probability of scattering into each energy interval. For neutrons scattered once by hydrogen,

$$T_1' \text{ (min)} = 0; \ T_1'(\text{average}) = \frac{T_1}{2} \tag{16.61}$$

Thus, after a neutron is scattered by n hydrogen nuclei,

$$T_1'(\text{average}) \approx \left(\frac{1}{2}\right)^n T_1 \tag{16.62}$$

Thus, to reduce a 1 MeV neutron to thermal energies ($\sim 1/40$ eV) requires about 25 collisions with hydrogen nuclei.

16.6   Radiation Exposure and Dosimetry

Up to this point we have taken a very microscopic view of the propagation of beams of particles through material. We have described the degradation of the intensity and the energies of the beams in terms of individual interactions. Now we will take a more macroscopic view from the standpoint of the absorber.

As we have seen the passage of radiation through material causes ionization of the atoms and molecules. The creation of free electrons, recoiling positive ions, and in some cases transmuted nuclei can disrupt the chemical structure of the material. It is important to note that the effect of the passage of a single particle through a macroscopic object will usually cause a minimal overall effect due to the enormous number of atoms present in the object. Special devices are necessary to even observe the ionization from individual particles as described in the next chapter on radiation detectors. Physical changes in an everyday object will be observed when it has been exposed to large amounts of radiation. At the same time we should realize that certain materials will be relatively

immune to the ionization caused by photons and fast electrons, whereas neutron irradiation of the same material can have a substantial effect. For example, a metal lattice is characterized by delocalized electrons, and the local ionization caused by a Compton scattering or photoelectric absorption will be quickly neutralized (or repaired). Whereas, neutron absorption by a metal will generally lead to β decay and the transmutation after β-decay of one atom into the neighboring element. On the other hand, local ionization created by photons and electrons in insulating materials like glasses will persist for a long time because the migration of charge is hindered. Similarly, lattice defects caused by atomic recoil have to be removed by annealing, but atomic recoil has little effect in liquids (and none in gases). Thus, we can see that the effects of radiation on a material will depend in great detail on the type and amount of radiation and on the physical and chemical nature of the material being irradiated.

We have seen that the neutral forms of radiation, photons, and neutrons are very penetrating and can pass through layers of material without interacting. In these cases, we need to distinguish between the amount of *radiation exposure* and the amount of energy absorbed by the material. Photons such as X-rays, bremsstrahlung, and γ rays play an important role in nuclear medicine, but they are not strongly absorbed by tissue. The *exposure* to these photons is not equal to the dose. In the case of highly ionizing radiation such as charged particles, the exposure will correspond to the absorbed energy except for very thin materials that allow the particle to pass through. In order to characterize radiation effects, we need to know the amount of energy absorbed by the material, which is called the *absorbed dose*.

The unit of radiation exposure is the roentgen (*R*). It is a historical unit of the exposure and characterizes the radiation incident on an absorbing material without regard to the character of the absorber. The unit was formalized in 1928 as "The amount of radiation which produces one electrostatic unit of ions (esu), either positive or negative, per cubic centimeter of air at standard temperature and pressure." Translated in modern units,

$$1 \text{ R} = 2.58 \times 10^{-4} \text{ C/kg} - \text{air} = 0.3336 \text{ nC/cm}^3 \text{ at STP} \qquad (16.63)$$

This value corresponds to an absorbed energy of ∼8.8 mJ/kg using the effective ionization energy of 34 eV per ion pair in air. The roentgen is most often used to describe the intensity of a photon source such as a medical X-ray machine or other irradiator. The exposure should be measured at some distance from the source so that the radiation field is uniform compared to the dimensions of the detector. The detector is usually an ion chamber filled with dry air that is sensitive to picoCoulombs of charge.

As studies of the effects of exposure to all types of radiation went on, it became clear that these effects were correlated with the amount of absorbed energy, which is generally less than the exposure. In 1962 the "rad" was formally defined as a special unit of energy called the "radiation absorbed dose" with

a value of 100 ergs/g of absorbing material. The rad is a convenient physical standard that correlates well with chemical and biological effects of radiation, whereas the roentgen defined in terms of an air ionization measurement was left for exposure. More recently, the gray (Gy) was introduced as the SI unit for the absorbed dose with the relationships

$$1 \text{ Gy} = 1 \text{ J/kg} = 100 \text{ rad} = 6.24 \times 10^{12} \text{ MeV/kg} \qquad (16.64)$$

so that 1 centigray (0.01 Gy) is exactly 1 rad. Notice that a gray corresponds to a relatively large amount of energy to be absorbed from a radiation source per unit mass. For example, 1 Gy in water corresponds to 18 mJ/mol. Modern dosimeters routinely measure doses at the few millirad (mr) level or few tens of a microGy.

The acronym "kerma" for "kinetic energy released in absorbing material" has been used to conceptually connect the energy deposited by ionizing radiation with the radiation field. It is defined to include the kinetic energy, which is locally absorbed from products of interaction with the particular medium such as Compton electrons, photoelectrons, and pair production while excluding the energy, which is not locally absorbed, from Compton scattered photons, characteristic fluorescence radiation, and annihilation photons. The kerma is defined as

$$K = \frac{\phi E \mu_x}{\rho} \qquad (16.65)$$

where ϕ is the particle fluence (m^{-2}), E is the energy of the radiation, μ_x is a linear energy attenuation coefficient (energy/m), and ρ is the mass density (kg/m^3). The dimensions of the kerma are thus joule per kilogram or gray. The concept of kerma in air is very close to the roentgen (as a unit of exposure) times a factor for the amount of energy necessary to create an ion pair. However, bremsstrahlung photons are lost as secondary particles but included in the definition of the roentgen, but they represent a small loss term under most conditions.

Just as the effect of radiation on a specific material depends on the dose or amount of absorbed amount of energy in contrast to the exposure, the effect of radiation on biological systems depends on the energy density and not just the energy. One can imagine that a biological system could survive the formation of a single ion pair and the following chemical transformations from a photoelectric event. However, if a large number of direct ionization events take place in a small volume due to the passage of a heavy charged particle through some biological material, the resulting chemical changes could be profound. The important distinguishing parameter is linear energy transfer, LET, which is very close to the specific energy loss $-dE/dx$ discussed earlier in this chapter. The value of LET for a given particle is smaller than the value of $-dE/dx$ because the LET does not include the radiative energy loss term, as the bremsstrahlung radiation is not absorbed "locally." Recall that the radiative energy loss term was only significant for high-energy electrons. Typical values of LET for photons and fast

Table 16.4 Radiation Weighting Factors

Radiation	γ	β	Proton (> 2MeV)	α	Fast Neutron (2–20 MeV)	Thermal Neutron
Factor	1	1	5	20	10	5

electrons are a few megaelectron volt per millimeter but are one or two orders of magnitude larger for heavy charged particles.

The concept of dose equivalent has developed over time to quantify the more damaging effects of high LET radiation. The original definition of the absorbed dose in rads was multiplied by a quality factor, $Q > 1$. The quality factor increased with increasing LET. The historical unit for dose equivalent is called a *rem* for "roentgen equivalent man," and measurements of dose equivalents to biological systems, especially people, are most commonly reported in millirem (mrem). With the more recent SI dose unit of gray, a new SI unit of dose equivalent (or as it is now called equivalent dose) was introduced called the sievert (Sv). The sievert and rem are different by a factor of 100 in the same way as the rad is smaller than the gray:

$$1 \text{ Sv} = 100 \text{ rem, or } 10 \text{ } \mu\text{Sv} = 1 \text{ mrem} \tag{16.66}$$

The equivalent dose in Sv = absorbed dose in grays $\times$ w_R (radiation weighting factor, formerly called the quality factor). The absorbed dose for low LET radiation, β and γ rays, is taken as having a radiation weighting factor of unity, thus, $w_R = 1$. The radiation weighting factor has been defined to increase in proportion to the log of the LET. Thus, the radiation weighting factor for α particles in tissue is about 20. The factor for neutrons takes an intermediate value due to the high probability for scattering protons in tissue. A listing of radiation weighting factor values for various types of radiation is shown in Table 16.4.

Notice that the dose has a strict definition of energy per unit mass of the absorber and, in principle, can be measured for a given radiation at a certain energy in a specific material. The equivalent dose is a relative unit in that a radiation weighting factor is applied to a measured quantity. The dose can be measured from ionization in an electronic radiation detector; the equivalent dose must take into account the type of radiation causing the ionization.

Problems

16.1 Calculate dE/dx for a 10 MeV α particle interacting with aluminum.

16.2 At what kinetic energy does an electron have the same energy loss as a 6 MeV α particle interacting with aluminum?

16.3 Calculate dE/dx for an 8 MeV α particle interacting with Mylar.

16.4 It has been said α particles and protons having the same speed have approximately the same range in matter. Why is this false? Which has the longer range and why?

16.5 Verify that the minimum ionization for heavy charged particles takes place at $\beta \sim 0.96$.

16.6 A thin nickel foil is used to slow down monoenergetic 10 MeV protons. What is the maximum thickness that can be used if one wants the straggling to be <1% of the mean transmitted energy? What is the mean transmitted energy in this case?

16.7 Calculate the thickness of aluminum foil needed to degrade a beam of 10 MeV/u ^{12}C ions to 3 MeV/nucleon.

16.8 Calculate the energy loss of a 6 MeV α particle in passing through 50 μ g/cm^2 of natural nickel.

16.9 Assuming no energy losses occur, calculate the heating of a 500 μg/cm^2 foil of ^{208}Pb when bombarded with 1 particle microampere of ^{86}Kr^{19+} ions.

16.10 Devise a way, using measurements of dE/dx and E, to build a particle identification system.

16.11 Calculate the range in aluminum of (a) an 80 MeV ^{80}Br ion, (b) a 12 MeV α particle, and (c) a 1 MeV electron.

16.12 A Geiger counter window is made of mica, $NaAl_3Si_3O_{10}(OH)_2$, with a thickness of 2 mg/cm^2. (a) What is the minimum energy β-particle that can penetrate this window? (b) What is the minimum energy α particle that can penetrate this window?

16.13 Repeat the calculation outlined in the previous problem (#12) for a skin thickness 1 mm with an average density of 1 g/cm³. Assume skin is 65% O, 18% C, 10% H and 7% N.

16.14 Particles of kinetic energy 400 MeV are incident on a medium of index of refraction of 1.888. One observes Cherenkov radiation with an opening angle of $\theta = \cos^{-1}(0.55)$. Identify the particles if they are minimum ionizing.

16.15 How far does a ^{32}P β^- particle ($E_{\text{max}} = 1.7$ MeV) penetrate in P-10 counter gas? (P-10 is a gas used extensively in radiation detectors that is 10% methane and 90% argon.)

16.16 Suppose you have a sample that contains radionuclides that emits 1 MeV β-particles and 1 MeV γ-rays. Devise an attenuation technique that would allow you to count the γ-rays without interference from the β-particles.

16.17 What is the fractional attenuation of a beam of 1 MeV photons in 2.5 cm of Pb?

16.18 Prove that a photon with $E_\gamma > 1.022$ MeV cannot undergo pair production in free space.

16.19 Lead is thought to be a "better" absorber of photons than aluminum. At what γ ray energies is the mass absorption coefficient of lead greater than that of aluminum? Why?

16.20 A 1 MeV photon undergoes Compton scattering through angles of 0°, 90°, and 180°. What is the energy of the scattered photon in each case?

16.21 What is the mean free path of a 0.1, a 1.0, and a 3.0 MeV photon in NaI? (Large crystals of this salt are very useful radiation detectors.)

16.22 Calculate the mean free path of a 200 keV photon in water.

16.23 How much lead shielding will it take to reduce the radiation exposure level to <10 mrem/h at 1 ft from a 5 mCi ^{137}Cs source?

16.24 Prove the scattering angle is 90° for $A + A$ elastic scattering.

16.25 Consider a particle with mass m_1 scattering elastically from a particle (at rest) with mass m_2. If $m_1 > m_2$, show that the scattering angle cannot exceed $\sin^{-1}(m_2/m_1)$.

16.26 In graphite, how many collisions are necessary to reduce the kinetic energy of a 1 MeV neutron to thermal energy? What is the approximate time scale for this process?

Bibliography

R.D. Evans, *The Atomic Nucleus* (McGraw-Hill, New York, 1955) The "bible" of this subject due to its detailed examination of all aspects of the subject. The text is dated but very accurate.

H. Geissel, C. Schiedenberger, and H. Weick, https://web-docs.gsi.de/~weick/atima. The ATIMA code is a modern energy-loss code that is particularly well suited to heavy ions at the highest energies.

B.G. Harvey, *Introduction to Nuclear Physics and Chemistry*, 2nd Edition (Prentice-Hall, Englewood Cliffs, 1969). The same information as Meyerhof from a chemist's perspective.

M.G. Hollaway and M.S. Livingston, Phys. Rev. **54**, 29 (1938).

F. Hubert, R. Bimbot, and H. Gauvin, At. Data Nucl. Data Tables **46**, 1 (1990). This reference contains ranges and stopping powers for the interaction of 2.5 to 100 MeV/nucleon heavy ions with matter.

G.F. Knoll, *Radiation Detection and Measurement*, 4th Edition (John Wiley & Sons, Inc., New York, 2010). An important, easy to read summary of this subject.

W.R. Leo, *Techniques for Nuclear and Particle Physics Experiments* (Springer-Verlag, Berlin, 1987).

K.H. Lieser, *Nuclear and Radiochemistry: Fundamentals and Applications* (VCH, New York, 1997). Covers a number of the practical aspects of the subject that are important to radiochemists.

P. Marmier and E. Sheldon, *Physics of Nuclei and Particles*, Volume I (Academic, New York, 1969). Detailed theoretical treatment of many of the important concepts. Still a useful reference.

W.E. Meyerhof, *Elements of Nuclear Physics* (McGraw-Hill, New York, 1967). A condensed treatment that captures the essential details.

L.P. Nielson, Dan. Mat. Fys. Medd. **33**, 6 (1961).

L.C. Northcliffe and R.P. Schilling, At. Data Nucl. Data Tables **A7**, 233 (1970). This older data compilation is a useful reference for estimating the stopping powers and ranges of slow ($E < 2.5$ MeV/nucleon heavy ions in matter).

N. Tsoulfanidis and S. Landsberger, *Measurement and Detection of Nuclear Radiation*, 4th Edition (CRC Press, Boca Raton, 2015). Many detailed numerical examples.

C.H. Wang, D.L. Willis, and W.D. Loveland, *Radiotracer Methodology in the Biological, Environmental and Physical Sciences* (Prentice-Hall, Englewood Cliffs, 1975). Noted for its discussion of liquid scintillation counting, this book served as a model for much of the discussion of this chapter.

G.F. Williamson, J.P. Boujot, and J. Picard, CEA—R03A2, (1966).

J. Ziegler and J.P. Biersack, http://www.srim.org. This website and the references cited therein represent the largest and most widely used compilation about the stopping of energetic ions in matter. The computer programs SRIM (stopping and range tables) and TRIM (transport of radiation in matter) found here are used widely to estimate stopping powers, ranges and straggling.

Radiation Detectors

17.1 Introduction

A fundamental feature of nuclear processes is that the energy released is larger than the binding energies of atomic electrons. Thus, any emitted particles will have sufficient energy to ionize atoms and molecules. Nuclear radiation is called "ionizing radiation"; therefore, detecting this ionization allows us to observe nuclear processes. Radiations that interact with matter via the electromagnetic force, that is, electrons, charged particles, and photons, can directly ionize or excite atoms. These radiations are readily detected. Neutrons interact with nuclei only via the nuclear force and are detected through indirect or secondary ionization processes. We should note that though the energy released in nuclear processes is several (even many) orders of magnitude larger than atomic binding energies, the total number of ion pairs that can be created when radiation interacts with matter is small on a macroscopic scale. For example, typical electron binding energies are about 10 eV. If the total energy available from a 1 MeV nuclear decay is completely converted into electron/ion pairs, then the total number of pairs would be $\sim 10^5$, corresponding to a charge of $\sim 10^{-14}$ C. Even this estimate of the charge created is optimistic because it is unlikely that all of the energy will create ion pairs. (The "effective" ionization energy of most gases is about 35 eV/ion pair because some ion pairs recombine and some energy goes into internal excitation.)

To measure the radiation, the primary ionization must be preserved and not be lost to recombination or scavenging by nonmobile electronegative atoms. Metals are generally not useful for creating radiation detectors. At the same time, the created ions must be mobile so that they can be collected. This rules out insulating materials in most cases for detectors that collect ionization. The small electrical signals must be amplified to be observed, and so electronic instrumentation plays a role in modern nuclear chemistry.

Although the various types of radiation detectors differ in many respects, several common criteria can be used to evaluate the performance of any detector

type. The criteria used for this purpose are as follows, and each class of detector will be discussed in this framework:

1. The sensitivity of the detector. What types of radiation will the detector detect? For example, solid scintillation detectors are normally not used to detect α-particles from radioactive decay because the α-particles cannot penetrate the detector covering.
2. The energy resolution of the detector. Will the detector measure the energy of the radiation striking it, and if so, how precisely does it do this? If two γ-rays of energies 1.10 and 1.15 MeV strike the detector, can it distinguish between them?
3. The time resolution of the detector or its pulse-resolving time. How high a counting rate will be measured by the detector without error? How accurately and precisely can one measure the time of arrival of a particle at the detector?
4. The detector efficiency. If 100 γ-rays strike a detector, exactly how many will be detected?

In this chapter we will consider the techniques developed to detect and quantitatively measure how much ionization and/or excitation is caused by different nuclear radiations. All radiation creates ionization and/or excitation as discussed in Chapter 16. Here we will separate the discussion of detection methods according to the general techniques used to collect and amplify the results of the interaction of the primary radiation with matter rather than by the type of radiation. These detection methods can be classified as (a) collection of the ionization produced in a gas or solid, (b) detection of secondary electronic excitation in a solid or liquid scintillator, or (c) detection of specific chemical changes induced in sensitive emulsions. A brief summary of these detector types is given in the following text.

17.1.1 Gas Ionization

Several detector types take advantage of the ionizing effect of radiation on gases. The ion pairs can be separated and the charges collected. When an electrical potential gradient is applied between two electrodes in a gas-filled ion chamber, the positively charged molecules move to the cathode and the negative ions (electrons) swiftly to the anode, thereby creating a measurable current. Such current pulses can be readily measured by the associated devices as individual events or integrated current.

17.1.2 Ionization in a Solid (Semiconductor Detectors)

In a semiconductor radiation detector, the incident radiation interacts with the detector material, such as Si, Ge, or materials like GaAs, to create hole–electron

pairs. These hole–electron pairs are collected on charged electrodes on the surface of the material with the electrons migrating to the positive electrode and the holes to the negative electrode, thereby creating an electrical current. Such current pulses contain information on the energy, time of arrival, and number of particles arriving per unit time. The important features of semiconductor detectors are their superior energy resolution due to a low ionization potential and compact size.

17.1.3 Solid Scintillators

Some of the energy of ionizing radiation is converted into visible light. This process can be enhanced by transferring excitation energy to fluor molecules (i.e., compounds that can produce fluorescence) in insulating crystalline solids. The transfer process is enhanced when the excited energy levels of the fluor are well matched to the bandgap in the insulator. De-excitation of the fluor results in the emission of the absorbed energy as electromagnetic radiation in the visible or near-ultraviolet (UV) region (called scintillations). Observing these weak scintillations visually under certain circumstances is possible (see Figure 17.1), but visual observation is normally not a feasible detection method. Instead a photomultiplier attached to the solid crystal with the fluor is employed. The photomultiplier converts the photons into photoelectrons, which are greatly amplified by secondary electron emission by a series of electrodes (called dynodes) to cause a sizable electrical pulse. Thus, the original excitation energy is transformed into a measurable pulse.

17.1.4 Liquid Scintillators

Liquid scintillators are quite similar in principle to solid scintillators. Here, however, the radioactive sample and the fluor (usually an organic molecule) are solutes in a liquid medium, usually a nonpolar solvent. The absorption of the nuclear radiation first excites the solvent molecules. Some of this excitation energy is transferred to fluor molecules that then emit photons. The photons are detected by a photomultiplier as with the solid scintillators.

17.1.5 Nuclear Emulsions

The process involved here is chemical and essentially the same as that in film-based photography. A small grain-size photographic emulsion or film is exposed to ionizing radiation. The radiation can usually penetrate the light tight covering and the emulsion is always kept in the dark. The radiation interacts with the silver halide grains suspended in the photographic emulsion to reduce the silver. The subsequent development of the film produces tracks and so permits a semi-quantitative estimate of the radiation coming from the sample.
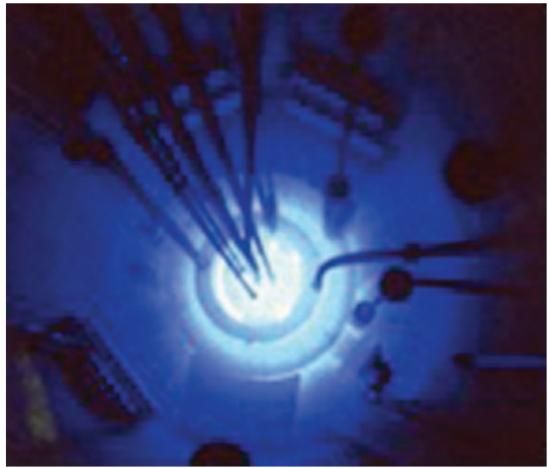
Figure 17.1 Image of the operating core of a TRIGA reactor illuminated by Cherenkov radiation. (*See insert for color representation of the figure.*)

Sample Problem 17.1: Visual Detection of Radiation

Can nuclear radiation be directly observed by humans?

Solution

The energy per decay is small so that only extremely large sources generate enough energy that they warm up and glow in the visible region. The human eye is not sensitive to photons in the X-ray and γ-ray regions, and so individual transitions are not "visible." Only indirect observation of Cherenkov radiation emitted by very energetic electrons from the β-decay of fission products and Compton-scattered electrons from γ-decay in nuclear reactors is possible. During reactor operation, very neutron-rich fission products are produced that rapidly emit very penetrating β-particles and Compton-scattered electrons. These electrons can leave the fuel rods and enter the cooling water. The energetic electrons are relativistic and travel with velocities very close to the speed of light. However, because the speed of light is lower in liquid water than in a vacuum, the electrons emit characteristic blue photons—called Cherenkov radiation—as they adjust their speed downward (Fig. 17.1). This Cherenkov radiation lies in the blue region of the spectrum. Large power reactors do not have viewing ports, but the cores of research reactors are usually visible. The cores are surrounded by an eerie blue glow from Cherenkov radiation when the reactors are operating.

17.2 Detectors Based on Collecting Ionization

Many detectors have been developed to collect and amplify the primary ionization created by nuclear particles. In principle, the careful measurement of this ionization provides the most information about the initial particle and its

energy. The devices with the highest resolution are these detectors based upon ionization. Broadly speaking, ionization-based detectors have the common feature that the incident radiation creates ion pairs in an active volume of the device. An electric field is applied to the active volume to separate the charge pairs and sweep the ions to the electrodes.

Ionization-based detectors have mostly used gases as the active medium. Very few devices use liquids because extremely pure materials are needed to preserve the primary ionization. Gas-filled detectors are easy to construct and operate but the density of the stopping material is low. The effective ionization potential is large, typically ~ 20 eV. Semiconductor solids are $\sim 10^3$ times denser than gases and have lower "ionization potentials," ~ 2 eV, but producing large volumes of suitably pure material is expensive. Liquids also have high densities, but successful devices have only been made with liquefied rare gases, liquid argon, and xenon. The impurity level and cryogenic nature of these liquids have limited the applicability of these devices.

17.2.1 Gas Ionization Detectors

As an energetic charged particle passes through a gas, the Coulomb interaction can dislodge orbital electrons from atoms sufficiently close to its path. In each case, the negatively charged electron dislodged and the more massive positive ion, that is, the remainder of the atom, form an ion pair. The *minimum* energy (in electron volts) required for such ion pair formation in a given gas is called the ionization potential. This value differs markedly for different gases. A more meaningful value is the *average* energy lost by the particle to producing one ion pair, which is nearly independent of particle energy and type (and is about 35 eV).

The *rate of energy loss* will depend on the energy and type of charged particle. α-Particles create intense ionization (10^4–10^5 ion pairs/cm of path length), whereas β^- particles produce less intense ionization (10^2–10^3 ion pairs/cm), and the passage of γ-rays results in only weak ionization (1–10 ion pairs/cm). How can we use this primary ionization to produce a detectable signal?

Ion Chambers

The first class of devices to be discussed is the *pulse-type ion chamber*. A sketch of such a device (a parallel-plate ion chamber) is shown in Figure 17.2. Note that one electrode has been connected to the negative terminal of the voltage source, making it the cathode, while the other electrode acts as the anode.

If a 3.5 MeV α-particle traverses an air-filled ion chamber, intense ionization will occur along its short path. Since about 35 eV are expended, on the average, in forming an ion pair in air, the 3.5 MeV α-particle would form $\sim 1 \times 10^5$ ion pairs before dissipating all of its kinetic energy (KE). The electrical potential applied to the chamber electrodes will cause the ions to migrate rapidly to
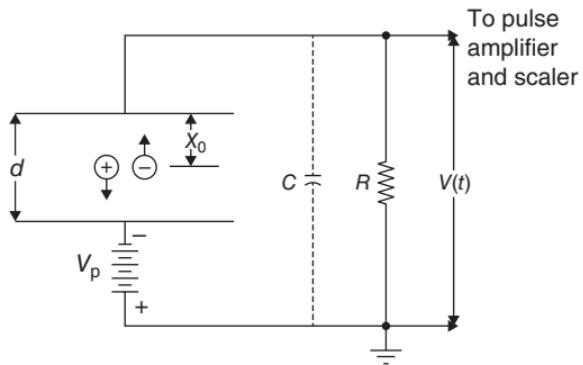
Figure 17.2 Schematic representation of a parallel-plate ionization chamber in which one ion pair has been formed. V_p is the voltage source, R denotes output resistor, C denotes the effective of stray capacitance of the plates, and $V(t)$ is the time-dependent voltage to be measured (O'Kelley (1962). Reproduced with the permission of NAS-NS-3105).

the respective electrodes. The less-massive electrons move very quickly to the anode and produce a rapid buildup of charges there. (Because the positive ions move about 1000 times slower than the electrons, their effect can be neglected for the moment.) The time for collection of the electron charge is about 0.1–1 µs depending on the volume of the chamber and the voltage gradient. The magnitude of this charge due to the electrons can be simply calculated as the charge on the electron times the number of ion pairs:

$$10^5 \text{ e}^- \times 1.6 \times 10^{-19} \text{ C/e}^- = 1.6 \times 10^{-14} \text{ C} \tag{17.1}$$

Using Figure 17.2 as a guide, the collected charge flows through the external circuit as a surge, or pulse. If the capacitance of the chamber is 20 picofarad (pF), then the total size of the voltage pulse, V, which would be observed on the external resistor, R, is
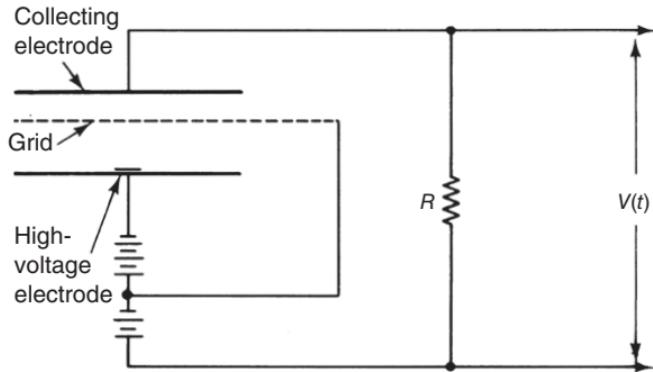
$$V = \frac{Q}{C} = \frac{1.6 \times 10^{-14} \text{ C}}{20 \times 10^{-12} \text{ F}} \tag{17.2}$$

where Q is the charge that we just calculated (Coulombs) and C is the capacitance (farads). For this example, $V = 0.0008$ V or 0.8 mV. The precise measurement of such small pulses is difficult and sensitive low-noise electronic modules are needed to measure the signals accurately. Note that in these ion chambers, there is no amplification of the primary ionization.

The discussion so far has not been completely accurate in that the effect of the positive ions on charge collection has been neglected. In practice, the positive ions can be troublesome. Although they move very slowly to the cathode, as they move, they induce a charge on the negative electrode ending in their collection on the surface. If no correction is made for this induced charge, the shape of the output pulse will depend on the position of the particle track in the chamber volume. A simple method for eliminating this induced charge is the addition of a grid to the ionization chamber, as shown in Figure 17.3.

The role of the grid in the ion chamber is to screen the anode from the motion of the electrons but allow the electrons to pass through and be collected on the

Figure 17.3 Schematic diagram of a gridded ionization chamber (O'Kelley (1962). Reproduced with the permission of NAS-NS-3105).
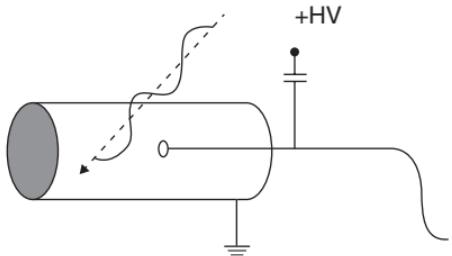
anode. Thus, the grid should be positively charged with respect to the cathode, but less positive than the anode or collecting electrode. The grid, called a Frisch grid after the inventor, should also be placed relatively close to the anode so that the induced charge from the motion of the electrons is short in time.

The electronic signals from the passage of individual particles through an ion chamber can be measured as a function of position inside the volume by segmenting the anode. As we have seen in Chapter 16, the rate of ionization is a characteristic of the energy and nature of the radiation. For example, devices with multiple anodes arranged parallel to the ion's path have been constructed to take samples of the rate of ionization (Fig. 17.4).
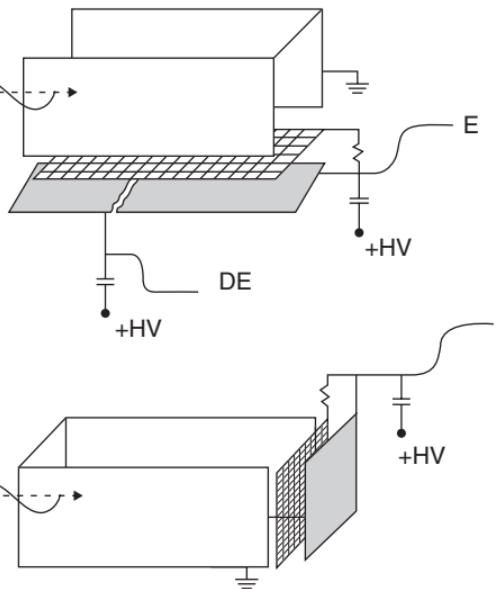
The so-called Bragg curve detectors determine the relative ionization *along* the path of the particle by measuring the time distribution of ions as they arrive at an anode that is perpendicular to the ion's path; see Figure 17.4. These detectors require sophisticated electronic readout to continuously measure the ionization collected as a function of time after a particle passed through the gas volume. Therefore, Bragg curve detectors and segmented anode ionization chambers are usually only used to detect charged particles from nuclear reactions.

The most sophisticated gas ionization detector is the *time projection chamber* (TPC). It is a large gas-filled volume that is usually used to track particles that move through or react in the gas. In most cases, the particles move parallel to the anode, which is segmented in thousands or even tens of thousands of individual pads. Each pad has its own electronic readout. Electrons produced by the ionizing radiation passing through the chamber drifts (down) to the anode (that can have a grid) are collected, and the amplitude on each pad is recorded. An overview of the signals from all of the pads provides a view of the particle track and thus a projection of the time that the particle was in the chamber. The TPC can be placed in a large magnetic field that will cause charged particles to curve due to the Lorentz force so that the track will provide additional information on the magnetic rigidity of the particle. A TPC can also record
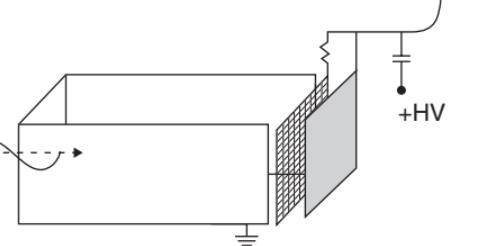
Figure 17.4 (a) A schematic diagram of a simple Geiger counter that provides no information on the incident particle's path. (b) A schematic diagram of an ion chamber that drifts the ionization perpendicular to the particle's path. In this case, the anode is segmented and the relative rate of ionization along the path can be determined. The device also contains a Frisch grid between the anode and chamber to improve the pulse-shape response of the device. (c) A schematic version of a detector that drifts the ionization along the particle's path, called a Bragg counter. The time distribution of the output signal will contain information on the relative rate of ionization all along the particle's path.

multiple tracks, for example, from reaction products, if all of the pads are read out independently. A recent variation of the TPC has been developed in which the electrons are multiplied near a transparent anode, and the light produced by this process and recombination is detected and measured with a digital camera. In this device, called an optical TPC, the pads and electronic readouts are replaced by the millions of pixels in the digital camera.

Gas-filled ionization counters that collect the primary electrons on an anode wire, as opposed to an anode plate, can automatically amplify the initial ionization. The cylindrical electric field near thin wire anodes ($\sim$50 μm) can be very large, causing the primary electrons to be accelerated past the point at which they can create secondary ionization (Fig. 17.5). The secondary ions so formed continue to be accelerated by the increasing potential gradient, thereby producing still more ionization. Thus, a geometrical increase in the number of ion pairs can result in a veritable torrent of electrons moving inside the chamber. Note that the electrons will be collected very quickly since they were mostly created
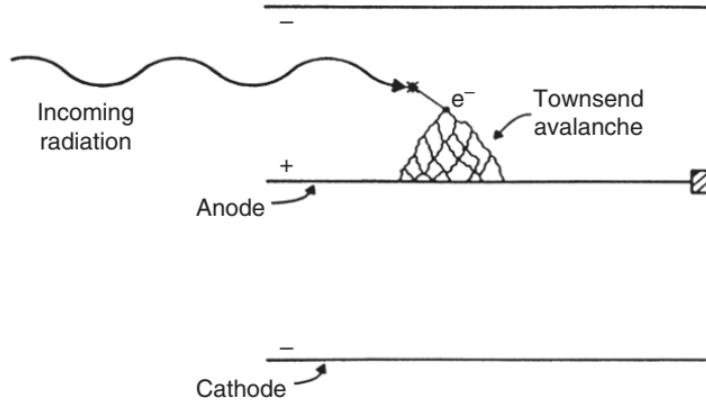
Figure 17.5 Cartoon illustration of a Townsend avalanche in a gas ionization device. The avalanche occurs extremely close to the wire in reality (Knoll (2010). Reproduced with the permission of John Wiley & Sons).

very close to the anode, but the positive (and slower) ions will have to move a larger distance to the cathode. The process described is known as *gas amplification*; the flood of electrons is termed the *Townsend avalanche*, in honor of the discoverer of this phenomenon. In gas amplification, most of the electrons are collected at the anode within a microsecond or less from the entrance of a single charged particle into the chamber. A strong pulse is thereby formed, fed into the external circuit, and directly measured after only low amplification. Note that the voltage applied to the anode will first be screened by the large number of nearby electrons before collection and then modified by positive ions as they drift away toward the cathode.

As the potential gradient between the electrodes in the ionization chamber is further increased, the number of electrons, mostly secondary, reaching the anode rises sharply for a given number of primary electrons created by a charged particle. Eventually a potential will be reached at which the chamber is said to "break down" and undergo a continuous electrical discharge and is no longer usable as a detector. There are two distinct potential regions between the ion chamber region (no amplification) and continuous discharge that are useful for gas ionization devices. They are called the proportional region and Geiger–Müller (GM) region.

Proportional Counters

Radiation detectors that operate in the *proportional region* use a small amount of gas amplification so that the number of electrons in output pulse is very much greater than, yet still proportional to, the number formed by the initial ionization. Gas amplification factors of about 10^3–10^4 are generally used. The amplification factor is primarily dependent on the diameter of the anode wire, the composition of the chamber filling gas, and the potential gradient.

At a given potential for a fixed geometry and fill gas, the amplification factor will be the same for all ionizing events. Consequently, if an α-particle traversing the ionization chamber creates 10^5 primary ion pairs, with an amplification factor of 10^3, a charge equivalent to 10^8 electrons would be collected at the anode. An incident β-particle, on the other hand, producing only 10^3 ion pairs, would, after amplification by the same factor of 10^3, result in a collected charge equivalent to only 10^6 electrons, and the two kinds of events would be easily distinguishable.

As with simple ionization chambers, then, it is possible to differentiate between various charged particles in the proportional region based on pulse size. This is one advantage of operating a detector in the proportional region. Because the amplification factor in the proportional region is so heavily dependent on the applied potential, highly stable high-voltage supplies are necessary.

The avalanche of electrons in proportional detectors is collected only on a small section of the anode wire. Furthermore, only a small fraction of the gas volume of the ionization chamber is involved in the formation of ions. These factors result in a very short *dead time*, that is, the interval during which ion pairs from a previous ionization event are being collected and the chamber is rendered unresponsive to a new ionizing particle. Ionization chambers operating in the proportional region are usually inactive for only 1–2 μs following each ionization event. Dead times as low as 0.2–0.5 μs can be achieved, but if a proportional counter is used for spectroscopy purposes, the average time between pulses may need to be ~10 μs or greater due to the slower operation of the external amplifiers and other electronics.

Two schematic designs for proportional counters are shown in Figure 17.6. In the cylindrical detector, a very thin window of split mica or aluminized Mylar plastic covers one end of the tube. It can be so thin (down to 150 μg/cm^3) that the absorption of α-particles by the window is not extensive. An even more efficient arrangement is found with the hemispherical detector, where the radioactive sample can be introduced directly into the detector chamber. In the hemispherical detector, one detects ~50% of all the particles emitted by the source. Such *windowless* detectors are widely used for counting sources that emit α- and low-energy β-particles.

With either ultrathin end-window or windowless detectors, a certain amount of air can leak into the counting chamber. Both the oxygen and the water vapor of the air reduce the detection efficiency by scavenging some of the primary electrons. Detectors of this variety, therefore, must be purged with the counting gas before the measurement is started and must be continually flushed with gas at a pressure above the ambient pressure at a low flow rate during the counting operation. Consequently, such chambers are often called *gas-flow detectors*.

The operating potential of the chamber is largely determined by the ionization potential of the fill gases. A mixture of 90% argon with 10% methane known
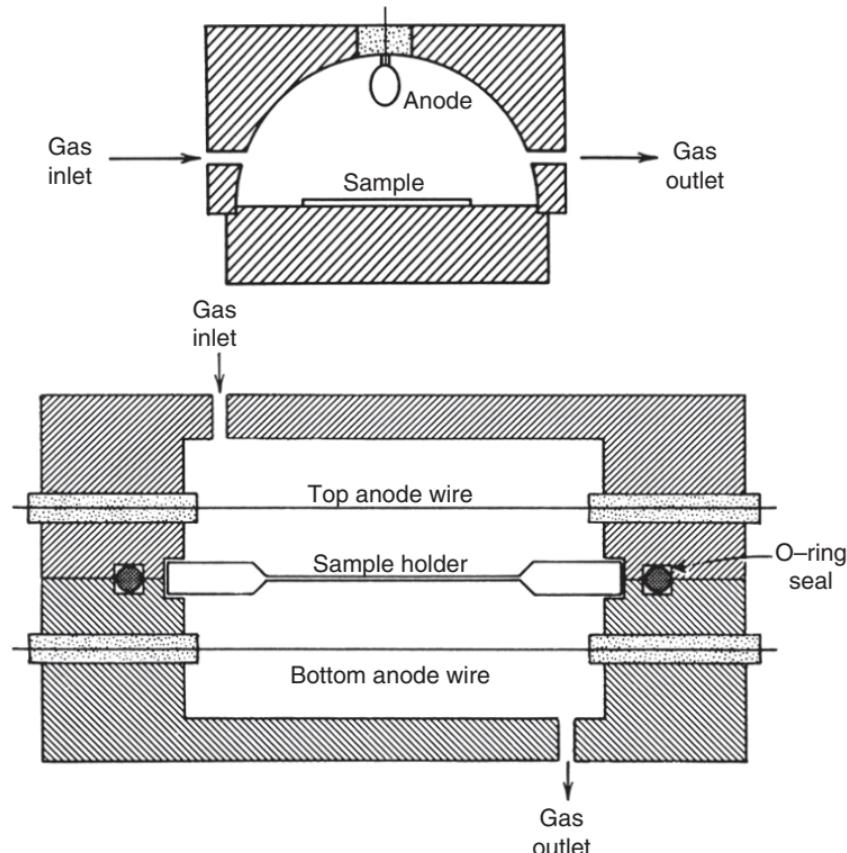
Figure 17.6 (Top) Diagram of a 2π gas-flow proportional counter. The sample is introduced by sliding out the bottom of the chamber and the anode is a loop to avoid a very large electric field on the tip of a straight wire. (Bottom) Diagram of a 4π gas-flow proportional counter for absolute counting.

as P-10 gas and a mixture of 4% isobutane plus 96% helium mixture known as Q-gas are some commonly used counting gases. Other high-purity gases and gas mixtures are used to fill the detectors. Often argon is used for its relatively high density, but fluorocarbons like CF_4 and C_2F_6 and hydrocarbons like isooctane and isobutane are also used in devices designed to detect heavy charged particles that create dense ionization tracks. A variant on the gas-flow counter is *internal gas counting* where the radioactive gas to be counted is mixed with the normal counting gas.

A schematic diagram of the basic electronic components necessary to operate a proportional counter is shown in Figure 17.7. Pulses from the detector pass through a preamplifier and amplifier, where they are shaped and amplified. Emerging from the amplifier, the pulses go to a discriminator. The discriminator is set so as not to fire on noise pulses but rather to fire on radiation pulses
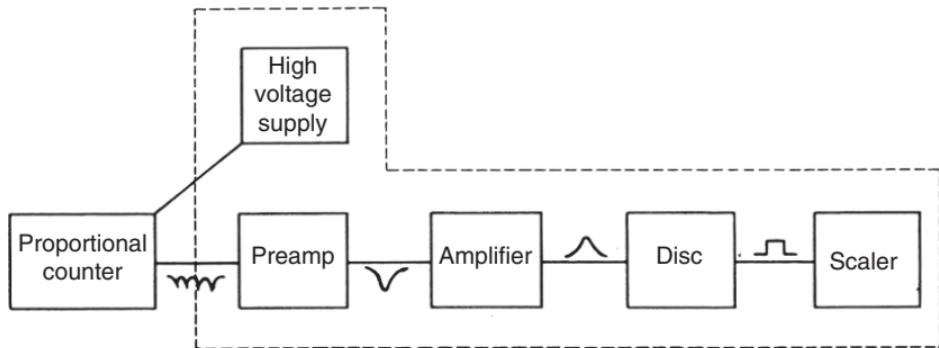
Figure 17.7 Schematic block diagram of the electronic components necessary to operate a proportional counter.
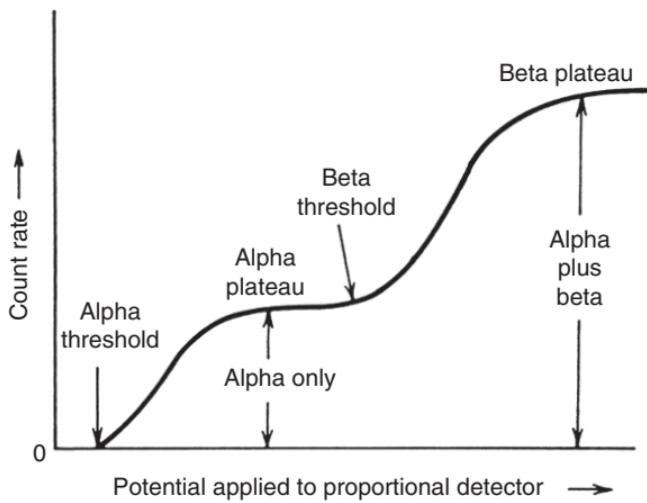
Figure 17.8 Example of the characteristic response curve for a gas-flow proportional counter versus applied voltage.

of any larger size. The number of discriminator pulses produced is recorded by the scaler.

When the counting rate of a sample emitting both α- and β-particles is determined over the voltage range of a proportional detector, a characteristic behavior is seen as a function of voltage, for example, as in Figure 17.8. The characteristic curve for a proportional detector exhibits two plateaus. The plateau at the lower voltage represents the response to α-radiation alone because, at this applied voltage, only the α-particles, with their much greater specific ionization, produce pulses large enough to trigger the discriminator. Not only may the α-particles thus be counted separately from any accompanying β-radiation at this potential, but also the background radiation counting rate (primarily cosmic rays and γ-rays) is extremely low, on the order of a few counts per hour.

As the potential gradient between the anode and cathode is increased, the amplification factor becomes exponentially greater. Eventually the primary ions produced by energetic (weakly ionizing) β-particles are amplified sufficiently to produce pulses large enough to be recorded. This point represents the β threshold. Further increases in potential gradient allow even the pulses from the weaker β-particles to be registered. The β plateau in the operating voltage has now been reached. The count rate here actually represents α plus β radiation, if both are present. A good proportional counter has a β plateau slope of <0.2% per 100 V. The efficiency of proportional detectors for γ radiation is so low that they are seldom used for γ counting. Often, in discussions of the proportional counter, one forgets to mention that the proportional counter is an excellent spectrometer (i.e., an energy measuring instrument) for low-energy radiation, such as X-rays.

Geiger–Müller Counters

At still higher potential gradients inside the chamber, the gas amplification factor may reach 10^8. Now even a weak β-particle or γ-ray can create a sufficient number of ion pairs to completely saturate the available "ion space" in the chamber. The amount of charge collected on the anode no longer depends on the number of primary ion pairs, and it is no longer possible to distinguish between the various types of radiation. This potential level is called the GM region, after Hans Geiger (a student of Rutherford) and his student Walther Müller who first investigated the behavior. Ionization chambers operated in this potential region are commonly called GM counters. Since the maximal gas amplification is realized in this region, the size of the output pulse from the detector will remain the same over a considerable voltage range until breakdown; continuous discharge occurs. This fact makes it possible to use a less expensive high-voltage supply than that required for proportional detectors.

The very high amplification factor in the GM region is not without problems. One problem is the longer dead time of the chamber. Following the passage of an ionizing particle through a detector, an electron avalanche occurs along the entire anode wire, resulting in a cylindrical sheath of positive ions around the anode. The number of such positive ions per pulse will be one or more orders of magnitude greater than that in chambers operated in the proportional region. To be neutralized, the positive ions must migrate to the cathode wall. Being much more massive than the electrons, these ions move at a slower velocity in the electrical field. During this migration, the chamber is somewhat unresponsive to any new ionizing particles passing through it. Thus, the dead time of a detector operated in the GM region is from 100 to 300 μs or more. A detector that behaves in this way is said to be "paralyzable" and care must be taken when making a reading.

Detector systems come in two groups with respect to dead time. If the detector requires a fixed amount of time to respond and measure a signal, then it is

said to be "non-paralyzable." Events that occur when a signal is being processed are just ignored in such detectors. On the other hand, if the detector is affected by the event while another event is being processed (e.g., a gas-amplified detector), then the detector is said to be "paralyzable." The measured counting rate will actually decrease at very high counting rates in a paralyzable detector system.

The correction for "dead time losses" in a non-paralyzable detector can be made with the value of the dead-time per event τ. If the true counting rate is R ($\tau = 0$), and R_{obs} is the measured rate, we have

$$R = \frac{R_{obs}}{(1 - R_{obs}\tau)} \quad \text{Non-paralyzable} \tag{17.3}$$

This is a single valued expression that is easy to evaluate for non-paralyzable detector systems. On the other hand, the expression for the true counting rate is double valued for a paralyzable detector system:

$$R_{obs} = Re^{-R\tau} \quad \text{Paralyzable} \tag{17.4}$$

Sample Problem 17.2: Dead Time and Counting Rates

What is the true counting rate if we measure a counting rate of 1000 counts per second (cps) with a detector that has a dead time of 250 μs if (a) it is non-paralyzable and (b) paralyzable?

Solution

(a) The true counting rate for a non-paralyzable detector is

$$R_T = \frac{R_M}{(1 - R_M\tau)} \quad \text{Non-paralyzable}$$

$$R_T = \frac{1000}{[1 - (1000 \times 250 \times 10^{-6})]} = 1333 \text{ cps}$$

thus the measured counting rate being low by 33%.

(b) The true counting rate for a paralyzable detector is

$$R_{obs} = Re^{-R\tau} \quad \text{Paralyzable}$$

$$1000 = Re^{-R \times 250 \times 10^{-6}}$$

This expression has two solutions, $R = 1440$ and $R = 8610$. Which is right?

Another important problem is the self-perpetuation of ionization in the chamber. The primary cause of multiple discharges from a single event is

associated with the neutralization of positive ions, primarily at the cathode wall of a detector. Notice that the fill gas is mostly rare-gas atoms (and not molecules). These atoms have relatively high ionization potentials and emit UV radiation when electrons fill the inner orbitals. The UV radiation is most likely to strike the chamber wall and can emit a photoelectron from the metal surface. This electron can go on to cause another avalanche! As a result, we need a means of terminating or quenching the perpetual ionization caused by UV from the recombination of the rare-gas atoms in the detector. This quenching is accomplished by introducing polyatomic organic compounds or halogen gases into the counter gas. The rare-gas ions will transfer their ionization to the molecules due to the lower ionization potentials of the molecules. These molecules will emit lower energy photons and can also vibrationally dissipate the energy, which stops the discharge. Since some of the molecules are destroyed during the quenching process, the lifetime of a GM tube is typically limited from 10^8–10^9 pulses.

One of us (GTS), as a graduate student in 1936, was involved with the discovery of the quenching phenomenon in GM counters. He and a fellow graduate student, David C. Grahame, were plagued with erratic GM counter behavior until they discovered the beneficial effect of water vapor, which was introduced by accident into the argon gas in their counter. They found that reliable behavior also followed the admixture of small amounts of other gases, such as ammonia and natural gas. They didn't publish a description of this discovery and were quite interested to read in 1937 the publication by Trost (1937) of his observation that ethyl alcohol had a similar quenching effect leading to reliable operations of such counters.

17.2.2 Semiconductor Detectors (Solid State Ionization Chambers)

As mentioned at the beginning of this section, the primary ionization must be collected to make a direct measurement of the energy of nuclear radiation. Condensed phases have much higher densities than gases and so provide more efficient stopping of the radiation per unit length. However, metals allow rapid recombination of the electron/positive ion pairs and insulators inhibit the collection of the charge. Therefore, only semiconductors have been used extensively for radiation detectors. Metals and insulators (like concrete) are used extensively in radiation shielding, and some transparent inorganic crystals have a special sensitivity to radiation that is discussed in the following text.

Silicon and germanium are the most common semiconductors used to construct "solid state ionization chambers." These materials must be extremely pure to observe the primary ionization ($\sim 10^5$ electrons), and, as we will see below, germanium devices must be cooled to reduce the thermal noise to even observe the signals. The properties of small-scale devices based on Group III/Group V materials, for example, GaAs, are well known, but no large-scale applications
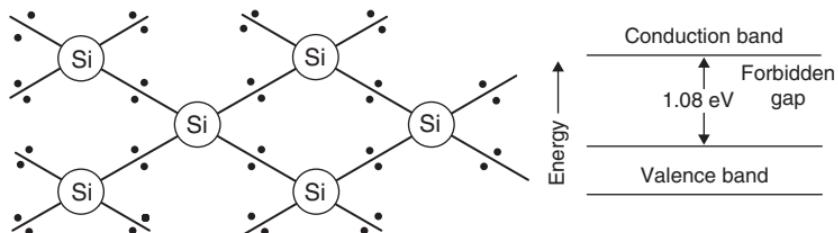
Figure 17.9 (Left) Schematic view of the crystal lattice of silicon. The true lattice is a three-dimensional diamond lattice. The dots represent electron pair bonds between the Si atoms. (Right) Schematic diagram of the electron energy bands in crystalline silicon.

have been made. The size and shape of the available semiconductors have grown over time but are still severely limited by production techniques and the availability of ultra pure materials. Early solid-state devices relied on observing the ionization in intrinsic semiconductors and were impractical due to the requirement of extremely pure material. Modern devices are based on semiconductor junction diodes. These diodes have a rectifying junction that only allows the flow of current in one direction. Incident radiation creates ionization inside the bulk of the diode and creates a pulse of current that flows in the opposite direction to the normal current flow through a diode and so is straightforward to detect.

To understand how semiconductor radiation detectors operate, it is necessary to review a little of the basic chemistry of semiconductors. Consider a typical Group IV element, such as Si or Ge. It will crystallize in the diamond lattice structure, as shown schematically in Figure 17.9. Each silicon atom is bound by four electron pair bonds to adjacent silicon atoms. The electrons are not free to migrate through the crystal, and therefore pure silicon is a poor conductor of electricity. A representation of the important electron energy levels of silicon is shown in Figure 17.9. The valence electron levels are so close together that they form a nearly continuous "band" of energies, known as the *valence band*. In pure silicon, there is a small region of energies above the valence band in which there are no allowed energy levels. This energy region is called the forbidden gap (or *bandgap*) and corresponds to ~1.08 eV for silicon. Just above the forbidden gap is the *conduction band*, another band of energies that allows free electron migration through the crystal, that is, the conduction of electricity. Suppose we replace a silicon atom in the silicon lattice with a Group V atom, such as phosphorus. Then we will have the situation depicted in Figure 17.10. Recall that phosphorus has five valence electrons and after forming four electron pair bonds to the adjacent silicon atoms, there is one electron left over. This leftover electron will be very loosely bound to the phosphorus atom and will be easily removed to conduct electricity through the crystal.
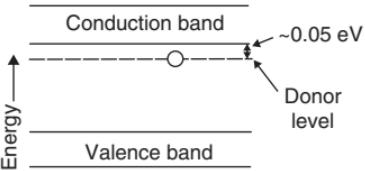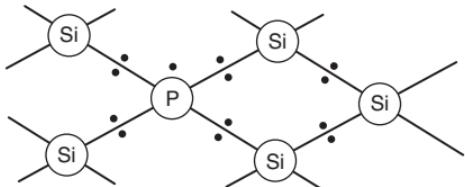
Figure 17.10 (Left) Schematic diagram of a typical n-type or donor impurity in a silicon crystal lattice. (Right) A schematic diagram of the energy levels of crystalline silicon with a donor impurity.
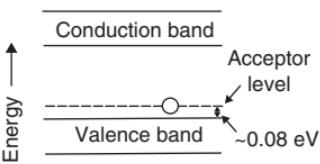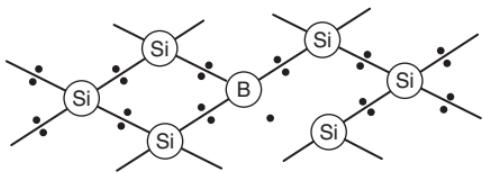
Figure 17.11 (Left) A schematic diagram of a silicon crystal lattice with a p-type impurity in the lattice. (Right) Schematic diagram of the energy levels of silicon with a p-type impurity in the lattice.

In terms of our diagrams of the crystalline electron energy levels with a Group V impurity, we have the situation shown in Figure 17.10. The "extra" phosphorus electron occupies a "donor level" very close to the conduction band and is easily promoted into this conduction band. Silicon containing Group V impurities, such as phosphorus, is called *n-type silicon* because the species that carries charge through the crystal is negative.

On the other hand, what would happen when a Group III atom, like boron, replaces an atom in the silicon lattice? The situation is shown in Figure 17.11. Boron has three valence electrons and can form electron pair bonds with three of its neighbors. It has no electron to pair up with the electron on the fourth silicon atom. We say we have an electron hole in the silicon lattice. In terms of our energy level diagrams, we have the situation illustrated in Figure 17.11. The hole occupies an energy level very close to the valence band (an "acceptor level") and can be easily promoted into the valence band. Promotion of a hole into the valence band simply means that an electron in the valence band and a hole in the acceptor level switch places, so that a hole is created in the valence band.

We must realize (unphysical as it may sound) that a hole in the valence band can conduct electricity as well as an electron in the conduction band. How does this work? Consider the lattice shown schematically in Figure 17.12. Imagine that electron 1 moves to fill hole 0. This step creates a hole at position 1. Electron 2 moves to fill this hole, leaving a hole at position 2. Electron 3 fills the hole at position 2, leaving a hole at position 3, and so forth. Thus, as the hole moves
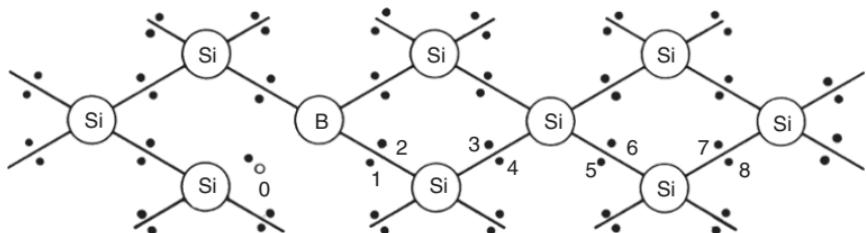
Figure 17.12 Schematic diagram of a silicon crystal lattice with a p-type impurity boron, at one lattice point. The hole is labeled 0, while the electrons are denoted as 1, 2, and so on.
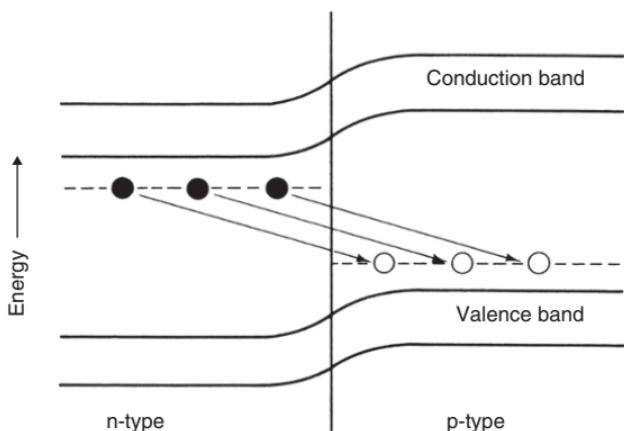
Figure 17.13 Schematic diagram of the band structure at a p–n junction.

to the right in Figure 17.12, negative charge is moving toward the left. Since electricity is the movement of charge, the motion of the hole corresponds to the flow of electricity. Silicon containing Group III impurities is said to be *p-type silicon* because of the positive charge carriers (the holes).

A silicon semiconductor radiation detector of a layer of p-type silicon in contact with a layer of n-type Si is shown in Figure 17.13. What happens when such a *p–n junction* is created? The electrons from the n-type silicon will migrate across the junction and fill the holes in the p-type silicon to create an area around the p–n junction in which there is no excess of either holes or electrons. (We say that a *depletion region* has been formed at the junction.) Imagine that we apply a positive voltage to the n-type material and a negative voltage to the p-type material (the junction is now said to be reverse biased). The electrons will be "pulled farther away" from the junction by the positive voltage on the n-type material, thus creating a much thicker depletion region around the p–n junction. The exact thickness of the depletion region, d, is given by

$$d \propto (\rho V)^2 \tag{17.5}$$

where ρ is the *resistivity* (a measure of purity) of the silicon and V is the magnitude of the applied reverse bias voltage. Note that the depletion of the depletion region can be varied by changing the voltage applied to the detector.

The depletion region acts as the sensitive volume of the detector. The passage of ionizing radiation through this region will create holes in the valence band and electrons in the conduction band. The electrons will migrate to the positive charge on the *n* side, while the holes will migrate to the negative voltage on the *p* side, thereby creating an electrical pulse at the output of the device.

The average energy necessary to create a hole–electron pair in silicon is ~3.6 eV. This average energy is about three times the forbidden gap energy (~1.1 eV) because most electrons are promoted from deep in the valence band to high in the conduction band. The energy required to create a hole–electron pair is independent of particle charge and mass, thus rendering semiconductor detector response independent of particle type. If we remember that the average energy to create an ion–electron pair in a gas ionization device was ~35 eV, then we see that, for the same energy deposit in the detector, we get $35/3.6 \approx 10$ times more ion pairs. If we note that the energy resolution of a detector, $\Delta E/E$, is proportional to $1/\sqrt{N}$ where N is the number of charge pairs formed, we can see that the energy resolution of a semiconductor is $\sim 10^{1/2} = 3.2$ times better than the energy resolution of a gas ionization detector. (Furthermore, as we will see later, the average energy deposit required by a γ-ray interaction in a scintillator to create one photoelectron at the cathode of a photomultiplier tube is ≈ 1000 eV. Then we can say that the resolution of a semiconductor detector is $(1000/3.6)^{1/2} \approx 17$ times better than that of a scintillation detector.) More detailed considerations show that the observed resolution can be smaller than the estimate based on the statistics of ion pair formation due to correlations between processes giving rise to ion pair formation.

For some semiconductor detectors, germanium is used instead of silicon for the detector material. The reasons for this substitution are as follows: (a) The average energy needed to create a hole–electron pair in germanium is 2.9 eV rather than the 3.6 eV in Si. Thus, the energy resolution for germanium should be $(3.6/2.9)^{1/2} = 1.1$ times better than silicon. (b) The atomic number of germanium (32) is much higher than that of silicon (14), leading to increased probability of γ-ray interactions in the detector material. Consequently, germanium is preferred to silicon for γ-ray detection. The forbidden gap is so small, however, for germanium (0.66 eV) that room-temperature thermal excitation leads to the formation of hole–electron pairs in the solid. Therefore, germanium detectors are operated at liquid nitrogen temperature (77K) to prevent this thermal electron noise from overwhelming the small signals from the primary ionization.

The silicon-based solid-state detectors fall into three general categories: surface barrier devices, PIN diodes, and Si(Li)(pronounced "silly") devices. These detectors are used to measure short-ranged radiation: charged particles in the first two cases and very energetic protons, low energy γ rays, and X-rays in the third case. The detector consists of a thin layer of silicon material (often
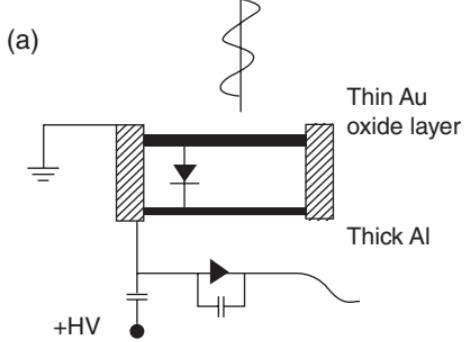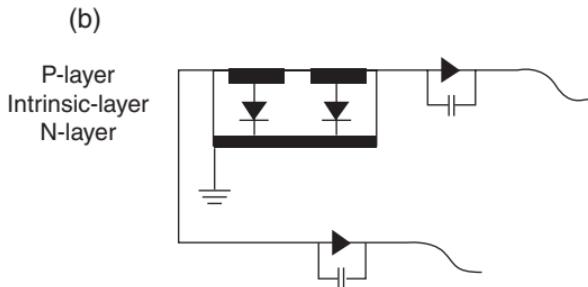
Figure 17.14 Representation of silicon diodes with readouts, (a) simple SSB and (b) a PIN device with two segments.

~200μm thick, but thicknesses from 5 μm up to 5 mm are available). An electric field (typically ~V/μm) is applied in the direction opposite to the "normal" flow of current through the diode to create the depletion layer. Radiation creates hole–electron pairs that are swept to the electrodes by the electric field and induce a current. These signals are amplified in an external circuit.

Silicon surface barrier (SSB) detectors generally consist of a thin cylindrical piece of high resistivity (10^3 Ω-cm), pure n-type silicon with a thin gold contact on one side and an aluminum contact on the other. The gold contact consists of a thin layer through which the radiation enters the silicon. Just under the gold is an oxide layer that creates the semiconductor junction (or barrier); see Figure 17.14. The gold layer is sensitive to physical wear and the oxide layer can be depleted by extended exposure to vacuum. The oxide layer is also very sensitive to organic molecules but can be reconstituted with proper treatment. During use, these detectors must be shielded from visible light as hole–electron pairs can be created by photons that enter the silicon through the thin gold contact. The gold and oxide layers are also thin to reduce the amount of KE lost by the particle before it enters the active depleted region. The top layers make up a dead layer that can be significant in alpha spectroscopy. Recently, silicon-based detectors with very thin and uniform dead layers have been created with an ion-implanted junction rather then the oxide layer. A thin layer of boron ions is implanted near the surface of n-type silicon to form the junction that is more robust than the oxide layer.

"Ruggedized" SSB detectors are available where the radiation enters the silicon through the thicker and light tight aluminum contact. The bulk of the material is p-type silicon, and a negative bias is applied to the gold contact so that the entry window can remain at ground potential. Another design of a "rugged" surface barrier detector replaces the gold contact with a thicker nickel contact. The nickel is resilient enough to be wiped clean.

Silicon surface barrier detectors have found widespread application in α-particle spectroscopy and in nuclear reaction studies. These detectors can be used in stacks to identify particles uniquely. Consider the situation in which a penetrating ion with a total KE passes through a thin SSB detector and is stopped in a second, thicker SSB detector. Such a stack of two detectors is called a *silicon detector telescope* and provides two signals, the energy lost in the thinner detector, ΔE, and the remainder, KE $- \Delta E$. Recall from Chapter 16 that the rate of energy loss for a charged particle in matter is approximately given by the simple expression

$$\frac{dE}{dX} \propto \frac{mZ^2}{\text{KE}} \tag{17.6}$$

where m is the ion's mass and Z is the charge. Z would be the atomic number if the ion is fully stripped of electrons. When the first detector is thin, dE/dX is approximately constant and $\Delta E \approx (dE/dX)\Delta X$, where ΔX is the thickness of the first detector. Thus, ΔE will be a hyperbolic function of KE for each ion with a given value of mZ^2. Therefore, the components of a mixture of penetrating charged particles emitted by nuclear reactions can be identified by their relative values of ionization. Stacks of SSBs with several thin detectors followed by a thick or stopping detector are used when unambiguous particle identification through redundant measurements is necessary. Variations in the thickness of the silicon in the manufacturing process place a practical limit on the particle identification. Thickness variations as small as 1 μm are currently achievable.

Detection of fission fragments with semiconductor detectors poses special challenges. The first of these is the "pulse height defect" where one observes that the pulse height (collected charge) for a fission fragment is substantially less than that of a light ion of the same energy. This is due to energy losses of the fission fragments in the entrance window and dead layer of the detector, the loss of energy by nuclear collisions where fewer electron–hole pairs are created, and, most importantly, a higher rate of electron–hole recombination along the densely ionized fission fragment track.

There is another related phenomenon of the "plasma delay time." When there is dense ionization, as with fission fragments, the collection of the charge is delayed due to the formation of a plasma-like charge cloud. For fission fragments the resulting pulses are delayed 2–5 ns relative to an ordinary ion.

One way to decrease these effects is to take advantage of the fact that the rate of energy loss of a charged particle in a semiconductor detector will depend

upon the orientation of its path relative to the crystal axis of the stopper. Ions traveling parallel to the crystal axes lose energy at a lower rate than particles traveling in an arbitrary direction in the crystal. This phenomenon is called "channeling," and detectors can be manufactured so that ions striking the detector face along the 110 crystal axes that undergo channeling (and experience less recombination and plasma delay effects) are minimized.

Semiempirical corrections exist to correct for the pulse height defects and plasma delay effects.

The typical resolution of a single detector is ~20 keV but depends on the detector geometry, in particular, on the detector capacitance. Notice that SSB detectors have parallel electrodes separated by a thin dielectric; the capacitance of such an object will increase with increasing area and with decreasing thickness. Thus, thin large area devices will have the largest capacity and thus the poorest intrinsic resolution.

Silicon PIN diodes are a more recent class of detectors that have become available, in large part, due to the growth of the semiconductor industry. These devices are constructed with a p-type layer on one side of an intrinsic silicon wafer and an n-type layer on the opposite, for a *p-I-n* sandwich. The detectors are available in a much larger range of sizes and shapes than surface barrier detectors. For example, 25 cm^2 devices with single or multiple specially shaped contacts are routinely available. The contacts on the front and back of PIN diodes can have different shapes and sizes. Consider a 5 cm × 5 cm rectangular wafer that has two horizontal electrical contacts on the front and two vertical contacts on the back. The divided contacts define four quadrants of silicon that are electrically separate. A particle that enters the detector will generate two signals, one on the front and another on the back that uniquely identifies the quadrant of silicon. Rectangular devices are often used with 40 stripes on the front and 40 stripes on the back and provide very accurate position measurements in nuclear reaction studies. In addition, the silicon wafers can be cut in various shapes such as circles or arcs with corresponding electrode patterns to make customized, high efficiency charged-particle detectors.

All solid-state detectors are damaged by long exposures to charged particles. The threshold dose for observable damage (in particles/cm^2) is ~3×10^8 for fission fragments, 10^{11} for α-particles, 10^{14} for fast neutrons, and 10^{14} or more for fast electrons. Notice that the particles generally come to rest in the silicon and stay there. Except for electrons, of course, the lattice will be disrupted and poisoned by the presence of many stopped particles. If the entering particles have the same energy (same range), then all of the particles will stop in a very narrow band of the silicon and can create a dead layer inside the silicon. The timing performance of the detector will be affected at lower doses than the energy resolution. Higher electric fields in the detector and cooling will help to mitigate these effects.

Lithium-drifted silicon detectors were originally developed for measurements of β-particles. Electrons are more penetrating than heavier charged particles and so these devices, usually called Si(Li) detectors, have to be much thicker than heavy-ion detectors. Si(Li) detectors are commonly 5 mm thick. Such large volumes of very pure silicon are not readily available, so the technique of drifting lithium ions into the bulk p-type material to compensate for internal lattice defects in the silicon was developed. A layer of lithium metal is applied to the surface and some atoms diffuse into the bulk silicon under heating. A bias can be applied to the silicon that causes the lithium ions to migrate from the coated surface into the lattice. The lithium atoms are mobile in the silicon and migrate to trapping centers; there they readily donate an electron into the conduction band and become ions. The migrating ions will be trapped by negative impurities in the lattice, thus "compensating" for the effect of the impurity site. The lithium ions retain their high mobility in the lattice, and the detectors have to be stored with a small retaining bias if they are stored for long periods at room temperature.

Bulk p-type germanium can be compensated by lithium drifting in a manner similar to silicon. Si(Li) detectors are favored over Ge(Li) detectors for β detection because of their low sensitivity to γ-rays and the lower backscattering probability (by a factor of ∼1/3 to ∼1/2). The energy resolution of Si(Li) detectors for electrons is ∼1–2 keV for electron energies up to 1000 keV. The detection efficiency of Si(Li) detectors for β⁻ particles ranges from one-half that of a gas counter for a low-energy β emitter like ^{14}C to greater than that of a gas counter for an energetic β⁻ emitter such as ^{32}P. The background of these detectors is exceptionally low, because of their small size for a given stopping power, and they do not require any peripheral gas supply. Very good energy resolution for X-rays is also possible. A resolution of 180 eV for the 5.9 keV Mn K$_\alpha$ X-ray have been obtained with Si(Li) detectors, whereas the best energy resolution available from a scintillation detector for this transition is about 1000 eV.

Silicon detectors can be cooled to reduce the thermal noise that produces a background under all of the induced signals. The thermal noise is created by random fluctuations that promote an electron across the bandgap into the conduction band resulting in an hole–electron pair. The number of promoted electrons will be proportional to a Boltzmann function containing the bandgap Δ and the temperature T:

$$N_{\text{thermal}} \propto e^{\Delta/k_{\text{B}}T}. \tag{17.7}$$

For practical reasons, silicon detectors are usually cooled from room temperature down to approximately −20°C; cooling below −60°C is not useful because the system noise becomes dominated by noise in the external electronic circuit. Temperatures below −20°C are also not used because the internal physical

stresses from differences in the thermal expansion coefficients of the construction materials become important. Specially prepared detectors should be used for cooling to the lower temperatures.

We can estimate the factor by which the thermal noise will be reduced with the Boltzmann expression

$$\frac{N(T = -20°C)}{N(T = +25°C)} \propto e^{253/298} = 2.3 \tag{17.8}$$

Cooled silicon detectors are particularly useful in experiments in which the measured particles are expected to cause significant damage to the crystal lattice during the experiment. If the detector is not cooled, the thermal noise will dramatically change during the measurement, and the detector resolution will decrease with time.

Germanium detectors have the highest resolution of any large-scale direct ionization devices due to the small bandgap of germanium of 0.73 eV (at 80K). The effective ionization potential of 2.95 eV of Ge allows the creation of a large number of ion pairs for a given amount of absorbed energy. The bandgap is also small enough that the number of hole–electron pairs created by thermal fluctuations causes very significant electronic noise. The noise is reduced by enclosing the germanium and the first stage of the amplification circuit in a cryostat and cooling both to liquid nitrogen temperature.

Other things being equal, the size of the signals produced in a germanium diode compared with those in a silicon diode should be larger by the inverse ratio of the effective ionization potentials, $(3.76/2.95) \sim 1.27$ (at 80K). However, the thermal noise will be larger in proportion to a Boltzmann exponential distribution with the bandgaps, so the noise in the germanium will be larger by the factor

$$\frac{e^{-\Delta_{Ge}/k_B T}}{e^{-\Delta_{Si}/k_B T}} = e^{\Delta_{Si} - \Delta_{Ge}} = 1.54 \tag{17.9}$$

These facts would appear to favor the use of silicon detectors strongly. However, the "stopping power" of matter for photons is much lower than that for charged particles, giving photons long penetration depths in all materials. Moreover, the probability of a photoelectric interaction with an atom, which contributes significantly to the absorption of the full energy of photons, increases in proportion to Z^5. This makes high-Z materials more effective absorbers of photons. Also from the practical standpoint, manufacturing techniques have been developed to produce very high-purity germanium (HPGe) crystals that are much larger than silicon crystals.

Germanium detectors are used almost exclusively to detect γ radiation. Energetic photons can easily penetrate the cryostat, and the high resolution of germanium detectors are well suited to the very precise energies of the γ rays emitted by the de-excitation of nuclear levels. There are two main classes of germanium detectors: an older style that uses lithium-compensated material,

called Ge(Li) (pronounced like jelly), and modern, intrinsic germanium, also called HPGe.

Ge(Li) detectors are similar in principle to the Si(Li) detectors described previously. Large ingots (~1 L) of p-type germanium material are prepared in a relatively pure state. Lithium metal is applied to the surface, some atoms diffuse into the lattice and donate their electron into the conduction band, and the ions are subsequently drifted through the material. The mobility of lithium ions is much higher in germanium than in silicon. This allows not only very effective compensation of the impurities in large volumes of germanium but also the rapid loss of compensation by the lattice at room temperature. The hallmark of Ge(Li) detectors is that the germanium crystals must be kept at liquid nitrogen temperatures for their *entire* useful lifetime. If the detectors are allowed to warm up, even for a very short time, the lithium compensation is lost to some extent, and their high resolution is degraded. The crystals can be re-drifted by the manufacturer.

The shape of the germanium crystal is generally cylindrical with the lithium applied to the outer surface and drifted in toward the center. The lithium contact produces an n-type region on the surface of the crystal, the bulk becomes intrinsic through compensation, and a small p-type region is deliberately left un-drifted to produce a P-I-N diode structure. The detector thus has coaxial p- and n-type "electrodes" and is sometimes called a coax detector. A reverse bias is applied to the germanium diode, as to the silicon detectors, and the small current pulses from the primary ionization events are collected and amplified. The requirement that Ge(Li) detectors must be kept very cold during their entire lifespan and the excellent resolution have spurred the development of germanium purification techniques. Large volumes of intrinsic germanium material can now be produced in sufficient quantity to produce PIN diode detectors without lithium drifting. These detectors are referred to as HPGe-detectors. These devices can be stored at room temperature and only need to be cooled when they are used. The n-type region is prepared by lithium diffusion without drifting or phosphorus implantation, and an extremely thin p-type region is prepared by implanting boron ions. The crystals are generally cylindrical with coaxial electrodes. Other shapes, such as thin planar detectors for low energy γ- and X-rays and crystals with hollow wells with large geometrical efficiency, are available. Recent developments include producing close-fitting germanium shapes with segmented electrodes on the outer surface to measure the interaction position of the photon in the crystal. These devices are especially useful to detect and track photons emitted by nuclear reaction products for Doppler correction.

For γ-ray detection, the detector of choice uses Ge due to its superior energy resolution. Various higher atomic number materials are available for scintillation detectors, but their energy resolution (discussed in the following text) is significantly worse. An energy resolution of 1.75 keV for the 1332 keV γ-ray
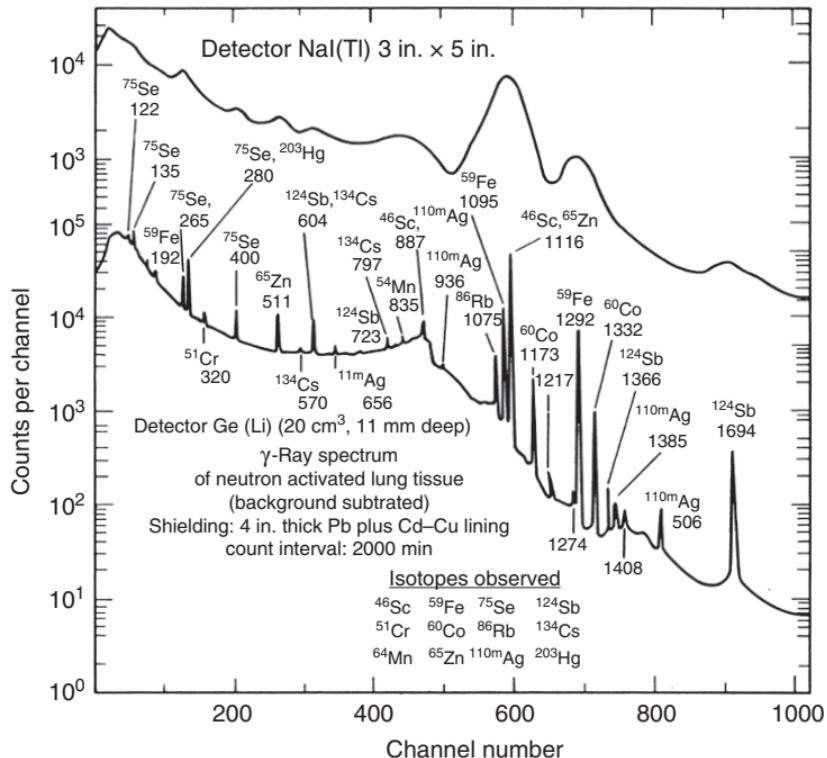
Figure 17.15 The γ-ray spectrum of neutron-activated lung tissue as measured with a 3 × 3 in. NaI(Tl) detector compared with that taken with a Ge detector (Cooper (1971). Reproduced with the permission of BNWL-SA-3603).

emitted by the decay of ^{60}Co can be routinely obtained (compared with the typical 90–100 keV for a 3 × 3 in. NaI(Tl) detector). What this means in terms of the ability to resolve complex γ-ray spectra can be appreciated from the comparison shown in Figure 17.15.

17.3 Scintillation Detectors

In a scintillation detector, a fraction of the energy deposited by the primary radiation in the detector is converted to light that, in turn, is converted into an electrical signal. Conceptually, the process can be divided into the scintillation process itself (energy → light), the collection and conversion of the light into electrons, and the multiplication of the electrons to make a macroscopic signal. We will divide our discussion similarly.

As discussed in Chapter 16, as radiation interacts with matter, it will lose energy by ionizing or exciting matter. As we have seen previously, only a few materials have the right properties to allow the collection of the primary
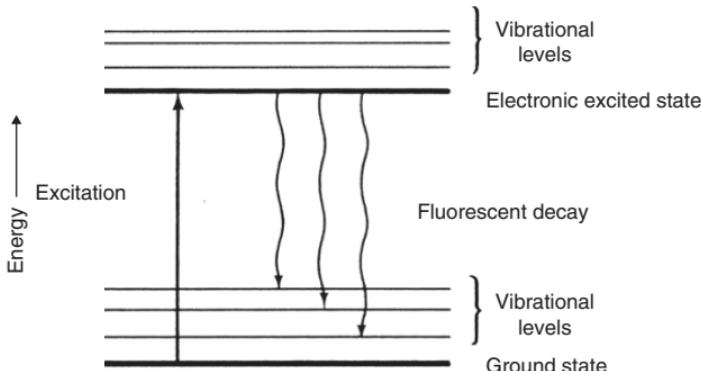
Figure 17.16 A schematic view of the band structure of an insulator and the levels in the general scintillation process in organic crystals.

ionization from nuclear radiation. If the ionization is not preserved and collected, the electron/positive ion pairs are expected to eventually recombine. During this recombination, the energy used to separate the charges will be re-emitted to the surroundings, very often as lattice vibrations and heat. Occasionally, a triplet electronic excited state is populated and the energy from such states is released as visible (or UV) photons. This emission process is well known as atomic or molecular *fluorescence* and is called *scintillation*, when it is caused by external irradiation. We will use the term "visible light" loosely in the present discussion. The wavelengths of the fluorescent photons from excited electronic states are characteristic of the material and range from UV to red. These visible, secondary photons can be easily detected and amplified with photomultiplier tubes.

The details of the scintillation process are complicated and depend very much on the molecular structure of the scintillator. In organic crystals, the molecules of the organic solid are excited from their ground states to their electronic excited states (see Fig. 17.16). The decay of the small number of triplet states by the emission of photons occurs in about 10^{-8} s (fluorescence). In general the energy of fluorescent photons is less than that of absorbed photons, often due to dissipation in vibrational modes or lattice vibrations before or after the photon emission. As a result, the crystal will generally transmit its own fluorescent radiation without absorption.

There are three common types of *organic* scintillators. The first type is a pure crystalline material, such as anthracene. The second type is a liquid scintillator, that is, the solution of an organic scintillating molecule in an organic liquid, such as a solution of p-terphenyl in toluene ($\approx$3 g solute/L solution). The third type is the solution of an organic scintillating molecule, again, such as p-terphenyl, in a solid plastic such as polystyrene.

All these organic scintillators are characterized by short fluorescence lifetimes, that is, 2–3 ns. The short lifetime allows their use in high count rate
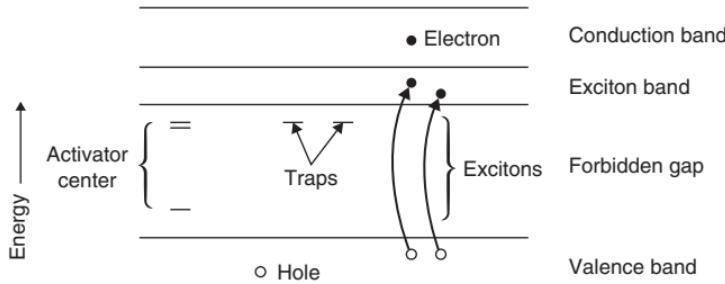
Figure 17.17 The electronic energy bands in an ionic crystal with the relative positions of trapping and the dopant/activator levels.

situations or for fast time measurements. The light output is modest, being 10–50% of that of the common *inorganic* scintillator NaI(Tl) (discussed in the following text). Because of the low atomic numbers of the organic scintillators, they are primarily used in the detection of heavy charged particles or electrons. The plastic scintillators are easily machined into a variety of shapes and/or made in thin films. Energy resolution of about 10–14% is typical. Liquid scintillators are used to assay low-energy β-emitters, like ^{14}C and ^{3}H, and the radioactive material is dissolved or suspended in the scintillator solution. Another application involves the use of liquid scintillators for large-volume (several m^3) detectors where the liquid scintillator has been "loaded" with a neutron absorbing material, such as gadolinium. The gadolinium captures neutrons producing fast electrons and γ-rays that are detected by the scintillator.

The scintillation process in inorganic scintillators differs from that in organic scintillators. Consider the band structure of an insulating ionic crystal, as shown in Figure 17.17. When an energetic electron passes through the crystal, it may raise bound valence electrons into the conduction band. The electron vacancy in the valence band resulting from this ionization is a "hole" as discussed previously, in the valence band. The electron in the conduction band and the hole in the valence band can migrate independently to the bottom of the conduction band and the top of the valence band, respectively. In an intrinsic scintillator, they recombine by the emission of a photon that corresponds to the bandgap. There may be trapping centers that create levels that reside in the bandgap and photon emission from these levels would result in slightly lower photon energies.

Alternatively, another excitation process can occur in which a valence band electron is excited to an unoccupied energy level in the conduction band. The electron remains bound to the hole in the valence band forming a pair called an *exciton*. The pair can also move through the crystal. Excitons form a band of effective energy levels called the exciton band (see Fig. 17.17) that lies in the bulk crystal bandgap. The hole–electron pair eventually collapses and emits a photon that is somewhat lower in energy than the bandgap energy.

More commonly, a dopant or activator is mixed into the alkali halide crystal with an excitation energy gap less than the bandgap of the bulk crystal. The relative few energy level pairs of the activator will lie in the forbidden gap of the bulk material. Hole–electron pairs will migrate to lower energy and a fraction will be transferred onto the excited states of the activator atoms. Figure 17.17 shows the energy levels of a typical alkali halide crystal, including the dopant/activator centers and traps. (Atomic thallium is a common activator for alkali halide crystals.)

Excitons, electrons, and holes produced by the interaction of radiation with the crystal can wander through the crystal until they encounter an activator center or trap. Migration of an exciton in a crystal may be thought of as a 6–8 eV excited iodide ion I^{-*}, transferring its energy to an adjacent stable I^-, which, in turn, becomes excited. Thus, energy may be transferred from I^- to I^- in the crystal lattice until final capture by either an activator center or crystal impurity. By exciton capture or hole–electron capture, the activator centers are raised from their ground state to an excited state. The de-excitation of this activator center by emission of light occurs in a time about 0.3 μs in typical crystals. Hence, the energy deposited by the radiation in the scintillator is mostly emitted as light by the activator center (usually Tl). The amount of light emitted by the entire crystal is directly proportional to the amount of energy deposited in the crystal by the incident radiation. The fraction of the deposited energy converted into fluorescence photons is small, about 10%.

Thallium–activated sodium iodide (NaI(Tl)) is the most widely used inorganic scintillator at present. This material is used extensively to detect γ-rays because it is relatively inexpensive, has a high stopping power for photons, and is rugged and easy to use. The fluorescence light output has a relatively slow decay time of almost 230 ns, limiting the count rate in such detectors. The energy resolution of NaI(Tl) detectors is rarely better than 6% for the 1332 keV γ-ray of ^{60}Co (as compared with the 0.13% typically seen with Ge detectors). NaI(Tl) detectors are very efficient for detecting γ-radiation (with typical detection efficiencies of 1–10%). The efficiency of a 3-in. diameter right cylinder, that is, 3 in. long, is the reference standard for γ-ray detectors. Other inorganic scintillators of note include bismuth germanate ($Bi_4Ge_3O_{12}$, BGO), which is a high-Z, high-density material. Its low light output (only 10–20% that of NaI(Tl)) limits its use to situations where a high efficiency (with poorer resolution) is needed. Barium fluoride (BaF_2) is a high-Z material with a fast light output ($\tau < 1$ ns) also with reduced light output. It is used in situations where its high density, high Z, and fast timing are important. A recent addition to the set is cerium-doped lanthanum bromide ($LaBr_3(Ce)$) that has a higher light output than NaI(Tl), having a typical resolution of 3% for ^{137}Cs. At present only relatively small $LaBr_3$ crystals are commercially available. Another type of scintillation detector is the *phoswich detector* on which two different scintillators are optically coupled and mounted on a phototube. Events in each scintillator

are distinguished on the basis of the different time response of each scintillator. These detectors can be used to detect low energy radiation in the presence of high backgrounds of energetic radiation.

How is the light emitted by the scintillator converted into an electrical signal? To answer this question, let us consider a schematic diagram of a typical scintillation detector (Fig. 17.18). The photons of visible light emitted by the activator centers, such as Tl^+ ions in a NaI(TI) crystal, pass through the transparent bulk crystal and out through a clear window to impinge on an adjacent photocathode. The typical photocathode is composed of a thin, photosensitive layer (commonly a cesium–antimony alloy) on the inner surface of the end of the photomultiplier tube. Here impinging photons, particularly those having wavelengths between 3000 and 6000 Å, are absorbed, with a consequent emission of photoelectrons. The number of photoelectrons ejected is slightly less than, but directly related to, the number of incident photons. Such a burst of photoelectrons resulting from a single γ-ray interaction in the crystal is still far too weak to be registered directly.

Amplification occurs by means of a series of electrodes, called dynodes, spaced along the length of the photomultiplier tube (see Fig. 17.18). Each dynode is maintained at a higher potential (usually about 50 V higher) than the preceding one. The photoelectrons emitted from the photocathode are focused by the focusing electrode to hit the first dynode. Striking the dynode surface, they cause the secondary emission of a larger number of electrons. This new burst of electrons is attracted by the potential gradient to the second dynode in the series, where a still larger number of electrons are dislodged. This electron-multiplying process continues at each dynode until at last the collecting anode is struck by $10^5 - 10^6$ electrons for each original photoelectron ejected from the photocathode. Thus the size of the output pulse from the photomultiplier is directly related to the quantity of energy dissipated by the incident γ-ray photon in the fluor.

To present a quantitative example of the energy conversions involved in scintillation detection, we trace the results of the interaction of a single 1.17-MeV γ-ray from ^{60}Co with a NaI(Tl) crystal:

1. If 20% of the energy of the γ-ray results in exciton production in the dopant, and if it is assumed that 7 eV is needed to produce an exciton, then ~33,000 excitons could result from this γ-ray photon.
2. Assuming that only 10% of the excitation events result in the production of photons of visible light seen by the adjacent photocathode, this would mean that about 3300 photons would reach the photocathode.
3. This number of photons striking a photocathode with a conversion efficiency of 10% would eject ~330 photoelectrons. Note that the highest photoelectron efficiencies are only about 25%.
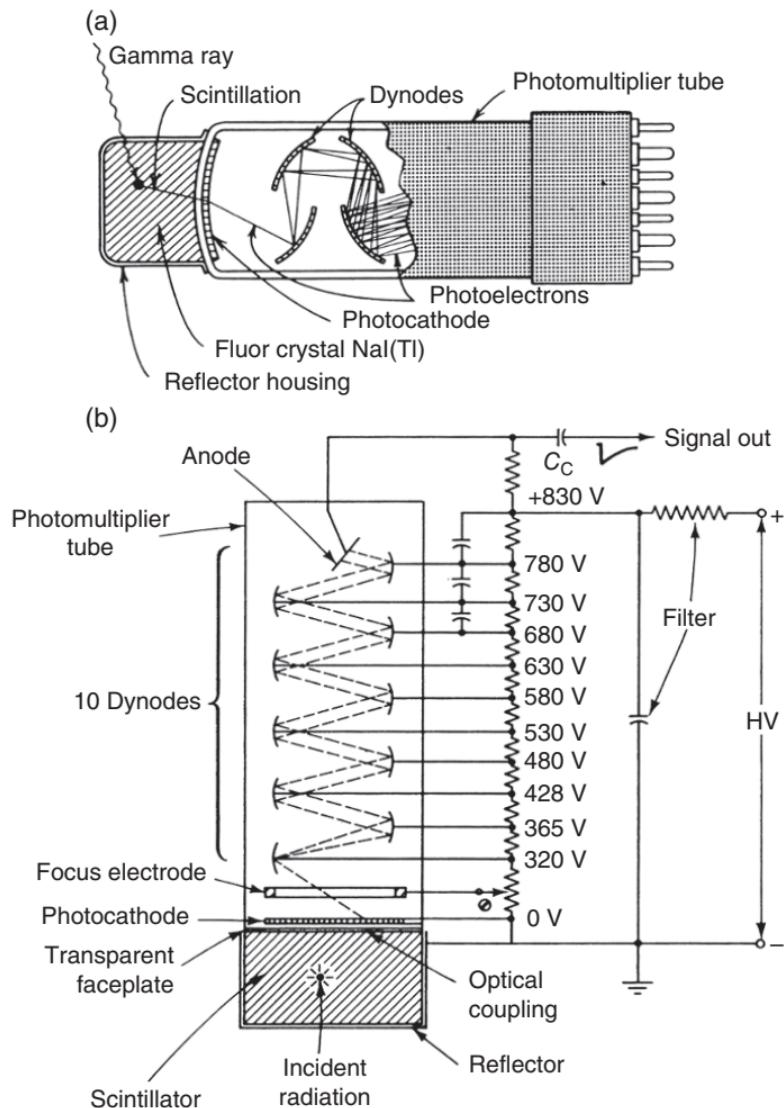
Figure 17.18 (a) Cutaway diagram of a typical cylindrical scintillation detector with a schematic illustration of how the light from the scintillator is converted and how the photoelectrons are amplified in a photomultiplier tube. (b) A typical wiring diagram is shown for a 10-stage photomultiplier operated with a positive high-voltage supply (O'Kelley (1962). Reproduced with the permission of Elsevier).

4. The successive dynodes of a photomultiplier operated at an overall gain of 10^6 could then amplify this quantity of photoelectrons so that $\sim 3.3 \times 10^8$ electrons would be collected at the photomultiplier anode, or a charge of $\sim 5 \times 10^{-11}$ C.

5. This charge could then be transformed by a preamplifier circuit with a capacitance of 30 pF into an output pulse of 1.8 V. A pulse of this size would be capable of directly triggering a scaler.

Note that the statistical resolution of this measurement will be determined by the smallest number in this chain, the number of photoelectrons, with a contribution from the multiplication process. In this case, the resolution would be expected to be $\sim 1/\sqrt{330} = 0.055$. ^{60}Co emits two γ-rays per disintegration. The other γ-ray has an energy of 1.33 MeV. Following the preceding analysis, the 1.33 MeV γ-ray would result in an output pulse of about 2.05 V from the electronic circuit.

17.4   Nuclear Track Detectors

The passage of highly ionizing radiation through an insulating solid leaves a wake of destruction in the material. In covalently bonded materials, the chemical structure of the material along the track can be significantly and permanently changed by the passage of a single energetic ion. Certain polymeric (plastic) materials and the mineral mica (a form of silicon dioxide) are particularly sensitive to such radiation damage. The original radiation damage remains localized on the molecular scale but is not visible without enhancement. However, the track can be expanded by chemical etching from the molecular scale (nanometers) up to the microscopic scale (μm).

Nuclear track detectors are very simple and very efficient detectors of rare events that produce highly ionizing radiation. Carefully prepared and scanned track detectors have been used to identify even *individual* rare decays. The detectors are integrating in that the damage caused by a track is not spontaneously repaired. The drawback to track detectors is that the developed tracks are small and can only be observed with a microscope. In the past, scanning by eye was extremely labor intensive and prone to error. Modern computer-controlled scanning has improved the speed and reliability of the analysis. Plastic track detectors that are sensitive to α-particles are used extensively in commercial radon detectors.

Chemical etching of the material takes place on all surfaces that are exposed to the etching solution. The exposed surfaces of the material are eroded along with the material along the track. Therefore, the rate of etching has to be carefully controlled to get the maximum amount of information from the track. Notice that etching of a uniform track will generally form a circular cone because the material will be more easily removed from the surface than from deep along the track. Mica tracks are diamond shaped due to the lattice structure as opposed to being conical.

Nuclear emulsions are closely related "track detectors" that trace their origins to the original discovery of radiation by Becquerel. Nuclear emulsions are very

fine-grained photographic films. The film is "exposed" by the passage of radiation through it, and the grains of AgCl are activated (the silver is reduced) by the ionization. The film is developed, and with careful handling and microscopic observation, the track or path of individual particles can be traced. Occasionally, a particle interacts with a nucleus in the emulsion, creating many fragments or particles, and the tracks of the reaction products can be traced. The emulsion is also sensitive to the rate of ionization and the nature of the particle in each track can often be determined. On the other hand, most people are familiar with the shadow images of skeletal features taken with X-rays. The X-rays are absorbed and scattered more efficiently by the heavy elements in bones (essentially calcium) than by the light elements in soft tissue (carbon, oxygen, hydrogen) and create a shadow. The grains in the emulsion are then exposed by the transmitted X-rays and are developed to form the negative image.

17.5   Neutron Detectors

As remarked in Chapter 16, neutrons interact with matter primarily via nuclear reactions. Since the probability of these interactions is very much less than the ionizing interactions of charged particles or protons with matter, neutrons are harder to detect. Most neutron detectors operate with the idea of "converting" the neutron into a charged particle via a nuclear reaction and then detecting the resulting charged particle. Examples of such "conversion" reactions are $^{10}B(n,\alpha)^7Li$, $^3He(n,p)$, and $^{235}U(n,f)$.

A widely used detector for "slow" neutrons ($E_n < 0.5$ eV) is the $^{10}BF_3$ proportional counter. $^{10}BF_3$ (at a pressure of 0.5–1 atm) serves as both the counter gas and the conversion medium for neutrons striking the detector. Both the α-particle ($E_\alpha = 1.47$ MeV) and the ^7Li ion ($E_{Li} = 0.84$ MeV) are collected. (The $^{10}B(n, \alpha)$ cross section is 3840 barns.) These proportional counters are typically cylindrical cathode tubes with a small diameter central wire anode. Typical detector efficiencies for thermal neutrons are ~90%.

The cross section for the $^3He(n, p)^3H$ reaction is 5400 barns for thermal neutrons, making it an important "conversion" reaction. The resulting reaction products, the proton and the triton, can be detected in a proportional counter that uses ^3He as a counting gas. As with the $^{10}BF_3$ detectors, some fraction of the events involve interactions of the reaction products with the counter walls, resulting in a range of deposited energies. For the ^3He detector, this wall effect is more serious, leading to some events that are difficult to separate from background events such as those due to γ-ray interactions with the detector. The gas pressures in these detectors are ~4–10 atm to minimize these wall effects.

Fission chambers are ionization chambers that detect fission fragments from (n, f) reactions in deposits of fissile material in the interior of the detector. Typically, the inner walls of the chamber are coated with fissionable material. If the fissile nucleus is ^{235}U, then the detector will respond primarily to thermal neutrons (due to the $1/v$ behavior of the fission cross section). Loading the detector with ^{238}U will make it sensitive to fast neutrons. These detectors only count neutrons but do not give information directly about the details of the neutron energy. Because of the large magnitude of the fission fragment signals, these detectors have low background rates, and small neutron fluxes are easily measured.

In fast neutron detectors, the "conversion" reaction is H(n, p) elastic scattering. The recoiling protons can be easily detected and the cross section for this reaction is large. Typically the interaction of fast neutrons is with hydrogen-containing scintillators. The scintillators can be organic crystals like stilbene or anthracene, liquid organic scintillators dissolved in a hydrogen-containing solvent and plastic scintillators. Liquid scintillators have the advantage of being able to use pulse shape discrimination to separate neutron events from γ-ray events. (The pulses resulting from γ-ray interactions with the scintillator are ~10× faster than the pulses resulting from neutron interactions with the scintillator.) The light output from these liquid scintillators is a complex function of the neutron energy. In Figure 17.19 the response of a common scintillator material NE-213 to monoenergetic neutrons is shown.
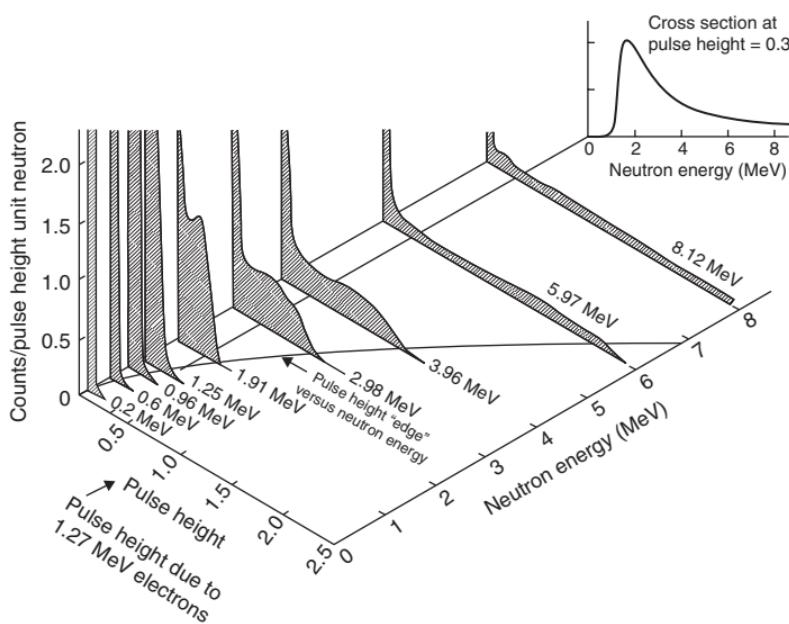
Figure 17.19 Response function of NE-213 scintillator to monoenergetic neutrons (Burris and Verbinski (1969). Reproduced with the permission of NAS-NS-3105).

The efficiency of these detectors must be determined with neutron sources whose spectrum resembles the spectrum of the neutrons being measured. Settings of lower-level discriminators will affect not only the range of neutron energies being studied but also the efficiency of detecting all neutrons.

17.6 Nuclear Electronics and Data Collection

As we have seen, essentially all of the nuclear radiation detectors produce electronic pulses in response to the interaction of some ionizing radiation. These signals are processed by standardized NIM (*nuclear instrumentation modules*) electronics to supply the high voltages, amplify and shape the current pulses, and analyze or just count the number of pulses. In addition, computer-based electronic modules in the older *computer automated measurement and control* (CAMAC) system are used to measure the time relationships of pulses, the pulse heights, and the signal shapes. More modern electronic modules use the *versa module Europa* (VME) standard that incorporates a computer memory standard to transfer information. The signals are recorded and stored by computers for later analysis. The boundary between electronic modules and computers is shifting. The most modern systems use fast data processing to analyze and record individual pulses using components similar to those in digital oscilloscopes. An important feature of scientific studies with radioactivities and with nuclear beams is that the data must be collected as rapidly as possible, usually during a very limited time. A radioactive source will decay after being produced and cannot be "stopped" because the scientist is not ready to use it. Similarly, the nuclear reactions induced by particle beams take place in a very short time and must be recorded when they occur. Then after a set of events has been collected "online," the data are analyzed later "offline."

We will give a very brief overview of the kinds of modules used. VME, CAMAC, and NIM electronics fall into three broad categories: linear electronics that maintain a linear relationship to the size of the input signal, logic circuits that provide only a standard (or single-sized) pulse indicating that a given logical condition was met, and data acquisition modules to measure the signals and record the data. One should realize that with modern, high-density electronics, the functions that we will describe can be carried out by a single electronic module or may be condensed into a single integrated circuit. Therefore, we will only describe the functions performed by the electronic modules and not specific equipment.

The output of most detectors is an electrical pulse that carries information about the energy deposited in the detector, the time of the interaction, and so on. Linear electronics are circuits/modules that preserve and extract information about the energy deposited in the detector from the detector signal. An overview of these modules and their function is given in Table 17.1.

Table 17.1 Summary of Common Pulse-Processing Circuits/Modules.

Linear In/Out	Input Signal	Output Signal
Preamplifier	Linear charge pulse from detector	Linear tail pulse (exponential tail)
Linear amplifier	Linear tail pulse	Amplified, Gaussian-Shaped linear pulse
Biased amplifier	Shaped linear pulse	Linear pulse proportional to input above a bias cut
Pulse stretcher	Linear Gaussian pulse	Linear flat-top pulse
Summing amplifier	Two or more shaped pulses	Shaped pulse proportional to sum of coincident pulses
Delay amplifier	Linear pulse	Identical pulse after given time delay
Linear gate	Linear pulse and logic gate pulse	Linear pulse that overlaps gate
Amplitude to digital convertor (ADC)	Linear pulse	Digital word
Time to amplitude convertor (TAC)	Two logic pulses	Linear pulse proportional to time between two pulses

Linear in/Logic out	Input Signal	Output Signal
Discriminator	Linear pulse	Logic pulse when input amplitude exceeds threshold
Single-channel analyzer	Linear pulse	Logic pulse when input amplitude lies within two limits
Time pickoff	Fast or shaped linear pulse	Logic pulse synchronized with a feature of input pulse

Logic In/Logic Out	Logic In/Logic Out	Logic In/Logic Out
Coincidence (AND)	≥Two logic pulses	Logic pulse during time overlap of pulses
Fan-in (OR)	≥Two logic pulses	Logic pulse whenever one or more pulse is present
Scaler	Logic pulse	Counts number of pulses
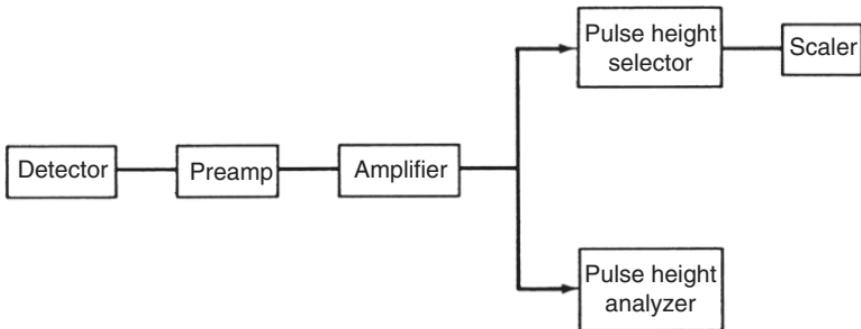
Figure 17.20 Schematic diagram of the electronic components in a simple pulse height analysis system for nuclear spectroscopy.

A conceptual diagram of a typical pulse height analysis system is shown in Figure 17.20. The signal from the detector is given a preliminary amplification and shaping by a *preamp* before being sent through a coaxial cable to a *linear amplifier*. The preamp is necessary to prevent noise in the cable from interfering with the tiny detector signal. In the amplifier the signal is further amplified and shaped to remove both low and high frequency noise before analysis. The height of the shaped pulse is proportional to the energy deposited in the detector. The analog-to-digital converter (ADC) converts the signal from the amplifier into a digital word, thus measuring its size. The ADC could be contained on a plug-in card in a personal computer (e.g., to measure the distribution of pulses from a single detector monitoring a radioactive source) or it might be one of many identical ADC units in a VME or CAMAC module (used to record the signals from many detectors simultaneously monitoring nuclear collisions).

Logic modules are used to monitor the counting rates of detectors and the relative times at which radiation is detected. Generally a fast signal derived from the detector itself, the preamp, or from a timing-filter amplifier is sent to a *discriminator*. The discriminator produces an output pulse with a fixed shape and size (generally square) for the period that the input signal crosses a reference threshold. Discriminators usually have multiple identical output signals. The logic pulses can be sent to a scaler that simply counts the number of pulses, to a count rate meter to provide a visual monitor of radiation rates or doses, or to a time-to-amplitude converter (TAC) to measure the relative times of arrival of two or more logic signals.

17.7 Nuclear Statistics

Radioactive decay is a random process and nuclear reactions occur at random times when a beam interacts with a target. The number of nuclei in a sample

Table 17.2 Data from Replicate Measurements of the Activity of a Long-Lived Source (^{170}Tm)[a].

Measurement Number	Counts/6 s	$(x_i - x_m)$	$(x_i - x_m)^2$
1	1880	−18	324
2	1887	−11	121
3	1915	17	289
4	1851	−47	2209
5	1874	−24	576
6	1853	−45	2025
7	1931	33	1089
8	1886	−32	1024
9	1980	82	6724
10	1893	−5	25
11	1976	78	6084
12	1876	−22	484
13	1901	3	9
14	1979	81	6561
15	1836	−62	3844
16	1832	−66	4536
17	1930	32	1024
18	1917	19	361
19	1899	1	1
20	1890	−8	64

[a]We are indebted to Prof. R.A. Schmitt for providing these data.

of radioactive material that decays in any time period is not a fixed number but will differ due to the randomness of the process and the changing number of atoms present. This point can be readily shown by making repeated measurements of the activity of a long-lived radionuclide, each for the same time duration. The results of such an experiment are shown in Table 17.2. Note that in these measurements show a large range of values for the activity with a clustering near the center of the range. We can plot the distribution of these data by "binning" the data, that is, dividing the data set into small, equal-sized ranges (see Fig. 17.21). We can now ask ourselves if we can understand this distribution function. Statisticians have given us mathematical models that describe
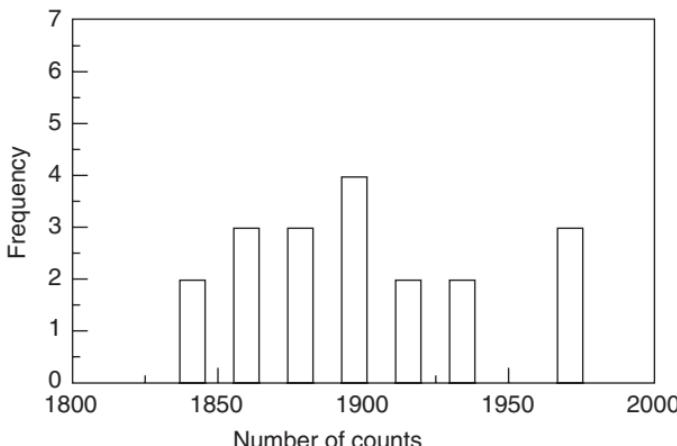
Figure 17.21 Example of the distribution of a small number of duplicate measurements of the activity of a long-lived sample. The data are shown in Table 17.2.

these and other similar distribution functions. As a background for our discussion of how to extract the maximum amount of information from these data, let us consider some of these models.

17.7.1 Distributions of Data and Uncertainty

The most general model to describe radioactive decay is the *binomial distribution*. For a process that has two outcomes (success or failure, decay or no decay), we can write for the distribution function $P(x)$ the predicted probability of getting x successes as

$$P_{\text{binomial}}(x) = \frac{n!}{(n-x)!x!}p^x\,(1-p)^{n-x} \tag{17.10}$$
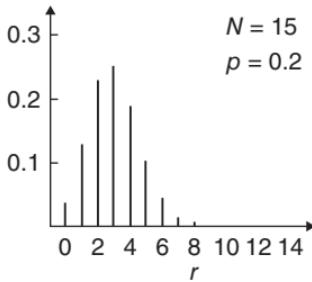
where n is the number of trials where each trial has a probability of success p. Applying this distribution to radioactivity, $P(x)$ can be taken as the probability of getting x counts in a given time interval, and therefore $p = \lambda\Delta t$ where Δt is a small time interval compared with the measurement time and the half-life. Note that x, the number of decays, and n, the number of tries, are both integers. Some examples of binomial distribution functions are shown in Figure 17.22.

The binomial distribution function is cumbersome and most useful for small values of n. However, a good approximation to this function is possible when the probability of success, p, is small (i.e., $p \ll 1$). This would occur when the measurement time is very short compared with the half-life. In this case we can approximate the binomial distribution by the *Poisson distribution*. The Poisson distribution is written as
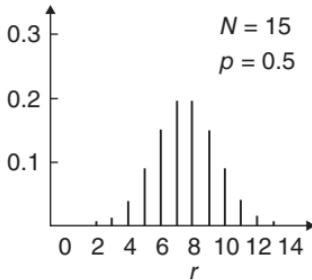
$$P_{\text{Poisson}}(x) = (x_m)^x\,\frac{e^{-x}}{x!} \tag{17.11}$$
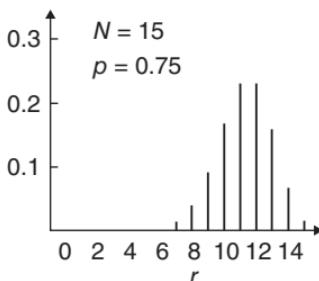
Figure 17.22 Binomial distributions for various values of *N* and *p* (Leo (1987). Reproduced with the permission of Springer).

where the mean, x_m, is the product $p \times n$. Thus, the Poisson distribution is characterized by one parameter, x_m, compared with the two parameters, p and n, in the binomial distribution. Notice that the Poisson distribution is an asymmetric distribution as shown in Figure 17.23. Besides being a more tractable function, the Poisson distribution has certain important properties that we will use in analyzing radioactivity data, particularly low counting rate data.

Let us consider another parameter, the variance or σ^2, which contains information on the spread of the distribution of values about the mean, x_m. We can calculate σ^2 for a set of N measurements with the expression

$$\sigma^2 = \frac{\sum_{i=1}^{N}(x_i - x_m)^2}{N - 1} \tag{17.12}$$

For reference, the data in Table 17.2 gives $x_m = 1898$ and $\sigma = 44.2$. A little algebra will show that $\sigma^2 = np(1 - p)$ for a binomial distribution. For the Poisson distribution, $\sigma^2 = x_m$ or $\sigma = \sqrt{x_m}$. Calculating the variance of the data in Table 17.2, we get $\sigma_{\text{Poisson}} = 43.6$, which is slightly smaller than the value for the binomial distribution. This difference illustrates the important point
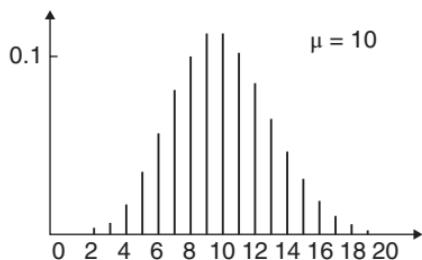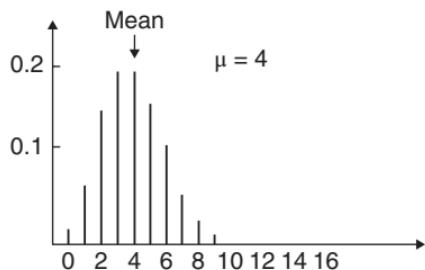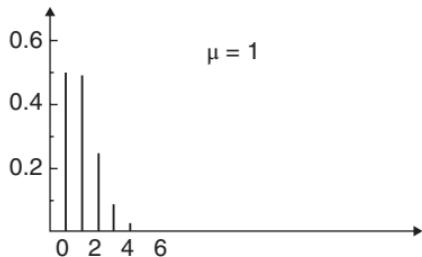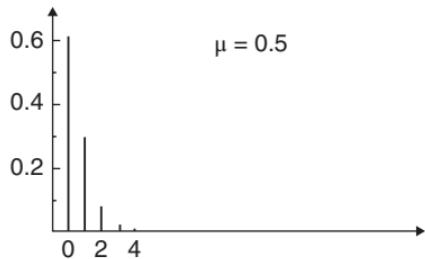
Figure 17.23 Poisson distribution for various values of x_m (Leo (1987). Reproduced with the permission of Springer).

that these distribution functions are *models* of the data, not physical laws, and when they are applied to finite data sets, their predictions may deviate from each other and the observations.

The Poisson distribution can be applied also to describe the action of detectors. For example, suppose the interaction of a γ-ray photon with an inefficient scintillator produced, on average, only 3.3 photoelectrons from the photocathode. The probability of producing no photoelectrons (not seeing the event) is given by the Poisson distribution by the expression

$$P_{\text{Poisson}}(0) = (3.3)^0 \frac{e^{-3.3}}{0!} = e^{-3.3} = 0.037 \tag{17.13}$$
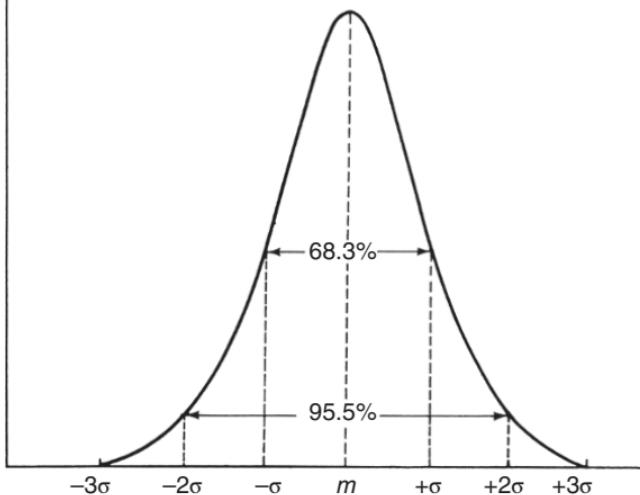
Thus, 3.7% of the events will be missed due to "statistical fluctuations" in the small number of photoelectrons produced at the photocathode.

A further simplification of the parent binomial distribution can be made when the number of successes, *n*, is relatively large but *p* remains small, for example, more than about 30 counts in a measurement. In this case the binomial distribution can be approximated by the *normal* or *Gaussian* distribution. The Gaussian function is written as

$$P_{\text{Gausian}}(x) = \frac{1}{\sqrt{2\pi x_m}} \exp\left(-\frac{(x - x_m)^2}{2x_m}\right) \tag{17.14}$$

The Gaussian function is symmetric as shown in Figure 17.24; one can show that 68.3% of the measured values lie within ±1σ of the mean value, x_m. Further, 95.5% of all measurements lie within ±2σ of the mean, and 99.7% lie within

Figure 17.24 A plot of the normal or Gaussian distribution function with the mean, x_m, 1σ, and 2σ indicated.
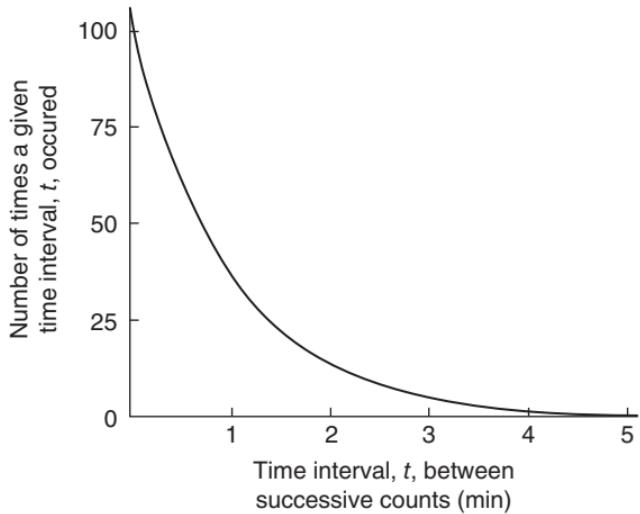
±3σ of the mean. Also the full width at half maximum (FWHM) is $\sigma\sqrt{2\ln 2} \approx 2.3548\sigma$.

As an example, imagine one makes a single measurement of a radioactive source and gets 100 counts; this is our estimate of the mean value, x_m. Our estimate of the square root of the variance, also called the *standard deviation*, σ, using the normal distribution is 10. The results can be interpreted as one has a 68.3% chance of being correct that the *true* number was between ±1σ or between 90 and 110. With 95.5% certainty, one could say the true rate lies between 80 and 120. Generalizing, we can quote the results of a measurement as $x \pm n\sigma$ where n is related to the probability that an infinite number of measurements would give a value within the quoted range. Specifically for $n = 0.6745, 1, 1.6449, 1.96, 2, 2.5758,$ and 3, the "confidence limits" are 50%, 68.3%, 90%, 95%, 95.5%, 99%, and 99.7%, respectively. Commonly people will quote the results of measurements as $x \pm \sigma$. One should remember that doing so implies that the true number will be outside the limits 31.7% of the time. If this risk is not acceptable, one should pick a greater confidence level, that is, 2σ, 3σ, etc.

Another distribution function of interest relates to the distribution of time intervals between successive counts. We know the average time between events is 1/(counting rate). The actual distribution of time between random events is given by the *interval distribution*. This distribution (applicable to all random events) states that for a process with an average time between events t_m, the probability of getting a time t between successive events, $I(t)$, is

$$I(t) = \frac{1}{t_m} e^{-t/t_m} dt \tag{17.15}$$

Figure 17.25 A graph of the frequency of occurrence of a time interval t between successive events, where the average rate is 1 cpm.

Note that this is a decreasing exponential distribution so that the most likely time between random events is zero. Random events (counts, natural disasters, etc.) occur in bunches. Recall that for radioactive decay $t_m = 1/\lambda$ so that

$$I_{\text{decay}} = \lambda e^{-\lambda t} dt \tag{17.16}$$

which is the familiar exponential decay law. An example of this distribution function is shown in Figure 17.25.

Let us summarize how we can describe the statistical uncertainty in measurements of radioactivity. If we measure the total activity of a sample, S, in the presence of a background, B, to be 64 counts in 1 min, then we have the activity

$$(S + B) = 64 \text{ cpm with } \sigma_{S+B} = \sqrt{64} = 8 \text{ cpm} \tag{17.17}$$

If a second measurement without a sample found a background of 10 counts in 1 min, then we would then estimate that

$$B = 10 \text{ cpm with } \sigma_B = \sqrt{10} = 3.2 \text{ cpm} \tag{17.18}$$

What is the net sample rate and its uncertainty? This raises the general question of calculating the uncertainty in the result of some mathematical operations using *uncertain* numerical input. If we consider two independently determined numbers and their uncertainties (standard deviations), $A \pm \sigma_A$, $B \pm \sigma_B$, we can derive the results shown in Table 17.3 for the rules for the propagation of the uncertainty in the result of some common mathematical operations.

As an example of the use of the relations outlined in Table 17.3, we would calculate that for our sample and background counting case previously mentioned, the activity of the sample or the *net* number of counts:

$$\text{Activity} = (\text{Sample} + \text{Background}) - (\text{Background})$$
$$= 64 - 10 = 54 \text{ cpm} \tag{17.19}$$

Table 17.3 Propagation of Uncertainties for Algebraic Operations.

Operation	Answer	Uncertainty
Addition	$A + B$	$(\sigma_A^2 + \sigma_B^2)^{1/2}$
Subtraction	$A - B$	$(\sigma_A^2 + \sigma_B^2)^{1/2}$
Multiplication	$A \times B$	$(A \times B)\,[(\sigma_A/A)^2 + (\sigma_B/B)^2]^{1/2}$
Division	A/B	$(A/B)\,[(\sigma_A/A)^2 + (\sigma_B/B)^2]^{1/2}$

$$\sigma_A = \sqrt{8^2 + 3.2^2} = 8.6 \text{ cpm} \tag{17.20}$$

Up to this point we have carefully restricted our discussion of nuclear statistics to numbers of counts. If the number of counts recorded in exactly 1 min was x, then the counting rate should be quoted as $x \pm \sqrt{x}$ cpm. Suppose, however, that we recorded 160 counts in exactly 5 min? What would be the standard deviation of the average counting rate (in cpm)? The best estimate of the mean number of counts in the 5-min period would by $160 \pm \sqrt{160}$, which is 160 ± 13 counts. The average *rate* using integers would be $160/5 \pm 13/5 = 32 \pm 3$ cpm. In general, therefore, the rate R is given as the number of observed counts, x, divided by the measurement time, t, and the square root of the variance or standard deviation in the rate, σ_R, is

$$\sigma_R = \frac{\sqrt{x}}{t} = \frac{\sqrt{R \times t}}{t} = \sqrt{\frac{R}{t}} \tag{17.21}$$

Thus for the preceding simple example, we could have calculated σ_R directly as

$$\sigma_R = \sqrt{\frac{R}{t}} = \sqrt{\frac{32}{5}} = 3.53 \approx 3 \tag{17.22}$$

Often we wish to compute the average of two numbers, x_1, and x_2, both of which have an uncertainty denoted by their standard deviations σ_1 and σ_2, respectively. The best average of these two numbers is not the simple average but weighted average x_m, given by the expression

$$x_m = \frac{\left(\frac{x_1}{\sigma_1^2} + \frac{x_2}{\sigma_2^2}\right)}{\left(\frac{1}{\sigma_1^2} + \frac{1}{\sigma_2^2}\right)} \tag{17.23}$$

or

$$x_m = \frac{x_1 + w x_2}{1 + w} \text{ where } w = \left(\frac{\sigma_1}{\sigma_2}\right)^2 \tag{17.24}$$

In short, each number is weighted by the inverse of its standard deviation squared. For the weighted average of N values, x_i, each with a standard deviation, σ_i, we should calculate the sums

$$x_m = \frac{\sum_{i=1}^{N} \left(\frac{x_1}{\sigma_1^2} \right)}{\sum_{i=1}^{N} \left(\frac{1}{\sigma_1^2} \right)} \qquad (17.25)$$

The uncertainty or standard deviation of x is given by the expression

$$\sigma_{x_m} = \sqrt{\frac{1}{\sum_{i=1}^{N} \left(\frac{1}{\sigma_1^2} \right)}} \qquad (17.26)$$

For example, suppose that we make two independent measurements of an activity, obtaining results of 35 ± 10 cpm and 46 ± 2 cpm. The weighted average of the two measurements using the weighting parameter, w, is

$$w = \left(\frac{10}{2} \right)^2 = 25 \ \text{ and } \ x_m = \frac{(35)(1 + 25(46))}{(1 + 25)} \approx 46 \ \text{cpm} \qquad (17.27)$$

and the standard deviation of the weighted average is

$$\sigma_{x_m} = \sqrt{\frac{(100 + (25^2)(2^2))}{(1 + 25)^2}} \approx 2 \ \text{cpm} \qquad (17.28)$$

Thus we would write that the average observed rate was 46 ± 2 cpm.

17.7.2 Rejection of Abnormal Data

In our discussions so far, we have only considered the uncertainty in the experimental data due to the randomness of radioactive decay or the occurrences of reactions. But there may also be other (unidentified) errors that contribute to the overall uncertainty in the data. As a result, when we make repeated measurements of a sample activity under seemingly identical situations, we will find occasionally one measurement that differs from the others by a large amount. If included in the average, this abnormal observation may cause significant error. When are we justified in rejecting such data? One criterion for rejecting such data is to reject suspected values that deviate from the mean by more than 2σ or 3σ. The probabilities of occurrence of such deviations are 4.5 and 0.27%, respectively.

What about the question of whether a detector or counting system is working properly? For example, the data in Table 17.2 do not exactly match either a Poisson or a normal distribution. Was the counting system malfunctioning at some point? One parameter that we can calculate that will help us answer such questions is χ^2 (chi-squared) or the reduced chi-squared $\chi^2/(N-1)$. The value of the reduced chi-squared should be close to one, which indicates that the average deviation from the mean is one sigma. Formally

$$\chi^2 = \frac{\sum_{i=1}^{N} \left(x_i - x_m \right)^2}{x_m} \qquad (17.29)$$
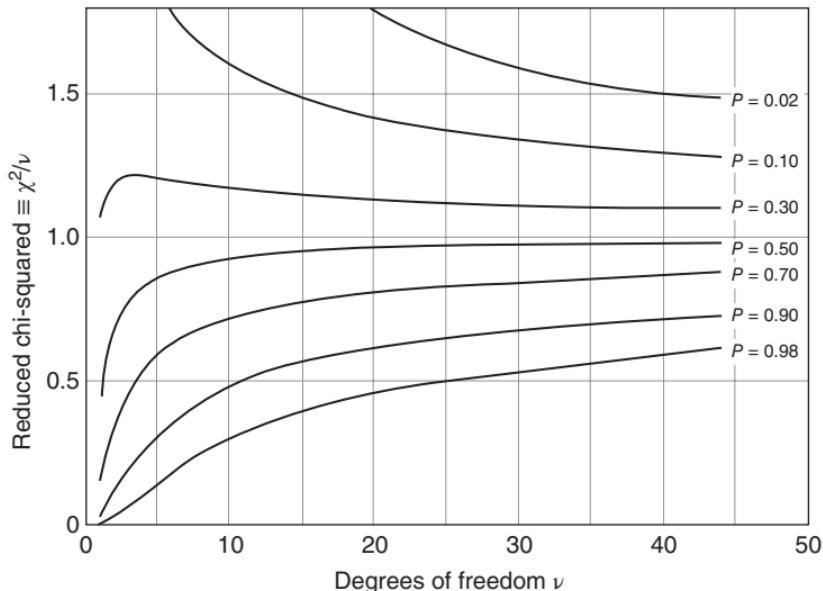
Figure 17.26 A plot of the reduced chi-squared distribution as a function of the degrees of freedom in the data set $(N - 1)(=\nu)$ and the probability, P. For each curve, P is the probability that a random sample of N values from a Poisson distribution would have a larger value of χ^2_ν.

Using the data in Table 17.2, we calculate that $\chi^2 = 37194/1898 = 19.60$. Another way of expressing this number is the *reduced χ^2 value*, $\chi^2/N - 1 \equiv \chi^2_\nu$ where N is the number of measurements. $N - 1$ is also referred to as ν, the number of degrees of freedom. In our example, $\chi^2/N - 1 = 1.03$. (Informally we expect the value of χ^2_ν to be ~1 for a good fit.) More formally we can look at Figure 17.26 where we plot the expected values of χ^2_ν as a function of ν for various values of P, the probability that a random sample of N values from a Poisson distribution would have a larger value of χ^2_ν than the ordinate value. For our value of $\chi^2_\nu = 1.03$ with $\nu = 19$, we see that the probability of getting a larger value of χ^2_ν is ~0.5, which is fine. If χ^2_ν was 1.5, the probability of getting a larger value would be ~0.08, not so likely. Generally speaking, a good fit will have $\chi^2_\nu \approx 1$ and $P(\chi^2, \nu) \approx 0.5$. A poor fit will have $\chi^2_\nu \ll 1$ or $\chi^2_\nu > 3$ and $P(\chi^2, \nu)$ near 1 or $P(\chi^2, \nu) < 10^{-4}$.

17.7.3 Setting Upper Limits When No Counts Are Observed

Suppose your experiment failed to detect a type of decay you were seeking: What can you say about the probability that it will not occur at all? The simplest answer is what is termed the *one-event upper limit.* One assumes that one event was in fact detected and calculates the resulting decay rate, cross section, or whatever, taking into account detection efficiencies, solid angles, using that one count.

A more sophisticated result can be obtained by using the properties of a Poisson distribution. Recall that the probability of observing n events if the mean value of events is x_m with the Poisson distribution is

$$P_{\text{Poisson}}(n, x_m) = \frac{x_m^n}{n!} e^{-x_m} \tag{17.30}$$

If we have a process (e.g., a decay) that is occurring at a *mean rate, r,* then mean number of *expected events* is $x_m = r \times T$. The probability of observing zero events in a time period T with a mean number of x_m is

$$P_{\text{Poisson}}(0, x_m) = \frac{x_m^0}{0!} e^{-x_m} = e^{-x_m} = e^{-rT} \tag{17.31}$$

So that the probability that no events at all will be observed decreases with time if the expected rate is nonzero.

It can be shown that the upper limit on the rate (when zero counts are observed) r_0 is given by the expression

$$r_0 = -\frac{1}{T} \ln(1 - \text{CL}) \tag{17.32}$$

where CL is the confidence limit you wish to attach to your upper limit. If you want to quote an upper limit on the rate with 95% confidence, then use CL = 0.95. For example, suppose you are attempting to observe a process that is expected to produce 1 decay per week and you observe no counts (with a 100% efficient detector) in 4 weeks of observation. At the 95% confidence level, the upper limit on the decay rate (using the usual symbol for the decay rate λ) is

$$\lambda_0 = -\frac{1}{4 \text{ weeks}} \ln(1 - 0.95) = 0.75/\text{week} \tag{17.33}$$

Problems

17.1 Describe a radiation detector that would be appropriate to detect the following. Please give your reasoning. (a) 0.1 µCi ^{32}P, (b) a mixture of 0.1 µCi ^{3}H and 0.5 µCi ^{14}C, (c) a mixture of 10 nCi each of ^{235}U and ^{238}U, and (d) 50 Bq ^{60}Co.

17.2 An advertisement for a high-purity Ge detector quoted its relative efficiency as being 200%. Is that possible? Please explain.

17.3 How would you detect 10 MeV neutrons?

17.4 How many counts would you have to collect to have 90% confidence in the quoted number of counts?

17.5 How would you detect the individual β-particles, γ-rays, and delayed neutrons from a fission product mixture?

17.6 What is the maximum allowed counting rate with a scintillation detector with a 0.25 μs dead time if you can only tolerate a 3% counting loss?

17.7 Five replicate measurements of the counting rate of a long-lived sample were 2712, 2753, 2708, 2739, and 2726. Do a chi-squared test to see if these data are consistent with a Poisson distribution.

17.8 How many counts do you need to collect to have a 2% uncertainty in your result?

17.9 Sketch a diagram of the nuclear modules that you would need to measure two coincident γ rays from a radioactive source on a very fast time scale (∼10s of ns) that are observed in two high-purity germanium detectors.

17.10 If a sample has an average counting rate of 16 cts/h and you read out the data every hour for each of 1000 h, how many times will you get 2, 8, 16, and 32 counts?

Bibliography

J.B. Birks, *Scintillation Counters* (McGraw-Hill, New York, 1953). The classic work on scintillators.

W.R. Burris and V.V. Verbinski, Nucl. Instru, Meth. **67**, 181 (1969).

J.A. Cooper, "Applied Ge(Li) gamma ray spectroscopy," BNWL-SA-3603, 1971.

R.D. Evans, *The Atomic Nucleus* (McGraw-Hill, New York, 1955). Noted for its discussion of statistics.

K. Kleinknecht, *Detectors for Particle Radiation*, 2nd Edition (Cambridge University Press, Cambridge, 1998). An excellent discussion from a high energy physics perspective.

G.F. Knoll, *Radiation Detection and Measurement*, 4th Edition (John Wiley & Sons, Inc., New York, 2011). The current "Bible" of radiation detection.

W.R. Leo, *Techniques for Nuclear and Particle Physics Experiments*, 2nd Edition (Springer-Verlag, Berlin, 1994). A very good summary of the properties of detectors and nuclear electronics.

G.D. O'Kelley, *Detection and Measurement of Nuclear Radiation* (NAS-NS-3105, 1962). An excellent, but simple discussion.

A. Trost, Z. Phys. **105**, 399 (1937).

N. Tsoulfanidis and S. Landsberger, *Measurement and Detection of Radiation*, 4th Edition (CRC Press, Boca Raton, 2015). Similar to Knoll, but with more details.

C.H. Wang, D.L. Willis, and W.D. Loveland, *Radiotracer Methodology in the Biological, Environmental and Physical Sciences* (Prentice-Hall, Englewood Cliffs, 1975). Noted for its discussion of liquid scintillation counting, this book served as a model for much of the discussion of this chapter.

D.H. Wilkinson, *Ionization Chambers and Counters* (Cambridge University Press, Cambridge, 1950). The classic discussion of ionization chambers, proportional counters, and Geiger-Muller counters.

18

Nuclear Analytical Methods

18.1 Introduction

As mentioned previously, one of the compelling reasons to use nuclear analytical methods is their high sensitivity. The radiation from the decay or excitation of a single nucleus can be readily detected. Even when one has to have the intervening step of a nuclear reaction to produce or excite the decaying species, the ability to detect very small quantities of material still occurs. This chapter deals with these nuclear analytical methods. The techniques to be discussed are known for their sensitivity; their ability to do nondestructive analysis of a large number of samples, sometimes quickly; and their ability to analyze the surfaces of materials. All of these techniques are *elemental analysis techniques* and do not, in general, give information about the chemical form of the element or isotope, any attached ligands, and so on. This lack of information on *speciation* is generally a drawback to these methods.

18.2 Activation Analysis
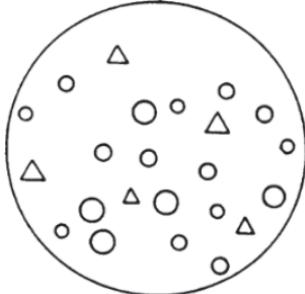
18.2.1 Basic Description of the Method

Activation analysis (AA) is an analytical technique that allows one to determine the amount of a given element X contained in some material Y. The basic steps in the activation technique are as follows:
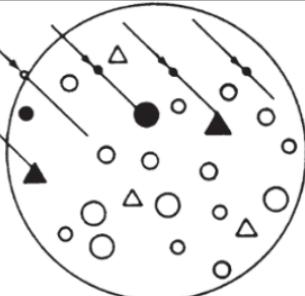
- Irradiate Y with a source of ionizing radiation so that some generally very small amount of X will change into X^*, a radioactive isotope of X.
- Using chemical or instrumental techniques, "isolate" X and X^* from all other elements in Y (not necessarily quantitatively) and measure the activity of X^*. Chemical "isolation" of the activity of interest is performed simply by separating it chemically from all other activities. Instrumental "isolation" of the activity of interest involves the detection of radiation that can uniquely

Figure 18.1 A schematic representation of the activation analysis procedure (Corliss (1963). Reproduced with the permission of USAEC).
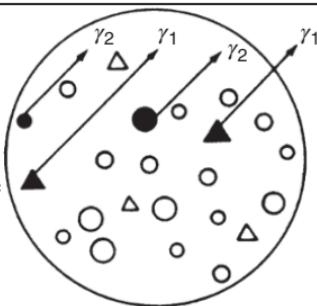
The sample consists of a base material ○ with traces of another material △

Neutrons

The sample is irradiated by neutrons, making some of the atoms in it radioactive ▲ ●

The gamma rays given off by the sample reveal the identity on the trace element

identify the nuclide in question and in some cases does not require chemical separation.
• Calculate the amount of X present.

These basic steps are shown schematically for neutron activation analysis (NAA) in Figure 18.1, but how does one calculate the amount of X present, knowing the activity of X^* produced in the irradiation? Since the radioactivity was produced in a nuclear reaction, it can be shown that the activity A_{X^*} as a function of time is $A_{X^*} = N_X \sigma \phi (1 - \exp(-\lambda_{X^*} t_i)) \exp(-\lambda_{X^*} t_d)$ where N_X is the number of X nuclei present initially, σ is the nuclear reaction cross section, ϕ is the flux of activating particles, t_i is the length of the irradiation, λ_{X^*} is the decay constant of X^*, and t_d is the time of decay after the end of irradiation. From this equation one could calculate N_X from A_{X^*}, if all of the other variables are known. (This equation for A_{X^*} is valid for "thin targets," that is, samples that absorb <5% of the flux of activating particles.)

The method of analysis just described is called *absolute activation analysis* and is rarely done. The reasons for this are the need for detailed knowledge of the flux and energy of the bombarding particles in the sample and the compounding of the nuclear uncertainties such as the cross sections, decay branching ratios, *and so on* in the final results. A simpler technique is to irradiate and count a known amount of pure X under the same conditions used for the mixture of X in Y. Then,

$$\text{Mass of X in Y} = (\text{Known mass X}) \left(\frac{\text{Activity of X}^* \text{ in Y}}{\text{Activity of X}^* \text{ in pure X}} \right) \quad (18.1)$$

which is known as the *comparator technique* and is the most widely used method of AA. The method only depends on irradiating and counting standards of known amounts of pure material using the same conditions as the samples being analyzed.

18.2.2 Advantages and Disadvantages of Activation Analysis

Using AA is straightforward since we know that the measured activity A is simply equal to $\epsilon \lambda N$ where ϵ is a constant representing the detection efficiency, λ is the decay constant, and N is the number of radioactive nuclei present. Moreover, we know that just a few radioactive nuclei are needed to give measurable activities so that AA can measure elemental abundances on the order of 10^{-6} to 10^{-12} g. The actual detection sensitivities for AA of various elements, as practiced by a commercial AA service, are shown in Figure 18.2. One can detect microgram levels for more than 2/3 of the elements using AA.

Although the high sensitivity of AA is perhaps its most striking advantage, there are a number of other favorable aspects as well. AA is fundamentally a multielemental technique. That is, many elements in the sample will become radioactive during the irradiation, and if each of these elements can be "isolated" either chemically or instrumentally, their abundances may be simultaneously determined. AA can be a nondestructive method of analysis. Numerous tests have shown that with careful experimental manipulation, AA is an accurate (∼1% accuracy) and precise (∼5% precision) method of measuring elemental concentrations.

AA is not without its drawbacks, however. Among them are the need to use expensive equipment and nuclear irradiation facilities; the inability to determine the chemical state of the elements under study; the potential need to work with significant levels of radioactivity, with their attendant radiation safety and legal problems; the long times (due to weak source strengths) needed to complete some analyses; and the complex analysis sometimes needed to unscramble the γ-ray spectra in a given experiment.

The ultimate test of the utility of AA as an analytical technique is whether there are competitive technologies that have the advantages of AA with fewer drawbacks. One candidate to be considered is *inductively coupled plasma mass*

Periodic table of elements
Activation analysis sensitivities

Sensitivities are expressed as the micrograms of the naturally occurring element that must be present in the entire sample to be detected and determined by the Activation Analysis Service at General Atomics. By special arrangement, the sensitivities of many of the elements can be increased up to 100-fold. Sensitivities are for interference-free conditions.

1 H NA																	2 He NA
3 Li 0.0008 p	4 Be 15. p											5 B 1.1 p	6 C 0.1c	7 N 1.c	8 O 1.c	9 F 0.4	10 Ne 2.
11 Na 0.004	12 Mg 0.5											13 Al 0.004	14 Si 1. FS	15 P 0.2 b	16 S 4. bFS	17 Cl 0.05	18 Ar 0.002
19 K 0.2	20 Ca 4.	21 Sc 0.001	22 Ti 0.1	23 V 0.002	24 Cr 0.3	25 Mn 0.0001	26 Fe 2.Fs	27 Co 0.01	28 Ni 0.7	29 Cu 0.002	30 Zn 0.1	31 Ga 0.002	32 Ge 0.1	33 As 0.005	34 Se 0.01	35 Br 0.003	36 Kr 0.01
37 Rb 0.02	38 Sr 0.005	39 Y 0.4	40 Zr 0.8	41 Nb 3.	42 Mo 0.1	43 Tc NA	44 Ru 0.04	45 Rh 0.005	46 Pd 0.03	47 Ag 0.004	48 Cd 0.005	49 In 0.00006	50 Sn 0.03	51 Sb 0.007	52 Te 0.03	53 I 0.002	54 Xe 0.1
55 Cs 0.001	56 Ba 0.02	57 L La 0.005	72 Hf 0.0006	73 Ta 0.1	74 W 0.004	75 Re 0.0008	76 Os 1.	77 Ir 0.0003	78 Pt 0.1	79 Au 0.0005	80 Hg 0.08	81 Ti 1.b	82 Pb 0.5 p	83 Bi 1.b	84 Po NA	85 At NA	86 Rn NA
87 Fr NA	88 Ra NA	89 A Ac NA															

L

58 Ce 0.2	59 Pr 0.03	60 Nd 0.03	61 Pm NA	62 Sm 0.001	63 Eu 0.0001	64 Gd 0.007	65 Tb 0.03	66 Dy 0.00003	67 Ho 0.003	68 Er 0.002	69 Tm 0.02	70 Yb 0.02	71 Lu 0.0003

A

90 Th 0.2	91 Pa NA	92 U 0.003	93 Np NA	94 Pu NA	95 Am NA	96 Cm NA	97 Bk NA	98 Cf NA	99 Es NA	100 Fm NA	101 Md NA	102 No NA	103 (Lw) NA

Key
Atomic number → 33 As ← Symbol
0.005 ← Sensitivities in micrograms (interference-free)

FS - Fast neutron fission spectrum, *b* - Beta count, *p* - Reactor pulse, *c* - Bremsstrahlung radiation required, *NA* - Analysis not normally performed at GGA

Figure 18.2 Table of activation analysis sensitivities as offered by General Atomics Company, San Diego, CA.

spectroscopy (ICP-MS). The detection limits in modern ICP-MS are certainly very close to those achieved by AA. In addition, an ICP-MS apparatus is frequently connected to traditional chemical separation techniques, such as liquid chromatography (LC), thus allowing a sensitive determination of both the amount and chemical species present for both metals and nonmetals. In recent years, there has been increasing use of ICP-MS techniques to replace those of AA although there still are a large number of applications of AA each year, especially in the geological sciences.

18.2.3 Practical Considerations in Activation Analysis

To better understand the practical details of how AA may be applied to a given problem in elemental analysis, let us consider the various practical aspects of a typical AA problem. To make our discussion more concrete, let us consider a specific problem, the measurement of the aluminum content of rocks and meteorites (cf. Loveland et al., 1969). The choice of this example problem comes from its pedagogic simplicity and the fact that conventional chemical analyses of aluminum in rocks are known to be inaccurate at low aluminum concentrations and, in general, not very precise.

The first step in an AA procedure is sample preparation. The unknown and known samples (sometimes referred to as the unknown and standard samples) should have the same size, composition, and homogeneity insofar as possible, to insure that any attenuation of the incoming radiation or of the radiation emitted by the sample during counting or any count rate-dependent effects are exactly the same. In practice, this sample preparation is accomplished by making sure that the unknown and known samples have the same physical volume, are irradiated in a homogenous flux, and are counted under exactly the same conditions (geometry, detector, etc.). Pre-irradiation handling and treatment of the sample should be kept to a minimum so as to lessen the possibility of sample contamination. The standards are generally either aqueous solutions of the elements in question or multielemental standard reference materials whose composition is certified by a national or international agency such as the IAEA, the US NIST, and so on.

The second step in an AA is the choice of nuclear reaction to change X into X*, plus identification the irradiation facility in which the reaction will be carried out. As part of these considerations, the length of irradiation and decay prior to counting must be chosen, so the produced X* activity is enhanced relative to all other activities produced. Most AA is done with thermal neutrons produced in nuclear reactors for the following reasons:

- Many elements have high cross sections for the absorption of thermal neutrons in (n, γ) reactions.
- Copious fluxes of thermal neutrons (e.g., $\phi \sim 10^{12}$ n/cm^2/s) are available in nuclear reactors.

- Neutrons penetrate matter easily, and therefore there are few problems related to attenuation of the neutron flux in the sample.
- The major elements carbon, nitrogen, and oxygen are only very weakly activated by thermal neutrons, making detection of other (perhaps more interesting) elements easier.

Although most AA is done with reactor thermal neutrons, several other nuclear reactions and irradiation facilities can be used. Spontaneous fission of ^{252}Cf creates 3.8 neutrons per fission, and fluxes of up to 10^9 n/cm^2/s are available from large ^{252}Cf isotopic neutron sources. Cockroft–Walton accelerators can be used to accelerate deuterons to energies of ~150 keV, and then the ^{3}H(d, n) reaction can create ~14 MeV neutrons (fast neutrons) for activation. Typical neutron generators of this type give fluxes also on the order of 10^9 n/cm^2/s of the 14 MeV neutrons. Fast neutrons are useful for activating some light elements, such as silicon, nitrogen, fluorine, and oxygen, via (n, p) or (n, α) reactions, leading to sensitivities on the order of 50–200 ppm and, thus, provides complementary sensitivity to slow NAA.

Charged particle and photon-induced reactions can also be used to activate samples. The typical charged particles used are protons, deuterons, ^{3}He, and α-particles. Charged particle activation analysis (CPAA) is also complementary to NAA since NAA has poor sensitivity for the lighter elements while CPAA has good sensitivity. The limited penetrating power of charged particles in matter either requires thin samples or limits CPAA to surface analysis. This attenuation of the primary radiation by the sample puts especially stringent requirements on sample preparation.

Activation by photons (PAA) usually takes place via the (γ, n) reaction although other reactions such as (γ, p), (γ, α), and so on are possible. Of special interest is the determination of lead by PAA that has a detection limit of ~0.5 μg. (Lead is very hard to detect using NAA as indicated in Fig. 18.2). Photon sources are usually electron accelerators, which produce high-energy photons through the bremsstrahlung process when the electrons strike a heavy metal target.

For the example problem of determining the aluminum content in rocks, the activating nuclear reaction was chosen to be ^{27}Al(n, γ)^{28}*Al*, with the irradiation source being a nuclear reactor. The product ^{28}Al decays with a 2.2 min half-life and emits a β$^-$ particle and a high-energy (1.78 MeV) γ-ray.

Note that even if you have chosen to irradiate a sample with thermal neutrons from a nuclear reactor, you may be surprised to learn that several other neutron energies may be present and cause reactions. For the popular TRIGA design of reactor, only ~25% of the neutrons at a typical irradiation position are truly "thermal" neutrons ($0 < E_n < 0.05$ eV). The rest of the neutrons have higher energies; neutrons with 0.05 eV $< E_n < 0.1$ MeV are called *epithermal* neutrons, and neutrons with $0.1 < E_n < 15$ MeV are called *fast* neutrons. The

capture cross sections for epithermal neutrons frequently involve resonance capture (cf. Chapters 10 and 11) and can have very large cross sections in some cases (e.g., $>10^4$ barns). Usually one uses epithermal neutrons as the activating particle when one wants to avoid interfering activities in the sample due to thermal neutron capture. For example, suppose a sample has a high sodium content. Sodium is easily activated via the ^{23}Na(n, γ) reaction, giving rise to copious amounts of 15 h ^{24}Na in the sample, which may interfere with the detection and measurement of other activities. How do we get rid of this sodium? We can surround our sample with a metallic cadmium cover (~0.1 cm thick). Cadmium has a very large capture cross section for neutrons in the energy region below 1.0 eV and effectively "cuts off" or removes these neutrons by nuclear absorption. The resulting neutron flux in the sample consists of the higher-energy (epithermal) neutrons. Frequently one measures a "Cd ratio" for activation of a specific element to get some idea of how much of the produced activity is due to epithermal activation. In such measurements the Cd ratio R is defined as

$$R = \frac{\text{Activity}_{\text{no cover}}}{\text{Activity}_{\text{with cover}}} \qquad (18.2)$$

Typical values of R range from 2 to 1000 depending on the reactor irradiation position. Epithermal activation is advantageous for Ag, As, Au, Ba, Cs, Ga, In, Mo, Pt, Rb, Sb, Se, Sr, Tb, Th, Tm, U, W, Zn, and Zr among other elements.

Once the nuclear reaction and an irradiation facility have been selected, the possibility of interfering reactions must be carefully considered. Interfering means that quite often, although X will change to X* during the irradiation, some other elemental component Z may also change to X* during the irradiation. Thus, the activity of X* is proportional to the abundances of Z and X in the sample, not just X. This effect is referred to as an interfering reaction or interference, and a correction must be made for it. In the case of the aluminum analysis, there is a very important interference—namely, the occurrence of the ^{28}Si(n,p)^{28}Al reaction whereby silicon in the rock is converted into ^{28}Al by reactions involving fast neutrons present in any reactor (along with the desired thermal neutrons). Thus, the measured ^{28}Al activity will be due to the activation of ^{27}Al and ^{28}Si. By irradiating a known amount of silicon and counting it and from the well-known silicon abundances of rocks, a correction for the ^{28}Al produced by the ^{28}Si(n,p)^{28}Al reaction can be calculated. Other possible interferences are the fission of any uranium in the sample or the occurrence of two nuclides that happen to emit γ-rays with very similar energies that cannot be resolved by the detector, although one might measure the half-lives of the two components to separate the contributions.

The final decision concerning irradiation conditions involves the determination of the flux and duration of the irradiation. A simple rule of thumb is that the longer one irradiates the sample and the longer one lets the sample

decay before counting, the greater the activity of the long-lived species relative to the short-lived species. One should recall that each activity is limited by saturation so that it rarely pays to irradiate any material for a length of time more than about two half-lives of the desired activity. In the example aluminum analysis, a sample irradiation time of 1.0 min and a neutron flux of 5×10^{10} n/cm^2/s were used. For reactors of the TRIGA design, an advantage in producing short-lived nuclei can be gained by using a reactor pulse to activate the sample. The advantage factor (activity produced by a pulse irradiation/activity produced by a steady state irradiation = $50/t_{1/2}(s)$." (H.R. Lukens, Jr., H.P. Yule, and V.P. Guinn, Nucl. Instru. Meth. 3**3**, 273 (1965).

Multiple irradiations of a sample are frequently carried out for different lengths of time. The first irradiation is generally short (minutes) to determine the short-lived radioisotopes (of Ag, Al, Ba, Br, Ca, Cl, Co, Cu, Dy, F, I, In, K, Mg, Mn, Na, Se, Sb, Si, Sr, Ti, U, and V) and the subsequent irradiations are long (hours) to determine the intermediate (As, Au, Br, Cd, Ga, Ge, Hg, Ho, K, La, Mo, Na, Pd, Sb, Sm, U, W, and Zn) or long-lived (Ag, Ce, Cr, Cs, Co, Eu, Fe, Hf, Hg, Lu, Nd, Ni, Rb, Sb, Sc, Se, Sn, Sr, Ta, Tb, Th, Tm, Yb, Zn, and Zr) radionuclides. Following the long irradiations, it is common to let the sample "decay" for several days to get rid of the 15 h ^{24}Na.

The next major step in any AA procedure is the selection of a method to "isolate" the activity of interest, X^*, to measure it. Two methods of "isolating" X^* are commonly used – *instrumental activation analysis (IAA)* and *radiochemical activation analysis (RAA)*. IAA uses the characteristic energies of the γ-rays emitted by the radionuclides in the activated sample for identification, and the corresponding photopeak areas measure the amounts of the activities. IAA is nondestructive, allowing further use of the sample. Furthermore, it permits the use of short-lived activities to identify various elements that might not be possible if a lengthy chemical separation would precede the counting. Also, IAA lends itself to automation and reduces the time spent per sample in the analysis. The use of germanium semiconductor detectors with excellent energy resolution has made IAA the preferred method of AA.

Although most investigators prefer to use IAA, in some situations radiochemical work must be carried out prior to counting the sample, to isolate the activity of interest. An example when radiochemistry is necessary is the determination of trace elements in biological materials, such as blood, which have a very high sodium content. Large quantities of ^{24}Na are produced via the ^{23}Na(n, γ)^{24}Na reaction mentioned previously, and the strong decay radiation from this isotope tends to "mask" the trace element activities in the blood by creating a large Compton background in the region where the photopeaks of other trace-element activities are found (see the discussion in Chapter 17 on γ-ray detectors). In addition, the intense γ-ray emission can overwhelm the germanium detector and force the samples to be counted with a very low efficiency.

One solution to this problem of sodium contamination is to chemically separate the sodium from the irradiated blood (for example by using ion exchange with hydrated antimony pentoxide) and then to instrumentally analyze the purified blood. This example does illustrate a feature of modern RAA, that is, not completely separating the element of interest, but making a group separation producing a relatively small number of activities in the sample and then further resolving these activities by γ-ray spectroscopy.

All of our discussions up to now have focused on detecting the γ-rays from the decaying activation products. There is another approach that has been used in some cases called *prompt γ-ray activation analysis* (PGAA) in which one detects the so-called prompt γ-radiation emitted during the actual activation nuclear reaction. In PGAA using neutron activation via the (n, γ) reaction, one detects the γ-rays emitted immediately following the neutron capture. Such analyses must be carried out with neutron beams (not in the reactor core for obvious reasons) and usually involves detecting relatively high-energy (>5 MeV) γ-rays. Because of these constraints, this relatively rapid analysis method is restricted usually to the determination of the major elemental constituents of the sample.

18.2.4 Applications of Activation Analysis

The number of applications of AA is quite large. In the physical sciences, AA is used in trace-element analysis of semiconductor materials, metals, meteorites, lunar samples, and terrestrial rocks. In most cases, the multielemental analysis feature of AA is used to measure the concentrations of several trace elements simultaneously. From these detailed studies of trace element abundance patterns, one has been able to deduce information about the thermal and chemical history of the Earth, moon, Mars, and meteorites, as well as the source or age of an object.

The use of AA in criminal investigations (forensic AA) is also well established. The basic idea in this application is to match the trace-element distributions found in bullets, paint, oil, and so on found at the scene of a crime with the trace-element distributions in objects associated with criminal suspects or specific sources. Such identification is rapid and nondestructive (allowing the actual evidence to be presented in court). Moreover, the probability of the correct identification or association can be ascertained quantitatively. Other prominent examples of the use of forensic AA involve confirmation of the notion that Napoleon was poisoned (by finding significant amounts of arsenic in hair from his head) and the finding that the AA of the wipe samples taken from a suspect's hand can reveal not only if he or she has fired a gun recently but also the type of gun and ammunition used.

Applications of AA in the environmental sciences are routine. Determinations of the trace element components in urban atmospheres, lakes, streams,

and similar areas have been used to trace the flow of pollutants in various ecosystems. In addition, a few of the trace elements whose abundances have been measured by AA have turned out to be biologically significant by themselves. The classic biological example is mercury and significant mercury concentrations in fish, and other foodstuffs is revealed by AA. A particular combination of AA and radiotracer methods has found important applications in the environmental sciences. This combination involves the use of unique sets of stable isotopes (instead of radioactive isotopes) as tracers in various systems, followed by AA of the samples after dispersal where the unique tag provides the key to the tracer concentrations. This technique avoids the need to introduce radioactive materials into a system (such as the environment with its subsequent health and legal complications) and yet retains the selectivity and sensitivity of radiation measurements. The stable isotopes are called *stable activable tracers.* Kruger (1971) has described their use.

In summary, AA is a multielemental, nondestructive, and very accurate method of elemental analysis. In the best case the sensitivities reach picograms per gram with a strong variation from element to element (due to the nuclear properties of the isotopes). AA is best suited for the bulk analysis of solid samples and can be "tuned" by changing the irradiation conditions, particles, and post-irradiation sample treatment. Disadvantages in AA are the long analysis times, the need for access to an irradiation facility, (usually a reactor), the need to handle radioactivity, the labor-intensive nature of sample counting, and the inability to get speciation information.

18.3 PIXE

Particle-induced X-ray emission (PIXE) is an analytical technique based on observing fluorescent X-rays that are characteristic of the elements present in a sample. As such, PIXE is not strictly a nuclear technique, since it involves an atomic process, X-ray emission. But the atomic electron shell vacancies that are filled when the X-ray is emitted are created using particle-accelerator beams, and one uses nuclear techniques and semiconductor radiation detectors, Si(Li) detectors, to measure the X-rays.

The essential features of a PIXE setup are shown schematically in Figure 18.3. A very narrow beam of charged particles from a small accelerator, typically 2–4 MeV protons, impinges on a thin sample in a vacuum chamber. The protons collide with the electrons in the material, and some inner shell electrons are ejected from the atoms in the sample. A Faraday cup is used to collect the charge deposited by the incident protons, and this is integrated electronically to monitor the beam current. The sample is typically a very thin, uniform deposit of the material to be analyzed on a thin backing material. The characteristic X-rays from the sample are detected with a Si(Li) detector that is

Figure 18.3 A schematic diagram of a PIXE analysis setup (Ehmann and Vance (1991). Reproduced with the permission of John Wiley & Sons).
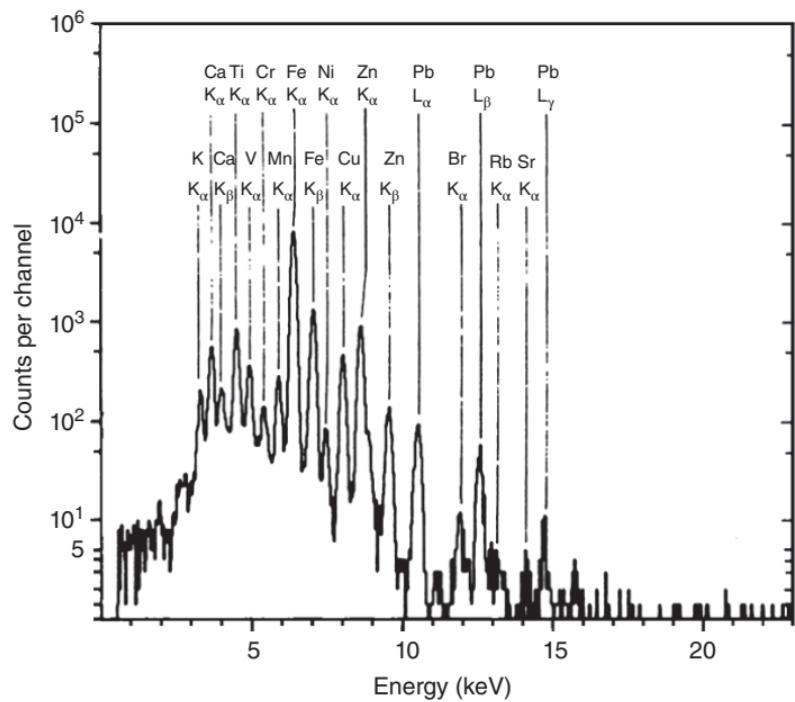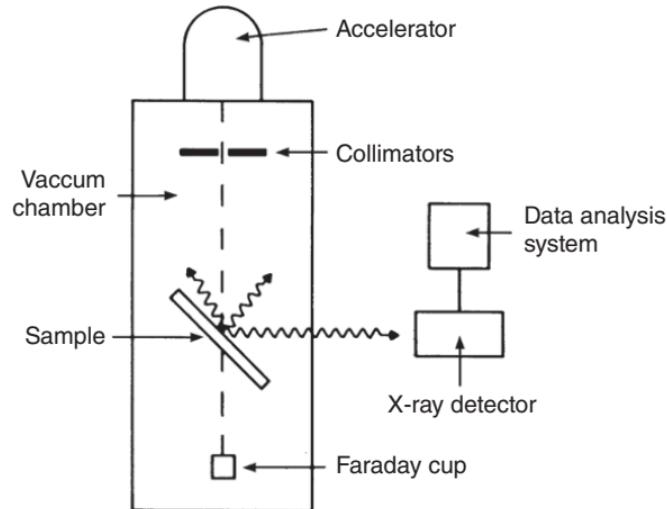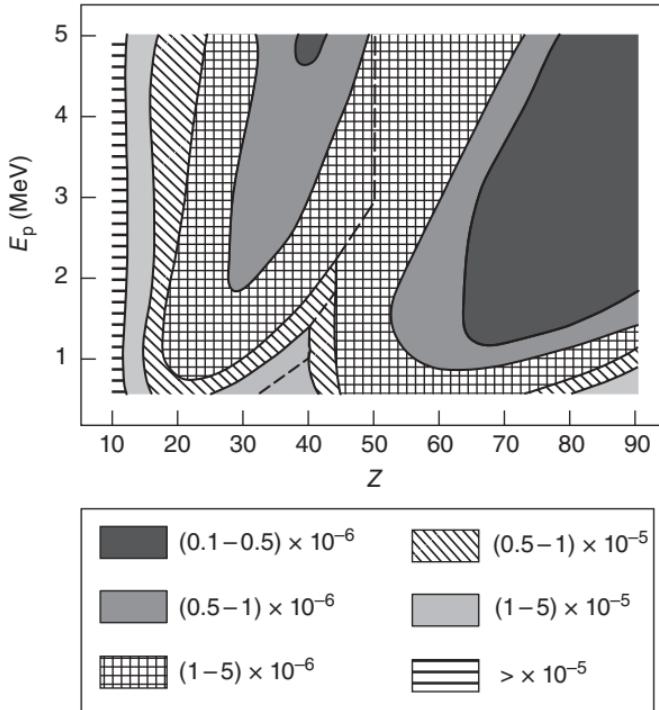
Figure 18.4 Example of the PIXE spectrum of a rainwater sample (Johansson and Johansson (1976). Reproduced with the permission of Elsevier).

sensitive to photons in this energy region. A typical spectrum from a PIXE experiment is shown in Figure 18.4. The spectrum consists of many discrete X-ray peaks superimposed on a continuous background of bremsstrahlung. One can observe a sequence of K_α and K_β lines of the lighter elements (from the filling of K shell vacancies in these atoms) and the L lines of the heaviest

Figure 18.5 Detection limits in a PIXE analysis of a biological sample (Ishii and Morita (1990). Reproduced with the permission of World Scientific Publishing Co Pte Ltd).

Legend:
- $(0.1-0.5) \times 10^{-6}$
- $(0.5-1) \times 10^{-6}$
- $(1-5) \times 10^{-6}$
- $(0.5-1) \times 10^{-5}$
- $(1-5) \times 10^{-5}$
- $> \times 10^{-5}$

elements. The peaks corresponding to a given element are integrated to give peak areas and the amounts of that element obtained either from a knowledge of the *absolute* ionization cross sections ($\sim 1-10^4$ barns) combined with fluorescence yields (0.1–0.9), beam current, and detector efficiency or on a relative basis by comparison to results obtained with thin elemental standards under identical conditions. Note that the term *fluorescence yield* refers to the fraction of the electron vacancies that lead to X-ray emission versus the ejection of Auger electrons.

Typical detection limits for PIXE analysis of various elements in a biological sample are shown in Figure 18.5. The sensitivity of PIXE is at the ppm level for many elements. About 25% of the applications of PIXE are in biology and medicine. The light element matrices lead to smaller continuous backgrounds, and many trace and toxic elements are easily detected by PIXE. (There are no "holes" in detection limits as there are in AA as all the elements emit some X-rays although the fluorescent yields of the lightest elements are extremely small.) Considerable attention has been and must continue to be devoted to the preparation of thin, representative samples. Note that PIXE is only sensitive to the elemental composition of the sample and not to the *isotopic* composition.

One of the most successful applications of PIXE has been in the analysis of particulate matter in air pollution. Atmospheric particulate matter is typically collected by impaction on a filter paper, which provides an ideal thin sample for PIXE analysis. The ability to analyze a large number of samples in a short time is an aspect of PIXE that is very important for the analysis of aerosol samples. PIXE analyses typically take less than a minute, and the entire irradiation, counting, sample changing, and analysis procedure can be completely automated.

Another non-destructive, reproducible and relatively quick technique applies a phenomenon called Particle Induced Gamma Emission, or PIGE, an analysis technique that is closely related to PIXE except that the nuclei are excited and emit characteristic gamma rays. The de-excitation gamma rays provide unique signatures for the elements (isotopes) present in a sample. An important recent application of PIGE is the detection of fluorine in environmental samples. Chemical compounds with a strong carbon-fluorine bond, or perfluorinated compounds, were developed and used extensively to make everyday materials stain resistant, water resistant and nonstick, including many textiles, food packaging wrappers and cooking utensils. However, more recently it was shown that these materials don't break down in the environment and are also bioaccumulative; that is, their concentration builds up in animal and human bodies over time. Elemental fluorine has only one stable isotope, ^{19}F, that is not very sensitive to NAA and its x-rays are low energy making them difficult to detect. The fluorine gamma rays have energies of 100 and 197 keV. Since PIGE excites the nuclei instead of destroying them, a given sample can be tested multiple times and in different laboratories for cross comparisons.

An important modern version of PIXE is called *micro-PIXE*. The accelerator is tuned to provide a proton beam whose spatial dimension is ~0.5 μm (rather than the more common 1–10 mm); one can determine the trace element content in very small samples or portions of a sample, giving one a "trace-element microscope." Micro-PIXE has become important in probing biological and medical samples since the size of a human cell is 1–10 μm. A closely related device called the *electron microprobe* has been developed where the ionization is caused by electron impact since it is somewhat easier to produce energetic electron beams compared to proton beams.

18.4 Rutherford Backscattering

One of the earliest experiments in nuclear physics was Rutherford's interpretation in 1909 of the large angle scattering of α-particles by gold nuclei observed by his graduate students Hans Geiger and Ernest Marsden. This experiment established the existence of an extremely small nucleus at the center of the atom (Chapter 10). In *Rutherford scattering* the repulsive Coulomb force acts
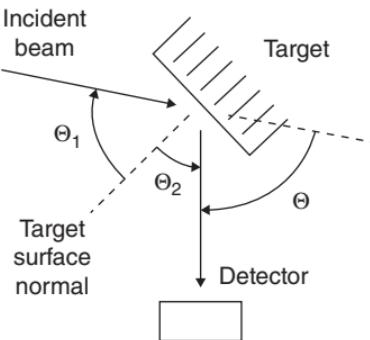
Figure 18.6 Schematic diagram of a Rutherford backscattering experiment. The incident beam is deflected by an angle, Θ, from the incident direction (Rauhala (1994). Reproduced with the permission of Wiley).

between the positively charged nuclei when they are close together and deflects the beam. The amount of deflection is characteristic of the nuclear charges, the beam energy, and the distance of closest approach. The schematic diagram of Rutherford backscattering spectrometry (RBS) experiment is shown in Figure 18.6 where the angle Θ measures the deflection of the incident beam.

Rutherford scattering is an elastic event, that is, the total kinetic energy is conserved, the nuclei do not come in contact, and no internal excitation of either the projectile or target nuclei occurs. Due to conservation of energy and momentum in the interaction, the kinetic energy of the scattered ion E_1 is always less than that of the incident ion E_0. The ratio of these energies is called the kinematic factor K which is given by the expression

$$K = \frac{E_1}{E_0} = \left[\frac{(M_2^2 - M_1^2 \sin^2 \Theta)^{1/2} + M_1 \cos \theta}{M_1 + M_2} \right]^2 \tag{18.3}$$

where M_1 and M_2 are the masses of the incident and target atoms, respectively, and Θ is the angle between the direction of the incident and scattered ions. Note that the relative shift in energy in the collision depends only on the masses of the ions and the angle of the detector. If one measures the scattering angle and the energy shift, one can calculate the mass (identity) of the scattering atom. The largest change in energy occurs for $\Theta = 180°$ where

$$K_{180} = \left[\frac{M_2 - M_1}{M_1 + M_2} \right]^2 \tag{18.4}$$

The geometry of the measurement is usually set so that the scattered particles are observed at very large angles, and thus the technique is called RBS.

The probability or cross section for Rutherford scattering as a function of solid angle (see discussion in Chapter 10) was given by Segre (1977) by the expression

$$\frac{d\sigma}{d\Omega} = \left(\frac{Z_1 Z_2 e^2}{4E} \right)^2 \frac{4}{\sin^4 \Theta} \frac{[\cos \Theta + (1 - x^2 \sin^2 \Theta)^{1/2}]^2}{(1 - x^2 \sin^2 \Theta)^{1/2}} \tag{18.5}$$
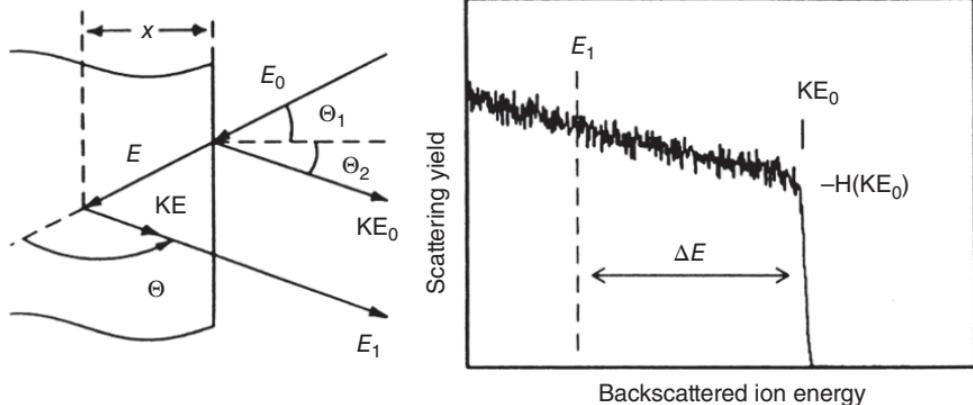
Figure 18.7 General relationship of the kinetic energy of the beam and backscattered ion with depth in a single pure material due to energy loss (Rauhala 1994). Reproduced with the permission of Wiley).

for a beam with Z_1, M_1 on a target with Z_2, M_2, where $x = M_1/M_2$, e^2 is the square of the electric charge, and E is the kinetic energy of the incident ion. Note that the probability of scattering increases with $(Z_1Z_2)^2$ and as $1/E^2$. At this point, we would expect a spectrum of backscattered particles to consist of a peak for each element in the sample with a relative height (area) that is proportional to Z_2^2. The elemental abundances could be calculated using the relation

$$N = \frac{D}{\phi \int (d\sigma/d\Omega)d\Omega} \tag{18.6}$$

where N is the number of target atoms, D is the number of detected events, and ϕ is the incident ion flux. This expression is only valid for thin films of target material or for scattering particles from heavy nuclei on the surface of a supporting material with a much lower atomic number.

The situation is actually more complicated because the incident ions will lose energy as they penetrate into the sample, continuously decreasing the value of E and thus increasing the probability of scattering and changing the energies of the scattered particles. The resulting spectrum for scattering α particles at varying depths from a single chemical element is shown in Figure 18.7, where the incident ion energy is E_0, the energy of ions scattered from the surface is KE_0, and the energy of ions scattered from a depth x is E_1. In this case, note that kinetic energy is lost twice as the particle traverses into and back out of the foil. Given a thickness N_x the energy loss ΔE is given by the expression

$$\Delta E = KE_0 - E = [\epsilon]_{RBS}N_x \tag{18.7}$$
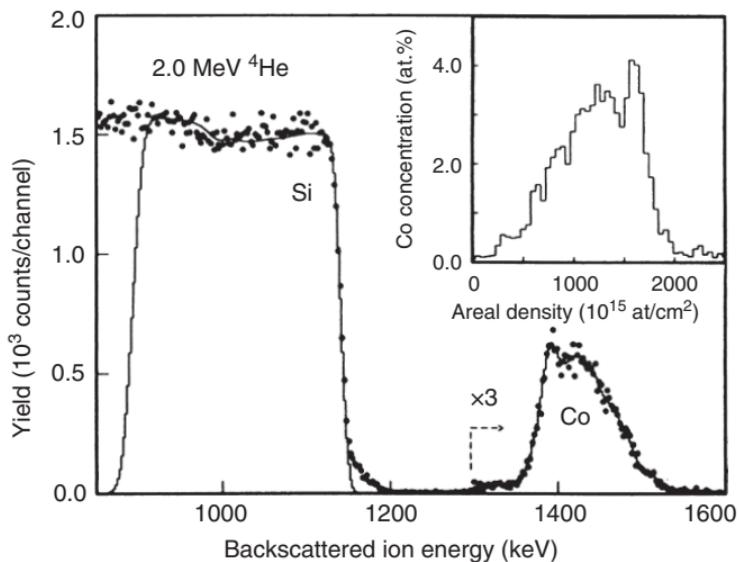
Figure 18.8 Example of data from Rutherford backscattering of 2.0 MeV ^{4}He ions incident on a Si(Co) sample. The dots represent the experimental data while the solid line is a simulated spectrum. Scattering angle was $\Theta = 170°$ with $\Theta_1 = \Theta_2 = 5°$. The concentration of cobalt from the analysis is shown in the inset (upper right) as a function of depth in the material (Saarilahti and Rauhala (1992). Reproduced with the permission of Elsevier).

where the reduced energy is

$$[\epsilon]_{RBS} = \frac{K\epsilon_{in}}{\cos\Theta_1} + \frac{\epsilon_{out}}{\cos\Theta_2} \tag{18.8}$$

with ϵ_{in} and ϵ_{out} being the energy dependent stopping cross sections on the inward and outward paths, respectively, of the ion. These cross sections are discussed by Ziegler (1990).

Rutherford backscattering is an important method for determining the composition and structure of surfaces and thin films. In Figure 18.8, the results of an RBS measurement with 2.0 MeV ^{4}He particles incident on a silicon surface with a cobalt impurity that was diffused into the bulk material are shown. One can clearly detect scattering from the Co atoms and their depth profile in the bulk material.

Another important application of this technique has been to determine the elemental composition of the lunar and Martian surfaces. Turkevich et al. (1969) constructed a rugged device to measure the backscattering of α-particles from the lunar surface. Copies of the device flew on three *Surveyor* missions in 1967–1968 and yielded the first complete and accurate elemental analysis of the lunar surface. The α-particles came from a radioactive source (^{242}Cm) that was part of the instrument package. The results of these experiments, which showed an unexpected and comparatively high abundance

of titanium, were confirmed by later laboratory analysis of lunar samples gathered during the *Apollo* lunar landing missions. Since that time, this technique continues to be used to study Martian rocks and soil.

18.5 Accelerator Mass Spectrometry (AMS)

Accelerator mass spectrometry (AMS) is an analytical technique for measuring the amounts of long-lived radionuclides present in a sample. The material to be analyzed is ionized, and the resulting ions are accelerated to megaelectron volts energies rather than the usual electron volts energies used in ordinary mass spectrometry. The resulting energetic ions are separated by mE/q^2 in an analyzing magnet (magnetic dipole) and then subjected to further separation by electrostatic analyzers and/or velocity filters. These final "filters" remove an unwanted ions and molecular fragments. The separated ions are then detected by charged particle detectors, or the ion current is measured in a Faraday cup. A schematic diagram of a typical AMS setup is shown in Figure 18.9.

By counting single ions rather than detecting their decay, sample sizes are reduced, and detection sensitivity improves. For example, in measuring ^{14}C, the needed sample size is reduced by a factor of 1000, and the measuring time is 100 times less. Using AMS, one can measure $^{14}C/^{12}C$ ratios of 10^{-15} that is equivalent to being able to count a ^{14}C sample activity of 10^{-7} Bq. A 10,000-year-old sample can be dated to within ± 40 years in <30 min. As a consequence of this, most (90%) of the applications of AMS involve measuring ^{14}C with over 100,000 samples being measured each year. ^{14}C AMS is done with Tandem van de Graaff accelerators where the initial ions are negatively charged (thus eliminating interference from the isobar ^{14}N that does not form a stable negative ion.) In AMS, one usually measures the ratio of isotopic abundances rather than the absolute isotopic abundance. Thus, for ^{14}C, one measures the $^{14}C/^{12}C$ ratio.
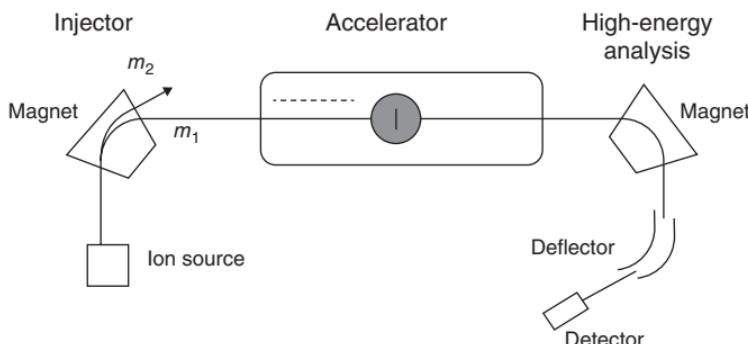
Figure 18.9 A schematic diagram of a typical AMS setup (Lehto and Hou (2011). Reproduced with the permission of Wiley-VCH).

Table 18.1 Long-Lived Radionuclides Measured by AMS.

Radionuclide	^{10}Be	^{14}C	^{26}Al	^{36}Cl	^{41}Ca	^{129}I
Half-life (My)	1.51	0.00573	0.705	0.301	0.103	15.7
Minimum sample size (mg)	0.5	0.02	1	1	20	2
Isotopic ratio sensitivity ($\times 10^{-15}$)	2	0.8	2	1	5	50
Detection limit (atoms/sample)	10^5	2×10^4	10^5	10^5	10^6	10^6

^{14}C is not the only radionuclide that can be determined using AMS. Table 18.1 shows some other radionuclides that are determined using AMS.

^{10}Be with its 1.6×10^6 year half-life is an important cosmogenic radionuclide that can be used to data geologic events on a much longer time scale than ^{14}C. The ^{10}Be concentration in ice and marine sediments can be used to infer solar fluctuations as these fluctuations will affect the cosmic ray fluxes striking the earth. The nuclides ^{10}Be, ^{14}C, ^{26}Al, ^{35}Cl, and ^{41}Ca are used to study the exposure ages of rocks. These nuclides are due to cosmic rays that penetrate the first few meters of a rock. ^{129}I is anthropogenic in origin and has been used to trace migration of nuclear waste. In addition to these nuclides, there are the actinides, ^{236}U, ^{239}Pu, ^{240}Pu, and ^{242}Pu that can be used to characterize the forensic history of fissionable material.

18.6 Other Mass Spectrometric Techniques

Two mass spectrometric techniques that are frequently used by nuclear and radiochemists are thermal ionization mass spectrometry (TIMS) and resonant ionization mass spectrometry (RIMS). TIMS is frequently used to determine the isotopic ratios of the actinides. An actinide sample is ionized by being deposited on a filament that is heated. The resulting 0.1–0.2 eV ions are focused into an ion beam and passed through a bending magnet to separate them by their mass-to-charge ratios (m/q). A multi-collector system is then used to determine the isotopic ratios. The TIMS sensitivities for U, Np, and Pu are comparable to AMS. The sample preparation and cleanup times for TIMS analyses are long and restrict the use of this technique for some purposes.

RIMS is a highly selective, very sensitive mass spectrometric technique. The sample material is vaporized and atomized and selectively ionized by laser resonant optical techniques. The laser ionization is a multistep (typically 2–3) process. Isobaric interferences are strongly suppressed ($>10^8$). Detection limits are 10^{-18} to 10^{-15} g with isotopic sensitivities of $>10^{13}$.

Problems

18.1 For each of the following analyses, indicate what role, if any, activation analysis could or should play. Be sure to clearly state the reasons for your choice.
   (a) Determination of the oxygen content of steel
   (b) Verification of the authenticity of ancient paintings
   (c) Determination of the radionuclides present in fallout from nuclear weapon testing
   (d) Determination of the extent to which radionuclides leaking from nuclear waste storage facilities contaminate the water of nearby streams
   (e) Determination of lithium impurities in thin films of GaAs

18.2 (a) Calculate the activity (in microcuries) of ^{49}Ca produced when 2.7 g of CaO are irradiated in a flux of 3×10^{12} n/cm^2/s for 10 min. (b) Repeat this calculation for the situation when the bombarding particle is 21 MeV deuterons, and the deuteron beam current is 10 μA. Assume the (d, p) cross section is 50 mbarns.

18.3 Using the Chart of the Nuclides as a guide to the cross sections, estimate the sensitivity (minimum quantity that can be detected) of neutron activation analysis for europium using a thermal neutron flux of 3×10^{12} n/cm^2/s. Assume no irradiation may last more than one hour and the minimum detectable activity is 10 dpm.

18.4 For the following analyses, indicate whether radiochemical neutron activation analysis would be preferred to instrumental neutron activation analysis. If radiochemistry is indicated, briefly sketch a separation procedure that could be used.
   (a) the determination of ppm levels of Mo in fathead minnows.
   (b) the determination of the trace element content of agricultural field-burning particulate matter.
   (c) the use of stable activable tracers to determine flow patterns in an ocean estuary.
   (d) the determination of Dy in pine needles.

18.5 Imagine that you want to trace the deposition of particulate matter using the stable activable tracer indium. The dilution factor between the point of release and the point of sampling is 10^6. Assume the samples that are collected are activated in a thermal neutron flux of 3×10^{12} n/cm^2/s for 10 min. Further assume a 1% efficiency for detecting the emitted photons. Determine the minimum amount of In that must be

released to ensure the uncertainty in the measured sample concentrations is 5%.

18.6 Two thin 1 mg samples of dysprosium are irradiated and counted in a similar manner, except for the use of a Cd cover foil on one sample. A Cd ratio of 7 was measured, and the saturation activity of the bare foil was found to be 1×10^4 dpm. Calculate the thermal neutron flux at the irradiation position in the reactor.

18.7 Devise an activation analysis scheme for determining the concentration of nitrogen in a sample of plant material. Assume the analysis must be nondestructive and rapid. Suggest an appropriate reaction, irradiation, and counting conditions and indicate possible interferences in your analysis.

18.8 Consider the following results obtained by neutron activation analysis of lake water samples for their manganese content. Assume the sample volumes are all one liter. A 10 mg Mn standard gave a counting rate of 5000 cpm. What is the Mn content of the lake water and its uncertainty?

Sample	EOB Activity (cpm)
1	1204
2	1275
3	940
4	1350

18.9 Compute the "advantage factor" for using a reactor neutron pulse to produce the 20 s $^{46}\text{Sc}^{\text{m}}$ activity for analysis compared to the activity produced by steady-state irradiation. Assume the reactor is of the TRIGA type and can produce a 15 ms long 3000 MW pulse with a peak instantaneous flux of 21×10^{15} n/cm^2/s whereas the steady-state operation of this reactor is at 1 MW.

18.10 Imagine you wish to detect ppm levels of aluminum in a matrix containing iron, calcium, and silicon. Assume you have access to a modern nuclear reactor. Describe an activation analysis procedure to do this analysis. Be sure to describe the irradiation conditions, any pre- or post-irradiation chemistry, and the counting strategy. Indicate how you would deal with any interferences in the analysis.

Bibliography

E. Segre, *Nuclei and Particles*, 2nd Edition (Benjamin, Reading, 1977).

General References about Nuclear Analytical Methods

Z.B. Alfassi, Editor, *Chemical Analysis by Nuclear Methods* (John Wiley & Sons Ltd, Chichester, 1994). A series of essays on various aspects of nuclear analytical chemistry. Most of them are quite good.

D. Brune, B. Forkman, and B. Persson, *Nuclear Analytical Chemistry* (Chartwell-Bratt, London, 1984).

W.D. Ehmann and D.E. Vance, *Radiochemistry and Nuclear Methods of Analysis* (John Wiley & Sons, Inc., New York, 1991) One of the best general references on nuclear analytical methods.

J. Lehto and X. Hou, *Chemistry and Analysis of Radionuclides* (Wiley-VCH, Weinheim, 2011). A highly recommended modern textbook on radiochemistry and radiochemical techniques.

References about Activation Analysis

D.J. Hughes, *Pile Neutron Research* (Addison-Wesley, Cambridge, 1953). The bible (old testament) of reactor neutron physics.

P. Kruger, *Principles of Activation Analysis* (John Wiley & Sons, Inc., New York, 1971). The best textbook approach to activation analysis.

D. de Soete, R. Gijbels, and J. Hoste, *Neutron Activation Analysis* (John Wiley & Sons, Inc., New York, 1974). An encyclopedic work.

References about PIXE

S.A.E. Johansson and J.L. Campbell, *PIXE: A Novel Technique for Elemental Analysis* (John Wiley & Sons Ltd, Chicester, 1988).

S.A.E. Johansson, J.L. Campbell, and K.-G. Malmqvist, *PIXE* (John Wiley & Sons, Inc., New York, 1995).

References about RBS

J.F. Ziegler, P.J. Scanlon, W.A. Lanford, and J.L. Duggan, Editors, *Ion Beam Analysis* (North-Holland, Amsterdam, 1990).

Specific References

W.R. Corliss, *Neutron Activation Analysis* (USAEC, Oak Ridge, 1963).

R. Heilborg and G. Skog, Mass Spectrom. Rev. **27**, 398 (2008).

M. Hotchkis, D. Fink, C. Tuniz, and S. Vogt, Appl. Radiat. Isot. **53**, 31 (2001).

K. Ishii and S. Morita, Int. J. PIXE **1**, 1 (1990).

S.A.E. Johansson and T.B. Johansson, Nucl. Instrum. Methods **137**, 473 (1976).

W. Loveland., R.A. Schmitt, and D.E. Fisher, Geochim. Cosmochim. Acta **33**, 375 (1969).

E. Rauhala, in *Chemical Analysis by Nuclear Methods*, Z.B. Alfassi, Ed. (John Wiley & Sons, Ltd, Chichester, 1994).

J. Saarilahti and E. Rauhala, Nucl. Instrum. Methods Phys. Res., Sect. B **64**, 734 (1992).

A. Turkevich, E.F. Franzgrote, and J.H. Patterson, Science **165**, 277 (1969).

19

Radiochemical Techniques

19.1 Introduction

Radiochemistry has been defined as "the chemical study of radioactive elements, both natural and artificial, and their use in the study of chemical processes" (Stein, 1984). Operationally radiochemistry is defined by the activities of radiochemists, that is, (a) nuclear analytical methods, (b) the application of radionuclides in areas outside of chemistry such as medicine, (c) the physics and chemistry of the radioelements, (d) the physics and chemistry of high activity level matter, and (e) radiotracer studies. We have dealt with several of these topics in Chapters 4, 14, 15, and 18. In this chapter, we will discuss the basic principles behind radiochemical techniques and some details of their application.

Because of the small physical amounts of material involved, the presence of radioactivity which implies certain regulatory and safety concerns and the general desire to deal with short-lived nuclei. These techniques are not the same as ordinary chemical techniques. Specialized techniques have evolved from the early part of the 20th century when chemistry was a principal tool in identifying the basic nature of radioactive decay through the extensive use of chemistry in the Manhattan Project during World War II up to the present, "high tech" character of many radiochemical manipulations. These techniques are quite important for they are often the key to a successful experiment even though they may get scant mention in descriptions of the experiment. Often the successful application of these techniques requires careful, painstaking attention to detail, frequent practice to develop the necessary manipulative skills, and a thorough knowledge of the underlying chemical principles. In addition to the discussions of these topics in textbooks such as this, there are excellent textbooks that focus primarily on radiochemistry (Adloff and Guillamont, 1984; Ehmann and Vance, 1991; Lehto and Hou, 2011).

19.2 Unique Aspects of Radiochemistry

Radiochemistry involves the application of the basic ideas of inorganic, organic, physical, and analytical chemistry to the manipulation of radioactive material. However, the need to manipulate radioactive materials imposes some special constraints (and features) upon these endeavors. The first of these involves the number of atoms involved and the solution concentrations. The range of activity levels in radiochemical procedures spans from pCi to MCi. For the sake of discussion, let us assume that the activity level A, typical for radiotracer experiments, is $1\,\mu Ci\,(= 3.7 \times 10^4\,dis/s = 3.7 \times 10^4\,Bq)$, for a nucleus with mass number ~ 100. If we assume a half-life for this radionuclide of 3 days, the number of nuclei present can be calculated from the equation,

$$N = \frac{A}{\lambda} = 1\,\mu Ci(3.7 \times 10^4\,dps/\mu Ci)\frac{3\,days \times 24\,h/day \times 3600\,s/h}{\ln(2)} \quad (19.1)$$

using the relation that λ, the decay constant of the nuclide, is $\ln(2)/t_{1/2}$. The result is that $N = 1.4 \times 10^{10}$ atoms, and the mass of the sample would be 2.3×10^{-12} g. This quantity of material, if prepared as an aqueous 1 L solution would have a concentration of $\sim 10^{-14}$ mol/L. This simple calculation demonstrates a number of the important features of radiochemistry, that is, (a) the manipulation of radiochemical samples involving infinitesimal quantities of material, (b) the power of nuclear analytical techniques (since $1\,\mu Ci$ is a significant, easily detectable quantity of radioactivity), and (c) in an extension of the calculation, the decay of a single heavy element atom might occur by α-particle emission with 100% detection efficiency, allowing one to do chemistry one atom at a time.

The small number of atoms involved in some radiochemical procedures can give unexpected behavior. Although time-dependent processes obeying first-order kinetics are not affected by changes in concentration, the same is not true of second-order kinetics. For example, at 10^{-2} M, isotopic exchange between U(IV) and U(VI) has a lifetime of ~ 2 h while at 10^{-10} M; the same lifetime is ~ 400 days. Another example is Np(V) that is unstable with respect to disproportionation and yet $\mu Ci/L$ solutions of NpO_2^+ are stable. The extreme dilution in some solutions can mean that equilibrium is not reached due to kinetic limitations. The plutonium in fallout, present in the aqueous environment at concentrations of 10^{-18} to 10^{-17} M, has not reached equilibrium in over 40 years.

In addition to the limitations posed by kinetics or thermodynamics, there are certain practical problems associated with solutions at very low concentrations. An important problem is the adsorption of tracer levels of radioactivity on the surfaces of laboratory glassware. Glass has an ion exchange capacity of 10^{-10} mol/cm² along with a similar number of chemisorption sites. A 100 mL

beaker can thus absorb $\sim 10^{-8}$ mol, which is significant if the concentration of the tracer is $\leq 10^{-6}$ M. One suppresses this absorption by having high [H^+] (thus blocking adsorption sites), by treating glass surfaces with nonadsorbing silicone coatings or by loading the glass sites with holdback carriers (see in the following text).

Conventional analytical techniques generally operate at the ppm or higher levels. Some techniques such as laser photo acoustic spectroscopy are capable of measuring phenomena at the 10^{-8} to 10^{-6} mol/L level. The most sensitive conventional analytical techniques, time-resolved laser-induced fluorescence, and inductively coupled plasma mass spectrometry (ICP-MS) are capable of measuring concentrations at the part per trillion level, that is, 1 part in 10^{12}, but rarely does one see detection sensitivities at the single atom level that are routinely obtained in some radioanalytical techniques. While techniques such as ICP-MS are replacing the use of neutron activation analysis in the routine measurement of ppb concentrations, there can be no doubt about the unique sensitivity associated with radioanalytical methods.

Along with the unique sensitivity and small quantities of material associated with radiochemistry, there is the need to comply with the regulations governing the safe use and handling of radioactive material. This task is a primary focus in the design and execution of radiochemical experiments and is often a significant factor in the cost of the experiment. Because so many of these rules are site specific, they are not treated in this chapter.

There are some chemical effects that accompany high specific activities that are unique to radiochemistry and are worth noting. Foremost among these are the chemical changes accompanying radioactive decay. The interaction of ionizing radiation from a radioactive source with air can result in the generation of ozone and the nitrous oxides, which can lead to corrosion problems. Sources containing Ra or Rn produced from the decay of heavier elements, such as U, will emanate Rn gas as the decay product of Ra. The decay products of gaseous Rn are particulates that deposit on nearby surfaces, such as the interior of the lungs, leading to contamination problems. In high activity aqueous solutions, one can make various species such as the solvated electron, e_{aq}^-; hydroxyl radicals, $OH^\bullet$; and the solvated proton, H_3O^+. The hydroxyl radical, $OH^\bullet$, is a strong oxidizing agent as indicated in

$$OH^\bullet + e^- \rightarrow OH^-, \ \ E_0 = 2.8 \text{ V} \tag{19.2}$$

while the solvated electron is a strong reducing agent,

$$e_{aq}^- + H^+ \rightarrow \frac{1}{2}H_2, \ \ E_0 = 2.77 \text{ V} \tag{19.3}$$

Solutions involving high activity levels will change their redox properties as a function of time. For example, all the atoms in a 100 Bq/mL (10^{-7} mol/L)

Table 19.1 Product Yields (*G* Values in µmol/J) Created in Irradiated Neutral Water.

Radiation	H_2O Loss	H_2	H_2O_2	e^-_{aq}	$H^\bullet$	$OH^\bullet$
γ Rays and fast electrons	0.43	0.047	0.073	0.062	0.28	0.0027
12 MeV α's	0.29	0.12	0.11	0.028	0.056	0.007

solution of ^{239}Pu will undergo a redox change in a period of about 1 year. In general, it is hard to keep high specific activity solutions stable. Reagents, column materials, and others can suffer radiation damage as well. In radiotracer studies, the self-decomposition (radiolysis) of ^{3}H- and ^{14}C-labeled compounds can lead to a variable concentrations and variable number of products from reactions.

Many of these effects of radioactive decay can be treated quantitatively using "*G* values." Historically the *G* value was defined as the number of molecules or species decomposed or formed per 100 eV of absorbed energy. A newer (SI) definition of the *G* value is the number of moles of molecules or species formed or decomposed per Joule of energy absorbed. (Note that 1 mol/J = 9.76×10^6 mol/100 eV.) *G* values depend on the radiation and the medium being irradiated and its physical state. Table 19.1 shows some typical *G* values for the irradiation of neutral liquid water. The actual final products of radiolysis are the result of a complex set of chemical reactions, see for example Section 15.7.1. Detailed quantitative estimates of product yields are therefore more complicated and beyond the scope of this book. The reader is referred to other textbooks that discuss how these estimates are made (Mozumder 1999; Woods et al. 1990).

Radioactive decay also causes chemical transmutations. The daughter nucleus in α- or β-decay is a different chemical element than the mother nucleus, but it is in the same chemical environment as the mother nucleus. In addition, the recoil energy is usually much larger than chemical bond or even ionization potentials so changes of oxidation state or bonding are possible.

In α decay, one expects all chemical bonds to the decaying atom to be broken as the recoil energy of the daughter nucleus far exceeds chemical bond energies. Surprisingly, the oxidation state of the daughter nucleus is frequently that of the parent nucleus after all electronic and atomic rearrangements have taken place. An obvious exception is when the daughter cannot exhibit the parent's oxidation state such as the α-decay of U(VI) initially as UO_2^{2+} where the Th daughter does not exhibit the 6^+ oxidation state.

In β$^-$ decay, especially for low-energy β$^-$ emitters such as ^{14}C and ^{3}H, the effects on chemical bonding are modest. For example, for the decay of ^{14}C in methane,

$$^{14}CH_4 \rightarrow {}^{14}NH_4^+ + \beta^- + \overline{\nu}_e \qquad (19.4)$$

the β^- decay can be considered an oxidizing process. In fact, β^- decay (of $^{83}SeO_4^{2-}$ and $^{242}AmO_2^+$) was used successfully to prepare new higher oxidation states (of $^{83}BrO_4^-$ and $^{242}CmO_2^{2+}$) of some elements. In electron capture or internal conversion decay, there are massive rearrangements of the atomic electrons, which make these considerations more complicated.

Some tracers (usually cations) in solution behave as colloids rather than true solutions. Such species are termed *radiocolloids* and are aggregates of 10^3–10^7 atoms, with a size of the aggregate in the range 0.1–500 nm. They are quite often formed during hydrolysis, especially of the actinides in high oxidation states. One can differentiate between real radiocolloids and pseudo-colloids, in which a radionuclide is sorbed on an existing colloid, such as humic acid or $Fe(OH)_3$. Formation of real colloids can be prevented by using solutions of low pH or by addition of complexing agents. The chemical behavior of these radiocolloids is difficult to predict, as the systems are not at equilibrium.

There are certain unique features to the chemical separations used in radiochemistry compared with those in ordinary analytical chemistry that are worth noting. First of all, high yields are not necessarily needed, provided the yields of the separations can be measured. Emphasis is placed on radioactive purity, expressed as decontamination factors, rather than chemical purity. Chemical purity is usually expressed as the ratio of the number of moles (molecules) of interest in the sample after separation to the number of *all* the moles (molecules) in the sample. Radioactive purity is usually expressed as the ratio of the activity of interest to the activity of all the radionuclides in the sample. The decontamination factor is defined as the ratio of the radioactive purity after the separation to that prior to the separation. Decontamination factors of 10^5–10^7 are routinely achieved with higher values possible. In the event that the radionuclide(s) of interest are short-lived, then the time required for the separation is of paramount importance, as it does no good to have a very pure sample in which most of the desired activity has decayed during the separation.

As indicated above, frequently the amount of material involved in a radio-chemical procedure is quite small. To obviate some of the difficulties associated with this, a weighable amount (e.g., ~mg) of inactive material, the *carrier*, is added during an early stage of the procedure. It is essential that this carrier and the radionuclide (tracer) be in the same chemical form. This is achieved usually by subjecting the carrier plus tracer system to one or more redox cycles prior to initiating any chemical separations to ensure that the carrier and tracers are in the same oxidation state.

Carriers frequently are stable isotopes of the radionuclide of interest, but they need not be. Non-isotopic carriers are used in a variety of situations. *Scavengers* are non-isotopic carriers used in precipitations that carry/incorporate other radionuclides into their precipitates indiscriminately. For example, the precipitation of $Fe(OH)_3$ frequently carries, quantitatively, many other cations that are

absorbed on the surface of the gelatinous precipitate. Such scavengers are frequently used in chemical separations by precipitation in which a radionuclide is put in a soluble oxidation state; a scavenging precipitation is used to remove radioactive impurities and then the nuclide is oxidized/reduced to an oxidation state where it can be precipitated. In such scavenging precipitations, so-called *holdback carriers* are introduced to dilute the radionuclide atoms by inactive atoms and thus prevent them from being scavenged.

It is certainly possible, although usually more difficult, to do *carrier-free* radiochemistry in which one works with the radionuclides in their low, tracer-level concentrations. Such carrier-free radiochemistry is used when the presence of the additional mass of carrier atoms would lead to problems of sample thickness (α-emitters), biological side effects (radiopharmaceuticals), or where high specific activities are needed (synthesis of labeled compounds). Formally, specific activity is the activity per mass unit, such as mCi/mg or μCi/μmol.

19.3 Availability of Radioactive Material

One obviously needs radioactive materials to carry out radiochemistry. As indicated in Chapter 3, radionuclides are classified as primordial (remnants of nucleosynthesis), cosmogenic (being continuously generated by the action of cosmic rays with the upper atmosphere), or anthropogenic (made by man). Most of the radionuclides used in radiochemistry work are of the latter type, that is, made artificially in response to perceived needs. In Table 19.2, we summarize the commonly used radionuclides and their methods of production. As indicated in that table, a large number of these nuclides can be made by neutron irradiation in a nuclear reactor using (n, γ) reactions. Such nuclei are, of course, not carrier-free, are largely β^- emitters, and have low specific activities. Charged-particle-induced reactions, using cyclotrons, are used to synthesize neutron-deficient nuclei, that decay by EC or β^+-emission. The short-lived nuclei used in PET or other procedures in nuclear medicine fall into this category.

The transuranium nuclei are a special class of radionuclides, being made by both reactor irradiation and production in charged-particle accelerators. In Table 19.3, we summarize the properties and available amounts for research in the United States by qualified individuals in 2015. One should also note that while large quantities of ^{239}Pu have been produced, it is classified as a *special nuclear material* because of its use in weaponry, and very strict regulations govern the possession and use of this nuclide (along with ^{233}U and ^{235}U).

Table 19.2 Commonly Used Radionuclides.

Nuclide	Method of Production	Half-Life	Decay Type and Energy (MeV)
^{3}H(T)	R	12.33 years	β^- 0.018
^{14}C	R	5730 years	β^- 0.156
^{22}Na	C	2.60 years	β^+, γ 1.274
^{24}Na	R	15.0 h	γ 1.369
^{32}P	R	14.3 days	β^- 1.71
^{33}P	R	25.3 days	β^- 0.249
^{35}S	R	87.4 days	β^- 0.167
^{36}Cl	R	3.0×10^5 years	β^- 0.71
^{45}Ca	R	162.6 days	β^- 0.257
^{47}Ca	R	4.54 days	β^- 1.99 γ 1.297
^{51}Cr	R	27.7 days	γ 0.320
^{54}Mn	R	312 days	γ 0.835
^{55}Fe	R	2.73 years	EC
^{59}Fe	R	44.5 days	γ 1.292, 1.099
^{57}Co	C	271.7 days	γ 0.122
^{60}Co	R	5.27 years	γ 1.173, 1.332
^{63}Ni	R	100.1 years	β^- 0.067
^{65}Zn	C,R	244.3 days	γ 1.116
^{75}Se	R	119.8 days	γ 0.265, 0.136
^{86}Rb	R	18.6 days	β^- 1.77
^{85}Sr	R,C	64.8 days	γ 0.514
^{99}Mo/^{99}Tc$^{\text{m}}$	F	65.9 h/6.01 h	γ 0.143
^{106}Ru	F	373.6 days	β^- 0.039
^{110}Ag$^{\text{m}}$	R	249.8 days	β^- 3.0
^{109}Cd	C	461 days	γ 0.088
^{111}In	C	2.80 days	γ 0.171
^{125}I	R	59.4 days	γ 0.035
^{131}I	R	8.02 days	β^- 0.606, γ 0.365
^{137}Cs	F	30.1 years	γ 0.662
^{153}Gd	R	240.4 days	γ 0.103
^{201}Tl	C	72.9 h	γ 0.167
^{210}Pb	R	22.3 years	β^- 0.017, 0.064

C, cyclotron; R, reactor; F, fission product.

Table 19.3 Availability of Transuranium Element Materials.

Nuclide	$t_{1/2}$	Decay Mode(s)	Available Amount	Specific Activity (dpm/µg)
^{237}Np	2.14×10^6 years	α, SF(10^{-10}%)	g	1565.0
^{238}Pu	8.77×10^1 years	α, SF(10^{-7}%)	mg	3.8×10^7
^{239}Pu	2.41×10^4 years	α, SF(10^{-4}%)	mg	1.38×10^5
^{240}Pu	6.56×10^3 years	α, SF(10^{-6}%)	mg	5.04×10^6
^{241}Pu	1.44×10^1 years	β, α(10^{-3}%)	mg	2.29×10^8
^{242}Pu	3.76×10^5 years	α, SF(10^{-3}%)	mg	8.73×10^3
^{243}Am	7.38×10^3 years	α, SF(10^{-8}%)	mg	4.4×10^5
^{244}Cm	1.81×10^1 years	α, SF(10^{-4}%)	mg	1.80×10^8
^{248}Cm	3.40×10^5 years	α, SF(8.3%)	µg	9.4×10^3
^{249}Bk	3.20×10^2 days	β, α(8.3%), SF(10^{-8}%)	µg	3.6×10^9
^{249}Cf	3.51×10^2 years	α, SF(10^{-7}%)	µg	9.1×10^6
^{252}Cf	2.60×10^0 years	α, SF(3.1%)	µg	1.2×10^9

19.4 Targetry

As indicated earlier, a combination of reactor and cyclotron irradiations is used to prepare most radionuclides. While many of these radionuclides are commercially available, some are not. In addition, nuclear structure, nuclear reactions, and heavy element research require accelerator or reactor irradiations to produce short-lived nuclei or to study the dynamics of nuclear collisions and others. One of the frequent chores of radiochemists is the preparation of accelerator targets and samples for reactor irradiation. It is this chore that we address in this section.

The first question to be addressed in preparing accelerator targets or samples for irradiation is the question of impurities and/or other chemical constituents of the sample. For neutron irradiation, one generally prefers metals or inorganic salts with a non-activable counterion. The salts usually include nitrates, sulfates, and others, but not halides (especially not chlorides due to the strong activation of chlorine) nor sodium, nor potassium salts. In general, one avoids materials that undergo radiolysis although it is possible, with suitable precautions, to even irradiate materials such as gasoline, oil, and other flammable materials in reactors. Liquid samples can be irradiated in reactors easily, but

one must generally pay attention to pressure buildup in the irradiation container due to radiolytic decomposition of water or other liquid. Unless purged with nitrogen, water will contain dissolved argon, which will activate to form ^{41}Ar, and the gaseous radioactive atoms will be released upon opening the irradiation container. For irradiations of a few hours in a moderate reactor flux ($\sim10^{12}$ n/cm^2/s), the samples to be irradiated may be heat sealed in polyethylene vials, usually using double encapsulation. For long irradiations or higher fluxes ($\sim10^{15}$ n/cm^2/s), encapsulation in quartz is required. One never uses Pyrex or other boron-containing glasses due to their high cross sections for neutron absorption. When irradiating larger samples, one must pay attention to self-shielding in the samples. For example, the flux reduction in a 0.5 mm thick Au foil is about 27% due to self-absorption. However, in irradiations of most liquid samples or geological samples, these self-absorption corrections can be neglected.

Preparation of the targets for charged-particle irradiations requires more effort due to the high rate of energy loss of charged particles in matter. In general, the material to be irradiated must be placed in vacuum, thus making the irradiation of liquids and gases more difficult. Solids must be in the form of thin foils or deposits on backing material. Typical backing materials are carbon, aluminum, beryllium, and titanium. High power irradiations with protons are made with thick metal targets with water-cooled backing. The typical measure of thickness of accelerator targets is in units of areal density (mass/unit area, i.e., mg/cm^2). The thickness expressed in units of areal density (mg/cm^2) is the linear thickness (cm) multiplied by the density (mg/cm^3). One can weigh very thin samples and determine their area and thus their areal density. Typical thicknesses for accelerator targets are $\sim$0.1–5 mg/cm^2 but depend, of course, on the rate of energy loss of the irradiating ion in the target material. Target backings for heavy ions are frequently 10–100 µg/cm^2. Such thicknesses qualify as "thin," that is, easily breakable and require special preparation techniques.

Because of the high rate of energy loss of heavy charged particles in matter, one must pay attention to cooling the targets or, in some way, dissipating the energy deposited in the target material as the beam passes through it. For example, consider the irradiation of a 0.5 mg/cm^2 ^{208}Pb target by 450 MeV ^{86}Kr ions. Each Kr ion passing through the target deposits $\sim$8.1 MeV. If the Kr beam intensity is 1 particle-µA (6.24×10^{12} ions/s), then the rate of energy deposit in the target is $\sim5 \times 10^{13}$ MeV/s $\approx$ 8.1 J/s (W). If the foil has an area of 2 cm^2, it would have a mass of 1 g. The specific heat of Pb is only 0.130 J/g/°C. Thus, in the absence of any cooling, the temperature of the target would rise 8.1°/s and the foil would soon melt. Since the foil will generally be in vacuum, without further intervention, it would only cool by thermal radiation, which will not suffice to remove the heat. Heat transfer from such a foil can occur by clamping it to the front of a cooled block (remembering now that the entire beam energy will

be dumped into the cooling block since the beam will pass through the target and into the block). Alternately a jet of a light gas such as helium can be used to cool the backside of the foil or the particle beam can be spread over a larger area foil, thus reducing the temperature increase.

Over the years, a number of specialized techniques have been developed for the preparation of accelerator targets. These techniques are also used in the preparation of thin sources for counting, such as those used in α or β spectroscopy. The first and simplest technique for depositing a target material on a backing foil is by simple *evaporation* of a solution of the desired material on the foil. Generally this is a poor choice as the solute tends to deposit at the edges of the drying droplet, leading to variations of up to a factor of 100 in thickness over the area of the deposit. This is the familiar phenomena that leads to milk rings after a drop of milk evaporates to dryness. Uniformity can be improved by using a wetting agent such as insulin to coat the surface of the backing material prior to evaporation.

A method that was widely used in the past is *electrospraying*. A solution of the nuclide to be deposited is prepared in a volatile, nonconducting liquid like acetone, alcohol, and others. A capillary is drawn out to a fine point such that no liquid can escape under normal conditions and filled with the solution. A fine wire is threaded though the capillary to within a few millimeters of the tip. A high voltage (3 to −10 kV) is applied between the wire in the tube and the backing material on which the deposit is to be made. One gets a spray of charged drops that are collected on the backing material, placed ∼1 cm from the capillary. The volatile solvent evaporates leaving a uniform film. This technique is widely used to introduce organic and biological samples into mass spectrometers. The deposit can then be calcined.

Another widely used technique for preparing thin deposits on a backing material is *electrodeposition*. Two types of electrodeposition are commonly used: (a) the direct deposit of a metal on a cathodic surface by reduction and (b) precipitation of a cationic species in an insoluble form on an electrode. This latter technique is widely used to deposit actinides and lanthanides. A 10–100 μL aqueous solution of the actinide or lanthanide is mixed with ∼15 mL of isopropyl alcohol and placed in a plating cell as indicated in Figure 19.1. The inorganic material forms a positively charged complex in which the inorganic molecule is surrounded by a cluster of solvent molecules. A large voltage (∼600 V) is applied between a rotating anode and the cathodic backing material. The positively charged complex is attracted to the cathode of the cell. The lanthanides and/or actinides precipitate as hydrous oxides near the cathode, which is a region of high pH. The alcohol is withdrawn from the cell and the deposit is dried and calcined. This technique is called *molecular plating* because the film is not that of the metal but some molecular form of it. Deposit thicknesses are restricted to <0.5 mg/cm^2, but the deposition is rapid
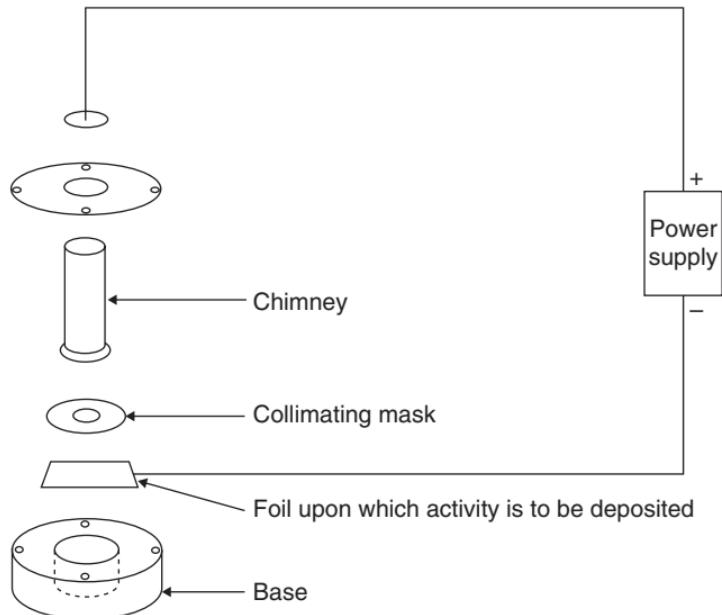
Figure 19.1 Schematic diagram of molecular plating cell (Wang et al. (1975). Reproduced with the permission of Prentice-Hall, Englewood Cliffs).

and quantitative and allows the use of active metals such as Al as backing foils (Parker and Slatis, 1966).

Vacuum deposition is a well established technique for making very uniform deposits of non-refractory materials on a backing material. Figure 19.2 shows a typical simple evaporation apparatus. The material to be evaporated is placed in a sample holder. Frequently these sample holders are just indented strips of W, Ta, or Mo, or wire baskets of the same metals, or carbon crucibles. These sample holders can be heated resistively by passing a large current through them, thus melting and then volatilizing the material while the heavy metal strips remain solid. Alternatively the sample holder can be bombarded by low-energy electrons to heat the sample. The entire process takes place in vacuum. Without the presence of air, most materials can be melted and the liquid evaporated. The substrate on which the vapors from the heated sample are condensed is placed some distance (often short) from the source of evaporating material. The distance generally depends on the expense of the target material and the required uniformity of the deposit. The area of the deposit may be defined (restricted) by collimators. The deposits produced by vacuum evaporation can be very uniform, but the process is not efficient, with <1% of the sample material being deposited in typical applications. Self-supporting deposits can be prepared if the substrate on which the vapors condense is coated with a release
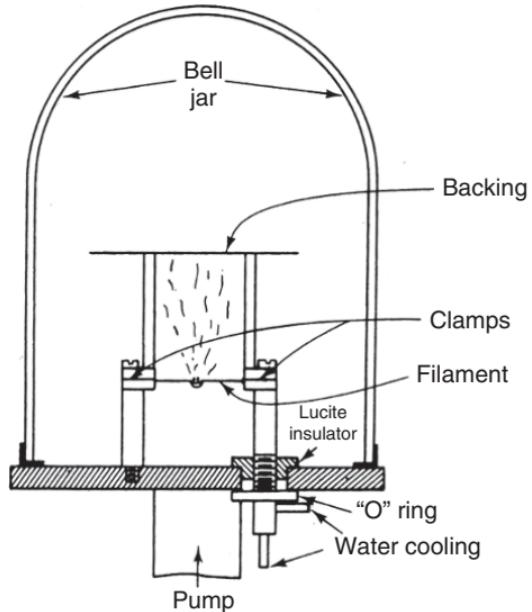
Figure 19.2 Simple schematic diagram of a vacuum deposition apparatus in a glass bell jar (Wang et al. (1975). Reproduced with the permission of Prentice-Hall, Englewood Cliffs).

agent prior to evaporation or can be removed chemically after the deposit is formed.

The thicknesses of these thin targets can be measured using a variety of techniques. The simplest and most reliable method is weighing. One weighs a known area of target material and computes its areal density. Such a technique will give the average deposit thickness but no information about its uniformity or composition. The most accurate measurements are destructive in that a well-defined area is punched out of the target for weighing. The uniformity of targets or thin foils can be measured with α-particle thickness gauges. In such devices, a collimated beam of α-particles (usually from a radioactive source) passes through the foil whose thickness is to be measured. Changes in count rate are noted as the beam scans over the area of the target or foil. To get absolute thicknesses from such devices, calibration with foils of known thickness is needed. This technique works best when the energy of the α-particle is so low that it barely pass through the foil. In this case, small changes in thickness are magnified in the observed count rate. X-ray fluorescence or neutron activation analysis can be used to determine the elemental composition of the target or source material. Approximate values of the target thicknesses can also be obtained by noting the energy loss of monoenergetic ions (or even α particles) as they pass through a foil. The thicknesses are calculated from the observed dE/dx and empirical stopping power relationships.

19.5 Measuring Beam Intensity and Fluxes

Measurement of charged-particle beam intensities is largely done using physical methods, although some older radiochemical methods are used occasionally. The most common technique to measure the intensity of a charged-particle beam is to use a *Faraday cup*. The Faraday cup has to be thick enough to full stop the beam and should be shielded so that any secondary or backscattered electrons do not leave the cup as shown in Figure 19.3. The collected charge is measured with an electrometer that functions as a current integrator. The beam intensity is just the current divided by the charge on each ion. Care must be taken regarding the loss of secondary electrons since an energetic beam will liberate secondary electrons in the material in which it stops. If these electrons escape, their positive ion partners will add to the positive charges of the stopped positive ions, thus causing an overestimate of the beam current and vice versa for an electron beam. The Faraday cup is thus made as a long cylinder to inhibit electron escape geometrically, and a magnetic or electric field can be applied to the cup along with a suppressing voltage to further prevent electron loss.

When the energy of the charged-particle beam is too high to easily stop the beam in a Faraday cup, the beam intensity is frequently monitored by a secondary ionization chamber. These ion chambers have thin entrance and exit windows and measure the differential energy loss when the beam traverses them. They must be calibrated to give absolute beam intensities. Alternatively, one can use a secondary emission chamber that simply has several metal foils
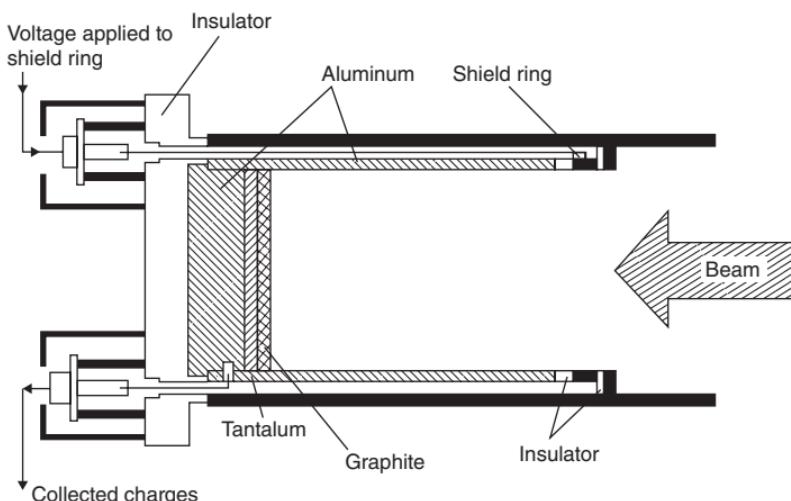
Figure 19.3 Schematic diagram of a shielded Faraday cup to measure the electrical current from a beam of heavy-ions (LeFort (1968). Reproduced with the permission of Van Nostrand).

and one measures the induced current due to the secondary electrons kicked out of the foils by the beam. These devices must also be calibrated in some way. If the charged-particle beam intensity is relatively low ($<10^6$ particles/s), then individual particles can be counted in a plastic scintillator detector mounted on a photomultiplier tube.

When performing irradiations with neutrons or high-energy protons, it is common to measure the beam intensity using a *monitor reaction*. A thin foil of a pure element is placed in the irradiating flux near the target and irradiated simultaneously with the target. Then both the reaction products from the target foil and the monitor foil are collected and counted. The flux is calculated using the previously known cross section for the monitor reaction.

Assuming that the monitor and target foils are exposed to the same irradiating flux, we have, for the activity of the monitor and target foils, A_{mon} and A_{tgt}, respectively, at the end of the irradiation one calculates

$$A_{tgt} = N_r \sigma_r \phi (1 - e^{-\lambda_r t}) \tag{19.5}$$

$$A_{mon} = N_m \sigma_m \phi (1 - e^{-\lambda_m t}) \tag{19.6}$$

where N_i, σ_i, and λ_i are the number of target atoms, cross section, and product decay constant, respectively, for the *i*th reaction. The cross section for the reaction of interest, σ_r, is, of course,

$$\sigma_r = \frac{A_{tgt}}{N_r \phi (1 - e^{-\lambda_r t})} \tag{19.7}$$

Substituting for ϕ in terms of the monitor reaction parameters, we get

$$\sigma_r = \frac{A_{tgt}}{A_{mon}} \times \frac{N_r}{N_m} \times \frac{(1 - e^{-\lambda_m t})}{(1 - e^{-\lambda_r t})} \times \sigma_m \tag{19.8}$$

If the irradiation is long enough to produce saturation activities in *both* the target and monitor foils, we get the slightly simpler formula,

$$\sigma_r = \frac{A_{tgt}}{A_{mon}} \times \frac{N_r}{N_m} \times \sigma_m \tag{19.9}$$

The typical monitor reactions for high-energy protons are $^{27}Al \rightarrow {}^{24}Na$, $^{27}Al \rightarrow {}^{22}Na$, $^{12}C \rightarrow {}^{7}Be$, $^{27}Al \rightarrow {}^{18}F$, $^{197}Au \rightarrow {}^{149}Tb$, and $^{12}C(p, pn)^{11}C$ where the arrows indicate a (possibly) complex set of reaction paths leading from the initial nucleus to the product nucleus. Care must be taken in the case of reactions producing ^{24}Na or ^{11}C to correct for secondary neutron-induced reactions that produce these nuclides. In high-energy reactions, the loss of recoils from the monitor or target foils can be corrected for by irradiating a stack of three identical foils and only counting the center foil. The forward-going recoils from the first foil enter the second foil and compensate

for its forward recoil loss. The backward recoils from the third foil enter the second foil and compensate for its backward recoil loss.

The measurement of neutron fluxes by foil activation is more complicated because the neutrons are not monoenergetic and the monitor cross sections are usually energy dependent. The simplest case is monitoring slow neutron fluxes. Radiative capture (n, γ) reactions have their largest cross sections at thermal energies and are thus used in slow neutron monitors. Typical slow neutron activation detectors are Mn, Co, Cu, Ag, In, Dy, and Au. Each of these elements has one or more odd A isotopes with a large thermal (n, γ) cross section, 1–2000 barns. The (n, γ) reaction products should have half-lives ranging from minutes to hours. The activation cross sections generally vary as $1/v$ although some nuclides have resonances in the capture cross sections for neutrons with energies between 1 and 1000 eV. A correction for such resonance capture can be made by irradiating the monitor foils with and without a Cd cover. The (n, γ) cross section for Cd below 0.4 eV is very large and is small for energies above this and thus very few low-energy neutrons penetrate the Cd cover. Irradiation of a foil without a Cd cover will cause reactions induced by both thermal and resonance neutrons, while the Cd-covered foil will just respond to resonance neutrons.

One can also use so-called "threshold monitor detectors" where the activating reaction has an energy threshold, such as the (n, α) , (n, p), and (n, 2n) reactions. By exposing a set of threshold detectors (involving different reactions with different thresholds) to a neutron flux, one can determine the relative amounts of different energy groups in the neutron spectrum. Further information about the use of activation detectors to measure neutron fluxes can be found in the textbooks by Knoll (2010) and Tsoulfanidis and Landsberger (2015).

19.6 Recoils, Evaporation Residues, and Heavy Residues

In a nuclear reaction, the momentum transfer to the struck nucleus is not negligible. If an $A = 100$ nucleus fuses completely with a 100 MeV α-particle projectile, the kinetic energy of the completely fused system is ∼4 MeV. A similar fusion of an $A = 100$ nucleus with a 100 MeV ^{16}O projectile will give the completely fused system an energy of 13.8 MeV. These energies are extremely large compared with chemical bond energies. Depending upon the position in the target foil where the nuclear reaction takes place, some or all of these recoiling nuclei may escape from the target foil. These recoil nuclei, which are usually radioactive, can be collected or studied using physical or radiochemical techniques. In reactor irradiations, the recoil energy from the capture of a

low-energy neutron is small relative to that in the charged-particle reactions but still substantial relative to chemical bonds, and the recoils often produce "contamination" on the inner surfaces of irradiation containers.

When these heavy recoil nuclei are the result of a complete fusion of the projectile and target nuclei, they are usually called evaporation residues (EVRs) because they result from the de-excitation of the primary complete fusion product by particle evaporation (emission). In intermediate energy and relativistic nuclear collisions, the momentum transfer to the target nucleus is much smaller and the energy of the recoiling nucleus is ~5–100 keV/nucleon. Such recoils are usually called heavy residues. It should be noted that in this discussion we are tacitly assuming "normal" or "forward" reaction kinematics with the lighter nucleus being the projectile (i.e., in motion before the collision) and the heavier collision partner being at rest in the laboratory system, In reactions studied using "inverse kinematics" with a heavier projectile striking a lighter target nucleus, the momentum of the recoiling heavy nucleus is approximately the same as that of the projectile nucleus. In inverse kinematics reactions, the energies of the EVRs or heavy residues are large, and their spatial and energy distribution is compressed accordingly. Collection of these recoils is relatively easy, but high resolution is needed for detailed measurements of their properties because of the spatial and energy compression.

There are a variety of ways to collect the recoiling heavy products of a nuclear reaction. One radiochemical technique is the so-called thick-target–thick-catcher method. Here a target foil whose thickness exceeds the average range of the recoils is surrounded by catcher foils of C or Al or some other material whose thickness exceeds the range of the recoiling product nucleus that cannot produce the nuclide of interest. The average range of the recoiling product, $\langle R \rangle$, which can be related to its total kinetic energy, is given as

$$\langle R \rangle = \frac{N_\text{C} W}{N_\text{C} + N_\text{W}} \tag{19.10}$$

where N_C is the number of recoils that escape from the target, N_W is the number that remains in the target, and W is the thickness of the target. The fraction of product nuclei that recoil into the forward catcher foil, F, and the fraction that recoil into the backward catcher foil, B, can be used to deduce something about the relative velocity imparted to the recoiling nucleus by the initial projectile–target interaction, v, followed by an isotropic velocity kick, V, given to it by successive momentum kicks by sequential particle emission. Formally we define the quantity η where $\eta = v/V$. The value of η is related to F and B through the expression

$$\eta = \frac{(F/B)^{1/2} - 1}{(F/B)^{1/2} + 1} \tag{19.11}$$

So the thick-target–thick-catcher method can provide some information on the kinematics of the nuclear reaction under study (Harvey, 1960). This technique has been used to advantage in the study of intermediate energy and relativistic nuclear collisions where the energy of the heavy residues is low (∼10–100 keV/nucleon). In this case, most of the residues stop in the target foil and cannot be studied any other way.

For the study of recoils in low-energy and some intermediate energy reactions, one can use a thin target (e.g., <0.5 mg/cm^2). The energy loss of the recoils in emerging from such thin targets is negligible or calculable and manageable. With thin-target irradiations, one can stop the recoiling nuclei in a catcher foil, which can be counted separately, perhaps after intervening chemical separations to isolate the products of interest. The "catcher foil" can take the form of a tape or rotating wheel that can rapidly transport the activity to a remote, low background location for counting. Alternatively, the "catcher foil" can take the form of a stack of thin foils that stop the products. These foils, upon disassembly and counting, can be used to construct a differential range distribution for products of interest. Catcher foils or stacks of foils can be mounted at various angles with respect to the incident beam and can be used to measure product angular or energy distributions. These catcher foil techniques are now only used to study reactions with very low cross sections where their use provides a high detection sensitivity.

The "catcher foil" can take the form of a jet of rapidly moving gas, a helium jet. The atoms produced in a nuclear reaction recoil out of a thin target and are stopped in 1 atm of helium gas in the target chamber. The gas contains an aerosol, typically an alkali halide, to which charged reaction product recoils attach themselves via van der Waals forces. The helium gas (and the aerosol particles) escapes through a small orifice to a vacuum chamber, with the gas achieving sonic velocity. The gas and aerosol can be transported for substantial distances in thin capillary tubes. The aerosol particles (and the attached atoms) are collected by allowing the gas stream to strike a collector surface. The resulting deposit can be counted directly or dissolved for further chemical processing. Note that the aerosol-loaded gas stream (jet) can also be used to transport the atoms through a thin capillary a distance of several meters in a few seconds. If the carrier gas is extremely pure helium gas, then the residues will remain ionized and can be collected using electrostatic devices. Alternatively the aerosol particles can be directed into a plasma ion source and disintegrated. The released activity can be skimmed off provided in a low-energy ion beam. An interesting version of these gas jet systems use carbon clusters as the aerosol particles. The carbon can be burned in an ion source and provide a very clean source of ions. More recent versions of the gas jet system involve thermalizing the recoils or reaction products in pure helium gas without any aerosols. The reaction products remain ionized in ultra pure helium and can be collected using electrodes while the neutral carrier gas is pumped away.

The principal limitation of the isolation devices discussed previously (tapes, jets, etc.) is that the reaction product must be stopped and mechanically transported to radiation detectors before product identification can occur. This restricts their use to studies of nuclei whose $t_{1/2}$ is greater than a few ms. For detection and identification of species whose $t_{1/2}$ is less than a few ms, one needs to use instruments that use direct collection and separation using magnetic and/or electrostatic deflection of target recoils. The most spectacularly successful of these devices is probably the velocity filter SHIP (Fig. 14.8). EVRs produced in compound nucleus reactions emerge from the target and pass through a thin carbon foil, which has the effect of equilibrating the ionic charge distribution of the residues. The ions then pass through two filter stages consisting of electric deflectors, dipole magnets, and a quadruple triplet for focusing. The solid angle of acceptance of the separator is 2.7 msr with a separation time for the reaction products of ~2 μs with a total efficiency of collecting EVRs of ~20% for $A_{\text{proj}} > 40$. Since complete fusion of EVRs have very different velocities and angular distributions compared to target-like transfer and deep inelastic products (a factor of ~2 difference in velocity between transfer products and EVRs) and beam nuclei, the separator with its ±5% velocity acceptance range and narrow angular acceptance very effectively separates the EVRs from the other reaction products and the beam. Following separation, the residues pass through a large area time-of-flight detector and are stopped in an array of position-sensitive detectors. From their time of flight and the energy deposited as they stop in the position-sensitive detectors, a rough estimate of their mass may be obtained ($dA/A \sim 0.01$). The final genetic identification of the residues is made by recording the time correlations between the original position signals from the detectors and subsequent decay signals from the same location (due to α or spontaneous fission decay) and/or signals from γ- or X-ray detectors placed next to the position-sensitive detector. This device for studying heavy element EVRs was used in the discovery of elements 107–112 (Chapter 14).

An alternate method of recoil collection and separation from other reaction products is the gas-filled separator. Unlike the vacuum separators SHIP at GSI or the fragment mass analyzer at ANL that can only accept a limited range of charge-to-mass ratios, a gas-filled separator is a magnetic separator that is filled with a low pressure (~1 Torr) gas (usually H or He). EVRs emerging from the target undergo charge changing collisions in the gas and quickly equilibrate to a common average charge state. The change in recoil charge states with gas pressure in a gas-filled magnet is shown in Figure 19.4. At a pressure of ~1 Torr, the recoils have a common average charge state. This charge state will differ depending on the charge of the projectile nuclei or other reaction products. This charge equilibration allows very efficient collection of the recoils but with a loss of the detailed mass selection obtained in vacuum separators like SHIP that use both electric and magnetic fields for separation. The appropriate magnetic
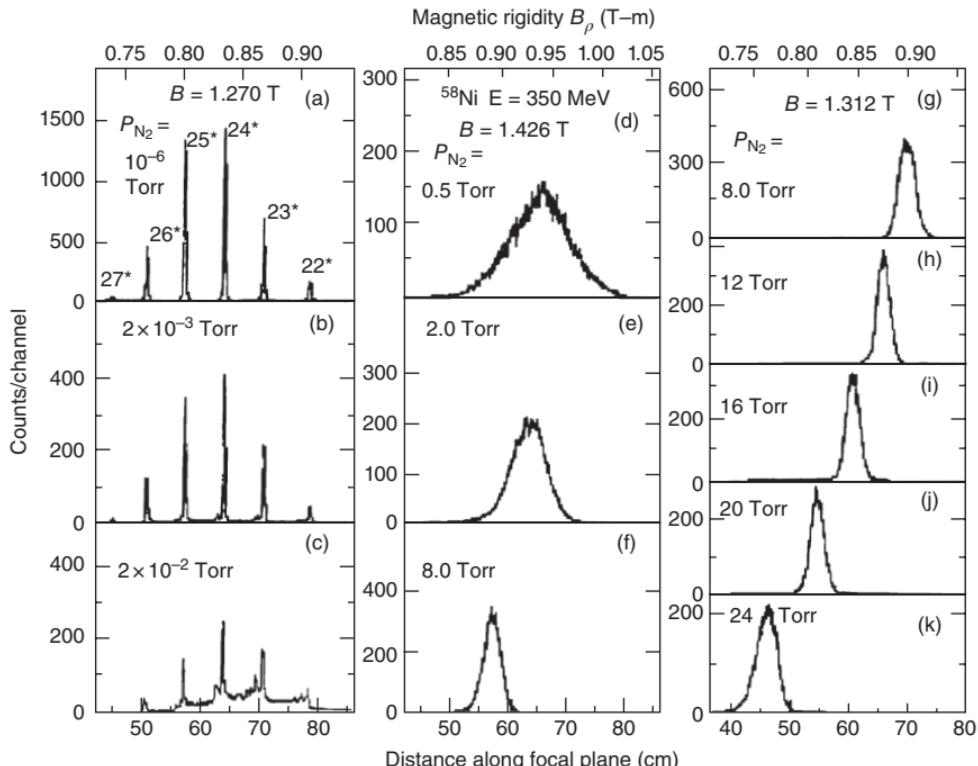
Figure 19.4 Changes in focal plane distributions in a gas-filled magnet for the reaction involving 350 MeV ^{58}Ni ions reacting with a Au target are shown as a function of gas pressure (Paul (1989). Reproduced with the permission of Elsevier).

rigidity to collect a given product nuclide with a gas-filled separator can be roughly described by the simple formula:

$$B\rho = \frac{mv}{q_{avg}} \approx \frac{mv}{(v/v_0)eZ^{1/3}} = \frac{0.0227\,A}{Z^{1/3}}\,Tm \tag{19.12}$$

where m, Z, and v are the mass, atomic number, and velocity of the recoiling ion, respectively, and v_0 is the Bohr velocity, 2.18×10^6 m/s. (In reality, q_{avg} is a sensitive function of the atomic structure of the recoiling ion and the gas (Ghiorso et al., 1988). The magnetic rigidity is proportional to the recoil velocity so that recoils of the same charge and velocity are focused. The primary beam is separated from the recoils right after the target by a dipole bending magnet followed by two quadrupole magnets that focus the beam onto the focal plane. For the study of heavy element production reactions, collection efficiencies of 25–50% can be achieved.
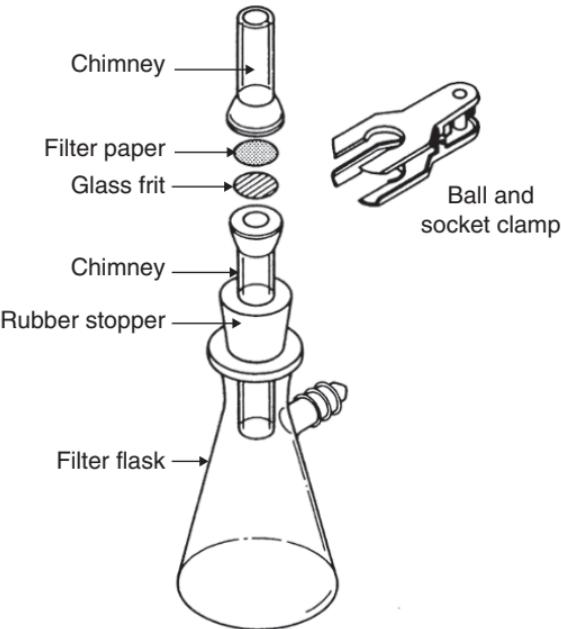
19.7 Radiochemical Separation Techniques

In the study of nuclear reactions, nuclear structure, and the heaviest elements, one frequently needs to chemically separate the nuclide(s) of interest from other radioactive species that are present. This is done by performing radiochemical separations that involve the conventional separation techniques of analytical chemistry adapted to the special needs of radiochemistry. For example, radiochemical purity is generally more important than chemical purity. When dealing with short-lived nuclides, speed may be more important than yield or purity. The high cost of remediating radioactive waste may require unusual waste minimization steps. As noted earlier, radiochemical separations need not be quantitative. One only needs to know the yield. With the availability of modern high resolution counting equipment, such as Ge γ-ray spectrometers, modern radiochemical separations frequently are designed only to reduce the level of radioactive impurities in the sample rather than producing an extremely pure sample. (The counting instrumentation is used to "isolate" the nuclide(s) of interest from other nuclides.) Thus, modern procedures sometimes are similar to qualitative analysis schemes, breaking products into chemically similar groups and using instrumentation to further separate the group members. A review summarizes some developments of relevance to radiochemistry (Bond et al., 1999). There are compilations of the best procedures to isolate and count every radioelement (http://library.lanl.gov/radiochemistry/elements.htm) along with textbooks that give general summaries of the relevant radiochemistry (Lehto and Hou, 2011).

19.7.1 Precipitation

The oldest, most well-established chemical separation technique is *precipitation*. Because the amount of the radionuclide present may be very small, carriers are frequently used, as discussed earlier. The carrier is added in macroscopic quantities and insures the radioactive species will be part of a kinetic and thermodynamic equilibrium system. Recovery of the carrier also serves as a measure of the yield of the separation. It is important that there is an isotopic exchange between the carrier and the radionuclide. There is the related phenomenon of *coprecipitation* wherein the radionuclide is incorporated into or adsorbed on the surface of a precipitate that does not involve an isotope of the radionuclide or isomorphously replaces one of the elements in the precipitate. Examples of this behavior are the sorption of radionuclides by $Fe(OH)_3$ or the coprecipitation of the actinides with LaF_3. Separation by precipitation is largely restricted to laboratory procedures and, apart from the bismuth phosphate process used in WWII to purify Pu, has little commercial application.

Figure 19.5 Schematic diagram of a filtration apparatus used in radiochemistry (Wang et al. (1975). Reproduced with the permission of Prentice-Hall, Englewood Cliffs).

As a practical matter, precipitation is usually carried out in hot, dilute aqueous solutions to allow the slow formation of large crystals. The pH of the solution is chosen to minimize colloid formation. After precipitation, the precipitate is washed carefully to remove impurities, dissolved, and re-precipitated to cause further purification. The precipitate is collected by filtration, as indicated in Figure 19.5. The filter paper is supported by a glass frit clamped between two glass tubes. The precipitate is washed finally with acetone or alcohol to dry it. The precipitate is chosen to have a known stoichiometry to allow calculation of the yield of the separation and should not absorb water or CO_2 so that an accurate weight can be obtained. The filter paper used in the filtration must be treated with all the reagents beforehand, dried, and weighed so that any material loss in filtration is minimized.

19.7.2 Solvent Extraction

Separation by liquid–liquid extraction (solvent extraction) has played an important role in radiochemical separations. Ether extraction of uranium was used in early weapons development, and the use of tributyl phosphate (TBP) as an extractant for U and Pu was recognized in 1946, resulting in the commercial PUREX process for reprocessing spent reactor fuel (see Chapter 15). In recent years, there has been a good deal of development of solvent extraction processes for the removal of the transuranic elements, ^{90}Sr and ^{137}Cs from acidic high-level waste. Laboratory demonstrations of the TRUEX process that uses the neutral extractant
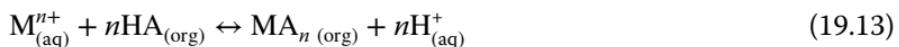
octyl(phenyl)-*N*,*N*-diisobutylcarbamoyl-methylphosphine oxide (CMPO) to separate the transuranium elements from acidic high-level waste have been successful. More recently crown ethers have been used as specific extractants for Sr and Cs.

In solvent extraction, the species to be separated is transferred between two immiscible or partially miscible phases, such as water and a nonpolar organic phase. To achieve sufficient solubility in the organic phase, the species must be in the form of a neutral, non-hydrated species. The transfer between phases is achieved by selectively complexing the species of interest causing its solubility in water to decrease with a concomitant increase in its solubility in the organic phase.

A hydrated metal ion (M^{q+}) will always prefer the aqueous phase to the organic phase. To get the metal ion to extract, some or all of the inner hydration sphere must be removed. The resulting complex must be electrically neutral and organophilic, that is, have an organic "surface" that interacts with the organic solvent. This can be done by:

1) Forming a neutral complex MA_Z by coordination with organic anions A^-
2) Replacing water in the inner coordination sphere by large organic molecules B such that one forms MB_N^{q+}, which is extracted into the organic phase as an ion association complex $(MB_N)^{q+}L_X^{q-}$
3) Forming metal complexes of the form ML_N^{q-N} with ligands (L^-) such that they combine with large organic cations RB^+ to form ion pair complexes $(RB^+)_{N-q}(ML_N)^{N-q}$

The extracting agents are thus divided into three classes: polydentate organic anions A^-, neutral organic molecules B, or large organic cations RB^+. Polydentate organic anions, which form chelates (ring structures of 4–7 atoms), are important extracting agents. Among these are the β-diketonates, such as acetylacetonate, the pyrazolones, benzoylacetonate, and thenoyltrifluoroacetone (TTA), with the extraction increasing strongly through this sequence. Representing the organic chelating agent as HA, the overall reaction involved in the chelate extraction of a metal ion, M^{n+}, is

$$M^{n+}_{(aq)} + nHA_{(org)} \leftrightarrow MA_{n\ (org)} + nH^+_{(aq)} \tag{19.13}$$

When an aqueous solution containing extractable metal ions is brought into contact with an organic phase containing chelating agent, the chelating agent dissolves in the water phase, ionizes, and complexes the metal ion, and the metal chelate dissolves in the organic phase. The low solubility of the metal complexes and their slow rates of formation limit the industrial use of this type of anionic extraction.

However, a number of organophosphorus compounds are efficient extractants as they and their complexes are very soluble in organic solvents. The most important of these are monobasic diethylhexylphosphoric acid (HDEHP) and
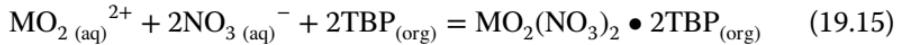
dibutylphosphoric acid (HDBP). The actinide MO_2^{2+} ions are very effectively extracted by these reagents as are the actinide (IV) ions.

Among the *neutral extractants*, alcohols, ethers, and ketones have been used extensively. The most famous example of these is the extraction of uranyl nitrate into diethyl ether, the process used in the Manhattan Project to purify the uranium used in the first reactors. In one of the early large-scale processes (the redox process) to recover uranium and plutonium from irradiated fuel, methyl isobutyl ketone was used to extract the actinides as nitrates.

The most widely used neutral extractants, however, are the organophosphorus compounds, of which the ester, tributylphosphate (TBP), is the most important. TBP forms complexes with the actinide elements thorium, uranium, neptunium, and plutonium by bonding to the central metal atom via the phosphoryl oxygen in the structure

$$(C_4H_9O)_3P^+O^- \tag{19.14}$$

The overall reactions are

$$MO_{2\ (aq)}^{\ 2+} + 2NO_{3\ (aq)}^{\ -} + 2TBP_{(org)} = MO_2(NO_3)_2 \bullet 2TBP_{(org)} \tag{19.15}$$

or

$$M_{(aq)}^{\ 4+} + 4NO_{3\ (aq)}^{\ -} + 2TBP_{(org)} = M(NO_3)_4 \bullet 2TBP_{(org)} \tag{19.16}$$
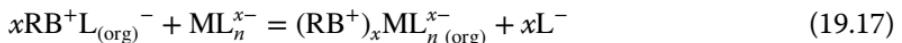
These equilibria can be shifted to the right, increasing the degree of extraction by increasing the concentration of uncombined TBP in the organic phase or by increasing the concentration of the aqueous nitrate anion. The latter increase is achieved by adding a salting agent such as HNO_3 or $Al(NO_3)_3$. These extraction equilibria are the basis of the PUREX process, used almost exclusively in all modern reprocessing of spent nuclear fuel.

A third group of extractants, called *cationic extractants*, are amines, especially tertiary or quarternary amines. These strong bases form complexes with actinide metal cations. The efficiency of the extraction is improved when the alkyl groups have long carbon chains, such as trioctylamine or triisooctylamine. The extraction is conventionally thought of as a "liquid anion exchange" in that the reaction for metal extraction can be written as an anion exchange, that is,

$$xRB^+L_{(org)}^{\ -} + ML_n^{x-} = (RB^+)_xML_{n\ (org)}^{x-} + xL^- \tag{19.17}$$

where ML_n^{x-} is the metal anion complex being extracted and RB^+ is the ammonium salt of the amine. Hexavalent and tetravalent actinides are efficiently extracted using this technique while trivalent actinides are not well extracted under ordinary conditions.

As a practical matter, the distribution ratio D is defined as

$$D = \frac{[M]_{org}}{[M]_{aq}} \tag{19.18}$$

where $[M]_i$ is the metal ion concentration in the ith phase. The relevant equilibria, for example, to describe the extraction in systems of lipophilic acidic chelating agents are

$$HL_{(org)} = HL_{(aq)} \tag{19.19}$$

$$HL_{(aq)} = H_{(aq)}^+ + L_{(aq)}^- \tag{19.20}$$

$$M_{(aq)}^{3+} + 3HL_{(org)} = (ML_3)_{(org)} + 3H_{(aq)}^+ \tag{19.21}$$

where K_{Eq3} is the equilibrium constant for the last reaction. The distribution coefficient D can be written as

$$D = \frac{[ML_{3\,(org)}]}{[M_{(aq)}^{3+}]} = \frac{K_{Eq\,3}[HL_{(org)}]^3}{[H_{(aq)}^+]^3} \tag{19.22}$$

If one introduces a water soluble complexing anion, X^-, into the system, the $[M_{(aq)}^{3+}]$ should be replaced by $[M^{3+}] + [MX^{2+}] + [MX_2^+] + \cdots$, and the measured distribution ratio will include these species as well. The separation factor between two ions, S, is given by the ratio of their distribution coefficients,

$$S = \frac{D_A}{D_B} \tag{19.23}$$

Thus, the most effective separations will involve cases where the target ion interacts strongly with the extractant but is less strongly complexed by the aqueous ligand X. The percent extraction is given by

$$\% \text{ Extraction} = \frac{100D}{D + (V_{aq}/V_{org})} \tag{19.24}$$

where V_i is the volume of the ith phase.

19.7.3 Ion Exchange

Ion exchange is one of the most popular radiochemical separation techniques due to its high selectivity coupled with the ability to rapidly perform separations. In ion exchange, a solution containing the ions to be separated is brought into contact with a synthetic organic resin containing specific functional groups that selectively bind the ions in question. In a later step the ions of interest can be removed from the resin by elution with another suitable solution that differs from the initial solution. Typically the solution containing the ions is run through a column packed with resin beads. The resins are typically cross-linked polystyrenes with attached functional groups. Most cation exchangers (such as Dowex 50) contain free sulfonic acid groups, SO_3H, where the cation displaces the hydrogen ion. Anion exchangers (such as Dowex 1) contain quaternary amine groups, such as $CH_2N(CH_3)_3Cl$ where the anion replaces the chloride

ion. The resin particles have diameters of 0.08–0.16 mm and exchange capacities of 3–5 mEq/g of dry resin.

It is common to absorb a group of ions on the column material and then selectively elute them. Complexing agents, which form complexes of varying solubility with the absorbed ions, are used as eluants. A competition between the complexing agent and the resin for each ion occurs, and each ion will be exchanged between the resin and the complexing agent several times as it moves down the column. This is akin to a distillation process. The rates at which the different ions move down the column vary, causing a spatial separation between "bands" of different ions. The ions can be collected separately in successive eluant fractions (see Fig. 19.6).

The most widely cited application of ion exchange techniques is the separation of the rare earths or actinides from one another. This is done with cation exchange using a complexing agent of α-hydroxyisobutyric acid ("α-but"). The order of elution of the ions from a cation exchange column is generally in order
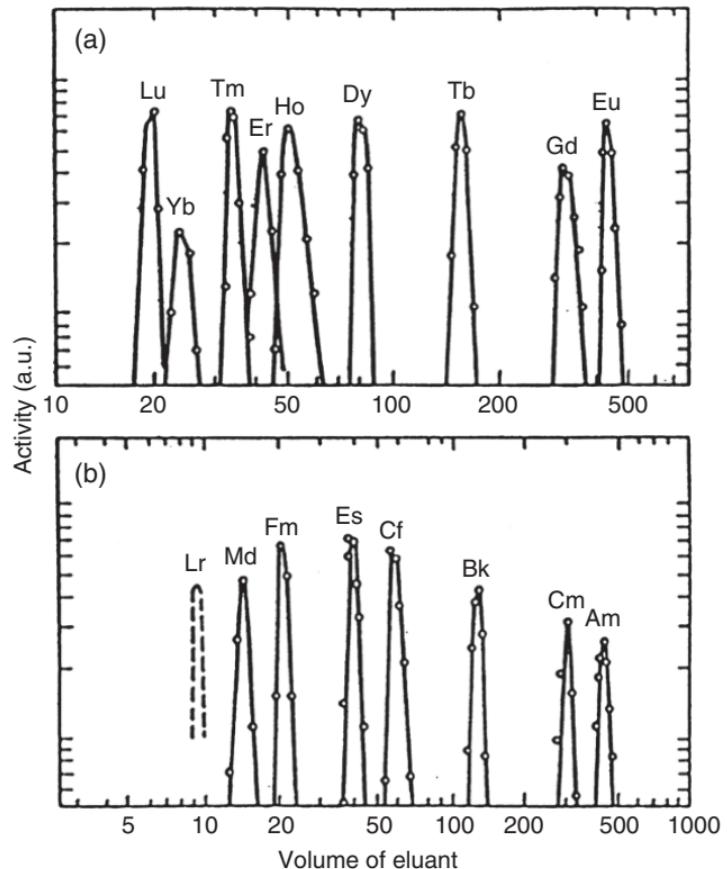
Figure 19.6 Example of the elution of tripositive lanthanide (a) and actinide (b) ions from a Dowex-50-filled column.

of the radii of the hydrated ions with the largest hydrated ions leaving first; thus lawrencium elutes first and americium last among the tri-positive actinide ions. As seen in the data shown in Figure 19.6, the separation between adjacent cations and the order of elution is derived from the comparative stability of the aqueous actinide or lanthanide complexes with α-hydroxyisobutyrate. Figure 19.6 also shows a strikingly analogous behavior in the elution of the actinides and lanthanides that allowed chemists to prove the identity of new elements in the discovery of elements 97–102 (Bk–No). For cation exchange, the strength of absorption goes as $M^{4+} > M^{3+} > MO_2^{2+} > M^{2+} > MO_2^+$.

The anion exchange behavior of various elements has been extensively studied. For example, consider the system of Dowex 1 resin with an HCl eluant. Typical distribution ratios for various elements as a function of $[Cl^-]$ are shown in Figure 19.7. Note that groups 1, 2, and 3 are not absorbed on the column. One usually sees a rise in the distribution coefficient D until a maximum is reached and then D decreases gradually with further increases in $[Cl^-]$. The maximum occurs when the number of ligands bonding to the metal atom equals the initial charge on the ion. The decrease in D continues with increasing eluant concentration due to free anions from the eluant competing with the metal complexes for ion exchange resin sites. Figure 19.7 and other data from similar measurements can be used to plan separations. For example, to separate Ni(II) and Co(II), one needs simply to pass a 12M HCl solution of the elements through a Dowex 1 column. The Co(II) will stick to the column, while the Ni(II) will not be absorbed. A mixture of Mn(II), Co(II), Cu(II), Fe(III), and Zn(II) can be separated after placement on a Dowex 1 column by eluting with 12 M HCl, followed by elutions of 6 M HCl (Mn), 4 M HCl (Co), 2.5 M HCl (Cu), 0.5 M HCl (Fe), and 0.005 M HCl (Zn).

In addition to the organic ion exchange resins, some inorganic ion exchanges, such as the zeolites, have been used. Inorganic ion exchange materials are used in situations where heat and radiation might preclude the use of organic resins although the establishment of equilibria may be slow.

Newer developments have emphasized the preparation of more selective resins. Among these are the chelating resins (such as Chelex 100) that contain functional groups that chelate metal ions. Typical functional groups include iminodiacetic acids, 8-hydroxyquinoline, or macrocyclic units such as the crown ethers, calixarenes, or cryptands. The bifunctional chelating ion exchange material, Diphonix resin—a substituted diphosphonic acid resin—shows promise in treating radioactive waste. Important newer resins include those with immobilized phosphorus ligands (Bond et al., 1999).

19.7.4 Extraction Chromatography

Extraction chromatography is an analytical separation technique that is closely related to solvent extraction. Extraction chromatography is a form of solvent
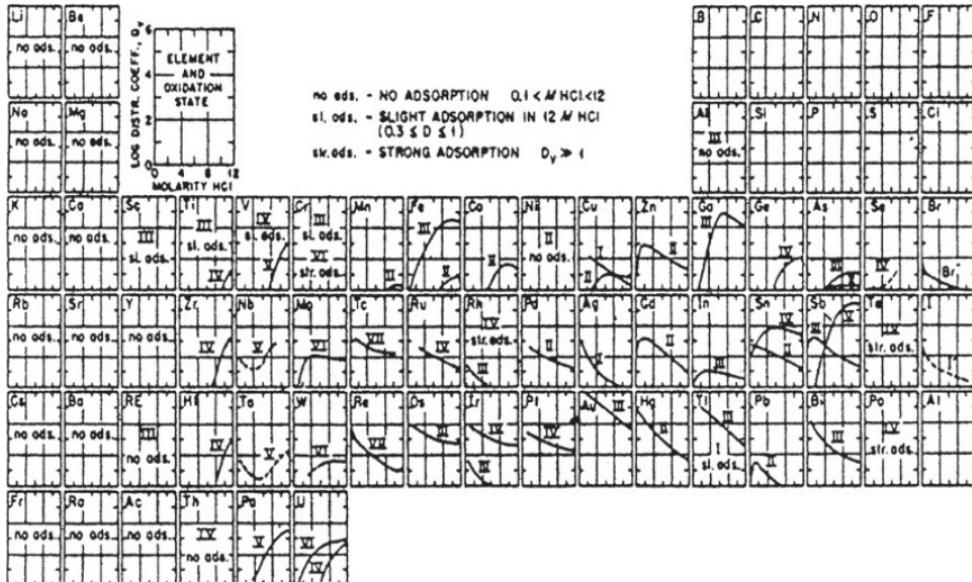
Figure 19.7 Elution curves of the elements from anion exchange resin (Kraus and Nelson (1956). Reproduced with the permission of Geneva Conference).

extraction where one of the liquid phases is made stationary by adsorption on a solid support. The other liquid phase is mobile. Either the aqueous or the organic phase can be made stationary. Extraction chromatography has the selectivity of solvent extraction and the multistage character of a chromatographic process. It is generally used for laboratory scale experiments although some attempts have been made to use it in larger-scale operations. The common applications involve the adsorption of an organic extractant onto a variety of inorganic substrates such as silica or alumina or organic substrates such as cellulose or styrene-divinyl benzene copolymers. When the stationary phase is organic, the technique is referred to as reversed-phase high-performance liquid chromatography. The stationary phase is used in a column just as in ion exchange chromatography. High pressure pumps are usually used to force the liquid phase through these columns, just as in conventional high-performance liquid chromatography.

The same extracting agents as used in solvent extraction can be used in extraction chromatography. Early applications of extraction chromatography have employed various traditional extractants such as the acidic organophosphorus compounds (di-(2-ethylhexyl) phosphoric acid, HDEHP) or TBP as extractants for the actinide elements. Recent advances have led to a variety of new solvent exchange extractants such as the crown ethers, cryptands, or bifunctional organophosphorus compounds. A particularly successful application is the selective sorption of actinides on TRU resins, involving solutions of carbamolymethylphosphoryl (CMPO) compounds in TBP sorbed on Amberlite XAD-7. This resin has found a number of applications in the isolation and subsequent determination of the actinides in complex matrices.

19.7.5 Rapid Radiochemical Separations

Many of the separation techniques we have described take hours to perform. Many interesting nuclei, such as the heavier actinides, the transactinides, or the light nuclei used in PET studies, have much shorter half-lives. Thus, we will briefly review the principles of rapid radiochemical separations (procedures that take seconds to minutes) and refer the reader to (Herrman and Trautman, 1982; Meyer, 1979; Schädel, 1988; Trautman, 1995) for details. In most chemical separation procedures, the goal is to selectively transfer the species of interest from one phase to another, leaving behind any unwanted species. The phase-to-phase transfer is rapid, but the procedures to place the species in the proper form for transfer to occur are slow. The goal of rapid radiochemical separations is to speed up existing chemical procedures or to use new, very fast chemical transformations.

Two procedures are commonly used for rapid radiochemical separations: the batch approach and the continuous approach. In the batch approach, the desired activities are produced in a short irradiation, separated, and counted

with the procedure being repeated many times to reduce the statistical uncertainty in the data. In the continuous approach, the production of the active species is carried out continuously, and the species is isolated and counted as produced.

One of the most widely used techniques for rapid chemical separation is that of gas chromatography, which has been developed for use with the transuranium elements by Zvara and coworkers (1972). In gas chromatography, volatile elements or compounds are separated from one another by their differences in distribution between a mobile gas phase and a stationary solid phase. Thermochromatography involves passing a gas through a column whose temperature decreases continuously with distance from the entrance. Thus the less volatile species condense on the column walls first with the more volatile species depositing last. Measurement of the migration times, the deposition temperature, the temperature gradient in the column, and others can allow one to deduce the molar enthalpy of absorption of the compound on the column material. This physical quantity can be compared to quantum chemical calculations of this quantity to gain insight into the bonding properties of the element in question. This technique was used to show the chemical properties (Düllmann et al., 2002; Eichler et al., 2000; Schadel et al., 1997) of the transactinides Rf to Hs and their behavior relative to their chemical congeners.

Another rapid chemical separation technique is separation by volatilization. There are a variety of volatile compounds that can be released from an irradiated material upon dissolution that can, with proper conditions, serve to rapidly chemically separate the elements involved. Examples of such volatile species include I_2, At, $GeCl_4$, $AsCl_3$, $SeCl_4$, OsO_4, RuO_4, Re_2O_7, Tc_2O_7, and others. Separation by volatilization has largely been used for the elements forming volatile hydrides, As, Se, Sn, Sb. and Te.

19.8 Low-Level Measurement Techniques

One of the areas in which the skills of radiochemists are used is the area of low-level chemistry and low-level counting. Areas as diverse as the detection of solar neutrinos or the study of environmental radioactivity involve low-level techniques. For example, even with increasing the concentration of the radiotracers of interest during sampling procedures in environmental studies, quite often one is left with a sample containing a small quantity <10 dpm of radioactivity that must be assayed. Such assays are referred to as *low-level techniques*. Let us begin our discussion of low-level techniques by considering any chemical manipulations of the sample that must be made prior to counting it. Understandably the fact of having activity levels <10 dpm puts severe restrictions on the nature of low-level chemistry. Among the requirements for *low-level chemistry* are a small constant blank, high chemical yields for all procedures,

high radiochemical purity for all reagents employed, and the ability to place the sample in suitable chemical form for counting.

19.8.1 Blanks

A *blank* in low-level chemistry is used to identify any contribution of the added reagents and other sample constituents to the activity being measured. The blank is determined by performing the chemical procedures without the radioactive sample being present. Care must be taken to ensure that the blank is properly measured and includes all possible contributions to the activity that would be encountered in a real system. For example, in the determination of fission product ^{144}Ce in seawater, the blank must be determined for each new bottle of reagents used due to the high variability of the ^{144}Ce content in chemical reagents.

Clearly one of the most effective ways of dealing with a blank correction is to reduce it to the lowest possible level. Among the factors contributing to the blank correction that can be reduced with care is *radiochemical contamination of analytical reagents used in chemical procedures*. DeVoe (1961) and Sugihara (1961) have written extensive review articles on this subject, and their work should be consulted for detailed information. Typical contamination of most reagents is in the range of ~10–100 ppm/g reagent, although individual reagents may contain activity levels of >10,000 ppm/g. Some especially troublesome reagents are rare earths (Ce salts in particular), chlorine, or sulfur-containing reagents that may contain ^{32}P contamination, cesium salts (which may contain ^{40}K or ^{87}Rb) and potassium salts, and other obvious offenders. Precipitating agents, such as tetraphenylborates and chloroplatinates, are also particularly pernicious with regard to contamination problems.

Airborne contamination is another possible contribution to the blank correction. Here one is chiefly dealing with sample contamination with the daughters of ^{222}Rn, which have half-lives in the 30–40 min range. Steps that can be taken to avoid this problem include eschewing the use of suction filtration in chemical procedures, prefiltering of room air, and use of radon traps.

Further lowering of the blank correction occurs when *non-isotopic carriers* in chemical procedures are used to replace inert carriers of the element of interest when it is difficult to obtain the inert carrier in a contamination-free condition. Obviously only clean glassware should be used, reagents should not be reused, and the laboratory should be kept in an immaculate condition. Separations that have high chemical yields and high radiochemical purity reduce the blanks.

19.8.2 Low-Level Counting: General Principles

Once the low-level radioactive sample has been collected and any chemical procedures carried out prior to counting, the sample is ready for counting. Because

of the extremely small disintegration rates generally encountered, special techniques, called *low-level counting*, must be used to assay the sample. We shall survey some of the highlights of this area, which has been the subject of many articles and monographs (Knoll, 2010).

What are the most important characteristics the detector must possess for low-level counting? The first general characteristic is one of stability. Low-level counting frequently requires counting periods of long duration; hence counter stability is quite important. If the sample count rate S (source + background) is only slightly larger than the background rate B, one's detector should be picked to maximize the ratio S^2/B, that is, provide a low background and a high efficiency. If the sample count rate is large with respect to background, one needs only to maximize S, that is, one can choose a high efficiency detector.

19.8.3 Low-Level Counting: Details

For *low-level* α-*particle counting*, the detector choice lies generally between a gas-filled ionization chamber and a semiconductor detector system. The former can have a counting efficiency of ~50% and a background of ~3–4 cpm, while the latter can have a background rate of ~0.5 cph and a detection efficiency that approaches 50%. The semiconductor detector is usually the detector of choice although large sample sizes may be better assayed with gas-filled ionization chambers. Background radiation is primarily due to α-emitting impurities in the counter, counter support material, and so on, plus the occurrence of cosmic ray-induced (n, α) reactions. Because of its Ra content, Al is not used in constructing α-spectrometers.

Low-level counting of "soft" radiation has its own techniques. The term *soft radiation counting* generally refers to detecting EC and low-energy β^- emitters where the self-absorption of the radiation in the sample is important. To solve this problem, one typically tries to incorporate the radionuclide to be counted into the detector itself. One typical method of assay is liquid scintillation counting, which is used to assay samples whose activity is >10 pCi. Typical liquid scintillation counter backgrounds can be as high as ~100 counts per minute (cpm), whereas special counters have been built with background rates of ~10 cpm or less. Liquid scintillation counting is a speedy, simple method of low-level counting. Another technique that has been used to count low-level soft radiation samples involves the use of gas-filled proportional counter. The sample to be counted is converted to gaseous form and added to the counter gas at a concentration of ~0.05 mol % or less. This method of low-level counting, although tedious and time consuming, allows one to assay samples whose activity is <0.5 pCi. Typical counter backgrounds are ~1–2 cpm with 100% counting efficiency for energies as low as ~10 eV.

The counting of tritium in water presents a special problem about which much has been written. Current methods for assay of tritium in water have

a range of 0.1–5000 tritium units (TU), which has the value of 7.2 dpm/L. The most desirable feature of a tritium measuring system is to be able to measure a large number of samples rapidly, simply, and cheaply as possible with an uncertainty of $\sim \pm 10\%$, or better. It is generally more important to assay 100 samples with an uncertainty of $\pm 10\%$ in a given period of time than to assay 10 samples with an uncertainty of $\pm 3\%$ in the same amount of time.

The basic feature of low-level β^- counting that distinguishes it from ordinary β^- counting is the use of an anticoincidence shield around the β^- detector volume. An anticoincidence shield is a single detector, or array of detectors that surround the primary detector. The output of the anticoincidence detector is fed to an anticoincidence circuit along with the output of the primary detector. When nuclear radiation passes through both detectors simultaneously, as in the case of a highly penetrating cosmic ray striking both detectors, no output is signaled by the anticoincidence circuit. When the anticoincidence circuit receives a signal only from the primary detector, an output signal is given. The net effect is that the anticoincidence shield detector "guards" or shields against exterior radiation background radiation entering the primary detector. Typical ring assemblies reduce the background rate in the primary counter by a factor of ~ 50. A well-designed guard ring will allow several different types of central counters to be inserted into it. Low background β^- counters constructed of especially pure materials with anticoincidence shields have exhibited background rates of ~ 1 cph with efficiencies of $\sim 50\%$.

Low-level counting of γ-ray emitters using solid scintillation counters is an extensively used technique. The most important consideration in low-level solid scintillation counting is to decrease the counter background. Typical contributions to a solid scintillation counter's background rate from various sources are listed in Table 19.4. Four factors can be seen to be the major

Table 19.4 Components of a NaI(Tl) Scintillation Counter Background.

Location	Source	Counting Rate (cpm)
Outside shield	**Total**	**29,200**
Inside shield		
	Cosmic ray mesons	116.4
	^{222}Rn daughters	25.9
	Cosmic ray neutrons	19.4
	^{40}K	8.6
	Others	33.1
	Total	203.4

Source: Stenberg and Olsson (1968).

contributors to the detector background rate in a shielded system: (a) the cosmic ray shield, (b) the atmosphere surrounding the detector, (c) the detector itself, and (d) the cosmic rays. For the cosmic ray shield around the detector, it is advisable to use *old* or so-called virgin lead, that is, lead that was purified over 100 years ago, thus allowing any ^{210}Pb present from the natural decay series to decay. One should expect ~1 cpm/g shield material. Iron can also be used in constructing the detector shield, but care must be taken to ensure that the iron or steel is pre-1945 in origin due to the production of fallout during atmospheric weapons testing and the fact that some iron processed in the post-1945 period has ^{60}Co contamination (due to its use in some blast furnace operations). Mercury is a very good, easily purified shield material but is quite expensive and hazardous. "Graded" shields consisting of an outer thick layer of Pb lined with Cd that in turn is lined with Cu are used to reduce the production of X-rays in the outer shield materials. The main portion of the atmospheric contribution to the detector background is due to radon and its daughters. Particularly troublesome in this regard is the fact that atmospheric radon concentrations can fluctuate by a factor of 40 during the course of a day. Once again the problem is best handled by filtering the room air, rapid air turnover, and the use of inert atmospheres inside counting assemblies (e.g., N_2 from evaporation of liquid nitrogen used to cool germanium γ-ray detectors). A NaI(Tl) detector will contain some ^{40}K impurity, which will contribute to the background. The detector housing is also a potential contributor to the background. Copper appears to be the best material for detector housing with aluminum being the least preferred, for it can be expected to contain ~10^{-13} Ci of Ra per gram of Al. In reducing the cosmic ray component of the background one tries to stop the "soft" cosmic rays (electrons, X- and γ-rays) in the detector shield while using an anticoincidence system to stop the "hard" component of the cosmic radiation (mesons).

At first one might think that germanium detectors with their low detection efficiencies would have little in low-level counting. However such is not the case because of the complexity of a radionuclide mixture found in environmental samples, it is very difficult to draw significant conclusions from spectra obtained with NaI(Tl) detectors due to poor energy resolution. Clearly there are many cases in which the very good energy resolution of the germanium detector is a necessity. Furthermore, recent developments in detector fabrication techniques allow the production of germanium detectors with detector efficiencies comparable or even greater than that of the standard (3 in. × 3 in.) NaI(Tl) detector.

A number of special techniques have evolved to increase the detection sensitivity in γ-ray counting. One of the most important is the suppression of the Compton scattering events in the γ-ray spectrum by the use of anticoincidence annulus around the central γ-ray detector. The idea behind a Compton suppression spectrometer is that most events in which the incident photon undergoes

one or more Compton scattering events in the central detector will result in partial energy deposition in the detector and a low-energy photon will escape that detector. Suppression is accomplished by setting up an anticoincidence between the central detector signal and any signal coming from the annulus. A photon that is Compton scattered from the central detector will probably give rise to a signal in a well-designed and close-fitting annulus. Thus, such events will not be accepted. Other events, such as photoelectric events in the central detector will not produce signals from the annulus and will be counted. This reduction in number of Compton scattering events in the γ-ray spectrum leads to a more easily interpreted spectrum since the peak to Compton ratios are much higher. Typically the use of such annuli reduces the number of Compton events tenfold. More sophisticated designs have been used to further improve the rejection of Compton scattering events by increasing the coverage of area behind and in front of the central detector.

19.8.4 Limits of Detection

Suppose you have performed a low-level experiment and you wish to state your results in a statistically meaningful manner. You wish to answer questions such as Is there a result/signal/event? What is the chance it will be detected with my apparatus? How big will the signal be? Currie (1968) has provided answers to these questions by defining three different limits of detection:
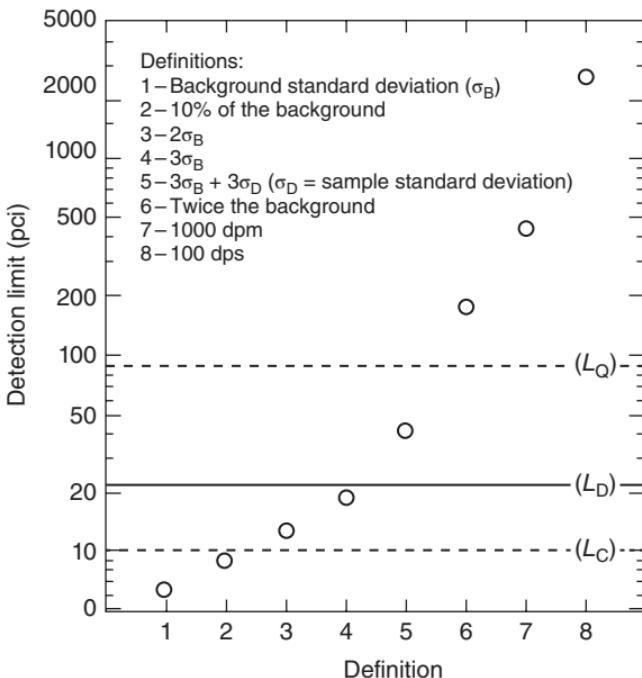
1) The critical level L_C, the signal level above which an observed instrument response may be reliably recognized as being "detected."
2) The detection limit L_D, the true net signal that may be expected a priori to lead to detection.
3) The determination limit L_Q, the signal level above which a quantitative measurement can be performed with a stated relative uncertainty.

Operationally, the recipes for calculating these limits in terms of the standard deviation of the background, σ_B, are as follows:

	L_C	L_D	L_Q
Paired observations	$2.33\sigma_B$	$4.65\sigma_B$	$14.1\sigma_B$
"Well-known" blank	$1.64\sigma_B$	$3.29\sigma_B$	$10\sigma_B$

For example, if the background under a photopeak of interest in a γ-ray spectrum was 100 cpm, then $\sigma_B = \sqrt{100} = 10$ cpm. According to the recipes given earlier, one would need to observe a photopeak area of 23 cpm to determine that a nuclide was present and would need to detect at least 141 cpm to measure the amount of nuclide present. One would need a counting rate of 47 cpm to insure, before making the measurement, that the nuclide in question could

Figure 19.8 A comparison of the different definitions used for detection limits in low-level counting (Currie (1968). Reproduced with the permission of ACS Publications)

be detected. The relationship of these limits to other measures used to describe low-level counting is shown in Figure 19.8.

Problems

19.1 A beam of 1 particle microampere of 200 MeV ^{48}Ca ions is incident on an Al foil that is 5 mg/cm^2 thick. (a) Estimate the energy deposit per second in the foil. (b) If the foil has an area of 4 cm^2 and it is mounted in a vacuum with no cooling, how long will it take until the foil reaches the melting point of Al (660°C)? Assume the specific heat of Al is independent of temperature and is 0.25 cal/deg/g.

19.2 Au foils are to be used as flux monitors in a nuclear reactor. What is the maximum thickness that can be used if the self-shielding corrections are to be <10%?

19.3 The reaction ^{27}Al(p,3pn)^{24}Na is to be used to measure the proton flux in an irradiation with 300 GeV protons. The cross section for this reaction is known to be 10.1 mbarn. The flux monitor is 5.0 mg/cm^2. One measures a ^{24}Na— counting rate (background corrected) of 10,000 cpm (in a 2% efficient detector) 24 h after a 0.5 h irradiation. What was the average proton flux during the irradiation?

19.4 Imagine you have for your use a nuclear reactor with a flux of 10^{13} n/cm^2/s in an irradiation facility and a cyclotron with a beam of 10.5 MeV protons, 21 MeV deuterons, and 42 MeV α-particles. What would be the best way to prepare samples of (a) ^{140}Ba, (b) carrier-free ^{99}Tc^m, (c) carrier-free ^{144}Ce, (d) ^{237}Np, (e) ^{254}Es, and (f) carrier free ^{18}F for incorporation into glucose? Outline the target and reaction to be used, how the target would be prepared, and any chemical separations to be done following irradiation.

19.5 What value of magnetic rigidity, $B\rho$, would you use in a gas-filled separator if you wanted to select ^{254}No produced in the reaction of 215 MeV ^{48}Ca with ^{208}Pb? You may assume q_{ave} for ^{254}No in 1 Torr He gas is 17$^+$.

19.6 As a radiochemist, you have been asked to prepare the following accelerator targets for your research group. They are (a) ^{226}Ra, (b) ^{208}Pb, (c) ^{238}U, (d) ^{244}Pu, (e) ^{90}Zr, and (f) ^{124}Sn. Assume all targets are to be 0.5 mg/cm^2. For each target, outline the best method of target preparation, the backing foil used, if any, and the reasons for your choice. Describe any anticipated problems in each procedure.

Bibliography

M. Paul, Nucl. Instrum. Meth. **A277**, 418 (1989).

A. Stenberg and I.U. Olsson. Nucl. Instr. Meth. **61**, 125 (1968).

Specific to Chapter

J.P. Adloff and R. Guillamont, *Fundamentals of Radiochemistry* (CRC Press, Boca Raton, 1984).

A.H. Bond, M.L. Dietz, and R.D. Rogers, Editors, *Metal Ion Separations and Preconcentration*, ACS Symposium Series 716 (ACS, Washington, DC, 1999).

L.A. Currie, Anal. Chem. **40**, 586 (1968).

J.R. DeVoe, *Radioactive Contamination of Materials Used in Scientific Research*, NAS-NRC 895 (National Research Council, Washington, 1961).

C.E. Düllmann, et al., *GSI Scientific Report 2001*; (GSI, Darmstadt, 2002), p. 179.

W.D. Ehmann and D.E. Vance, *Radiochemistry and Nuclear Methods of Analysis* (John Wiley & Sons, Inc., New York, 1991).

R. Eichler, et al. Nature **407**, 63 (2000).

A. Ghiorso, et al., Nucl. Instrum. Meth. **A269**, 192 (1988)

B.G. Harvey, Ann. Rev. Nucl. Sci. **10**, 235 (1960).

G. Herrman, and N. Trautman, Ann. Rev. Nucl. Part. Sci. **32**, 117 (1982).

G.F. Knoll, *Radiation Detection and Measurement*, 4th Edition (John Wiley & Sons, Inc., New York, 2010).

K. Kraus and D. Nelson, Paper 837, Geneva Conference, Volume 7 (1956).

J. Lehto and X. Hou, *Chemistry and Analysis of Radionuclides* (Wiley-VCH, Weinheim, 2011).

R.A. Meyer, and E.A. Henry, Proc. Workshop Nucl. Spectrosc. Fission Products, Grenoble 1979, (Bristol, London, 1979), pp. 59–103.

A. Mozumder, *Fundamentals of Radiation Chemistry* (Academic, New York, 1999).

Y.T. Oganessian, et al., Phys. Rev. **C64**, 064309 (2001).

W.C. Parker and H. Slatis, in *Alpha-, Beta- And Gamma-Ray Spectroscopy*, Volume 1, K. Siegbahn, Ed. (North Holland, Amsterdam, 1966), pp. 379–408.

M. Schädel, et al., Nucl. Instrum. Meth. Phys. Res. **A264**, 308 (1988).

M. Schädel, et al. Nature **388**, 55 (1997).

The Random House College Dictionary, Revised Edition (Random House, New York, 1984).

T.T. Sugihara, *Low Level Radiochemical Separations*, NAS-NRC 3103, 1961.

N. Trautmann, Radiochim. Acta **70/71**, 237 (1995).

N. Tsoulfanidis and S. Landsberger, *Measurement and Detection of Radiation*, 4th Edition (CRC Press, Boca Raton, 2015).

R.J. Woods, J.W.T. Spinks, and B. Spinks, *An Introduction to Radiation Chemistry* (John Wiley & Sons, Inc., New York, 1990).

I. Zvara, et al. Sov. Radiochem. **14**, 115 (1972).

General to Subject

J.P. Adloff and R. Guillamont, *Fundamentals of Radiochemistry* (CRC Press, Boca Raton, 1984).

D. Brune, B. Forkman, and G. Persson, *Nuclear Analytical Chemistry* (Chartwell-Brandt, Lund, 1984).

G.R. Choppin, *Experimental Nuclear Chemistry* (Prentice-Hall, Englewood Cliffs, 1961).

G. Choppin, J.-O. Liljenzin, and J. Rydberg, *Radiochemistry and Nuclear Chemistry*, 3rd Edition (Butterworth-Heinemann, Woburn, 2002).

W.D. Ehmann and D.E. Vance, *Radiochemistry and Nuclear Methods of Analysis* (John Wiley & Sons, Inc., New York, 1991).

G. Friedlander, J.W. Kennedy, J.M. Miller, and E.S. Macias, *Nuclear and Radiochemistry* (John Wiley & Sons, Inc., New York, 1981).

M. LeFort, *Nuclear Chemistry* (Van Nostrand, Princeton, 1968).

J. Lehto and X. Hou, *Chemistry and Analysis of Radionuclides* (Wiley-VCH, Weinheim, 2011).

W.C. Parker and H. Slatis, in *Alpha-, Beta- and Gamma-Ray Spectroscopy*, Volume 1, K. Siegbahn, Ed. (North Holland, Amsterdam, 1966), pp. 379–408.

G.T. Seaborg and W. Loveland, *The Elements Beyond Uranium* (John Wiley & Sons, Inc., New York, 1990).

C.H. Wang, D.L. Willis, and W. Loveland, *Radiotracer Methods in the Biological, Physical and Environmental Sciences*, (Prentice-Hall, Englewood Cliffs, 1975).

Nuclear Forensics

20.1 Introduction

One of the fastest growing areas of nuclear and radiochemistry is that of **nuclear forensics**. Nuclear forensics has been defined as "the investigation of nuclear materials to find evidence of the source, the trafficking, and the enrichment of the material" (Moody et al., 2005). Alternatively, it has been defined as "a methodology that aims at *reestablishing* the history of nuclear material of unknown origin". (Mayer et al., 2011) From these definitions, we can begin to understand the character and scope of the field. Nuclear forensics involves a partnership between nuclear scientists and governmental and law enforcement personnel. The nuclear scientist brings a knowledge of nuclear phenomena, radiation detection and measurement techniques, and radioanalytical and conventional analytical methods along with a practical understanding of nuclear weapons, reactors, accelerators, and the nuclear fuel cycle. It is not by accident that we chose to discuss nuclear forensics in the last chapter of this textbook as it combines essentially all aspects of nuclear chemistry discussed in previous chapters.

What do nuclear forensic scientists do to "reestablish" the history of nuclear material? They have to identify the source of a sample of nuclear material and the procedures used to construct the material. In the case of an explosion, they can try to identify the character of the "device." In the case of construction, they can attempt to answer the following questions: What is the material? How was it constructed? When was it made? Where was it made? By whom? And perhaps, Why? Establishing the "age" of clandestine material is very important. (In this context, "age" is taken to mean the time since production or last purification.) In the case of an explosion, can one use the debris to establish properties like the pre-explosion isotopic abundances in the sample?
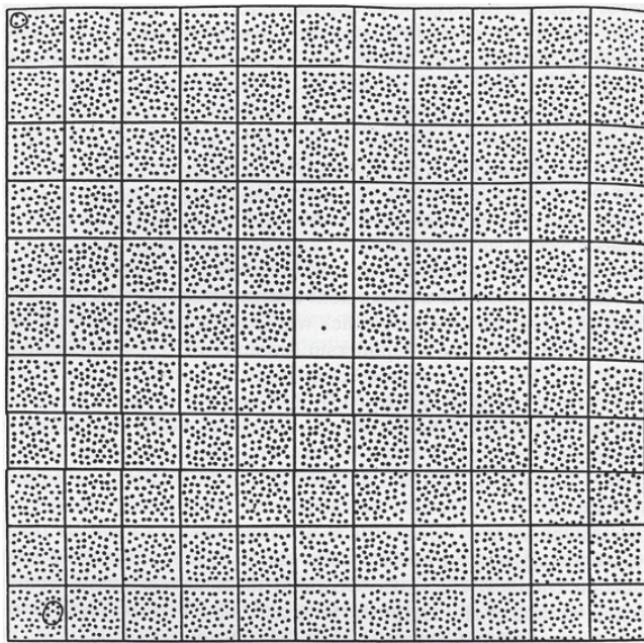
There is another activity, **attribution**, that is an important component of forensic endeavors (Nuclear Forensics, 2012). Attribution is a political, legal,

and forensic process to establish the origin and route of transmission of clandestine nuclear material as well as the design of explosive nuclear devices. Attribution seeks to establish *who* is responsible for nuclear material or nuclear explosions. Attribution involves the cooperative efforts of nuclear forensic scientists, law enforcement personnel, and the intelligence community. Rapid and accurate attribution are important for swift response and retaliation to any event. Because of the consequences, attribution requires a high degree of certainty. Another related and more political question is what sort of response is justified in the wake of a given incident. The certainty of successful attribution can be an important deterrent to the theft of nuclear material or acts of terrorism.

Before going further, we need to establish a small glossary of certain terms and abbreviations. By the term "nuclear material" we mean radioactive material albeit with special attention given to special nuclear materials (SNMs, e.g., ^{233}U, ^{235}U, and ^{239}Pu). The term radiological dispersal device (RDD) or "dirty bomb" is an explosive device that uses conventional explosives to disperse radioactive material. It is referred to as a weapon of mass disruption as its goal is to disrupt society. An improvised nuclear device (IND) is a theoretically illicit nuclear weapon bought, stolen, or otherwise originating from an existing nuclear state, or a weapon fabricated by a terrorist group from illegally obtained SNM that produces a nuclear explosion. The acronym HEU stands for highly enriched uranium, that is, uranium containing >90% ^{235}U, while LEU refers to low enrichment uranium, that is, uranium containing <20% ^{235}U. "Weapons grade" nuclear material is > 90% ^{235}U and has < 7% ^{240}Pu. "Reactor grade" material has < 20% ^{235}U and > 19% ^{240}Pu. "Weapons usable" material has > 20% ^{235}U.

There are certain "realities" about the availability and natural distribution of nuclear materials that underlie any discussion of nuclear forensics. From the end of WWII to the early 1990s, there was an "arms" race between the United States and the former Soviet Union. The United States produced 100 tonnes of weapons grade Pu and $\approx$1000 tonnes of HEU. The Soviet Union produced similar amounts. During this period of time, the United States and the USSR conducted a number of atmospheric and underground tests of nuclear weapons. At its peak in 1962, 72 M tonnes of fission products/year were injected into the atmosphere. Over the entire testing program about 5000 kg of ^{239}Pu was injected into the biosphere. The insanity of this situation was graphically illustrated by Hofstadter (1985) in a famous cartoon that we reproduce as Figure 20.1. In this figure, the world armaments situation is depicted in terms of the firepower of WWII. The one dot in the central square represents the firepower of WWII, including the nuclear weapons dropped on Hiroshima and Nagasaki. All the other dots represent the nuclear weaponry of that time (6000 WWIIs). The encircled three dots in the upper left corner represent the weaponry of one Poseidon submarine. The encircled group in the

Figure 20.1 A 1985 view of the world armaments situation. The one dot in the central square represents the firepower of WWII, including the nuclear weapons dropped on Hiroshima and Nagasaki. All the other dots represent the nuclear weaponry in 1985 (6000 WWIIs); see the text (Hofstadter (1985). Reproduced with the permission of Basic).

lower left corner represents the power of one Trident submarine, the power to destroy every major city in the northern hemisphere. Two squares on this chart represent the firepower to destroy all the large and medium-sized cities on the planet Earth. Since the end of the cold war, there has been a concerted effort to reduce these stockpiles of nuclear weapons. At present (2015) there are about 15,800 nuclear weapons held by the world's nuclear nations with about 4,120 of these weapons classified as "deployed strategic" weapons (Kristensen and Norris, 2016)

Plutonium is an SNM used in weapons and there is a well-recognized tie between Pu and nuclear power. Specifically a 1 GWe nuclear reactor generates about 200 kg of Pu per year by neutron capture on ^{238}U as discussed before. That is roughly the amount of material needed to make ≈50 nuclear weapons. The world production of Pu from the present operation of nuclear power plants is about 70 tonnes of Pu per year. Given this production rate, it should not come as a surprise that the world inventory of Pu is about 2200 tonnes with about 90–100 tonnes being associated with military applications. There are about 3800 tonnes of fissile material with about 2000 tonnes in weapons usable form.

A current concern is that the PUREX/MOX fuel cycle (discussed previously) produces, in routine operation, material that can be converted to weapons usable material, The MOX fuel cycle has led to the accumulation of 25,000 weapons worth of Pu in Europe, Russia, and Japan (Beckjord, 2003) where the process is carried out. The projected growth of nuclear power will exacerbate this problem. However, the history of the burning of nuclear fuel and its particular processing can provide clues for the forensic scientist.

20.1.1 Basic Principles of Forensic Analysis

What are the general principles of nuclear forensic analysis? Whether one is examining intercepted material or bomb debris, there are certain common nuclear forensic procedures that are applicable. (Mayer et al., 2011; Nuclear Forensics, 2012) One usually starts with a general radiological examination of any sample that involves survey measurements of the total activity of the sample using α, β, and γ detectors. One will swipe the exterior of any sample to determine if there is any removable contamination. From these initial measurements, one can assess the radiological hazards associated with handling the sample and determine the extent where further investigations are necessary or even possible.

One follows this initial radiological examination with a physical characterization of the sample. Here one relies on visual inspection, photography, size measurements, mass measurements, optical microscopy, and radiography to establish the mass and macroscopic dimensions of the overall sample and of the radioactive sample, if possible. Follow-up measurements using scanning electron microscopy with energy dispersive X-ray analysis can provide information on the elemental composition of the sample and its microstructure. The crystal structure of the sample can be determined using X-ray diffraction.

Traditional forensic analysis of fingerprints, fibers, and DNA can be applied to some samples. Initial isotopic analysis is done with γ-ray spectroscopy followed by more detailed measurements using SIMS, TIMS, ICP-MS, and α-spectroscopy of chemically separated samples. A general chemical analysis of the sample can be done with ICP-MS, XRF, and traditional analytical methods. The typical sensitivities of these forensic analytical techniques are given in Table 20.1.

Suppose as a nuclear forensic analyst, you are presented with some contraband material. Your first responsibility is to determine if the sample contains radioactive material. If so, could it be naturally occurring radioactive material (NORM) or medical or hospital waste? Is it nuclear waste from a reactor or fuel cycle facility? Does it contain Pu or U? If it is U, is it HEU? If it is Pu, what are the isotopic ratios? Is it weapons grade material? What is the age of the sample? What is its chemical composition? In Table 20.2 we show the typical timeline for experimental procedures used to investigate intercepted material. Note the division of the analysis into different time regimes. First responders, civil authorities, and others need certain descriptive information within a matter of hours. Other more time-consuming procedures can be done later.

Similarly, suppose as a nuclear forensic analyst, you are presented with debris from an exploded device. Once again, your first responsibility is to determine if the sample contains radioactive material but time is now of the essence. Not only do you have to determine the radiological hazards, but also the radioactive products that contain important information will be decaying. In Table 20.3,

Typical Forensic Analytical Techniques.

nique	Type of Information	Detection Li
n res. γ-spec	Isotopic	ng–µg
mical assay	Elemental	mg
iochemistry	Isotopic	fg–pg
IS	Isotopic	pg–ng
-MS	Isotopic	pg–ng
MS	Isotopic	0.1–10 ppm
F	Elemental	10 ppm
D	Molecular	5 atom %
MS	Molecular	ppm
	Molecular	ppm
al	Macroscopic	
ical microscopy	Microscopic	
M	Microscopic	
M	Microscopic	
-MS	Elemental	pg–ng
IS	Isotopic	pg–ng
S	Elemental	0.1 ppb–10
M-EDS	Elemental	0.1–2 atom
D	Molecular	5 atom %

Atomic Energy Agency (2006).

Forensic Investigation of Intercepted Material.

h	1 Week	1 Mo
timated total activity		
ose rate (α, γ, n)		
rface contamination		
sual inspection	SEM(EDS)	TEM
diography	XRD	
otography	Organics	
eight		
mension		
ptical microscopy		
ensity		
ngerprints, fibers		
Spectroscopy	Mass spectrometry	Radic
Spectroscopy	(SIMS, TIMS, ICPMS)	Mass
	ICP-MS	GC-
	XRF	
	ICP-OES	

2).

Forensic Investigation of Post-Detonation Debris.
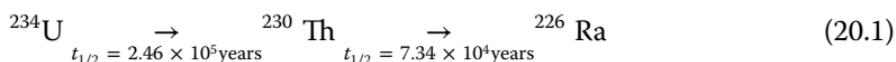
easing Time Since Event)	Information Gained
oscopy	Initial "picture" of device, y
	Starting point for laboratory
es	Initial look at fuel type (U o
spec	Improved knowledge of fue
	Device design, fuel material
spec)	
	Burnup, fuel origin
	Route

12).

we show the timeline for the experimental characterization of post-detonation debris. The needs of first responders are clearly paramount. Help is needed to assess the dispersal of radioactive material and to begin consequence management. Reliable information is very important. The possibility of a second device or attack needs to be addressed on the political front.

20.2   Chronometry

One of the important tasks for the nuclear forensic analyst is to establish the age of a sample of radioactive material. Using our discussion of radioactive decay kinetics in Chapter 3 as a basis, let's consider the basis chronometric concepts. Taking as an example, consider the following segment of the $4n + 2$ decay series:

$$^{234}\text{U} \underset{t_{1/2}\,=\,2.46\,\times\,10^5\,\text{years}}{\rightarrow} {}^{230}\text{Th} \underset{t_{1/2}\,=\,7.34\,\times\,10^4\,\text{years}}{\rightarrow} {}^{226}\text{Ra} \tag{20.1}$$

We can write the following equations to describe the time evolution of this decay sequence:

$$N_{234} = N_0^{234} e^{-\lambda_{234} t} \tag{20.2}$$

$$N_{230} = \frac{\lambda_{234}}{\lambda_{230} - \lambda_{234}} N_0^{234} \left(e^{-\lambda_{234} t} - e^{-\lambda_{230} t} \right) \tag{20.3}$$

where the numerical subscripts refer to ^{234}U and ^{230}Th. One can rearrange these equations to give the age (the time since the last purification or removal of the daughters) of a ^{234}U sample as

$$t = \frac{1}{\lambda_{234} - \lambda_{230}} \ln \left(1 - \frac{N_{230}}{N_{234}} \left(\frac{\lambda_{230} - \lambda_{234}}{\lambda_{234}} \right) \right) \tag{20.4}$$

where the unknowns are the numbers of atoms or simply their ratio. Thus, a measurement of this ratio of the number of ^{230}Th nuclei to the number of ^{234}U nuclei in a uranium sample gives an estimate of the time since the last purification or age of that sample.

The ^{234}U/^{230}Th chronometer is a general and important measure of the age of uranium samples. Figure 20.2 shows the dependence of the ^{234}U/^{230}Th atom ratio on the age of a uranium sample. Notice this ratio is approximately linear at the shorter times most applicable to nuclear forensic work (0–40,000 years).

The astute student will note that we have neglected the precursor ^{238}U ($t_{1/2} = 4.47 \times 10^9$ years) in the $4n + 2$ chain that decays to ^{234}Th ($t_{1/2} = 24.1$ day), then decays to ^{234}Pa ($t_{1/2} = 6.7$ h), and then produces the ^{234}U. This part of the chain that starts with ^{238}U is not generally useful as a chronometric set of isotopes due to the relatively short half-lives of the progeny (although the ^{234}Th/^{238}U ratio can be used to date materials whose age is < 6 months). Another $4n + 2$ nuclide that we have also neglected is ^{238}Pu ($t_{1/2} = 87.7$ years). The atom ratios
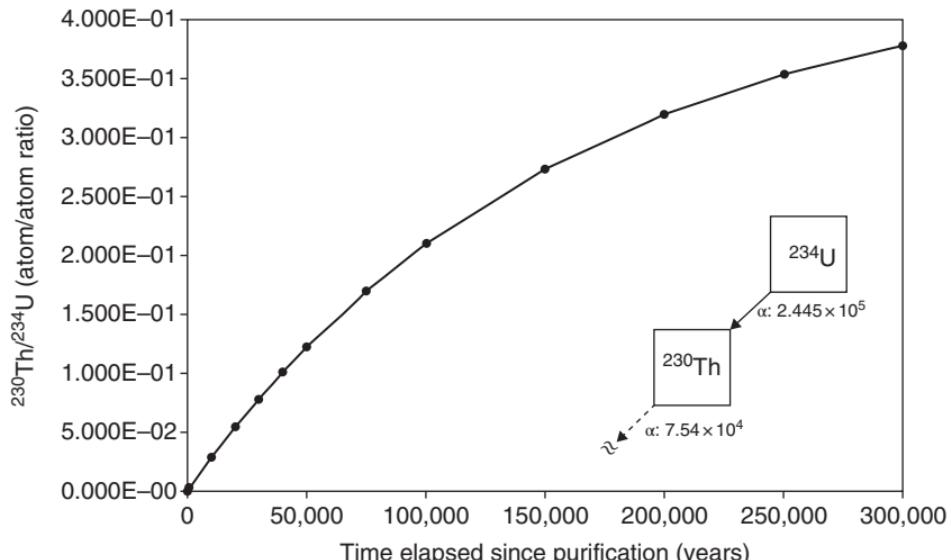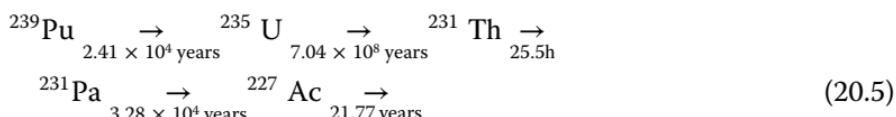
Figure 20.2 Dependence of the of the ^{234}U/^{230}Th atom ratio on the age of a purified uranium sample (National Planning Scenarios). Reproduced with permission of Royal Society of Chemistry).
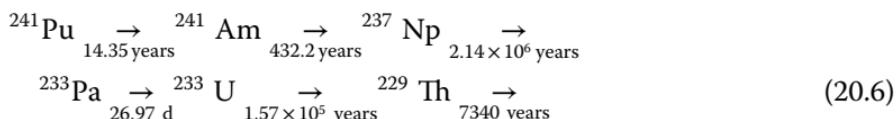
of ^{234}U/^{238}Pu, ^{234}Th/^{238}Pu, and ^{226}Ra/^{238}Pu can be used to date ^{238}Pu samples (Moody et al., 2015) and similar ratios can be used to date Th samples.

The $4n + 3$ decay series beginning with ^{239}Pu:

$$^{239}\text{Pu} \underset{2.41 \times 10^4 \text{ years}}{\rightarrow} {}^{235}\text{U} \underset{7.04 \times 10^8 \text{ years}}{\rightarrow} {}^{231}\text{Th} \underset{25.5\text{h}}{\rightarrow}$$
$$^{231}\text{Pa} \underset{3.28 \times 10^4 \text{ years}}{\rightarrow} {}^{227}\text{Ac} \underset{21.77 \text{ years}}{\rightarrow} \tag{20.5}$$

is also useful in dating ^{239}Pu samples (Figure 20.3), but ^{231}Th is too short-lived to be useful in this regard.

The $4n + 1$ decay series beginning with ^{242}Pu

$$^{241}\text{Pu} \underset{14.35 \text{ years}}{\rightarrow} {}^{241}\text{Am} \underset{432.2 \text{ years}}{\rightarrow} {}^{237}\text{Np} \underset{2.14 \times 10^6 \text{ years}}{\rightarrow}$$
$$^{233}\text{Pa} \underset{26.97 \text{ d}}{\rightarrow} {}^{233}\text{U} \underset{1.57 \times 10^5 \text{ years}}{\rightarrow} {}^{229}\text{Th} \underset{7340 \text{ years}}{\rightarrow} \tag{20.6}$$

is the basis for the interesting chronometric pair of ^{241}Am and ^{241}Pu. This pair is technically important since both the ^{241}Am and ^{241}Pu activities and thus the atom ratio can be measured by γ-ray spectroscopy allowing a nondestructive analysis. Note that there is a small side branch for the decay of the ^{241}Pu decay where 0.00245% goes to the short-lived (6.75 day) ^{237}U nuclide that itself decays to ^{237}Np and increases the number of ^{237}Np atoms in the sample. The ^{241}Am/^{241}Pu chronometer sometimes gives a larger age for a mixed Pu/U sample than do the U chronometers. This seems to be due to the incomplete removal of Am during the last purification of the Pu that occurs in the PUREX process.
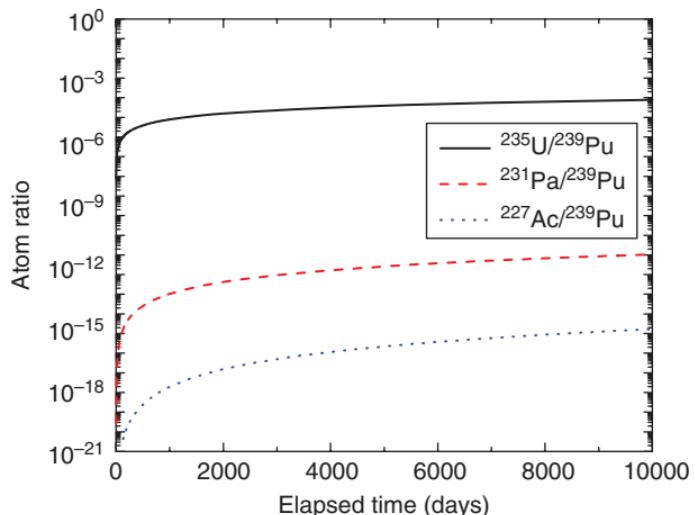
Figure 20.3 Chronometric atom ratios arising from the decay of ^{239}Pu as a function of sample age.

The variability of chemical processing should lead us to inquire what the principal uncertainties in chronometric determinations are. One key assumption in chronometry is that the initial purification of the sample was perfect, that is, the absence of any daughter activities. If some daughter activity was left in the sample, the measured age will be too large. A similar concern is whether the parent–daughter system is closed or open in terms of chemical speciation, since open systems can lead to loss of progeny. Finally one assumes that all of the half–life values are well–known although that may not always be the case (Williams and Gaffney, 2011). The use of multiple chronometers to date samples can help to reduce the uncertainties.

20.3 Nuclear Weapons and Their Debris

In this section we shall examine the nuclear forensic analysis that is used today to study nuclear bombs through the forensic signatures in the post-explosion debris. We shall focus our attention on two postulated scenarios, an RDD and a 10 kT weapon. (National Planning Scenarios, 2006).

20.3.1 RDD or Dirty Bombs

A postulated *dirty bomb scenario* (National Planning Scenarios, 2006) involves the detonation of conventional explosives to disperse radioactivity in three medium-sized cities simultaneously by a terrorist group. The radioactive material to be dispersed is ^{137}Cs ($t_{1/2}$ = 30 years), which undergoes β decay and then emits a 662 keV γ-ray. The chemical form of the activity is CsCl, an

easily dispersed salt. Note that ^{137}Cs is widely used in irradiation devices for food, medicine, and medical therapy and, thus, it is plausible that a terrorist group could obtain this material. It is estimated that there will be 180 fatalities, 270 injuries, and 20,000 people with detectable contamination at each site depending on the size of the explosion and the amount of radioactive material. It is widely thought that the residual contamination, although small and easily diluted due to the chemical form, will cause extensive distress. The contaminated region is assumed to be about 36 square blocks in each city, including business, residential, and shopping areas and schools. Economic losses (post-explosion) are estimated to be billions of dollars due to the contamination and its long-term psychological affects. An important aftermath of the attack is the perceived damage, which may be greater than the actual damage (Burns and Slovic, 2012; Giesecke et al., 2012). A highly recommended gripping portrayal of this scenario can be found in the BBC film Dirty War (2004)

What is the role of the nuclear forensic analysis in this scenario? The first action is to recognize the presence of radioactive material and make the identification of the dispersed material as ^{137}Cs. This determination is most likely to be made using widely available, modern, handheld commercial survey meters that can easily identify and quantify nuclides like ^{137}Cs and might even be triggered by some claim from the terrorists since radioactive decay is not detectable by human senses. First responders and/or forensic analysts should be able to make this identification within 15 min after the explosion. (It should be noted that there is some skepticism as to whether forensic analysis is up to this challenge (Baxter, 2016), and the tip-off from the terrorists may be very important.) Establishing the extent of the contamination will be harder as the cesium salt will be dispersed by prevailing winds, and cesium chloride is readily soluble in water. In fact, weather conditions will play a very important role in the dispersal of contamination.

Following the initial determination of the nature and severity of the event, the role of the nuclear forensic analyst is to assist civil authorities to define the hazard areas and to assist in radioactive and hazardous contamination mitigation, decontamination, and contamination control. For example, many nuclear scientists were drawn into the evaluation of the extent of contamination during the earliest stages of the Fukushima reactor disaster in Japan. Other areas where technical assistance may be requested include victim care and public protection from secondary problems, investigation of the incident, and who caused it.

A suggested protocol (Moody et al., 2015) for forensic labs for investigating an RDD event involves:

(1) Visible trace evidence (hairs, fibers, etc.) is removed from external surfaces.
(2) The condition of the evidence as received is photographed and documented.

(3) Latent finger mark examination is conducted, including stripping off and investigating any tape; additional trace evidence, if present, is isolated.
(4) Tape is examined for polymer content and end-match assessment.
(5) Material residues are collected from the high explosive containment vessel.
(6) Toolmark examination is conducted.
(7) Metallurgical exams of unusual or significant metals are conducted.
(8) Device components and functions are assessed.

One should remember that DNA evidence could survive an RDD explosion and attempts should be made to capture such evidence as well.

20.3.2 Nuclear Explosions

A postulated *nuclear weapon scenario* (National Planning Scenarios, 2006) involves the detonation of a 10 kT device utilizing HEU in a major US city, perhaps understandably Washington, DC. The numbers of casualties would be very large, $\sim$ 100,000–1,000,000 people, with most of these people being killed, and the contaminated area is postulated to be $\sim$8,000 km^2 with a net economic impact $\sim$10^{11} dollars. About one million people (most likely all of the remaining people) would flee the city with $\sim$100,000 people needing decontamination before exiting the contaminated area. Recovery time from such an incident is measured in years, if not decades. As a background for this scenario, one notes that as of 2016, 40 countries have HEU, 7 of which have Pu-based bombs, and another 6 have enough Pu to develop a bomb (Nuclear Forensics, 2012).

In the face of a catastrophic event like this, a forensic response will be difficult. One can expect general chaos immediately after the event. First responders, including forensic personnel, who enter the high radiation areas could suffer incapacitating or fatal radiation doses. Nonetheless, it will be important to have a source of reliable information about the incident and its consequences that is informed and self-correcting. Nuclear forensics is expected to fill this role using a protocol similar to that outlined in Table 20.3. The extent of the damage should clearly indicate the use of a nuclear explosive. In a few hours after the explosion, handheld dosimetry should be able to detect the general perimeter for the radioactivity although prevailing weather conditions will be important. Visual and seismic observations along with radiation measurements should confirm the occurrence of a nuclear explosion.

The next task is to collect representative samples of the bomb debris. In the explosion of the nuclear weapon, one must remember that *all* of the components of the weapon and its debris will be vaporized along with the materials in the immediate surroundings and mixed with pulverized building materials, soil, and so on. The fission products, unreacted fissile material, and structural material will be carried up by the rising fireball. As the fireball cools, most of the nuclidic vapors will condense on particulates and may combine

with other vapors to form a wide variety of solid particles. This "fractionation" will change the relative composition of the fission fragment fallout (and unreacted fissile material) as a function of distance from ground zero. Fractionation can be described as being "geometrical" or "chemical." Geometrical fragmentation refers to the sorting of debris by particle size, whereas chemical fractionation refers to the sorting of debris by volatility of the material. In chemical fractionation, one categorizes debris as as either "refractory" or "volatile," depending on when they condense from the fireball. The refractory elements condense first and then the volatile elements condense. The refractory elements in bomb debris include metals such as Zr, Ta, Th, Np, Pu, Am, and Cm, but not U. One must also remember that the precursor of a fission-product nuclide could be volatile, while the nuclide itself is refractory, As the fallout cools, the refractory elements condense early and are included throughout the volume of the particles, while the volatile elements condense on the surface. This leads to the situation where small particles are richer in volatiles (higher surface-to-volume ratio), while larger particles are enriched in refractory elements. Thus the volatile/refractory ratio will vary as r^{-1}, where r is the radius of the fallout particle. The refractory elements are also likely to be found closer to ground zero.

Some of the plasma condensate from the weapon will end up in the explosion crater, mixed with glass-like material from molten rocks. That debris fraction will be very radioactive and probably not accessible for a long time. However, most of the plasma condensate will be associated with dust particles that will fall in the region downwind from the explosion. A smaller fraction will remain suspended in the atmosphere and will travel great distances from the explosion site. To get a representative sample of the bomb debris, one will have to collect many samples of the fallout at various distances from ground zero. To get a "representative" distribution of fission products, one measures the nominal distribution with the $A = 91, 140, 141$ mass chains to define the refractory/volatile ratios and adjusts this ratio empirically to account for volatile loss. (Hicks, 1982). Continued forensic analysis of the bomb debris over a period of days after the explosion will attempt to identify the type of device involved and how it is delivered or detonated, the yield of the weapon, and whether uranium or plutonium (or both) formed the basis of the weapon.

A method for attacking the general problem of identifying the type of fissile material is to determine the detailed yields of the fission products produced in the explosion. Using γ ray spectroscopy and radiochemistry, one can measure the yields of numerous fission products that β decay along constant mass chains. The most easily interpreted data come from the *independent yields* (IY) that do not have significant β decay feeding although the cumulative yields are also usable as long as the time of the measurement relative to the explosion is known. Of special importance are the few shielded nuclides, which can only be made directly in fission and not by the β^- decay of a parent. Examples of such nuclei are ^{126}Sb, ^{136}Cs, and ^{148}Pm.

Suppose one detects the fission product ^{140}Ba (a γ-ray emitter with a 12.8 day half-life) in the fallout debris. The cumulative yield of ^{140}Ba is 5.99%, that is, the yield of this nuclide plus that of all of its β decay parents. From this observation combined with the well-known fission yields of the fissile nuclei, one can deduce the total number of fission events of a given fissile nuclide that occurred to give rise to this sample of ^{140}Ba. If one knows a fraction of the total amount debris represented by this sample of ^{140}Ba, not an easy problem, one can calculate the number of fissions that occurred in the explosion. Using rough guidelines (Glasstone and Dolan, 1977) such as 3×10^{23} fission events corresponding to an explosive yield of 1 kT, one can estimate the explosive yield of the weapon.

However, suppose the weapon contains some mixture of ^{235}U, ^{238}U, and ^{239}Pu. Let us further assume that the weapon is sophisticated enough to be a fusion-boosted fission device, that is, a thermonuclear explosion is used to enhance a fission weapon. One should recognize that this is a sophisticated device that is probably not consistent with a terrorist attack but this assumption is the most conservative one for testing nuclear forensic capabilities. In this case, one would have to postulate that the fission products have six contributions, the low-energy (fission spectrum) neutron-induced fission of ^{235}U, ^{238}U, and ^{239}Pu plus the 14 MeV neutron-induced fission of these three nuclides. (One has assumed that the thermonuclear reaction is the DT reaction, ^{2}H + ^{3}H →^{4}He +n where the neutrons have a kinetic energy of ~14 MeV.) The postulated cumulative fission product yields from these six components are shown in Figure 20.4. In principle, one would then take the measured fission product yields and do a nonlinear least-squares fitting of that data to decompose it into the six postulated components. However, one should notice the large differences among the various components for the symmetric and high mass yields so that a simpler comparison of the measured symmetric and high mass yields might suffice to determine the U/Pu ratios for the weapon and the type of weapon that is involved. (One should note that Figure 20.4 relates to data from US weapons and other designs could have different yield patterns.)

Chronology of the bomb debris is not likely to be useful to the mixing of uranium and thorium contained in the soil in the bomb debris. A possible exception to this would be the ^{241}Am/^{241}Pu chronometer, which should not be affected by soil contamination since these isotopes are not present in nature.

Mass spectrometry of the explosion debris along with high resolution α-spectroscopy of radiochemically separated samples should give information on the uranium (^{232,233,234,235,236,238}U) and plutonium (^{238,239,240,241,242}Pu) isotopic ratios. These, in turn, can provide information on the device history and isotopic makeup. One should note, for example, that radiation and mass spectrometry measurements ~60 years after the explosion were able
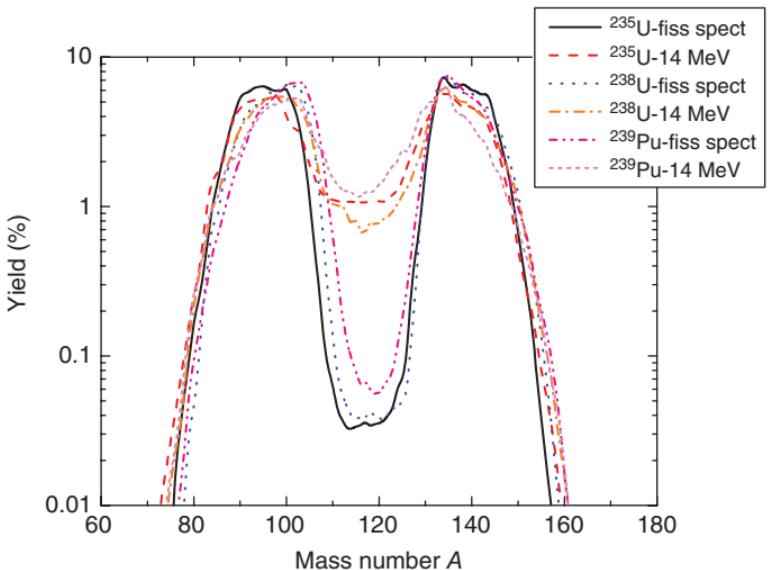
Figure 20.4 Fission product mass yield distributions for the postulated components of a fusion-boosted nuclear fission weapon (England and Rider (1993). Reproduced with the permission of ENDF-349).

to characterize the trinitite debris from the original Trinity test as being a plutonium-based weapon. (Fahey et al., 2010).

The plutonium isotopic ratios are important in that, under certain circumstances, they may indicate the reactor in which the Pu was made. Due to neutron absorption by protons to form deuterium, ordinary water is not used as a moderator in a Pu production reactor. Rather either graphite or D_2O is used to moderate the reactors. The graphite-moderated reactors have two designs, the water-cooled Hanford style and the gas-cooled Calder–Hill style. The heavy water-moderated reactors also have two designs, the H_2O-cooled NRX style and the D_2O-cooled Dimona style. According to neutronics calculations, one can distinguish material from some of these designs by comparing the ^{238}Pu/total Pu and $^{242}Pu/^{240}Pu$ ratios. The ^{238}Pu abundance reflects the initial ^{235}U level in the fuel while the $^{242}Pu/^{240}Pu$ ratio is sensitive to the reactor neutron spectrum, that is, the softer the spectrum, the higher the ratio. Better discrimination is obtained by comparison to actual samples from the reactors. Some (Mayer et al., 2012) have concluded that the Pu isotopic composition is definitive as to the type of reactor that produced the Pu.

In certain types of devices, that is, gun-type weapons involving HEU, the uranium isotopic ratios have been shown to shift very little during the explosion, and thus one can use the observed ratios in the debris to infer the initial U isotope ratios. However, identification of the weapons through the uranium

isotope ratios can be "swamped" by the U isotope ratios in the upswept soil, making it difficult to reach any conclusions about the weapons. But the relative ^{232}U atom ratios can be used to discriminate between samples from the Hanford and NRX reactor types since ^{232}U is not present in soils. Additional information about the device structure may be obtained from the neutron activation products on the nonnuclear components of the weapons.

20.4 Deducing Sources and Routes of Transmission

In this section we examine the nuclear forensic techniques used to deduce the origin and routes of transmission of intercepted nuclear material. In the last 15 years, 17 kg of HEU have been reported to have been intercepted along with 400 g of Pu. The verified history of seizures of weapons-usable nuclear materials, involves < 20 incidents in the period from 1992 to 2011. One can notice a decrease in the number of incidents per year over time. Two criticisms of these data are that "weapons-usable material" excludes the radioactive material that would enable a RDD and if, for example, LEU is successfully smuggled, then it may be possible to smuggle HEU.

When one has intercepted material, there are many questions to be answered regarding the source and history of the material: What type of material is it? SNM or weapons usable or other? What is the origin of the material? Was the material diverted from a legitimate use? How did the authorities get the material? When was the material acquired? What future problems does this material pose? Some of the questions specific to the route of the material include: What was the route the material followed? Was the route of transmission of the material unique? Is the acquisition of this material a unique event or is this a systematic problem? Who are the "perps," i.e, who is responsible for the smuggling of this material? What is the estimated end use of the material? Given this large number and variety of questions, it should be clear that it may not be possible to answer them all, but the goal of a nuclear forensic analyst is to answer as many as possible.

In Table 20.2, we outlined the steps in the nuclear forensic analysis of intercepted material. Following the initial radiological inspection of the material, one seeks to make a physical characterization of the material. For macroscopic objects, one wants to know their size, shape, and texture. For example, the size and shape of fuel pellets from a reactor can be used to help establish the reactor type from which they originated. For granular material, a determination of the particle size distribution is important. For material originating somewhere in the nuclear fuel cycle, these distributions can give information on which conversion processes were applied to the sample. In this and subsequent examination of the sample, one prefers, if possible, to use empirical, measured signatures of processes to characterize materials as opposed to using predictive
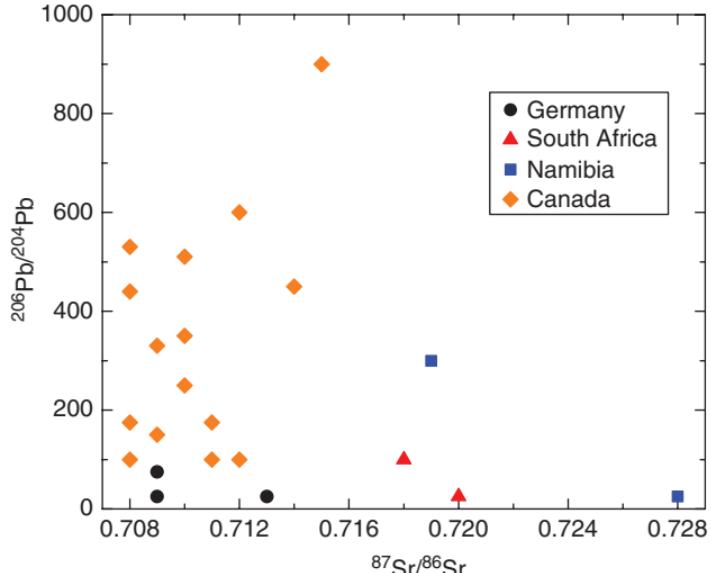
Figure 20.5 Diagram of $^{206}Pb/^{204}Pb$ ratios versus $^{87}Sr/^{86}Sr$ ratios for uranium ore concentrates showing the correlation of the ratios with the origin of the ores (Moody et al. (2015). Reproduced with the permission of CRC Press).

signatures that are based on modeling of the chemistry and physics of the fuel cycle and weapons manufacture.

The isotopic signatures of the material are generally critical. From measurements of the atom percentages of ^{235}U and ^{239}Pu, one can characterize the material as weapons grade, weapons usable, or reactor grade. The simple chemical stoichiometry of the sample is also very informative since U_3O_8 is 84.8 % U, UO_2 is 88.15 % U, while UO_3 is 83.2 % U. One notes that unlike weapons debris, there is no mixing of soil components or fractionation in an intercepted sample to complicate the isotopic signatures. Also the presence of ^{236}U or ^{232}U means the sample has been in a reactor as these nuclides do not occur naturally. Since there are no masking soil or other components, chronometry should be instructive in establishing the history of the samples. If the isotopic ratios are those of natural uranium, then one can deduce that the source of the material is an ore, while altered isotopic ratios indicate processing in a reactor. As indicated previously in connection with weapons debris, the Pu isotopic ratios can indicate the type of reactor used to make the Pu, the neutron spectrum of the reactor, and the enrichment of the uranium target material in the reactor.

An intriguing sidelight of the use of U/Pu isotopic abundances to identify a source of "unknown" intercepted material was the recent use by Norman et al. (2015) of X-ray and γ-ray spectroscopy to identify the presence of ^{239}Pu (and its amount, 2.0 ± 0.3 μg) in an "unknown" historical source that proved to be the first sample of ^{239}Pu (Cunningham and Werner, 1949; Seaborg, 1977) that was large enough to be weighed.
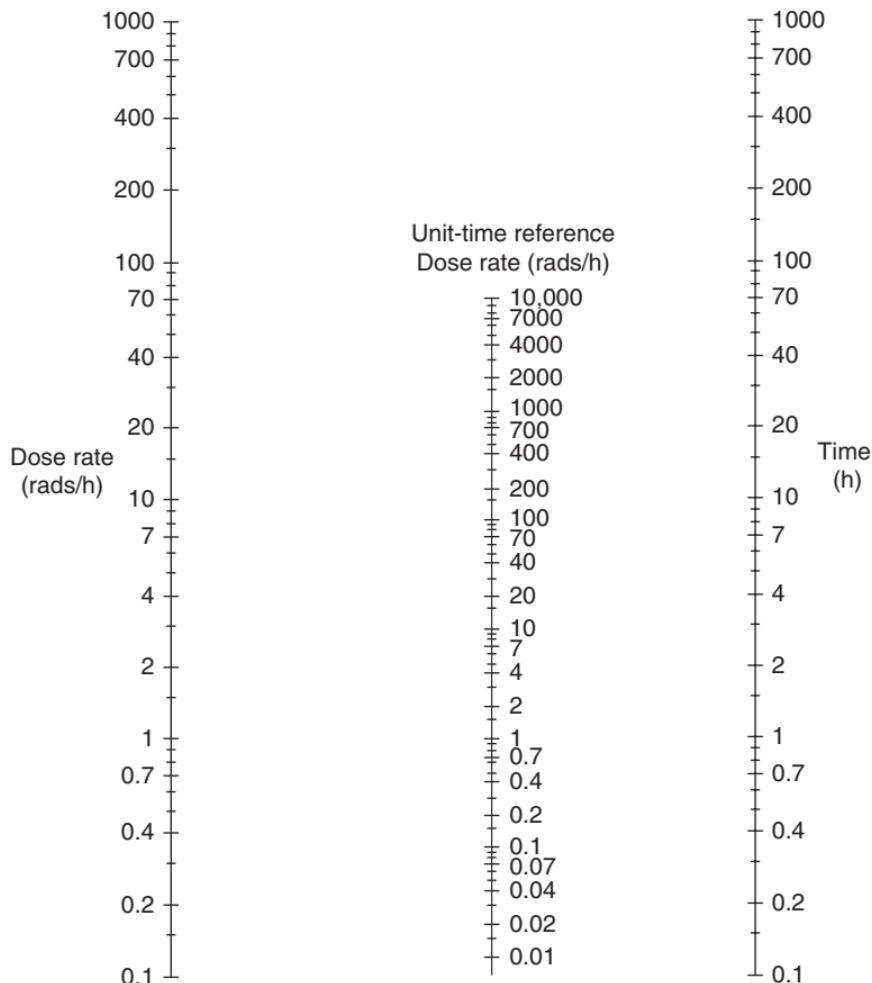
Figure 20.6 A nomograph for calculating approximate dose rates from early fallout (Glasstone and Dolan, (1977). Reproduced with the permission of Walter de Gruyter GmbH).

Trace element (nonradioactive) abundances in an intercepted sample can also be used to characterize the material and its history. Gd and Er are reactor poisons and Ga is frequently used for the phase stabilization of Pu in the nuclear fuel cycle. The rare earth abundances can be used to identify particular geologic formations. Isotope correlation diagrams such as the one shown in Figure 20.5 can be used to characterize the origin of certain ores.

Problems

20.1 There are at least four groups needed for an act of nuclear terrorism. They are (a) the terrorist group itself, (b) nuclear specialists whose

expertise is needed for certain procedures, (c) a supplier state who supplies the weapons or weapons usable materials, and (d) intermediates who provide transportation, funding, and so on. Describe the role of nuclear forensics has with regard to each of these groups.

20.2 Derive Equation 20.4

20.3 Using the nomograph in Figure 20.6 and the information that the radiation dose rate due to fallout is 1 rad/h at 10 h after a nuclear explosion, calculate the dose rate at 100 h after the event. Comment on your answer.

20.4 In our discussions of the ^{230}Th/^{234}U chronometer, we neglected the decay of ^{238}Pu that might be present in the sample into ^{234}U. Quantitatively evaluate effect of any ^{238}Pu present in the sample on the ^{230}Th/^{234}U chronometer by computing the ^{230}Th/^{234}U atom ratio (as a function of age) from the ^{230}Th/^{238}Pu and ^{234}U/^{238}Pu ratios and comparing this to the normal ^{230}Th/^{234}U chronometer.

20.5 Consider the ^{234}Th/^{238}U chronometer. Plot the ^{234}Th/^{238}U atom ratio as a function of the age of a U sample. Comment on the utility of this chronometer.

20.6 Assuming a yield of 3×10^{23} fission product nuclei are formed per kT of fission energy yield, calculate the mass of ^{140}Ba nuclei formed in the explosion of a 10 kT weapon. Assume the cumulative yield of ^{140}Ba is 5.99% from fission spectrum neutron-induced fission of ^{235}U. How would this estimate change if the weapon were known to be a "boosted" weapon?

20.7 Show that $\sim 3 \times 10^{23}$ fission product nuclei are formed per kT of fission energy yield

20.8 Describe the procedure(s) you would use to measure the Pu isotopic ratios of fallout debris.

Bibliography

P. Baxter, The False Hope of Nuclear Forensics? Assessing the Timeliness of Forensics Intelligence. https://fas.org/pir-pubs/the-false-hope-of-nuclear-forensics-assessing-the-timeliness-of-forensics-intelligence/ (accessed October 4, 2016).

BBC, *Dirty War* (film). https://en.wikipedia.org/wiki/Dirty-War-(film)(accessed October 4, 2016).

E.S. Beckjord, *The Future of Nuclear Power, An Interdisciplinary MIT Study* (Massachusetts Institute of Technology MIT, 2003).

W.J. Burns and P. Slovic, Risk Anal. **32**, 579 (2012).

B.B. Cunningham and L.B. Werner, J. Am. Chem. Soc. **71**, 1521 (1949).

T.R. England and B.F. Rider, LA-UR-94-3106, ENDF-349, Evaluation and Compilation of Fission Product Yields (Los Alamos National Laboratory, Los Alamos, 1993).

A.J. Fahey, C.J. Zeissler, D.E. Newbury, J. Davis, and R.M. Lindstrom, PNAS **107**, 20207 (2010).

J.A. Giesecke, W.J. Burns, A. Barrett, E. Bayrak, A. Rose, P. Slovic, and M. Suher, Risk Anal. **32**, 583 (2012).

S. Glasstone and P.J. Dolan, *The Effects of Nuclear Weapons*, 3rd Edition (U.S. Department of Defense, Washington, 1977).

H.G. Hicks, Health Phys. **42**, 585 (1982).

D.R. Hofstadter, *Metamagical Themas* (Basic, New York, 1985).

International Atomic Energy Agency, *Nuclear Forensics Support Reference Manual* (IAEA, Vienna, 2006).

H.M. Kristensen and R.S. Norris, Status of World Nuclear Forces. http://fas.org/issues/nuclear-weapons/status-world-nuclear-forces/ (accessed October 4, 2016).

K. Mayer et al., J. Phys. Conf. Series 312, 062003 (2011).

K. Mayer, M. Wallenius, and Z. Vargu, Chem. Rev. **113**, 884 (2012).

K.J. Moody, P.M. Grant, and I.D. Hutcheon, *Nuclear Forensic Analysis*, 2nd Edition (CRC Press, Boca Raton, 2015) — This book is the "bible" for nuclear forensics and the most authoritative source for information.

National Planning Scenarios 1, 11, 15. National Planning Scenarios Version 21.3 2006 Final Draft. http://publicintelligence.net/national-planning-scenarios-version-21-3-2006-final-draft (accessed October 4, 2016).

E.B. Norman, K.J. Thomas, and K.E. Telhami, Am. J. Phys. **83**, 843 (2015).

Nuclear Forensics, Role. State of the Art, Program Needs. Joint Working Group of the American Physical Society and the American Association for the Advancement of Science. December 2012.

G.T. Seaborg, *History of the MET Lab Section C-1, April 1942 to April 1943*, (Lawrence Berkeley Laboratory, Berkeley, 1977), p. 228.

F.E. Stanley, J. Anal. At. Spectrom. **27**, 1821 (2012).

R.W. Williams and A.M. Gaffney, Proc. Radiochim. Acta **1**, 31 (2011).

Fundamental Constants and Conversion Factors

Table A.1 Fundamental Constants.

Quantity	Symbol (Expression)	Value	SI Units	cgs Units
Speed of light (in vacuum)	c	2.99792458	10^8 m/s^1	10^{10} cm/s^1
Elementary charge	e	1.6021766208	10^{-19} C	10^{-20} emu
Planck constant	h	6.626070040	10^{-34} J s	10^{-27} ergs
	$\hbar = h/2\pi$	1.054571800	10^{-34} J s	10^{-27} ergs
Boltzmann constant	k_B	1.38064852	10^{-23} J/K^1	10^{-16} erg K^1
Avogadro's number	N_A	6.022140857	10^{23}/mol^1	10^{23}/mol^1
Molar gas constant	R	8.3144598	J/mol^{-1}/K^1	10^7 erg/mol^1/K^1
Rydberg constant	$R_\infty = m_e\alpha^2/2h$	1.0973731568	10^7/m^1	10^5/cm^1
Bohr magneton	$\mu_B = eh[c]/2m_e c$	9.274009994	10^{-24}/J T^1	10^{-21}/erg G^1
Nuclear magneton	$\mu_N = eh[c]/2m_p c$	5.050783699	10^{-27}/J T^1	10^{-24}/erg G^1
Fine structure constant	$\alpha = [4\pi\epsilon_0]^{-1}e^2/hc$	7.2973525664		
	$1/\alpha$	137.035999139		
Permittivity (free space)	ϵ_0	8.854187817	10^{-12}C^2/N^1/m^2	

(*Continued*)

Quantity	Symbol (Expression)	Value	SI Units	cgs Units
Atomic mass unit	u	1.660539040	10^{-27}kg	10^{-24}g
Electron rest mass	m_e	9.10938356	10^{-31}kg	10^{-28}g
Proton rest mass	m_p	1.672621898	10^{-27}kg	10^{-24}g
Neutron rest mass	m_p	1.674927471	10^{-27}kg	10^{-24}g
Muon rest mass	m_μ	1.883531594	10^{-28}kg	10^{-25}g
Bohr radius	$a_0 = r_e/\alpha^2$	5.2917721067	10^{-11} m	10^{-9}cm
Electron classical radius	$r_e = \alpha h/m_e c$	2.8179403227	10^{-15}m	10^{-13}cm
Compton wavelengths				
Electron	$\lambda_{c,e} = h/m_e c$	2.4263102367	10^{-12}m	10^{-10}cm
Proton	$\lambda_{c,p} = h/m_p c$	1.32140985396	10^{-15}m	10^{-13}cm
Neutron	$\lambda_{c,n} = h/m_n c$	1.31959090481	10^{-15}m	10^{-13}cm
Magnetic dipole moments				
Electron	μ_e	−1.00115965218091	μ_B	
Proton	μ_p	2.7928473508	μ_N	
Neutron	μ_n	−1.91304273	μ_N	
Proton gyromagnetic ratio	γ_p	2.675221900	$10^8/s^1/T^1$	$10^4/s^1/G^1$

Table A.2 Conversion Factors and Handy Units.

Quantity	Symbol	Value
Atomic mass unit	u	931.4940954 MeV
Electron mass	m_e	0.5109989461 MeV
Proton mass	m_p	938.2720813 MeV
Neutron mass	m_n	939.5654133 MeV
Electron volt	1 eV	$1.6021766208 \times 10^{19}$ J
Electron volt per particle	$1 \text{ eV}/k_B$	11,604.5221 K
Planck constant	h	$6.582119514 \times 10^{-22}$ MeV s
	$\hbar c$	197.3269788 MeV fm
	$(\hbar c)^2$	0.389379 GeV mb
Rydberg constant	$R_\infty hc$	13.605693009 eV
1 degree	°	1.7453×10^{-2} rad
1 calorie	cal	4.184 J
1 British thermal unit	Btu	1,054.350 J
1 erg	erg	10^{-7} J
1 ton (equivalent of TNT)		4.184×10^9 J
1 fermi	fm	10^{-15} m
1 light year	ly	9.4605284×10^{15} m
1 parsec	pc	$3.08567759 \times 10^{16}$ m
1 atmosphere	atm	101,325 Pa
1 torr (mm Hg, 0°C)		133.322368 Pa
1 day	d	86,400 s
1 year (365.25636 d)	year	3.1558150×10^7 s
1 curie	Ci	3.7×10^{10} Bq (exact)
1 rad		10^{-2} Gy
1 rem		10^{-2} Sv
1 roentgen	R	2.580×10^{-4} C/k

Appendix C

6	7	8	9	10	11	12	13	
IB	VIIB	-	VIII	-	IB	IIB	IIIA	I
							B	
							5	
							Al	
							13	
Cr	Mn	Fe	Co	Ni	Cu	Zn	Ga	C
24	25	26	27	28	29	30	31	
Mo	Tc	Ru	Rh	Pd	Ag	Cd	In	
42	43	44	45	46	47	48	49	
W	Re	Os	Ir	Pt	Au	Hg	Tl	
74	75	76	77	78	79	80	81	
Sg	Bh	Hs	Mt	Ds	Rg	Cn	Nh	
106	107	108	109	110	111	112	113	
m	Sm	Eu	Gd	Tb	Dy	Ho	Er	T
61	62	63	64	65	66	67	68	
Np	Pu	Am	Cm	Bk	Cf	Es	Fm	N
93	94	95	96	97	98	99	100	1

Alphabetical List of the Elements

Name	Symbol	Z	Name	Symbol	Z	Name	Symbol	Z
Actinium	Ac	89	Germanium	Ge	32	Potassium	K	19
Aluminum	Al	13	Gold	Au	79	Praseodymium	Pr	59
Americium	Am	95	Hafnium	Hf	72	Promethium	Pm	61
Antimony	Sb	51	Hassium	Hs	108	Protactinium	Pa	91
Argon	Ar	18	Helium	He	2	Radium	Ra	88
Arsenic	As	33	Holmium	Ho	67	Radon	Rn	86
Astatine	At	85	Hydrogen	H	1	Rhenium	Re	75
Barium	Ba	56	Indium	In	49	Rhodium	Rh	45
Berkelium	Bk	97	Iodine	I	53	Rubidium	Rb	37
Beryllium	Be	4	Iridium	Ir	77	Ruthenium	Ru	44
Bismuth	Bi	83	Iron	Fe	26	Rutherfordium	Rf	104
Bohrium	Bh	107	Krypton	Kr	36	Samarium	Sm	62
Boron	B	5	Lanthanum	La	57	Scandium	Sc	21
Bromine	Br	35	Lawrencium	Lr	103	Seaborgium	Sg	106
Cadmium	Cd	48	Lead	Pb	82	Selenium	Se	34
Cesium	Cs	55	Lithium	Li	3	Silicon	Si	14
Calcium	Ca	20	Livermorium	Lv	116	Silver	Ag	47
Californium	Cf	98	Lutetium	Lu	71	Sodium	Na	11
Carbon	C	6	Magnesium	Mg	12	Strontium	Sr	38
Cerium	Ce	58	Manganese	Mn	25	Sulfur	S	16
Chlorine	Cl	17	Mendelevium	Md	101	Tantalum	Ta	73
Chromium	Cr	24	Mercury	Hg	80	Technetium	Tc	43

Name	Symbol	Z	Name	Symbol	Z	Name	Symbol	Z
Cobalt	Co	27	Molybdenum	Mo	42	Tellurium	Te	52
Copernicium	Cn	112	Moscovium	Mc	115	Tennessine	Ts	117
Copper	Cu	29	Neodymium	Nd	60	Terbium	Tb	65
Curium	Cm	96	Neon	Ne	10	Thallium	Tl	81
Dubnium	Db	105	Neptunium	Np	93	Thorium	Th	90
Dysprosium	Dy	66	Nickel	Ni	28	Thulium	Tm	69
Einsteinium	Es	99	Nihonium	Nh	113	Tin	Sn	50
Erbium	Er	68	Niobium	Nb	41	Titanium	Ti	22
Europium	Eu	63	Nitrogen	N	7	Tungsten	W	74
Fermium	Fm	100	Nobelium	No	102	Uranium	U	92
Flerovium	Fl	112	Oganesson	Og	118	Vanadium	V	23
Fluorine	F	9	Osmium	Os	76	Xenon	Xe	54
Francium	Fr	87	Oxygen	O	8	Ytterbium	Yb	70
Gadolinium	Gd	64	Palladium	Pd	46	Yttrium	Y	39
Gallium	Ga	31	Phosphorus	P	15	Zinc	Zn	30
			Platinum	Pt	78	Zirconium	Zr	40
			Plutonium	Pu	94			
			Polonium	Po	84			

Elements of Quantum Mechanics

Quantum mechanics provides a correct description of phenomena on the atomic or subatomic scale, where the ideas of classical mechanics are not generally applicable. As we describe nuclear phenomena, we will use many results and concepts from quantum mechanics. While it is *not* our goal to have the reader, in general, perform detailed quantum mechanical calculation, it is important that the reader understands the basis for many of the descriptive statements made in the text. Therefore, we present, in this appendix, a brief summary of the essential features of quantum mechanics that we shall use. For more detailed discussion of these features, we refer the reader to the bibliography at the end of this appendix.

E.1 Wave Functions

All the knowable information about a physical system (i.e., energy, angular momentum, etc.) is contained in the wave function of the system. We shall restrict our discussion to one-body systems for the present. (We could easily generalize to many body systems.) The wave function can be expressed in terms of space coordinates and time or momenta and time. In the former notation we write $\Psi(x, y, z, t)$ or just Ψ. These wave functions must be "well behaved," that is, they (and their derivatives with respect to the space coordinates) must be continuous, finite, and single valued. The functions Ψ are solutions to a second order differential equation called the Schrödinger equation (see following text).

The probability of finding a particle within a volume element of the Cartesian coordinate system $dx\,dy\,dz$, written as $W\,dx\,dy\,dz$, is given by the expression

$$W dx dy dz = \Psi^* \Psi \, dx \, dy \, dz \tag{E.1}$$

where Ψ^* is the complex conjugate of Ψ. (To form the complex conjugate of any complex number, replace all occurrences of i (where $i = \sqrt{-1}$) with $-i$. For example, real numbers are their own complex conjugates, whereas $6 - 5i$ is the

complex conjugate of $6 + 5i$ and the product of a function with its complex conjugate $(a + ib)(a + ib)^* = (a + ib)(a - ib) = a^2 + b^2$.) The probability per unit volume, called the *probability density*, is $W = \Psi^*\Psi$. If we look everywhere in a closed system, then we must find the particle so that the integrated probability must be one:

$$\int \Psi^* \, \Psi \, d\tau = 1 \tag{E.2}$$

where we have used the shorthand $d\tau$ for the volume element $dx \, dy \, dz$ in Cartesian coordinates. Wave functions possessing this numerical property are said to be *normalized*. If the value of some physical quantity P is a function of the position coordinates, the average of P is given by

$$\langle P \rangle = \int \Psi^* \, P \, \Psi \, d\tau \tag{E.3}$$

This average over the wave function is called the expectation value, and it represents the average outcome of a large number of measurements of the property P.

E.2 Operators

Often we want to compute values of quantities that are not simple functions of the space coordinates, such as the y component of the momentum p_y where the averaging procedure shown earlier is not applicable. To get around the limitation, we say that corresponding to every classical (observable) variable, there is a *quantum mechanical operator*. An operator is a symbol that directs us to do some mathematical operation. For example, the momentum operators are

$$\hat{p}_x = -i\hbar \frac{\partial}{\partial x}; \hat{p}_y = -i\hbar \frac{\partial}{\partial y}; \hat{p}_z = -i\hbar \frac{\partial}{\partial z} \tag{E.4}$$

while the *total* energy operator $\hat{E}$ is given by the expression

$$\hat{E} = i\hbar \frac{\partial}{\partial t} \tag{E.5}$$

Thus, to calculate the expectation value of the x-component of the momentum p_x we should write

$$\langle p_x \rangle = \int \Psi^* \left(-i\hbar \frac{\partial}{\partial x} \right) \Psi \, d\tau \tag{E.6}$$

$$= -i\hbar \int \Psi^* \, \frac{\partial \Psi}{\partial x} d\tau \tag{E.7}$$

Recall that the classical expression for the kinetic energy is $T = p^2/2m$, which when translated into quantum mechanical terms is the kinetic energy operator $\widehat{T}$ in Cartesian coordinates:

$$\widehat{T} = \frac{-\hbar}{2m}\left(\frac{\partial^2}{\partial x^2} + \frac{\partial^2}{\partial y^2} + \frac{\partial^2}{\partial z^2}\right) \tag{E.8}$$

or using the Laplacian operator ∇^2 for conciseness:

$$\widehat{T} = \frac{-\hbar}{2m}\nabla^2 \tag{E.9}$$

where ∇^2 in Cartesian coordinates is, of course,

$$\nabla^2 = \frac{\partial^2}{\partial x^2} + \frac{\partial^2}{\partial y^2} + \frac{\partial^2}{\partial z^2} \tag{E.10}$$

E.3 The Schrödinger Equation

In 1926, Erwin Schrödinger found that behavior on the atomic or subatomic scale was correctly described by a differential equation of the form

$$\frac{\hbar^2}{2m}\nabla^2\Psi + V\Psi = i\hbar\frac{\partial\Psi}{\partial t} \tag{E.11}$$

where V represents the potential energy and Ψ the wave function of the system. Substituting for the expression for the total energy of the system from earlier, we can write

$$\frac{\hbar^2}{2m}\nabla^2\Psi + V\Psi = E\Psi \tag{E.12}$$

This equation is an example of a general class of equations called *eigenvalue equations* of the form $\widehat{\Omega}\Psi = \omega\Psi$ where $\widehat{\Omega}$ is an operator and ω is the *eigenvalue* (German for "one value") of an observable corresponding to that operator. (The mathematical expression Ψ that satisfies this relationship is thus referred to as an *eigenfunction* of the operator $\widehat{\Omega}$.)

To use the Schrödinger equation to gain information about a physical system, we must perform a set of steps that are as follows:

1) Specify the potential energy function of the system, that is, specify the forces acting (Section 1.8.1).
2) Find a mathematical function, Ψ, which is a solution to the differential equation, the Schrödinger equation.
3) Of the many functions that satisfy the equation, reject those that do not conform to certain physical constraints on the system, known as boundary conditions.

Before illustrating this procedure for several cases of interest to nuclear chemists, we can point out another important property of the Schrödinger equation. If the potential energy V is independent of time, we can separate the space and time variables in the Schrödinger equation and write

$$\Psi(x, y, z, t) = \psi(x, y, z)\, \tau(t) \tag{E.13}$$

Substituting this separated expression back into the general equation earlier and separating the time-dependent terms,

$$\frac{1}{\Psi}\frac{-\hbar^2}{2m}\nabla^2\Psi + V = \frac{i\hbar}{\tau}\frac{\partial\tau(t)}{\partial t} \tag{E.14}$$

This equality can only be true if each side of the equation is equal to a constant. Otherwise the RHS with a function of time would have to be equal to the LHS, which would be a function of spatial variables. If we call this result of the separation the "constant," E, we can write

$$\frac{1}{\psi}\frac{-\hbar^2}{2m}\nabla^2\psi + V = E \tag{E.15}$$

or in the more well-known form, which is called the *time-independent Schrödinger equation*,

$$\frac{-\hbar^2}{2m}\nabla^2\psi + V\psi = E\psi \tag{E.16}$$

and the time-dependent side would become

$$i\hbar\frac{\partial\tau(t)}{\partial t} = E\tau(t) \tag{E.17}$$

A solution to this time-dependent equation is

$$\tau(t) = C^{\,-iE\,t/\hbar} \tag{E.18}$$

where C is a constant. Using the Euler relation that $e^{i\theta} = \cos\theta + i\,\sin\theta$, we can rewrite the solution as

$$\tau(t) = \cos(\omega\,t) - i\sin(\omega\,t) \tag{E.19}$$

where $\tau(t)$ is thus a periodic function with an angular frequency $\omega = E/\hbar$. The separation constant E can be shown to be the total energy, that is, the sum of the kinetic and potential energies, $T + V$.

E.4   The Free Particle

To illustrate how the Schrödinger equation might be applied to a familiar situation, consider the case of a "free" particle, that is, a particle moving along at a constant velocity with no force acting on the particle ($V = 0$) as indicated
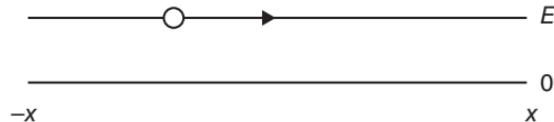
Figure E.1 Schematic representation of a free particle moving in the positive *x*-direction over a constant potential energy, $V = 0$.

in Figure E.1. For simplicity, let us consider motion in one dimension, the *x*-direction. For the time-independent Schrödinger equation, we have

$$\frac{-\hbar^2}{2m}\frac{d^2\psi}{dx^2} = E\psi \tag{E.20}$$

using the simple derivative since it is a one-dimensional problem. Collecting constants on the RHS,

$$\frac{d^2\psi}{dx^2} = k^2\,\psi, \text{ with } k^2 = \frac{2mE}{\hbar^2} \tag{E.21}$$

The allowed values of the energy E will be given by the expression

$$E = \frac{k^2\hbar^2}{2m} \tag{E.22}$$

where k can assume any value (i.e. E is not quantized). Since $V = 0$ in this simple case, E is just the kinetic energy of a particle with momentum $p = hk$. From de Broglie, we know that all moving particles have a wavelength given by the momentum, $\lambdabar = \hbar/p$, so that we can associate k with the wave number as $k = 1/\lambdabar$.

Combining the two separate parts of the solution for the Schrödinger equation in this one-dimensional problem, we have

$$\Psi(x, t) = A\,\exp[ikx - i\omega t] + B\,\exp[-ikx - i\omega t] \tag{E.23}$$

where $k = \sqrt{2mE}/\hbar$ and $\omega = E/\hbar$ as given earlier. This solution is the equation for a wave traveling to the right (+x direction, the first term) and to the left (−x direction, second term). We can impose a boundary condition, namely, we can specify the particle is traveling in the +x direction. Then we have

$$\Psi(x, t) = A\,\exp[ikx]\,\exp[-i\omega t] \tag{E.24}$$

We can now calculate the values of any observable for which we can write an operator. For example, to calculate the value of the momentum p, we write (see earlier text for the momentum operator)

$$\langle p_x \rangle = \int_{-\infty}^{+\infty} \psi^* \left(-i\hbar\frac{\partial}{\partial x}\right) \psi\,dx = \sqrt{2mE} \tag{E.25}$$

which after some calculus agrees, of course, with the classical result.
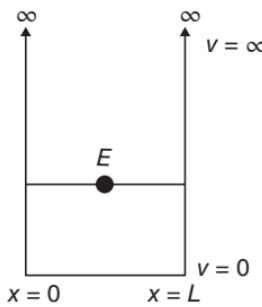
Figure E.2 Schematic representation of a particle in a one-dimensional box with a "flat" bottom, $V = 0$. The particle is free to move between $x = 0$ and $x = L$ but not allowed to have $x < 0$ or $x > L$.

E.5   Particle in a Box (One Dimension)

Continuing our survey of some simple applications of wave mechanics to problems of interest to the nuclear chemist, let us consider the problem of a particle confined to a one-dimensional box as indicated in Figure E.2. The potential energy is flat across the bottom of the box and then rises to infinity at the walls and remains infinity everywhere outside the box. This can be expressed as

$$V(x) = \infty \text{ for } x < 0 \tag{E.26}$$
$$V(x) = 0 \text{ for } 0 \leq x \leq L \tag{E.27}$$
$$V(x) = \infty \text{ for } x > L \tag{E.28}$$

and the particle can move freely between 0 and L but is excluded from the regions with $x < 0$ and $x > L$. Inside the box, the Schrödinger equation has the *form* developed earlier for the free particle, but there are added constraints or *boundary conditions*. The general time-independent solution can be written as

$$\psi(x) = A \sin kx + B \cos kx \tag{E.29}$$

But we know that $\psi(x)$ must be zero at $x = 0$ and at $x = L$ (the particle can't be in the wall). Thus, due to the properties of the cosine function, B must be zero, leaving both

$$A \sin(0) = 0 \text{ and } A \sin(k L) = 0 \tag{E.30}$$
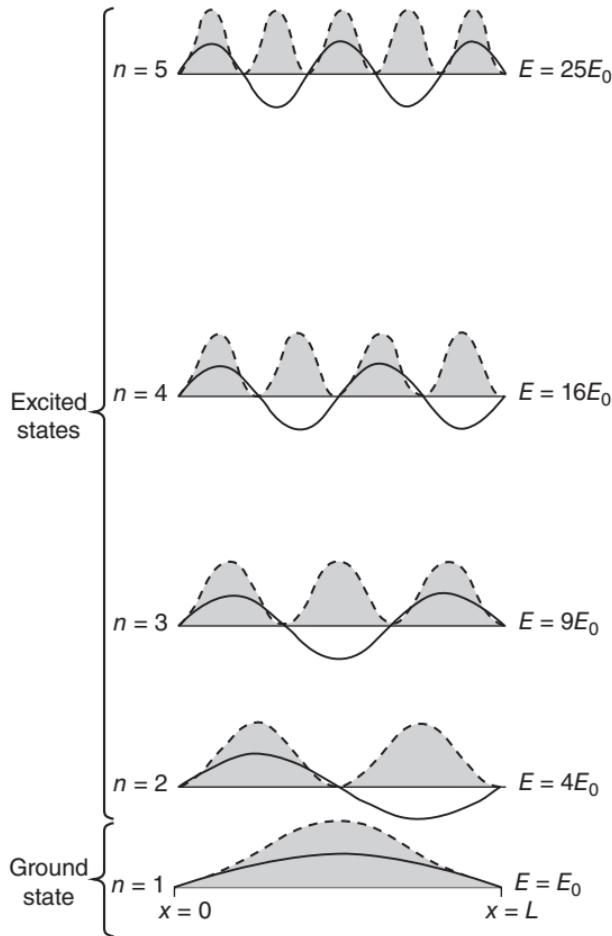
The sine of zero is zero, but the second condition $\sin(kL) = 0$ is true for all integer multiples of π. Thus,

$$kL = n\pi \text{ where } n = 1, 2, \ldots \tag{E.31}$$

Now using the result for the energy of the free particle earlier, we find a *quantized* set of energies:

$$E_n = \frac{\hbar^2 k^2}{2m} = \frac{\hbar^2 \pi^2}{2m} n^2 \tag{E.32}$$

Figure E.3 Schematic representation of the allowed energy levels of a particle in a one-dimensional box. The wave function is shown as a solid line for each level, while the shaded area indicates the probability density.

In this case with the boundary conditions, only certain values of the energy are allowed. One can also show the normalization condition is satisfied if

$$\psi_n(x) = \sqrt{\frac{2}{L}} \sin\left(\frac{n\pi x}{L}\right) \tag{E.33}$$

The allowed energy levels, the probability densities, and the wave functions are shown for the first few levels of this potential in Figure E.3.

Sample Problem E.1: Particle in a Box

Suppose a neutron is confined to a box that is approximately the size of a nucleus, 10^{-14}m. (a) What is the energy of the first excited state? (b) What amount of energy will be necessary to promote the neutron from the ground state up to the first excited state? (c) What is the probability of finding the neutron within a region corresponding to 20% of the width of the box, that is, between 0.4×10^{-14} and 0.6×10^{-14}m when it is in the fourth excited state?

Solution

(a) The energy of the ground state can be obtained from the formula earlier with $n = 1$.

$$\begin{aligned}
E_0 &= \frac{\hbar^2 \pi^2 (n)^2}{2mL^2} \\
&= \frac{(1.05 \times 10^{-34} \text{Js})^2 (3.141)^2 (1)^2}{2(1.66 \times 10^{-27} \text{kg})(10^{-14})^2} \\
&= 3.3 \times 10^{-13} \text{ J} = 2.0 \text{ MeV}
\end{aligned}$$

(b) Note that the energy of the first excited state, $n = 2$, will be $4E_0$ and the energy spacing between the first excited state and the ground state will be $3E_0 = 6$ MeV.

(c) The probability comes from integrating the square of the wave function between the given limits:

$$\begin{aligned}
P(n = 5) &= \int_{x1}^{x2} \psi^* \psi \, dx = \int_{x1}^{x2} \left(\sqrt{\frac{2}{L}} \sin\left(\frac{5\pi x}{L}\right) \right)^2 dx \\
&= \left(\frac{x}{L} - \frac{1}{5\pi} \sin\left(\frac{5\pi x}{L}\right) \right) \Big|_{x1}^{x2} \\
&= 0.20
\end{aligned}$$

This result can be confirmed by inspection of the ψ^2 curve shown in Figure E.3.

E.6   Harmonic Oscillator (One Dimensional)

One of the classic problems of quantum mechanics that is very important for our study of nuclei is the *harmonic oscillator*. For a simple harmonic oscillator, the restoring force is proportional to the distance from the center, that is, $F = -kx$ so that the potential energy $V(x) = k x^2/2$. This is a parabolic potential energy that only becomes infinite at infinite distance from the center. The Schrödinger equation for this system is

$$\frac{-\hbar^2}{2m} \frac{d^2\psi}{dx^2} + \frac{1}{2} k x^2 \psi = E\psi \tag{E.34}$$

The solution of this equation is mathematically complicated and leads to wave functions of the form

$$\psi_n(x) = N_n \, e^{-\beta^2/2} \, H_n(\beta) \tag{E.35}$$
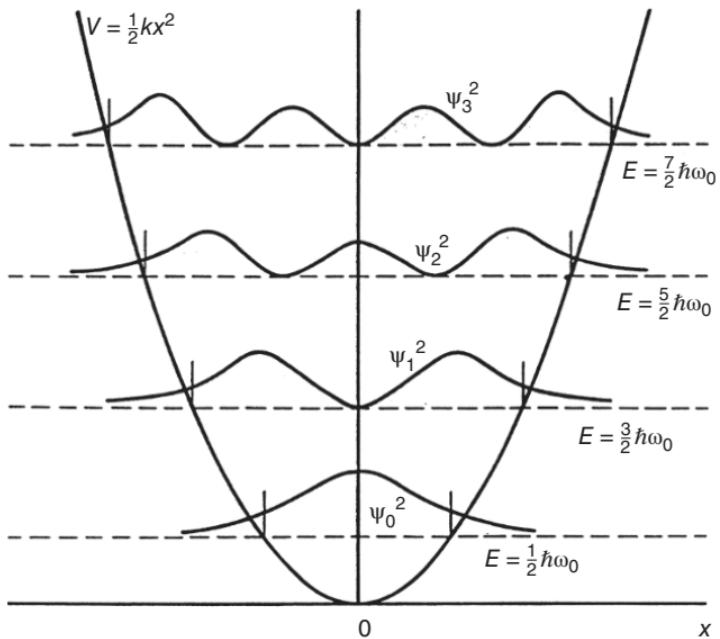
Figure E.4 Representation of the low-lying levels, their energies, and associated probability densities in a 1-D harmonic oscillator.

where

$$\beta = \sqrt{\alpha}\, x \tag{E.36}$$

$$\alpha = \frac{2\pi\, m}{\hbar}\, \nu_0 \tag{E.37}$$

and the fundamental oscillator frequency ν_0 is

$$\nu_0 = \frac{1}{2\pi} \sqrt{\frac{k}{m}} \tag{E.38}$$

with a normalization constant that depends on the quantum number n as

$$N_n = \left(\sqrt{\frac{\alpha}{\pi}} \frac{1}{2^n\, n!} \right)^{1/2} \tag{E.39}$$

The expression $H_n(\beta)$ is the n-th Hermite polynomial (which can be found in various handbooks of mathematical functions). Finally, the energy eigenvalues can be shown to be

$$E_n = \left(n + \frac{1}{2} \right)\, h\nu_0 \tag{E.40}$$

where in this case $n = 0, 1, 2, \ldots$. Notice that the ground state corresponds to the $n = 0$ state for this set of equations; the reason for the difference stems from the uncertainty relation. The energy levels are equally spaced in a harmonic
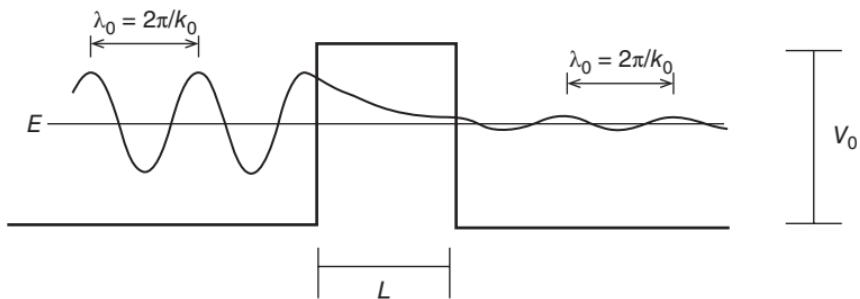
Figure E.5 A schematic diagram of a particle with energy *E* incident on a barrier of height V_0 and thickness *L*. The variation of the wave function ψ in each region is also shown.

oscillator, starting with the zero point energy $h\nu_0$ as indicated in Figure E.4. Note also that the solutions have the property that there is some probability of finding the particle in classically forbidden regions, that is, the particle penetrates into the walls.

E.7 Barrier Penetration (One Dimensional)

Another important quantum mechanical problem of interest to nuclear chemists is the penetration of a one-dimensional potential energy barrier by a beam of particles. The results of solving this problem (and more complicated variations of the problem) will be used in our study of nuclear α-decay and nuclear reactions. The situation is indicated schematically in Figure E.5. A beam of particles originating at $-\infty$ is incident on a barrier of thickness *L* and height V_0 that extends from $x = 0$ to $x = L$. Each particle has a total energy *E*. (Classically, we would expect if $E < V_0$, the particles would bounce off the barrier, while if $E > V_0$, the particles would pass by the barrier with no change in their properties. Both conclusions are altered significantly in quantum mechanics.)

It is conventional to divide the space into three regions, I, II, and III, shown in Figure E.5. In regions I and III, we have the "free particle" problem treated earlier. In region I, we have particles moving to the left (the incident particles) and particles moving to the right (reflected particles). So we expect a wave function with two components, whose time-independent part can be written as

$$\psi_I = A_I e^{ik_I x} + B_I e^{-ik_I x} = \psi_{I\rightarrow} + \psi_{I\leftarrow} \tag{E.41}$$

where the wave number in region I is

$$k_I = \sqrt{\frac{2mE}{\hbar}} \tag{E.42}$$

In region III, we have no particles incident from $+\infty$, so, at best, we can only have particles moving in the $+x$ direction ($B_{\text{III}} = 0$). Thus,

$$\psi_{\text{III}} = A_{\text{III}} \, e^{ik_1 x} = \psi_{\text{III}\rightarrow} \tag{E.43}$$

The time-independent Schrödinger equation for region II is

$$\frac{d^2\psi_{\text{II}}}{dx^2} = k_2 \psi_{\text{II}} \tag{E.44}$$

where $k_2 = [2m(V_0 - E)]^{1/2}/\hbar$ assuming $V_0 > E$. The solution is

$$\psi_{\text{II}} = A_{\text{II}} \, e^{k_2 x} + B_{\text{II}} \, e^{-k_2 x} \tag{E.45}$$

Notice that the wave length λ is the same in regions I and III, but the amplitude of the wave beyond the barrier is much less than in front of the barrier. It can be shown that the probability of transmitting particles through the barrier is

$$T = \frac{|\psi_{\text{III}\rightarrow}|^2 \, v}{|\psi_{\text{III}\rightarrow}|^2 \, v} = \frac{|A_{\text{III}}|^2}{|A_{\text{I}}|^2} \tag{E.46}$$

where v is the particle speed. To determine the ratio $A_{\text{III}}/A_{\text{I}}$, we need to eliminate the other constants B_{I}, A_{II}, and B_{II} by applying the requirements that ψ and $d\psi/dx$ be continuous through all space for a valid wave function. After much algebra (see, e.g., the textbook by Evans), we have

$$T = \left[1 + \frac{V_0^2}{4E(V_0 - E)} \, \sinh^2 k_2 L \right]^{-1} \tag{E.47}$$

For nuclear applications, the barriers are quite thick ($k_2 L \gg 1$), in which case, $\sinh^2 k_2 L \approx \frac{1}{4} e^{2k_2 L}$ and

$$T \approx 16 \frac{E}{V_0} \left(1 - \frac{E}{V_0} \right) e^{-2k_2 L} \tag{E.48}$$

The dominant term in this expression is the exponential. As an example, for a 6 MeV α-particle and a nucleus with $V_0 = 20$ MeV and $L = 10^{-14}$ m, we get

$$k_2 \approx \frac{\sqrt{2 \times 4 \times 1.6 \times 10^{-27} \times (20 - 6) \times 1 \times 10^{-12}}}{1.05 \times 10^{-34}} \tag{E.49}$$

$$k_2 \approx 5.1 \times 10^{15} \text{ m}^{-1} \text{ and } e^{-2k_2 L} = e^{-102} = 5.1 \times 10^{-45} \tag{E.50}$$

and the transmission

$$T \approx 16 \times \left(\frac{8}{20} \right) \left(1 - \left(\frac{8}{20} \right) \right) (5.1 \times 10^{-45}) = 1.9 \times 10^{-44} \tag{E.51}$$

Given the relative magnitudes, the pre-exponential term is generally ignored for nuclear reactions, and the transmission is simply written as $T \approx e^{-2G}$, where

$2G = 2k_2L = 2\sqrt{2m(V_0 - E)}/\hbar$. For an arbitrarily shaped potential that would be more pertinent to nuclear α-decay, one can show that

$$2G = \frac{2}{\hbar} \int_{x_1}^{x_2} \sqrt{2m(V(x) - E)} \, dx \tag{E.52}$$

where the limits of integration x_1 and x_2 are the points where $E = V(x)$.

What about the case where $E > V_0$? In regions I and III, the situation will be similar to that discussed earlier except that the reflected amplitude will be smaller. In region II, however, the wave functions will be traveling waves:

$$\psi_{II} = A_{II} \, e^{ik_{II}x} + B_{II} \, e^{-ik_{II}x} = \psi_{II\rightarrow} + \psi_{II\leftarrow} \tag{E.53}$$

where

$$k_2 = \frac{\sqrt{2m(E - V_0)}}{\hbar} \tag{E.54}$$

Since the wave length in this region λ_{II} is $1/k_2$, we can see by comparing the equations that $\lambda_{II} > \lambda_{I}$ and the momentum $p_{II} = \sqrt{2mk_2}$ is less than p_{I}. In other words, the particle is scattered by the barrier in the potential energy, even when the particle's energy is above the barrier.

E.8   Schrödinger Equation in Spherical Coordinates

Many problems in nuclear physics and chemistry involve potential energy functions, such as the Coulomb potential, which are spherically symmetric. In these cases, it is advantageous to express the time-independent Schrödinger equation in spherical coordinates. The definitions are shown in Figure E.6, and transformations from a Cartesian coordinate system (x, y, z) to spherical coordinates (r, θ, ϕ) are

$$x = r \, \sin\theta \, \cos\phi \quad y = r \, \sin\theta \, \sin\phi \quad z = r \, \cos\theta \tag{E.55}$$

Applying these transformations the time-independent Schrödinger equation in spherical coordinates becomes
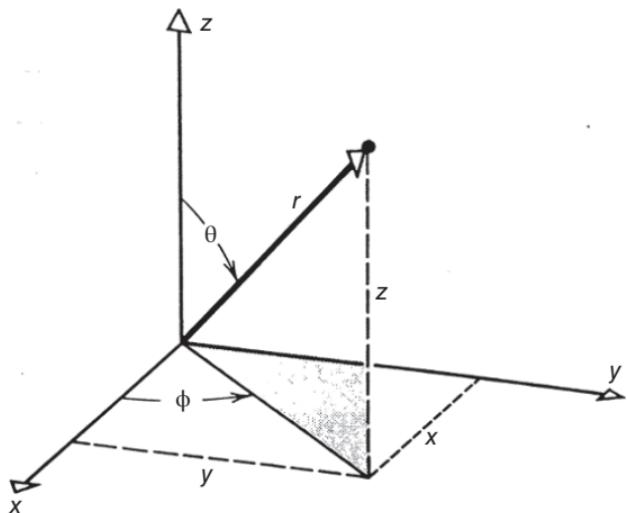
$$\frac{-\hbar^2}{2m} \left[\frac{1}{r^2} \frac{\partial}{\partial r}(r^2 \frac{\partial\psi}{\partial r}) + \frac{1}{r^2 \sin^2\theta} \frac{\partial}{\partial\theta}(\sin^2\theta \frac{\partial\psi}{\partial\theta}) + \frac{1}{r^2 \sin^2\theta} \frac{\partial^2\psi}{\partial\phi^2} \right] + V\psi = E\psi \tag{E.56}$$

When the potential is spherically symmetric, $v = v(r)$, and it does not have an angular dependence, then the wave function can be written as

$$\psi(r, \theta, \phi) = R(r) \, Y_{\ell,m}(\theta, \phi) \tag{E.57}$$

where $Y_{\ell,m}$ are the spherical harmonic functions.

Figure E.6 Definitions used in the spherical–polar coordinate system.

If we substitute this wave function in the Schrödinger equation and collect terms, we find that all functions of r can be separated from the functions of θ and ϕ. Specifically, notice that the LHS contains the radial behavior and the RHS contains the angular behavior:

$$\frac{1}{R}\frac{d}{dr}(r^2\frac{dR}{dr}) + \frac{2mr^2}{\hbar^2}(E - V) = \frac{1}{Y_{\ell,m}}\left[\frac{1}{\sin\theta}\frac{\partial}{\partial\theta}(\sin\theta\frac{\partial Y}{\partial\theta} + \frac{1}{\sin^2\theta}\frac{\partial^2 Y}{\partial\phi^2}\right] \tag{E.58}$$

Using the idea earlier that this expression is only true when both sides equal a constant, in this case $\ell(\ell + 1)$, where $\ell = 0, 1, 2...$, we have

$$\left[\frac{1}{\sin\theta}\frac{\partial}{\partial\theta}(\sin\theta\frac{\partial Y}{\partial\theta} + \frac{1}{\sin^2\theta}\frac{\partial^2 Y}{\partial\phi^2}\right] = \ell(\ell + 1)Y_{\ell,m} \tag{E.59}$$

and

$$\frac{d}{dr}(r^2\frac{dR}{dr}) + \frac{2mr^2}{\hbar^2}(E - V)\,R = \ell(\ell + 1)\,R \tag{E.60}$$

Using a change of variables, $R(r) = u(r)/r$, the radial expression can be converted to a simpler form:

$$\frac{d^2u}{du^2} + \frac{2m}{\hbar^2}\left((E - V(r) - \frac{\ell(\ell + 1)\hbar^2}{2mr^2}\right)u = 0 \tag{E.61}$$

This equality is called the *radial wave equation*. Apart from the term involving ℓ, this expression is the same as the one-dimensional time-independent Schrödinger equation; a fact that is useful, of course, in its solution. The third term inside the parenthesis is referred to as the *centrifugal potential*, that is, a potential energy function whose first derivative with respect to r gives the centrifugal force.

It is important to note that the angular part of the whole equation does not contain a potential energy term. Thus, its solutions will apply to all cases where V does not depend on θ and ϕ, that is, all so-called central potentials. The wave functions $Y_{\ell,m}(\theta, \phi)$ are known as the spherical harmonic functions and are tabulated in many places. The indices ℓ and m are related to the orbital angular momentum, L, of the particle relative to a reference axis. ℓ is called the orbital angular momentum quantum number, while m is the magnetic quantum number, in reference to the different energies of the m states in a magnetic field (the Zeeman effect). The magnitude of L is $[\ell(\ell + 1)]h$ and has $2\ell+1$ possible projections on the reference axis given $m\hbar$ with $m = 0, \pm1, \pm2, \ldots$. (In more formal language, $\langle \ell^2 \rangle = \ell(\ell + 1)\hbar^2$ and $\langle \ell_z \rangle = m\hbar$.) It follows, therefore, that the specification of a particular spherical harmonic function (as a solution to the angular equation) uniquely specifies the particle's orbital angular momentum and its z-component relative to an external reference axis.

E.9 Infinite Spherical Well

As an application of the Schrödinger equation, expressed in spherical coordinates, to a problem of interest in nuclear chemistry, let us consider the problem of a particle in an infinite spherical well with a "flat bottom" as indicated in Figure E.7. This potential energy function is closely related to the particle in a one-dimensional linear box. Here the one dimension is the radius: $V(r) = 0, r < a$ and $V(r) = +\infty, r > a$.

Following our discussion of a spherical potential energy earlier, we expect the solution of the Schrödinger equation to have the form $\psi = R_\ell(r)\, Y_{\ell,m}(\theta, \phi)$ and the radial part of the wave function to be a solution to

$$\frac{1}{r^2}\frac{d}{dr}\left(r^2 \frac{dR_\ell}{dr}\right) + \frac{2m}{\hbar^2}\left((E - \frac{\ell(\ell + 1)\hbar^2}{2mr^2}\right)R_\ell = 0 \tag{E.62}$$

inside the well. The solutions of this equation are the spherical Bessel functions:

$$R_\ell(r) = j_\ell(kr) = \left(-\frac{r}{k}\right)^\ell \left(\frac{1}{r}\frac{d}{dr}\right)^\ell \left(\frac{\sin kr}{kr}\right) \tag{E.63}$$
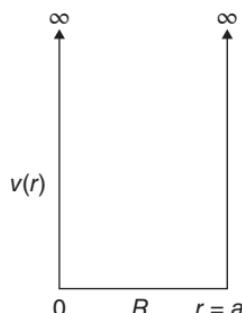
Figure E.7 Simple representation of the radial dependence of the infinite spherical well with a flat bottom.
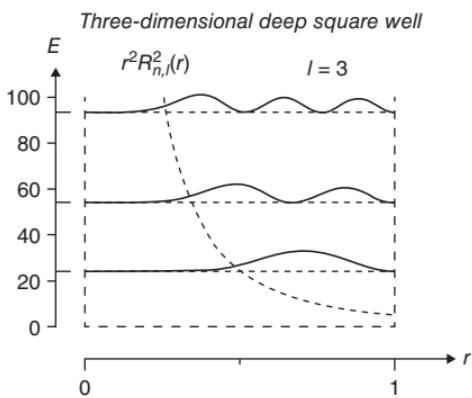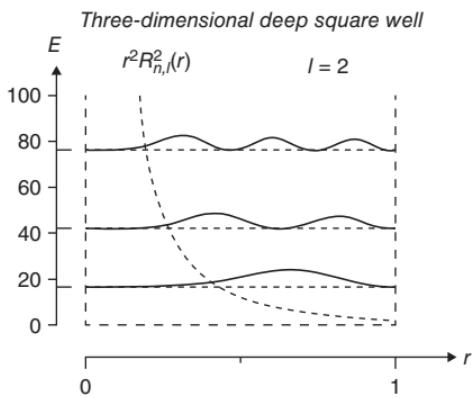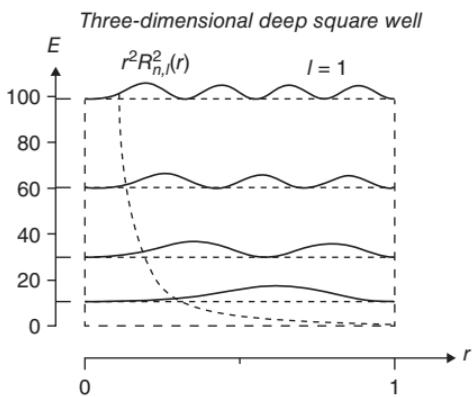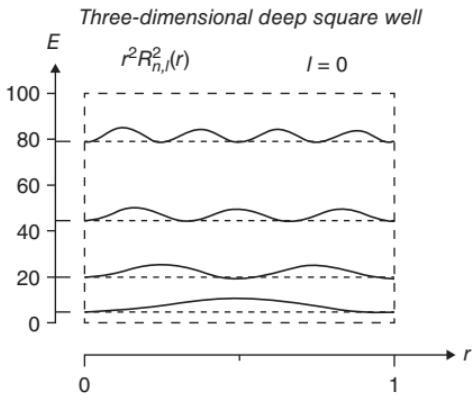
Figure E.8 Representations of the energy levels of an infinitely deep spherical well with a flat bottom. The radical probability density functions, $r^2 R_{n,\ell}^2(r)$, are shown for different values of ℓ.

where $k = \frac{\sqrt{2mE}}{\hbar}$. The boundary conditions require $\psi = 0$ at $r = 0$ and at $r = a$. This will occur for values of k times a that force the Bessel functions to 0 (the so-called "zeros" of these functions and each ℓ value will have its own set of zeros). These resulting values of k can be used to calculate the allowed energy levels, for example, see Figure E.8. Each level is labeled with a number $(1, 2, 3, \ldots)$ and a letter (s, p, d, e, etc.). The letter follows the usual spectroscopic notation for angular momentum, ℓ ($\ell = 0$, s; $\ell = 1$, p, etc.), while the number designates how many times that letter has occurred (the first d level is 1d; the second 2d, etc.). The radial probability distributions are given by the function $r^2 R_{n,\ell}^2(r)$, and a few of the lower values are also shown in Figure E.8, while some of the angular distribution functions, $\Theta_{n,\ell,m}^2(r, \theta)$ not derived here, are shown in Figure E.9.
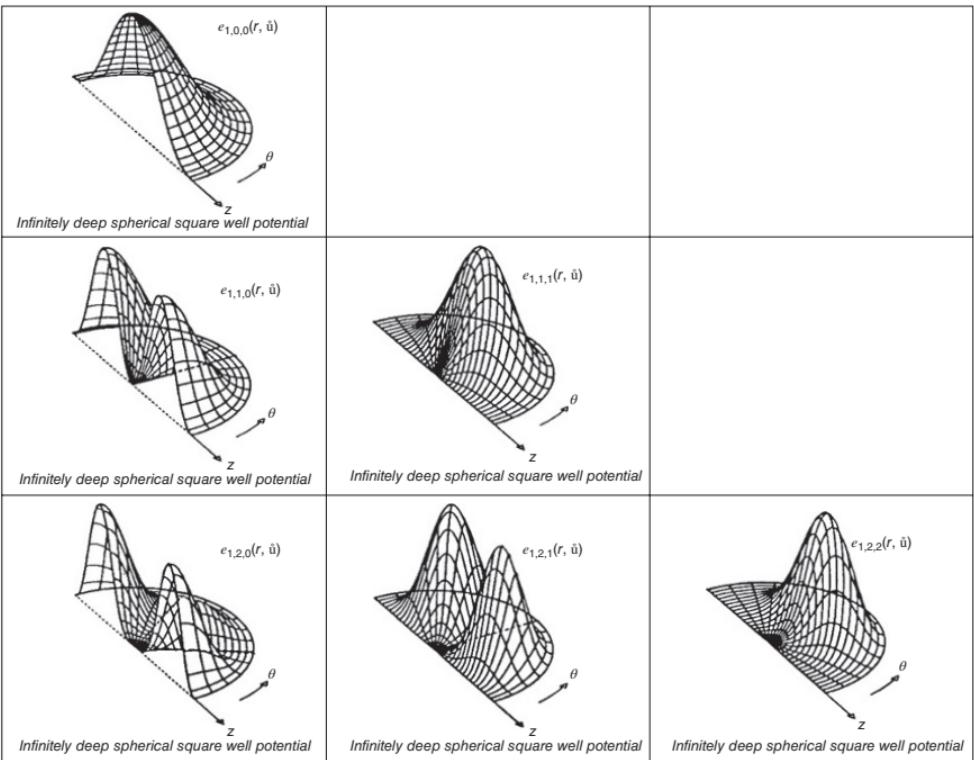
Figure E.9 The three-dimensional probability densities, $\Theta^2_{n,\ell,m}(r, \theta)$, for an infinitely deep three-dimensional square well.

E.10 Angular Momentum

Classically the angular momentum of a particle moving with respect to a reference axis can be written as $\vec{\ell} = \vec{r} \times \vec{p}$ (cf. Section 1.8.1). From this classical expression, we can write down the classical components of the vector $\vec{\ell}$ using spherical coordinates:

$$\ell_x = yp_z - zp_x \quad \ell_y = zp_x - xp_z \quad \ell_z = xp_y = yp_z \tag{E.64}$$

These classical expressions can be converted to the operator language of quantum mechanics by substitutions (e.g., $x \to x, p_x \to i\hbar(\partial/\partial x)$), yielding Cartesian and spherical forms:

$$\ell_x = -i\hbar \left(y\frac{\partial}{\partial z} - z\frac{\partial}{\partial y} \right) = -i\hbar \left(-\sin\phi\frac{\partial}{\partial\theta} - \cot\theta\cos\phi\frac{\partial}{\partial\phi} \right) \tag{E.65}$$

$$\ell_y = -i\hbar \left(z\frac{\partial}{\partial x} - x\frac{\partial}{\partial z} \right) = -i\hbar \left(-\cos\phi\frac{\partial}{\partial\theta} - \cot\theta\sin\phi\frac{\partial}{\partial\phi} \right) \tag{E.66}$$

$$\ell_z = -i\hbar \left(x\frac{\partial}{\partial y} - y\frac{\partial}{\partial x} \right) = -i\hbar\frac{\partial}{\partial\phi} \tag{E.67}$$
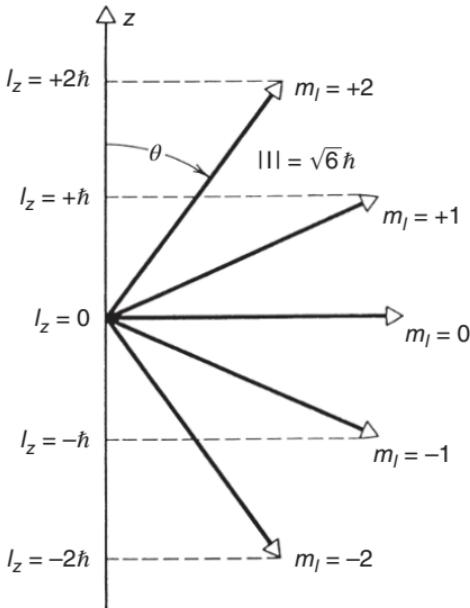
As indicated already earlier, the expectation values of $\langle \ell_z \rangle$ and $\langle \ell^2 \rangle$ for a central potential are

$$\langle \ell_z \rangle = m_\ell \ \text{ where } \ m_\ell = 0, \pm 1, \pm 2, \ldots \pm \ell \ \text{ and } \ \langle \ell^2 \rangle = \ell(\ell + 1)\hbar^2 \tag{E.68}$$

We can give these mathematical results a pictorial interpretation that is worth studying. Consider a system in a state with a definite orbital angular momentum, ℓ; the numerical value of the angular momentum is $\ell = \sqrt{\ell(\ell + 1)}\hbar$. The projection of this angular momentum on a reference axis, z, can be any value from $\ell_z = m_\ell = -\ell\hbar$ up to $\ell_z = m_\ell = +\ell\hbar$. The possible values of ℓ_z can be visualized as the projections of a vector of fixed length ℓ onto the z axis as shown in Figure E.10. This situation is referred to as spatial quantization. Only fixed values of ℓ^2 are allowed, and due to the uncertainty principle; the values of ℓ_x and ℓ_y are completely uncertain. Using the image in Figure E.10, the vector representing ℓ is imagined to be rotating about the z axis so that ℓ and ℓ_z remain constant, but ℓ_x and ℓ_y are continuously changing during the rotation.

We found that to complete description of the quantum state of an electron in an atom, we had to introduce another quantum number, the intrinsic angular momentum or spin of the electron. This quantum number is designated as S. By analogy to the orbital angular momentum quantum number ℓ we have $\langle S^2 \rangle = S(S + 1)\hbar^2$ and $S_z = -S \ to \ +S$; however, the electron spin is $1/2$ so that $m_S = \pm 1/2$. Nucleons also have an intrinsic spin quantum number of $S = 1/2$, like the electrons, and can have an orbital angular momentum inside the nucleus.

Figure E.10 The spatial orientation axis z and the z projections of a vector with $\ell = 2$.

The *total angular momentum* of a nucleon is given the symbol j and is written as the vector sum $\vec{j} = \vec{\ell} + \vec{S}$. The usual quantum mechanical rules apply to j, that is,

$$\langle j^2 \rangle = j(j+1)\hbar^2 \quad \text{and} \quad \langle j_z \rangle = m_j \hbar = \langle \ell_z + S_z \rangle \tag{E.69}$$

where $m_j = -j, -j+1 \ldots j-1, +j$. Thus, we could have written $m_j = m_\ell + m_S = m_\ell \pm 1/2$. Since m_ℓ is always an integer, then m_j and j must be half integers, due to the nucleon spin, that is, either $j = \ell - 1/2$ or $j = \ell + 1/2$. Alternatively, for a given value of ℓ, we have two possible values of j, $j = \ell - 1/2$ or $j = \ell + 1/2$. For example, for $\ell = 1$ (a p state), we have two configurations for the total angular momentum of that nucleon: $j = \ell - 1/2 = 1/2$ or $j = \ell + 1/2 = 3/2$. We designate these states as $p_{1/2}$ and $p_{3/2}$ states, respectively.

E.11 Parity

Parity, with the symbol π, is a description of the inversion symmetry of a wave function (and thus of a quantum mechanical state). A wave function is said to have positive (or even) parity if its numerical value does not change sign by inversion through the origin, thus

$$\text{If} \quad \psi(-x, -y, -z) = \psi(x, y, z), \quad \text{then} \quad \text{parity} = + \ (\pi = +) \tag{E.70}$$

Similarly, if inversion through the origin produces a change of sign, then the parity of the wave function is said to be negative:

$$\text{If} \quad \psi(-x, -y, -z) = -\psi(x, y, z), \quad \text{then} \quad \text{parity} = - \ (\pi = -) \tag{E.71}$$
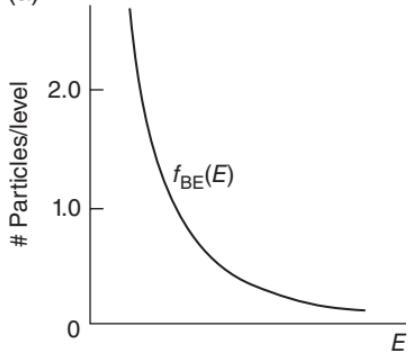
When ψ is expressed in spherical coordinates as $\psi(r, \theta, \phi)$, then "inversion through the origin" is accomplished by replacing θ and φ by $(\pi - \theta)$ and $(\pi + \phi)$, respectively. Notice that r cannot change sign as it is just the distance from the origin. In other words, the parity of the wave function is determined ONLY by its angular part. For spherically symmetric potentials, the value of ℓ uniquely determines the parity since m_ℓ is simply an orientation in space: $\pi = (-1)^\ell$. An important corollary of this is that for a system of particles, the total parity of the wave function is *even* if the sum of the individual orbital angular momentum quantum numbers $\Sigma \ell$ is *even*; the total parity is odd if $\Sigma \ell$ s odd. The excited states of a nucleus need not have the same parity as the ground state since the individual nucleons in an excited state are generally not in the same orbitals as when they are in the ground state.

Parity is important in our discussion of nuclei reactions and nuclear decays. For example, parity is conserved in nuclear reactions; however, parity conservation is violated in beta decay; a fact that tells us that a different force, the weak interaction, must be acting in beta decay compared with nuclear reactions. The γ-ray transitions between nuclear excited states depend on the change in parity between the states, and observation of the angular distributions of the photons (and thus their multipolarity and angular momentum) should be used to determine the parity of nuclear states.
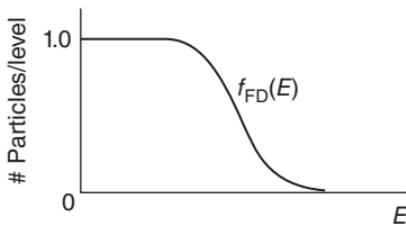
E.12   Quantum Statistics

We just saw that the parity of a system is related to the symmetry properties of the spatial portion of the wave function. Another important quantum mechanical property of a system containing two or more identical particles is the effect on the wave function of exchanging the coordinates of two particles. If there is no change in the wave function when the spatial *and* spin coordinates are exchanged, then we say the wave function is *symmetric* and the particles obey *Bose–Einstein statistics*. On the other hand, if upon exchange of the spatial and spin coordinates of the two particles the wave function changes sign, the wave function is said to be *antisymmetric* and the particles obey *Fermi–Dirac statistics.* The "statistics" that these particles follow profoundly affects the overall behavior of an assembly of such particles. Notice that particles with half-integer spins, such as individual neutrons, protons, and electrons, are fermions and obey Fermi–Dirac statistics, have antisymmetric wave functions, and as a consequence, obey the Pauli principle. (No two particles can have identical values of the quantum numbers m, ℓ, $m/$, S, and m_S.) Photons, *pairs* of nucleons, or other particles with integer spins, such as the π-meson, are bosons, obey Bose–Einstein statistics, have symmetric wave functions, and do not obey the Pauli principle.
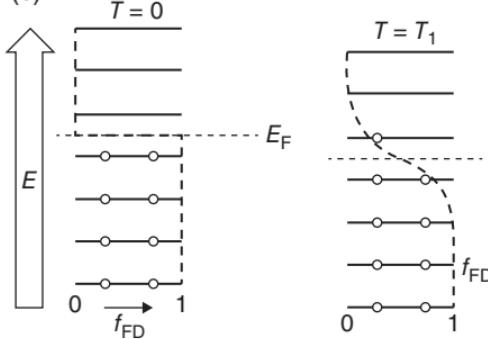
Figure E.11 (a) Schematic representation of the Bose–Einstein distribution function for bosons in a set of uniformly spaced levels at a finite temperature. (b) Similar for the Fermi–Dirac distribution function. (c) The filling of equally-spaced levels by fermions at $T = 0$ and $T = T_1 > 0$ illustrating the Fermi–Dirac distribution. The dashed line indicates the so-called Fermi energy, E_F, in each case.

The fundamental difference between fermions and bosons is primarily reflected in how they occupy quantum mechanical states, especially as a function of temperature. Consider the system shown in Figure E.11. At zero temperature ($T = 0$), the bosons will be able to all occupy the lowest energy state (a Bose–Einstein condensate), while fermions will be distributed among the same set of states with only one particle per quantum state. At high temperatures the distributions will become similar and approach the Maxwell–Boltzmann distribution function.

The Fermi–Dirac distribution is given as a function of the total excitation energy E of the system by the equation

$$f_{F.D}(E) = \left(1 + e^{-(E-E_F)/k_B T}\right)^{-1} \tag{E.72}$$

where $f_{F.D}(E)$ is the number of particles per quantum state, k_B is Boltzmann's constant, and E_F is the Fermi energy (see, e.g., Fig. E.11c). At $T = 0$, all energy levels up to E_F are occupied ($f_{F.D} = 1$) and all energy levels above E_F are empty

($f_{F.D} = 0$). As the temperature T increases, some levels above E_F become occupied (i.e., they have some excitation energy) by particles that were below E_F at lower temperatures.

Bibliography

C. Cohen-Tannoudji, B. Diu, and F. Laloe, *Quantum Mechanics* (John Wiley & Sons, Inc., New York, 1991). An encyclopedic treatment.

R.M. Eisberg, *Fundamentals of Modern Physics* (John Wiley & Sons, Inc., New York, 1964). A comprehensive treatment of modern physics.

K.S. Krane, *Modern Physics* (John Wiley & Sons, Inc., New York, 3rd Edition, 2012). A well written introductory treatment of quantum physics.

E. Merzbacher, *Quantum Mechanics* (John Wiley & Sons, Inc., New York, 3rd Edition 1998). Another treatment with several nuclear physics applications.

M. Scharff, *Elementary Quantum Mechanics* (Wiley-Interscience, London, 1969). A very lucid, elementary treatment of quantum mechanics, emphasizing physical insight rather than formal theory.

L.I. Schiff, *Quantum Mechanics* (McGraw-Hill, New York, 1968). An old classic treatment that contains several applications of interest.

Index

Figure 1.1 Schematic representation of the relative sizes of a lithium atom and its nucleus. The nucleus is too small to be represented in the image of the atom even with the smallest printable dot.

3×10^{-10} m

5×10^{-15} m

Figure 2.10 Nuclear density distribution: (a) in a schematic presentation and (b) in an artist's conception (Mackintosh et al. (2001)). Reproduced with the permission of The Johns Hopkins University Press).

(a)

ρ

ρ_0

$\frac{\rho_0}{2}$

t

R

r

(b)

Figure 2.12 Artistic representation of the relative sizes of the halo nucleus ^{11}Li and ^{208}Pb.

Figure 4.9 Amyvid-PET images are shown for three subjects where red in the highest standard uptake value ratio (SUVr). Top row, normal subject with no β-amyloid plaques, middle row moderate load of β-amyloid plaques associated with early stage Alzheimer's disease, and bottom row high load of β-amyloid plaques associated with late stage Alzheimer's disease (From Butler Hospital).
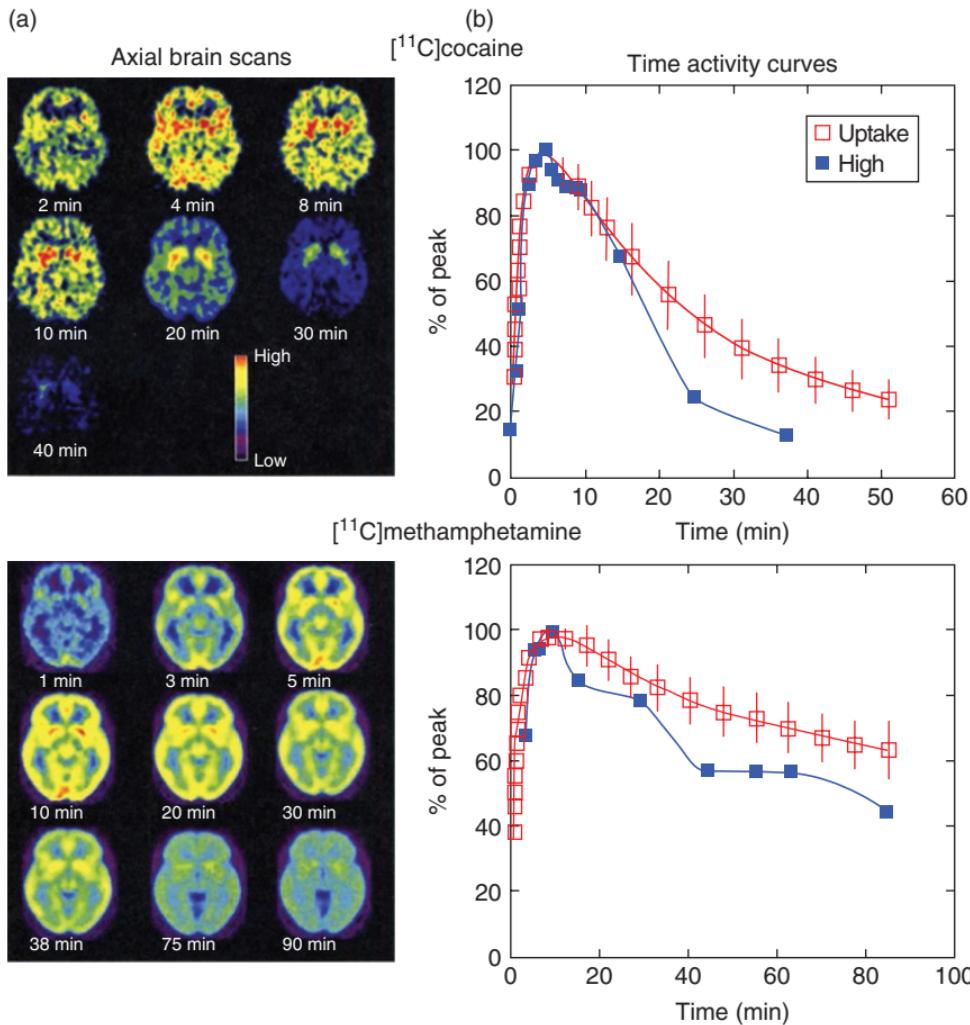
Figure 4.10 Pharmacokinetics of cocaine and methamphetamine in the human brain. (a) Axial brain scans (b) Time activity curves. The fast brain uptake of the drugs corresponds to the user "high". Reproduced with permission from Annu. Rev. Pharmcol. Toxicol. **52**, 321 (2012).
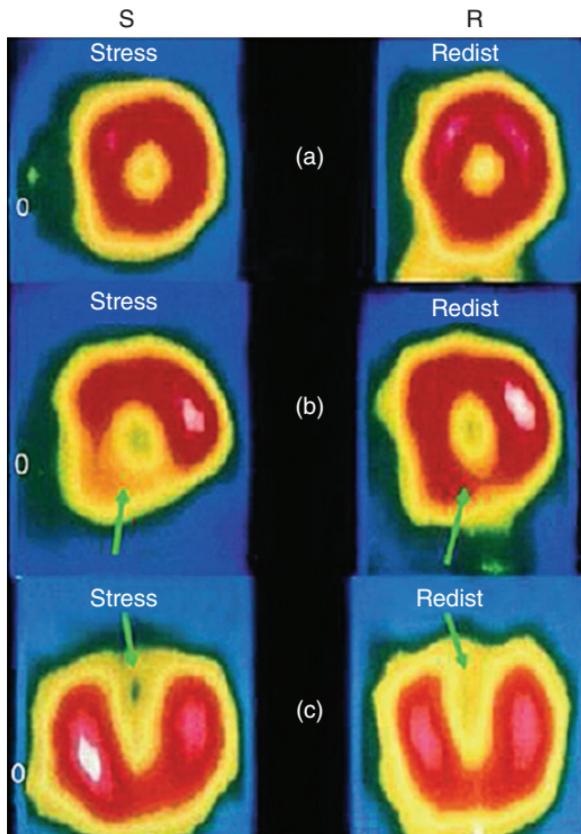
Figure 4.11 Images from ^{201}Tl cardiac imaging (Saha (2010). Reproduced with the permission of Springer).

Figure 9.12 Energy level diagram of two members of the $A = 57$ mass chain. ^{57}Co decays to excited states of ^{57}Fe, which result in the M1 transition from the $3/2^-$ state at 14.41 keV to the $1/2^-$ ground state.
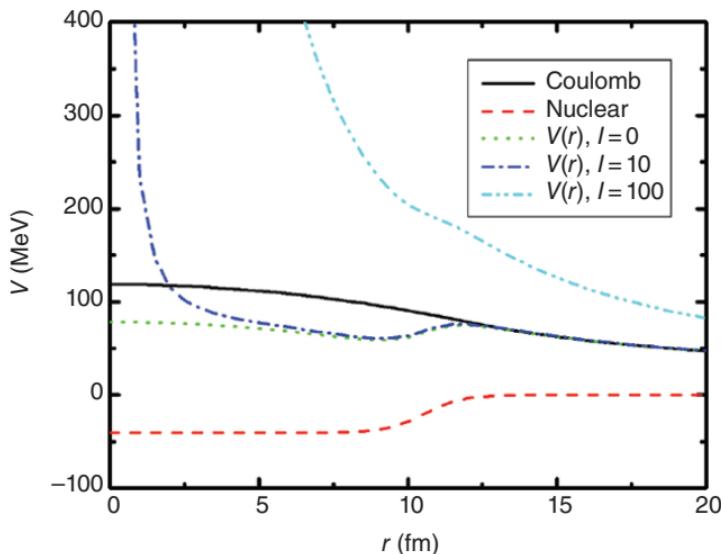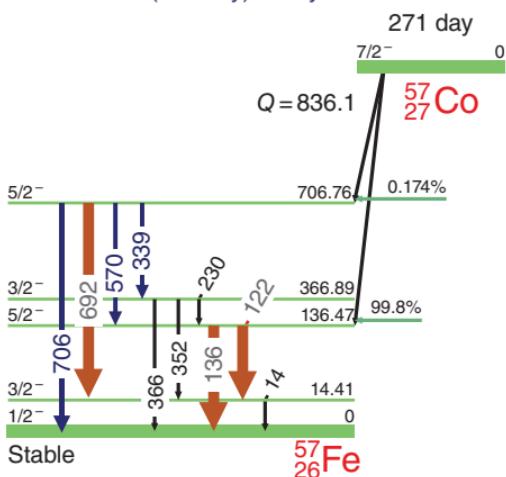

Figure 10.11 The nuclear Coulomb and total potentials for the interaction of ^{16}O with ^{208}Pb for several values of the orbital angular momentum.

Fission isomers
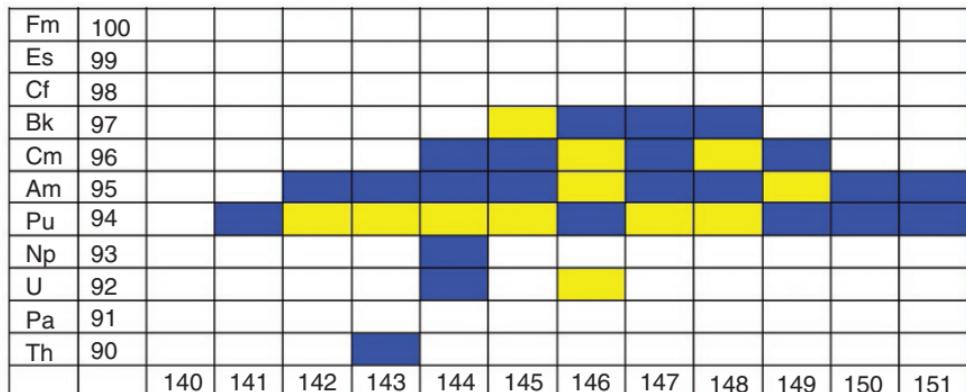
		140	141	142	143	144	145	146	147	148	149	150	151
Fm	100												
Es	99												
Cf	98												
Bk	97						�	▰	▰	▰	▰		
Cm	96				▰	▰	▢	▰	▢	▰			
Am	95			▰	▰	▰	▢	▰	▰	▢	▰	▰	
Pu	94		▰	▢	▢	▢	▢	▰	▢	▢	▰		▰
Np	93				▰								
U	92				▰		▢						
Pa	91												
Th	90				▰								

Figure 11.6 The positions of the known spontaneously fissioning isomers in the high mass end of the chart of nuclides. The dark-colored boxes indicate one isomeric state, while the light-colored boxes indicate two isomeric states (Vandenbosch and Huizenga (1973). Reproduced with the permission of Elsevier).
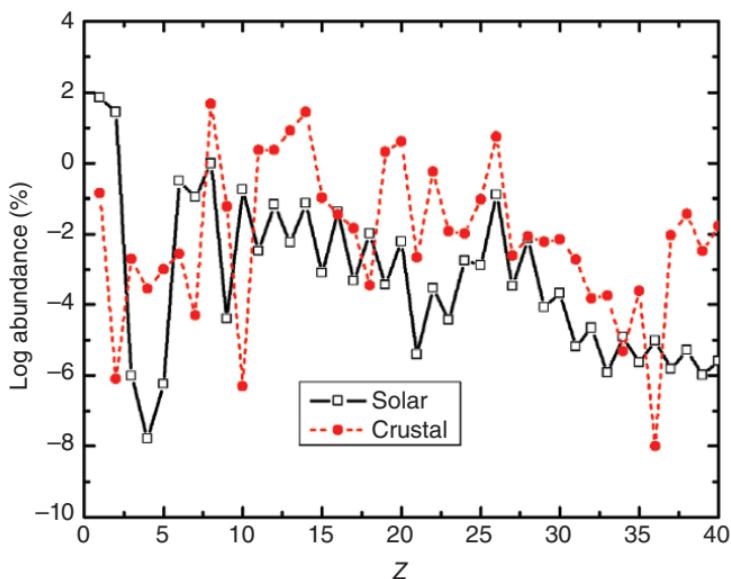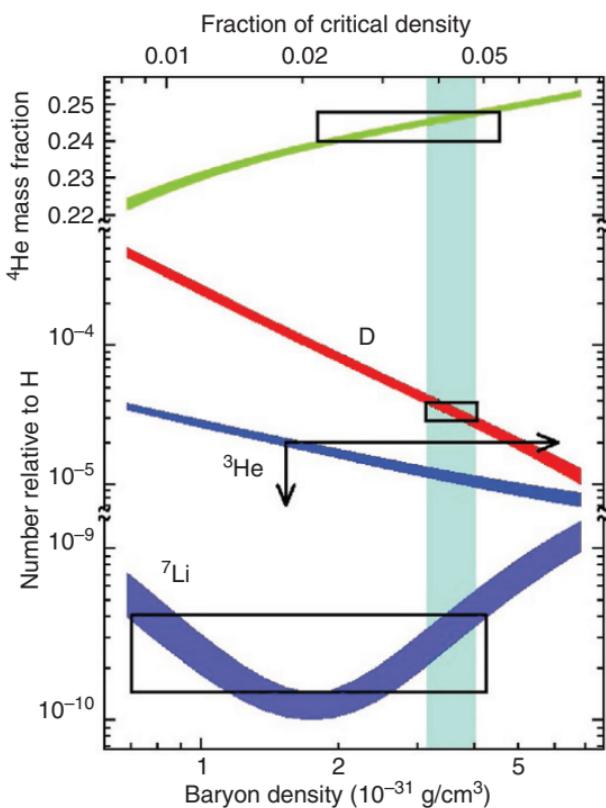
Figure 12.1 The abundances of the first 40 elements as a percentage by mass of the earth's crust (filled circles) and in the solar system (open squares) (Reproduced with the permission of Haynes et al. (1994)).

Figure 12.6 The variation of the relative abundances of the big bang nuclei (bottom) and the ^{4}He mass fraction (top) versus the baryon density. The boxes indicate the measured values and estimates of their uncertainty. The curves indicate the dependence of the yield on the baryon density in the big bang models and the vertical bar indicates the region of overlap.

Figure 12.19 A summary of the comparison between standard solar model predictions and experimental measurements emphasizing the effects of neutrino oscillations in detector systems that are sensitive to only one form of neutrino (Bahcall, Reproduced with the permission of Bahcall website).

Figure 14.2 The half-lives of the known transuranium nuclei plotted as a function of Z and N (Karpov et al. (2012). Reproduced with the permission of World Scientific Publishing Co Pvt Ltd).

Figure 14.3 The dominant decay modes of the nuclei shown in Firgure 14.2 (Karpov et al. (2012). Reproduced with the permission of World Scientific Publishing Co Pvt Ltd).

Theoretical half-lives of transuranium nuclei
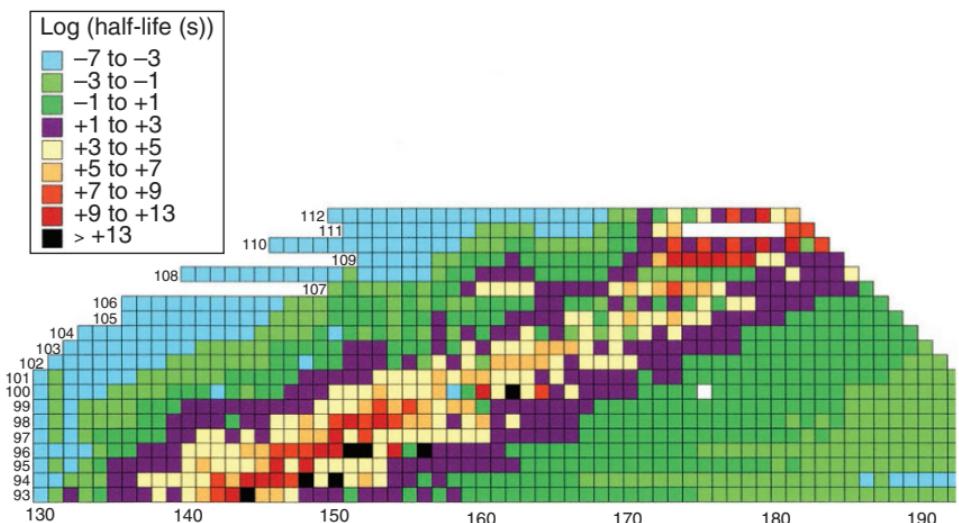
Figure 14.4 The predicted half-lives of the transuranium nuclei with $Z \leq 112$ (Möller (1997). Reproduced with the permission of John Wiley & Sons).
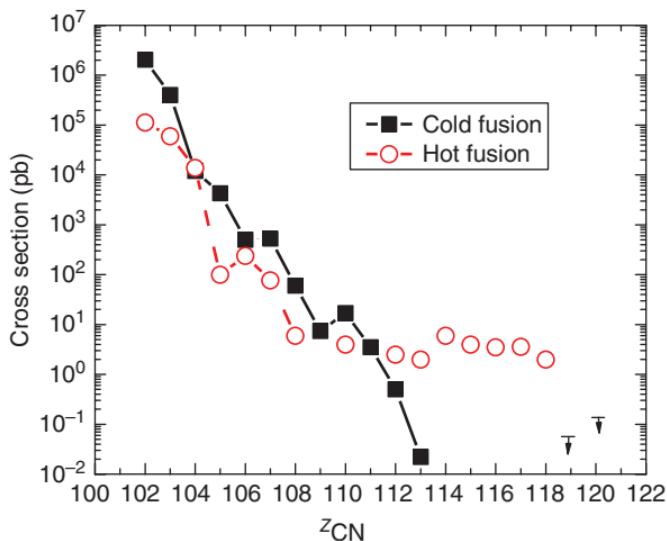
**Figure 14.5** The observed cross sections for the production of heavy elements by the "cold" and "hot" fusion reactions.
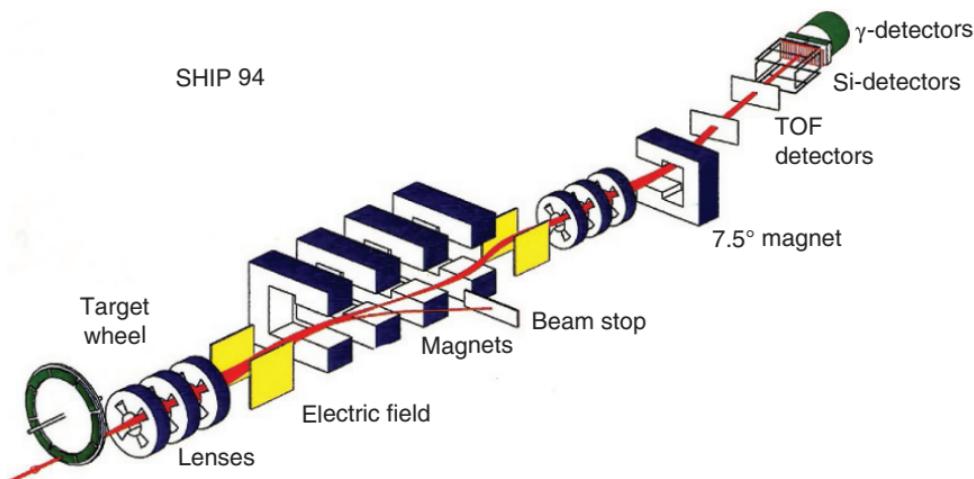
Figure 14.9 A schematic diagram of the SHIP velocity filter separator at the GSI in Germany.
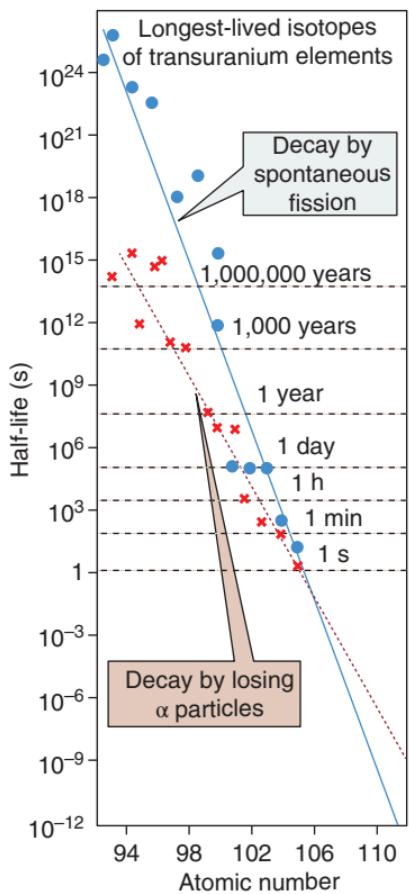
Figure 14.11 Half-lives of the longest-lived isotope of the heaviest elements versus atomic number, *Z*, circa 1970.
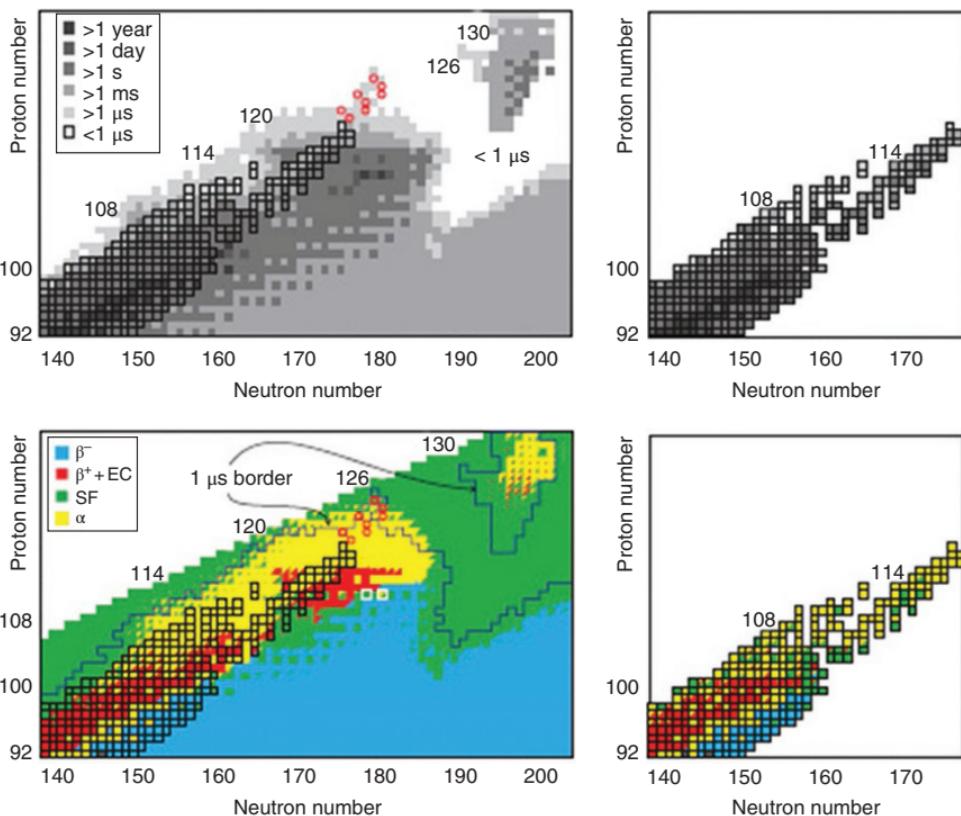
Figure 14.13 Total half-lives (top) and decay modes (bottom) of the transuranium nuclei. The left panels are predictions and the right panels are observations (Karpov et al. (2012). Reproduced with the permission of World Scientific Publishing Co Pvt Ltd).

Figure 15.4 Ammonium diuranate (yellowcake) after solvent extraction (Photo from UIC).


Vitrified waste

Radioactive material is immobilized in a glass matrix and is only released as the glass is dissolved.

Overpack (steel container)

The vitrified HLW is encapsulated in an overpack (steel container) to prevent contact with groundwater during the time when its radioactivity and beat generation are high.

Buffer (compacted day)

The buffer is mainly bentonite clay compacted to high density so as to have low permeability, which slows the movement of dissolved radioactive waste. The buffer is also designed to protect the overpack.

Figure 15.13 Schematic diagram of the final steps in putting vitrified waste into a geologic repository.
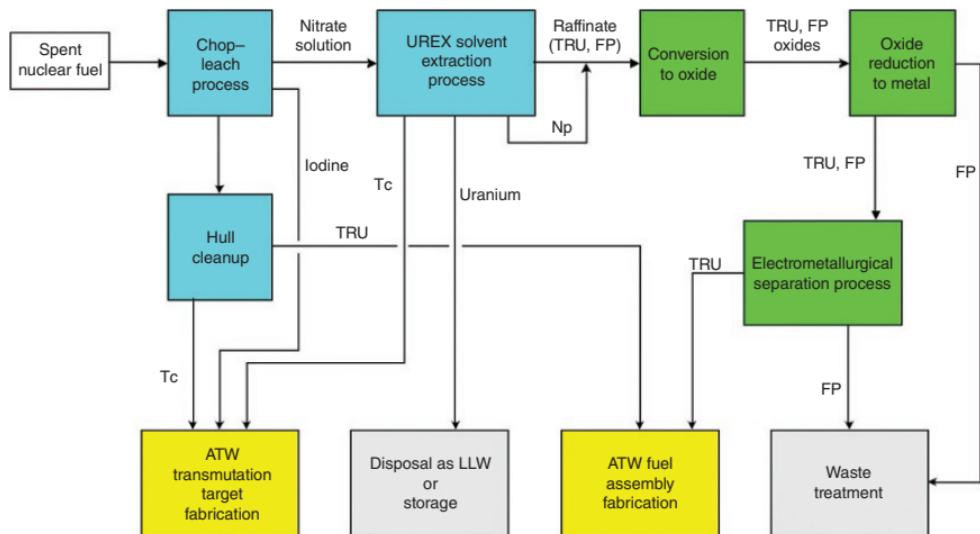
**Figure 15.15** Schematic representation of the new schemes for the processing of SNF.

Figure 17.1 Image of the operating core of a TRIGA reactor illuminated by Cherenkov radiation.